# NANOMATERIALS FOR SOLAR CELL APPLICATIONS

EDITED BY

SABU THOMAS

EL HADJI MAMOUR SAKHO

NANDAKUMAR KALARIKKAL

SAMUEL OLUWATOBI OLUWAFEMI

JIHUAI WU

ELSEVIER

# Nanomaterials for Solar Cell Applications

This page intentionally left blank

# Nanomaterials for Solar Cell Applications

Edited by

**SABU THOMAS**
School of Chemical Sciences,
Mahatma Gandhi University, Kottayam, India;
International and Inter University,
Centre for Nanoscience and Nanotechnology,
Mahatma Gandhi University, Kottayam, India

**EL HADJI MAMOUR SAKHO**
Department of Chemical Sciences
(Formerly Applied Chemistry),
University of Johannesburg

**NANDAKUMAR KALARIKKAL**
International and Inter University,
Centre for Nanoscience and Nanotechnology,
Mahatma Gandhi University, Kottayam, India

**SAMUEL OLUWATOBI OLUWAFEMI**
Department of Chemical Sciences
(Formerly Applied Chemistry),
University of Johannesburg

**JIHUAI WU**
Professor of Materials and Chemistry, Vice-President of Huaqiao University, Director of Engineering Research Center of Environment-Friendly Functional Materials, Ministry of Education, Director of Institute of Materials Physical Chemistry, Huaqiao University, Xiamen, Fujian, P.R. China

ELSEVIER

Elsevier
Radarweg 29, PO Box 211, 1000 AE Amsterdam, Netherlands
The Boulevard, Langford Lane, Kidlington, Oxford OX5 1GB, United Kingdom
50 Hampshire Street, 5th Floor, Cambridge, MA 02139, United States



Notices

Knowledge and best practice in this field are constantly changing. As new research and experience broaden our understanding, changes in research methods, professional practices, or medical treatment may become necessary.

Practitioners and researchers must always rely on their own experience and knowledge in evaluating and using any information, methods, compounds, or experiments described herein. In using such information or methods they should be mindful of their own safety and the safety of others, including parties for whom they have a professional responsibility.

To the fullest extent of the law, neither the Publisher nor the authors, contributors, or editors, assume any liability for any injury and/or damage to persons or property as a matter of products liability, negligence or otherwise, or from any use or operation of any methods, products, instructions, or ideas contained in the material herein.

**British Library Cataloguing-in-Publication Data**
A catalogue record for this book is available from the British Library

**Library of Congress Cataloging-in-Publication Data**
A catalog record for this book is available from the Library of Congress

ISBN: 978-0-12-813337-8



*Publisher:* Matthew Deans
*Acquisition Editor:* Christina Gifford
*Editorial Project Manager:* Ali Afzal - Khan
*Production Project Manager:* R. Vijay Bharath
*Cover Designer:* Matthew Limbert

Typeset by MPS Limited, Chennai, India

# Contents

# List of Contributors

**Antonio Abate**
Helmholtz Center for Materials and Energy, Berlin, Germany

**Y. Akila**
Department of Physics, Coimbatore Institute of Technology, Coimbatore, India

**Alexander V. Akkuratov**
Institute for Problems of Chemical Physics of Russian Academy of Sciences, Chernogolovka, Russian Federation

**Marcie Black**
Advanced Silicon Group, Lincoln, MA, United States

**Daniel Chemisana**
Applied Physics Section of the Environmental Science Department, Polytechnic School, University of Lleida, Lleida, Spain

**Saniat Ahmed Choudhury**
Independent University, Bangladesh (IUB), Dhaka, Bangladesh

**Mustafa Habib Chowdhury**
Independent University, Bangladesh (IUB), Dhaka, Bangladesh

**Wenqi Duan**
Electrical and Computer Engineering Department, University of Iowa, Iowa City, IA, United States

**Fatema Fairooz**
Independent University, Bangladesh (IUB), Dhaka, Bangladesh

**Leandro A. Faustino**
Laboratory of Photochemistry and Materials Science, Institute of Chemistry, Federal University of Uberlandia, Uberlandia, Brazil

**Naoki Fukata**
International Center for Materials Nanoarchitectonics, National Institute for Materials Science, Tsukuba, Japan

**Bingtao Gao**
Electrical and Computer Engineering Department, University of Iowa, Iowa City, IA, United States

**Peng Gao**
CAS Key Laboratory of Design and Assembly of Functional Nanostructures, and Fujian Key Laboratory of Nanomaterials, Fujian Institute of Research on the Structure of Matter, Chinese Academy of Sciences, Fuzhou, P.R. China; Laboratory of Advanced Functional Materials, Xiamen Institute of Rare Earth Materials, Haixi Institute, Chinese Academy of Sciences, Xiamen, P.R. China

**Chang Kook Hong**
Polymer Energy Materials Laboratory, School of Applied Chemical Engineering, Chonnam National University, Gwangju, South Korea

**Rajan Jose**
Nanostructures Renewable Energy Materials Laboratory, Faculty of Industrial Sciences & Technology, Universiti Malaysia Pahang, Gambang, Malaysia

**Hyungjin Kim**
Polymer Energy Materials Laboratory, School of Applied Chemical Engineering, Chonnam National University, Gwangju, South Korea

**P. Senthil Kumar**
Department of Chemical Engineering, SSN College of Engineering, Chennai, India

**Iliya E. Kuznetsov**
Institute for Problems of Chemical Physics of Russian Academy of Sciences, Chernogolovka, Russian Federation

**Chrysovalantou Lamnatou**
Applied Physics Section of the Environmental Science Department, Polytechnic School, University of Lleida, Lleida, Spain

**Junming Li**
Helmholtz Center for Materials and Energy, Berlin, Germany

**Xiaoxiao Lin**
CAS Key Laboratory of Design and Assembly of Functional Nanostructures, and Fujian Key Laboratory of Nanomaterials, Fujian Institute of Research on the Structure of Matter, Chinese Academy of Sciences, Fuzhou, P.R. China; Laboratory of Advanced Functional Materials, Xiamen Institute of Rare Earth Materials, Haixi Institute, Chinese Academy of Sciences, Xiamen, P.R. China

**Sawanta S. Mali**
Polymer Energy Materials Laboratory, School of Applied Chemical Engineering, Chonnam National University, Gwangju, South Korea

**Andressa V. Muller**
Federal University of ABC, Santo André, Brazil

**N. Muthukumarasamy**
Department of Physics, Coimbatore Institute of Technology, Coimbatore, India

**Mu. Naushad**
Department of Chemistry, College of Science, King Saud University, Riyadh, Saudi Arabia

**Barbara N. Nunes**
Laboratory of Photochemistry and Materials Science, Institute of Chemistry, Federal University of Uberlandia, Uberlandia, Brazil

**Takeo Oku**
Department of Materials Science, The University of Shiga Prefecture, Hikone, Japan

**Oluwatobi S. Oluwafemi**
Centre for Nanomaterials Science Research, University of Johannesburg, Johannesburg, South Africa; Department of Chemical Sciences (Formerly Applied Chemistry), University of Johannesburg, Doornfontein Campus, Johannesburg, South Africa

**Gerko Oskam**
Departamento de Física Aplicada, CINVESTAV-IPN, Mérida, México

**Sundararajan Parani**
Department of Chemical Sciences (Formerly Applied Chemistry), University of Johannesburg, Doornfontein Campus, Johannesburg, South Africa; Centre for Nanomaterials Science Research, University of Johannesburg, Johannesburg, South Africa

**Jyoti V. Patil**
Polymer Energy Materials Laboratory, School of Applied Chemical Engineering, Chonnam National University, Gwangju, South Korea; Thin Film Materials Laboratory, Department of Physics, Shivaji University, Kolhapur, India

**Pramod S. Patil**
Thin Film Materials Laboratory, Department of Physics, Shivaji University, Kolhapur, India

**Antonio Otavio T. Patrocinio**
Laboratory of Photochemistry and Materials Science, Institute of Chemistry, Federal University of Uberlandia, Uberlandia, Brazil

**K. Grace Pavithra**
Department of Chemical Engineering, SSN College of Engineering, Chennai, India

**Andre S. Polo**
Federal University of ABC, Santo André, Brazil

**Dena Pourjafari**
Departamento de Física Aplicada, CINVESTAV-IPN, Mérida, México

**Rashid Ahmed Rifat**
Independent University, Bangladesh (IUB), Dhaka, Bangladesh

**A. Riverola**
Applied Physics Section of the Environmental Science Department, Polytechnic School, University of Lleida, Lleida, Spain

**El Hadji Mamour Sakho**
Department of Chemical Sciences (Formerly Applied Chemistry), University of Johannesburg, Doornfontein Campus, Johannesburg, South Africa; Centre for Nanomaterials Science Research, University of Johannesburg, Johannesburg, South Africa

**Subramani Thiyagu**
International Center for Young Scientists (ICYS), National Institute for Materials Science, Tsukuba, Japan; International Center for Materials Nanoarchitectonics, National Institute for Materials Science, Tsukuba, Japan

**Sabu Thomas**
International and Inter University Centre for Nanoscience and Nanotechnology, Mahatma Gandhi University, Kottayam, India

**Fatima Toor**
Electrical and Computer Engineering Department, University of Iowa, Iowa City, IA, United States

**Pavel A. Troshin**
Institute for Problems of Chemical Physics of Russian Academy of Sciences, Chernogolovka, Russian Federation; Skolkovo Institute of Science and Technology, Moscow, Russian Federation

**R. Jose Varghese**
International and Inter University Centre for Nanoscience and Nanotechnology, Mahatma Gandhi University, Kottayam, India; Department of Chemical Sciences (Formerly Applied Chemistry), University of Johannesburg, Doornfontein Campus, Johannesburg, South Africa; Centre for Nanomaterials Science Research, University of Johannesburg, Johannesburg, South Africa

**Dhayalan Velauthapillai**
Department of Chemical Sciences (Formerly Applied Chemistry), University of Johannesburg, Johannesburg, South Africa

**A. Vossier**
CNRS-PROMES, Odeillo, France

**Qamar Wali**
NUTECH School of Applied Sciences and Humanities, National University of Technology, Islamabad, Pakistan

**Qiong Wang**
Helmholtz Center for Materials and Energy, Berlin, Germany

**Jihuai Wu**
Professor of Materials and Chemistry, Vice-President of Huaqiao University, Director of Engineering Research Center of Environment-Friendly Functional Materials, Ministry of Education, Director of Institute of Materials Physical Chemistry, Huaqiao University, Xiamen, Fujian, P.R. China

# Preface

The interests of developing renewable, sustainable, and clean energy sources have become very high because of the emergence of global warming and the vast use of nonrenewable energy sources, such as natural gas, oil, and coal. Several renewable energy sources, such as wave and tidal power, wind turbines, hydropower, solar cells, fuel cells, and solar thermal are being investigated to evaluate their potential to address large-scale demand. Among these sources, solar photovoltaic (PV) technology, which uses solar radiation energy, has been considered as the most abundant, inexhaustible, clean, and sustainable energy resource. Solar cells directly convert the incident solar radiation into electricity via the PV effect and can convert up to about 20% of incoming solar radiation. Solar cells are classified into three generations, which are based on their materials and manufacturing process. Silicon (Si) single crystal wafers and bulk polycrystalline Si wafers are the first generation of solar cells. These cells, according to the manufacturing procedures and wafer quality, give solar conversion efficiencies between 12% and 16% and are largely leading the solar cells market. The thin-film solar cells that are made from different materials, such as amorphous silicon, a-Si, cadmium telluride, cadmium indium selenide, or thin silicon films on indium tin oxide, t-Si, are the second generation of solar cells. This technology provides less expensive solar cells with lower solar energy conversion in comparing to the silicon wafers technology. The third and emerging solar cells generation, which can produce high efficiency devices at low production costs of solar cells, are based on polymer solar cells, dye synthesized solar cells, quantum dots solar cells, and perovskite solar cells.

Recently, nanomaterials have emerged as the new building blocks to construct solar cell assemblies. The use of nanomaterials in solar cell application is gaining tremendous interest and building great expectations in the academic community, industry, and governments. A motivation to develop high efficiency and cost-effective nanostructured materials for solar cells is growing and a specific contribution of nanotechnology to various solar energy is being developed. Nanomaterials provide new methods to approach solar energy conversion with a flexible and promising material platform. Therefore nanostructured materials, such as metal oxide, quantum dots, perovskite, graphene, carbon nanotubes, and

fullerene play a significant role in solar cell applications. Hence, it has been demonstrated that nanostructured materials can improve the performance of solar cells by enhancing both light trapping and photo-carrier collection. Furthermore, the synthesis, characterizations, and utilization of these novel nanostructures lie at the interface among physics, chemistry, engineering, and materials science. The structure, size, and shape of these nanomaterials have significant effect over the efficiency of the solar energy conversion.

Over the last two decades there are numerous research papers on nanostructured materials for solar cell applications. A few research papers are based on metal oxide-based solar cells, quantum dot sensitized solar cells, dye sensitized solar cells, and polymer nanocomposites solar cells. Recently, nano-carbon based materials such as graphene, graphene derivatives, carbon nanotube, and fullerene have been extensively investigated on solar cells. However, up to now, no systematic efforts have been made to come out with a book that exclusively covers the synthesis, characterizations, and properties of nanomaterials for solar cell applications that are very much required for academe and industry.

Thus this book reports on the developments in the synthesis and characterizations of nanomaterials for solar cells. The book starts with a discussion on the fundamentals of nanomaterials for solar cells, including a discussion on the life-cycle assessments and characterization techniques. It then follows with a review of the various types of solar cells: thin film, metal oxide, nanowire, nanorods, and nanoporous materials, and concludes with nanocarbon materials. In addition, it includes a review of quantum dot sensitized, perovskite, and polymer nanocomposites-based solar cells.

PART I

# Fundamental of nanomaterials for solar cells

This page intentionally left blank

# CHAPTER 1

# Fundamentals of solar cells

**A. Riverola[1], A. Vossier[2] and Daniel Chemisana[1]**
[1]Applied Physics Section of the Environmental Science Department, Polytechnic School, University of Lleida, Lleida, Spain
[2]CNRS-PROMES, Odeillo, France

## Contents



## 1.1 Introduction

During the last decades, photovoltaics (PVs) have become one of the most promising renewable energy technologies, with installed capacity of PV panels approaching 100 GW in 2018. High conversion efficiencies at reasonable costs undoubtedly represent a *sine-qua-non* condition to be fulfilled toward promoting an even wider deployment of solar electricity.

*Nanomaterials for Solar Cell Applications*
DOI: https://doi.org/10.1016/B978-0-12-813337-8.00001-1

The development of strategies aiming at an improved PV efficiency has instigated a broad range of research activities in the most recent decades. With this objective, strategies involving nanomaterials, implementation of nanoobjects, or manipulation of light at a nanometer scale, has prompted a considerable amount of research. These different strategies will be carefully reviewed in the next book chapters. In this chapter, we aim to provide several fundamental concepts necessary to better grasp the underlying physical mechanisms governing PV cells (A detailed explanation of these concepts can be found in other textbooks [1,2]).

The PV effect, which was discovered by Edmund Becquerel in 1839, basically implies direct conversion of sunlight into electricity using a PV cell made of a semiconductor material tailored to ensure both a high absorption of sunlight and an efficient extraction of the photogenerated carriers.

## 1.2 The solar resource, solar energy

The spectral distribution of sunlight spans a broad range of wavelengths ranging from the ultraviolet to the near infrared. The relation between the photon energy ($E$) and its wavelength ($\lambda$) is given by:

$$E = \frac{hc}{\lambda} \tag{1.1}$$

where $c$ is the light speed in vacuum (approximately $3.00 \times 10^8$ m s$^{-1}$) and $h$ is the Planck's constant ($6.63 \times 10^{-34}$ J s).

The spectral distribution of sunlight may vary noticeably depending on (1) the position of the sun in the sky (which is function of the characteristic latitude of the site where the PV cell is supposed to operate, the time of the day, and the day in the year) and (2) typical atmospheric parameters values, which are likely to change noticeably depending on the climatic and atmospheric conditions.

Air mass (AM) is the atmospheric variable to which the solar spectrum is normally more sensitive. It is defined as the distance, relative to the shortest (vertical) path length, that sunrays traverse through the atmosphere before impacting on the Earth's surface. AM can simply be defined as:

$$\mathrm{AM} = \frac{1}{\cos\theta} \tag{1.2}$$

where $\theta$ is the so called *solar zenith angle*, that is, the angle between the zenith and the center of the sun's disc.

Nonetheless, a more accurate expression that considers the Earth's curvature is commonly used to predict or define the solar spectrum [3]

$$\mathrm{AM} = \frac{1}{\cos\theta + 0.50572 \cdot (96.07995 - \theta)^{-1.6364}} \tag{1.3}$$

Fig. 1.1 shows two commonly used solar spectra: AM0 (standard extraterrestrial solar spectrum mainly used by the aerospace community) and AM1.5 Global (where the receiving surface is defined as an inclined plane at 37 degrees tilt toward the equator, facing the sun).

The spectral distribution corresponding to AM0 solar spectrum can be approximated, with a good accuracy, to the spectrum of a blackbody at 5758K (The spectral distribution for blackbody radiation being only determined by its temperature, as stated by Planck's law).

The AM1.5 Global spectrum often serves as the terrestrial standard (reference), and is measured on a surface that faces the sun, with a tilt angle of 37 degrees over the horizontal plane, under specified atmospheric conditions [aerosol optical depth (AOD) of 0.084, precipitable water

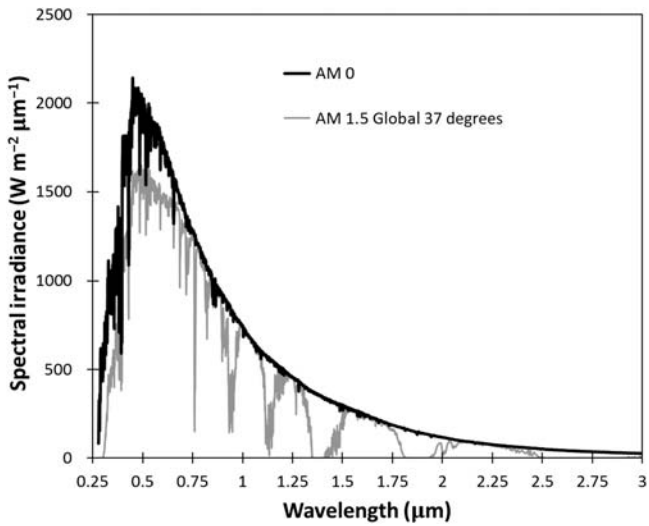


**Figure 1.1** Extraterrestrial solar spectrum (AM0) and the standard terrestrial spectrum (AM1.5 Global). *Retrieved from ASTM, G173-03 Standard tables for reference solar spectral irradiances: direct normal and hemispherical on 37° tilted surface, Book of Standards, 14.04.2004 [4].*

(PW) of 1.42 cm and total column ozone equivalent of 0.34 cm]. An AM of 1.5 corresponds to a solar zenith angle of approximately 48 degrees. Passing through the atmosphere, the spectrum is attenuated differently for each wavelength due to absorption or scattering by atmospheric particles. For instance, water vapor absorption bands are mainly located in the near-infrared and infrared regions of the spectrum (around 0.94, 1.10, and 1.40 μm). The amplitude of light scattering in the atmosphere is correlated to the AM value: the higher the AM, the higher the light scattering by atmospheric molecules (such as nitrogen and oxygen). Consequently, the terrestrial irradiance (which is commonly normalized to 1000 $W\,m^{-2}$) is lower than the extraterrestrial irradiance (around 1353 $W\,m^{-2}$). The peak solar irradiance, which corresponds to wavelengths typically comprised between 0.4 and 0.8 μm, is associated with "visible" light in the sense that human vision evolved to be particularly sensitive to this spectral range. One should distinguish different definitions for solar irradiance: direct normal irradiance (DNI) refers to the photons coming directly from the sun. It should be noted that the definition of DNI is not univocal. This ambiguity stems from the fact that the angular distance from the center of the sun and the penumbra function are not well limited. Several definitions of DNI can be found in the literature, explicitly or implicitly referring to different limit angles and penumbra functions, which inherently lead to varying amounts of integrated radiance in the vicinity of the sun [5]. Global Horizontal Irradiance refers to the total irradiance received from above by a horizontal surface, and includes both the contributions of DNI and diffuse radiation, associated to photons scattered in the atmosphere. The amount of diffuse radiation changes depending on the climate (and especially the cloud cover) and the latitude, and typically represent ~15% of the total radiation. AM1.5D solar spectrum is commonly used as a reference spectrum for the characterization of concentrator solar cells (because of the fundamental inability of these cells to concentrate diffuse light).

The other atmospheric variables that significantly affect the solar spectrum characteristics are AOD and PW. AOD characterizes the radiative strength of aerosols (urban haze, smoke particles, desert dust, sea salt ...) in the vertical direction while PW is the amount of condensed water corresponding to the total water vapor contained in a vertical atmospheric column above any location. Water vapor has strong absorption bands in the near infrared, which directly impacts the spectrum.

## 1.3 Principles of photovoltaic energy conversion

Solar cells should be designed to ensure maximum absorption of photons coming from the sun, and to promote electrons to high-energy states where they are able to move. The material should have at least two energetically separated bands to guarantee an efficient extraction of the charges carried from the PV cell. The bandgap ($E_g$) of PV cell corresponds to the energy gap separating the maximum energy level in the low-energy band [referred as "valence band" (VB)], from the minimum energy level in the high-energy band [known as "conduction band" (CB)], where the electrons should be promoted. The typical time during which the electron is maintained in a high-energy state should be high enough to guarantee an efficient extraction of the excited carriers [a constraint that may be fulfilled if the bandgap is higher than the thermal energy $k_BT$ (where $k_B$ is the Boltzmann's constant and $T$ the temperature)].

Only photons with energy higher than $E_g$ are able to pump electrons from the VB to the CB. The charge separation mechanism, which is required to extract charge carriers from the PV cells, involves the use of a "membrane" to separate the different charge carriers. This is commonly achieved with an electric field originating from the potential difference between contacts.

Semiconductor materials have historically been seen as a very attractive option toward efficiently converting sunlight into electricity using the PV effect. Emerging technologies using organic or/and inorganic substances such as Perovskite or polymer solar cells are currently instigating a great amount of research work, but these technologies will not be addressed in this chapter, since the underlying physical mechanisms are sensibly different (the reader should refer to the following chapters for deeper insights into these technologies).

## 1.4 Semiconductors

Materials can be classified into three main categories, depending on their typical electronic properties: Semiconductors and insulators both show an energy gap between their valence and CBs, whereas metals show an overlap between energy levels in the VB and the CB (and, as a consequence, no energy gap). The development of efficient PV cells requires both an efficient absorption of solar photons, and the establishment of two distinct charge carrier populations, which can only be achieved with semiconductor materials.

In this section, some basic concepts related to semiconductor physics will be introduced. Electrons, holes, and electronic bands will first be explained. The principles of semiconductor doping will then be detailed, before concluding this section, by a description of generation and recombination of electron−holes pairs in semiconductors.

### 1.4.1 Bands, electrons, and holes

In an atom, electrons move in orbitals around the nucleus and can only have certain energy values, called *energy levels*. In a solid material consisting of an immensely high number of atoms, the original orbitals are combined to form orbitals with a large number of energy levels. Because of the huge number of atoms involved, these levels are very close one from another so that they form *energy bands*. The bonds between atoms and their electronic properties determine the bands' energy distribution, as well as the crystalline structure. For instance, silicon atoms share four electrons of the outermost shell (valence shell) with the neighboring atoms, creating stable and strong covalent bonds that result in a diamond lattice type crystalline structure.

The atoms' chemical properties are determined to a great extent by the number of electrons in the valence shell. In a similar manner, the last occupied bands define the electronic properties of crystals. The occupied band with the highest energy, which contains the valence electrons, is called the Valence Band (VB), whereas the unoccupied band with the lowest energy is called the Conduction Band (CB). The energy between both bands is the previously mentioned bandgap energy ($E_g$).

In metals, electrons move without difficulty from one energy level to another, since the valence and the conduction bands overlap in energy ($E_g = 0$), giving rise to a high electrical conductivity. In semiconductors, the valence and conduction bands are separated ($0.5 < E_g < 3$ eV), and the VB is filled with bonded electrons that do not have sufficient energy to overcome the energy gap and freely move in the crystalline network. At a temperature higher than 0K, a fraction of these electrons has sufficiently high thermal energy to be expelled to the CB (this fraction being a function of both the temperature and the energy gap of the semiconductor material). Insulators have very high bandgaps, which practically avoid electrons from the VB to be ejected to the CB because of the high energy required to overcome the bandgap. As a consequence, the absence of free electrons in the CB precludes efficient electrical transport, and these materials are characterized by a low conductivity. Fig. 1.2 shows a scheme of insulators, semiconductors, and conductors.

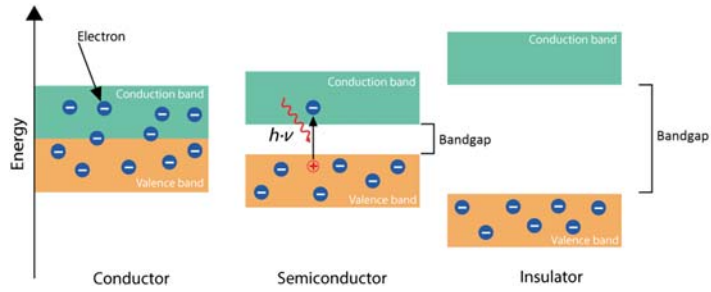


**Figure 1.2** Scheme of conductor, semiconductor, and insulator bandgaps.

Electrons with energy high enough to overcome the electronic gap of the material, because of their thermal energy or after absorption of a solar photon, may break free from the atoms and become a free electron in the CB. The remaining broken bond in the VB is associated with a vacancy referred as a "hole." Semiconductor theory predicts that holes behave as if they were positive charges. In the presence of holes (or vacancies), other valence electrons in the VB can move into these vacancies, thus leading to an apparent movement of "holes" in the opposite direction. Because the concentration of electrons in the VB largely outnumbers the concentration of the remaining vacancies associated with electrons ejected in the CB, it is practically more convenient to describe this mechanism as a "holes" movement.

Semiconductors characterized by identical concentrations of free electrons and holes are called "intrinsic." The concentration of free carriers (often referred to as "intrinsic carrier concentration"), is correlated to both the electronic gap of the semiconductor and the temperature, and translates the ability of charge carriers to move from one band to another under the sole effect of temperature. Therefore, the higher the temperature, the higher number of electrons in the CB and the higher the conductivity (unlike conductor materials that show decreasing conductivity with increasing temperature).

### 1.4.2 Doping, n and p types

As previously explained, the conductivity of semiconductors increases as the temperature rises and the bandgap decreases. For example, the electrical conductivity of Gallium Arsenide (GaAs), which has a bandgap of 1.42 eV, is two orders of magnitude lower than the conductivity of Silicon (1.11 eV).

A mean to control the conductivity of semiconductors, known as *doping*, consists of introducing impurity atoms in the crystalline network, characterized by different electronic structure (and, in particular, a different number of valence electrons). One can distinguish two different kinds of impurity atoms:

- Donor: They possess one extra valence electron that is shared with the lattice, as a free electron. In a silicon structure, consisting of four valence electrons, phosphorous atoms are typical *donor* impurities. These atoms, which comprise five valence electrons, share four of them with their neighboring Si atoms under the form of covalent bonds, the remaining one being free to move in the crystalline network. The phosphorous atoms become ionized (positively charged) and both the electron density and the electrical conductivity are increased, relative to intrinsic silicon.
- Acceptor: Unlike *donors*, *acceptor* atoms comprise fewer valence electrons than the bulk atoms, and their introduction in the network gives rise to the generation of extra *holes*: The impurity atoms become negatively ionized by taking a valence electron from another bond and then releasing a *hole* to the band, thus leading to increased *hole* concentration as well as higher conductivity. Boron atoms are typical acceptor atoms in silicon lattices.

*Doping* is thus the process by which both the conductivity and the concentration of one kind of charge carriers (either electrons or holes) are increased, through the introduction of impurity atoms showing different electronic properties than the bulk atoms. Doping allows increasing the conductivity without any external energy input (light, heat …), and

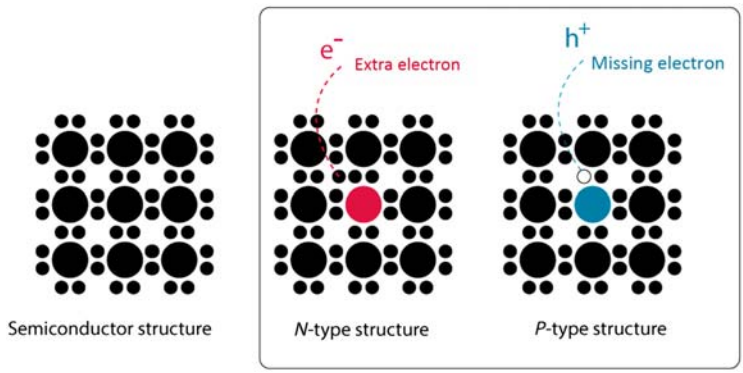


**Figure 1.3** Structures of an intrinsic, *n-type* and *p-type* semiconductors.

semiconductors with electronic properties controlled using this means are known as *extrinsic* semiconductors.

The type of doping is governed by the nature of the impurity atoms introduced in the network: if the *donor* impurity concentration exceeds the intrinsic carrier concentration, the doping is *n-type*. Conversely, if the *acceptor* impurity concentration exceeds the intrinsic carrier concentration, the semiconductor becomes *p-type*. Fig. 1.3 schematically illustrates intrinsic and extrinsic semiconductors.

## 1.4.3 Generation and recombination of electron–holes pairs

The process by which electrons are excited from the VB to the CB, creating an electron–hole pair, is called *generation*. The inverse process is called *recombination* and involves the relaxation of free electrons from the CB to a vacancy (hole) in the VB, thus leading to the annihilation of an electron–hole pair. Under thermal equilibrium, *Generation* and *Recombination* occurs at the same rate within the cell to maintain the populations of electrons and holes.

If the *generation* process requires an input energy provided by photons, phonons (vibrational energy of the lattice), or kinetic energy of other particles, *recombination* is a relaxation process in which energy is released through the same mechanisms.

### *1.4.3.1 Absorption*

Photogeneration is the process leading to the creation of an e–h pair in the cell after photon absorption. Only photons with energies higher than the bandgap may give rise to the generation of e–h pairs. Photons with energy lower than the bandgap cannot participate to the photogeneration process. In addition, photons with energy exceeding the bandgap are only partially used: the difference between the incident photon energy and the electronic gap of the cell is wasted as heat. The process by which excited electrons quickly release their excess energy until they reach the edge of the CB is known as *thermalization* (see Fig. 1.4). This cooling process is very fast (typically occurring at a picosecond timescale) and fundamentally explains, together with the transparency of PV cells to low-energy photons, the wide discrepancy between the high efficiency with which it is theoretically possible to convert sunlight into electricity ($\sim$90%) and the best PV efficiency experimentally achievable (which does not exceed 29% for single-junction solar cells). Photogeneration is characterized by the *absorption coefficient* ($\alpha$) that quantifies the semiconductor absorption as

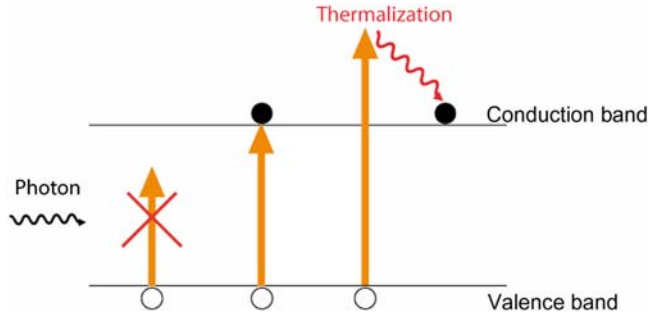


**Figure 1.4** Sketch of the photogeneration process, depicting (left) transparency loss mechanism, (center) photogeneration, (right) thermalization loss.

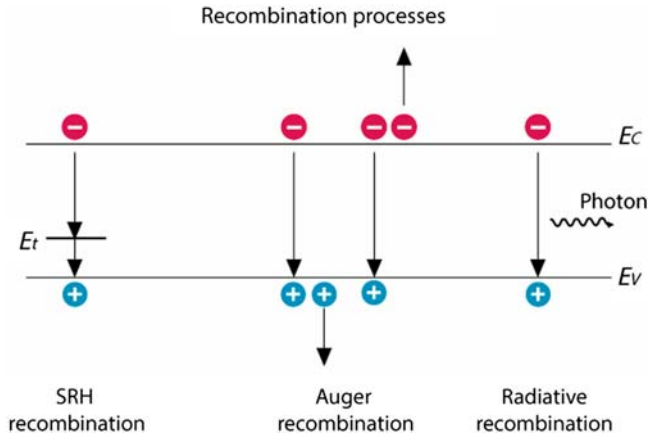


**Figure 1.5** Scheme of the main recombination processes [Shockley–Read–Hall (SRH), Auger, and Radiative].

a function of wavelength, and which translates the ability for a photon of a given wavelength to be efficiently absorbed in the PV cell. The absorption process is easier in direct bandgap semiconductors due to their band structures, leading to very high absorption coefficient and, as a consequence, reduced thicknesses (the material thickness required to ensure complete absorption of the incident light being much smaller than in the case of indirect bandgap semiconductors, such as silicon).

There are three main recombination processes (Fig. 1.5), whose amplitude largely depend on the nature and the quality of the semiconductor materials involved, as well as on the typical density of charge carriers in the cell: (1) *band-to-band* recombination refers to the annihilation of an e–h pair followed by the emission of a photon of corresponding energy. These *unavoidable* recombination (in the sense that, unlike other recombination

mechanisms, they must occur in any PV cell) are particularly effective in direct bandgap materials, such as GaAs. (2) *Shockley–Read–Hall* (SRH) recombination involves impurities or defects in the crystalline structure, giving rise to unwanted energy levels acting like traps in the forbidden gap: annihilation of an e–h pair may occur if both a free electron in the CB, and a hole in the VB, simultaneously fall into an impurity trap.

SRH recombination is often strong in many semiconductor materials, and a particular care should be brought toward minimizing the defect density in the PV cell through appropriate fabrication and doping conditions.

Trap states are also likely to appear at the surface of the cell because of material discontinuities. These recombination mechanisms, known as surface recombination, may be minimized with high-quality surface passivation.

(3) *Auger* recombination refers to a three-particle mechanism where the energy of an electron in the CB (or, alternatively, the energy of a hole in the VB) is transferred to another electron (or hole). The excess energy is rapidly dissipated as heat in the crystalline network.

*Carrier lifetime ($\tau$)* is a measure of the mean lifetime of a free charge carrier before recombination occurs. This parameter, which should be kept long enough to ensure an efficient carrier extraction from the PV cell, is largely dependent on the semiconductor and the doping.

The *diffusion length (L)* expresses the mean distance that a free carrier can travel in the cell before a recombination event occurs. The diffusion length, which should be high enough to guarantee that the carriers travel the distance separating them from the p–n junction, is related to the lifetime and the diffusivity ($D$) by the following equation:

$$L = \sqrt{D\tau} \tag{1.4}$$

The diffusivity determines how carriers repeal each other, whereas the mobility ($\mu$) allows calculating the carriers' velocity under an electric field. These quantities are related by Einstein equation:

$$D = \frac{k_B T}{e}\mu \tag{1.5}$$

## 1.5 Solar cell structure, operation, and main parameters

### 1.5.1 p–n Junction

Efficient photogeneration of free charge carriers is a fundamental requirement in PV cells. However, separate collection of holes on one electrode,

and electrons on the other, requires an additional mechanism to effectively extract these two types of carriers. This charge separation is usually achieved using a p–n junction: the electric field appearing at the interface between the *p-side* and the *n-side* of the solar cell acts as a membrane, repelling the different charge carriers in different regions of the cell where they can be separately extracted (Fig. 1.6).

The p–n junction is realized by bringing together an n-type and a p-type semiconductor layer.

On the n-side, electrons move by diffusion toward the p-side (where their concentration is orders of magnitude lower), leaving positively charged ions behind them. Similarly, holes on the p-side tend to diffuse to the n-side (where their concentration is significantly lower), thus creating negatively charged ions. The presence of negatively and positively charged ions in close contact gives rise to an electric field at the interface between the two regions, repelling electrons in the n-side and holes in the p-side. The region where the electric field arises is commonly referred as *depletion region* (*D*) since it is depleted of carriers. Consequently, two competing mechanisms constitute the driving forces for the movement of charge carriers in the cell: *diffusion*, caused by the gradient in carrier concentration, represents the main driving force in the p and n neutral regions, whereas *drift*, caused by the interaction between the electric field and the electrical charges hold by electrons and holes, principally controls the movement of charge carriers in the depletion region.

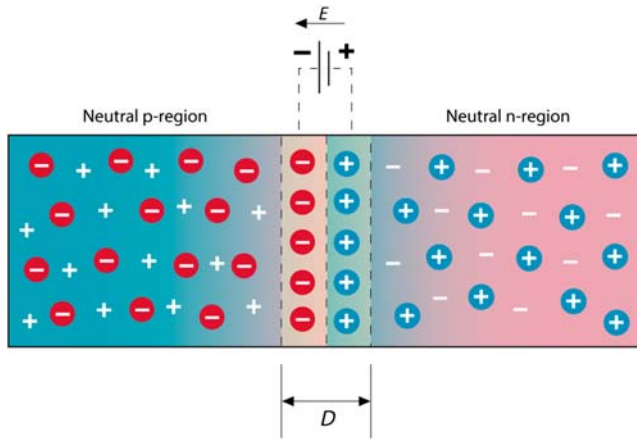


**Figure 1.6** Scheme of the p–n junction showing the depletion region (*D*), the neutral regions, and the electric field originated (*E*).

### 1.5.2 Structure, operation, and main parameters of solar cells

In practice, solar cells are a two-terminal device that can provide electrons to an external circuit while illuminated with sufficiently high-energy photons. Metal front and back contacts are used to extract carriers. Since the presence of a metal grid on top of the cell may avoid a significant fraction of the incident light to be absorbed, the front contact should be designed to minimize shading on the cell. However, because the metal grid geometry is also constrained by series resistance losses, the optimal grid geometry stems from a compromise between shading and series resistance.

The front surface is commonly textured to both increase the light absorption and lower the reflectivity. In addition, antireflection coatings with adequate refractive indexes are deposited atop of the texture to reduce Fresnel losses.

Fig. 1.7 summarizes the operation of a PV cell: (1) light is absorbed in the cell and creates e−h pairs (2) charge carriers move under the combined effect of *diffusion* (in the neutral regions) and *drift* (in the depletion region) (3) the p−n junction at the interface between the n- and p-side behaves as a membrane, repelling electrons in the n-side and holes in the p-side (4) electrons and holes are separately collected and injected in the external circuit.

Applying a voltage between the electrical contacts of the cell will affect the cell operation: when no voltage is applied (or, alternatively, when the cell is short-circuited), the cell is said to operate in *short-circuit*, and the corresponding current, which is called *short-circuit* current ($I_{SC}$),

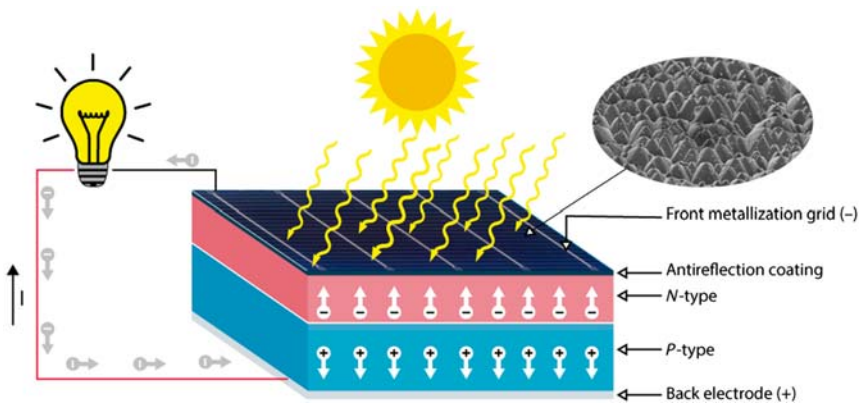


**Figure 1.7** Sketch of a photovoltaic (PV) cell.

represents the maximum electrical current one can extract from a PV cell. Applying a voltage bias on the PV cell leads to larger *diffusion* current associated with the flow of electrons from the n-side to the p-side, and holes from the p-side to the n-side. This current, which flows in opposite direction to the photogenerated current, grows exponentially with the applied voltage, and lowers the total current one can extract from the PV cell. For a sufficiently high value of the applied voltage, the diffusion current equals the photogenerated current, and the total current extractable from the cell is thus equal to zero. The corresponding voltage value is known as *open-circuit* voltage ($V_{OC}$), and corresponds to the maximum voltage that can be extracted from a PV cell.

The short-circuit current depends on the spectral distribution of the incident sunlight: Achieving high $I_{SC}$ necessarily requires an important fraction of the incoming photons to possess an energy exceeding the electronic gap of the cell. In addition, each photon with sufficiently high energy should ideally be converted into an electron−hole pair. The ability of any particular cell to fulfill this requirement is usually characterized by *quantum efficiency* (QE) measurements, which indicate the probability that a given photon of a certain wavelength ($\lambda$) will provide an electron to the external circuit.

Fig. 1.8 shows the QE of a crystalline silicon solar cell. QE curves provide key information for solar cell manufacturers, such as the ability of the cell to efficiently collect charge carriers, the amplitude of front surface recombination, or reflection losses.

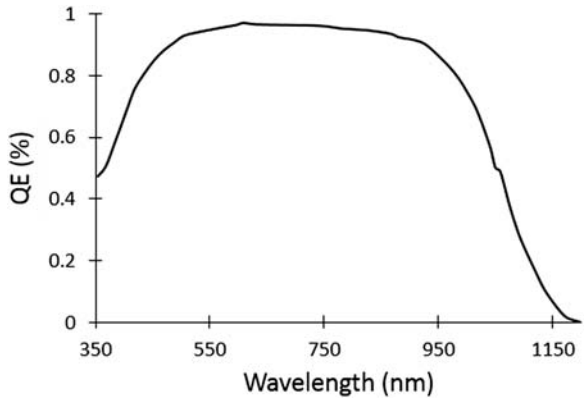


**Figure 1.8** Quantum efficiency (QE) of a crystalline silicon solar cell.

Considering that the spectral incident photon flux density $F(\lambda)$ is known, the short-circuit current can be obtained using the following equation:

$$I_{SC} = eA \int F(\lambda) \mathrm{QE}(\lambda) \frac{\lambda}{hc} d\lambda \tag{1.6}$$

where $e$ is the electron charge and $A$ is the solar cell area.

The spectral response (SR) of a solar cell is analogous to the QE but expressed in amperes-per-watt of incident light. Both are related by the following equation:

$$\mathrm{SR}(\lambda) = e \frac{\lambda}{hc} QE(\lambda) \tag{1.7}$$

#### 1.5.2.1 Dark current due to voltage

Applying a potential difference between the electrical contacts gives rise to a reverse current flowing in opposite direction to the photogenerated current, which is called *dark current*. This current, which is associated with the flow of majority carriers (electrons from the n-side to the p-side, holes from the p-side to the n-side), grows exponentially with the voltage, thus reducing noticeably the current extractable from the cell at high voltage values. The dark current ($I_D$) can be expressed as a function of the potential difference ($V$) by the following equation:

$$I_D(V) = I_o\left(e^{eV/mTk_B} - 1\right) \tag{1.8}$$

where $I_o$ is the diode reverse saturation current (associated to the movement of minority charge carriers in reverse bias), $m$ the diode ideality factor, and $T$ the temperature in Kelvin. The diode reverse saturation current depends largely on the temperature, as well as on the material quality. The ideality factor typically ranges from 1 to 2.

#### 1.5.2.2 Superposition and IV curve

Solar cells follow the superposition principle, which means that the current–voltage curve of a PV cell under illumination simply corresponds to the sum of the dark $IV$ curve and the photogenerated current. The equation governing PV cell operation can thus be written:

$$I(V) = I_{SC} - I_D(V) = I_{SC} - I_o\left(e^{eV/mTk_B} - 1\right) \tag{1.9}$$

Note that, for simplicity, the sign of the photogenerated current is commonly considered as positive in the sign convention. The *IV* curve of the cell is thus deduced by subtracting the dark current from the photogenerated current.

Fig. 1.9 shows the *IV* (current−voltage) curve of a solar cell that follows Eq. (1.9). The photogenerated current shifts the *IV* curve up, enhancing the available power to be extracted. Under low-voltage values, the output current remains close to the short-circuit value. However, as the voltage increases, the dark current grows exponentially and the output current decreases.

The open-circuit voltage, which corresponds to the point of the *IV* curve where the dark current and the photogenerated current compensate each other, leading to an output current equal to zero, can simply be derived from Eq. (1.9):

$$V_{OC} = \frac{mk_B T}{e} \ln\left(\frac{I_{SC}}{I_0} + 1\right) \tag{1.10}$$

Achieving high $V_{OC}$ requires the short-circuit current to be as high as possible, and the dark saturation current to be as low as possible. Mechanisms giving rise to increased dark saturation currents (such as high operating temperature or high recombination rates) may thus significantly lower the open-circuit voltage.

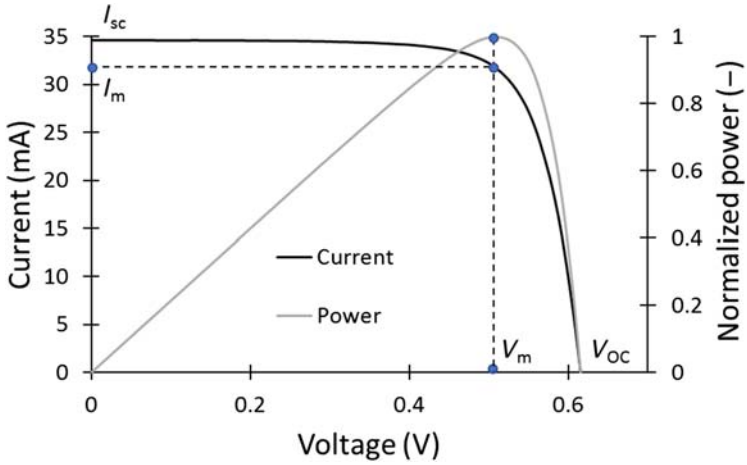


**Figure 1.9** *IV* Curve of a photovoltaic (PV) cell, showing the main solar cell parameters.

Solar cells can be electrically modeled by a current generator in parallel with a diode. The generator produces a photogenerated current with an intensity function of the illumination level to which the cell is submitted, while the diode accounts for the dark current. In real solar cells, a precise description of the electrical behavior requires power dissipation through series resistance losses to be taken into account. These are electrically modeled by a resistance in series $R_s$ (originating from bulk, emitter, front contact, and metal grid) and by a resistance in parallel $R_{sh}$ (associated with the presence of electrical paths allowing current leakage in the cell) as depicted in Fig. 1.10.

The $IV$ curve of a more realistic solar cell, including both series and shunt resistance, can be written:

$$I = I_{SC} - I_o\left(e^{(eV+IR_s)/mTk_B} - 1\right) - \frac{V + R_sI}{R_{sh}} \tag{1.11}$$

The temperature dependence of PV cells mainly stems from two different mechanisms (as shown in Fig. 1.11): (1) the decrease in the semiconductor bandgap with increasing temperature, which leads to slightly higher photogenerated current values (the fraction of the incident photons likely to create electron–holes pairs being larger); (2) the increase in the intrinsic carrier concentration with increasing temperature, giving rise to higher dark current and, in turn, lower open-circuit voltage [see Eq. (1.10)]. The negative effect of temperature on the open-circuit voltage being more significant than the positive effect on short-circuit current, there is an overall detrimental effect of temperature on the cell efficiency (with a temperature coefficient typically comprised between −0.28% and 0.52%/°C for Si) [6].

The electrical power delivered by a solar cell is simply calculated as the product of the current and the voltage output.

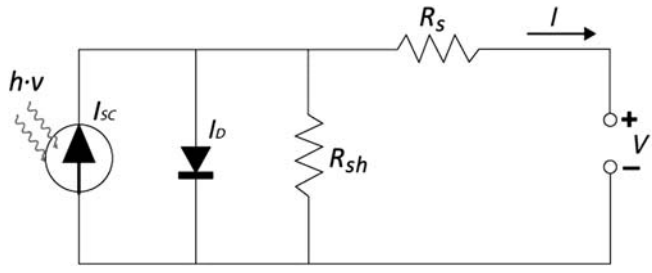


**Figure 1.10** Equivalent circuit of a solar cell.

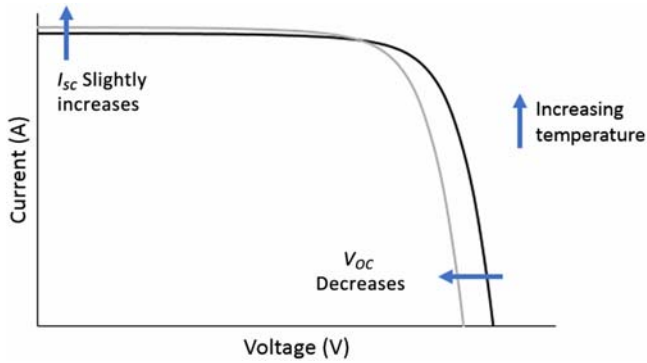


**Figure 1.11** Effects of temperature on the *IV* curve of a PV cell.

The electrical power output, depicted in Fig. 1.9 together with the corresponding *IV* curve, shows a peak value denoted $P_m$, characterized by a voltage value $V_m$ and a current value $I_m$. Achieving the highest solar to electricity conversion efficiency thus requires applying a load equal to $V_m/I_m$.

The fill factor is defined as:

$$\mathrm{FF} = \frac{I_m V_m}{I_{SC} V_{OC}} \tag{1.12}$$

Finally, the most important parameter to characterize the cell ability to convert sunlight into electricity efficiently is the conversion efficiency, which can simply be written:

$$\eta = \frac{I_{SC} V_{OC} \mathrm{FF}}{A P_S} \tag{1.13}$$

where $P_S$ is the incident power per unit area.

## 1.6 Upper limit for solar energy conversion

The high temperature of the sun (5700K) has two important consequences on the ability of solar energy to be used efficiently as a source of electrical power. First, the radiated power density reaches a value of around 1000 W $m^{-2}$ at ground level ($\sim$1300 W $m^{-2}$ outside the atmosphere), a value that is sufficiently high to consider sunlight as a good candidate for providing electricity to the world; and, second, the upper bound for sunlight-to-electricity conversion efficiency is higher than 90% in the Carnot limit, the upper limit value for conversion of solar energy into entropy-free energy (also known as Landsberg limit [7]) being $\sim$85%.

In fact, the practical efficiencies of the best solar cells fall well below these values, with maximum efficiencies typically being in the range 10%–30% (~13% for organic PV cells, ~23% for perovskite cells, 26.7% for crystalline Silicon solar cells, and 28.8% for GaAs solar cells, the most efficient PV cell among all the single-junction solar cell technologies) [8].

A fundamental reason explaining the wide discrepancy among the theoretical limits for solar energy to electricity conversion and the best practical efficiencies obtained to date stems from the inadequacy between the broad solar spectrum, covering a range of wavelengths comprised between ~350 and 2500 nm, and the absorption properties of the semiconductor materials used, which only allows a narrow range of solar photons to be converted efficiently.

The main losses mechanisms in a PV cell as a function of the electronic bandgap have been studied in details [9], showing the extent to which "practical" PV cells may approach the theoretical limit for sunlight into electricity conversion. The three main fundamental loss mechanisms (Boltzmann losses, thermalization losses, and below-$E_g$ losses), typically representing between 60% and 90% of the solar radiation impinging the cell, are responsible for restricting the maximum electrical power one can extract from a PV cell to no more than ~33% of the incident power.

Boltzmann losses basically stem from the angular asymmetry between the incoming solar radiation, providing from a reduced region of the sky (the solar disk representing ~1/46,000th of the full hemisphere) and the radiation emitted by the PV cell as a result of band-to-band recombination, which covers the entire hemisphere.

Below-$E_g$ losses (also known as transparency losses) are associated with long-wavelength photons with energy not sufficient to create an e–h pair in the cell. These losses being related to the fraction of the solar spectrum not absorbed by the PV cell, the use of low bandgap semiconductors materials allows to mitigate drastically their amplitude.

As it was previously explained, thermalization losses refer to the imperfect conversion of photons where the energy exceeds the electronic gap of the semiconductor material. Photons with sufficient energy for being absorbed in the PV cell quickly dissipate their excess kinetic energy (i.e., the difference between the photon energy and the electronic gap) through interactions with phonons in the semiconductor lattice. The amplitude of these losses being proportional to the difference between the

photon energy and the electronic gap, the use of high bandgap materials allows lessening their effect.

The optimum electronic gap values for which the PV efficiency peaks is shown to be comprised between ~1.1 and 1.4 eV. PV cells involving low bandgap materials are inherently limited in their ability to convert sunlight into electricity by thermalization losses, while high bandgap materials are too inefficient in their capacity to absorb the broad solar spectrum to ensure high PV conversion efficiency.

The development of strategies aiming to overcome the main fundamental mechanisms preventing solar cells to achieve ultra-high conversion efficiencies has instigated a significant amount of research efforts over the recent decades. One should differentiate two distinct paths, targeting different fundamental losses mechanisms. Strategies aiming at reduced Boltzmann losses, through manipulation of the angular properties of the incoming solar radiation or the radiation emitted by the cell as a result of band-to-band recombination and strategies aiming at reduced thermalization and/or below-$E_g$ losses. These tactics basically imply solar cells with modified architecture to better convert the broad solar spectrum. It is worth stressing that these two strategies may be combined to further improve the solar to electricity conversion efficiency.

## 1.7 Reducing Boltzmann losses: optical concentration and angular restriction

The maximum open-circuit voltage attainable in a PV cell can be written as:

$$qV_{OC} = \left(1 - \frac{T_0}{T_S}\right)E_g + k_B T_0 \ln\left(\frac{T_S}{T_0}\right) - k_B T_0 \ln\left(\frac{\varepsilon_{\text{out}}}{\varepsilon_{\text{in}}}\right) \tag{1.14}$$

where $T_0$ and $T_S$ are the ambient and the sun temperature. $\varepsilon_{\text{out}}$ and $\varepsilon_{\text{in}}$ denote the étendue of the emitted (resulting from band-to-band recombination in the cell) and absorbed beams [10], where

$$\varepsilon = \iint_{(A,\omega)} \cos\theta \, dA d\omega \tag{1.15}$$

where $dA$ is an element of the cross sectional area of the beam, $d\omega$ is an element of the solid angle, and $\theta$ is the angle between the normal to $dA$ and the direction of the beam [11]. In the case of a light cone incident on

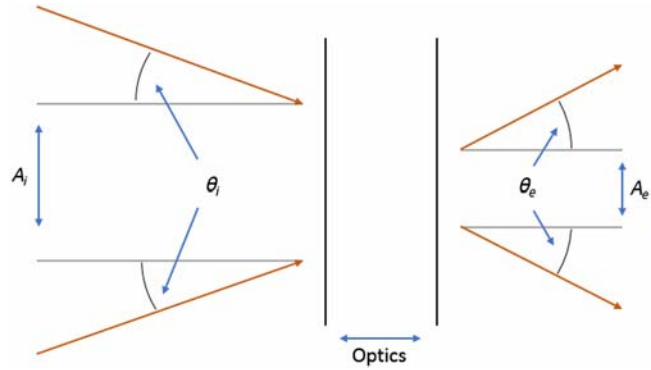


**Figure 1.12** Illustration of the étendue conservation principle.

a planar surface with an area $A$, and characterized by a half-angle $\theta$, the étendue can simply be written [12]:

$$\varepsilon = A \sin^2\theta \tag{1.16}$$

A fundamental limitation causing solar cells to avoid achieving very high conversion efficiency arises from the discrepancy in the étendue of the absorbed and emitted beam: because of the limited size of the solar disk, the optical étendue of the absorbed beam is significantly smaller than the étendue of the emitted beam, which covers the full hemisphere. This asymmetry in the angular properties of the beams gives rise to optical entropy [last term in the left-hand side of Eq. (1.14)], thus lowering the maximum open-circuit voltage attainable (Fig. 1.12).

### 1.7.1 Optical concentration

Attaining higher PV electrical output can be achieved by increasing the solid angle subtended by the sun, using an appropriate optical concentrator. The maximum concentration factor attainable with any kind of optical concentrator can be derived from the conservation of optical étendue. In the case of a beam passing through an area $\delta A$ and characterized by a solid angle $\delta\omega$, the element of étendue $\delta\omega$ can be written:

$$\delta\varepsilon = n^2 \cos\theta \delta\omega \delta A \tag{1.17}$$

where $n$ is the refractive index of the media where the light propagates, and $\theta$ is angle between the direction of propagation and the normal to $\delta A$.

The conservation of optical étendue implies that the maximum sunlight concentration attainable equals

$$C_{\max} = n^2 \frac{\sin^2\theta_e}{\sin^2\theta_s} \tag{1.18}$$

where $\theta_e$ is the exit angle of the concentrator, and $\theta_s$ refers to the apparent size of the sun, which includes the intrinsic size of the sun, the optical errors associated with tracking and the imperfect optical quality of the concentrator.

Assuming an apparent size of the sun of 47 mrad (i.e., no optical losses), the maximum concentration achievable using a 2D concentrator is 46,200 suns. It should be stressed that using a high-index media concentrator optic can provide a significant boost in the maximum concentration attainable, assuming a good optical match (i.e., similar refractive index) between the concentrator and the absorber.

#### *1.7.1.1 Practical concentrators*

Optical concentrators for thermal or PV applications cover a wide range of concentration factors and optical powers, including static concentrators for low illuminations (typically 1−3 suns); 1D concentrator systems, such as parabolic troughs for medium concentration (5−30 suns) (Fig. 1.13); and 2D concentrators (such as parabolic dishes of Fresnel lenses) able to

**Figure 1.13** Example of Fresnel-transmission optical concentrator used in concentrating photovoltaics systems.

achieve illumination levels exceeding 1000 suns. The nature of the optical concentrator involved in any particular PV system is constrained by the type of PV cell used: conventional single-junction solar cells are mainly used together with low or medium optical concentrator systems, while highly efficient MJ cells are commonly associated with high-concentration parabolic dishes or Fresnel lenses.

## 1.7.2 Angular restriction

Bridging the gap in the angular extent between absorbed and emitted photon beams can be achieved by narrowing the angular range of the emitted photons, rather than increasing the angular extent of the incident photons through sunlight concentration.

This alternative strategy, which has been carefully scrutinized in recent years, appears at first sight as a complementary solution to sunlight concentration, where the apparent size of the sun is artificially increased using an optical concentrator. In fact, the underlying physical mechanisms governing the ability of each approach to achieve high efficiencies are rather different: while concentrated PV cells are limited by series resistance losses, improving PV efficiency through angular restriction requires very high external radiative efficiencies (i.e., very high band-to-band recombination rate in the cell, together with an efficient extraction of these radiative photons from the cell).

### *1.7.2.1 Optics for angular restriction*

There are currently two main families of optical devices considered for restricting the angular distribution of the light emitted by PV cells: (1) compound parabolic concentrator (CPC)-like optics and (2) angular-selective filters.

The nature of the physical processes involved in the angular control of the emitted light differ noticeably between these two optical devices families: CPC-like devices involve multiple reflections inside a nonimaging optical component tailored to narrow the angular extent of the light exiting the device. Angular-selective filters are usually characterized by a critical angle $\theta_c(\lambda)$ that defines the acceptance range of the filter, and which is usually dependent on the wavelength $\lambda$ of the incident photons. Photons hitting the filter with an angle greater than the cutoff angle are reflected back to the cell, while photons with an angle smaller than the cutoff angle are transmitted by the filter. More details and examples of CPC-like

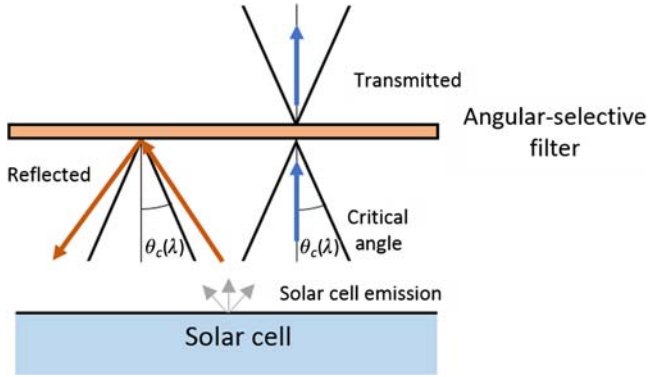


**Figure 1.14** Scheme of an angular-selective filter for the angular restriction of the emitted light.

devices and angular-selective filters can be respectively found in Refs. [13,14] (Fig. 1.14).

## 1.8 Reducing thermalization and below-$E_g$ losses: advanced concepts of photovoltaic cells

A number of original concepts have been further explored in the last decades to optimize the conversion of solar photons, either by increasing the number of photons absorbed in the cell or by reducing the thermalization losses, which both represent major fundamental mechanisms preventing ultra-high PV efficiency to be achieved. These concepts will be briefly reviewed here.

### 1.8.1 Multijunction (MJ) solar cells

Multijunction concentrator solar cells undoubtedly represent the most advanced and mature technology among the strategies suggested to overcome the fundamental loss mechanisms described in the previous section. A multijunction solar cell (also known as "tandem" cell in the literature) basically consists in a stack of p–n junctions characterized by different bandgaps, each of them converting different parts of the solar spectrum. High-energy photons are absorbed by the top-junction of the device, involving a high bandgap semiconductor material, while lower-energy photons are transmitted to the junctions underneath, basically consisting in lower bandgap semiconductors (Fig. 1.15). Tailoring the absorption properties of the solar cell to the broad energy distribution of the solar

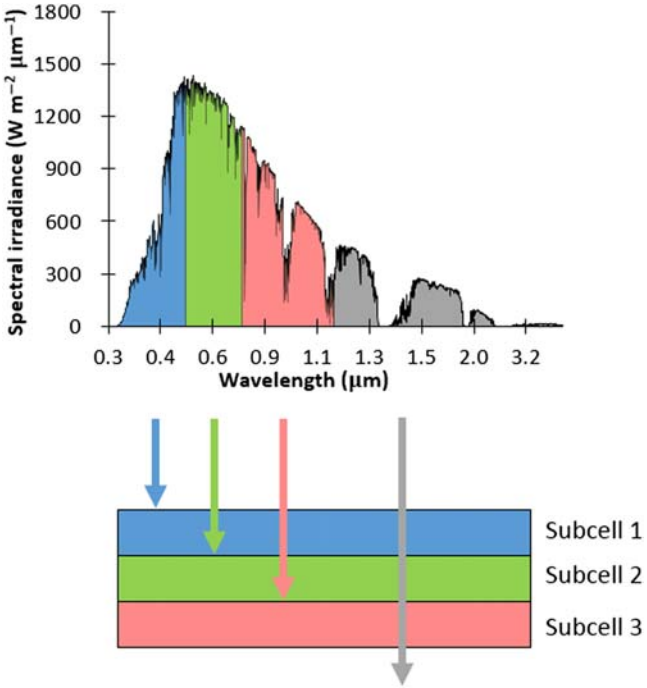


**Figure 1.15** Sketch of a multijunction solar cell with three subcells.

spectrum through the use of multiple p−n junction allows a significant decrease in both the thermalization and the below-$E_g$ losses. As a result, multijunction solar cells are likely to significantly outperform the best single-junction solar cells currently available. The highest PV conversion efficiency to date has been measured on a quadruple-junction solar cell with a solar to electricity conversion efficiency of 46% [8].

Multijunction solar cells involve multiple p−n junctions electrically and optically interconnected, and are designed to ensure simultaneously

1. An effective transmission of the photons to the appropriate p−n junction.
2. Similar photogenerated current values. Since the different subcells involved in the MJ stack are usually connected in series, the output current is determined by the lowest current generated by each individual subcell. As a result, an efficient operation of MJ cells requires each individual subcell to be tailored to generate similar current values. This can be achieved by appropriate bandgap engineering, and by an optimization of each semiconductor layer thickness (the number of

photons absorbed in each junction being a function of both the semiconductor bandgap and the subcell thickness).

3. An effective electrical interconnection between subcells. This is usually achieved by growing "tunnel junctions" between two neighboring subcells, which basically consists of very thin layers of highly doped semiconductor materials, allowing carriers to be transported from one junction to the other. In addition, tunnel diodes should be perfectly transparent to the solar spectrum (in order not to block the light) and should show very low series resistance values, to prevent any significant voltage drop.

A major limitation in the development of highly efficient multijunction concentrator solar cells stems from the limited range of alloys with lattice constants close to that of Ge, GaAs, or InP (commonly used in those devices). Different strategies have been followed to achieve high efficiencies: the "lattice-matched" approach involves stacking subcells with identical lattice constants, while "metamorphic" cells are based on the incorporation of non lattice-matched subcells with more optimal bandgaps. These two designs are constrained by either lack of flexibility in choosing the subcell bandgaps (in the lattice-matched case) or by increased defects density leading to extra-recombination losses (for the metamorphic design). Inverted metamorphic solar cells are grown inverted in comparison to conventional multijunction cell architectures: The top cell is grown first, while the bottom cell is grown last. Using such an approach allows the growth of high-quality top-cell material because of lower threading dislocations.

Recent conversion efficiency records measured on quadruple-junction solar cells were obtained on wafer-bonded solar cell architectures, a technology used to combine two lattice mismatched materials without creating dislocations. The two materials are brought into contact after a specific surface preparation of the material, creating atomic bonds at the interface.

## 1.8.2 Other concepts

### *1.8.2.1 Quantum solar cells*

Quantum wells (2D), quantum wire (1D), and quantum dots (0D) basically consist in the inclusion of a lower bandgap semiconductor material inside a higher bandgap matrix material (Fig. 1.16).

In most quantum well (QW) solar cells, the carrier escape from the well is assumed to be faster than the competing recombination

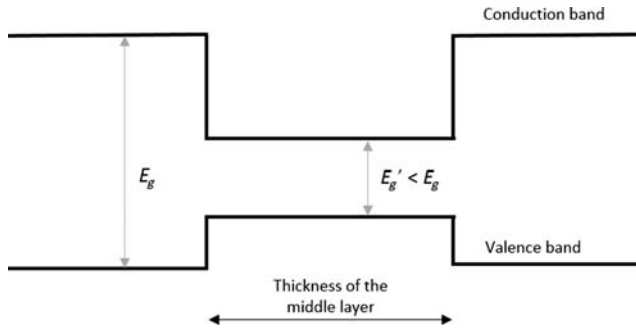


**Figure 1.16** Band structure of a quantum well (QW) with the inclusion of a lower bandgap semiconductor.

mechanisms, meaning that all the photocarriers generated in the wells participate in the current generation, thus leading to an enhanced photogenerated current relative to the equivalent bulk cell without any QWs. On the other hand, open-circuit voltage suffers from a drop—basically caused by the inclusion of lower bandgap material in a higher bandgap cell—whose effect can, however, be more than compensated by the increase in photocurrent when submitted to concentrated sunlight, giving rise to an increase in the QW cell efficiency relatively to the bulk cell.

Strain constraining the QWs allows increasing the anisotropy of light emission from the wells, resulting in reduced radiative recombination losses and thus higher efficiencies.

Incorporation of QWs in the top and/or middle junction of a conventional triple junction solar cell has also been suggested as a solution better to match the absorption edges of the top two junctions without introducing any dislocations (unlike metamorphic cells) [15].

### *1.8.2.2 Intermediate band solar cells*

Another strategy toward better absorbing the solar spectrum can be achieved through the introduction of narrow, intermediate bands (IBs) located inside the bandgap of wide bandgap semiconductor material. Three different absorption processes are involved in IBSC, namely from VB to IB, from IB to CB and from VB to CB, leading to the creation of three different quasi-Fermi levels describing the electron and holes population within the three different bands (Fig. 1.17). A fundamental motivation for IBSC lies in the high efficiencies that can theoretically be achieved [63.1% for a solar cell containing a single IB, 74.6% for a solar

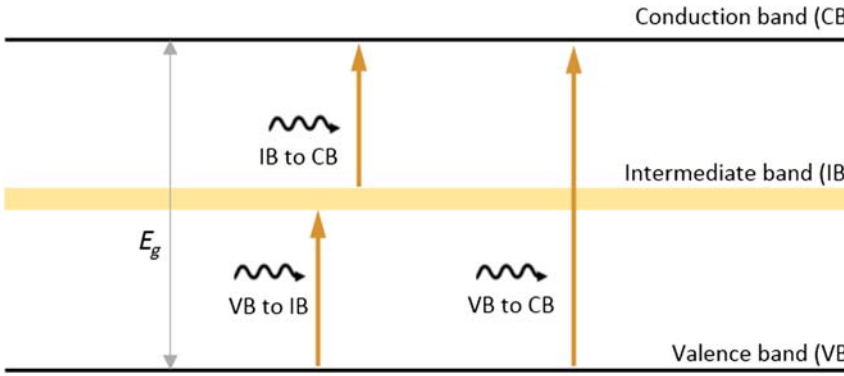


**Figure 1.17** Sketch of an intermediate band solar cell.

cell containing 4 IBs without the need for a complex stacking of multiple p−n junction (as opposed to multijunction solar cells)].

The introduction of IBs in the cell can be achieved through the implementation of bulk semiconductors, molecular-based materials, or quantum dots (which are preferred over QWs or quantum wires due to the fact that (1) quantum dots provide a true 0 density of states between the confined states and the CB and (2) due to symmetry selection rules in QWs, photon absorption causing transitions from the IB to the CB would be forbidden, which is highly undesirable).

A strong reduction in open-circuit voltage was experimentally observed on many IBSC—a consequence of the increased nonradiative recombination induced by the IB—which can be significantly improved by the use of concentrated illumination.

A complete study about IB solar cells can be found in Ref. [16].

#### *1.8.2.3 Hot carrier solar cells*

Hot carrier solar cells lie on the better exploitation of the excess energy of "hot" electrons, which is usually dissipated as heat in the lattice (thermalization losses) in solar cells. One of the main challenges lies in the decrease in the rate of photoexcited carrier cooling (in most bulk semiconductors, the carrier cooling happens in less than 0.5 ps) in order to allow extraction of "hot" carriers from the cell, thus allowing higher voltages to be achieved from the cell.

Temperature gradients can be used to obtain higher voltages by means of an absorber and energy-selective contacts to extract carriers with a specific range of energy. Using such contact may prevent entropy losses

associated with the cooling of hot carriers and thus increase the work extractable from the cell (compare $E_{ext}$ to $E_g$ in Fig. 1.18). It has been shown that the hot carrier cooling rate is related to the photogenerated carrier density, the higher the carrier density the slower the cooling rate.

A detailed work about hot carrier solar cells can be consulted in [17].

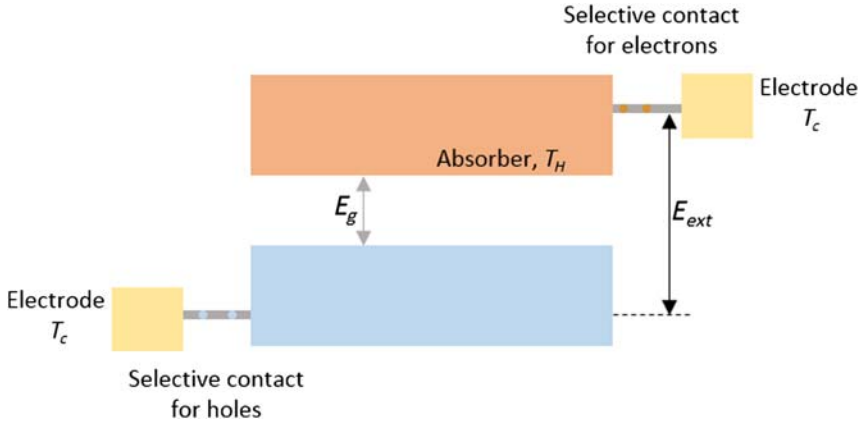


**Figure 1.18** Sketch of a hot carrier solar cell. The hot carriers are extracted from the absorber (at a temperature $T_H$) to the selective contact (at temperature $T_C$).

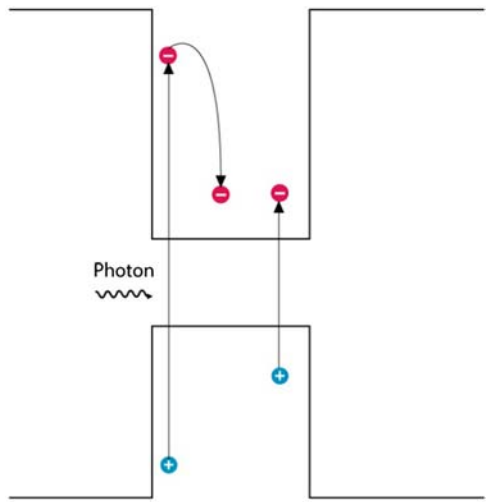


**Figure 1.19** Generation of two electron–hole pairs in a multiple exciton generation (MEG) solar cell with a quantum dot by one photon (reverse to Auger recombination).

#### 1.8.2.4 Multiple exciton generation

Another approach suggested to better exploit hot electron–holes pairs consists in using their excess kinetic energy to generate extra electron–hole pairs. This process, known as "impact-ionization" (II) in the case of bulk semiconductor materials and "Multiple exciton generation" (MEG) when the material involves quantized states, is shown to lead to conversion efficiency reaching 45% under 1 sun illumination. This relatively modest conversion efficiency in comparison to other third-generation concepts stems from the fundamental inability of photons with energy comprised between $E_g$ and $2E_g$ to generate an extra electron–hole pair (Fig. 1.19).

The amplitude of II in bulk semiconductor materials is known to be relatively weak for photons energy corresponding to the solar spectrum, thus rendering this physical process rather ineffective in better exploiting high-energy photons. On the other hand, MEG yield in quantum dots is particularly high due to the spatial confinement of electrons and holes, which makes quantum-dots solar cells a promising option toward increasing solar cell efficiency through multiple exciton effect.

## References

[1] J. Nelson, The Physics of Solar Cells, Imperial College Press, 2003. Available from: <https://books.google.es/books/about/The_Physics_of_Solar_Cells.html?id = s5NN34HLWO8C&redir_esc = y> (accessed 20.03.18).
[2] P. Würfel, Physics of Solar Cells: From Principles to New Concepts, Wiley, Weinheim, 2005. Available from: https://doi.org/10.1002/9783527618545.
[3] F. Kasten, A.T. Young, Revised optical air mass tables and approximation formula, Appl. Opt. 28 (22) (1989) 4735. Available from: https://doi.org/10.1364/AO.28.004735.
[4] ASTM, G173-03 Standard Tables for Reference Solar Spectral Irradiances: Direct Normal and Hemispherical on 37° Tilted Surface, Book of Standards, 14.04.2004.
[5] P. Blanc, B. Espinar, N. Geuder, C. Gueymard, R. Meyer, R. Pitz-Paal, et al., Direct normal irradiance related definitions and applications: the circumsolar issue, Solar Energy 110 (2014) 561–577. Available from: https://doi.org/10.1016/J.SOLENER.2014.10.001.
[6] B. Marion, Comparison of predictive models for photovoltaic module performance, in: 2008 33rd IEEE Photovolatic Specialists Conference. IEEE, 2008, pp. 1–6, doi:10.1109/PVSC.2008.4922586.
[7] P.T. Landsberg, V. Badescu, Carnot factor in solar cell efficiencies, J. Phys. D: Appl. Phys. 33 (22) (2000) 3004–3008. Available from: https://doi.org/10.1088/0022-3727/33/22/320.
[8] M.A. Green, Y. Hishikawa, E.D. Dunlop, H.D. Levi, J. Hohl-ebinger, A.W.Y. Hobaillie, Solar cell efficiency tables (version 51), Prog. Photovoltaics Res. Appl. 26 (2018) 3–12. Available from: https://doi.org/10.1002/pip.2978.
[9] L.C. Hirst, N.J. Ekins-Daukes, Fundamental losses in solar cells, Prog. Photovoltaics Res. Appl. 19 (3) (2011) 286–293. Available from: https://doi.org/10.1002/pip.1024.

[10] T. Markvart, Solar cell as a heat engine: energy-entropy analysis of photovoltaic conversion, Phys. Status Solidi A 205 (12) (2008) 2752–2756. Available from: https://doi.org/10.1002/pssa.200880460.
[11] T. Markvart, Thermodynamics of losses in photovoltaic conversion, Appl. Phys. Lett. 91 (6) (2007) 64102. Available from: https://doi.org/10.1063/1.2766857.
[12] M. Peters, J.C. Goldschmidt, B. Bläsi, Angular confinement and concentration in photovoltaic converters, Sol. Energy Mater. Sol. Cells 94 (8) (2010) 1393–1398. Available from: https://doi.org/10.1016/J.SOLMAT.2010.04.009.
[13] E.D. Kosten, J.H. Atwater, J. Parsons, A. Polman, H.A. Atwater, Highly efficient GaAs solar cells by limiting light emission angle, Light: Sci. Appl. 2 (1) (2013) e45. Available from: https://doi.org/10.1038/lsa.2013.1.
[14] M. Peters, C. Ulbrich, J.C. Goldschmidt, J. Fernandez, G. Siefer, B. Bläsi, Directionally selective light trapping in a germanium solar cell, Opt. Express 19 (S2) (2011) A136. Available from: https://doi.org/10.1364/OE.19.00A136.
[15] J.G.J. Adams, B.C. Browne, I.M. Ballard, J.P. Connolly, N.L.A. Chan, A. Ioannides, et al., Recent results for single-junction and tandem quantum well solar cells, Prog. Photovoltaics Res. Appl. 19 (7) (2011) 865–877. Available from: https://doi.org/10.1002/pip.1069.
[16] A. Luque, A. Martí, C. Stanley, Understanding intermediate-band solar cells, Nat. Photonics 6 (3) (2012) 146–152. Available from: https://doi.org/10.1038/nphoton.2012.1.
[17] D. König, K. Casalenuovo, Y. Takeda, G. Conibeer, J.F. Guillemoles, R. Patterson, et al., Hot carrier solar cells: principles, materials and design, Physica E: Low-Dimens. Syst. Nanostruct. 42 (10) (2010) 2862–2866. Available from: https://doi.org/10.1016/J.PHYSE.2009.12.032.

## Further reading

G.W. Neudeck, The PN Junction Diode, Addison-Wesley, 1983.
W. Shockley, H.J. Queisser, Detailed balance limit of efficiency of p-n junction solar cells, J. Appl. Phys. 32 (3) (1961) 510–519. Available from: https://doi.org/10.1063/1.1736034.
A. Vossier, A. Riverola, D. Chemisana, A. Dollet, C.A. Gueymard, Is conversion efficiency still relevant to qualify advanced multi-junction solar cells? Prog. Photovoltaics Res. Appl. 25 (3) (2017) 242–254. Available from: https://doi.org/10.1002/pip.2853.

This page intentionally left blank

# CHAPTER 2

# Life-cycle assessment of photovoltaic systems

**Chrysovalantou Lamnatou and Daniel Chemisana**
Applied Physics Section of the Environmental Science Department, Polytechnic School, University of Lleida, Lleida, Spain

## Contents



*Nanomaterials for Solar Cell Applications*
DOI: https://doi.org/10.1016/B978-0-12-813337-8.00002-3

## List of symbols and abbreviations

| | |
|---|---|
| **AC** | alternating current |
| **BA** | building-added |
| **BA PV** | building-added photovoltaic |
| **BA PVT** | building-added photovoltaic/thermal |
| **BI** | building-integrated |
| **BICPV** | building-integrated concentrating photovoltaic |
| **BICPVT** | building-integrated concentrating photovoltaic/thermal |
| **BIPV** | building-integrated photovoltaic |
| **BIPVT** | building-integrated photovoltaic/thermal |
| **CAES** | compressed air energy storage |
| **CdS** | cadmium sulfide |
| **CdTe** | cadmium telluride |
| **CED** | cumulative energy demand |
| **CIGS** | copper indium gallium diselenide |
| **CIS** | copper indium diselenide |
| **CML-IA** | CML-IA method |
| **$CO_2$ PBT** | payback time based on $CO_2$ emissions |
| **$CO_{2.eq}$ PBT** | payback time based on $CO_{2.eq}$ emissions |
| **$CO_{2.eq}$** | $CO_{2.equivalent}$ |
| **CPV** | concentrating photovoltaic |
| **CPVT** | concentrating photovoltaic/thermal |
| **CR** | concentration ratio |
| $E_{agen}$ | electricity generated (annually) by the PV system |
| **Ecological footprint** | Ecological footprint method |
| $E_{EOL}$ | primary energy demand for end-of-life management |
| **EI95** | Eco-indicator 95 method |
| **EI99** | Eco-indicator 99 method |
| **EI99 PBT** | payback time based on EI99 method |
| $E_{inst}$ | primary energy demand for PV-system installation |
| $E_{manuf}$ | primary energy demand for PV-system manufacturing |
| $E_{mat}$ | primary energy demand for manufacturing of the materials of the PV system |
| $E_{O;M}$ | annual primary energy demand for the phase of operation and maintenance |
| **EPBT** | energy payback time |
| **EPS 2000** | EPS 2000 method |
| **EROI** | energy return on investment |
| $E_{trans}$ | primary energy demand related to the transportation of the materials utilized during the life-cycle |
| **GaInAs** | gallium indium arsenide |
| **GaInP** | gallium indium phosphide |
| **GHG** | greenhouse gas |
| **GHG PBT** | greenhouse-gas payback time |
| **GWP** | global warming potential |

| | |
|---|---|
| **GWP 100a** | global warming potential for a time horizon of 100 years |
| **GWP 20a** | global warming potential for a time horizon of 20 years |
| **GWP 500a** | global warming potential for a time horizon of 500 years |
| **IMPACT 2002 +** | IMPACT 2002 + method |
| **IMPACT World +** | IMPACT World + method |
| **IPCC 2007** | IPCC 2007 method |
| **IPCC 2013** | IPCC 2013 method |
| **IPCC** | Intergovernmental Panel on Climate Change |
| **LCA** | life-cycle assessment |
| **LCI** | life-cycle inventory |
| **LCIA** | life-cycle impact assessment |
| **Li-ion** | lithium ion |
| $n_G$ | grid efficiency (the average primary energy to electricity conversion efficiency with respect to the demand side) |
| **PbA** | lead-acid |
| **PBT** | payback time |
| **PCM** | phase change material |
| **PHS** | pumped hydroelectric storage |
| **PV** | photovoltaic |
| **PV-Bitumen** | photovoltaic roof with bitumen-layer below the PV panels |
| **PV-Gravel** | photovoltaic roof with gravel-layer below the PV panels |
| **PV-Green** | photovoltaic roof with plants below the PV panels |
| **PVT** | photovoltaic/thermal |
| **PVT/air** | photovoltaic/thermal with air as working fluid |
| **PVT/water** | photovoltaic/thermal with water as working fluid |
| **ReCiPe** | ReCiPe method |
| **ReCiPe PBT** | payback time based on ReCiPe method |
| **$SnO_2$** | tin oxide |
| **TRACI** | TRACI method |
| **USEtox** | USEtox method |
| **ZnO** | zinc oxide |

## 2.1 Introduction

In the frame of sustainable development, solar energy systems offer multiple advantages, especially for countries with high solar irradiance. Among solar energy systems, options based on Photovoltaic (PV) technology have been widely used in the frame of different configurations: Building-Added Photovoltaic (BA PV), Building-Integrated Photovoltaic (BIPV), Building-Added Photovoltaic/Thermal (BA PVT), Building-Integrated Photovoltaic/Thermal (BIPVT), Concentrating Photovoltaic (CPV), Concentrating Photovoltaic/Thermal (CPVT), etc. By taking into account that the inputs that are needed for PV-cell material manufacturing and the energy produced during PV-system phase of usage, it can be seen

that PVs show interest from a Life-cycle assessment (LCA)/environmental point of view. In the report "Environmental Aspects of PV Power Systems" by Nieuwlaar and Alsema [1], it was concluded that the use of PVs, as a replacement for the generation of electricity based on fossil fuels, provides remarkable environmental advantages, and it seems that there are no considerable bottlenecks that cannot be overcome. Moreover, Fthenakis [2] highlighted that PV technology is under a transition to a new generation of efficient and low-cost products that are based on thin films of photoactive materials. Furthermore, Fthenakis [2] noted that PV technology shows environmental benefits in comparison to competing electricity generation technologies, and PV industry is based on a life-cycle approach in order to avoid environmental damage in the future and to sustain the environmental benefits.

In light of the issues mentioned above, it can be noted that in the literature there are studies about different PV technologies from an LCA/environmental point of view. Some of these investigations focus on a certain PV technology (for example, Perez et al. [3] presented a stydy about LCA of a BIPV system based on monocrystalline PV cells), whereas other references compare different PV technologies (for instance, Serrano-Luján et al. [4] conducted an LCA about crystalline silicon, thin-film cadmium telluride (CdTe) and organic polymer-based PV cells). Moreover, Pérez-López et al. [5] proposed a tool which offers worldwide information about the environmental profile of PV systems, based on multicriteria assessment (the user can compare the environmental performance of a PV system with the environmental impact of the electricity mix of a certain country). On the other hand, in the literature there are reviews about PV LCA, placing emphasis on different issues such as BIPVs [6], perovskite solar cells [7], PVT systems [8], nanomaterials in PVs [9], light absorbing materials/reliability/control/storage/concentrators and environmental aspects [10], and solar-energy projects [11].

By considering the importance of investigating LCA/environmental aspects of PVs, the present study is about PV LCA. Selected literature references are presented (based on certain criteria) and critical parameters are highlighted. Firstly, general issues about LCA and Life-Cycle Impact Assessment (LCIA) methods as well as environmental indicators for PV LCA are presented. Secondly, representative literature references about different PV technologies (separated into different subsections according to PV technology) are cited. Finally, important parameters about LCA of PV systems (sunlight concentration, storage, durability of the materials, end-of-life and disposal, recycling, etc.) are discussed.

## 2.2 Life-cycle assessment: general issues

In recent years, there have been concerns about environmental problems and the depletion of the natural resources. In this context, there is a new tendency for "greener" products and "greener" processes. Therefore it can be seen that it is important to evaluate the environmental profile of products and processes, and this is why certain companies examine solutions in order to reduce the environmental impact of their products and processes [12]. Based on the issues mentioned above, in the frame of sustainable production and consumption, the concepts of life-cycle thinking and LCA (for business decisions, environmental policies, etc.) play an important role [13]. At this point it should be clarified that life-cycle includes the major activities during the life span of a product (manufacturing, use/maintenance, final disposal). The raw material acquisition necessary for product manufacturing is included [12]. In the report by Fthenakis et al. [14], it was noted that LCA is a method that is comprehensive, structured, and useful for quantifying material-, and energy-flows and their impacts during the life-cycle of a product.

In the frame of LCA, the resources that are consumed and the emissions of a certain product are compiled and documented in Life-Cycle Inventory (LCI). Then, an impact assessment is performed, considering the natural environment, human health, and the use of natural resources [13].

The standards ISO 14040 [15], 14044 [16] provide the indispensable framework for conducting LCA, including four phases [12,15,16]:

1. *Goal/scope definition*: The product (or the process or the activity) should be described. The context of the assessment (boundaries, environmental effects, etc.) should be established.
2. *LCI*: Identification and quantification of energy, materials, and water usage as well as environmental releases (solid waste, air emissions, wastewater, etc.).
3. *LCIA*: Potential ecological and human effects of energy, material, and water usage, environmental releases.
4. *Interpretation*: Evaluation of the results of the inventory analysis and impact assessment ( issues such as uncertainty and assumptions should be taken into account).

## 2.3 Life-cycle impact assessment methods

### 2.3.1 Embodied energy, embodied carbon, energy payback time, greenhouse-gas payback time

Hammond and Jones [17] discussed the notions of embodied energy and embodied carbon. It was noted that for LCA in an energy context, it is important the estimation of the primary energy inputs to produce a given product (or service) so as to find the least energy-intensive industrial process. Embodied energy shows the quantity of energy needed to process and supply to the construction site a certain material. In the same context, the emissions of energy-related pollutants (e.g., $CO_2$ emissions) can be examined (for instance, for the life-cycle of a product) and, in this way, the notion of embodied carbon arises [17].

The primary energy demand related to the life-cycle of a system can be used, for example, for the calculation of the energy metric Energy Payback Time (EPBT). EPBT is the time period that needs a renewable-energy system in order to produce the same amount of energy (primary energy equivalent) that was used for the production of the system itself [14]. For the evaluation of the EPBT of PV systems, the following equation [14,18] can be adopted:

$$\mathrm{EPBT} = \frac{E_{mat} + E_{manuf} + E_{trans} + E_{inst} + E_{EOL}}{\left(E_{agen}/n_g\right) - E_{O;M}} \tag{2.1}$$

where $E_{mat}$ represents the primary energy demand needed to produce the materials of the PV system, $E_{manuf}$ is the primary energy demand necessary to manufacture the PV system, $E_{trans}$ stands for the primary energy demand related to the transportation of the materials that have been utilized during the life-cycle, $E_{inst}$ is the primary energy demand for the installation of the PV system, $E_{EOL}$ represents the primary energy demand with respect to end-of-life management, $E_{agen}$ stands for the electricity generated (annually) by the PV system, $E_{O\&M}$ is the annual primary energy demand for the phase of operation and maintenance, $n_G$ represents the grid efficiency (more specifically, it is the average primary energy to electricity conversion efficiency, with respect to the demand side).

In the same way, Greenhouse-Gas Payback Time (GHG PBT) can be evaluated. LCA studies which include GHG PBT calculations have been presented: for instance, by Chow and Ji [19] for different PVT systems and by Lamnatou et al. [20] for a Building-Integrated Concentrating Photovoltaic (BICPV) configuration. The equation of GHG PBT has the

same formula with the equation of EPBT but, instead of the primary energy quantities, $CO_{2.eq}$ emissions (over the life-cycle of the studied PV system) are taken into account.

Moreover, based on EPBT, another energy metric, which in the literature is known as Energy Return on Investment (EROI), can be evaluated. The notion of EROI shows how "easy" (from an energetic point of view) it is to exploit the available primary energy sources by investing an amount of energy that one has at one's disposal. EROI can be evaluated by the following equation [21]:

$$\text{EROI} = \frac{\text{system lifetime}}{\text{EPBT}} \tag{2.2}$$

### 2.3.2 Methods which include midpoint and/or endpoint approaches

Concerning the Eco-indicator 99 (EI99) method, the first concept that should be clarified is that EI99 is a successor to Eco-indicator 95 and both methods use a damage-oriented approach. For the characterization of the emissions, multiple impact categories (carcinogens, respiratory organics, respiratory inorganics, etc.) are taken into account. For the damage assessment, the damages of the impact categories result in three types of damages (in terms of human health, ecosystem quality, and resources) [22].

Regarding the IMPACT 2002 + (acronym: IMPact Assessment of Chemical Toxics) method, it combines midpoint with damage approach. IMPACT 2002 + connects all types of LCI results via 14 midpoint categories (human toxicity, respiratory effects, ionizing radiation, ozone layer depletion, etc.) to four damage categories (in terms of human health, ecosystem quality, climate change, and resources) [22].

Furthermore, ReCiPe represents another method, and it is a successor of EI99 and CML-IA. ReCiPe includes integration of the problem-oriented approach (midpoint) and the damage-oriented approach. At the midpoint level, ReCiPe has 18 impact categories (ozone depletion, human toxicity, ionizing radiation, photochemical oxidant formation, etc.). At the endpoint level, most of the midpoint impact categories are multiplied by damage factors and, then, they are aggregated into three endpoint categories (in relation to human health, ecosystems, and resource surplus costs). The three endpoint categories are normalized, weighted, and aggregated into a single-score [22].

Moreover, CML-IA method refers to midpoint approach, whereas EPS 2000 is a damage-oriented method [22].

At this point, it should be noted that by having as reference the methods discussed above, some additional PBTs can be evaluated. For instance, by using ReCiPe endpoint score, ReCiPe PBT can be calculated [23].

In addition, it should be clarified that in the case of Building-Integrated (BI) solar systems, the PBTs can also be evaluated with an alternative way: by considering that there is material replacement and this is because BI systems replace a building component (e.g., façade). For example, Chow and Ji [19] discussed the option of evaluating EPBTs and GHG PBTs (for PVT systems) by taking into account material replacement.

### 2.3.3 Other methods

In the present subsection, some additional methods are presented [22]:

- *USEtox*: It is an environmental model for characterizing human and eco-toxicological impacts.
- *Cumulative Energy Demand (CED)*: It includes characterization factors for energy resources (nonrenewable and renewable impact categories are included).
- *GHG protocol*: It is an accounting standard for GHG emissions.
- *IPCC 2013*: It provides information about Global Warming Potential (GWP) based on time horizons of 20 (GWP 20a), 100 (GWP 100a), and 500 (GWP 500a) years.
- *Ecological footprint*: It is about the biologically productive land and water a population needs so as to produce the resources it consumes and to absorb a part of the waste generated by the consumption of fossil and nuclear fuel. Regarding characterization, in the frame of LCA, ecological footprint (e.g., in the case of a product) is the sum of time integrated (direct and indirect) land occupation, with respect to nuclear energy utilization and the $CO_2$ emissions due to the use of fossil energy [22].

In Table 2.1, the methods mentioned above (Sections 2.3.2 and 2.3.3) are briefly presented and important issues are highlighted. Table 2.1 is mainly based on the classification presented in the report by PRé [22]. In the literature, classifications based on other criteria can also be found.

**Table 2.1** Brief presentation of certain methods, based on the report by PRé [22].

| Methods | Basic information |
|---|---|
| ***Single issue*** | |
| CED | Energy resources (nonrenewable and renewable impact categories) |
| GHG protocol | GHG emissions |
| IPCC 2013 | GWP for time horizons of 20, 100, and 500 years (GWP 20a, GWP 100a, and GWP 500a, respectively) |
| USEtox | Human and eco-toxicological impacts |
| Ecological footprint | Land occupation related to nuclear energy use and $CO_2$ emissions from fossil-energy use |
| ***Midpoint/Endpoint*** | |
| CML-IA | Problem-oriented (midpoint) approach |
| EPS 2000 | Damage-oriented (endpoint) approach |
| IMPACT 2002 + | Combination midpoint/endpoint approach |
| ReCiPe | Combination midpoint/endpoint approach |
| ***Superseded*** | |
| EI95 | Damage-oriented (endpoint) approach |
| EI99 | Damage-oriented (endpoint) approach |

*CED*, Cumulative energy demand; *GHG*, greenhouse gas; *GWP*, global warming potential; *IMPACT*, impact assessment of chemical toxics; *IPCC*, Intergovernmental Panel on Climate Change.

## 2.4 Life-cycle assessment and metrics—environmental indicators for photovoltaics

In Fig. 2.1, a schematic which shows life-cycle stages of PV modules is illustrated and it can be seen that the life-cycle begins with the extraction of the raw materials, then follows material manufacturing phase (in the factory), then follows use phase (phase of usage: the time period during which the PV module is utilized for the production of electricity, for example, in the building sector). Then, the phase of end-of-life/disposal of the materials follows. It should be noted that, in the life-cycle, additional stages such as transportation and installation of the system can also be included.

### 2.4.1 Metrics and indicators for photovoltaic life-cycle assessment

Anctil and Fthenakis [18] highlighted the following metrics (for PV LCA):

1. GHG emissions (e.g., in kg $CO_{2.eq}$) of a PV system during its life-cycle, with a GWP time horizon of 100 years.

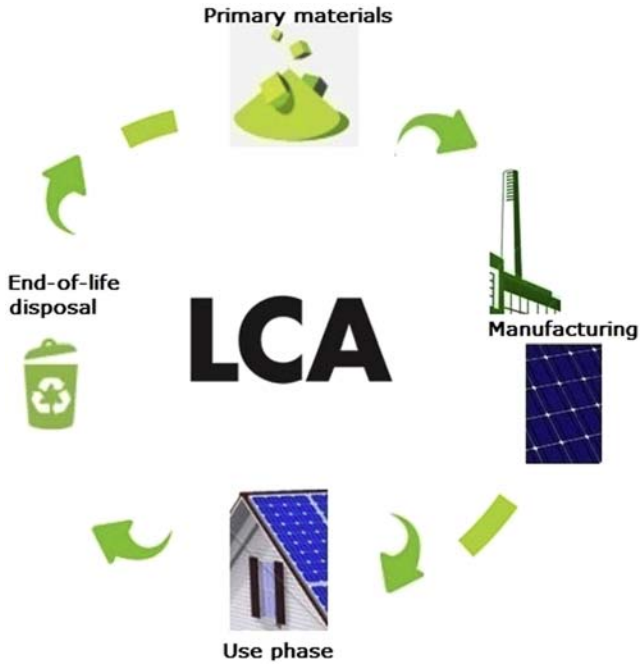


**Figure 2.1** Life-cycle stages of PV modules. *PV*, Photovoltaic.

2. CED: It includes direct uses as well as indirect (known as gray) consumption of energy.
3. Acidification potential: $NO_X$, $NH_3$, and $SO_2$ are considered as major acidifying substances.
4. Ozone-depletion potential: Stratospheric ozone-layer depletion has negative impacts on terrestrial ecosystems, aquatic ecosystems, human health, animal health, biochemical cycles, and materials.
5. Human toxicity: It refers to the impacts of toxic substances on human health.
6. Ecotoxicity: It is about the impacts of toxic substances on ecosystems (aquatic, terrestrial, sedimentary).
7. Land use and water use: These are environmental impacts of growing importance.

In relation to the primary energy required during the life-cycle of a PV system, EPBT (presented in Section 2.3.1) provides useful information (from an energetic point of view). Anctil and Fthenakis [18], except of the common equation of EPBT, presented and discussed the option of nonrenewable EPBT (the time necessary to compensate for nonrenewable

energy needed during PV system life-cycle), EROI and mitigation potentials for climate change.

### 2.4.2 Methodological framework for assessing (based on life-cycle assessment) the environmental impacts of photovoltaic systems

Evon et al. [24] conducted a study about the methodological framework for PV LCA. As a first step, the product category should be defined. Certain product categories were presented:

1. Above 0 kVA and under 36 kVA; low-voltage single phase or three phases; In this case the system can be integrated into (or connected to) a building or (another option) installed on the roof of a building.
2. Strictly above 36 kVA and under 250 kVA; low-voltage three phases; There are two options: (1) system integrated into (or connected to) a building or installed on the roof of a building, (2) system installed on the ground.
3. Strictly above 250 kVA; medium voltage; There are two options: (1) system integrated into (or connected to) a building or installed on the roof of a building, (2) system installed on the ground.

Another step is the definition of the scope of the LCA study (including functional unit, system boundaries, etc.). Moreover, Evon et al. [24] highlighted that the categories of climate change, respiratory inorganics, resource depletion/water, primary energy consumption/renewable, and primary energy consumption/nonrenewable are obligatory.

## 2.5 Life-cycle assessment of photovoltaic technologies

In the present section selected references about LCA of PV technologies, separated into subsections according to each technology, are presented.

### 2.5.1 Silicon

Silicon is considered as the most developed and best understood semiconductor material. In terms of the market, multicrystalline-silicon PVs have the greatest market share (followed by monocrystalline silicon, followed by CdTe thin-film) [25].

Different solar-cell architectures can be compared (from an environmental point of view). For example, Luo et al. [26] investigated two solar-cell architectures: the conventional aluminum back-surface-field and the state-of-the-art passivated emitter and rear cell.

It should be noted that in the broad category of silicon PV technology can also be included the technology of silicon heterojunction. Louwen et al. [27] noted that silicon heterojunction cells offer high efficiencies and several benefits in the production process in comparison to conventional crystalline silicon solar cells. A study about GHG emissions (on a life-cycle basis) and EPBT of current and prospective silicon heterojunction solar-cell designs was conducted. Louwen et al. [27] found that for current designs the life-cycle GHG emissions could be 32 g $CO_{2.eq}$/kW h for complete silicon heterojunction PV systems (module efficiency: 18.4%). In the case of conventional monocrystalline-silicon PV systems (module efficiency: 16.1%), the indicator mentioned was calculated to be 38 g $CO_{2.eq}$/kW h. Regarding EPBT, for all the silicon heterojunction designs, a value of 1.5 years was found. For the monocrystalline PV system, EPBT was calculated to be 1.8 years. Moreover, Louwen et al. [27] highlighted that an increase in terms of cell efficiency, adoption of thin silicon wafers and replacement of silver-based with copper-based metallization could reduce the life-cycle GHG emissions to 20 g $CO_{2.eq}$/kW h for silicon heterojunction systems (and to 25 g $CO_{2.eq}$/kW h for monocrystalline silicon system). At the same time, EPBTs could also be reduced to 0.9 and 1.2 years, respectively.

On the other hand, some LCA studies are about the specific category of BIPV. For instance, Perez et al. [3] investigated a BIPV system (completely integrated curtain-wall façade spanning 12 floors of the "Solaire Building" in New York City). Perez et al. [3] concluded that façade-integrated BIPV shows an environmental impact that is comparable to that of optimally oriented roof or ground-mounted PV systems. Moreover, it was mentioned that this environmental advantage is associated with the fact that BIPV replaces the materials of the façade and, therefore, there is an avoided environmental impact. Regarding BIPV, Wang et al. [28] presented a comparison of BA PV with BIPV and it was concluded that both systems offer environmental benefits and the BIPV system showed a better environmental profile in comparison to the BA one.

Regarding PV roofs, Lamnatou and Chemisana [23] investigated different types of roofing systems: (1) PV-Green (PV panels over a "green" layer of plants), (2) PV-Gravel (PV panels over a gravel roof), (3) PV-Bitumen (PV panels over a bitumen roof). Fig. 2.2 illustrates the results for the option without recycling. For the PV-Green system several scenarios (in terms of the PV-output increase due to the interaction of the

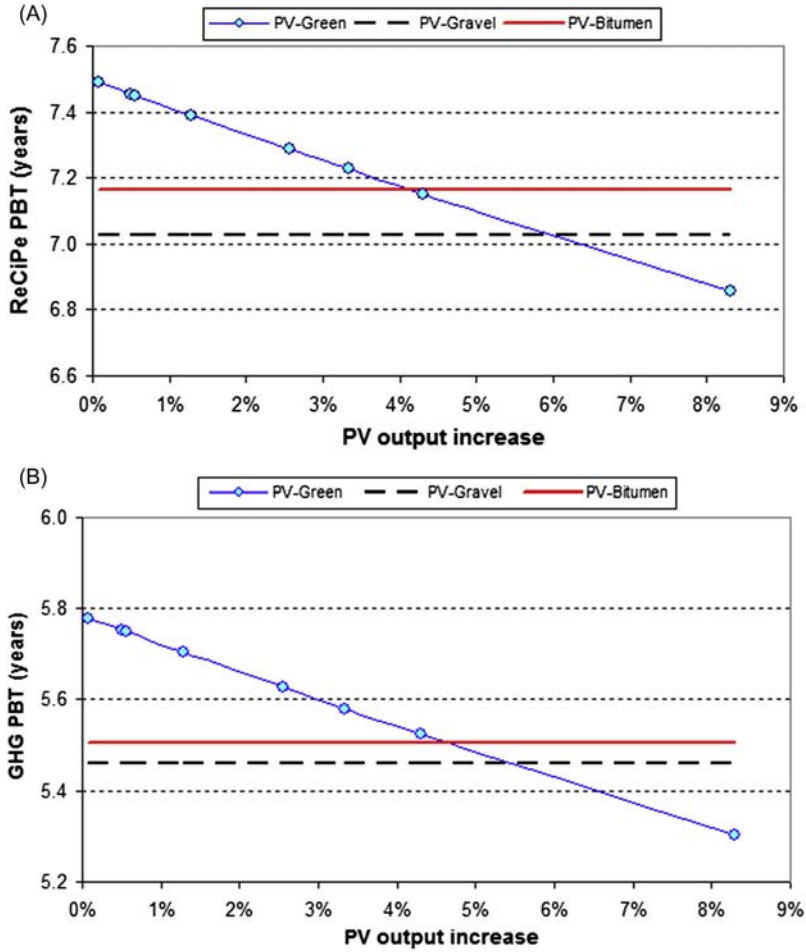


**Figure 2.2** Different PV roofs (PV-Green; PV-Gravel; PV-Bitumen) for the scenario "'without recycling": (A) ReCiPe PBT values and (B) GHG PBT values. *GHG*, Greenhouse gas; *PBT*, payback time; *PV*, photovoltaic. *C. Lamnatou, D. Chemisana, Evaluation of photovoltaic-green and other roofing systems by means of ReCiPe and multiple life cycle-based environmental indicators, Build. Environ. 93 (2015) 376–384.*

plants with the PV panels) were evaluated. Fig. 2.2A reveals that there is a critical point (at 6% PV-output increase) that is associated with the comparison of the PV-Green with the PV-Gravel. Moreover, in Fig. 2.2A, there is another critical point (at 4.2% PV-output increase) that is for the comparison of the PV-Green with the PV-Bitumen. From Fig. 2.2B two additional critical points at 4.7% and 5.5% PV-output increase (regarding the comparison of the PV-Green with the PV-Bitumen and PV-Gravel,

respectively; GHG PBTs; scenario without recycling) are identified. These critical points demonstrate the critical PV-output increase after which the PV-Green roof pays back its additional environmental impact (due to its "green" layer), and it becomes more eco-friendly than the other two PV roofs. The increase of 4%–6% in terms of PV-output increase, according to the literature, can be considered as reasonable (in certain climatic conditions). ReCiPe PBTs and GHG PBTs were also evaluated for the scenario with recycling: Recycling resulted in a reduction of around 0.4–0.6 years in both ReCiPe and GHG PBTs.

In Table 2.2, selected literature references about LCA on silicon-based PV are presented and it can be seen that:

1. In recent years, there is an increasing interest for PV LCA studies.
2. Most of the investigations are about multi- and monocrystalline-silicon PV cells.
3. Embodied energy, EPBT, $CO_2$, and GHG emissions are the most commonly studied environmental issues/indicators.
4. There are few PV LCA studies based on methods with endpoint and/or midpoint approaches (ReCiPe, EI99, IMPACT 2002 + , etc.).
5. Most of the cases are about BA systems, and there are few investigations about BI configurations.
6. The systems have been examined for different climatic conditions (Europe, China, United States, etc.).
7. The results reveal that there are multiple factors which influence the environmental profile of a PV system such as climatic conditions, latitude, type of integration into the building (BA vs. BI) and roof material (gravel, bitumen, plants, etc.) in the case of PVs for building applications, type of PV technology, and the electricity mix of a country (for certain environmental indicators).
8. Most of the studied PV systems presented EPBTs around 2–3 years (considerably lower than the life span of these types of systems: for instance, 30 years).
9. GHG PBT is strongly influenced by the electricity mix of a country. Countries with electric mixes of low $CO_2$ emissions present high GHG PBT values [37].

### 2.5.2 Multijunction

Multijunction devices of high-efficiency utilize multiple bandgaps (or junctions) which are tuned in order to absorb a certain part of the solar

**Table 2.2** Selected references about photovoltaic (PV) life-cycle assessment of silicon-based PVs.

| Reference | PV technology | Information about the system | Location | Methods/environmental issues studied |
|---|---|---|---|---|
| Jungbluth et al. [29] | Multicrystalline and monocrystalline silicon | Different grid-connected PV systems (each of them: 3 $kW_p$) for roof and façade applications | Switzerland | CED; EI99; ecological scarcity; EI99 PBT and other PBTs based on global warming, human toxicity, etc. |
| Battisti and Corrado [30] | Multicrystalline silicon | Grid-connected PV systems, retrofitted on a tilted roof | Italy | GWP; CED; EPBT; $CO_{2,eq}$ PBT; EI95 |
| Nawaz and Tiwari [31] | Monocrystalline silicon | Open-field and rooftop PV systems with battery | India | EPBT; embodied energy; $CO_2$ emissions |
| Bravi et al. [32] | Thin-film technology in dual silicon layers | Grid-connected PV system of 1 $kW_p$ | Switzerland | EI99; GHG emissions; EPBT; Gross energy requirement |
| Bayod-Rújula et al. [33] | Multicrystalline silicon | PV system of 26.46 $kW_p$ (configurations with/without sun tracking) | Spain; Germany | IPCC 2007 GWP 100a; CED; EI99; EPBT; EI99 PBT; $CO_2$ PBT; energy return factor |
| Perez et al. [3] | Monocrystalline silicon | BIPV curtain-wall array | United States | EPBT; EROI; GWP; carbon-equivalent PBT |
| Desideri et al. [34] | Multicrystalline silicon | Ground-mounted 1778 $kW_p$ PV plant | Italy | EI99; EPBT; Energy return on energy invested, $CO_2$ emissions; GWP 100a |
| Lamnatou and Chemisana [35] | Multicrystalline silicon | PV-Green, PV-Gravel roofs | Spain | EI99; IMPACT 2002 + ; CED; EPBT; avoided $CO_2$ emissions; avoided gasoil |
| Nicholls et al. [36] | Multicrystalline silicon | PV system (3 kW, rooftop) with batteries | Australia | GHG emissions; embodied energy; EPBT |

(*Continued*)

**Table 2.2** (Continued)

| Reference | PV technology | Information about the system | Location | Methods/environmental issues studied |
|---|---|---|---|---|
| Lamnatou et al. [37] | Monocrystalline silicon | BICPV | France; Spain; United Kingdom; Ireland | Embodied energy; embodied carbon; EPBT; GHG PBT; EROI |
| Wetzel and Borchers [38] | Monocrystalline and multicrystalline silicon modules | PV modules of 60 cells: 243 $W_p$ for the multicrystalline one and 260 $W_p$ for the monocrystalline one | Europe | EPBT; $CO_2$ emissions |
| Fu et al. [39] | Multicrystalline silicon | Module of 200 $W_p$ | China | Primary energy demand; EPBT; CML |
| Lamnatou and Chemisana [23] | Multicrystalline silicon | PV-Green, PV-Bitumen, PV-Gravel roofs | Spain | IPCC 2013; GHG PBT; ReCiPe; ReCiPe PBT; Ecological footprint; USEtox |
| Louwen et al. [27] | Different silicon heterojunction solar-cell designs | PV modules with balance-of-system | Netherlands, Southern Europe | CED; IPCC 2007 GWP 100a; EPBT |
| Collins et al. [40] | Monocrystalline and multicrystalline silicon | PV system with 80% performance ratio (impacts normalized to 1 $W_p$) | United States; China | CED; EPBT; TRACI |
| Chen et al. [41] | Monocrystalline silicon | 1 $kW_p$ mono-Si PV-cell production (functional unit) | China | EPBT; and other types of PBTs; IMPACT 2002 + ; ReCiPe; TRACI; CML |

| | | | | |
|---|---|---|---|---|
| Hong et al. [42] | Multicrystalline silicon | 1 $kW_p$ multi-Si PV-cell production (functional unit) | China | IMPACT 2002 + ; ReCiPe; TRACI; IMPACT World + |
| Tiago Filho et al. [43] | Crystalline silicon | PV system with batteries | Brazil; Japan; Germany; United States; China | EPBT; $CO_2$ emissions; effectively clean-energy-production time; emission−factor ratio |
| Lamnatou et al. [44] | Monocrystalline silicon | BICPV | Spain; Ireland; United Kingdom | ReCiPe; EI99; USEtox; Ecological footprint; ReCiPe PBT; EI99 PBT |
| Wang et al. [28] | Monocrystalline and multicrystalline silicon | BA PV; BIPV | China | EPBT; GHG PBT; emissions ($SO_2$, NOx , etc.) |
| Kristjansdottir et al. [45] | Monocrystalline and multicrystalline silicon | Different configurations (BA PV, BIPV, with/ without batteries, etc.) | Norway | IPCC GWP 100a; $CO_{2.eq}$; GHG PBT |
| Beccali et al. [46] | Multicrystalline silicon | Grid-connected and stand-alone PV systems | Switzerland; Italy | Global energy requirement; EPBT; Energy return ratio; GWP; PBT in terms of GWP |
| Petrillo et al. [47] | Monocrystalline silicon | Small-scale stand-alone PV system with batteries | Egypt | EI99 |
| Hou et al. [48] | Monocrystalline and multicrystalline silicon | Grid-connected PV systems | China | GHG emissions; EPBT; energy yield ratio; energy consumption |

(*Continued*)

**Table 2.2** (Continued)

| Reference | PV technology | Information about the system | Location | Methods/environmental issues studied |
|---|---|---|---|---|
| Gazbour et al. [49] | Comparison of bifacial PV with classic and updated monocrystalline-silicon PV | PV system of 570 $kW_p$ | Europe (average irradiation) | IPCC 2013 GWP100a; GHG emissions; CED; EPBT |
| Jones et al. [50] | Monocrystalline silicon | Rooftop PV system with batteries | United Kingdom | $CO_2$ emissions; $CO_2$ savings |
| Yu et al. [51] | Multicrystalline silicon | Grid-connected PV system of 1 $MW_p$ | China | EPBT; IPCC 2007; IMPACT 2002 + ; CML 2002; energy conservation and emission reduction and other indicators |
| Palacios-Jaimes et al. [52] | Monocrystalline silicon | BIPV façade-integrated | Spain | EI99; EPS 2000; IPCC 2013 |
| Akinyele et al. [53] | Monocrystalline silicon | PV system of 1.5 kW | Nigeria | GHG emissions; CED; EPBT; net energy ratio; fuel consumption rate of a diesel generator |
| Murphy and McDonnell [54] | Monocrystalline silicon | Roof-mounted panels (roof area: 784 $m^2$) | Ireland | GHG emissions; EPBT |
| Huang et al. [55] | Multicrystalline silicon | Five modules (200 $W_p$ each of them) | China | ReCiPe |
| Luo et al. [26] | Multicrystalline silicon | Roof-integrated PV systems (60-cell PV modules) | Singapore | EPBT; CED; IPCC 2013 GWP 100a |

*BICPV*, Building-integrated concentrating photovoltaic; *BA PV,* building-added photovoltaic; *BIPV*, building-integrated photovoltaic; *CED*, cumulative energy demand; *EPBT*, energy payback time; *EROI*, energy return on investment; *GHG*, greenhouse gas; *GWP*, global warming potential; *IMPACT*, impact assessment of chemical toxics; *IPCC*, Intergovernmental Panel on Climate Change; *PBT*, payback time.

spectrum. For these types of solar cells, efficiencies higher than 45% have been recorded. Multijunction devices utilize a high-bandgap top cell for the absorption of high-energy photons (in addition to this, lower-energy photons pass through). A material that has a slightly lower bandgap is placed below the high-bandgap junction, and the role of this configuration is the absorption of photons with slightly less energy (longer wavelengths). The cells which are characterized as typical multijunction cells utilize two or more absorbing junctions, and there is an increase of the theoretical maximum efficiency with the number of the junctions which are included [56].

Fthenakis and Kim [57] presented an LCA study about Amonix 7700 high-concentrating PV system with tracking and Concentration Ratio (CR) 500×. The cells of the system are multijunction GaInP/GaInAs/Ge grown on germanium substrate (37% efficiency under the test conditions). The aperture area is 267 $m^2$ and the capacity of the unit is 53 $kW_p$ AC (test conditions: 850 $W/m^2$ direct normal insolation; 20°C ambient temperature; 1 m/s wind velocity). The EPBT for operation in Phoenix, AZ, United States, was found to be 0.9 years and the GHG emissions were calculated to be 27 g $CO_{2.eq}$/kW h and around 16 g $CO_{2.eq}$/kW h, for 30-year and 50-year operation, respectively.

Sandwell et al. [58] presented an LCA about a high-CPV system based on III−V multijunction PV cells and 625 × CR. Different scenarios (for instance for different countries: United States, Spain, Saudi Arabia, China, Australia and Chile) were examined. The EPBTs were found to be 0.22−0.33 years and the GHG emissions showed values of 6.5−9.8 g $CO_{2.eq}$/kW h (depending on the location).

Espinosa and Krebs [59] conducted an LCA study about organic tandem solar cells. An overview of research findings on how the energy consumption influences the energy balance when adopting single and multijunction solar cells was presented. The minimum efficiency that the tandem or multijunction cell should show in order to achieve the minimum EPBT was calculated. It was noted that the increase in terms of the materials used and the complexity of the tandem configuration are compensated by the fact that there is better performance.

Additional LCA studies about multijunction PV cells have been presented by Kim and Fthenakis [60], Stucki and Itten [61], and Itten and Stucki [62].

### 2.5.3 Copper indium gallium diselenide

Thin-film copper indium gallium diselenide (CIGS) PV modules are promising. CIGS technology presents competitive cell efficiencies and performances under a variety of environments (in comparison to traditional technologies which are based on silicon) [63]. Recent developments in terms of the cost and the efficiency of thin-film BIPV technologies, in particular CIGS, brought new design options, providing advantages such as low weight, customizable shapes, and esthetically pleasing designs for BI applications [64,65].

Jayathissa et al. [64] presented an LCA study about BIPV configurations which include adaptive shading with façade-integrated solar tracking. CIGS PV panels were selected as thin-film panels because they have high efficiency, low cost, and they can be deposited on a polymer or aluminum substrate. Several scenarios were examined and Jayathissa et al. [64] concluded that BIPV systems and adaptive shading elements complement each other and they offer an improvement of PV-technology environmental profile, creating new options for esthetic integration of PV panels over glazed building surfaces.

Amarakoon et al. [63] investigated the manufacturing of CIGS modules, placing emphasis on LCA and environmental issues. The findings revealed that during the manufacturing phase of CIGS PV cells, there are certain critical factors related to environmental/toxicity impacts: (1) the silver utilized in stringer and screen printing processes, (2) the metals of the CIGS layer, (3) the surface washing of the stainless steel substrate, and (4) the copper included in the balance of system. In addition, Amarakoon et al. [63] noted that the zinc oxysulfide alternative presents lower overall impacts in comparison to cadmium sulfide (CdS). Moreover, substitution of the integrated-cell-interconnect system reduced the impacts of the CIGS system, by reducing the silver needed.

### 2.5.4 Cadmium telluride

CdTe thin-film PV panels consist of layers of CdTe and CdS. In terms of Cd, it should be noted that it is a by-product of zinc mining. On the other hand, the rare metal tellurium (Te) is a by-product of copper, lead, and gold mining, and its scarcity could be considered as a bottleneck for the production of CdTe cells. Regarding hazards, the main health and safety concerns related to the manufacture of CdTe cells are due to the

use of cadmium, CdS, cadmium chloride, and thiourea. At this point, it should be highlighted that Cd is carcinogen and extremely toxic [66].

Raugei et al. [67] conducted a study about LCA of thin-film CdTe PV modules in the frame of the European research project PVACCEPT. The investigation is based on actual production data (from the former project partner ANTEC Solar GmbH). The following findings were presented: 60 g abiotic matter/kW h, 32 g $CO_{2.eq}$/kW h, and EPBT of 0.9 years, despite the fact that the modules had low energy-conversion efficiency (8%).

Kim et al. [68] presented an LCA about power generation systems, based on CdTe PVs (100 $kW_p$), in Malaysia. It was noted that CdTe PV systems presently show a GWP of 15.1 g $CO_{2.eq}$/kW h (in Malaysia). The CdTe PV panel is responsible for the greatest part (47.8%) of the GWP of the system. More specifically, the electricity for the process of semiconductor deposition was found to be the main contributor in terms of the GWP of the CdTe PV panel. PBTs were also evaluated and the results showed values of 0.94 years and 0.76 years for EPBT and $CO_2$ PBT, respectively (relatively short PBTs in comparison with other PV power plants).

Additional studies about LCA of thin-film CdTe modules have been presented by Held and Ilg [69], Held [70], and Rix et al. [71].

### 2.5.5 Perovskite

Assadi et al. [72] analyzed recent progress in perovskite solar cells. It was noted that organic and inorganic hybrid halide perovskite solar cells are viable and comparable to other PV configurations. Moreover, it was highlighted that the large charge carrier diffusion length of 1 μm in the case of mixed-halide perovskite thin films is much higher than for other thin films processed in low-temperature solution. Another advantage related to perovskite solar cells is their excellent optoelectronic characteristic of their organometal halide perovskite material. Environmental aspects and photostabilities should be defined for the devices which are utilized at a commercial level. Materials for encapsulation and methods with humidity-resistance and photo-stability are necessary to be established. For achieving environmental-friendly perovskite solar cells, instead of Pb, other elements should be adopted. Assadi et al. [72] also highlighted that perovskite technology can offer high quantities in production of solar cells, with cost reduction in terms of the manufacturing processes.

Ibn-Mohammed et al. [7] presented a review article about perovskite solar cells, highlighting that, at present (year of the study [7]: 2017), there is a limited number of environmental assessments of perovskite-structured solar cells. The main findings revealed that perovskite-structured solar cells are more environmentally friendly and sustainable in comparison with other PV technologies. In addition, the review by Ibn-Mohammed et al. [7] included pathways for future PV designs in the frame of cleaner production.

Lunardi et al. [73] investigated three perovskite/silicon tandem cell structures with silver (Ag), gold (Au), and aluminum (Al) as top electrodes in comparison to p−n junction and heterojunction with intrinsic inverted layer silicon solar cells. The study was based on LCA. More analytically, EPBT, GWP, human toxicity, freshwater eutrophication, freshwater ecotoxicity, and abiotic depletion potential impacts were evaluated. The results of the investigation by Lunardi et al. [73] revealed that the replacement of the metal electrode with indium tin oxide/metal grid in the tandem cell offers a remarkable reduction in the environmental impacts (compared to the perovskite cell). In addition, it was noted that for all the impacts that were examined, it was found that the perovskite/silicon tandem with Al as top electrode shows better environmental performance in comparison to the other tandem structures which were studied.

Celik et al. [74] studied perovskite solar cells and conventional-silicon PV technologies. It was found that the environmental impact for the manufacturing of the perovskite solar cells was lower than that of the monocrystalline-silicon ones. Moreover, Celik et al. [74] noted that the environmental impact based on the unit of electricity generated was higher than all the commercial PV technologies and this is mainly associated with the fact that perovskite solar cells show lower lifetimes.

Studies about LCA of perovskite solar cells have also been presented by Zhang et al. [75], Espinosa et al. [76], and Gong et al. [77].

### 2.5.6 Organic

In recent years, there are developments in the field of organic PV solar cells (thin-film cells based on organic/polymer materials which absorb sunlight and convert it into electricity). Chatzisideris et al. [78] highlighted that organic PVs are promising (in comparison with conventional PVs which are based on silicon) for improving the environmental and economic performance of PVs offering advantages (e.g., for BI applications)

such as low weight, flexibility, easy installation, and semitransparency. However, organic PVs show shorter lifetimes and lower power conversion efficiencies in comparison with conventional PV technologies.

Chatzisideris et al. [78] modeled the self-consumption of electricity generation of a system which is based on organic PVs and batteries. The life-cycle impacts in terms of climate change and human toxicity in an iron/metal industry were examined. It was found that the installation of an organic PV system without storage can offer decrease in the impact related to climate change, but it can increase human-toxicity impacts (in comparison to the electricity consumption from the Danish electricity grid). A specific case that was examined included coupling of an organic PV system with a sodium/nickel chloride battery. It was found that the sodium/nickel chloride battery is responsible for a considerable part of the environmental impact of the combined organic PV/battery system. Moreover, it was highlighted that the electricity mix of the country significantly influences the results [78].

Furthermore, dos Reis Benatto et al. [79] conducted an LCA study about organic PVs applied in the frame of a commercial product (solar charged power bank). The proposed configuration has a portable organic PV panel which offers the possibility to be charged from the sun (and not only from the grid). Issues related to the environmental impact and the phases of disposal and recycling were examined.

Hengevoss et al. [80] presented a work about LCA and eco-efficiency of prospective, flexible, tandem, and organic PV modules. It was found that the production of 1 $m^2$ tandem organic PV module shows only 3%–10% of the impact of 1 $m^2$ multicrystalline or CdTe module (in terms of GWP, CED, ecotoxicity, and metal depletion). Hengevoss et al. [80] concluded that for applications where the PV modules cannot be optimally oriented towards the sun, a flexible tandem organic PV could be a better alternative solution (in comparison to multicrystalline silicon and CdTe modules).

Additional studies about LCA of organic PVs have been presented by Anctil and Fthenakis [18], Lizin et al. [81], and Tsang et al. [82,83].

### 2.5.7 Dye-sensitized

Dye-sensitized is a specific category of solar cells. Greijer et al. [84] presented a configuration with Kay's monolithic series connected with a nanocrystalline dye-sensitized PV module. The process included chemical

vapor deposition of a transparent conducting coating such as fluorine doped $SnO_2$ as well as additional treatments. It was noted that the dye is adsorbed onto the photoelectrode and the electrolyte is filled in the porous layers. Greijer et al. [84] investigated environmental aspects about electricity generation based on nanocrystalline dye-sensitized solar cells, and they noted that these cells are very interesting for the future because of their simple construction and use of cheap and relatively benign materials.

Furthermore, de Wild-Scholten and Veltkamp [85] conducted an LCA study about dye-sensitized solar cells. The findings showed that the major contribution to the environmental impact in terms of the production phase is due to the glass substrate. Additional contributions are related to the energy consumption during the production of the dye-sensitized solar cells and the adoption of ruthenium, platinum, and silver in the modules. For Southern Europe (for a complete PV system with 8% efficient dye-sensitized modules) an EPBT of around 0.8 years was found. Moreover, the life-cycle GHG emissions were calculated to be 20 g $CO_{2.eq}$/kW h, depending on the life span of the systems.

Parisi and Basosi [86] conducted LCA of dye-sensitized solar cells. It was noted that this PV technology is interesting because it shows a potential for low-cost production and reduction in the environmental impact (in comparison to traditional silicon-based PV cells). However, these PV cells (at the moment; year of the study [86]: 2015) are not efficient enough to be competitive at industrial level. The environmental performance, based on LCA, of a virtual rooftop grid-connected PV system based on dye-sensitized solar cells was investigated.

### 2.5.8 Studies comparing different photovoltaic technologies

In the literature there are studies which compare different PV technologies, revealing which option is more environmentally friendly in each case. In the following paragraphs, selected references of this category are presented.

Perez-Gallardo et al. [87] investigated grid-connected PV systems according to technical, economic, and environmental criteria (for the environmental part of the study, IMPACT 2002 + method was used). Different PV technologies were examined: monocrystalline silicon, multicrystalline silicon, amorphous silicon, CdTe, and Copper Indium Diselenide (CIS). In addition, the PBT of investment and the EPBT were

evaluated. For each PV technology, a score, based on multiple criteria, was found. The option with the lowest total score was found to be amorphous silicon. Moreover, by taking into account the environmental impact per kW h of produced electricity, CIS showed the best results.

Itten and Stucki [62] investigated the environmental impact of monolithic silicon heterojunction organometallic perovskite tandem cells and single-junction organometallic perovskite solar cells. The study included comparisons with the impacts of crystalline silicon-based solar cells. The life-cycle results revealed that the environmental impact of monolithic silicon heterojunction organometallic perovskite tandem cells and single-junction organometallic perovskite solar cells is similar to or lower than the impact of conventional crystalline-silicon solar cells (having as basis comparable life spans) with the exception of the impact categories of mineral and fossil resource depletion.

Serrano-Luján et al. [4] investigated (based on LCA) crystalline silicon, thin-film (CdTe), and organic polymer-based PVs. Different countries were evaluated (in order to find the best geographical combination manufacturer-installation). The $CO_2$ emissions per $kW_p$ of installed PV capacity were evaluated.

Tsang et al. [83] compared (based on LCA) organic PVs with conventional-silicon PV technologies. It was found that the environmental advantages which are offered by the organic PVs extend beyond the material manufacturing phase and further reduction of their impact can be achieved by integrating organic PVs into simpler devices with flexibility. Organic PV charging units showed life-cycle impacts considerably lower in comparison to silicon-based configurations. Moreover, Tsang et al. [83] noted that recent developments in organic PV technology verify that this technology shows several advantages (easily printable; light, thin, and flexible solar panels; fast manufacturing).

Additional studies, which compare (from an environmental point of view) different PV technologies/configurations, have been presented by Frankl et al. [88], Alsema and Nieuwlaar [89], Fthenakis and Kim [90], Ling-Chin et al. [91], and Ito et al. [92].

### 2.5.9 Photovoltaic/thermal

PVT systems are a specific type of PV systems which produce, by means of one single device, electrical, and thermal energy. Depending on the working fluid PVT systems can be classified, for instance, into PVT/air

and PVT/water. Tripanagnostopoulos et al. [93,94] investigated, based on LCA, several PVT configurations (PVT/air, PVT/water, with/without reflectors, etc.). Michael and Selvarasan [95] conducted an LCA study about roof-mounted PVT systems. Menoufi et al. [96] presented an LCA work about a Building-Integrated Concentrating Photovoltaic/Thermal (BICPVT) scheme. By taking into account the fact that PVT configurations offer both electricity and thermal energy, it can be seen that they show interest from an LCA/environmental point of view [8]. In the literature about PVT, several review studies have been presented: Charalambous et al. [97], Daghigh et al. [98], Chow et al. [99], Reddy et al. [100], Besheer et al. [101], Lamnatou and Chemisana [8], and Joshi and Dhoble [102].

## 2.6 Life-cycle assessment of photovoltaic systems

### 2.6.1 Materials and manufacturing phase

Wolden et al. [103] note that it is expected that various type of crystalline silicon will dominate the market and there is potential to improve the first generation PV cells. In addition, in the global market, thin-film CdTe plays a pivotal role. Moreover, CIGS has gained a foothold in PV manufacturing. On the other hand, it was highlighted that even if there is a progress in dye-sensitized solar cells and organic PVs, these technologies are still limited (year of the study [103]: 2011) by their low efficiency and stability. With respect to glass, unless glass can be replaced, costs will remain high. Another challenge is related to material availability, if material availability becomes a constraint factor in relation to TW/year manufacturing, this will probably favor the PV technologies which are based on silicon [103].

### 2.6.2 The role of sunlight concentration

Solar concentrators are devices that concentrate sunlight. PVs can be combined with concentrators, and these systems are known as CPV. In the case of CPVs, sunlight is focused onto the PV cell, for example, by means of reflective or refractive optical devices, and CPVs are characterized by their CR [104]. CR is the ratio between the aperture area of the primary concentrator and the active cell area [105].

In general, CPV systems show higher efficiencies in comparison to PV systems without concentration. However, this can be achieved in an

effective way by keeping PV temperature as low as possible because temperature is a critical factor [104]. Certainly, higher PV output during CPV system life-cycle is favorable for certain environmental indicators which include the lifetime energy output of a system. Another critical factor for CPV systems is the uniform distribution of the concentrated solar radiation on PV surface [104].

Regarding materials, the use of devices for sunlight concentration means that less PV-cell material is used and, in this way, there is replacement of the expensive PV cells with a cheaper concentrating device [104]. Furthermore, the use of less PV-cell material offers benefits from an environmental point of view [105].

Concerning CR, it should be highlighted that CR affects CPV environmental profile. In the literature about CPV LCA, there is a study (based on LCA) with sensitivity analysis (according to EI99 method) for a BICPVT scheme and for different CRs [96]. The results demonstrated that, in general terms, the increase of CR reduces CPV system environmental impact but this needs further investigation because CR increase results in higher optical losses [96].

### 2.6.3 Nanomaterials and nanofluids

In the literature about PVs, there are some studies which place emphasis on the role of nanomaterials in PV technology. For instance, Kumar et al. [106] presented a review about different generations of solar cells, focusing on nanomaterial-based solar cells such as quantum dot sensitized solar cells. It was mentioned that, in recent years, there are considerable improvements in terms of the energy-conversion efficiency of the solar cells mentioned above. Kumar et al. [106] also noted that these solar cells are promising alternatives to conventional crystalline and thin-film PVs, offering advantages such as high performance, low cost, and easy fabrication.

In addition, Yu et al. [107] presented a review article about nanomaterials and nanostructures for efficient light absorption and PV cells. Several advantages which are provided by nanomaterials/nanostructures (in comparison to their thin-film/bulk counterparts) were highlighted: remarkable improvement in terms of photon capturing and photo-carrier collection capability, PV mechanism exceeding thermo-dynamic limits, low cost. Different materials and structures were presented: nanowires, nanopillars, nanocones, nanodomes, nanoparticles, and other configurations,

including materials such as crystalline silicon, amorphous silicon, CdS, cadmium selenide, CdTe, ZnO, and CIS.

With respect to nanomaterials for PV conversion, Davenas et al. [108] highlighted the strong influence of molecular morphology on the nanocomposite properties. The considerable improvements which can be obtained in terms of the performances of the organic solar cells were discussed. In light of the studies mentioned above, Brennan et al. [109] conducted a study about carbon nanomaterials for dye-sensitized solar cell applications. Chen et al. [110] presented a review about nanomaterials for PVs and it was noted that nanochemical interface engineering of nanoparticle surfaces and junction-interfaces offer enhanced charge separation and collection. The issue of harvesting underutilized ultraviolet and unutilized infrared photons was discussed. In addition, Sharma et al. [111] investigated a nanoenhanced Phase Change Material (PCM) for thermal management of a BICPV system.

In the case of PV modules which offer production of electricity and heat (PVT modules), the working fluid plays an important role. For example, there is a study about a PVT operating with water and nanofluid. A detailed thermal model for the collector was developed and validated. It was found that the nanofluid results in a higher thermal performance in all the operating conditions which were examined [112].

### 2.6.4 Storage and materials

Given the fact that batteries are commonly used as storage for PV applications, the present subsection places emphasis on these types of storage systems.

Barnhart and Benson [113] investigated the reduction in energetic and material demands of electrical energy storage, based on different technologies: Lithium ion (Li-ion), sodium sulfur and lead-acid (PbA) batteries; vanadium redox batteries and zinc bromine flow batteries; Pumped Hydroelectric Storage (PHS) and Compressed Air Energy Storage (CAES). Barnhart and Benson [113] noted that electrochemical storage technologies are expected to impinge on global energy supplies whereas PHS and CAES are less energy intensive. On the other hand, an increase in electrochemical storage cycle life by tenfold would remarkably relax the energetic constraints of grid-storage [113].

Regarding batteries, their life span and, therefore, their replacements during the phase of usage, can considerably affect the environmental performance of a storage system. Kabir and Demirocak [114] highlighted that

the degradation of Li-ion batteries can have chemical as well as mechanical origins.

Hiremath et al. [115] presented a comparative LCA, based on CED and GWP, for four stationary battery technologies: lithium ion, PbA, sodium–sulfur, and vanadium-redox-flow. The study included a complete utilization of the cycle life and six different stationary applications. A qualitative analysis of the lithium-ion option was conducted so as to examine the impacts related to its process chains based on midpoint impact categories of ReCiPe 2008 method. The findings demonstrated that, in general, the use phase of the batteries considerably influences their life-cycle impacts. Hiremath et al. [115] suggested the development of batteries with higher round-trip efficiencies.

Vandepaer et al. [116] conducted an LCA study, according to IMPACT 2002 + method, in order to evaluate the environmental impact of lithium-metal-polymer and lithium-ion stationary batteries. It was found that battery manufacturing is responsible for the major part of the environmental impact. Based on global warming and ozone depletion, Li-ion batteries showed remarkably higher impacts in comparison to lithium-metal-polymer ones. Furthermore, the results of the study by Vandepaer et al. [116] demonstrated that lithium-metal-polymer batteries presented higher impacts in terms of aquatic eutrophication.

At this point it should be noted that, with the exception of the storage systems mentioned above, there is also the solution of hydrogen. An example is the project MYRTE (Mission hYdrogène Renouvelable pour l' inTégration au réseau Electrique) at the laboratory "Sciences Pour l'Environnement" (Centre de Recherches Scientifiques Georges Peri, Ajaccio, France, University of Corsica). MYRTE includes a storage system with hydrogen and fuel cells for a PV system [117].

On the other hand, another storage solution is the use of PCMs which are materials with high latent heat and other desirable thermophysical properties, appropriate for different applications, for instance in buildings. An example is the study by Sharma et al. [111] about PCM for thermal management of BICPV configurations.

### 2.6.5 Roles of the heat transfer fluid (for photovoltaic/thermal) and integration into the building (relative to photovoltaics for buildings)

It is known that the heat transfer fluid influences the environmental profile of a PVT system. Tripanagnostopoulos et al. [93] mentioned that

natural or forced air circulation is a low-cost and simple solution to remove heat from PV panels but it is less effective at low latitudes with high ambient air temperatures. In addition, Tripanagnostopoulos et al. [94] presented comparisons between PVT/air and PVT/water systems. It was highlighted that cost PBTs, EPBTs, and $CO_2$ PBTs were found to be higher for the studied PVT/air configurations (in comparison to the PVT/water ones) because of the lower thermal efficiency of the air heat extraction. At this point it should be noted that, with the exception of the above-mentioned configurations of PVT/water and PVT/air, there are also bifluid PVT systems [118].

In the specific case of BI applications, literature studies show that the building integration of a solar system (apart from the benefits that offers: high esthetic value, etc.) may reduce the energy production of the system and, therefore, the environmental performance of the BI solar system is influenced [119,120].

### 2.6.6 Life span, durability of the materials, recycling, end-of-life

The durability of the materials/components, for example, of a solar system is an important factor because it is related to its ability to resist wear and tear during the phase of usage; and therefore the durability influences the environmental profile of a system. More durable components with longer lifetime need few (or no) replacements during the use phase of a system [119,120].

Certainly, a product that can be easily recycled will normally be preferable in a comparison to a product that cannot be recycled. For example, building industry includes materials which have poor durability and low recycling potential whereas there are other materials that can be recycled several times. The potential for material recycling depends on the purity of an item and it should be taken into account that, in certain cases, the separation of different constituents can be a difficult process, costly or near impossible [121].

Fthenakis [2] noted that PV recycling is feasible from a technological and an economical point of view; however, there is a need for careful forethought. A recycling program was examined. Issues such as reclaiming metals from used solar panels, smelting and refining were discussed. Fthenakis [2] mentioned that separating the PV materials from the glass leads to a considerable decrease in the amount of waste generated.

Corcelli et al. [122] mentioned that, by taking into account PV-market growth, it is important to evaluate the impacts associated with the end-of-life of PV panels. Furthermore, it was noted that, in recent years, there is a development of many industrial processes for recycling of PV panels. One recycling process for crystalline-silicon PV technology is based on thermal treatment in order to separate the PV cells from the glass. Corcelli et al. [122] highlighted that this treatment may include certain hazardous materials (e.g., Cd, Pb, and Cr) and, therefore, there is a need for accurate handling. The results of Corcelli et al. [122] revealed that the studied recovery process shows a positive effect in terms of all the analyzed impact categories, especially in terms of the following impact categories: freshwater eutrophication, human toxicity, terrestrial acidification, and fossil depletion. It was noted that the major environmental advantages are related to the recovery of aluminum and silicon. In addition, the recovered materials (e.g., silicon, aluminum, and copper) offer benefits from an economic point of view [122].

Perez-Gallardo et al. [123] investigated the advantages (based on environmental and techno-economic criteria) of including PV-module recycling at the initial design stages of PV grid-connected systems. Recycling scenarios for crystalline-silicon and CdTe PV modules were examined. An eco-design methodology was applied. In the case of crystalline-silicon PVs, recycling considerably reduced EPBT as well as GWP. For thin-film CdTe PVs, the findings verified the environmental advantages due to glass-cullet and copper recycling. Perez-Gallardo et al. [123] noted that PV-module end-of-life management should be studied in-depth in order to evaluate potential benefits from an environmental and an economic point of view. Moreover, the importance of the end-of-life management for silicon-based and CdTe PV panels has been highlighted by Vellini et al. [124].

Bogacka et al. [125] presented PV LCA, placing emphasis on PV-cell waste scenarios. Silicon standard PV cells and ReCiPe method were adopted. It was noted that in the future, rapid increase in the volume of PV-cell waste is expected.

Latunussa et al. [126] investigated, based on LCA, a process for recycling of crystalline-silicon PV panels. The process includes mechanical and thermal treatments followed by processes with acid leaching and electrolysis. Latunussa et al. [126] noted that the impacts are mainly related to the incineration of the encapsulation layers of the panels, followed by the treatments for recovering of the silicon metal, silver, copper, and aluminum.

Goe and Gaustad [127] estimated direct climate impacts of end-of-life PV recovery, placing emphasis on the United States. A case study was examined and the findings showed that the PV-waste environmental impacts depend on different parameters such as the emission factors of electricity and the geographic dispersion.

Held [70] noted that the PV manufacturers identified that there is a need for research on the treatment of used PV modules and recycling processes. In terms of thin-film technologies, the recycling of the used modules can offer recovery of rare metals such as Te or indium. Held [70] investigated recycling of CdTe modules and the importance of recycling (in the case of CdTe modules) was highlighted.

## 2.7 Conclusions

The present chapter is an overview about LCA of different PV technologies. Selected literature references are cited. In addition, a critical discussion is provided.

The literature review shows that there are investigations for multiple climatic conditions and different PV technologies, but most of these studies are about monocrystalline and multicrystalline silicon. Therefore it can be seen that more LCA investigations about other types of PV technologies (multijunction, CIGS, CdTe, perovskite, organic, etc.) are necessary. Moreover, the issues most commonly studied are embodied energy, EPBT, $CO_2$, and GHG emissions and, consequently, there is a need for more LCA studies based on methods with midpoint and/or endpoint approaches. In the case of PVs for building applications, it can be noted that most of the studied PV systems are BA, and this means that more LCA investigations about BI configurations are needed.

On the other hand, the literature studies demonstrate that there are multiple parameters that affect the environmental performance of a PV system such as the latitude, the climatic conditions, the type of integration into the building (in the case of PVs for building applications), the electricity mix of a country (for certain environmental indicators), PV-cell material, the processes during material manufacturing phase, the use (or not) of solar concentrating devices, the storage materials, recycling, end-of-life, and durability of the adopted materials.

## References


[1] E. Nieuwlaar, E. Alsema, Environmental Aspects of PV Power Systems. IEA PVPS Task 1. Workshop 25–27 June 1997, Utrecht, The Netherlands, 1997. Report no. 97072. December 1997.

[2] V.M. Fthenakis, End-of-life management and recycling of PV modules, Energy Policy 28 (2000) 1051–1058.

[3] M.J.R. Perez, V.M. Fthenakis, H.-C. Kim, A.O. Pereira, Facade BIPV—the environmental life-cycle value proposition, in: Proc. ASES National Solar Conference, May 17–21, 2011, Raleigh, NC, 2011.

[4] L. Serrano-Luján, N. Espinosa, J. Abad, A. Urbina, The greenest decision on photovoltaic system allocation, Renew. Energy 101 (2017) 1348–1356.

[5] P. Pérez-López, B. Gschwind, P. Blanc, et al., ENVI-PV: an interactive Web Client for multi-criteria life cycle assessment of photovoltaic systems worldwide, Prog. Photovolt.: Res. Appl. 25 (2017) 484–498.

[6] M. Tripathy, P.K. Sadhu, S.K. Panda, A critical review on building integrated photovoltaic products and their applications, Renew. Sustain. Energy Rev. 61 (2016) 451–465.

[7] T. Ibn-Mohammed, S.C.L. Koh, I.M. Reaney, et al., Perovskite solar cells: an integrated hybrid lifecycle assessment and review in comparison with other photovoltaic technologies, Renew. Sustain. Energy Rev. 80 (2017) 1321–1344.

[8] Chr. Lamnatou, D. Chemisana, Photovoltaic/thermal (PVT) systems: a review with emphasis on environmental issues, Renew. Energy 105 (2017) 270–287.

[9] J. Kim, J.L. Rivera, T.Y. Meng, et al., Review of life cycle assessment of nanomaterials in photovoltaics, Solar Energy 133 (2016) 249–258.

[10] B. Parida, S. Iniyan, R. Goic, A review of solar photovoltaic technologies, Renew. Sustain. Energy Rev. 15 (2011) 1625–1636.

[11] M. Grágeda, M. Escudero, W. Alavia, et al., Review and multi-criteria assessment of solar energy projects in Chile, Renew. Sustain. Energy Rev. 59 (2016) 583–596.

[12] SAIC, Life Cycle Assessment: Principles and Practice, Scientific Applications International Corporation (SAIC), May 2006. Contract No. 68-C02-067. Work Assignment 3-15. EPA/600/R-06/060.

[13] ILCD Handbook, International Reference Life Cycle Data System, Analysis of Existing Environmental Impact Assessment Methodologies for Use in Life Cycle Assessment, European Commission, Joint Research Centre, Institute for Environment and Sustainability, Italy, 2010.

[14] V. Fthenakis, R. Frischknecht, M. Raugei, et al., Methodology Guidelines on Life Cycle Assessment of Photovoltaic Electricity. Second ed. IEA PVPS Task 12, International Energy Agency. Photovoltaic Power systems Programme, 2011.

[15] ISO 14040:2006, Environmental Management – Life Cycle Assessment – Principles and Framework, 2006.

[16] ISO 14044:2006, Environmental Management – Life Cycle Assessment – Requirements and Guidelines, 2006.

[17] G.P. Hammond, C.I. Jones, Embodied energy and carbon in construction materials, Proc. Inst. Civ. Eng. Energy 161 (2) (2008) 87–98.

[18] A. Anctil, V. Fthenakis, in: V. Fthenakis (Ed.), Life Cycle Assessment of Organic Photovoltaics, Third Generation Photovoltaics, InTech, 2012. 978-953-51-0304-2 Available from: <http://www.intechopen.com/books/third-generation-photovoltaics/life-cycle-assessment-of-organicphotovoltaics>.

[19] T.T. Chow, J. Ji, Environmental life-cycle analysis of hybrid solar photovoltaic/thermal systems for use in Hong Kong, Int. J. Photoenergy 2012 (2012) 101968. Available from: https://doi.org/10.1155/2012/101968. 9 pages.

[20] Chr. Lamnatou, H. Baig, D. Chemisana, T.K. Mallick, Dielectric-based 3D building-integrated concentrating photovoltaic modules: an environmental life-cycle assessment, Energy Build. 138 (2017) 514–525.
[21] M. Raugei, P. Fullana-i-Palmer, V. Fthenakis, The energy return on energy investment (EROI) of photovoltaics: methodology and comparisons with fossil fuel life cycles, Energy Policy 45 (2012) 576–582.
[22] PRé, Various Authors. SimaPro Database Manual. Methods Library. Report Version 2.6, May 2014.
[23] Chr. Lamnatou, D. Chemisana, Evaluation of photovoltaic-green and other roofing systems by means of ReCiPe and multiple life cycle-based environmental indicators, Build. Environ. 93 (2015) 376–384.
[24] B. Evon, J. Payet, I. Blanc, et al., Methodological framework for assessing the environmental impacts of photovoltaics systems using the LCA method, in: 6th International Conference on Life Cycle Management, August 2013, Gothenburg, Sweden, 2013.
[25] V. Fthenakis, Photovoltaics: Present Status and Future Prospects, Center for Life Cycle Analysis, Columbia University, New York, 2012. 56 pp.
[26] W. Luo, Y.S. Khoo, A. Kumar, et al., A comparative life-cycle assessment of photovoltaic electricity generation in Singapore by multicrystalline silicon technologies, Solar Energy Mater. Solar Cells 174 (2018) 157–162.
[27] A. Louwen, W.G.J.H.M. van Sark, R.E.I. Schropp, et al., Life-cycle greenhouse gas emissions and energy payback time of current and prospective silicon heterojunction solar cell designs, Prog. Photovolt.: Res. Appl. 23 (2015) 1406–1428.
[28] W. Wang, Y. Liu, X. Wu, et al., Environmental assessments and economic performance of BAPV and BIPV systems in Shanghai, Energy Build. 130 (2016) 98–106.
[29] N. Jungbluth, C. Bauer, R. Dones, R. Frischknecht, Life cycle assessment for emerging technologies: case studies for photovoltaic and wind power, Int. J. LCA 10 (1) (2005) 24–34.
[30] R. Battisti, A. Corrado, Evaluation of technical improvements of photovoltaic systems through life cycle assessment methodology, Energy 30 (2005) 952–967.
[31] I. Nawaz, G.N. Tiwari, Embodied energy analysis of photovoltaic (PV) system based on macro- and micro-level, Energy Policy 34 (2006) 3144–3152.
[32] M. Bravi, M.L. Parisi, E. Tiezzi, R. Basosi, Life cycle assessment of a micromorph photovoltaic system, Energy 36 (2011) 4297–4306.
[33] Á.A. Bayod-Rújula, A.M. Lorente-Lafuente, F. Cirez-Oto, Environmental assessment of grid connected photovoltaic plants with 2-axis tracking versus fixed modules systems, Energy 36 (2011) 3148–3158.
[34] U. Desideri, S. Proietti, F. Zepparelli, et al., Life cycle assessment of a ground-mounted 1778 $kW_p$ photovoltaic plant and comparison with traditional energy production systems, Appl. Energy 97 (2012) 930–943.
[35] Chr. Lamnatou, D. Chemisana, Photovoltaic-green roofs: a life cycle assessment approach with emphasis on warm months of Mediterranean climate, J. Clean. Prod. 72 (2014) 57–75.
[36] A. Nicholls, R. Sharma, T.K. Saha, Financial and environmental analysis of rooftop photovoltaic installations with battery storage in Australia, Appl. Energy 159 (2015) 252–264.
[37] Chr. Lamnatou, H. Baig, D. Chemisana, T.K. Mallick, Life cycle energy analysis and embodied carbon of a linear dielectric-based concentrating photovoltaic appropriate for building-integrated applications, Energy Build. 107 (2015) 366–375.
[38] T. Wetzel, S. Borchers, Update of energy payback time and greenhouse gas emission data for crystalline silicon photovoltaic modules, Prog. Photovolt.: Res. Appl. 23 (2015) 1429–1435.

[39] Y. Fu, X. Liu, Z. Yuan, Life-cycle assessment of multi-crystalline photovoltaic (PV) systems in China, J. Clean. Prod. 86 (2015) 180–190.
[40] K. Collins, B. Powell, A. Anctil. Life cycle assessment of Silicon Solar Panels manufacturing in United States. in: 2015 IEEE 42nd Photovoltaic Specialist Conference (PVSC), 14–19 June 2015. IEEE, New Orleans, LA, 2015.
[41] W. Chen, J. Hong, X. Yuan, J. Liu, Environmental impact assessment of monocrystalline silicon solar photovoltaic cell production: a case study in China, J. Clean. Production 112 (2016) 1025–1032.
[42] J. Hong, W. Chen, C. Qi, et al., Life cycle assessment of multicrystalline silicon photovoltaic cell production in China, Solar Energy 133 (2016) 283–293.
[43] G.L. Tiago Filho, C.A. Rosa, R.M. Barros, et al., Study of the energy balance and environmental liabilities associated with the manufacture of crystalline Si photovoltaic modules and deployment in different regions, Solar Energy Mater. Solar Cells 144 (2016) 383–394.
[44] Chr. Lamnatou, H. Baig, D. Chemisana, T.K. Mallick, Environmental assessment of a building-integrated linear dielectric-based concentrating photovoltaic according to multiple life-cycle indicators, J. Clean. Production 131 (2016) 773–784.
[45] T.F. Kristjansdottir, C.S. Good, M.R. Inman, et al., Embodied greenhouse gas emissions from PV systems in Norwegian residential Zero Emission Pilot Buildings, Solar Energy 133 (2016) 155–171.
[46] M. Beccali, M. Cellura, S. Longo, F. Guarino, Solar heating and cooling systems versus conventional systems assisted by photovoltaic: application of a simplified LCA tool, Solar Energy Mater. Solar Cells 156 (2016) 92–100.
[47] A. Petrillo, F. De Felice, E. Jannelli, et al., Life cycle assessment (LCA) and life cycle cost (LCC) analysis model for a stand-alone hybrid renewable energy system, Renew. Energy 95 (2016) 337–355.
[48] G. Hou, H. Sun, Z. Jiang, et al., Life cycle assessment of grid-connected photovoltaic power generation from crystalline silicon solar modules in China, Appl. Energy 164 (2016) 882–890.
[49] N. Gazbour, G. Razongles, C. Schaeffer, C. Charbuillet, Photovoltaic power goes green, in: 2016 Electronics Goes Green 2016 + (EGG), IEEE, 2016.
[50] C. Jones, V. Peshev, P. Gilbert, S. Mander, Battery storage for post-incentive PV uptake? A financial and life cycle carbon assessment of a non-domestic building, J. Clean. Prod. 167 (2017) 447–458.
[51] Z. Yu, W. Ma, K. Xie, et al., Life cycle assessment of grid-connected power generation from metallurgical route multi-crystalline silicon photovoltaic system in China, Appl. Energy 185 (2017) 68–81.
[52] G.Y. Palacios-Jaimes, P. Martín-Ramos, F.J. Rey-Martínez, I.A. Fernández-Coppel, Transformation of a University Lecture Hall in Valladolid (Spain) into a NZEB: LCA of a BIPV system integrated in its Façade, Int. J. Photoenergy 2017 (2017) 2478761. Available from: https://doi.org/10.1155/2017/2478761. 11 pages.
[53] D.O. Akinyele, R.K. Rayudu, N.K.C. Nair, Life cycle impact assessment of photovoltaic power generation from crystalline silicon-based solar modules in Nigeria, Renew. Energy 101 (2017) 537–549.
[54] F. Murphy, K. McDonnell, A feasibility assessment of photovoltaic power systems in Ireland; a case study for the dublin region, Sustainability 2017 (9) (2017) 302. Available from: https://doi.org/10.3390/su9020302.
[55] B. Huang, J. Zhao, J. Chai, et al., Environmental influence assessment of China's multi-crystalline silicon (multi-Si) photovoltaic modules considering recycling process, Solar Energy 143 (2017) 132–141.
[56] US Department of Energy, Multijunction III-V Photovoltaics Research, <https://www.energy.gov/eere/solar/multijunction-iii-v-photovoltaics-research>.

[57] V.M. Fthenakis, H.C. Kim, Life cycle assessment of high-concentration photovoltaic systems, Prog. Photovolt.: Res. Appl. 21 (2013) 379–388.
[58] P. Sandwell, G. Duggan, J. Nelson, N. Ekins-Daukes, The environmental impact of lightweight HCPV modules: efficient design and effective deployment, Prog. Photovolt.: Res. Appl. 24 (2016) 1458–1472.
[59] N. Espinosa, F.C. Krebs, Life cycle analysis of organic tandem solar cells: when are they warranted? Solar Energy Mater. Solar Cells 120 (2014) 692–700.
[60] H.C. Kim, V.M. Fthenakis, Comparative life-cycle energy payback analysis of multi-junction a-SiGe and nanocrystalline/a-Si modules, Prog. Photovolt.: Res. Appl. 19 (2011) 228–239.
[61] M. Stucki, R. Itten, High efficient 3rd generation multi-junction solar cells using silicon heterojunction and perovskite technology: life cycle based environmental impacts. Available from: <https://pd.zhaw.ch/publikation/upload/213148.pdf>, 2017.
[62] R. Itten, M. Stucki, Highly efficient 3rd generation multi-junction solar cells using silicon heterojunction and perovskite tandem: prospective life cycle environmental impacts, Energies 10 (2017) 841. Available from: https://doi.org/10.3390/en10070841.
[63] S. Amarakoon, C. Vallet, M.A. Curran, et al., Life cycle assessment of photovoltaic manufacturing consortium (PVMC) copper indium gallium (di)selenide (CIGS) modules, Int. J. Life Cycle Assess 23 (4) (2017) 851–866.
[64] P. Jayathissa, M. Jansen, N. Heeren, et al., Life cycle assessment of dynamic building integrated photovoltaics, Solar Energy Mater. Solar Cells 156 (2016) 75–82.
[65] M. Kaelin, D. Rudmann, A.N. Tiwari, Low cost processing of CIGS thin film solar cells, Solar Energy 77 (2004) 749–756.
[66] SVTC, Toward a Just and Sustainable Solar Energy Industry, A silicon valley toxics coalition. White Paper, 14 January 2009.
[67] M. Raugei, S. Bargigli, S. Ulgiati, Energy and life cycle assessment of thin film CdTe photovoltaic modules, 2005. Available from: <www.civil.uwaterloo.ca/beg/Downloads/NREL_PV_Embodied_Energy.pdf>.
[68] H. Kim, K. Cha, V.M. Fthenakis, et al., Life cycle assessment of cadmium telluride photovoltaic (CdTe PV) systems, Solar Energy 103 (2014) 78–88.
[69] M. Held, R. Ilg, Life cycle assessment (LCA) of CdTe thin film PV modules and material flow analysis (MFA) of cadmium within EU27, in: 23rd European Photovoltaic Solar Energy Conference and Exhibition, 1–5 September 2008, Valencia, Spain, 2008, https://doi.org/10.4229/23rdEUPVSEC2008-3BV.4.25.
[70] M. Held, Life cycle assessment of CdTe module recycling, in: 24th European Photovoltaic Solar Energy Conference, 21–25 September 2009, Hamburg, Germany, 2009, https://doi.org/10.4229/24thEUPVSEC2009-3CO.7.4.
[71] A.J. Rix, J.D.T. Steyl, J. Rudman, et al., First Solar's CdTe Module Technology – Performance, Life Cycle, Health and Safety Impact Assessment, Stellenbosch University. Centre for Renewable and Sustainable Energy Studies, 15 December 2015.
[72] M.K. Assadi, S. Bakhoda, R. Saidur, H. Hanaei, Recent progress in perovskite solar cells, Renew. Sustain. Energy Rev. 81 (2018) 2812–2822.
[73] M.M. Lunardi, A.W.Y. Ho-Baillie, J.P. Alvarez-Gaitan, et al., A life cycle assessment of perovskite/silicon tandem solar cells, Prog. Photovolt.: Res. Appl. 25 (2017) 679–695.
[74] I. Celik, Z. Song, A.J. Cimaroli, et al., Life cycle assessment (LCA) of perovskite PV cells projected from lab to fab, Solar Energy Mater. Solar Cells 156 (2016) 157–169.
[75] J. Zhang, X. Gao, Y. Deng, et al., Comparison of life cycle environmental impacts of different perovskite solar cell systems, Solar Energy Mater. Solar Cells 166 (2017) 9–17.

[76] N. Espinosa, L. Serrano-Luján, A. Urbina, F.C. Krebs, Solution and vapour deposited lead perovskite solar cells: ecotoxicity from a life cycle assessment perspective, Solar Energy Mater. Solar Cells 137 (2015) 303–310.
[77] J. Gong, S.B. Darling, F. You, Perovskite photovoltaics: life-cycle assessment of energy and environmental impacts, Energy Environ. Sci. 8 (2015) 1953–1968.
[78] M.D. Chatzisideris, A. Laurent, M.Z. Hauschild, F.C. Krebs, Environmental impacts of electricity self-consumption from organic photovoltaic battery systems at industrial facilities in Denmark, CIRP Ann. Manuf. Technol. 66 (2017) 45–48.
[79] G.A. dos Reis Benatto, N. Espinosa, F.C. Krebs, Life-cycle assessment of solar charger with integrated organic photovoltaics, Adv. Eng. Mater. 19 (2017) 1700124.
[80] D. Hengevoss, C. Baumgartner, G. Nisato, C. Hugi, Life cycle assessment and eco-efficiency of prospective, flexible, tandem organic photovoltaic module, Solar Energy 137 (2016) 317–327.
[81] S. Lizin, S.V. Passel, E. De Schepper, et al., Life cycle analyses of organic photovoltaics: a review, Energy Environ. Sci. 6 (2013) 3136.
[82] M.P. Tsang, G.W. Sonnemann, D.M. Bassani, A comparative human health, ecotoxicity, and product environmental assessment on the production of organic and silicon solar cells, Prog. Photovolt.: Res. Appl. 24 (2015) 645–655.
[83] M.P. Tsang, G.W. Sonnemann, D.M. Bassani, Life-cycle assessment of cradle-to-grave opportunities and environmental impacts of organic photovoltaic solar panels compared to conventional technologies, Solar Energy Mater. Solar Cells 156 (2016) 37–48.
[84] H. Greijer, L. Karlson, S.-E. Lindquist, A. Hagfeldt, Environmental aspects of electricity generation from a nanocrystalline dye sensitized solar cell system, Renew. Energy 23 (2001) 27–39.
[85] M.J. de Wild-Scholten, A.C. Veltkamp, Environmental Life Cycle Analysis of Dye Sensitized Solar Devices; Status and Outlook, ECN, Netherlands, 2007.
[86] M.L. Parisi, R. Basosi, Environmental life cycle analysis of nonconventional thin-film photovoltaics: the case of dye-sensitized solar devices, in: B. Reddy, S. Ulgiati (Eds.), Energy Security and Development, Springer, New Delhi, 2015, pp. 195–210.
[87] J.R. Perez-Gallardo, C. Azzaro-Pantel, S. Astier, et al., Ecodesign of photovoltaic grid-connected systems, Renew. Energy 64 (2014) 82–97.
[88] P. Frankl, A. Masini, M. Gamberale, D. Toccaceli, Simplified life-cycle analysis of PV systems in buildings: present situation and future trends, Prog. Photovolt.: Res. Appl. 6 (1998) 137–146.
[89] E.A. Alsema, E. Nieuwlaar, Energy viability of photovoltaic systems, Energy Policy 28 (2000) 999–1010.
[90] V.M. Fthenakis, H.C. Kim, Greenhouse-gas emissions from solar electric- and nuclear power: a life-cycle study, Energy Policy 35 (2007) 2549–2557.
[91] J. Ling-Chin, O. Heidrich, A.P. Roskilly, Life cycle assessment (LCA) – from analysing methodology development to introducing an LCA framework for marine photovoltaic (PV) systems, Renew Sustain. Energy Rev. 59 (2016) 352–378.
[92] M. Ito, S. Lespinats, J. Merten, et al., Life cycle assessment and cost analysis of very large-scale PV systems and suitable locations in the world, Prog. Photovolt.: Res. Appl. 24 (2016) 159–174.
[93] Y. Tripanagnostopoulos, M. Souliotis, R. Battisti, A. Corrado, Energy, cost and LCA results of PV and hybrid PV/T solar systems, Prog. Photovolt.: Res. Appl. 13 (2005) 235–250.
[94] Y. Tripanagnostopoulos, M. Souliotis, R. Battisti, A. Corrado, Performance, cost and life-cycle assessment study of hybrid PVT/AIR solar systems, Prog. Photovolt.: Res. Appl. 14 (2006) 65–76.

[95] J.J. Michael, I. Selvarasan, Economic analysis and environmental impact of flat plate roof mounted solar energy systems, Solar Energy 142 (2017) 159–170.
[96] K. Menoufi, D. Chemisana, J.I. Rosell, Life cycle assessment of a building integrated concentrated photovoltaic scheme, Appl. Energy 111 (2013) 505–514.
[97] P.G. Charalambous, G.G. Maidment, S.A. Kalogirou, K. Yiakoumetti, Photovoltaic thermal (PV/T) collectors: a review, Appl. Thermal Eng. 27 (2007) 275–286.
[98] R. Daghigh, M.H. Ruslan, K. Sopian, Advances in liquid based photovoltaic/thermal (PV/T) collectors, Renew. Sustain. Energy Rev. 15 (2011) 4156–4170.
[99] T.T. Chow, G.N. Tiwari, C. Menezo, Hybrid solar: a review on photovoltaic and thermal power integration, Int. J. Photoenergy 2012 (2012) 307287. Available from: https://doi.org/10.1155/2012/307287. 17 pages.
[100] S.R. Reddy, M.A. Ebadian, C.-X. Lin, A review of PV–T systems: thermal management and efficiency with single phase cooling, Int. J. Heat Mass Trans. 91 (2015) 861–871.
[101] A.H. Besheer, M. Smyth, A. Zacharopoulos, et al., Review on recent approaches for hybrid PV/T solar technology, Int. J. Energy Res. 40 (2016) 2038–2053.
[102] S.S. Joshi, A.S. Dhoble, Photovoltaic–thermal systems (PVT): technology review and future trends, Renew. Sustain. Energy Rev. 92 (2018) 848–882.
[103] C.A. Wolden, J. Kurtin, J.B. Baxter, et al., Photovoltaic manufacturing: present status, future prospects, and research needs American Vacuum Society, J. Vac. Sci. Technol. A 29 (3) (2011) 030801. Available from: https://doi.org/10.1116/1.3569757.
[104] Y. Tripanagnostopoulos, Aspects and improvements of hybrid photovoltaic/thermal solar energy systems, Solar Energy 81 (2007) 1117–1131.
[105] D. Chemisana, Building integrated concentrating photovoltaics: a review, Renew. Sustain. Energy Rev. 15 (2011) 603–611.
[106] S. Kumar, M. Nehra, A. Deep, et al., Quantum-sized nanomaterials for solar cell applications, Renew. Sustain. Energy Rev. 73 (2017) 821–839.
[107] R. Yu, Q. Lin, S.-F. Leung, Z. Fan, Nanomaterials and nanostructures for efficient light absorption and photovoltaics, Nano Energy 1 (2012) 57–72.
[108] J. Davenas, A. Ltaief, V. Barlier, et al., Nanomaterials for photovoltaic conversion, Mater. Sci. Eng., C 28 (2008) 744–750.
[109] L.J. Brennan, M.T. Byrne, M. Bari, Y.K. Gun'ko, Carbon nanomaterials for dye-sensitized solar cell applications: a bright future, Adv. Energy Mater. 1 (2011) 472–485.
[110] G. Chen, J. Seo, C. Yang, P.N. Prasad, Nanochemistry and nanomaterials for photovoltaics, Chem. Soc. Rev. 42 (2013) 8304–8338.
[111] S. Sharma, L. Micheli, W. Chang, et al., Nano-enhanced phase change material for thermal management of BICPV, Appl. Energy 208 (2017) 719–733.
[112] E. Bellos, C. Tzivanidis, Yearly performance of a hybrid PV operating with nanofluid, Renew. Energy 113 (2017) 867–884.
[113] C.J. Barnhart, S.M. Benson, On the importance of reducing the energetic and material demands of electrical energy storage, Energy Environ Sci. 6 (2013) 1083–1092.
[114] M.M. Kabir, D.E. Demirocak, Degradation mechanisms in Li-ion batteries: a state-of-the-art review, Int. J. Energy Res. 41 (14) (2017) 1963–1986.
[115] M. Hiremath, K. Derendorf, T. Vogt, Comparative life cycle assessment of battery storage systems for stationary applications, Environ. Sci. Technol. 49 (2015) 4825–4833.

[116] L. Vandepaer, J. Cloutier, B. Amor, Environmental impacts of lithium metal polymer and lithium-ion stationary batteries, Renew. Sustain. Energy Rev. 78 (2017) 46–60.
[117] MYRTE. Available from: <http://myrte.univ-corse.fr/La-plateforme_a4.html>.
[118] Y.B. Assoa, C. Menezo, G. Fraisse, et al., Study of a new concept of photovoltaic–thermal hybrid collector, Solar Energy 81 (2007) 1132–1143.
[119] Chr. Lamnatou, G. Notton, D. Chemisana, C. Cristofari, Life cycle analysis of a building-integrated solar thermal collector, based on embodied energy and embodied carbon methodologies, Energy Build. 84 (2014) 378–387.
[120] Chr. Lamnatou, G. Notton, D. Chemisana, C. Cristofari, The environmental performance of a building-integrated solar thermal collector, based on multiple approaches and life-cycle impact assessment methodologies, Build. Environ. 87 (2015) 45–58.
[121] B. Berge, The Ecology of Building Materials (translated by C. Butters, F. Henley), second ed. Elsevier, Architectural Press, 2009.
[122] F. Corcelli, M. Ripa, E. Leccisi, et al., Sustainable urban electricity supply chain – indicators of material recovery and energy savings from crystalline silicon photovoltaic panels end-of-life, Ecol. Indic. 94 (2018) 37–51.
[123] J.R. Perez-Gallardo, C. Azzaro-Pantel, S. Astier, A multi-objective framework for assessment of recycling strategies for photovoltaic modules based on life cycle assessment, Waste Biomass Valor. 9 (2018) 147–159. Available from: https://doi.org/10.1007/s12649-017-9878-0.
[124] M. Vellini, M. Gambini, V. Prattella, Environmental impacts of PV technology throughout the life cycle: importance of the end-of-life management for Si-panels and CdTe-panels, Energy 138 (2017) 1099–1111.
[125] M. Bogacka, K. Pikoń, M. Landrat, Environmental impact of PV cell waste scenario, Waste Manage. 70 (2017) 198–203.
[126] C.E.L. Latunussa, F. Ardente, G.A. Blengini, et al., Life cycle assessment of an innovative recycling process for crystalline silicon photovoltaic panels, Solar Energy Mater. Solar Cells 156 (2016) 101–111.
[127] M. Goe, G. Gaustad, Estimating direct climate impacts of end-of-life solar photovoltaic recovery, Solar Energy Mater. Solar Cells 156 (2016) 27–36.

This page intentionally left blank

# CHAPTER 3

# Introduction to nanomaterials: synthesis and applications

**R. Jose Varghese[1,2,3], El hadji Mamour Sakho[2,3], Sundararajan Parani[2,3], Sabu Thomas[1,*], Oluwatobi S. Oluwafemi[2,3] and Jihuai Wu[4]**

[1]International and Inter University Centre for Nanoscience and Nanotechnology, Mahatma Gandhi University, Kottayam, India
[2]Department of Chemical Sciences (Formerly Applied Chemistry), University of Johannesburg, Doornfontein Campus, Johannesburg, South Africa
[3]Centre for Nanomaterials Science Research, University of Johannesburg, Johannesburg, South Africa
[4]Professor of Materials and Chemistry, Vice-President of Huaqiao University, Director of Engineering Research Center of Environment-Friendly Functional Materials, Ministry of Education, Director of Institute of Materials Physical Chemistry, Huaqiao University, Xiamen, Fujian, P.R. China

## Contents



## 3.1 Introduction to nanotechnology

### 3.1.1 History of nanotechnology

Nanotechnology involves the synthesis and application of materials in dimensions of the order of a billionth of a meter ($1 \times 10^{-9}$). This categorizes them under ultrafine particles. Fig. 3.1 reveals the size comparison of the nanoparticles against different living and nonliving species. The properties of nanoparticles vary from their bulk counterpart and their chemistry [1]. The electronic structure, reactivity, and thermal and mechanical properties

*Nanomaterials for Solar Cell Applications*
DOI: https://doi.org/10.1016/B978-0-12-813337-8.00003-5

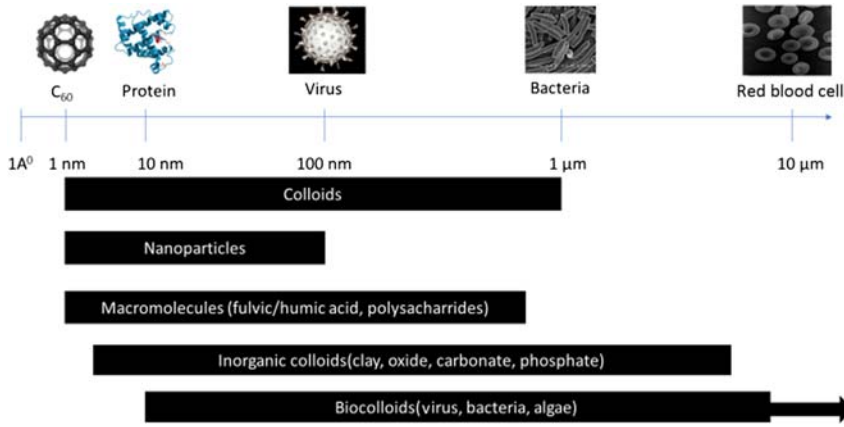


**Figure 3.1** Size comparison of different structures (living and nonliving).

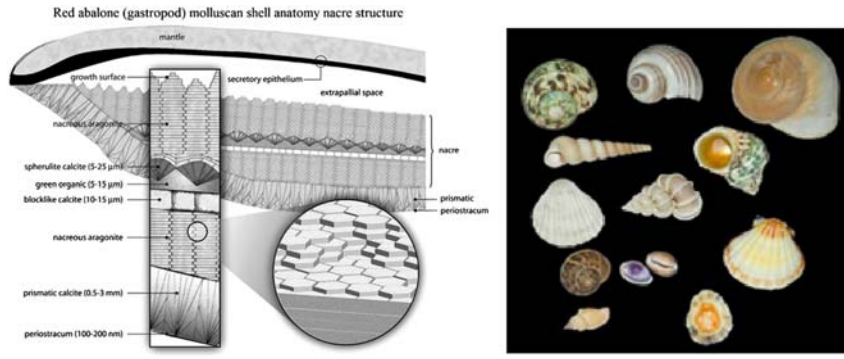


**Figure 3.2** Mollusk shell.

tend to change when the particles reach the nanoscale. Through nanotechnology, we can build materials and devices with control down to the level of individual atoms and molecules. In the past two decades, there were reports of colloids and nanoparticles designed by nature [2,3].

Abalone shells (Fig. 3.2) are an example of nature's Nanoassembly [4]. The shells of these mollusks are made by nanopatterning of calcium carbonate, which is same as limestone, but harder. The molecules in these shells are clumped and stacked up in a row pattern that makes them much harder. Another wonder of nanotechnology in nature is the spider, which synthesizes silk (Fig. 3.3) from protein polymer to form a fiber with strength similar to high-tensile steel [5].

Nanotechnology has been applied by humans for over a thousand years unknowingly from painting to making steel. Medieval stained-glass

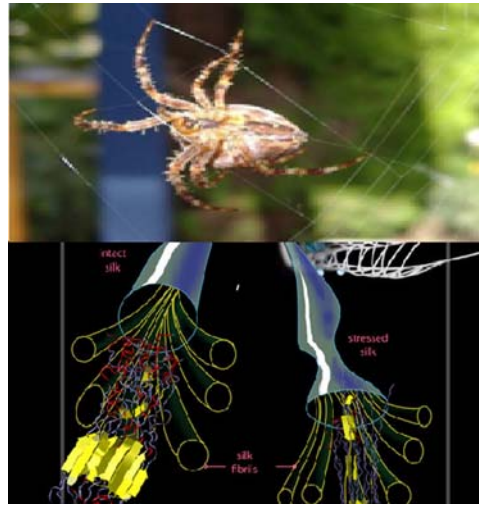


**Figure 3.3** Spider web.

**Figure 3.4** Medieval stained-glass of an ancient church.

(Fig. 3.4), which originated in Europe, is one of the examples of the oldest nanotechniques known in history. Different staining of the glass is due to the entrapment of different nanoparticle in the glass matrix, which was unintentional. For instance, the ruby red color was due to the entrapment of gold nanoparticles (AuNPs) in the glass matrix, whereas the formation of silver nanoparticles (AgNPs) within the glass matrix was responsible for the deep yellow color [6,7].

Deruta ceramics is an iridescent ceramic material developed in Italy during the early medieval age. The metallic glaze of this material was due to the presence of copper and silver particles in nanometer range (Fig. 3.5) [8]. The Chinese used AuNPs to create a red color in the ceramic porcelains (Fig. 3.6).

The Lycurgus Cup (Fig. 3.7) is a dichroic cup made by Romans in the 4th century. The color of the cup changes with respect to the incident light. When it is looked at in reflected light or daylight, it appears green. However, when light is shown into the cup and transmitted through the glass, it changes to red. This color variation is due to the presence of gold and AgNPs [9]

**Figure 3.5** Deruta maiolica plate.

**Figure 3.6** Chinese ceramic porcelain.

**Figure 3.7** Lycurgus Cup.

In 1861, James Clark Maxwell produced the first color photograph. Later, in 1883, American inventor George Eastman designed a film consisting of a long paper strip coated with an emulsion containing silver halides that are in nanoparticle range. So, the technology based on nanosized materials is not new. Michael Faraday, in 1857, published an article in "Experimental relations of gold (and other metals) to light" in which he attempted to explain how metal particles affect the color of church windows [10].

Richard Zsigmondy, the 1925 Nobel Prize Laureate in chemistry, proposed the term "nanometer." Later, Richard Feynman, an American theoretical physicist, presented a lecture on "There's plenty of room at the bottom," at the meeting of American Physical Society on December 29, 1959, which led to the birth of theoretical nanotechnology [11,12]. He proposed a theory on manipulation of individual atoms to make new small structures having very different properties.

### 3.1.2 Size effects of nanomaterials

The size of the nanoparticles has a great influence on their properties (Fig. 3.8). When a particle is in its bulk state compared to its size in its microscale, there is not much difference in its properties. However, when the particle reaches a size less than 100 nm, the properties changes significantly compared to its bulk state. In this scale (1−100 nm), quantum size

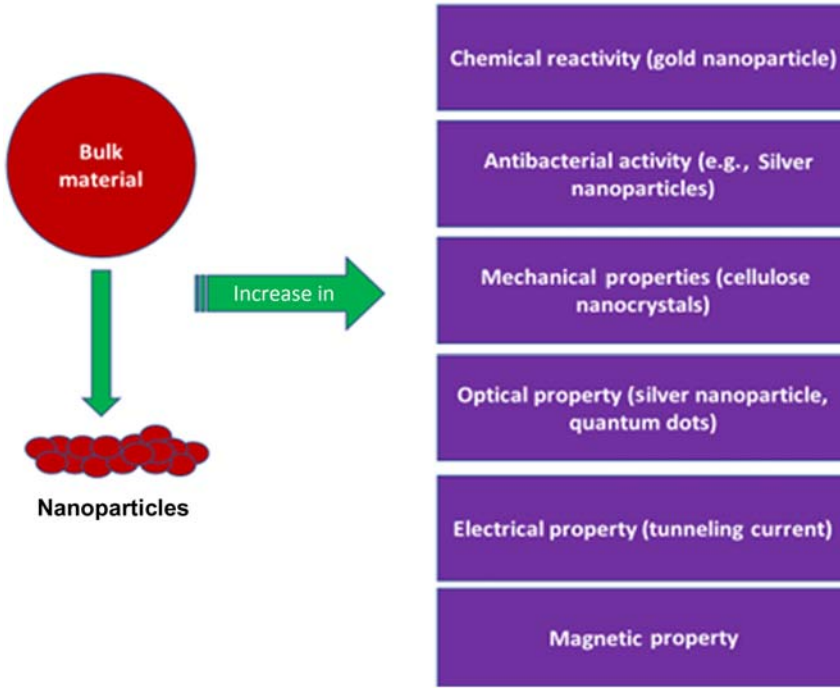


**Figure 3.8** Schematic representation of properties of nanoparticle.

effects decide the properties of particles, such as chemical, thermal, mechanical, optical, electrical, and magnetic [12–14].

The size-dependent properties of AuNPs have been explained well in the last few decades [7,9,10,14,15]. Fig. 3.9 shows the size-dependent color of AuNPs. At nanoscale, gold particle exhibits purple color different from the bulk, which was yellow colored. This color change is attributed to the change in their band type from continuous to discrete due to confinement effect (Fig. 3.10).

These quantum effects in the nanoscale are the basic reasons behind the "tunability" of properties. By simply tuning the particle size, we can change the material property of our interest (such as fluorescence).

### 3.1.3 Carbon nanomaterials

The element carbon plays an important role in nature due to its ability to bond in so many ways. If we investigate the nature of most important biological compounds, such as DNA and proteins, they are largely based on carbon linked to nitrogen, hydrogen, and oxygen. Carbon with

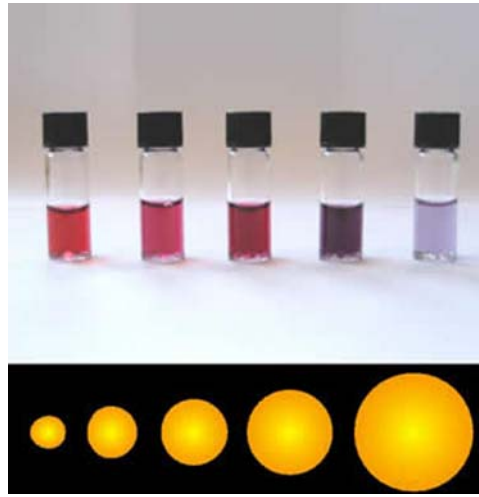

**Figure 3.9** Size–color dependence of gold particles.

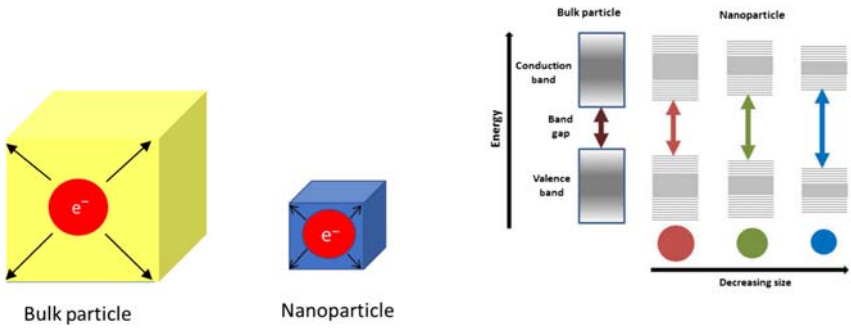


**Figure 3.10** Schematic representation of confinement of electron and change in band gap with size.

electronic configuration of 1s2 2s2 2p2 can form different crystalline and amorphous materials, because it can exist in $sp^2$ $sp^3$ and $sp^1$ hybridization. For a long time, carbon was thought to exist only in two allotropic forms, such as graphite and diamond. The difference in properties of the above materials is explained through its structure. When we look into graphite, the large amount of delocalized bonding, promotes the electrical conductivity of graphite, whereas the strong covalent bond of $sp^3$ carbons in diamond promotes the hardness of the diamond. But, in 1985, the research focus on carbon changed after the discovery of fullerene, another form of carbon (Fig. 3.11) [16]. This led to the birth of synthetic carbon

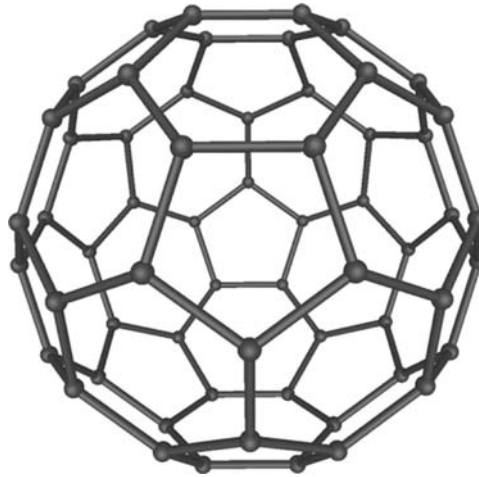

**Figure 3.11** Structure of fullerene.

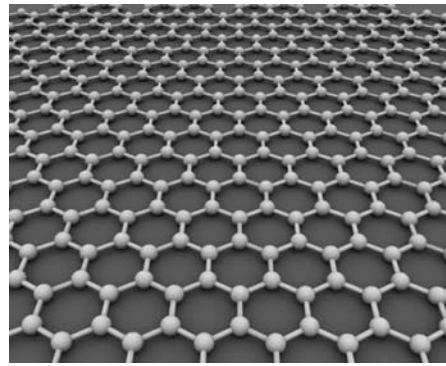

**Figure 3.12** Structure of graphene sheet [19].

nanomaterials. This discovery was followed by carbon nanotubes (CNTs) in 1991 and graphene at 2004 [17,18] (Figs. 3.12 and 3.13).

The fullerenes were discovered accidentally by Kroto and Smalley in 1985 when they observed a strange result in the mass spectra of vaporized carbon. $C_{60}$ is found to be most stable fullerene. $C_{60}$ consists of 60 equivalent carbon atoms, which is $sp^2$ hybridized. The approximate diameter of reported $C_{60}$ is 0.7 nm [16]. CNT is described as rolled up graphene sheets of one atom thick and made up of hexagonal rings similar to benzene rings of carbon atoms. The properties such as metallic and semiconducting properties of this material depend on the chirality of carbon atom. The actual discovery of CNTs is credited to Sumio Lijima, who worked

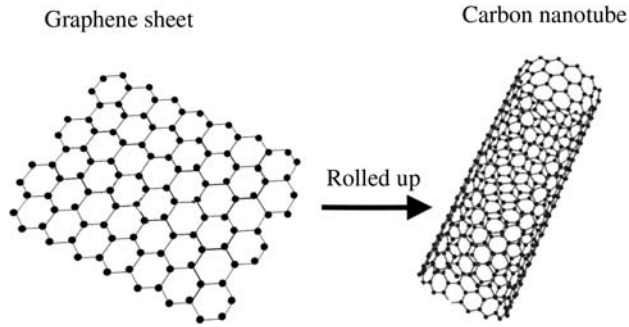


**Figure 3.13** Structure of carbon nanotube [20].

at NEC Corporation in 1991 and synthesized CNT with the help of the arc-discharge method. The reported CNT diameter was about 4−30 nm and length of 1 μm [21]. These structures were similar to a Russian doll-like coaxial packing that was later named multiwall CNTs (MWCNT). Later, in 1993, Lijima et al. and Bethune et al. reported the CNTs that were composed of single-layered graphene with a diameter of 1.37 nm [16,21] and named single-walled CNTs (SWNT). CNTs have been applied as a filler in composite material to improve structural properties, electronic applications, solar cells/batteries, and also in biologicals as sensors.

Graphene is composed of a one-atom-thick sheet of $sp^2$-bonded carbon atoms arranged in hexagonal pattern. This structure is considered as the basic building block of other carbon nanomaterials. For example, it can be rolled into CNTs or stacked into a graphite. It can be transformed into a fullerene by the addition of pentagons. From the electronic point of view, graphene is considered to be zero gap semiconductor, more like metals. This unique property led to many electronic properties, like ballistic transport (transport of charge carriers in a medium), pseudospin chirality, and conductivity in the absence of charge carriers that can be utilized for future applications [23]. Graphene has the fastest electron mobility, greater than silver; high mobility of temperature-independent charge carriers (200 times higher than Si); and effective Fermi velocity similar to the speed of light. Graphene has good mechanical and thermal properties. Due to its unique properties, graphene can replace graphite, CNTs, and metals. Graphene found its application as transparent electrodes, solar cells, and photoelectrodes [24]. The electrical conductivity can be tuned by doping with different impurities. The higher mobility can be utilized for high-frequency applications. The transparent property can be utilized for touch screens and solar cells in which it can replace the expensive indium titanium oxide.

Basically, the physical and chemical properties of fullerens, CNTs, and graphene are related to each other. Compared to CNTs, which has various types (helicites, single-walled, multiwall), graphene is reported to be a more uniform material. The covalent modification to graphene is possible from both sides, compared to CNTs and fullerene, which exhibit exo- and endofaces. The applications of these nanostructures are vast. Practically, the applications for the bulky ball are quiet few. More research is done in the utilization of CNTs. Graphene can be used extensively to replace steel, because it can be recyclable and manufactured in a sustainable way.

## 3.2 Quantum dots

The realization of dependency of band gap against its particle size in 1980 was the birth of quantum dots (QDs). From then, scientists started to study the excited electronic states of smaller nanocrystals (2−10 nm). The results of these studies were compared with their bulk counterpart, and it was learned that these small nanocrystals displayed unique electronic properties compared to those of bulk semiconductors. This variation in property is also due to its high surface-to-volume ratio and quantum confinement [25]. The quantum confinement occurs when the size of the particle is smaller than the excitonic Bohr radii (distance between electron hole pair). For example, Bohr exciton radius of the bulk PbSe is 46 nm with a band gap 0.28 eV. But as if the size of PbSe was reduced to 4.8 nm, the band gap changes to 0.82 eV, which gives a strong confined blue shift of >500 m eV compared to the bulk PbSe. The most observed property is the fluorescence of these materials where they can exhibit different wavelengths depending on the size of the particle. When the size of the particle is smaller than Bohr radius, the energy level will become quantized (Pauli's exclusion principle). This discretion of energy level can be compared to the molecules rather than bulk materials.

## 3.3 Metal nanoparticles

Similar to QDs, metal nanoparticles also exhibit size-dependent optical properties that are called surface plasmon resonance (SPR). The most studied SPR is of silver and AuNPs. When the metal nanoparticle is photoactivated, the plasmon will couple with excitation light and result in

an increase in the electromagnetic field in the particle [19,20,26–31]. The interaction between the incident photon and electric field will lead to the scattering and absorption of light. The research on surface plasma resonance is very active in scientific community and industry [32].

AuNPs: AuNPs are reported to be the most stable metal nanoparticles. Size-dependent electronic and optical properties are very well studied. As we discussed earlier, the size-dependent color change of AuNPs explains the surface plasma band (SPB). The SPB is reported to be absent for AuNPs with a diameter less than 2 nm. AuNPs are mostly used in medical diagnostics, catalysis, optics, solar cells, and as inks, sensors, and in surface coating. They are also used as the electron-dense labeling agents in the areas of histochemistry and cytochemistry.

AgNPs: The unique property of AgNPs compared to other metal nanoparticles is their antimicrobial property. AgNPs are reported to be very effective against bacteria, viruses, and other eukaryotic microorganisms [33,34]. Even though it has been applied in many commercial products, the toxicity of AgNPs to the useful microorganisms and human body is yet to be evaluated. The mechanism of antibacterial property of Ag nanoparticle is under debate. Some reported that there is an interaction between AgNPs and the bacterial membrane that leads to the damage in cell walls [34]. Another explanation is the creation of reactive oxygen species when the AgNPs inhibit the respiratory enzyme of bacteria [35,36]. The absorption of AgNPs is reported to be in the range from 380 to 450 nm by localized SPR [37,38]. The antibacterial property was also reported to be dependent on the SPRs [39].

Copper nanoparticles (CuNPs): Cu is a naturally abundant material with low-cost synthesis procedure [40–44]. The application of CuNPs in various fields is restricted by their instability due to oxidation. Research has been conducted in order to solve this issue by making more complex structures with CuNPs, like core/shell CuNPs. To prepare highly active, selective, and stable nanocatalysts, CuNPs can be anchored to different supports, such as iron oxides, $SiO_2$, carbon-based materials, and polymers. Cu is represented among 3D transition metals and has some unique physical and mechanical properties. Cu has four oxidation states ($Cu^0$, $Cu^{1+}$, $Cu^{2+}$, $Cu^{3+}$), which lead to one and two electron pathways. Due to these unique properties, CuNPs have found applications in nanocatalysis [45–50].

## 3.4 Synthesis of nanomaterials

### 3.4.1 Top-down approaches

#### *3.4.1.1 Mechanical milling*

Through mechanical milling, size of bulk material can be reduced to nanoscale. This method can also be utilized to blend different phases. For large-scale production, this method is more suitable. The basic principle behind this process is the transfer of energy to the sample from the balls during the process [51]. Commonly used ball materials are steel and tungsten because of the fact that dense materials are required for the milling purpose [52]. The temperature generated during the process depends on the kinetic energy of the ball and the sample powder characteristics. The final particle shape and structure also depends on the strain-rated during the collision of the balls [53].

#### *3.4.1.2 Mechanochemical processing*

During the milling, there can be deformation, fracture, and welding of powder if the conditions are not right. There is a development of plastic deformation of the powder due to the development of shear bands that finally decompose into subgrains. When the milling process is continued, the subgrain size decreases to nanoscale [54]. The unique property of mechanochemical processing is the processing speed in yielding to nanoscale. The nanometer powder enhances the reaction kinetics, which induces chemical reactions that basically requires high temperature [55].

#### *3.4.1.3 Electroexplosion*

In 1962 Karioris and Fish discovered a method that can be used to generate aerosols of the following metals: Au, Ag, Al, Cu, Fe, W, Mo, Ni, Th, U, Pt, Mg, Pb, Sn, and Ta. The particle size formed was around 30–50 nm. This is basically the electrical explosion of metal wires that fabricated nanoparticles with high activity. High-density electric pulse (104–106 $A/mm^2$) is passed through a metal wire, which results in the increase in heat (20,000°C–30,000°C) and explodes and forms products that are converted to nanoparticles by the passage of gas [55–57]. Through this method, it is possible to fabricate powders with unique properties that are difficult to fabricate through other methods.

#### 3.4.1.4 Sputtering

It was first observed by Grove in 1852. He noted the sputtering of the cathode surface of the discharge tube by energetic ions and the material was deposited inside of the discharge tube. Today this technique is utilized by the bombardment of a sample surface with energetic gaseous ions, which results in the ejection of surface atoms or small clusters. The sputtering is performed in the following different ways: DC-diode, RF-diode, and mag-neutron sputtering. Argon plasma is mostly used for sputtering. Unlike other vapor phase techniques, there is no melting of the samples [58].

#### 3.4.1.5 Laser ablation

Laser ablation (LA) is a complex process. The laser penetrates to the sample surface, depending on the wavelength of the laser and the refractive index of the target material. The high electric field generated due to laser light is enough to remove electrons from the bulk sample. The generated free electron collides with the atoms of the bulk sample, in which transfer of energy occurs. This leads to the heating of the surface, which is followed by vaporization [59]. When the laser flux is high enough, the material will transfer to the plasma state, including atoms, molecules, ions, clusters. The pressure difference between the seed plasma and the atmosphere lead to a rapid expansion and cooling of the plasma. LA takes place in either a vacuum or gaseous environment. LA combined with a tube furnace is called a pulsed LA technique. This technique allows better control over growth temperature, flowing gas type rate, and pressure.

#### 3.4.1.6 Lithography

Micro and nanolithography technology have been utilized for decades to fabricate integrated circuits. This technique can create patterns with size in the nanometer range. Lithography is usually combined with deposition and etching to yield high-resolution topography. Lithography can be divided into masked lithography and maskless lithography. In masked lithography, masks or molds will be used to fabricate patterns. The types of masked lithography include photolithography [60–64], soft lithography [65,66], and nanoimprint lithography [67–72]. Maskless lithography yields arbitrary patterns without the use of masks. For example, electron beam lithography [73–75], focused ion beam lithography [76,77], and scanning probe lithography [78,79].

#### 3.4.1.7 Aerosol-based techniques

Aerosol is a mixture of solid/liquid particles in a gaseous environment. The advantage of aerosol methods over others is due to its high-purity product yield with less toxicity to the environment. Aerosol methods are classified as follows: (1) furnace method; (2) flame method; (3) electrospray; (4) chemical vapor deposition (CVD); and (5) physical vapor deposition method. Electrospray method is reported to be the most favorable method to fabricate nanoparticle production, but the process is slow [80].

#### 3.4.1.8 Electrospinning

Electrospinning technique was developed during the last decade (from 2012) for the fabrication of continuous fibers in submicron to nanometer scale range. This method is utilized to fabricate nanofibers of polymers, metals, ceramics, and composites. Nanoparticles are mixed with polymers and electrospun to produce scaffolds. Electrospinning is also used for the assembly of nanoparticles through the alignment with fibers and thus reduce the Gibbs Free energy [81]. The other advantage of electrospinning is that it does not require any functionalization process, it needs only a solvent that can disperse nanoparticles and dissolve the polymer. Electrospinning basically depends on the high electrostatic forces. Factors that influence the electrospinning process are polymer concentration, solution viscosity and flowrate, electric field intensity, the work distance, and air humidity.

### 3.4.2 Bottom-up approaches

#### 3.4.2.1 Chemical vapor deposition

In this method, a sample material is deposited in a vapor medium with the help of chemical reaction. The material is deposited in the form of thin film, powder or a single crystal. The advantages of the CVD is its excellent throwing power, thin films with uniform thickness with low percentage of porosity, and selective deposition on desired pattern. CVD is applied in thin films for dielectric, conductors, passivation layer, oxidation layer, conductive oxides, tribological and corrosion resistant coatings, heat resistant coatings, etc. Other applications include fabrication of solar cells and high-temperature fiber composites [82].

#### 3.4.2.2 Plasma arcing

Plasma is basically an ionized gas. Plasma is created by conduction of electricity through gas with the help of a potential difference that is created

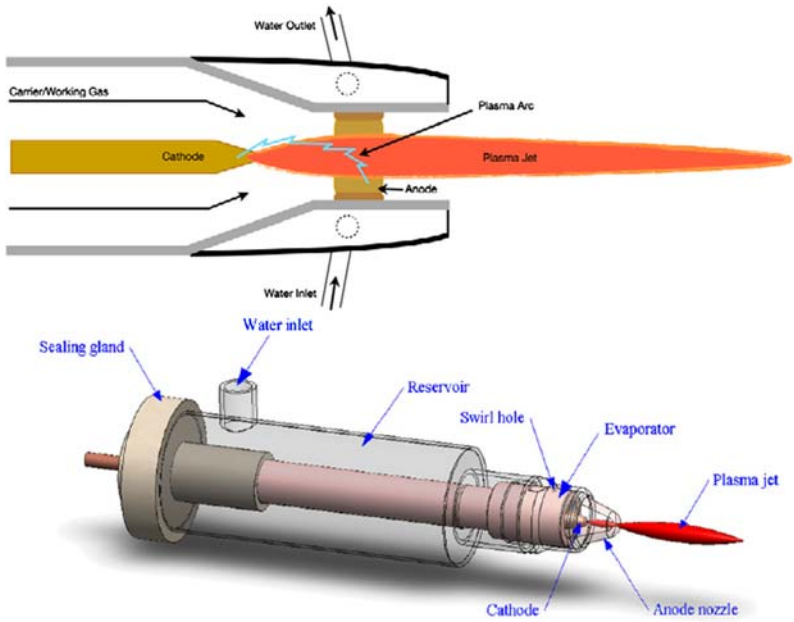


**Figure 3.14** Plasma torch.

between two electrodes. A plasma torch (Fig. 3.14) is used to generate a contracted plasma arc, using an inert gas.

For example, an arc-discharge method is typically used to fabricate MWNTs and SWNTs. For this, it generally involves the use of a graphite electrode as the anode and cathode. The electrodes get vaporized by the passage of DC current (~100 A). When the arc discharge is completed for a period of time, carbon rods are created at the cathode side. This method is usually used to fabricate MWCNTs, but with the help of metal catalyst such as Fe, Ni, Mo, SWCNT can be fabricated [83].

#### *3.4.2.3 Wet chemical methods*

This method is used to synthesize uniform nanoparticles with desired size. This method achieved a great success because of the control over size, shape, and crystallinity. Wet chemical synthesis is mostly used to synthesize inorganic nanomaterials due to low cost and easy application. This method also has many disadvantages when it comes to the industrial scale due to long mixing time and uncontrollable nucleation and growth [84].

#### 3.4.2.4 Solvothermal/Hydrothermal synthesis

The reaction occurring in solvents contained in sealed vessels by heating to their critical point under autogenous pressure is called hydrothermal/solvothermal process. It is basically a crystallization process that consists of crystal nucleation and its growth. Particle morphology can be controlled by tuning the temperature, pH, and reactant concentrations [85].

#### 3.4.2.5 Reverse micelle method

Surfactants are made up of hydrophilic head and a hydrophobic chain. These amphiphilic molecules can self-assemble into variable structures under certain conditions. For reverse micelles the structure is characterized through polar cores formed with hydrophilic heads. These solutions can be called microemulsions, which are thermodynamically stable and optically transparent. Water–oil microemulsions consist of droplets in 5–100 nm size range. The reverse micelles can be tuned to nanometer scale by changing the parameters, such as molar ratio of water, to surfactant. With the adsorption of surfactants with the inorganic materials, it is possible to use these micelles for the synthesis of nanostructures with controlled morphology [86].

#### 3.4.2.6 Sol–gel method

This method is mainly used to synthesize metal oxide NPs and mixed oxide composites with desired nanostructures. Typical sol–gel method includes the following steps: hydrolysis, condensation, and drying process. Initially, the metal precursor undergoes hydrolysis and yields metal hydroxide, followed by condensation to form gels. The final gel is dried and converted to xerogel/aerogel [87].

## 3.5 Conclusion

The field of nanotechnology has found applications in all the fields, and this chapter has reviewed the field at an introductory level. It has been seen that nanomaterials are different from their bulk moieties and cannot be studied as same as bulk or small molecules due to their unique properties in nanoscale. The properties of nanomaterials depend on composition, chemistry, particle dimension, and interactions with other materials. Their intrinsically small dimension and higher surface area is critically studied. There are various methods to fabricate nanoparticles, depending on type of material and composition. Even though there are lot of advantages,

unique characteristic of nanoparticle is a big concern in determining their toxicological and ecotoxicological properties and will be discussed in further chapters.

## References


[1] SCENIHR, 2005. Request for a scientific opinion on the appropriateness of existing methodologies to assess the potential risks associated with engineered and adventitious nanotechnologies: SCENIHR/002/05; J.M. Zachara, J.F. McCarthy, ES&T features: subsurface transport of contaminants, Exp. Sci. Technol. 23 (5) (1989) 496–502.

[2] N.S. Wigginton, K.L. Haus, M.F. Hochella Jr, Aquatic environmental nanoparticles, J. Environ. Monit. 9 (12) (2007) 1306–1316.

[3] Y. Shao, H.P. Zhao, X.Q. Feng, Optimal characteristic nanosizes of mineral bridges in mollusk nacre, RSC Adv. 4 (61) (2014) 32451–32456.

[4] S. Keten, M.J. Buehler, Atomistic model of the spider silk nanostructure, Appl. Phys. Lett. 96 (15) (2010) 153701.

[5] Wikipedia Contributors, Mollusc Shell, Wikipedia, The Free Encyclopedia 25, 2019.

[6] S. Link, M.A. El-Sayed, Size and temperature dependence of the plasmon absorption of colloidal gold nanoparticles, J. Phys. Chem. B 103 (21) (1999) 4212–4217.

[7] Wikipedia Contributors, Medieval Stained Glass, Wikipedia, The Free Encyclopedia 23, 2018.

[8] Wikipedia Contributors, Deruta Ceramics, Wikipedia, The Free Encyclopedia 6, 2018.

[9] Wikipedia Contributors, Lycurgus Cup, Wikipedia, The Free Encyclopedia 9, 2018.

[10] A. Junk, F. Riess, From an idea to a vision: there's plenty of room at the bottom, Am. J. Phys. 74 (9) (2006) 825–830.

[11] J. Polte, Fundamental growth principles of colloidal metal nanoparticles–a new perspective, CrystEngComm 17 (36) (2015) 6809–6830.

[12] C.Q. Sun, Size dependence of nanostructures: impact of bond order deficiency, Prog. Solid State Chem. 35 (1) (2007) 1–159.

[13] M. Brust, M. Walker, D. Bethell, D.J. Schiffrin, R. Whyman, Synthesis of thiol-derivatised gold nanoparticles in a two-phase liquid–liquid system, J. Chem. Soc., Chem. Commun. (7) (1994) 801–802.

[14] M.C. Daniel, D. Astruc, Gold nanoparticles: assembly, supramolecular chemistry, quantum-size-related properties, and applications toward biology, catalysis, and nanotechnology, Chem. Rev. 104 (1) (2004) 293–346.

[15] Wikipedia Contributors, Colloidal Gold, Wikipedia, The Free Encyclopedia 9, 2019.

[16] S. Iijima, T. Ichihashi, Single-shell carbon nanotubes of 1-nm diameter, Nature 363 (6430) (1993) 603.

[17] K.S. Novoselov, A.K. Geim, S.V. Morozov, D.A. Jiang, Y. Zhang, S.V. Dubonos, et al., Electric field effect in atomically thin carbon films, Science 306 (5696) (2004) 666–669.

[18] Wikipedia Contributors, Fullerene, Wikipedia, The Free Encyclopedia, Wikipedia, The Free Encyclopedia 26, 2019.

[19] A. Otto, I. Mrozek, H. Grabhorn, W. Akemann, Surface-enhanced Raman scattering, J. Phys.: Condens. Matter 4 (5) (1992) 1143.

[20] Z.Q. Tian, B. Ren, D.Y. Wu, Surface-enhanced Raman scattering: from noble to transition metals and from rough surfaces to ordered nanostructures, J. Phys. Chem. 106 (37) (2002) 9463–9483.

[21] D.S. Bethune, C.H. Kiang, M.S. De Vries, G. Gorman, R. Savoy, J. Vazquez, et al., Cobalt-catalysed growth of carbon nanotubes with single-atomic-layer walls, Nature 363 (6430) (1993) 605–607.
[22] T. Ando, The electronic properties of graphene and carbon nanotubes, NPG Asia Mater. 1 (1) (2009) 17.
[23] I. Childres, L.A. Jauregui, J. Tian, Y.P. Chen, Effect of oxygen plasma etching on graphene studied using Raman spectroscopy and electronic transport measurements, New J. Phys. 13 (2) (2011) 025008.
[24] M.A. Kastner, Artificial atoms, Phys. Today 46 (1993) 24.
[25] D.L. Jeanmaire, R.P. Van Duyne, Surface Raman spectroelectrochemistry: Part I. Heterocyclic, aromatic, and aliphatic amines adsorbed on the anodized silver electrode, J. Electroanal. Chem. Interfacial Electrochem. 84 (1) (1977) 1–20.
[26] S. Eustis, M.A. El-Sayed, Why gold nanoparticles are more precious than pretty gold: noble metal surface plasmon resonance and its enhancement of the radiative and nonradiative properties of nanocrystals of different shapes. Chem. Soc. Rev. 35 (3) (2006) 209–217.
[27] E. Hao, G.C. Schatz, Electromagnetic fields around silver nanoparticles and dimers, J. Chem. Phys. 120 (1) (2004) 357–366.
[28] K. Kneipp, H. Kneipp, J. Kneipp, Surface-enhanced Raman scattering in local optical fields of silver and gold nanoaggregates from single-molecule Raman spectroscopy to ultrasensitive probing in live cells, Acc. Chem. Res. 39 (7) (2006) 443–450.
[29] S.A. Maier, H.A. Atwater, Plasmonics: localization and guiding of electromagnetic energy in metal/dielectric structures, J. Appl. Phys. 98 (1) (2005) 10.
[30] M. Moskovits, Surface-enhanced Raman spectroscopy: a brief perspective, Surface-Enhanced Raman Scattering, Springer, Berlin, Heidelberg, 2006, pp. 1–17.
[31] M. Moskovits, Surface-enhanced spectroscopy, Rev. Mod. Phys. 57 (3) (1985) 783.
[32] G. Mie, Beiträge zur Optik trüber Medien, speziell kolloidaler Metallösungen, Ann. Phys. 330 (3) (1908) 377–445.
[33] P. Gong, H. Li, X. He, K. Wang, J. Hu, W. Tan, et al., Preparation and antibacterial activity of $Fe_3O_4$@Ag nanoparticles, Nanotechnology 18 (28) (2007) 285604.
[34] I. Sondi, B. Salopek-Sondi, Silver nanoparticles as antimicrobial agent: a case study on E. coli as a model for Gram-negative bacteria, J. Colloid. Interface. Sci. 275 (1) (2004) 177–182.
[35] S. Pal, Y.K. Tak, J.M. Song, Does the antibacterial activity of silver nanoparticles depend on the shape of the nanoparticle? A study of the gram-negative bacterium *Escherichia coli*, Appl. Environ. Microbiol. 73 (6) (2007) 1712–1720.
[36] J.R. Morones, J.L. Elechiguerra, A. Camacho, K. Holt, J.B. Kouri, J.T. Ramírez, et al., The bactericidal effect of silver nanoparticles, Nanotechnology 16 (10) (2005) 2346.
[37] M. Sastry, K.S. Mayya, V. Patil, D.V. Paranjape, S.G. Hegde, Langmuir–Blodgett films of carboxylic acid derivatized silver colloidal particles: role of subphase pH on degree of cluster incorporation, J. Phys. Chem. B 101 (25) (1997) 4954–4958.
[38] M. Sastry, V. Patil, S.R. Sainkar, Electrostatically controlled diffusion of carboxylic acid derivatized silver colloidal particles in thermally evaporated fatty amine films, J. Phys. Chem. B 102 (8) (1998) 1404–1410.
[39] A. Syafiuddin, M.R. Salim, A. Beng Hong Kueh, T. Hadibarata, H. Nur, A review of silver nanoparticles: research trends, global consumption, synthesis, properties, and future challenges, J. Chin. Chem. Soc. 64 (7) (2017) 732–756.
[40] G. Evano, N. Blanchard, M. Toumi, Copper-mediated coupling reactions and their applications in natural products and designed biomolecules synthesis, Chem. Rev. 108 (8) (2008) 3054–3131.

[41] H. Huang, W. Huang, Y. Xu, X. Ye, M. Wu, Q. Shao, et al., Catalytic oxidation of gaseous benzene with ozone over zeolite-supported metal oxide nanoparticles at room temperature, Catal. Today 258 (2015) 627–633.
[42] A. Ahmed, P. Elvati, A. Violi, Size- and phase-dependent structure of copper (II) oxide nanoparticles, RSC Adv. 5 (44) (2015) 35033–35041.
[43] J. Mondal, A. Biswas, S. Chiba, Y. Zhao, Cu0 nanoparticles deposited on nanoporous polymers: a recyclable heterogeneous nanocatalyst for Ullmann coupling of aryl halides with amines in water, Sci. Rep. 5 (2015) 8294.
[44] N.B.R. Baig, R.S. Varma, Copper modified magnetic bimetallic nano-catalysts ligand regulated catalytic activity, Curr. Org. Chem. 17 (20) (2013) 2227–2237.
[45] B.C. Ranu, R. Dey, T. Chatterjee, S.C. Ahammed, Copper nanoparticle-catalyzed carbon-carbon and carbon-heteroatom bond formation with a greener perspective, ChemSusChem. 1 (2012) 22–44.
[46] S.E. Allen, R.R. Walvoord, R. Padilla-Salinas, M.C. Kozlowski, Aerobic copper-catalyzed organic reactions, Chem. Rev. 113 (8) (2013) 6234–6458.
[47] O. Amadine, H. Maati, K. Abdelouhadi, A. Fihri, S. El Kazzouli, C. Len, et al., Ceria-supported copper nanoparticles: a highly efficient and recyclable catalyst for N-arylation of indole, J. Mol. Catal. A: Chem. 395 (2014) 409–419.
[48] K. Pan, H. Ming, H. Yu, Y. Liu, Z. Kang, H. Zhang, et al., Different copper oxide nanostructures: synthesis, characterization, and application for C-N cross-coupling catalysis, Cryst. Res. Technol. 46 (11) (2011) 1167–1174.
[49] Z.Y. Shih, A.P. Periasamy, P.C. Hsu, H.T. Chang, Synthesis and catalysis of copper sulfide/carbon nanodots for oxygen reduction in direct methanol fuel cells, Appl. Catal., B: Environ. 132 (2013) 363–369.
[50] R. Kaur, B. Pal, Cu nanostructures of various shapes and sizes as superior catalysts for nitro-aromatic reduction and co-catalyst for $Cu/TiO_2$ photocatalysis, Appl. Catal., A: Gen. 491 (2015) 28–36.
[51] S.C. Tjong, H. Chen, Nanocrystalline materials and coatings, Mater. Sci. Eng., R 45 (1–2) (2004) 1–88.
[52] D.L. Zhang, Processing of advanced materials using high-energy mechanical milling, Prog. Mater. Sci. 49 (3–4) (2004) 537–560.
[53] C.C. Koch, Synthesis of nanostructured materials by mechanical milling: problems and opportunities, Nanostruct. Mater. 9 (1–8) (1997) 13–22.
[54] F. Muller, F. Koch, A. Kohl, IR detection using subband absorption in delta-doping layers, Semicond. Sci. Technol. 6 (12C) (1991) C133.
[55] B. Gabriele, G. Salerno, M. Costa, Oxidative carbonylations, Catalytic Carbonylation Reactions, Springer, Berlin, Heidelberg, 2006, pp. 239–272.
[56] F.D. Bennett, High temperature exploding wires, Prog. High Temp. Phys. Chem. 2 (1) (1968) 1–63.
[57] S.G. Psakhie, K.P. Zolnikov, D.S. Kryzhevich, A.V. Abdrashitov, M.I. Lerner, Stage character of cluster formation in metal specimens in electrothermal pulse dispersion, Phys. Mesomech. 13 (3–4) (2010) 184–188.
[58] P. Williams, The sputtering process and sputtered ion emission, Surf. Sci. 90 (2) (1979) 588–634.
[59] M. Hashida, H. Mishima, S. Tokita, S. Sakabe, Non-thermal ablation of expanded polytetrafluoroethylene with an intense femtosecond-pulse laser, Opt. Express 17 (15) (2009) 13116–13121.
[60] R.F. Pease, S.Y. Chou, Lithography and other patterning techniques for future electronics, Proc. IEEE 96 (2) (2008) 248–270.
[61] B.D. Gates, Q. Xu, M. Stewart, D. Ryan, C.G. Willson, G.M. Whitesides, New approaches to nanofabrication: molding, printing, and other techniques, Chem. Rev. 105 (4) (2005) 1171–1196.

[62] R. Menon, A. Patel, D. Gil, H.I. Smith, Maskless lithography, Mater. Today 8 (2) (2005) 26–33.
[63] G.T. Chiu, J.M. Shaw, Optical lithography: introduction, IBM J. Res. Dev. 41 (1.2) (1997) 3–6.
[64] W.M. Moreau, Semiconductor Lithography: Principles, Practices, and Materials, Springer Science & Business Media, 2012.
[65] C.D. Bain, G.M. Whitesides, Modeling organic surfaces with self-assembled monolayers, Angew. Chem. Int. Ed. 28 (4) (1989) 506–512.
[66] A.M. Dickson, Design and Applications of Metal Oxide Nanostructures From Electrospun Carbon Templates, State University of New York at Binghamton, 2010.
[67] S.Y. Chou, P.R. Krauss, P.J. Renstrom, Imprint lithography with 25-nanometer resolution, Science 272 (5258) (1996) 85–87.
[68] S.Y. Chou, P.R. Krauss, Imprint lithography with sub-10 nm feature size and high throughput, Microelectron. Eng. 35 (1–4) (1997) 237–240.
[69] J. Haisma, M. Verheijen, K. Van Den Heuvel, J. Van Den Berg, Mold-assisted nanolithography: a process for reliable pattern replication, J. Vac. Sci. Technol. B: Microelectron. Nanometer Struct. Process. Meas. Phenom. 14 (6) (1996) 4124–4128.
[70] J. Chen, J. Shi, D. Decanini, E. Cambril, Y. Chen, A.M. Haghiri-Gosnet, Gold nanohole arrays for biochemical sensing fabricated by soft UV nanoimprint lithography, Microelectron. Eng. 86 (4–6) (2009) 632–635.
[71] A. Cattoni, E. Cambril, D. Decanini, G. Faini, A.M. Haghiri-Gosnet, Soft UV-NIL at 20 nm scale using flexible bi-layer stamp casted on HSQ master mold, Microelectron. Eng. 87 (5–8) (2010) 1015–1018.
[72] J. Chen, J. Shi, A. Cattoni, D. Decanini, Z. Liu, Y. Chen, et al., A versatile pattern inversion process based on thermal and soft UV nanoimprint lithography techniques, Microelectron. Eng. 87 (5–8) (2010) 899–903.
[73] M.J. Madou, Fundamentals of Microfabrication: The Science of Miniaturization, CRC Press, New York, 2002.
[74] M. Altissimo, E-beam lithography for micro-/nanofabrication, Biomicrofluidics. 4. (2010) 3–6.
[75] C. Vieu, F. Carcenac, A. Pepin, Y. Chen, M. Mejias, A. Lebib, et al., Electron beam lithography: resolution limits and applications, Appl. Surf. Sci. 164 (2000) 111–117.
[76] J. Melngailis, Focused ion-beam technology and applications, J. Vac. Sci. Technol. B 5 (1987) 469–495.
[77] S.R.R. Puers, A review of focused ion beam applications in microsystem technology, J. Micromech. Microeng. 11 (2001) 287–300.
[78] A.A. Tseng, A. Notargiacomo, T.P. Chen, Nanofabrication by scanning probe microscope lithography: a review, J. Vac. Sci. Technol. B 23 (2005) 877–894.
[79] C.F. Cooper, George Whitesides: molecular self-assembly and the invention of soft lithography, J. Franklin. Inst. 348 (2011) 544–554.
[80] G. Biskos, V. Vons, C.U. Yurteri, A. Schmidt-Ott, Generation and sizing of particles for aerosol-based nanotechnology, KONA Powder Part. J. 26 (2008) 13–35.
[81] F. Ko, Y. Gogotsi, A. Ali, N. Naguib, H.H. Ye, G.L. Yang, et al. Electrospinning of continuous carbon nanotube-filled nanofiber yarns. Advanced materials, 15 (14) (2003) 1161–1165.
[82] J.M. Carlsson, P.M. Martin, Chemical Vapor Deposition, third ed., William Andrew Publishing, 2010, pp. 314–363.
[83] L.N. Mishra, K. Shibata, H. Ito, N.N. Yugami, Characterization of pulsed discharge plasma at atmospheric pressure, Surf. Coat. Technol. 201 (13) (2007) 6101–6104.
[84] C.Z. Tan, H. Zhang, Wet-chemical synthesis and applications of non-layer structured two-dimensional nanomaterials, Nat. Commun. 6 (2015) 7873.

[85] G. Zou, H. Li, Y. Zhang, K.Q. Xiong, Y. Qian, Solvothermal/Hydrothermal route to semiconductor nanowires, Nanotechnology 17 (11) (2006) 313.
[86] J. Zhang, L. Sun, C.Y. Liao, C. Yan, Size control and photoluminescence enhancement of CdS nanoparticles prepared via reverse micelle method, Solid State Commun. 124 (1–2) (2002) 45–48.
[87] D.H. Chen, X.R. He, Synthesis of nickel ferrite nanoparticles by sol-gel method, Mater. Res. Bull. 36 (7–8) (2001) 1369–1377.

## Further reading

Wikipedia Contributors, Spider Web, Wikipedia, The Free Encyclopedia 27.
K.A. Duncan, C. Johnson, K. McElhinny, S. Ng, K.D. Cadwell, G.M. Zenner Petersen, et al., Art as an avenue to science literacy: Teaching nanotechnology through stained glass, J. Chem. Educ. 87 (10) (2010) 1031–1038.
P. Fermo, G. Padeletti, The use of nano-particles to produce iridescent metallic effects on ancient ceramic objects, J. Nanosci. Nanotechnol. 12 (11) (2012) 8764–8769.
I. Freestone, N. Meeks, M. Sax, C. Higgitt, The Lycurgus cup—a Roman nanotechnology, Gold Bull. 40 (4) (2007) 270–277.
M. Faraday, The Bakerian lecture. Experimental relations of gold (and other metals) to light, Philos. Trans. R. Soc. London 147 (1857) 145–181.
H.W. Kroto, J.R. Heath, S.C. O'Brien, R.F. Curl, R.E. Smalley, C60: Buckminsterfullerene, Nature 318 (6042) (1985) 162.
Wikipedia Contributors, Graphene, Wikipedia, The Free Encyclopedia. Wikipedia, The Free Encyclopedia, 12, Web 13.
Wikipedia Contributors, Carbon Nanotube, Wikipedia, The Free Encyclopedia, Wikipedia, The Free Encyclopedia 9.
S. Iijima, Helical microtubules of graphitic carbon, Nature 354 (6348) (1991) 56.

This page intentionally left blank

# CHAPTER 4

# Characterization techniques for nanomaterials

**P. Senthil Kumar**[1], **K. Grace Pavithra**[1] **and Mu. Naushad**[2]
[1]Department of Chemical Engineering, SSN College of Engineering, Chennai, India
[2]Department of Chemistry, College of Science, King Saud University, Riyadh, Saudi Arabia

## Contents



## 4.1 Introduction

Nanotechnology is used in sectors of science and technology such as energy, medicine and drugs, nanobiotechnology, nanodevices, optical engineering, cosmetics, bioengineering, nanofabrics, and also in the defense sector because of its large surface-area-to-volume ratio. Nanomaterials draw attention due to their unique physical, chemical, and mechanical properties from bulk solids and molecules. Nanomaterials are classified based upon their origin and structure. The classifications which depend upon the origin are: natural nanomaterials, artificial nanomaterials, zero-dimensional, one-dimensional, two-dimensional, and three-dimensional. Structural classification nanomaterials are classified into four types: carbon-based, metal-based, dendrimers, and composites. Size distribution is the most important information in dealing with nanomaterials. With decrease in size there is increase in portion of surface atoms. Nanoparticles make a connection between bulk materials and atomic structures [1,2]. When comparing to bulk materials, nanomaterials which are considered as low-dimensional material have unique thermophysical

*Nanomaterials for Solar Cell Applications*
DOI: https://doi.org/10.1016/B978-0-12-813337-8.00004-7

properties and thermophysical characterization, which was found to be important in the field of nanoscience and nanotechnology. Small size, high surface area, easy blend with liquids, deep access to cells, strength, and ductility are some of the advantages found in nanomaterials. Some challenges, such as safety-related issues in exposure to engineered nanomaterials mainly in air and in water, loss of jobs in manufacturing and farming and easy availability of automated weapons are current concerns in the field of nanomaterials. The usage of nanomaterials has increased in various fields such as carbon nanotubes, medicine, information technology, nanorobots, nanocomputers, solar cells, and paper batteries, before labeling a nanomaterial, characterization of the material is needed. This chapter deals with the characterization techniques which are currently in practice within the field of nanomaterials [3,4].

## 4.2 Characterization techniques for nanomaterials

Nanomaterials have large surface-area-to-volume ratio that differs in orders of magnitude greater from the macroscopic materials. The size and structure of the nanomaterials depend upon factors such as surfactant additives, reactant concentrations, temperature, solvent conditions on the time of synthesis, and salt. In order to develop reproducible synthesis of nanomaterials, characterization of nanomaterials is found to be important. Characterization refers to the study of composition, structure, and other properties such as physical, chemical, electrical, and magnetic. Many techniques are available for the characterization of nanomaterials, but a degree of uncertainty is seen in each technique [5,6].

### 4.2.1 Characterization based upon nanomaterial properties

#### *4.2.1.1 Optical characterization techniques*

##### 4.2.1.1.1 Confocal laser scanning microscopy

The main feature of confocal microscopy is its ability to produce images which are blur-free from thick specimens in different depths. Point to point information about images is gathered and reconstructed with a computer instead of projecting into an eyepiece. Depth of field, elimination of image degradation when images are out-of-focus and collection of images from thick specimens are some of the advantages of laser scanning confocal microscopy as compared to optical microscopy. Fig. 4.1 shows schematic representation of confocal laser scanning microscopy. The advantage is elimination of out-of-focus light by using spatial filtering

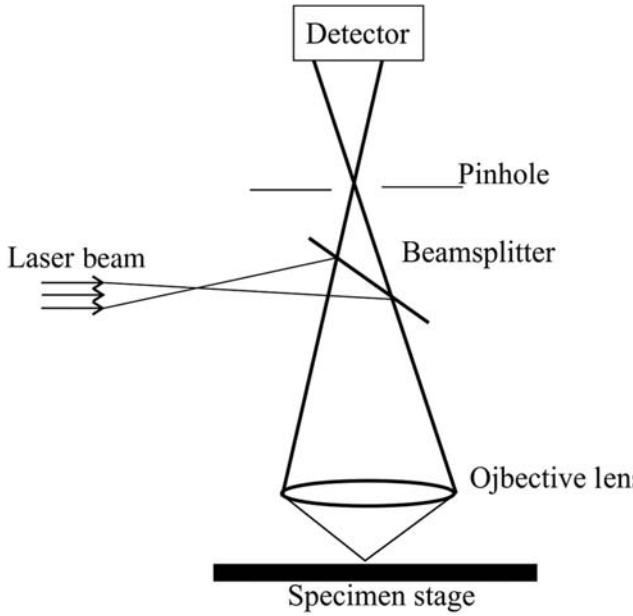


**Figure 4.1** Schematic representation of confocal laser scanning microscopy.

when the specimen is thicker than the plane of focus. Different imaging modes such as single, double, triple, or multiple illumination modes are seen. Confocal microscopy uses raster scanning and scans the specimen point by point. The detection process was found to be slow and the axial resolution was found to be slow as compared to lateral resolution. Instead of illuminating the optical section, confocal microscopy illuminates the entire column and it causes photodamage [7].

#### 4.2.1.1.2 Scanning near-field optical microscopy

The topography and the optical properties of nanomaterials can be measured using near-field optical microscopy. This method also provides details about the surface of the nanofeatures and their optical, as well as electronic, properties. The near-field scanner has an arbitrarily small aperture and it is illuminated at the back side with constant distance. The samples are scanned at a small distance below the aperture, and optical resolution of transmitted or reflected light is limited by the diameter of the aperture. 60−100 nm of optical resolution is normally attained, and the optical images are obtained by scanning the sample surface point by point and line by line. Some of the advantages of scanning near-field

optical microscopy (SNOM) include: high resolution of images up to 25 nm, analyzing of multiple properties and usage for different kinds of samples. Some of the disadvantages include: this type of scanning is limited to very low working distance and at extremely shallow depth of field, does not provide details of nonconductive soft materials and takes long scan times for large sample areas. This type of microscopy is generally seen in the field of nanotechnology, nanophotonics, nanooptics, life sciences, and in material research. Single-molecule detection is possible and dynamic properties at subwavelength scale are done using SNOM [8].

#### 4.2.1.1.3 Two-photon fluorescence microscopy

Two-photon fluorescence Microscopy is used for studying biological systems. It is a nonlinear process which involves absorption of two photons whose combined energy is greater than the energy gap between the excited states and the molecule's ground. This energy gap is sufficient to make an excited electronic state in molecular transition. Two-photon absorptions by a fluorescent molecule is an excitation radiance's quadratic function. Deeper tissue penetration and less photodamage are some of advantages of two-photon fluorescence microscopy and lower resolution is the main drawback. This type of scanning is mainly seen in the fields of physiology, neurobiology, embryology, and tissue engineering. Two-photon fluorescence microscopy finds its special application in noninvasive optical biopsy [9,10].

#### 4.2.1.1.4 Dynamic light scattering

Dynamic light scattering (DLS) is used for measuring the size of the particle and the measurement of molecules in suspension. Alternative names for DLS are photon correlation spectroscopy or quasielastic light scattering. Hydrodynamic size, shape, structure, aggregation state, and biomolecular confirmation can be obtained using scattering techniques. From submicron to nanometers of polymers scattering modalities, size distribution is obtained using a monochromatic light source. The temporal fluctuations are monitored using DLS. The particles which follow Brownian movement are measured by this technique, and the particle size, sample viscosity, and temperature influences the speed. Brownian motion causes the particle to diffuse through the medium. This instrument measures the scattered intensity at a fixed scattering angle with time. The static light scattering measures the scattered intensity as a function of angle. The

timescale of light intensity fluctuations and temporal fluctuations are measured using DLS, and it also provides information regarding average size, size distribution, and polydispersity of molecules, as well as particles in solution. Experiment durations are found to be short. Precision in accuracy of hydrodynamic size of samples, measuring diluted samples, analyzing a wide range of concentrations and giving reproducible measurements represent many of the positive aspects of DLS. In addition, costs are found to be less. Some of the disadvantages of DLS include: sensitivity to mechanical disturbances, lack of selectivity, low signal strength, analyzation with heterogeneous size distributions, unsuitability in the measurement of nonspherical nanomaterials and applicability only for transparent samples. The particles, including proteins, polymers, micelles, carbohydrates, and nanoparticles, are measured using DLS as it concentrates mainly on the size of the particle. If the system is not dispersing in size, the diameter of the particle is noted as its size and the measurement purely depend upon the core particle size, surface structure's size, the concentration of the particle and the types of ions in the medium [10,11].

#### 4.2.1.1.5 Brewster angle microscopy

Thin films on liquid surfaces are imaged using a Brewster angle microscope. Based on the principle that if p-polarized light is used, no light is reflected from the air–water interface under Brewster's angle incidence but there is a change in its principle when there is a constant angle of incidence which leads to the formation of a monolayer on the water surface. This monolayer alters the Brewster angle condition. This type of microscopy is used for imaging adsorbed or spread monolayers. Brewster angle microscopy is used for studying phase transitions, characterization of domain microstructure, phase separation in mixed monolayers and changes due to complex formation. This technique focuses more on optical anisotropy of monolayers. A refractive index different from that of water can also be analyzed [12,13].

### *4.2.1.2 Physicochemical characterization*

#### 4.2.1.2.1 Fluorescence correlation spectroscopy

Spontaneous intensity fluctuations, such as those where quantitative information such as hydrodynamic radii, average concentrations, chemical reaction rate, and diffusion coefficients are yielded using fluorescence correlation spectroscopy (FCS). FCS and its derivatives analyze the binding kinetics between donor and acceptor. The advantage of FCS over DLS is

the requirement of a small amount of fluorescent particles for monitoring probe particles. FCS also prevents interfering contributions from the medium. The advantages of FCS lie with the proper selection of fluorophore with extinction coefficient, high quantum yield and low photobleaching. The disadvantages include the lack of models, which limits the applications of FCS. Fig. 4.2 provides the block diagram for FCS.

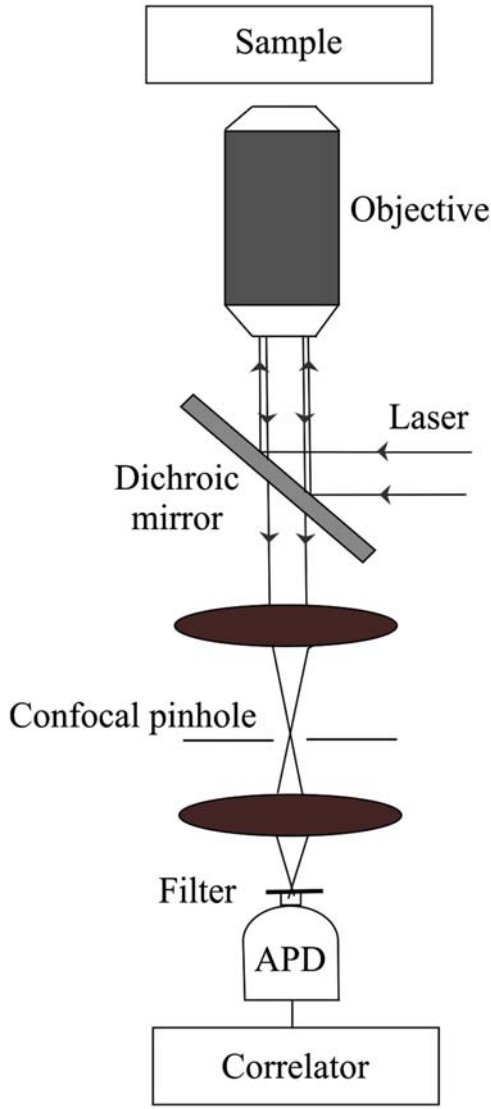


**Figure 4.2** Fundamental block diagram of fluorescence correlation spectroscopy.

#### 4.2.1.2.2 Raman scattering

Structural characterization of nanomaterials is done using Raman scattering (RS). The principle of RS resides in measuring the inelastic scattering of photons possessing different frequencies from the incident light after interacting with electric dipoles of the molecule. RS is found to be complementary to infrared (IR) spectroscopy. Raman caterers are found to be weak in water molecules used for studying about biological samples in aqueous solutions and further tissue abnormalities can be identified using RS. It has advantages which include analyzing average size and size distribution. Disadvantages of RS include lagging in spatial resolution in delineating the applications in nanotechnology, smaller cross sections, the demand for intensive laser excitation, and the requirement for large amounts of samples to provide sufficient RS signals. In addition to RS, the implementation of surface-enhanced RS (SERS) strongly influences RS signals. In order to gain surface enhancement in Raman signals, tip-enhanced Raman spectroscopy (TERS) uses an aperture with a less metallic tip than that of the optical fiber. When compared to RS, SERS, and TERS, RS provides information regarding topological data in addition to the structure, chemical, and electronic properties of the nanomaterials in question [14,15].

#### 4.2.1.2.3 Nuclear magnetic resonance

The atomic nuclei which possess both magnetic moments and angular momentum when subjected to an external magnetic field are handled using nuclear magnetic resonance (NMR). NMR acts as a transformational molecular characterization tool and provides exceptional detail regarding the chemical environments of constituent atomic nuclei. Chemical structure, reactions, and even dynamics are analyzed using NMR. The schematic representation of NMR is explained in Fig. 4.3. NMR is extremely sensitive to the magnetic environment of nuclei and observes the individual spectral lines of nuclei in different environments. NMR magnetically orders materials and deals with atomic nuclei possessing both magnetic moments and angular momentum that are subjected to a magnetic field [16,17]. The phenomenon of NMR depends upon the nuclei of atoms which have magnetic properties that can be utilized to yield chemical information. The physiochemical characteristics, including the structure, purity, and functionality in dendrimers and fullerene derivatives, are analyzed. In recent studies pulsed field gradient NMR has been implemented to evaluate the diffusivity of nanomaterials, under

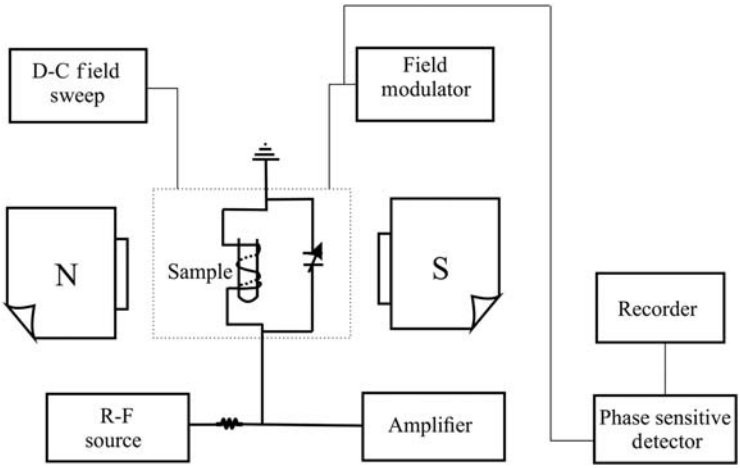


**Figure 4.3** Schematic representation of nuclear magnetic resonance.

which the size and species interaction are investigated. Smaller amounts of sample preparation, low detection sensitivity, and time consumption represent some of the drawbacks [18,19].

#### 4.2.1.2.4 Mass spectrometry

Mass, elemental composition, and the chemical structure of the molecules are determined using an analytical technique called mass spectrometry (MS). Using various MS procedures, several physiochemical characteristics of nanomaterials, such as mass, composition, and structure, can be determined. The principle of MS rests on the way it distinguishes charged particles with different masses using their mass-to-charge ratio. It gives high precision and high sensitivity in detection. In the fields of nanotechnology, environmental, and toxicological studies, MS is currently used for characterization and quantification. For inductively coupled plasma (ICP), MS is used to vaporize, atomize, and ionize the elements, and also provides elemental chemical analysis. This combination gives reliable quantification and elemental composition of metallic nanoparticles and impurities in nonmetallic nanoparticles. It provides high accuracy and measurement with precision. Some of the disadvantages, such as the equipment cost and lack in databases for the identification of species, have been identified. [15,20].

#### 4.2.1.2.5 Zeta potential

Charged particles with oppositely charged ions form a thin layer called the "stern" layer in an ionic solution with a diffusive layer at the outer

area containing loosely associated ions. These two layers are responsible for electric double layers. Instead of ions staying in the bulk dispersant on the outside layer, the movement of a charged particle shears ion migrates in the diffused layer. Shear surface electric potential is known as zeta potential and it is usually determined by the velocity of charged species toward the electrode with an external electric field in a sample solution. Maintenance of 30 mV zeta potential is mandatory. Less than 30 mV leads to coagulation, aggregation, instability, etc. To measure zeta potential electrophoretic light scattering is used. This measures the velocity of a charged particle in a liquid state. But an electroosmotic effect is the major problem with this method because it reduces the precision. The disadvantages of zeta potential measurement are that it is subjected to environmental changes which include pH, ionic strength, etc. [21–23].

#### 4.2.1.2.6 X-ray diffraction

In order to find the average size of the particle and structure, diffraction techniques are used. This type of information includes variations in crystal structure, phase quantification and identification, shape and size of crystallite, distortion of lattice, size, and periodicity of noncrystalline and orientation, etc., The crystal which is going to be measured is mounted on the goniometer and it is bombarded using X-rays with gradual rotation. Using Fourier transform (FT) the two-dimensional images are converted to three-dimensional images. When the crystals are too small, poor resolution or error may occur. Crystals are considered as arrays of atom and X-rays are known as electromagnetic radiation. A regular array of caterers produces spherical waves of regular arrays. According to Bragg's law, the waves are constructively added in specific directions.

$$2d \sin \theta = n\lambda$$

where $d$ is spacing between diffracting angles, $\theta$ is incident angle, $n$ is integer, and $\lambda$ is wavelength of the beam.

X-ray diffraction (XRD) is a well-established technique and, at atomic scale, high-resolution images are seen. The limitations, such as the single confirmation state in which the sample is accessible and the low intensity compared to electron diffraction, have been noted [15,24].

### *4.2.1.3 Thermogravimetric measurement technique*

Under programmed conditions, mass change of a nanomaterials can be analyzed using thermogravimetric analysis. This type of measurement is used to understand events like absorption, desorption, adsorption,

sublimation, decomposition, oxidation, and reduction in cases like loss of volatile or gaseous products during chemical reactions, especially in nanomaterials. Polymers, paints, films, etc. can be analyzed using this method. The instrument consists of an electronic microbalance, sample holder, furnace, temperature programmer, and recorder. The purpose of the microbalance is to record the changes which are associated with the sample mass. Two types of balance are available. These balances include the deflection type and null-point type. The sample holder is also known as a crucible, where the samples are investigated. The crucible is attached to the weighing arm of the microbalance. The differing types of crucible are deep, loosely covered, retort cup, and shallow pan type. Furnaces are designed in such a manner as to achieve a linear heating rate throughout the analysis. Thermocouples are used to measure the temperature, and the temperature programmer controls the heating rate when the temperature increases during the analysis [25–27].

#### 4.2.1.3.1 Evolved gas analysis

The number of volatile products formed during the thermal degradation of materials is determined using a technique known as evolved gas analysis (EGA). EGA generally analyses the chemical pathway of degradation reactions by analyzing the decomposition products of composition. Two approaches, namely simultaneous analysis and combined analysis, are seen in EGA. Thermogravimetric FT-IR spectroscopy and thermogravimetric mass spectroscopy fall under simultaneous analysis wherein the decomposition products which are evolved from the materials are monitored simultaneously. In the combined analysis technique, more than one sample is analyzed and is not viable for use in real-time applications [28,29].

- Thermogravimetric analysis-coupled FT-IR spectrometry. These types of systems are generally used for analysis. The released components during combustion or volatilization are transferred to an IR cell for identifications. For simple components like carbon dioxide or solvents, this type of coupled instrument is useful.
- Thermogravimetric analysis–mass spectroscopy. Low level of impurities in real time are analyzed using this system. For every minute, components present in the evolved gas are identified. In departments like quality control and safety and in product development these techniques are found to be useful [30–32].

## 4.2.2 Characterization technique based upon instruments

### *4.2.2.1 Scanning electron microscopy techniques*

Scanning electron microscopy (SEM) is considered a versatile technique for micro- and nanostructures analysis with a large range of applications. The SEM technique provides information regarding composition and topography of surfaces and Fig. 4.4 represents the working principle of SEM. The advantages of SEM include adjustable magnifications from reading glass magnification and imposition of structure visualization. It achieves information from the signals originating from specific interactions onto the material compositions. SEM falls under the category of a surface-imaging method in which the sample surface scans across an electron beam. It reflects the topographic detail and atomic composition by generating signals with sample interactions. Characteristics such as topography, morphology, composition, and crystallographic information are obtained using SEM. Before placing a sample, the surface of the sample is viewed using SEM. The resolution attained by SEM is around 1 nm and it mainly depends upon the operating parameters, properties of the

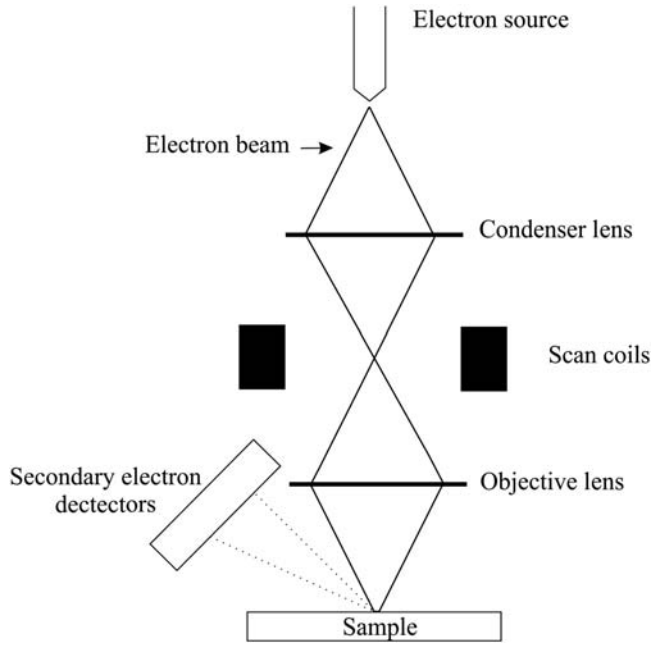


**Figure 4.4** Working principle of scanning electron microscopy techniques.

specified sample. They work on electrons that are generated, accelerated, and focused toward the sample.

#### 4.2.2.1.1 Near-field scanning optical microscopy

This type of microscope is limited to the diffraction phenomenon of illuminating light. In a conventional optical microscope, visible light is used and optical microscopy is not useful for dealing with nanostructured investigations. The concepts of both surface-probe microscopy and optical microscopy to exceed far-field resolution limits are seen in near-field scanning optical microscopy (NSOM). The working principle of NSOM is represented in Fig. 4.5. Instead of equipping objective lenses, the laser light is adjusted to emit optical fiber to the tip of the aperture which is closer in proximity to the object. The NSOM consists of phase contrast,

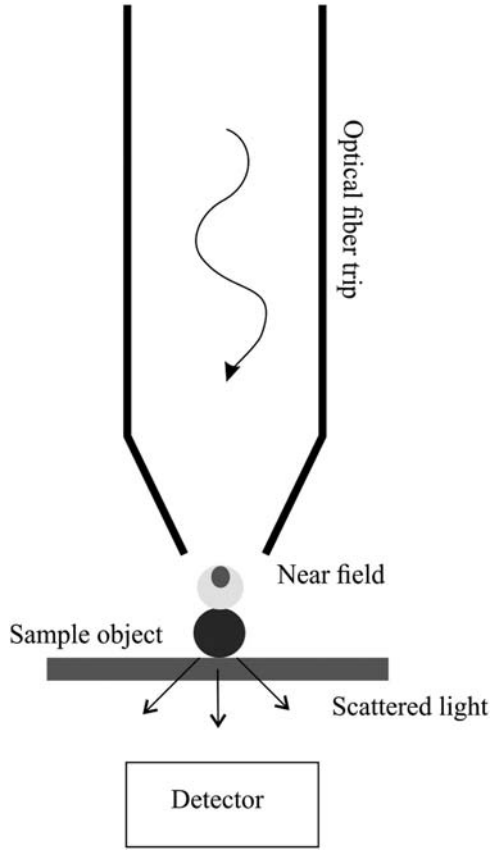


**Figure 4.5** Working principle of near-field scanning optical microscopy.

polarization, fluorescence, and staining, which are seen in optical microscopy. In addition, NSOM includes distribution of single molecules on the surfaces of cells and associations in protein− Nanoparticle (NP) conjugates at nanoscaled spatial determinations which facilitates for characterization of nanomaterials. The disadvantages of NSOM include high-resolution images as output, excitation of weak fluorescent molecules, hindrance in low incident light intensity, and imaging of surface features [33,34].

#### 4.2.2.1.2 Transmission electron microscopy

Transmission electron microscopy (TEM) is considered to be the most popular technique in characterizing nanomaterials in electron microscopy. The chemical information and images of nanomaterials at a spatial resolution equal to the level of atomic dimensions are provided using TEM. The electron beam through which incident light is transmitted via a thin foil specimen is transformed into elastically or inelastically scattered electrons when the electron beam interacts with the specimen. The ratio of distance between the objective lens, the specimen, and the image plane are considered as magnified by the lens. Both TEM and SEM show the size, degree of aggregation, and dispersion, as well as the heterogeneity of nonmaterial. When compared to SEM, TEM has more advantages in providing spatial resolution in good quality and analytical measurements. Precise particle size of bright field images as well as dark field images are provided by the TEM, and it provides details regarding nanoparticles as it utilizes energetic electrons to provide information regarding morphologic, compositional, and crystallographic information. Imaging, spectroscopy, and diffraction techniques are the three main techniques seen in TEM techniques. The classification and working principle of TEM are explained in Figs. 4.6 and 4.7, respectively.

TEM functions under the principle of optical microscopy. The electrons are replaced by photons, glass lenses are replaced by electromagnetic lenses, and images are viewed in a screen instead of an eyepiece. The advantages of TEM include powerful magnification and the provision of information regarding compound and element structures. TEM requires special maintenance and expensive, black-and-white images are considered as output [35].

#### 4.2.2.1.3 Atomic force microscopy

Atomic force microscopy (AFM) works on the principle of Hook's law wherein the probe travels near the surface of the specimen. The local

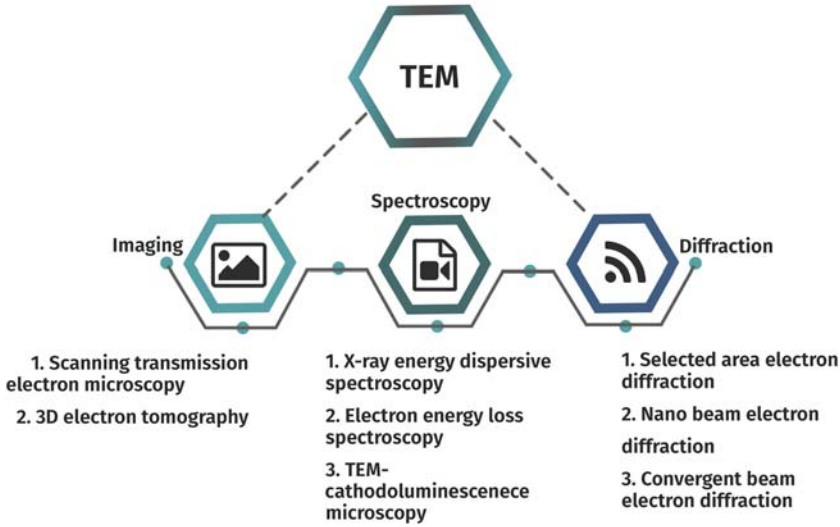


**Figure 4.6** Classification of TEM. *TEM*, Transmission electron microscopy.

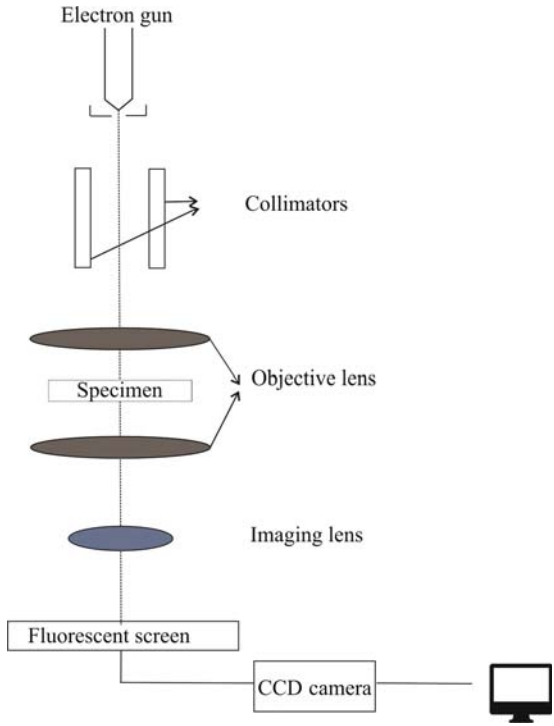


**Figure 4.7** Working principle of TEM. *TEM*, Transmission electron microscopy.

properties like height, friction, and magnetism with probe are measured using AFM. AFM is a kind of scanning probe microscopy (SPM). The probe scans over the small area of the sample while measuring the local property of the sample simultaneously. The principles of AFM are as follows: the cantilever provides a sharp tip to scan onto the sample surface. By using the optical lever, the AFM measures the vertical as well as lateral deflections of the cantilever. The optical lever reflects the laser and the laser strikes the position-sensitive photodetector which consists of four segments. The position of the laser spot on the detector and the angular deflections of the cantilever are achieved by the differences between the segments of the photodetector of signals. Piezo-ceramics are placed in the tip with higher resolution and Fig. 4.8 shows the function of AFM. With the help of a voltage gradient, AFM expands or contracts. In measuring the force on the sample, AFM also regulates the force and allows capturing of images at low forces. Tube scanners are seen in the feedback loop, which controls the tip height, the cantilever, and the optical lever. The cantilever deflection is kept constant by adjusting the voltage applied in the feedback circuit. The height, to the order of several micrometers

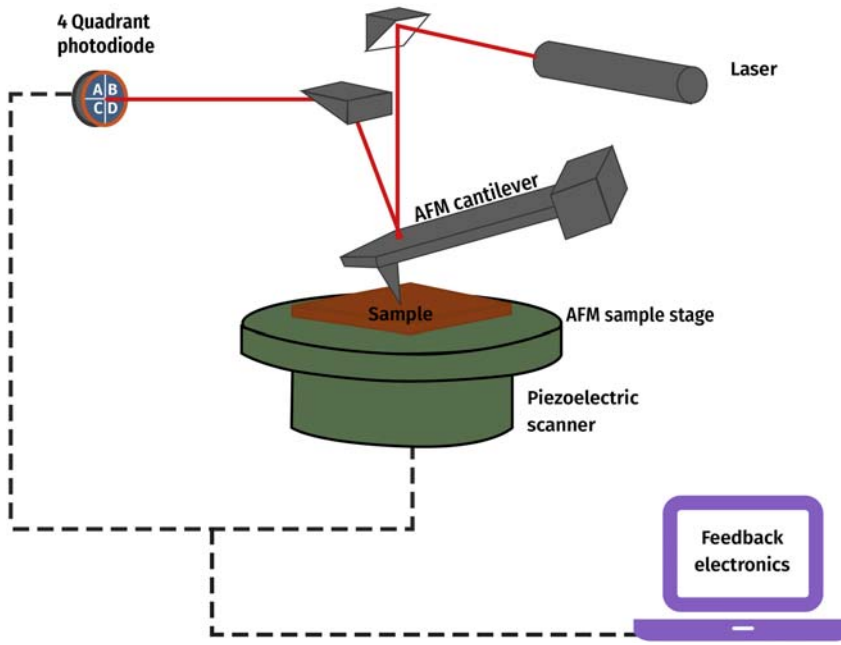


**Figure 4.8** Schematic diagram of AFM principle. *AFM*, Atomic force microscopy.

only, is covered by AFM. Another drawback is that the quality of the image is limited to its curvature of the probe tip [15,36].

#### 4.2.2.1.4 Energy-dispersive X-ray microanalysis

Generally referred to as microanalysis and used to measure micrometer dimensions, energy-dispersive X-ray (EDX) performs with a sample matrix, electron beam energy which produces interaction volume and resolution which is of the order of a few cubic micrometers. These items are generally attached with SEM or TEM, depending upon the specimen of interest. EDX offers elemental mapping as well as image analysis of samples. Its application is mainly seen in analyzing contaminated samples and in forensic science investigations. Without any preliminary sample preparation, nondestructive analysis of the sample can be done. Rapid identification of contaminant and source, control over environmental factors, greater production yield, and identification of source of problem are some of the advantages of using EDX [37].

#### 4.2.2.1.5 Environmental scanning electron microscopy

This type of instrument allows variable pressures into the microscope sample chamber while maintaining an ultrahigh vacuum which is essential for beam generation in the column. Environmental scanning electron microscopy (E-SEM) is also referred to as "variable-pressure SEM" or "low-vacuum SEM," which purely depends upon the instrument manufacturer and the range of pressure variations. E-SEM is the separation of the two different pressure levels in the microscope chamber where the sensitive sample is positioned and the ultrahigh vacuum is required in the column. Used for analyzing morphology and topography down to the resolution of 1.2 nm. E-SEM has an ability to perform the measurement under humid conditions. Signal-to-noise ratio and spatial resolution are significantly improved by the use of a field emission gun [37,38].

#### 4.2.2.1.6 Cryo-scanning microscopy

Some samples require cooling before analyzing with SEM. For such situations the sample has to be prepared using cryo-conditions and the cold sample must be transferred to the microscope. Two approaches are available for preparing the sample under cryo-conditions: (1) Using the device like a plunger, cryo-ultramicrotome, and freeze dryer. The cold sample is prepared and transferred to the SEM chamber into a cryo-stage. (2) Samples are prepared inside the cryo-SEM.

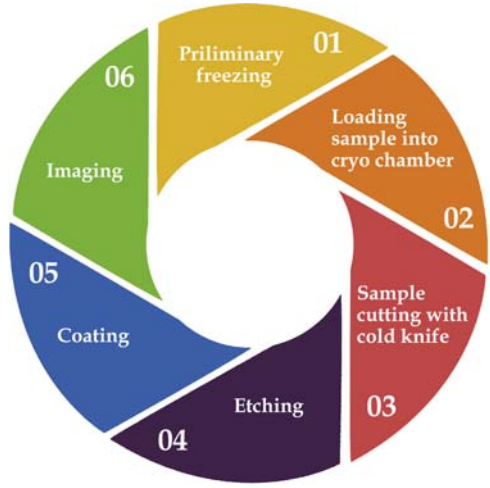


**Figure 4.9** Operating procedure for cryo-SEM. *SEM*, Scanning electron microscopy.

Before loading into the cryo-SEM the sample containing moisture has to be frozen using liquid nitrogen. By the help of an airlock system, the frozen sample is loaded into the specimen process stage. In order to examine the internal structure, the sample is cleaved using a cold knife. Etching has to be done on the cleaved surface in a controlled manner to remove the ice and the sample has to be coated with Au for imaging. The working procedure for cryo-SEM is explained in Fig. 4.9. No chemicals are added to the specimens so that ultrastructural details are not altered. The main disadvantages are the low-contrast images, the costly nature of the machinery, and the tedious method required for the sectioning of samples in the frozen state [39,40].

### *4.2.2.2 Spectroscopic techniques*

#### 4.2.2.2.1 Ultraviolet–visible absorption

For characterizing different types of organic, inorganic, and biological materials, Ultraviolet (UV)–visible spectroscopy is used. This method measures the light passing through a sample. It is used as a tool for identifying, characterizing, and studying nanomaterials, and the schematic representation of UV–visible spectroscopy. The schematic representation of UV–visible spectroscopy is explained in Fig. 4.10. To study the relationship between absorbance spectra and particle size distributions of quantum-sized nanocrystals, UV spectroscopy is used. In characterizing metal nanoparticles, UV spectroscopy was found to be one of the great

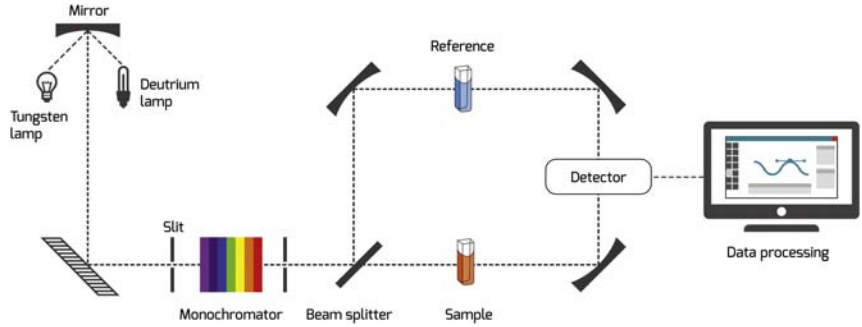


**Figure 4.10** Schematic representation of UV spectroscopy. *UV*, Ultraviolet.

tools for analyzing the size, shape, and surface property in the form of colloidal dispersion system. In addition to this, UV spectroscopy also detects the amount of precursor metal ions used during the formation of metal nanoparticles. Because of its two advantages, easy use and quick analysis of substance, a UV–visible spectrometer is used in the field of medicine, research, forensic analysis, etc., When the mirrors of a double-beam UV–visible spectrometer is covered by dust or grime, the performance of the device degrades, and the replacement cost is double that of the capital investment. The device sensitivity and measurement accuracy is decreased by the noise generated from the sample source or the electronic components within the instrument [41,42].

#### 4.2.2.2.2 Infrared spectroscopy

By measuring the vibrational frequencies of the chemical bonds, the presence of functional groups is analyzed by FT-IR spectroscopy. When the vibrational excitation energy of molecules is in the range of $10^{13}$–$10^{14}$ Hz it corresponds to IR radiation and the vibrational transitions of the functional groups on the nanoparticle surface are observed by IR spectroscopy, both qualitatively and quantitatively. The experimental process is summarized in Fig. 4.11 and the first step deals with the activation of the surface by means of heating or some other means. Thermal treatment is normally used because it cleans up the surface of the sample from physisorbed and chemisorbed species, which are weak, and it purely depends upon the temperature. Lewis acids and basic sites, as well as Bronsted acids and basic sites, correspond to an electron acceptor, an electron donor as well as a proton donor and proton acceptor. It is a noninvasive and nondestructive technique but has high signal-to-noise ratio, and

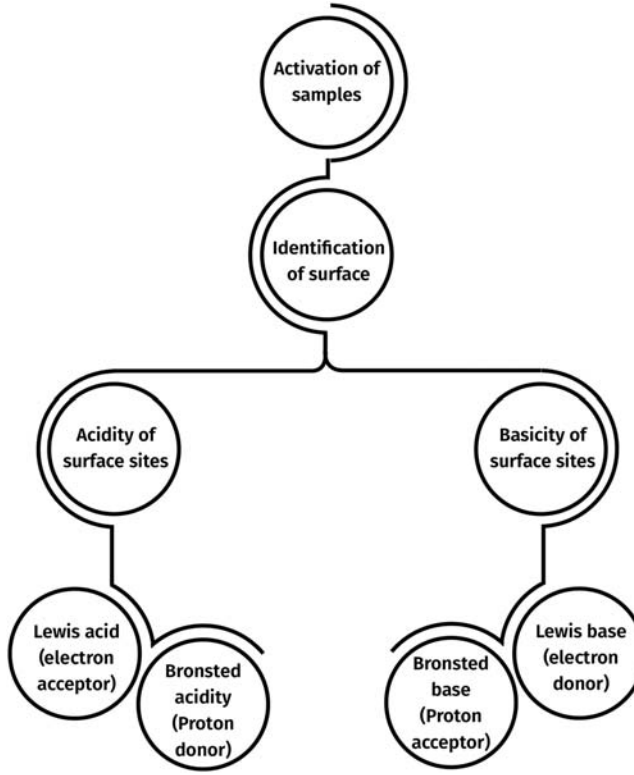


**Figure 4.11** Experimental procedure for IR. *IR*, Infrared.

the samples with low transmission and weak spectra are difficult to do with FT-IR. For characterization of carbon nanomaterials, core-shell, metallic NPs, and hybrid nanoparticles, FT-IR is utilized and the schematic representation of IR spectroscopy is explained in Fig. 4.12. The oxidation state and the surface structure of metal-oxide nanoparticles are demonstrated using $CeO_2$ NPs by IR observing O−H stretching modes presence or absence associated with O−H−O−H complexes present in fully oxidized NPs [43]. The size of the nanoparticle is analyzed using IR, near-IR Fourier transform near-infrared spectroscopy in the diffuse reflectance mode (DR-FTNIR) (spectroscopy combined with back-propagation artificial neural network). Multivariate algorithms are implemented in a research work in order to estimate the size of $TiO_2$ NPs. IR-ATR (attenuated total reflection infrared spectroscopy) is used to identify agent-induced alterations occurring within the cell, and the use of multivariate techniques like principle component analysis and linear

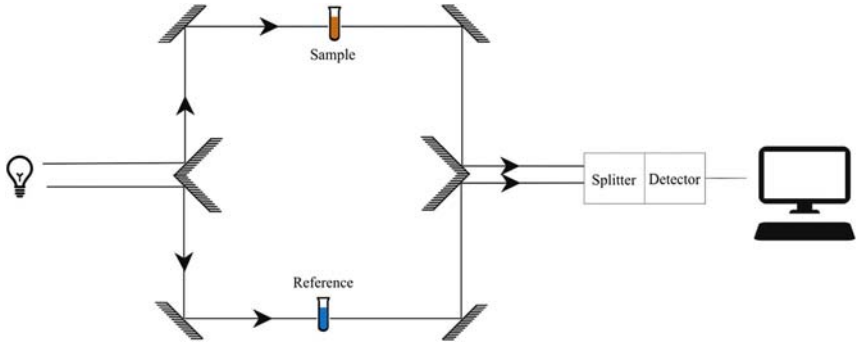


**Figure 4.12** Schematic representation of IR. *IR*, Infrared.

discriminant analysis reveal the difference between the inferred IR spectra and the combination of ATR. Multivariate algorithms are used for analyzing carbon nanoparticles. In a research work, IR-ATR spectroscopy is combined with scanning electrochemical microscopy and with AFM providing, molecule-specific IR details during electrochemical experiments. This will be considered as a next-generation tool for analyzing nanomaterials. Miniaturization of IR-sensing devices with advanced light sources, which include quantum cascade lasers and interbank cascade lasers with both a planar waveguide as well as a thin-film diamond waveguide, improves the quality of IR spectra. Different ligands attached to nanoparticles are identified using vibrational signatures in a rapid and precise manner. The drawbacks include that the molecular weight of the substance is not known, the relative position of different functional groups of a molecule are not known and, while dealing with an unknown substance, the purity of the substance cannot be determined using the IR technique [44,45].

#### 4.2.2.2.3 Surface-enhanced Raman scattering

RS is considered to be a nondestructive, efficient, and easy technique while being widely applied for the characterization of nanoparticles. Low sensitivity is considered a limitation in normal Raman spectroscopy. SERS is used in characterizing nanoparticles. It is considered a powerful technique that enhances RS. For the enhancement effect, two mechanisms, surface Plasmon resonance and resonance enhancement, are responsible. A combination of atomic force and scanning tunneling microscopes is referred to as "nano-Raman" when the above pieces of equipment are connected with a Raman spectrometer.

#### *4.2.2.3 Probe characterization techniques*

##### 4.2.2.3.1 Electron probe characterization

**4.2.2.3.1.1 Scanning probe electron microscopy** SPM represents a tool which makes images for nanoscale structures and surfaces. It uses light waves for imaging, and the interaction power between the surface and the tip is monitored. The surface of the material is scanned using a sharp probe which is kept at a few angstroms or nanometers, and three-dimensional topographic images are obtained due to the interactions between the sharp probe and the surface of the nanomaterial. Two modes are available for scanning: contact and noncontact. AFM, magnetic force microscopy, and scanning tunneling microscopes fall under this technique. Some of the advantages of SPM are that it measures small differences in object height, and the specialized probes provide faster, more efficient specimen images with less effort. The disadvantages are that it cannot be used for solid–solid or liquid–liquid surfaces, as the maximum image size is smaller. The idea of topography, electrical, as well as magnetic properties of the nanomaterials is acquired using SPM. Using SPM information can also be transferred to sample.

**4.2.2.3.1.2 Electron probe microanalysis** Electron probe microanalysis (EPMA) is used to determine the local chemical composition of materials in multiphase. It gives the detailed image of the sample with nondestructive in situ chemical analysis. This technique is based upon the X-rays excited from the specimen. It is based upon the principle of bombardment by an accelerated and focused electron beam onto the solid material, and the incident electron beam has energy to liberate matter and energy from the sample. The electron–sample interaction liberates heat, derivative electrons, and X-rays. These X-rays are used for analyzing the surface and average composition of the material. The geological materials are analyzed using EPMA. The lightest elements are unable to detect and different valence states are nondetectable with EPMA. Individual phases are analyzed using EPMA. In some cases, the age of the mineral can be obtained without isotopic ratios.

**4.2.2.3.1.3 Scanning transmission electron microscopy** Scanning TEM combines the principle of TEM and SEM, and analysis is performed on any of the two instruments. When the electron probe interacts with the specimen inside the scanning transmission electron microscopy, a variety of electron, electromagnetic, and other signals can be generated. This signal can be used to form images of the specimen. It provides

information regarding imaging, diffraction as well as spectroscopic information [46,47].

#### 4.2.2.3.2 Photon probe characterization

**4.2.2.3.2.1 Photoelectron spectroscopy** The electrons emitted from solids, gases, or liquids by photoelectric effect are measured by determining the binding energies measured in the electrons present in the substance. This process is very expensive, and high vacuum as well as large areas are required for analysis. Photoelectron spectroscopy (PES) has two types:

1. UV PES: The photon energy ranges from 10 to 50 eV are used to study the valence energy levels and chemical bonding, particularly the bonding character of molecular orbitals.
2. X-ray PES (XPS): Known as surface-sensitive spectroscopic technique that measures in the range of parts per thousand. By irradiating the beam of X-rays and simultaneously measuring the kinetic energy and number of escaped electrons of the material being analyzed. XPS is also known as electron microscopy and used for chemical analysis.

**4.2.2.3.2.2 Ultraviolet–visible spectroscopy** The light of the UV region is absorbed by the molecule. The UV radiation results in excitation of the electrons from the ground state to the higher energy state. The difference between the ground state and the higher state is equal to the UV radiation that is absorbed. The electromagnetic radiation between 190 and 800 nm and this region is divided into UV (190–400 nm) and visible (400–800 nm) regions. Beer–Lambert law is used in UV spectroscopy. Beer–Lambert law obeys the principle that the greater the number of molecules capable of absorbing light of a given wavelength, the greater the extent of light absorption. For quantitative determination of analyses UV–visible spectroscopy is used. The device performance degrades if there is dust or grime in the mirror, and the noise generated by the sample source as well as from the electronic components also degrades the measurement accuracy.

**4.2.2.3.2.3 Atomic absorption spectroscopy** Atomic absorption spectroscopy determines chemical elements by using absorption of optical radiation with the help of free atoms in a gaseous state. It relies on Beer–Lambert law, where it establishes the relation between the sample concentration which is needed in order to be analyzed, and the standards which come from known analysis. This is a sensitive instrument which measures to parts per billion. Some of the disadvantages in atomic

absorption spectroscopy are as follows: only solutions can be analyzed, this method requires a large sample and it also has problems with refractory elements.

**4.2.2.3.2.4 Inductively coupled plasma spectroscopy** ICP spectroscopy is a type of mass spectroscopy which is capable of detecting metals and nonmetals at concentrations less than 1 part in $10^{15}$. The samples are ionized using ICP, and the separation/quantification part is done using a mass spectrometer. ICP has greater speed and precision, as well as sensitivity, when compared to atomic absorption spectroscopy. This type of instrument is used for isotope ratio measurements and not for routine milt-elemental analysis.

**4.2.2.3.2.5 Fluorescence spectroscopy** Fluorescence spectroscopy is a type of electromagnetic spectroscopy which analyses fluorescence from the sample. The two-photon emission processes, such as fluorescence and phosphorescence, occur during molecular relaxation from an electronic excited state. The transition between vibrational and electronic states of polyatomic fluorescent molecules occurs in the photonic process. Excitation occurs and, after excitation, the molecules are relaxed to the vibrational level of the excited state. The excitation occurs within femtoseconds to picoseconds, and is used in fields like DNA sequencing, forensics, genetic analysis, and biotechnology. The components which have fluorescence capability will be identified using this technique. Contamination in the fluorescence sample may lead to a false reading [48,49].

### 4.2.2.3.3 Ion particle probe characterization

**4.2.2.3.3.1 Rutherford backscattering** Rutherford backscattering spectrometry (RBS) is an ion scattering technique used for thin-film analysis without using reference standards. In RBS analysis, high energy ions are passed onto the sample and the energy distribution while a backscattered yield at a given angle is measured. This method analyses contamination level and can make a determination of thickness density of the silicide layer. RBS provides lower accuracy for lower elements in the periodic table [50].

**4.2.2.3.3.2 Small-angle scattering** This technique gives information regarding shape, size, and orientation of structures, and it is utilized for large-scale structures from 10 Angstrom to several tens of thousands of angstroms. This method is used for analyzing the inner structure of a disordered system.

**4.2.2.3.3.3 Small-angle neutron scattering** For materials of only a few nanometers to a millimeter in length, neutron scattering techniques are often used. The shape and size of the particle dispersed in a homogenous medium is studied using this technique. The principle of small-angle neutron scattering (SANS) rests in the scattering of a monochromatic beam of neutron and the measurement of scattered neutron intensity as a function of scattering angle. The major disadvantage of SANS is that it does not work on thin films and substrates.

**4.2.2.3.3.4 Small-angle X-ray scattering** By characterizing the average particle size and shapes, small-angle X-ray scattering (SAXS) provides detailed structural analysis and physical information for a sample between 1 and 100 nm. Information such as pore size, surface-to-volume ratio, lattice type, and dimensions are determined using this technique. XRD is limited to crystalline materials, but SAXS provides many characteristics regarding crystalline or amorphous materials. In this technique, part of incident X-rays are elastically scattered. From the sample forms a scattering pattern on a 2D X-ray detector which is perpendicular to the direction of the incident X-ray beam. The scattered X-ray collected within the scattering angle gives the details about size distribution, shape, orientation, and structure of a variety of nanomaterials and polymers. It provides holistic information of the structure and gives the information of a nonrepeating structure while following a nondestructive method. The disadvantage of this method is obtainment of low-resolution images [51].

**4.2.2.3.3.5 Cathodoluminescence** Cathodoluminescence is a combination of optical and electromagnetic phenomena. It is the inverse of a photoelectric effect, where irradiation with photons induces electron emission. Cathodoluminescence is considered a tool for obtaining composition, optical as well as electrical properties of the material and comparing, with microstructure, composition, and morphology in SEM. It gives full details about the given sample with correlations. The drawback of this technique is that only the sample which has a luminescence property can be analyzed by this technique [20,52].

## 4.3 Advanced measurement techniques

New combinations of techniques are innovated in order to find the characteristics of nanomaterials. Asymmetric flow field flow fractionation

(AF4) is a liquid phase size separation technique which can be coupled with many numbers of downstream detectors. It consists of perpendicular cross flow which pushes the particles against a semipermeable membrane. Brownian motion is seen in the smallest particles and the particle diffuses into the center of the channel, where the elution is higher. The retention time of AF4 can provide equivalent sphere hydrodynamic diameter. AF4 provides better results than microscopy-based techniques. The power of AF4 can be amplified with the addition of downstream detectors. When AF4 couples, inductively coupled plasma mass spectroscopy (ICP-MS) provides a wealth of information about each particle size in a heterogeneous mixture. Metallic clusters smaller than 1 nm can be measured using AF4-ICP-MS [53,54]. Electrospray differential mobility analysis (ES-DMA) is an aerodynamic sizing technique used in nanoparticle characterization where the aerodynamic diameter is obtained by measuring the ballistic distance traveled by the particle under an applied voltage. AF4 can be coupled with ES-DMA for robust analysis of complex nanoparticle synthesis products. TEM combined with electron energy loss spectroscopy provides a high degree of spatial resolution for elemental mapping of TEM images [55].

## 4.4 Conclusion

Increase in demand and requirements has led to development in the field of nanomaterials. Characterization of nanomaterials is necessary to analyze the properties of nanomaterials. A discussion about characterization of nanomaterials in detail is included in this chapter. On the whole, this chapter provides a clear-cut idea regarding characterization of nanomaterials in terms of optical, thermal, and physiochemical properties, and in terms of instruments. The process, advantages, drawbacks, and applications of each individual technique are discussed briefly. The properties of samples, such as material type, composition, dimensions, and the environment in which the study is conducted, are found to be limiting factors in characterization techniques. Some of the major material characterization techniques are covered in this chapter. Apart from that, some techniques such as low energy electron diffraction, nuclear reaction analysis, fast neutron analysis, and nuclear reaction analysis are used for chemical analysis. In addition, small changes in radiation source, such as electrons or ion beams, can reveal different information about nanomaterials.

## References


[1] S. Henning, R. Ashikari, Scanning Electron Microscopy and X-ray Diffraction, vol. 1, Elsevier (Ed), 2017.

[2] C.J.C. Rayil, J. Abraham, R.K. Mishra, S.C. Georgeand, S. Thomas, Instrumental Techniques for the Characterization of Nanoparticles, vol. 3, Elsevier (Ed), 2017.

[3] P. Alessio, P.H.B. Aoki, L.N. Furini, A.E. Aliaga, C.J.L. Constantino, Spectroscopic techniques for characterization of nanomaterials, Nanocharacterization Tech. (3) (2017) 65–98.

[4] Y. Dahman, Nanotechnology and Functional Materials for Engineers, Elsevier (Ed), 2017.

[5] P. Lin, S. Lin, P.C. Wang, R. Sridhar, Techniques for physicochemical characterization of nanomaterials, Biotechnol. Adv. 32 (4) (2014) 711–726.

[6] H.J. Fecht, K. Brühne (Eds.), Carbon-Based Nanomaterials and Hybrids: Synthesis, Properties, and Commercial Applications, CRC Press, 2014.

[7] V. Rai, N. Dey, The basics of confocal microscopy, laser scanning, theory and applications, in: C.-C. Wang (Ed.), 2012. ISBN: 978-953-307-205-0.

[8] R. Xu, Light scattering: a review of particle characterization applications, Particuology 18 (2015) 11e21.

[9] S.K. Brar, M. Verma, Measurement of nanoparticles by light-scattering techniques, TrAC Trends Anal. Chem. 30 (1) (2012) 4e17.

[10] S. Thomas, R. Thomas, A.K.Z. Achariah, R.K. Mishra (Eds.), Thermal and Rheological Measurement Techniques for Nanomaterials Characterization, Elsevier, 2017.

[11] J. Lim, S.P. Yeap, H.X. Che, S.C. Low, Characterization of magnetic nanoparticle by dynamic light scattering, Nanoscale Res. Lett. 8 (2013) 381.

[12] H.D. Mobius, Direct visualization of monolayers at the air-water interface by Brewster angle microscopy, J. Phys. Chem. 95 (1991) 4590e4592.

[13] K.J. Stine, Brewster angle microscopy, in: Supramolecular Chemistry: From Molecules to Nanomaterials, 2012.

[14] J.R. Laconic (Ed.), Principles of Fluorescence Spectroscopy, Springer Science & Business Media, 2013.

[15] J.P. Lavigne, P. Espinal, C. Dunyach-Remy, N. Messad, A. Pantel, A. Sotto, Mass spectrometry: a revolution in clinical microbiology? Clin. Chem. Lab. Med. 51 (2013) 257–270.

[16] K.E. MacArthur, The use of annular dark-field scanning transmission electron microscopy for quantitative characterisation, Johnson Matthey Technol. Rev. 60 (2016) 117.

[17] K.E. Sapsford, K.M. Tyner, B.J. Dair, J.R. Deschamps, I.L. Medintz, Analyzing nanomaterial bioconjugates: a review of current and emerging purification and characterization techniques, Anal. Chem. 83 (2011) 4453–4488.

[18] S. Deshayes, V. Maurizot, M.C. Clochard, T. Berthelot, C. Baudin, G. Déléris, Synthesis of specific nanoparticles for targeting tumor angiogenesis using electron-beam irradiation, Radiat. Phys. Chem. 79 (2010) 208–213.

[19] D.G. Mullen, M. Fang, A. Desai, J.R. Baker, B.G. Orr, M.M. Banaszak Holl, A quantitative assessment of nanoparticle–ligand distributions: implications for targeted drug and imaging delivery in dendrimer conjugates, ACS Nano 4 (2010) 657–670.

[20] H. Günther, NMR Spectroscopy: Basic Principles, Concepts and Applications in Chemistry, John Wiley & Sons, 2013.

[21] K.E. Sapsford, K.M. Tyner, B.J. Dair, J.R. Deschamps, I.L. Medintz, Analyzing nanomaterial bioconjugates: a review of current and emerging purification and characterization techniques, Anal. Chem. 83 (2011) 4453–4488.

[22] J. Clogston, A. Patri, Zeta potential measurement, in: S.E. McNeil (Ed.), Characterization of Nanoparticles Intended for Drug Delivery, Humana Press, 2011, pp. 63–70.
[23] T.L. Doane, C.H. Chuang, R.J. Hill, C. Burda, Nanoparticle ζ-potentials, Acc. Chem. Res. 45 (2011) 317–326.
[24] R. Xu, Progress in nanoparticles characterization: sizing and zeta potential measurement, Particuology 6 (2008) 112–115.
[25] H.N. Chapman, P. Fromme, A. Barty, T.A. White, R.A. Kirian, A. Aquila, et al., Femtosecond X-ray protein nanocrystallography, Nature 470 (2011) 73–77.
[26] L. Wang, B. Chenlu, Y. Wei, Y. Hu, L. Song, R.K.K. Yuen, et al., Influence of iron hydroxyl phosphate particles on the thermal stability and combustible properties of polymethyl methacrylate, in: Fire Safety Science Proceedings of the Eleventh International Symposium, 2014, pp. 860–873.
[27] Z.B. Marta, D. Chelminiak, H. Kaczmarek, K.K. Anna, Effect of side substituents on thermal stability of the modified chitosan and its nanocomposites with magnetite, J. Therm. Anal. Calorim. 124 (2016) 1267–1280.
[28] R.B. Valapa, G. Pugazhenthi, V. Katiyar, Thermal degradation kinetics of sucrose palmitate reinforced poly(lactic acid) biocomposites, Int. J. Biol. Macromol. 65 (2014) 275–283.
[29] C.D. Varganici, N. Marangoci, L. Rosu, B.M. Cristian, D. Rosu, M. Pinteala, et al., TGA/DTA-FTIR-MS coupling as analytical tool for confirming inclusion complexes occurrence in supramolecular host–guest architectures, J. Anal. Appl. Pyrol. 115 (2015) 132–142. Available from: https://doi.org/10.1016/j.jaap.2015.07.006.
[30] D.K. Ojha, R. Vinu, Fast co-pyrolysis of cellulose and polypropylene using Py-GC/MS and Py-FT-IR, RSC Adv. 5 (2015) 66861–66870.
[31] E. Mansfield, K.M. Tyner, C.M. Poling, J.L. Blacklock, Determination of nanoparticle surface coatings and nanoparticle purity using microscale thermogravimetric analysis, Anal. Chem. 86 (2014) 1478–1484.
[32] R. Kotcherlakota, A.K. Barui, S. Prashar, M. Fajardo, D. Briones, R.D. Antonio, et al., Curcumin loaded mesoporous silica: an effective drug delivery system for cancer treatment, Biomater. Sci. 4 (2016) 448–459.
[33] S. Loganathan, A.K. Ghoshal, Amine tethered pore-expanded MCM-41: a promising adsorbent for $CO_2$ capture, Chem. Eng. J. 308 (2017) 827–839.
[34] N. de Jonge, F.M. Ross, Electron microscopy of specimens in liquid, Nat. Nanotechnol. 6 (2011) 695–704.
[35] D. Su, Advanced microscopy characterization of nanomaterial for catalysis, Green Energy Environ. 2 (2017) 70–83.
[36] Y.F. Dufrêne, M.F. Garcia-Parajo, Recent progress in cell surface nanoscopy: light and force in the near-field, Nano Today 7 (2012) 390–403.
[37] I.V. Gmoshinski, S.A. Khotimchenko, V.O. Popov, B.B. Dzantiev, A.V. Zherdev, V.F. Demin, Nanomaterials and nanotechnologies: methods of analysis and control, Russ. Chem. Rev. 82 (2013) 48.
[38] A. Alagarasi, Introduction to Nanomaterials, National Center for Environmental Research, 2011.
[39] S.K. Shukla, A.K. Mishra, O.A. Arotiba, B.B. Mamba, Chitosan-based nanomaterials: a state-of-the-art review, Int. J. Biol. Macromol. 59 (2013) 46–58.
[40] N. Jayarambabu, B. Siva Kuamri, K. Venkateswara Rao, Y.T. Prabhu, Germination and growth characteristics of mungbean seeds (*Vigna radiata* L.) affected by synthesized zinc oxide nanoparticles, Int. J. Curr. Eng. Technol. 4 (2014) 3411–3416.
[41] Y.N. Chang, M. Zhang, L. Xia, J. Zhang, G. Xing, The toxic effects and mechanisms of CuO and ZnO nanoparticles, Materials 5 (12) (2012) 2850–2871.

[42] X. Huang, M.J. Beck, Determining the oxidation state of small, hydroxylated metal-oxide nanoparticles with infrared absorption spectroscopy, Chem. Mater. 27 (2015) 2965–2972.
[43] M. Khanmohammadi, A.B. Garmarudi, N. Khoddami, K. Shabani, M. Khanlari, A novel technique based on diffuse reflectance near-infrared spectrometry and back-propagation artificial neural network for estimation of particle size in $TiO_2$ nanoparticle samples, Microchem. J. 95 (2010) 337–340.
[44] M.J. Riding, F.L. Martin, J. Trevisan, V. Llabjani, I.I. Patel, K.C. Jones, et al., Concentration-dependent effects of carbon nanoparticles in Gram-negative bacteria determined by infrared spectroscopy with multivariate analysis, Environ. Pollut. 163 (2012) 226–234.
[45] L. Wang, C. Kranz, B. Mizaikoff, Monitoring scanning electrochemical microscopy approach curves with mid-infrared spectroscopy—towards a novel current-independent positioning mode, Anal. Chem. 82 (2010) 3132–3138.
[46] R. Vurgaftman, M. Weih, J.R. Kamp, C.L. Meyer, C.S. Canedy, M. Kim, et al., Interband cascade lasers, J. Phys. D Appl. Phys. 48 (2015).
[47] K.E. MacArthur, The use of annular dark-field scanning transmission electron microscopy for quantitative characterization, Johnson Matthey Technol. Rev. 60 (2016) 117.
[48] J.R. Lakowicz (Ed.), Principles of Fluorescence Spectroscopy, Springer Science & Business Media, 2013.
[49] F. Boldon, F. Laliberte, L. Liu, Review of the fundamental theories behind small angle X-ray scattering, molecular dynamics simulations, and relevant integrated application, Nano Rev. Exp. 6 (2015) 25661.
[50] N. Colthup, Introduction to Infrared and Raman Spectroscopy, Elsevier, 2012.
[51] S.L. Zhang, Raman Spectroscopy and Its Application in Nanostructures, John Wiley & Sons, 2012.
[52] L.F. Marvin, M.A. Roberts, L.B. Fay, Matrix-assisted laser desorption/ionization time-of-flight mass spectrometry in clinical chemistry, Clin. Chim. Acta 337 (1) (2003) 11–21.
[53] M.E. Hoque, K. Khosravi, K. Newman, C.D. Metcalfe, Detection and characterization of silver nanoparticles in aqueous matrices using asymmetric-flow filed flow fractionation with inductively coupled plasma mass spectrometry, J. Chromatogr. A 1233 (2012) 109–115.
[54] D.H. Tsai, T.J. Cho, S.R. Elzey, J.C. Gigault, V.A. Hackley, Quantitative analysis of dendron-conjugated cisplatin-complexed gold nanoparticles using scanning particle mobility mass spectrometry, Nanoscale 5 (12) (2013) 5390–5395.
[55] D.H. Tsai, S.R. Elzey, F.W. DelRio, R.I. MacCuspie, S. Guha, M.R. Zachariah, Tumor necrosis factor interaction with gold nanoparticles, Nanoscale 4 (10) (2012) 3208–3217.

## Further reading

E.P. Gray, T.A. Bruton, C.P. Higgins, R.U. Halden, P. Westerhoff, J.F. Ranville, Analysis of gold nanoparticle mixtures: a comparison of hydrodynamic chromatography (HDC) and asymmetrical flow filed-flow fractionation (AF4)coupled to ICP-MS, J. Anal. At. Spectrom. 27 (9) (2011) 1532–1539.

PART II

# Metal oxide-based solar cells

This page intentionally left blank

# CHAPTER 5

# $TiO_2$-based dye-sensitized solar cells

**Y. Akila[1], N. Muthukumarasamy[1] and Dhayalan Velauthapillai[2]**
[1]Department of Physics, Coimbatore Institute of Technology, Coimbatore, India
[2]Department of Chemical Sciences (Formerly Applied Chemistry), University of Johannesburg, Johannesburg, South Africa

## Contents



## 5.1 Introduction

Dye-sensitized solar cells (DSSCs), placed in the category of third generation photovoltaics, were proposed as low-cost alternatives to the conventional amorphous silicon solar cells owing to the simplicity of their fabrication procedure under ambient conditions. Modern DSSCs, or Gratzel cells, were invented in 1988 by Brian O'Regan and Michael Gratzel. During the search for better performance electrodes for electrochemical cells, it was discovered in the late 1960s that illuminated organic dyes can generate electricity at oxide electrodes. Followed by this, various efforts were made to understand the primary process in photosynthesis which led to many experiments for electric power generation via the DSSC since 1972. Generally a DSSC consists of (Fig. 5.1) (1) an anode-thin layer of suitable metal oxide coated on the transparent conductive oxide (TCO) followed by sensitization of the metal oxide film with dye while the (2) cathode−TCO glass plate is usually coated with Pt film and (3) an electrolyte, preferably an iodide/tri-iodide solution.

At the Ecole Polytechnique Federale de Lausene in 1991, Gratzel et al. succeeded to produce the "Gratzel cell," known as the DSSC by

*Nanomaterials for Solar Cell Applications*
DOI: https://doi.org/10.1016/B978-0-12-813337-8.00005-9

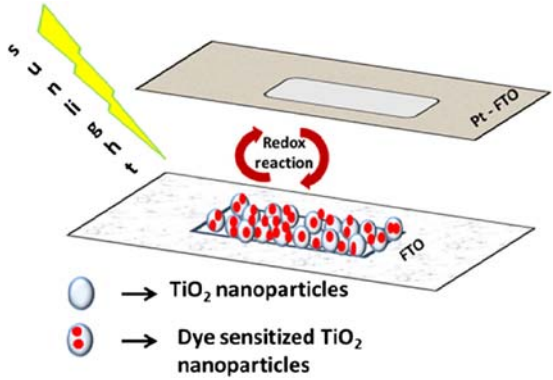


**Figure 5.1** Schematic representation of a $TiO_2$-based DSSC. *DSSC*, Dye-sensitized solar cell.

sensitizing a nanocrystalline $TiO_2$ film using a novel Ru biprydine complex which obtained an efficiency of 7%. This outcome triggered a boom in research in DSSC [1–4].

## 5.2 Why $TiO_2$ in dye-sensitized solar cells?

The large band gap, suitable band edge levels for charge injection and extraction, long lifespan of excited electrons, exceptional resistance to photo corrosion, nontoxicity and low cost have made $TiO_2$ a popular material for solar energy applications. $TiO_2$ occurs naturally in three crystalline forms: anatase (tetragonal), rutile (tetragonal), and brookite (orthorhombic). For DSSCs, anatase is the most commonly used phase due to its superior charge transport nature [5–7]. The band gap of n-type semiconducting single-crystal anatase $TiO_2$ is approximately 3.2 eV and the resistivity is $10^{15}\ \Omega$ cm [8]. Mesoporous $TiO_2$ nanoparticle (NP) films are used as photoanodes for high-efficiency DSSCs to absorb far more of the incident light [9]. Due to low electron mobility of $TiO_2$, alternate oxides, including ZnO, that possess high electron mobility are being investigated for photoanodes in DSSCs [10]. Though the transport rate of electrons is faster in ZnO compared to $TiO_2$, the recombination rate is also higher [11]. On the other hand $TiO_2$ is advantageous in terms of electron recombination, as it is relatively inert to single-electron redox mediators.

## 5.3 $TiO_2$-based dye-sensitized solar cell

An efficient solar cell sensitizer should adsorb strongly to the surface of the semiconductor oxide via anchoring groups, exhibit intense absorption in the visible part of the spectrum, and possess an appropriate energy level alignment of the dye excited state and the conduction band (CB) edge of the semiconductor [9]. Sensitization of the semiconductor in DSSCs has been achieved using numerous chemical compounds, such as phthalocyanines [12], coumarin 343 [13], carboxylated derivatives of anthracene [14,15], and porphyrins [16,17]. The dye must carry attachment groups such as carboxylate or phosphonate to firmly graft itself to the $TiO_2$ surface. The function of the carboxylate group in the dye is to attach the semiconductor oxide substrate by chemisorption [14]. The attachment group of the dye ensures that it spontaneously assembles as a molecular layer upon exposing the oxide film to a dye solution. This creates a high probability that, once a photon is absorbed, the excited state of the dye molecule will relax by electron injection to the semiconductor CB.

Gratzel's achievement with 7% efficiency in DSSC attracted various researchers to explore DSSCs. Followed by Gratzel, Hagfeldt et al. [18] in the year 1994, have analyzed the practical problems associated with the fabrication procedure of the solar cell as described by Nazeeruddin et al. [19]. They came out with the suggestions that (1) fill factor (FF) and $J_{SC}$ depend on the series resistance of the cell (2) FF is affected by the choice of the solvent for the electrolyte and (3) a decrease in the viscosity of the solvent increases the FF and $J_{SC}$ due to better diffusion of the redox couple [10,11]. On the other hand, in the year 1998, Deb et al. [20] studied the effect of surface treatment on $V_{OC}$, $J_{SC}$, FF and consequently the cell efficiency. Among various surface treatments an $NH_3$-treated electrode showed an improvement in $V_{OC}$ to 0.81 V with an increase in efficiency to 7.8%.

A hybrid $TiO_2$ electrode-based DSSC which contains a sputter-deposited layer and a nanocrystalline layer exhibited a higher solar-to-electric energy conversion efficiency $\sim$8.1%, FF 0.56, $J_{sc} = 20.8$ mA cm$^{-2}$ and open-circuit $V_{oc} = 682$ mV [21]. Tan et al. [22] improved the efficiency from 6.7% to 8.6% by the addition of 20 wt.% of nanowires to $TiO_2$ NPs. With the NP/nanowire composites it is possible to utilize the advantages of both building blocks, that is, the high surface area of NP aggregates and the long electron diffusion length and light-scattering effect of single-crystalline nanowires. In the year 2009,

Lee et al. [23] obtained a good efficiency of around 9.52% for $TiCl_4$ post treated with $TiO_2$ nanorod (NR)-based photoelectrodes prepared by electrospun, calcined $TiO_2$ composite fibers. NR-DSSCs showed a $V_{oc}$, $J_{sc}$, FF, and power conversion efficiency (PCE) of 788 mV, 15.32 mA $cm^{-2}$, 74.5%, and 9.00%, respectively. Posttreatment of $TiO_2$ with $TiCl_4$ does not make much difference in recombination life time but improved the inter-rod connectivity and electron diffusion, as well as exhibiting an efficiency of 9.52% ($V_{oc} = 761$ mV, $J_{sc} = 17.6$ mA $cm^{-2}$, FF = 70.0%).

Aggregation of the NP has to be prevented while preparing $TiO_2$ films for DSSC since it leads to a lower diffusion coefficient ($D_n$). A peculiar morphology of coral-like $TiO_2$ films, showed a superior light scattering property because of the existent aggregate units of nano-$TiO_2$ particles and micropores in the film synthesized by Fan et al. [24]. The nature of the coral-like $TiO_2$ nanostructure, including the particle shape, surface status, and aggregation form, was expected to contribute to the high $D_n$ of the film. The film exhibited a red-shifted Incident photon conversion efficiency (IPCE), a higher photocurrent (15.24 mA $cm^{-2}$) and an improved PCE of 8.57%. In the year 2010 the vision of improving the performance of DSSC spread out by using various new perspectives such as the performance of DSSC-based tests on anatase $TiO_2$ nanosheets (NSs) with (0 0 1) facets, modification of the $TiO_2$ layer, incorporation of graphene over $TiO_2$ films, tuning of the Ru complex containing bipyridine ligands, synthesis of $TiO_2$ nanotubes (NTs) by anodization using Ti mesh, hydrothermal method and performance analysis of bilayers that is, $TiO_2$NR-NP layer, $TiO_2$ NT-nanowire layer etc. Alivov et al. [25] used a unique method for fabrication of truncated pyramid-shaped $TiO_2$ NP layers by transformation of $TiO_2$ NTs through thermal annealing, and the latter was grown by electrochemical anodization of titanium (Ti) foil in ethylene glycol, followed by annealing in a fluorine environment. The formed NPs had a truncated bipyramid shape with a high reactive (0 0 1) surface area. The size of NPs depends on fluorine concentration and can be controlled within a 20−500 nm range. The XRD pattern of the NP layer transformed from the NT film had anatase (1 0 1), (1 0 3), (0 0 4), (1 1 2), and (2 0 0) diffraction peaks at 25.3°, 36.95°, 37.75°, 38.45°, and 47.95°, respectively. It was found that the efficiency of DSSCs greatly depends on NP size ($d$) varying in the range 1.45% ($d = 350$ nm) to 9.05% ($d = 65$ nm). The highest short-circuit current density $J_{sc} = 22.7$ mA $cm^{-2}$ was observed for sample with NP sized = 90 nm.

A new version of DSSCs, in which the transparent electrode having an opened-end $TiO_2$ NT (O-TiNT) film oriented perpendicular to the flourine doped tin oxides (FTO) glass was introduced by Lin et al. [26]. This electrode was fabricated using a facile process involving removal of the anodic TiNT-array film from a Ti-metal substrate to open the closed bottom and to strongly adhere it onto the FTO glass by sol–gel processed NP-$TiO_2$ paste and sintering at a high temperature. A simple and environment-friendly method with oxalic acid solution as the etching agent was used to remove the closed bottom caps of the TiNT film. With the O-TiNT film, the $J_{sc}$ of the cell dramatically increased up to 18.5 mA $cm^{-2}$, with $V_{oc}$ of 0.770 V, FF of 0.64 and $\eta$ of 9.1%. The opened-end NTs allow the redox electrolyte to easily access the NP-$TiO_2$ under-layer which shows a significant increase in the photocurrent at the longer wavelength.

In DSSCs the dye adsorption strongly depends on the lattice plane exposed on the $TiO_2$ nanocrystal surface, which greatly affects DSSC performance. DSSCs fabricated using anatase $TiO_2$ nanocrystals exposing a specific lattice plane on the surface were studied by Wen et al. [27]. To prepare anatase $TiO_2$ nanocrystals by mainly exposing the (0 1 0) plane on the surface, a layered titanate ($H_{1.07}Ti_{1.73}O_4$) with lepido crocite-like structure, was treated in a tetrabutyl ammonium hydroxide (TBAH) solution to exfoliate the layered titanate into its NSs. A sample with quadrate morphology ($AN_Q$) was obtained by the hydrothermal reaction of a titanate NS solution of TBAH at 120°C and pH 1.8. A sample with nanoleaf-like ($AN_L$) morphology was obtained by the hydrothermal reaction of a titanate NS solution of *n*-propylamine at 135°C and pH 11.3. The diffraction spots of the (2 0 0), (1 0 1), and (0 0 4) planes of the anatase structure were observed in selected-area electron diffraction, suggesting that the (0 1 0) plane was vertical to the observation direction. This result indicates that the surface of the quadrate nanocrystal corresponds to the (0 1 0) plane. The $J_{sc}$, $V_{oc}$, ff, and $\eta$ values of the solar cell fabricated using $AN_Q$ and $AN_L$ (20%) composite photo electrode were 20.6 mA $cm^{-2}$, 0.685 V, 0.55, and 7.8%, respectively.

Incorporating nanoleaf-like particles can enhance the electron transport properties of the $TiO_2$ film resulting in an improvement in FF and $J_{sc}$. $TiO_2$ nanocrystals, exhibiting mainly the (0 1 0) plane on the surface, have a high dye adsorption capacity and a high $V_{oc}$ which is close to the maximum value theoretically evaluated by Tachibana et al. [28], suggesting a potential application in high performance DSSCs fabricated by using

a mixture of $AN_Q$ (80%) and $AN_L$ (20%) nanocrystals exposing mainly the (0 1 0) plane on their surfaces. One step synthesis of anatase $TiO_2$ tetragonal faceted-nanorods (ATTFNRs) with a large percentage of {0 1 0} facets obtained by tuning the amount of TBAH has been reported by Yang et al. [29]. The PCE of a DSSC fabricated using ATTFNRs (PCE—7.73%) exhibited a significant improvement (37%) and was compared to that of the anatase $TiO_2$ NPs-based cells (PCE—5.65%). $J_{sc}$ was found to increase by 31% from 12.6 to 16.5 mA $cm^{-2}$, and concomitantly the FF increased from 0.62 to 0.66. The two roles played by TBAH as an organic morphology controlling agent in the formation of the ATTFNRs are (1) the selective adherement of $Bu_4N^+$ cations from TBAH to {010} facets favoring the growth of {010} facets; (2) the preferential adsorption of $OH^-$ anions from TBAH onto {010} surfaces favoring the formation of *O*-terminated (010) which stabilizes the {010} facets.

The application of $HfO_2$ as an efficient material to modify the $TiO_2$ electrodes in DSSCs was demonstrated by Ramasamy et al. [30]. The X-ray photoelectron spectroscopy (XPS) studies revealed the presence of peak at 213.7 eV which can be attributed to the presence of an $HfO_2$ blocking layer, uniformly coated on the surface of $TiO_2$ NPs. The higher basicity of the $HfO_2$-coated surface favors dye attachment through its carboxylic acid groups, which results in the increased dye absorption and increased short-circuit photocurrent ($J_{sc}$). The DSSCs having the $HfO_2$ layer over the $TiO_2$ have an increased diffusion coefficient ($D_n$), increased lifetime ($\tau_e$) of the photoelectrons, reduced recombination rate at the $TiO_2$ and dye/electrolyte interface, larger $V_{oc}$ (715 mV) and appreciably higher $J_{sc}$ (20.23 mA $cm^{-2}$) values, which leads to significant increase in the photo conversion efficiency from 5.67% to 9.59%. A one-step hydrothermal method to directly convert commercial P25 powders into monodisperse anatase $TiO_2$ containing 3D urchin-like structures with an average diameter of about 2 μm was developed by Cheng et al. [31] (Fig. 5.2).

A trilaminar-layer photoanode for DSSCs was constructed using urchin-like $TiO_2$ hierarchical microspheres and P25. The DSSCs based on the photoanode with a tripartite-layer structure exhibited a high short-circuit photocurrent density of 18.97 mA $cm^{-2}$ and energy conversion efficiency of 8.80%. The great improvement of photocurrent density and energy conversion efficiency for hierarchical $TiO_2$ microspheres are mainly attributed to the presence of considerable surface area (nitrogen

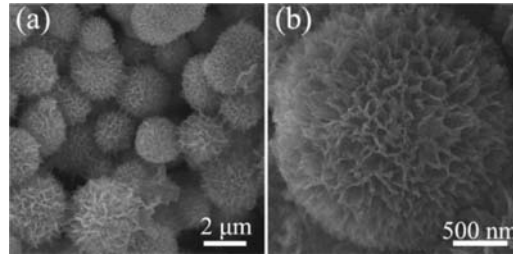


**Figure 5.2** SEM images of urchin-like $TiO_2$ hierarchical microspheres with different magnifications.

adsorption analysis), higher light scattering ability, and slower electron recombination rate.

A fast and effective procedure for the preparation of high efficiency hybrid photoanodes for DSSCs, based on nanocrystalline $TiO_2$ with limited addition of multiwall carbon mulliwall carbon nanotubes (MWCNTs) (0.01%) has been reported by Dembele et al. [32]. In Raman spectra, instead, the D and G bands of MWCNTs at about 1350 and 1582 $cm^{-1}$, which can be attributed to MWCNT defects, a disorder-induced mode, and in-plane $E_{2g}$ zone-center mode, are clearly visible even for low MWCNT concentrations (0.010%) which confirm the presence of MWCNTs in the nanocomposite. The concentration of MWCNTs (0.010% − 0.020%) does not affect the optical properties of the $TiO_2$ layer, whereas enhanced electron lifetime and reduced charge recombination resulted in highly increased short circuit current density and overall photo conversion efficiency from 13.6 to 16.0 mA $cm^{-2}$ and from 7.0% to 9.0%, respectively, corresponding to the bare $TiO_2$.

Different kinds of $TiO_2$ nanostructures have gained great importance due to their promising physico-chemical properties. $TiO_2$ nanostructure shapes such as rice- (∼1.10 μm), star- (∼3.60 μm), and flower-like (3.75 μm) structures were obtained by hydrothermal method using different hydrothermal conditions by Lekphet et al. [33]. Among them, the star-like $TiO_2$ photoanode based DSSC exhibited the highest PCE of 9.56%. For 240°C heat treatment (TH-0), the formation of star-like $TiO_2$ microstructures consisting of sixfold symmetry with a diameter of about 3.6 μm was observed. Among the cells coated with scattering layers, photoanodes with star-shaped microstructures (a-$TiO_2$/TH-0, 240°C for 3 hours) exhibited the best PCE of 9.56% ($J_{sc}$ of 17.97 mA $cm^{-2}$, open-circuit voltage of 0.76 V and FF of 0.70). The highest $J_{sc}$ shown was

attributed to the better dye loading and the strongest light scattering property exhibited by these structures.

The highest PCE for a DSSC, 11.13% using a liquid electrolyte, N719-dye and a $TiO_2$ film with highly exposed (0 0 1)-facets anatase microspheres synthesized via facile hydrothermal method, was first reported by Peng et al. [34]. Analysis of XRD pattern and High-Resolution transmission electron microscopy (HRTEM) images of $TiO_2$ film suggests the dominance of the (0 0 1)-facets crystalline anatase phase. Brunauer–Emmett–Teller surface area measurement shows the specific surface area of the $TiO_2$ film as 112.2 $m^2\ g^{-1}$. The DSSC with (0 0 1)-facets $TiO_2$ photo anode exhibited a $J_{SC}$ of 19.15 ± 0.2 mA $cm^{-2}$, a $V_{OC}$ of 784.9 ± 2.2 mV, a FF of 0.741 ± 0.003 and a cell efficiency ($\eta$) of 11.13% ± 0.1%. A possible explanation for the better performance can be that the (0 0 1)-facets of $TiO_2$, owing to their mirror-like plane structure, scatter the incident light to all directions within the bulk of the $TiO_2$ and thereby utilize the incident light in the whole wavelength region to a higher degree. To add value to this point diffuse reflectance spectra ($R$) also showed that even in the infrared region above 700 nm, the (001)-facets $TiO_2$ maintains a high $R$ value of about 55%, whereas the reference-$TiO_2$ shows a value lower than 40% in this region. In the same year Peng et al. [35], improved the PCE to 11.43% using porphyrin dye (YD2-O-C8) and cobalt electrolyte. Well-defined (001)-facets (10%, 36%, 58%, and 84%) anatase $TiO_2$ was synthesized by a facile hydrothermal route. Due to the presence of a higher content of (001)-$TiO_2$, the S84-$TiO_2$ [84% (001) facet $TiO_2$] film exhibited an extraordinarily high dye coverage of 29.7%. This high coverage has resulted in a 14.2% increase in $J_{SC}$ (16.2 mA $cm^{-2}$) and a 34 mV increase in $V_{OC}$ (918 mV) with a PCE of 11.43%.

Sheng et al. [36], observed an increase in particle size and a change in morphology due to the presence of ammonia in the synthesis of highly crystalline $TiO_2$ hierarchical microspheres. From the ammonia solution, $NH_4^+$ was adsorbed on the NPs surface, which enhanced the interfacial surface tension and helps crystal growth. The ammonia played an important role in the crystallization process of $TiO_2$ hierarchical spheres, of which crystallization was found to be higher in the mixture solution with higher ammonia concentration. The DSSC fabricated using these $TiO_2$ photoanodes exhibited the highest conversion efficiency, 11.43% with a $V_{oc}$ of 720 mV, a $J_{sc}$ of 22.92 mA $cm^{-2}$ and a FF of 69%. $TiO_2$ NPs synthesized by a modified solvothermal method involving mixed solvent

technique, when used as photoanodes for DSSC yielded a PCE of 5.02%. This was further improved to 5.92% when post treated with $TiCl_4$ [37]. The influence of crystallite size and facet on the dye adsorption capability, electron recombination, and photovoltaic characteristics were analyzed by Wu et al. [38]. Anatase nanocrystallites with different morphologies and sizes ranging from 5 to 30 nm were synthesized in one pot via the microwave solvothermal method using different types of alcohol solvents, namely, *n*-propanol (NPA), isopropanol, and octanol (OCT) with no ionic additives. The TEM and HRTEM images demonstrate that the NPA and OCT NPs with sizes of 12−15 nm and 5−7 nm, respectively, were mainly exposed at the {101} facet. The best PCE of DSSC with a $TiO_2$ photo anode synthesized using OCT was 9.58% and the film thickness was only 10.6 μm. No scattering layer was used.

Hierarchical $TiO_2$ sub-microrods (HTRs) assembled by tiny NPs and NRs were synthesized by Guo et al. [39] using a titanate glycolate rod as a self-template through a facile hydrothermal method. The as-prepared HTRs possessed a higher surface area (103 $m^2\ g^{-1}$) and act as scattering centers. Composite photoanodes for DSSCs were prepared by integrating the prepared (20 wt.%) HTRs and P25 NPs and a photovoltaic conversion efficiency of 8.09% was obtained. Relatively larger submicro particle size offers a direct pathway for charge carrier transfer and reduces the recombination as well. The co-sensitization process is using the combination of two or more dyes having complementary absorption properties as a strategy to broaden the light harvesting property. A better efficiency around 8.27% was achieved by Singh et al. [40] by a stepwise co-sensitization process using N719 and metal-free dye, that is, TA−St−CA which resulted in higher values of $J_{sc}$ and overall PCE. The DSSCs co-sensitized with N719/TA−St−CA exhibited a good performance with $J_{sc} = 16.22$ mA $cm^{-2}$, $V_{oc} = 0.68$ V, FF = 0.75, and PCE = 8.27% when compared to the cells sensitized using the individual dyes N719 and TA−St−CA.

The remarkable PCE for DSSCs of 10.5% by Wang et al. [41], 11.6% by Ozawa et al. [42] and a maximum of 12.3% was obtained by Yella et al. [43] were based on black dye, black dye co-sensitized with organic dye and Co(II/III) redox electrolyte, respectively. Wang et al., used $TiCl_4$-treated, HCl pre-treated $TiO_2$ photo anodes sensitized by black dye and obtained a conversion efficiency of 10.5%, 21.49 mA $cm^{-2}$ of $J_{sc}$, 0.700 V of $V_{oc}$, and 0.699 of FF. The HCl pretreatment resulted in a significant increase in dye adsorption, a positive shift of the flat band for

$TiO_2$, reduced dark current and increased resistance at the $TiO_2$/dye/electrolyte interface. Ozawa et al. [42] achieved a conversion efficiency of 11.46% (Fig. 5.3) by co-sensitization of black dye with D131 in the presence of deoxycholic acid, as the former suppress the black dye aggregation and later disrupt the remaining dye aggregations. This prevents the backward electron transfer from the CB of $TiO_2$.

Mesoscopic solar cells that incorporate a Co(II/III) tris(bipyridyl)—based redox electrolyte in conjunction with a custom synthesized donor-π-bridge-acceptor zinc porphyrin dye as a sensitizer (designated YD2-O-C8) has been reported by Yella et al. [43]. The specific molecular design of YD2-O-C8 greatly retards the rate of interfacial back electron transfer from the CB of the nanocrystalline titanium dioxide film to the oxidized cobalt mediator. Co-sensitization of YD2-O-C8 with another organic dye (Y123) further enhances the performance of the device, leading to a measured PCE of 12.3% under simulated air mass 1.5 global sunlight. The YD2-O-C8 dye lacks absorption in the 480—630 nm range, as evidenced by the IPCE spectra. Hence a co-sensitizer (Y123), added to the dye, exhibited better photovoltaic performance with cumulative increase of $J_{sc}$ (17.66 mA $cm^{-2}$), $V_{OC}$ (935 mV), and FF (0.74) resulting in an efficiency of 12.3%.

The performance of rutile $TiO_2$ as photo anodes was analyzed by Park et al. [44], $\eta = 5.6\%$ for rutile and $\eta = 7.1\%$ for anatase and they have observed that the rate of electron transport in rutile $TiO_2$ is found to be one order of magnitude lesser than in anatase $TiO_2$. The possible factor behind the slow electron transport in rutile $TiO_2$ was found to be the

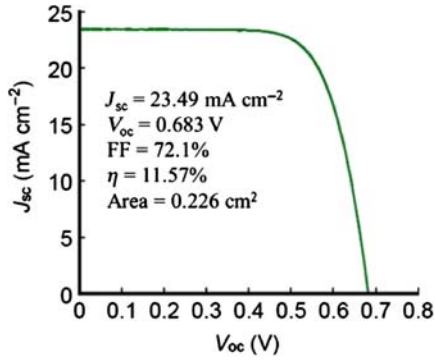


**Figure 5.3** *J—V* Curve of $TiO_2$ film-sensitized with black dye co-sensitized with D131 and DCA. *DCA*, deoxycholic acid.

lower inter-particle connection per unit volume than that of anatase film. This enroutes to the smaller number of pathways to the collecting electrode and lowers the electron diffusion coefficient in the rutile [12]. Thus they have concluded that increasing the surface area of the rutile film by producing a more densely packed film of smaller particles is expected to improve the photocurrent. As nanostructures help in improving the surface area of the film, researchers focused on structured rutile $TiO_2$. A PCE of 6.03% was achieved by Yang et al. [45], 7.91% by Lv et al. [46] for $TiO_2$ NR arrays and 9.6% ($TiO_2$ nanowire arrays), by Li et al. [47].

Natural dyes are considered a viable alternative to synthetic ones because of their many advantages, such as easy preparation, low cost, eco-friendliness, biodegradability and wide availability. In nature, the fruit, flower and leaf of plants show various colors from red to violet and contain various natural dyes which can be extracted by simple procedures. Some natural dyes as sensitizers of DSSC have been reported by Calogero et al (PCE using red turnip—1.7% [48]), Zhou et al. (PCE using mangosteen—1.17%, [49]), Sathyajothi et al. (PCE using beetroot—1.3%, henna dye—1.08% [50]). Kumara et al. [51], used the different technology of mixed dye made up of a shisonin and chlorophyll combination and achieved a maximum conversion efficiency of 1.31%. Many researchers have focused toward natural DSSCs, but due to the poor absorption, fast degradation in the presence of sunlight, less repeatability and poor lifespan of the cell, a presumption of the instability of natural dye based DSSCs has been formed.

## 5.4 Doped $TiO_2$-based dye-sensitized solar cell

An effective way of modifying the electronic properties of $TiO_2$ is doping, the deliberate insertion of impurities into the $TiO_2$ lattice [52]. Doping has a major effect on the band structure and trap states of $TiO_2$, which in turn affect important properties such as the CB energy, charge transport, recombination and collection. Doping can be achieved by either replacing the $Ti^{4+}$ cation or the $O^{2-}$ anion. Cationic dopants are typically metals, whereas anionic dopants are non-metals. Since the lower edge of the CB is made up of $Ti^{4+}$ 3D bands, replacing $Ti^{4+}$ by a different cation is thus expected to heavily affect the CB structure. The upper edge of the valence band (VB) consists of $O^{2-}$ 2p bands and replacing $O^{2-}$ by a different anion affects the VB energy.

In short, doping can affect five different properties of anatase $TiO_2$: (1) Flat-band potential: $V_{FB}$ can be shifted either positively or negatively; a positive shift is indicative of a downward shift of the CB and $E_F$ (increases $J_{SC}$), while a negative $V_{FB}$ shift indicates an upward shift of CB and $E_F$ (decreases $J_{SC}$ and $V_{OC}$) (2) Recombination rate: A decrease in the number of defect states usually enhances the electron lifetime and reduces recombination rate (3) Electron transport rate (4) Dye adsorption and (5) Phase transition: Doping can inhibit the anatase-to-rutile phase transition, reducing rutile instigated charge recombination. The defect states of $TiO_2$ are highly dependent on the synthesis method and thus the effect of doping may vary for different synthesis techniques, making it difficult to compare the suitability of different dopants.

DSSCs based on a tantalum (Ta)-doped $TiO_2$ thin film prepared by the hydrothermal method which showed a photovoltaic efficiency of 8.18%, $J_{SC} = 19.1$ mA cm$^{-2}$, $V_{OC} = 665$ mV, and FF = 65% has been reported by Liu et al. [53]. The Mott–Schottky plot indicates that the Ta-doped $TiO_2$ photoanode shifts the flat band potential positively and increases the electron density, which is confirmed from the improved electron transport properties measured from intensity-modulated photocurrent spectroscopy. Moreover, when Ta is implanted into the $TiO_2$, the electron concentration in the film increases because Ta has a $5^+$ valence and one more electron than that of Ti. Despite the reduced open-circuit photo voltage (due to the positive shift of the Fermi level), Ta-doping improves the cell conversion efficiency from 7.40% (for undoped $TiO_2$ film) to 8.18%. Liu et al. [54] have reported that the PCE of Zn + Mg co-doped $TiO_2$ based DSSC is 9.07% when the dopant concentration was 2.0 mol.%. XRD results indicated that Zn + Mg co-doped $TiO_2$ sintered at 450°C had polycrystalline structures consisting of an anatase $TiO_2$ phase characterized with primary (101), (004), and (200) peaks, suggesting that Zn and Mg have been incorporated homogeneously into the $TiO_2$ matrix. The results of Intensity–modulated photocurrent spectroscopy (IMPS) measurement shows a faster electron transport, due to the positive shift of the flat band in the Zn + Mg co-doped $TiO_2$ films, which contributes to the observed higher $J_{sc}$ of DSSCs. The photovoltaic characteristics of Zn + Mg-doped $TiO_2$ based DSSC like $J_{sc}$, $V_{oc}$, FF, and $\eta$ were 20.1 mA cm$^{-2}$, 625 mV, 0.73, and 9.07%, respectively. 1% Sn-doped $TiO_2$ NR arrays were grown over a 1% Sn-doped $TiO_2$ seed layer synthesized by a hydrothermal and dip-coating method respectively. The prepared Sn-doped $TiO_2$ films were post-treated using zirconium

oxide, followed by ruthenium dye sensitization and yielded a PCE of 4.96% [55].

Photoanodes for DSSCs based on composites of carbon NTs and titanium dioxide NPs were realized by Barberio et al. [56]. They have used two different photoanode hybrid composites of $TiO_2$ doped with multiwalled carbon NTs and three-layer sandwich $TiO_2$/CNT/$TiO_2$ photoanodes. scanning electron microscope (SEM) and Atomic force microscopy (AFM) images of $TiO_2$/CNT hybrid nanocomposites show the formation of a network of carbon NT bundles uniformly decorating the $TiO_2$ grains in the entire volume of the photo anode with dimensions of about 50 nm. Cells obtained with the three-layer sandwich $TiO_2$/CNT (0.2%–0.4%)/$TiO_2$ photoanode show a PCE of 10.5%, with a FF of 70%, indicating the strong enhancements in charge transport with the presence of a high amount of carbon NT (the decreases in dye adsorption are limited by the presence of two layers of $TiO_2$).

A systematic study of various anatase $TiO_2$ surfaces interacting with N719 dye by means of Density functional theory (DFT) calculations in combination with microscopic techniques reports that an (0 0 1) surface interacting with an N719 will have the lowest work function, leading to the best photovoltaic performance. To further increase the efficiency, an Nb dopant was incorporated into the anatase $TiO_2$ nanocrystals by Jiang et al. [57]. Highly crystallized Nb-doped anatase (0 0 1) and (1 0 0) oriented $TiO_2$ NSs were synthesized and a PCE as high as 10.0% was obtained for Nb-doped (0 0 1) dominated $TiO_2$ NSs photo anode based DSSC. All XRD peaks indicated that the anatase nanocrystalline structure is retained after Nb doping.

High-performance DSSCs-based g-$C_3N_4$ modified $TiO_2$ NSs as photoanodes and $Co_9S_8$ acicular nanotube arrays (ANTAs) as counter electrodes have been fabricated by Yuan et al. [58]. The coupling of g-$C_3N_4$ with $TiO_2$ to form a heterojunction extends the optical response behavior of $TiO_2$ to visible-light region, and simultaneously restrains the recombination rate of photo-generated charges, thus greatly enhancing the photovoltaic performance of $TiO_2$ based DSSC. The size of the g-$C_3N_4$ modified $TiO_2$ NSs is in the range of 40–50 nm, which were obtained as uniform square NSs. Pore volume of the $TiO_2$ NSs decreases after introducing g-$C_3N_4$. The Photoluminescence (PL) emission intensity of $TiO_2$/g-$C_3N_4$ nanocomposites significantly decreases, suggesting that the recombination rate of the photoinduced charge carrier decreases. $Co_9S_8$ hollow nanoneedle arrays were prepared by a template-assisted

method. $Co_9S_8$ ANTAs are arranged uniformly and cover the full surface of FTO substrates. It can be seen that the value of $\eta$ of the DSSCs based on $TiO_2$/g-$C_3N_4$ electrodes (8.07%) is much higher than the $TiO_2$ photoanodes (6.19%), which is ascribed to the fact that the g-$C_3N_4$ layer can act as a blocking layer to efficiently prevent charge recombination at the $TiO_2$/electrolyte interface.

## 5.5 Conclusion

The wide history of DSSC has given a better explanation of various factors involved in improving the photovoltaic parameters of DSSC and in turn to increase the PCE of DSSC. It was concluded that the charge collection, light harvesting efficiency and charge separation were found to influence the $J_{SC}$. In addition to $J_{SC}$ and $V_{OC}$, FF is found to be an important parameter to determine the cell performance, which is dependent on the series and shunt resistance of the cell. Apart from the absorption profile, the amount of dye loading is an important factor for enhanced PCE of DSSCs. The fast hydrolysis rate of Ti complexes leads to difficulty in well-dispersed, uniform hierarchial $TiO_2$ films. The rapid electron transport in the $TiO_2$ film plays a vital role against recombination and dark current. Uncovered $TiO_2$ sites in FTO, specific surface area and crystallinity are the influencing factors towards the photocatalytic activity and efficiency of $TiO_2$-based DSSC. DSSC progressively showed its improvement in PCE by rectifying the above all controlling parameters toward its performance, but still lags behind silicon solar cells when considered for commercialization. To have an economically viable, nonhazardous and eco-friendly DSSC, it has to travel a long way to complete the requirements.

## References

[1] B. O'Regan, M. Grätzel, A low-cost, high-efficiency solar cell based on dye-sensitized colloidal $TiO_2$ films, Nature 353 (1991) 737. Available from: https://doi.org/10.1038/353737a0.

[2] H. Gerischer, The impact of semiconductors on the concepts of electrochemistry, Electrochim. Acta 35 (11) (1990) 1677–1699. Available from: https://doi.org/10.1016/0013-4686(90)87067-C.

[3] A. Heller, Conversion of sunlight into electrical power and photoassisted electrolysis of water in photoelectrochemical cells, Acc. Chem. Res. 14 (5) (1981) 154–162. Available from: https://doi.org/10.1021/ar00065a004.

[4] A. Fujishima, K. Honda, Electrochemical photolysis of water at a semiconductor electrode, Nature 238 (1972) 37. Available from: https://doi.org/10.1038/238037a0.

[5] D.Y.C. Leung, X. Fu, C. Wang, M. Ni, M.K.H. Leung, X. Wang, et al., Hydrogen production over titania-based photocatalysts, ChemSusChem 3 (6) (2010) 681–694. Available from: https://doi.org/10.1002/cssc.201000014.
[6] M.A. Rauf, M.A. Meetani, S. Hisaindee, An overview on the photocatalytic degradation of azo dyes in the presence of $TiO_2$ doped with selective transition metals, Desalination 276 (1) (2011) 13–27. Available from: https://doi.org/10.1016/j.desal.2011.03.071.
[7] H. Park, Y. Park, W. Kim, W. Choi, Surface modification of $TiO_2$ photocatalystfor environmental applications, J. Photochem. Photobiol., C 15 (2013) 1–20. Available from: https://doi.org/10.1016/j.jphotochemrev.2012.10.001.
[8] H.K. Ardakani, Electrical and optical properties of in situ "hydrogen-reduced" titanium dioxide thin films deposited by pulsed excimer laser ablation, Thin Solid Films 248 (2) (1994) 234–239. Available from: https://doi.org/10.1016/0040-6090(94)90017-5.
[9] N. Vlachopoulos, P. Liska, J. Augustynski, M. Graetzel, Very efficient visible light energy harvesting and conversion by spectral sensitization of high surface area polycrystalline titanium dioxide films, J. Am. Chem. Soc. 110 (4) (1988) 1216–1220. Available from: https://doi.org/10.1021/ja00212a033.
[10] A.K. Chandiran, M. Abdi-Jalebi, M.K. Nazeeruddin, M. Grätzel, Analysis of electron transfer properties of ZnO and $TiO_2$ photoanodes for dye-sensitized solar cells, ACS Nano 8 (3) (2014) 2261–2268. Available from: https://doi.org/10.1021/nn405535j.
[11] J. Fan, Y. Hao, A. Cabot, E.M.J. Johansson, G. Boschloo, A. Hagfeldt, Cobalt(II/III) redox electrolyte in ZnO nanowire-based dye-sensitized solar cells, ACS Appl. Mater. Interfaces 5 (6) (2013) 1902–1906. Available from: https://doi.org/10.1021/am400042s.
[12] L. Giribabu, V.K. Singh, T. Jella, Y. Soujanya, A. Amat, F. De Angelis, et al., Sterically demanded unsymmetrical zinc phthalocyanines for dye-sensitized solar cells, Dyes Pigm. 98 (3) (2013) 518–529. Available from: https://doi.org/10.1016/j.dyepig.2013.04.007.
[13] K. Hara, Y. Tachibana, Y. Ohga, A. Shinpo, S. Suga, K. Sayama, et al., Dye-sensitized nanocrystalline $TiO_2$ solar cells based on novel coumarin dyes, Sol. Energy Mater. Sol. Cells 77 (1) (2003) 89–103. Available from: https://doi.org/10.1016/S0927-0248(02)00460-9.
[14] K.R. Justin Thomas, P. Singh, A. Baheti, Y.-C. Hsu, K.-C. Ho, J.T.S. Lin, Electro-optical properties of new anthracene based organic dyes for dye-sensitized solar cells, Dyes Pigm. 91 (1) (2011) 33–43. Available from: https://doi.org/10.1016/j.dyepig.2011.02.006.
[15] J.A. Mikroyannidis, A. Kabanakis, P. Balraju, G.D. Sharma, Novel broadly absorbing sensitizers with cyanovinylene 4-nitrophenyl segments and various anchoring groups: synthesis and application for high-efficiency dye-sensitized solar cells, J. Phys. Chem. C 114 (28) (2010) 12355–12363. Available from: https://doi.org/10.1021/jp101945z.
[16] N. Xiang, W. Zhou, S. Jiang, L. Deng, Y. Liu, Z. Tan, et al., Synthesis and characterization of trivalent metal porphyrin with NCS ligand for application in dye-sensitized solar cells, Sol. Energy Mater. Sol. Cells 95 (4) (2011) 1174–1181. Available from: https://doi.org/10.1016/j.solmat.2010.12.051.
[17] W. Zhou, B. Zhao, P. Shen, S. Jiang, H. Huang, L. Deng, et al., Multi-alkylthienyl appended porphyrins for efficient dye-sensitized solar cells, Dyes Pigm. 91 (3) (2011) 404–412. Available from: https://doi.org/10.1016/j.dyepig.2011.05.017.
[18] A. Hagfeldt, B. Didriksson, T. Palmqvist, H. Lindström, S. Södergren, H. Rensmo, et al., Verification of high efficiencies for the Grätzel-cell. A 7% efficient solar cell

based on dye-sensitized colloidal $TiO_2$ films, Sol. Energy Mater. Sol. Cells 31 (4) (1994) 481–488. Available from: https://doi.org/10.1016/0927-0248(94)90190-2.

[19] M.K. Nazeeruddin, A. Kay, I. Rodicio, R. Humphry-Baker, E. Mueller, P. Liska, et al., Conversion of light to electricity by *cis*-X2bis (2,2′-bipyridyl-4,4′-dicarboxylate)ruthenium(II) charge-transfer sensitizers (X = Cl-, Br-, I-, CN-, and SCN-) on nanocrystalline titanium dioxide electrodes, J. Am. Chem. Soc. 115 (14) (1993) 6382–6390. Available from: https://doi.org/10.1021/ja00067a063.

[20] S.K. Deb, R. Ellingson, S. Ferrere, A.J. Frank, B.A. Gregg, A.J. Nozik, et al., Photochemical solar cells based on dye-sensitization of nanocrystalline $TiO_2$, AIP Conf. Proc. 462 (1) (1999) 473–482. Available from: https://doi.org/10.1063/1.57993.

[21] H. Han, X. Zhao, J. Liu, Enhancement in photoelectric conversion properties of the dye-sensitized nanocrystalline solar cells based on the hybrid $TiO_2$ electrode, J. Electrochem. Soc. 152 (1) (2005) A164–A166.

[22] B. Tan, Y. Wu, Dye-sensitized solar cells based on anatase $TiO_2$ nanoparticle/nanowire composites, J. Phys. Chem. B 110 (32) (2006) 15932–15938. Available from: https://doi.org/10.1021/jp063972n.

[23] B.H. Lee, M.Y. Song, S.-Y. Jang, S.M. Jo, S.-Y. Kwak, D.Y. Kim, Charge transport characteristics of high efficiency dye-sensitized solar cells based on electrospun $TiO_2$ nanorod photoelectrodes, J. Phys. Chem. C 113 (51) (2009) 21453–21457. Available from: https://doi.org/10.1021/jp907855x.

[24] S.Q. Fan, R.J. Cao, Y.X. Xi, M. Gao, M.D. Wang, G. Wang, et al., Improved performance of dye-sensitized solar cell by using a coral-like $TiO_2$ film, Optoelectron. Adv. Mater. Rapid Commun. 3 (2) (2009) 101–105.

[25] Y. Alivov, F. Zhaoyang, Dye-sensitized solar cells using $TiO_2$ nanoparticles transformed from nanotube arrays, J. Mater. Sci. 45 (2010) 2902–2906. Available from: https://doi.org/10.1007/s10853-010-4281-2.

[26] C.-J. Lin, W.-Y. Yu, S.-H. Chien, Transparent electrodes of ordered opened-end $TiO_2$-nanotube arrays for highly efficient dye-sensitized solar cells, J. Mater. Chem. 20 (6) (2010) 1073–1077. Available from: https://doi.org/10.1039/b917886d.

[27] P. Wen, Z. Tao, Y. Ishikawa, H. Itoh, Q. Feng, Dye-sensitized solar cells based on anatase $TiO_2$ nanocrystals exposing a specific lattice plane on the surface, Appl. Phys. Lett. 97 (13) (2010) 131906. Available from: https://doi.org/10.1063/1.3494087.

[28] Y. Tachibana, K. Hara, K. Sayama, H. Arakawa, Quantitative analysis of light-harvesting efficiency and electron-transfer yield in ruthenium-dye-sensitized nanocrystalline $TiO_2$ solar cells, Chem. Mater. 14 (6) (2002) 2527–2535. Available from: https://doi.org/10.1021/cm011563s.

[29] W. Yang, Y. Wang, W. Shi, One-step synthesis of single-crystal anatase $TiO_2$ tetragonal faceted-nanorods for improved-performance dye-sensitized solar cells, CrystEngComm 14 (1) (2012) 230–234. Available from: https://doi.org/10.1039/c1ce05844d.

[30] P. Ramasamy, M.-S. Kang, H.-J. Cha, J. Kim, Highly efficient dye-sensitized solar cells based on $HfO_2$ modified $TiO_2$ electrodes, Mater. Res. Bull. 48 (1) (2013) 79–83. Available from: https://doi.org/10.1016/j.materresbull.2012.10.006.

[31] P. Cheng, S. Du, Y. Cai, F. Liu, P. Sun, J. Zheng, et al., Tripartite layered photoanode from hierarchical anatase $TiO_2$ urchin-like spheres and P25: a candidate for enhanced efficiency dye sensitized solar cells, J. Phys. Chem. C 117 (46) (2013) 24150–24156. Available from: https://doi.org/10.1021/jp406849j.

[32] K.T. Dembele, G.S. Selopal, C. Soldano, R. Nechache, J.C. Rimada, I. Concina, et al., Hybrid carbon nanotubes – $TiO_2$ photoanodes for high efficiency dye-sensitized solar cells, J. Phys. Chem. C 117 (28) (2013) 14510–14517. Available from: https://doi.org/10.1021/jp403553t.

[33] W. Lekphet, T.-C. Ke, C. Su, S. Kathirvel, P. Sireesha, S.B. Akula, et al., Morphology control studies of $TiO_2$ microstructures via surfactant-assisted hydrothermal process for dye-sensitized solar cell applications, Appl. Surf. Sci. 382 (2016) 15–26.

[34] J.-D. Peng, C.-M. Tseng, R. Vittal, K.-C. Ho, Mesoporous anatase-$TiO_2$ spheres consisting of nanosheets of exposed (0 0 1)-facets for [Co(byp)3]2 + /3 + based dye-sensitized solar cells, Nano Energy 22 (2016) 136–148. Available from: https://doi.org/10.1016/j.nanoen.2016.01.025.

[35] J.-D. Peng, H.-H. Lin, C.-T. Lee, C.-M. Tseng, V. Suryanarayanan, R. Vittal, et al., Hierarchically assembled microspheres consisting of nanosheets of highly exposed (0 0 1)-facets $TiO_2$ for dye-sensitized solar cells, RSC Adv. 6 (17) (2016) 14178–14191. Available from: https://doi.org/10.1039/c5ra26307g.

[36] J. Sheng, L. Hu, L.E. Mo, J. Ye, S. Dai, $TiO_2$ hierarchical sub-wavelength microspheres for high efficiency dye-sensitized solar cells, Phys. Chem. Chem. Phys. 18 (47) (2016) 32293–32301. Available from: https://doi.org/10.1039/c6cp06916a.

[37] V.M. Ramakrishnan, M. Natarajan, A. Santhanam, V. Asokan, D. Velauthapillai, Size controlled synthesis of $TiO_2$ nanoparticles by modified solvothermal method towards effective photo catalytic and photovoltaic applications, Mater. Res. Bull. 97 (2018) 351–360. Available from: https://doi.org/10.1016/j.materresbull.2017.09.017.

[38] Y.C. Wu, C.-K. Hung, C.-Y. Tsai, Y.-L. Guo, Y.-H. Chiang, P. Chen, Clean and flexible synthesis of $TiO_2$ nanocrystallites for dye-sensitized and perovskite solar cells, Sol. Energy Mater. Sol. Cells 159 (2017) 336–344. Available from: https://doi.org/10.1016/j.solmat.2016.09.033.

[39] D. Guo, S. Xiao, K. Fan, J. Yu, Hierarchical $TiO_2$ submicrorods improve the photovoltaic performance of dye-sensitized solar cells, ACS Sustainable Chem. Eng. 5 (2) (2017) 1315–1321. Available from: https://doi.org/10.1021/acssuschemeng.6b01671.

[40] M. Singh, R. Kurchania, R.J. Ball, G.D. Sharma, et al., Efficiency enhancement in dye sensitized solar cells through step wise cosensitization of $TiO_2$ electrode with N719 and metal free dye, Indian J. Pure Appl. Phys. 54 (2016) (2016) 656–664.

[41] Z.-S. Wang, T. Yamaguchi, H. Sugihara, H. Arakawa, Significant efficiency improvement of the black dye-sensitized solar cell through protonation of $TiO_2$ films, Langmuir 21 (10) (2005) 4272–4276. Available from: https://doi.org/10.1021/la050134w.

[42] H. Ozawa, R. Shimizu, H. Arakawa, Significant improvement in the conversion efficiency of black-dye-based dye-sensitized solar cells by cosensitizationwith organic dye, RSC Adv. 2 (8) (2012) 3198–3200. Available from: https://doi.org/10.1039/c2ra01257j.

[43] A. Yella, H.-W. Lee, H.N. Tsao, C. Yi, A.K. Chandiran, M.K. Nazeeruddin, et al., Porphyrin-sensitized solar cells with cobalt(II/III)-based redox electrolyte exceed 12 percent efficiency, Science 334 (6056) (2011) 629.

[44] H. Park, Y. Park, W. Kim, W. Choi, Surface modification of $TiO_2$ photocatalyst for environmental applications, J. Photochem. Photobiol., C 15 (2013) 1–20. Available from: https://doi.org/10.1016/j.jphotochemrev.2012.10.001.

[45] W. Yang, F. Wan, Y. Wang, C. Jia, Achievement of 6.03% conversion efficiency of dye-sensitized solar cells with single-crystalline rutile $TiO_2$ nanorod photoa node, Appl. Phys. Lett. 95 (2009) 133121.

[46] M. Lv, D. Zheng, M. Ye, J. Xiao, W. Guo, Y. Lai, et al., Optimized porous rutile $TiO_2$ nanorod arrays for enhancing the efficiency of dye-sensitized solar cells, Energy Environ. Sci. 6 (5) (2013) 1615–1622. Available from: https://doi.org/10.1039/c3ee24125d.

[47] H. Li, Q. Yu, Y. Huang, C. Yu, R. Li, J. Wang, et al., Ultralong rutile $TiO_2$ nanowire arrays for highly efficient dye-sensitized solar cells, ACS Appl. Mater. Interfaces 8 (21) (2016) 13384–13391. Available from: https://doi.org/10.1021/acsami.6b01508.

[48] G. Calogero, G. Di Marco, S. Cazzanti, S. Caramori, R. Argazzi, A. Di Carlo, et al., Efficient dye-sensitized solar cells using red turnip and purple wild sicilian prickly pear fruits, Int. J. Mol. Sci. 11 (1) (2010) 254–267. Available from: https://doi.org/10.3390/ijms11010254.

[49] H. Zhou, L. Wu, Y. Gao, T. Ma, Dye-sensitized solar cells using 20 natural dyes as sensitizers, J. Photochem. Photobiol., A 219 (2) (2011) 188–194. Available from: https://doi.org/10.1016/j.jphotochem.2011.02.008.

[50] S. Sathyajothi, R. Jayavel, A.C. Dhanemozhi, The fabrication of natural dye sensitized solar cell (DSSC) based on $TiO_2$ using henna and beetroot dye extracts, Mater. Today Proc. 4 (2, Part A) (2017) 668–676. Available from: https://doi.org/10.1016/j.matpr.2017.01.071.

[51] G.R.A. Kumara, S. Kaneko, M. Okuya, B. Onwona-Agyeman, A. Konno, K. Tennakone, Shiso leaf pigments for dye-sensitized solid-state solar cell, Sol. Energy Mater. Sol. Cells 90 (9) (2006) 1220–1226. Available from: https://doi.org/10.1016/j.solmat.2005.07.007.

[52] R.L.Z. Hoye, K.P. Musselman, J.L. MacManus-Driscoll, Research update: doping ZnO and $TiO_2$ for solar cells, APL Mater. 1 (060701) (2013) 2013. Available from: https://doi.org/10.1063/1.4833475.

[53] J. Liu, H. Yang, W. Tan, X. Zhou, Y. Lin, Photovoltaic performance improvement of dye-sensitized solar cells based on tantalum-doped $TiO_2$ thin films, Electrochim. Acta 56 (1) (2010) 396–400. Available from: https://doi.org/10.1016/j.electacta.2010.08.063.

[54] Q. Liu, Y. Zhou, Y. Duan, M. Wang, Y. Lin, Improved photovoltaic performance of dye-sensitized solar cells (DSSCs) by Zn + Mg co-doped $TiO_2$ electrode, Electrochim. Acta 95 (2013) 48–53. Available from: https://doi.org/10.1016/j.electacta.2013.02.008.

[55] Y. Akila, N. Muthukumarasamy, S. Agilan, S. Senthilarasu, D. Velauthapillai, Zirconium oxide post treated tin doped $TiO_2$ for dye sensitized solar cells, Mater. Sci. Semicond. Process. 57 (2017) 24–31. Available from: https://doi.org/10.1016/j.mssp.2016.09.028.

[56] M. Barberio, D.R. Grosso, A. Imbrogno, F. Xu, Preparation and photovoltaic properties of layered $TiO_2$/carbon nanotube/$TiO_2$ photoanodes for dye-sensitized solar cells, Superlattices Microstruct. 91 (2016) 158–164. Available from: https://doi.org/10.1016/j.spmi.2016.01.012.

[57] L. Jiang, L. Sun, D. Yang, J. Zhang, Y.-J. Li, K. Zou, et al., Niobium-doped (0 0 1)-dominated anatase $TiO_2$ nanosheets as photoelectrode for efficient dye-sensitized solar cells, ACS Appl. Mater. Interfaces 9 (11) (2017) 9576–9583. Available from: https://doi.org/10.1021/acsami.6b14147.

[58] Z. Yuan, R. Tang, Y. Zhang, L. Yin, Enhanced photovoltaic performance of dye-sensitized solar cells based on Co9S8 nanotube array counter electrode and $TiO_2$/g-C3N4 heterostructure nanosheet photoanode, J. Alloys Compd. 691 (2017) 983–991. Available from: https://doi.org/10.1016/j.jallcom.2016.08.136.

# CHAPTER 6

# ZnO-based dye-sensitized solar cells

**Dena Pourjafari and Gerko Oskam**
Departamento de Física Aplicada, CINVESTAV-IPN, Mérida, México

## Contents



*Nanomaterials for Solar Cell Applications*
DOI: https://doi.org/10.1016/B978-0-12-813337-8.00006-0

## 6.1 Introduction

Energy and environment issues are the most important concerns for human health in the 21th century. Due to the depletion of fossil fuels, but mostly, their crucial effects on environment and climate, the search for alternative energy sources is vital. Among all the renewable, clean and environment-friendly sources of energy, solar energy provides the most promising strategy due to its abundance and continuous supply. Photovoltaic (PV) technology has demonstrated the potential to solve the environmental problems and it can be considered a fast growing technology both in research and industrialization. An efficient PV technology must meet high-efficiency/low-cost requirements. First generation solar cells based on bulk crystalline silicon (c-Si) wafers dominate today's market because of their good performance and high stability, demonstrating 24.4% of efficiency for a c-Si module consisting of 108 cells with 13,177 $cm^2$ of designated illumination area (da) fabricated by Kaneka Corporation [1]. Binary III−V semiconductors, such as GaAs, GaAlAs, GaInAsP, InAs, InSb, and InP also fall into the first generation of solar cells. The fabrication cost of this PV technology has been declining over the past 10 years and, although the technology is economically viable, upfront installation costs are still too high for worldwide commercialization and installation. The second generation of solar cells consists of amorphous silicon (a-Si) and thin-film technologies, including Si and chalcogenides. This generation is focused on the aim of cost reduction by elimination of unnecessary and expensive materials by adopting a thin-film configuration. In this category, copper indium gallium selenide mini-modules with the area of approximately 16 $cm^2$ have achieved 18.7% of efficiency [1]. In addition, CdTe-based PV technology has been successfully commercialized, reaching an efficiency of 18.6% for a mini-module with 7038.8 $cm^2$ of designated illumination area [2]. Despite the more efficient solar absorption and potentially lower fabrication cost of these materials compared to c-Si, reproducibility and uniformity issues remain on larger substrate areas. Over the last three decades, the efforts to reduce the fabrication cost even more led to the development of third generation solar cells using organic/inorganic materials such as dye-sensitized solar cells (DSSCs), organic PVs, and more recently hybrid perovskite solar cells [3−5]. After the breakthrough report of O'Regan and Grätzel in 1991 [6] introducing the DSSC, intensive investigation has been performed worldwide to improve the performance of both small cells and mini-modules to

achieve a reasonable production cost per peak Watt of solar-to-electrical energy conversion. DSSCs are easy to fabricate at ambient temperature using inexpensive and reproducible techniques, such as screen printing and roll-to-roll processing for large-scale PVs [7–9]. The low-cost manufacturing methods on both rigid and flexible substrates, and the capability to perform well under cloudy conditions as well as diffuse light, make DSSCs also an excellent choice for indoor applications.

This chapter starts with an introduction to the DSSC, describing the components of the solar cell and the mechanism of the energy conversion. Then the general information on ZnO crystallographic structure and its properties, synthesis, morphology and deposition methods are provided. The advantages and disadvantages of ZnO in DSSCs are discussed in detail, mentioning the main challenges in the fabrication process by modifying the substrate, dye and type of electrolyte. The criteria for the choice of an appropriate dye and redox couple are discussed as important factors to improve the performance of ZnO-based DSSCs. The influence of dye chemistry on the injection efficiency of electrons into the ZnO nanostructured network is explained. Finally, the performance of the cells with different architectures and the advantages and drawbacks of each are reviewed. The advanced analysis of the solar cell behavior using electrochemical characterization techniques, such as electrochemical impedance spectroscopy (EIS), intensity-modulated photovoltage spectroscopy (IMVS) and intensity-modulated photocurrent spectroscopy (IMPS), is explained and discussed in detail. Some examples from literature are interpreted and used to compare the performance of different types of ZnO-based solar cells and to elucidate the fundamental processes governing the observed performance. The chapter ends with a brief explanation of the design parameter optimization, aspects of technology scale-up, and conclusions.

### 6.1.1 Dye-sensitized solar cells

In 1991 O'Regan and Grätzel proposed a new type of solar cell working on the principal of plant photosynthesis and taking advantage of nanotechnology that achieved an efficiency of 7.1%, and they named it a "DSSC" [6]. A DSSC consists of two electrodes assembled in a sandwich configuration, and contains three basic components: a wide band gap semiconductor, dye or sensitizer, and electrolyte [3,10,11]. The electrode is a transparent conducting oxide (TCO) layer, such as fluorine-doped tin oxide (FTO) or indium tin oxide (ITO), deposited on a glass substrate.

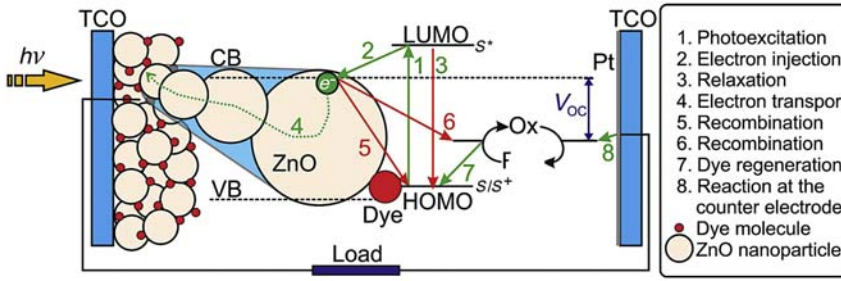


**Figure 6.1** Schematic view of the architecture and operating principals of the DSSC.

The working electrode (WE) (photoanode) is a nanostructured semiconducting metal oxide material with a monolayer of dye molecules bonded to its surface. The counter electrode (CE) (cathode) is a TCO coated with (usually) platinum as a catalyst [12,13]. A generally nonaqueous electrolyte containing a redox couple mediator is placed between WE and CE. Fig. 6.1 presents a schematic view of the architecture and operating principals of the DSSC.

In the past 25 years, many research groups have reported fabrication processes of these cells with different components in order to study and improve their performance. DSSCs operate based on three principal processes including charge carrier generation, charge transport and charge collection [3,14]. Dye molecules adsorbed at the photoanode nanostructured metal oxide absorb incident solar energy and, as a result, the dye is brought into the excited state. The dye is oxidized by injection of an electron from the excited stated into the conduction band (CB) of the semiconductor. The electrons are then transported through the mesoporous, nanostructured network of the semiconductor to reach the TCO substrate of the WE, and are then transported through the external circuit to the CE. Oxidized dye molecules receive electrons from the redox mediator in the electrolyte and the dye is regenerated; back into the ground state, the dye can again absorb a photon for continued photocurrent generation. The oxidized redox species in the electrolyte is regenerated by a reduction reaction at the CE, thus completing the electronic circuit. The photocurrent generation process described here is, of course, balanced by loss processes under open circuit conditions. The two most important recombination processes are the electron transfer from the semiconductor CB to the oxidized dye, and to the redox electron acceptor in the electrolyte, the latter of which also results in a dark current

[11,15–18]. Eqs. (6.1)–(6.6) represent the photoelectrochemical processes, which occur during operation of a DSSC:

$$S + h\upsilon \rightarrow S^{*}\ (\text{dye excitation}) \tag{6.1}$$

$$S^{*} \rightarrow S^{+} + e^{-}\ (\text{CB})\ (\text{electron injection to semiconductor CB} - \text{ps scale}) \tag{6.2}$$

$$S^{+} + e^{-}\ (\text{electrolyte}) \rightarrow S\ (\text{dye regeneration;}\ \ \mu\text{s scale}) \tag{6.3}$$

$$\text{Ox} + e^{-}\ (\text{CE}) \rightarrow \text{Red}\ (\text{reduction of oxidized species at the CE}) \tag{6.4}$$

$$e^{-}(\text{CB}) + S^{+} \rightarrow S\ (\text{recombination to oxidized dye} - \mu\text{s/ms scale}) \tag{6.5}$$

$$e^{-}(\text{CB}) + \text{Ox} \rightarrow \text{Red}\ (\text{recombination to the electrolyte} - \text{ms/s scale}) \tag{6.6}$$

where $S$ is the dye molecule in the ground state, $S^{*}$ represents the dye in the excited state, $S^{+}$ is the oxidized dye, $h$ is Planck's constant, $\nu$ is the frequency and Ox and Red are oxidized and reduced species of the redox couple in the electrolyte solution.

Titanium dioxide ($TiO_2$) is the most studied metal oxide as working electrode in DSSCs [19–26]. However, there are also many reports on zinc oxide (ZnO) [27–31] and tin dioxide ($SnO_2$) [32–35]. The metal oxide must be nanostructured and mesoporous to provide a high surface area and guarantee a good light harvesting efficiency by the dye molecules, which should be well bonded to the surface of the nanostructure [36–41]. The first DSSC was fabricated using a dye with three ruthenium metallic centers [6]. Ruthenium-complex dyes are the most commonly used dyes in DSSCs fabrication. To date, most of the highly efficient and reproducible $TiO_2$-based DSSCs contain ruthenium-based dyes such as N3, the black dye, N719, C101 and Z991, with reproducible efficiencies between 10% and 12% [42–46]. However the ruthenium-based dyes are not suitable for cost-effective device production since ruthenium is a rare and expensive metal. This drawback has led to the development of new dyes using either cheaper metal (metal-complex porphyrin dyes) [47,48] or metal-free (organic) dyes, such as oligothiophene, coumarin and indoline derivatives, which have also reached efficiencies up to 10% or higher [49–51].

The choice of the different components of the DSSC is an important factor to fabricate a highly efficient PV system by optimizing the parameters, which have a direct influence on the open circuit voltage ($V_{OC}$) and short circuit current density ($J_{SC}$) of the solar cell. The energy levels at the semiconductor/sensitizer/electrolyte interfaces should be well matched to ensure efficient electron injection and dye regeneration processes. The electrolyte must be optimized for each dye; it should not absorb light in the visible region, it should have a high electrical conductivity and low viscosity for faster ion diffusion, and it should provide good interfacial contacts with the metal oxide and CE. Also the electrolyte should not have a tendency to detach the adsorbed dye molecules from the semiconductor surface [52]. The iodide/triiodide ($I^-/I_3^-$) redox mediator is the best known and classically used electrolyte in DSSCs due to its excellent stability, fast electron donation by $I^-$, which results in fast dye regeneration, and slow electron capture of $I_3^-$ at the metal oxide surface, which reduces the recombination rate [53–55]. However, because of a large overpotential for dye regeneration, the open circuit voltage of the solar cell is relatively low for this redox couple. Also, the iodide/triiodide redox mediator is strongly corrosive; hence, it is not suitable for large-scale applications where metallic parts may come in contact with the electrolyte. As a result, the search for new redox couples has been the center of research in the DSSC field in the past 10 years. One-electron redox couples, such as cobalt or copper complexes, are interesting alternatives for the conventional iodide/triiodide redox mediator. To date, the confirmed highest efficiency DSSC was reported by Komiya et al. in 2011, for a $TiO_2$-based cell of 1.005 $cm^2$ active area, with an open circuit voltage of 0.74 V, a short circuit current of 22.47 mA $cm^{-2}$, and a fill factor of 71.2%, thus achieving a 11.9% efficiency [1].

There are extensive and detailed studies in literature on $TiO_2$-based DSSCs [11,41]. However, zinc oxide is also an interesting material due to its structural, optical and electrical properties, as well as its thermal, mechanical and chemical stability. The band gap and CB edge of ZnO are similar to those of anatase $TiO_2$. However, single-crystalline ZnO has much higher electron mobility than anatase, which may improve the electron conduction [56,57]. As a result, it has been widely used in a vast range of technological applications such as light emitting diodes, sensors (UV, chemical, gas and biosensors), transistors, laser, transparent electronic and optoelectronic devices, smart windows, piezoelectronic devices and DSSCs [58–62].

### 6.1.2 Properties of ZnO

Under ambient conditions, the most thermodynamically stable crystallographic structure of ZnO is wurtzite, characterized by hexagonal unit cells with space group $P6_3mc$ and lattice parameters $a = 3.29$ Å and $c = 5.24$ Å, in which each $Zn^{2+}$ is surrounded by a tetrahedral coordination of $O^{2-}$ and vice-versa [62,63]. Nonuniform distribution of the cations and anions results in formation of several polar surfaces with positive and negative charges. The polar and nonpolar surfaces are responsible for growth phenomena and some unique characteristics of ZnO, such as piezoelectric properties, as well as electronic, chemical and physical properties. The two most common face terminations of wurtzite ZnO are the positively charged Zn-(0001) and negatively charged O-$(000\bar{1})$, which are polar faces along the *c*-axis. The two most common nonpolar faces are $(11\bar{2}0)$ and $(10\bar{1}0)$ along the *a*-axis [64]. The optical and electrical properties of ZnO, as well as its thermal, chemical and mechanical stability, significantly depend on the ZnO morphology [65–68]. The differently charged polar Zn- or O-terminated surfaces determine the morphology due to their distinct reactivity and thus growth behavior. Hence, the properties of ZnO nanostructures are different from one morphology to another. In the following sections, these properties are briefly reviewed in general terms.

The optical and electrical properties of ZnO are significantly affected by the followed synthesis method, which has a direct influence on the growth mechanism and rate, as well as the morphology of the final product. This may lead to the presence of point defects and impurities in the ZnO structure, affecting its properties [66]. In general, ZnO is a direct band gap semiconductor with piezoelectric properties, a band gap of 3.3 eV and a relatively large exciton binding energy of 60 meV, which makes the exciton stable at room temperature. ZnO has almost the same refractive index as $TiO_2$. However, due to the lower electron effective mass of ZnO (0.26 $m_e$) compared to $TiO_2$ (9 $m_e$), ZnO has a much higher electron mobility (205–300 $cm^2\,V^{-1}\,s^{-1}$ at 300K) than $TiO_2$ (0.1–4 $cm^2\,V^{-1}\,s^{-1}$ at 300K) resulting in a faster electron transport in both bulk and nanostructured ZnO; the electron diffusion coefficient of bulk ZnO is 5.2 $cm^2\,s^{-1}$ while it is 0.5 $cm^2\,s^{-1}$ for $TiO_2$ [13,28,56].

Many oxide materials are stable at high temperature. ZnO has excellent stability in air up to 1300°C with a decomposition temperature of above 2200K. ZnO shows good electrical conductivity over a wide range of temperatures, which makes it suitable for thermoelectric generators that

operate at very high temperature [69–71]. The chemical stability of ZnO is relatively poor in acidic and alkali media, hence this is an aspect that needs to be considered in specific applications of ZnO. However, in spite of or related to its poor chemical stability, there is a vast variety of synthesis methods in a wide range of pH environments that result in the formation of ZnO nanostructures with many different morphologies [68,72]. Depending on the orientation of the perpendicular crystallographic planes to the principal *c*-axis, the mechanical properties of ZnO vary. *c*-Axis oriented ZnO (5 GPa) is harder than *a*-axis oriented ZnO (2 GPa), which is why one-dimensional (1D) ZnO nanostructures have been widely used in piezoelectric applications. 1D ZnO has a high aspect (length to diameter) ratio resulting in good mechanical stability [67]. Recently, 2D ZnO materials such as nanosheets and nanoplates have shown promising mechanical stability related to their high surface-to-volume ratio [73].

### 6.1.3 Advantages, disadvantages and challenges in ZnO-based dye-sensitized solar cell fabrication

Although ZnO has almost the same band gap and CB edge as $TiO_2$, it has higher bulk electron mobility than that of $TiO_2$, resulting in faster bulk electron transport in a ZnO photoanode, which may lead to an increase in the collection efficiency [74]. ZnO is a direct band gap semiconductor and because of its crystallographic properties, an ample diversity of nanostructured photoanodes can be produced on different substrates. Due to these advantages, ZnO is expected to be one of the alternative candidates to $TiO_2$ in DSSCs. However, the highest achieved efficiency for ZnO-based DSSCs is still much lower than the record value for $TiO_2$-based DSSCs, which may also be related to the strong focus of the community on $TiO_2$. ZnO nanostructures have shown a somewhat lower porosity and surface area, which may result in a lower quantity of dye adsorbed at the semiconductor surface [52]. As mentioned previously, ZnO has poor chemical stability in acidic solutions, including dye solutions with or without complexing agents, related to its isoelectric point of 9; note that the isoelectric point is about 6 for $TiO_2$ [75]. Beside partial ZnO dissolution in this media, $Zn^{2+}$ cations may interact with dye ligands and $Zn^{2+}$– dye complexes can be formed. This undesirable side product tends to cover the semiconductor surface preventing efficient charge injection and charge separation [51,68]. Another reason for the limited performance of ZnO-based DSSCs are the slower injection kinetics in the range of picoseconds, compared to that for $TiO_2$-based DSSCs,

which is on the femtosecond scale [76]. This is related to the formation of intermediate states at the semiconductor/dye interface in the presence of metal-complex based dyes. Due to the intrinsic electronic properties of the CB of ZnO, electron−cation pairs are formed after dye excitation. This suggests that the electrons are considered to be delayed at the ZnO/dye interface via these intermediate states [68,76,77]. One important factor in order to fabricate a high performance DSSC, is the optimization of the basic principles of cell operation, such as light harvesting, electron injection, electron transport and charge collection phenomena by adequate material choice.

To increase dye adsorption at the ZnO surface and improve light harvesting of the PV device, research on new dyes that are compatible with the ZnO structure and cell electrolyte should be addressed. In the presence of some electrolytes, the dye tends to detach from the ZnO surface, and a dye weakly bonded to the ZnO surface is undesirable. In addition to new dyes, structure modification of commonly used dyes in order to tailor the acidity and modify complexing agent chemistry could be considered as a solution for better ZnO/dye interactions. The dye concentration and pH of the solution, as well as the dye-sensitization time, strongly depend on the dye structure, and must be optimized for each dye in order to avoid reaction with the ZnO surface and formation of $Zn^{2+}$− dye complexes. A better control of the surface properties of ZnO structure such as morphology and surface chemistry should be achieved in order to increase the ZnO porosity and surface area, and its interaction with dye and electrolyte [52,56,68,76].

## 6.2 Synthesis methods and nanostructure morphology of ZnO for dye-sensitized solar cell applications

Thanks to the nature and crystallographic structure of ZnO, there are many routes to synthesize a wide range of nanostructure morphologies. Synthesis methods influence the growth rate, mechanism and material orientation and, accordingly, the optoelectrical properties of the final product. High-quality ZnO nanostructures can be synthesized from high temperature and pressure methods such as vapor-liquid-solid (VLS) [78,79], chemical vapor deposition (CVD) [80−82], thermal evaporation [83,84], sputtering [85,86], pulsed laser deposition [87,88], molecular beam epitaxy [89,90] and physical vapor deposition [91,92], among others. Also, ZnO can be synthesized through solution-based methods such as hydrothermal [93,94], solvothermal [95,96],

sol–gel [97–99], microwave-assisted synthesis [100,101], template-assisted synthesis [102,103] and electrodeposition (ED) [104–106]. These synthesis methods result in different ZnO nanostructures, including 1D structures such as nanotubes, nanorods, nanopillars and nanowires, as well as thin films, nanoparticles (NPs), nanosheets, nanoflowers, nanoflakes, nanocombs, nanobelts, nanodisks, tetrapod, etc. [107–109]. In the next section we focus on ZnO synthesis and morphology specifically for DSSCs applications.

Among the various ZnO synthesis routes for DSSC fabrication, the solution-based methods such as wet chemical, hydrothermal, solvothermal and ED are the most common and efficient methods due to their low cost of process and materials [110–113]. These methods usually start from an aqueous or alcohol solution containing Zn salts such as zinc acetate, zinc nitrate or zinc chloride and pH-control additives or capping-agents [114–116]. ZnO nanostructures generally form in a low-temperature process. Sometimes an annealing process of up to 400°C is needed to obtain good-quality ZnO crystals.

### 6.2.1 ZnO morphology and morphological parameters: size, surface area, porosity

The synthesis experimental conditions and parameters, such as solution concentration, pH, temperature, additives or capping-agent, type of substrate, presence of a seed layer, stirring, applied voltage and current, reaction time and heat treatment have significant influence on the growth rate and orientation of the formed ZnO. A small change in experimental condition may result in a significant change in morphology and, hence, properties. Several review articles provide detailed information on different ZnO morphologies and morphological parameters [28,117]. Changing the synthesis route and experimental conditions is one way to modify the size of fabricated nanostructures. Depending on these synthesis conditions for ZnO NPs, the reported average diameter is in the range of 5–60 nm [118–122] and for 1D ZnO nanostructures including nanowires, nanofibers, nanorods and nanotubes this value is in the range of 50–300 nm. The length of 1D ZnO varies from several hundreds of nanometers to several micrometers [123–128]. For ZnO nanospheres both as an active layer and scattering layer, a diameter in the range of 300–600 nm has been reported [129–132]. Metal oxide porosity depends on the morphological properties of nanostructures such as diameter, length and aspect ratio. In general, reported values of the ZnO specific surface area are smaller than that of $TiO_2$, which could be a reason for the lower performance

of ZnO-based DSSCs. There are some reports on the value of the specific surface area calculated by Brunauer–Emmett–Teller (BET) technique for ZnO nanostructures, demonstrating that modifying the synthesis conditions such as changing the precursor concentration and pH, precursor addition rate, temperature of the synthesis, using a capping agent and dopant and also applying post-treatment, directly affect the morphology and, hence, the porosity of the obtained ZnO nanostructures [114,133–141]. To our knowledge, the lowest and the highest reported values for BET surface area of ZnO nanostructures are about 0.04 and 230.8 $m^2 g^{-1}$, respectively, both for ZnO NPs [136,142]. However, usually the reported specific surface area values for ZnO with different nanostructures morphology are in the range of 20–60 $m^2 g^{-1}$ [133–135,140,143–152]. This value for commercial ZnO NPs with 20 nm in diameter is 24.1 $m^2 g^{-1}$ [153]. Fig. 6.2 shows scanning electron microscopy (SEM) images of different ZnO nanostructures that have been used in ZnO-based DSSCs.

## 6.3 Deposition techniques

In a variety of synthesis methods, the ZnO nanostructures are deposited on the substrate at the same time of the synthesis process; that is, the substrates are used as a starting point for ZnO nucleation and growth to a desirable film thickness. In these methods the substrate is dipped into or covered by a, in some cases metastable solution containing a precursor and reactant for the formation of ZnO. Some examples of these deposition techniques are; drop coating [171], dip coating [172], spin coating [167], chemical bath deposition (CBD) [145,173], electrochemical [174,175] and electrophoretic deposition (EPD) [176]. In most of these methods the substrate is immersed in the soluble Zn salt bath, such as zinc acetate, zinc nitrate or zinc chloride. The $Zn^{2+}$ and $O^{2-}$ from the solution are deposited onto the substrate and a ZnO layer is formed by modifying the experimental conditions. In the drop coating method, drops of precursor solution are spread onto the substrate and the thickness of ZnO layer is varied by controlling the number of added drops and the concentration of the colloidal ZnO solution [139,177]. In dip coating, the entire substrate is immersed into the precursor solution containing zinc salt or ZnO colloidal solutions at room temperature for a short period of reaction time [172,178,179]. In both drop and dip coating, the substrate should be compatible with the solution and resist the experimental

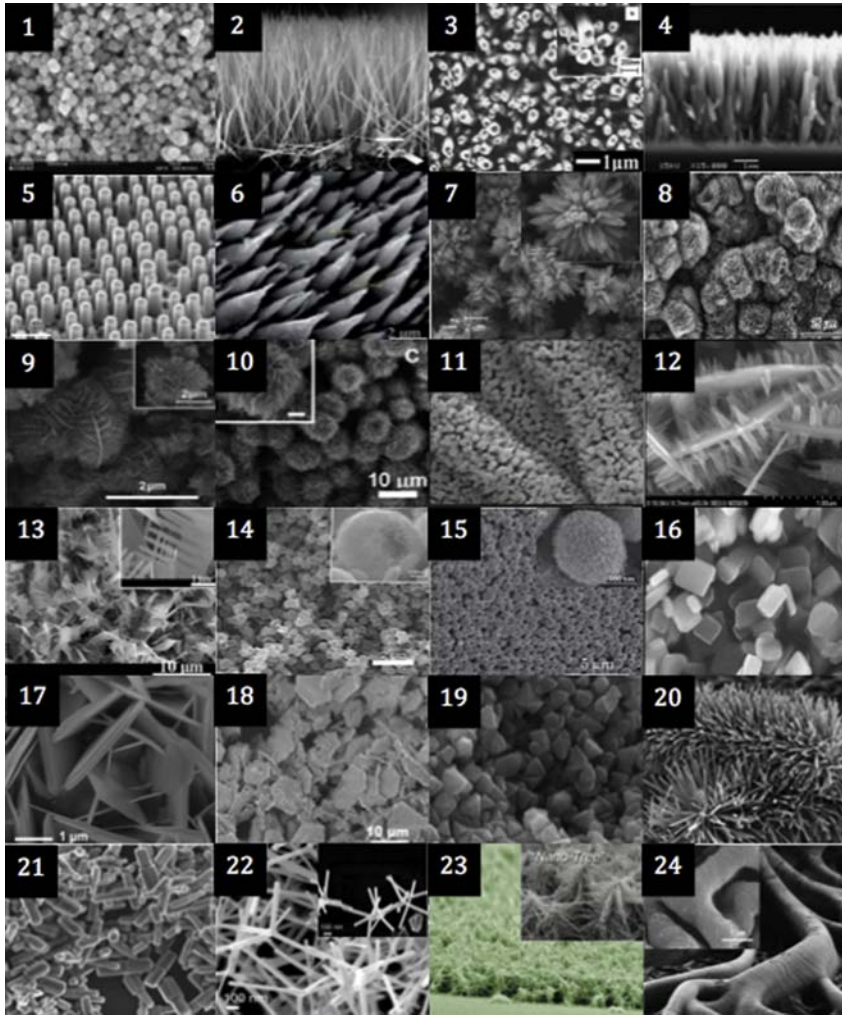


**Figure 6.2** SEM images of different ZnO nanostructures morphologies: (1) nanoparticles [154], (2) nanowires [123], (3) nanotubes [155], (4) nanorods [156], (5) pillar arrays [103], (6) microtips [157], (7) nanoflowers [158], (8) cauliflower-like [159], (9) panel-like [152], (10), microsphere [143], (11) Garland-like [160], (12) nanospike decorated sheets [161], (13) nanocombs [162], (14) hollow spheres [130], (15) nanospheres [129], (16) rectangular prisms [163], (17) nanosheets [164], (18) disk-like [165], (19) nanocons [166], (20) caterpillars [167], (21) hexagonal clubs [168], (22) tetrapods [169], (23) nanoforest [111], (24) banyan-root structured [170].

conditions. In the spin coating method, the diluted paste or colloidal dispersion of ZnO nanostructures is dropped onto the spinning substrate. The thickness of the layer is determined by controlling the rotation speed. Sometimes a two-step process is required; the first step at low or moderate speed to evenly spread the solution onto the substrate, and the second step at higher speed to achieve the desired thickness of the coating [122,180]. In the drop, dip and spin coating methods, usually the coated substrate is heated in the range of 200°C−400°C to ensure the formation of zinc oxide, and to eliminate the unwanted organic components. In CBD, films of ZnO are grown onto the substrate, which is immersed into the solution containing appropriate precursors at relatively low temperature for a specific period of time to deposit films of desired thickness [181,182]. Another low-temperature deposition technique is ED, in which the substrate as working electrode is immersed in the zinc containing precursor solution. Various experimental conditions such as type, concentration, temperature and pH of the solution as well as the applied voltage, current density, distance between the WE and CE, area of the electrodes, stirring and deposition time must be controlled in order to achieve uniform deposition films [183,184]. Besides the advantages of ED as a fast, low-cost, low temperature and scalable technique suitable for various types of substrate, it can also be considered as one-step method to obtain the hybrid film of ZnO/dye simultaneously [175,185]. EPD has also been used to deposit ZnO films and like ED, it is a low-temperature method and compatible with TCO-covered glass and plastic, as well as metal substrates. Usually in EPD, the substrate is dipped into a ZnO suspension using a higher DC voltage than that used in ED, since in this technique the NPs move to the substrate under influence of the electrical field. Depending on the experimental conditions, for example, if the oxygen source is sufficient in ED, it is not always necessary to sinter the ZnO films after deposition [176,186].

Printing methods, such as doctor blade and screen printing are other techniques for ZnO deposition. In these methods, an as-prepared ZnO nanomaterial is first converted to a colloidal solution or paste in order to deposit a film onto the substrate [120,153]. In this case, a sintering process should be carried out to remove all organic chemicals or binders that are generally used in paste preparation. For solar cell applications and large-scale fabrication, the deposition technique should be easy, low-cost and reproducible, and often printing techniques are preferred [8,187].

## 6.4 ZnO-based dye-sensitized solar cells with different architecture

ZnO-based DSSCs can be fabricated in different architectures by changing the components that are used in cell assembly, such as the substrate, the electrolyte and the dye. The substrate varies from rigid conductive glass to conductive flexible plastic and metal substrates. Dye molecules are divided into three categories; organometallic dyes, metal-free (organic) dyes, and natural dyes, and the electrolyte can be either a liquid, a quasi solid or a solid, using different redox couples. These architectures are explained in the following sections.

### 6.4.1 Type of substrate: glass, flexible plastic and metal substrates

The fabrication parameters, such as ZnO deposition method, process temperature, cell configuration and sealing process, depend on the type of the substrate. Glass substrates are the most common substrates used in DSSCs due to their stability under a wide range of experimental conditions, including relatively high temperature and pressure, and high and low pH. Therefore, many fabrication methods mentioned above can be applied to fabricate ZnO-based DSSCs on glass substrates. Typical DSSC photoanodes require sintering at high temperature (450°C−550°C) in order to obtain good electrical connection and necking between NPs, to improve charge transport [188]. The flexible substrates can be transparent plastics such as polyethylene terephthalate coated with ITO (ITO/PET), and their low thermal stability (degradation $\geq 150$°C) restricts them to be used only in low-temperature deposition processes.

A number of methods, such as low temperature hydrothermal growth, hot water treatment, ED, EPD, low-temperature sintering with ultraviolet light, mechanical compression, microwave irradiation, binder-free coating, successive ionic layer adsorption and the reaction method have been reported for the fabrication of DSSCs on polymer substrates [117,183,187−193]. The relatively high sheet resistance of the TCO film either on glass or plastic substrates, especially in the production of large area devices, is the main reason to use top-illuminated DSSCs based on metal foils or plastic foils with metal coatings [194]. The various metal substrates such as Ti, Al, Ag, Ni, W, Zn and stainless steel have been used for DSSC manufacture [194,195]. Screen printing, doctor blading, spin coating and EPD are the most common methods using in DSSCs

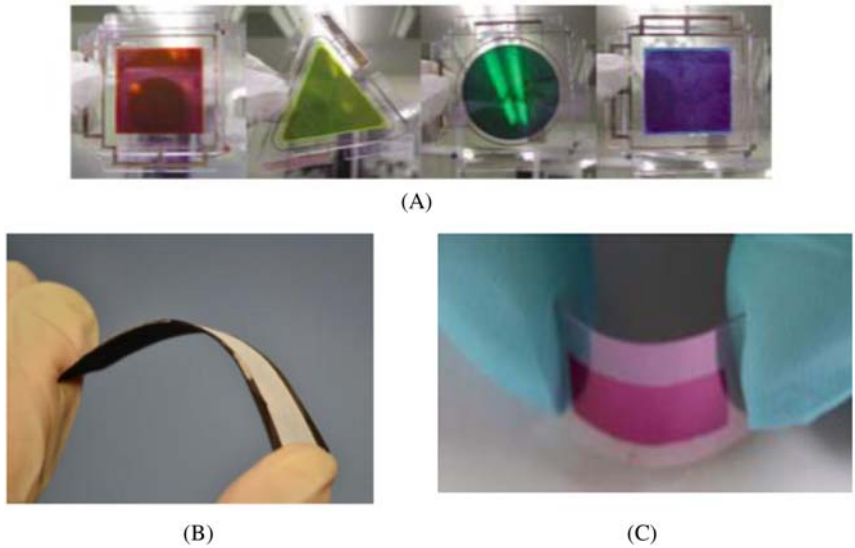


**Figure 6.3** Examples of ZnO-based DSSCs on plastic and metal substrates, (A) plastic solar cells in various color by combination of three primary colors, yellow, magenta, and cyan [198]. (B) Flexibility of DSSCs on Ni coated paper substrates; [199] (C) Photo of a plastic D149-sensitized ZnO electrode [176].

fabrication on metal substrates [195–197]. Fig. 6.3 shows some examples of ZnO-based DSSCs on plastic and metal substrates.

### 6.4.2 Dyes

One of the strategies to enhance DSSC performance is to achieve a higher efficiency of the electron injection process, which depends on the identity of the sensitizer dye. For ZnO, electron injection occurs within 0.1–100 ps, as calculated from femtosecond transient absorption measurements [200–202]. ZnO-based DSSCs have shown good efficiencies but poor performance stability using dyes based on Ru-complexes (N719, N3, Z907, black dye, K27, K28, K313, HMP-09, HMP-11, CYB-1) [138,146,203–206] due to the formation of $Zn^{2+}$– dye micrometer-sized structures, which suppress the electron injection process by blocking the ZnO surface in the form of aggregates. Several studies reported the formation mechanism of these aggregates and the linkage of dye molecules to the ZnO surface [77,207–209]. In addition to the sensitizer type, the dye concentration, dye loading time, type of solvent and the thickness of metal oxide semiconductor are important factors influencing the cell

performance [177,184,210,211]. Cao et al. studied the effect of dye concentration and loading time on the performance of the ZnO/N3 cell [177]. Saito and Fujihara reported a ZnO/N719 cell with an efficiency of 4.53% and $J_{SC}$ of 13.76 mA $cm^{-2}$ using a dye loading time of 90 minutes. The cell performance was improved by fabrication of thicker ZnO films that adsorbed more dye molecules, thus achieving 6.58% efficiency and a $J_{SC}$ of 18.11 mA $cm^{-2}$, showing very good cell performance with this Ru-complex dye [153]. However, to prevent the undesirable aggregates at the ZnO surface, many studies suggest the replacement of Ru-complex dyes with metal-free and organic dyes. ZnO-based DSSCs with metal-free dyes, such as indoline-based dyes (D149, D205, D102) [122,131,166], have reached efficiencies of more than 5%. Other metal-free dyes that have been used to fabricate ZnO-based DSSCs are heptamethine–cyanine dyes (KFH-2, KFH-3), coumarin dyes (C206, C220, C218, SK1), benzothiadiazole (BT)-based dyes, carbazole dyes (SD4, JM1, JM2), xanthene dyes (DJ104), mercurochrome, eosin-Y and anthocyanins [117,119,149,212–219]. To improve the long-term stability of ZnO-based DSSCs, research has focused on synthesis of new dyes in order to obtain a dye with less acidity, broad range of visible light adsorbed by the dye, and compatibility with redox species. Yoshida et al. proposed DN-7 dye in which the hydrophobic interactions between adjacent molecules are expected to be smaller than those of D149 dye, making DN-7 less prone to form aggregates than D149 [184]. Ho et al. synthesized CR147 and measured the ZnO-based DSSC performance for different dye loading times. They reported less agglomeration compared to N719, achieving 6.89% of power conversion efficiency (PCE) [171]. Also, natural dyes such as extracts from walnuts, rhubarb, pomegranate, etc., have been used in ZnO-based DSSCs. However, they have shown very low performance [147]. Fig. 6.4 shows the molecular structure of the most common and high-efficiency dyes for ZnO-based DSSCs. The inset figure shows colorful ZnO cells fabricated by Sankapal et al. [213].

### 6.4.3 Redox couples

In the DSSC, the open circuit voltage is determined by the difference between the quasi-Fermi level of the semiconductor metal oxide and the redox potential of the electrolyte. Due to the advantages of the $I^-/I_3^-$ redox couple, such as small size, high solubility, fast electron donation by $I^-$ (which ensures a quick dye regeneration), and slow electron transfer from the metal

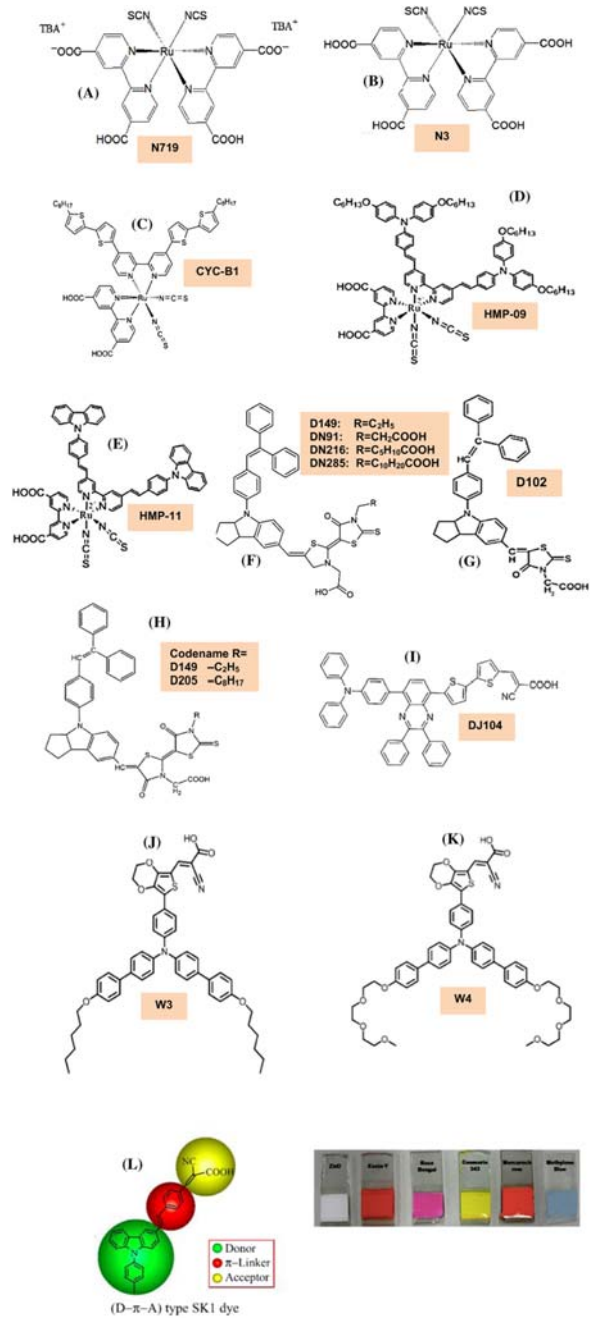


**Figure 6.4** Molecular structure of (A) N719 [220], (B) N3 [220], (C) CYC-B1 [206], (D) HMP-09 [203], (E) HMP-11 [203], (F) indoline-based dyes [221], (G) D102 [122], (H) D149 and D205 [131], (I) DJ104 [119], (J) W3 [222], (K) W4 [222], (L) SK1 [149] and the inset shows colorful ZnO cells fabricated by Sankapal et al. [213].

oxide to $I_3^-$ (which decrease the recombination rate), the most efficient DSSCs remain those that are based on this conventional redox mediator and Ru-based dyes. However, some drawbacks exist, including corrosiveness, competitive light absorption, and direct redox quenching of highly polarizable dyes such as conjugated prophyrins [223]. Recently a variety of redox couples such as $Br^-/Br_3^-$, $SCN^-/(SCN)_2$, $SeCN^-/(SeCN)_3^-$, $Fe(CN)_6^{3-/4-}$, Co(II)/Co(III) complexes and Cu(I)/Cu(II) complexes have been introduced to $TiO_2$-based DSSCs in order to achieve a higher $V_{OC}$ [41,193,224–229] and to prevent electrode and metal electrical contact corrosion by the iodide/triiodide species; this latter aspect has significantly complicated the commercialization of DSSCs [41]. One-electron redox mediators with weak visible light absorption are less corrosive than iodide. The $V_{OC}$ of solar cells based on these alternative redox couples may be high ($>1000$ mV) because of the more positive redox potential of the complexes, which can easily be tuned. It is possible to adjust the redox potential by changing the coordination sphere of the complexes resulting in the large amount of commercially available ligands [53,230]. Compared with $I^-/I_3^-$, cobalt-based electrolytes require less energy for dye-regeneration, which may increase the open-circuit voltage, however it has also been found that for these new redox couples, unwanted properties such as slower dye regeneration and faster electron recombination may occur, which in some cases can be slowed down by applying an adequate intermediate blocking layer in the cell fabrication process [224].

Recently, the most efficient ZnO-based DSSC was reported by Xie et al., containing the conventional $I^-/I_3^-$ electrolyte, and achieving 8.22% of PCE [138]. The iodide/triiodide redox couple in a volatile solvent such as acetonitrile or the mixture of acetonitrile and valeronitrile, is the most studied electrolyte species in the majority of literature on ZnO-based DSSCs. There are some reports on other types of electrolytes including$I^-/I_3^-$ in less volatile solvents such as methoxyacetonitrile, 3-methoxypropionitrile, and propylene carbonate, Co-based electrolytes, ionic liquid electrolytes, solid-state or gel electrolytes like polyethylene oxide (PEO) and spiro-OMeTAD. However, the efficiencies of these solar cells are still lower than those of iodide/triiodide-based electrolytes [135,159,166,193,219,231–236].

### 6.4.4 Advantages and drawbacks of different architectures

As mentioned before, ZnO can be deposited onto both glass and flexible substrates coated with a TCO and forming a vast range of nanostructure

morphologies. Glass substrates have good thermal and chemical stability and ZnO can be deposited on glass substrates under a wide range of experimental conditions. However, rigid glass makes these cells unsuitable for some applications. Flexible, plastic substrates cannot resist high temperature fabrication and deposition methods, which restricts the applied experimental conditions. However their light weight, flexibility, lower sheet resistance and cheaper cost, make them suitable for both investigation and industrial applications where roll-to-roll mass production is needed.

Liquid electrolyte ZnO-based DSSCs have shown good performance, however, due to the leakage or evaporation of the volatile electrolyte, the technical problems, such as sealing, must be solved for large-scale devices. The alternative solutions are using a high viscosity and less volatile solvent or using a solid-state electrolyte. For devices with a one-electron redox mediator and faster recombination rate, a blocking layer must be introduced in the device architecture in order to slow down the recombination reactions.

### 6.4.5 State-of-the-art performance of ZnO-based dye-sensitized solar cells

Although the conversion efficiencies for ZnO are much lower than that of for $TiO_2$, ZnO is still considered a viable alternative to $TiO_2$ due to its ease of synthesis, crystallization and higher electron mobility. In fact, the first report on dye-sensitization of a ZnO semiconductor was by Gerischer and Tributsch in early 1969 [237]. In past years, there have been many improvements in efficiency and performance of ZnO-based DSSCs. Two main topics are involved with ZnO-based DSSCs; PCE and long-term stability. The efficiency of ZnO-based DSSCs can achieve higher values considering some strategies. One is improving the ZnO surface area to adsorb more dye molecules: [128,143,146] Liu et al. achieved 35.8% enhancement in efficiency of a ZnO nanoflowers-based cell compared to ZnO NPs-based cell by changing the morphology, porosity and surface area of ZnO from 27 $m^2 g^{-1}$ for NPs to 74 $m^2 g^{-1}$ for nanoflowers ZnO [238]. For the same flower-like morphology, Murugan et al. reported an efficiency of 5.64% for urchin-rod, flower-like ZnO combined with rice grain-like ZnO, showing that hybrid or mixed structures is one strategy to combine morphological properties, transport and recombination behavior of different ZnO nanostructures to achieve better cell performance [151]. One of the morphologies that resulted in high

efficiency ZnO-based DSSCs is the nanosheet structure. Ho et al. fabricated a ZnO-based DSSC with ZnO nanosheets by CBD. They obtained 6.06% of cell efficiency, a short circuit current density of 18.01 mA $cm^{-2}$ and open circuit voltage of 0.53 V with the D149 dye [173]. Another example of how to improve the performance of ZnO-based DSSCs is using doped ZnO nanostructures. Mahmood and Park reported a cell fabricated with ZnO nanosheets doped with boron and the N3 dye, achieving a PCE of 6.75%, 19.3 mA $cm^{-2}$ and 0.64 V for $J_{SC}$ and $V_{OC}$, respectively [134]. One way to reach a higher open circuit voltage and reduce the recombination rate through the substrate, is by isolating the substrate from an electrolyte solution by incorporation of a compact layer of ZnO, $TiO_2$ or $SnO_2$ between a substrate and the ZnO nanostructured active layer. Usually this layer is deposited onto the substrate by spray pyrolysis or simply just by immersion of the substrate into a solution containing these metal precursors following by heat treatment to obtain the metal oxide [171,184,239–242]. Luo et al. fabricated a DSSC consisting of 8 μm of porous ZnO active layer on top of a 200 nm ZnO compact layer prepared by ED, showing 0.605 V open circuit voltage and 5.08% PCE [174]. Also, coating nanostructured ZnO with a thin layer of insulating or semiconducting oxide may help to suppress carrier recombination and improve the PCE. Yang et al. covered ZnO nanowires by introducing a layer of $Al_2O_3$ and $TiO_2$ deposited by atomic layer deposition (ALD), forming a shell around the ZnO core. They reported better cell performance and suggested that $Al_2O_3$ and $TiO_2$ shells could act as an energy barrier that increases the physical separation between photoinjected electrons and the oxidized redox species in the electrolyte. These shells also form a tunneling barrier that corrals electrons within the conducting cores of the film. Finally, they passivated recombination centers on the ZnO surface. The efficiency of the cells without a shell was enhanced from 0.85% to 2.1% for the cell with a shell. Similarly, an enhancement ($\approx$240 mV) was observed in the $V_{OC}$ of bare ZnO after passivation with an ALD-deposited layer [243]. To improve the stability of ZnO-based DSSCs, ionic liquid and solid-state electrolytes are considered as a promising architecture to overcome the volatility problems of the conventional liquid electrolyte. A high efficiency (6.46%) ZnO-based DSSC with ZnO nanostructures, N719 and PEO was fabricated by Ma et al. From the electrochemical characterization of their cells and compared to liquid electrolytes, they proposed that using a polymer gel electrolyte can be

considered an effective strategy to ensure high efficiency and good stability [140]. In Table 6.1, a summary of the ZnO synthesis method and morphology, morphological parameters, type of substrate, dye, electrolyte and performance parameters for the corresponding ZnO-based DSSCs with efficiencies higher than 1% are listed.

## 6.5 Advanced characterization of ZnO-based dye-sensitized solar cells

The majority of studies related to ZnO-based DSSCs have been focused on synthesis methods, especially for 1D ZnO nanostructures, and research on new dyes that are compatible with ZnO. However, in comparison with $TiO_2$-based DSSCs, there are few detailed studies of electron transport and recombination for ZnO-DSSCs. In order to understand and identify the factors that are responsible for low performance of ZnO-based cells, and to improve the PV parameters, it is necessary to provide advanced studies and characterizations. Detailed characterization methods based on small-signal perturbations such as EIS, IMVS and IMPS are powerful tools to obtain quantitative information on electron transport, charge transfer and recombination processes. Using these techniques allows a comparison of chemical capacitance, charge transfer resistance, electron lifetime and electron diffusion coefficient between different systems [287–290]. The concepts, detailed study, analysis and interpretation of these techniques are beyond the scope of this chapter, however vast information on definition, experimental parameters and conditions, fitting the results and data analysis can be found in literature [287–300].

### 6.5.1 Electrochemical impedance spectroscopy

Electrochemical impedance measurements are generally performed under illumination at the voltage corresponding to open circuit conditions; the voltage can be varied by changing the light intensity. From EIS spectra the chemical capacitance and recombination resistance can be obtained by fitting the results using, for example, Zview software to the electrical circuit model developed by Bisquert et al. [288,292,296,299], shown in Fig. 6.5.

The differential chemical capacitance describes the dependence of the density of electrons stored in the nanostructured metal oxide film, and is generally found to exponentially increase with the open circuit voltage [289,300]. The recombination resistance, $R_{rec}$, describes the charge transfer

**Table 6.1** Summary of ZnO-based dye-sensitized solar cells fabrication and performance parameters.

| Synthesis method | Morphology | Morphological parameters | | | | Deposition technique: substrate | Dye | Electrolyte | Cell parameters | | | | References |
|---|---|---|---|---|---|---|---|---|---|---|---|---|---|
| | | *D* (nm) | *L* (μm) | *t* (μm) | BET ($m^2\ g^{-1}$) | | | | $J_{SC}$ ($mA\ cm^{-2}$) | $V_{OC}$ (V) | FF | $\eta$ (%) | |
| Solid-state | Rod-like | 50 | 100 | – | 15.6 | Drop blade: FTO | N719 | $I_2$-based | 23.26 | 0.62 | 0.57 | 8.22 | [138] |
| Solid-state | Sponge-like | – | – | 10 | – | – | – | – | 22.18 | 0.60 | 0.60 | 8.03 | [244] |
| Spray pyrolysis | Nanosheets: NAs | 200–1000 | – | 3–5 | – | Dip-coating: FTO | N719 | $I_2$-based | 21.73 | 0.61 | 0.60 | 7.95 | [172] |
| Microemulsion-assisted synthesis | Hexagonal clubs NP, hexagonal plate | 500<br>20–50<br>600 | 1<br>–<br>– | –<br>–<br>250 | –<br>–<br>– | Drop coating: FTO | DJ104 | $I_2$-based in AN/MPN | 15.84 | 0.69 | 0.68 | 7.40 | [119] |
| Multibatch, CFI | NWs: NPs | 15 (NPs) | 25 | – | – | Doctor blade: FTO | N719 | – | 17.01 | 0.70 | 0.60 | 7.14 | [120] |
| – | NC | – | – | – | – | ITO | N3, HMP9, HMP-11 | $I_2$-based | 23.4 | 0.61 | 0.49 | 7.09 | [203] |
| Two-step chemical method | Coral-like ZnO hexagonal clubs-like ZnO crystals | – | – | – | – | Drop coating: FTO | CR147 | $I_2$-based | 13.32 | 0.76 | 0.68 | 6.89 | [171] |
| Electrospraying | Nanosheets: boron | | – | 1.5–2 | 79 | Electrospraying: FTO | N3 | $I_2$-based | 19.3 | 0.64 | 0.54 | 6.75 | [134] |
| Heating ZnO: C powder | Tetrapods, NWs NRs, Nanobelts | – | – | – | – | Coated: ITO | Rose bengal | $I_2$-based | 17.52 | 0.71 | 0.56 | 6.74 | [245] |
| – | Commercial | 20 | – | 7 | 24.1 | Screen-printing: FTO | N719 | $I_2$-based in MPN | 18.11 | 0.62 | 0.58 | 6.58 | [153] |
| Solid-state synthesis | Nanostructures | – | – | 15.3 | 19.02 | Doctor blade: FTO | N719 | PEO polymer gel | 13.14 | 0.69 | 0.71 | 6.46 | [140] |
| CBD | Nanosheets | – | – | 12 | 52.4 | CBD: FTO | D149 | $I_2$-based | 18.01 | 0.52 | 0.63 | 6.06 | [173] |
| Solution-based | NAs, cluster | 30–700 | – | – | – | Solution-based: FTO | N719 | $I_2$-based | 12.05 | 0.75 | 0.66 | 6.01 | [246] |
| Solution-based/Microwave | Nanoflowers NPs | – | – | 8.5 | 27, 74 | Doctor blade: FTO | N719 | $I_2$-based | 13.5 | 0.68 | 0.64 | 5.96 | [238] |
| Sonochemical | Hierarchical structures | – | – | 20.1 | 26.6 | Doctor blade: FTO | N719 | Gel (PEO) | 11.99 | 0.71 | 0.69 | 5.88 | [135] |
| Solvothermal | Graphene/ZnO HSN | – | – | 9 | – | Doctor blade: FTO | N719 | $I_2$-based | 17.11 | 0.67 | 0.42 | 5.86 | [247] |

| Synthesis method | Morphology | Morphological parameters | | | | Deposition technique: substrate | Dye | Electrolyte | Cell parameters | | | | References |
|---|---|---|---|---|---|---|---|---|---|---|---|---|---|
| | | *D* (nm) | *L* (μm) | *t* (μm) | BET ($m^2 g^{-1}$) | | | | $J_{SC}$ (mA $cm^{-2}$) | $V_{OC}$ (V) | FF | $\eta$ (%) | |
| Solution-based | NWs<br>NPs | 40<br>(NWs) | – | 5–7<br>8–10 | 19.3<br>26.9 | Solution-based: FTO | SK1 | Co-based | 12.04 | 0.72 | 0.64 | 5.7 | [149] |
| Microwave-assisted | 4 Different flower-like | – | – | 17–23 | 22.24 | Doctor blade: FTO | N719 | $I_2$-based | 14.33 | 0.58 | 0.68 | 5.64 | [151] |
| – | Commercial | 20 | – | 14–35 | – | Screen-Printing: FTO | N719 | $I_2$-based | 11.95 | 0.68 | 0.69 | 5.61 | [211] |
| Template assisted-hydrothermal | Hollow microsphere | 1 μm | – | 12 | – | Doctor blade: FTO | N719 | $I_2$-based | 14.2 | 0.63 | 0.63 | 5.6 | [248] |
| Hybrid electrodeposition | ZnO/Eosin-Y Film | – | – | – | – | Electrodeposition: FTO ITO/PET | D149 | $I_2$-based (EC: AN) | 12.23 | 0.69 | 0.65 | 5.6 | [175] |
| Solution-based | Commercial NPs<br>Active layer of Microcubes/NPs | – | – | BL: 0.4 – 2AL: 15.9 | – | Spray pyrolysis: FTO<br>Casting: FTO + BL | N719 | $I_2$-based | 15.25 | 0.63 | 0.58 | 5.6 | [242] |
| Solution-based | Panel-like | – | – | 28.7 | 34.93 | Doctor blade: FTO | N719 | Gel (PEO) | 11.09 | 0.69 | 0.72 | 5.59 | [152] |
| Solution-based | NPs | 5–10 | – | 2–10 | – | Spin coating: ITO | D102 | – | 17.43 | 0.63 | 0.48 | 5.44 | [122] |
| CBD | Nanosheets | – | – | 25 | 52.4 | CBD: Ti foil | D149 | $I_2$-based | 18.9 | 0.54 | 0.53 | 5.41 | [145] |
| Solution-based | ZnO films scattering ZnO | ~200–500 | – | 18, 21, 27, 32 | – | Screen-printing: FTO | D149 D205 + CDCA | $I_2$-based | 12.17 | 0.65 | 0.67 | 5.34 | [249] |
| – | NWs-caterpillar | – | – | – | – | Spin coating: FTO | – | – | 15.20 | 0.69 | 0.50 | 5.20 | [167] |
| Hydrothermal (autoclave) | Microspheres (nanosheets) | 4–6 μm | – | 27 | 18.26 | Doctor blade: FTO | N719 | $I_2$-based | 14.73 | 0.57 | 0.61 | 5.16 | [143] |
| CBD | Nanocactus/Nanosheets mix on NWs | 60–120<br>(NWs) | 2.8<br>(NWs) | 9 | – | CBD: ITO | D149 | $I_2$-based | 11.22 | 0.71 | 0.64 | 5.14 | [182] |

(*Continued*)

**Table 6.1** (Continued)

| Synthesis method | Morphology | Morphological parameters | | | | Deposition technique: substrate | Dye | Electrolyte | Cell parameters | | | | References |
|---|---|---|---|---|---|---|---|---|---|---|---|---|---|
| | | *D* (nm) | *L* (μm) | *t* (μm) | BET ($m^2\ g^{-1}$) | | | | $J_{SC}$ (mA $cm^{-2}$) | $V_{OC}$ (V) | FF | $\eta$ (%) | |
| Electrodeposition | BL (200 nm) + Nanoporous film | – | – | 8 | – | Electrodeposition: FTO | N3 | $I_2$-based (commercial) | 6.98 | 0.60 | 0.64 | 5.08 (53 mW $cm^{-2}$) | [174] |
| – | Commercial NPs Nanosphere: PMMA | 20 | – | – | – | Doctor blade: FTO | N3/CYC-B1 | $I_2$-based (MPN) | 13.76 | 0.56 | 0.63 | 4.85 | [206] |

| Synthesis method | Morphology | Morphological parameters | | | | Deposition technique: substrate | Dye | Electrolyte | Cell parameters | | | | References |
|---|---|---|---|---|---|---|---|---|---|---|---|---|---|
| | | *D* (nm) | *L* (μm) | *t* (μm) | BET ($m^2\ g^{-1}$) | | | | $J_{SC}$ (mA $cm^{-2}$) | $V_{OC}$ (V) | FF | $\eta$ (%) | |
| Hydrothermal | Hollow microsphere | 15–20 | – | 15 | – | Spread: FTO | N719 | $I_2$-based (MPN) | 11.8 | 0.62 | 0.58 | 4.3 | [250] |
| Electrodeposition | Porous film | – | – | – | – | Electrodeposition: FTO | D149, DN91 DN285, DN216 | $I_2$-based | 10.38 | 0.60 | 0.68 | 4.29 | [221] |
| Electrodeposition | Nanosheets/NPs | – | – | 12 | – | Electrodeposition: FTO | D149 | $I_2$-based | 11.40 | 0.55 | 0.65 | 4.12 | [251] |
| Solution-based | ZnO:Mg banyan-root structure | – | – | 4 | – | Solution-based: FTO | N719 | $I_2$-based | 9.98 | 0.71 | 0.58 | 4.11 | [170] |
| Electrodeposition | Hierarchical | | 5 | 5 | | Electrodeposition: FTO | D149 | $I_2$-based | 12.3 | 0.57 | 0.58 | 4.08 | [252] |
| Solution-based | NC: NR | 70–200 | 4.5 | 7 | 21,51,65 | Solution-based: FTO | N3 | – | 12.6 | 0.62 | 0.51 | 4.0 | [146] |
| Forced hydrolysis | NPs | 15–25 | – | – | 54 | Doctor blade: FTO + CL | N719 | $I_2$-based | 11.8 | 0.65 | 0.52 | 4.0 | [31] |
| Solution-based | NPs | Av.27.7 | – | – | – | Solution-based: FTO | N719 | $I_2$-based | 16.84 | 0.55 | 0.43 | 3.92 | [118] |
| | Microsphere | 700 | – | 5.4 | 18 | | N719 | $I_2$-based | 11.35 | 0.60 | 0.54 | 3.91 | [139] |

| | | | | | | | | | | | | | |
|---|---|---|---|---|---|---|---|---|---|---|---|---|---|
| Aqueous chemical synthesis | | | | | | Drop coating: FTO, ITO/PET | | | | | | | |
| Electrodeposition | NRs | 198–306 | 287–545 | – | – | Electrodeposition: FTO | N719 | $I_2$-based | 10.40 | 0.64 | 0.56 | 3.75 | [183] |
| Solution-based | Nanostructure | – | – | 8 | – | Doctor blade: FTO | N719 | $I_2$-based | 8.04 | 0.68 | 0.67 | 3.68 | [253] |
| Solution-based | Nanobullets, nanoflakes | – | – | 10 | – | Doctor blade: FTO | N719 | $I_2$-based | 11.6 | 0.62 | 0.50 | 3.64 | [254] |
| – | Commercial NPs | – | – | – | – | Doctor blade: FTO, ITO/PEN | D149 | $I_2$-based (MPN) | 7.58 | 0.68 | 0.68 | 3.54 | [240] |
| Chemical bath | Prism array ZnO:F | 100–1500 | 5 | 5 | – | Chemical bath: FTO | N719 | $I_2$-based | 10.75 | 0.53 | 0.54 | 3.43 | [255] |
| – | Commercial NPs | 20 | – | 28 | – | Screen-printing: FTO | N719, W3, W4 | $I_2$-based | 6.45 | 0.68 | 0.77 | 3.38 | [222] |
| Hydrothermal | Hexagonal clubs | 100–300 | 250–600 | 20 | – | Drop coating: FTO | N719 | $I_2$-based in MPN | 10.80 | 0.52 | 0.59 | 3.36 | [168] |
| CBD | NWs, nanocactus, nanodentrite | – | – | 3.3 | | CBD: FTO | D149 | $I_2$-based | 7.20 | 0.66 | 0.70 | 3.32 | [256] |

| Synthesis method | Morphology | Morphological parameters | | | | Deposition technique: substrate | Dye | Electrolyte | Cell parameters | | | | References |
|---|---|---|---|---|---|---|---|---|---|---|---|---|---|
| | | *D* (nm) | *L* (μm) | *t* (μm) | BET ($m^2\ g^{-1}$) | | | | $J_{SC}$ (mA $cm^{-2}$) | $V_{OC}$ (V) | FF | $\eta$ (%) | |
| Solution-based | RP | 200–300 | – | RP: 100 | 10.8 | FTO | N719 | $I_2$-based | 8.91 | 0.72 | 0.51 | 3.3 | [163] |
| Solution-based | Nanodisks contains NPS commercial ZnO | – | – | – | 24.75 34.35 | Screen-printing: FTO posttreatment with $TiCl_4$ | N719 | $I_2$-based (Dyesol) | 5.83 | 0.798 | 0.70 | 3.27 | [257] |
| Metal vapor transport-oxidation | Nanotetrapods | 40 (arm) | 0.5–0.8 | 31.2 | 18.5 | Metal vapor transport-oxidation: FTO | N719 | $I_2$-based | 9.71 | 0.61 | 0.55 | 3.27 | [169] |
| – | Commercial NPs | 20 | – | 20 | – | Electrophoretic: FTO ITO/PEN | D149 + CDCA | $I_2$-based | 8.16 | 0.57 | 0.69 | 3.13 | [186] |
| Electrodeposition | Hierarchical NRs-NShs | – | – | 7 | – | Electrodeposition: ITO | N719 | $I_2$-based | 10.85 | 0.74 | 0.38 | 3.12 | [164] |
| Hydrothermal | Nanosheets | – | – | 20 | – | Hydrothermal: Ti | N719 | $I_2$-based | 6.77 | 0.68 | 0.64 | 2.97 | [258] |
| Solution-based | ZnO Sphere | 100 | – | 2–10 | | Drop coating: FTO | N3 | $I_2$-based | 9.45 | 0.70 | 0.43 | 2.89 | [177] |
| Solution-based | ZnO:ZnS NWs | – | 5.3 | – | – | Solution-based: FTO | N719 | $I_2$-based | 11.66 | 0.53 | 0.44 | 2.72 | [259] |

(*Continued*)

**Table 6.1** (Continued)

| Synthesis method | Morphology | Morphological parameters | | | | Deposition technique: substrate | Dye | Electrolyte | Cell parameters | | | | References |
|---|---|---|---|---|---|---|---|---|---|---|---|---|---|
| | | *D* (nm) | *L* (μm) | *t* (μm) | BET ($m^2\ g^{-1}$) | | | | $J_{SC}$ (mA $cm^{-2}$) | $V_{OC}$ (V) | FF | $\eta$ (%) | |
| Commercial | Nanopowder | 20, 50 | – | 8 | – | Doctor blade: FTO | JG1007, D358 | ILE, OLE | 8.72 | 0.67 | 0.45 | 2.70 | [260] |
| Solvothermal | NPs with polyoxometalates | 60 | – | – | | Screen-printing: FTO | N719 | $I_2$-based | 8.23 | 0.54 | 0.60 | 2.70 | [261] |
| Spray pyrolysis | Commercial NPs | – | – | 800 (nm) | – | Spray pyrolysis: FTO Buffer and active layers | B18, CPTD-R BTD-R | $I_2$-based | 8.88 | 0.54 | 0.56 | 2.68 | [239] |
| Solution-based | Nanodisks | 150 | – | – | – | Solution-based: FTO | N719 | $I_2$-based | 5.99 | 0.66 | 0.66 | 2.63 | [262] |
| Hydrothermal | Hierarchical NWs | 30–50 | 13 | 13 | – | Hydrothermal: FTO | N719 | $I_2$-based | 8.78 | 0.68 | 0.53 | 2.63 | [111] |
| – | Commercial NPs | – | – | – | – | EPD: ITO/PET | N719 | $I_2$-based | 7.88 | 0.57 | 0.58 | 2.63 | [189] |
| Solution-based | NRs | 103–291 | – | 7.4 | – | Spin coating: FTO/$SnO_2$ | N719 | $I_2$-based | 7.35 | 0.66 | 0.54 | 2.62 | [263] |
| Capping agents-assisted hydrothermal | Sheet-sphere | 4 μm | – | – | 13.1 | Doctor blade: F TO | N719 | $I_2$-based | 12.3 | 0.55 | 0.48 | 2.6 | [114] |
| Solution-based | NPs | – | – | 10.5, 17.5 | – | Doctor blade: FTO | SD4, JM1, JM2 | Co-based $I_2$-basedd | 6.91 | 0.53 | 0.70 | 2.55 | [219] |

| Synthesis method | Morphology | Morphological parameters | | | | Deposition technique: substrate | Dye | Electrolyte | Cell parameters | | | | References |
|---|---|---|---|---|---|---|---|---|---|---|---|---|---|
| | | *D* (nm) | *L* (μm) | *t* (μm) | BET ($m^2\ g^{-1}$) | | | | $J_{SC}$ (mA $cm^{-2}$) | $V_{OC}$ (V) | FF | $\eta$ (%) | |
| – | Commercial ZnO | 20–200 | – | – | 16.7 | Doctor blade: FTO | N719 | $I_2$-based | 6.2 | 0.66 | 0.62 | 2.54 | [264] |
| Solution-based | Nanospikes on Nanosheets | 80–100 | 150–200 (nm) | – | – | Autoclave: FTO | N719 | $I_2$-based | 6.07 | 0.68 | 0.60 | 2.51 | [161] |
| Forced hydrolysis | NRs | 24–26 | 209–289 | – | – | Hydrolysis: ITO | K27, K28, K13 | $I_2$-based | 7.19 | 0.55 | 0.63 | 2.51 | [205] |
| Hydrothermal | Hexagonal disk-like | 210 (μm) | – | 20 | – | Blade method: FTO | N719 | $I_2$-based | 6.92 | 0.69 | 0.52 | 2.49 | [165] |
| | Rod-cluster | – | – | – | – | Coating: FTO | N719, | $I_2$-based | 7.29 | 0.57 | 0.58 | 2.42 | [116] |

| Synthesis method | Morphology | Morphological parameters | | | | Deposition technique: substrate | Dye | Electrolyte | Cell parameters | | | | References |
|---|---|---|---|---|---|---|---|---|---|---|---|---|---|
| | | $D$ (nm) | $L$ (μm) | $t$ (μm) | BET ($m^2\ g^{-1}$) | | | | $J_{SC}$ ($mA\ cm^{-2}$) | $V_{OC}$ (V) | FF | $\eta$ (%) | |
| Solution-based | | | | | | | | | | | | | |
| Commercial | ZnO powder with $Al_2O_3$ and $SiO_2$ | – | – | – | – | Screen-printing: FTO | N719 | - | 9.22 | 0.53 | 0.48 | 2.4 | [265] |
| ALD | – | – | – | – | – | ALD: FTO | N719 | $I_2$-based (MPN) | 8.32 | 0.60 | 0.48 | 2.4 | [266] |
| Solution-based | NRs | 40 | 1 | – | – | Solution-based: FTO | Z907 | $I_2$-based | 6.4 | 0.72 | 0.49 | 2.3 | [204] |
| – | NRs, NPs, NRs: NPs | 100 | – | 15 | | Doctor blade: Ti foil | N719 | $I_2$-based | 7 | 0.60 | 0.52 | 2.19 | [267] |
| CBD | Cauliflower-like | – | – | 8 | – | CBD: FTO | N719 | $I_2$-based (PC) | 6.08 | 0.66 | 0.55 | 2.18 | [159] |
| – | Nanostructures | – | – | 8–10 | – | Spread on: FTO | N719, N3 | $I_2$-based (MPN) | - | - | - | 2.1 | [207] |
| Hydrothermal | NWs | – | – | – | – | Hydrothermal: ITO | N719 | $I_2$-based | 8.1 | 0.55 | 0.44 | 2 | [268] |
| Hydrothermal | Nanorods | 100 | 0.85 | 0.85 | – | Hydrothermal: FTO | N719 | $I_2$-based | 8.7 | 0.52 | 0.44 | 1.93 | [269] |
| Hydrothermal | Nanoflowers | 200 | – | 11 | – | | N719 | $I_2$-based | 5.5 | 0.65 | 0.53 | 1.9 | [270] |
| Solution-based | NPs/Al-boron dopes (AZB) | – | – | 10 | – | Doctor blade: AZB | N719, D149, N3 | Gel-electro-lyte (PEO) | 5.1 | 0.68 | 0.53 | 1.84 | [235] |
| Wet chemical | Jack-likes NRs | 120–140 | 3–4 | 3–4 | – | Wet chemical: ITO | N719 | $I_2$-based | 5.52 | 0.59 | 0.54 | 1.82 | [110] |
| Solvothermal | Nanorods | 150–220 | 12 | 8.9 | – | CVD: FTO | N719, D149 | $I_2$-based | 15.7 | 0.55 | 0.21 | 1.82 | [271] |
| Solution-based | Granular | – | – | – | – | Doctor blade: FTO | N719 | $I_2$-based (MPN) | 4.6 | 0.73 | 0.54 | 1.82 | [272] |
| Solution-based/ED | $TiO_2$ + ZnO/ ZnO NRs | 65–101 | 200–245 | 2.69 5.09 | – | Spin coating: FTO/ $TiO_2$ + ZnO films | N719 | $I_2$-based | 7.92 | 0.61 | 0.37 | 1.81 | [180] |
| Commercial colloid | ZnO powder | 20 | – | 10–15 | – | Spread on: FTO | N719 | $I_2$-based (PC) | 6 | 0.70 | 0.42 | 1.8 | [216] |

(*Continued*)

**Table 6.1** (Continued)

| Synthesis method | Morphology | Morphological parameters | | | | Deposition technique: substrate | Dye | Electrolyte | Cell parameters | | | | References |
|---|---|---|---|---|---|---|---|---|---|---|---|---|---|
| | | *D* (nm) | *L* (μm) | *t* (μm) | BET ($m^2 g^{-1}$) | | | | $J_{SC}$ (mA $cm^{-2}$) | $V_{OC}$ (V) | FF | $\eta$ (%) | |
| Precipitation | Nanorods | – | – | – | – | Doctor blade: FTO | N719 | $I_2$-based | 4.76 | 0.69 | 0.52 | 1.73 | [273] |
| Solution-based | NWs | 100–120 | 14 | 14 | – | Solution-based: FTO | N719 | Idolyte (Solaronix) | 6.79 | 0.54 | 0.50 | 1.7 | [115] |
| Magnetron Sputtering | Nanofibrous | – | – | 5 | – | Magnetron sputtering: FTO | D149 | $I_2$-based | 8.45 | 0.49 | 0.40 | 1.7 | [274] |
| Electrodeposition | NRs | – | 4 | 4 | – | Electrodeposition: FTO | D149 | $I_2$-based | 5.97 | 0.56 | 0.48 | 1.66 | [275] |
| Anodization on Zn foil/ED | NWs/ Hierarchical | – | – | – | – | Coating: FTO | N719, | $I_2$-based (MAN) | 5.10 | 0.60 | 0.54 | 1.63 | [234] |
| ALD/Template | Nanotubes | – | – | Tens of μm | | ALD: AAO | N719 | $I_2$-based (MPN) | 3.3 | 0.74 | 0.64 | 1.6 | [276] |
| Thermal evaporation | NRs: NPs | Tens of nm | 2 | 30 | | Thermal-evaporation: FTO | N719 | $I_2$-based | 5.12 | 0.46 | 0.45 | 1.56 | [277] |
| Solvothermal | Branched NWs | 150–250 | 7–8 | 8 | – | Solution-based: FTO | N719 | $I_2$-based | 4.27 | 0.67 | 0.52 | 1.51 | [112] |
| Sol–gel | NWs | 5–50 | 3 | 3 | – | Spin coating: ITO | N3 | $I_2$-based | 5.6 | 0.62 | 0.43 | 1.49 | [278] |
| Solution-based/ Hydrothermal | Different nanostructures nanosheets/ rods | – | – | 18 | 21.96 | Doctor blade: FTO | N719 | $I_2$-based (Dyesol) | 6.48 | 0.73 | 0.31 | 1.47 | [150] |
| Solution-based | Nanotubes | 200–300 | – | – | – | Solution-based: ITO | N719 | $I_2$-based | 17 | 0.23 | 0.36 | 1.44 | [279] |
| Solution-based | NRs | 600 | – | 12 | 42 | Doctor blade: FTO | N719 | $I_2$-based | 6.1 | 0.60 | 0.37 | 1.38 | [148] |
| Hydrothermal | Nanoflowers | 500–1000 | 5–6 | 5–6 | – | Doctor blade: FTO | N719 | - | 5.23 | 0.55 | 0.48 | 1.37 | [158] |

| | | | | | | | | | | | | | |
|---|---|---|---|---|---|---|---|---|---|---|---|---|---|
| Magnetron sputtering | – | – | – | – | – | Magnetron sputtering: ITO | N719 Rose Bengal | $I_2$-based | 4.74 | 0.74 | 0.39 | 1.37 | [280] |
| Sol–gel | NWs | | 40 | 40 | – | Dip coating: FTO | N719 | $I_2$-based | 4.26 | 0.69 | 0.42 | 1.31 | [178] |
| MOCVD | NPs: NWs | 20 | 0.1 | – | – | MOCVD: FTO | N719 | $I_2$-based | 3.5 | 0.84 | 0.44 | 1.3 | [281] |
| CBD | Nanobeads | 3–5 | – | 2 | – | CBD: FTO | Rhodamine B | $I_2$-based | 4.61 | 0.45 | 0.61 | 1.26 | [181] |

| Synthesis method | Morphology | Morphological parameters | | | | Deposition technique: substrate | Dye | Electrolyte | Cell parameters | | | | References |
|---|---|---|---|---|---|---|---|---|---|---|---|---|---|
| | | *D* (nm) | *L* (μm) | *t* (μm) | BET ($m^2\ g^{-1}$) | | | | $J_{SC}$ (mA $cm^{-2}$) | $V_{OC}$ (V) | FF | $\eta$ (%) | |
| Solution-based | NWs | 50 ± 30 | 10 | 10 | – | Solution-based: FTO | C220 | $I_2$-based | 5.49 | 0.52 | 0.43 | 1.25 | [218] |
| Electrodeposition | Nanostructured films | – | – | 3/7–9 | – | Electrodeposition: FTO | KFH-3, KFH-2 | $I_2$-based | 3.34 | 0.49 | 0.76 | 1.23 | [212] |
| Solution-based | Nanorods | 50–130 | 3–5 | | | Solution-based: ITO | N719 | $I_2$-based | 4.2 | 0.62 | 0.46 | 1.2 | [282] |
| Solution-based | Nanotubes | – | – | 2 | – | Solution-based: ITO | N3 | $I_2$-based | 4.70 | 0.38 | 0.67 | 1.2 | [155] |
| Chemical solution method | Star-like | – | – | – | – | Coating: FTO | N719 | $I_2$-based (MPN) | 4.70 | 0.59 | 0.50 | 1.16 | [283] |
| Solution-based | NRs, nanosheets | 125 | 11 | 11 | 15.73 | Drop and spin coating: ITO | N719 | $I_2$-based | 4.80 | 0.53 | 0.43 | 1.13 | [284] |
| Solution-based: Hydrothermal | Nanostructures | – | – | 7 | 87.8 203.8 | Drop cast: ITO | N719 | $I_2$-based | 3.83 | 0.74 | 0.39 | 1.12 | [142] |
| Sol–gel | Hexagonal shape | 14–16 | – | – | | Doctor blade: ITO | Eosin-Y | $I_2$-based | 2.36 | 0.54 | 0.53 | 1.11 | [285] |
| Solution-based | Nanopyramids | 17.9 | – | 8.9 | 31.26 | Blade: FTO | N719 | $I_2$-based | 4.98 | 0.64 | 0.33 | 1.07 | [144] |
| Solution-based | Nanospheres | 400–600 | – | – | – | Drop cast: FTO | N719 | $I_2$-based | 5.31 | 0.64 | 0.29 | 1.03 | [129] |
| Microwave | Nanoflowers, nanoplates | – | – | – | – | Doctor blade: FTO | Eosin Y, N719 | $I_2$-based (PC) | 4.36 | 0.63 | 0.37 | 1.03 | [233] |
| ED | Porous film | – | – | 3.4 | – | Electrodeposition: ITO | N719 | Idolyte (solaronix) | 4.63 | 0.58 | 0.38 | 1.02 | [286] |
| Hydrothermal | Nanorods | 80–120 | 1.5 | 1.5 | – | Hydrothermal: FTO | C206 | $I_2$-based | 3.9 | 0.61 | 0.44 | 1.0 | [214] |

*NAs*, nanoaggregates; *NPs*, nanoparticles; *AN*, acetonitrile; *MPN*, 3-methoxypropionitrile; *CFI*, continuous flow injection; *NWs*, nanowires; *NC*, nanocrystallite; *NRs*, nanorodes; *PEO*, polyethylene oxide; *HSN*, hierarchically structured nanoparticle; *EC*, ethylene carbonate; *BL*, blocking layer; *AL*, active layer; *PMMA*, poly(methyl methacrylate); *RP*, rectangular prism; *NSh*s, nanosheets; *ILE*, ionic liquid electrolyte; *OLE*, organic liquid electrolyte; *ALD*, atomic layer deposition; *PC*, propylene carbonate; *AZB*, aluminum-boron co-doped ZnO; *CVD*, chemical vapor deposition; *AAO*, anodic aluminum oxide; *MOCVD*, metalorganic chemical vapor deposition.

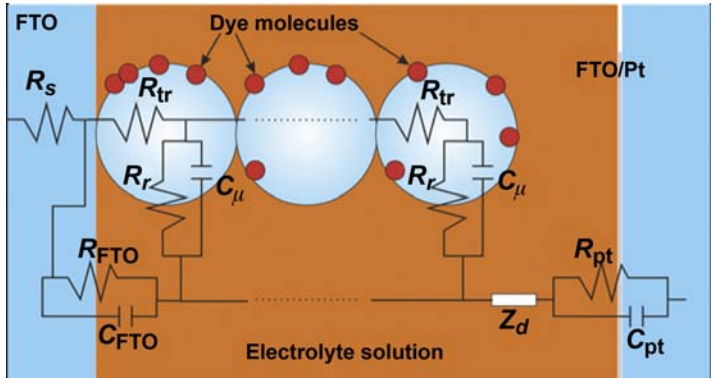


**Figure 6.5** The equivalent circuit generally used for the interpretation of EIS measurements on DSSCs: $R_s$ is the FTO series resistance; $R_{FTO}$ and $C_{FTO}$ correspond to the substrate not covered by the $TiO_2$ nanoparticles; $R_{tr}$ represents the resistance for electron transport; $R_r$ is the charge transfer or recombination resistance (in some reports it is shown as $R_{rec}$ or $R_{ct}$ as well); $C\mu$ is the chemical capacitance; $Z_d$ is the Warburg impedance corresponding to diffusion of the redox species in the electrolytic solution; $R_{pt}$ stands for the charge transfer resistance; and $C_{pt}$ for the Helmholtz capacitance at the counter electrode/electrolyte interface.

kinetics of electrons to the acceptor in the electrolyte solution, and can give information on whether the recombination process is faster or slower for certain materials, surface facets or redox electrolytes [288,292,298].

In order to accurately compare between different systems it is important to change one parameter and then compare the systems under the same experimental conditions. For example, one can compare cells with different ZnO morphology, but using the same dye, electrolyte and substrate, or analyze cells with the same ZnO morphology using a different dye and electrolyte, in order to understand the influence of each element on cell performance. An example on the effect of morphology on charge transport is the work of Vega-Poot et al. for ZnO NPs of different diameters synthesized from a wet-chemistry technique and vertically aligned nanocolumnar morphology obtained from a plasma-enhanced CVD (PECVD) technique. Their results showed very similar $R_{ct}$ for different particle sizes or crystalline texture ZnO cells with the same dye and electrolyte. However, $C_\mu$ slightly increased with the thickness of the deposited films. The electron lifetime obtained from EIS confirmed the similarity of the recombination rate as well as similar values of $V_{OC}$ yielded by both the nanoparticulate material and the PECVD films [301].

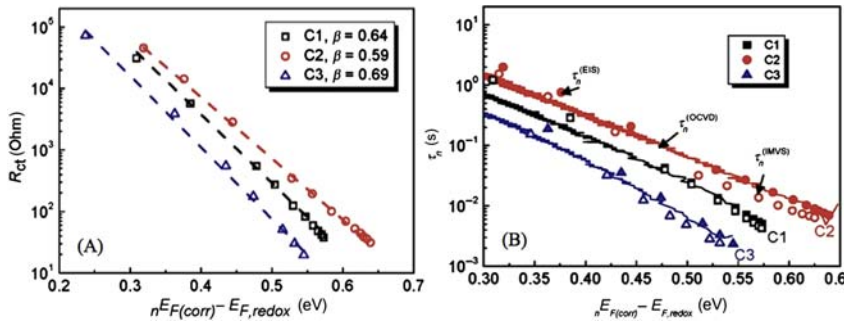


**Figure 6.6** (A) Charge transfer resistance obtained by fitting EIS spectra at various open circuit voltages, (B) Electron lifetime for the three-cell configurations extracted from open circuit photovoltage decay (OCVD) (*lines*), EIS (*solid symbols*), and IMVS (*open symbols*) [230].

Post-treatment on ZnO nanostructures can also change the transport and recombination behaviors of systems with the same dye, electrolyte and ZnO morphology as Bang et al. showed a higher charge transport resistance and, thus, longer electron lifetime and $V_{OC}$ for ZnO nanodisks treated by $TiCl_4$ compared to bare ZnO nanodisks. They mentioned that this improvement may be due to the decrease in surface traps by passivation as a result of the $TiCl_4$ treatment [257]. Anta et al. compared the systems consisting of (C1) ZnO/N719/organic solvent electrolyte, (C2) ZnO/D149/organic solvent electrolyte and (C3) ZnO/N719/ionic liquid electrolyte, which is shown in Fig. 6.6A and B. The best performance cell with the highest current density was C2 using indoline dye as a suitable dye for ZnO cells [230]. C3 has the lowest charge transfer resistance and open circuit voltage (0.52 V) and C1 exhibits slightly faster recombination than C2. The difference in open circuit voltage between C1 (0.63 V) and C2 (0.61 V) suggests that the role of the dye in the recombination of electrons with the oxidized species might be important. Fig. 6.6B shows good agreement between the electron lifetime extracted from three different techniques. Configuration C3 yields the shortest lifetime at the same position of the Fermi level. This explains the much smaller open circuit photovoltage found for this cell.

Ho et al. demonstrated the effect of types of sensitizers on the performance of ZnO-based DSSCs, and calculated the electron diffusion coefficient and resistance related to the charge transfer process at the ZnO/dye/electrolyte interface. The EIS spectra of this study are shown in Fig. 6.7 [206]. The diffusion coefficient for CYC-B1 was higher

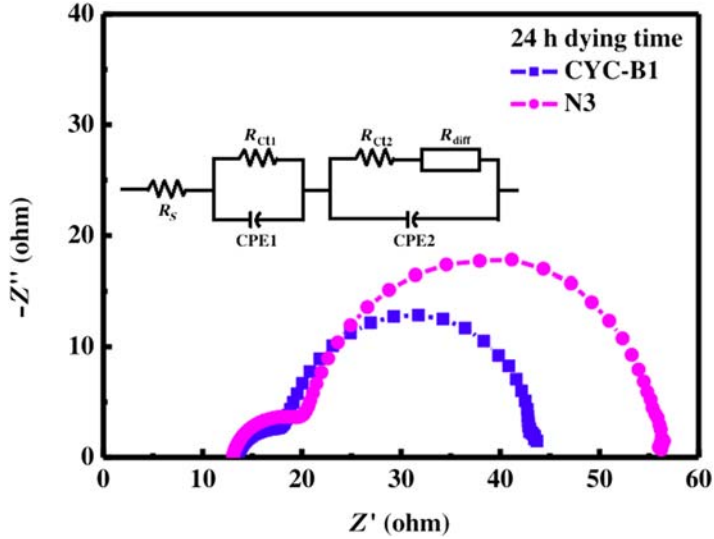


**Figure 6.7** Electrochemical impedance spectra of the cells measured at 100 mW $cm^{-2}$ light intensity under the open-circuit voltage. The inset shows the equivalent circuit [206].

($2.24 \times 10^{-3}$ $cm^2$ $s^{-1}$) compared to that of cells with the N3 dye ($1.64 \times 10^{-3}$ $cm^2$ $s^{-1}$), indicating better electron transport in ZnO films for cells fabricated with the CYC-B1 dye.

Table 6.2 summarizes the results of EIS measurements on ZnO-based DSSCs, and provides a comparison of different cell architectures.

### 6.5.2 Intensity-modulated photovoltage spectroscopy

Like EIS, IMVS is performed at the open circuit potential and, in general, a single semicircular arc is observed, and the electron lifetime is obtained from the frequency at the apex: $\tau_{IMVS} = 1/\omega_{min}$ where $\omega_{min}$ is the minimum angular frequency [288,293,316]. Yang et al. fabricated a cell containing ZnO nanosheets as a bottom layer and a layer of ZnO nanocrystalline aggregates as a scattering layer, achieving 7.95% of PCE, which was almost twice compared with a DSSC composed of only ZnO nanosheets, with an efficiency of 4.38%. The electron lifetime was calculated from the IMVS spectra and it was 18 ms for the mixture of ZnO nanosheets and aggregates, which was longer than for only ZnO nanosheets (12 ms), and resulted in much better performance of the mixed architecture [172]. Another example is the work by Vega-Poot et al. where they compared the transport behavior of ZnO nanoparticles with

**Table 6.2** Comparison parameters by electrochemical impedance spectroscopy (EIS) measurement for ZnO-based dye-sensitized solar cells.

| Comparison parameter | References |
|---|---|
| Different film thickness for hybrid electrodeposited ZnO and ionic liquid electrolyte (PYR14TFSI) | [302] |
| Deposition technique (doctor blade vs electrodeposition) | [303] |
| Different ZnO annealing time | [304] |
| Morphology comparison (wet-chemistry technique vs electrodeposition) | [301] |
| NPs of different diameters compared with commercial ZnO | [264] |
| Effect of type of dye (N719, W3, W4) | [222] |
| Morphology comparison (NPs vs nanodisks) and effect of post-treatment with $TiCl_4$ | [257] |
| Effect of synthesis pH | [137] |
| Morphology comparison (coral-like vs hexagonal clubs-like) | [171] |
| Morphology comparison (nanosheests vs NPs) on Ti foil, comparison of CE (glass vs flexible substrate) | [258] |
| Different indoline dyes (D149, DN91, DN216, DN285) | [221] |
| Morphology comparison (ZnO spheres vs ZnO cluster aggregation) | [246] |
| Morphology comparison (ZnO nanosheets vs ZnO nanoaggregates) | [172] |
| EIS study of ZnO nanotips | [305] |
| Effect of ZnO surface activation and pressing process on ITO/PEN substrate | [306] |
| Effect of annealing temperature | [118] |
| Effect of compression pressure on ZnO films on plastic substrate | [186] |
| Morphology comparison (NRs, NPs and combination of NRs and NPs) | [267] |
| Effect of NRs thickness for NRs: NPs mixture systems | [307] |
| Morphology comparison (ZnO nanorods vs nanorods: nanosheets) | [284,308] |
| Effect of thermal heating temperature and type of electrolyte (liquid vs gel) | [140] |
| Morphology comparison (ZnO NPs vs NRs) | [277] |
| Effect of synthetic parameters (precursor concentration) | [135] |
| Morphology comparison (ZnO NWs vs NPs) | [120] |
| Morphology comparison (ZnO nanosheets vs ZnO NPs and $TiO_2$ NPs/ZnO nanosheets) | [173] |
| Morphology comparison (commercial ZnO vs coral-like ZnO) | [309] |
| Morphology comparison (NPs, NWs and NPs: NWs) | [179] |
| EIS study of nanofibrous ZnO | [274] |

| Comparison parameter | References |
|---|---|
| Effect of changing the diameter of ZnO nanograss | [310] |
| ZnO:$TiO_2$ configuration: different ratio | [311] |
| Morphology comparison (ZnO film vs Nanosheets) | [312] |
| Comparison between ZnO NWs and NPs in $I_2$-based and Co-based electrolyte | [149] |
| Type of dye (N3, HMP-09, HMP-11) | [203] |
| Effect of dye loading time on nanosheets: NPs composite | [251] |
| Morphology comparison (NWs, brushed-like nanoforest, willow-like nanoforest) | [313] |
| Morphology comparison (microrod vs nanosheet) | [150] |
| Morphology comparison (mixed structure of different flower-like ZnO) | [151] |
| Morphology comparison (star-like ZnO with different diameter) | [283] |
| Morphology comparison (nanoflowers vs NPs) | [238] |
| Morphology comparison (tetrapod: short-arm vs long-arm) and effect of TBP concentration in electrolyte | [141] |
| Morphology comparison (tetrapod vs commercial ZnO) | [314] |
| Morphology comparison (porous nanosheets microflowers vs porous dispersed ZnO nanosheets) | [143] |
| Performance study of cauliflower-like ZnO | [159] |
| Effect of type of dye: comparison between CYC-B1 and N3 | [206] |
| Morphology comparison (nanoaggregates vs nanoclusters) | [246] |
| Changing time of post-treatment with PFDTES | [138] |
| Comparison of N719 and grapheme quantum dots | [315] |
| Configuration comparison of ZnO NPs and ZnO double layer device | [171] |
| Post-treatment: effect of changing the concentration | [168] |
| Morphology comparison (pH effect) | [137] |
| Electrolyte effect | [204] |
| Effect of dye loading time | [184,211] |
| Effect of type of dye (D358 vs JG1007), effect of electrolyte (ILE vs OLE) | [260] |
| Effect of type of organic dyes (B18, CPTD-R, BTD-R) | [239] |
| Effect of post-treatment | [257] |
| Morphology comparison (NWs vs branched-NWs) | [112] |
| Effect of tetrapod film thickness | [169] |
| Morphology comparison (NWs of different lengths) | [178] |
| Effect of sputter-deposition time of Pt on the counter electrode | [145] |
| Effect of doping (ZnO vs ZnO:I) | [133] |
| Morphology comparison (NWs vs NWs: NC) | [252] |
| Morphology comparison (NC vs monodisperes aggregates), bailayer and underlayer configuration | [146] |
| Morphology comparison (branch-free vs jack-like) | [110] |

*ITO/PEN*, ITO-coated polyethylene naphthalate; *TBP*, tert-butylpyridine; *PFDTES*, perfluorodecyltriethoxysilane.

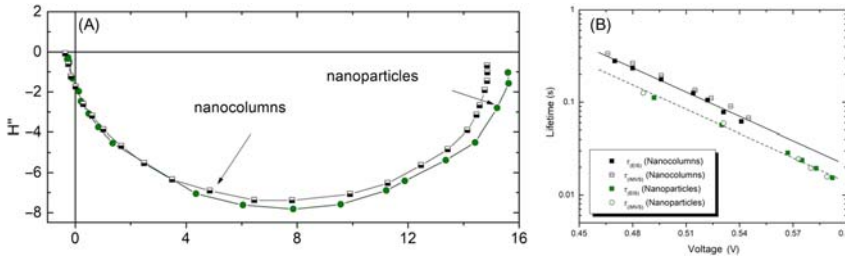


**Figure 6.8** (A) Typical IMVS curves for ZnO-based DSSCs studied in this work, (B) Electron lifetime versus $V_{OC}$ measured by EIS and IMVS [317]. *H"* represents the transfer function, dividing the modulated cell response (in this case, the open circuit voltage) by the modulated light intensity; the scale is in arbitrary units. *Adapted from J. Idígoras, L. Pellejà, E. Palomares, J.A. Anta, The redox pair chemical environment influence on the recombination loss in dye-sensitized solar cells, J. Phys. Chem. C 118 (8) (2014) 3878–3889 [316].*

ZnO nanocolumns [317]. They obtained the electron lifetime from EIS and IMVS, which exponentially decreases with increasing open circuit volatege, that is, light intensity. Both techniques provided similar values for the electron lifetime at the same voltage. However, the electron lifetime was significantly longer for the nanocolumn structure as compared to that of the NP structure, confirming the EIS results of recombination resistance, which was found to be larger for ZnO nanocolumns. Fig. 6.8A and B show the typical IMVS curve and the measured electron lifetime by EIS and IMVS techniques respectively for the studied ZnO structures.

### 6.5.3 Intensity-modulated photocurrent spectroscopy

IMPS is performed under short circuit conditions and is the most suitable method to characterize transport. The spectra generally consist of a single semicircular arc and the transport time constant can be determined from $\tau_{\text{IMPS}} = 1/\omega_{\text{min}}$ and the electron diffusion coefficient is calculated from $D_n(\text{cm}^2\ \text{s}^{-1}) = d^2/\gamma \times \tau_{\text{IMPS}}$ where $d$ is the semiconductor thickness and $\gamma$ is a constant [318,319].

An example of IMPS in ZnO-based DSSCs is the work of Luo et al. showing the transport parameters of ZnO nanosheets frameworks (NSFs) and ZnO NPs both on Ti foil substrate with an efficiency of 3.23% and 1.23 %, respectively. From IMPS spectra the electron transport time for NSFs is shorter than for NPs at the same light intensity, indicating slower electron transport for ZnO NPs on Ti foil than for the NSFs [258]. Another example is the IMPS measurements for synthesized ZnO NPs

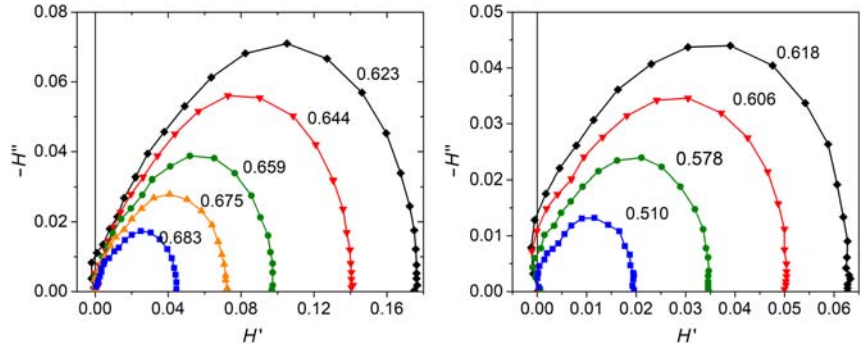


**Figure 6.9** Nyquist-type plots of the IMPS measurements. Left: Sample S1 (synthesized nanoparticulate ZnO). Right: ZnO films obtained from PECVD [301]. *H″* represents the transfer function, dividing the modulated cell response (in this case, the short circuit photocurrent) by the modulated light intensity; the scale is in arbitrary units. *Adapted from J. Halme, Linking optical and electrical small amplitude perturbation techniques for dynamic performance characterization of dye solar cells, Phys. Chem. Chem. Phys. 13 (27) (2011) 12435–12446 [300].*

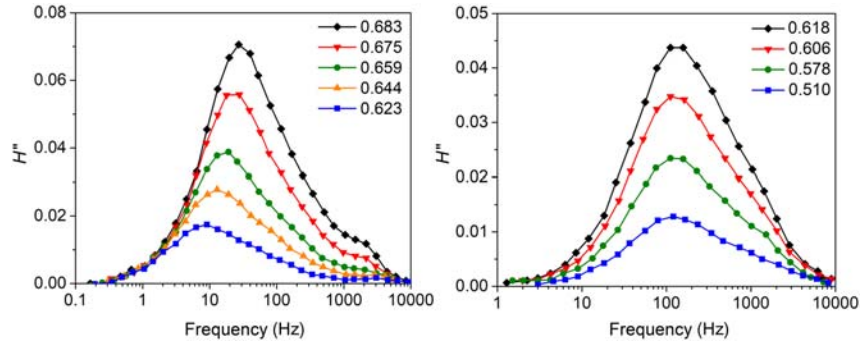


**Figure 6.10** Imaginary IMPS response versus frequency for nanoparticulate (left); and nanocolumnar (right) ZnO electrodes [301]. *Adapted from J. Halme, Linking optical and electrical small amplitude perturbation techniques for dynamic performance characterization of dye solar cells, Phys. Chem. Chem. Phys. 13 (27) (2011) 12435–12446 [300].*

and ZnO films obtained from plasma-enhanced chemical vapor deposition (PECVD) in the study of Vega-Poot et al. as is shown in Fig. 6.9 [301].

They mentioned that in spite of the different morphology, the recombination features are very similar for both nanoparticulate films and texturized PECVD films. In contrast to recombination, electron transport can be affected by both surface and bulk electronic states. Fig. 6.10 shows the imaginary part of the IMPS response versus the frequency.

They explained that in contrast with the results of the nanoparticulate ZnO electrodes, the maxima in the spectra obtained for the texturized PECVD samples are effectively independent of the bias illumination, and hence of the Fermi level, illustrating that electron transport is not anomalous in ZnO nanocolumns [301].

## 6.6 Performance improvement strategies and scale-up

In an efficient DSSC with a characteristic high surface area photoanode covered with a dye with moderate extinction, the separation of the injected electron-oxidized dye pair takes, at most, tens of femtoseconds, resulting in charge separation efficiencies approaching unity. Also in an efficient DSSC, the charge collection efficiency depends on the difference between charge transport and charge recombination rates. As charge transport through the nanostructured semiconductor oxide may be slow (100 μs scale), a redox pair such as iodide/triiodide of very slow electron accepting rate must be introduced to minimize the difference between charge transport and recombination rates. For this reason, up to now, the most efficient DSSCs include $TiO_2$ and iodide/triiodide because of its good electron collection efficiency. ZnO can be considered an alternative to $TiO_2$ related to its better electrical properties. However, the highest reported PCE for ZnO-based DSSCs is still lower than that of $TiO_2$-based DSSCs. There are several strategies to improve the performance of ZnO cells including morphology modification, post-treatment of ZnO nanostructures, new electrolyte solutions and new dyes that are compatible with ZnO, and using doped ZnO, core–shell or mixed structures. Improved performance of ZnO-based solar cells and modules may be achieved by optimization of structural parameters such as morphology, diameter, length, or aspect ratio of ZnO nanostructures and film porosity in order to enhance the surface area of the photoanode, which may result in a higher photocurrent. Also, the operational parameters, such as recombination resistance, electron lifetime, electron diffusion coefficient and length, must be studied and modified in order to find the best match for ZnO nanostructures/dye/electrolyte systems. In order to improve the photovoltage, a redox couple with smaller overpotential must be employed in the cell architecture. However, simply replacing one redox couple with another is not sufficient, since without changing other cell components, such as photoanode architecture and type of dye, one cannot expect a significant change in cell performance. To fabricate large-scale

devices it is first necessary to solve the operational problems of small cells and find the best semiconductor/dye/electrolyte system with a good overall performance; subsequently, it is essential to overcome technical issues associated with large-scale area devices such as cost-effectiveness and uniform deposition technique, homogeneous deposition of compact or blocking layer, dye loading process, electrolyte injection process, sealing of the entire device, and long-term stability due to leakage and volatilization of organic solvents. For the scale-up of ZnO-based DSSCs, electrodeposition may be considered an easy, fast and low-cost method suitable for large area glass and plastic substrate. In addition hybrid ED or co-deposition of ZnO and dye at the same time may even reduce the fabrication costs more. Minura and Yoshida reported the ED of ZnO and eosin Y at the same time for miniature cells (0.2 $cm^2$) on a plastic substrate achieving 4% of PCE. For a set of 28 interconnected cells to power a mobile phone, this efficiency decreased to 1.4% due to the high internal resistance [175]. Recently Wark et al. have reported a ZnO module with 40 $cm^2$ active area fabricated using the ED of ZnO/eosin Y hybrid thin films of a thickness of 9 μm, which achieved an efficiency of 2.58% under low light intensity [185].

### 6.6.1 Design optimization of ZnO-based dye-sensitized solar cells

One strategy to improve the performance of ZnO-based DSSCs is morphology modification. Cheng et al. fabricated two types of architecture with bare ZnO NWs and branched NWs with efficiency of 2.37% and 4.27% respectively. The cell performance was improved by changing the morphology resulting in the enlargement of the internal surface area within the photoelectrode without increasing interparticle hops [112]. Also, using mixed ZnO structures is one way to improve the performance of cells as reported by Xu et al.: using only ZnO nanosheets resulted in a 2.3% efficiency compared to 4.8% for the mixture of nanosheets and nanowires. The mixture architecture provides better light scattering behavior and thus more efficient light harvesting [113]. The use of core–shell structures is another strategy to increase cell performance. Liang et al. showed that, compared with the bare ZnO nanorod electrode, a ZnO/$TiO_2$ core–shell electrode exhibits higher photocurrent density and open-circuit voltage due to the better dye adsorption performance. The energy barrier formed at the interface between the core and shell offers a two-fold improvement of PV efficiency [214]. Another

example of core–shell architecture is using a ZnS shell on ZnO nanowires, which improved the cell performance as compared to that found for bare ZnO NWs [259]. DSSCs containing I-doped or F-doped ZnO nanostructures have shown significant enhancement of PV performance compared to ZnO cells without doping agent [133,255]. Looking for a new electrolyte or changing the electrolyte composition is a solution to overcome low performance of ZnO-based cells. Qiao et al. reported an increase in PCE of ZnO DSSCs based on BMII/$I_2$/TBP compared to that of LiI/$I_2$ due to reduction of the recombination rate and increase in electron lifetime [204]. In order to fabricate an efficient ZnO-based DSSCs with ruthenium acidic dyes, Nguyen et al. have optimized the number of carboxylic acid groups in the dye structure, since the presence of carboxyl protons in the Ru-complex dyes promote etching of the ZnO surface during dye loading, resulting in the formation of $Zn^{2+}$–dye complexes, and thereby less efficient electron injection [117]. Research on new dye structures that are compatible with ZnO is an important strategy to enhance cell performance. Ho et al. proposed BT-containing new dyes achieving more than 5% PCE with a ZnO photoanode [215]. Post-treatment of ZnO nanostructures also is a factor resulting in improvement in DSSCs. He and Xie fabricated sponge-like ZnO photoanodes with high porosity and optical density using low temperature and pressure air plasma reaching 8.03% of efficiency [244]. The last but not the least strategy to improve ZnO cell performance is the introduction of a blocking layer in cell architecture in order to reduce the recombination rate.

### 6.6.2 Aspects of scale-up

Since the PCE of $TiO_2$-based DSSCs is higher than for ZnO-based DSSCs, there are many reports on scale-up of $TiO_2$ large-scale, dye-sensitized mini-modules, and still there is a lack of information related to ZnO dye-sensitized mini-modules in literature. The first report on scale-up of the DSSC was in 1996 by Grätzel's group, in which they reported a solar mini-module with a total surface area of 21.06 $cm^2$ and an efficiency of 5.65% with respect to its active area [320]. Several research groups have tried to overcome the challenges of DSSC industrialization, which include the deposition of uniform semiconductor metal oxide films on a large substrate, electrolyte leakage and sealing, long-term stability, ohmic losses associated with the larger area substrates, and efficient module design [321,322]. There are various reports in literature on types of large

substrate, reproducibility, stability, semiconductor deposition methods, and configuration of dye-sensitized solar modules [323–330]. For large-scale applications, usually screen printing and roll-to-roll deposition techniques are the most suitable methods. However, as mentioned before, ED also can be considered to be a low-cost and fast method, applicable to scale-up especially for ZnO-based dye-sensitized solar cells [175,185]. Solid-state electrolytes are the best choice in order to overcome the liquid electrolyte leakage or evaporation at high temperature.

## 6.7 Conclusions and outlook

As mentioned before, the three main components of a DSSC are the semiconductor metal oxide, sensitizer, and electrolyte. The correct choice of each component is a key factor to enhance the PV performance of the solar cell. To obtain high current density in ZnO-based DSSCs, one way is to increase the ZnO porosity and surface area, which may be achieved by nanostructure modification and optimization, or the development of a new synthesis method and new morphologies. ZnO particle pretreatment is one way to modify the surface chemistry of the semiconductor and improve the quantity of adsorbed dye on a ZnO surface. High porosity ZnO adsorbs more dye molecules, resulting in more efficient light harvesting. Also the ZnO layer should be thick enough to adsorb more dye molecules. The dye structure must be compatible with ZnO to prevent the $Zn^{2+}$– dye complex aggregates in the presence of acidic dyes. The dye molecular structure, dye loading time and dye solution concentration are the parameters that can be optimized to ensure a good linkage between dye molecules and ZnO surface, sufficient dye adsorption and good electron injection from the dye into ZnO. The electrolyte has a strong influence on the long-term stability and light-to-electricity conversion efficiency of the devices. Thus, the correct choice of solvent, electrolyte additives and redox couple concentrations are critical for reaching long-term stability and less recombination especially for large-scale dye-sensitized devices. Besides the three main elements (ZnO semiconductor, dye and electrolyte), other factors, such as the blocking layer, scattering layer, and sealing quality, have strong influence on cell performance and stability. Also, advanced electrochemical analysis of ZnO-based DSSCs provides useful information on fundamental cell parameters, such as recombination resistance, electron lifetime and diffusion coefficient, which ensures the proper choice of ZnO/dye/electrolyte system. For scale-up,

the fabrication process is even more challenging, since uniform deposition of ZnO onto a large substrate using low-cost and time-saving methods, as well as high-quality sealing, are necessary to obtain high-performing and stable devices.

## Acknowledgments

The authors gratefully acknowledge CONACYT, SENER and IER-UNAM for funding through the Mexican Center for Innovation in Solar Energy (CeMIE-Sol), Project P-27. DP acknowledges the Fondo de Sustentabilidad, CONACYT-SENER, for a postdoctoral fellowship.

## References

[1] M.A. Green, K. Emery, Y. Hishikawa, W. Warta, E.D. Dunlop, D.H. Levi, et al., Solar cell efficiency tables (version 49), Prog. Photovoltaics Res. Appl. 25 (2017) 3–13.
[2] First Solar Press Release, First solar achieves world record 18.6% thin film module conversion efficiency, First Solar (2015).
[3] E. Stathatos, Dye sensitized solar cells as an alternative approach to the conventional photovoltaic technology based on silicon—recent developments in the field and large scale applications, in: L.A. Kosyachenko (Ed.), Solar Cells—Dye Sensitized Devices, 2011, pp. 471–492.
[4] G. Conibeer, Third-generation photovoltaics, Mater. Today 10 (11) (2007) 42–50.
[5] M.A. Green, Third generation photovoltaics: ultra-high conversion efficiency at low cost, Prog. Photovoltaics Res. Appl. 9 (2) (2001) 123–135.
[6] B. O'Regan, M. Grätzel, A low-cost, high-efficiency solar cell based on dye-sensitized colloidal $TiO_2$ films, Nature 353 (1991) 737–740.
[7] C.G. Granqvist, Transparent conductors as solar energy materials: a panoramic review, Sol. Energy Mater. Sol. Cells 91 (17) (2007) 1529–1598.
[8] P. Mariani, L. Vesce, A. Di Carlo, The role of printing techniques for large-area dye sensitized solar cells, Semicond. Sci. Technol. 30 (10) (2015) 104003.
[9] W.J. Lee, E. Ramasamy, D.Y. Lee, J.S. Song, Dye-sensitized solar cells: scale up and current-voltage characterization, Sol. Energy Mater. Sol. Cells 91 (18) (2007) 1676–1680.
[10] N. Asim, K. Sopian, S. Ahmadi, K. Saeedfar, M.A. Alghoul, O. Saadatian, et al., A review on the role of materials science in solar cells, Renew. Sustain. Energy Rev. 16 (8) (2012) 5834–5847.
[11] J. Gong, K. Sumathy, Q. Qiao, Z. Zhou, Review on dye-sensitized solar cells (DSSCs): advanced techniques and research trends, Renew. Sustain. Energy Rev. 68 (2017) 234–246.
[12] W. Rho, H. Jeon, H. Kim, W. Chung, J.S. Suh, B. Jun, Recent progress in dye-sensitized solar cells for improving efficiency: $TiO_2$ nanotube arrays in active layer, J. Nanomater. 2015 (2015) 1–17.
[13] A.P. Uthirakumar, Fabrication of ZnO based dye sensitized solar cells, in: L.A. Kosyachenko (Ed.), Solar Cells – Dye-Sensitized Devices, 2011, pp. 435–456.

[14] K.E. Splan, A.M. Massari, J.T. Hupp, A porous multilayer dye-based photoelectrochemical cell that unexpectedly runs in reverse, J. Phys. Chem. B 108 (13) (2004) 4111–4115.
[15] H.A. Ribeiro, P.M. Sommeling, J.M. Kroon, A. Mendes, C.A.V. Costa, Dye-sensitized solar cells: novel concepts, materials, and state-of-the-art performances, Int. J. Green Energy 6 (3) (2009) 245–256.
[16] M.A.M. Al-Alwani, A.B. Mohamad, N.A. Ludin, A.A.H. Kadhum, K. Sopian, Dye-sensitised solar cells: development, structure, operation principles, electron kinetics, characterisation, synthesis materials and natural photosensitisers, Renew. Sustain. Energy Rev. 65 (2016) 183–213.
[17] U. Mehmood, S.-U. Rahman, K. Harrabi, I.A. Hussein, B.V.S. Reddy, Recent advances in dye sensitized solar cells, Adv. Mater. Sci. Eng. 2014 (2014) 1–12.
[18] S. Shalini, R. Balasundaraprabhu, T.S. Kumar, N. Prabavathy, S. Senthilarasu, S. Prasanna, Status and outlook of sensitizers/dyes used in dye sensitized solar cells (DSSC): a review, Arch. Thermodyn. 40 (2016) 1303–1320.
[19] L. Kavan, M. Grätzel, Highly efficient semiconducting prepared by aerosol, Electrochim. Acta 40 (5) (1995) 643–652.
[20] H. Lindström, A. Holmberg, E. Magnusson, L. Malmqvist, A. Hagfeldt, A new method to make dye-sensitized nanocrystalline solar cells at room temperature, J. Photochem. Photobiol., A 145 (1) (2001) 107–112.
[21] S. Ito, P. Chen, P. Comte, P.L. Mohammad Khaja Nazeeruddin, P. Péchy, M. Grätzel, Fabrication of screen-printing pastes from $TiO_2$ powders for dye-sensitised solar cells seigo, Prog. Photovolt Res. Appl. 15 (2007) 603–612.
[22] E.C. Muniz, M.S. Góes, J.J. Silva, J.A. Varela, E. Joanni, R. Parra, et al., Synthesis and characterization of mesoporous $TiO_2$ nanostructured films prepared by a modified sol-gel method for application in dye solar cells, Ceram. Int. 37 (3) (2011) 1017–1024.
[23] S. Kathirvel, H.-S. Chen, C. Su, H.-H. Wang, C.-Y. Li, W.-R. Li, Preparation of smooth surface $TiO_2$ photoanode for high energy conversion efficiency in dye-sensitized solar cells, J. Nanomater. 2013 (2013) 1–8.
[24] A.R. Pascoe, D. Chen, F. Huang, N.W. Duffy, R.A. Caruso, Y.-B. Cheng, Charge transport in photoanodes constructed with mesoporous $TiO_2$ beads for dye-sensitized solar cells, J. Phys. Chem. C 118 (30) (2014) 16635–16642.
[25] X. Wei, J. Liu, X.-W. Liu, Ultrafine dice-like anatase $TiO_2$ for highly efficient dye-sensitized solar cells, Sol. Energy Mater. Sol. Cells 134 (2015) 133–139.
[26] S.H. Lee, J. Kwon, D.Y. Kim, K. Song, S.H. Oh, J. Cho, et al., Enhanced power conversion efficiency of dye-sensitized solar cells with multifunctional photoanodes based on a three-dimensional $TiO_2$ nanohelix array, Sol. Energy Mater. Sol. Cells 132 (2015) 47–55.
[27] E. Guillén, C. Fernández-Lorenzo, R. Alcántara, J. Martín-Calleja, J.A. Anta, Solvent-free ZnO dye-sensitised solar cells, Sol. Energy Mater. Sol. Cells 93 (10) (2009) 1846–1852.
[28] B.Q. Zhang, C.S. Dandeneau, X. Zhou, G. Cao, ZnO nanostructures for dye-sensitized solar cells, Adv. Mater. 21 (2009) 4087–4108.
[29] S.K. Sharma, A.I. Inamdar, H. Im, B.G. Kim, P.S. Patil, Morphology dependent dye-sensitized solar cell properties of nanocrystalline zinc oxide thin films, J. Alloys Compd. 509 (5) (2011) 2127–2131.
[30] T.-H. Lee, H.-J. Sue, X. Cheng, Solid-state dye-sensitized solar cells based on ZnO nanoparticle and nanorod array hybrid photoanodes, Nanoscale Res. Lett. 6 (1) (2011) 517–524.
[31] G. Pérez-Hernández, A. Vega-Poot, I. Pérez-Juárez, J.M. Camacho, O. Arés, V. Rejón, et al., Effect of a compact ZnO interlayer on the performance of ZnO-based dye-sensitized solar cells, Sol. Energy Mater. Sol. Cells 100 (2012) 21–26.

[32] K. Tennakone, G.R.Ra Kumara, I.R.M. Kottegoda, V.P.S. Perera, An efficient dye-sensitized photoelectrochemical solar cell made from oxides of tin and zinc, Chem. Commun. 0 (1) (1999) 15–16.
[33] A. Birkel, Y.-G. Lee, D. Koll, X. Meerbeek, Van, S. Frank, et al., Highly efficient and stable dye-sensitized solar cells based on $SnO_2$ nanocrystals prepared by microwave-assisted synthesis, Energy Environ. Sci. 5 (1) (2012) 5392–5400.
[34] Y. Duan, J. Zheng, N. Fu, Y. Fang, T. Liu, Q. Zhang, et al., Enhancing the performance of dye-sensitized solar cells: doping $SnO_2$ photoanodes with Al to simultaneously improve conduction band and electron lifetime, J. Mater. Chem. A 3 (6) (2015) 3066–3073.
[35] H.J. Snaith, C. Ducati, $SnO_2$-based dye-sensitized hybrid solar cells exhibiting near unity absorbed photon-to-electron conversion efficiency, Nano Lett. 10 (4) (2010) 1259–1265.
[36] S. Ito, T.N. Murakami, P. Comte, P. Liska, C. Grätzel, M.K. Nazeeruddin, et al., Fabrication of thin film dye sensitized solar cells with solar to electric power conversion efficiency over 10%, Thin Solid Films 516 (14) (2008) 4613–4619.
[37] R. Mori, T. Ueta, K. Sakai, Y. Niida, Y. Koshiba, L. Lei, et al., Organic solvent based $TiO_2$ dispersion paste for dye-sensitized solar cells prepared by industrial production level procedure, J. Mater. Sci. 46 (5) (2011) 1341–1350.
[38] H. Abdullah, M.Z. Razali, M.A. Yarmo, Preparation of titanium dioxide paste for dye sensitized solar cells (DSSCs), Adv. Mater. Res. 139–141 (2010) 153–156.
[39] T.C. Liu, C.C. Wu, C.H. Huang, C.M. Chen, Effects of ethyl cellulose on performance of titania photoanode for dye-sensitized solar cells, J. Electron. Mater. 45 (12) (2016) 6192–6199.
[40] A. Hagfeldt, Brief overview of dye-sensitized solar cells, Ambio 41 ((SUPPL.2) (2012) 151–155.
[41] J. Gong, J. Liang, K. Sumathy, Review on dye-sensitized solar cells (DSSCs): fundamental concepts and novel materials, Renew. Sustain. Energy Rev. 16 (8) (2012) 5848–5860.
[42] M.K. Nazeeruddin, A. Kay, I. Rodicio, R. Humphry-Baker, E. Müller, P. Liska, et al., Conversion of light to electricity by *cis*-X2bis (2,2′-bipyridyl-4,4ctdicarboxylate) ruthenium(II) charge-transfer sensitizers (X = $Cl^-$, $Br^-$, $I^-$, $CN^-$, and $SCN^-$) on nanocrystalline $TiO_2$ electrodes, J. Am. Chem. Soc. 115 (14) (1993) 6382–6390.
[43] M.K. Nazeeruddin, P. Péchy, T. Renouard, S.M. Zakeeruddin, R. Humphry-Baker, P. Cointe, et al., Engineering of efficient panchromatic sensitizers for nanocrystalline $TiO_2$-based solar cells, J. Am. Chem. Soc. 123 (8) (2001) 1613–1624.
[44] M.K. Nazeeruddin, F. De Angelis, S. Fantacci, A. Selloni, G. Viscardi, P. Liska, et al., Combined experimental and DFT-TDDFT computational study of photoelectrochemical cell ruthenium sensitizers, J. Am. Chem. Soc. 127 (48) (2005) 16835–16847.
[45] F. Gao, Y. Wang, D. Shi, J. Zhang, M. Wang, X. Jing, et al., Enhance the optical absorptivity of nanocrystalline TiO2 film with high molar extinction coefficient ruthenium sensitizers for high performance dye-sensitized solar cells, J. Am. Chem. Soc. 130 (2008) 10720–10728.
[46] M. Grätzel, Recent advances in sensitized mesoscopic solar cells, Acc. Chem. Res. 42 (11) (2009) 1788–1798.
[47] W.M. Campbell, K.W. Jolley, P. Wagner, K. Wagner, P.J. Walsh, K.C. Gordon, et al., Highly efficient porphyrin sensitizers for dye-sensitized solar cells, J. Phys. Chem. C 111 (32) (2007) 11760–11762.
[48] H.P. Lu, C.Y. Tsai, W.N. Yen, C.P. Hsieh, C.W. Lee, C.Y. Yeh, et al., Control of dye aggregation and electron injection for highly efficient porphyrin sensitizers adsorbed on semiconductor films with varying ratios of coadsorbate, J. Phys. Chem. C 113 (49) (2009) 20990–20997.

[49] N. Koumura, Z.S. Wang, S. Mori, M. Miyashita, E. Suzuki, K. Hara, Alkyl-functionalized organic dyes for efficient molecular photovoltaics, J. Am. Chem. Soc. 128 (44) (2006) 14256–14257.
[50] Z.S. Wang, Y. Cui, Y. Dan-oh, C. Kasada, A. Shinpo, K. Hara, Thiophene-functionalized coumarin dye for efficient dye-sensitized solar cells: electron lifetime improved by coadsorption of deoxycholic acid, J. Phys. Chem. C 111 (19) (2007) 7224–7230.
[51] T. Horiuchi, H. Miura, K. Sumioka, S. Uchida, High efficiency of dye-sensitized solar cells based on metal-free indoline dyes, J. Am. Chem. Soc. 126 (39) (2004) 12218–12219.
[52] S. Suhaimi, M.M. Shahimin, Z.A. Alahmed, J. Chyský, A.H. Reshak, Materials for enhanced dye-sensitized solar cell performance: electrochemical application, Int. J. Electrochem. Sci. 10 (2015) 2859–2871.
[53] S.M. Feldt, E.A. Gibson, E. Gabrielsson, L. Sun, G. Boschloo, A. Hagfeldt, Design of organic dyes and cobalt polypyridine redox mediators for high efficiency dye-sensitized solar cells, J. Am. Chem. Soc. 132 (46) (2010) 16714–16724.
[54] M. Wang, C. Grätzel, S.M. Zakeeruddin, M. Grätzel, Recent developments in redox electrolytes for dye-sensitized solar cells, Energy Environ. Sci. 5 (11) (2012) 9394.
[55] A. Listorti, O. Brian, J.R. Durrant, Electron transfer dynamics in dye-sensitized solar cells, Chem. Mater. 23 (2011) 3381–3399.
[56] A.K. Chandiran, M. Abdi-Jalebi, M.K. Nazeeruddin, M. Grätzel, Analysis of electron transfer properties of ZnO and $TiO_2$ photoanodes for dye-sensitized solar cells, ACS Nano 8 (3) (2014) 2261–2268.
[57] C.M. Firdaus, M.S.B.S. Rizam, M. Rusop, S.R. Hidayah, Characterization of ZnO and ZnO: $TiO_2$ thin films prepared by sol-gel spray-spin coating technique, Procedia Eng. 41 (Iris) (2012) 1367–1373.
[58] W.I. Park, G.C. Yi, Electroluminescence in N-ZnO nanorod arrays vertically grown on p-GaN, Adv. Mater. 16 (1) (2004) 87–90.
[59] S.L. Chang, M.C. Park, Q. Kuang, Y. Deng, A.K. Sood, D.L. Polla, et al., Giant enhancement in UV response of ZnO nanobelts by polymer surface-functionalization, J. Am. Chem. Soc. 129 (40) (2007) 12096–12097.
[60] H.C. Wu, Y.C. Peng, T.P. Shen, Electronic and optical properties of substitutional and interstitial Si-doped ZnO, Materials (Basel) 5 (11) (2012) 2088–2100.
[61] M.H. Huang, Room-temperature ultraviolet nanowire nanolasers, Science 292 (5523) (2001) 1897–1899.
[62] Z.L. Wang, ZnO nanowire and nanobelt platform for nanotechnology, Mater. Sci. Eng. R Rep. 64 (3–4) (2009) 33–71.
[63] H. Morkoç, Ü. Özgür, Zinc Oxide: Fundamentals, Materials and Device Technology, WILEY-VCH Verlag GmbH & Co, 2009.
[64] C. Jagadish, S. Pearton, Zin Oxide Bulk, *Thin Films and Nanostructures*, Elsevier Ltd., 2006.
[65] A.B. Djurišić, Y.H. Leung, Optical properties of ZnO nanostructures, Small 2 (8–9) (2006) 944–961.
[66] A. Janotti, C.G. Van De Walle, Fundamentals of zinc oxide as a semiconductor, Rep. Prog. Phys. 72 (12) (2009) 126501–126530.
[67] G.J. Soldano, F.M. Zanotto, M.M. Mariscal, Mechanical stability of zinc oxide nanowires under tensile loading: is wurtzite stable at the nanoscale? RSC Adv. 5 (54) (2015) 43563–43570.
[68] J.A. Anta, E. Guillén, R. Tena-Zaera, ZnO-based dye-sensitized solar cells, J. Phys. Chem. C 116 (21) (2012) 11413–11425.

[69] K.P. Ong, D.J. Singh, P. Wu, Analysis of the thermoelectric properties of N-type ZnO, Phys. Rev. B 83 (11) (2011) 1–5.
[70] C. Zno, A. Co, H.D. Co, Thermoelectric properties of ZnO-based materials, Mater. Sci. Lett. 16 (1997) 155–157.
[71] P. Veluswamy, S. Sathiyamoorthy, K.H. Chowdary, O. Muthusamy, K. Krishnamoorthy, T. Takeuchi, et al., Morphology dependent thermal conductivity of ZnO nanostructures prepared via a green approach, J. Alloys Compd. 695 (2017) 888–894.
[72] S. Heinonen, J.-P. Nikkanen, E. Huttunen-Saarivirta, E. Levänen, Investigation of long-term chemical stability of structured ZnO films in aqueous solutions of varying conditions, Thin Solid Films 638 (2017) 410–419.
[73] K.H. Kim, B. Kumar, K.Y. Lee, H.K. Park, J.H. Lee, H.H. Lee, et al., Piezoelectric two-dimensional nanosheets/anionic layer heterojunction for efficient direct current power generation, Sci. Rep. 3 (2013) 1–6.
[74] M. Quintana, T. Edvinsson, A. Hagfeldt, G. Boschloo, Comparison of dye-sensitized ZnO and $TiO_2$ solar cells: studies of charge transport and carrier lifetime, J. Phys. Chem. C 111 (2) (2007) 1035–1041.
[75] G.A. Parks, The isoelectric points of solid oxides, solid hydroxides, and aqueous hydroxo complex systems, Chem. Rev. 65 (2) (1965) 177–198.
[76] M. Borgwardt, M. Wilke, T. Kampen, S. Mähl, M. Xiao, L. Spiccia, et al., Charge transfer dynamics at dye-sensitized ZnO and $TiO_2$ interfaces studied by ultrafast XUV photoelectron spectroscopy, Sci. Rep. 6 (2016) 1–7.
[77] A. Furube, R. Katoh, K. Hara, S. Murata, H. Arakawa, M. Tachiya, Ultrafast stepwise electron injection from photoexcited Ru-complex into nanocrystalline ZnO film via intermediates at the surface, J. Phys. Chem. B 107 (17) (2003) 4162–4166.
[78] Q.X. Zhao, P. Klason, M. Willander, Growth of ZnO nanostructures by vapor-liquid-solid method, Appl. Phys. A Mater. Sci. Process. 88 (1) (2007) 27–30.
[79] A. Marcu, L. Trupina, R. Zamani, J. Arbiol, C. Grigoriu, J.R. Morante, Catalyst size limitation in vapor-liquid-solid ZnO nanowire growth using pulsed laser deposition, Thin Solid Films 520 (14) (2012) 4626–4631.
[80] S. Ohnishi, Y. Hirokawa, T. Shiosaki, A. Kawabata, Chemical vapor deposition of single-crystalline ZnO film with smooth surface on intermediately sputtered ZnO thin film on sapphire, Jpn. J. Appl. Physics, Part 1 17 (5) (1978) 773–778.
[81] K. Minegishi, Y. Koiwai, Y. Kikuchi, K. Yano, M. Kasuga, A. Shimizu, Growth of P-type zinc oxide films by chemical vapor deposition, Jpn. J. Appl. Phys. 36 (1997) 1453–1455.
[82] L.V. Podrezova, S. Porro, V. Cauda, M. Fontana, G. Cicero, Comparison between ZnO nanowires grown by chemical vapor deposition and hydrothermal synthesis, Appl. Phys. A 113 (3) (2013) 623–632.
[83] S.N. Fatimah Hasim, M.A. Abdul Hamid, R. Shamsudin, A. Jalar, Synthesis and characterization of ZnO thin films by thermal evaporation, J. Phys. Chem. Solids 70 (12) (2009) 1501–1504.
[84] O.A. Fouad, A.A. Ismail, Z.I. Zaki, R.M. Mohamed, Zinc oxide thin films prepared by thermal evaporation deposition and its photocatalytic activity, Appl. Catal. B Environ. 62 (1–2) (2006) 144–149.
[85] W. Gao, Z. Li, ZnO thin films produced by magnetron sputtering, Ceram. Int. 30 (7) (2004) 1155–1159.
[86] W.L. Dang, Y.Q. Fu, J.K. Luo, A.J. Flewitt, W.I. Milne, Deposition and characterization of sputtered ZnO films, Superlattices Microstruct. 42 (1–6) (2007) 89–93.
[87] Y.Y. Villanueva, D. Liu, P. Tzu, Pulsed laser deposition of zinc oxide, Thin Solid Films 501 (2006) 366–369.

[88] J.B. Franklin, B. Zou, P. Petrov, D.W. McComb, M.P. Ryan, M.A. McLachlan, Optimised pulsed laser deposition of ZnO thin films on transparent conducting substrates, J. Mater. Chem. 21 (22) (2011) 8178.
[89] S.P. Wang, C.X. Shan, B. Yao, B.H. Li, J.Y. Zhang, D.X. Zhao, et al., Electrical and optical properties of ZnO films grown by molecular beam epitaxy, Appl. Surf. Sci. 255 (9) (2009) 4913–4915.
[90] M. Opel, S. Geprägs, M. Althammer, T. Brenninger, R. Gross, Laser molecular beam epitaxy of ZnO thin films and heterostructures, J. Phys. D. Appl. Phys. 47 (3) (2014) 034002 (17pp).
[91] G. Jimenez-Cadena, E. Comini, M. Ferroni, A. Vomiero, G. Sberveglieri, Synthesis of different ZnO nanostructures by modified PVD process and potential use for dye-sensitized solar cells, Mater. Chem. Phys. 124 (1) (2010) 694–698.
[92] L. Wang, X. Zhang, S. Zhao, G. Zhou, Y. Zhou, J. Qi, Synthesis of well-aligned ZnO nanowires by simple physical vapor deposition on c-oriented ZnO thin films without catalysts or additives, Appl. Phys. Lett. 86 (2) (2005) 84–87.
[93] B. Liu, H.C. Zeng, Hydrothermal synthesis of ZnO nanorods in the diameter regime of 50 Nm, J. Am. Chem. Soc. 125 (15) (2003) 4430–4431.
[94] B. Baruwati, D.K. Kumar, S.V. Manorama, Hydrothermal synthesis of highly crystalline ZnO nanoparticles: a competitive sensor for LPG and EtOH, Sens. Actuators, B: Chem. 119 (2) (2006) 676–682.
[95] P. Rai, W.-K. Kwak, Y.-T. Yu, Solvothermal synthesis of ZnO nanostructures and their morphology-dependent gas-sensing properties, ACS Appl. Mater. Interfaces 5 (8) (2013) 3026–3032.
[96] W. Feng, P. Huang, B. Wang, C. Wang, W. Wang, T. Wang, et al., Solvothermal synthesis of ZnO with different morphologies in dimethylacetamide media, Ceram. Int. 42 (2) (2016) 2250–2256.
[97] M.F. Khan, A.H. Ansari, M. Hameedullah, E. Ahmad, F.M. Husain, Q. Zia, et al., Sol-gel synthesis of thorn-like ZnO nanoparticles endorsing mechanical stirring effect and their antimicrobial activities: potential role as nano-antibiotics, Sci. Rep. 6 (May) (2016) 1–12.
[98] J.N. Hasnidawani, H.N. Azlina, H. Norita, N.N. Bonnia, S. Ratim, E.S. Ali, Synthesis of ZnO nanostructures using sol-gel method, Procedia Chem. 19 (2016) 211–216.
[99] J. Qiu, W. Yu, X. Gao, X. Li, Sol-gel assisted ZnO nanorod array template to synthesize $TiO_2$ nanotube arrays, Nanotechnology 17 (18) (2006) 4695–4698.
[100] M. Hasanpoor, M. Aliofkhazraei, H. Delavari, Microwave-assisted synthesis of zinc oxide nanoparticles, Procedia Mater. Sci. 2015 (11) (2014) 320–325.
[101] G.P. Barreto, G. Morales, M.L.L. Quintanilla, Microwave assisted synthesis of ZnO nanoparticles: effect of precursor reagents, temperature, irradiation time, and additives on nano-ZnO morphology development, J. Mater. 2013 (1) (2013) 1–12.
[102] C. Ou, P.E. Sanchez-Jimenez, A. Datta, F.L. Boughey, R.A. Whiter, S.-L. Sahonta, et al., Template-assisted hydrothermal growth of aligned zinc oxide nanowires for piezoelectric energy harvesting applications, ACS Appl. Mater. Interfaces 8 (22) (2016) 13678–13683.
[103] H.J. Fan, W. Lee, R. Hauschild, M. Alexe, G. Rhun, Le, et al., Template-assisted large-scale ordered arrays of ZnO pillars for optical and piezoelectric applications, Small 2 (4) (2006) 561–568.
[104] B.N. Illy, A.C. Cruickshank, S. Schumann, R. Da Campo, T.S. Jones, S. Heutz, et al., Electrodeposition of ZnO layers for photovoltaic applications: controlling film thickness and orientation, J. Mater. Chem. 21 (34) (2011) 12949.

[105] T. Mahalingam, V.S. John, M. Raja, Y.K. Su, P.J. Sebastian, Electrodeposition and characterization of transparent ZnO thin films, Sol. Energy Mater. Sol. Cells 88 (2) (2005) 227–235.
[106] M. Kumar, C. Sasikumar, Electrodeposition of nanostructured ZnO thin film: a review, Am. J. Mater. Sci. Eng. 2 (2) (2014) 18–23.
[107] S.K. Arya, S. Saha, J.E. Ramirez-Vick, V. Gupta, S. Bhansali, S.P. Singh, Recent advances in ZnO nanostructures and thin films for biosensor applications: review, Anal. Chim. Acta 737 (2012) 1–21.
[108] A. Kolodziejczak-Radzimska, T. Jesionowski, Zinc oxide-from synthesis to application: a review, Materials (Basel) 7 (4) (2014) 2833–2881.
[109] F. Xu, L. Sun, Solution-derived ZnO nanostructures for photoanodes of dye-sensitized solar cells, Energy Environ. Sci. 4 (3) (2011) 818–841.
[110] P. Sudhagar, R.S. Kumar, J.H. Jung, W. Cho, R. Sathyamoorthy, J. Won, et al., Facile synthesis of highly branched jacks-like ZnO nanorods and their applications in dye-sensitized solar cells, Mater. Res. Bull. 46 (9) (2011) 1473–1479.
[111] S.H. Ko, D. Lee, H.W. Kang, K.H. Nam, J.Y. Yeo, S.J. Hong, et al., Nanoforest of hydrothermally grown hierarchical ZnO nanowires for a high efficiency dye-sensitized solar cell, Nano Lett. 11 (2) (2011) 666–671.
[112] H.-M. Cheng, W.-H. Chiu, C.-H. Lee, S.-Y. Tsai, W.-F. Hsieh, Formation of branched ZnO nanowires from solvothermal method and dye-sensitized solar cells applications, J. Phys. Chem. C 112 (42) (2008) 16359–16364.
[113] F. Xu, M. Dai, Y. Lu, L. Sun, Hierarchical ZnO nanowire—nanosheet architectures for high power conversion efficiency in dye-sensitized solar cells, J. Phys. Chem. C 114 (2010) 2776–2782.
[114] M.S. Akhtar, M.A. Khan, M.S. Jeon, O.B. Yang, Controlled synthesis of various ZnO nanostructured materials by capping agents-assisted hydrothermal method for dye-sensitized solar cells, Electrochim. Acta 53 (2008) 7869–7874.
[115] Y. Gao, M. Nagai, T.-C. Chang, J.-J. Shyue, Solution derived ZnO nanowire array film as photoelectrode in dye-sensitized solar cells, Cryst. Growth Des. 7 (2007) 2467–2471.
[116] Y. Meng, Y. Lin, J. Yang, Synthesis of rod-cluster ZnO nanostructures and their application to dye-sensitized solar cells, Appl. Surf. Sci. 268 (2013) 561–565.
[117] R. Vittal, K.-C. Ho, Zinc oxide based dye-sensitized solar cells: a review, Renew. Sustain. Energy Rev. 70 (December 2016) (2017) 920–935.
[118] L. Lu, R. Li, K. Fan, T. Peng, Effects of annealing conditions on the photoelectrochemical properties of dye-sensitized solar cells made with ZnO nanoparticles, Sol. Energy 84 (2010) 844–853.
[119] C.P. Lee, C.T. Li, M.S. Fan, S.R. Li, Y.J. Huang, L.Y. Chang, et al., Microemulsion-assisted zinc oxide synthesis: morphology control and its applications in photoanodes of dye-sensitized solar cells, Electrochim. Acta 210 (2016) 483–491.
[120] L.-Y. Chen, Y.-T. Yin, Hierarchically assembled ZnO nanoparticles on high diffusion coefficient ZnO nanowire arrays for high efficiency dye-sensitized solar cells, Nanoscale 5 (2013) 1777–1780.
[121] C. Magne, T. Moehl, M. Urien, M. Grätzel, T. Pauporté, Effects of ZnO film growth route and nanostructure on electron transport and recombination in dye-sensitized solar cells, J. Mater. Chem. A 1 (6) (2013) 2079–2088.
[122] S.B. Ambade, R.S. Mane, S.H. Han, S.H. Lee, M.M. Sung, O.S. Joo, Indoline-dye immobilized ZnO nanoparticles for whopping 5.44% light conversion efficiency, J. Photochem. Photobiol., A 222 (2011) 366–369.
[123] D.I. Suh, S.Y. Lee, T.H. Kim, J.M. Chun, E.K. Suh, O.B. Yang, et al., The fabrication and characterization of dye-sensitized solar cells with a branched structure of ZnO nanowires, Chem. Phys. Lett. 442 (2007) 348–353.

[124] G. Hua, Y. Zhang, J. Zhang, X. Cao, W. Xu, L. Zhang, Fabrication of ZnO nanowire arrays by cycle growth in surfactantless aqueous solution and their applications on dye-sensitized solar cells, Mater. Lett. 62 (25) (2008) 4109–4111.
[125] S. Li, X. Zhang, X. Jiao, H. Lin, One-step large-scale synthesis of porous ZnO nanofibers and their application in dye-sensitized solar cells, Mater. Lett. 65 (2011) 2975–2978.
[126] A. Qurashi, M.F. Hossain, M. Faiz, N. Tabet, M.W. Alam, N.K. Reddy, Fabrication of well-aligned and dumbbell-shaped hexagonal ZnO nanorod arrays and their dye sensitized solar cell applications, J. Alloys Compd. 503 (2010) L40–L43.
[127] J. Chung, J. Lee, S. Lim, Annealing effects of ZnO nanorods on dye-sensitized solar cell efficiency, Phys. B: Condens. Matter 405 (2010) 2593–2598.
[128] V.M. Guérin, J. Rathousky, T. Pauporté, Electrochemical design of ZnO hierarchical structures for dye-sensitized solar cells, Sol. Energy Mater. Sol. Cells 102 (2012) 8–14.
[129] Y.-Z. Zhang, L.-H. Wu, Y.-P., Liu, E.-Q., Xie, D. Yan, J.-T. Chen, Preparation of ZnO nanospheres and their applications in dye-sensitized solar cells, Chin. Phys. Lett. 26 (2009) 038201.
[130] C.X. He, B.X. Lei, Y.F. Wang, C.Y. Su, Y.P. Fang, D.B. Kuang, Sonochemical preparation of hierarchical ZnO hollow spheres for efficient dye-sensitized solar cells, Chemistry 16 (2010) 8757–8761.
[131] H.-M. Cheng, W.-F. Hsieh, High-efficiency metal-free organic-dye-sensitized solar cells with hierarchical ZnO photoelectrode, Energy Environ. Sci. 3 (2010) 442–447.
[132] C. Sima, C. Grigoriu, O. Toma, S. Antohe, Study of dye sensitized solar cells based on ZnO photoelectrodes deposited by laser ablation and doctor blade methods, Thin Solid Films 597 (2015) 206–211.
[133] Y.Z. Zheng, X. Tao, Q. Hou, D.T. Wang, W.L. Zhou, J.F. Chen, Iodine-doped ZnO nanocrystalline aggregates for improved dye-sensitized solar cells, Chem. Mater. 23 (2011) 3–5.
[134] K. Mahmood, S.B. Park, Highly efficient dye-sensitized solar cell with an electrostatic spray deposited upright-standing boron-doped ZnO (BZO) nanoporous nanosheet-based photoanode, J. Mater. Chem. A 1 (2013) 4826–4835.
[135] Y. Shi, C. Zhu, L. Wang, C. Zhao, W. Li, K.K. Fung, et al., Ultrarapid sonochemical synthesis of ZnO hierarchical structures: from fundamental research to high efficiencies up to 6.42% for quasi-solid dye-sensitized solar cells, Chem. Mater. 25 (2013) 1000–1012.
[136] M. Navaneethan, J. Archana, M. Arivanandhan, Y. Hayakawa, Functional properties of amine-passivated ZnO nanostructures and dye-sensitized solar cell characteristics, Chem. Eng. J. 213 (2012) 70–77.
[137] F.I. Lizama-Tzec, R. García-Rodríguez, G. Rodríguez-Gattorno, E.J. Canto-Aguilar, A.G. Vega-Poot, B.E. Heredia-Cervera, et al., Influence of morphology on the performance of ZnO-based dye-sensitized solar cells, RSC Adv. 6 (2016) 37424–37433.
[138] Y. Xie, X. Zhou, H. Mi, J. Ma, J. Yang, J. Cheng, High efficiency ZnO-based dye-sensitized solar cells with a 1*H*,1*H*,2*H*,2*H*-perfluorodecyltriethoxysilane chain barrier for cutting on interfacial recombination, Appl. Surf. Sci. 434 (2018) 1144–1152.
[139] X.H. Lu, Y.Z. Zheng, J. Zhao, J.F. Chen, X. Tao, Aqueous chemical synthesis of large-scale ZnO aggregates with high-efficient light-scattering and application in dye-sensitized solar cells, Electrochim. Acta 90 (2013) 649–655.
[140] Y. Shi, K. Wang, Y. Du, H. Zhang, J. Gu, C. Zhu, et al., Solid-state synthesis of ZnO nanostructures for quasi-solid dye-sensitized solar cells with high efficiencies up to 6.46%, Adv. Mater. 25 (2013) 4413–4419.

[141] C.H. Lee, W.H. Chiu, K.M. Lee, W.H. Yen, H.F. Lin, W.F. Hsieh, et al., The Influence of tetrapod-like ZnO morphology and electrolytes on energy conversion efficiency of dye-sensitized solar cells, Electrochim. Acta 55 (2010) 8422–8429.
[142] A.K. Patra, A. Dutta, A. Bhaumik, Self-assembled ultra small ZnO nanocrystals for dye-sensitized solar cell application, J. Solid State Chem. 215 (2014) 135–142.
[143] Z. Li, Y. Zhou, G. Xue, T. Yu, J. Liu, Z. Zou, Fabrication of hierarchically assembled microspheres consisting of nanoporous ZnO nanosheets for high-efficiency dye-sensitized solar cells, J. Mater. Chem. 22 (29) (2012) 14341–14345.
[144] R. Marczak, F. Werner, R. Ahmad, V. Lobaz, D.M. Guldi, W. Peukert, Detailed investigations of ZnO photoelectrodes preparation for dye sensitized solar cells, Langmuir 27 (2011) 3920–3929.
[145] Y.-H. Lai, C.-Y. Lin, H.-W. Chen, J.-G. Chen, C.-W. Kung, R. Vittal, et al., Fabrication of a ZnO film with a mosaic structure for a high efficient dye-sensitized solar cell, J. Mater. Chem. 20 (2010) 9379–9385.
[146] Y.-Z. Zheng, J. Zhao, H. Zhang, J.-F. Chen, W. Zhou, X. Tao, Dual-functional ZnO nanorod aggregates as scattering layer in the photoanode for dye-sensitized solar cells, Chem. Commun. 47 (2011) 11519–11521.
[147] T.M. El-Agez, A.A. El Tayyan, A.A. Al-Kahlout, S.S. Taya, M. Abdel-Latif, Dye-sensitized solar cells based on ZnO films and natural dyes, Int. J. Mater. Chem. 2 (3) (2012) 105–110.
[148] A. Jana, P.P. Das, S.A. Agarkar, P. Sujatha Devi, A comparative study on the dye sensitized solar cell performance of solution processed ZnO, Sol. Energy 102 (2014) 143–151.
[149] D. Barpuzary, A.S. Patra, J.V. Vaghasiya, B.G. Solanki, S.S. Soni, M. Qureshi, Highly efficient one-dimensional ZnO nanowire-based dye-sensitized solar cell using a metal-free, D-π-A-type, carbazole derivative with more than 5% power conversion, ACS Appl. Mater. Interfaces 6 (2014) 12629–12639.
[150] J. Fang, H. Fan, H. Tian, G. Dong, Morphology control of ZnO nanostructures for high efficient dye-sensitized solar cells, Mater. Charact. 108 (2015) 51–57.
[151] R. Krishnapriya, S. Praneetha, A. Vadivel Murugan, Energy-efficient, microwave-assisted hydro/solvothermal synthesis of hierarchical flowers and rice grain-like ZnO nanocrystals as photoanodes for high performance dye-sensitized solar cells, CrystEngComm 17 (2015) 8353–8367.
[152] Y. Shi, C. Zhu, L. Wang, W. Li, K.K. Fung, N. Wang, Asymmetric ZnO panel-like hierarchical architectures with highly interconnected pathways for free-electron transport and photovoltaic improvements, Chemistry 19 (2013) 282–287.
[153] M. Saito, S. Fujihara, Large photocurrent generation in dye-sensitized ZnO solar cells, Energy Environ. Sci. 2 (2008) 280–283.
[154] T.J. Koplin, M. Siemons, C. Océn-Valéntin, D. Sanders, U. Simon, Workflow for high throughput screening of gas sensing materials, Sensors 6 (4) (2006) 298–307.
[155] Z. Liu, C. Liu, J. Ya, E. Lei, Controlled synthesis of ZnO and $TiO_2$ nanotubes by chemical method and their application in dye-sensitized solar cells, Renew. Energy 36 (4) (2011) 1177–1181.
[156] J. Chen, C. Li, J.L. Song, X.W. Sun, W. Lei, W.Q. Deng, Bilayer ZnO nanostructure fabricated by chemical bath and its application in quantum dot sensitized solar cell, Appl. Surf. Sci. 255 (17) (2009) 7508–7511.
[157] F. Xu, L. Sun, Solution-derived ZnO nanostructures for photoanodes of dye-sensitized solar cells, Energy Environ. Sci. 4 (3) (2011) 818–841.
[158] C.X. Wang, X.D. Zhang, D.F. Wang, Z.H. Yang, W.W. Ji, C.S. Zhang, et al., Synthesis of nanostructural ZnO using hydrothermal method for dye-sensitized solar cells, Sci. China Technol. Sci. 53 (2010) 1146–1149.

[159] Y. Wang, X. Cui, Y. Zhang, X. Gao, Y. Sun, Preparation of cauliflower-like ZnO films by chemical bath deposition: photovoltaic performance and equivalent circuit of dye-sensitized solar cells, J. Mater. Sci. Technol. 29 (2) (2013) 123–127.
[160] M. Thambidurai, N. Muthukumarasamy, D. Velauthapillai, C. Lee, Synthesis of garland like ZnO nanorods and their application in dye sensitized solar cells, Mater. Lett. 92 (2013) 104–107.
[161] S. Ameen, M. Shaheer Akhtar, H.S. Shin, Growth and characterization of nanospikes decorated ZnO sheets and their solar cell application, Chem. Eng. J. 195–196 (2012) 307–313.
[162] A. Umar, Growth of comb-like ZnO nanostructures for dye-sensitized solar cells applications, Nanoscale Res. Lett. 4 (9) (2009) 1004–1008.
[163] F.A. Al-Agel, M. Shaheer Akhtar, H. Alshammari, A. Alshammari, S.A. Khan, Solution processed ZnO rectangular prism as an effective photoanode material for dye sensitized solar cells, Mater. Lett. 147 (2015) 119–122.
[164] J. Qiu, M. Guo, X. Wang, Electrodeposition of hierarchical ZnO nanorod-nanosheet structures and their applications in dye-sensitized solar cells, ACS Appl. Mater. Interfaces 3 (7) (2011) 2358–2367.
[165] J.X. Wang, C.M.L. Wu, W.S. Cheung, L.B. Luo, Z.B. He, G.D. Yuan, et al., Synthesis of hierarchical porous ZnO disklike nanostructures for improved photovoltaic properties of dye-sensitized solar cells, J. Phys. Chem. C 114 (31) (2010) 13157–13161.
[166] J. Chang, R. Ahmed, H. Wang, H. Liu, R. Li, P. Wang, et al., ZnO nanocones with high-index $\{10\bar{1}1\}$ facets for enhanced energy conversion efficiency of dye-sensitized solar cells, J. Phys. Chem. C 117 (2013) 13836–13844.
[167] M. McCune, W. Zhang, Y. Deng, High efficiency dye-sensitized solar cells based on three-dimensional multilayered ZnO nanowire arrays with "caterpillar-like" structure, Nano Lett. 12 (7) (2012) 3656–3662.
[168] C.-P. Lee, J.-C. Lin, Y.-C. Wang, C.-Y. Chou, M.-H. Yeh, R. Vittal, et al., Synthesis of hexagonal ZnO clubs with opposite faces of unequal dimensions for the photoanode of dye-sensitized solar cells, Phys. Chem. Chem. Phys. 13 (47) (2011) 20999.
[169] W. Chen, H. Zhang, I.M. Hsing, S. Yang, A new photoanode architecture of dye sensitized solar cell based on ZnO nanotetrapods with no need for calcination, Electrochem. Commun. 11 (5) (2009) 1057–1060.
[170] C.J. Raj, K. Prabakar, S.N. Karthick, K.V. Hemalatha, M.K. Son, H.J. Kim, Banyan root structured Mg-doped ZnO photoanode dye-sensitized solar cells, J. Phys. Chem. C 117 (6) (2013) 2600–2607.
[171] C.P. Lee, P.W. Chen, C.T. Li, Y.J. Huang, S.R. Li, L.Y. Chang, et al., ZnO double layer film with a novel organic sensitizer as an efficient photoelectrode for dye-sensitized solar cells, J. Power Sources 325 (2016) 209–219.
[172] Y.-X. Wang, Z.-C. Shen, D.-D. Huang, Z.-S. Yang, High-performance ZnO nanosheets/nanocrystalline aggregates composite photoanode film in dye-sensitized solar cells, Mater. Lett. 214 (2018) 88–90.
[173] C.-Y. Lin, Y.-H. Lai, H.-W. Chen, J.-G. Chen, C.-W. Kung, R. Vittal, et al., Highly efficient dye-sensitized solar cell with a ZnO nanosheet-based photoanode, Energy Environ. Sci. 4 (2011) 3448–3455.
[174] Z. Chen, Y. Tang, L. Zhang, L. Luo, Electrodeposited nanoporous ZnO films exhibiting enhanced performance in dye-sensitized solar cells, Electrochim. Acta 51 (2006) 5870–5875.
[175] H. Minoura, T. Yoshida, Electrodeposition of ZnO/dye hybrid thin films for dye-sensitized solar cells, Electrochemistry 76 (2) (2008) 109–117.

[176] X. Yin, X. Liu, L. Wang, B. Liu, Electrophoretic deposition of ZnO photoanode for plastic dye-sensitized solar cells, Electrochem. Commun. 12 (9) (2010) 1241–1244.
[177] T.P. Chou, Q. Zhang, G. Cao, M. Science, V. Uni, R. Hall, Effects of dye loading conditions on the energy conversion efficiency of ZnO and $TiO_2$ dye-sensitized solar cells, J. Phys. Chem. C 111 (2007) 18804–18811.
[178] J. Qiu, X. Li, F. Zhuge, X. Gan, X. Gao, W. He, et al., Solution-derived 40 Mm vertically aligned ZnO nanowire arrays as photoelectrodes in dye-sensitized solar cells, Nanotechnology 21 (19) (2010) 195602.
[179] E. Puyoo, G. Rey, E. Appert, V. Consonni, D. Bellet, Efficient dye-sensitized solar cells made from ZnO nanostructure composites, J. Phys. Chem. C 116 (34) (2012) 18117–18123.
[180] T. Marimuthu, N. Anandhan, Growth and characterization of ZnO nanostructure on $TiO_2$-ZnO films as a light scattering layer for dye sensitized solar cells, Mater. Res. Bull. 95 (2017) 616–624.
[181] P.K. Baviskar, J.B. Zhang, V. Gupta, S. Chand, B.R. Sankapal, Nanobeads of zinc oxide with rhodamine B dye as a sensitizer for dye sensitized solar cell application, J. Alloys Compd. 510 (1) (2011) 33–37.
[182] W.T. Jiang, C. Wu, Te, Y.H. Sung, J.J. Wu, Room-temperature fast construction of outperformed ZnO nanoarchitectures on nanowire-array templates for dye-sensitized solar cells, ACS Appl. Mater. Interfaces 5 (3) (2013) 911–917.
[183] T. Marimuthu, N. Anandhan, R. Thangamuthu, Electrochemical synthesis of one-dimensional ZnO nanostructures on ZnO seed layer for DSSC applications, Appl. Surf. Sci. 428 (2018) 385–394.
[184] Y. Sakuragi, X.F. Wang, H. Miura, M. Matsui, T. Yoshida, Aggregation of indoline dyes as sensitizers for ZnO solar cells, J. Photochem. Photobiol., A 216 (1) (2010) 1–7.
[185] F. Bittner, T. Oekermann, M. Wark, Scale-up of the electrodeposition of ZnO/eosin Y hybrid thin films for the fabrication of flexible dye-sensitized solar cell modules, Materials (Basel) 11 (2) (2018).
[186] H.W. Chen, C.Y. Lin, Y.H. Lai, J.G. Chen, C.C. Wang, C.W. Hu, et al., Electrophoretic deposition of ZnO film and its compression for a plastic based flexible dye-sensitized solar cell, J. Power Sources 196 (10) (2011) 4859–4864.
[187] C.Y. Jiang, X.W. Sun, K.W. Tan, G.Q. Lo, A.K.K. Kyaw, D.L. Kwong, High-bendability flexible dye-sensitized solar cell with a nanoparticle-modified ZnO-nanowire electrode, Appl. Phys. Lett. 92 (14) (2008) 90–93.
[188] M.S.H. Choudhury, N. Kishi, T. Soga, Compression of ZnO nanoparticle films at elevated temperature for flexible dye-sensitized solar cells, J. Alloys Compd. 656 (2016) 476–480.
[189] M.S. Haque Choudhury, N. Kishi, T. Soga, Hot-compress: a new postdeposition treatment for ZnO-based flexible dye-sensitized solar cells, Mater. Res. Bull. 80 (2016) 135–138.
[190] H. Utsunomiya, S. Ueno, S. Fujihara, Fabrication of nanostructured zinc oxide films on plastic substrates by pyrolysis method and their application to dye-sensitized solar cells, Key Eng. Mater. 582 (2014) 206–209.
[191] H. Lu, X. Zhai, W. Liu, M. Zhang, M. Guo, Electrodeposition of hierarchical ZnO nanorod arrays on flexible stainless steel mesh for dye-sensitized solar cell, Thin Solid Films 586 (2015) 46–53.
[192] T. Yoshida, K. Terada, Electrochemical self assembly of nanoporous ZnO eosin Y thin films and their sensitized photoelectrochemical performance, Adv. Mater. 12 (2000) 1214–1217.

[193] E.J. Canto-Aguilar, M. Rodríguez-Pérez, R. García-Rodríguez, F.I. Lizama-Tzec, A.T. De Denko, F.E. Osterloh, et al., ZnO-based dye-sensitized solar cells: effects of redox couple and dye aggregation, Electrochim. Acta 258 (2017) 396–404.
[194] A.K.K. Kyaw, X.W. Sun, J.L. Zhao, J.X. Wang, D.W. Zhao, X.F. Wei, et al., Top-illuminated dye-sensitized solar cells with a room-temperature-processed ZnO photoanode on metal substrates and a Pt-coated Ga-doped ZnO counter electrode, J. Phys. D. Appl. Phys. 44 (4) (2011) 45102–451028.
[195] S. Ito, N.-L.C. Ha, G. Rothenberger, P. Liska, P. Comte, S.M. Zakeeruddin, et al., High-efficiency (7.2%) flexible dye-sensitized solar cells with Ti-metal substrate for nanocrystalline-$TiO_2$ photoanode, Chem. Commun. No. 38 (2006) 4004–4006.
[196] K. Onoda, S. Ngamsinlapasathian, T. Fujieda, S. Yoshikawa, The superiority of Ti plate as the substrate of dye-sensitized solar cells, Sol. Energy Mater. Sol. Cells 91 (13) (2007) 1176–1181.
[197] W. Tan, X. Yin, X. Zhou, J. Zhang, X. Xiao, Y. Lin, Electrophoretic deposition of nanocrystalline $TiO_2$ films on Ti substrates for use in flexible dye-sensitized solar cells, Electrochim. Acta 54 (19) (2009) 4467–4472.
[198] T. Yoshida, K. Hiramatsu, H. Koike, T. Yane, K. Funabiki, M. Matsui, et al., Colorful and plastic solar cells with electrodeposited nanostructured zinc oxide, Galvanotechnik 1 (2009) 164–168.
[199] B. Wang, L.L. Kerr, Dye sensitized solar cells on paper substrates, Sol. Energy Mater. Sol. Cells 95 (8) (2011) 2531–2535.
[200] J.B. Asbury, E. Hao, Y. Wang, H.N. Ghosh, T. Lian, Ultrafast electron transfer dynamics from molecular adsorbates to semiconductor nanocrystalline thin films, J. Phys. Chem. B 105 (20) (2001) 4545–4557.
[201] R. Katoh, A. Furube, K. Hara, S. Murata, H. Sugihara, Efficiencies of electron injection from excited sensitizer dyes to nanocrystalline ZnO films as studied by near-IR optical absorption of injected electrons, J. Phys. Chem. B 106 (2002) 12957–12964.
[202] T. Yoshihara, R. Katoh, A. Furube, M. Murai, Y. Tamaki, K. Hara, et al., Quantitative estimation of the efficiency of electron injection from excited sensitizer dye into nanocrystalline ZnO film, J. Phys. Chem. B 108 (2004) 2643–2647.
[203] T. Ganesh, H.-M. Nguyen, R.S. Mane, N. Kim, D.V. Shinde, S.S. Bhande, et al., Promising ZnO-based DSSC performance using HMP molecular dyes of high extinction coefficients, Dalt. Trans. 43 (2014) 11305–11308.
[204] Y. Xie, P. Joshi, S.B. Darling, Q. Chen, T. Zhang, D. Galipeau, et al., Electrolyte effects on electron transport and recombination at ZnO nanorods for dye-sensitized solar cells, J. Phys. Chem. C 114 (2010) 17880–17888.
[205] K. Ocakoglu, E. Harputlu, P. Guloglu, S. Erten-Ela, The photovoltaic performance of new ruthenium complexes in DSSCs based on nanorod ZnO electrode, Synth. Met. 162 (2012) 2125–2133.
[206] C.P. Lee, C.Y. Chou, C.Y. Chen, M.H. Yeh, L.Y. Lin, R. Vittal, et al., Zinc oxide-based dye-sensitized solar cells with a ruthenium dye containing an alkyl bithiophene group, J. Power Sources 246 (2014) 1–9.
[207] K. Keis, J. Lindgren, S.E. Lindquist, A. Hagfeldt, Studies of the adsorption process of Ru complexes in nanoporous ZnO electrodes, Langmuir 16 (2000) 4688–4694.
[208] C. Bauer, G. Boschloo, E. Mukhtar, A. Hagfeldt, Electron injection and recombination in $Ru(Dcbpy)_2(NCS)_2$ sensitized nanostructured ZnO, J. Phys. Chem. B 105 (2001) 5585–5588.
[209] H. Horiuchi, R. Katoh, K. Hara, M. Yanagida, S. Murata, H. Arakawa, et al., Electron injection efficiency from excited N3 into nanocrystalline ZnO films: effect of ($N3–Zn^{2+}$) aggregate formation, J. Phys. Chem. B 107 (2003) 2570–2574.

[210] F. Yan, L. Huang, J. Zheng, J. Huang, Z. Lin, F. Huang, et al., Effect of surface etching on the efficiency of ZnO-based dye-sensitized solar cells, Langmuir 26 (2010) 7153–7156.
[211] W.C. Chang, C.H. Lee, W.C. Yu, C.M. Lin, Optimization of dye adsorption time and film thickness for efficient ZnO dye-sensitized solar cells with high at-rest stability, Nanoscale Res. Lett. 7 (2012) 1–10.
[212] K. Funabiki, H. Mase, A. Hibino, N. Tanaka, N. Mizuhata, Y. Sakuragi, et al., Synthesis of a novel heptamethine–cyanine dye for use in near-infrared active dye-sensitized solar cells with porous zinc oxide prepared at low temperature, Energy Environ. Sci. 4 (6) (2011) 2186.
[213] P.K. Baviskar, D.P. Dubal, S. Majumder, A. Ennaoui, B.R. Sankapal, "Basic idea, advance approach": efficiency boost by sensitization of blended dye on chemically deposited ZnO films, J. Photochem. Photobiol., A 318 (2016) 135–141.
[214] M. Wang, C. Huang, Y. Cao, Q. Yu, Dye-sensitized solar cells based on nanoparticle-decorated ZnO/$TiO_2$ core/shell nanorod arrays, J. Phys. D. Appl. Phys. 42 (2009) 155104 (6pp).
[215] R.Y.-Y. Lin, C.-P. Lee, Y.-C. Chen, J.-D. Peng, T.-C. Chu, H.-H. Chou, et al., Benzothiadiazole-containing donor–acceptor–acceptor type organic sensitizers for solar cells with ZnO photoanodes, Chem. Commun. 48 (99) (2012) 12071.
[216] E. Guillén, F. Casanueva, J.A. Anta, A. Vega-Poot, G. Oskam, R. Alcántara, et al., Photovoltaic performance of nanostructured zinc oxide sensitised with xanthene dyes, J. Photochem. Photobiol., A 200 (2–3) (2008) 364–370.
[217] I.B. Karki, J.J. Nakarmi, P.K. Mandal, S. Chatterjee, Effect of organic dyes on the performance of ZnO based dye-sensitized solar cells, Appl. Sol. Energy 49 (1) (2013) 40–45.
[218] J.S. Bendall, L. Etgar, S.C. Tan, N. Cai, P. Wang, S.M. Zakeeruddin, et al., An efficient DSSC based on ZnO nanowire photo-anodes and a new D-π-A organic dye, Energy Environ. Sci. 4 (2011) 2903–2908.
[219] Y. Kusumawati, J. Massin, C. Olivier, T. Toupance, A.L. Ivansyah, M.A. Martoprawiro, et al., Combined computational and experimental study of carbazole dyes for iodide- and cobalt-based ZnO DSSCs, J. Photochem. Photobiol., A 341 (2017) 69–77.
[220] S. Ito, Investigation of dyes for dye-sensitized solar cells: Ruthenium-complex dyes, metal-free dyes, metal-complex porphyrin dyes and natural dyes, in: L. A. Kosyachenko (Ed.), Solar Cells – Dye-Sensitized Devices, 2011, pp. 19–48.
[221] J. Falgenhauer, F. Fiehler, C. Richter, M. Rudolph, D. Schlettwein, Consequences of changes in the ZnO trap distribution on the performance of dye-sensitized solar cells, Phys. Chem. Chem. Phys. 19 (24) (2017) 16159–16168.
[222] S.M. Chang, C.L. Lin, Y.J. Chen, H.C. Wang, W.C. Chang, L.Y. Lin, Improved photovoltaic performances of dye-sensitized solar cells with ZnO films co-sensitized by metal-free organic sensitizer and N719 dye, Org. Electron. 25 (2015) 254–260.
[223] V.O. Williams, N.C. Jeong, C. Prasittichai, O.K. Farha, M.J. Pellin, J.T. Hupp, Fast transporting ZnO-$TiO_2$ coaxial photoanodes for dye-sensitized solar cells based on ALD-modified $SiO_2$ aerogel frameworks, ACS Nano 6 (7) (2012) 6185–6196.
[224] H. Nusbaumer, S.M. Zakeeruddin, J.E. Moser, M. Grätzel, An alternative efficient redox couple for the dye-sensitized solar cell system, Chemistry 9 (2003) 3756–3763.
[225] T. Daeneke, Y. Uemura, N.W. Duffy, A.J. Mozer, N. Koumura, U. Bach, et al., Aqueous dye-sensitized solar cell electrolytes based on the ferricyanide-ferrocyanide redox couple, Adv. Mater. 24 (2012) 1222–1225.

[226] Y. Cao, Y. Saygili, A. Ummadisingu, J. Teuscher, J. Luo, N. Pellet, et al., 11% Efficiency solid-state dye-sensitized solar cells with copper(II/I) hole transport materials, Nat. Commun. 8 (2017) 15390. 8pp.
[227] Z. Shen, B. Xu, P. Liu, Y. Hu, Y. Yu, H. Ding, et al., High performance solid-state dye-sensitized solar cells based on organic blue-colored dyes, J. Mater. Chem. A 5 (2017) 1242–1247.
[228] Y. Zhao, J. Zhai, J. He, X. Chen, L. Chen, L. Zhang, et al., High-performance all-solid-state dye-sensitized solar cells utilizing imidazolium-type ionic crystal as charge transfer layer, Chem. Mater. 20 (2008) 6022–6028.
[229] A. Lennert, M. Sternberg, K. Meyer, R.D. Costa, D.M. Guldi, Iodine-pseudohalogen ionic liquid-based electrolytes for quasi-solid-state dye-sensitized solar cells, ACS Appl. Mater. Interfaces 9 (2017) 33437–33445.
[230] E. Guillén, L.M. Peter, J.A. Anta, Electron transport and recombination in ZnO-based dye-sensitized solar cells, J. Phys. Chem. C 115 (45) (2011) 22622–22632.
[231] S.S. Kanmani, K. Ramachandran, S. Umapathy, Eosin yellowish dye-sensitized ZnO nanostructure-based solar cells employing solid PEO redox couple electrolyte, Int. J. Photoenergy 2012 (2012) 1–8.
[232] I.Y.Y. Bu, M.T. Cole, One-pot synthesis of intercalating ZnO nanoparticles for enhanced dye-sensitized solar cells, Mater. Lett. 90 (2013) 56–59.
[233] N. Mir, M. Salavati-Niasari, F. Davar, Preparation of ZnO nanoflowers and Zn glycerolate nanoplates using inorganic precursors via a convenient rout and application in dye sensitized solar cells, Chem. Eng. J. 181–182 (2012) 779–789.
[234] Y.T. Kim, J. Park, S. Kim, D.W. Park, J. Choi, Fabrication of hierarchical ZnO nanostructures for dye-sensitized solar cells, Electrochim. Acta 78 (2012) 417–421.
[235] V. Kumar, N. Singh, V. Kumar, L.P. Purohit, A. Kapoor, O.M. Ntwaeaborwa, et al., Doped zinc oxide window layers for dye sensitized solar cells, J. Appl. Phys. 114 (2013) 134506. 6pp.
[236] L. Schlur, A. Carton, P. Lévêque, D. Guillon, G. Pourroy, Optimization of a new ZnO nanorods hydrothermal synthesis method for solid state dye sensitized solar cells applications, J. Phys. Chem. C 117 (6) (2013) 2993–3001.
[237] H. Tributsch, H. Gerischer, The use of semiconductor electrodes in the study of photochemical reactions, Ber. Bunsenges. Phys. Chem. 73 (8–9) (1969) 850–854.
[238] X. Chen, Y. Tang, W. Liu, Efficient dye-sensitized solar cells based on nanoflower-like ZnO photoelectrode, Mol. Commun. 22 (2017) 1–6.
[239] G.S. Selopal, H.-P. Wu, J. Lu, Y.-C. Chang, M. Wang, A. Vomiero, et al., Metal-free organic dyes for $TiO_2$ and ZnO dye-sensitized solar cells, Sci. Rep. 6 (1) (2016) 18756.
[240] F. Hu, Y. Xia, Z. Guan, X. Yin, T. He, Low temperature fabrication of ZnO compact layer for high performance plastic dye-sensitized ZnO solar cells, Electrochim. Acta 69 (2012) 97–101.
[241] C.-Y. Huang, P.-H. Chen, Y.-J. Wu, H.-P. Chiang, J.-S. Hwang, P.-T. Lin, et al., Enhanced performance of ZnO-based dye-sensitized solar cells using $TiO_2$/graphene nanocomposite compact layer, Jpn. J. Appl. Phys. 56 (4) (2017) 045201.
[242] G.S. Selopal, N. Memarian, R. Milan, I. Concina, G. Sberveglieri, A. Vomiero, Effect of blocking layer to boost photoconversion efficiency in ZnO dye-sensitized solar cells, ACS Appl. Mater. Interfaces 6 (2014) 11236–11244.
[243] M. Law, L.E. Greene, A. Radenovic, T. Kuykendall, J. Liphardt, P. Yang, ZnO-$Al_2O_3$ and ZnO-$TiO_2$ core-shell nanowire dye-sensitized solar cells, J. Phys. Chem. B 110 (2006) 22652–22663.
[244] Y. He, J. Hu, Y. Xie, High-efficiency dye-sensitized solar cells of up to 8.03% by air plasma treatment of ZnO nanostructures, Chem. Commun. 51 (90) (2015) 16229–16232.

[245] S.A. Mahmoud, O.A. Fouad, Synthesis and application of zinc/tin oxide nanostructures in photocatalysis and dye sensitized solar cells, Sol. Energy Mater. Sol. Cells 136 (2015) 38–43.
[246] M.H. Jung, High efficiency dye-sensitized solar cells based on the ZnO nanoparticle aggregation sphere, Mater. Chem. Phys. 202 (2017) 234–244.
[247] F. Xu, J. Chen, X. Wu, Y. Zhang, Y. Wang, J. Sun, et al., Graphene scaffolds enhanced photogenerated electron transport in ZnO photoanodes for high-efficiency dye-sensitized solar cells, J. Phys. Chem. C 117 (17) (2013) 8619–8627.
[248] Z. Dong, X. Lai, J.E. Halpert, N. Yang, L. Yi, J. Zhai, et al., Accurate control of multishelled ZnO hollow microspheres for dye-sensitized solar cells with high efficiency, Adv. Mater. 24 (8) (2012) 1046–1049.
[249] H.-M. Cheng, W.-F. Hsieh, Electron transfer properties of organic dye-sensitized solar cells based on indoline sensitizers with ZnO Nanoparticles, Nanotechnology 21 (48) (2010) 485202.
[250] L. Wang, C. Ma, X. Ru, Z. Guo, D. Wu, S. Zhang, et al., Facile synthesis of ZnO hollow microspheres and their high performance in photocatalytic degradation and dye sensitized solar cells, J. Alloys Compd. 647 (2015) 57–62.
[251] C.-W. Kung, H.-W. Chen, C.-Y. Lin, Y.-H. Lai, R. Vittal, K.-C. Ho, Electrochemical synthesis of a double-layer film of ZnO nanosheets/nanoparticles and its application for dye-sensitized solar cells, Prog. Photovoltaics Res. Appl. 22 (2014) 440–451.
[252] V.-M. Guérin, T. Pauporté, From nanowires to hierarchical structures of template-free electrodeposited ZnO for efficient dye-sensitized solar cells, Energy Environ. Sci. 4 (8) (2011) 2971.
[253] H. Li, Z. Xie, Y. Zhang, J. Wang, The effects of ethyl cellulose on PV performance of DSSC made of nanostructured ZnO pastes, Thin Solid Films 518 (2012) e68–e71.
[254] J. Mou, W. Zhang, J. Fan, H. Deng, W. Chen, Facile synthesis of ZnO nanobullets/nanoflakes and their applications to dye-sensitized solar cells, J. Alloys Compd. 509 (3) (2011) 961–965.
[255] L. Luo, W. Tao, X. Hu, T. Xiao, B. Heng, W. Huang, et al., Mesoporous F-doped ZnO prism arrays with significantly enhanced photovoltaic performance for dye-sensitized solar cells, J. Power Sources 196 (2011) 10518–10525.
[256] C.-T. Wu, J.-J. Wu, Room-temperature synthesis of hierarchical nanostructures on ZnO nanowire anodes for dye-sensitized solar cells, J. Mater. Chem. 21 (35) (2011) 13605.
[257] S.A. Kim, M.A. Abbas, L. Lee, B. Kang, H. Kim, J.H. Bang, Control of morphology and defect density in zinc oxide for improved dye-sensitized solar cells, Phys. Chem. Chem. Phys. 18 (2016) 30475–30483.
[258] Q.P. Luo, B. Wang, Y. Cao, Single-crystalline porous ZnO nanosheet frameworks for efficient fully flexible dye-sensitized solar cells, J. Alloys Compd. 695 (2017) 3324–3330.
[259] J. Chung, J. Myoung, J. Oh, S. Lim, Synthesis of a ZnS shell on the ZnO nanowire and its effect on the nanowire-based dye-sensitized solar cells, J. Phys. Chem. C 114 (2010) 21360–21365.
[260] N.M. Gómez-Ortíz, J. Idígoras, E. Guillén, A. Hernández, A. Sastre-Santos, F. Fernández-Lázaro, et al., Influence of dye chemistry and electrolyte solution on interfacial processes at nanostructured ZnO in dye-sensitized solar cells, J. Photochem. Photobiol., A 264 (2013) 26–33.
[261] J. Li, X. Sang, W. Chen, C. Qin, S. Wang, Z. Su, et al., The application of ZnO nanoparticles containing polyoxometalates in dye-sensitized solar cells, Eur. J. Inorg. Chem. No. 10–11 (2013) 1951–1959.

[262] M. Navaneethan, J. Archana, M. Arivanandhan, Y. Hayakawa, Chemical synthesis of ZnO hexagonal thin nanodisks and dye-sensitized solar cell performance, Phys. Status Solidi RRL 6 (3) (2012) 120–122.
[263] N.K. Huu, D.Y. Son, I.H. Jang, C.R. Lee, N.G. Park, Hierarchical $SnO_2$ nanoparticle-ZnO nanorod photoanode for improving transport and life time of photoinjected electrons in dye-sensitized solar cell, ACS Appl. Mater. Interfaces 5 (3) (2013) 1038–1043.
[264] X. Liu, G. Wang, A. Ng, F. Liu, Y.H. Ng, Y.H. Leung, et al., Towards low temperature processed ZnO dye-sensitized solar cells, Appl. Surf. Sci. 357 (2015) 2169–2175.
[265] Z. Qin, Y. Huang, J. Qi, L. Qu, Y. Zhang, Improvement of the performance and stability of the ZnO nanoparticulate film electrode by surface modification for dye-sensitized solar cells, Colloids Surf., A: Physicochem. Eng. Aspects 386 (1–3) (2011) 179–184.
[266] T.W. Hamann, A.B.F. Martinson, J.W. Elam, M.J. Pellin, J.T. Hupp, Aerogel templated ZnO dye-sensitized solar cells, Adv. Mater. 20 (8) (2008) 1560–1564.
[267] L.Y. Lin, M.H. Yeh, C.P. Lee, C.Y. Chou, R. Vittal, K.C. Ho, Enhanced performance of a flexible dye-sensitized solar cell with a composite semiconductor film of ZnO nanorods and ZnO nanoparticles, Electrochim. Acta 62 (2012) 341–347.
[268] Y. Wei, C. Xu, S. Xu, C. Li, W. Wu, Z.L. Wang, Planar waveguide-nanowire integrated three-dimensional dye-sensitized solar cells, Nano Lett. 10 (6) (2010) 2092–2096.
[269] P. Uthirakumar, J.H. Kang, S. Senthilarasu, C.H. Hong, The different types of ZnO materials on the performance of dye-sensitized solar cells, Physica E 43 (9) (2011) 1746–1750.
[270] C.Y. Jiang, X.W. Sun, G.Q. Lo, D.L. Kwong, J.X. Wang, Improved dye-sensitized solar cells with a ZnO-nanoflower photoanode, Appl. Phys. Lett. 90 (26) (2007) 2005–2008.
[271] M.H. Lai, M.W. Lee, G. Wang, M.F. Tai, Photovoltaic performance of new-structure ZnO-nanorod dye-sensitized solar cells, Int. J. Electrochem. Sci. 6 (2011) 2122–2130.
[272] M.M. Rahman, N.C.D. Nath, K.-M. Noh, J. Kim, J.-J. Lee, A facile synthesis of granular ZnO nanostructures for dye-sensitized solar cells, Int. J. Photoenergy 2013 (2013) 1–6.
[273] C. Justin Raj, S.N. Karthick, A. Dennyson Savariraj, K.V. Hemalatha, S.K. Park, H.J. Kim, et al., Electrochemical properties of $TiO_2$ encapsulated ZnO nanorod aggregates dye sensitized solar cells, J. Alloys Compd. 537 (2012) 159–164.
[274] O. Lupan, V.M. Guérin, L. Ghimpu, I.M. Tiginyanu, T. Pauporté, Nanofibrous-like ZnO layers deposited by magnetron sputtering and their integration in dye-sensitized solar cells, Chem. Phys. Lett. 550 (2012) 125–129.
[275] Y. Meng, Y. Lin, Y. Lin, Electrodeposition for the synthesis of ZnO nanorods modified by surface attachment with ZnO nanoparticles and their dye-sensitized solar cell applications, Ceram. Int. 40 (1) (2014) 1693–1698.
[276] A.B.F. Martinson, J.W. Elam, J.T. Hupp, M.J. Pellin, ZnO nanotube based dye-sensitized solar cells, Nano Lett. 7 (8) (2007) 2183–2187.
[277] G.J. Fodjouong, Y. Feng, M. Sangare, X. Huang, Synthesis of ZnO nanostructure films by thermal evaporation approach and their application in dye-sensitized solar cells, Mater. Sci. Semicond. Process. 16 (3) (2013) 652–658.
[278] M.-C. Kao, H.-Z. Chen, S.-L. Young, C.-C. Lin, C.-Y. Kung, Structure and photovoltaic properties of ZnO nanowire for dye-sensitized solar cells, Nanoscale Res. Lett. 7 (1) (2012) 260.

[279] Y. Xi, W.Z. Wu, H. Fang, C.G. Hu, Integrated ZnO nanotube arrays as efficient dye-sensitized solar cells, J. Alloys Compd. 529 (2012) 163–168.
[280] M.A. Borysiewicz, S. Chusnutdinow, M. Wzorek, T. Wojciechowski, Dye aggregation influence on dye sensitized solar cell performance in nanocoral ZnO-based thin film cells sensitized with N-719 and rose bengal dyes, Acta Phys. Pol. A 130 (5) (2016) 1187–1189.
[281] J.B. Baxter, E.S. Aydil, Dye-sensitized solar cells based on semiconductor morphologies with ZnO nanowires, Sol. Energy Mater. Sol. Cells 90 (5) (2006) 607–622.
[282] Z.H. Chen, Y.B. Tang, C.P. Liu, Y.H. Leung, G.D. Yuan, L.M. Chen, et al., Vertically aligned ZnO nanorod arrays sentisized with gold nanoparticles for Schottky barrier photovoltaic cells, J. Phys. Chem. C 113 (30) (2009) 13433–13437.
[283] Huang, P.; Ma, C.-W.; Hung, W.; Yang, Y. Synthesis of star-like ZnO nanoparticles and its application in dye-sensitized solar cell. **2012**, 4.
[284] S. Zhu, L. Shan, X. Chen, L. He, J. Chen, M. Jiang, et al., Hierarchical ZnO architectures consisting of nanorods and nanosheets prepared via a solution route for photovoltaic enhancement in dye-sensitized solar cells, RSC Adv. 3 (9) (2013) 2910.
[285] S. Rani, P. Suri, P.K. Shishodia, R.M. Mehra, Synthesis of nanocrystalline ZnO powder via sol-gel route for dye-sensitized solar cells, Sol. Energy Mater. Sol. Cells 92 (12) (2008) 1639–1645.
[286] Y.Y. Xi, Y.F. Hsu, A.B. Djurišić, W.K. Chan, Electrochemical synthesis of ZnO nanoporous films at low temperature and their application in dye-sensitized solar cells, J. Electrochem. Soc. 155 (9) (2008) D595.
[287] F. Fabregat-Santiago, G. Garcia-Belmonte, I. Mora-Seró, J. Bisquert, Characterization of nanostructured hybrid and organic solar cells by impedance spectroscopy, Phys. Chem. Chem. Phys. 13 (20) (2011) 9083.
[288] J. Bisquert, F. Fabregat-Santiago, I. Mora-Seró, G. Garcia-Belmonte, E.M. Barea, E. Palomares, A review of recent results on electrochemical determination of the density of electronic states of nanostructured metal-oxide semiconductors and organic hole conductors, Inorganica Chim. Acta 361 (3) (2008) 684–698.
[289] J. Bisquert, Chemical capacitance of nanostructured semiconductors: its origin and significance for nanocomposite solar cells, Phys. Chem. Chem. Phys. 5 (24) (2003) 5360.
[290] T. Hoshikawa, M. Yamada, R. Kikuchi, K. Eguchi, Impedance analysis of internal resistance affecting the photoelectrochemical performance of dye-sensitized solar cells, J. Electrochem. Soc. 152 (2) (2005) E68.
[291] M. Adachi, M. Sakamoto, J. Jiu, Y. Ogata, S. Isoda, Determination of parameters of electron transport in dye-sensitized solar cells using electrochemical impedance spectroscopy, J. Phys. Chem. B 110 (28) (2006) 13872–13880.
[292] J. Bisquert, Theory of the impedance of electron diffusion and recombination in a thin layer, J. Phys. Chem. B 106 (2) (2002) 325–333.
[293] R. Kern, R. Sastrawan, J. Ferber, R. Stangl, J. Luther, Modeling and interpretation of electrical impedance spectra of dye solar cells operated under open-circuit conditions, Electrochim. Acta 47 (26) (2002) 4213–4225.
[294] A. Hauch, A. Georg, Diffusion in the electrolyte and charge-transfer reaction at the platinum electrode in dye-sensitized solar cells, Electrochim. Acta 46 (22) (2001) 3457–3466.
[295] F. Fabregat-Santiago, J. Bisquert, G. Garcia-Belmonte, G. Boschloo, A. Hagfeldt, Influence of electrolyte in transport and recombination in dye-sensitized solar cells

studied by impedance spectroscopy, Sol. Energy Mater. Sol. Cells 87 (1–4) (2005) 117–131.
[296] F. Fabregat-Santiago, G. Garcia-Belmonte, J. Bisquert, A. Zaban, P. Salvador, Decoupling of transport, charge storage, and interfacial charge transfer in the nanocrystalline $TiO_2$/electrolyte system by impedance methods, J. Phys. Chem. B 106 (2) (2002) 334–339.
[297] Q. Wang, J.-E. Moser, M. Grätzel, Electrochemical impedance spectroscopic analysis of dye-sensitized solar cells, J. Phys. Chem. B 109 (31) (2005) 14945–14953.
[298] J. Bisquert, A. Zaban, P. Salvador, Analysis of the mechanisms of electron recombination in nanoporous $TiO_2$ dye-sensitized solar cells. Nonequilibrium steady-state statistics and interfacial electron transfer via surface states, J. Phys. Chem. B 106 (34) (2002) 8774–8782.
[299] J. Bisquert, V.S. Vikhrenko, Interpretation of the time constants measured by kinetic techniques in nanostructured semiconductor electrodes and dye-sensitized solar cells, J. Phys. Chem. B 108 (2004) 2313–2322.
[300] J. Halme, Linking optical and electrical small amplitude perturbation techniques for dynamic performance characterization of dye solar cells, Phys. Chem. Chem. Phys. 13 (27) (2011) 12435–12446.
[301] A.G. Vega-Poot, M. Macías-Montero, J. Idígoras, A. Borrás, A. Barranco, A.R. Gonzalez-Elipe, et al., Mechanisms of electron transport and recombination in ZnO nanostructures for dye-sensitized solar cells, ChemPhysChem 15 (2014) 1088–1097.
[302] E. Azaceta, J. Idigoras, J. Echeberria, A. Zukal, L. Kavan, O. Miguel, et al., ZnO–ionic liquid hybrid films: electrochemical synthesis and application in dye-sensitized solar cells, J. Mater. Chem. A 1 (35) (2013) 10173.
[303] T. Pauporté, C. Magne, Impedance spectroscopy study of N719-sensitized ZnO-based solar cells, Thin Solid Films 560 (2014) 20–26.
[304] F. Wang, Y. Chen, C. Liu, Q. Ma, T. Zhao, M. Wang, Photoelectrochemical study on the electron transport and recombination kinetics in an urchin-like Zn/ZnO hierarchical nanostructure, RSC Adv. 4 (65) (2014) 34531–34538.
[305] Z. Yang, T. Xu, U. Welp, W.K. Kwok, Enhanced electron transport in dye-sensitized solar cells using short ZnO nanotips on a mirco-textured metal anode, MRS Proc. 1211 (2009) 20521–20526.
[306] W. Chen, Y. Qiu, S. Yang, A new ZnO nanotetrapods/$SnO_2$ nanoparticles composite photoanode for high efficiency flexible dye-sensitized solar cells, Phys. Chem. Chem. Phys. 12 (32) (2010) 9494.
[307] L.Y. Lin, M.H. Yeh, C.P. Lee, C.Y. Chou, K.C. Ho, Flexible dye-sensitized solar cells with one-dimensional ZnO nanorods as electron collection centers in photoanodes, Electrochim. Acta 88 (2013) 421–428.
[308] S. Zhu, L. Shan, X. Tian, X. Zheng, D. Sun, X. Liu, et al., Hydrothermal synthesis of oriented ZnO nanorod-nanosheets hierarchical architecture on zinc foil as flexible photoanodes for dye-sensitized solar cells, Ceram. Int. 40 (8) (2014) 11663–11670.
[309] J.-C. Lin, C.-P. Lee, K.-C. Ho, Zinc oxide synthesis via a microemulsion technique: morphology control with application to dye-sensitized solar cells, J. Mater. Chem. 22 (4) (2012) 1270–1273.
[310] S. Zhu, X. Chen, F. Zuo, M. Jiang, Z. Zhou, D. Hui, Controllable synthesis of ZnO nanograss with different morphologies and enhanced performance in dye-sensitized solar cells, J. Solid State Chem. 197 (2013) 69–74.
[311] J. Liu, A. Wei, Y. Zhao, K. Lin, F. Luo, Dye-sensitized solar cells based on ZnO nanoflowers and $TiO_2$ nanoparticles composite photoanodes, J. Mater. Sci. Mater. Electron. 25 (2) (2014) 1122–1126.

[312] M. Zi, M. Zhu, L. Chen, H. Wei, X. Yang, B. Cao, ZnO photoanodes with different morphologies grown by electrochemical deposition and their dye-sensitized solar cell properties, Ceram. Int. 40 (6) (2014) 7965–7970.
[313] X. Sun, Q. Li, J. Jiang, Y. Mao, Morphology-tunable synthesis of ZnO nanoforest and its photoelectrochemical performance, Nanoscale 6 (15) (2014) 8769–8780.
[314] K.M. Lee, W.H. Chiu, C.Y. Hsu, H.M. Cheng, C.H. Lee, C.G. Wu, Ionic liquid diffusion properties in tetrapod-like ZnO photoanode for dye-sensitized solar cells, J. Power Sources 216 (2012) 330–336.
[315] G. Zamiri, S. Bagheri, Fabrication of green dye-sensitized solar cell based on ZnO nanoparticles as a photoanode and graphene quantum dots as a photo-sensitizer, J. Colloid Interface Sci. 511 (2018) 318–324.
[316] J. Idígoras, L. Pellejà, E. Palomares, J.A. Anta, The redox pair chemical environment influence on the recombination loss in dye-sensitized solar cells, J. Phys. Chem. C 118 (8) (2014) 3878–3889.
[317] A.G. Vega-Poot, M. Macias-Montero, A. Barranco, A. Borras, A.R. Gonzalez-Elipe, G. Oskam, et al., Performance of porous, nanocolumnar ZnO electrodes obtained at low temperature by plasma-enhanced chemical vapor deposition in dye-sensitized solar cells, Energy Environ. Focus 2 (4) (2013) 270–276.
[318] L. Dloczik, O. Ileperuma, I. Lauermann, L.M. Peter, E.A. Ponomarev, G. Redmond, et al., Dynamic response of dye-sensitized nanocrystalline solar cells: characterization by intensity-modulated photocurrent spectroscopy, J. Phys. Chem. B 101 (49) (1997) 10281–10289.
[319] A.J. Frank, N. Kopidakis, J. van deLagemaat, Electrons in nanostructured $TiO_2$ solar cells: transport, recombination and photovoltaic properties, Coord. Chem. Rev. 248 (13–14) (2004) 1165–1179.
[320] A. Kay, M. Grätzel, Low cost photovoltaic modules based on dye sensitized nanocrystalline titanium dioxide and carbon powder, Sol. Energy Mater. Sol. Cells 44 (1) (1996) 99–117.
[321] E. Ramasamy, W.J. Lee, D.Y. Lee, J.S. Song, Portable, parallel grid dye-sensitized solar cell module prepared by screen printing, J. Power Sources 165 (1) (2007) 446–449.
[322] M. Späth, P.M. Sommeling, J.A.M. Van Roosmalen, H.J.P. Smit, N.P.G. Van Der Burg, D.R. Mahieu, et al., Reproducible manufacturing of dye-sensitized solar cells on a semi-automated baseline, Prog. Photovoltaics Res. Appl. 11 (3) (2003) 207–220.
[323] S. Dai, K. Wang, J. Weng, Y. Sui, Y. Huang, S. Xiao, et al., Design of DSC panel with efficiency more than 6%, Sol. Energy Mater. Sol. Cells 85 (3) (2005) 447–455.
[324] H. Pettersson, T. Gruszecki, C. Schnetz, M. Streit, Y. Xu, L. Sun, et al., Parallel-connected monolithic dye-sensitised solar modules, Prog. Photovoltaics Res. Appl. 18 (5) (2010) 340–345.
[325] T.C. Wei, S.P. Feng, Y.H. Chang, S.J. Cherng, Y.J. Lin, C.M. Chen, et al., Fabrication and characterization of interconnected grid-type dye-sensitized solar modules, Int. J. Electrochem. Sci. 7 (12) (2012) 11904–11916.
[326] G.R.A. Kumara, S. Kawasaki, P.V.V. Jayaweera, E.V.A. Premalal, S. Kaneko, Large area dye-sensitized solar cells with titanium based counter electrode, Thin Solid Films 520 (12) (2012) 4119–4121.
[327] L. Han, A. Fukui, Y. Chiba, A. Islam, R. Komiya, N. Fuke, et al., Integrated dye-sensitized solar cell module with conversion efficiency of 8.2%, Appl. Phys. Lett. 94 (2009) 013305 (3pp).
[328] Y. Jun, J. Kim, M.G. Kang, A study of stainless steel-based dye-sensitized solar cells and modules, Sol. Energy Mater. Sol. Cells 91 (9) (2007) 779–784.

[329] W.J. Lee, E. Ramasamy, D.Y. Lee, J.S. Song, Grid type dye-sensitized solar cell module with carbon counter electrode, J. Photochem. Photobiol. A Chem. 194 (1) (2008) 27–30.
[330] Y. Liu, H. Wang, H. Shen, W. Chen, The 3-dimensional dye-sensitized solar cell and module based on all titanium substrates, Appl. Energy 87 (2) (2010) 436–441.

# CHAPTER 7

# $SnO_2$ dye-sensitized solar cells

**Qamar Wali**[1] **and Rajan Jose**[2]
[1]NUTECH School of Applied Sciences and Humanities, National University of Technology, Islamabad, Pakistan
[2]Nanostructures Renewable Energy Materials Laboratory, Faculty of Industrial Sciences & Technology, Universiti Malaysia Pahang, Gambang, Malaysia

## Contents



## 7.1 Introduction

It has been previously shown that $TiO_2$ is the most employed photoanode material in dye-sensitized solar cells (DSSCs). Despite the high surface area of $TiO_2$, it is characterized by slow electron diffusion

*Nanomaterials for Solar Cell Applications*
DOI: https://doi.org/10.1016/B978-0-12-813337-8.00007-2

($\sim 10^{-5}$ cm$^2$ s$^{-1}$) and lower $\mu_e$ ($<1$ cm$^2$ V$^{-1}$ s$^{-1}$), consequently resulting in high charge recombination at the $TiO_2$/electrolyte interface [1]. ZnO is another widely employed photoanode material that has similar band gap ($\sim 3.2$ eV) to $TiO_2$ while providing higher $\mu_e$ than the latter. However, it is chemically unstable with the successful Ru commercial dyes due to the fact that the carboxylic group present in the dye dissolves the ZnO and creates a $Zn^{2+}$/dye aggregate, which consequently affects the electron injection to the metal oxide semiconductor (MOS) [2,3]. Furthermore, $SnO_2$ has a lower Conduction band (CB) edge (more positively located, i.e., $\sim 300-500$ eV) [4–6] than $TiO_2$ (Fig. 7.1B) as it is made of lower energy orbitals (s orbitals) [7]. The lower CB position enables electron injection from the low-lying Lowest unoccupied molecular orbitals (LUMO) sensitizer, such as perylene dyes [9] and PbS quantum dots [10]. The incorporation of such sensitizers may lead to the utilization of the near-infrared part of the solar spectrum. Although $SnO_2$ is one of the earliest materials that showed the photovoltaic effect in the 1980s [11,12], its intrinsic lower CB ($\sim 300$ eV lower than $TiO_2$) results in routinely achieving a low $V_{OC} \sim 500$ mV ($V_{OC}$ for $TiO_2 \sim 800$ mV) despite the high $J_{SC} \geq 15$ mA cm$^{-2}$. Inspired from the high $\mu_e$ of $SnO_2$, a number of researchers have attempted doping various transition metals to uplift its Fermi energy level; for example, Zn-doped $SnO_2$ resulted in a $V_{OC} \sim 780$ mV [13]. Various semiconductor divalent metal oxides, such as Cd, Ni, Cu, and Pb are doped in $SnO_2$ to improve its performance in DSSCs [14]. Such dopants enhanced the surface area, the dye loading, raised its flat-band potentials, and eventually enhanced the $\eta$ compared to a pure $SnO_2$-based DSSCs. Despite these advancements, $\eta$ of $SnO_2$-based DSSCs remains lower than that of the state-of-the-art $TiO_2$.

Another issue with $SnO_2$ is its low iso-electric point (IEP) (pH $\sim 4-5$) compared to that of $TiO_2$ (pH $\sim 6-7$) and ZnO (pH $\sim 9$) [15], which makes weak bonding with the carboxylic groups upon dye anchoring, and consequently yielding low photocurrent in DSSCs. Toward this end, a number of $SnO_2$ morphologies other than nanoparticles (NPs), such as nanotubes (NTs), core–shell structures, and composite nanostructures are employed in DSSCs. These structures provide two advantages: (1) provide larger surface area for dye loading and (2) a directed transport path for electron diffusion. Such developments have brought $SnO_2$ to deliver $\eta$ as high as $\sim 4\%$ in its pure form and 7.6% in hybrid photoanodes [16].

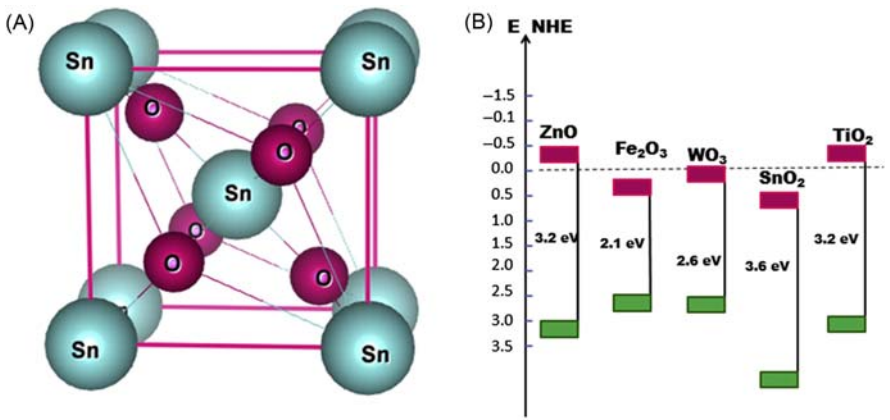


**Figure 7.1** (A) Shows the crystal structure of rutile $SnO_2$ where the big balls atoms are tin and the small balls are oxygen [7], (B) compare the energy band diagram of various MOS [8]. *MOS*, Metal oxide semiconductor.

### 7.1.1 Tin oxide

Tin oxide ($SnO_2$) is an archetypical *n*-type MOS with high transparency and conductivity, which shows outstanding performance in many electronic devices such as DSSCs [6,16,17], lithium ion batteries [18], catalysis [19], and gas sensors [20]. The $SnO_2$ crystallizes into the following polymorphs: rutile type ($P4_2/mnm$), pyrite type (Pa3), $CaCl_2$ type ($Pnnm$), $ZrO_2$ type orthorhombic phase I (*Pbca*), α-$PbO_2$ type (*Pbcn*) [20]. Among these, the most important naturally occurring polymorph is the cassiterite $SnO_2$ which crystallizes in rutile tetragonal structure at ambient temperature with space group $P4_2/mnm$. Its crystal structure diagram is shown in Fig. 7.1A. The unit cell of $SnO_2$ consists of six atoms: two tin (Sn) and four oxygen atoms where each Sn atom exists at the center of a regular octahedron. Among the various MOS, $SnO_2$ possess the lowest CB as shown in Fig. 7.1B. The top of the valence band is made of O (2p) orbital states, whereas the bottom of the CB has Sn (4s) and O (2p) states [7,20]. The lattice parameters of $SnO_2$ are $a = b \sim 4.74$ Å, $c \sim 3.18$ Å, and the interplanar spacing are $d_{1\,1\,0} = 3.35$ Å, $d_{1\,0\,1} = 2.65$ Å, $d_{2\,0\,0} = 2.37$ Å, $d_{2\,1\,1} = 1.77$ Å, and $d_{2\,2\,0} = 1.68$ Å, with unit cell volume = 71.54 $Å^3$ [20].

## 7.2 Various $SnO_2$ nanostructures employed as photoanodes in dye-sensitized solar cells

Various $SnO_2$ nanostructures have been employed as a photoanode in DSSCs with specific purposes. For instance, NPs function for large surface area while nanospheres (NSs) perform best for light scattering and harvesting purposes. On the other hand, one-dimensional (1D) nanostructures include nanorods (NRs), NTs and nanowires (NWs), which are expected to enhance the charge transport properties in the photoanode. Moreover, three-dimensional (3D) nanomorphologies are employed, such as flower or mixing of NPs and 1D nanostructures in order to perform dual functions in the photoanode of the DSSCs, such as allow a large amount of dye loading as well as superior charge transport properties.

### 7.2.1 Pure $SnO_2$ nanostructures based on nanoparticles in dye-sensitized solar cells

A tin oxide NPs and multifunctional NPs−NSs were synthesized in order to achieve a high surface area and superior light harvesting properties by

controlling the annealing temperature. The materials thus synthesized were developed for DSSCs electrodes, and scientists evaluated their performance. The details of material characteristics, optical properties of the electrodes developed, and results of solar cell testing are described.

## 7.2.2 Characterization of synthesized nanostructures

### *7.2.2.1 X-rays diffraction analysis*

Three samples were synthesized at three temperatures, viz. 150°C, 180°C, and 200°C, which are labeled as sample 150°C, sample 180°C, sample 200°C, respectively. The X-rays diffraction (XRD) patterns of these samples show similarity in the peak position and intensity distribution as can be seen in Fig. 7.2. All the peaks could be indexed to the tetragonal rutile $SnO_2$ (cassiterite phase, space group $P4_2/mnm$, JCPDS file card #41-1445). The samples synthesized at lower temperatures (≦180°C) showed (1 1 0), (1 0 1) (2 0 0), (2 1 1), and (3 0 1) planes. However, few extra planes (2 2 0), (0 0 2), (3 1 0), and (2 0 2) are observed in the sample synthesized at 200°C, which is due to its higher crystallinity. The crystallinity of the materials was evaluated from the full width at half maximum (FWHM) of the major reflections, that is, (1 1 0), (1 0 1), and (2 1 1) plane employing the Scherrer equation and shown in Table 7.1. Clearly, as the temperature increased from 150°C to 200°C the crystallite size increased from 0.8 to 10.6 nm. The calculated lattice parameters from the XRD patterns are $a = b \sim 4.738$ Å and $c \sim 3.187$ Å, which are in good

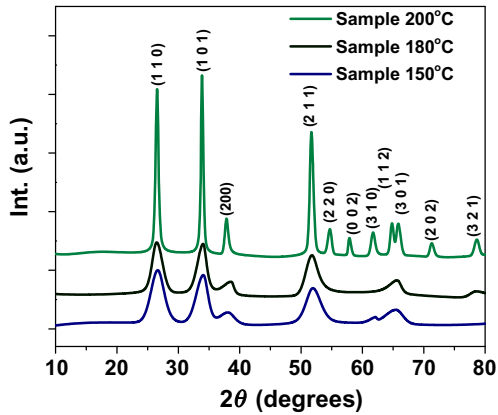


**Figure 7.2** XRD pattern of the synthesized samples at three different temperatures (150°C, 180°C, and 200°C).

**Table 7.1** FWHM (B) of the three principal (1 1 0), (1 0 1), and (2 1 1) planes and their crystallite sizes of the $SnO_2$ synthesized nanostructures at temperatures (150°C, 180°C, and 200°C) calculated using Scherrer's equation.

| Synthesized samples (°C) | (1 1 0) | | (1 0 1) | | (2 1 1) | |
|---|---|---|---|---|---|---|
| | FWHM (B) (degrees) | Crystallite size (nm) | FWHM (B) (degrees) | Crystallite size (nm) | FWHM (B) (degrees) | Crystallite size (nm) |
| 150 | 2.54 | 0.78 | 2.27 | 1.59 | 2.85 | 1.05 |
| 180 | 1.98 | 0.99 | 1.80 | 1.60 | 2.34 | 1.29 |
| 200 | 0.55 | 3.02 | 0.43 | 10.58 | 0.67 | 2.26 |

**Table 7.2** XRD data of the $SnO_2$ nanostructures synthesized at three temperatures (150°C, 180°C, and 200°C) by hydrothermal method.

| $2\theta$ (degrees) | $d$ (Å) | ($h$ $k$ $l$) | $I/I_o$ | | |
|---|---|---|---|---|---|
| | | | 150°C | 180°C | 200°C |
| 26.46 | 3.36 | (1 1 0) | 1 | 1 | ~0.94 |
| 33.82 | 2.64 | (1 0 1) | 0.91 | 0.97 | 1 |
| 37.76 | 2.38 | (2 0 0) | 0.28 | 0.54 | 0.43 |
| 51.63 | 1.76 | (2 1 1) | 0.7 | 0.85 | 0.77 |
| 54.49 | 1.68 | (2 2 0) | – | – | 0.39 |
| 58.00 | 1.58 | (0 0 2) | – | – | 0.36 |
| 61.62 | 1.50 | (3 1 0) | 0.20 | – | 0.38 |
| 64.71 | 1.43 | (1 1 2) | – | – | 0.42 |
| 65.66 | 1.42 | (3 0 1) | 0.33 | 0.56 | 0.41 |
| 71.42 | 1.32 | (2 0 2) | – | – | 0.34 |
| 78.29 | 1.22 | (3 2 1) | 0.64 | 0.43 | 0.35 |

agreement with that reported (JCPDS file card #41-1445). The XRD data of the materials are given in Table 7.2.

#### *7.2.2.2 Morphological study*

The morphologies and surface analysis of the three samples (150°C, 180°C, and 200°C) were studied using field emission scanning electron microscope (FESEM) analysis. Fig. 7.3A shows that the sample 150°C consists of uniform NPs distribution with a diameter in the range of ~10 to ~30 nm. The particles are distributed in a wide range with less agglomeration revealing porosity in the nanostructure. When the temperature is increased to 180°C, the FESEM images in Fig. 7.3C show a bimodal distribution of spheroidal particles one of which centered at 10–30 nm (as for the sample 150°C) and the other centered at ~700–800 nm.

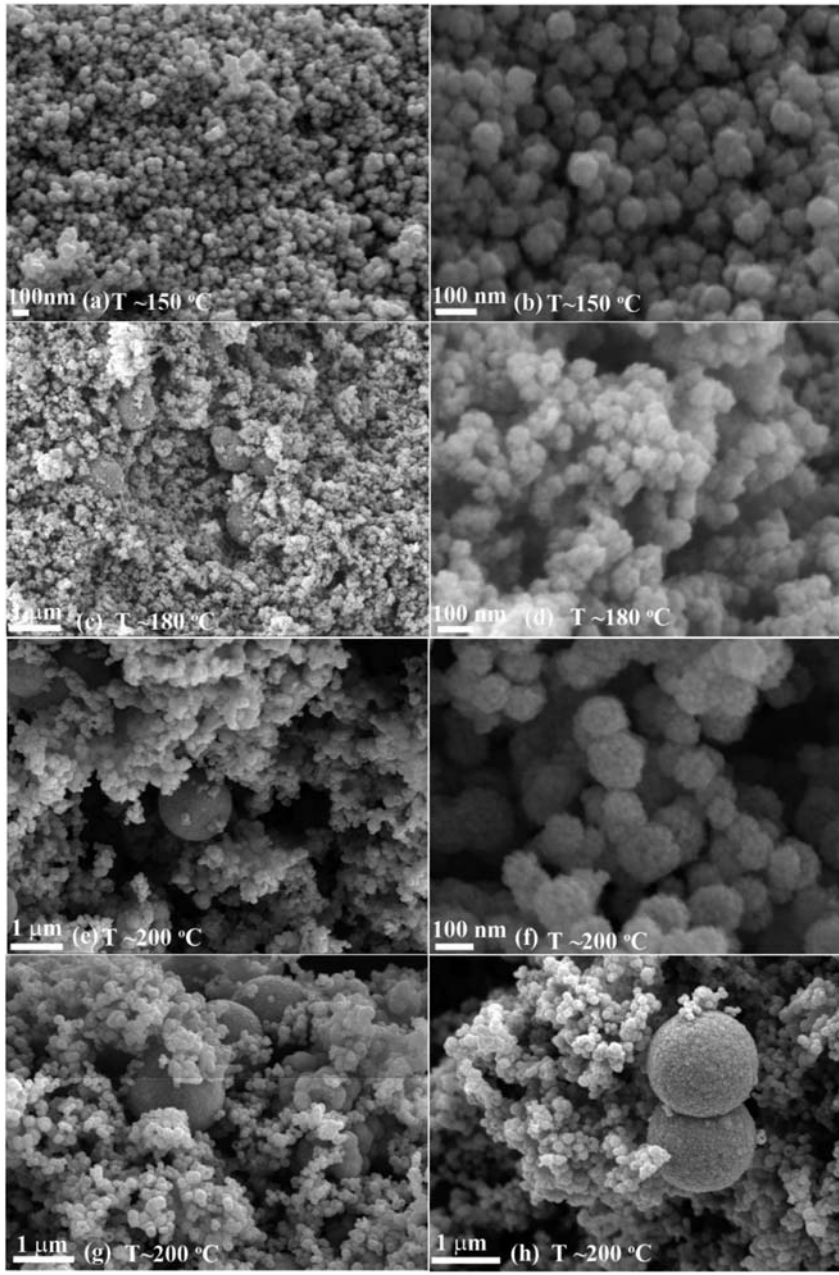


**Figure 7.3** FESEM images of the synthesized nanostructures (A and B) "sample 150° C", (C and D) "sample 180°C", and (E—H) "sample 200°C".

However, a close examination (Fig. 7.3D) shows that the basic building blocks of the bigger particle remained at ~10–30 nm. Bigger particles further grow >1 μm at 200°C with relatively large size distribution and wider gaps among the individual particles as shown in Fig. 7.3E–H. Moreover, hollow NPs are also observed having size in a nanometric scale (~50–100 nm). This unique nanostructure "sample 200°C" having a hollow nature and wider gaps among the NPs was further investigated using TEM analysis in order to elaborate its nature.

It can be observed from Fig. 7.3C, G, and H that the distribution of small NPs and big spheres are not uniform. The proportion of small NPs (~100 nm) are about 70% while only about 30% for the big spheres (>1 μm). The hydrothermal method exploits that by increasing temperature and pressure, the fundamental properties of water and thus its abilities as a solvent changes. Important characteristics such as the ionic product, density, thermal conductivity, viscosity, heat capacity and the dielectric constant are all highly pressured and temperature dependent. By tuning the synthesis parameters, specific solvent properties can be obtained. The theory of the hydrothermal process uses simple thermodynamic functions to describe the formation of the nuclei that lead to particle formation. This activity is described by a process called nucleation. Generally, atoms in solvent liquid phase fluctuate due to thermal motion. This fluctuation of atoms leads to the formation of atomic assemblies with local structures similar to those found in solid phase. When stable nuclei have formed in the solid/liquid interface, the particle starts growing to form a bigger particle. This leads to re-dissolution of the newly formed particles, creating a concentration gradient in the solution. Uniformity of the concentration is reestablished by material diffusion toward the larger particles, thus leading to a kind of particle growth called Ostwald ripening. Fig. 7.4A shows a typical TEM images of the sample 200°C. Spherical multifunctional (NPs–NSs) of large size distribution in the range of ~50 nm–1 μm was observed; particles in each particle remain practically constant at ~10 nm. All multifunctional particles, including the smaller ones, showed partial transparency to the electron beam. From this it is inferred that the multifunctional specimens are hollow. The hollow nature of the multifunctional (NPs–NSs) could also be observed from SEM (Fig. 7.3G and H). The crystallinity of the sample was judged from the high-resolution transmission electron microscopy (HRTEM) lattice images and selected area electron diffraction (SAED) patterns, which are shown in Fig. 7.4B.

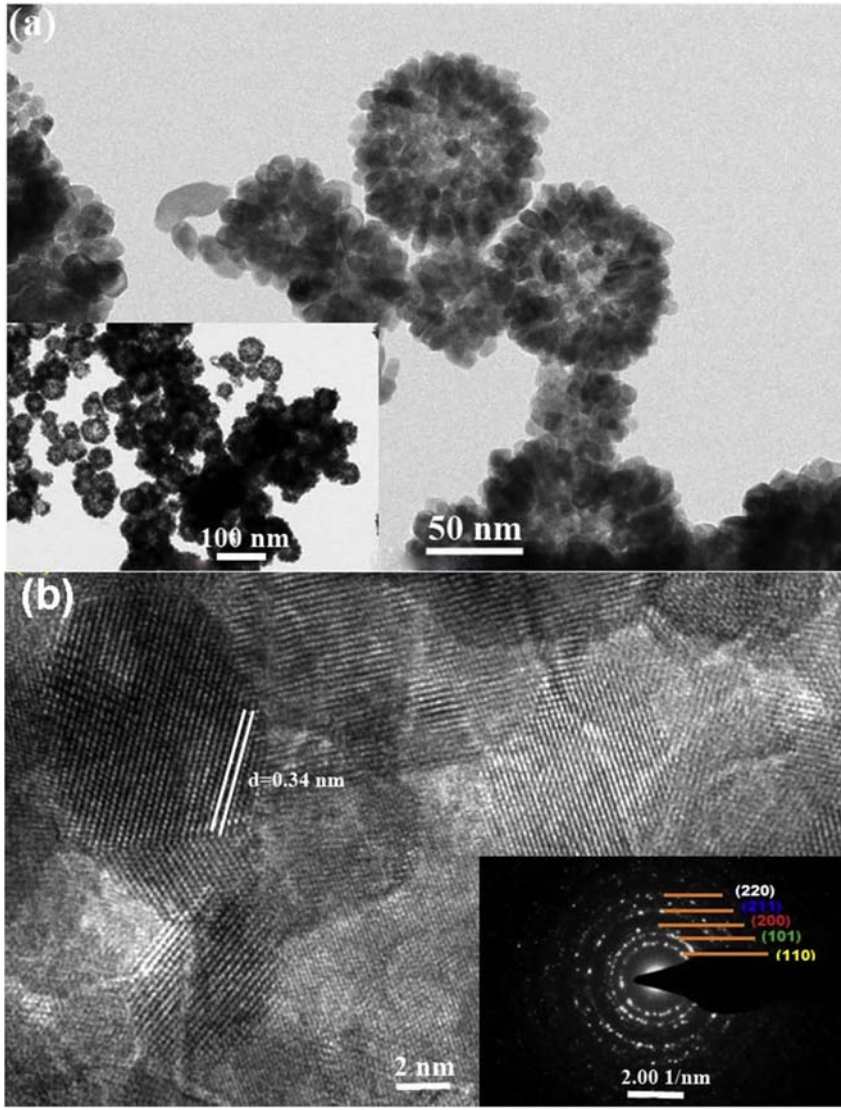


**Figure 7.4** TEM images (A) at low magnification and (B) magnified HRTEM and (inset SAED image) of the sample synthesized at 200°C.

The HRTEM images showed multifunctional (NPs−NSs) specimens of defect-free nanograins with lattice fringe ∼0.34 nm and SAED pattern (shown in the inset of the Fig. 7.4B) revealed diffraction spots oriented along a circle where the bright circles represent the polycrystalline nature of the structure and could be related to the XRD data. These observations

**Table 7.3** BET surface area, pore sizes, and pore volume distribution of the synthesized samples at three temperatures.

| Sample | BET ($m^2\ g^{-1}$) | Pore size (nm) | Pore volume ($cm^3\ g^{-1}$) |
|---|---|---|---|
| 150°C | 50 | 11.7 | 0.09 |
| 180°C | 45 | 13.1 | 0.15 |
| 200°C | 29 | 15.1 | 0.19 |

show that the particles are of high crystallinity. In the XRD pattern, sharp and intense peaks of the sample 200°C reveal that they are highly crystalline, as observed from the HRTEM images and SAED patterns. Smaller particles with superior crystallinity are recommended for efficient charge transport in DSSCs while anchoring a large amount of dyes [21].

#### *7.2.2.3 Gas adsorption studies*

The specific surface area, pore size, and volume distribution were studied by Brunner-Emmett-Teller (BET) method in a nitrogen adsorption and a desorption environment. The particulate properties of the samples, such as surface area, pore size and volume distributions are listed in Table 7.3. The BET surface area was $\sim 50$, $\sim 46$, and $\sim 29\ m^2\ g^{-1}$, respectively, for samples 150°C, 180°C, and 200°C. The lowering of surface area could be due to the formation of multifunctional (NPs−NSs) at high temperature for samples 180°C and 200°C. The high surface area and varying pore size are beneficial for the DSSCs as they help in large dye loading and help improving permeations of the electrolyte. The adsorption−desorption isotherm of the three samples correspond to type IV isotherm are shown in Fig. 7.4. The area under hysteresis loops increased with the processing temperature thereby indicating increasing the pore size distribution (Fig. 7.5).

### 7.2.3 Dye-sensitized solar cells fabrication and testing

#### *7.2.3.1 Morphology and thickness of the electrodes*

Fig. 7.6 shows a typical FESEM image (sample 200°C) showing the cross-section of the electrode of thickness $\sim 8.5-12\ \mu m$. The particles were well sintered onto Fluorine doped Tin Oxide (FTO); a closer examination shows sporadic distribution of larger particles as well as their shell structure (Fig. 7.6F). The hollow structures retained their initial morphology even after extensive mechanical agitation during the paste-making

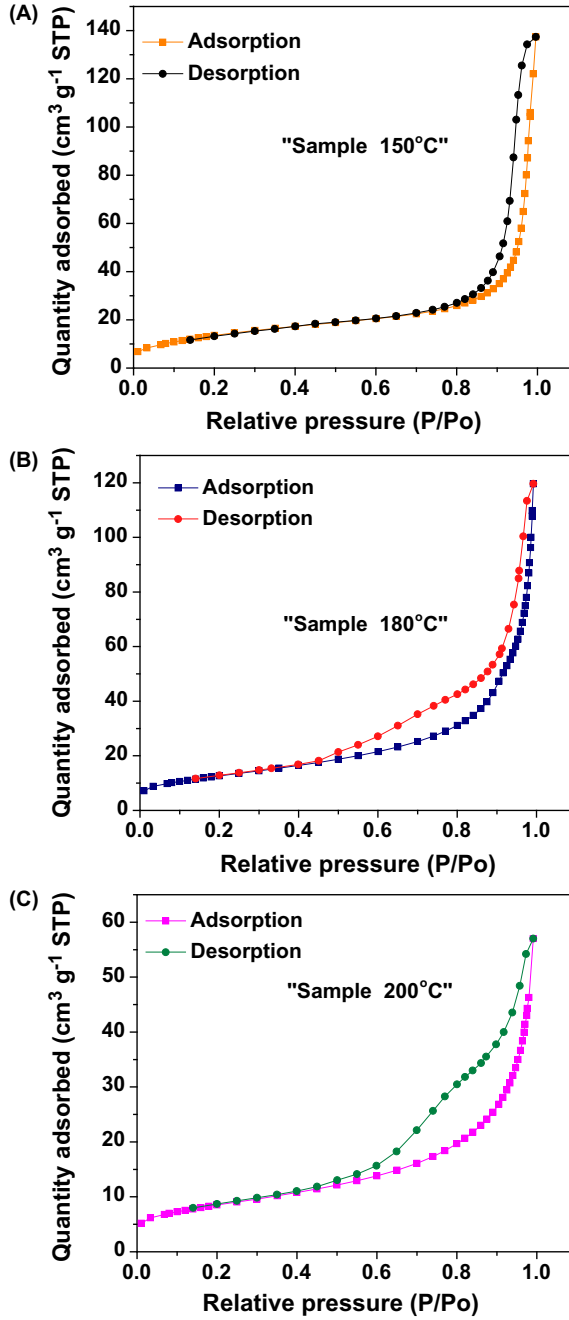


**Figure 7.5** Gas adsorption–desorption isotherm curve of (A) sample 150°C, (B) sample 180°C, and (C) sample 200°C.

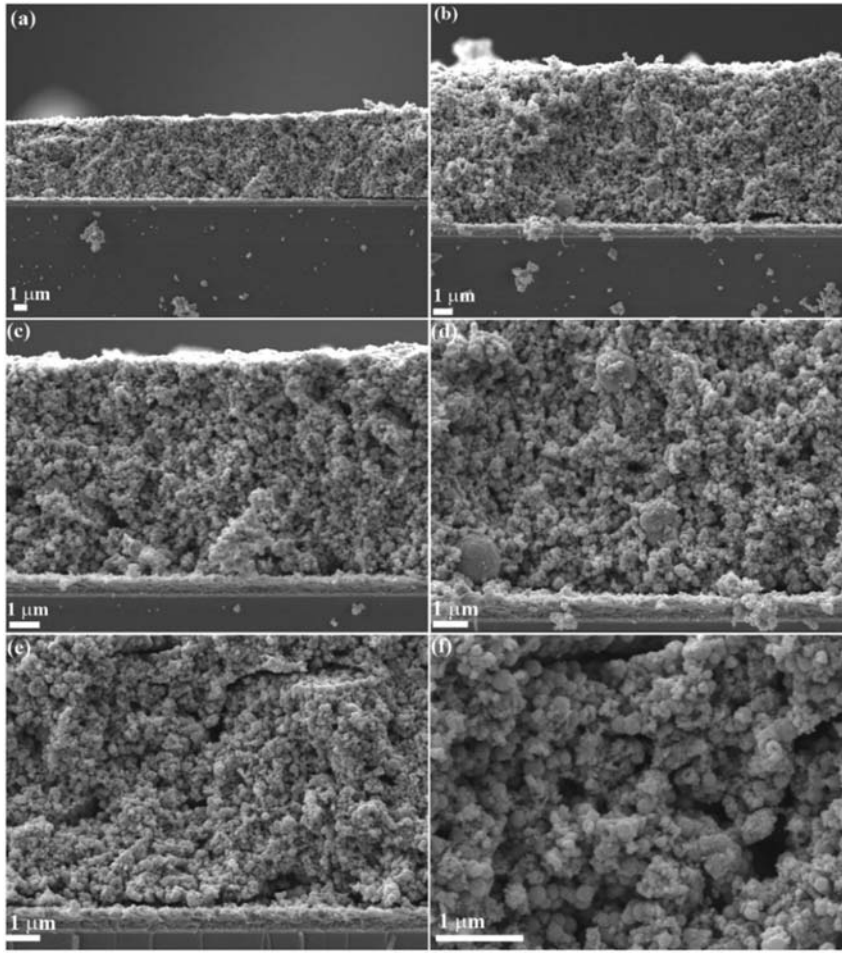


**Figure 7.6** SEM cross-section of the fabricated DSSC electrode using sample 200° C at various magnifications (a–f), where the magnification level increase from (a) to (f).

procedure and subsequent thermal annealing. No agglomeration was found in the WE film; ensuring high porosity for electrolyte permeation.

#### *7.2.3.2 Light scattering properties of the dye-anchored electrodes*

The light harvesting properties of the dye-anchored working electrode (WE) were studied by UV–vis–NIR absorption spectroscopy. The light scattering properties of the electrodes were studied by recording their absorbance (Fig. 7.7), transmittance (Fig. 7.8), and reflectance spectra

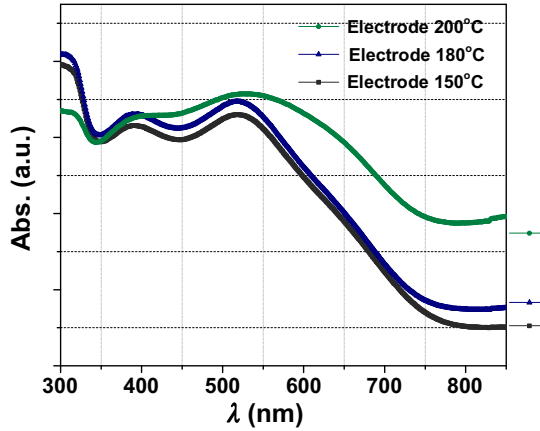


**Figure 7.7** Absorption spectra of three dye-anchored photoanodes synthesized at different temperatures (150°C, 180°C, and 200°C).

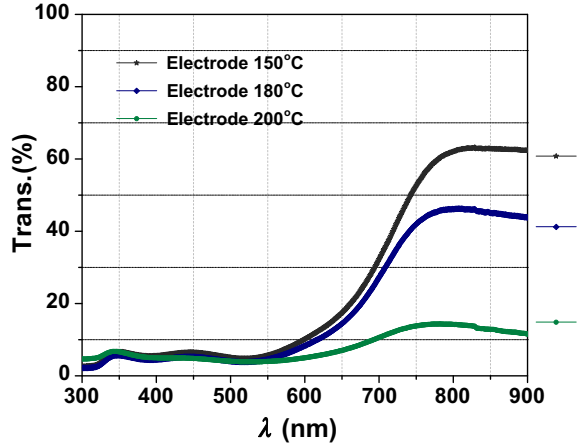


**Figure 7.8** Transmission spectra of three dye-anchored electrodes.

(Fig. 7.9). Fig. 7.7 shows that electrodes of samples 150°C and 180°C showed similar absorbance, although slightly improved absorbance was observed for the latter in spite of lower dye loading. Light scattering by the larger particles is responsible for this increment in absorbance. The electrode of sample 200°C showed a larger absorption cross-section (i.e., the area under the absorbance curve due to the presence of larger particles in spite of its inferior dye loading) than that of the other two samples (150°C and 108°C).

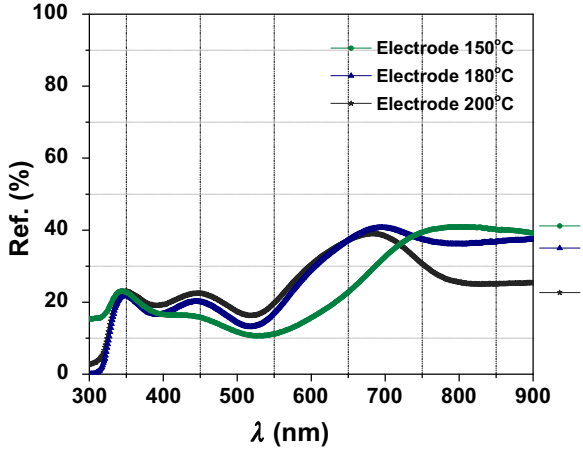


**Figure 7.9** Reflection spectra of three dye-anchored electrodes (150°C, 180°C, and 200°C).

The superior light harvesting property of the electrode 200°C is more obvious in the transmittance spectra (Fig. 7.8). As the size of the particles in sample 200°C corresponds to the wavelength of the vis (∼360−700 nm) and NIR (∼700 nm to ∼2.5 μm) regions of the light, a strong light scattering could be expected. Moreover, the presence of micron and mesoporous sized NPs would increase the reflection of light and eventually enhance the optical path length for incident photons [22]. The transmittance of the electrodes were ∼34%, ∼30%, and <10% at the dye's absorption wavelength range for electrodes 150°C, 180°C, and 200°C, respectively. Thus ∼90% of the incident light is absorbed by the electrode 200°C, whereas a considerable portion of the incoming light is transmitted in the other electrodes (150°C and 180°C).

In a diffuse reflection (Fig. 7.9), incident photons are reflected in all directions by the photoanode, thereby increasing the light harvesting efficiency (LHE). If the internal diffuse reflection is taken into consideration, electrode 200°C has a higher reflectance >700 nm owing to its comparable size together with macro and mesopores, which is expected to increase the incident light reflected and scattered inside the photoanode. However, if the external reflectance is taken into consideration, the electrode 200°C possesses lower reflectance in the 350−700 nm range than electrodes 150°C and 180°C. This low reflectance of the electrode 200°C reveals high absorbance; and therefore, leads to high PV parameters.

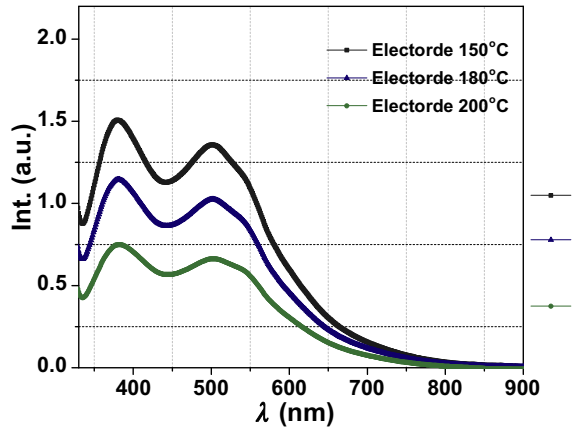


**Figure 7.10** Absorption spectra of unloaded dye of electrodes (150°C, 180°C, and 200°C).

Dye loading of the dye-anchored electrodes was measured by a desorption test as shown in Fig. 7.10. The spectra of the desorbed dye solution show that the electrode of 150°C has the highest absorption, while the least was shown for the 200°C. The calculated dye loading values were ~278, ~203, and ~131 nmol $cm^{-2}$ for 150°C, 180°C, and 200°C electrodes, respectively. The difference in the dye loading is due to the fact that they have differences in BET surface area, and also due to their varying pores and volumetric size distribution (Table 7.3). It is a well-known fact that small particles possess high surface area and, consequently, this causes an anchoring of large amounts of dye and vice versa.

#### *7.2.3.3 Photovoltaic characteristics of fabricated dye-sensitized solar cells*

To observe the performance of the NPs and multifunctional (NPs–NSs) as WE in DSSCs, $J-V$ characteristics were performed under a standard solar simulator at 1 Sun condition as illustrated in Fig. 7.11. The photovoltaic (PV) parameters of DSSCs based on the sample (150°C, 180°C, and 200°C) are tabulated in Table 7.4. The $\eta$ of the DSSCs increased in the order of $\eta_{DSSC\ 200°C} > \eta_{DSSC\ 180°C} > \eta_{DSSC\ 150°C}$, respectively. The DSSCs 200°C showed the highest $J_{SC}$ compared to the other two types (DSSC 150°C and 180°C), which could be attributed to the increased light scattering properties of the former electrode as discussed in the earlier section. The DSSCs of 200°C showed the comparable $\eta \sim 4.0\%$ to date using a pure form of $SnO_2$ with other PV parameters such as

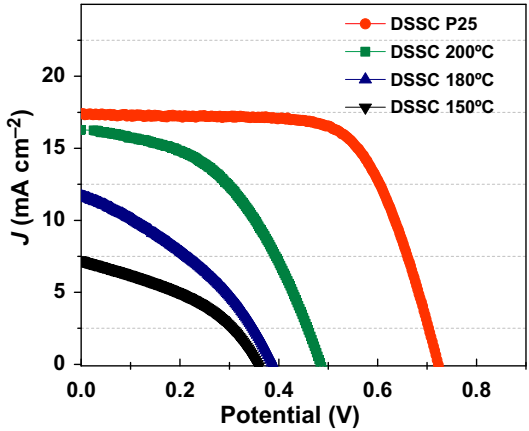


**Figure 7.11** PV characteristic curves of DSSCs based on 150°C, 180°C, 200°C, and P25 NPs at 1 Sun condition. *DSSC*, Dye-sensitized solar cell.

**Table 7.4** Photovoltaic parameters of dye-sensitized solar cells (DSSCs) [$J_{SC}$, $V_{OC}$, fill factor (FF), $\eta$ and dye loading] based on synthesized samples 150°C, 180°C, 200°C, and P25 nanoparticles, respectively.

| Devices | $J_{SC}$ (mA cm$^{-2}$) | $V_{OC}$ (V) | FF | $\eta$ (%) | Dye loading (nmol cm$^{-2}$) |
|---|---|---|---|---|---|
| DSSC 150°C | 07.2 | 0.37 | 0.38 | 1.02 | 278 |
| DSSC 180°C | 11.1 | 0.40 | 0.37 | 1.62 | 203 |
| DSSC 200°C | 16.3 | 0.49 | 0.50 | 4.0 | 131 |
| DSSC P25 | 16.4 | 0.72 | 0.61 | 7.2 | 702 |

$J_{SC} \sim 16.3$ mA cm$^{-2}$, $V_{OC} \sim 491$ mV, and fill factor (FF) $\sim 0.50$ achieved so far. For comparison, a DSSC based on commercial $TiO_2$ P25 was also prepared as a reference, and its PV parameters are listed in Table 7.4 and the IV characteristic curve is shown in Fig. 7.11. Both the DSSCs, that is, DSSC 200°C and P25 DSSC, resulted in a similar $J_{SC}$, however, the latter has far higher FF and $V_{OC}$.

In addition, a systematic improvement in $V_{OC}$ [$V_{OC\ (DSSC\ 200°C)} > V_{OC\ (DSSC\ 180°C)} > V_{OC\ (DSSC\ 150°C)}$] was observed in the three sets of devices despite the chemical similarity of the WE material. This increase in $V_{OC}$ could be due to increased light scattering achieved using varying particle size and crystallinity. In terms of FF, DSSCs 200°C have better value compared to the other two types of DSSCs 150°C and 180°C. This improved FF might be due to the pore widening of the pore-size distribution of the former sample. Chen et al. synthesized

mesoporous $TiO_2$ beads with surface areas up to 108 $m^2\ g^{-1}$ with pore sizes (pore diameters varying from 14.0 to 22.6 nm) via a facile combination of sol–gel and solvothermal processes [23]. In comparison, our fabricated nanostructures possess lower surface area with almost the same pore size distribution and shape diameter, however, the higher $J_{SC}$ could be attributed to the multiple factors including improved light scattering and high $\mu_e$ of $SnO_2$. The observed higher $J_{SC}$ of the DSSCs 200°C can be credited to (1) the presence of small hollow NPs providing more sites (inner and outer surface) for dye anchoring, whereas micrometer sized spheres offer less grain boundaries and therefore minimize the loss of electrons during transportation and (2) this type of nanostructure with varying particle size can have more chances for an electrolyte penetration owing to its high porosity.

#### 7.2.3.4 Charge transport parameters

An impedance spectroscopy analysis of DSSC 200°C was compared with DSSC P25 as shown in Fig. 7.12. The Nyquist plot of DSSC 200°C shows a smaller diameter than that of DSSC P25, as can be seen in Fig. 7.12A. This thereby resulted in a sever electron recombination with the electrolyte species. To further identify the lower performance of DSSC 200°C as compared to the $TiO_2$ counterpart, the charge transport parameters were extracted using Z-view software of the well-known Bisquert transmission line model [24]. The DSSC 200°C exhibits an inferior $R_{CT}$ value (i.e., the value was $\sim$19 Ω for DSSC 200°C and $\sim$70 Ω for DSSC P25). On the other hand, DSSC 200°C shows a surprisingly lower $R_T$ ($\sim$10 Ω) and it was very high for DSCC P25 ($\sim$43 Ω). It is a well-known fact that $TiO_2$ NPs possess detrimental grain boundaries between individual NPs and also characterized by low $\mu_e$, thereby leading to higher $R_T$ value [25–27].

The $\tau_n$ was calculated for both DSSCs using the mid frequency of the bode-phase plots (Fig. 7.12B) using a relation $\tau_n = 1/2\pi f_o$ [28] where $f_o$ is the maximum frequency at the mid peak. The calculated value of $f_o$ was $\sim$18.0 and $\sim$29.3 Hz, with corresponding $\tau_n \sim 8.85$ and $\sim$5.3 ms for DSSC 200°C and DSSC P25, respectively.

The difference in $\eta_{cc}$ of the DSSCs was investigated using the incident photon to current efficiency (IPCE) spectra. Fig. 7.13 compares the IPCE spectra of the DSSC 200°C and DSSC P25. The highest IPCE was $\sim$78% for DSSC 200°C and $\sim$72% for DSSC P25 at a particular $\lambda \sim 520$ nm near the peak absorbance of the N3 sensitizer. The enhanced

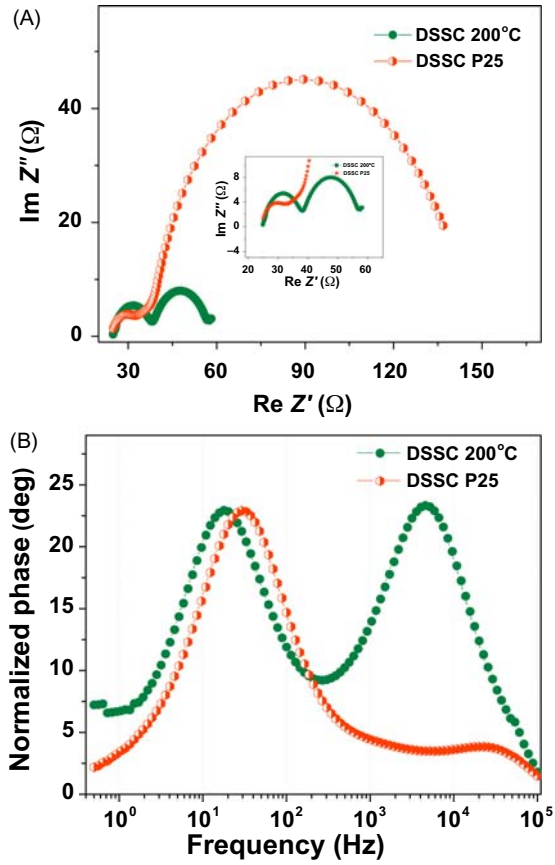


**Figure 7.12** (A) Shows the Nyquist plot, while (B) depicts bode-phase plots of DSSC 200°C and DSSC P25. *DSSC*, Dye-sensitized solar cell.

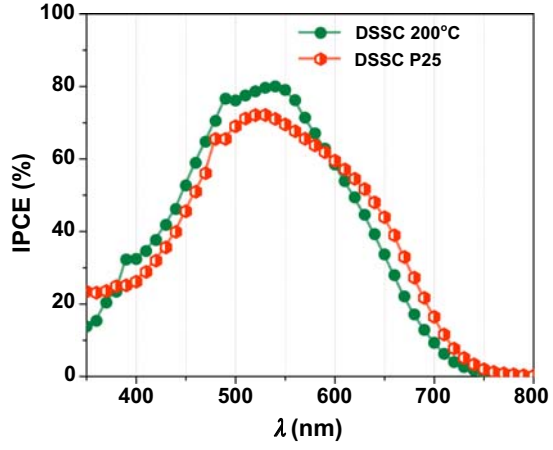


**Figure 7.13** IPCE characteristic curve of DSSC 200°C and DSSC P25. *DSSC*, Dye-sensitized solar cell.

IPCE curve of DSSC 200°C could be due to the improved light scattering capability of the multifunctional (NPs−NSs) composed of variable particle sizes, despite the fact that it resulted in low surface area ($\sim 29\ m^2\ g^{-1}$) and subsequently inferior dye loading. Furthermore, the $J-V$ data was validated from the IPCE measurements of the DSSCs by calculating the $J_{SC}$ using a relation.

The integrated IPCE over the entire wavelength ($\lambda \sim 300-800$ nm) was used to calculate the $J_{SC}$ as depicted in Fig. 7.13. The calculated $J_{SC}$ of the DSSC 200°C ($\sim 14\ mA\ cm^{-2}$) and PDSSC P25 ($\sim 15\ mA\ cm^{-2}$) agrees with their measured $J_{SC}$ (Table 7.4).

The measured open-circuit voltage decay (OCVD) curves of the DSSC 200°C and DSSC P25 are shown in Fig. 7.14A while Fig. 7.14B compares the $\tau_n$ of both DSSCs measured from the OCVD curves using the following relation:

$$\tau_n = -\left(\frac{k_B T}{e}\right)\left(\frac{dV_{OC}}{dt}\right)^{-1}$$

In the OCVD curve, both the DSSCs show a similar decaying over the entire time, although $SnO_2$ has shown low $R_{CT}$ (i.e., recombination of photo-induced electrons with electrolyte is faster for $SnO_2$ than $TiO_2$). On the other hand, DSSC 200°C exhibits comparable $\tau_n$ over the low voltage range to that of DSSC P25. However, at a typical voltage of $\sim 300$ mV, the calculated $\tau_n$ for the former was $\sim 0.7$ and $\sim 1.5$ seconds for the latter. The detailed PV parameters of $SnO_2$ NPs and multifunctional NPs in pure form employed as photoanode in DSSCs are listed in Table 7.5.

Similarly, other reports showed improved performance employing NPs photoanodes. For instance, $SnO_2$ NPs (surface area ranging from $\sim 44$ to $57\ m^2\ g^{-1}$) have been employed as bi-layered nanostructures (having sizes $\sim 15-20$ and $\sim 50-150$ nm) photoanode and demonstrated $\eta \sim 4\%$ [31]. Another report on NPs/NSs by Wang et al., employing $SnO_2$ NSs by hydrothermal method (surface area of $\sim 64.2\ m^2\ g^{-1}$) resulted in $\eta \sim 0.86\%$ using pure NSs which enhanced 8 times ($\eta \sim 6.02\%$) upon $TiCl_4$ aqueous solution treatment. Surprisingly, despite its higher surface area ($\sim 64.2\ m^2\ g^{-1}$), the $\eta$ is lower ($\sim 0.86\%$) than that reported by Cojocaru et al. [31]. These results show that the performance of DSSC does not depend on surface area alone. This is also evidenced by the work of Reda et al. showing that $SnO_2$ NPs of high surface area

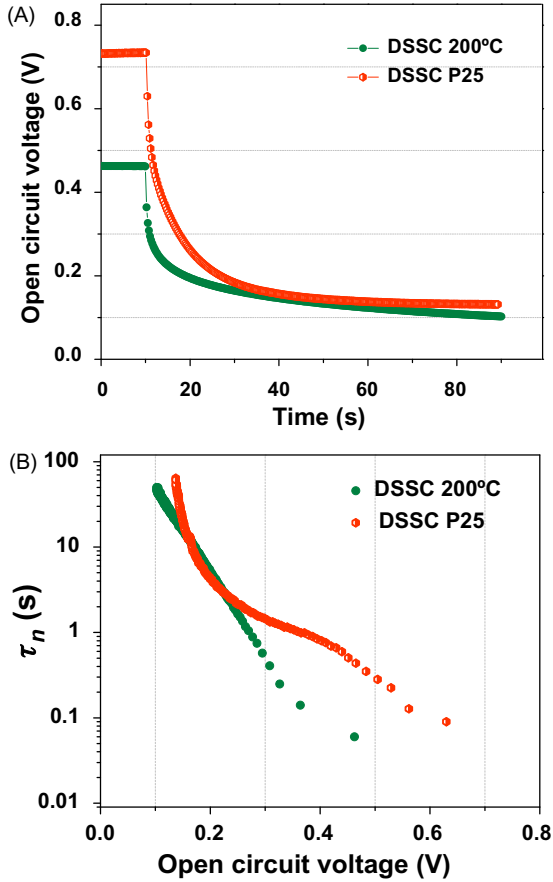


**Figure 7.14** (A) Shows the OCVD curve of DSSC 200°C versus DSSC P25 and (B) illustrates $\tau_n$ versus $V_{OC}$ for the respective devices. *DSSC*, Dye-sensitized solar cell.

($\sim 140\ m^2\ g^{-1}$) as a photoanode and Erythrosine dye gave $\eta \sim 0.06\%$ ($J_{SC} < 1\ mA\ cm^{-2}$ and $V_{OC}$ of $\sim 200\ mV$) [72]. A similar report by Li et al., which performed a comparative study between bigger size macroporous particles possessing less surface area versus smaller NPs of size $\sim 10\ nm$ with high surface area, resulted in a 10% improvement in $\eta$ in the former based DSSCs, despite the fact that the latter possess larger dye loading [73].

These studies revealed that factors besides surface area, such as light scattering and charge collection efficiency also contributed to the PV performance. Although NPs usually provide high surface area, they are characterized by trap-limited electron transport, which eventually limits their

**Table 7.5** Photovoltaic parameters of dye-sensitized solar cell (DSSC) of pure $SnO_2$ photoanode based on nanoparticles (NPs), one-dimensional and core−shell or nanospheres.

| Sample | Dye | $J_{SC}$ (mA cm$^{-2}$) | $V_{OC}$ (mV) | FF (%) | $\eta$ (%) |
|---|---|---|---|---|---|
| ***Nanoparticles pristine $SnO_2$ morphologies*** | | | | | |
| $SnO_2$ NPs [29] | N719 | 12.7 | 677 | 50 | 4.3 |
| Mesoporous NPs $SnO_2$ [30] | Z907 | 17.1 | 450 | 47 | 3.7 |
| $SnO_2$ NPs [31] | N719 | 11.1 | 517 | 54 | 3.1 |
| Nano-$SnO_2$−octa $SnO_2$ NPs [31] | N719 | 09.5 | 437 | 59 | 2.4 |
| $SnO_2$ NPs [32] | N3 | 07.9 | 467 | 55 | 2.0 |
| $SnO_2$ NPs [33] | N719 | 11.0 | 356 | 36 | 2.0 |
| $SnO_2$ NPs [34] | N3 | 17.2 | 280 | 37 | 1.8 |
| $SnO_2$ NPs [35] | N719 | 8.02 | 345 | 49 | 1.4 |
| $SnO_2$ NPs [36] | N719 | 3.64 | 510 | 55 | 1.0 |
| $SnO_2$ NPs [14] | Ru 535 | 7.63 | 350 | 43 | 1.1 |
| $SnO_2$ NPs [37] | N719 | 11.9 | 347 | 41 | 1.7 |
| $SnO_2$ NPs [38] | N719 | 04.9 | 401 | 51 | 1.0 |
| $SnO_2$ NPs [39] | N719 | 04.2 | 412 | 53 | 0.9 |
| $SnO_2$ NPs [40] | N719 | 02.9 | 560 | 52 | 0.9 |
| $SnO_2$ NPs [41] | N3 | 11.2 | 250 | 26.4 | 0.7 |
| $SnO_2$ NPs [42] | N719 | 05.0 | 400 | 33 | 0.7 |
| $SnO_2$ NPs [43] | N719 | 06.1 | 292 | 37 | 0.7 |
| $SnO_2$ NPs [44] | N719 | 02.4 | 516 | 41 | 0.5 |
| $SnO_2$ NPs [45] | | 01.7 | 470 | 40 | 0.5 |
| $SnO_2$ NPs [46] | N719 | 04.2 | 330 | 34 | 0.5 |
| $SnO_2$ NPs [47] | N719 | 02.0 | 414 | 50.6 | 0.4 |
| $SnO_2$ NPs [48] | | 03.8 | 320 | 33 | 0.4 |
| $SnO_2$ NPs [49] | Rose Bengal | 00.9 | 385 | 60 | 0.3 |
| $SnO_2$ NPs [50] | D102 | 00.8 | 0.03 | 23 | 0.06 |
| ***One-dimensional pristine $SnO_2$ morphologies*** | | | | | |
| $SnO_2$ NFs [29] | N719 | 14.9 | 702 | 50 | 5.4 |
| $SnO_2$ MPNFs [51] | N719 | 18.0 | 510 | 51 | 4.3 |
| $SnO_2$ nanocrystal [52] | D149 | 09.3 | 524 | 50 | 2.2 |
| $SnO_2$ NWs [33] | N719 | 05.7 | 522 | 50 | 2.1 |
| PNFs $SnO_2$ [51] | N719 | 10.0 | 440 | 45 | 2.0 |
| $SnO_2$ nanograins [53] | N719 | 07.5 | 465 | 47.7 | 1.7 |
| $SnO_2$ NFs [54] | N719 | 07.0 | 506 | 38 | 1.3 |
| $SnO_2$ NTs [55] | N719 | 08.0 | 490 | 27 | 1.0 |
| $SnO_2$ NTs [56] | N719 | 5.89 | 489 | 35 | 1.0 |
| $SnO_2$ NFs [57] | N3 | 03.0 | 600 | 38 | 0.7 |
| $SnO_2$ NFs [56] | N719 | 04.5 | 499 | 31 | 0.7 |
| $SnO_2$ NWs [33] | N719 | 01.2 | 560 | 59 | 0.6 |

(*Continued*)

**Table 7.5** (Continued)

| Sample | Dye | $J_{SC}$ (mA cm$^{-2}$) | $V_{OC}$ (mV) | FF (%) | $\eta$ (%) |
|---|---|---|---|---|---|
| ***Core–shell or 3D spheres pristine $SnO_2$ morphologies*** | | | | | |
| $SnO_2$ nanobelt [19] | N719 | 16.9 | 690 | 51 | 5.7 |
| HMs $SnO_2$ [58] | N719 | 09.0 | 709 | 55.6 | 3.6 |
| [a]HM-$SnO_2$ spheres [59] | N719 | 12.3 | 520 | 58 | 3.7 |
| [a]HM-$SnO_2$ spheres [59] | N719 | 10.7 | 560 | 57 | 3.4 |
| $SnO_2$ nanoflowers [57] | N3 | 07.3 | 700 | 60 | 3.0 |
| $SnO_2$ NPs + NWs [44] | N719 | 09.9 | 525 | 49 | 2.5 |
| $SnO_2$ NWs–NPs [33] | N719 | 06.3 | 484 | 53 | 2.3 |
| [b]NP-$SnO_2$ spheres [59] | N719 | 07.8 | 490 | 58 | 2.2 |
| [c]Cauliflower-like $SnO_2$ HMS* [58] | @@ | 07.5 | 587 | 56 | 2.5 |
| Cauliflower-like $SnO_2$ HMS* [58] | @@ | 07.6 | 551 | 51 | 2.1 |
| [d]NP-$SnO_2$ spheres [59] | N719 | 06.3 | 520 | 56 | 1.9 |
| $SnO_2$ crystallite [60] | – | 10.7 | 388 | 42 | 1.7 |
| $SnO_2$ nanostructure [61] | N719 | 05.7 | 510 | 56 | 1.6 |
| $SnO_2$ HNS [62] | N179 | 08.5 | 495 | 36 | 1.5 |
| $SnO_2$ urchin microsphere [63] | N719 | 07.6 | 380 | 50 | 1.4 |
| [e]$SnO_2$ MHSs [38] | N719 | 07.4 | 398 | 48 | 1.4 |
| $SnO_2$ nanosheets [64] | N719 | 08.3 | 430 | 39 | 1.4 |
| NRs-based $SnO_2$ microsphere [65] | N719 | 05.3 | 410 | 63 | 1.4 |
| Bare $SnO_2$ mesoporous [66] | N719 | 05.1 | 549 | 45 | 1.3 |
| Coral-like porous $SnO_2$ hollow [67] | | 03.6 | 520 | 56 | 1.0 |
| $SnO_2$ spherical crystallite [68] | N719 | 07.4 | 320 | 41 | 1.0 |
| Hollow NSs $SnO_2$ [69] | N719 | 06.4 | 390 | 34 | 0.9 |
| $SnO_2$ nanosheets [47] | N719 | 02.4 | 417 | 57.3 | 0.6 |
| Spherical $SnO_2$ [67] | | 04.2 | 330 | 31 | 0.4 |
| $SnO_2$ nanoplates [47] | N719 | 01.9 | 348 | 35.8 | 0.3 |
| $SnO_2$ nanoflowers [70] | N719 | 05.4 | 440 | 43.5 | 1.0 |
| $SnO_2$ microsphere [71] | N719 | 00.5 | 553 | 61.5 | 0.2 |
| $SnO_2$ thin film [72] | Erythrosin | 00.8 | 210 | 40 | 0.06 |

*3D*, Three-dimensional; *FF*, fill factor; *NF*, nanofiber; *NP*, nanoparticle; *NR*, nanorod; *NS*, nanosphere; *NT*, nanotube; *NW*, nanowire; *PNF*, porous nanofiber.
[a]HM, hierarchical mesoporous.
[b]Used liquid electrolyte in DSSCs.
[c]@@ = CdS/CdSe/ZnS QDs.
[d]Used solid electrolyte in DSSCs.
[e]MHSs stands for multilayered hollow microspheres.
*hollow microspheres (HMS).

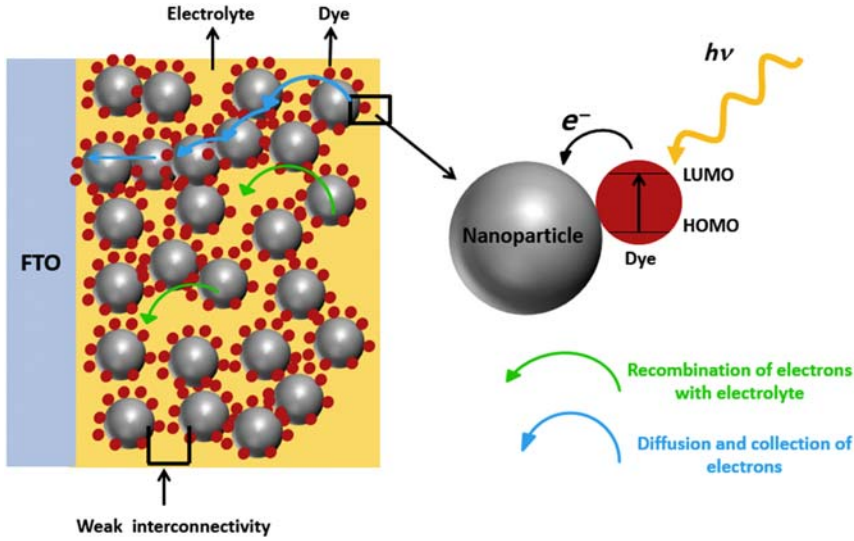


**Figure 7.15** Trapping and de-trapping phenomena in a NPs-based photoanode, where the top four arrow shows electron diffusion and the below two shows recombination of electrons with electrolyte species. Electrons can also be lost due to the weak interconnectivity of the successive NPs in the WE [74,75]. *NP*, Nanoparticle.

performance, as shown in Fig. 7.15. Another issue for the low performance of pure NPs is their poor interconnectivity, which detrimentally reduces the number of photo-induced electrons [74,76]. Therefore the progress in a NPs-based photoanode is hindered and other alternatives, such as 1D nanostructure alone or their composites with NPs, are attempted in an $SnO_2$-based photoanode. The details of PV and photoanode materials employed appear in Fig. 7.15.

Although surface area is the crucial factor for the photoanode materials, the additional light scattering and harvesting are playing a vital role. Small NPs synthesized at low temperature ($\sim$150°C) resulted in a highest BET surface area ($\sim 50\ m^2\ g^{-1}$) while show a lack in light harvesting characteristics. On the other hand, the unique (combination of hollow NPs along with a micron size sphere) morphology synthesized at a higher temperature ($\sim$200°C) performed tremendously when employed as a photoanode in DSSCs. This nanostructure possesses the two desired features, that is, high surface area and superior light scattering capability, as can be seen from the light absorption analysis. Moreover, $SnO_2$-based DSSC showed comparable IPCE and lifespan to that of the $TiO_2$ counterpart. Finally, the sample 200°C showed an overall $\eta \sim 4\%$ with $J_{SC}$ as

high as $\sim 16.3\ \text{mA cm}^{-2}$. The overall performance of $SnO_2$ was lower than the $TiO_2$ counterpart because the conduction band and valence band energies of the former are much lower than the latter, which increases the overall potential and charge recombination. Multiporous tin oxide nanofibers result.

Multifunctional $SnO_2$ comprising its NPs−NSs was developed by hydrothermal reaction at 200°C. When used as a photoanode in DSSCs, it offered superior light scattering and charge transport properties although it has relatively lower surface area. They showed superior PV parameters with $\eta \sim 4\%$ ($J_{SC} \sim 17\ \text{mA cm}^{-2}$) compared to the other samples synthesized at lower temperatures (150°C and 180°C). Electrochemical impedance spectroscopy measurements show that the multifunctional $SnO_2$ supports longer electron lifespan and charge transport parameters.

## 7.3 Photoanode based on $SnO_2$ one-dimensional nanostructures

1D nanostructures such as NRs, NWs, and NTs are conceived to overcome the poor transport in NPs photoanode in DSSCs. These 1D nanostructures provide a direct path for photoinjected electrons, and therefore lead to a possibility of the complete electron collection at the WE [77]. However, these nanostructures are characterized by a poor surface area that leads to lower dye anchoring. Shang et al. synthesized $SnO_2$ NRs and NPs in order to compare their performance in DSSCs [78]. The PV parameters for NRs DSSCs were higher, that is, $J_{SC}$ ($\sim 4.58\ \text{mA cm}^{-2}$) than NPs DSSCs ($\sim 4.02\ \text{mA cm}^{-2}$) due to improved electron transport properties. The slight increment in the NRs devices was due to the lower surface area ($12.2\ \text{m}^2\ \text{g}^{-1}$), which therefore, led to lower dye adsorption than the NPs counterpart ($15.1\ \text{m}^2\ \text{g}^{-1}$). The charge transport parameters were calculated using the bode-phase diagram by the following relation:

$$\tau_n = \frac{1}{2\pi f_{\max}}$$

where $\tau_n$ is the electron lifespan and $f_{\max}$ is the mid-peak frequency in the bode-phase diagram. The calculated $\tau_n$ was $\sim 13$ and $\sim 2.2$ ms for NRs and NPs-based DSSCs, respectively, a 6-times higher value for NRs due to their 1D nature.

To further elaborate the different performances of the two nanostructure architectures, Akilavasan et al. performed a comparative study of pure

$SnO_2$ NPs and NRs and demonstrated remarkably enhanced performance for NRs-based DSSCs. The NRs-based DSSCs exhibited enhanced $\tau_n$ and reduced recombination, which led to a twofold improvement in FF, fivefold increase in $\eta$, twofold increment in $J_{SC}$ and also slightly higher $V_{OC}$ [79]. Still the $\eta$ based on 1D photoanode DSSCs is far lower, therefore further improvement is required in order to combine the two desired features of the two different morphologies in a single photoanode (i.e., NPs for high surface area and 1D nanostructure for reduced electron recombination and faster charge transport).

## 7.3.1 Porous and multiparous tin oxide nanofiber

Porous nanofibers (PNFs) and multiporous NFs (MPNFs) were synthesized, characterized, and subsequently followed by their testing as a WE in DSSCs. The MPNFs resulted in a higher specific surface area $\sim 80\ m^2\ g^{-1}$, many fold to that of PNFs, expected to anchor large amounts of dye that can lead to a superior photocurrent.

## 7.3.2 Characterization of porous and multiporous nanofibers

### *7.3.2.1 Precursor concentration versus viscosity of the solutions*

The synthesis method of the $SnO_2$ electrospun 1D nanostructures is described. The tin precursor concentration in the polymeric solution for electrospinning was varied in five steps, that is, 5.5 ($C_0$), 7.0 ($C_1$), 8.5 ($C_2$), 10.0 ($C_3$), and 11.5 mM ($C_4$), respectively, where $C$ stands for concentration. Table 7.6 summarizes the precursor concentration and viscosity of the solution used for electrospinning. In the electrospinning polymeric solution, the tin precursor was increased gradually in a systematic way while other parameters were kept constant. It is obvious from Table 7.6 that an increase in tin precursor concentration in the polymeric

**Table 7.6** Characteristics parameters of the electrospinning solution such as precursor concentration, solution viscosity and % increments.

| Sample label | Precursor concentration (mM) | Solution viscosity (cP) | Increase in precursor (%) | Increase in viscosity (%) |
|---|---|---|---|---|
| $C_0$ | 5.5 | 256.7 | 0 | 0 |
| $C_1$ | 7.0 | 298.1 | 27.3 | 16.1 |
| $C_2$ | 8.5 | 304.9 | 54.6 | 18.8 |
| $C_3$ | 10 | 321.5 | 81.8 | 25.2 |
| $C_4$ | 11.5 | 344.2 | 109.1 | 34.1 |

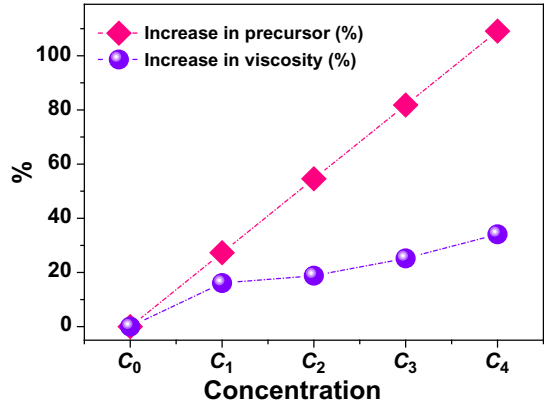


**Figure 7.16** Illustration of the % increase in concentration versus % increase in the viscosity of the five ($C_0$–$C_4$) concentration solution.

solution monotonously raised the viscosity of the solution. Fig. 7.16 shows the % increase in concentration versus % increase in viscosity of the five solutions ($C_0$–$C_4$). It can be observed that the precursor concentration increased sharply from concentration $C_0$ (0%) to $C_4$ (109.1%). On the other hand, the viscosity of the solution ($C_0$–$C_4$) showed a sharp increase with the first addition, whereas the magnitude of increase is less pronounced for subsequent additions.

#### *7.3.2.2 Crystal structure of the annealed samples*

The phase purity and crystallinity of the synthesized electrospun annealed ($C_0$–$C_4$) nanostructures were examined using XRD technique with $2\theta$ range from 10 to 80 degrees as shown in Fig. 7.17. All the peaks in the XRD pattern could be indexed to the tetragonal structure of $SnO_2$ with space group $P4_2/mnm$. No impurity was found in all five types of synthesized nanostructures and the highest intensity peaks are centered at $2\theta \sim 26.8$, $\sim 32$, and $\sim 53$ degrees ascribed to (1 1 0), (1 0 1), and (2 1 1) planes, respectively. It can be seen from the figure that all materials have a similar XRD pattern; however, there were a few extras planes appearing for $C_1$ and $C_2$. These extra planes are expected to be due to the high crystallinity of the respective samples. The calculated values of the lattice parameters were similar that is, $a = b \sim 4.635$ Å and $c \sim 3.165$ Å, which are in close agreement with the standard data (JCPDS card #41-1445).

The $D$ values of these nanostructures ($C_0$–$C_4$) were calculated using Scherrer's equation $D = \kappa\lambda/B\cos\theta_B$. The principal (1 1 0) plane of all

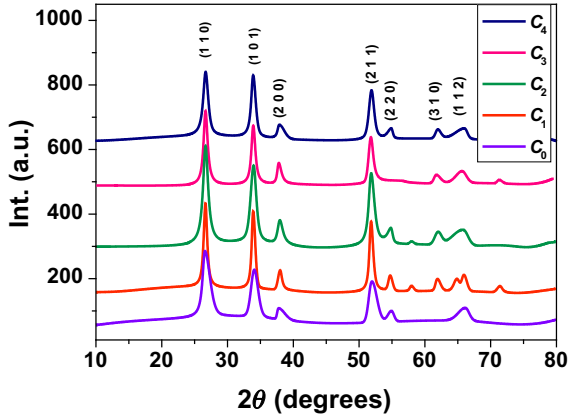


**Figure 7.17** XRD pattern of the electrospun annealed ($C_0$–$C_4$) nanostructures.

**Table 7.7** FWHM, crystallite size, pore size, and pore volume of the synthesized ($C_0$–$C_4$) samples.

| Sample | FWHM (B) (degrees) | Crystallite size ($D$) (nm) | | Pore size (nm) | Pore volume ($cm^3\ g^{-1}$) |
|---|---|---|---|---|---|
| | | XRD | HRTEM | | |
| $C_0$ | 1.48 | 10.6 | – | 60.7 | 0.064 |
| $C_1$ | 0.79 | 19.9 | ~10–15 | 12.2 | 0.069 |
| $C_2$ | 1.01 | 15.3 | ~10–20 | 16.1 | 0.071 |
| $C_3$ | 0.81 | 19.0 | – | 22.5 | 0.165 |
| $C_4$ | 1.04 | 15.0 | – | 18.9 | 0.094 |

nanostructures was used to calculate the FWHM by fitting it with a single Gaussian peak. It can be seen from Table 7.7 that the $D$ is the highest for $C_1$ and $C_3$ (~20 nm), while it is the lowest for $C_0$ (~10.6 nm) owing to the difference in their FWHM. Large $D$ are beneficial for superior conductivity [80]; therefore the $SnO_2$ synthesized from the solutions $C_1$ and $C_2$ is expected to provide superior charge transport properties.

Crystal structure and the difference in microstructure between the materials were further studied by TEM. Samples from only two concentrations were selected for the TEM analysis $C_1$ and $C_2$, because (1) XRD shows similar pattern for all samples, and (2) these two nanostructures show significantly different morphologies which are explained in detail in the next subsection detailing the FESEM results. Fig. 7.18A, B, D, and E shows TEM images of $C_2$ and $C_1$, respectively. A highly porous and

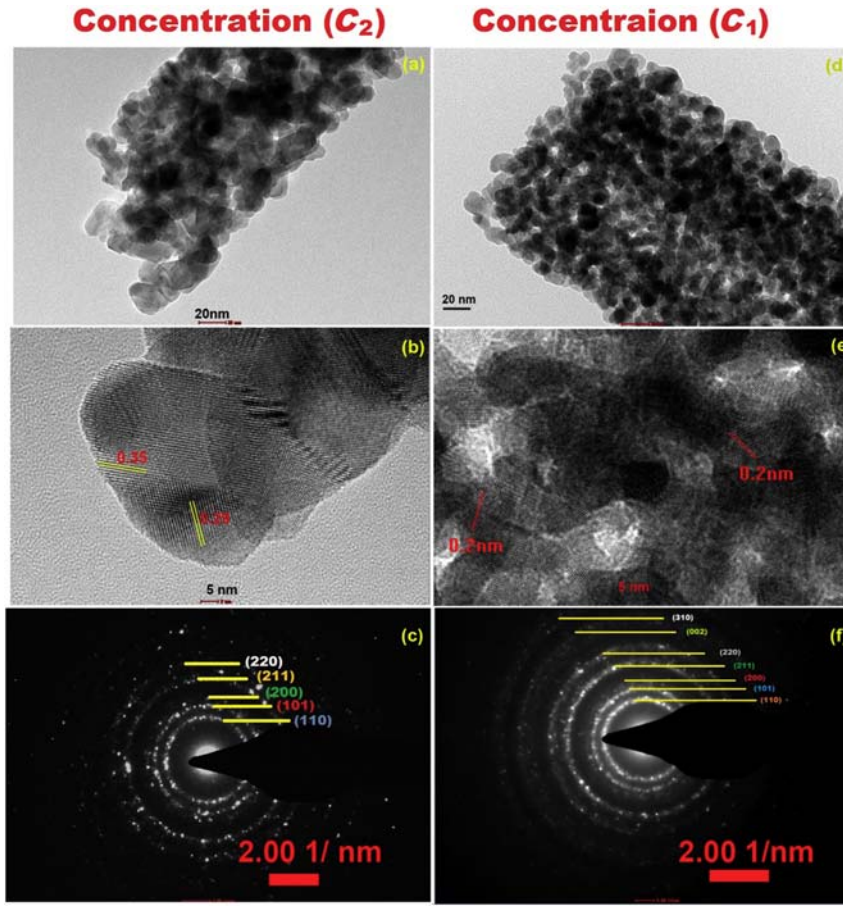


**Figure 7.18** TEM images (A) $C_2$ and (D) $C_1$ low magnification (B) $C_2$ and (E) $C_1$ at high magnification, (C) and (F) SAED pattern of the annealed samples ($C_1$ and $C_2$).

hollow structure is visible in both cases. The $C_1$ were formed with grains of size 10−15 nm, which are smaller than the grains forming the $C_2$ (15−20 nm). The smaller grains and many pores in $C_1$ could lead to large surface area. The HTREM images (Fig. 7.18B and E) of the $C_2$ and $C_1$ have clear lattice fringes of ∼0.3 and ∼0.2 nm, assuring high crystallinity of these nanostructures, respectively. The smaller lattice fringe for the $C_1$ could be attributed to its smaller grain sizes as compared to PNFs. The SAED (C) and (F) in Fig. 7.18 show concentric circles which are due to polycrystallinity in both nanostructures; however, the $C_2$ have a relatively spotty pattern. In Table 7.8, the lattice spacing determined from XRD

**Table 7.8** Lattice spacing of the samples ($C_1$ and $C_2$) using XRD and TEM techniques.

| Annealed sample | XRD | | | | HRTEM |
|---|---|---|---|---|---|
| | Lattice spacing (*d*) (nm) | | | | Lattice spacing (*d*) (nm) |
| | (1 1 0) | (1 0 1) | (2 1 1) | Ave | |
| $C_1$ | 0.3345 | 0.2645 | 0.1764 | 0.2584 | ~0.20 |
| $C_2$ | 0.3365 | 0.2639 | 0.1766 | 0.259 | ~0.35 |

and SAED patterns of the respective samples are compared. The extra XRD peaks appearing in sample $C_1$ are clearly reflected in its SAED pattern (Fig. 7.17).

#### *7.3.2.3 Concentration dependent morphology of the tin oxide*

Conventionally, the tin precursor dispersed electrospun Polyvinylpyrrolidone (PVP) fibrous mats are annealed at between 500°C and 600°C to obtain the pure $SnO_2$ fibers [44,56,81,82]; therefore the as-spun polymeric fibers were annealed at 600°C in this study. The surface morphology of the annealed fibers was studied by FESEM analysis. Fig. 7.19 shows FESEM surface morphology of the annealed electrospun nanofibers for samples $C_0$ (A1–A3), $C_1$ (B1–B3), $C_2$ (C1–C3), $C_3$ (D1–D3), and $C_4$ (E1–E3). For the sample $C_0$, porous solid NFs were formed with diameter ranging from ~100 to 170 nm. The FESEM image of the sample prepared from $C_0$ shows that it has a smooth surface morphology; the higher magnification images show that the nanostructure is composed of grains of ~10–20 nm uniformly distributed throughout the structure with considerable surface roughness. A slightly small increase in the precursor concentration (7 mM, $C_1$) resulted in nanofibers with slightly larger diameter (120–190 nm); however, the grains are larger (20–30 nm) as can be seen in the high-magnification FESEM images. Further increase in the precursor concentration to 8.5 mM ($C_2$) resulted in fibers having diameters in the range ~160–220 nm, where the surface seems more porous than $C_0$. However, these fibers also came with smaller particle size than that of $C_1$. Similar NFs have been achieved to that of $C_2$ when the tin precursor was increased to 10 mM ($C_3$). Finally, when the precursor concentration was increased to more than double that of the initial value (i.e., 11.5 mM, $C_4$), fibers with a significantly varying diameter (210–340 nm) resulted, which is in accordance with the previous

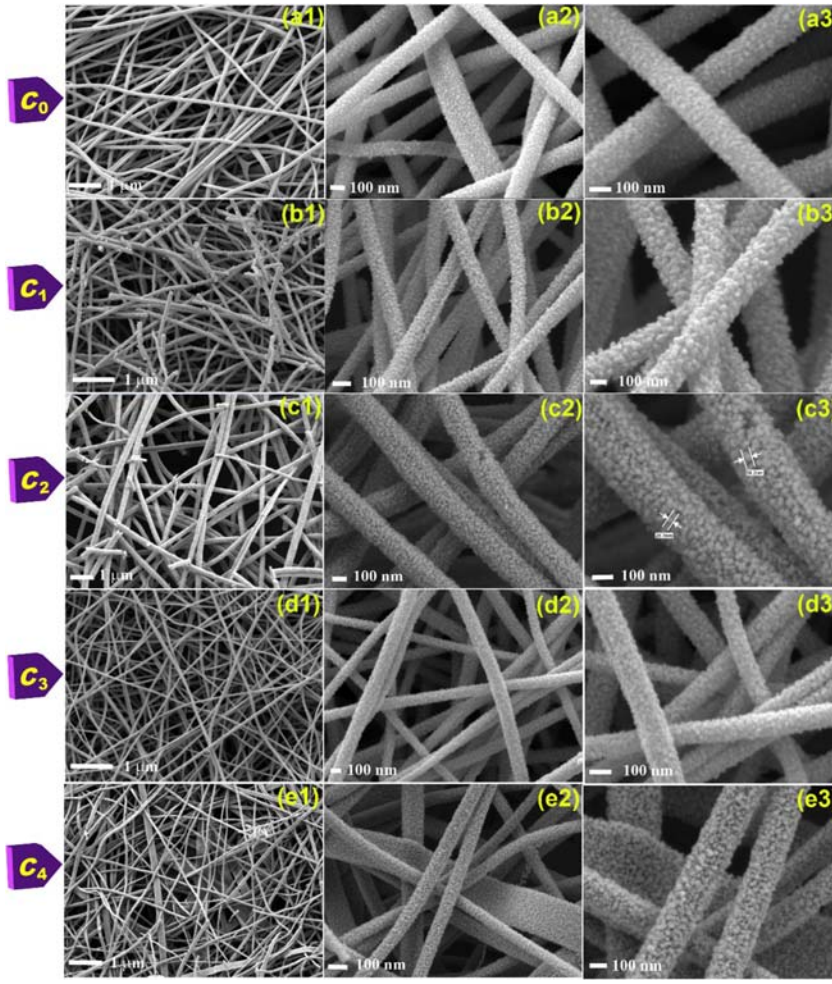


**Figure 7.19** FESEM surface morphologies (A1−A3) show $C_0$ solid NFs, (B1−B3) $C_1$ MPNFs, (C1−C3 and D1−D3) $C_2$ and $C_3$ for PNFs and $C_4$, (E1−E3) present the formation of porous nanostructure developed by electrospinning. *NF*, Nanofiber; *PNF*, porous nanofiber.

report on electrospinning of $SnO_2$ NFs [83]. The morphological features of the annealed electrospun NFs ($C_0$−$C_4$) are summarized in Table 7.9. Image J software was used to measure the particle size and diameter of the NFs.

The cross-sectional FESEM view of the annealed nanofibers of the samples $C_0$ (A1−A3), $C_1$ (B1−B3), $C_2$ (C1−C3), $C_3$ (D1−D3), and $C_4$ (E1−E3) is shown in Fig. 7.19. It can be observed that the cross-section

**Table 7.9** Morphology, grain size, and diameter of the annealed electrospun nanostructures.

| Sample label | Morphology | Diameter distribution (nm) | Grain size (nm) |
|---|---|---|---|
| $C_0$ | NFs | 114–170 | 10–20 |
| $C_1$ | NFs | 124–191 | 20–30 |
| $C_2$ | NFs | 162–224 | 15–25 |
| $C_3$ | NFs | 170–195 | 10–25 |
| $C_4$ | NFs | 213–337 | 20–30 |

*NF*, Nanofiber.

**Table 7.10** Morphology, channel's diameter, surface area, % increase in surface area of the annealed nanostructures.

| Sample label | Morphology | Channel's diameter (nm) | Surface area ($m^2\ g^{-1}$) | % Increase ($m^2\ g^{-1}$) | Channel |
|---|---|---|---|---|---|
| $C_0$ | NFs | – | 7 | 0 | 0 |
| $C_1$ | MPNFs | 30–50 | 78 | 1014 | 1–4 |
| $C_2$ | PNFs | 50–100 | 12 | 71 | 1 |
| $C_3$ | PNFs | 50–100 | 10 | 42 | 1 |
| $C_4$ | NFs | – | 10 | 42 | 0 |

*NF*, Nanofiber; *PNF*, porous nanofiber.

of concentration $C_0$ is solid. A slight increase in the precursor concentration (7 mM, $C_1$) shows that the NFs are transformed to a hollow structure and composed of multiple pores inside a single fiber termed multiporous NFs (MPNFs). The number of pores in the MPNFs varied from 2 to 4 with their inner diameters ranging from 30 to 70 nm. Further increase in the precursor concentration ($C_2$ and $C_3$) resulted in a hollow structure consisting of a single channel per nanofiber named porous NFs (PNFs) having an inner diameter $\sim$50–100 nm; that is, increase in the precursor concentration in samples $C_2$ and $C_3$ resulted in significant decrease in the pore diameter and ultimately the pores vanished in the sample $C_4$. Table 7.10 shows the features of the cross-sectional view of the synthesized nanostructures ($C_0$–$C_4$) such as morphology, surface area, and channel's diameter, respectively (Fig. 7.20).

A significant question that needs to be addressed focuses on the mechanism of formation of variable porosity, and the changes in the sizes of the particles composing the fibers with change in concentration of the precursor. It can be seen that $C_0$ and $C_4$ resulted in solid NFs, while $C_1$ and ($C_2$ and $C_3$) resulted in PNFs and MPNFs, respectively.

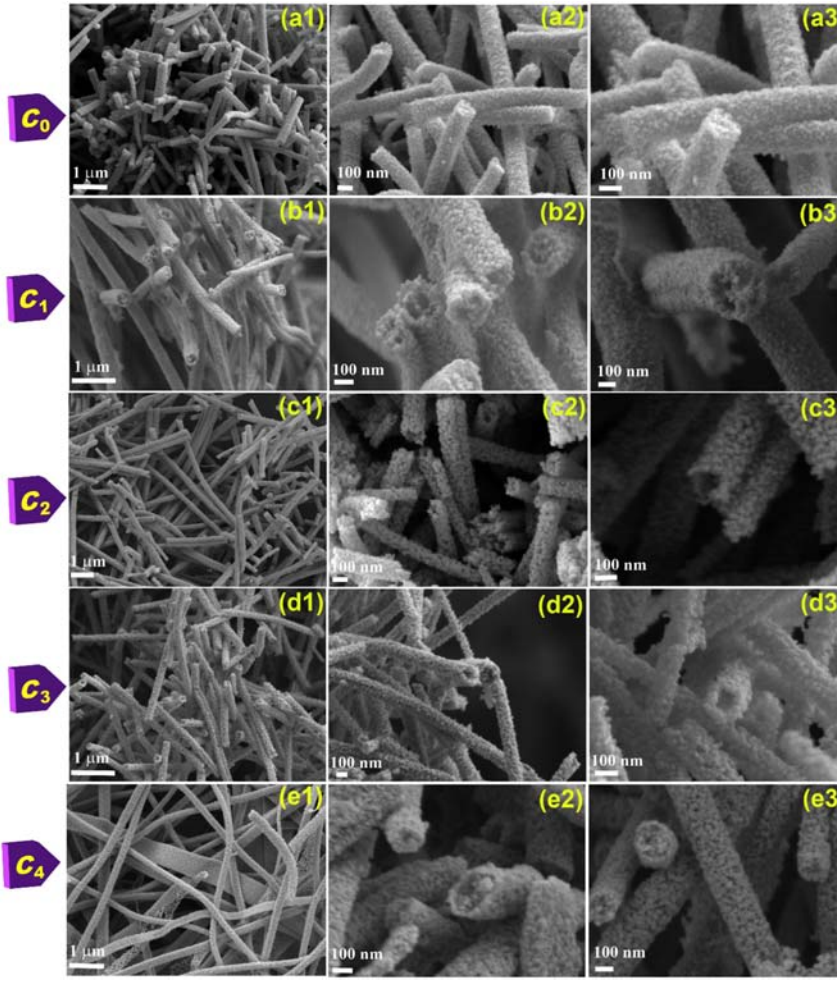


**Figure 7.20** FESEM cross-sectional view (A1−A3) show $C_0$ NFs, (B1−B3) depict $C_1$ MPNFs, (C1−C3 and D1−D3) demonstrate $C_2$ and $C_3$ for PNFs and $C_4$, (E1−E3) present the formation of porous nanostructure developed by electrospinning. *NF*, Nanofiber; *PNF*, porous nanofiber.

To see whether there is any clue about the formation of PNFs and MPNFs, FESEM images of the as-spun fibers were recorded (Fig. 7.21). The as-spun polymeric mats had a conventional fiber morphology with similar fiber diameter (∼300−400 nm) cross-section and cylindrical surface (i.e., no significant change was observed in the morphology of the as-spun fibers, which appears unable to explain the formation of variable porosity in the annealed fibers).

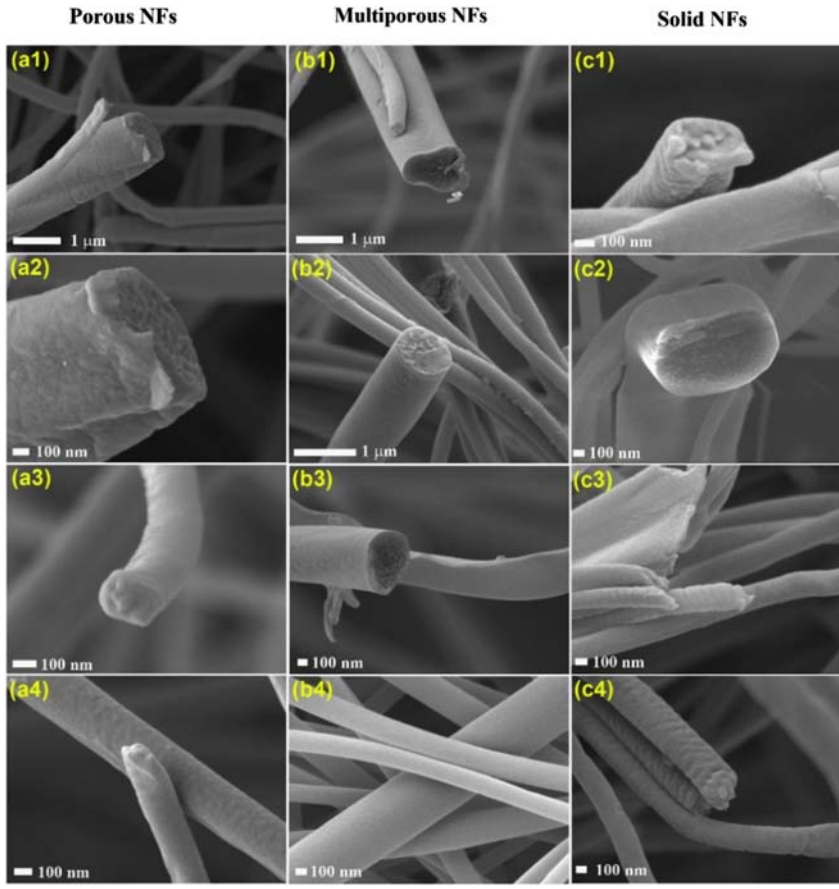


**Figure 7.21** FESEM cross-section view of the synthesized as-spun nanostructure for (A1−A4) PNFs, (B1−B4) MPNFs, (C1−C4) solid NFs at varying magnification level. *NF*, Nanofiber; *PNF*, porous nanofiber.

To further examine whether there is any structural change in the as-spun polymeric fibers, XRD analysis was performed. Fig. 7.22 shows the XRD pattern of the $C_0$, $C_1$, and $C_2$, pure PVP nanofibers without any tin precursor. The XRD pattern of the pure PVP showed a typical amorphous powder diffraction pattern containing a broad and diffused peak at ~23 degrees. Inorganic crystalline phases (judged from the sharp peaks) were observed in the as-spun polymeric samples. To check whether these peaks belong to unreacted tin chloride or tin hydroxide $Sn(OH)_4$ upon hydrolysis of $SnCl_4 \cdot 5H_2O$, the XRD patterns of these materials were

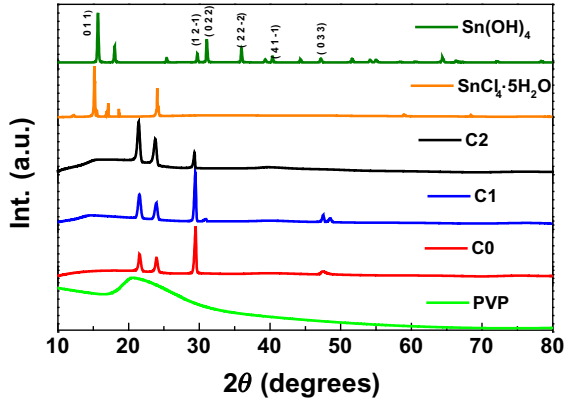


**Figure 7.22** XRD pattern of the as-spun fibers of concentration $C_0$, $C_1$, and $C_2$ compared along with pure PVP nanofibers, $SnCl_4 \cdot 5H_2O$ precursor, and $Sn(OH)_4$.

recorded and compared in the Fig. 7.22. The $Sn(OH)_4$ was synthesized by precipitating a clear $SnCl_4 \cdot 5H_2O$ aqueous solution using ammonium hydroxide. It is clear from the XRD patterns that the phases in the polymeric fibers are neither from $SnCl_4$ nor from $Sn(OH)_4$. The crystal structure of the phases could not be identified; however, the peaks show a reversal of intensity for $C_2$ (PNFs) compared to $C_1$ (MPNFs) indicating the change in orientation of the crystallites, which might be causing variable porosity upon changing the precursor concentration.

Furthermore, chemical analysis of the three as-spun ($C_0$, $C_1$, and $C_2$) fibers was made by Fourier transform infrared spectroscopy (FTIR), and compared with PVP fibers and $SnCl_2 \cdot 5H_2O$ precursor. It can be seen from Fig. 7.23 that the major absorption band lies at $\sim 1630\ cm^{-1}$ for as-spun ($C_0 - C_1$) fibers, PVP fibers, and $SnCl_2 \cdot 5H_2O$ showing similar functional groups. Another principal absorption band centered (at $\sim 1200\ cm^{-1}$) was observed for the three as-spun fibers arising from the adsorbed moisture in the sample. Therefore the FTIR spectra do not convey a profound inference on the chemical structure of the respective fibers.

#### *7.3.2.4 Gas adsorption studies of the annealed samples*

The surface properties of the above nanostructures were measured using BET surface analyzer. Briefly, the BET surface area of the samples varied in the range of $7-78\ m^2\ g^{-1}$, that is, $C_0 \sim 7$, $C_1 \sim 78$, $C_2 \sim 12$, $C_3 \sim 10$,

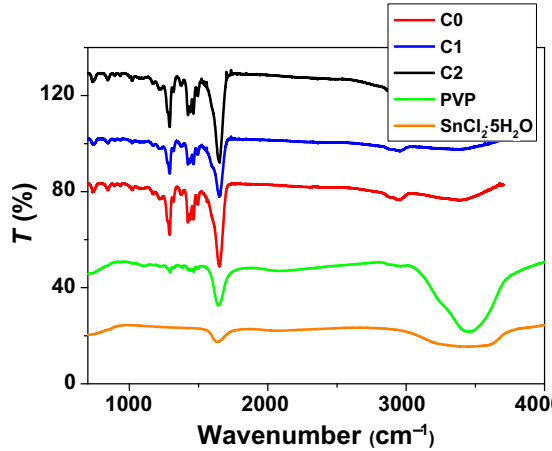


**Figure 7.23** FTIR curves of the three ($C_0$, $C_1$, and $C_2$) as-spun fibers along with PVP fibers and $SnCl_2 \cdot 5H_2O$ precursor. *FTIR*, Fourier transform infrared spectroscopy.

and $C_4 \sim 10\ m^2\ g^{-1}$. In addition, the difference in the pore size and volume distribution between these nanostructures was studied by adsorption–desorption test in the $N_2$ atmosphere. Fig. 7.24A–F presents the adsorption–desorption isotherms for the samples ($C_0$–$C_4$), and pore diameter distribution, respectively. According to the International Union of Pure and Applied Chemistry (IUPAC) classification of adsorption isotherm, the type IV curve describes the nanostructure, which is composed of mesopores (2–50 nm). The Barrett, Joyner, and Halenda (BJH) method is commonly employed to determine the volume and size distribution of mesopores and micropores [84–86]. Characteristic features of the type IV isotherm plots are its hysteresis loop, which is associated with the filling and emptying of mesopores by a phenomena called capillary condensation. In the present experiment, all five types of samples exhibit type IV isotherms, and their average pore and volume size. It is observed that sample $C_0$ contains the highest pore diameter ($\sim$60.7 nm) and $C_1$ the lowest (12.2 nm).

Therefore, to summarize, although various characterization methods such as SEM, XRD, and FTIR have been conducted in order to understand the formation mechanism of the MPNFs and PNFs, there was no clear evidence obtained using these techniques.

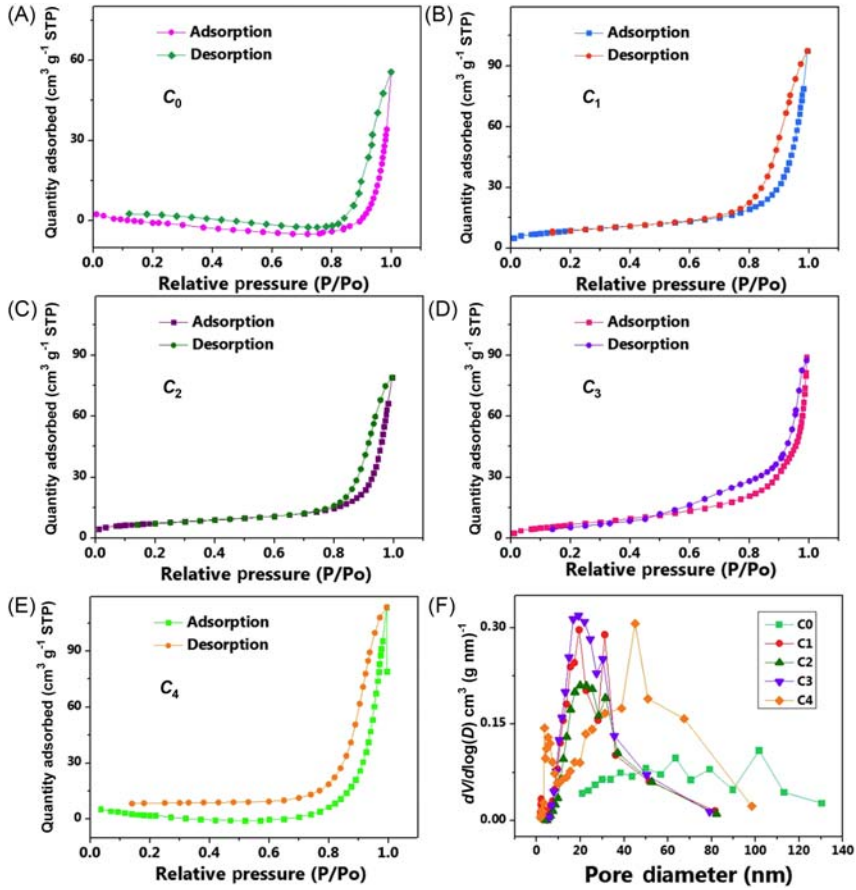


**Figure 7.24** Gas adsorption–desorption isotherm curves (A–E) for sample $C_0$, $C_1$, $C_2$, $C_3$, and $C_4$, respectively, and (F) pore diameter distribution of the respective samples.

## 7.4 Dye-sensitized solar cells fabrication and testing

### 7.4.1 Morphology and thickness of the electrodes

To see any changes in the morphology of the synthesized PNFs and MPNFs after passing through an extensive mechanical agitation during the paste-making procedure and then thermal annealing, images of the prepared coated electrodes were recorded. In Fig. 7.25, the FESEM images are displayed showing the cross-sectional view of the photoanodes fabricated using PNFs and MPNFs. Thickness of the films measured from the FESEM images was $17 \pm 0.5$ μm. It is interesting to note that the PNFs and MPNFs retained their morphologies even after extensive

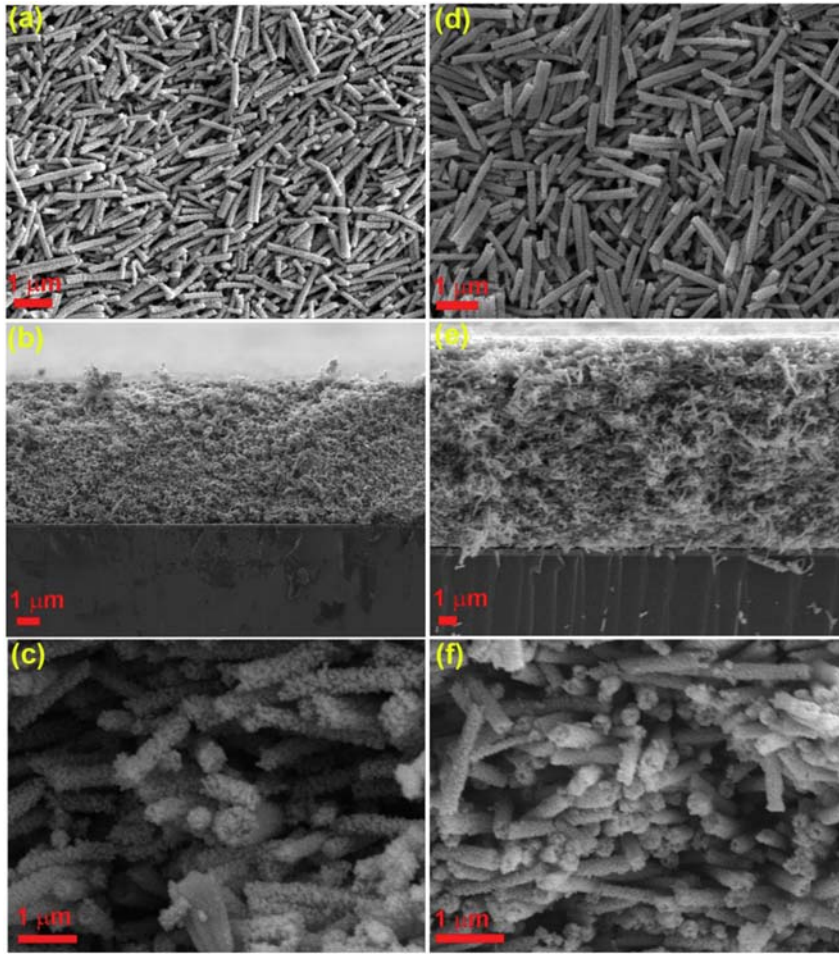


**Figure 7.25** FESEM top view of the coated FTO substrates (A and D), while (B and E) and (C and F) illustrate the cross-section view at low and high magnification of PNFs and MPNFs electrodes. *PNF*, Porous nanofiber.

mechanical agitation during the paste-making procedure and subsequent thermal annealing. No agglomeration was found in the photoanode film; ensuring high porosity for efficient electrolyte penetration and superior charge transport [73].

## 7.4.2 Light scattering properties of the dye-anchored electrodes

Light harvesting properties of the dye-anchored WE were studied by UV–vis–NIR absorption spectroscopy. The light scattering properties of

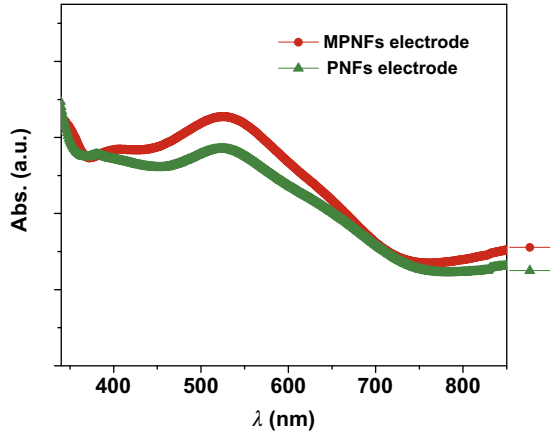


**Figure 7.26** Absorption spectra of the PNFs and MPNFs dye-anchored electrodes. *PNF*, Porous nanofiber.

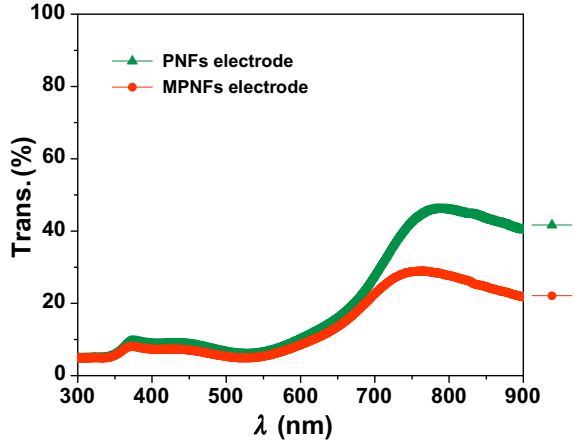


**Figure 7.27** Transmission spectra of the PNFs and MPNFs dye-anchored electrodes. *PNF*, Porous nanofiber.

the electrodes were studied by recording their absorbance (Fig. 7.26) and transmittance (Fig. 7.27). Fig. 7.26 shows that an electrode prepared using PNFs and MPNFs showed similar absorption curve although slightly improved absorbance was observed for the latter due to its high specific surface area.

The superior light harvesting property of the electrode synthesized using MPNFs is more obvious in the transmission spectra (Fig. 7.27). This is due to the fact that MPNFs are highly porous and contain

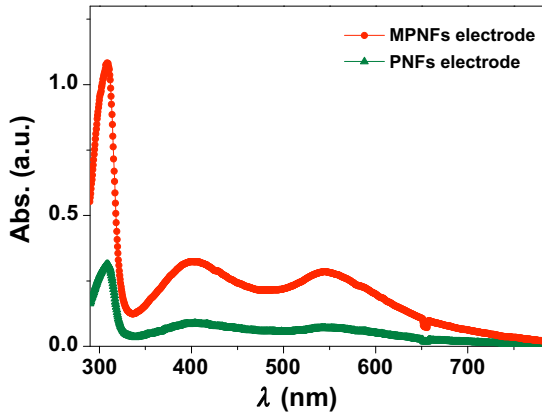


**Figure 7.28** UV–vis–NIR absorption spectra of the desorbed dye of the electrodes fabricated using PNFs and MPNFs. *PNF*, Porous nanofiber.

multichannels inside a single fiber so that the reflection of light can increase and eventually enhance the optical path length for incident photons [22]. The transmittance of the electrodes was $<20$ and $\sim 40$ at the $\lambda \sim 600-750$ nm for MPNFs and PNFs, respectively. Thus $\sim 80\%$ of the incident light is absorbed by the MPNFs electrode, whereas considerable portion of the incoming light is transmitted in the PNFs electrode.

The dye loading on photoanodes was calculated by the desorption test and their curves are shown in Fig. 7.28. The calculated dye loading of MPNFs is $3.38 \times 10^{-7}$ nmol $cm^{-2}$ which is over 4 times larger than that of PNFs ($0.83 \times 10^{-7}$ nmol $cm^{-2}$). The significantly enhanced dye loading is attributed to the higher surface area of MPNFs. Besides, they have highly porous morphology, that is, multiple channels inside a single NF, which ultimately provides more bonding sites on the outer as well as inner side for the dye-anchoring group as compared to the single channel fiber counterpart. A control electrode of $TiO_2$ was also fabricated using commercial P25 paste. The dye loading of the P25-based electrode ($7.02 \times 10^{-7}$ mol $cm^{-2}$) is twice that of the MPNFs-based electrodes owing to its twofold higher surface area ($\sim 100-150$ $m^2$ $g^{-1}$) than the later. The lower surface area of the $SnO_2$ MPNFs is owing to the lower IEP ($\sim 4-5$ at pH) thereby make weak bonding to the carboxylic groups of the ruthenium-based dyes. On the other hand, $TiO_2$ NPs possess IEP ($\sim 6-7$, at pH) and therefore make a strong bonding group with carboxylic groups and consequently enhance the dye loading.

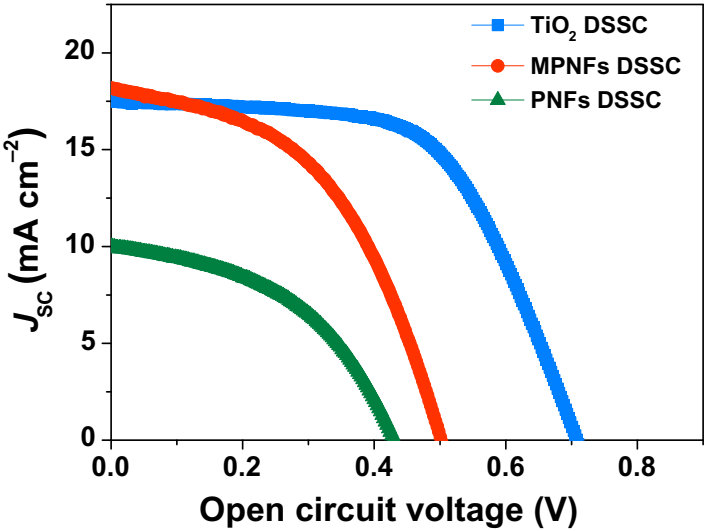


**Figure 7.29** Current voltage characteristic curve of DSSCs fabricated using synthesized PNFs, MPNFs and a reference cell based on $TiO_2$ P25 NPs under standard 1 Sun condition with intensity of 1000 W $m^{-2}$. *DSSC*, Dye-sensitized solar cell; *NP*, nanoparticles; *PNF*, porous nanofiber.

**Table 7.11** PV parameters, $J_{SC}$, $V_{OC}$, fill factor (FF), $\eta$ and dye loading of dye-sensitized solar cells (DSSCs) fabricated using porous nanofibers (PNFs), MPNFs and P25 nanoparticles (NPs), respectively (film thickness of the devices kept at $\sim$17 $\mu$m).

| DSSCs | $J_{SC}$ (mA $cm^{-2}$) | $V_{OC}$ (V) | FF | $\eta$ (%) | Dye loading (nmol $cm^{-2}$) |
|---|---|---|---|---|---|
| PNFs | 10 | 0.45 | 0.45 | 2.0 | 83 |
| MPNFs | 18 | 0.51 | 0.49 | 4.3 | 338 |
| P25 NPs | 17.4 | 0.72 | 0.61 | 7.6 | 702 |

## 7.4.3 Photovoltaics characteristics of tin oxide nanostructures

To realize the effect of increased surface area in MPNFs, photoanodes were fabricated for DSSCs. $I-V$ analysis of the DSSCs is shown in Fig. 7.29 and the corresponding PV parameters are listed in the Table 7.11 As expected from high surface area of MPNFs, a high $J_{SC} \sim 18$ mA $cm^{-2}$ and $\eta \sim 4.3\%$ were obtained for the MPNFs DSSCs, while those for PNFs DSSCs are ($J_{SC} \sim 10$ mA $cm^{-2}$ and $\eta \sim 2\%$). The $V_{OC}$ in MPNFs DSSCs showed an increment of $\sim$0.57 mV as a consequence of the enhanced $J_{SC}$. The FF of both DSSCs remained practically the same (0.49 in MPNFs and 0.45 in PNFs). As the thickness of both

electrodes was the same, the presence of multichannels in MPNFs and their smaller $D$ value compared to PNFs, which resulted in up to 8 times increased surface area and up to 5 times larger dye loading, is attributed to the higher $J_{SC}$. A reference P25 DSSC was fabricated to show its comparison with $SnO_2$-based DSSCs. The P25 DSSC resulted in $\eta \sim 7.6\%$ with other PV parameters ($V_{OC} \sim 0.72$ V, $J_{SC} \sim 17.4$, and FF $\sim 0.61$), which shows ($\sim 45\%$) higher $V_{OC}$ and (20%) large FF than the PNFs and MPNFs DSSCs. However, MPNFs DSSC exhibit superior photocurrent than that of $TiO_2$-based DSSC (Table 7.11). The low $V_{OC}$ and FF are the main issues in $SnO_2$-based DSSCs due to its lower conduction band edge [4], which results in high electron recombination with the electrolyte species [33,87,88]. A remedy for this issue has been developed and is explained in the following segments.

### 7.4.4 Charge transport properties of dye-sensitized solar cells

Electrochemical impedance analysis (EIS) is a useful tool used to explore the charge transport and transfer mechanism in the DSSC. The EIS for the PNFs DSSC and MPNFs DSSC was studied under dark conditions. The Nyquist and Bode-phase plots of both devices are shown in Fig. 7.30. The intermediate peak in the Nyquist plot (Fig. 7.30A) of the MPNFs DSSC shows large diameter as compared to that of PNFs DSSC assuring high recombination resistance and consequently resulted in long $\tau_n$ as $\tau_n = (C\mu \times R_{CT})^{1/2}$ [24]. In bode-phase plot, the MPNFs DSSC peak shifts (Fig. 7.30B) toward lower frequency than that of PNFs counterpart showing long $\tau_n$. The calculated $\tau_n$ for both devices from the mid-peak frequency of the bode-phase plots using a relation $\tau_n = 1/2\pi f_o$ [28] where $f_o$ is the maximum frequency at the mid peak. The calculated values of $f_o$ were $\sim 14$ and $\sim 29$ Hz with corresponding $\tau_n \sim 11$ and $\sim 5$ ms for the MPNFs DSSC and PNFs DSSC, respectively. Long $\tau_n$ implies that electrons could survive for a long time in the photoanode material before recombining with electrolyte species and consequently leading to high PV performance [25]. Although both nanostructures possess a 1D nature and are prepared from the same materials, the better performance of MPNFs over PNFs could be due to its multichannel status inside a single fiber.

To further analyze the better performance of the MPNFs DSSC, an OCVD measurement was performed. It is a simple technique to investigate real-time recombination kinetics in DSSCs by changing their

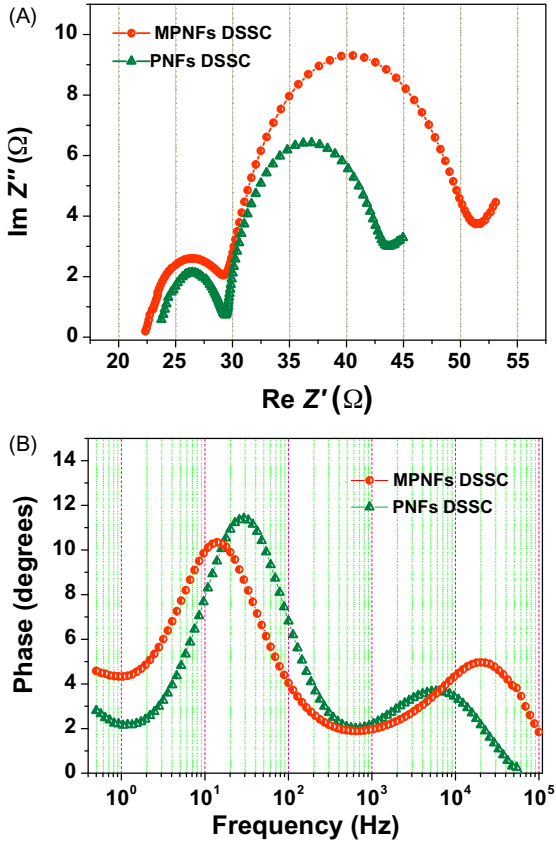


**Figure 7.30** (A) Shows Nyquist plot and (B) bode-phased plots for PNFs and MPNFs DSSC. *DSSC*, Dye-sensitized solar cell; *PNF*, porous nanofiber.

equilibrium state from illuminated to dark. Fig. 7.31A illustrates OCVD curves of the PNFs, MPNFs, and P25 DSSC, respectively. It is evident that the $V_{OC}$ decay rate was significantly lower for MPNFs DSSC as compared to PNFs and P25 DSSC suggesting low recombination of photoexcited electrons. Fig. 7.31B compared the $\tau_n$ of the (PNFs, MPNFs, and P25 DSSC), which was calculated using their OCVD curves. The MPNFs DSSC showed the highest $\tau_n$; for example, at 0.3 V, MPNFs gave $\tau_n \sim 7$ seconds whereas it was 2.3 and 1.47 seconds for PNFs and P25 DSSC, respectively. The calculated $\tau_n$ for P25 DSSC in our case is similar to that obtained by Ref. [89] that is ($\sim$20 ms−1 second) for a P25 NPs–based high-efficiency DSSCs. The high $\tau_n$ observed in $SnO_2$ can be attributed to their 1D morphology as well as improved charge mobility throughout.

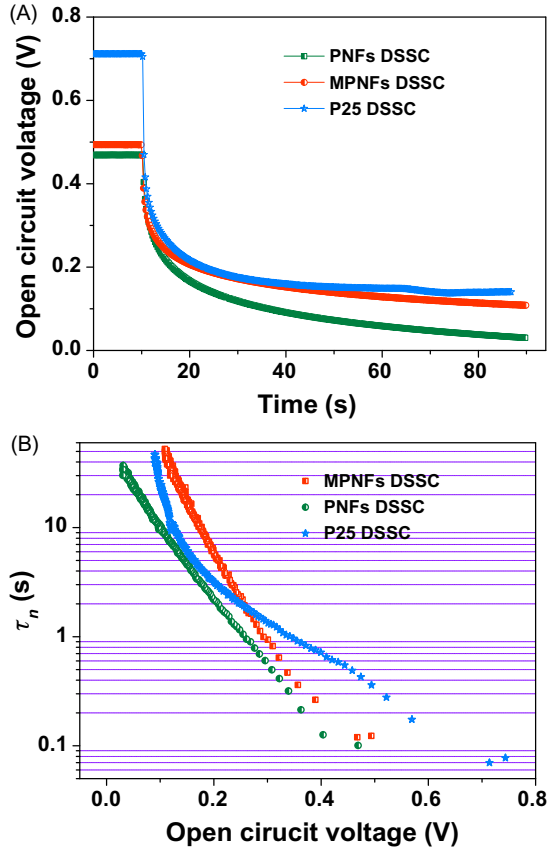


**Figure 7.31** (A) Shows OCVD and (B) shows the $\tau_n$ calculated from the OCVD curve versus $V_{OC}$ of the MPNFs, PNFs, and P25 DSSCs. *PNF*, Porous nanofiber.

$\eta_{cc}$ of the PNFs, MPNFs, and P25 DSSC was compared from $\tau_n$ and electron transit time ($\tau_d$) by using an expression $\eta_{cc} = 1/1 + (\tau_n/\tau_d)$. It is obvious from Fig. 7.32 that MPNFs DSSCs showed ~21% increased charge collection than that of P25 DSSC and slightly improved charge collection against PNFs DSSC in photoanodes of similar thickness ($17 \pm 0.5$ μm). This increment is owing to the fact that the diffusion length $L_n = L\sqrt{R_{CT}/R_T}$ (i.e., the distance traveled by the photoinjected electrons before they recombine with the electrolyte specie in MPNFs-based photoanodes) is 2–3 times higher than that of P25 DSSC. The $L_n$, which is ~70–75 μm in MPNFs DSSC, ~65–70 μm in PNFs, and ~30–35 μm in P25 DSSC (Fig. 7.32B), clearly establishes the nature of the porous nanostructures. Thus an enhanced $\tau_n$ and significantly higher $L_n$

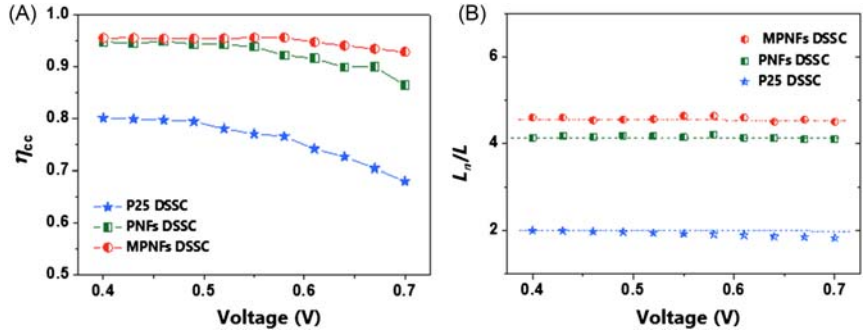


**Figure 7.32** (A) Charge collection efficiency of the PNFs, MPNFs, and P25 DSSC, (B) electron diffusion length calculated using a well-known electrical equivalent model for both devices. *DSSC*, Dye-sensitized solar cell; *PNF*, porous nanofiber.

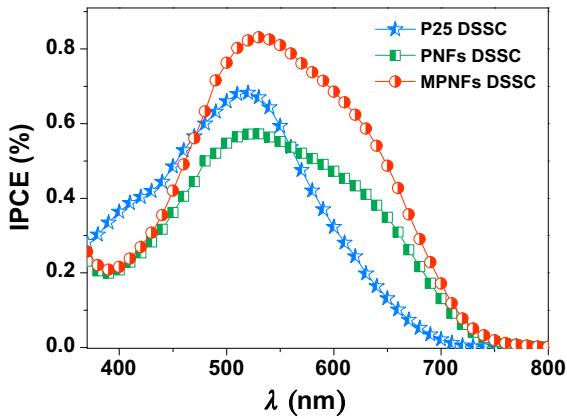


**Figure 7.33** Incident photon to current conversion efficiency curves of the PNFs, MPNFs, and P25 DSSCs. *DSSC*, Dye-sensitized solar cell; *PNF*, porous nanofiber.

demonstrate the beneficial effects when 1D nanomaterial MPNFs architecture is employed as a photoanode material.

Furthermore, to validate the higher photocurrent of the MPNFs DSSCs, an IPCE measurement was performed. The IPCE curves of the three devices (PNFs, MPNFs, and P25 DSSC) are shown in Fig. 7.33. The integrated IPCE over the entire $\lambda$ was used to calculate the $J_{SC}$. The calculated $J_{SC}$ of the MPNFs, PNFs, and P25 DSSC was $\sim$17.8, $\sim$10.3, and $\sim$15.2 mA cm$^{-2}$, respectively, which agrees closely with their measured $J_{SC}$ from the $I-V$ measurements (Table 7.11). A significant increase in the IPCE of the MPNFs over the other two was observed. The highest IPCE for MPNFs, PNFs, and P25 DSSCs are $\sim$83%, $\sim$57%, and

$\sim$68%, respectively. The increased IPCE of the MPNFs DSSCs over the PNFs could be attributed to its significantly larger dye loading and desirable charge transport characteristics. However, its dye loading is only half of that associated with P25 DSSC, thereby indicating that improved $J_{SC}$ of the MPNFs results from both dye loading and desirable charge transport characteristics.

Moreover, an enhanced light scattering in the case of both MPNFs and PNFs is noticed at $\lambda > 560$ nm which is attributed to the bigger size of 1D porous material than that of P25 particles. An improved charge transport in $SnO_2$ can be normally expected due to its many fold increased $\mu_e$ compared to that of the $TiO_2$. The charge transport parameters such as $L_n$, $\tau_n$, and IPCE of the three DSSCs are compared in Table 7.11. It is clear from the data that MPNFs DSSC possesses superior charge transport properties over the PNFs as well as P25 DSSC.

While 1D nanostructure routinely produces low surface area, MPNFs showed tremendously high surface area ($\sim 80\ m^2\ g^{-1}$) due to their hollow nature and the presence of multichannels inside a single fiber. High surface area MPNFs adsorbed large amounts of dye molecules and therefore achieved a significantly high photocurrent. In addition, MPNFs DSSC exhibit significantly superior charge transport properties, such as high crystallinity, high IPCE, long diffusion length and long lifespan comparative to that of their PNFs counterpart. An overall final $\eta \sim 4.3\%$ was achieved using MPNFs as a photoanode material, while PNFs yielded $\eta$ merely half of it.

## 7.5 Photoanode based on $SnO_2$ composite or hybrid

In order to combine the desired features, such as large surface area, favored band alignment and directed paths in a single photoanode, composite or hybrid nanostructures, are widely employed. Such nanostructures are formed by combining $SnO_2$ with other MOS of high surface area and CB edge. Chen et al. reported ZnO Nanotetrapods-$SnO_2$ NPs composite with surface area $\sim 109\ m^2\ g^{-1}$, notably higher than a pure $SnO_2$ NP analogue ($98.7\ m^2\ g^{-1}$). They also achieved improved $\eta$ from $\sim$2% to $\sim$6.18% [90] and other PV parameters which are tabulated in Table 7.12. In another report by Wang et al., $SnO_2$ NFs-NPs composite, which achieved $\eta \sim 6.3\%$, $a \sim 30\%$ higher than a pure counterpart ($\sim$4.30%) [29]. Ito et al. also reported a record PV parameters using composite $SnO_2$ NPs—ZnO submicron particles with a FF$\sim$0.71, a high

**Table 7.12** Charge transport parameters (diffusion length, electron lifespan using bode-phase plot, OCVD, and IPCE) for the porous nanofibers (PNFs), MPNFs, and P25 dye-sensitized solar cell (DSSC).

| Devices | $L_n$ (μm) | $\tau_n$ (ms) Bode phase | $\tau_n$ (s) OCVD | IPCE (%) |
|---|---|---|---|---|
| PNFs DSSC | ~68 | 5 | 2.3 | 57 |
| MPNFs DSSC | ~72 | 11 | 7 | 83 |
| P25 DSSC | 32 | 5.3 | 1.47 | 68 |

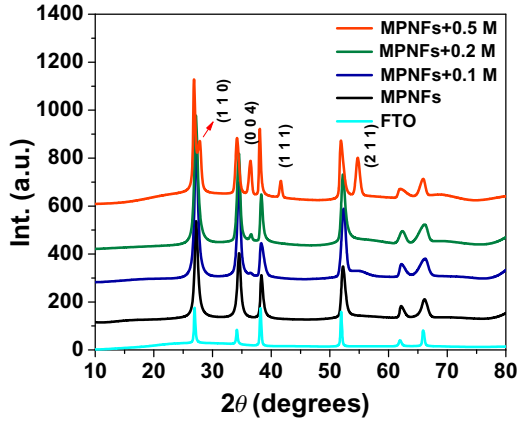


**Figure 7.34** XRD pattern of the various treated electrodes along with FTO substrate as a reference.

$V_{OC}$ ~721 mV and $\eta$ ~6.34% [91]. These reports suggest that composite WEs tremendously enhanced the PV parameters of DSSCs and can serve as a possible avenue to further enhance the $\eta$ in $SnO_2$ DSSCs.

## 7.5.1 Characterization of composite nanostructures

### *7.5.1.1 Phase and crystallinity of composite nanostructures*

The phase and crystallinity of the pure $SnO_2$ MPNFs and $TiCl_4$-treated electrodes were examined by XRD technique (Fig. 7.34). The crystal structure of the composite $SnO_2$ MPNFs showed a tetragonal cassiterite phase, space group $P4_2/mnm$ with lattice parameters $a = b = 4.635$ Å and $c = 3.165$ Å. The values match exactly to the standard data (JCPDS card #41-1445). All XRD patterns reflect the presence of pure $SnO_2$ peaks; however, new peaks appeared in the composite architectures showing the existence of $TiO_2$, particularly at a higher $TiCl_4$ molar concentrations. A new (0 0 4) plan is observed at $2\theta$ ~36.48 degrees in the $SnO_2$–$TiO_2$

composite, corresponding to anatase $TiO_2$, the intensity of which increased systematically with increasing $TiO_2$ NPs concentration, that is, from 0.1 to 0.5 M. However, at a higher molar concentration (0.5 M) a rutile phase is also observed, as evidenced by (1 1 0) and (1 1 1) peaks at ~28 and ~41.61 degrees, respectively.

Furthermore, an additional anatase peak (2 1 1) at ~54.76 degrees is also observed due to the excess $TiO_2$ NPs formation using 0.5 M. Electrodes were also prepared using higher $TiCl_4$ molar concentrations such as (~0.75 and 1 M). However, thicker layers tend to vanish in the $TiCl_4$ solution or crack upon heat treatment as reported previously [92]. The major peaks of the anatase structure were not seen (in all $TiCl_4$ composite nanostructures) after annealing at ~450°C due to the fact that the $TiCl_4$ layers are extremely thin (below ~250 nm). On the other hand, it is expected that a $TiCl_4$ layer with thickness above ~1 μm must have the anatase structure [92]. Although characterization to realize the thickness of the $TiO_2$ overlayer is not carried out in our study, the absence of XRD peaks in $TiO_2$ at lower molar concentrations coupled with the presence of $TiO_2$ peaks at high concentration suggest that the systematic change in $TiCl_4$ concentration is correlated with the $TiO_2$ overlayer thickness as observed by Ref. [92].

The XRD analysis (Fig. 7.35) of electrospun ($SnO_2$−$TiO_2$) NFs from a single precursor solution also showed principal peaks for $SnO_2$ such as (1 1 0), (1 0 1) and (2 1 1); however, these peaks are broader than those observed in previous composites (those formed from two different precursor solutions). The composite XRD was also compared with pure $SnO_2$ NFs and $TiO_2$ (anatase and rutile) in order to investigate the broadened FWHM of the former. The widening of the composite peaks can be attributed to the combined chemical behavior of $SnO_2$ and $TiO_2$.

To further understand the variation in the crystallinity of chemically synthesized $SnO_2$−$TiO_2$ composites, we employed HTREM and SAED (Fig. 7.36). The lattice spacing of the HTREM images are clear throughout the materials and index to ~0.3−0.34 nm, which are in close agreement with both $SnO_2$ and $TiO_2$ values. The SAED pattern showed concentric circles, which reveals that the material is polycrystalline. The bright concentric circles also corroborate with the XRD peaks of the composite NFs. This suggests the key difference between the two types of composites; while the mixing of two types of nanostructures or posttreatment of one ($TiO_2$) on the surface of another ($SnO_2$) formed a composite which may still have dominant separate chemical identities, a composite

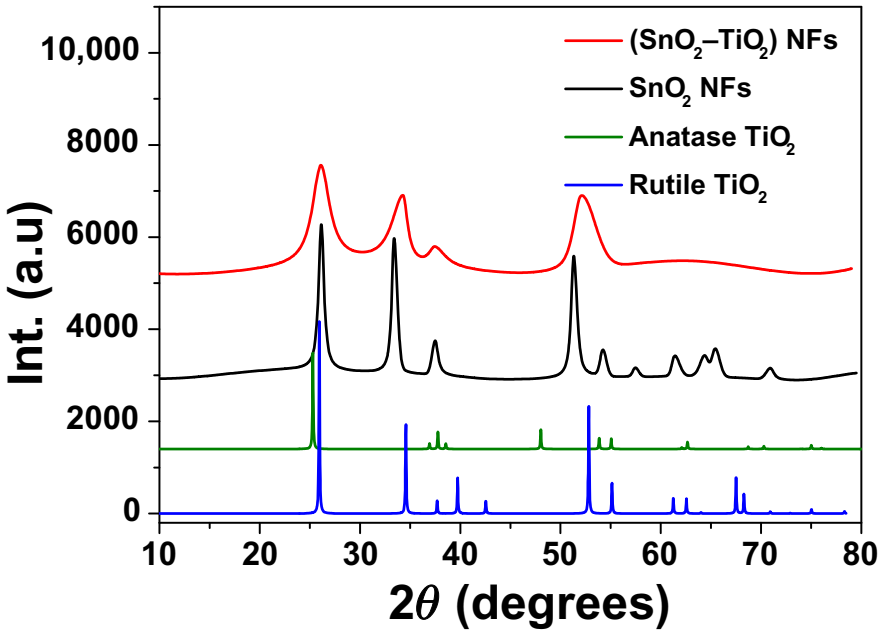


**Figure 7.35** XRD pattern of the electrospun ($SnO_2$—$TiO_2$) NFs along with pure $SnO_2$ NFs and $TiO_2$ (anatase and rutile). *NF*, Nanofiber.

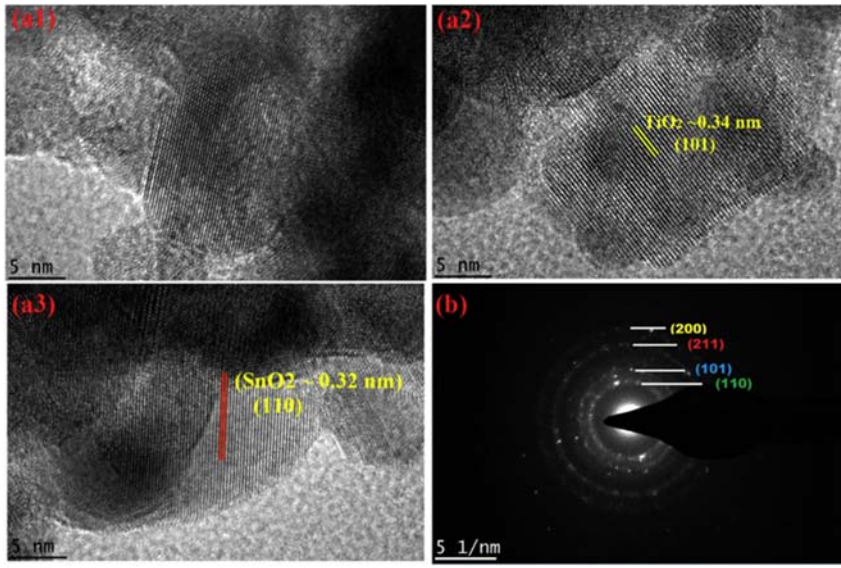


**Figure 7.36** HRTEM images show the (A1−A3) and (B) SAED pattern of the electrospun ($SnO_2$−$TiO_2$) NFs composite. *NF*, Nanofiber.

formed chemically from a single solution, on the other hand, tends to have a single chemical identity and the two different materials are scarcely distinct.

### *7.5.1.2 Morphological properties of composite photoanodes*

As it was shown that the MPNFs yielded significantly higher PV parameters compared to those of PNFs, they have been chosen in order to further tailor their PV performance to match $TiO_2$ counterparts. The calcined MPNFs-coated electrodes were treated with various $TiCl_4$ molar concentration (0.1, 0.2, and 0.5 M) aqueous solutions. The effect of various $TiCl_4$ concentrations on the MPNFs surface morphology is shown in Fig. 7.37. The pure $SnO_2$ MPNFs exhibit porous morphology; however, upon $TiCl_4$ posttreatment, the pores in the MPNFs start to fill (Fig. 7.37D1 and D2) evidencing the formation of thin $TiO_2$ particles eventually resulting in a $SnO_2$−$TiO_2$ nanocomposite. Although the effect is not very apparent for lower $TiCl_4$ molar concentration (0.1 M) treatment, as can be seen from the surface of NFs, which might be due to a conformal $TiO_2$ coating over a $SnO_2$ MPNFs surface. The higher concentrations steadily developed NPs of size (∼5−10 nm), which formed a

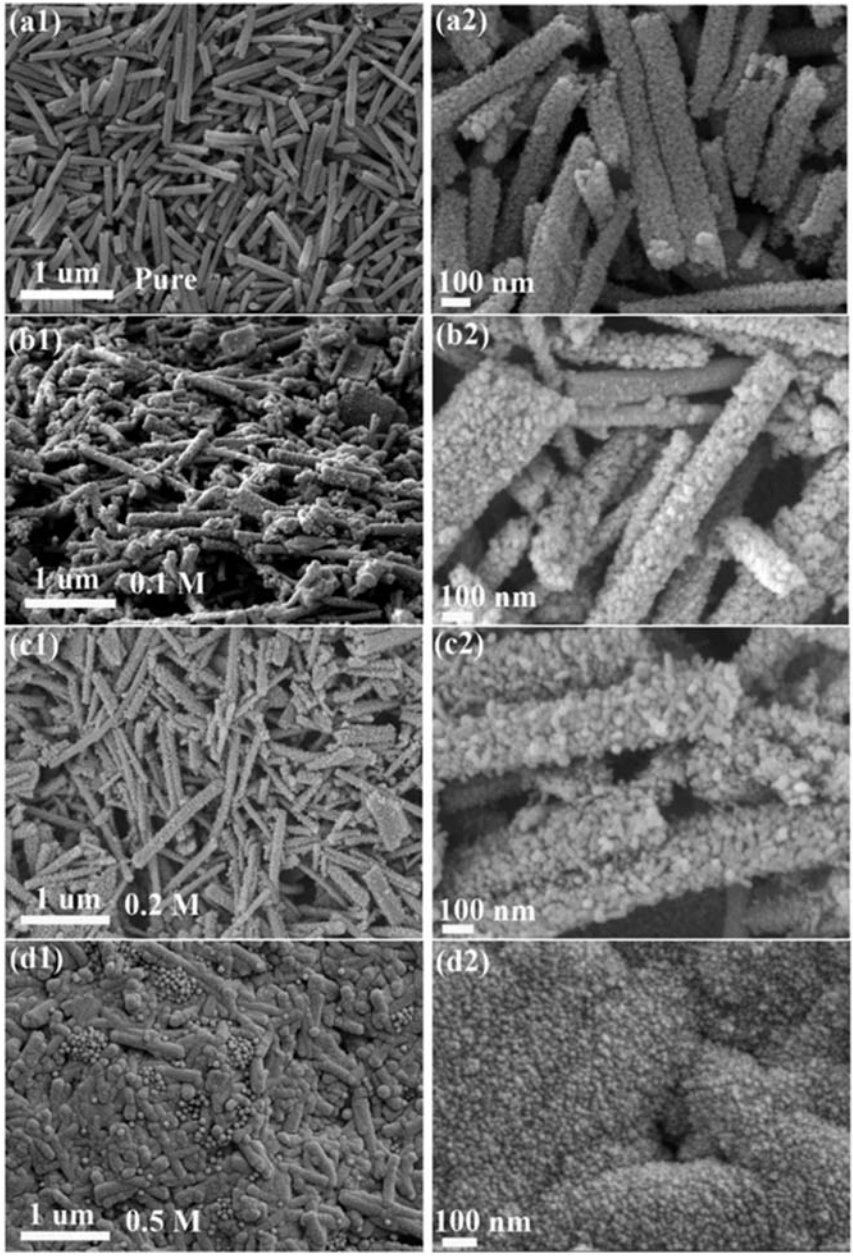


**Figure 7.37** FESEM surface images (A1 and A2) show pure $SnO_2$ MPNFs electrodes and (B1−D2) demonstrate (0.1, 0.2, and 0.5 M) $TiCl_4$ molar concentrations on pure $SnO_2$ MPNFs electrodes.

thin $TiO_2$ overlayer on MPNFs and also filled the gaps between them resulting in an improved interconnectivity of the grains.

An improved physical interconnection (i.e., the voids between the NFs are filling due to the access number of $TiO_2$ NPs increasing from 0 to 0.5 M) of NFs in the photoanode film upon $TiCl_4$ posttreatment can be easily seen from their cross-sectional images (Fig. 7.38B1–D2). Although porous photoanode materials help electrolyte penetration and enhance dye uptake, it increases grain boundary density and decreases particle–particle interconnectivity thereby suppressing charge transport properties [93]. $TiO_2$ NPs served as a medium to fill the voids in pure MPNFs (Fig. 7.38D1 and D2), which is expected to increase the transport properties in the photoanodes of the DSSCs.

The decrease in porosity and filling voids can also be seen upon increasing $TiCl_4$ molar concentration (Fig. 7.37B1–D2). Interestingly, the $SnO_2$ MPNFs film thickness remains unchanged upon $TiO_2$ NPs via $TiCl_4$ solution process; however, it merely filled the spaces between the NFs. This suggests that the overlayer formed by $TiCl_4$ is too thin to be separately realized by FESEM in composite morphology.

#### 7.5.1.3 Morphological features of electrospun composite

The synthesized electrospun composite nanostructures were examined by FESEM analysis. Fig. 7.39 demonstrates the surface morphology of the annealed composite NFs, which shows smooth surface morphology. The diameter of the fibers ranges between 200 and 300 nm as can be seen from the higher FESEM magnification images.

Cross-sectional view (Fig. 7.40) of the synthesized nanocomposites reveal that, contrary to the surface analysis, the composite NFs are in fact hollow in nature, similar to those of MPNFs. This additional feature offered by composite NFs, as typical $TiO_2$ NFs formed by electrospinning, is solid and does not offer tubular morphology.

In order to confirm the formation of ($SnO_2$–$TiO_2$) NFs composite energy-dispersive X-ray spectroscopy (EDX) analysis was performed. During the EDX measurement different areas were focused and the corresponding peaks are shown in Fig. 7.41A–C. Both $SnO_2$ and $TiO_2$ can be seen in the synthesized composite nanostructure in the EDX spectrum. In spectrum 1, the quantity of Sn, Ti, and O were 9.67, 10.71, and 79.62, respectively, while in spectrum 2, the values were 11.67, 13.48, and 74.85 measured in atomic % for Sn, Ti, and O, respectively. Details of the three

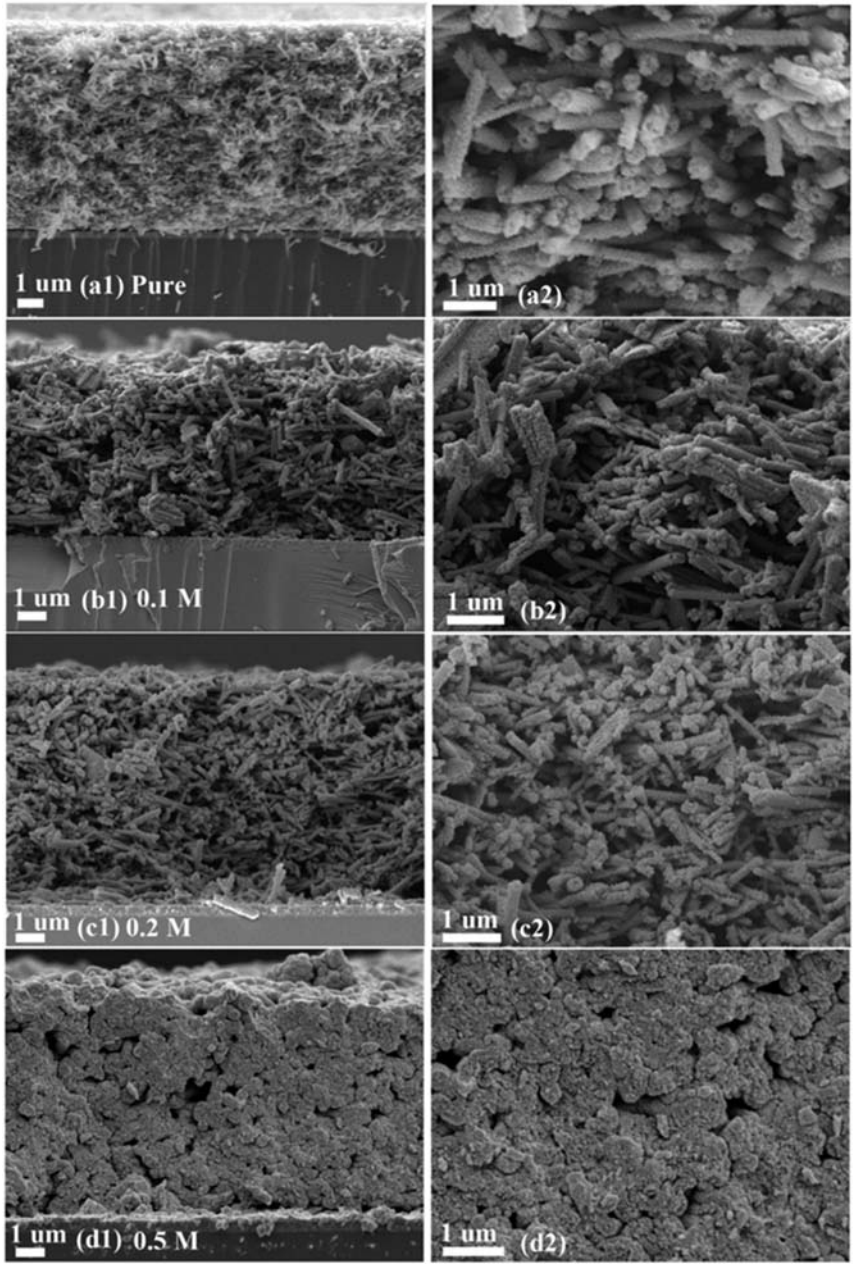


**Figure 7.38** FESEM cross-section images of the pristine $SnO_2$ MPNFs (A1 and A2) and passivated electrodes (B1—D2) using 0.1, 0.2, and 0.5 M $TiCl_4$ molar concentrations at different magnifications.

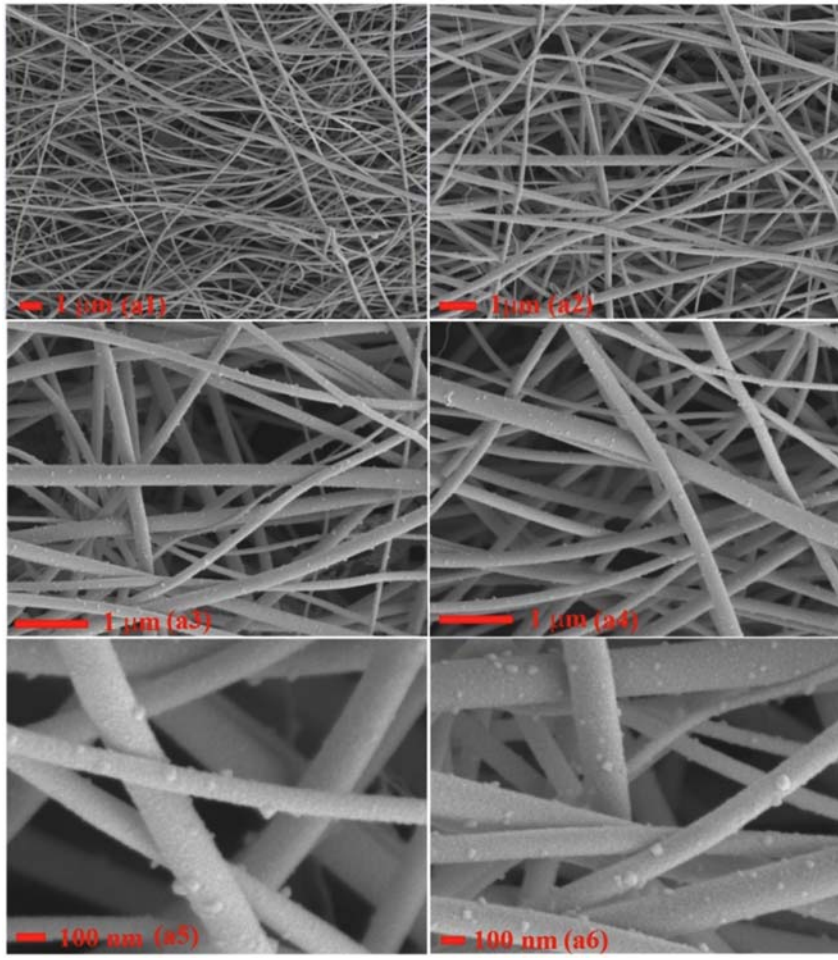


**Figure 7.39** FESEM surface morphology images of ($SnO_2$—$TiO_2$) NFs from low to high magnification (A1—A6). *NF*, Nanofiber.

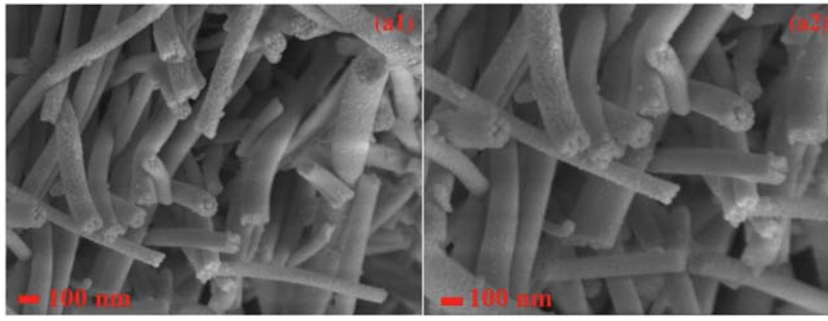


**Figure 7.40** FESEM cross-sectional morphology images of ($SnO_2$—$TiO_2$) NFs from low to high magnification (a1 and a2). *NF*, Nanofiber.

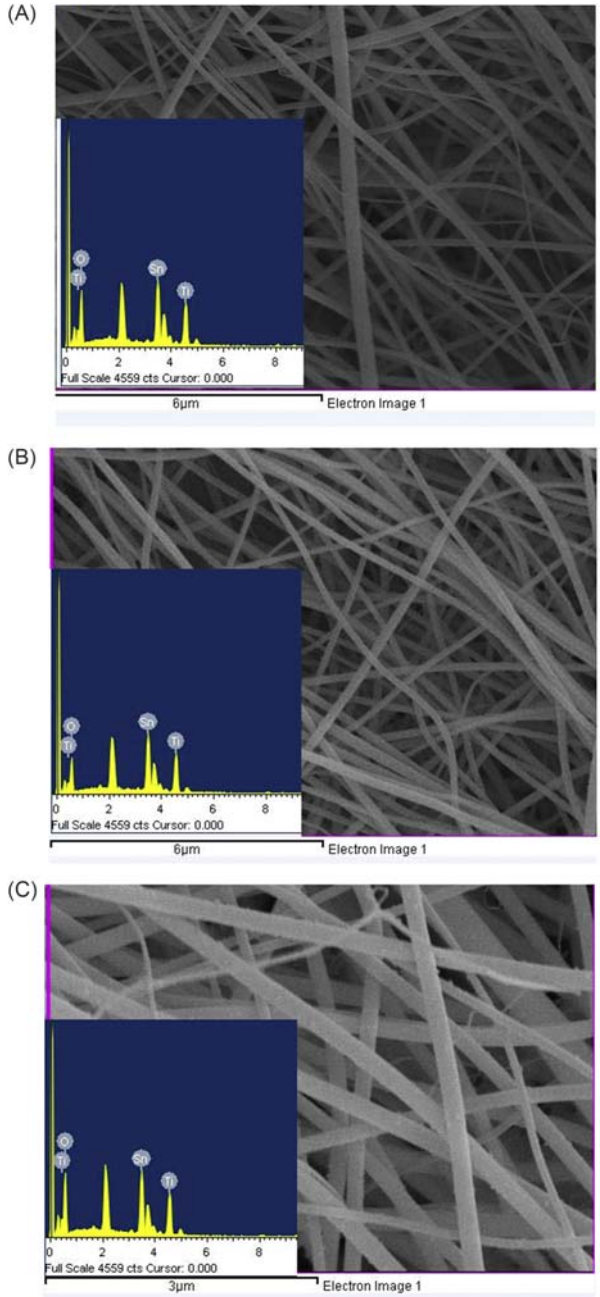


**Figure 7.41** (A) EDX pattern of the electrospun ($SnO_2$—$TiO_2$) NFs composite (spectrum 1). (B) EDX pattern of the electrospun ($SnO_2$—$TiO_2$) NFs composite (spectrum 2). (C) EDX pattern of the electrospun ($SnO_2$—$TiO_2$) NFs composite (spectrum 3). *NF*, Nanofiber.

**Table 7.13** EDX weight ratio of electrospun ($SnO_2$−$TiO_2$) nanofibers nanocomposite using three spectrums focused on three distinct areas.

| ($SnO_2$−$TiO_2$) composite | Tin (Sn) | | Titanium (Ti) | | Oxygen (O) | |
|---|---|---|---|---|---|---|
| | Weight (%) | Atomic (%) | Weight (%) | Atomic (%) | Weight (%) | Atomic (%) |
| Spectrum 1 | 39.10 | 9.67 | 17.48 | 10.71 | 43.41 | 79.62 |
| Spectrum 2 | 42.91 | 11.67 | 19.99 | 13.48 | 37.10 | 74.85 |
| Spectrum 3 | 37.05 | 8.86 | 17.37 | 10.29 | 45.58 | 80.85 |

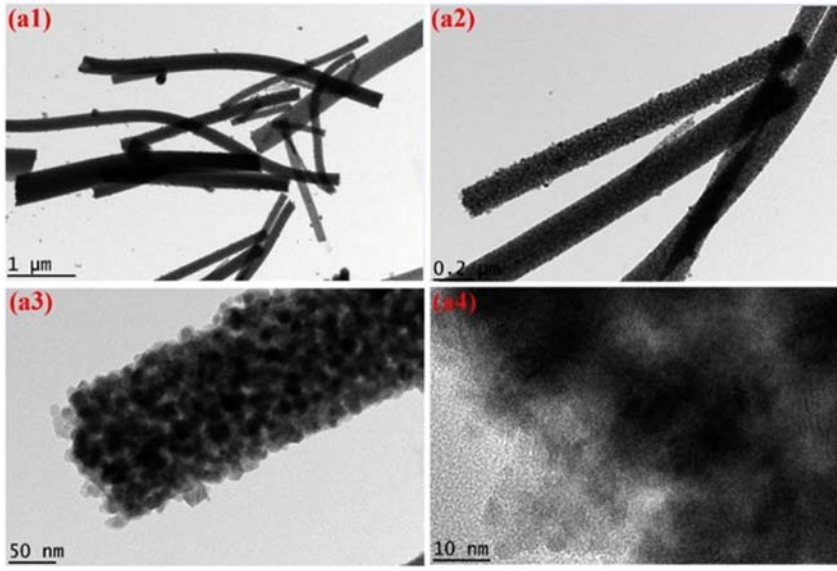


**Figure 7.42** (A1−A4) Depict TEM images of the electrospun ($SnO_2$−$TiO_2$) NFs composite. *NF*, Nanofiber.

EDX spectra of the electrospun ($SnO_2$−$TiO_2$) NFs values measured in atomic and weight % are listed in Table 7.13.

To further investigate the morphology of ($SnO_2$−$TiO_2$) NFs composite, TEM analysis was performed. Fig. 7.42 shows TEM images of the composite nanostructure at low magnification where highly smooth NFs' surface can be seen, corroborating the findings of FESEM images. The NFs vary in diameter and also show a partial transparency to an electron beam, from which it is deduced that the NFs are porous. The composite NFs possess grain size (10−20 nm) and a visible grain boundary can be seen throughout the composite material.

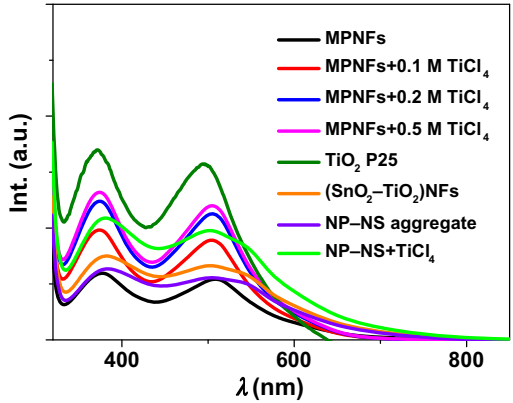


**Figure 7.43** UV–vis–NIR absorption spectra of the desorbed photoanodes for pure $SnO_2$ MPNFs, multifunctional NPs–NSs, $TiO_2$ P25 NPs, ($SnO_2$–$TiO_2$), and posttreated electrodes at different $TiCl_4$ concentrations (0.1, 0.2, and 0.5 M) on MPNFs and multifunctional particles. *NP*, Nanoparticle; *NS*, nanosphere.

## 7.5.2 Dye-sensitized solar cells fabrication and testing

### *7.5.2.1 Dye loading of the electrodes*

Dye loading of the dye-anchored electrodes was measured by a desorption test as shown in Fig. 7.43. The spectra of the desorbed dye solution show that MPNFs electrodes treated with 0.5 M concentration exhibit significantly higher dye loading (262 nmol $cm^{-2}$) than other molar treatments. The dye loading dramatically decreased for the lower $TiCl_4$ concentration as can be observed from the Fig. 7.43. Moreover, electrospun $SnO_2$–$TiO_2$ NFs composite electrodes show inferior dye loading due to the lower surface area while the hydrothermal multifunctional (NPs–NSs) showed dramatic increase when treated with $TiCl_4$. On the other hand, $TiO_2$ P25 surpass the dye loading owing to the nature of these particles which possess the highest surface area ($\sim 150\ m^2\ g^{-1}$). Dye loading values of the pure and $TiCl_4$-treated electrodes are listed in Table 7.14.

### *7.5.2.2 Photovoltaic characteristics of the dye-sensitized solar cells*

It has been revealed that hydrothermal multifunctional NPs–NSs and electrospun MPNFs performed notably better than other $SnO_2$ morphologies and generated a comparable $J_{SC}$ ($\sim 17$–$18\ mA\ cm^{-2}$) to that of the $TiO_2$. However, the $V_{OC}$ ($\sim 480$–$500$ mV) and FF ($\sim 45\%$–$50\%$) were far lower than that of $TiO_2$ (typically $\geq 800$ mV and 60%–70%) and therefore DSSCs made from their composite photoanodes were investigated.

**Table 7.14** Photovoltaic parameters of dye-sensitized solar cells (DSSCs) [$J_{SC}$, $V_{OC}$, fill factor (FF), $\eta$ and dye loading based on pure multifunctional nanoparticles (NPs)–nanospheres (NSs), and MPNFs], passivated MPNFs electrodes with (0.1, 0.2, and 0.5 M) $TiCl_4$ aqueous solution and an electrospun composite of ($SnO_2$–$TiO_2$) nanofibers (NFs).

| DSSC/WE | $J_{SC}$ (mA $cm^{-2}$) | $V_{OC}$ (V) | FF | $\eta$ (%) | Dye loading (nmol $cm^{-2}$) |
|---|---|---|---|---|---|
| Pure (NPs–NSs) | 16.3 | 0.490 | 0.49 | 4.0 | 131 |
| Pure MPNFs | 17.5 | 0.491 | 0.50 | 4.3 | 119 |
| MPNFs + 0.1 M $TiCl_4$ | 18.3 | 0.570 | 0.50 | 5.2 | 192 |
| MPNFs + 0.2 M $TiCl_4$ | 19.1 | 0.620 | 0.50 | 5.9 | 245 |
| MPNFs + 0.5 M $TiCl_4$ | 22.0 | 0.720 | 0.53 | 7.9 | 262 |
| (NPs–NSs) + $TiCl_4$ | 21.33 | 0.705 | 0.53 | 7.5 | 180 |
| ($SnO_2$–$TiO_2$) NFs | 16.0 | 0.732 | 0.64 | 7.5 | 173 |
| P25 NPs | 17.49 | 0.730 | 0.60 | 7.6 | 745 |

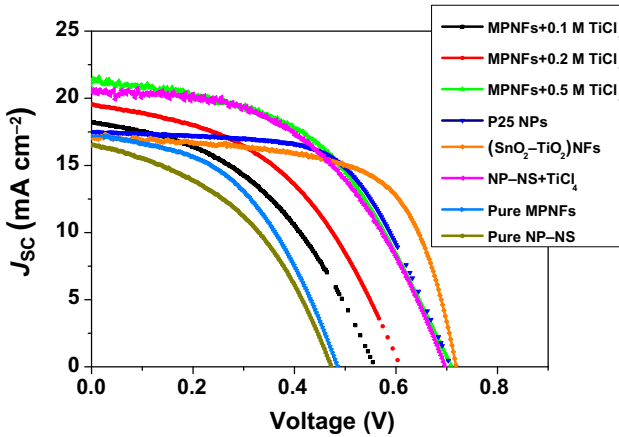


**Figure 7.44** Current voltage characteristics curves of DSSCs based on multifunctional NPs–NSs and MPNFs, passivated MPNFs electrodes with 0.1, 0.2, and 0.5 M $TiCl_4$ aqueous solution, and electrospun composite of ($SnO_2$–$TiO_2$) NFs. *DSSC*, Dye-sensitized solar cell; *NF*, nanofiber; *NP*, nanoparticle; *NS*, nanosphere.

*J–V* characteristics of the best-performing devices are shown in Fig. 7.44. The PV parameters of pure and composite DSSCs are listed in Table 7.14. It is obvious that the $\eta$ of the DSSCs increased in the order that is, multifunctional NPs–NSs $\left(\eta_{\text{multifunctional NPs–NSs+TiCl}_4} > \eta_{\text{multifunctional NPs–NSs}}\right)$, which showed $\sim$80% higher $\eta(\sim 7.5\%)$ than the parent device (Table 7.14). Although the $TiCl_4$-treated DSSCs yielded a higher $J_{SC}$ ($\sim$21%) than the

P25 DSSC, $a \sim 20\%$ lower FF of the former restricts its performance than its $TiO_2$ counterpart. On the other hand, MPNFs electrodes were treated using various $TiCl_4$ concentrations, which yielded $(\eta_{MPNFs+0.5\ MTiCl_4} > \eta_{MPNFs+0.2\ MTiCl_4} > \eta_{MPNFs+0.1\ MTiCl_4} > \eta_{Pure\ MPNFs})$.

The pure MPNFs showed an enhanced $J_{SC}$ ($\sim 18$ mA cm$^{-2}$), however, limited in $V_{OC}$ ($\sim 470-500$ mV) and FF ($\sim 45\%-50\%$). Initially, the MPNFs electrode was treated with 0.1 M $TiCl_4$, which increased the $J_{SC}$ (from 18 to 18.3 mA cm$^{-2}$), $V_{OC}$ ($\sim 490-570$ mV) and a slightly increase in FF was observed with overall $\eta$ of $\sim 5.2\%$ with a subsequent 0.2 M $TiCl_4$ solution posttreatment dramatically increased the $V_{OC}$ up to $\sim 620$ mV with a marginal increase in the $J_{SC}$ and FF that resulted a final $\eta$ of $\sim 5.9\%$. Nonetheless, the $\eta$ was still far lower than the most successful employed MOS $TiO_2$ ($\sim 14.3\%$). Finally, the pure MPNFs electrode was passivated with higher $TiCl_4$ molar concentration (0.5 M), which resulted in an exceptional $\eta \sim 8\%$ with $V_{OC} \sim 720$ mV close to that of $TiO_2$-based DSSCs in our experiments ($\sim 730$ mV) and yielded notably higher $J_{SC} \sim 22$ mA cm$^{-2}$ ($J_{SC}$ of $TiO_2 \sim 17$ mA cm$^{-2}$). On increasing the $TiCl_4$ concentration during posttreatment, the photoanode films cracked during the hydrolysis process or upon sintering, which is in close agreement with the reported results [94]. It appears that the $TiCl_4$ posttreatment only increases the $V_{OC}$ and $J_{SC}$ significantly and has only a minor impact on the FF of the devices. The increment in $J_{SC}$ is attributed to the enhanced dye loading upon $TiCl_4$ posttreatment (Fig. 7.43), which also has its impact on $V_{OC}$. Similar improvements in $J_{SC}$ are observed by Refs. [93,95]. The achieved FF ($\sim 45\%-50\%$) of $SnO_2$ is still far lower than that of $TiO_2$ ($\sim 60\%-70\%$).

From the comparative experiments of pure $SnO_2$ multifunctional NPs–NSs and MPNFs-based DSSCs and their $TiCl_4$ posttreated analogues it is obvious that $SnO_2$ possesses lower IEP (at pH $\sim 4-5$) and thereby make weak bonding to the carboxylic groups of the ruthenium-based dyes. The weak bonding resulted in inferior dye anchoring and eventually lower $J_{SC}$. On the contrary, $TiO_2$ has a high IEP (at pH $\sim 6-7$) therefore making a strong bonding group with carboxylic groups. Thus the increase in $J_{SC}$ values of the $SnO_2$ electrodes passivated with $TiCl_4$ solution can be understood from the surface passivation which changes adsorption properties of pure $SnO_2$ resulting in higher amounts of dye loading (Fig. 7.43) and a surge in $J_{SC}$.

Another significant improvement in composite photoanodes is the increase in $V_{OC}$. The lower $V_{OC}$ ($\sim 470-500$ mV) in pure $SnO_2$ CB is

due to its lower CB than $TiO_2$ with respect to the most successful ruthenium-based sensitizers. The increase in $V_{OC}$ in $SnO_2$ photoanodes upon $TiCl_4$ posttreatment is attributed to the formation of a $TiO_2$ NPs thin layer. The physical barrier reduces electron back recombination from $SnO_2$ CB to dye, or with electrolytes so that to increase the number of accommodated electrons in the CB of the $SnO_2$, and eventually enhance the lower $V_{OC}$, as reported. There are two possible electron-injection routes for the photoinjected electrons to be injected from the dye's LUMO to the CB of $SnO_2$ (1) it can pass direct to $SnO_2$ through the $TiO_2$ NPs thin layer via tunneling or (2) it may first jump into the $TiO_2$ CB and then into $SnO_2$ CB owing to the downhill transition. As the $V_{OC}$ and the $J_{SC}$ are correlated [96], the above studies showed that $TiCl_4$ posttreatment on the pure $SnO_2$ nanostructures electrodes only improved the $V_{OC}$ and $J_{SC}$, however, the FF remained unchanged throughout the study. The enhancement in $V_{OC}$ and $J_{SC}$ reveals that the injection efficiency of photogenerated electrons into MOS and the blocking behavior of the MOS-electrolyte interface is improved as also observed by Ref. [94].

In order to combine the synergistic properties of $SnO_2$ higher $\mu_e$ and $TiO_2$ favorable CB in a single photoanode in DSSCs, electrospun ($SnO_2$−$TiO_2$) NFs composites were developed. The DSSCs made using the composite NFs resulted in FF ~ 64%, similar to that of $TiO_2$ NPs and a similar $V_{OC}$ ~ 732 mV, however, a slight decrease in the $J_{SC}$ is noticed (Fig. 7.44).

### 7.5.2.3 Origin of high open circuit voltage

DSSCs based on pure $SnO_2$ yielded inferior PV parameters owing to its lower $V_{OC}$ and FF using conventional electrolytes ($I^-/I_3^-$) and ruthenium-based sensitizers. These two quantities affect the performance of the device as $= V_{OC} \times J_{SC} \times$ FF. Higher $V_{OC}$ could be achieved if the photoinjected electrons from the LUMO of the dye molecule into the CB of $SnO_2$ and the transfer of electrons from the CE to an electrolyte become equal. The increase in $V_{OC}$ is owing to the suppression of the back reaction (originates between the CB electrons and $I_3^-$ species of the electrolyte at the $SnO_2$/electrolyte interface). Although the MOS surface is covered with the dye, the $I_3^-$ species either penetrate the anchored dye and recombine with electrons in the MOS or access the unanchored exposed MOS surface where the dye molecules are not anchored by the following equation [96]:

$$I_3^- + 2e_{CB}^-(\text{MOS}) \rightarrow 3I^-$$

It is obvious that the photo-induced electrons combine faster in an $SnO_2$ photoanode owing to its lower CB than $TiO_2$ when conjugated with most employed ruthenium-based dyes. However, the increase in the $V_{OC}$ in $SnO_2$ electrode upon $TiCl_4$ posttreatment could be due to the minimized loss in potential between the LUMO of the dye because of an upward shift in CB of the $SnO_2-TiO_2$ composite. Moreover, the thin $TiO_2$ layers formed by $TiCl_4$ treatment on the surface of the $SnO_2$ electrodes sufficiently hinder the recombination of photoinjected electrons with $I_3^-$ species resulting in higher $V_{OC}$ for the passivated electrodes [97].

$$V_{OC} = \frac{kT}{e}\left(\frac{J_{inj}}{n_{cb}k_{rec}[I_3^-]}\right)$$

where $kT$ is the thermal energy, $e$ is the elementary charges, $J_{inj}$ is the injected electron flux, $k_{rec}$ $[I_3^-]$ is the rate constant for $I_3^-$ reduction, and $n_{cb}$ is the electron density in CB or electron's concentration in the CB in the dark. Another reason for an enhanced $V_{OC}$ could be the injection rate in composite NFs (i.e., as an electron can easily jump to the $TiO_2$ CB as compared to that of $SnO_2$ CB).

#### 7.5.2.4 Charge transport properties

The achieved high $V_{OC}$ and the suppression of electron recombination by the $TiCl_4$ blocking layer were evaluated from the charge transport parameters using EIS technique. The Nyquist plot of the DSSCs shows three semicircles. The first small circle of Nyquist plot at the high-frequency region ($>1$ kHz) represents the charge transport resistance, while the recombination of electrons at the dye-anchored WE/electrolyte interface is deduced from the second semicircle at frequency ($1000\ \text{Hz} < f < 1\ \text{Hz}$). The third semicircle at low frequency ($<1$ Hz) reveals the ions' diffusion in the electrolyte [3]. Typically for high-performing DSSCs, $R_{CT} \gg R_T$ and the second semicircle are much larger than the first. A similar trend is observed in our experiments, which is shown in Fig. 7.45. Similarly, MPNFs + 0.5 M DSSCs exhibit larger diameter than the pure analogues and passivated DSSCs at lower molar concentrations, thereby, evidencing the suppression of electron recombination and consequently long $\tau_n$.

The $\tau_n$ was calculated for the respective DSSCs using the mid frequency of the bode-phase plots (Fig. 7.46) and by using the relation $\tau_n = 1/2\pi f_o$ where $f_o$ is the maximum frequency at the mid peak. The

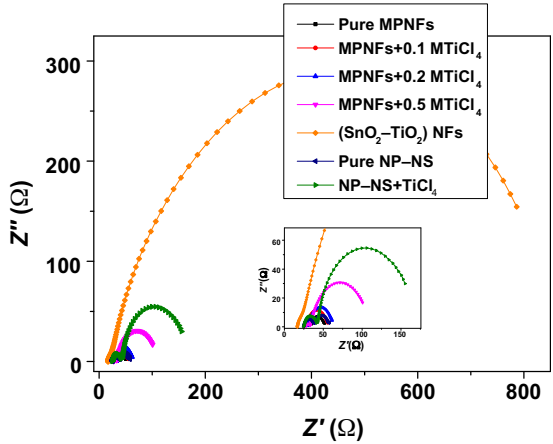


**Figure 7.45** Nyquist plots recorded for the pure multifunctional NPs−NSs and MPNFs, 0.1−0.5 M $TiCl_4$ posttreated MPNFs, NPs−NSs + $TiCl_4$, and $SnO_2$−$TiO_2$ NFs. *NF*, Nanofiber; *NP*, nanoparticle; *NS*, nanosphere.

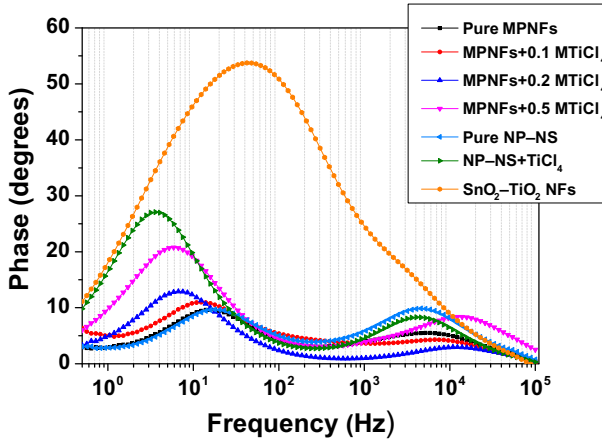


**Figure 7.46** Bode-phase plots recorded for the pure multifunctional NPs−NSs and MPNFs, 0.1−0.5 M $TiCl_4$ MPNFs, multifunctional NPs−NSs + $TiCl_4$, and $SnO_2$−$TiO_2$ NFs. *NF*, Nanofiber; *NP*, nanoparticle; *NS*, nanosphere.

calculated values of $f_o$ were ∼18.0, 17.0; ∼3.6; 12.34, 6.65, 5.88; and 42.8 for NPs−NSs DSSCs, MPNFs DSSCs, NPs−NSs DSSCs + $TiCl_4$, and 0.1−0.5 M $TiCl_4$ DSSCs, respectively, and their corresponding $\tau_n$ are listed in Table 7.15. Long $\tau_n$ values for the composite nanostructures show that the electrons could survive for a longer time before recombination which leads to higher $J_{SC}$ and $V_{OC}$ in DSSCs employing them.

**Table 7.15** Electron lifespan using OCVD and electrochemical impedance analysis (EIS) of dye-sensitized solar cells (DSSCs) based on pure [multifunctional nanoparticles (NPs)−nanospheres (NSs) and MPNFs], their composite and composite of ($SnO_2$−$TiO_2$) nanofibers (NFs).

| DSSC/WE | OCVD ($\tau_n$ s) | | | EIS ($\tau_n$ ms) |
|---|---|---|---|---|
| | $V_{OC}\sim 0.2$ V | $V_{OC}\sim 0.3$ V | $V_{OC}\sim 0.4$ V | |
| Pure NPs−NSs | 4.8 | 0.40 | 0.50 | 28.0 |
| Pure MPNFs | 0.39 | 0.11 | 0.05 | 28.0 |
| MPNFs + 0.1 M $TiCl_4$ | 4.9 | 0.90 | 0.14 | 19.4 |
| MPNFs + 0.2 M $TiCl_4$ | 5.0 | 1.6 | 0.84 | 10.5 |
| MPNFs + 0.5 M $TiCl_4$ | $>100$ | $>100$ | 1.9 | 9.2 |
| NPs−NSs + $TiCl_4$ | $>100$ | 16.0 | 2.5 | 5.6 |
| ($SnO_2$−$TiO_2$) NFs | $>100$ | 13.5 | 3.6 | 66.5 |
| $TiO_2$ P25 | 4.1 | 1.5 | 0.8 | − |

To further explore the effect of $TiCl_4$-treated DSSCs and the electrospun ($SnO_2$−$TiO_2$) NFs composite, OCVD measurement was performed. It is a useful technique to know the electron recombination kinetics and explore the built-in potential particularly in $TiCl_4$-treated DSSCs. Under illumination at standard condition, the device under test attained a state of equilibrium due to the electron injection into the MOS, thus the Fermi level raised to its optimum level. However, when an illumination is interrupted, the $V_{OC}$ started decaying with time as can be seen in Fig. 7.47. The OCVD measurement is always made in the dark so that no electrons could recombine with oxidized dye molecules as the dye is not oxidized in dark. Consequently, electrons can merely recombine with electrolyte species. Owing to the recombination, the Fermi level starts to move toward the valence band. When all the photo-induced electrons disappear, the Fermi level touches the valence band of the MOS and results in the $V_{OC}$ approaching zero.

It can be seen from Fig. 7.48 that $V_{OC}$ decays slowly for all passivated and ($SnO_2$−$TiO_2$) NFs devices, while there was an abrupt drop in pure $SnO_2$ multifunctional NPs−NSs and MPNFs. Such a slower decay revealed that the passivated DSSCs not only assures that the electron could retain for a long time and subsequently long $\tau_n$, but also opens a new idea that a built-in potential is formed between the two MOS having different CB and other physio-chemic properties.

To further study the recombination kinetics in detail, $\tau_n$ is derived from OCVD curves and compared with the $V_{OC}$ (Fig. 7.48). At lower

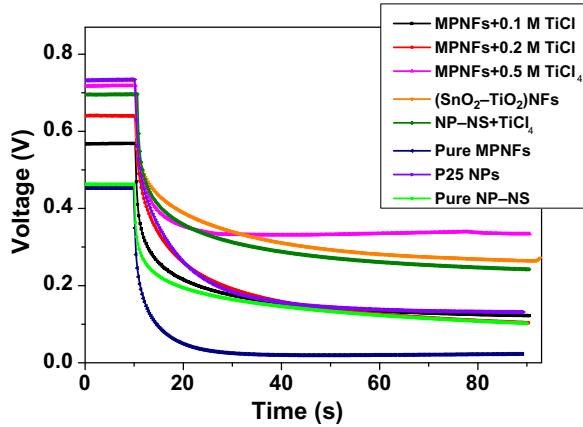


**Figure 7.47** OCVD measurement where voltage decaying with the passage of time for pure $SnO_2$ (NPs−NSs and MPNFs), (0.1−0.5 M $TiCl_4$ MPNFs), multifunctional NPs−NSs + $TiCl_4$ and P25 NPs. *NP*, Nanoparticle; *NS*, nanosphere.

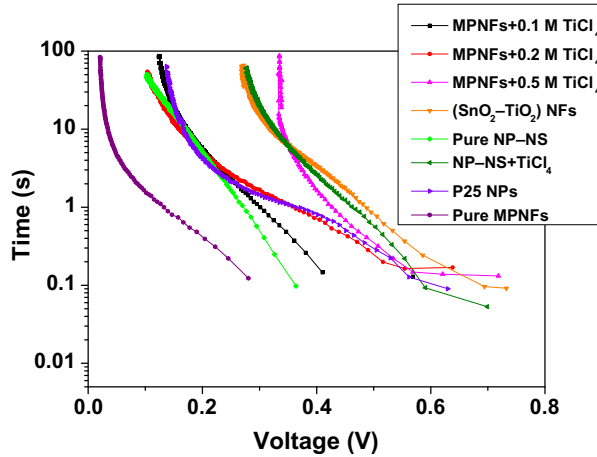


**Figure 7.48** Electron lifespan from OCVD measurement of the pure (NPs−NSs and MPNFs), (0.1−0.5 M $TiCl_4$ MPNFs), multifunctional NPs−NSs + $TiCl_4$, and P25 NPs. *NP*, Nanoparticle; *NS*, nanosphere.

range of $V_{OC}$, the passivated DSSCs (NPs−NSs and MPNFs) with $TiCl_4$ and ($SnO_2$−$TiO_2$) NFs composite show very high $\tau_n$ compared to the pure counterparts (multifunctional NPs−NSs and MPNFs), respectively. The $\tau_n$ calculated from OCVD curves at ∼0.2, 0.3, and ∼0.4 V are listed in Table 7.15. Therefore the composite DSSCs show significantly higher $\tau_n$ than the pure analogues due to the suppression of electron recombination at the $SnO_2$ WE/electrolyte interfaces.

The primary issue of pure $SnO_2$ nanostructures, that is, inferior $V_{OC}$ and FF, is significantly enhanced by compositing with $TiO_2$ using two different approaches. Initially, pure $SnO_2$ photoanodes were passivated with aqueous $TiCl_4$ solution with varying molar concentrations which dramatically enhanced the $V_{OC}$ from $\sim$500 to $\sim$730 mV with final $\eta \sim 8\%$. However, the FF remained unchanged ($\sim$50%) for both the devices. In the next approach, an electrospun NFs composite was developed by chemically combining the inherent feature of both the $SnO_2$ and $TiO_2$. The resulted composite significantly improved the FF$\sim$64% comparable to that of a reference $TiO_2$-based DSSC and also a $V_{OC} \sim 732$ mV. This enhancement in PV parameters is due to the suppression of electron recombination, enhanced dye loading and Fermi level shift photoanode (14.3%). This brings into account a multishell architecture around a single core by Dong et al. A systematic increase in the number of $SnO_2$ shells, which enhanced the surface area from $\sim 22\ m^2\ g^{-1}$ in a single shell to $\sim 38\ m^2\ g^{-1}$ in quintuple shells [98]. It also showed a direct effect on their PV performance; the $\eta$ increased to 7.18% in quintuple shells from 5.21% in a conventional single-shell architecture (all $SnO_2$ DSSCs WE were passivated with $TiCl_4$ aqueous solution). Although the work reported the highest $\eta$ in $SnO_2$-based DSSCs, so far it requires further optimization to elevate the $\eta$ closer to that of $TiO_2$-based devices.

## 7.6 Doped photoanode

Another way to improve the PV parameters in pure $SnO_2$ DSSCs, especially the low $V_{OC}$ and FF, is to simply dope $SnO_2$ with other elements having similar ionic radii [13,99,100]. Various transition metals such as niobium ($Nb^{5+} \sim 0.78$ Å), Zinc ($Zn^{2+}$), magnesium ($Mg^{2+}$), gallium ($Ga^{3+} \sim 0.76$ Å), tungsten ($W^{4+} \sim 0.74$ Å), titanium ($Ti^{4+}$, 0.75 Å), and indium ($In^{3+} \sim 0.76$ Å) are doped in $SnO_2$ toward this end. Among these, $Zn^{2+}$, $Ga^{3+}$, and $Mg^{2+}$ showed outstanding performance when doped with tin ($Sn^{4+} \sim 0.69$ Å) [16]. Dou et al. reported $\sim$20% doping of Zn in $SnO_2$ and achieved a substantial increment in the $V_{OC}$ ($\sim$0.78 V in doped and $\sim$0.52 V in pure) [101]. The Zn doping is suspected of replacing some Sn atoms from its crystal structure, which resulted in an upward shift of the Fermi Level of the $SnO_2$ and consequently achieved a higher $V_{OC}$.

In a similar report, Li et al. compared PV parameters of Zn-doped $SnO_2$ and pure $SnO_2$-based DSSCs. The pure $SnO_2$ photoanodes resulted

in $V_{OC} \sim 0.41$ V, $J_{SC} \sim 5.10$ mA cm$^{-2}$, FF $\sim 0.53$, and $\eta \sim 1.13\%$, whereas, doped analogues showed notable improvement ($\sim 0.59$ V, $\sim 9.22$ mA cm$^{-2}$, $\sim 0.74$ and $\sim 4.15\%$, respectively) [100]. It is revealed that Zn-doped $SnO_2$ photoanodes provide better electron transport and slowed down the recombination with electrolytes, which resulted in improved FF and about 150% enhanced $\tau_n$ from $\sim 5.3$ to $\sim 12.5$ ms. Pang et al. reported $>200\%$ increment in $\eta$ in Mg-doped $SnO_2$ compared to a pure $SnO_2$ device primarily owing to the increased $J_{SC}$ from $\sim 3$ to $\sim 7$ mA cm$^{-2}$ [40]. Teh et al. employed Gallium-doped $SnO_2$ nano-cuboids as a photoanode in DSSCs and achieved a remarkable $V_{OC} \sim 0.74$ and FF $\sim 74\%$ without any further surface passivation of the WE [99]. The $V_{OC}$ in Ga-doped $SnO_2$, which is similar to $TiO_2$, results from the suppression of charge recombination as evidenced by Mott–Schottky analysis in their work. The flat-band potentials consistently shifted upon Ga-doping ($-0.34$ and $-0.81$ V for 0% and 5% Ga precursor, respectively), which explains the origin of high $V_{OC}$ and FF in their report.

In conclusion, the photoanode is the crucial part of the DSSCs due to the fact that it not only supports the sensitizers but also acts as an electron acceptor and conducts the photo-induced electrons. $TiO_2$ is the primarily-employed photoanode material in the DSSCs owing to its high surface area ($\sim 150$ m$^2$ g$^{-1}$) and suitable conduction band alignment with the most successful Ruthenium-based sensitizers. However, it is characterized by a low electron mobility ($<1$ cm$^2$ V$^{-1}$ s$^{-1}$). On the other hand, $SnO_2$ offers a high electron mobility ($\sim 250$ cm$^2$ V$^{-1}$ s$^{-1}$"/>0"/>) and wider band gap ($\sim 3.6$ eV) compared to that of $TiO_2$. However, it shows 3–4 times lower photoconversion efficiency ($\eta \sim 4\%$) compared to the latter ($\eta \sim 14.3\%$). In reality, $SnO_2$ typically results in $\sim 300$ mV lower $V_{OC}$ and significantly inferior FF in its pure form than $TiO_2$ mainly owing to its lower-lying conduction band edge [4]. In addition, $SnO_2$ also results in a lower specific surface area due to its lower IEP (at pH $\sim 4$–5) versus $TiO_2$ (at pH $\sim 6$–7) resulted in poor dye loading and consequently lowered the photocurrent [88]. Innovative approaches are required to combine the large surface area of $TiO_2$ and superior electron mobility of $SnO_2$ in a single photoanode of the DSSCs. Efforts have been made to overcome these limitations by introducing $SnO_2$ composite nanostructures with other MOS of high CB and doping with suitable transition metals to uplift its Fermi energy level. Such efforts reported a comparable $V_{OC}$ ($\sim 780$ mV) and FF ($\sim 70\%$) to that of $TiO_2$

with a maximum $\eta \sim 10\%$. Although the $\eta$ is still lower than the best-performing $TiO_2$ counterpart. Recent developments in $SnO_2$ DSSCs made it a runner-up material and also paved a way for its further development.

## 7.7 Three-dimensional $SnO_2$ nanostructures

In order to achieve strong light scattering and harvesting properties in the WE, 3D nanostructures, which are composed of submicron aggregates (size equivalent to that of the wavelength of visible light), are employed. The 3D nanostructures increase light scattering in the photoanodes, and thereby, improve the charge collection efficiency ($\eta_{CC}$). However, owing to their relatively larger sizes than those of NPs, they are characterized by a lower surface area. Recently, Ganapathy et al. reported cauliflower-like $SnO_2$ hollow microspheres as a WE of the DSSCs and in quantum dot-sensitized solar cells, which showed $\eta \sim 3\%$ and $\sim 2.5\%$, respectively, using a carbon-based CE. In another report Kumar et al. developed 3D flower-shaped structure, where $\eta$ ($\sim 3\%$ with a $V_{OC} \sim 700$ mV) has been achieved, which was higher $\sim 4$ times compared to that of 1D conventional NFs (0.7%) [57]. The $SnO_2$ nanostructure in pure form shows inferior performance when tested as a photoanode in the DSSCs. Therefore a composite with high CB MOS is required in order to enhance its low PV parameters.

Various ways have been adopted in order to enhance the performance of pure $SnO_2$ photoanodes in the DSSCs. For instance, making a composite nanostructure of the $SnO_2$ with another high CB MOS earlier and then utilizing it as a photoanode material, or fabricating a composite directly via a deposition process on the FTO of the DSSCs can produce such a performance enhancement. Another way to improve the performance is making a core–shell nanocomposite, where the core and shell possess distinct characteristics. Finally, by incorporating a trace of a suitable element to $SnO_2$ via the doping process for the enhancement of the PV parameter, progress can be made. The $SnO_2$ composite photoanodes employed in DSSCs are tabulated in Table 7.16.

## 7.8 Photoanodes based on $SnO_2$ core–shell

Although $SnO_2$ is a well-known MOS for its high $\mu_e$, a high-efficiency DSSCs similar to the state-of-the-art $TiO_2$ analogues is yet to be seen.

**Table 7.16** PV parameters of composite and doped $SnO_2$ photoanodes of dye-sensitized solar cell based on nanoparticles (NPs), one-dimensional and core−shell or nanospheres (NSs).

| Sample | Dye | $J_{SC}$ (mA $cm^{-2}$) | $V_{OC}$ (mV) | FF (%) | $\eta$ (%) |
|---|---|---|---|---|---|
| ***Nanoparticles composite/doped $SnO_2$ morphologies*** | | | | | |
| $SnO_2$ NPs−Al (0.02%)−$TiO_2$ [32] | N3 | 16.6 | 650 | 64 | 6.9 |
| Mesoporous $SnO_2$−MgO [30] | Z907 | 15.7 | 670 | 61 | 6.4 |
| Pt-electrode $SnO_2$/$TiO_2$ NPs [102] | N719 | 12.5 | 730 | 71 | 6.5 |
| Carbon-electrode $SnO_2$ NPs/$TiO_2$ [102] | N719 | 13.0 | 740 | 64 | 6.2 |
| $SnO_2$ MHSs−$TiO_2$ [38] | N719 | 14.6 | 664 | 58 | 5.7 |
| $SnO_2$ NPs−Al (0.01%)−$TiO_2$ [32] | N3 | 14.6 | 611 | 62 | 5.5 |
| $SnO_2$ NPs−$CaCO_3$ [37] | N719 | 11.4 | 681 | 69 | 5.4 |
| $SnO_2$ NPs (10%)−$TiO_2$ [103] | N719 | 10.8 | 740 | 66 | 5.3 |
| $SnO_2$ NPs (15%)−$TiO_2$ [103] | N719 | 10.3 | 750 | 67 | 5.2 |
| $SnO_2$ NPs (5%)−$TiO_2$ [103] | N719 | 10.6 | 730 | 66 | 5.1 |
| $SnO_2$ NPs/ZnO nanotetrapods [104] | N719 | 12.0 | 684 | 60 | 5.0 |
| $SnO_2$ NPs−$TiO_2$ [105] | N719 | 11.1 | 641 | 67 | 4.7 |
| Commercial $SnO_2$ NPs/$TiCl_4$ [69] | N719 | 09.7 | 758 | 62 | 4.6 |
| $SnO_2$ NPs−$TiO_2$ [73] | N719 | 13.9 | 670 | 49 | 4.4 |
| $SnO_2$ NPs−Al (0.005%)−$TiO_2$ [32] | N3 | 11.8 | 563 | 66 | 4.4 |
| $SnO_2$ NPs−$TiO_2$ [38] | N719 | 10.3 | 665 | 62 | 4.2 |
| $SnO_2$ NPs−Zn [106] | N719 | 08.6 | 756 | 67 | 4.2 |
| $SnO_2$ NPs−Al (0.03%)−$TiO_2$ [32] | N3 | 11.5 | 607 | 60 | 4.9 |
| Mg−$SnO_2$−$TiO_2$ [40] | N719 | 09.7 | 670 | 61 | 4.2 |
| $SnO_2$ NPs@$TiO_2$ [42] | N179 | 11.5 | 590 | 57 | 3.8 |
| $SnO_2$ NPs/$TiO_2$/Cu anode [107] | Cds/Cdse | 17.4 | 477 | 45 | 3.7 |
| $SnO_2$ NPs−Ni [106] | N719 | 07.6 | 690 | 69 | 3.6 |
| $SnO_2$ NPs/Al (0.02%) [32] | N3 | 12.8 | 555 | 51 | 3.5 |
| $SnO_2$ NPs/$TiO_2$/Pt anode [107] | Cds/Cdse | 16.2 | 458 | 46 | 3.4 |
| Nano-$SnO_2$−$SrTiO_3$ (24.23%) [52] | D149 | 09.5 | 580 | 62 | 3.4 |
| $SnO_2$ NPs/$TiO_2$ [32] | N3 | 09.3 | 540 | 66 | 3.3 |
| $SnO_2$ NPs−$TiCl_4$ [106] | N719 | 06.9 | 684 | 70 | 3.2 |
| Nano-$SnO_2$−$SrTiO_3$ (27.43%) [52] | D149 | 07.6 | 615 | 63 | 2.9 |
| Nano-$SnO_2$−$SrTiO_3$ (20.74%) [52] | D149 | 08.5 | 569 | 60 | 2.9 |

(*Continued*)

**Table 7.16** (Continued)

| Sample | Dye | $J_{SC}$ (mA cm$^{-2}$) | $V_{OC}$ (mV) | FF (%) | $\eta$ (%) |
|---|---|---|---|---|---|
| $SnO_2$ NPs/Al (0.01%) [32] | N3 | 11.0 | 512 | 51 | 2.8 |
| $SnO_2$ NPs−$TiO_2$−MgO [50] | D102 | 06.6 | 710 | 59 | 2.8 |
| $SnO_2$ NPs/Al (0.005%) [32] | N3 | 09.8 | 490 | 55 | 2.6 |
| $SnO_2$ NPs−$TiO_2$ [34] | N3 | 19.7 | 330 | 40 | 2.6 |
| $SnO_2$ NPs/Al (0.03%) [32] | N3 | 10.0 | 535 | 46 | 2.4 |
| $SnO_2$ NPs−ZnO [108] | N719 | 06.6 | 597 | 62 | 2.4 |
| Mg−$SnO_2$ NPs [40] | N719 | 06.7 | 570 | 53 | 2.0 |
| $SnO_2$ NPs−MgO [108] | N719 | 08.8 | 447 | 52 | 2.0 |
| Nano-$SnO_2$−$SrTiO_3$ (30%) [52] | – | 05.3 | 599 | 64 | 2.0 |
| Ni−$SnO_2$ NPs [14] | Ru 353 | 07.0 | 460 | 58 | 1.9 |
| Cd−$SnO_2$ NPs [14] | Ru 535 | 08.8 | 450 | 46 | 1.8 |
| Cu−$SnO_2$ NPs [14] | Ru 353 | 06.7 | 470 | 57 | 1.8 |
| $SnO_2$ NPs−MgO [50] | D102 | 09.5 | 430 | 42 | 1.8 |
| Zn−$SnO_2$ NPs [14] | Ru 535 | 08.5 | 420 | 48 | 1.7 |
| $SnO_2$ NPs−$TiO_2$ [42] | N719 | 05.5 | 760 | 45 | 1.7 |
| $SnO_2$−MgO [45] | | 03.3 | 710 | 48 | 1.2 |
| $SnO_2$ NPs−NiO [108] | N719 | 03.9 | 598 | 52 | 1.2 |
| Pb−$SnO_2$ NPs [14] | Ru 535 | 05.8 | 380 | 50 | 1.1 |
| $SnO_2$ NPs−$TiO_2$ [50] | D102 | 02.5 | 520 | 49 | 0.6 |
| $SnO_2$ NPs−CuO [108] | – | 00.9 | 475 | 70 | 0.3 |
| ***One-dimensional composite/doped $SnO_2$ morphologies*** | | | | | |
| $SnO_2$ NRs−$TiO_2$ [109] | N719 | 19.6 | 644 | 68 | 8.6 |
| [a]$SnO_2$ NT@TNS/OM−$TiO_2$ [110] | N719 | 17.1 | 760 | 61 | 7.9 |
| MPNFs/$TiO_2$ | N719 | 23.7 | 660 | 47 | 7.4 |
| $SnO_2$ NF−$TiO_2$ [54] | N719 | 20.5 | 713 | 48 | 7.0 |
| $SnO_2$ NRs@$TiO_2$ [111] | | 16.2 | 780 | 55 | 7.0 |
| Zn−$SnO_2$−$TiO_2$ 10 μm [101] | N719 | 13.8 | 800 | 59 | 6.8 |
| $SnO_2$ NFs−$TiO_2$ (1:1) [112] | | 13.5 | 730 | 63 | 6.2 |
| Zn−$SnO_2$−$TiO_2$ nanoflowers 8 μm [101] | N719 | 10.0 | 800 | 63 | 5.2 |
| $SnO_2$ NTs−$TiO_2$ [56] | – | 14.7 | 723 | 48 | 5.2 |
| $SnO_2$−ZnO nanoneedle [113] | N719 | 09.8 | 590 | 57 | 4.7 |
| $SnO_2$ NR−$TiCl_4$ [112] | N719 | 12.9 | 650 | 55 | 4.6 |
| $SnO_2$ NFs−$TiO_2$ [56] | N719 | 12.7 | 742 | 49 | 4.6 |
| $SnO_2$ NWs−$TiO_2$ NPs [33] | N719 | 08.6 | 686 | 49 | 4.1 |
| $SnO_2$ NRs−$TiO_2$ [111] | N719 | 09.9 | 660 | 60 | 4.0 |
| PNFs/$TiO_2$ | N719 | 13.5 | 570 | 45 | 3.5 |
| $SnO_2$ NTs−$TiO_2$ [55] | N719 | 09.9 | 680 | 49 | 3.5 |
| NRs $SnO_2$/NaOH [114] | N719 | 08.9 | 575 | 61.4 | 3.1 |
| Zn−$SnO_2$ 10 μm [101] | N719 | 06.0 | 780 | 62 | 3.0 |
| Zn−$SnO_2$ nanoflowers 8 μm [101] | N719 | 04.5 | 700 | 65 | 2.1 |

(*Continued*)

**Table 7.16** (Continued)

| Sample | Dye | $J_{SC}$ (mA $cm^{-2}$) | $V_{OC}$ (mV) | FF (%) | $\eta$ (%) |
|---|---|---|---|---|---|
| ***Core–shell or 3D composite/doped $SnO_2$ morphologies*** | | | | | |
| Five-shell-$SnO_2$–HMSs/P25 [98] | N719 | 20.1 | 750 | 63.2 | 9.5 |
| [b]$SnO_2$ HS@TNS/OM–$TiO_2$ [110] | N719 | 18.2 | 760 | 60 | 8.2 |
| ($SnO_2$ crystallites)ZnO/ZnO [115] | N3 | 18.8 | 660 | 64 | 8.0 |
| $SnO_2$ crystallites/ZnO [115] | N3 | 16.9 | 665 | 65 | 7.3 |
| $SnO_2$ crystallite–MgO [60] | N719 | 14.2 | 758 | 67 | 7.2 |
| Quintuple-shelled/$TiO_2$ [98] | N719 | 17.6 | 720 | 56.6 | 7.2 |
| $SnO_2$ nanobeans–$TiO_2$ HS [116] | | 13.0 | 754 | 67.2 | 6.6 |
| $SnO_2$ HNS*–$TiO_2$ [62] | N719 | 18.3 | 744 | 48 | 6.5 |
| $SnO_2$ NPs/NFs–$TiO_2$ [29] | N719 | 16.8 | 711 | 53 | 6.3 |
| $SnO_2$ microsphere–$TiO_2$ [117] | N719 | 14.1 | 803 | 55 | 6.3 |
| Hollow NSs $SnO_2$/$TiCl_4$ [69] | N719 | 14.6 | 765 | 54 | 6.1 |
| $SnO_2$ microsphere–$TiO_2$ [63] | N719 | 14.7 | 740 | 56 | 6.0 |
| $SnO_2$–$TiO_2$ [61] | N719 | 17.0 | 620 | 53 | 5.6 |
| $SnO_2$ nanoflowers–$TiCl_4$ [70] | N719 | 12.7 | 760 | 58 | 5.6 |
| $SnO_2$@$TiO_2$–ZnO nanoplate [118] | N719 | 15.0 | 711 | 51 | 5.6 |
| $SnO_2$ microsphere–$TiO_2$ [117] | N719 | 12.1 | 801 | 54 | 5.3 |
| $SnO_2$ nanosheets–MgO [64] | N719 | 15.9 | 690 | 48 | 5.3 |
| $SnO_2$ nanosheets–$CaCO_3$ [64] | N719 | 16.0 | 720 | 45 | 5.2 |
| $SnO_2$ nanobeans–$TiCl_4$ [116] | | 11.0 | 720 | 65 | 5.1 |
| $SnO_2$ microsphere–$TiO_2$ [117] | N719 | 10.7 | 800 | 59 | 5.0 |
| $TiO_2$–mesosphere $SnO_2$–$TiO_2$ [66] | N719 | 10.6 | 745 | 63 | 5.0 |
| $SnO_2$ microsphere–$TiO_2$ [117] | N719 | 09.2 | 792 | 55 | 4.0 |
| Macro-$SnO_2$ [73] | N719 | 14.7 | 690 | 49 | 4.9 |
| $SnO_2$ nanobelt–ZnO [19] | N719 | 15.9 | 650 | 47 | 4.7 |
| NWs-based $SnO_2$/$Zn_2SnO_2$ HMs [65] | N719 | 11.0 | 590 | 730 | 4.7 |
| Mesosphere $SnO_2$–$TiO_2$ [66] | N719 | 10.9 | 754 | 54 | 4.4 |
| $SnO_2$@$TiO_2$ [118] | N719 | 12.7 | 677 | 50 | 4.3 |
| $SnO_2$ HMs/$TiO_2$ (600 nm) [119] | Z907 | 09.4 | 662 | 67 | 4.1 |
| $SnO_2$ HMs/$TiO_2$ (200 nm) [119] | Z907 | 08.8 | 679 | 68 | 4.0 |
| Nano-cuboids $SnO_2$/Ga [99] | N719 | 07.4 | 740 | 74 | 4.0 |
| $SnO_2$ nano-grain–ZnO [53] | N719 | 08.7 | 648 | 70 | 4.0 |

(*Continued*)

**Table 7.16** (Continued)

| Sample | Dye | $J_{SC}$ (mA cm$^{-2}$) | $V_{OC}$ (mV) | FF (%) | $\eta$ (%) |
|---|---|---|---|---|---|
| $SnO_2$ nanosheets−$ZrO_2$ [64] | N719 | 13.0 | 690 | 47 | 4.0 |
| Cubic meso-$SnO_2$/$TiO_2$ [39] | N719 | 10.4 | 711 | 51 | 3.8 |
| Meso-$SnO_2$/$Al_2O_3$ [39] | – | 10.1 | 705 | 51 | 3.6 |
| [c]Cauliflower-like $SnO_2$ HMS−$TiO_2$ [58] | N719 | 09.0 | 709 | 55.6 | 3.6 |
| $SnO_2$−ZnO [43] | N719 | 07.0 | 610 | 83 | 3.6 |
| Nanocrystalline−$SnO_2$−Zn [120] | | 08.6 | 590 | 65 | 3.3 |
| $SnO_2$ nanosheets−ZnO [64] | N719 | 10.2 | 650 | 48 | 3.2 |
| NWs-based $SnO_2$/$Zn_2SnO_2$ Ms [65] | N719 | 07.2 | 570 | 74 | 3.0 |
| $SnO_2$ nanocrystallite−ZnO [68] | N719 | 09.5 | 610 | 51 | 3.0 |
| [d]Cauliflower-like $SnO_2$ HMS−$TiO_2$ [58] | N719 | 07.8 | 733 | 53.3 | 3.0 |
| $SnO_2$ crystal/KOH [114] | N719 | 09.4 | 526 | 56 | 2.8 |
| Nano-$SnO_2$/$TiO_2$ [39] | – | 06.6 | 707 | 58 | 2.7 |
| $TiO_2$−$SnO_2$ mesosphere [66] | N719 | 07.0 | 683 | 55 | 2.7 |
| Spherical $SnO_2$/$NH_4OH$ [114] | N719 | 09.5 | 405 | 41.6 | 1.6 |
| Sieve-liked $SnO_2$ sheet/$TiCl_4$ [36] | N719 | 04.4 | 610 | 47.5 | 1.3 |
| $SnO_2$ MSs/$Zn_2SnO_4$ [71] | N719 | 01.6 | 707 | 42.6 | 0.5 |
| $SnO_2$/MgO [121] | – | 15.4 | 654 | 65 | 6.0 |
| Sb−$SnO_2$−MgO [121] | – | 07.3 | 473 | 65 | 1.8 |
| Nano-$SnO_2$ NPs/$TiCl_4$ [31] | N719 | 11.9 | 503 | 59 | 3.6 |

*3D*, Three-dimensional; *FF*, fill factor; *MHS*, multilayered hollow microsphere; *NF*, nanofiber; *NR*, nanorod; *NT*, nanotube; *NW*, nanowire; *PNF*, porous nanofiber.
[a]SNT@TNS: $SnO_2$ nanotube−$TiO_2$ nanosheet double-shell nanostructures, OM is organized mesoporous.
[b]SHS@TNS = $SnO_2$ hollow sphere−$TiO_2$ nanosheet double-shell nanostructures.
[c]Pt counter electrode was used.
[d]Carbon nanofibers counter electrodes used.
*hollow nanospheres (HNS).

This is due to the lower-lying CB of $SnO_2$, which favors electron recombination by the holes present in the electrolyte. Core−shell nanostructure−based WE is one of the several strategies used to resolve such recombination in $SnO_2$-based DSSCs. In core−shell structures, $SnO_2$ serves as a core material because of its higher $\mu_e$ whereas the shell is made using insulating oxides or MOS of higher CB ($Nb_2O_5$, $TiO_2$, ZnO, MgO, $Al_2O_3$, $Y_2O_3$, and $ZrO_2$) [30,88,122,123]. The shell serves as an energy barrier at the MOS/electrolyte interface and also improves the dye anchoring due to its higher surface area originating from the high IEP. There are two ways to fabricate a core−shell NPs photoanode as shown

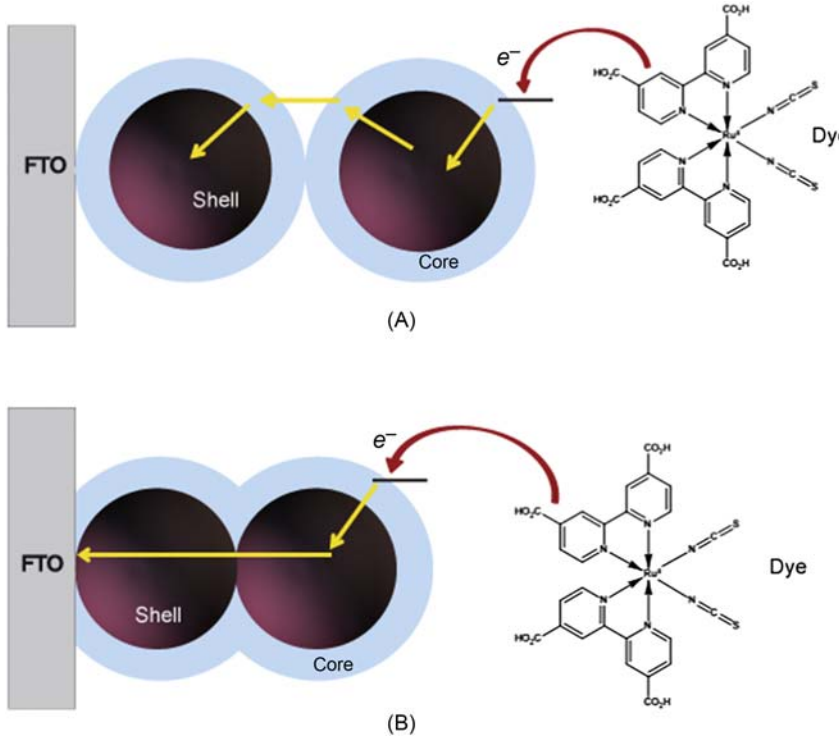


**Figure 7.49** Schematic representation of a core–shell photoanode using two different approaches [124,125]. (A) shows that both particles have separate shell while in (B) only one shell for the both particles.

in Fig. 7.49: (1) synthesize $SnO_2$ NPs as a core followed by coating an overlayer as a shell on its surface (Fig. 7.49A) and then employing the material in the photoanodes, and (2) fabricate $SnO_2$ NPs photoanode first followed by applying an overlayer of a shell on it (Fig. 7.49B). In the first approach, the barrier is formed between successive NPs (serving as a core) and electrolytes, whereas in the second approach the barrier is formed between the core and the electrolyte. The latter has more advantages over the former due to the fact that electron recombination is lower and it also facilitates faster electron transport.

It is important to note that the core and shell material should be chosen to favor a downhill transition, that is, dye's LUMO-shell–core material-FTO. To allow such a transition, the CB of the core must be lower than the CB of the shell and the LUMO of the dye molecule must be at a higher energy level than the CB of the shell as shown in

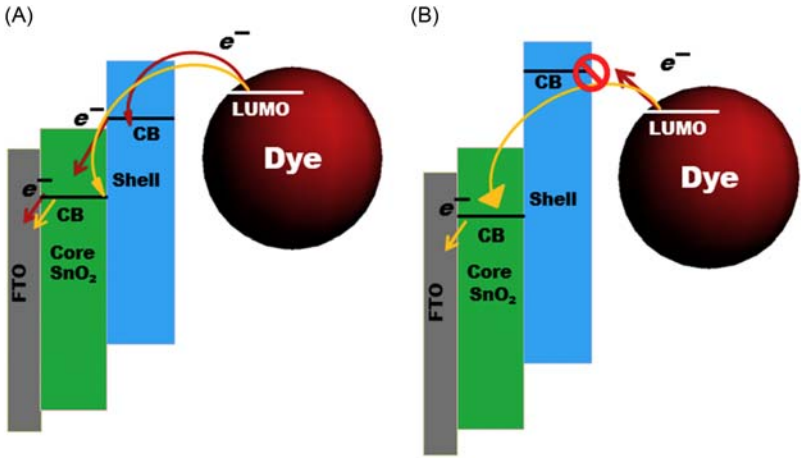


**Figure 7.50** Core–shell mechanism (A) depicts the suitable core–shell adjustment where electrons can easily jump to the CB of the shell, then follow to the core material or it can diffuse through the tunneling process while (B) shows unfavorable injection phenomena between dye LUMO and CB of the shell material where electrons can only diffuse via the tunneling process [76].

Fig. 7.50A. Electrons can reach to the core material via their injection into the CB of the shell from the dye LUMO followed by downhill movement to the core materials or it can also directly be injected into the core by a tunneling process via the shell materials. On the other hand, Fig. 7.50B illustrates the unfavorable core–shell structure, where the CB of the shell lies at a higher position than the LUMO of the dye, and therefore electrons can only diffuse through the tunneling process. Tunneling of electrons can take place when the shell layer is extremely thin (a few angstrom thick).

A number of papers reported the core–shell DSSCs, which have shown remarkable improvement in DSSC's parameters. Pang et al. employed $SnO_2$–ZnO core–shell as a photoanode in DSSCs. Owing to the thin shell layer of ZnO, electron recombination was largely suppressed and achieved five times higher $\eta \sim 7.3\%$ compared to pure $SnO_2$ DSSCs ($\eta \sim 1.3\%$) [115]. It also showed twofold increments in FF and $V_{OC}$ (Table 7.16). Similarly, insulating oxides ($Al_2O_3$ and MgO) and MOS such as, $TiO_2$ and ZnO, are also found to increase the dye loading and the $J_{SC}$ thereby. This is because of the fact that the surface of these insulating oxides is more basic in nature than that of pure $SnO_2$, which makes the former more favorable with carboxyl groups. This could be evidenced

from a study that the pure $SnO_2$ photoanodes have weak coloration, whereas the coloration was strongly enhanced by the systematic increase of $TiO_2$ NPs thin layer on its surface resulted in enhanced $J_{SC}$. The differences in coloration could be due to the low acidity and low IEP (pH ~ 4–5) of $SnO_2$ as compared to the $TiO_2$ which has IEP (pH ~ 6–7). Similarly, when the $SnO_2$ photoanode was passivated with $SiO_2$, a material of lower Isoelectric Point (IEP) (pH ~ 2.0), it resulted in significantly inferior dye loading owing to the more acidic nature of the $SiO_2$. In contrast, significant improvement in dye adsorption and coloration was achieved when the insulating layers of high IEP, such as MgO (IEP at pH ~ 12), $Al_2O_3$ (IEP, at pH ~ 9), and $Y_2O_3$ (IEP, at pH ~ 9) were overcoated on the $SnO_2$ surface [88]. Thus a shell layer not only acts as an interfacial barrier for charge recombination but also may affect the dye-loading characteristics of the $SnO_2$ photoanode.

It is obvious that the thickness of a shell layer has a significant effect on the PV performance of core–shell materials–based DSSCs. Grätzel et al. reported a $Y_2O_3$ insulating layer on $TiO_2$ and $SnO_2$ and showed that an increase in the thickness of the insulating layer gives rise to the $V_{OC}$. However, this is accomplished at the expense of $J_{SC}$. The diminishing of the $J_{SC}$ could be due to the thickness of the insulating layer. Although it suppresses back electrons, it also acts as a physical barrier in the tunneling process. However, still the $\eta \sim 5.2\%$ of DSSCs employing a single shell of insulating oxides around a core of $SnO_2$ [88] is far lower than the $TiO_2$ mesoporous NPs.

## 7.9 Outlook and future recommendations

The questions that need to be answered are: *(1) how far could the efficiency of $SnO_2$ dye-sensitized solar cells be increased? (2) What strategies are required for this increase?*

First, it is clear that there is a theoretical limit of 31% for a single-junction solar cell and the best reported $\eta$ in DSSCs based on $TiO_2$ to date is ~11.9% by engineering various parts of the basic embodiment such as photoanodes architecture, sensitizers, electrolyte, and counter electrodes. However, the best-performing DSSCs using $SnO_2$ nanocrystalline as a photoanode resulted in a maximum ~3%–4% in pure and ~7%–8% in a composite with other MOS. This is due to the low CB with respect to the most employed ruthenium-based sensitizers (lower $V_{OC}$ and lower FF). Although this study showed $SnO_2$ DSSCs simultaneously

yielding comparable $V_{OC}$ and FF to those of $TiO_2$-based analogues, the photocurrent is limited in such devices due to the lower surface roughness. One promising direction in this scenario is to further develop the composite wires with high surface area and increase the surface roughness. Moreover, multiporous $SnO_2$ nanofibers have a potential application in sensors, catalysis, and lithium ion batteries owing to their desirable charge transport properties associated with high specific surface area.

## References

[1] A. Fakharuddin, R. Jose, T.M. Brown, F. Fabregat-Santiago, J. Bisquert, A perspective on the production of dye-sensitized solar modules, Energy Environ. Sci. 7 (2014) 3952–3981.
[2] K. Keis, J. Lindgren, S.-E. Lindquist, A. Hagfeldt, Studies of the adsorption process of Ru complexes in nanoporous ZnO electrodes, Langmuir 16 (2000) 4688–4694.
[3] R. Jose, V. Thavasi, S. Ramakrishna, Metal oxides for dye-sensitized solar cells, J. Am. Ceram. Soc. 92 (2009) 289–301.
[4] L.A. Harris, R.H. Wilson, Semiconductors for photoelectrolysis, Annu. Rev. Mater. Sci. 8 (1978) 99–134.
[5] D.E. Scaife, Oxide semiconductors in photoelectrochemical conversion of solar energy, Solar Energy 25 (1980) 41–54.
[6] I. Bedja, S. Hotchandani, P.V. Kamat, Preparation and photoelectrochemical characterization of thin $SnO_2$ nanocrystalline semiconductor films and their sensitization with bis(2,2′-bipyridine)(2,2′-bipyridine-4,4′-dicarboxylic acid)ruthenium(II) complex, J. Phys. Chem. 98 (1994) 4133–4140.
[7] K.G. Godinho, A. Walsh, G.W. Watson, Energetic and electronic structure analysis of intrinsic defects in $SnO_2$, J. Phys. Chem. C 113 (2008) 439–448.
[8] R. Vogel, P. Hoyer, H. Weller, Quantum-sized PbS, CdS, $Ag_2S$, $Sb_2S_3$, and $Bi_2S_3$ particles as sensitizers for various nanoporous wide-bandgap semiconductors, J. Phys. Chem. 98 (1994) 3183–3188.
[9] S. Ferrere, A. Zaban, B.A. Gregg, Dye sensitization of nanocrystalline tin oxide by perylene derivatives, J. Phys. Chem. B 101 (1997) 4490–4493.
[10] H.C. Leventis, F. O'Mahony, J. Akhtar, M. Afzaal, P. O'Brien, S.A. Haque, Transient optical studies of interfacial charge transfer at nanostructured metal oxide/PbS quantum dot/organic hole conductor heterojunctions, J. Am. Chem. Soc. 132 (2010) 2743–2750.
[11] M. Shimura, K. Shakushiro, Y. Shimura, Photo-electrochemical solar cells with a $SnO_2$-liquid junction sensitized with highly concentrated dyes, J. Appl. Electrochem. 16 (1986) 683–692.
[12] R. Memming, F. Schröppel, Electron transfer reactions of excited ruthenium(II) complexes in monolayer assemblies at the $SnO_2$-water interface, Chem. Phys. Lett. 62 (1979) 207–210.
[13] X. Dou, D. Sabba, N. Mathews, L.H. Wong, Y.M. Lam, S. Mhaisalkar, Hydrothermal synthesis of high electron mobility Zn-doped $SnO_2$ nanoflowers as photoanode material for efficient dye-sensitized solar cells, Chem. Mater. 23 (2011) 3938–3945.
[14] M.-H. Kim, Y.-U. Kwon, Semiconducting divalent metal oxides as blocking layer material for $SnO_2$-based dye-sensitized solar cells, J. Phys. Chem. C 115 (2011) 23120–23125.

[15] G.A. Parks, The isoelectric points of solid oxides, solid hydroxides, and aqueous hydroxo complex systems, Chem. Rev. 65 (1965) 177–198.
[16] Q. Wali, A. Fakharuddin, R. Jose, Tin oxide as a photoanode for dye-sensitised solar cells: current progress and future challenges, J. Power Sources 293 (2015) 1039–1052.
[17] Z.M. Jarzebski, J.P. Marton, Physical properties of $SnO_2$ materials: I. Preparation and defect structure, J. Electrochem. Soc. 123 (1976) 199C–205C.
[18] J. Lin, Z. Peng, C. Xiang, G. Ruan, Z. Yan, D. Natelson, et al., Graphene nanoribbon and nanostructured $SnO_2$ composite anodes for lithium ion batteries, ACS Nano 7 (2013) 6001–6006.
[19] S.A. Mahmoud, O.A. Fouad, Synthesis"/>1"/> and application of zinc/tin oxide nanostructures in photocatalysis and dye sensitized solar cells, Sol. Energy Mater. Sol. Cells 136 (2015) 38–43.
[20] S. Das, V. Jayaraman, $SnO_2$: a comprehensive review on structures and gas sensors, Prog. Mater. Sci. 66 (2014) 112–255.
[21] P. Archana, A. Gupta, M.M. Yusoff, R. Jose, Tungsten doped titanium dioxide nanowires for high efficiency dye-sensitized solar cells, Phys. Chem. Chem. Phys. 16 (2014) 7448–7454.
[22] M. Grätzel, Recent advances in sensitized mesoscopic solar cells, Acc. Chem. Res. 42 (2009) 1788–1798.
[23] D. Chen, F. Huang, Y.-B. Cheng, R.A. Caruso, Mesoporous anatase $TiO_2$ beads with high surface areas and controllable pore sizes: a superior candidate for high-performance dye-sensitized solar cells, Adv. Mater. 21 (2009) 2206–2210.
[24] J. Bisquert, Theory of the impedance of electron diffusion and recombination in a thin layer, J. Phys. Chem. B 106 (2002) 325–333.
[25] A. Fakharuddin, I. Ahmed, Z. Khalidin, M.M. Yusoff, R. Jose, Channeling of electron transport to improve collection efficiency in mesoporous titanium dioxide dye sensitized solar cell stacks, Appl. Phys. Lett. 104 (2014) 053905.
[26] A. Fakharuddin, P.S. Archana, Z. Kalidin, M.M. Yusoff, R. Jose, Standardization of photoelectrode area of dye-sensitized solar cells, RSC Adv. 3 (2013) 2683–2689.
[27] R. Jose, A. Fakharuddin, P.S. Archana, M.M. Yusoff, On the scalability of dye-sensitized solar cells: effects of photoelectrode area on the photovoltaic and charge transport parameters, in: Abstracts of Papers of The American Chemical Society, American Chemical Society, Washington, DC, 2013.
[28] A. Le Viet, R. Jose, M.V. Reddy, B.V.R. Chowdari, S. Ramakrishna, $Nb_2O_5$ photoelectrodes for dye-sensitized solar cells: choice of the polymorph, J. Phys. Chem. C 114 (2010) 21795–21800.
[29] Y.-F. Wang, K.-N. Li, W.-Q. Wu, Y.-F. Xu, H.-Y. Chen, C.-Y. Su, et al., Fabrication of a double layered photoanode consisting of $SnO_2$ nanofibers and nanoparticles for efficient dye-sensitized solar cells, RSC Adv. 3 (2013) 13804–13810.
[30] P. Docampo, P. Tiwana, N. Sakai, H. Miura, L. Herz, T. Murakami, et al., Unraveling the function of an MgO interlayer in both electrolyte and solid-state $SnO_2$ based dye-sensitized solar cells, J. Phys. Chem. C 116 (2012) 22840–22846.
[31] L. Cojocaru, C. Olivier, T. Toupance, E. Sellier, L. Hirsch, Size and shape fine-tuning of $SnO_2$ nanoparticles for highly efficient and stable dye-sensitized solar cells, J. Mater. Chem. A 1 (2013) 13789–13799.
[32] Y. Duan, J. Zheng, N. Fu, Y. Fang, T. Liu, Q. Zhang, et al., Enhancing the performance of dye-sensitized solar cells: doping $SnO_2$ photoanodes with Al to simultaneously improve conduction band and electron lifetime, J. Mater. Chem. A 3 (2015) 3066–3073.
[33] S. Gubbala, V. Chakrapani, V. Kumar, M.K. Sunkara, Band-edge engineered hybrid structures for dye-sensitized solar cells based on $SnO_2$ nanowires, Adv. Funct. Mater. 18 (2008) 2411–2418.

[34] H. Yang, P. Li, J. Zhang, Y. Lin, $TiO_2$ compact layer for dye-sensitized $SnO_2$ nanocrystalline thin film, Electrochim. Acta 147 (2014) 366–370.
[35] K. Asdim, T. Manseki, T. Sugiura, Yoshida, Microwave synthesis of size-controllable $SnO_2$ nanocrystals for dye-sensitized solar cells, New J. Chem. 38 (2014) 598–603.
[36] J.J. Teh, G.H. Guai, X. Wang, K.C. Leong, C.M. Li, P. Chen, Nanoporous tin oxide photoelectrode prepared by electrochemical anodization in aqueous ammonia to improve performance of dye sensitized solar cell, J. Renew. Sustain. Energy 5 (2013) 023120.
[37] K.A.T.A. Perera, S.G. Anuradha, G.R.A. Kumara, M.L. Paranawitharana, R.M.G. Rajapakse, H.M.N. Bandara, The interconnected $CaCO_3$ coated $SnO_2$ nanocrystalline dye-sensitized solar cell with superior performance, Electrochim. Acta 56 (2011) 4135–4138.
[38] J. Qian, P. Liu, Y. Xiao, Y. Jiang, Y. Cao, X. Ai, et al., $TiO_2$-coated multilayered $SnO_2$ hollow microspheres for dye-sensitized solar cells, Adv. Mater. 21 (2009) 3663–3667.
[39] E. Ramasamy, J. Lee, Ordered mesoporous $SnO_2$-based photoanodes for high-performance dye-sensitized solar cells, J. Phys. Chem. C 114 (2010) 22032–22037.
[40] H. Pang, H. Yang, C.X. Guo, C.M. Li, Functionalization of $SnO_2$ photoanode through Mg-doping and $TiO_2$-coating to synergically boost dye-sensitized solar cell performance, ACS Appl. Mater. Interfaces 4 (2012) 6261–6265.
[41] Z. Liu, K. Pan, M. Liu, M. Wang, Q. Lü, J. Li, et al., $Al_2O_3$-coated $SnO_2/TiO_2$ composite electrode for the dye-sensitized solar cell, Electrochim. Acta 50 (2005) 2583–2589.
[42] F. Gu, W. Huang, S. Wang, X. Cheng, Y. Hu, C. Li, Improved photoelectric conversion efficiency from titanium oxide-coupled tin oxide nanoparticles formed in flame, J. Power Sources 268 (2014) 922–927.
[43] N.G. Park, M.G. Kang, K.M. Kim, K.S. Ryu, S.H. Chang, D.K. Kim, et al., Morphological and photoelectrochemical characterization of core–shell nanoparticle films for dye-sensitized solar cells: ZnO type shell on $SnO_2$ and $TiO_2$ cores, Langmuir 20 (2004) 4246–4253.
[44] T. Krishnamoorthy, M.Z. Tang, A. Verma, A.S. Nair, D. Pliszka, S.G. Mhaisalkar, et al., A facile route to vertically aligned electrospun $SnO_2$ nanowires on a transparent conducting oxide substrate for dye-sensitized solar cells, J. Mater. Chem. 22 (2012) 2166–2172.
[45] A.N.M. Green, E. Palomares, S.A. Haque, J.M. Kroon, J.R. Durrant, Charge transport versus recombination in dye-sensitized solar cells employing nanocrystalline $TiO_2$ and $SnO_2$ films, J. Phys. Chem. B 109 (2005) 12525–12533.
[46] M. Dadkhah, M. Salavati-Niasari, Dye-sensitized solar cells based on tin dioxide nanoparticles prepared by a facile hydrothermal method, Mater. Sci. Semicond. Process 20 (2014) 41–48.
[47] X. Xu, F. Qiao, L. Dang, Q. Lu, F. Gao, Porous tin oxide nanosheets with enhanced conversion efficiency as dye-sensitized solar cell electrode, J. Phys. Chem. C 118 (2014) 16856–16862.
[48] M. Dadkhah, M. Salavati-Niasari, Controlled synthesis of tin dioxide nanostructures via two simple methods and the influence on dye sensitized solar cell, Electrochim. Acta 129 (2014) 62–68.
[49] S. Arote, V. Tabhane, S. Jadkar, H. Pathan, Optimization of dye loading time for $SnO_2$ based Rose Bengal dye-sensitized solar cell, Indian J. Phys. 88 (2014) 1067–1071.
[50] H.J. Snaith, C. Ducati, $SnO_2$-based dye-sensitized hybrid solar cells exhibiting near unity absorbed photon-to-electron conversion efficiency, Nano Lett. 10 (2010) 1259–1265.

[51] Q. Wali, A. Fakharuddin, I. Ahmed, M.H. Ab Rahim, J. Ismail, R. Jose, Multiporous nanofibers of $SnO_2$ by electrospinning for high efficiency dye-sensitized solar cells, J. Mater. Chem. A 2 (2014) 17427–17434.
[52] G.M.L.P. Aponsu, T.R.C.K. Wijayarathna, I.K. Perera, V.P.S. Perera, A.C.P.K. Siriwardhana, The enhancement of photovoltaic parameters in dye-sensitized solar cells of nano-crystalline $SnO_2$ by incorporating with large $SrTiO_3$ particles, Spectrochim. Acta A: Mol. Biomol. Spectrosc. 109 (2013) 37–41.
[53] J.-H. Lee, N.-G. Park, Y.-J. Shin, Nano-grain $SnO_2$ electrodes for high conversion efficiency $SnO_2$–DSSC, Sol. Energy Mater. Sol. Cells 95 (2011) 179–183.
[54] C. Gao, X. Li, X. Zhu, L. Chen, Z. Zhang, Y. Wang, et al., Branched hierarchical photoanode of titanium dioxide nanoneedles on tin dioxide nanofiber network for high performance dye-sensitized solar cells, J. Power Sources 264 (2014) 15–21.
[55] U.V. Desai, C. Xu, J. Wu, D. Gao, Hybrid $TiO_2$–$SnO_2$ nanotube arrays for dye-sensitized solar cells, J. Phys. Chem. C 117 (2013) 3232–3239.
[56] C. Gao, X. Li, B. Lu, L. Chen, Y. Wang, F. Teng, et al., A facile method to prepare $SnO_2$ nanotubes for use in efficient $SnO_2$-$TiO_2$ core-shell dye-sensitized solar cells, Nanoscale 4 (2012) 3475–3481.
[57] E.N. Kumar, R. Jose, P.S. Archana, C. Vijila, M.M. Yusoff, S. Ramakrishna, High performance dye-sensitized solar cells with record open circuit voltage using tin oxide nanoflowers developed by electrospinning, Energy Environ. Sci. 5 (2012) 5401–5407.
[58] V. Ganapathy, E.-H. Kong, Y.-C. Park, H.M. Jang, S.-W. Rhee, Cauliflower-like $SnO_2$ hollow microspheres as anode and carbon fiber as cathode for high performance quantum dot and dye-sensitized solar cells, Nanoscale 6 (2014) 3296–3301.
[59] J.T. Park, C.S. Lee, J.H. Kim, One-pot synthesis of hierarchical mesoporous $SnO_2$ spheres using a graft copolymer: enhanced photovoltaic and photocatalytic performance, RSC Adv. 4 (2014) 31452–31461.
[60] M.K.I. Senevirathna, P.K.D.D.P. Pitigala, E.V.A. Premalal, K. Tennakone, G.R.A. Kumara, A. Konno, Stability of the $SnO_2$/MgO dye-sensitized photoelectrochemical solar cell, Sol. Energy Mater. Sol. Cells 91 (2007) 544–547.
[61] S.F. Shaikh, R.S. Mane, O.-S. Joo, Spraying distance and titanium chloride surface treatment effects on DSSC performance of electrosprayed $SnO_2$ photoanodes, RSC Adv. 4 (2014) 35919–35927.
[62] L. Chen, X. Li, Y. Wang, C. Gao, H. Zhang, B. Zhao, et al., Low-temperature synthesis of tin dioxide hollow nanospheres and their potential applications in dye-sensitized solar cells and photoelectrochemical type self-powered ultraviolet photodetectors, J. Power Sources 272 (2014) 886–894.
[63] A. Thapa, J. Zai, H. Elbohy, P. Poudel, N. Adhikari, X. Qian, et al., $TiO_2$ coated urchin-like $SnO_2$ microspheres for efficient dye-sensitized solar cells, Nano Res. 7 (2014) 1154–1163.
[64] S.S. Bhande, D.V. Shinde, K.K. Tehare, S.A. Patil, R.S. Mane, M. Naushad, et al., DSSCs synergic effect in thin metal oxide layer-functionalized $SnO_2$ photoanodes, J. Photochem. Photobiol. A 295 (2014) 64–69.
[65] Z. Li, Y. Zhou, W. Mao, Z. Zou, Nanowire-based hierarchical tin oxide/zinc stannate hollow microspheres: enhanced solar energy utilization efficiency for dye-sensitized solar cells and photocatalytic degradation of dyes, J. Power Sources 274 (2015) 575–581.
[66] G. Shang, J. Wu, M. Huang, J. Lin, Z. Lan, Y. Huang, et al., Facile synthesis of mesoporous tin oxide spheres and their applications in dye-sensitized solar cells, J. Phys. Chem. C 116 (2012) 20140–20145.
[67] J. Liu, T. Luo, S. Mouli T, F. Meng, B. Sun, M. Li, et al., A novel coral-like porous $SnO_2$ hollow architecture: biomimetic swallowing growth mechanism and enhanced

photovoltaic property for dye-sensitized solar cell application, Chem. Commun. 46 (2010) 472–474.
[68] S.F. Shaikh, R.S. Mane, O.-S. Joo, Mass scale sugar-mediated green synthesis and DSSCs application of tin oxide nanostructured photoanode: effect of zinc sulphide layering on charge collection efficiency, Electrochim. Acta 147 (2014) 408–417.
[69] H. Wang, B. Li, J. Gao, M. Tang, H. Feng, J. Li, et al., $SnO_2$ hollow nanospheres enclosed by single crystalline nanoparticles for highly efficient dye-sensitized solar cells, CrystEngComm 14 (2012) 5177–5181.
[70] H. Niu, S. Zhang, R. Wang, Z. Guo, X. Shang, W. Gan, et al., Dye-sensitized solar cells employing a multifunctionalized hierarchical $SnO_2$ nanoflower structure passivated by $TiO_2$ nanogranulum, J. Phys. Chem. C 118 (2014) 3504–3513.
[71] M. Liu, J. Yang, S. Feng, H. Zhu, J. Zhang, G. Li, et al., Composite photoanodes of $Zn_2SnO_4$ nanoparticles modified $SnO_2$ hierarchical microspheres for dye-sensitized solar cells, Mater. Lett. 76 (2012) 215–218.
[72] A.Y. El-Etre, S.M. Reda, Characterization of nanocrystalline $SnO_2$ thin film fabricated by electrodeposition method for dye-sensitized solar cell application, Appl. Surf. Sci. 256 (2010) 6601–6606.
[73] K.-N. Li, Y.-F. Wang, Y.-F. Xu, H.-Y. Chen, C.-Y. Su, D.-B. Kuang, Macroporous $SnO_2$ synthesized via a template-assisted reflux process for efficient dye-sensitized solar cells, ACS Appl. Mater. Interfaces 5 (2013) 5105–5111.
[74] J. Nelson, R.E. Chandler, Random walk models of charge transfer and transport in dye sensitized systems, Coord. Chem. Rev. 248 (2004) 1181–1194.
[75] J. van de Lagemaat, N.G. Park, A.J. Frank, Influence of electrical potential distribution, charge transport, and recombination on the photopotential and photocurrent conversion efficiency of dye-sensitized nanocrystalline $TiO_2$ solar cells: a study by electrical impedance and optical modulation techniques, J. Phys. Chem. B 104 (2000) 2044–2052.
[76] Q. Zhang, G. Cao, Nanostructured photoelectrodes for dye-sensitized solar cells, Nano Today 6 (2011) 91–109.
[77] P. Poudel, Q. Qiao, One dimensional nanostructure/nanoparticle composites as photoanodes for dye-sensitized solar cells, Nanoscale 4 (2012) 2826–2838.
[78] G. Shang, J. Wu, S. Tang, L. Liu, X. Zhang, Enhancement of photovoltaic performance of dye-sensitized solar cells by modifying tin oxide nanorods with titanium oxide layer, J. Phys. Chem. C 117 (2013) 4345–4350.
[79] J. Akilavasan, K. Wijeratne, A. Gannoruwa, A.R.M. Alamoud, J. Bandara, Significance of $TiCl_4$ post-treatment on the performance of hydrothermally synthesized titania nanotubes-based dye-sensitized solar cells, Appl. Nanosci. 4 (2014) 185–188.
[80] P.S. Archana, R. Jose, C. Vijila, S. Ramakrishna, Improved electron diffusion coefficient in electrospun $TiO_2$ nanowires, J. Phys. Chem. C 113 (2009) 21538–21542.
[81] Z. Fu, X. Li, G. Xu, Novel electrospun $SnO_2$@carbon nanofibers as high performance anodes for lithium-ion batteries, Cryst. Res. Technol. 49 (2014) 441–445.
[82] S. Sigdel, H. Elbohy, G. Jiawei, N. Adhikari, K. Sumathy, Q. Hui, et al., Dye-sensitized solar cells based on porous hollow tin oxide nanofibers, electron devices, IEEE Trans. Electron Devices 62 (2015) 2027–2032.
[83] N.K. Elumalai, R. Jose, P.S. Archana, V. Chellappan, S. Ramakrishna, Charge transport through electrospun $SnO_2$ nanoflowers and nanofibers: role of surface trap density on electron transport dynamics, J. Phys. Chem. C 116 (2012) 22112–22120.
[84] J. Rouquerol, D. Avnir, C.W. Fairbridge, D.H. Everett, J.M. Haynes, N. Pernicone, et al., Recommendations for the characterization of porous solids (technical report), Pure Appl. Chem. 66 (1994) 1739.

[85] K.S.W. Sing, D.H. Everett, R.A.W. Haul, L. Moscou, R.A. Pierotti, J. Rouquerol, et al., Reporting physisorption data for gas/solid systems, Handbook of Heterogeneous Catalysis, Wiley-VCH Verlag GmbH & Co. KGaA, 2008.
[86] J.P. Olivier, Improving the models used for calculating the size distribution of micropore volume of activated carbons from adsorption data, Carbon 36 (1998) 1469–1472.
[87] S. Ito, M.K. Nazeeruddin, P. Liska, P. Comte, R. Charvet, P. Péchy, et al., Photovoltaic characterization of dye-sensitized solar cells: effect of device masking on conversion efficiency, Prog. Photovolt. Res. Appl. 14 (2006) 589–601.
[88] A. Kay, M. Grätzel, Dye-sensitized core-shell nanocrystals: improved efficiency of mesoporous tin oxide electrodes coated with a thin layer of an insulating oxide, Chem. Mater. 14 (2002) 2930–2935.
[89] A. Zaban, M. Greenshtein, J. Bisquert, Determination of the electron lifetime in nanocrystalline dye solar cells by open-circuit voltage decay measurements, ChemPhysChem 4 (2003) 859–864.
[90] W. Chen, Y. Qiu, Y. Zhong, K.S. Wong, S. Yang, High-efficiency dye-sensitized solar cells based on the composite photoanodes of $SnO_2$ nanoparticles/ZnO nanotetrapods, J. Phys. Chem. A 114 (2010) 3127–3138.
[91] S. Ito, Y. Makari, T. Kitamura, Y. Wada, S. Yanagida, Fabrication and characterization of mesoporous $SnO_2$/ZnO-composite electrodes for efficient dye solar cells, J. Mater. Chem. 14 (2004) 385–390.
[92] L. Kavan, B. O'Regan, A. Kay, M. Grätzel, An international journal devoted to all aspects of electrode kinetics, interfacial structure, properties of electrolytes, colloid and biological electrochemistry preparation of $TiO_2$ (anatase) films on electrodes by anodic oxidative hydrolysis of $TiCl_3$, J. Electroanal. Chem. 346 (1993) 291–307.
[93] N.G. Park, G. Schlichthörl, J. van de Lagemaat, H.M. Cheong, A. Mascarenhas, A. J. Frank, Dye-sensitized $TiO_2$ solar cells: structural and photoelectrochemical characterization of nanocrystalline electrodes formed from the hydrolysis of $TiCl_4$, J. Phys. Chem. B 103 (1999) 3308–3314.
[94] L. Kavan, B. O'Regan, A. Kay, M. Grätzel, Preparation of $TiO_2$ (anatase) films on electrodes by anodic oxidative hydrolysis of $TiCl_3$, J. Electroanal. Chem. 346 (1993) 291–307.
[95] C.J. Barbé, F. Arendse, P. Comte, M. Jirousek, F. Lenzmann, V. Shklover, et al., Nanocrystalline titanium oxide electrodes for photovoltaic applications, J. Am. Ceram. Soc. 80 (1997) 3157–3171.
[96] M.K. Nazeeruddin, A. Kay, I. Rodicio, R. Humphry-Baker, E. Mueller, P. Liska, et al., Conversion of light to electricity by cis-X2bis(2,2′-bipyridyl-4,4′-dicarboxylate)ruthenium(II) charge-transfer sensitizers (X = Cl-, Br-, I-, CN-, and SCN-) on nanocrystalline titanium dioxide electrodes, J. Am. Chem. Soc. 115 (1993) 6382–6390.
[97] M.L. Rosenbluth, N.S. Lewis, "Ideal" behavior of the open circuit voltage of semiconductor/liquid junctions, J. Phys. Chem. 93 (1989) 3735–3740.
[98] Z. Dong, H. Ren, C.M. Hessel, J. Wang, R. Yu, Q. Jin, et al., Quintuple-shelled $SnO_2$ hollow microspheres with superior light scattering for high-performance dye-sensitized solar cells, Adv. Mater. 26 (2014) 905–909.
[99] J.J. Teh, S.L. Ting, K.C. Leong, J. Li, P. Chen, Gallium-doped tin oxide nanocuboids for improved dye sensitized solar cell, ACS Appl. Mater. Interfaces 5 (2013) 11377–11382.
[100] Z. Li, Y. Zhou, T. Yu, J. Liu, Z. Zou, Unique Zn-doped $SnO_2$ nano-echinus with excellent electron transport and light harvesting properties as photoanode materials for high performance dye-sensitized solar cell, CrystEngComm 14 (2012) 6462–6468.

[101] X. Dou, D. Sabba, N. Mathews, L.H. Wong, Y.M. Lam, S. Mhaisalkar, Hydrothermal synthesis of high electron mobility Zn-doped $SnO_2$ nanoflowers as photoanode material for efficient dye-sensitized solar cells, Chem. Mater. 23 (2011) 3938–3945.
[102] W. Sun, X. Sun, T. Peng, Y. Liu, H. Zhu, S. Guo, et al., A low cost mesoporous carbon/$SnO_2$/$TiO_2$ nanocomposite counter electrode for dye-sensitized solar cells, J. Power Sources 201 (2012) 402–407.
[103] H. Chae, D. Song, Y.-G. Lee, T. Son, W. Cho, Y.B. Pyun, et al., Chemical effects of tin oxide nanoparticles in polymer electrolytes-based dye-sensitized solar cells, J. Phys. Chem. C 118 (2014) 16510–16517.
[104] W. Chen, Y. Qiu, S. Yang, A new ZnO nanotetrapods/$SnO_2$ nanoparticles composite photoanode for high efficiency flexible dye-sensitized solar cells, Phys. Chem. Chem. Phys. 12 (2010) 9494–9501.
[105] M. Peng, X. Cai, Y. Fu, X. Yu, S. Liu, B. Deng, et al., Facial synthesis of $SnO_2$ nanoparticle film for efficient fiber-shaped dye-sensitized solar cells, J. Power Sources 247 (2014) 249–255.
[106] A.E. Shalan, M. Rasly, I. Osama, M.M. Rashad, I.A. Ibrahim, Photocurrent enhancement by $Ni^{2+}$ and $Zn^{2+}$ ion doped in $SnO_2$ nanoparticles in highly porous dye-sensitized solar cells, Ceram. Int. 40 (2014) 11619–11626.
[107] M.A. Hossain, J.R. Jennings, Z.Y. Koh, Q. Wang, Carrier generation and collection in CdS/CdSe-sensitized $SnO_2$ solar cells exhibiting unprecedented photocurrent densities, ACS Nano 5 (2011) 3172–3181.
[108] C. Lee, G.-W. Lee, W. Kang, D.-K. Lee, M.J. Ko, K. Kim, et al., Suppression of charge recombination rate in nanocrystalline $SnO_2$ by thin coatings of divalent oxides in dye-sensitized solar cells, Bull. Korean Chem. Soc. 31 (2010) 3093.
[109] H. Song, K.-H. Lee, H. Jeong, S.H. Um, G.-S. Han, H.S. Jung, et al., A simple self-assembly route to single crystalline $SnO_2$ nanorod growth by oriented attachment for dye sensitized solar cells, Nanoscale 5 (2013) 1188–1194.
[110] S.H. Ahn, D.J. Kim, W.S. Chi, J.H. Kim, Hierarchical double-shell nanostructures of $TiO_2$ nanosheets on $SnO_2$ hollow spheres for high-efficiency, solid-state, dye-sensitized solar cells, Adv. Funct. Mater. 24 (2014) 5037–5044.
[111] J. Huo, Y. Hu, H. Jiang, W. Huang, C. Li, $SnO_2$ nanorod@$TiO_2$ hybrid material for dye-sensitized solar cells, J. Mater. Chem. A 2 (2014) 8266–8272.
[112] R. Kasaudhan, H. Elbohy, S. Sigdel, Q. Hui, W. Qufu, Q. Qiquan, Incorporation of nanoparticles into nanofibers for higher efficiency dye-sensitized solar cells, IEEE Electron. Device Lett. 35 (2014) 578–580.
[113] Y. Zhou, C. Xia, X. Hu, W. Huang, A.A. Aref, B. Wang, et al., Dye-sensitized solar cells based on nanoparticle-decorated ZnO/$SnO_2$ core/shell nanoneedle arrays, Appl. Surf. Sci. 292 (2014) 111–116.
[114] A. Birkel, Y.-G. Lee, D. Koll, X.V. Meerbeek, S. Frank, M.J. Choi, et al., Highly efficient and stable dye-sensitized solar cells based on $SnO_2$ nanocrystals prepared by microwave-assisted synthesis, Energy Environ. Sci. 5 (2012) 5392–5400.
[115] G.R.R.A. Kumara, K. Tennakone, I.R.M. Kottegoda, P.K.M. Bandaranayake, A. Konno, M. Okuya, et al., Efficient dye-sensitized photoelectrochemical cells made from nanocrystalline tin(IV) oxide–zinc oxide composite films, Semicond. Sci. Technol. 18 (2003) 312.
[116] C.-L. Wang, J.-Y. Liao, Y. Zhao, A. Manthiram, Template-free $TiO_2$ hollow submicrospheres embedded with $SnO_2$ nanobeans as a versatile scattering layer for dye-sensitized solar cells, Chem. Commun. 51 (2015) 2848–2850.
[117] Y.-F. Wang, X.-F. Li, D.-J. Li, Y.-W. Sun, X.-X. Zhang, Controllable synthesis of hierarchical $SnO_2$ microspheres for dye-sensitized solar cells, J. Power Sources 280 (2015) 476–482.

[118] Y.-F. Wang, W.-X. Zhao, X.-F. Li, D.-J. Li, Engineered interfacial and configuration design of double layered $SnO_2$@$TiO_2$-ZnO nanoplates ternary heterostructures for efficient dye-sensitized solar cells, Electrochim. Acta 151 (2015) 399–406.
[119] J. Chen, C. Li, F. Xu, Y. Zhou, W. Lei, L. Sun, et al., Hollow $SnO_2$ microspheres for high-efficiency bilayered dye sensitized solar cell, RSC Adv. 2 (2012) 7384–7387.
[120] N.-G. Park, M.G. Kang, K.S. Ryu, K.M. Kim, S.H. Chang, Photovoltaic characteristics of dye-sensitized surface-modified nanocrystalline $SnO_2$ solar cells, J. Photochem. Photobiol. A 161 (2004) 105–110.
[121] K. Tennakone, P. Jayaweera, P. Bandaranayake, Dye-sensitized photoelectrochemical and solid-state solar cells: charge separation, transport and recombination mechanisms, J. Photochem. Photobiol. A 158 (2003) 125–130.
[122] C. Prasittichai, J.T. Hupp, Surface modification of $SnO_2$ photoelectrodes in dye-sensitized solar cells: significant improvements in photovoltage via $Al_2O_3$ atomic layer deposition, J. Phys. Chem. Lett. 1 (2010) 1611–1615.
[123] E. Palomares, J.N. Clifford, S.A. Haque, T. Lutz, J.R. Durrant, Control of charge recombination dynamics in dye sensitized solar cells by the use of conformally deposited metal oxide blocking layers, J. Am. Chem. Soc. 125 (2003) 475–482.
[124] S. Chappel, S.-G. Chen, A. Zaban, $TiO_2$-coated nanoporous $SnO_2$ electrodes for dye-sensitized solar cells, Langmuir 18 (2002) 3336–3342.
[125] Y. Diamant, S. Chappel, S.G. Chen, O. Melamed, A. Zaban, Core–shell nanoporous electrode for dye sensitized solar cells: the effect of shell characteristics on the electronic properties of the electrode, Coord. Chem. Rev. 248 (2004) 1271–1276.

This page intentionally left blank

# CHAPTER 8

# $Nb_2O_5$ dye-sensitized solar cells

**Barbara N. Nunes[1], Leandro A. Faustino[1], Andressa V. Muller[2], Andre S. Polo[2] and Antonio Otavio T. Patrocinio[1]**
[1]Laboratory of Photochemistry and Materials Science, Institute of Chemistry, Federal University of Uberlandia, Uberlandia, Brazil
[2]Federal University of ABC, Santo André, Brazil

## Contents



## 8.1 Introduction

The development of cost-effective devices able to absorb and convert sunlight into fuels or electricity is a key step aiming at a sustainable society. Ideally, a wide range of new technologies employing earth-abundant materials could be available to be applied in different ways, from large-scale solar farms to smart building facades or wearable devices, so the solar harvesting can be maximized [1–8]. Dye-sensitized solar cells (DSSCs) are photoelectrochemical devices capable of converting sunlight into electricity based on photochemical processes. They have attracted much attention in recent decades due to their low cost, long-term durability; possibility of having different colors; transparency; and use of flexible substrates. [9,10].

DSSCs are comprised of two electrodes, the photoanode and the counter electrode. The photoanode has a mesoporous nanocrystalline semiconductor oxide layer deposited on the conductive surface of fluorine doped tin oxide conducting glass (FTO). The oxide layer is dye sensitized to improve the absorption of sunlight, thus a wide range of inorganic

*Nanomaterials for Solar Cell Applications*
DOI: https://doi.org/10.1016/B978-0-12-813337-8.00008-4

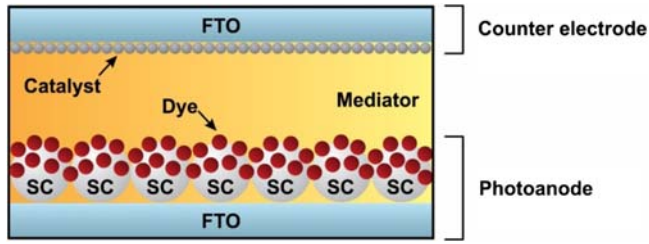


**Figure 8.1** Schematic representation of a DSSC. *DSSC*, Dye-sensitized solar cells; *FTO*, fluorine doped tin oxide conducting glass; *SC*, metal oxide semiconductor.

[11–16], organic [17–21], and natural [22–24] compounds has been investigated for this purpose. The counter electrode is another conducting glass covered by a thin layer of catalyst, such as platinum, graphite, or CoS [25,26]. Between these electrodes is placed a mediator, commonly a mixture of $I^-/I_3^-$ in nitriles [27]. A DSSC is schematically represented in Fig. 8.1. The dye sensitizer absorbs visible light and reaches its excited state, being capable of injecting an electron into the semiconductor conduction band. The injected electron percolates through the semiconductor film until it reaches the conducting substrate and then flows to the external circuit. The oxidized dye is rapidly regenerated by the mediator, which is also reduced in the counter electrode by a catalyzed reaction that uses the electrons from the external circuit [28].

The best performances up to date were achieved using $TiO_2$ as the mesoporous layer; however, $Nb_2O_5$ has interesting electronic properties to be evaluated as a possible substitute for $TiO_2$ [29] or even as under/top-layer to avoid recombination losses [30]. In this chapter, attention is focused on the application of $Nb_2O_5$ on DSSCs for solar energy conversion. First, the general properties of $Nb_2O_5$ are discussed, including its crystalline phases; preparation methods; and optical, electrical, and surface properties. In the following sections, these properties are correlated to the performance of DSSCs based on $Nb_2O_5$ thin films. Finally, other recent applications of $Nb_2O_5$ on other photoelectrochemical devices for solar energy conversion are briefly discussed, along with an outlook with future perspectives.

## 8.2 $Nb_2O_5$ and its thin films – preparation methods, typical morphology, crystalline phases, optical, and electronic properties

$Nb_2O_5$ is the most thermodynamically stable among the niobium oxides [31], with Brazil being the world's largest producer, with more than 90%

of known exploitable niobium mineral reserves [32]. The gross Brazilian production of niobium in 2015 was over 22 million tons [33]. A standout application for high purity (99.9%) niobium oxide is the manufacture of fine ceramics used mainly in the production of capacitors for electronics and optical lenses. It is estimated that around 500 tons of $Nb_2O_5$ are annually used worldwide, with Japan being responsible for almost 2/3 of this quantity [34]. $Nb_2O_5$ has interesting properties for film fabrication, such as high refractive index, low optical absorption in the visible and near infrared region, corrosion resistance, and thermal and chemical stability. Some of its applications are sensors, electronic devices, optical interference filters, and, more recently, solar cells [35].

$Nb_2O_5$ is a white solid powder, water insoluble, and stable in air. It has Bronsted and Lewis acid sites and can only be dissolved by fusion with acidic or alkaline fluxes, such as HF and NaOH [36]. The crystal structure of niobium pentoxide is commonly formed by $NbO_6$ octahedra; however, other phases formed from heptacoordinated ($NbO_7$) and octacoordinated ($NbO_8$) niobium species can also be found [37]. As an n-type metal oxide semiconductor, its conduction band is comprised of empty $Nb^{5+}$ 4d orbitals lying typically around 0.2−0.4 eV higher than the $TiO_2$ conduction band potential (Fig. 8.2). Depending on the crystalline phase, the $Nb_2O_5$ band-gap energy can vary from 3.2 eV to more resistive values such as 5 eV [38]. $Nb_2O_5$ is a typical polymorphic compound with more than 15 different structural configurations [38,39].

Different terminologies are found in the literature to differentiate the $Nb_2O_5$ polymorphs. One of them is based in a sequence of Greek letters ($\alpha$, $\beta$, $\gamma$), such as those applied for other metal oxides [40]. However, the nomenclature system proposed in 1941 by Brauer has been more largely employed. In this system, the different polymorphs are identified by the letters T, M and H [41]. These letters are correlated with the temperature in which the $Nb_2O_5$ crystalline form is obtained: T ($\gamma$), from the German word "tief," is used for the polymorphs prepared at relatively low-temperatures (about 773 K) and exhibits orthorhombic symmetry; M ($\beta$) for oxides prepared at medium-temperature (about 1103 K); and H ($\alpha$) for those submitted to high temperature (above 1273 K), exhibit both monoclinic symmetry [37,42], Fig. 8.3. Other subclasses proposed as new intermediates were found, such as "tief-tief" (TT) for polymorphs obtained at temperatures below those for the T phase [42]. Complementary, Schäfer and coworkers also proposed naming some polymorphs according to the shape or the particles: B ("Blätter," plates in German), N ("Nalden," needles) and R ("Prismen," prisms).

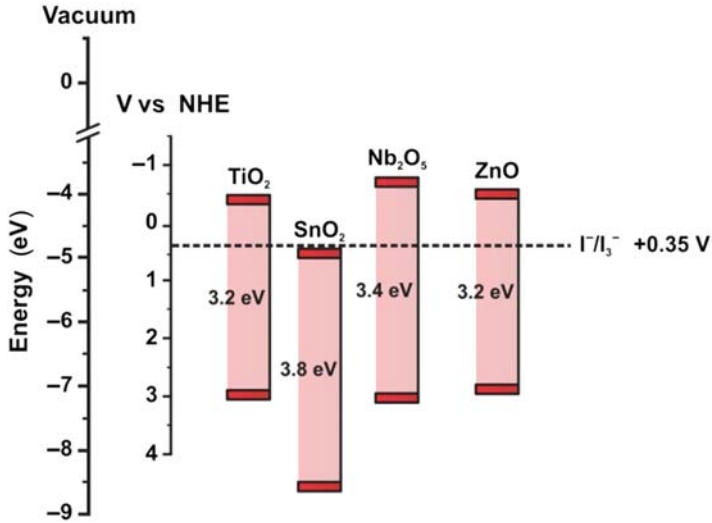


**Figure 8.2** Valence and conduction band energies of several semiconductors relative to the vacuum and the standard hydrogen electrode (NHE). The standard reduction potential of the $I^-/I_3^-$ pair, typically used in DSSCs is also shown. *DSSCs*, Dye-sensitized solar cells.

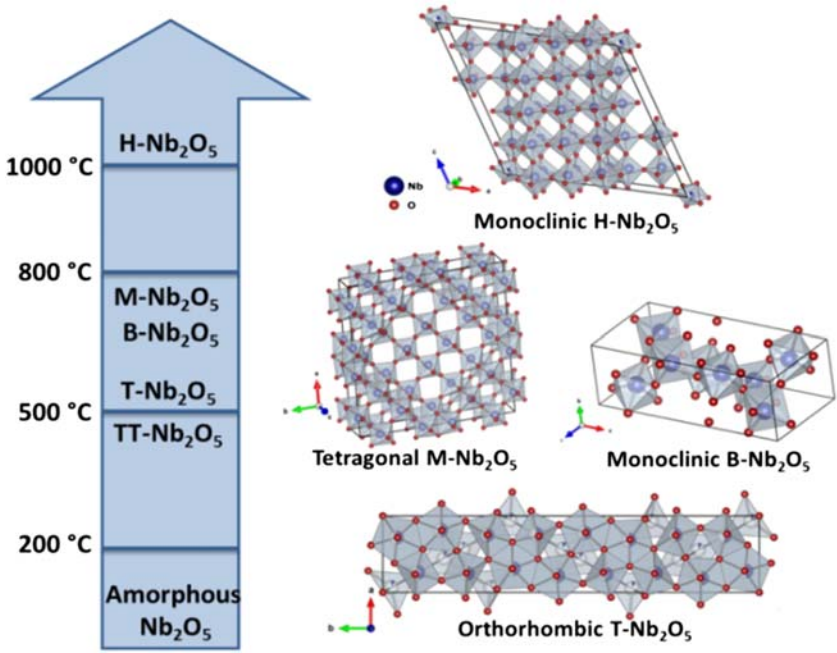


**Figure 8.3** $Nb_2O_5$ crystal phases as a function of temperature and some structural schemes. *Adapted from C. Nico, T. Monteiro, M. Graça, Niobium oxides and niobates physical properties: review and prospects. Prog. Mater. Sci. 80 (2016) 1−37 with permission. Copyright 2016, Elsevier.*

The synthesis of $Nb_2O_5$ is based on hydrolysis of alkali-metal niobates, niobium alkoxides, or niobium pentachloride, as well as through the precipitation from hydrofluoric acid solutions with alkali-metal hydroxides or ammonia. Then, the obtained amorphous hydrated oxide is calcined in a given temperature according to the desired crystal structure [36]. Following the advances in the production of nanostructured metal oxides, different methodologies have been used to produce $Nb_2O_5$ particles, such as hydrothermal treatment, sol–gel and electrodeposition. Thin films of the nanoparticles can also be obtained by screen printing, spray pyrolysis, and other coating techniques. Alternatively, gas phase deposition methods, such as physical and chemical vapor deposition, can also be used. These and other preparation methods were recently summarized by Rani et al. [38].

Among the polymorphs reported in the literature, the orthorhombic T-$Nb_2O_5$ form is the most recurrent for thin-film deposition and solar energy conversion applications, since the annealing temperature is between 500°C and 700°C [30,43,44]. In DSSCs, the annealing temperature is limited by the conductive glassy substrates (FTO), the optical and electrical properties of which are seriously affected after 600°C [30,45,46]. Liu et al. prepared $Nb_2O_5$ powders by electrochemical anodization of metallic niobium, which were used to prepare $Nb_2O_5$ pastes to coat a FTO glass substrate by the doctor-blading technique. The film was annealed at 550°C in air for 2 hours [47] and resulted in films with high crystallized orthorhombic phase. This same structural configuration was observed by Ok et al. [48] following a sol–gel route based on the hydrolysis of niobium ethoxide followed by annealing at 600°C.

The optical properties of $Nb_2O_5$ are highly dependent on the sintering temperature. For example, Lenzmann et al. [49] prepared $Nb_2O_5$ thin films by hydrolyzing niobium(V) ethoxide followed by autoclaving under hydrothermal conditions (230°C for 12 hours) and doctor-blading deposition. The authors observed a blue-shift of the absorption edge as the annealing temperature decreased (Fig. 8.4). The respective band-gap values were 3.15 eV for the film treated at 575°C and 3.25 eV for those treated at 500°C.

The optical, structural, and electrochromic properties of the different crystalline forms of $Nb_2O_5$ films were also investigated by Coşkun et al. [35]. These films were made by radio frequency magnetron sputtering using high temperature glass as substrates and, then, annealed at 400°C, 500°C, 600°C, and 700°C for 6 hours in the air. The optical transmission

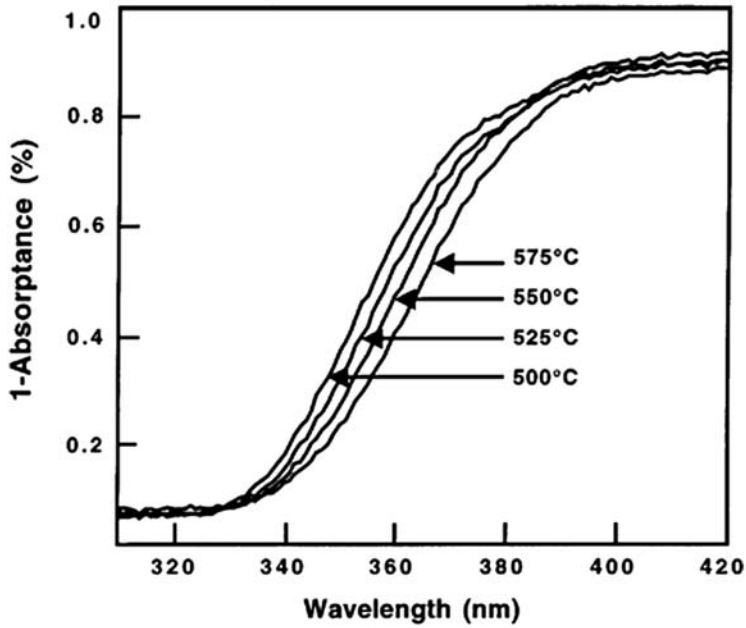


**Figure 8.4** UV–vis spectra of $Nb_2O_5$ thin films annealed at different temperatures. *Reprinted from F. Lenzmann, V. Shklover, K. Brooks, M. Grätzel, Mesoporous $Nb_2O_5$ films: influence of degree of crystallinity on properties. J. Sol-Gel Sci. Technol. 19 (1) (2000) 175–180 with permission. Copyright 2000, Springer Nature.*

spectra in visible and near-IR regions as a function of the annealed temperature are shown in Fig. 8.5. It was observed that, in general, the transmission decreased in the visible and near infrared region as the annealing temperature increased. These data agree with those presented by Lenzmann et al. [49] (Fig. 8.4). The authors ascribed the higher scatter/absorption of the oxides submitted to higher temperatures to the greater concentration of oxygen vacancies, which increases the presence of localized states in the band structure. These oxygen vacancies increase the presence of non-bridging $O^{2-}$ ions and shift the valance band to more negative energies. The band gap is also affected by changes in atomic distances with the annealing temperature. As shown in Table 8.1, the band-gap energies, the film thickness, and refractive indexes decreased as the sintering temperature increases.

Another parameter that also varies with the crystalline structure and the annealing temperature is the film roughness. More crystalline films exhibit higher roughness as a result of the larger grain size. By AFM

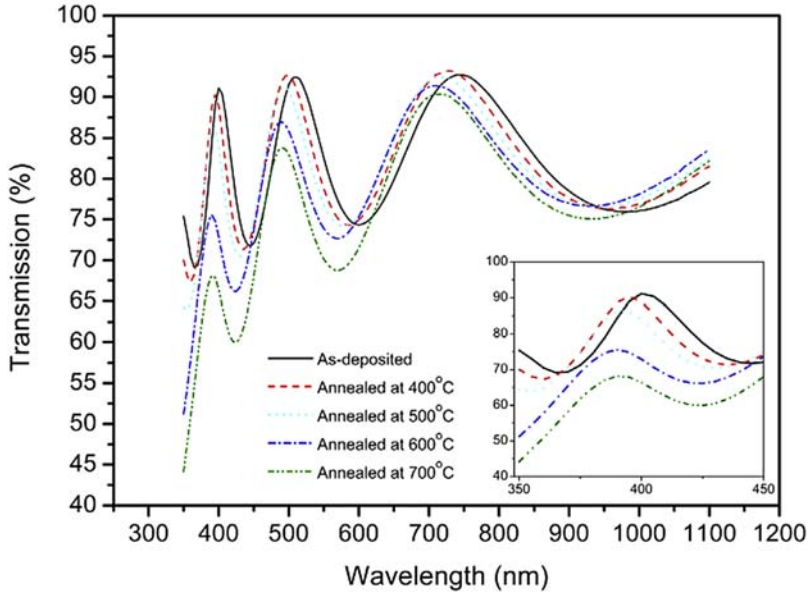


**Figure 8.5** Optical transmission of the $Nb_2O_5$ films annealed at different temperatures in air. *Reprinted from Ö.D. Coşkun, S. Demirel, G. Atak, The effects of heat treatment on optical, structural, electrochromic and bonding properties of $Nb_2O_5$ thin films. J. Alloys Compd. 648 (2015) 994–1004 with permission. Copyright 2015, Elsevier.*

images and X-ray diffractograms, Coşkun et al. were able to probe the conversion from amorphous to crystalline TT phase in $Nb_2O_5$ film, followed by an expected increase in the surface roughness. At 700°C, the T-$Nb_2O_5$ phase was observed and the film surface became needle-shaped, which is associated with the layered structure of the orthorhombic $Nb_2O_5$.

Brayner and Bozon-Verduraz investigated different conditions of soft chemical routes for production of $Nb_2O_5$ nanostructures and then compared some properties as crystalline phase, morphology, and optical properties, among others [50]. The oxide was prepared by digestion from the complex $[(NH_4)H_2[NbO(C_2O_4)_3](H_2O)]$ in aqueous ammonia (NbNH1) or hydrazine (NbNH2) solutions at 80°C for 144 hours. By XRD and DTA-TG measurements, it was observed that the temperatures for phase transformation were different depending on the preparation method. The conversion from amorphous to TT-$Nb_2O_5$ occurred at 550°C for NbNH1 and 600°C for NbNH2. The transformation from TT-$Nb_2O_5$ for T-$Nb_2O_5$ occurred approximately at 700°C for NbNH1

**Table 8.1** Optical band gaps, refractive indexes, film thickness, and root mean square surface roughness for sputtered $Nb_2O_5$ films submitted to different annealing temperatures.

| Sintering conditions | Band gap (eV) | Refractive index (550 nm) | Film thickness (nm) | Surface roughness (nm) |
|---|---|---|---|---|
| As-deposited | 3.75 | 2.09 | 377 | 1.93 |
| 400°C | 3.74 | 2.10 | 365 | 2.34 |
| 500°C | 3.70 | 2.09 | 362 | 2.61 |
| 600°C | 3.70 | 2.10 | 355 | 0.73 |
| 700°C | 3.60 | 2.22 | 340 | 3.98 |

*Source:* Reprinted from Ö.D. Coşkun, S. Demirel, G. Atak, The effects of heat treatment on optical, structural, electrochromic and bonding properties of $Nb_2O_5$ thin films. J. Alloys Compd. 648 (2015) 994–1004 with permission. Copyright 2015, Elsevier.

and at 800°C for NbNH2. After the annealing at 400°C, the sample morphologies were different with the NbNH1 presenting particles with size around 4 nm and NbNH2 with larger particles, between 40 and 100 nm and disk-shaped. The behavior of textural elements in relation to temperature in comparison to the commercial sample (HY), such as total pore volume and specific surface area can be seen in Fig. 8.6. At 400°C, it was observed that NbNH2 had lower porosity in comparison to NbNH1 as well as lower specific surface area. By EPR measurements, it could be shown that both NbNH1 and NbNH2 samples presented paramagnetic centers, which were identified as $Nb^{4+}$ species and ionized oxygen vacancies.

Ou et al. [51] reported the synthesis of an $Nb_2O_5$ crisscross nanoporous network by an elevated temperature anodization process. A niobium foil was anodized in ethylene glycol at 50°C and then annealed in air at 440°C for 20 min, resulting in a $Nb_2O_5$ orthorhombic structure. By SEM images, it was observed as a highly organized pore distribution with size from 30 to 50 nm. The synthesis conditions were important factors for achieving such morphology. The ethylene glycol was used instead of water for increasing the layer thickness to several micrometers and the relative higher temperature (50°C) was able to enhance the diffusion rate of the ions that improved the growth of the porous layer. Also, the anodic voltage selected and the fluoride concentration in electrolyte was essential for the formation of the desired configuration. The authors expected that the crisscross nanoporous network could provide better directional and

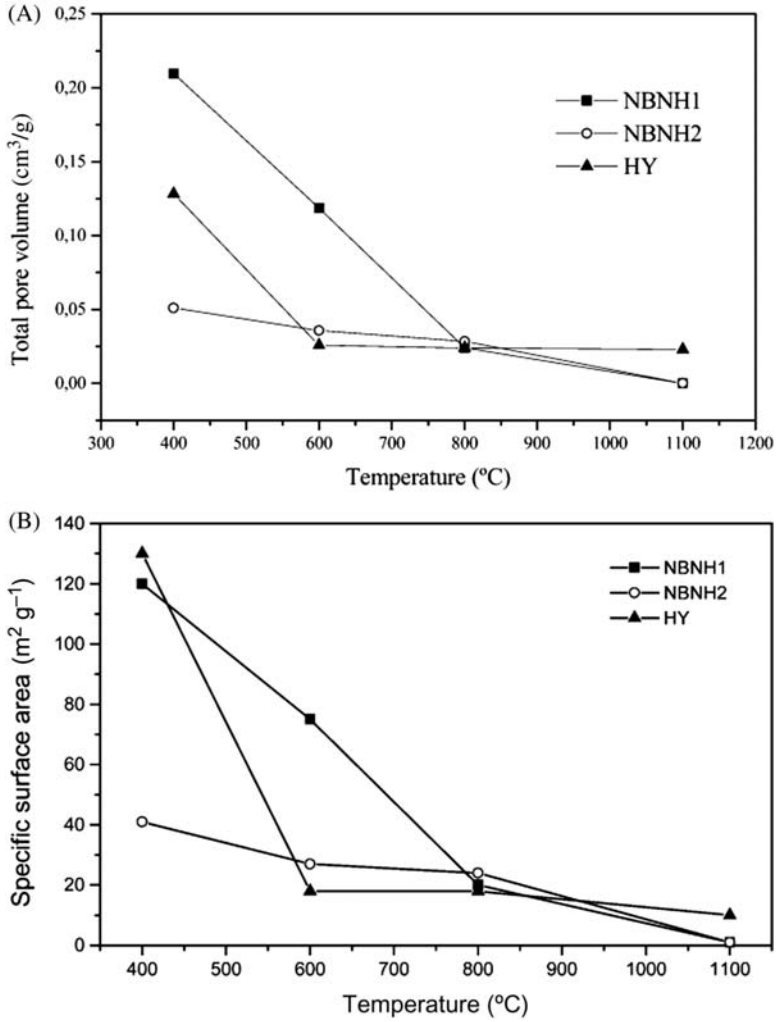


**Figure 8.6** (A) Total pore volume and (B) specific surface area versus calcination temperature for $Nb_2O_5$ samples. *Reproduced from R. Brayner, F. Bozon-Verduraz, Niobium pentoxide prepared by soft chemical routes: morphology, structure, defects and quantum size effect. Phys. Chem. Chem. Phys. 5 (7) (2003) 1457–1466 with permission of The Royal Society of Chemistry.*

continuous pathways for electron transfer when applied in DSSC photoanodes. Similar work was developed by Rani et al. in which highly ordered anodized $Nb_2O_5$ nanochannels were synthesized using a Nb foil in glycerol-based electrolyte at 180°C and then annealed in air at 450°C

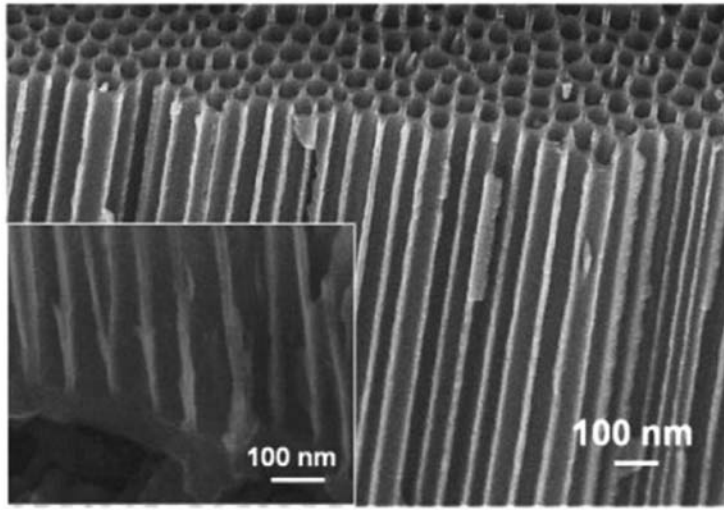


**Figure 8.7** Cross-sectional SEM image of $Nb_2O_5$ nanochannelled structure (inset: bottom view). *Reprinted from R. Abdul Rani, A.S. Zoolfakar, J. Subbiah, J.Z. Ou, K. Kalantar-zadeh, Highly ordered anodized $Nb_2O_5$ nanochannels for dye-sensitized solar cells, Electrochem. Commun. 40 (Suppl. C) (2014) 20–23 with permission. Copyright 2014, Elsevier.*

for 30 minutes [52]. The morphology of the $Nb_2O_5$ film can be observed in SEM image of Fig. 8.7.

Other interesting morphology was reported by Ghosh et al. [53] in a $Nb_2O_5$ photoanode with a nanoforest structure (vertically aligned bundles) by pulsed-laser deposition in FTO. The influence of the oxygen pressure and the number of laser shots were investigated. The obtained films were annealed at 500°C for 1 hour in air, resulting in orthorhombic $Nb_2O_5$ phase. With a background oxygen pressure of around 4 Pa, the films showed very low porosity, but at higher pressures more porous films were observed, along with segmentation into separated oxide columns vertically aligned that work as building blocks of the films, Fig. 8.8. The morphology obtained at higher pressures leads to a better dye adsorption and, consequently, more efficient light harvesting. Concerning the gas composition, it was observed that films prepared in the absence of oxygen during deposition were extremely compact and the authors concluded that oxygen is needed to enable the nanoforest formation, and the overall pressure required could be supplied by an inert component. This structure formation was also independent of the number of laser shots.

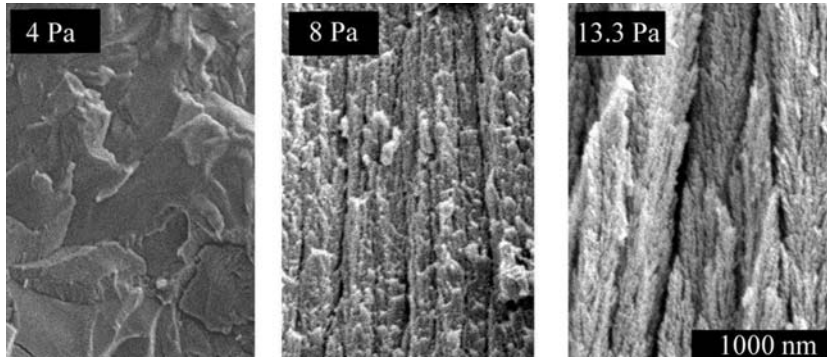


**Figure 8.8** SEM images of $Nb_2O_5$ films deposited at different background oxygen pressures. *Reprinted from R. Ghosh, M.K. Brennaman, T. Uher, M.-R. Ok, E.T. Samulski, L. E. McNeil, et al., Nanoforest Nb2O5 photoanodes for dye-sensitized solar cells by pulsed laser deposition. ACS Appl. Mater. Interfaces 3 (10) (2011) 3929–3935 with permission. Copyright 2011 American Chemical Society.*

Thus by knowing the different possibilities for $Nb_2O_5$ in relation to its crystalline phase, morphology, optical properties, and others, a strict control over the synthesis, deposition, and treatment methods is essential for obtaining suitable films for application in DSSCs. In the following section, the photoelectrochemical performance of DSSCs with different $Nb_2O_5$ thin films is discussed in detail and rationalized based on the intrinsic properties of the metal oxide as well as on its interaction with the other solar cell components.

## 8.3 $Nb_2O_5$ in dye-sensitized solar cells

### 8.3.1 Application as mesoporous layer

To achieve highly efficient devices, the rates of forward and backward electron transfer processes involved in the energy conversion are important, Fig. 8.9 [54]. After light absorption and excitation of the dye, the electron injection into $Nb_2O_5$ must be faster than the relaxation of the dye to its ground state; the regeneration of the dye must be fast enough to avoid the recombination of the injected electron with the oxidized specie; and the transport of electrons through the semiconductor oxide to reach the substrate and the external circuit must be effective to avoid the electron transfer to the oxidized dye molecules or to the electrolyte [44]. Molecular engineering of all components in DSSCs must take into

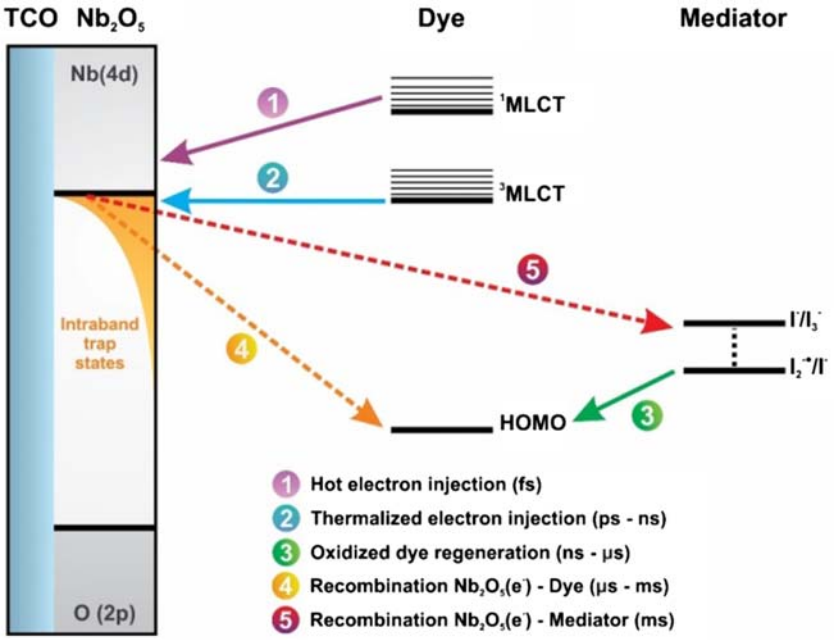


**Figure 8.9** Schematic representation of the main electron transfer processes in a $Nb_2O_5$ dye-sensitized solar cell and their respective time scales. *Adapted from R. Katoh, A. Furube, T. Yoshihara, K. Hara, G. Fujihashi, S. Takano, et al., Efficiencies of electron injection from excited N3 dye into nanocrystalline semiconductor ($ZrO_2$, $TiO_2$, ZnO, $Nb_2O_5$, $SnO_2$, $In_2O_3$) films, J. Phys. Chem. B 108 (15) (2004) 4818–4822; J.E. Moser, M. Wolf, F. Lenzmann, M. Grätzel, Photoinduced charge injection from vibronically hot excited molecules of a dye sensitizer into acceptor states of wide-bandgap oxide semiconductors, Z. Phys. Chem. 212 (1999) 85 [55].*

account these kinetic parameters to increase the photoelectrochemical performance.

#### *8.3.1.1 $Nb_2O_5$ sensitization*

The dye sensitizer is responsible for harvesting the solar light in DSSCs and must fulfill certain requisites for efficient energy conversion: it must exhibits intense visible light absorption, have an excited state energy negative enough to promote electron injection into the semiconductor conducting band and a ground state energy positive enough to be reduced by the mediator redox couple; and be chemically stable and allow the formation of a covalent linkage onto the semiconductor surface. The most used dyes in DSSCs are *cis*-di(isothiocyanato)*bis*-(2,2′-bipyridyl-4,4′-dicarboxylic acid)ruthenium(II), N3, or its doubly deprotonated analogous, N719,

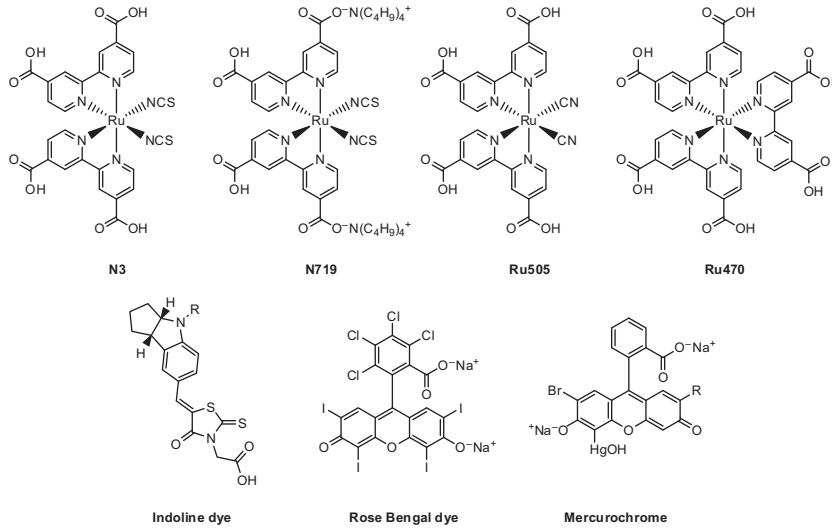


**Figure 8.10** Chemical structures of inorganic and organic dyes employed in DSSCs based on mesoporous $Nb_2O_5$. *DSSCs*, Dye-sensitized solar cells.

Fig. 8.10 [51,57,58], which have been employed as standards for $Nb_2O_5$ DSSCs. The high molar extinction coefficients for MLCT transitions ($\varepsilon \approx 10^4$ L mol$^{-1}$ cm$^{-1}$) and slow back electron transfer rates are key factors for reaching efficiencies up to 6% in $Nb_2O_5$ DSSCs [57,59]. Other Ru(II) dyes, as Ru505 and Ru470, also exhibited potential for $Nb_2O_5$ sensitization [44].

Alternative organic and natural dyes have also been investigated as sensitizers for $Nb_2O_5$ DSSCs. The best result was obtained using a metal-free indoline dye to sensitize single-crystal $Nb_2O_5$ nanobelts, but the 1.42% efficiency is still low in comparison to N3 [60]. Rose Bengal dye (4,5,6,7-tetrachloro-2′,4′,5′,7′-tetraiodofluorescein) and mercurochrome (2′,7′-dibromo-5′-(hydroxymercurio)fluorescein) were also investigated as low-cost alternative dyes, but yielded low photocurrents and poor efficiencies [61,62].

### 8.3.1.2 The influence of the electrolyte

The electrolyte is a key component of DSSCs. The reduced part of the redox couple regenerates the oxidized dye after electron injection, and the oxidized species diffuses to the counter electrode, where it is reduced by the electrons of the external circuit. The open-circuit voltage ($V_{OC}$) of DSSCs depends on the redox potential of the couple since it is established

by the Fermi level of the semiconductor and the redox potential of the mediator [53]. The redox couple also affects the electrochemical potential of the semiconductor through the recombination of injected electrons and oxidized redox species [27]. The only redox couple ever employed in electrolytes for mesoporous $NbO_5$ DSSCs was $I^-/I_3^-$, which yielded the most stable and efficient $TiO_2$-based DSSCs. Overall, the $I^-/I_3^-$ presents good solubility in organic solvents, it has a redox potential (0.35 V vs NHE) suitable for regeneration of most Ru(II) dyes, provides fast dye regeneration and very slow recombination kinetics between electrons injected in metal oxide conduction band.

The electrolyte composition has great impact on the performance of DSSCs, including those employing $Nb_2O_5$ as mesoporous layer. By changing it from an ionic liquid-based mixture (0.1 mol $L^{-1}$ LiI, 0.05 mol $L^{-1}$ $I_2$, 0.6 mol $L^{-1}$ 1,2-dimethyl-3-propylimidazolium iodide and 0.5 mol $L^{-1}$ *tert*-butylpyridine in acetonitrile) to 0.5 mol $L^{-1}$ LiI and 0.05 mol $L^{-1}$ $I_2$ in dried acetonitrile, the maximum incident photon-to-current efficiency (IPCE) improved from 28% to 40% [53]. This effect is ascribed to a higher concentration of $Li^+$ ions and the absence of *tert*-butylpyridine, being responsible for a shift of the oxide conduction band edge.

#### 8.3.1.3 Effect of $Nb_2O_5$ morphology in dye-sensitized solar cells

$Nb_2O_5$ can, in principle, overcome $TiO_2$ and other semiconductor oxides, such as $SnO_2$, $In_2O_3$, and $WO_3$, as mesoporous layer in DSSCs due to its wider band gap and more negative conduction band edge [29,63–65]. The conduction band edge of a material plays a significant role in the photovoltage of DSSCs because the $V_{OC}$ is dependent of the Fermi level of the oxide. Thus by increasing the conduction band edge of the material, an increase in $V_{OC}$ is expected, making $Nb_2O_5$ an ideal material for photoanodes for highly efficient DSSC applications. $Nb_2O_5$ has also the advantage of being more chemically stable than $TiO_2$ and exhibits a very low photocatalytic activity under UV light [29,52,66]. Photocatalytic decomposition of dye and organic solvents by the semiconductor is a serious problem under solar irradiation because even a slight gas evolution may destroy the sealed cell [29].

The actual mechanism of charge transport through mesoporous $Nb_2O_5$ needs to be further explored. In general, it was observed that the electron lifetime ($\tau_n$) value, which means the time it takes to recombine, is much higher in $Nb_2O_5$ than in $TiO_2$, due to its larger charge transfer

resistance [47,51]. However, the electron transport time ($\tau_c$) of $Nb_2O_5$, which means the time the electrons take to traverse the photoanode, is also usually longer than that of $TiO_2$ due to the lower electronic conductivity of $Nb_2O_5$, hence leading to smaller electron diffusion rates [51]. Fortunately, as the effect of the greater enhancement of $\tau_n$ in comparison to $\tau_c$, combined with the higher conduction band energy of $Nb_2O_5$, the electron diffusion length and charge collection efficiency ($\eta_{CC} = 1 - \tau_c/\tau_n$) are relatively high, conferring a great potential for $Nb_2O_5$ as mesoporous layer in DSSCs [47,67].

The potential of $Nb_2O_5$ as mesoporous layer was first demonstrated in 1998 when a series of different mesoporous oxide DSSCs was investigated and a dye-sensitized $Nb_2O_5$ cell exhibited the highest $V_{OC}$ among all semiconductor cells tested. It also exhibited the next highest $J_{SC}$ in comparison to the $TiO_2$ cell and comparable fill factor (ff), being all these parameters are much higher than for other materials [29]. So far, the best solar-to-electricity conversion efficiencies of $Nb_2O_5$ films have surpassed 6% using hydrothermally grown nanorods [57]. The photoelectrochemical parameters of some DSSC based on mesoporous $Nb_2O_5$ films are summarized in Table 8.2.

The intrinsic properties of $Nb_2O_5$ films should, in principle, result in higher solar energy conversion efficiencies. However, it is observed that DSSCs based on various $Nb_2O_5$ nanostructures have shown relatively poor performances in comparison to $TiO_2$ [38,63]. The crystal and surface structures of these two oxides are rather different [70] and most authors found evidences that the main issue is the larger size of the unit cell of $Nb_2O_5$, which can reduce its surface area and thereby the amount of dye adsorbed, thus it is a challenging task to obtain the optimal $Nb_2O_5$ morphology for DSSC applications [47,57,67]. The smaller amount of dye coverage limits the light harvesting and generation of photocurrent, leading to lower conversion efficiencies [47,60,63].

In order to overcome this issue, new strategies for preparation of $Nb_2O_5$ films have been developed aiming to increase the thickness and surface area to improve the amount of dye adsorbed. Decreasing the temperature of thermal treatment during preparation of $Nb_2O_5$ powder led to rougher films that resulted in a higher amount of dye adsorbed and therefore in higher photocurrents [29]. Treatment of sintered $Nb_2O_5$ nanoparticles with niobium alkoxides, followed by its calcination, also increased the roughness of the film and resulted in 1.2 times higher dye loading along with better conductivity between the particles, thus

**Table 8.2** Photoelectrochemical and device assembly parameters of some DSSC based on mesoporous $Nb_2O_5$ films.

| $Nb_2O_5$ film nanostructure | Deposition method | Crystal structure | Dye | Film thickness (μm) | Dye loading (nmol $cm^{-2}$) | $P_{irr}$ (mW $cm^{-2}$) | $V_{OC}$ (V) | $J_{SC}$ (mA $cm^{-2}$) | ff | $\eta$ (%) | Ref. |
|---|---|---|---|---|---|---|---|---|---|---|---|
| Nanoparticle | Doctor-blading | | N3 | 6–8 | 47 | 100 | 0.60 | 3.1 | 0.63 | 1.2 | [29] |
| Nanoparticle | Doctor-blading | | Mercurochrome | 19 | | 100 | 0.54 | 0.0041 | | | [62] |
| Nanoparticle with $Nb(OC_2H_5)_5$ treatment | Doctor-blading | | N3 | 6–8 | 56 | 100 | 0.63 | 4.9 | 0.66 | 2.0 | [29] |
| Sol–gel nanoparticle | Dip- and spin-coating | Mainly hexagonal | N3 | 6 | | 90 | 0.61 | 7.0 | 0.44 | 2.2 | [63] |
| Sol–gel nanoparticle | Dip- and spin-coating | Mainly hexagonal | N3 | 6 | | 10 | 0.57 | 1.6 | 0.56 | 4.9 | [63] |
| Sol–gel nanoparticles | Screen printing | | N719 | 12.1 | 112 | 100 | 0.662 | 11.57 | 0.611 | 4.68 | [57] |
| Microspheres aggregated from nanoparticles | Screen printing | Hexagonal | N719 | 8.5 | | 100 | 0.738 | 6.81 | 0.589 | 2.97 | [68] |
| Chemically synthesized nanoparticles | Doctor-blading | Orthorhombic | Rose Bengal | | | 15 | 0.53 | 0.13 | 0.22 | 0.016 | [61] |
| Nanorods | Hydrothermal reaction | Monoclinic | N719 | 11.2 | 139 | 100 | 0.749 | 12.20 | 0.660 | 6.03 | [57] |
| $Nb_3O_7(OH)$ nanorods | Hydrothermal reaction | Orthorhombic | N719 | 11.5 | 162 | 100 | 0.740 | 15.00 | 0.610 | 6.77 | [57] |
| Nanowires | Electrospinning | Pseudohexagonal | N3 | 30 | 330 | 100 | 0.77 | 6.68 | 0.5906 | 3.05 | [65] |
| Nanowires | Electrospinning | Orthorhombic | N3 | 25 | 96 | 100 | 0.77 | 5.99 | 0.5470 | 2.53 | [65] |
| Nanowires | Electrospinning | Monoclinic | N3 | 25 | 66 | 100 | 0.81 | 4.24 | 0.5607 | 1.92 | [65] |
| Nanotube powder | Doctor-blading | Orthorhombic | N3 | 10 | 83 | 100 | 0.738 | 6.234 | 0.683 | 3.15 | [47] |
| Single-crystal nanobelts (hydrothermal synthesis) | Screen printing | Orthorhombic | Metal-free indoline dye | 8–10 | | 100 | 0.580 | 3.93 | 0.621 | 1.42 | [60] |

| | | | | | | | | | | | |
|---|---|---|---|---|---|---|---|---|---|---|---|
| Nanochains (DNA-aided formation) | Screen printing | Hexagonal | 719 | | | 100 | 0.51 | 0.34 | 0.39 | 0.068 | [69] |
| Crisscross nanoporous network | Anodization | Orthorhombic | N3 | 4 | 73.7 | 100 | 0.7013 | 10.00 | 0.585 | 4.10 | [51] |
| Highly ordered nanochannels | Anodization | Orthorhombic | N3 | 10 | 109.75 | 100 | 0.639 | 17.6 | 0.398 | 4.48 | [52] |
| Nanoforest | Pulsed laser | Orthorhombic | N3 | 5.9 | 32.1 | 100 | 0.71 | 6.65 | 0.49 | 2.41 | [53] |
| Micromountain and nanoforest pancake structure with surface nanowires | Anodization | | N719 | 27.7 | 147 | 100 | 0.59 | 10.66 | 0.53 | 3.35 | [58] |

*ff*, Fill factor; $J_{SC}$, short-circuit current density; $P_{in}$, irradiated power density; $V_{OC}$, open-circuit potential; $\eta$, efficiency.

improving the $J_{SC}$, ff, IPCE, and the overall solar-to-electric conversion efficiency [29]. The photovoltaic performance of nanobelt films and of vertically aligned bundles of $Nb_2O_5$ nanocrystals fabricated by pulsed-laser deposition exhibited a strong dependence on film thickness, indicating that the dye loading dominates the light absorption and photocurrent generation in the DSSCs [53,60].

Aggregation of $Nb_2O_5$ nanoparticles into mesoporous microspheres (0.2−0.9 μm) through a solvothermal process followed by calcination resulted in electrodes with tunable porous structure and a large specific surface area for adsorbing more dye molecules. The microspheres exhibited higher surface area upon increasing its diameter and this contributed to more effective light harvesting. Moreover, its superior light scattering properties improved the light-harvesting efficiency and resulted in devices with efficiencies up to 2.97% [68]. However, the increase in microsphere size led to slower electron transport rate and faster recombination rates, resulting in lower $V_{OC}$ values, indicating that trap sites and recombination centers in the microspheres increased due to the presence of more interfaces [68]. Thus an adequate balance between photon absorption, electron transport and charge transfer properties is necessary to obtain the highest overall solar to electrical conversion efficiency.

Electron transport and recombination are highly dependent on the morphology of the $Nb_2O_5$ films. A major drawback of the use of nanoarchitectures based on nanoparticles is that the electron transport is dominated by random diffusion by a trapping-detrapping process (instead of drift), requiring $10^3$−$10^6$ interparticle hopping steps for an electron to percolate a layer a few micrometers thick, leading to a higher likelihood of electron entrapment [51,53,71,72]. This is a consequence of the high dielectric constant of $Nb_2O_5$ and the small particle size that shield the photogenerated electrons from significant electric fields coming from electrolyte, limiting the effective electron transport length [73]. The high density of grain boundaries also gives rise to defect states in the band gap that act as trap centers for free electrons, hence largely degrading the electron transport and favoring recombination [67,74].

Le Viet et al. [65] compared the photoelectrochemical performances of DSSCs based on three $Nb_2O_5$ polymorphic forms: pseudohexagonal, orthorhombic, and monoclinic, which the authors have called H-$Nb_2O_5$, O-$Nb_2O_5$, and M-$Nb_2O_5$, respectively. These polymorphs correspond to TT-$Nb_2O_5$, T-$Nb_2O_5$ and H-$Nb_2O_5$, respectively, according to the nomenclature system proposed by Brauer (Fig. 8.2). They were assembled

by electrospinning a polymeric solution and were subsequently annealed at 500°C, 800°C and 1100°C for 1 hour in air to yield $Nb_2O_5$ nanofibers. These fibers were dispersed with polyethylene oxide and ethyl cellulose in acetic acid solutions and deposited on FTO glass substrates by the doctor-blade technique. The films' structures were investigated by XRD (Fig. 8.11A) and the band gap of the materials was also determined (Fig. 8.11B).

By combining cyclic voltammograms and absorption spectra, the authors determined the conduction (CB) and valence (VB) bands edge of the $Nb_2O_5$ polymorphs comparing them with the values for anatase $TiO_2$ (Table 8.3). Since M-$Nb_2O_5$ exhibits a higher conduction band edge, it exhibit high open-circuit potentials, $V_{OC} = 0.81$ V, in DSSCs than those observed for the other polymorphs ($V_{OC} \sim 0.77$ V). The electron lifetime in the photoelectrodes was also calculated from Bode plots and the values were 49.5 ms for pseudohexagonal, 43.1 ms for orthorhombic, and 64.7 ms for monoclinic $Nb_2O_5$. As a drawback, the high annealing temperature for monoclinic phase reduced the specific surface area ($1.3\ m^2\ g^{-1}$) when compared with the pseudohexagonal ($55\ m^2\ g^{-1}$) and orthorhombic ($8\ m^2\ g^{-1}$) phases. If the photocurrent was normalized with respect to the dye loading, the monoclinic phase gave superior performance due to its attractive charge transport properties. Thus the authors concluded that monoclinic $Nb_2O_5$ might be a promising layer in DSSC photoanodes if mesoporous particles with higher surface area could be obtained.

In comparison to nanoparticles, long length one-dimensional (1-D) nanostructures greatly reduce intercrystalline $Nb_2O_5$ contacts, resulting in easier electron percolation and suppression of back electron transfer and thus their use can improve the photovoltaic performance of DSSCs [60]. Various strategies were employed to combine the high surface area of nanoparticles with the electron transport properties of 1-D structures [75]. The use of these advanced materials has been recently gaining increasing interest due to the simplicity, versatility, and possibility of scaling the preparation process. Vertically aligned bundles of $Nb_2O_5$ nanocrystals, nanorods, and a nanotube powder network increased the electron diffusion length, provided direct electron pathways, and significantly reduced recombination rate in comparison to $TiO_2$ [47,53,57].

As discussed in Section 8.2, ordered $Nb_2O_5$ crisscross nanoporous networks with low embedded impurities and high surface area were prepared to provide continuous and directional electron transfer pathways and have

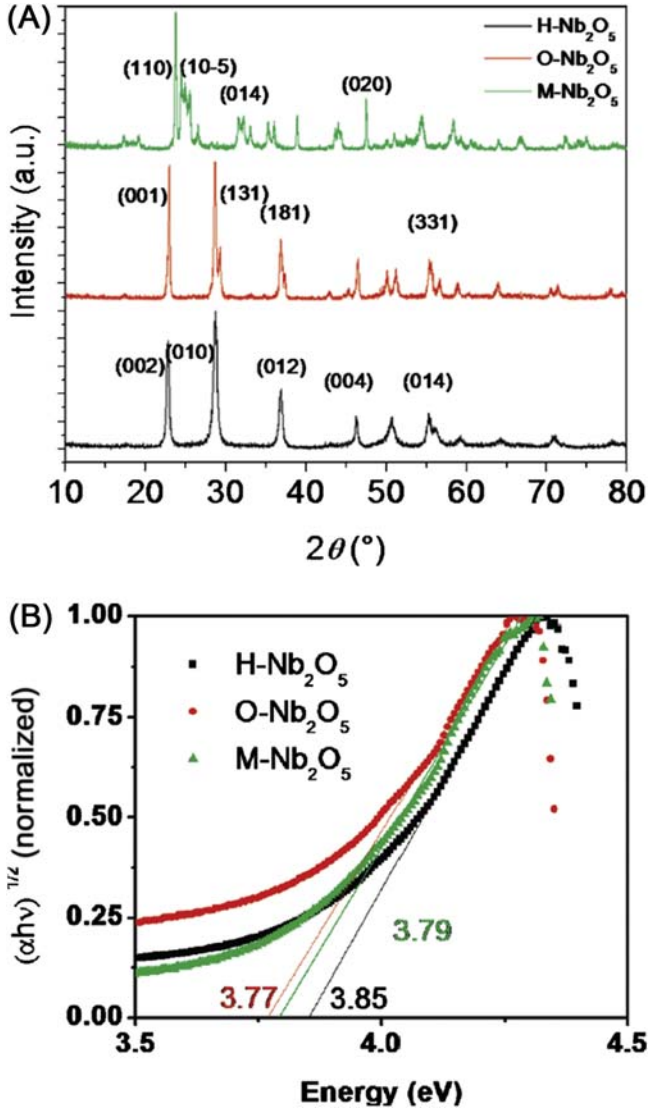


**Figure 8.11** (A) XRD patterns and (B) Tauc plots derived from the absorption spectra of the $Nb_2O_5$ polymorphs: pseudohexagonal (H-$Nb_2O_5$), orthorhombic (O-$Nb_2O_5$), and monoclinic (M-$Nb_2O_5$). *Reprinted from A. Le Viet, R. Jose, M. Reddy, B. Chowdari, S. Ramakrishna, $Nb_2O_5$ photoelectrodes for dye-sensitized solar cells: choice of the polymorph, J. Phys. Chem. C 114 (49) (2010) 21795−21800 with permission. Copyright 2010 American Chemical Society.*

**Table 8.3** Band gap, valence, and conduction bands values of the $Nb_2O_5$ polymorphs in comparison with that of the $TiO_2$ in vacuum level.

| Sample | Band gap (eV) | VB (eV) | CB (eV) |
|---|---|---|---|
| $TiO_2$ | 3.2 | − 7.4 | − 4.2 |
| Pseudohexagonal (TT) | 3.85 | − 7.23 | − 3.38 |
| Orthorhombic (T) | 3.77 | − 7.19 | − 3.42 |
| Monoclinic (H) | 3.79 | − 7.12 | − 3.33 |

*Source*: Reprinted from A. Le Viet, R. Jose, M. Reddy, B. Chowdari, S. Ramakrishna, $Nb_2O_5$ photoelectrodes for dye-sensitized solar cells: choice of the polymorph, J. Phys. Chem. C 114 (49) (2010) 21795–21800 with permission. Copyright 2010 American Chemical Society.

shown superior performances in comparison to their $TiO_2$ counterparts [51]. However, DSSCs only showed a maximum efficiency of 4.1% due to the lack of film integrity as the thickness exceed 5 μm [51]. This problem was solved using an anodization method that resulted in highly ordered $Nb_2O_5$ nanochannelled films having a thickness from 5 to 25 μm. Its large surface-to-volume ratio and highly porous structure led to a substantial amount of adsorbed dye, achieving $J_{SC} = 17.6\ mA\ cm^{-2}$ and $\eta = 4.48\%$ for 10 μm $Nb_2O_5$ films [52]. Similar to what happened with the $Nb_2O_5$ microspheres [68], thicker films of $Nb_2O_5$ nanochannels showed longer electron lifetimes and larger charge transfer resistances than those for thinner films, leading to a lower conversion efficiency.

Micromountain and nanoforest pancake $Nb_2O_5$ structures with nanowires on the surface were also prepared by anodization processes [58]. The thick oxide layers and high surface area of the vertical $Nb_2O_5$ bundles allowed adsorption of a high amount of dye, which resulted in enhanced light harvesting, achieving 3.35% conversion efficiency. They exhibited reduced charge recombination and provided direct conduction pathways along the crystalline $Nb_2O_5$ structures.

Although anodization is a strategy to achieve highly ordered $Nb_2O_5$ nanostructures with high surface area, a drawback of this method is that the prepared films are normally tightly adhered to the metallic Nb foil substrate. To use these films in DSSCs, the undesired back-side solar cell configuration is necessary, leading to losses due to light scattering and limited solar cell performance [47,51]. To produce photoanodes for front-side illuminated devices, films coated on transparent conductive substrates need to be prepared to improve light absorption in DSSCs. Some strategies include the direct anodization of sputtered or evaporated Nb films, synthesis, and transfer of free-standing membranes and fabrication,

dispersion, and coating of oxide powders onto transparent conductive oxide substrates [47,76]. The later strategy outstands due to the possibility of easily tuning the area and thickness of the films and is also suitable for large-scale production [47,77].

Besides morphology and crystallinity, other features of $Nb_2O_5$ films directly affect the efficiencies of devices. High porosity or incomplete coverage of the substrate leads to an increase in recombination sites and energy losses [53]. The presence of excessive defects may cause poor electron transport and a decrease in efficiency [53]. In nanoparticle films, obstructed pores, small pore sizes, and pore neck diameters are responsible for a decrease in efficiency at high light illumination intensities because $I^-/I_3^-$ ions of electrolyte cannot diffuse fast enough in and out of the pores to regenerate the dye molecules [59,63]. Moreover, the presence of large particles in the films can cause a high visible light scattering and the reflected photons scattered outward by semiconductor particles results in the loss of IPCE [29].

#### 8.3.1.4 Interfacial electron transfer and electron transport properties

The electron injection in $TiO_2$ conducting band is the first chemical process involved in the energy conversion process of DSSCs and mainly determines the photogenerated current mechanism. Thus it is fundamental for understanding the interfacial electron transfer to improve the performance of the devices. The rate and efficiency of this process depend strongly on the nature of the dye sensitizer and semiconductor oxide. The dye sensitizer is usually adsorbed onto $Nb_2O_5$ surface by an ester linkage, and electron injection to the $Nb_2O_5$ conduction band occurs mainly through these conjugated orbitals. The $Nb_2O_5$ conduction band is largely comprised of $Nb^{5+}$ 4d empty orbitals, and as $TiO_2$, the lower part of the d band consists of $\pi$ symmetry $t_{2g}$ orbitals, which allows strong electronic coupling with the electron-donating $\pi^*$ orbital of the adsorbed dye. The orbital overlap between the dye and the oxide is more advantageous if the conduction band of the oxide is comprised of d-orbitals instead of s-ones due to the orbital shape [29,78], thus the injection to $Nb_2O_5$ is expected to be more effective than observed for ZnO, $SnO_2$ or $In_2O_3$, whose conduction bands consist of s-orbitals [44,56].

An interesting aspect concerning the electron injection into $Nb_2O_5$ is that even N3 is the most used dye sensitizer, the energy level of the lowest $^3$MLCT excited state of the dye lies below the bottom of the conduction band of the oxide, where hardly any electron acceptor state is

available. In this condition, direct injection from this excited state into the $Nb_2O_5$ conduction band would not be possible and no photovoltaic effect would be seen [70]. However, experimentally, energy conversion is observed. This is only possible because electron injection dynamics is found to be biphasic, consisting of a significant efficient ultrafast component (<100 fs) and a slower component (300 ps to about 1 ns) [44,56]. The fast component is attributed to a hot electron injection from unthermalized, higher vibronic excited states, of the sensitizer to the conduction band of $Nb_2O_5$ (from $^1$MLCT in the case of Ru(II) dyes) that competes with intramolecular vibrational energy redistribution and relaxation that may occur after photoexcitation [79]. The slow component corresponds to the electron injection from thermalized excited states of the sensitizer (from $^3$MLCT in the case of Ru(II) dyes) to intraband gap states due to eventual defect states present below the conduction band edge of $Nb_2O_5$ [44,56].

According to the Marcus theory of interfacial electron transfer, the electron injection rate depends on the electronic coupling strength and the density of states of the semiconductor [80,81]. Upon raising the hot excited state energy of the dye, the fast injection component rate is expected to increase due to the high density of accepting states in the conduction band. On the other hand, lowering the relaxed excited state potential decreases the rate of slow injection due to reduced density of defect states [44].

The dependence of injection kinetics on the crystallinity of the $Nb_2O_5$ films also provides further evidence that the slow injection component originates from electron transfer into defect states present below the conduction band edge. The fast component amplitude is similar for crystalline and amorphous $Nb_2O_5$ films, while the slow injection rate is one order of magnitude slower for the crystalline film. The later has much smaller density of defect states below the conduction band edge than in an amorphous film, decreasing the injection rate from relaxed excited states [44,56,70].

#### 8.3.1.5 Composite mesoporous layers with $Nb_2O_5$

Since the $V_{OC}$ of DSSCs is determined by the difference between the redox potential of the electrolyte and the energy of the Fermi level of the semiconductor, it is expected to obtain a higher $V_{OC}$ by using an oxide with a higher conduction band edge potential. Additionally, since the $J_{SC}$ is affected by the dye coverage, a larger surface area is preferred to obtain

high photocurrents. Thus photoelectrochemical properties of DSSCs can be improved by tailoring the photoanode materials and their microstructure. By combining $Nb_2O_5$ with oxides with higher flat-band potential. such as $SrTiO_3$, $Ta_2O_5$, and $ZrO_2$, higher open-circuit voltages were obtained, but the $J_{SC}$ showed the opposite trend [82]. This relationship can be understood as the charge transfer from the conduction band of $Nb_2O_5$ to that of the other oxides becomes more difficult if the conduction band potential of the latter lies at a higher position, leading to a higher interfacial resistance and thus a lower current density.

Another approach is the combination of $Nb_2O_5$ and $TiO_2$. The open-circuit voltage of the cells using the $Nb_2O_5$–$TiO_2$ composite electrodes decreased with increasing $TiO_2$ content. On the other hand, $J_{SC}$ is augmented by increasing $TiO_2$ content due to its larger surface area. The balance between these two effects led to a higher conversion efficiency at $Nb_2O_5$:$TiO_2$ 8:2 in mass. Thus the combination of these two components has been found to be useful to improving photoelectrochemical properties [82].

Recently, graphene has been incorporated into photoanodes of DSSCs in several ways [83]. The inclusion of a strongly electrically conductive material, such as graphene into $Nb_2O_5$ photoanodes led to the formation of an impurity-free crystalline orthorhombic nanocomposite [84]. An improvement of light absorption due to the reduction of the band-gap energy along with an increase in the electrical conductivity was observed. As a result, improvements in charge collection efficiency and reduction in electron recombination rate in comparison to the unmodified $Nb_2O_5$ were achieved. Furthermore, DSSCs assembled with this nanocomposite exhibited a 52% increase in efficiency and 68% increase in ff when compared to cells made using $Nb_2O_5$ nanoparticles as photoanode.

### 8.3.2 Application as blocking layers

The electrons injected by the dye into the metal oxide conduction band semiconductor needs to percolate through the mesoporous layer and reach the conductive substrate. As the electrolyte can also percolate through the porous of the metal oxide film, electron recombination can occur in both, mesoporous metal oxide/electrolyte or conductive substrate/electrolyte, interfaces [85–88]. $Nb_2O_5$ has been employed as a blocking layer to avoid back electron transfer processes in these interfaces. For example, Zaban et al. [89] described a mesoporous electrode composed by inner

nanoporous $TiO_2$ matrix covered with a $Nb_2O_5$ thin layer, which exhibited higher performance in DSSCs than those for bare $TiO_2$ electrodes. Similar results were reported by other research groups [90–92], employing different preparation methods. It has been shown that both electron lifetime and electron diffusion coefficient are increased due to introduction of the $Nb_2O_5$ shell on $TiO_2$ nanoparticles [91].

Particularly, for the conductive substrate/electrolyte interface, several reports have shown the effectiveness of $Nb_2O_5$ as blocking layer in $TiO_2$-based DSSCs [93–97]. Besides being a physical barrier that avoids the direct contact of the electrolyte with the surface of the conductive substrate (Fig. 8.12), $Nb_2O_5$ imposes a potential barrier between the substrate and the mesoporous layer due its higher conduction band energy in relation to $TiO_2$ [93]. The control of the morphological properties of the $Nb_2O_5$ layer seems to be the key for achieving higher efficiencies. The underlayer has to be thin enough to not interfere in the electron transfer from $TiO_2$ to the conductive substrate but, it should also be compact and non-porous effectively to block the back electron transfer to the electrolyte. In Table 8.4, the improvements on DSSC efficiencies reported by different authors due to $Nb_2O_5$ underlayers are listed

In general, after the deposition of $Nb_2O_5$ on the surface of the transparent substrate, the electrode is subjected to a heat treatment. Suresh

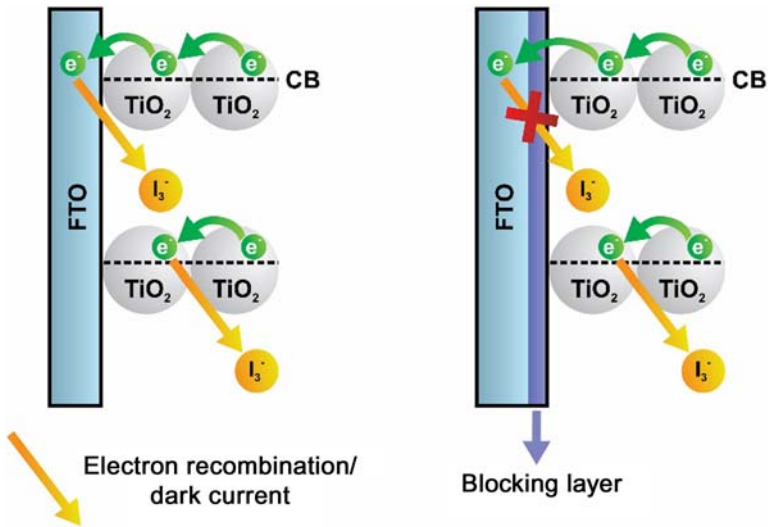


**Figure 8.12** Role of the compact blocking layers on DSSCs with liquid electrolytes. *DSSCs*, Dye-sensitized solar cells.

**Table 8.4** Photoelectrochemical parameters under 100 mW $cm^{-2}$ A.M. 1.5 irradiation DSSCs based on mesoporous $TiO_2$ films containing $Nb_2O_5$ as underlayer/blocking layer.

| Deposition method | Dye | Film thickness (nm) | $V_{OC}$ (V) | $J_{SC}$ (mA $cm^{-2}$) | ff | $\eta$ (%) | $\Delta\eta$ (%)[a] | Ref. |
|---|---|---|---|---|---|---|---|---|
| Sputtering | Z-907 | 400 | 0.71 | 11.4 | 0.66 | 5.5 | 2.0 | [96] |
| Spray pyrolysis | Z-907 | 100 | 0.63 | 8.1 | 0.66 | 3.35 | 0.5 | [99] |
| Screen printing | N719 | 400 | 0.67 | 12.9 | 0.68 | 5.9 | 1.5 | [100] |
| Layer-by-layer | N3 | 200 | 0.70 | 13.9 | 0.60 | 6.2 | 2.9 | [93] |

[a]Variation in relation to DSSCs without blocking layer and measured at same experimental conditions.

et al. [30] have investigated the role of the sintering temperature on the efficiency of the $Nb_2O_5$ underlayers and have found an optimal value around 550°C. The optimal thickness varies with the deposition method. While, for sputtered layers, Suresh reported 40 nm [30,98,99], Xia et al. reported 100 nm for films prepared by spray pyrolysis [97]. If the deposited film is too thick, it acts as insulating layer, decreasing considerably the photocurrent [97]. An elegant and effective solution to avoid this strong dependence on film thickness was introduced by us through the use of the layer-by-layer technique [93]. On this methodology, $Nb_2O_5$ nanoparticles are combined with $TiO_2$ ones through electrostatic interactions to yield $Nb_2O_5/TiO_2$ compact films. The ratio between the two oxides is easily controlled by the pH of the suspensions employed during deposition. As shown in Fig. 8.13, the resulting film exhibits non-porous morphology in relation to the mesoporous $TiO_2$ layer, and its use as blocking layer in DSSCs led to an expressive improvement in the overall conversion efficiency.

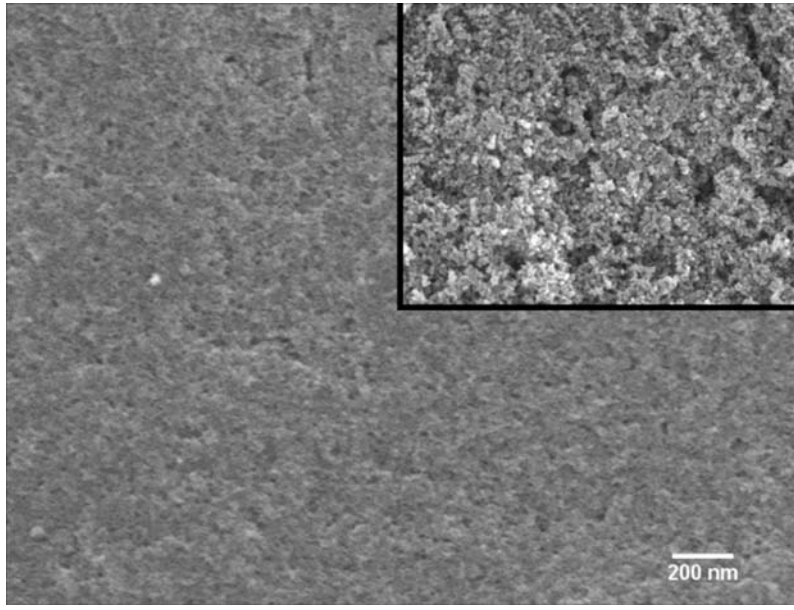


**Figure 8.13** Scanning electron microscopy of a $TiO_2/Nb_2O_5$ thin film prepared by layer-by-layer. Inset: mesoporous $TiO_2$ layer in the same magnification.

## 8.4 Other photoelectrochemical applications of dye-sensitized $Nb_2O_5$ films

As new architectures and devices for solar energy conversion are developed, $Nb_2O_5$ nanostructures have been tested as both mesoporous and blocking layers. One example is in the perovskite solar cells, PSCs, a new and emerging photovoltaic device that gained much attention recently due to their high efficiency and low cost [101]. The first attempt to use perovskites in third-generation solar cells was their use as sensitizers in DSSCs, which resulted in low efficiency and stability. These problems are due to the existence of an organic solvent in the mediator layer capable of dissolving the material [102]. Advances in PSCs were observed after the use of a solid hole conducting layer, which improved their performance and stability and resulted in a different device architecture [103–105].

$Nb_2O_5$ have been recently investigated to be used in PSCs. The first use of this oxide in these devices was as blocking layer in $Al_2O_3$-based PSCs and resulted in higher photovoltage than devices using $TiO_2$ for the same purpose. The increase in $V_{OC}$ was ascribed to a reduced recombination of the injected electron to the perovskite layer due to the presence of $Nb_2O_5$ blocking layer. Unfortunately, $J_{SC}$ values are also lower than those observed with the $TiO_2$ blocking layer, since the electron injection is also inhibited [106]. It was also observed that the thickness of the $Nb_2O_5$ blocking layer has strong influence on $J-V$ hysteresis, since devices having 50 nm of $Nb_2O_5$ have small or undetectable hysteresis [107]. Besides the material itself, its preparation and deposition method are responsible for the performance of the device using this oxide. $Nb_2O_5$ nanoparticles prepared by solution-based synthesis and deposited by electrophoresis were investigated by Huang et al. [108] and resulted in ultrathin and compact $Nb_2O_5$ blocking layer between mesoporous $TiO_2$ and FTO. This approach resulted in improvements in $V_{OC}$, $J_{SC}$, ff, and reduced hysteresis in comparison to solar cells without the blocking layer. Electron-beam deposition was also investigated to prepare $Nb_2O_5$ layers without need of thermal posttreatment and resulted in efficient PSCs using both glass or plastic substrates. The good performance is ascribed to the effectiveness of $Nb_2O_5$ as charge carrier extraction layer [109].

Other aspects investigated in PSCs using $Nb_2O_5$ are its use as window layer or electron selective contacts. Investigation of $Nb_2O_5$ in a planar PSC device reveals that the oxide has good optical performance to work as window layer, resulting in $J_{SC}$ values similar to $TiO_2$ and ZnO but

lower than $WO_3$ [110]. $Nb_2O_5$ was also tested as an electron selective contact in comparison with $SnO_2$ and $TiO_2$. All oxides were deposited by atomic layer deposition and investigation on operational principles of PSCs was carried out by electrochemical impedance spectroscopy [111].

Another application for $Nb_2O_5$ thin films are on the dye-sensitized photoelectrosynthesis cells (DSPECs). In these devices, the redox pair used in DSSCs is replaced by sacrificial reagents or just aqueous electrolytes and the radiant energy is used to promote the formation of fuels such as $H_2$ from water [112]. As in DSSCs, the standard mesoporous layer is $TiO_2$, but Luo et al. [113] evaluated the use of T-phase orthorhombic $Nb_2O_5$ as mesoporous layer. The authors have shown that the electrons injected by the Ru(II)-based sensitizer are located mainly in shallow band-tail trap sites, while on anatase $TiO_2$ a wide distribution of trap sites, including deep trap states, are found. The difference on the trap state distributions, conduction band energies, and interfacial barriers appear to contribute to a slower back electron transfer rate, a lower injection yield (on nanosecond time scale), and a lower open-circuit voltage for T-$Nb_2O_5$, compared to anatase $TiO_2$. Nevertheless, the quantum yield for $H_2$ evolution from EDTA aqueous solutions were very similar: 0.16 and 0.15, respectively, for T-$Nb_2O_5$- and $TiO_2$-based DSPECs.

Moreover, Mallouk's group also reported an interesting approach [43] involving the application of core–shell $TiO_2/Nb_2O_5$ nanoparticles as mesoporous layer in the DSPEC photoanode. It was observed as an enhancement in the quantum efficiency for oxygen evolution in relation to that for $TiO_2$ films, which is directly correlated to the charge injection and the back electron transfer kinetics. For 1–2 nm $Nb_2O_5$ layers, the lowest back electron transfer rates were observed, leading to optimal oxygen evolution. As the layer thickness was increased, the $O_2$ production decreased due to the smaller electron injection efficiency.

## 8.5 Final remarks and perspectives

In this chapter, recent applications of $Nb_2O_5$ in dye-sensitized photoelectrochemical cells were summarized. Despite the smaller conversion efficiencies than those observed for traditional $TiO_2$-based devices, the fundamental investigations on the different $Nb_2O_5$ nanostructures evidence the potential of this material for photoelectrochemical applications. It seems clear, however, that continuous research should be developed to control and understand the formation of the different morphologies and

crystalline phases of $Nb_2O_5$ better. These are key aspects for tuning the electronic properties such as conduction band potential, electron diffusion, and interfacial charge transfer rates. The recent advances on the synthetic methodologies and, particularly, the use of anodization and pulsed-laser methods to deposit thin films have allowed the preparation of well-oriented nanostructures (wires, rods, etc.) on the conductive substrates. As a result, better electron transport properties and improved conversion efficiencies were achieved. Still, the charge transport resistance on the $Nb_2O_5$ films increases considerably as they become thicker, which then limits the photocurrent.

$Nb_2O_5$ films were also successfully employed in the development of new solar energy conversion devices, such as PSCs or DSPECs. These films have been playing an important role as an electron blocking layer in PSCs, resulting in the improvement of the performance as well as reducing the hysteresis of the devices. In DSPECs, the presence of the $Nb_2O_5$ films also reduces the electron recombination in comparison to anatase $TiO_2$ ones and optimize oxygen evolution.

Hence, doping as well as preparation of nanocomposites involving $Nb_2O_5$ and other oxides can be a suitable strategy to overcome this limitation. During this chapter, successful examples of $Nb_2O_5$-based nanocomposites applied both as mesoporous or as blocking layers were described. Moreover, DSSCs based on $Nb_2O_5$ films would also benefit from the development of specific dyes, in which the thermally equilibrated triplet CT states (responsible for the slow electron injection) lies above the bottom of the $Nb_2O_5$ conduction band. So far, there are several fundamental questions on the photoelectrochemical properties of $Nb_2O_5$ thin films and their composites still to be answered, which encourages the research on these systems and that could lead to potential applications on solar energy conversion.

## References

[1] M.E. El-Khoulya, E. El-Mohsnawy, S. Fukuzumi, Solar energy conversion: from natural to artificial photosynthesis, J. Photochem. Photobiol. C 31 (2017) 36–83.
[2] M.E. Ragoussi, T. Torres (Eds.), New generation solar cells: concepts, trends and perspectives, Chem. Commun. 51 (19) (2015) 3957–3972.
[3] A. Fakharuddin, R. Jose, T.M. Brown, F. Fabregat-Santiago, J. Bisquert (Eds.), A perspective on the production of dye-sensitized solar modules, Energy Environ. Sci. 7 (12) (2014) 3952–3981.
[4] R. Tagliaferro, D. Gentilini, S. Mastroianni, A. Zampetti, A. Gagliardi, T.M. Brown (Eds.), Integrated tandem dye solar cells, RSC Adv. 3 (43) (2013) 20273–20280.

[5] G.Y. Chen, J. Seo, C.H. Yang, P.N. Prasad (Eds.), Nanochemistry and nanomaterials for photovoltaics, Chem. Soc. Rev. 42 (21) (2013) 8304–8338.
[6] R.R. Lunt, T.P. Osedach, P.R. Brown, J.A. Rowehl, V. Bulovic (Eds.), Practical roadmap and limits to nanostructured photovoltaics, Adv. Mater. 23 (48) (2011) 5712–5727.
[7] D. Lincot, Photovoltaics: a new responsibility for chemistry, Actual. Chim. 353-54 (2011) 52–60.
[8] S. Gong, W.L. Cheng (Eds.), Toward soft skin-like wearable and implantable energy devices, Adv. Energy Mater. 7 (23) (2017) 1700648.
[9] Jd.S. de Souza, L.O.M. de Andrade, A.V. Müller, A.S. Polo, F.L. Souza, E.R. Leite (Eds.), In *Nanoenergy: Nanotechnology Applied for Energy Production*, Springer International Publishing, Cham, 2018.
[10] S. Caramori, V. Cristino, R. Boaretto, R. Argazzi, C.A. Bignozzi, A. Di Carlo (Eds.), New components for dye-sensitized solar cells, Int. J. Photoenergy (2010). Article ID 458614.
[11] C.A. Bignozzi, R. Argazzi, R. Boaretto, E. Busatto, S. Carli, F. Ronconi (Eds.), The role of transition metal complexes in dye sensitized solar devices, Coord. Chem. Rev. 257 (9–10) (2013) 1472–1492.
[12] A. Reynal, E. Palomares (Eds.), Ruthenium polypyridyl sensitisers in dye solar cells based on mesoporous $TiO_2$, Eur. J. Inorg. Chem. 29 (2011) 4509–4526.
[13] A.V. Müller, P.S. Mendonça, S. Parant, T. Duchanois, P.C. Gros, M. Beley (Eds.), Effects of methyl-substituted phenanthrolines on the performance of ruthenium(II) dye-sensitizers, J. Braz. Chem. Soc. 26 (2015) 2224–2232.
[14] A.V. Muller, L.D. Ramos, K.P.M. Frin, K.T. de Oliveira, A.S. Polo (Eds.), A high efficiency ruthenium(II) tris-heteroleptic dye containing 4,7-dicarbazole-1,10-phenanthroline for nanocrystalline solar cells, RSC Adv. 6 (52) (2016) 46487–46494.
[15] F. Carvalho, E. Liandra-Salvador, F. Bettanin, J.S. Souza, P. Homem-de-Mello, A.S. Polo (Eds.), Synthesis, characterization and photoelectrochemical performance of a tris-heteroleptic ruthenium(II) complex having 4,7-dimethyl-1,10-phenanthroline, Inorg. Chim. Acta 414 (Suppl. C) (2014) 145–152.
[16] Y. Sun, A.C. Onicha, M. Myahkostupov, F.N. Castellano (Eds.), Viable alternative to N719 for dye-sensitized solar cells, ACS Appl. Mater. Interfaces 2 (7) (2010) 2039–2045.
[17] Y. Hu, N. Robertson (Eds.), Atypical organic dyes used as sensitizers for efficient dye-sensitized solar cells, Front. Optoelectron. 9 (1) (2016) 38–43.
[18] Z.S. Wang, N. Koumura, Y. Cui, M. Takahashi, H. Sekiguchi, A. Mori (Eds.), Hexylthiophene-functionalized carbazole dyes for efficient molecular photovoltaics: tuning of solar-cell performance by structural modification, Chem. Mater. 20 (12) (2008) 3993–4003.
[19] G. Sathiyan, E.K.T. Sivakumar, R. Ganesamoorthy, R. Thangamuthu, P. Sakthivel (Eds.), Review of carbazole based conjugated molecules for highly efficient organic solar cell application, Tetrahedron Lett. 57 (3) (2016) 243–252.
[20] K. Hara, T. Sato, R. Katoh, A. Furube, T. Yoshihara, M. Murai (Eds.), Novel conjugated organic dyes for efficient dye-sensitized solar cells, Adv. Funct. Mater. 15 (2) (2005) 246–252.
[21] K. Hara, Z.S. Wang, T. Sato, A. Furube, R. Katoh, H. Sugihara (Eds.), Oligothiophene-containing coumarin dyes for efficient dye-sensitized solar cells, J. Phys. Chem. B 109 (32) (2005) 15476–15482.
[22] S. Shalini, R.B. Prabhu, S. Prasanna, T.K. Mallick, S. Senthilarasu (Eds.), Review on natural dye sensitized solar cells: operation, materials and methods, Renew. Sust. Energy Rev. 51 (2015) 1306–1325.

[23] N.A. Ludin, A. Mahmoud, A.B. Mohamad, A.A.H. Kadhum, K. Sopian, N.S.A. Karim (Eds.), Review on the development of natural dye photosensitizer for dye-sensitized solar cells, Renew. Sust. Energy Rev. 31 (2014) 386–396.
[24] A.S. Polo, N.Y. Murakami Iha (Eds.), Blue sensitizers for solar cells: natural dyes from Calafate and Jaboticaba, Sol. Energy Mater. Sol. Cells 90 (13) (2006) 1936–1944.
[25] M. Congiu, M. Bonomo, M.L.D. Marco, D.P. Dowling, A. Di Carlo, D. Dini (Eds.), Cobalt sulfide as counter electrode in p-type dye-sensitized solar cells, Chemistry Select 1 (11) (2016) 2808–2815.
[26] J. Theerthagiri, A.R. Senthil, J. Madhavan, T. Maiyalagan (Eds.), Recent progress in non-platinum counter electrode materials for dye-sensitized solar cells, ChemElectroChem 2 (7) (2015) 928–945.
[27] G. Boschloo, A. Hagfeldt (Eds.), Characteristics of the iodide/triiodide redox mediator in dye-sensitized solar cells, Acc. Chem. Res. 42 (11) (2009) 1819–1826.
[28] M. Gratzel, Photoelectrochemical cells, Nature 414 (6861) (2001) 338–344.
[29] K. Sayama, H. Sugihara, H. Arakawa (Eds.), Photoelectrochemical properties of a porous $Nb_2O_5$ electrode sensitized by a ruthenium dye, Chem. Mater. 10 (12) (1998) 3825–3832.
[30] S. Suresh, T.G. Deepak, C.S. Ni, C.N.O. Sreekala, M. Satyanarayana, A.S. Nair (Eds.), The role of crystallinity of the $Nb_2O_5$ blocking layer on the performance of dye-sensitized solar cells, New J. Chem. 40 (7) (2016) 6228–6237.
[31] C. Nico, T. Monteiro, M. Graça (Eds.), Niobium oxides and niobates physical properties: review and prospects, Prog. Mater. Sci. 80 (2016) 1–37.
[32] O. Lopes, V. Mendonça, F. Silva, E. Paris, C. Ribeiro (Eds.), Óxidos de nióbio: uma visão sobre a síntese do $Nb_2O_5$ e sua aplicação em fotocatálise heterogênea, Quim. Nova 38 (1) (2015) 106–117.
[33] A.R. Alves, Ad.R. Coutinho (Eds.), The evolution of the niobium production in Brazil, Mater. Res. 18 (1) (2015) 106–112.
[34] F. Cardarelli, *Materials Handbook: A Concise Desktop Reference*, Springer Science & Business Media, London, 2008.
[35] Ö.D. Coşkun, S. Demirel, G. Atak (Eds.), The effects of heat treatment on optical, structural, electrochromic and bonding properties of $Nb_2O_5$ thin films, J. Alloys Compd. 648 (2015) 994–1004.
[36] S. Albrecht, C. Cymorek, J. Eckert (Eds.), Niobium and Niobium Compounds., vol. 24, Wiley-VCH, Weinheim, 2011.
[37] I. Nowak, M. Ziolek (Eds.), Niobium compounds: preparation, characterization, and application in heterogeneous catalysis, Chem. Rev. 99 (12) (1999) 3603–3624.
[38] R.A. Rani, A.S. Zoolfakar, A.P. O'Mullane, M.W. Austin, K. Kalantar-Zadeh (Eds.), Thin films and nanostructures of niobium pentoxide: fundamental properties, synthesis methods and applications, J. Mater. Chem. A 2 (38) (2014) 15683–15703.
[39] L.A. Reznichenko, V.V. Akhnazarova, L.A. Shilkina, O.N. Razumovskaya, S.I. Dudkina (Eds.), Invar effect in n-$Nb_2O_5$, αht-$Nb_2O_5$, and L-$Nb_2O_5$, Crystallogr. Rep. 54 (3) (2009) 483–491.
[40] F. Holtzberg, A. Reisman, M. Berry, M. Berkenblit (Eds.), Chemistry of the group VB pentoxides. VI. The polymorphism of $Nb_2O_5$, J. Am. Chem. Soc. 79 (9) (1957) 2039–2043.
[41] G. Brauer, Die oxyde des niobs, Zeitschrift für anorganische und allgemeine Chemie 248 (1) (1941) 1–31.
[42] H. Schäfer, R. Gruehn, F. Schulte (Eds.), The modifications of niobium pentoxide, Angew. Chem. Int. Ed. 5 (1) (1966) 40–52.
[43] S.H.A. Lee, Y.X. Zhao, E.A. Hernandez-Pagan, L. Blasdel, W.J. Youngblood, T.E. Mallouk (Eds.), Electron transfer kinetics in water splitting dye-sensitized solar cells based on core-shell oxide electrodes, Faraday Discuss. 155 (2012) 165–176.

[44] X. Ai, J. Guo, N.A. Anderson, T. Lian (Eds.), Ultrafast electron transfer from Ru polypyridyl complexes to $Nb_2O_5$ nanoporous thin films, J. Phys. Chem. B 108 (34) (2004) 12795–12803.
[45] S. Suresh, G.E. Unni, C. Ni, R.S. Sreedharan, R.R. Krishnan, M. Satyanarayana (Eds.), Phase modification and morphological evolution in $Nb_2O_5$ thin films and its influence in dye-sensitized solar cells, Appl. Surf. Sci. 419 (2017) 720–732.
[46] H. Zhao, J. Kiwi, C. Pulgarin, J. Yang (Eds.), Oxygen distribution of fluorine-doped tin oxide films coated on float glass along depth before and after heat treatment, Int. J. Appl. Glass Sci. 4 (3) (2013) 242–247.
[47] X. Liu, R. Yuan, Y. Liu, S. Zhu, J. Lin, X. Chen (Eds.), Niobium pentoxide nanotube powder for efficient dye-sensitized solar cells, New J. Chem. 40 (7) (2016) 6276–6280.
[48] M.-R. Ok, R. Ghosh, M.K. Brennaman, R. Lopez, T.J. Meyer, E.T. Samulski (Eds.), Surface patterning of mesoporous niobium oxide films for solar energy conversion, ACS Appl. Mater. Interfaces 5 (8) (2013) 3469–3474.
[49] F. Lenzmann, V. Shklover, K. Brooks, M. Grätzel (Eds.), Mesoporous $Nb_2O_5$ films: influence of degree of crystallinity on properties, J. Sol-Gel Sci. Technol. 19 (1) (2000) 175–180.
[50] R. Brayner, F. Bozon-Verduraz (Eds.), Niobium pentoxide prepared by soft chemical routes: morphology, structure, defects and quantum size effect, Phys. Chem. Chem. Phys. 5 (7) (2003) 1457–1466.
[51] J.Z. Ou, R.A. Rani, M.-H. Ham, M.R. Field, Y. Zhang, H. Zheng (Eds.), Elevated temperature anodized $Nb_2O_5$: a photoanode material with exceptionally large photoconversion efficiencies, ACS Nano 6 (5) (2012) 4045–4053.
[52] R. Abdul Rani, A.S. Zoolfakar, J. Subbiah, J.Z. Ou, K. Kalantar-zadeh (Eds.), Highly ordered anodized $Nb_2O_5$ nanochannels for dye-sensitized solar cells, Electrochem. Commun. 40 (Suppl. C) (2014) 20–23.
[53] R. Ghosh, M.K. Brennaman, T. Uher, M.-R. Ok, E.T. Samulski, L.E. McNeil (Eds.), Nanoforest $Nb_2O_5$ photoanodes for dye-sensitized solar cells by pulsed laser deposition, ACS Appl. Mater. Interfaces 3 (10) (2011) 3929–3935.
[54] R.N. Sampaio, A.V. Müller, A.S. Polo, G.J. Meyer (Eds.), Correlation between charge recombination and lateral hole-hopping kinetics in a series of cis-Ru(phen′)(dcb)$(NCS)_2$ dye-sensitized solar cells, ACS Appl. Mater. Interfaces 9 (39) (2017) 33446–33454.
[55] R. Katoh, A. Furube, T. Yoshihara, K. Hara, G. Fujihashi, S. Takano (Eds.), Efficiencies of electron injection from excited N3 dye into nanocrystalline semiconductor ($ZrO_2$, $TiO_2$, ZnO, $Nb_2O_5$, $SnO_2$, $In_2O_3$) films, J. Phys. Chem. B 108 (15) (2004) 4818–4822.
[56] J.E. Moser, M. Wolf, F. Lenzmann, M. Grätzel (Eds.), Photoinduced charge injection from vibronically hot excited molecules of a dye sensitizer into acceptor states of wide-bandgap oxide semiconductors., Z. Phys. Chem. 212 (1999) 85.
[57] H. Zhang, Y. Wang, D. Yang, Y. Li, H. Liu, P. Liu (Eds.), Directly hydrothermal growth of single crystal $Nb_3O_7(OH)$ nanorod film for high performance dye-sensitized solar cells, Adv. Mater. 24 (12) (2012) 1598–1603.
[58] B.-Y. Jeong, E.H. Jung (Eds.), Micro-mountain and nano-forest pancake structure of $Nb_2O_5$ with surface nanowires for dye-sensitized solar cells, Met. Mater. Int. 19 (3) (2013) 617–622.
[59] D.D.A. Barros Filho, P.P. Abreu Filho, O.L. Alves, D.W. Franco (Eds.), Sensitization of niobium pentoxide thin films by cis-dithiocyanate (2,2-bipyridyl-4,4′dicarboxylic acid) ruthenium(II) complex, J. Sol-Gel Sci. Technol 18 (3) (2000) 259–267.
[60] M. Wei, Z.-m Qi, M. Ichihara, H. Zhou (Eds.), Synthesis of single-crystal niobium pentoxide nanobelts, Acta Mater. 56 (11) (2008) 2488–2494.

[61] N.I. Beedri, S.A.A.R. Sayyed, S.R. Jadkar, H.M. Pathan (Eds.), Rose Bengal sensitized niobium pentaoxide photoanode for dye sensitized solar cell application, AIP Conf. Proc 2017 (1) (1832) 1–3.
[62] K. Hara, T. Horiguchi, T. Kinoshita, K. Sayama, H. Sugihara, H. Arakawa (Eds.), Highly efficient photon-to-electron conversion with mercurochrome-sensitized nanoporous oxide semiconductor solar cells, Sol. Energy Mater. Sol. Cells 64 (2) (2000) 115–134.
[63] P. Guo, M.A. Aegerter (Eds.), Ru(II) sensitized $Nb_2O_5$ solar cell made by the sol-gel process, Thin Solid Films 351 (1–2) (1999) 290–294.
[64] R. Vogel, H. Weller, *Sensitization of titanium dioxide and niobium pentoxide electrodes by strongly quantized semiconductor particles*, Optical Materials Technology for Energy Efficiency and Solar Energy, SPIE, Toulouse-Labege, France, 1992, p. 11.
[65] A. Le Viet, R. Jose, M. Reddy, B. Chowdari, S. Ramakrishna (Eds.), $Nb_2O_5$ photoelectrodes for dye-sensitized solar cells: choice of the polymorph, J. Phys. Chem. C 114 (49) (2010) 21795–21800.
[66] K. Sayama, H. Arakawa (Eds.), Effect of $Na_2CO_3$ addition on photocatalytic decomposition of liquid water over various semiconductor catalysis, J. Photochem. Photobiol. A 77 (2) (1994) 243–247.
[67] R. Jose, V. Thavasi, S. Ramakrishna (Eds.), Metal oxides for dye-sensitized solar cells, J. Am. Ceram. Soc. 92 (2) (2009) 289–301.
[68] X. Jin, C. Liu, J. Xu, Q. Wang, D. Chen (Eds.), Size-controlled synthesis of mesoporous $Nb_2O_5$ microspheres for dye sensitized solar cells, RSC Adv. 4 (67) (2014) 35546–35553.
[69] K. Karthick, U. Nithiyanantham, S.R. Ede, S. Kundu (Eds.), DNA aided formation of aggregated $Nb_2O_5$ nanoassemblies as anode material for dye sensitized solar cell (DSSC) and supercapacitor applications, ACS Sust. Chem. Eng. 4 (6) (2016) 3174–3188.
[70] F. Lenzmann, J. Krueger, S. Burnside, K. Brooks, M. Grätzel, D. Gal (Eds.), Surface photovoltage spectroscopy of dye-sensitized solar cells with $TiO_2$, $Nb_2O_5$, and $SrTiO_3$ nanocrystalline photoanodes: indication for electron injection from higher excited dye states, J. Phys. Chem. B 105 (27) (2001) 6347–6352.
[71] L. Vayssieres, K. Keis, A. Hagfeldt, S.-E. Lindquist (Eds.), Three-dimensional array of highly oriented crystalline ZnO microtubes, Chem. Mater. 13 (12) (2001) 4395–4398.
[72] J. van de Lagemaat, A.J. Frank (Eds.), Nonthermalized electron transport in dye-sensitized nanocrystalline $TiO_2$ films: transient photocurrent and random-walk modeling studies, J. Phys. Chem. B 105 (45) (2001) 11194–11205.
[73] W.H. Leng, P.R.F. Barnes, M. Juozapavicius, B.C. O'Regan, J.R. Durrant (Eds.), Electron diffusion length in mesoporous nanocrystalline $TiO_2$ photoelectrodes during water oxidation, J. Phys. Chem. Lett. 1 (6) (2010) 967–972.
[74] T.W. Hamann, R.A. Jensen, A.B.F. Martinson, H. Van Ryswyk, J.T. Hupp (Eds.), Advancing beyond current generation dye-sensitized solar cells, Energy Environ. Sci. 1 (1) (2008) 66–78.
[75] M. Grätzel, Dye-sensitized solar cells, J. Photochem. Photobiol., C 4 (2) (2003) 145–153.
[76] J.Y. Kim, J.H. Noh, K. Zhu, A.F. Halverson, N.R. Neale, S. Park (Eds.), General strategy for fabricating transparent $TiO_2$ nanotube arrays for dye-sensitized photoelectrodes: illumination geometry and transport properties, ACS Nano 5 (4) (2011) 2647–2656.
[77] J. Lin, L. Zheng, X. Liu, S. Zhu, Y. Liu, X. Chen (Eds.), Assembly of a high-scattering photoelectrode using a hybrid nano-$TiO_2$ paste, J. Mater. Chem. C 3 (26) (2015) 6645–6651.

[78] S. Anderson, E.C. Constable, M.P. Dare-Edwards, J.B. Goodenough, A. Hamnett, K.R. Seddon (Eds.), Chemical modification of a titanium (IV) oxide electrode to give stable dye sensitisation without a supersensitiser, Nature 280 (5723) (1979) 571–573.
[79] J.B. Asbury, N.A. Anderson, E. Hao, X. Ai, T. Lian (Eds.), Parameters affecting electron injection dynamics from ruthenium dyes to titanium dioxide nanocrystalline thin film, J. Phys. Chem. B 107 (30) (2003) 7376–7386.
[80] Y.Q. Gao, Y. Georgievskii, R.A. Marcus (Eds.), On the theory of electron transfer reactions at semiconductor electrode/liquid interfaces, J. Chem. Phys. 112 (7) (2000) 3358–3369.
[81] Y.Q. Gao, R.A. Marcus (Eds.), On the theory of electron transfer reactions at semiconductor/liquid interfaces. II. A free electron model, J. Chem. Phys. 113 (15) (2000) 6351–6360.
[82] K. Eguchi, H. Koga, K. Sekizawa, K. Sasaki (Eds.), $Nb_2O_5$-based composite electrodes for dye-sensitized solar cells, J. Ceram. Soc. Jpn. 108 (1264) (2000) 1067–1071.
[83] M.-N. Lu, C.-Y. Chang, T.-C. Wei, J.-Y. Lin (Eds.), Recent development of graphene-based cathode materials for dye-sensitized solar cells, J. Nanomater. 2016 (2016) 21.
[84] M. Jamil, Z.S. Khan, A. Ali, N. Iqbal (Eds.), Studies on solution processed Graphene-$Nb_2O_5$ nanocomposite based photoanode for dye-sensitized solar cells, J. Alloys Compd. 694 (Suppl. C) (2017) 401–407.
[85] A.O.T. Patrocinio, A.S. El-Bacha, E.B. Paniago, R.M. Paniago, N.Y.M. Iha (Eds.), Influence of the sol-gel pH process and compact film on the efficiency of $TiO_2$-based dye-sensitized solar cells, Int. J. Photoenergy (2012). Article ID 638571.
[86] L. Peter, Transport, trapping and interfacial transfer of electrons in dye-sensitized nanocrystalline solar cells, J. Electroanal. Chem. 599 (2) (2007) 233–240.
[87] P.J. Cameron, L.M. Peter, S. Hore (Eds.), How important is the back reaction of electrons via the substrate in dye-sensitized nanocrystalline solar cells? J. Phys. Chem. B 109 (2) (2005) 930–936.
[88] P.J. Cameron, L.M. Peter (Eds.), How does back-reaction at the conducting glass substrate influence the dynamic photovoltage response of nanocrystalline dye-sensitized solar cells? J. Phys. Chem. B 109 (15) (2005) 7392–7398.
[89] A. Zaban, S. Chen, S. Chappel, B. Gregg (Eds.), Bilayer nanoporous electrodes for dye sensitized solar cells, Chem. Commun. 22 (2000) 2231–2232.
[90] J. Xia, S. Yanagida (Eds.), Strategy to improve the performance of dye-sensitized solar cells: interface engineering principle, Sol. Energy 85 (12) (2011) 3143–3159.
[91] K.-S. Ahn, M.-S. Kang, J.-K. Lee, B.-C. Shin, J.-W. Lee (Eds.), Enhanced electron diffusion length of mesoporous $TiO_2$ film by using $Nb_2O_5$ energy barrier for dye-sensitized solar cells, Appl. Phys. Lett. 89 (1) (2006) 013103.
[92] E. Barea, X. Xu, V. González-Pedro, T. Ripollés-Sanchis, F. Fabregat-Santiago, J. Bisquert (Eds.), Origin of efficiency enhancement in $Nb_2O_5$ coated titanium dioxide nanorod based dye sensitized solar cells, Energy Environ. Sci. 4 (9) (2011) 3414–3419.
[93] L. Paula, R. Amaral, N.M. Iha, R. Paniago, A. Machado, A. Patrocinio (Eds.), New layer-by-layer $Nb_2O_5$–$TiO_2$ film as an effective underlayer in dye-sensitised solar cells, RSC Adv. 4 (20) (2014) 10310–10316.
[94] X. Li, Y. Qiu, S. Wang, S. Lu, R.I. Gruar, X. Zhang (Eds.), Electrophoretically deposited $TiO_2$ compact layers using aqueous suspension for dye-sensitized solar cells, Phys. Chem. Chem. Phys. 15 (35) (2013) 14729–14735.
[95] J. Xia, N. Masaki, K. Jiang, Y. Wada, S. Yanagida (Eds.), Importance of blocking layers at conducting glass/$TiO_2$ interfaces in dye-sensitized ionic-liquid solar cells, Chem. Lett. 35 (3) (2006) 252–253.

[96] J. Xia, N. Masaki, K. Jiang, S. Yanagida (Eds.), Sputtered $Nb_2O_5$ as an effective blocking layer at conducting glass and $TiO_2$ interfaces in ionic liquid-based dye-sensitized solar cells, Chem. Commun. 2 (2007) 138–140.
[97] J. Xia, N. Masaki, K. Jiang, S. Yanagida (Eds.), Sputtered $Nb_2O_5$ as a novel blocking layer at conducting glass/$TiO_2$ interfaces in dye-sensitized ionic liquid solar cells, J. Phys. Chem. C 111 (22) (2007) 8092–8097.
[98] S. Suresh, T. Deepak, C. Ni, M. Satyanarayana, A.S. Nair, V.M. Pillai, Electro chemical impedance spectrscopic analysis of Nb2O5 blocking layer in dye sensitised solar cells, 2016 International Conference on Electrical, Electronics, and Optimization Techniques (ICEEOT), IEEE, Chennai, India, 2016, pp. 3765–3769.
[99] J. Xia, N. Masaki, K. Jiang, S. Yanagida, Fabrication and characterization of thin $Nb_2O_5$ blocking layers for ionic liquid-based dye-sensitized solar cells, J. Photochem. Photobiol. A 188 (1) (2007) 120–127.
[100] T.-Y. Cho, K.-W. Ko, S.-G. Yoon, S.S. Sekhon, M.G. Kang, Y.-S. Hong (Eds.), Efficiency enhancement of flexible dye-sensitized solar cell with sol–gel formed $Nb_2O_5$ blocking layer, Curr. Appl. Phys. 13 (7) (2013) 1391–1396.
[101] Z. Zhao, W. Sun, Y. Li, S. Ye, H. Rao, F. Gu (Eds.), Simplification of device structures for low-cost, high-efficiency perovskite solar cells, J. Mater. Chem. A 5 (10) (2017) 4756–4773.
[102] A. Kojima, K. Teshima, Y. Shirai, T. Miyasaka (Eds.), Organometal halide perovskites as visible-light sensitizers for photovoltaic cells, J. Am. Chem. Soc. 131 (17) (2009) 6050–6051.
[103] M. Grätzel, The rise of highly efficient and stable perovskite solar cells, Acc. Chem. Res. 50 (3) (2017) 487–491.
[104] J. Seo, J.H. Noh, S.I. Seok (Eds.), Rational strategies for efficient perovskite solar cells, Acc. Chem. Res. 49 (3) (2016) 562–572.
[105] J.S. Manser, M.I. Saidaminov, J.A. Christians, O.M. Bakr, P.V. Kamat (Eds.), Making and breaking of lead halide perovskites, Acc. Chem. Res. 49 (2) (2016) 330–338.
[106] K. Atsushi, N. Youhei, I. Masashi, M. Tsutomu (Eds.), $Nb_2O_5$ blocking layer for high open-circuit voltage perovskite solar cells, Chem. Lett. 44 (6) (2015) 829–830.
[107] S.L. Fernandes, A.C. Véron, N.F.A. Neto, F.A. Nüesch, J.H. Dias da Silva, M.A. Zaghete (Eds.), $Nb_2O_5$ hole blocking layer for hysteresis-free perovskite solar cells, Mater. Lett. 181 (Suppl. C) (2016) 103–107.
[108] Y.-T. Huang, R. Cheng, P. Zhai, H. Lee, Y.-H. Chang, S.-P. Feng (Eds.), Solution-based synthesis of ultrasmall $Nb_2O_5$ nanoparticles for functional thin films in dye-sensitized and perovskite solar cells, Electrochim. Acta 236 (Suppl. C) (2017) 131–139.
[109] J. Feng, Z. Yang, D. Yang, X. Ren, X. Zhu, Z. Jin (Eds.), E-beam evaporated $Nb_2O_5$ as an effective electron transport layer for large flexible perovskite solar cells, Nano Energy 36 (Suppl. C) (2017) 1–8.
[110] L.J. Phillips, A.M. Rashed, R.E. Treharne, J. Kay, P. Yates, I.Z. Mitrovic (Eds.), Maximizing the optical performance of planar $CH_3NH_3PbI_3$ hybrid perovskite heterojunction stacks, Sol. Energy Mater. Sol. Cells 147 (Suppl. C) (2016) 327–333.
[111] A. Guerrero, G. Garcia-Belmonte, I. Mora-Sero, J. Bisquert, Y.S. Kang, T.J. Jacobsson (Eds.), Properties of contact and bulk impedances in hybrid lead halide perovskite solar cells including inductive loop elements, J. Phys. Chem. C 120 (15) (2016) 8023–8032.
[112] W.J. Song, Z.F. Chen, M.K. Brennaman, J.J. Concepcion, A.O.T. Patrocinio, N. Y.M. Iha (Eds.), Making solar fuels by artificial photosynthesis, Pure Appl. Chem. 83 (4) (2011) 749–768.
[113] H.L. Luo, W.J. Song, P.G. Hoertz, K. Hanson, R. Ghosh, S. Rangan (Eds.), A sensitized $Nb_2O_5$ photoanode for hydrogen production in a dye-sensitized photoelectrosynthesis cell, Chem. Mater. 25 (2) (2013) 122–131.

PART III

# Nanowire, nanorod and nanoporous materials-based solar

This page intentionally left blank

# CHAPTER 9

# Silicon nanowire-based solar cells

**Subramani Thiyagu**[1,2] **and Naoki Fukata**[2]
[1]International Center for Young Scientists (ICYS), National Institute for Materials Science, Tsukuba, Japan
[2]International Center for Materials Nanoarchitectonics, National Institute for Materials Science, Tsukuba, Japan

## Contents



## 9.1 Introduction

Photovoltaics (PV) have the potential to make a significant contribution to solving the energy-shortage crisis that our society currently faces. Silicon (Si) is the most abundant, stable, and nontoxic element, and has the best-known electronic properties. However, PV continues to struggle to hold a cost-competitive edge in industrial-scale manufacturing. The solar cell market is based mostly on crystalline Si wafers measuring between 180 and 300 μm in thickness. Because a significant fraction of a cell's price is due to the Si materials it contains [1], the demand for alternative, less expensive technology has become a major goal for the scientific and commercial communities [2]. Thin-film silicon solar cells would seem to be a suitable alternative [3] and have inspired major research interest. These devices utilize inexpensive substrates, such as plastic, glass,

*Nanomaterials for Solar Cell Applications*
DOI: https://doi.org/10.1016/B978-0-12-813337-8.00009-6

or stainless steel. However, the significantly reduced thickness of the silicon layer leads to insufficient sunlight absorption and the nonoptimized crystal structure leads to low carrier collection. Those factors inevitably lead to low energy conversion efficiency. Light-trapping technology provides broad-band and efficient light absorption enhancement that can boost the performance of thin-film solar cells. Light-trapping structures can take various forms such as nanowires, nanoholes, and nanocones to enhance optical absorption as well allowing the radial configuration of p−n junctions.

Many researchers have focused their efforts on silicon nanowires (SiNWs) due to their broad potential application in nanoscale electronic and optoelectronic devices [4], such as field effect transistors [5], field emitters [6], chemical sensors [7], and solar cells [8,9]. Significant progress has been made in recent years in the development of simple and controllable methods of SiNW fabrication [10]. There are two basic approaches to preparing SiNWs: the bottom-up approach and the top-down approach. The bottom-up approach includes laser ablation, physical vapor deposition, and chemical vapor deposition [11−13]. Lithography and etching are top-down approaches [14,15]. Research into SiNWs with sub-100-nm diameters and spacing's is strongly motivated by the desire to achieve ultra-low reflectance and optimal carrier collection efficiency in the radial direction. By configuring the p−n junctions in SiNWs radially, the light-trapping effect effectively increases and the carrier recombination rate is reduced due to the shorter carrier collection path.

Nanostructured solar cells have a large surface-to-volume ratio; this has both benefits and detriments to the solar cells' properties. The light absorption and junction area are greatly enhanced due to their structural properties, but the high recombination rate caused by surface and interfacial defects shorten the carrier lifetimes, resulting in lower efficiencies. The primary challenge is to reduce recombination losses by passivating the surfaces and interfaces of the nanostructures. There have been numerous reports on the effects of surface passivation. Passivation layers such as $SiN_x$, $Al_2O_3$, $SiO_2$, and hydrogenated amorphous Si have been investigated. Surface treatment processes applied to the nanostructure can also be used to reduce surface and interfacial defects. Annealing in various atmospheres, such as $H_2$, $N_2$, Ar, $O_3$ and the use of plasma treatments effectively reduce surface and interface recombination [16−19]. This chapter will focus on the formation of SiNWs, their structural properties, and passivation techniques. Finally, we describe the fabrication of nanostructured

core–shells of silicon solar cells using different fabrication techniques and the resultant solar cells' properties.

## 9.2 Formation of silicon nanowires

One-dimensional (1D) SiNWs are attracting intense interest as a promising material for solar energy conversion for the new-generation PV technology. SiNWs can be prepared by numerous methods. The vapor–liquid–solid (VLS) growth method is among the most popular methods for growing 1D SiNWs. The classical VLS growth mechanism for SiNWs is gold-catalyzed. However, Au is known to affect the carrier lifetime in Si. The other preparation methods for 1D nanostructures include top-down methods such as metal-catalyzed electroless etching (MCEE) and reactive ion etching (RIE). Even though metals are used in this process, they are much more easily removed from the nanowire structures. The above-mentioned three processes (VLS, RIE, and MCEE) will be described in this chapter.

### 9.2.1 The bottom-up approach

#### *9.2.1.1 Vapor–liquid–solid growth*

In the VLS method, Si precursor gas, typically silane ($SiH_4$), is decomposed on an Au metal catalyst, after which Si-metal liquid alloys are formed. Si atoms diffuse into the Si-metal alloy droplet, and Si precipitation occurs through Si supersaturation, causing SiNWs to grow. The growth of SiNWs depends on the growth temperature, the pressure of the precursor gas and other conditions. The bottom-up approach can readily grow SiNWs with diameters ranging from $\approx 5$ nm to several hundreds of nanometers and lengths from $\approx 100$ nm to tens of micrometers. SiNW morphology can generally be controlled by adjusting the substrate type, precursor flow gas, base pressure, and crystallographic orientation [20–22]. Fig. 9.1A is a schematic illustration of 1D SiNW formation by the VLS using $SiH_4$ and $N_2$ as the carrier gas. Fig. 9.1B shows an scanning electron microscope (SEM) image of SiNWs grown by VLS.

### 9.2.2 The top-down approach

#### *9.2.2.1 Nanoimprinting method (reactive ion etching)*

The SiNW arrays were fabricated by nanoimprinting and the Bosch process using a Si substrate. In this method, Si substrates were patterned with a 30-nm thick Cr layer by UV-imprint lithography and a lift-off process.

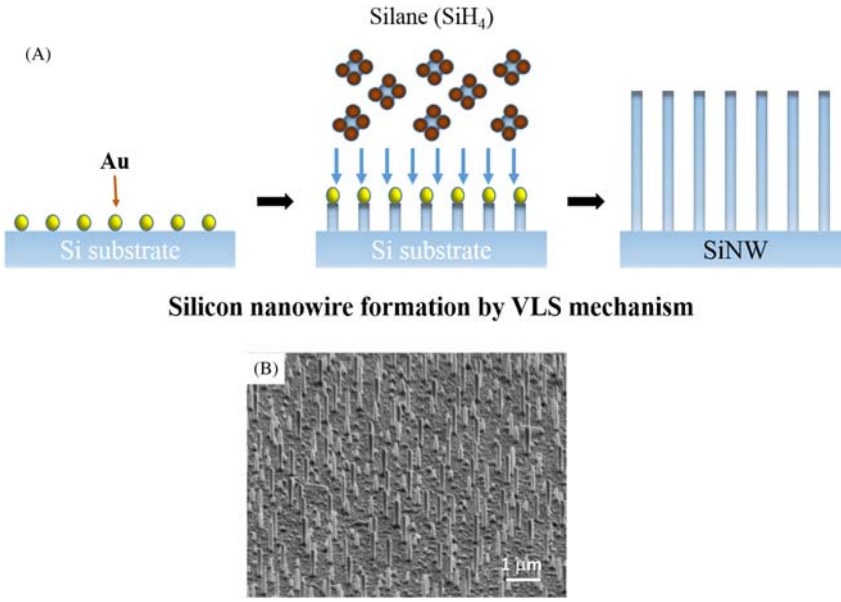


**Figure 9.1** (A) Schematic illustration for vapor–liquid–solid (VLS) mechanism and (B) SEM image of SiNWs formation by VLS. *SEM*, Scanning electron microscope; *SiNW*, silicon nanowire; *VLS*, vapor–liquid–solid.

The process involved coating photoresist on the Si substrate and employing a hard mold (mask) with a surface pattern to emboss the resist. Heat and pressure were typically utilized during the imprinting process. The mold was removed after imprinting, and the residual resists layer was then etched away to leave a patterned resist. The Cr layer was then deposited, followed by the lifting process. $SF_6$ plasma followed by $C_4F_8$ plasma or the Bosch process was then applied for deep Si etching to form the SiNW structure. The flow rates of $SF_6$ and $C_4F_8$ were both fixed at 35 sccm under a chamber pressure of 0.75 Pa and Radio Frequency (RF) power of 100 W [23]. Fig. 9.2A is a schematic illustration of 1D SiNWs formation by RIE etching, and Fig. 9.2B is a SEM image of SiNWs prepared by RIE etching growth.

#### *9.2.2.2 Metal-catalyzed electroless etching method*

For the MCEE process, a simple low-cost, one-step etching solution process was used to prepare 1D SiNWs. This technique is commonly used in solar cell and other electronic and optoelectronic applications. Wafer-scale

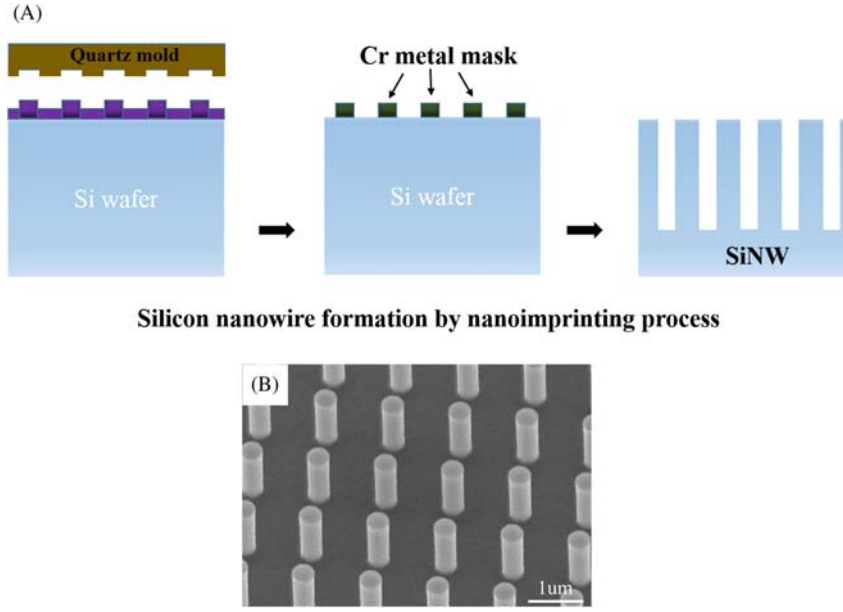


**Figure 9.2** (A) Schematic illustration for nanoimprinting process and (B) SEM image of SiNWs formation by the nanoimprinting method. *SEM*, Scanning electron microscope; *SiNW*, silicon nanowire.

SiNW arrays could be readily produced by electroless etching at room temperature by simply immersing Si wafers in an hydrofluoric (HF)–$AgNO_3$ solution. Significantly, highly oriented SiNW arrays and Si nanostructures can be produced using the MCEE process. SiNWs were fabricated in this way: the assisted metal was deposited on the silicon substrate prior to the etching process shown in Fig. 9.3A. Fig. 9.3B is an SEM image of SiNWs formed using the MCEE process. Full details of the fabrication process follow below [24–27].

A single-sided polished n-type (100) wafer was used (thickness $525 \pm 5$ μm, resistivity 1–10 Ω). First, we cleaned the Si wafer with deionized water, acetone, piranha clean ($H_2SO_4$: $H_2O_2$), and isopropanol for 5–10 minutes. Next, the cleaned silicon wafers were directly dipped in the etchant solution containing 0.023 M $Ag^+$ and 5.6 M HF. The $Ag^+$ and Si underwent a redox reaction, with the $Ag^+$ being reduced to Ag and deposited on the Si wafer to assist the HF etching in the [100] direction. At the same time, Si near the Ag nanoparticles was oxidized to silicon dioxide ($SiO_2$), located between the Ag and Si. The $SiO_2$ was

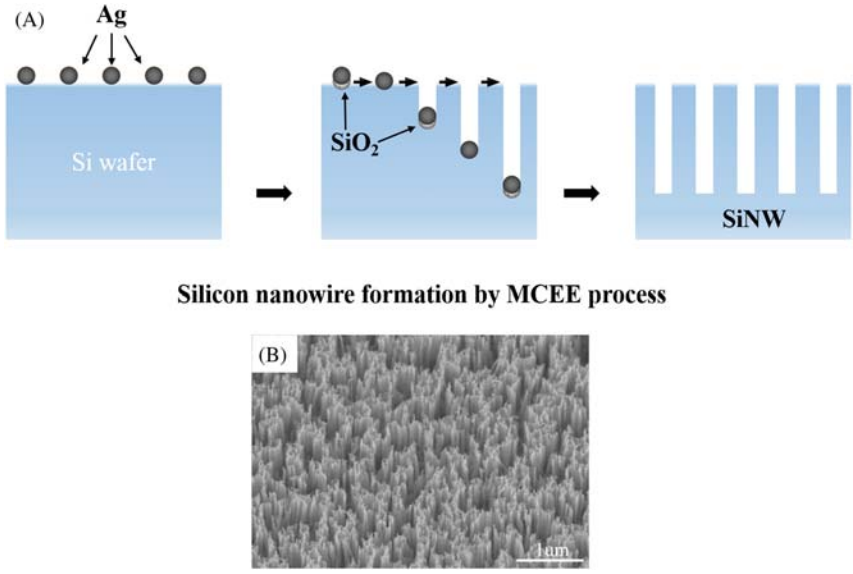


**Figure 9.3** (A) Schematic illustration for MCEE process and (B) SEM image of SiNWs formation using MCEE method. *MCEE*, Metal-catalyzed electroless etching; *SEM*, scanning electron microscope; *SiNW*, silicon nanowire.

instantly etched by HF. The Ag surface has a slightly negative charge that attracts $Ag^+$. Because the electronegativity of Ag (1.9) is greater than that of Si (1.8), the electrons of Si near the Ag nanoparticles distribute toward the Ag. In the etching solution, the silver ions agglomerate and attract electrons, causing Ag nanoparticles to form. Meanwhile, the Si underneath the Ag is oxidized to $SiO_2$, which is immediately etched by HF. The SiNW structures are obtained when the Ag penetration reaches a certain depth. The etching time was varied depending on the required length of the nanowires. After etching, the substrate was immersed in the dilute $HNO_3$ solution to remove the Ag film. The chemical reaction equations are shown below.

$$Ag^+ + e^- \rightarrow Ag \tag{9.1}$$

$$Si + 2H_2O \rightarrow SiO_2 + 4H^+ + 4e^- \tag{9.2}$$

$$SiO_2 + 4HF \rightarrow H_2SiF_6 + 2H_2O \tag{9.3}$$

## 9.3 Silicon nanostructure properties

### 9.3.1 Morphology characterization

The surface morphologies of SiNWs synthesized by MCEE and nanoimprinting, followed by the Bosch process, were investigated. Fig. 9.4 shows SEM images of n-SiNWs formed by nanoimprinting and the Bosch process. The SEM images of Fig. 9.4A–D show a tilted view of SiNW arrays with a diameter of 380, 230, 200, and 150 nm. SiNWs fabricated via the nanoimprinting method are well-ordered arrays, and we can define the diameter of the SiNW arrays by the photoresist patent, followed by a metal mask. The depth can be tuned by adjusting the RIE etching time.

SEM images of SiNW arrays fabricated by the MCEE process are shown in Fig. 9.5. The SEM images of Fig. 9.5A–F show a 45 degrees tilted view of the SiNW arrays with lengths of 50, 130, 170, 295, 470, and 570 nm. High-density nanowires, with an average diameter size of 25–30 nm, are homogeneously distributed on the Si wafer. The SEM images in Fig. 9.5 show some nanowires connecting with each other, and

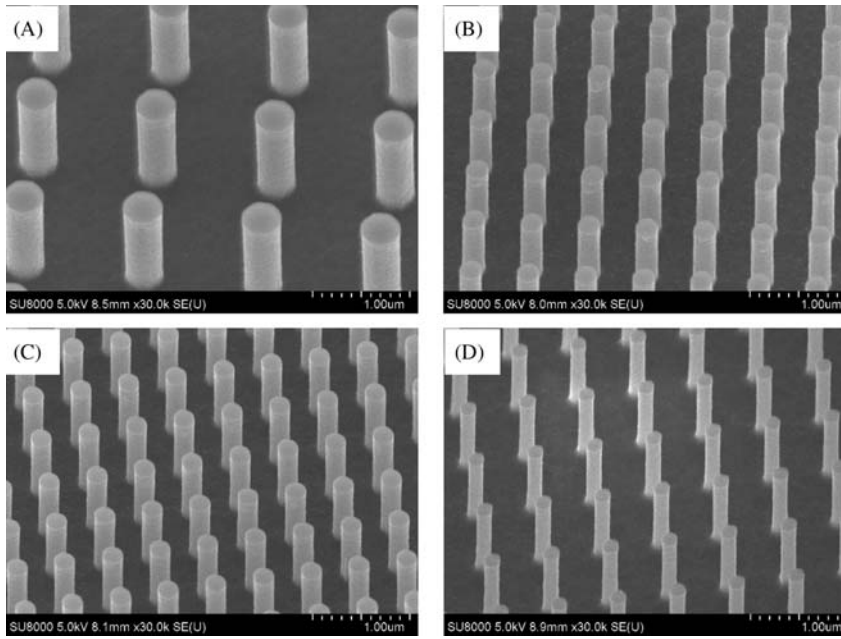


**Figure 9.4** SEM images of SiNW arrays fabricated by nanoimprinting method with different diameters: (A) 380 nm, (B) 230 nm, (C) 200 nm, and (D) 150 nm. *SEM*, Scanning electron microscope; *SiNW*, silicon nanowire.

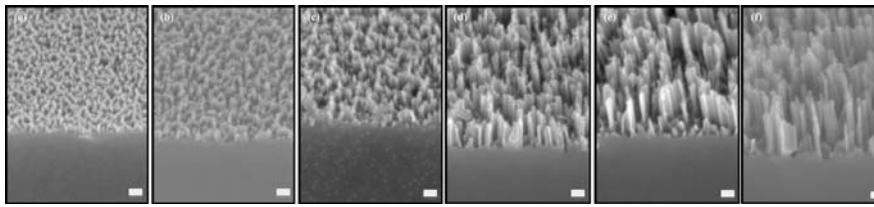

**Figure 9.5** SEM images of SiNW arrays with the etching times and lengths of (A) 50 nm, (B) 130 nm, (C) 170 nm, (D) 295 nm, (E) 470 nm, and (F) 570 nm. The scale bars in all of the figures represent 100 nm. *SEM*, Scanning electron microscope; *SiNW*, silicon nanowire.

the top of the substrate is rough. According to a previous report [26], when a one-step etching method is used to form SiNW arrays, some of the nanowires tend to aggregate as their lengths increase. Some of the gaps between the nanowires also shrink, and some places show increased gaps between the nanowires, as previously observed [28]. Aggregation is significant in this etching technique because the assisting metal is deposited during the etching process. The nanowires are directly fabricated via electroless metal deposition in $HF/AgNO_3$ solution. During this process, Ag nanoparticles are self-assembled via local reduction and oxidation between $Ag^+$ and Si; therefore, no photolithography or template assistance is needed [29,30].

The SiNW SEM images in Fig. 9.5 showed different lengths. The density of the nanostructure is calculated to express the morphology difference of the SiNW array. The density of SiNWs with lengths of 51, 130, 170, 295, 468, 565, and 710 nm are $3.49 \times 10^{10}$, $3.39 \times 10^{10}$, $3.35 \times 10^{10}$, $3.22 \times 10^{10}$, $3.02 \times 10^{10}$, $2.88 \times 10^{10}$, and $2.17 \times 10^{10}$ $cm^{-2}$, respectively.

## 9.3.2 Optical absorption

The SiNWs fabricated by MCEE process are randomly distributed, with a high-aspect ratio from around 25 to 100. This structure is similar to that of the antireflection nanostructures on the eyes of moths, where the outer surface of the cornea is covered with an array of conical protuberances [31,32]. One of the main purposes of Si nanostructures is to replace the conventional texture with an antireflection coating. Incident light undergoes multiple internal reflections, resulting in a long optical path before absorption. The prepared SiNW samples were black in appearance. As a consequence, the material was named "black silicon" [28]. The reflectance

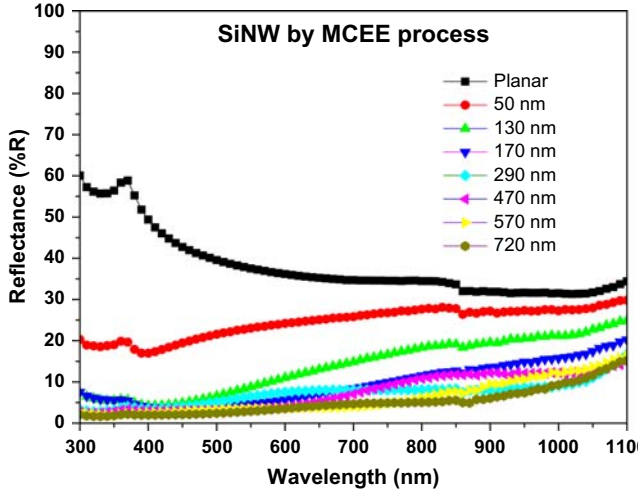


**Figure 9.6** The optical reflectance of SiNW arrays measured using an integrating sphere, including the average reflectance lengths of 50, 130, 170, 290, 470, 570, and 720 nm. The figure shown here uses the reflectance of a polished n-type Si wafer as a reference. *SiNW*, Silicon nanowire.

spectra of the SiNWs (of black appearance) and the polished bare n-Si are shown in Fig. 9.6. The SiNWs show low reflectance over the entire spectral range from 300 to 1100 nm. The high absorption of SiNWs causes low reflectance due to the strong internal light trapping property of the dense SiNWs. This remarkable feature suggests SiNW arrays are an appropriate candidate for antireflective surfaces and as absorption materials for use in photovoltaic cells. The spectral reflectance of the SiNWs for different etching times and different lengths are shown in Fig. 9.6. Even SiNWs that are just 50 nm long give a drastic decrease in reflectance from over 50% to less than 25% over the entire spectral range of 300–800 nm when compared to the surface of a polished Si wafer. SiNWs over 250 nm in length that are closely packed are a very efficient antireflection material. A further increase in etching time produces a more gradual decrease in reflectance.

### 9.3.3 Passivation techniques

Even though the SiNW structure has a very low reflectance, other problems need to be solved for solar cell applications. To realize higher efficiency in a solar cell, surface passivation is especially important because SiNW solar cells have a higher surface-to-volume ratio than bulk Si solar

cells. There are many passivation techniques that can be applied to SiNW structures, but here we focus on only three.

#### 9.3.3.1 $H_2$ annealing treatment

The first is two-step $H_2$ annealing [33]. Fig. 9.7 shows how two-step $H_2$ annealing was performed at 900°C for 10 minutes each after both n-SiNW formations and subsequent p-Si matrix shell layers for MCEE-SiNWs. The results of electron spin resonance (ESR) measurements at 4.2K at a microwave power of 0.5 mW, as displayed in Fig. 9.7A, show a reduction of defect signals with a *g*-value of 2.005. The defects are assigned to dangling bond-type defects present on the surface and inside the p-Si matrix. The crystallinity of the p-Si shell layers was also investigated by Raman and transmission electron microscope (TEM) measurements, as shown in Fig. 9.7B and C. The Si optical phonon peak with a small shoulder toward the lower wavenumbers was observed due to its polycrystalline properties. The peak position was the same as that for bulk Si, showing the good crystallinity of p-Si shell layers. The polycrystalline structures can be seen in the TEM image of Fig. 9.7C after the two-step $H_2$ annealing process. As-deposited p-Si layers had a high defect density, as evidenced by the high ESR signal. After $H_2$ annealing, the ESR defect signals dramatically decreased, showing that the annealing processes can effectively improve crystallinity and reduce defects in the CVD p-Si layer.

#### 9.3.3.2 UV−ozone treatment

The second passivation method is UV−ozone ($O_3$) treatments [25]. These were performed under 20 μW UV irradiation and 10 mTorr $O_2$ pressure at temperatures of 200°C−400°C. A schematic illustration of the UV−$O_3$ treatment system is shown in Fig. 9.8A. A UV lamp with a wavelength of 172 nm and a power density of 20 mW $cm^{-2}$ was used. The $O_2$ pressure was set at 10 mTorr. To minimize damage caused by direct irradiation of UV light, the samples are placed in the shade, as shown in the inset of Fig. 9.8A. Using ozone treatment causes atomic oxygen to diffuse into the p-type Si layer and passivate the dangling bonds. $O_3$ is more reactive than $O_2$, resulting in more efficient surface passivation of p-Si shell layers on n-type SiNWs prepared by the MCEE process. The results of ESR measurements at 4.2K shown in Fig. 9.8B and C show the reduction of defect signals with a *g*-value of 2.005. The signal intensity decreased with increased UV−$O_3$ treatment temperature and the reduction rate peaked at around 300°C−400°C.

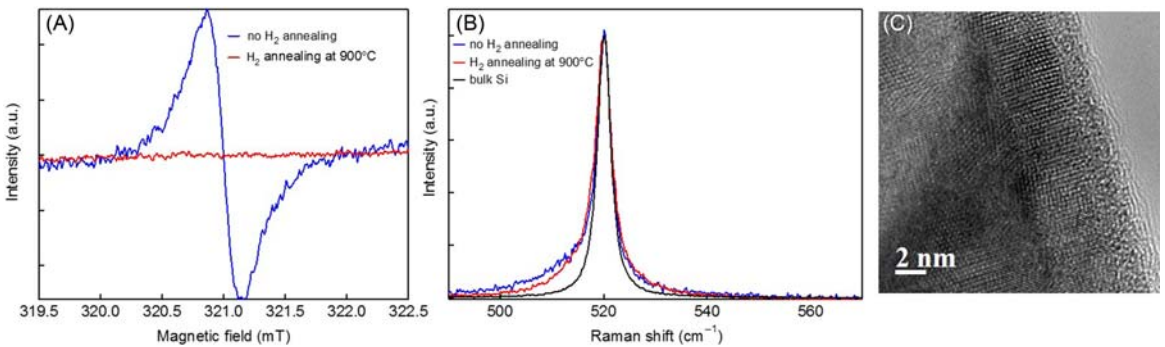


**Figure 9.7** (A) ESR spectra and (B) Raman spectra of MCEE-SiNW samples with and without $H_2$ annealing. (C) TEM image of a nanoimprinted-SiNW sample after two-step $H_2$ annealing at 900°C for 10 min. *ESR*, Electron spin resonance; *MCEE*, metal-catalyzed electroless etching; *SiNW*, silicon nanowire; *TEM*, transmission electron microscope.

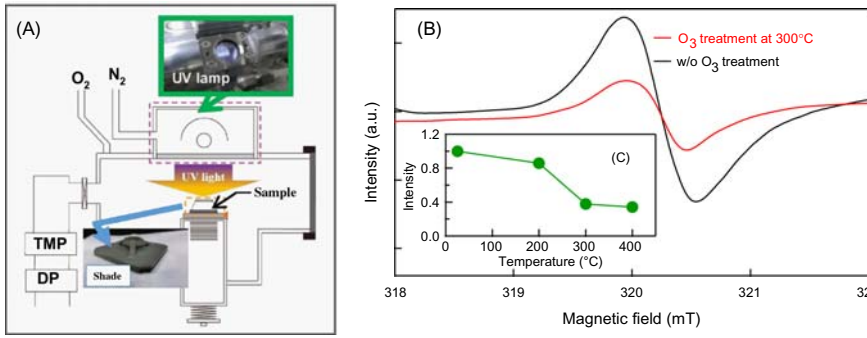


**Figure 9.8** (A) Schematic illustration of the ozone oxidation system. Photographs show the UV lamp and the sample stage with a shade to eliminate direct UV irradiation. (B) ESR signal and (C) dependence of ESR signal intensity on $O_3$ treatment temperature. *ESR*, Electron spin resonance.

#### *9.3.3.3 Chemical polishing etching treatment*

High-density surface defects easily trapped the photo-excited carriers. To reduce the surface defects and metal contamination of silicon nanostructures formed using the MCEE process, we further proceed to a feasible simple solution treatment. Applying the chemical polishing etching (CPE) treatment [27] to the silicon nanohole (SiNH) surface leads to a smooth and contamination-free surface. The surface modification of silicon nanostructures is performed using a CPE process containing HF and $HNO_3$. The working mechanism is as follows. First, $HNO_3$ oxidizes the Si, especially rough surface regions, to form $SiO_2$. Next, HF is used to etch the $SiO_2$. As a result, the rough surfaces of the silicon nanostructure are made smoother and surface defects are much reduced. The sample was immersed in this solution ($HF + HNO_3$) for different timings (5 and 10 seconds). A schematic diagram of the CPE process is shown in Fig. 9.9.

With CPE treatment, the density of the nanostructures decreases and the side walls of the nanostructures are smoothed. CPE treatment is a rapid process mostly used for polishing silicon surfaces. After 5 seconds of surface modification, SiNHs become Si nanotips (NTs). Fig. 9.10 displays high-resolution TEM (HR-TEM) images of an individual SiNH and silicon NT before and after CPE treatment. The atomically rough surface induces additional surface defects and causes severe carrier recombination. By utilizing the CPE treatment after fabricating a high-density SiNH structure, edge roughness decreased significantly and an atomically smooth surface was achieved, as shown in Fig. 9.10B. The effective carrier lifetime


**Figure 9.9** (A) Schematic diagram of the fabrication of silicon nanoholes with surface defects and metal contamination. (B) Schematic diagram of silicon nanostructures after CPE treatment. *CPE*, Chemical polishing etching.

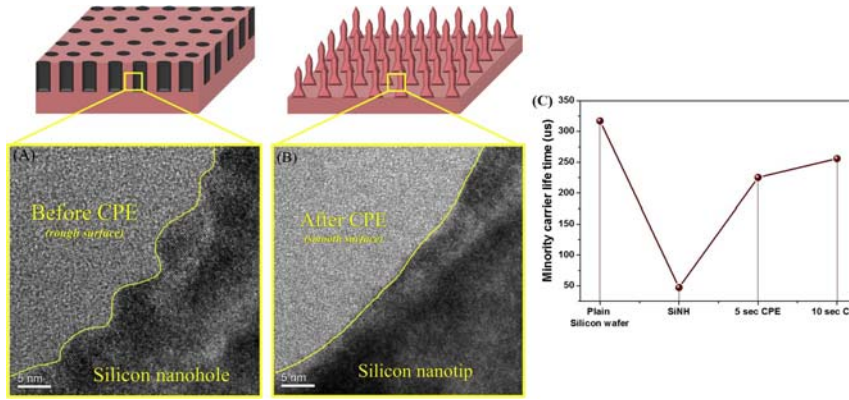


**Figure 9.10** HR-TEM images taken near the edge of the individual SiNH and silicon nanotip (A) before and (B) after CPE treatment. (C) Effective carrier lifetime for high-density SiNH and CPE treatment. *CPE*, Chemical polishing etching; *HR-TEM*, high-resolution transmission electron microscope; *SiNH*, silicon nanohole.

for high-density SiNH, 5 seconds CPE and 10 seconds CPE of all this structure after coating with poly(3,4-ethylene dioxythiophene):poly(styrenesulfonate) (PEDOT:PSS) for passivation is shown and summarized in Fig. 9.10C. The results show that the measured carrier lifetime dramatically drops after using metal-assisted chemical etching to fabricate SiNH, indicating that carrier-trapping centers and high-density surface defects are removed. The carrier lifetime significantly increases after applying the CPE treatment for 5 or 10 seconds to the SiNHs structure and turning them into silicon NTs.

## 9.4 Solar applications using silicon nanowires

### 9.4.1 Solar cell design and radial p–n junctions

A solar cell needs to have a p–n junction with a large surface area. In principle, light is predominately absorbed by Si. The p-type or n-type

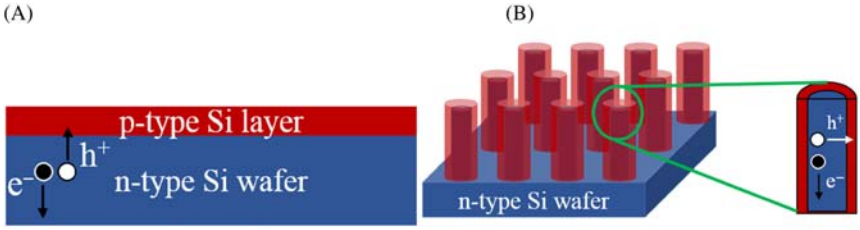


**Figure 9.11** Schematic diagram of (A) a planar junction and (B) a radial p−n junction.

materials should be thin enough to let the light to pass through the p−n junction. Electron-and-hole pairs are generated and separated by the driving force of the built-in electric field. The generation of electric current happens inside the depletion zone of the p−n junction. A schematic diagram of the p−n junction solar cell is shown in Fig. 9.11A. In planar junction solar cells, when the Si absorbs a photon of light, an electron-and-hole pair is generated. The generated charge carriers must, however, travel a long distance from the junction and reach an electrode without recombination. The diffusion distance of the charge carriers must therefore be long to produce electricity. On the other hand, nanostructure array solar cells have a significant advantage in that they effectively absorb light from all directions and generate charge carriers. In this design, the p−n junction is formed radially in core−shell structures. The generated charge carriers transport in the radial direction, resulting in a shorter diffusion length. Each nanowire also acts as a p−n junction. As a result, they have a much larger junction area than planar p−n junctions. Fig. 9.11B is a schematic diagram of a radial p−n junction solar cell.

## 9.4.2 Homojunction silicon nanowire solar cells

Radial homojunction SiNW solar cells are the most commonly fabricated and adopted type of SiNW solar cells. We fabricated SiNWs using the MCEE method on an n-type Si substrate. After removing the oxide layer, the substrates were immediately placed on a holder in the CVD chamber to undergo deposition of the B doped p-type Si shell layers. The total pressure was set at around 8 Torr by mixing with $N_2$ gas (30 sccm). For B doping, 0.5 sccm of diborane ($B_2H_6$) gas was injected into the CVD chamber with 19 sccm of silane ($SiH_4$) gas.

SEM images of nanoimprinted n-SiNWs with the different CVD deposition times of 0, 3, 5, 8, and 10 minutes are shown in

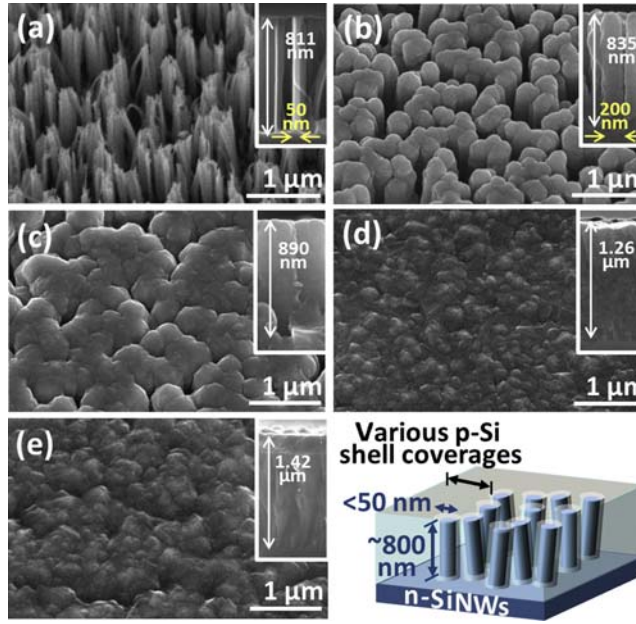


**Figure 9.12** SEM images of (A) n-SiNWs and (B) embedded nanoimprinted n-SiNWs in p-Si shell layers with various CVD deposition times of 3, (C) 5, (D) 8, and (E) 10 min. *SEM*, Scanning electron microscope; *SiNW*, silicon nanowire. *Reproduced with permission from W. Jevasuwan, K. C. Pradel, T. Subramani, J. Chen, T. Takei, K. Nakajima, Y. Sugimoto, N. Fukata, Jpn. J. Appl. Phys. 2017, 56, 04CP01. ©2017, The Japan Society of Applied Physics.*

Fig. 9.12A–E. High-density SiNW bunches approximately 800 nm in length and less than 50 nm in diameter were obtained using the MCEE method shown in Fig. 9.12A. After 3-minute CVD deposition, the average diameter of SiNWs grew to 200 nm with a small increase in length, and several nanowire bunches merged into large nanowires as shown in Fig. 9.12B. SiNWs were entirely covered with a p-Si shell after 8 minutes deposition: this was the optimum condition for p-Si coverage. We fabricated homojunction SiNW solar cells using the best conditions for p-Si shell growth, and also applied passivation treatment to these SiNW devices. Several other techniques were also employed to improve the performance of the solar cells by employing a back surface field (BSF) [33]. The BSF treatment is used to reduce electron-hole recombination at the rear surface of solar cells. The n + BSF layer is formed on the rear surface of n-Si substrates by phosphorus diffusion, which effectively reflects

**Table 9.1** Radial homojunction silicon nanowire (SiNW) solar cell properties.

| Samples | $J_{sc}$ (mA cm$^{-2}$) | $V_{oc}$ (V) | FF | Efficiency (%) |
|---|---|---|---|---|
| SiNW solar cell without any treatments | 16.5 | 0.38 | 0.38 | 2.4 |
| With $H_2$ annealing | 23.1 | 0.50 | 0.55 | 6.3 |
| With $H_2$ annealing and BSF | 23.4 | 0.50 | 0.68 | 7.9 |
| With $O_3$ treatment | 26.9 | 0.47 | 0.68 | 8.4 |
| With $O_3$ treatment and BSF | 32.7 | 0.47 | 0.71 | 10.9 |

*BSF*, Back surface field.

minority carriers (holes) so that efficiency can be improved. All the successful devices are summarized in Table 9.1.

### 9.4.3 Hybrid silicon nanowire polymer solar cells

Silicon nanostructure-organic polymer hybrid solar cells have also been widely investigated. Currently, traditional solar cells are manufactured utilizing expensive high-temperature diffusion and high-vacuum techniques. Another approach to reducing the cost of silicon solar cells is to reduce the quantity of silicon used, since most of the cost of a Si solar cells comes from the Si used. To ameliorate this problem, the conductive polymer is coated on the SiNWs to form heterojunction solar cells. These have several advantages, including large area coverage, low-temperature process capability, easy preparation, and low cost. SiNW arrays use an organic conductive material, PEDOT:PSS, to form heterojunction hybrid solar cells. The PEDOT:PSS acts as a hole-transporting layer and also passivates the Si nanostructure surfaces, reducing surface recombination. The lowest unoccupied molecular orbital of PEDOT:PSS is 3.5 eV, which is higher than the conduction band of Si, allowing the electron transportation direction to be regulated toward the cathode. Moreover, the highest occupied molecular orbital of PEDOT:PSS is 5.1 eV, which is near the valence band of Si, allowing holes to be transported from Si to PEDOT:PSS [34–36].

Regarding solar cell fabrication, n-type Si nanostructures were formed using a two-step MCEE process for n-type (1 0 0) Czochralski (CZ) wafers (thickness 525 μm, resistivity 1–10 Ω). In the first step, a cleaned Si wafer was dipped into an aqueous solution containing HF acid/$AgNO_3$ for just a few seconds to form independently distributed silver

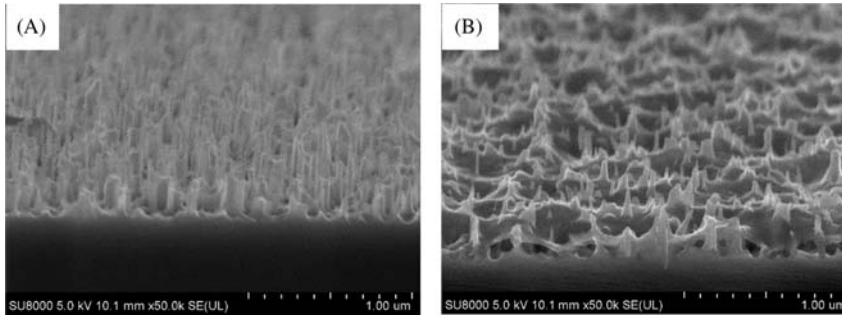


**Figure 9.13** (A) CPE treated and modified silicon nanostructure after 5 s treatment. (B) PEDOT:PSS covered silicon nanostructure. *CPE*, Chemical polishing etching; *PEDOT:PSS*, poly(3,4-ethylene dioxythiophene):poly(styrenesulfonate).

nanoparticles. Then, in the second step, the silver nanoparticle-coated wafer was immersed in an aqueous solution of HF and $H_2O_2$ to etch the Si wafer and form SiNHs. This is the two-step MCEE process. SiNHs usually show surface defects due to high density and Ag contamination. To remove these, CPE using a mixture solution of $HNO_3$ and HF was carried out for 5 seconds. After the CPE process, the high-density SiNHs were modified into SiNTs. The structural characterization of the silicon nanostructures was carried out by SEM measurements, as shown in Fig. 9.13. CPE etching reduced the density and depth of the nanostructures. As a result, the gaps between the nanostructures were widened, enabling the PEDOT:PSS to infiltrate easily. The key here is to cover the entire surface of the silicon nanostructure with PEDOT:PSS and form heterojunctions in all areas; otherwise, charge carrier recombination will occur in the uncovered areas [36].

The $J-V$ characteristics of the silicon nanostructure/PEDOT:PSS hybrid solar cells are shown in Fig. 9.14 and the results are summarized in Table 9.2. Hybrid solar cells fabricated with the nanohole structures formed through non-CPE treatment display the lowest efficiency of 10.08%, with a $J_{sc}$ of 33.50 mA $cm^{-2}$ and $V_{oc}$ of 0.475 V, due to a high carrier recombination rate resulting from a high density of surface defects. Compared to the non-CPE-treated sample, the hybrid cells with NTs have higher $V_{oc}$ and FF because of reduced surface defects, and complete coverage with PEDOT:PSS. The $V_{oc}$ is increased from 0.475 to 0.528 V for the 5 seconds CPE-treated sample, which is due to the reduced surface defects and improved carrier lifetime. As a result of this, the efficiency improved from 10.08% to 13.36%.

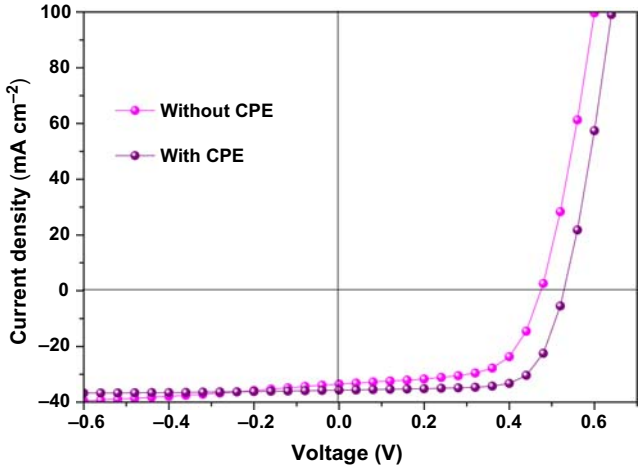


**Figure 9.14** Photo $J-V$ characteristics of Si nanostructure/PEDOT:PSS hybrid solar cell. *PEDOT:PSS*, Poly(3,4-ethylene dioxythiophene):poly(styrenesulfonate).

**Table 9.2** Hybrid silicon nanostructure solar cells.

| Samples | $J_{sc}$ (mA cm$^{-2}$) | $V_{oc}$ (V) | FF | Efficiency (%) |
|---|---|---|---|---|
| Without CPE treatment | 33.50 | 0.475 | 63.40 | 10.08 |
| With CPE treatment | 35.67 | 0.528 | 70.94 | 13.36 |

*CPE*, Chemical polishing etching.

Our group also proposed and demonstrated another way of improving power conversion efficiency. The method is called energy transfer (ET) and this phenomenon is new in solar cells. Nonradiative ET (NRET) is observed in heavy metal-containing compound semiconductor quantum dots, such as CdS, CdSe, and PbS quantum dots [37–39], and the same effect has been proven in silicon nanocrystal quantum dots (nc-Si QDs) [36,40], since nc-Si QDs offer a promising and safer alternative to II–VI QDs. The confinement effect in the nc-Si QDs, when the diameter is less than 5 nm, can cause emission in visible frequencies after absorbing the solar spectrum. This acts as RET. On the other hand, NRET also can be seen in nc-Si QDs. The key point is that nc-Si QDs have a higher ET rate in NRET than in RET [40]. ET in nc-Si QDs is not caused by the charge transfer effect, but by long-range dipole-dipole interaction. To transfer energy from nc-Si QDs to SiNW solar cells, the surface of the nc-Si QDs must be terminated with specific molecules. In our previous

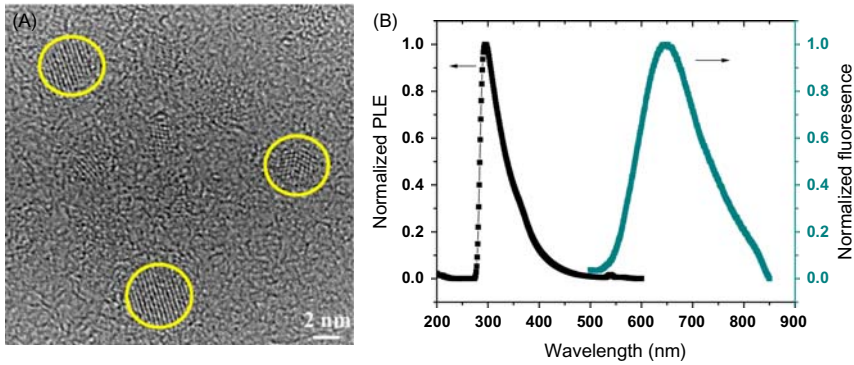


**Figure 9.15** (A) HR-TEM images of nc-Si QDs, and (B) Photoluminescence excitation (PLE) (left) and fluorescence (right) spectra. *HR-TEM*, High-resolution transmission electron microscope; *nc-Si QD*, silicon nanocrystal quantum dot.

report, nc-Si QDs were prepared from hydrogen silsesquioxane and the surfaces were ultimately terminated with 1-octadecene [36].

The HR-TEM image shown in Fig. 9.15A reveals the nearly spherical particle of a single nc-Si QD with an average diameter of 3.9 nm. The lattice fringes of Si QDs crystal exhibit an interplanar lattice spacing of 0.311 nm, corresponding to the d spacing of the [1 1 1] crystal plane of the diamond cubic structure of silicon. The fluorescence spectrum and absorption spectra were also measured to characterize the optical behavior of the nc-Si QDs. In Fig. 9.15B, the fluorescence spectrum of nc-Si QDs, measured under the excitation wavelength of 295 nm, gives an emission peak at around 648 nm. We checked the current density–voltage (J–V) characteristics in two configurations. In the first, hybrid solar cells with various concentrations of nc-Si QDs mixed with PEDOT:PSS on the silicon NTs are shown in Fig. 9.16A. The hybrid solar cell without nc-Si QDs exhibited a power conversion efficiency of 10.39% with a $J_{sc}$ of 34.07 mA $cm^{-2}$, $V_{oc}$ of 0.539 V, and FF of 56.5%.

The hybrid solar cell with 7 wt.% nc-Si QDs mixed with PEDOT:PSS exhibits higher performance due to higher concentrations of nc-Si QDs leading to higher $J_{sc}$. This indicates that more photons being absorbed by the nc-Si QDs and thus many more charge carriers are created by ET from the nc-Si QDs to the underlying silicon layer. The device with 7 wt.% of nc-Si QDs shows the highest $J_{sc}$ and FF of 36.30 mA $cm^{-2}$ and 59.14%, respectively, leading to the highest Power Conversion Efficiency (PCE) of 11.65%. On adding a greater concentration of nc-Si QDs, the performance of the hybrid solar cells began to

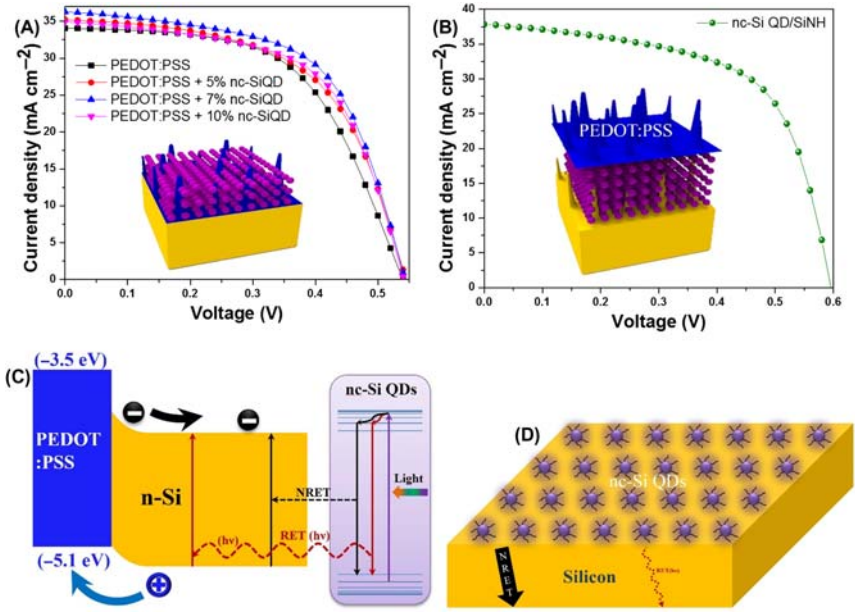


**Figure 9.16** $J-V$ characteristics of PEDOT:PSS/Si hybrid solar cells (A) without nc-Si QDs and with 5, 7, and 10 wt.% of nc-Si QDs mixed with PEDOT:PSS. A schematic diagram is shown in the inset of (A). (B) nc-Si QDs directly coated on silicon nanotip surfaces, followed by PEDOT:PSS coating. A schematic diagram is shown in inset (B). Illustration of energy transfer by both radiatively and nonradiatively induced light absorption in Si and subsequent charge separation and extraction by Schottky junctions (C) Energy band diagram and (D) Schematic diagram. *PEDOT:PSS*, Poly(3,4-ethylene dioxythiophene):poly(styrenesulfonate); *nc-Si QD*, silicon nanocrystal quantum dot. *Reproduced with permission from T. Subramani, J. Chen, Y. Sun, W. Jevasuwan, N. Fukata, Nano Energy 35 (2017) 154. ©2017, Elsevier Inc.*

decrease. However, nc-Si QDs mixed with the PEDOT:PSS configuration detract from the NRET effect, since NRET can generally occur within a distance of $\leq 10$ nm between the 1-octadecene-capped nc-Si QDs and Si solar cell layer. Due to the longer distance from the silicon NTs, the probability of the NRET rate from such nc-Si QDs decreases, resulting in lower power conversion efficiency.

To counter this disadvantage, we modified the configuration. nc-Si QDs were directly coated on the Si nanostructures and followed by PEDOT:PSS coating, as shown in Fig. 9.16B. In this case, all the nc-Si QDs effectively take part in the NRET. The device with direct coating of nc-Si QDs without PEDOT:PSS mixing showed a higher $J_{sc}$, $V_{oc}$, and FF of 37.85 mA cm$^{-2}$, 0.595 V, and 60.91%, respectively, leading to the

**Table 9.3** Photovoltaic parameters of poly(3,4-ethylene dioxythiophene):poly (styrenesulfonate) (PEDOT:PSS)/Si hybrid solar cells with silicon nanocrystal quantum dots (nc-Si QDs) on silicon nanostructure.

| Sample | $J_{sc}$ (mA cm$^{-2}$) | $V_{oc}$ (V) | FF (%) | PCE (%) |
|---|---|---|---|---|
| PEDOT:PSS/SiNTs | 34.07 | 0.539 | 56.51 | 10.39 |
| PEDOT:PSS + 5% nc-Si QDs/ SiNTs | 35.21 | 0.544 | 56.48 | 10.83 |
| PEDOT:PSS + 7% nc-Si QDs/ SiNTs | 36.30 | 0.542 | 59.14 | 11.65 |
| PEDOT:PSS + 10% nc-Si QDs/ SiNTs | 34.92 | 0.541 | 59.07 | 11.17 |
| PEDOT:PSS/nc-Si QDs/SiNTs | 37.85 | 0.595 | 60.91 | 13.73 |

*SiNT*, Silicon nanotip.

highest PCE of 13.73%. In this hybrid cell, the high $J_{sc}$ is due to the close contact between the nc-Si QDs and the silicon nanostructure: much more ET effectively occurs than with nc-Si QDs mixed with PEDOT: PSS. The energy band diagram of the hybrid solar cells and schematic diagram are shown in Fig. 9.16C and D. All these results related to PEDOT: PSS/Si nanostructure hybrid solar cells are summarized in Table 9.3.

## 9.5 Summary

In summary, the use of a silicon nanostructure is an effective way of fabricating high-performance and cost-effective solar cells because of their superior properties for carrier transport, charge separation, and light absorption. Radial p−n junction SiNW arrays offers a more viable approach to cost-effective Si-based solar cells than do conventional planar Si solar cells. Reflectance can be dramatically suppressed relative to that of planar Si substrates due to the formation of SiNW array structures over a broad range of spectral wavelengths of 300−1000 nm. By constructing p−n junctions radially in SiNWs, the light trapping effect effectively increases and the carrier recombination rate is also effectively reduced due to the shorter carrier collection path. SiNW-based solar cells appear to be promising candidates; however, many challenges need to be tackled; in particular, the carrier recombination problem at the interface caused by increased surface-to-volume ratio. We showed that three kinds of passivation techniques improve the performance of SiNW solar cells. As a result

of these enhancements, cell properties such as $J_{sc}$, $V_{oc}$, and FF increase, leading to higher power conversion efficiency. The NRET effect using nc-Si is a new way of improving solar cell properties. This technique can be simply and easily applied to any kind of Si solar cell. These approaches broaden the scope for developing cost-effective, large-area solar energy devices in industries at large scales.

## References

[1] R. Brendel, Thin-Film Crystalline Silicon Solar Cells: Physics and Technology, Wiley-VCH, Weinheim, 2003.
[2] V. Marroccoa, et al., Efficient plasmonic nanostructures for thin film solar cells, Proc. SPIE 7725 (2010) 77250L.
[3] T. Markart, L. Casatnar, Practical Handbook of Photovoltaics: Fundamentals and Applications, Elsevier, Oxford, UK, 2003.
[4] Y. Cui, C.M. Lieber, Functional nanoscale electronic devices assembled using silicon nanowire building blocks, Science 291 (2001) 851–853.
[5] J. Goldberger, A.I. Hochbaum, R. Fan, P.D. Yang, Silicon vertically integrated nanowire field effect transistors, Nano Lett. 6 (2006) 973–977.
[6] Q. Wang, J.J. Li, Y.J. Ma, X.D. Bai, Z.L. Wang, P. Xu, et al., Field emission properties of carbon coated Si nanocone arrays on porous silicon, Nanotechnology 16 (2005) 2919–2922.
[7] M.W. Shao, H. Yao, M.L. Zhang, N.B. Wong, Y.Y. Shan, S.T. Lee, Fabrication and application of long strands of silicon nanowires as sensors for bovine albumin detection, Appl. Phys. Lett. 87 (2005) 183106.
[8] K.-Q. Peng, S.-T. Lee, Silicon nanowires for photovoltaic solar energy conversion, Adv. Mater. 23 (2011) 198–215.
[9] S. Thiyagu, B.P. Devi, Z. Pei, Fabrication of large area high density, ultra-low reflection silicon nanowire arrays for efficient solar cell applications, Nano Res. 4 (2011) 1136–1143.
[10] Z. Fan, D.J. Ruebusch, A.A. Rathore, R. Kapadia, O. Ergen, P.W. Leu, et al., Challenges and prospects of nanopillar-based solar cells, Nano Res. 2 (2009) 829–843.
[11] N. Fukata, M. Mitome, Y. Bando, M. Seoka, S. Matsushita, K. Murakami, et al., Codoping of boron and phosphorus in silicon nanowires synthesized by laser ablation, Appl. Phys. Lett. 93 (2008) 203106.
[12] D.P. Yu, Z.G. Bai, Y. Ding, Q.L. Hang, H.Z. Zhang, J.J. Wang, et al., Nanoscale silicon wires synthesized using simple physical evaporation, Appl. Phys. Lett. 72 (1998) 3458–3460.
[13] N. Fukata, Impurity doping in silicon nanowires, Adv. Mater. 21 (2009) 2829.
[14] H.D. Tong, S. Chen, W.G. van der Wiel, E.T. Carlen, A. van den Berg, Novel top-down wafer-scale fabrication of single crystal silicon nanowires, Nano Lett. 9 (2009) 1015–1022.
[15] S. Thiyagu, Z. Pei, Y.H. Chen, J.C. Liu, Ultra-low reflectance, high absorption microcrystalline silicon nanostalagmite, Nanoscale Res. Lett. 7 (2012) 171.
[16] A.D. Mallorqui, E.A. Llado, I.C. Mundet, A. Kiani, B. Demaurex, S.D. Wolf, et al., Nano Res. 8 (2014) 673.
[17] K.T. Li, X.Q. Wang, P.F. Lu, J.N. Ding, N.Y. Yuan, Sol. Energy Mater. Sol. Cells 128 (2014) 11.

[18] H. Wang, J. Wang, L. Hong, Y.H. Tang, C.S. Tan, Nanoscale Res. Lett. 11 (2016) 311.
[19] S. Aouida, R.B. Zaghouani, N. Bachtouli, B. Bessais, Appl. Surf. Sci. 370 (2016) 49.
[20] N. Fukata, M. Mitome, T. Sekiguchi, Y. Bando, M. Kirkham, J. Hong, et al., Characterization of impurity doping and stress in Si/Ge and Ge/Si core shell nanowires, ACS Nano 6 (2012) 8887.
[21] N. Fukata, S. Ishida, S. Yokono, R. Takiguchi, J. Chen, T. Sekiguchi, et al., Segregation behaviors and radial distribution of dopant atoms in silicon nanowires, Nano Lett. 11 (2011) 651.
[22] N. Fukata, K. Sato, M. Mitome, Y. Bando, T. Sekiguchi, M. Kirkham, et al., Doping and Raman characterization of boron and phosphorus atoms in germanium nanowires, ACS Nano 4 (2010) 3807.
[23] W. Jevasuwan, K. Nakajima, Y. Sugimoto, N. Fukata, Jpn. J. Appl. Phys. 55 (2016) 065001.
[24] T. Subramani, C.-C. Hsueh, H.-J. Syu, C.-T. Liu, S.-T. Yang, C.-F. Lin, Interface modification for efficiency enhancement in silicon nanohole hybrid solar cells, RSC Adv. 6 (2016) 12374–12381.
[25] M. Dutta, N. Fukata, Low-temperature UV ozone-treated high efficiency radial p-n junction solar cells: N-Si NW arrays embedded in a p-Si matrix, Nano Energy 11 (2015) 219–225.
[26] S. Thiyagu, H.-J. Syu, C.-C. Hsueh, C.-T. Liu, T.-C. Lin, C.-F. Lin, Optical trapping enhancement from high density silicon nanohole and nanowire arrays for efficient hybrid organic-inorganic solar cells, RSC Adv. 5 (2015) 13224–13233.
[27] T. Subramani, H.-J. Syu, C.-T. Liu, C.-C. Hsueh, S.-T. Yang, C.-F. Lin, Low-pressure-assisted coating method to improve interface between PEDOT:PSS and silicon nanotips for high-efficiency organic/inorganic hybrid solar cells via solution process, ACS Appl. Mater. Interfaces 8 (2016) 2406–2415.
[28] H.J. Syu, S.C. Shiu, Y.J. Hung, C.C. Hsueh, T.C. Lin, S. Thiyagu, et al., Prog. Photovoltaics 21 (2013) 1400.
[29] K.Q. Peng, X. Wang, L. Li, X.L. Wu, S.T. Lee, J. Am. Chem. Soc. 132 (2010) 6872.
[30] T.G. Chen, P. Yu, S.W. Chen, F.Y. Chang, B.Y. Huang, Y.C. Cheng, et al., Prog. Photovoltaics 22 (2014) 452.
[31] Y.F. Huang, S. Chattopadhyay, Y.J. Jen, C.Y. Peng, T.A. Liu, Y.K. Hsu, et al., Improved broadband and quasi-omnidirectional anti-reflection properties with biomimetic silicon nanostructures, Nat. Nanotechnol. 2 (2007) 770–774.
[32] P.B. Clapham, M.C. Hutley, Reduction of lens reflection by moth eye principle, Nature 244 (1973) 281–282.
[33] W. Jevasuwan, K.C. Pradel, T. Subramani, J. Chen, T. Takei, K. Nakajima, et al., Jpn. J. Appl. Phys. 56 (2017) 04CP01.
[34] S.C. Shiu, J.J. Chao, S.C. Hung, C.L. Yeh, C.F. Lin, Morphology dependence of silicon nanowire/poly(3,4-ethylenedioxythiophene):poly(styrenesulfonate) heterojunction solar cells, Chem. Mater. 22 (2010) 3108–3113.
[35] K. Sato, M. Dutta, N. Fukata, Inorganic/organic hybrid solar cells: optimal carrier transport in vertically aligned silicon nanowire arrays, Nanoscale 6 (2014) 6092–6101.
[36] T. Subramani, J. Chen, Y. Sun, W. Jevasuwan, N. Fukata, Nano Energy 35 (2017) 154.
[37] H.M. Nguyen, O. Seitz, W. Peng, Y.N. Gartstein, Y.J. Chabal, A.V. Malko, Efficient radiative and nonradiative energy transfer from proximal CdSe/ZnS nanocrystals into silicon nanomembranes, ACS Nano 6 (2012) 5574–5582.

[38] O. Seitz, L. Caillard, H.M. Nguyen, C. Chiles, Y.J. Chabal, A.V. Malko, Optimizing non-radiative energy transfer in hybrid colloidal-nanocrystal/silicon structures by controlled nanopillar architectures for future photovoltaic cells, Appl. Phys. Lett. 100 (2012) 021902.
[39] M. Achermann, M.A. Petruska, S. Kos, D.L. Smith, D.D. Koleske, V.I. Klimov, Energy-transfer pumping of semiconductor nanocrystals using an epitaxial quantum well, Nature 429 (2004) 642–646.
[40] M. Dutta, L. Thirugnanam, P. Van Trinh, N. Fukata, High efficiency hybrid solar cells using nanocrystalline Si quantum dots and Si nanowires, ACS Nano 9 (2015) 6891–6899.

# CHAPTER 10

# Nanorod-based dye sensitized solar cells

**Sawanta S. Mali, Jyoti V. Patil, and Chang Kook Hong**
Polymer Energy Materials Laboratory, School of Applied Chemical Engineering, Chonnam National University, Gwangju, South Korea

## Contents



## 10.1 Introduction

Fabrication of cost-effective solar cells has become a rapidly expanding field in nonconventional, renewable energy source research area. The tuning of nano-morphologies of the metal oxides via green methods is a challenging task toward energy storage and conversion applications [1]. The global challenge to develop carbon-free renewable energy sources can be addressed by harnessing solar power using photovoltaics. In 1991, Grätzel and O'Regan experienced a scientific research blast for photovoltaic applications; after that as an alternative to conventional solar cells named dye sensitized solar cells (DSSCs) [2]. This third-generation photovoltaic technology with various nano-architectures of wide band-gap semiconductors and variety of dyes has been extensively studied [3–5]. The DSSC is a molecular approach to photovoltaic solar energy

*Nanomaterials for Solar Cell Applications*
DOI: https://doi.org/10.1016/B978-0-12-813337-8.00010-2

conversion technology. This is one of the emerging photovoltaic technologies that offers the potential to reduce the cost of photovoltaic electricity production. During the past two decades, nanoporous polycrystalline titania has been extensively used in DSSCs, which demonstrated to be a promising alternative to silicon-based solar cells due to their relatively high solar-to-electric power conversion efficiency (PCE) at low cost. Among wide band gap semiconductors, $TiO_2$, $SnO_2$, ZnO, and $WO_3$ are promising metal oxides for low-cost photovoltaics. The loading of visible band-gap sensitizers on nanostructured metal oxides is directly related to its density, surface area, phase purity, smooth charge transport, and nature of crystallinity. Thus, fabrication of crystalline, porous with high surface area wide band gap nanomaterials are major requirements for efficient DSSCs applications [6].

It is well known that the tuning of metal oxide nanomorphology is a key parameter in order to harvest solar energy effectively. So far, various morphologies of the $TiO_2$ have been developed by various chemical as well as physical techniques. In the case of the tuning of nano-architectures of the metal oxides, the solution process is the most promising route because of its low cost and is easy to control all chemical parameters [7–10]. In this chapter, we discussed the different one dimensional (1D) metal oxides for DSSCs' application developed by different chemical or physical techniques.

## 10.2 Dye-sensitized solar cells

### 10.2.1 Basic principle of dye-sensitized solar cells

The DSSC provides a technically and economically credible alternative concept to present-day $p-n$ junction photovoltaic devices. A schematic presentation of the operating principles of the DSSC is given in Fig. 10.1. At the heart of the system is a mesoporous titanium oxide (herein n-type metal oxide) layer composed of nanometer-sized particles that have been sintered together to allow for electronic conduction to take place. Attached to the surface of the nanocrystalline film is a monolayer of the charge transfer dye. Photoexcitation of the dye results in the injection of an electron into the conduction band (CB) of the oxide. The original state of the dye is subsequently restored by electron donation from the electrolyte, usually an organic solvent containing redox system, such as the iodide/triiodide couple. The regeneration of the sensitizer by iodide intercepts the recapture of the CB electron by the oxidized dye. The

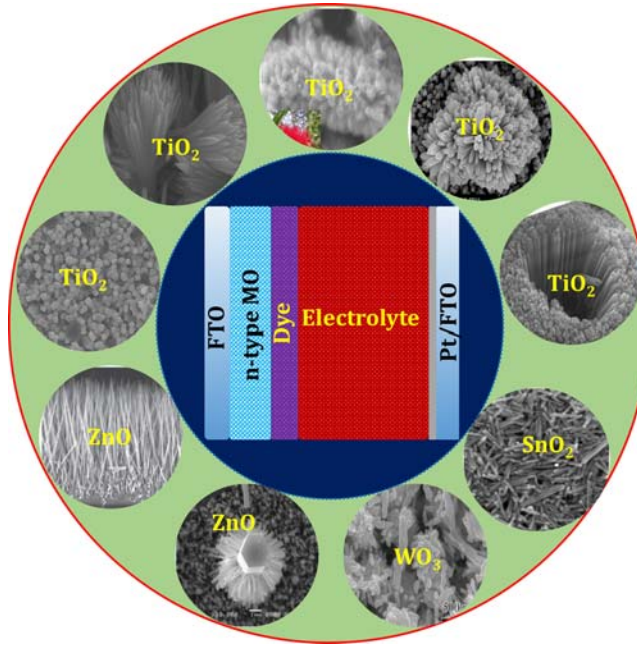


**Figure 10.1** Schematic representation of dye sensitized solar cells and different nanostructures of n-type metal oxides.

iodide is regenerated in turn by the reduction of triiodide at the counter electrode the circuit being completed via electron migration through the external load. The voltage generated under illumination corresponds to the difference between the Fermi level of the electron in the solid and the redox potential of the electrolyte. Overall the device generates electric power from light without suffering any permanent chemical transformation.

Upon illumination, the surface-anchored dyes are sensitized to the exited state (S*) by light absorption. This mode of carrier generation is also shared in organic, bulk junction solar cells where a light-absorbing organic polymer works as the sensitizer and a derivatized fullerene as the electron accepter. These devices are classified by Gregg as "excitonic solar cells," referring to the generation of a molecular excited-state or Frenkel exciton as the first step of a photovoltaic event [11]. In most other "excitonic" solar cells, photogenerated excitons have to diffuse a few nm to the interface before dissociating to an electron-hole pair. While in DSSCs, the excitons are generated right at the interface and they dissociate readily to create an electron-hole pair, with electrons subsequently

injected into the CB of the semiconductor. The dye ground state (S°) is then regenerated by electron donation from the redox system to the oxidized state of the sensitizer ($S^+$). The recuperation of redox system is realized by transporting holes to the counter electrode either in diffusion or hopping mechanism (depending on the transporting mediator). The whole process is finally completed by electron migration via the outer circuit and the device generates electric power from light without penalty of any permanent chemical transformation [12].

## 10.3 Conventional dye-sensitized solar cells

Conventional DSSCs are based on mesoporous $TiO_2$ loaded with N719 dye and reported >13% PCE [12–14]. However, a major drawback of the conventional $TiO_2$ nanoparticles photoelectrode in DSSCs is the slow electron transport speed [12]. This drawback can be overcome by the implementation of 1D nanostructured metal oxides, such as nanotubes, nanorods, and nanowires (NWs). For instance, the electron lifetime in films using nanorods or nanotubes can be enhanced by almost 3 times to that in nanoparticle films [8]. Therefore, we have overviewed the 1D nanorod-based DSSCs.

### 10.3.1 ZnO Nanorod-based dye-sensitized solar cells

The zinc oxide (ZnO) favors the formation of anisotropic structures, exhibits much higher electron mobility than $TiO_2$. Generally, ZnO exhibited 155 $cm^2\,V^{-1}\,s^{-1}$ while $TiO_2$ exhibits $10^{-5}$ $cm^2\,V^{-1}\,s^{-1}$ and higher exciton binding energy (60 meV) with wide band gap (3.37 eV), high breakdown strength, cohesion, exciton stability, and environmentally friendly material [15–17]. These properties make ZnO more promising in DSSC application. Law et al. first synthesized ZnO nanorods using a modified chemical method. This method includes the synthesis of ZnO quantum dot seeds followed by synthesis of ZnO NWs. A schematic of the construction of a NW DSSCs is shown in Fig. 10.2A. Arrays of ZnO NWs were synthesized in an aqueous solution using a seeded-growth process. In this method, authors used a thin layer ZnO quantum dots (dot diameter ~3–4 nm, film thickness ~10–15 nm) was deposited via a dip coating method followed by annealing. Then, the NWs were grown by immersing the seeded substrates in aqueous solutions containing 25 mM zinc nitrate hydrate, 25 mM hexamethylenetetramine, and 5–7 mM polyethylenimine (PEI) at 92°C for 2.5 hours. This process is also known as

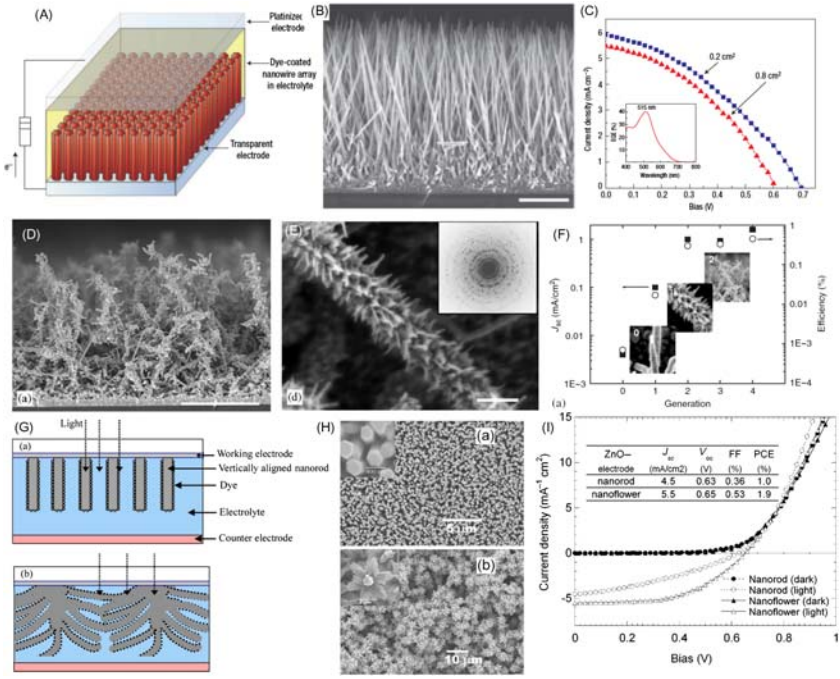


**Figure 10.2** The nanowire dye-sensitized cell, based on a ZnO wire array. (A) Schematic diagram of the cell. Light is incident through the bottom electrode. (B) Typical scanning electron microscopy cross-section of a cleaved nanowire array on FTO. The wires are in direct contact with the substrate, with no intervening particle layer. Scale bar, 5 μm. Traces of current density against voltage ($J$–$V$) for two cells with roughness factors of ~200. The small cell (active area: 0.2 $cm^2$) shows a higher $V_{oc}$ and $J_{sc}$ than the large cell (0.8 $cm^2$). The fill factor and efficiency are 0.37% and 1.51% and 0.38% and 1.26%, respectively.

aqueous chemical growth (ACG). The thickness and nanorod diameter can be easily controlled by growth time and nature of surfactant used in mother solution. In this process, PEI, a cationic polyelectrolyte, plays a key role in order to grow a variety of nanostructures of ZnO. Here, PEI serves to enhance the anisotropic growth of NWs. The synthesized NWs exhibit 125 aspect ratio and densities up to 35 billion wires per square centimeter. In addition, controlled parameters showed the longest length was 20–25 mm with 130–200 nm in diameter (Fig. 10.2B) [18]. It was found that the resistivity values of individual NWs ranged from 0.3 to 2.0 V cm, with an electron concentration of $1-5\times10^{18}$ $cm^3$ and a mobility of 1–5 $cm^2\ V^{-1}\ s^{-1}$. In addition, the single NW exhibited electron diffusivity $D_n = 0.05-0.5\ cm^2\ s^{-1}$, which is much higher than

conventional $TiO_2$ ($10^{-7} - 10^{-4}\,cm^2\,s^{-1}$) as well as ZnO ($10^{-5} - 10^{-3}\,cm^2\,s^{-1}$). This value is several hundred times larger than the highest reported electron diffusion coefficients for nanoparticle films in a DSSC configuration under operating conditions, that is, $10^{7}-10^{4}\,cm^2\,s^{-1}$ for $TiO_2$ and $10^{5}-10^{3}\,cm^2\,s^{-1}$ for ZnO. Moreover, the conductivity of the wire arrays increased by 5%–20% when they were bathed in the standard DSSC electrolyte. Furthermore, these ZnO NWs were used for fabrication of DSSCs. Fig. 10.2A shows the typical schematic DSSC device architecture based ZnO NWs. The ZnO NW arrays were first sensitized in a solution ($0.5\,mmol\,L^{-1}$) of $(Bu_4N)_2Ru(dcbpyH)_2(NCS)_2$ (N719 dye) in dry ethanol for one hour and then sandwiched together and bonded with thermally platinized fluorine doped tin oxide (FTO) counter electrodes separated by 40-μm-thick hot-melt spacers (Bynel, Dupont). The internal space of the cell was filled with a liquid electrolyte (0.5 M LiI, 50 mM I2, 0.5 M 4-tertbutylpyridine) in 3-methoxypropionitrile by capillary action. The fabricated devices were illuminated under solar simulator having a full sun intensity of 100 $mWcm^2$. The well optimized device exhibited short-circuit current densities ($J_{sc}$) of 5.3–5.85 mA $cm^2$, open-circuit voltages ($V_{oc}$) of 610–710 mV, fill factors (FF) of 0.36–0.38, and overall PCEs of 1.2%–1.5% (Fig. 10.2C).

Baxter et al. developed dendritic ZnO NWs by metalorganic chemical vapor deposition (MOCVD) method [19]; in typical method, zinc acetylacetonate hydrate [$Zn(C_5H_7O_2)_2\,xH_2O$, or $Zn(AcAc)_2$] and oxygen gas on conducting glass heated to 550°C in vacuum. Here, researchers used a two-step method in order to grow such dendritic type morphology. Initially, 100-nm-diameter ZnO NWs were grown by MOCVD followed by 20-nm secondary NW branches. Here, the NWs provide a direct path from the point of photogeneration to the conducting substrate and offer alternative semiconductor network morphologies to those possible with sintered nanoparticles. It was indicated that each of the NWs was crystalline with grain boundaries separating secondary NWs from the primary NW, called "second generation." It is noted that, after 2 hours, thinner NWs with the same dimensions as the secondary NWs also begin to nucleate from the substrate between the primary NWs. During the growth of a second generation of NWs, the secondary NWs act as nucleation sites. This process can also be continued for third and fourth generations for the attainment of a dendrite-like branched ZnO nanostructure. This dendrite architecture provides a much higher surface area, leading to improved light harvesting and overall efficiencies.

The fabricated DSSC devices based dendrite ZnO nanostructures exhibited much higher short-circuit density increased with increasing growth generation than smooth NWs due to the larger surface area, which in turn led to increased adsorption of dye molecules. Solar cells made from branched NWs showed photocurrents of 1.6 mA $cm^2$, internal quantum efficiencies of 70%, and overall efficiencies of 0.5%. Solar cells made from appropriate hybrid morphologies show photocurrents of 3 mA $cm^{-2}$ and overall efficiencies of 1.1%, while both the NW and hybrid cells show larger open circuit voltages than nanoparticle cells.

Jiang et al. used different morphology of ZnO called as "nanoflowers" consisting of upstanding NWs and outstretched branches and used in DSSCs with 1.9% efficiency [20]. Authors used hydrothermal technique for the synthesis of ZnO nanoflowers without seed coating. Both ZnO-nanoflower and upstanding nanorod films were grown with the same method but different substrate treatments, ammonia amounts, and growing times. In a typical method, 16 hours hydrothermal reaction time results in nanoflowers while 30 hours reaction time results in nanorod film. For the upstanding nanorod array, FTO glass substrate with a thin layer of densely and uniformly dispersed ZnO nanoparticles was used, which was deposited by spin coating of 0.75 M zinc acetate dehydrate [$Zn(CH_3COO) \cdot 2H_2O$] dissolved in a mixed solution of ethanolamine [$NH_2CH_2CH_2OH$] (0.75 M) and 2-methoxyethanol ($CH_3OCH_2{-}CH_2OH$). For deposition of the nanoflower film, a clear FTO substrate without any surface modification was used at 95°C. Fig. 10.2I shows the current–voltage (*IV*) characteristics for DSSCs constructed using nanorod and nanoflower films measured in dark and under a simulated illumination with a light intensity of 100 mW $cm^{-2}$. From Fig. 10.3, it can be seen that the $J_{sc}$, $V_{oc}$, and FF for the cell constructed using nanoflower film ($J_{sc} = 5.5$ mA $cm^2$, $V_{oc} = 0.65$ V, and FF = 0.53) represent clear improvement over the cell constructed using nanorod array ($J_{sc} = 4.5$ mA $cm^2$, $V_{oc} = 0.63$ V, and FF = 0.36). Due to much improved $J_{sc}$ and FF, the nanoflower-based cell reached a total PCE of 1.9%, outperforming that of the nanorod-based cell (1.0%) by 90%.

Pawar et al. used ACG route for the synthesis of different nanostructures of ZnO [21]. The seed solution was prepared in an absolute ethanol with 0.05 M zinc acetate ($Zn(CH_3COO)_2{\bullet}2H_2O$) and 0.05 M diethanolamine ($HN(CH_2CH_2OH)_2$, DEA). The cleaned FTO substrate was dip coated for 10 seconds in a seed solution and then kept at room temperature (RT) over night for drying. The dried films were annealed at 400°C for 5 minutes in air to yield a layer of ZnO seed on the substrate. The

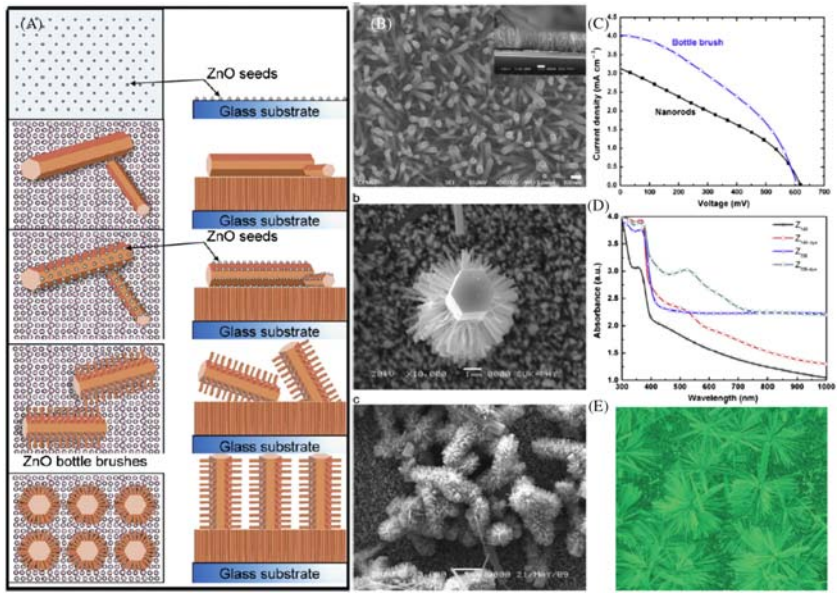


**Figure 10.3** (A) Growth model of ZnO bottle brush-like structure. (B) (a) SEM image of vertically aligned ZnO nanorods with an average diameter of 80 nm and about 2.5 μm length. Film recorded at × 50,000 magnification, (b) SEM micrograph of vertical ZnO bottle brush and secondary nanorods are emanated from vertical micro rod. Film recorded at × 10,000 magnification, and (c) SEM image of bottle brush indicates the formation of bottle brush over entire substrates. Film recorded at × 10,000 magnification. (C) *I*–*V* Characteristics for $Z_{NR}$ and $Z_{BB}$ films (D) Optical absorption spectra of $Z_{NR}$ and $Z_{BB}$ films without and with N3 dye (ZBR-dye and $Z_{BB}$-dye). (E) ZnO cactus like morphology. *Reproduced from R.C. Pawar, J.S. Shaikh, P.S. Shinde, P.S. Patil, Mater. Lett. 65 (2011) 2235.*

seeded substrates were placed vertically in 200 mL solution (growth solution) containing an equimolar (0.05 M) zinc acetate and hexamethylenetetramine (HMTA) and refluxed at 95 ± 3°C for 5 hours. The resulting film exhibits dense forest of vertically aligned ZnO NRs, and denoted as $Z_{NR}$. The refluxed film containing NRs array was re-seeded and re-refluxed at 90°C for 5 hours in growth solution to form ZnO bottle brush ($Z_{BB}$). The possible growth mechanism of bottle brush-like morphology is shown in Fig. 10.3A, which includes top and side views. Step-I: Shows formation of ZnO seed layer and their uniform distribution over the substrate. An average diameter of the seed, determined from SEM image, is about 30 nm. Step-II: when the ZnO seed pre-coated substrate is refluxed in the growth solution, nanorods emanate from the seeds. The length of

the nanorods depend on the reflux time, it is 2.5 μm for 5 hours. Step-III: The μR/NR film has been re-seeded in the seed solution. The seeds get nucleated on the surface of the μRs only. Step-IV: The secondary growth of NRs, which emanates from secondary seeds, takes place. The secondary NRs grow perpendicular to the μRs, leading to the bottle brush-like structure. The μRs are aligned parallel, inclined and perpendicular to the substrate (Step-V). The SEM micrograph demonstrates the vertically aligned ZnO nanorods and their uniform distribution over the substrate (Fig. 10.3B top). Their average rod diameter is about 80 nm and length is about 2.5 μm (inset). Fig. 10.3B (middle) shows the SEM micrograph of $Z_{BB}$. The dense secondary nanorods, with an average diameter of 125 nm and length of 1.2 μm, emanated from the primary vertical hexagonal microrods. Fig. 10.3B (bottom) shows the randomly distributed bottle brush over the entire substrate. Furthermore, the fabricated DSSC devices exhibited the $V_{oc}$ for both films is $\sim$600 mV. However, $J_{sc}$ is varied from 3.14 mA $cm^{-2}$ for $Z_{NR}$ to 4.02 mA $cm^{-2}$ for $Z_{BB}$ and the $\eta$ is improved from 0.7% to 1.0%. The nanostructure of ZnO plays a crucial role to improve light harvesting efficiency. The three-dimensional (3D) nanostructure provides direct path for electron transport and increases the specific surface area for more dye loading. Fig. 10.3C compares the variation in the optical absorption behavior of $Z_{BB}$ and $Z_{NR}$ films with ($Z_{BB}$-dye and $Z_{NR}$-dye) and without N3 dye. Both the films exhibit maximum absorption peak at 370 nm (3.35 eV) corresponding to band edge absorption of ZnO. After N3 dye loading, one more peak is observed at 523 nm (2.37 eV), which is attributed to the $t_2 \rightarrow \pi^*$ metal-to-ligand charge transfer. The optical absorption spectra revealed that the bottle brush-like structure induces effective absorption in the visible region due to increased surface area for dye loading. Moreover, the existence of higher visible absorption for $Z_{BB}$ suggests the light scattering effect, which increases the optical path length within the photoanode so as to increase the probability of interaction between the photons and the dye molecules [22]. The secondary NRs exhibit the size comparable to the wavelength of incident light, and hence act as major scattering centers. When these scattering centers are exposed transversely, the light is multiplied and scattered during its propagation. Therefore, absorption is increased for the $Z_{BB}$ film.

Wu et al., developed ZnO nanocactus (NC) array by the chemical bath deposition (CBD) on the ZnO NW array at RT surface etching method in NaOH solution [23]. Authors demonstrated that, compared to

the ZnO NW, the ZnO NC anode possesses a large surface area with a well-dye-matched characteristic, resulting in the superior $J_{sc}$, FF, and therefore efficiency of the ZnO NC DSSC. A DSSC efficiency of 3.32% with $V_{oc}$ of 0.67, $J_{sc}$ of 7.06 mA $cm^{-2}$, and FF of 0.68 is obtained using a 3.3 μm thick and D149-sensitized ZnO NC anode. This enhancement is almost 2 times that achieved for the ZnO ND-30/NC-20 electrode.

Jiang et al., developed a ZnO nanoarchitecture composed of NCs and nanosheets (NS) on the ZnO-NW-array template within 4 minutes by a facile room-temperature CBD for use in D149 based DSSCs [24]. A conventional seed coating method was adopted, followed by CBD for ZnO NWs. To synthesize the ZnO NPs, a 65 mL of methanolic solution of 0.03 M NaOH was added dropwise into a 125 mL of methanolic solution of 0.01 M zinc acetate at 60°C under vigorous stirring, and stirring of the solution was maintained for 2 hours at 60°C. For construction of the ZnO NS−NS frameworks on ZnO NWs, the (1250 rpm) aqueous solution of 0.062 M zinc acetate and 0.455 M NaOH at RT (Fig. 10.4).

A thick NC-NS framework was prepared for further increasing the efficiency of ZnO NC-NS DSSC. When using an 8-μm-thick ZnO NW

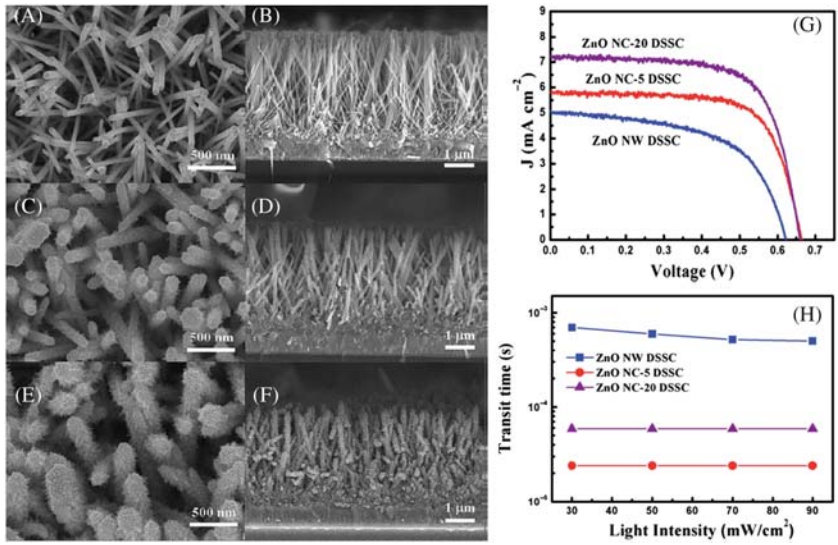


**Figure 10.4** Top-view and cross-sectional SEM images of the ZnO NW array (A), (B); the ZnO NC-5 array (C), (D); and the ZnO NC-20 array (E), (F). (A) *J*−*V* characteristics of the ZnO NW, ZnO NC-5 and ZnO NC-20 DSSCs. (B) Dynamics of charge transport in the three DSSCs. *DSSCs*, Dye sensitized solar cells. *Reproduced from C.T. Wu, J.J. Wu, J. Mater. Chem. 21 (2010) 13605.*

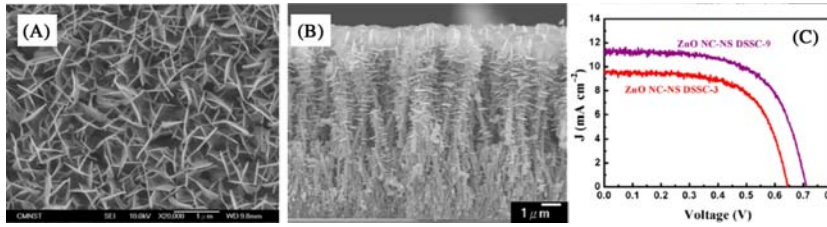


**Figure 10.5** (A) Top-view and (B) cross-sectional SEM image of the ZnO NC-NS framework. (B) $J-V$ curves of the D149-sensitized ZnO NC-NS DSSCs. *DSSCs*, Dye sensitized solar cells. *Reproduced from W.T. Jiang, C.-Te Wu, Y.H. Sung, J.-J. Wu, ACS Appl. Mater. Interfaces 5 (2013) 911.*

array as the template, the ZnO NCNS framework with a thickness of 9 μm was formed on ITO substrate by the RT CBD, as shown in Fig. 10.5a. It should be addressed here that the RT CBD was conducted for 4 minutes in this case to grow the hierarchical nanostructures fully covering the ZnO NW template. The photovoltaic performance of the ZnO NC-NS DSSC with anode thickness of 9 μm (named ZnO NC-NS DSSC-9 hereafter) is shown in Fig. 10.5B. The $J-V$ curve of the ZnO NC-NS DSSC with an anode thickness of 3.3 μm (named ZnO NC-NS DSSC-3 hereafter) is replotted in this figure for comparison. They indicate that the $J_{sc}$ and $V_{oc}$ are increased when elongating the ZnO NC-NS anode. Although the increment of $J_{sc}$ is not as significant as expected, a DSSC efficiency of 5.14% is achieved in the ZnO NC-NS DSSC-9 simply by the formation of hierarchical nanostructure on the 8-μm-thick ZnO NW anode at RT for 4 minutes.

## 10.3.2 $SnO_2$ Nanorod-based dye-sensitized solar cells

Tin-oxide ($SnO_2$) is a highly favorable material for applications in DSSCs. It is noted that $SnO_2$ is most favorable compared to $TiO_2$ due to its two key advantages. The $SnO_2$ exhibits a band gap of 3.8 eV. which is much larger than that of $TiO_2$ (3.2 eV). In addition, the electron mobility ($\sim 100-200\ cm^2\ V^{-1}\ s^{-1}$) of $SnO_2$ is over two orders of magnitude higher than that of anatase $TiO_2$ ($\sim 0.1-1\ cm^2\ V^{-1}\ s^{-1}$), indicating a faster electron diffusion inside the photoanode [25,26]. Furthermore, it generates many fewer oxidative holes under illumination, therefore improving the long-term stability of the DSSCs and minimizing the degradation rate of the dye. Therefore, developing 1D structured $SnO_2$ in DSSCs is a hot topic in the DSSCs field nowadays.

Huo et al. synthesized novel $SnO_2$ nanorod@$TiO_2$ hybrid materials by in situ coating a layer of $TiO_2$ on the surface of the $SnO_2$ nanorods using a modified flame spray pyrolysis (FSP) approach [27]. The as-prepared $SnO_2$ nanorod@$TiO_2$ hybrid materials have a length of up to about 150 nm and a diameter of about 40 nm. $TiO_2$ is uniformly coated on well-crystallized $SnO_2$ nanorods with a thickness of about 10 nm. Authors compared three different photoelectrodes for their photovoltaic performance. The electrode derived from the $SnO_2$ nanorod@$TiO_2$ hybrid materials shows a highest $J_{sc}$ of 16.15 mA $cm^{-2}$, $V_{oc}$ of 0.78 V, and FF of 0.55. The remarkable improvement of the $J_{sc}$ may be attributed to the high dye loading amount, high light harvesting efficiency, and the fast electron transport process. The increase of the $V_{oc}$ is attributed mainly to the low charge recombination rate due to the $SnO_2$ and $TiO_2$ hybrid. As a result, the electrode shows the highest PCE of 6.98%, 76.7% higher than the $SnO_2$ nanorods electrode (3.95%), and also much higher than the P25 electrode (5.27%). The $SnO_2$ nanorods electrode shows the lowest PCE, which is mainly a consequence of the lowest $J_{sc}$ of 8.64 mA $cm^{-2}$ (Fig. 10.6). This is also confirmed by amount of dye loading, the BET specific surface area, and incident photon-to-electron

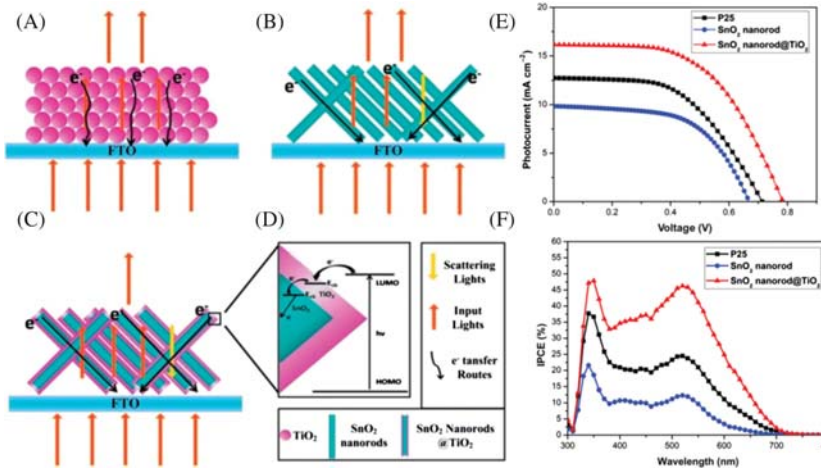


**Figure 10.6** Light scattering effect and electron transport routes in films based on (A) P25, (B) $SnO_2$ nanorods and (C) $SnO_2$ nanorod@$TiO_2$, and (D) electrons transport routes in the interface of $TiO_2$ and $SnO_2$. (E) DSSC performance of the three films based on P25, $SnO_2$ nanorods, and $SnO_2$ nanorod@$TiO_2$. (F) IPCE spectra. *DSSC*, Dye sensitized solar cells; *IPCE*, incident photon-to-electron conversion efficiency. *Reproduced from J. Huo, Y. Hu, H. Jiang, W. Huang, C. Li, J. Mater. Chem. A 2 (2014) 8266.*

conversion efficiency (IPCE) analysis. Authors results revealed that the $SnO_2$ nanorods have 11.9 $m^2 g^{-1}$, which is smaller than that of the $SnO_2$ nanorod@$TiO_2$ (34.7 $m^2 g^{-1}$) and P25 (49.6 $m^2 g^{-1}$) electrodes. The larger specific surface area of $SnO_2$ nanorod@$TiO_2$ over the $SnO_2$ nanorods is derived from the coating of $TiO_2$, which is beneficial for increasing the dye loading amount. Furthermore, the $SnO_2$ nanorod@$TiO_2$ cell shows the highest IPCE values and the cell of $SnO_2$ nanorods shows the lowest values. The increased IPCE value is mainly due to the increased dye loading amount and the suppression of electron combination provided by the $TiO_2$ and $SnO_2$ hybrid electrode.

It is well known that controlling the nano-architectures of photoanode is one of the important approaches for the improvement of solar cell performance. However, small-sized particles suffer from insufficient light scattering, thus resulting in low light-harvesting efficiency. However, Frank et al. discussed limitations of electron diffusion coefficient and electron collection time in such nanoparticulate samples, which stem mainly from the prevailing hopping mechanism in them [28]. To tackle these problems, 3D growth of hierarchical nanostructured metal oxides is the effective solution, which can provide a direct path, effective light harvesting, particle-to-particle light scattering, and low grain boundaries for the rapid collection of photogenerated electrons and reduce the charge recombination. Mali et al., synthesized $SnO_2$ by controlled hydrothermal process in aqueous NaOH medium and employed it successfully for DSSC applications [29]. However, most of the works have been only focused on the hierarchical $TiO_2$ or ZnO spheres. Fig. 10.7 shows typical TEM micrographs of $SnO_2$−16 (Fig. 10.7A) and SnO2−24 (Fig. 10.7B) sample after 24 hours hydrothermal reaction time. From Fig. 10.7A and B, it is clear that the microspheres are well grown and separated from each other. Moreover, the higher magnified FESEM images show that the microspheres are composed of nanoparticles with 15−20 nm size. Fig. 10.7A (a−d) shows the TEM images of a $SnO_2$−16 sample. From TEM analysis, it is clear that the synthesized microspheres are very compact in nature. The average size of the microsphere is 1.5 μm, which is well in agreement with FESEM analysis. In order to check its crystallinity, HRTEM images were recorded. Fig. 10.7A(e,f) shows the HRTEM images clearly revealing that these microspheres are crystalline in nature. In order to investigate the growth mechanism of such microspherical morphology of $SnO_2$, authors performed time-dependent hydrothermal process. Initially, 2.15 g of $SnCl_2$ was hydrolyzed in water to form white colored sol. After the

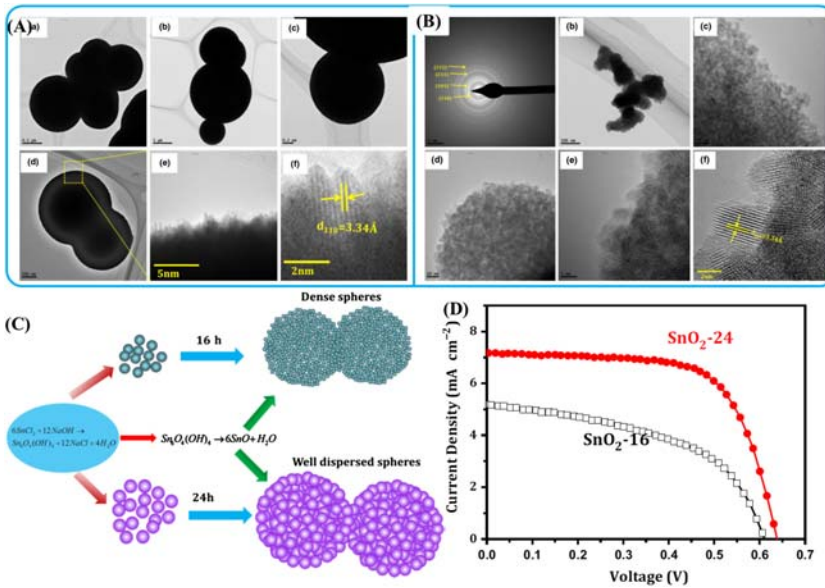


**Figure 10.7** Transmission electron microscopic images of $SnO_2$ microspheres deposited for 16 h by hydrothermal reaction at different magnifications. (A) (a–d) TEM images of $SnO_2$ microspheres at different magnifications, (e and f) HRTEM images transmission electron microscopic images of $SnO_2$ microspheres deposited for 24 h by hydrothermal reaction at different magnifications. (B) (a) SAED pattern of $SnO_2$–24 sample, (b–d) TEM images of $SnO_2$ microspheres at different magnifications, and (e and f) HRTEM images (C) Proposed growth mechanism of formation of compact and well-dispersed $SnO_2$ microspheres, (D) Current–voltage characteristics of the as-prepared dye sensitized solar cells based on $SnO_2$ photoelectrodes. *Reproduced from S.S. Mali, C.S. Shim, H.J. Kim, M.C. Lee, S.D. Patil, P.S. Patil, et al., J. Nanopart. Res. 17 (2015) 496.*

hydrolysis process, the pH of the solution was controlled by adding 50 mL of 1.35 g aqueous NaOH solution. In this process, yellow-colored $Sn_6O_4(OH)_4$ complex has been formed. The above process can be expressed as

$$6SnCl_2 + 12NaOH \rightarrow Sn_6O_4(OH)_4 + 12NaCl + 4H_2O \quad (10.1)$$

Tetragonal SnO was re-precipitated after the dissolution of $Sn_6O_4(OH)_4$ precursor, as expressed by the equation:

$$Sn_6O_4(OH)_4 \rightarrow 6SnO + H_2O \quad (10.2)$$

During this process, the hydrolyzed $Sn^{2+}$ is converted into $SnO_2$ nucleus. These $SnO_2$ nuclei provide high surface energy, resulting in the

formation of $SnO_2$ compact nanoparticles. This is a kind of self-assembly of nanoparticles by van der Waals interactions to reduce the overall energy. As deposition time increases, the compact microspheres are converted into well-dispersed $SnO_2$ microspheres, as illustrated in Fig. 10.7C. Initially, $SnO_2$ compact layer is converted into well-dispersed microspheres due to acid etching effect, and with the hydrothermal processing time increasing, the acidic etching becomes stronger. This structure may have formed due to selected surface etching of Sn species in acidic medium at a relatively higher deposition time. Such process is also known as recrystallization process, i.e. "dissolve and grow process." According to the "dissolve and grow" method, $Sn_6O_4(OH)_4$ is oxidized to $Sn^{2+}$ by reaction with dissolved oxygen. The $Sn^{2+}$complex ions are thus used as the growth units. Both the devices showed reasonably improved PCEs, all well above 1.5%, probably due to the good quality of the photoanode films. Device prepared with $SnO_2$−16 sample exhibited an efficiency of 1.68% and a $V_{oc}$ of 0.611 V, with FF = 0.50, while $SnO_2$−24 sample shows significantly high conversion efficiency of 3.12%, with $V_{oc} = 0.631$ V, $J_{sc} = 7.28$ mA cm$^{-2}$, and FF = 0.67 (Fig. 10.7D). This increase in efficiency can be attributed to high surface area and excellent crystallinity of the $SnO_2$−24 sample compared to the $SnO_2$−16 sample.

### 10.3.3 $WO_3$ nanorods for dye-sensitized solar cells

Tungsten oxide ($WO_3$) is a semiconductor oxide material with a bandgap of 2.6−3.0 eV [30], and it is becoming the focus of research attention due to its unique electronic properties. In particular, various $WO_3$ nanostructures (nanoparticles, nanoplatelets, nanorods, and NWs) are of special interest as promising candidates for photocatalyst, electrochromic devices [31], and gas sensors [32] because of their high surface area and novel properties [14]. Zheng et al. $WO_3$ nanostructures in DSSCs used for the first time with the 1.46% PCE via $TiCl_4$-treatment [33] as an alternative photoelectrode materials in DSSC. They used commercial $WO_3$ nanoparticles with a size of approximately 40 nm as the photoelectrode in DSSC and investigated the effect of various parameters on the cell performance. DSSCs based on $WO_3$ nanoparticles exhibited a conversion efficiency of 0.75%, which was enhanced to 1.46% by the surface modification [33]. However, the problem is that the efficiency is relatively lower than that of DSSCs based on the other semiconducting metal oxides, such as $TiO_2$, $SnO_2$, and ZnO.

Yong et al. used the hydrothermal method for the $WO_3$ nanorod synthesis [34]. The $W_{18}O_{49}$ nanorods were synthesized by dissolving 8.1 g of tungsten hexachloride in 200 mL of ethanol. Next, 10 mL of starting solution was mixed with 60 mL of ethanol under mild magnetic stirring at RT. The final solution was transferred into a 100 mL Teflon-lined stainless steel autoclave, which was sealed and maintained at 200°C for 10 hours in a preheated electric oven and then allowed to cool to RT. The products were collected and washed repeatedly with deionized water and ethanol and then dried at 60°C for 12 hours. Fig. 10.8E exhibits the current density-voltage ($J-V$) characteristics of the fabricated DSSCs based on photoelectrodes made of $WO_3$ nanorods and nanoparticles. A DSSC based on $WO_3$ nanorods showed $J_{sc}$ of 4.66 mA $cm^{-2}$, $V_{oc}$ of 0.383 V, and FF of 0.422 yielded 0.75% PCE. Authors mentioned that the lower $J_{sc}$ and FF compared to conventional $TiO_2$ are mainly attributed to a low isoelectric point (ISP) of $WO_3$, which is pH = 0.4–1. In other words, the

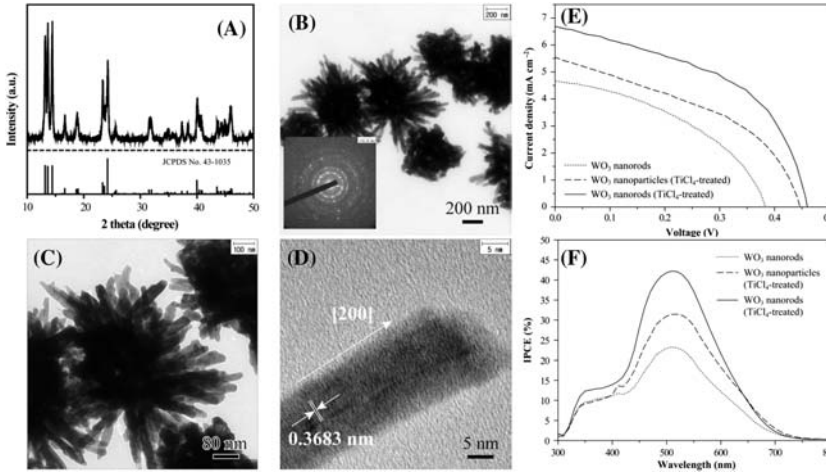


**Figure 10.8** (A) XRD pattern, (B) and (C) TEM, and (D) HR-TEM micrographs of the $WO_3$ nanorods obtained by the heat treatment of the $W_{18}O_{49}$ nanorods at 500°C for 30 min in air. Inset in (B) shows the electron diffraction pattern. (E) The current density–voltage ($J-V$) characteristics of the fabricated DSSCs based on photoelectrodes made of $WO_3$ nanorods (*dotted line*), $TiCl_4$-treated $WO_3$ nanorods (*straight line*), and $TiCl_4$-treated $WO_3$ nanoparticles (*dashed line*). The IPCE of the fabricated cells based on $WO_3$ nanorods (*dotted line*), $TiCl_4$-treated $WO_3$ nanorods (*straight line*), and $TiCl_4$-treated $WO_3$ nanoparticles (*dashed line*). *DSSCs*, Dye sensitized solar cells; *IPCE*, incident photon-to-electron conversion efficiency. *XRD*, X-ray diffraction; *TEM*, Transmission electron microscopy, *HR*, High-resolution. *Reproduced from S.-M. Yong, T. Nikolay, B. Tae Ahn, D.K. Kim, J. Alloys. Comp. 547 (2013) 113.*

$WO_3$ surface is negatively charged in the dye solution. Therefore, dye absorption on the $WO_3$ surface is poor because the anchoring ligand of the N719 dye is the negatively charged carboxylic group. The low dye loading results in the restriction of excited electron quantities and an increase of the dark current by the direct contact between the electrolyte and the $WO_3$ photoelectrode.

## 10.4 $TiO_2$ nanorod-based dye-sensitized solar cells

After the discovery of photoelectrochemical properties of nanostructured $TiO_2$, it is recognized as one of most promising wide-band gap semiconducting materials for photocatalysis, dye/quantum DSSCs (DSSC/QDSSC) and lithium ion batteries. The transportation of electrons through $TiO_2$ film and effective dye loading are the most important parameters in DSSCs. These two parameters depend upon the surface topography of the photoanode, surface area, and grain boundaries between two nanostructures and porosity of the photoanodes. Hence, the tailoring nanomorphology of photoanode is a key factor in the DSSCs application [2]. Titanium dioxide ($TiO_2$), also known as titanium (IV) oxide or titania, is a wide-band gap semiconducting material for multifunctional applications in areas such as solar cells, sensors, storage devices, self-cleaning coatings, photonic crystals, environmental remediation, water purification, cosmetics, and pigments.

Generally, $TiO_2$ has three crystalline polymorphs: anatase (tetragonal), rutile (tetragonal), and brookite (orthorhombic). The majority of authors have reported that the rutile $TiO_2$ has a direct band gap of 3.06 eV and an indirect band gap of 3.10 eV, while anatase $TiO_2$ has only an indirect band gap of 3.23 eV [35]. All three polymorphs contain more-or-less distorted ($TiO_6$) octahedra, however their linkage is different in the three polymorphic phases. In the bulk material, rutile is the most thermodynamically stable phase, while brookite and anatase are increasingly metastable and transform exothermally and irreversibly to rutile. Among these polymorphs of $TiO_2$, rutile phase is most important due to its excellent light-scattering efficiency, high refractive index, opacity, chemical inertness, and superb photocatalytic properties [36].

Different $TiO_2$ nanostructures have been synthesized by various methods, including template assistant approach, direct oxidation of Ti substrate, electrochemical anodization of titanium, metal–organic chemical vapor deposition, and hydrothermal synthesis. Until today, a variety of $TiO_2$

morphologies have been reported by hydrothermal route, which includes nanorods, nanoflowers, nanoparticles, nanostars, and so on. However, this tuning of the morphology was done by different experimental conditions and surfactant. The electron transportation through $TiO_2$ film and effective dye loading are the most important parameters in DSSCs. These two parameters depend upon the surface topography of the photoanode, surface area, grain boundaries between two nanostructures, and porosity of the photoanodes. Hence, tailoring nanomorphology of $TiO_2$ photoanode is a key factor in the DSSCs. It is well known that the nanoparticulate architecture also suffers from a large number of particles relative to particle grain boundaries, which hampers the fast flow of electrons and subsequently limits the efficiency. On the other hand, 1D nanostructures, such as rutile 1D $TiO_2$, provides fast electron flow through 1D crystal structure and low grain boundaries.

Hydrothermal technique is an important tool for advanced nanostructure material processing, covering the processing of electronics, catalysis, and ceramics. Kasuga et al. in 1998 introduced the hydrothermal method for $TiO_2$ [37]. This technique produces nano $TiO_2$ with homogeneity, high purity, crystal symmetry, metastable compounds with unique properties, and narrow particle size distributions. Many inorganic nanostructures, including $TiO_2$, have been fabricated via various ionic liquid (IL)-involved processes. However, to the best of our knowledge, few studies about the synthesis of rutile $TiO_2$ nanostructures have been reported in IL solutions [38–41]. Ding et al. successfully developed a route for the synthesis of high quality $TiO_2$ nanocrystals in IL via a microwave-assisted process. Initially, we have used bronsted acidic ionic liquid (BAIL) as a RT IL for hydrothermal technique and synthesized $TiO_2$ nanostructures. Initially we have synthesized 1D vertically aligned rutile $TiO_2$ nanorods (TNRs) by controlled hydrothermal method in an equal amount of $H_2O$: HCl (1:1 v/v). Briefly, titanium (IV) isopropoxide (0.5 mL) was added to equal volumes of distilled water and concentrated HCl. This method facilitates controlled nucleation growth with uniform nanoparticle size and well-crystallized structure due to the stable and low interfacial tension properties of the IL. Fig. 10.9A shows the $TiO_2$ nanoflowers with petals comprising a bunch of aligned nanorods, prepared in RTIL. It retains the rod-like array geometry but the nanorod diameter drastically decreased to ~62 nm Fig. 10.9B and C. Fig. 10.9A illustrates the mechanism for the aligned nanorods and nanoflowers formation. When the longer-chained 1:3-ethoxycarbonylethyl-1-methylimidazolium chloride [CMIM][$HSO_4$]

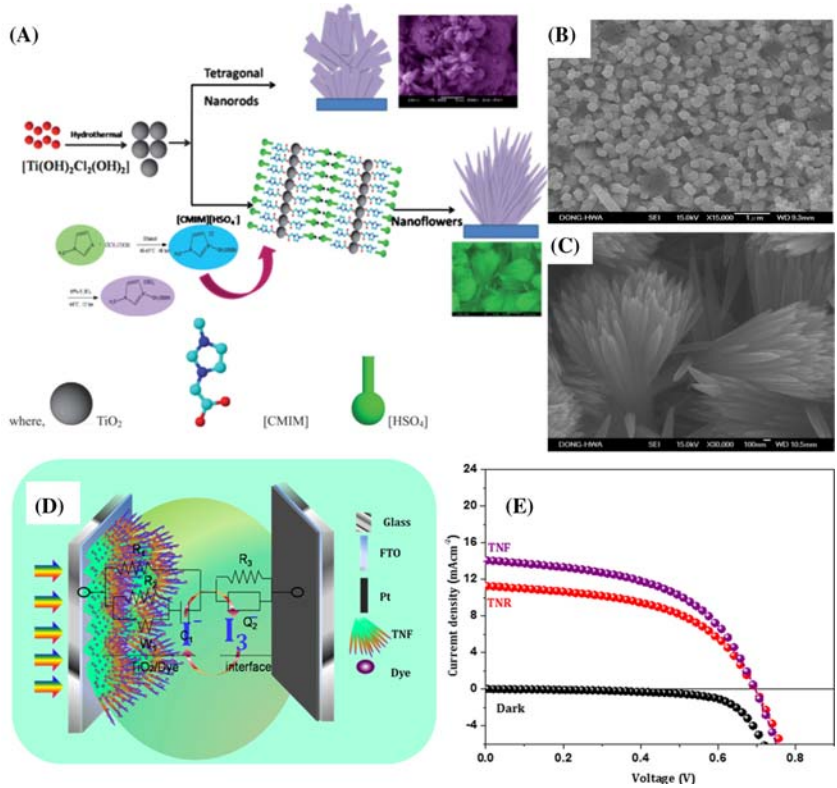


**Figure 10.9** (A) Schematic illustration for the growth process of the TNRs and TNFs (B) TNRs (without BAIL) and (C) nanoflowers (BAIL) (synthesized in Bronsted Acidic Ionic Liquid and schematic illustration for the growth process of the TNRs and $TiO_2$ nanoflowers (TNFs). FESEM images of TNRs and TNFs. (D) Schematic representation of fabricated DSSC device with its charge carrier dynamics (E) *J*–*V* curves of the DSSCs assembled respectively from TNR and TNF under simulated AM 1.5 G solar light (100 mW $cm^{-2}$). *DSSCs*, Dye sensitized solar cells; *TNR*, $TiO_2$ nanorod. *Reprinted with permission from (A and C) S.S. Mali, C.A. Betty, P.N. Bhosale, R.S. Devan, Y.R. Ma, S. S. Kolekar, et al., CrystEngComm 14 (2012) 1920. ©2012 Royal Society of Chemistry. (B and D) S.S. Mali, H.J. Kim, C.S. Shim, W.R. Bae, N.L. Tarwal, S.B. Sadale, et al., CrystEngComm 15 (2013) 5660. ©2014 Royal Society of Chemistry.*

RTIL is employed, nanoflowers comprising a bunch of aligned nanorods were obtained. The IL content in the precursor solution controlled formation of regular, titania-aligned nanorod arrays having ~62 nm size. This is due to the fact that a presence of 3-carboxymethyl-1-methylimidazoliurn bisulfate [CMIM][$HSO_4$] can effectively control the gathering of the nanoparticles and improve the dispersion in the reaction

system just like a surfactant. Because the RTIL can cap the surface of the nanocrystals, it provides a low agglomeration tendency, good dispersibility, and the potential to tailor the surface properties [42].

In the case of TNRs, it shows $J_{sc} = 11.24$ mA cm$^{-2}$, $V_{oc} = 0.699$ V, and FF = 0.62 results in 4.87% efficiency. While, the nanoflowers grown from RTIL [CMIM][$HSO_4$] resulted in a big enhancement of $J_{sc}$. The TNF sample shows $\eta$ of 6.63% ($J_{sc} = 13.15$ mA cm$^{-2}$, $V_{oc} = 0.699$ V, and FF = 0.67) (Fig. 10.9E). Therefore, TNF sample provides large surface area for dye adsorption, which results in increased efficiency. Further, $J_{sc}$ increased significantly because the size and width of nanoflowers are thinner, about ($\sim$61 nm), compared to the TNR ($\sim$250 nm) sample, denser and more aligned, which yielded more dye loading and faster electron diffusion.

For 3D $TiO_2$ nanostars with 1D TNR synthesis, we have varied precursor ration to 1:0.7 (v:v%) of $H_2O$:HCl solvent. The reaction time and temperature was kept similar to the TNR sample. Here we have controlled the hydrolysis rate of Ti species. These 3D $TiO_2$ nanostars (TNS) act as a scattering layer for DSSCs and that can be prepared by a single-step hydrothermal route (Fig. 10.10A). Compared to a nanorod based cell, the photovoltaic performance of the nanostars/nanorods $TiO_2$ cell exhibits excellent DSSCs performance, including superior light scattering, rapid electron transport, and lower electron recombination rate. The 3D/1D TNS/TNR based DSSCs cell exhibits 5.39% PCE (Fig. 10.10C), which is remarkably higher than that of the bare 1D nanorod based (3.74%) photoelectrode [43]. Further, we have developed the nanostructured bottle brushes with tetragonal nanorods of $\sim$75 nm diameter by changing the nature of the precursors and hydrothermal processing parameters. It is found that bottle brush provides effective large surface area 89.34 m$^2$ g$^{-1}$, which is much higher than TNRs' 63.70 m$^2$ g$^{-1}$. Such effective surface area can facilitate the effective light harvesting, and hence improve the dye adsorption and the photovoltaic performance of DSSCs, typically in short-circuit photocurrent and PCE (Fig. 10.10D). The optimized device shows a >6% PCE (Fig. 10.10F) [44].

Furthermore, we also have studied the effect of temperature from 100°C to 190°C and developed morphologies from nanoparticles to 3D dendritic hollow urchin like morphology using titanium butoxide (Ti($OC_4H_9$)$_4$) (TBT) precursor (Fig. 10.11A). The TBT was controlled hydrolyzed in hydrochloric acid and distilled water (1:1 v:v). The reaction temperature was varied from 100°C to 190°C while reaction time was

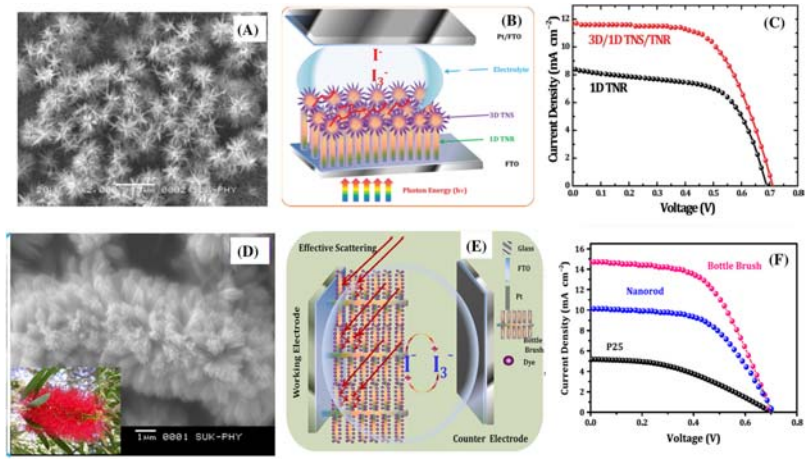


**Figure 10.10** FESEM images of synthesized 1D TNR and 3D/1D TNS/TNR deposited at 1:1 v:v and 1: 0.7 v:v of $H_2O$ and HCl, respectively; (B) and (D) show respective cross section images. *J–V* curves of the DSSCs assembled from 1D TNR and 3D/1D TNS/TNR samples under simulated AM1.5 solar light (100 mW $cm^{-2}$). The schematic representation of 3D/1D TNS/TNR nanoarchitecture based DSSCs device schematic representation of photocarrier dynamics of a $TiO_2$ nanorods and b $TiO_2$ bottle brush *J–V* curves of the DSSCs assembled from commercial P25 Degussa nanoparticles, $TiO_2$ nanorods, and $TiO_2$ bottle brush. *DSSCs*, Dye sensitized solar cells; *FESEM*, field emission scanning electron microscopy; *TNR*, $TiO_2$ nanorod. *Reprinted with permission from S.S. Mali, J.V. Patil, P.M. Kadam, H.P. Deshamukh, C.S. Shim, P.S. Patil, et al., J. Nanopart. Res. 16 (2014) 2406.*

kept constant and growth mechanism is studied systematically. The compact $TiO_2$ nanoparticles clusters are deposited on entire surface of the FTO substrate. The particle sizes of the deposited nanoparticles were found to be 25–35 nm, while tapered nanorods having 180 nm diameter was formed at 110°C. Interestingly, these large-size nanorods are made up from agglomeration of a number of small nanorods. Uniform distribution of vertically aligned nanorods covered throughout the substrate. The sample deposited at 160°C (i.e. Sample-$T_{160}$) shows novel nanoflower like morphology having bunch of aligned nanorods. The diameter of such flower is about 3 mm as shown Fig. 10.11A. However, $T_{170}$ sample shows well distributed $TiO_2$ nanoflowers over the substrate as shown in Fig. 10.11A. The image on right-hand side shows clearly these nanorods containing a bunch of aligned nanorods. The above process has been discussed by following reaction

$$2Ti + 6HCl \rightarrow 2TiCl_3 + 3H_2(g)$$

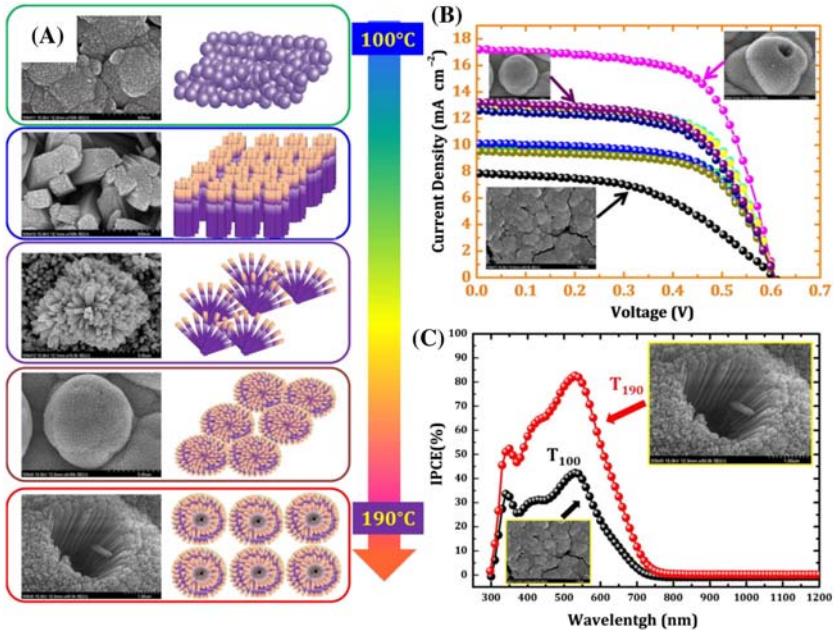


**Figure 10.11** SEM images of the nanostructured $TiO_2$ obtained at different temperatures from 100°C to 190°C. The figures at right show their corresponding possible growth mechanism (B) *J–V* curves of hydrothermally grown $TiO_2$ samples at different temperatures. (C) IPCE spectra of $T_{100}$ nanoparticulate and $T_{190}$ 3D dendritic hollow urchin samples. *IPCE*, Incident photon-to-current conversion efficiency. *Reprinted with permission from S.S. Mali, H.J. Kim, C.S. Shim, P.S. Patil, J.-H. Kim, C.K. Hong, Sci. Rep. 3 (2013) 3004.*

$$Ti^{3+} + 2H_2O \rightarrow TiOH^{2+} + H^+$$

$$TiOH^{2+} + 2O_2^- \rightarrow Ti(IV) - \text{oxospecies} + O_2^- \rightarrow TiO_2$$

This process is also known as "dissolve and grow process". Initially Ti species from TBT precursor start to react with $H^+$ ions from concentrated solution. It is well known that $Ti^{3+}$ species are not stable in an aqueous solution, therefore $TiOH^{2+}$ species are formed by hydrolysis of $Ti^{3+}$ species. According to the "dissolve and grow method," $TiOH^{2+}$ is oxidized to Ti(IV) by reaction with dissolved oxygen. The Ti(IV) complex ions are thus used as the growth units. The formation mechanism of the rutile $TiO_2$ NRs may be described as follows: For rutile $TiO_2$, a $TiO_6$ octahedron forms first by bonding of a Ti atom and six oxygen atoms. The $TiO_6$ octahedron then shares a pair of opposite edges with the next

octahedron, forming a chainlike structure. Because the growth rate of the different crystal faces depends on the numbers of corners and edges of the coordination polyhedra available, the growth of rutile NRs follows the sequence $(110) < (100) < (101) < (001)$. Thus, rutile $TiO_2$ NRs along [0 0 1] direction is formed. For nanoparticle $T_{100,}$ sample based DSSC device exhibited $J_{sc}$ of 7.85 mA $cm^{-2}$, $V_{oc}$ of 0.587 V, and FF of 48.2%, results in 2.34%. DSSC device based of $T_{110}$ sample shows $J_{sc} = 9.42$ mA $cm^{-2}$, $V_{oc} = 0.589$ V, FF = 54%, and $\eta = 2.99\%$. Sample $T_{120}$ shows 3.86% conversion efficiency with $J_{sc}$ of 9.53 mA $cm^{-2}$ and $V_{oc}$ of 0.599 $V_{oc}$. Interestingly, it was found that the current density (9.79 mA $cm^{-2}$), as well as efficiency (4.11%) of the $T_{130}$ sample, is larger than nanoparticulate clusters and compact nanorods pillars. This may be due to higher surface area beneficial for effective dye loading. The $T_{140}$ sample shows slightly higher 4.14% conversion efficiency. The $T_{150}$ sample shows $V_{oc} = 0.610$ V, $J_{sc} = 12.59$ mA $cm^{-2}$, FF = 61.1, and $\eta = 4.93\%$, while the 3D $TiO_2$ nanoflower sample shows drastic enhancement in PCE. These 3D nanoflowers (Sample-$T_{160}$) exhibit 5.16% PCE with $V_{oc}$ of 0.609 V, $J_{sc}$ of 13.22 mA $cm^{-2}$, and FF of 60.9%. This enhancement is due to effective light scattering among the 3D flowers. Further, $T_{170}$ sample shows slightly higher efficiency (5.32%). However, the 3D dendritic urchin samples ($T_{180}$ and $T_{190}$ hollow urchin) exhibit drastic enhancement in current density from 12.83 to 12.98 and 17.17 mA $cm^{-2}$, respectively. The PCE of the $T_{190}$ sample is 7.16% with $V_{oc} = 0.612$ V and FF = 64.7% (Fig. 10.11B). This morphology offers higher surface area and unique morphology that facilitates scattering of light and effective light harvesting. The enhancement in current density is also observed for IPCE analysis (Fig. 10.11C). This approach may pave the way to synthesize better and efficient $TiO_2$ electrodes for respective applications at low cost.

## 10.5 Conclusions and outlook

Various hierarchical nanostructures of n-type metal oxides have been successfully employed in DSSCs as photoanodes. These nanostructures facilitate a high surface area, low grain boundary and have light scattering ability. In this chapter, we discussed the low temperature process for the synthesis of 1D ZnO, $SnO_2$, $WO_3$, and $TiO_2$ nanostructured, which will be beneficial for the synthesis of flexible devices. The implementation of TRIL is another green approach to tune nanoflower morphology of $TiO_2$

with >7% PCE. These 3D dendrites and 3D dendritic hollow urchin containing bunch of aligned nanorod with 30 nm diameter show 5.32% and 7.16% conversion efficiency, respectively, which is much higher than clusters of nanoparticles as well as nanorods pillars. Moreover, these nanostructures are directly deposited on FTO substrate; therefore, they are free from tedious binder based process. The solution temperature, with or without surfactant, nature of the substrate surface, and reaction time are the key parameters for tuning the morphology. The 1D nanorods facilitate a low grain boundary and fast electron transportation; therefore, these nanostructures are useful for the various applications. Furthermore, these nanostructures could be useful as a promising electron transporting layer for recently started highly efficient perovskite solar cells. So far, a number of reports developed the various morphology of the metal oxides by changing their preparative parameters rigorously, but the fabrication of large area devices without hampering the device efficiency has certainly been increased in recent years. In view of the high efficiencies over a large area now reported from various groups, however, stability at more harsh conditions need to be monitored for upscaling this technology to meet the industrial manufacturing requirements.

## Acknowledgment

This work was supported by the Korea Research Fellowship Program through the National Research Foundation of Korea (NRF), funded by the Ministry of Science, ICT, and Future Planning (2016H1D3A1909289) for an outstanding overseas young researcher. This research was supported by the NRF grant funded by the Korea government (MSIT) (2018R1C1B6008218). This research work was also supported by the Priority Research Centre Program through the NRF, funded by the Ministry of Education, Science and Technology (NRF-2018R1A6A1A03024334).

## References

[1] A.Y. Hoekstra, T.O. Wiedmann, Science 344 (2014) 1114.
[2] B. O'Regan, M. Grätzel, Nature 353 (1991) 737.
[3] P.V. Kamat, J. Phys. Chem. C 112 (2008) 18737.
[4] V. Gonzaález-Pedro, X. Xu, I. Mora-Seroó, J. Bisquert, ACS Nano 4 (2010) 5783.
[5] M.A. Hossain, J.R. Jennings, C. Shen, J.H. Pan, Z.Y. Koh, N. Mathews, et al., J. Mater. Chem. 22 (2012) 16235.
[6] D. Chen, L. Cao, F. Huang, P. Imperia, Y.-B. Cheng, R.A. Caruso, J. Am. Chem. Soc. 132 (2010) 4438.
[7] J.-N. Nian, H. Teng, J. Phys. Chem. B 110 (2006) 4193.
[8] G. Melcarne, L.D. Marco, E. Carlino, F. Martina, M. Manca, R. Cingolani, et al., J. Mater. Chem. 20 (2010) 7248.

[9] R.-S. Chen, Y.-L. Liu, C.-H. Chan, Y.-S. Huang, Appl. Phys. Lett. 105 (2014) 153107.
[10] Z. Yang, B. Wang, H. Cui, H. An, Y. Pan, J. Zhai, J. Phys. Chem. C 119 (2015) 16905.
[11] L.M. Peter, J. Phys. Chem. C 111 (2007) 6601.
[12] S. Mathew, A. Yella, P. Gao, R. Humphry-Baker, B.F.E. Curchod, N. Ashari-Astani, et al., Nat. Chem. 6 (2014) 242.
[13] W. Zeng, Y. Cao, Y. Bai, Y. Wang, Y. Shi, M. Zhang, et al., Chem. Mater. 22 (2010) 1915.
[14] J.-H. Yum, E. Baranoff, F. Kessler, T. Moehl, S. Ahmad, T. Bessho, et al., Nat. Commun. 3 (2012) 631.
[15] H. Tang, K. Prasad, R. Sanjines, P.E. Schmid, F. Levy, J. Appl. Phys. 75 (1994) 2042.
[16] H.S. Bae, M.H. Yoon, J.H. Kim, S. Im, Appl. Phy. Lett. 83 (2003) 5313.
[17] U. Ozgur, Y.I. Alivov, C. Liu, A. Teke, M.A. Reshchikov, S. Dogan, et al., J. Appl. Phys. 98 (2005) 041301.
[18] M. Law, L.E. Greene, J.C. Johnson, R. Saykally, P.D. Yang, Nat. Mater. 4 (2005) 455.
[19] J.B. Baxter, E.S. Aydil, Sol. Energy Mat. Sol. C 90 (2006) 607.
[20] C.Y. Jiang, X.W. Sun, G.Q. Lo, D.L. Kwong, J.X. Wang, Appl. Phys. Lett. 90 (2007) 263501.
[21] R.C. Pawar, J.S. Shaikh, P.S. Shinde, P.S. Patil, Mater. Lett. 65 (2011) 2235.
[22] X. Sheng, Y. Zhao, J. Zhai, L. Jiang, D. Zhu, App Phys. A 87 (2007) 715.
[23] C.T. Wu, J.J. Wu, J. Mater. Chem. 21 (2010) 13605.
[24] W.T. Jiang, C.-Te Wu, Y.H. Sung, J.-J. Wu, ACS Appl. Mater. Interfaces 5 (2013) 911.
[25] P. Tiwana, P. Docampo, M.B. Johnston, H.J. Snaith, L.M. Herz, ACS Nano 5 (2011) 5158.
[26] X.C. Dou, D. Sabba, N. Mathews, L.H. Wong, Y.M. Lam, S. Mhaisalkar, Chem. Mater. 23 (2011) 3938.
[27] J. Huo, Y. Hu, H. Jiang, W. Huang, C. Li, J. Mater. Chem. A 2 (2014) 8266.
[28] G. Schlichthorl, N.G. Park, A.J. Frank, J. Phys. Chem. B 103 (1999) 782–791.
[29] S.S. Mali, C.S. Shim, H.J. Kim, M.C. Lee, S.D. Patil, P.S. Patil, et al., J. Nanopart. Res. 17 (2015) 496.
[30] F.G. Wang, C. Di Valentin, G. Pacchioni, ChemCatChem 4 (2012) 476.
[31] S.R. Bathe, P.S. Patil, Sol. Energy Mater. Sol. Cells 91 (2007) 1097.
[32] X.L. Li, T.J. Lou, X.M. Sun, Y.D. Li, Inorg. Chem. 43 (2004) 5442.
[33] H.D. Zheng, Y. Tachibana, K. Kalantar-zadeh, Langmuir 26 (2010) 19148.
[34] S.-M. Yong, T. Nikolay, B. Tae Ahn, D.K. Kim, J. Alloys Comp. 547 (2013) 113.
[35] A. Welte, C. Waldauf, C. Brabec, P. Wellmann, Thin Solid Films 516 (2008) 7256.
[36] I.C. Baek, M. Vithal, J.A. Chang, J.H. Yum, M.K. Nazeeruddin, M. Gratzel, et al., Electrochem. Commun. 11 (2009) 909.
[37] T. Kasuga, M. Hiramatsu, A. Hoson, T. Sekino, K. Niihara, Langmuir 14 (1998) 3160.
[38] N. Yu, L. Gong, H. Song, Y. Liu, D. Yin, J. Solid State Chem. 180 (2007) 799.
[39] H. Kaper, F. Endres, I. Djerdj, M. Antonietti, B.M. Smarsly, J. Maier, et al., Small 3 (2007) 1753.
[40] X. Jia, W. He, X. Zhang, H. Zhao, Z. Li, Y. Feng, Nanotechnology 18 (2007) 075602.
[41] S. Tian, H. Yang, M. Cui, R. Shi, H. Zhao, X. Wang, et al., Appl. Phys. A: Mater. Sci. Process 104 (2011) 149.

[42] S.S. Mali, C.A. Betty, P.N. Bhosale, R.S. Devan, Y.R. Ma, S.S. Kolekar, et al., CrystEngComm 14 (2012) 1920.
[43] S.S. Mali, H.J. Kim, C.S. Shim, W.R. Bae, N.L. Tarwal, S.B. Sadale, et al., CrystEngComm 15 (2013) 5660.
[44] S.S. Mali, J.V. Patil, P.M. Kadam, H.P. Deshamukh, C.S. Shim, P.S. Patil, et al., J. Nanopart. Res. 16 (2014) 2406.
[45] S.S. Mali, H.J. Kim, C.S. Shim, P.S. Patil, J.-H. Kim, C.K. Hong, Sci. Rep. 3 (2013) 3004.

## Further reading

Grätzel, 2005 M. Grätzel, Chem. Lett. 34 (2005) 8.

PART IV

# Others

This page intentionally left blank

# CHAPTER 11

# Quantum dots for solar cell applications

**El Hadji Mamour Sakho**[1,2] **and Oluwatobi S. Oluwafemi**[1,2]
[1]Department of Chemical Sciences (Formerly Applied Chemistry), University of Johannesburg, Johannesburg, South Africa
[2]Centre for Nanomaterials Science Research, University of Johannesburg, Johannesburg, South Africa

## Contents



## 11.1 Introduction

Fossil fuels, such as natural gas, oil, and coal are currently the world's primary energy sources. From the early days of the hunters and harvesters society to the current industrial society, the energy consumption per person per day has experienced an exponential growth. With rapidly growing global energy consumption, which is compensated by the use of these non-renewable energy sources, the world faces serious energy, environmental,

*Nanomaterials for Solar Cell Applications*
DOI: https://doi.org/10.1016/B978-0-12-813337-8.00011-4

and economic crises as a result of pollution, global warming, depleted stocks of fossil fuels, etc. [1–3]. In this sense, development of renewable, sustainable, and clean energy sources has become a matter/subject of urgency. Solar energy is sustainable, clean, and particularly abundant as the most promising energy source for humanity's future. Many technologies have been exploited to convert a solar photon into electricity, heat, fuel gas, and biomass for practical use [4–7]. Among these, solar cells (SC) are photovoltaic devices that directly convert a solar photon into electricity via the photoelectric effect (e.g., silicon/thin film SCs) or photochemical effect [e.g., dye-/quantum dot (QD)-sensitized SCs (DSSC/QDSSCs)]. Despite its great promise, the cost and efficiency of current photovoltaic cells (PVs) present great challenges to implement solar energy on a larger scale [8,9]. Therefore, designing low-cost and effective systems that can effectively gather, transfer, or store solar energy has become one of the most striking problems of the humankind. After over 30 years of slow development, the contribution of solar energy, including photovoltaic electricity, to global energy consumption is still marginal [10].

Nowadays, development of new and efficient PVs with substantially increased power conversion efficiency (PCE) is critical for converting sunlight energy from a promising clean renewable energy to a competitive primary energy source. Among the third generation of SCs, QDSSCs, developed during the last two years are promising for fulfilling this task. QDSSCs have the potential of theoretical PCE that surpassing Shockley–Queisser limit of 44% due to the possibility of extraction of hot electrons and multiple exciton generations (MEGs). Due to unique properties of QDs which include wide tunability of band gaps, easy solution processability, and impressive capability of generating multiple excitons and slowing down the cooling of hot electrons, QDSSCs have attracted tremendous research interest and have been considered as the most promising candidate for the next generation of photovoltaic devices. Until now, a maximum PCE of 13% has been reported for optimized DSSCs. Nevertheless, the high cost and fussy synthesis procedures of organic dyes along with limited PCE restrict the commercialization of dye sensitized SCs (DSSC). Thus, SC devices using QDs as sensitizers to substitute organic dyes are considered as promising alternatives to DSSCs. With QDs as a sensitizer, it is possible to realize the light absorption in the whole solar spectrum region by harvesting the underutilized ultraviolet and currently unutilized infrared (IR) by means of combining several types of QDs. Moreover, a direct bandgap semiconductor offers a stronger absorption

coefficient and QDs can generate multiple electron–hole pairs from a single incident photon absorption that lead to the maximum theoretical conversion efficiency up to 44%. Thus, QDSSCs have been considered as promising candidates among the third-generation SCs, and thus the number of relevant research articles is increasing rapidly year by year [10–17].

This chapter summarizes the development in QDSSCs over the recent years and it is divided into seven sections. In the first part, the general theoretical background of SCs is discussed, including quantum confinement, MEGs, and molar extinction coefficient. The second section gives an introduction on the operational principle of QDSSCs. In the third section, photoanodes in QDSSCs are addressed including semiconductor QDs as charges generator, graphene QDs as a new emerging material for QDSSCs and variety of deposition techniques. This is followed by a discussion on the electrolytes in QDSSCs. In the fifth section, counter electrodes (CEs) in QDSSCs are discussed. The sixth section covers the different electrical analysis performed in QDSSCs, such as current–voltage (IV) measurements and electrochemical impedance spectroscopy. The final section contains a brief summary of the discussed topics, the future outlook, and future perspectives of QDSSCs.

## 11.2 Theoretical background

### 11.2.1 Quantum confinement effect

One of the most popular terms in the nanoworld is quantum confinement effect, which is essentially due to the changes in the atomic structure as a result of the direct influence of the ultra-small length scale on the energy band structure [18–20]. Semiconductor QDs exhibit unique optical properties due to the combination of their band-gap energy and quantum-well phenomena. The most interesting property in QDs is the massive change in the optical properties as a function of size. The dots of a few nanometers behave similarly to three-dimensional (3-D) quantum wells. Electrons generated in the QD by absorption of a photon are confined in an infinite potential well. QDs have a discrete density of states with band gap inversely related to the size of the QD, as shown in Fig. 11.1. When the size is reduced, the electronic excitation is blue-shifted and the oscillator strength is concentrated into just a few of transitions [21,22]. The basic physical phenomena of quantum confinement is due to the change in the density electronic state and can be explained by considering the relationship between position and momentum in free and confined particles.

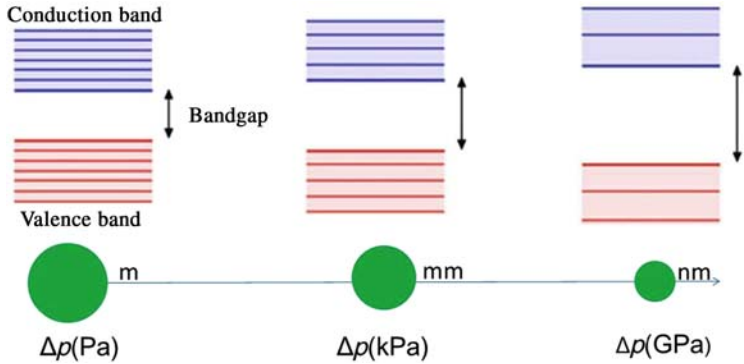


**Figure 11.1** The relationship between the band gap and the particle size explained through the Young–Laplace law in the classical mechanics.

For a free particle or a particle in the periodic potential of an extended solid, the crystal momentum and the energy can be both precisely defined, whereas the position cannot. For a localized particle, the energy may still be well defined, but the uncertainly in position decreases, so the momentum is no longer uncertain. The discrete energy functions of the particle can be viewed as a superposition of bulk momentum state. Given the relation between momentum and energy in the bulk solid, one can see how a series of nearby transitions occurring at slightly different energies in the bulk will be compressed by quantum confinement into a single, intense transition in the QD [23].

In quantum mechanics, a proper approach to the behavior of an exciton is the 3-D model of a particle in a box because the behavior of a particle is fundamentally described by the wavefunction $\Psi$ which is the solution of the time-independent Schrodinger equation. For a 3-D box, the wavefunctions and energies are given by the following equations.

$$\Psi_{n_x,n_y,n_z} = \sqrt{\frac{8}{L_x L_y L_z}} \sin\left(\frac{n_x \pi x}{L_x}\right) \sin\left(\frac{n_y \pi y}{L_y}\right) \sin\left(\frac{n_z \pi z}{L_z}\right) \tag{11.1}$$

$$E_{n_x,n_y,n_z} = \frac{h^2 \pi^2}{2m} \left[ \left(\frac{n_x}{L_x}\right)^2 + \left(\frac{n_y}{L_Y}\right)^2 + \left(\frac{n_z}{L_z}\right)^2 \right] \tag{11.2}$$

where the 3-D wavevector is

$$k_{n_x,n_y,n_z} = k_{n_x x} + k_{n_y y} + k_{n_z z} = \frac{n_x \pi}{L_x} x + \frac{n_y \pi}{L_y} y + \frac{n_z \pi}{L_z} \tag{11.3}$$

where $L$ is the length of the box and $x$, for example, denotes a unit vector along the $x$ direction. If an exciton is a spherical particle, the relationship between energy and radius of a particle is given by

$$E^{e,h} \propto \frac{1}{R^2} \tag{11.4}$$

On the other hand, the relation between the band gap and the particle size can also be explained by the classical Laplace–Young equation, namely

$$\Delta p = 2\gamma H = \gamma\left(\frac{1}{R_1} + \frac{1}{R_2}\right) = \frac{2\gamma}{R} \propto \frac{1}{R} \quad \text{when } R_1 = R_2 = R \tag{11.5}$$

where $\Delta p$ is the pressure difference across the fluid interface, $\gamma$ is the surface tension, $H$ is the mean curvature, and $R_1$ and $R_2$ are the two principal radii of curvature. At the nanoscale, the increase in pressure creates strong forces toward the interior of the particle that is responsible for the changes in interatomic interactions and the band gap [24,25], as schematically represented in Fig. 11.1. Therefore, panchromatically-light-absorbing QDSSCs can be designed by dealing with the band gap engineering of the quantum-dots.

### 11.2.2 Multiple exciton generations

MEG in quantum confined semiconductors involves the generation of multiple bound charge-carrier pairs per single high-energy photon (Fig. 11.2). MEG effects have been highlighted as particularly beneficial for SCs where they have the potential to enhance the energy conversion efficiency of QDSSCs significantly. The energy gap between electron states is too small to be ignored because the bulk semiconductor has many atoms in total volume. Thus, upon absorption in bulk semiconductors, solar photons with energy greater than the material band gap ($E_g$) generate excited charge-carrier pairs that are rapidly relaxed with low phonon energy and kinetic energy equal to $h\nu - E_g$. When the semiconductor material absorbs photon energy that is higher than its band gap, the photon energy in excess of the band gap is lost as heat through phonon emission following electron–phonon scattering (Fig. 11.3) [26–30]. The higher threshold photon energy is required for impact ionization (I.I.), the process in a material by which one energetic charge carrier can lose energy by the creation of other charge carriers because of crystal

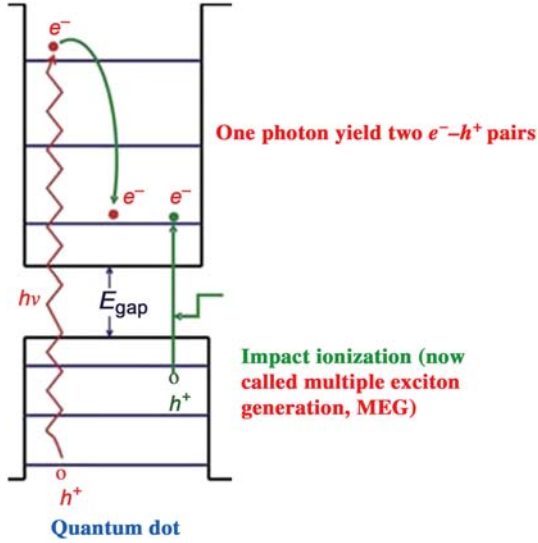


**Figure 11.2** Multiple electron–hole pair (exciton) generation (MEG) in quantum dots. *MEG*, Multiple exciton generation.

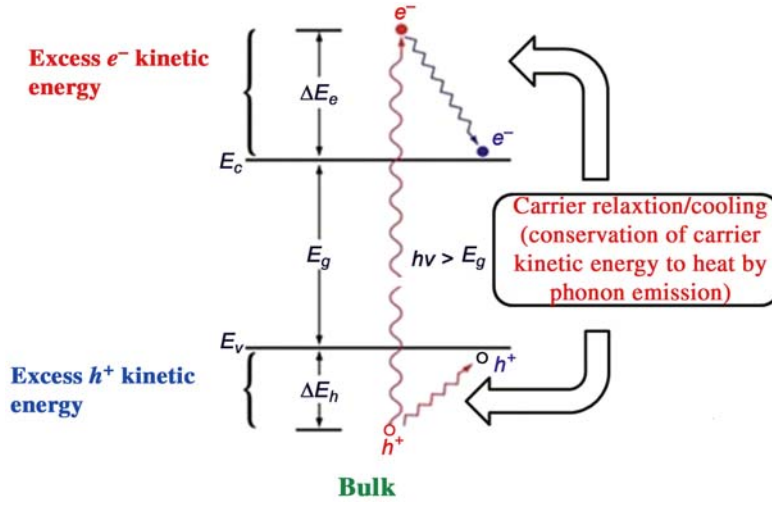


**Figure 11.3** Hot carrier relaxation/cooling in bulk semiconductors.

momentum ($k$) has to be conserved. This results in a low maximum quantum yield (QY) [31,32].

On the other hand, for SCs based on Si, CdTe, $CuIn_xGa_{1-x}Se_2$, or III–V semiconductors, I.I. cannot contribute to the improvement of QYs

because the maximum QY for I.I. does not exceed 1.0 until photon energies reach the ultraviolet region of the spectrum. In bulk semiconductors, the threshold photon energy for I.I. exceeds that required for energy conservation alone because, in addition to conserving energy, crystal momentum ($k$) must also be conserved. Moreover, the rate of I.I. must compete with the rate of energy relaxation by phonon emission through electron–phonon scattering. It has been demonstrated that the rate of I.I. becomes competitive with phonon scattering rates only when the kinetic energy of the electron is many times the band gap energy ($E_g$). The observed transition between efficient and inefficient I.I. occurs slowly; for example, in Si, the I.I. efficiency was found to be only 5% (i.e., total QY = 105%) at $h\upsilon \approx 4$ eV ($3.6E_g$), and 25% at $h\upsilon \approx 4.8$ eV ($4.4E_g$) [33]. This large blue shift of the threshold photon energy for I.I. in semiconductors prevents materials, such as bulk Si and GaAs, from yielding improved solar conversion efficiencies [34].

Nevertheless, for QDs, the rate of electron relaxation through electron–phonon interactions can be considerably reduced due to the discrete character of the $e^- - h^+$ spectra, and the rate of Auger processes, including the inverse Auger process of exciton multiplication, which is greatly enhanced due to carrier confinement and the concomitantly increased $e^- - h^+$ coulombic interaction. Furthermore, crystal momentum need not be conserved because momentum is not a good quantum number for 3-D confined carriers (from the Heisenberg Uncertainty Principle, the well-defined location of the electrons and holes in the nanocrystal makes the momentum uncertain). The concept of enhanced MEG in QDs is indicated in Fig. 11.2. Indeed, very efficient multiple $e^{2-} - h^+$ pair (multi exciton) creation by one photon has now been reported in six semiconductor QD materials: PbSe, PbS, PbTe, CdSe, InAs, and Si [30].

Moreover, quantum-dots have 100–10,000 atoms in total volume. It was demonstrated that the energy separation between quantized levels in QDs might be many times higher than the phonon energy. During the relaxation process, several phonons should be emitted via electron–phonon scattering to meet the energy conservation, which accompanies multiparticle scattering events. As a result, the rate of excited electron relaxation can be retarded by the existence of discrete quantized energy levels. The slowed relaxation of hot excitons via phonon emission allows other channels for relaxation, such as MEG, to become competitive and even dominant in QDs. Furthermore, the crystal momentum need not be conserved because the momentum is not a good quantum number for 3-D confined carriers

(from the Heisenberg Uncertainty Principle, the well-defined location of the electrons and holes in the nanocrystal makes the momentum uncertain). This shows that the maximum QY is very high due to the lower threshold photon energy.

In bulk semiconductors, the threshold photon energy for I.I. exceeds that required for energy conservation alone because, in addition to conserving energy, crystal momentum ($k$) must also be conserved [32].

For various QDs, the difference in carrier multiplication (CM) can be explained easily by using effective masses in simple bulk semiconductors without bringing up an exact structure of quantized states in these materials [35]. If one assumes that the energy required for an additional exciton is given by either the electron or the hole of an original exciton, then the CM threshold ($\hbar\omega_{CM}$) can be determined from the relation $\Delta E_{e(h)} = E_g$, where $\Delta E_{e(h)}$ is the energy of the electron (hole) excited by the photon in excess of the energy gap. This condition yields the following equation:

$$\hbar\omega_{CM} = \left(2 + \frac{m_e}{m_h}\right) E_g \tag{11.6}$$

### 11.2.3 Molar extinction coefficient

The molar extinction coefficient, also known as the molar absorptivity, is a measure of how well a chemical species absorbs a given wavelength of light. It helps to make comparisons about the probability of electronic transition between levels for different compounds without taking into account differences in concentration or solution length during measurements. The concept of the molar extinction coefficient is useful in analyzing optical data of QDs. The ratio of radiant power transmitted ($I$) by a sample to the radiant power incident ($I_o$) on the sample is called the transmittance $T$:

$$T = \frac{I}{I_o} \tag{11.7}$$

On the other hand, the absorbance ($A$) is defined by

$$A = -\log T = \log\left(\frac{1}{T}\right) \tag{11.8}$$

The transmittance and absorbance depend on the molar concentration ($c$), the light path length in centimeters ($L$), and the molar absorptivity ($\varepsilon$) for the dissolved substance [36].

$$T = 10^{-\varepsilon d} \text{ or } A_\lambda = \varepsilon d \tag{11.9}$$

Beer's Law states that, for a given substance dissolved in a given solute and measured at a given wavelength, the absorbance is proportional to the concentration and that the molar extinction coefficient is constant [37]. Since transmittance and absorbance are unitless, the units for molar absorptivity must cancel out the units measure in concentration and light path. Accordingly, the unit for molar absorptivity has $L^{-1}\,cm^{-1}$ or $M^{-1}\,cm^{-1}$. Most laboratory spectrophotometers are fitted for use with 1 cm width cuvettes. Thus, molar absorptivity is expressed as

$$A_\lambda = \varepsilon c L = \varepsilon c \quad \text{when } L = 1 \text{ cm} \tag{11.10}$$

### 11.2.4 The operational principle of quantum dot-sensitized solar cells

A classical architecture of DSSCs consists of three components: a dye-sensitized photoanode (working electrode), a CE and a salt electrolyte [37]. Photoanode is made by deposting a mesoporous wide-band gap semiconductor layer ($TiO_2$, $Nb_2O_5$, ZnO, $SnO_2$) with an optimal thickness of c. 10 mm and a porosity of 50%–60% on the conducting glass [38–42]. A monolayer of charge transfer dye is then adsorbed onto the surface of the mesoporous wide-band gap semiconductor nanostructures, leading to photon absorption and electron injection. This photoanode section is in contact with a redox salt electrolyte or hole conductor. The DSSCs' device is completed by coupling with a CE (cathode), as shown in Fig. 11.4. The evolution of DSSCs to QDSSCs does not take a big leap. The only physical difference between the DSSCs and QDSSCs is

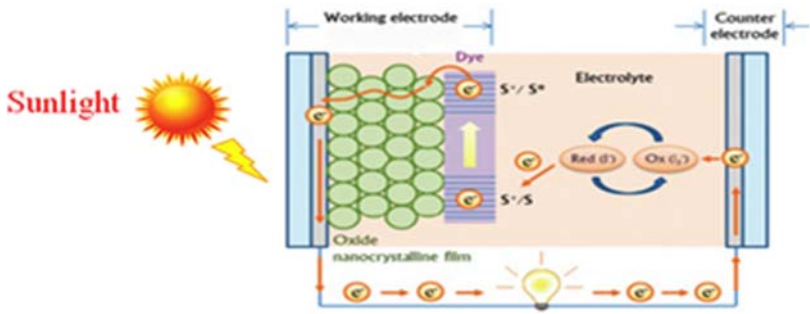


**Figure 11.4** Schematic representation of DSSCs. *DSSC*, Dye-sensitized solar cell.

the sensitizing materials. In the QDSSCs, the dye is replaced by the QDs [43–45]. The mesoporous wide bang semiconductor ($TiO_2$, $Nb_2O_5$, ZnO, $SnO_2$) is coated with these QDs using in situ fabrication or colloidal QDs. Charge carriers are created in the QDs as electron migrate from the valence band to the conduction band (CB) of QDs and injected into that mesoporous wide bang semiconductor upon illumination, leading to the oxidation of the photosensitizer. A general structure of a QDSSCs and its operation is shown in Fig. 11.5 The original state of the sensitizing material is regenerated through electron donation from the electrolyte, which is usually a redox system. For DSSCs, polyiodide ($I^-/I_3^-$) redox couples have been considered as one of the most effective and efficient electrolytes, however, it is not chemically compatible with QD-sensitizers in QDSSCs (mainly in the case of cadmium chalcogenides). Therefore, for stabilizing QDs over electrolytes, polysulfide ($S^{2-}/S_x^{2-}$) redox couples are generally used because polysulfide ($S^{2-}/S_x^{2-}$) redox couple is able to mediate the carrier for QDDSCs efficiently [46–48].

The oxidation that occurs at the photoanode-electrolyte interface can be explained as fellows: [23,49].

$$S^{2-} + 2h^+ \rightarrow S \tag{11.11}$$

$$S + s_{x-1}^{2-} \rightarrow s_x^{2-} (x = 2 - 5) \tag{11.12}$$

After oxidation, a regeneration process occurs on the CE, during which the oxidized groups $S_x^{2-}$ are re-reduced to $S^{2-}$. Hence, electrons migrate via the external load to complete the circuit [50,51].

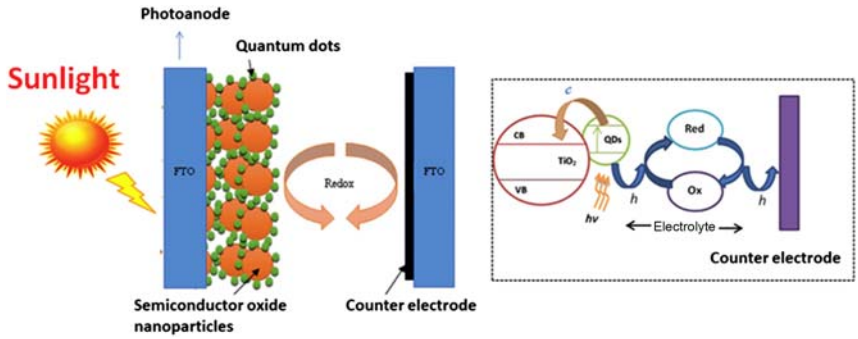


**Figure 11.5** Schematic representation of QDSSCs. *QDSSC*, QD-sensitized solar cell.

$$S_x^{2-} + 2e^- \rightarrow S_{x-1}^{2-} + S^{2-} \tag{11.13}$$

The external load is connected to the cell to complete the circuit through electron migration. When the cell is irradiated with sunlight, the potential difference between the photo-electrode (due to the Fermi level of the electrons) and electrolyte (due to the redox potential) produces a voltage across the load, and the solar energy conversion efficiency ($\eta$) of the cells is obtained as follows [52,53].

$$\eta = \frac{J_m V_m}{P} \tag{11.14}$$

where $P$ is the power density at the operating point, and $J_m$ and $V_m$ represent current density and voltage, respectively, at the actual maximum power.

## 11.3 Photoanode in quantum dot-sensitized solar cells

### 11.3.1 Quantum dot materials

With an aim to enhance the photovoltaic performances of QDSSCs, many researchers have focused their attention on materials selection and materials engineering. Thus, QDs as an essential part in QDSSCs should possess appropriate band-gap and high absorption coefficient energy to maximize the harvesting efficiency of the incident light [44,54,55]. The energy level of QDs employed in QDSSCs must match that of wide band-gap semiconductors. If the band-gap energy of the QDs is high, although a large open circuit voltage ($V_{oc}$) can be achieved, the wavelength range of light absorption will be narrowed concurrently. Contrarily, low band-gap energy of QDs may contribute to a wide wavelength region of light absorption but inevitably may lead to a low $V_{oc}$ [54]. Accordingly, enormous literature studies have reported the availability of different QDs with an appropriate band gap as light harvesters in QDSSCs that include CdSe [56–59], CdTe [60,61], CdS [62,63], ZnSe [64,65], $Ag_2Se$ [66], $Ag_2S$ [67,68], InAs [69,70], InP [71], $In_2O_3$ [72], PbS [73,74], $CuInS_2$ [75–78], $AgInS_2$ [79,80], $Bi_2S_3$ [81], $Cu_2ZnSnS_4$ [82,83], ZnCdSSe [84], Si [85], graphene [86,87], and so on.

Among various QDs, Cd chalcogenide (CdX, = S, Se or Te) QDs are preferred due to their relatively high stability in QDSSCs even though they may degrade upon visible illumination [88]. However, other kinds of QDs with narrow band gaps, such as PbS [73], PbSe [89], $Ag_2S$ [68], and

InAs [70], have also been considered because of their abilities to widen the light absorption into the IR region. Moreover, cosensitization of two or three types of QDs, for example, CdS/CdSe [90,91], CdS/CdTe [92], CdSe/CdTe [93], CdS/PbS [94], CdS/CdSe/PbS [58], $CuInS_2$/ZnS [95], $CuInS_2/In_2S_3$ [96], etc., is well accepted due to the complementary effect of extending the wavelength range of light harvesting, and/or facilitating the electron transfer process. More significantly, the design of alloy materials, which include $CdSe_xS_{1-x}$ [97], $CdSe_xTe_{1-x}$ [98–102], $CuInSe_xS_{2-x}$ [103], and Zn–Cu–In–Se [104], has recently attracted considerable attention since it is feasible to engineer the physical characteristics (e.g., band gaps, energy band positions and photoelectrical properties) of QDs by controlling the compositional ratio between each chalcogenide and metal element. For example, Zn–Cu–In–Se QDs with an absorption onset extending to $\approx$1000 nm were successfully fabricated for high-efficiency QDSCs with a champion PCE of 11.91% and a certified PCE of 11.61% [104]. The remarkably photovoltaic performance was supposed to be associated with the high loading capacity of QDs, broad light harvesting range stretching to near-IR (NIR) light and reduced charge recombination rate, and fast electron extraction from the special alloyed structure of Zn–Cu–In–Se QDs. To boost light harvesting, cosensitized photoanodes were fabricated by a sequential deposition of presynthesized Zn–Cu–In–Se and CdSe QDs on mesoporous $TiO_2$ films for high-efficiency QDSCs with PCE over 12%. Cosensitized cells were developed by introducing different sizes of CdSe QDs into Zn–Cu–In–Se based QDSSCs system. By the selective interaction between the QDs and the specific functional group contained in the bifunctional ligands, the mercaptopropionic acid (MPA)-modified QDs were anchored on $TiO_2$ with the desired remaining functional group, through which the loading capacity of ligand-modified QDs on $TiO_2$ was effectively tuned. Both Zn–Cu–In–Se and CdSe QDs were uniformly distributed throughout the $TiO_2$ film. Benefiting from the high extinction coefficient of CdSe and the wide light absorption of Zn–Cu–In–Se in visible light, the constructed Zn–Cu–In–Se/CdSe cosensitized cells exhibit a broad photocurrent response extending to the NIR region of $\approx$1100 nm and a high incident PCE (IPCE) value over 80% in the range from 400 to 600 nm [104]. On the basis of "simultaneous nucleation and growth" approach, Cu – In – Ga – Se QDs with light harvesting range of about 1000 nm were synthesized and used as a photosensitizer to construct QDSSCs with a champion efficiency of 11.49% [105].

### 11.3.2 Graphene quantum dots in quantum dot-sensitized solar cells

Graphene QDs (GQD), as defined, are a kind of zero dimension (0-D) carbon-nanomaterial with characteristics derived from both graphene and carbon dots (CDs), which can be regarded as incredibly small pieces of graphene [106–110]. By converting two-dimensional graphene sheets into 0-D GQDs, the GQDs exhibit new phenomena due to quantum confinement and edge effects, which are similar to CDs. Compared to conventional semiconductor QDs and organic dyes, GQDs are superior in terms of their unique properties, such as good biocompatibility, low toxicity, good chemical inertness, and high photostability against photobleaching and blinking [105,110]. Unlike, conventional 0-D materials, CDs, GQDs clearly hold a graphene structure inside the dots, regardless of the dot size, which endows them with some of the unusual properties of graphene. Moreover, GQDs have a size dependent band gap and large optical absorptivity, making them particularly interesting building blocks for solar energy conversion [111]. For these reasons, GQDs have gained tremendous attention in QDSSCs applications [112].

Owing to their attractive optoelectronic properties and solution processibility, GQDs are more promising for low-cost and high PCE QDSSCs. GQDs diverse roles include hole/electron transport agents and active layer additive in the donor/acceptor blends and sensitizers [113,114]. Zhong et al. reported the first successful modification of CdSe QDSSCs with GQDs [115]. The QDSSCs device was constructed by assembling CdSe-GQDs sensitized photonoanode and $Cu_2S$/brass CE with a blind clip separated by a scotch spacer. Polysulfide was used as the electrolytes and for the QDSSCs device. They reported that the optimized photovoltage ($V_{oc}$) of the CdSe-GQDs QDSSCs was higher than that of plain CdSe QDSSCs, consequently improving the photovoltaic performance of the resulting QDSSCs. Here, GQDs serve as a novel surface coating layer that can reduce electron–hole recombination occurring at the QDs/electrolytes interface. Tavakoli et al., through a solution-based hot injection approach, synthesized monodisperse PbS/GQDs nanocomposites as active layers of QDSSCs with an efficiency of 3.6%, which could be further improved to 4.1% by Cd doping [116]. They defined the hot-injection synthesis of the colloidal nanostructure as quasi core/shell PbS/graphene QDs because of their incomplete passivation of PbS surfaces with an ultrathin layer of graphene. Dutta et al. reported a

combination GQDs with ZnO nanowire (NW) as a potential candidate in solid-state SCs with $V_{oc}$ of 0.8 V. The ZnO NWs-GQDs composites were formed by infiltrating ZnO NWs with GQDs synthesized by the hydrazine reduction of GO cells [111].

### 11.3.3 Deposition techniques of quantum dots sensitizing layer

QD sensitizers are deposited on semiconductor coated electrode either by in situ or ex situ methods [117]. The in situ methods are simple, low-cost techniques and suitable for large-scale production. However, they do not provide precise control of the particle size distribution of the QDs. In addition, the in situ methods mainly include chemical bath deposition (CBD), successive ionic layer adsorption and reaction (SILAR), and electrochemical deposition (ED) and are commonly used for QDs preparations. They also perform better than the ex situ methods when used to assemble QDSSCs. In the ex situ methods, QDs are prepared separately and further deposited into the semiconductor coated electrode. The commonly used ex situ techniques for QD deposition in QDSSCs are electrophoretic deposition (EPD), molecular linker attachment, and direct adsorption (DA).

#### *11.3.3.1 Chemical bath deposition*

CBD has been used to deposit QD films onto wide-band gap semiconductors. It has been considered as a simple and cost-effective approach to grow QDs directly onto nanostructured photoanodes (usually a metal oxide) by immersing photoactive electrodes into a solution containing the cationic (e.g., Cd and Zn) and anionic (S and Se) precursors for the slow precipitation of the desired QDs [118,119]. Cationic and anionic solutions are prepared and separately placed in a container to form bath solution for slow reaction. QDs are grown on the wide-band gap semiconductor coated electrode by dipping the electrode into the bath solution for a specified period (Fig. 11.6A). Thus, QDs deposition is controlled by varying dipping time, precursor solution composition, and reaction temperature. CBD facilitates the dense deposition of QDs on a wide-band gap semiconductor layer and enhances the recombination resistance. This method also has many advantages, such as stable yield, robust adherence, and uniform and good reproducibility. However, QD deposition by CBD sometimes does not result in nanoparticles deposition, but results in nanocrystalline film pattern that blocks the narrow

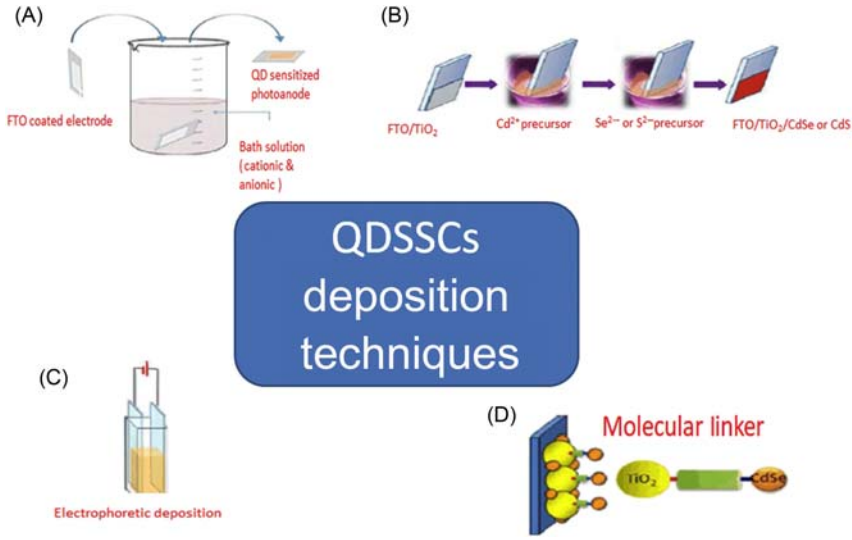


**Figure 11.6** Schematic illustration of the preparation of photoanode in QDs, (A) chemical bath deposition, (B) successive ionic layer adsorption and reaction, (C) electrophoretic deposition, and (D) molecular linker attachment. *QD*, Quantum dot.

pore channel if the pore size is in order of 5−7 nm. Therefore, CBD is suitable for nano-structured electrodes that offer large porosity of a wide-band gap semiconductor layer, for example nanorod, nanotubes, or 3-D hierarchical structures.

As CBD is a time-consuming process and suffers from above-discussed shortcomings, various research groups further modified CBD technique for fabrication of efficient and stable QDSSCs that has been used in the controlled sequential manner for sensitization of CdS over ZnO electrode. In this technique, microwave assisted CBD (MACBD) has been utilized for rapid nucleation and growth of QDs on $TiO_2$-deposited electrode. A CdS/CdSe cosensitized $TiO_2$ photo-anode has been fabricated through MACBD, which allowed direct and rapid deposition of QDs on $TiO_2$ thin film. It assisted in suppressing the surface defects of the QDs as well as form a good contact between QDs and the $TiO_2$ film, therefore, high $J_{sc}$ (16.1 mA $cm^{-2}$) and PCE (3.06%) were observed [122]. Microwaves assist in quick and homogenous heating of the aqueous solution that leads to faster nucleation and growth of the QDs. Thus, the deposition time is optimized. Microwave irradiation reduces the recombination of injected electrons from the $TiO_2$ to the hole present in the electrolyte because of the densely covered QDs layer as compared to the conventional CBD

process. MACBD also enhances the wettability of the $TiO_2$ surface that results in good contact between the QDs and $TiO_2$ layer. In a new development, electric field assisted CBD has been used for PbS QDs deposition on $TiO_2$ nanotube arrays (NTA). In the study, CBD was controlled by a low electric field, which assisted in increasing QDs loading in $TiO_2$ NTA resulting in high $J_{sc}$ (8.48 mA $cm^{-2}$) and PCE (3.41%) [123]. Choi et al. optimized the CBD precursor concentration ratio for deposition of CdSe QDs [124]. They found that the formation of an amorphous $SeO_2$ layer on the CdSe QDs significantly depends on the Cd:Se precursor ratio and this $SeO_2$ layer plays a critical role in the conversion efficiency of the assembled SCs.

#### *11.3.3.2 Successive ionic layer adsorption and reaction*

SILAR technique is an extension of the CBD method. In SILAR, cationic and anionic precursor solutions are prepared separately and placed in two different containers. Semiconductor coated electrode is first dipped into the cationic precursor solution followed by rinsing and drying. Then, it is dipped into the anionic precursor, again followed by rinsing and drying. The whole process of sequential dipping (of the semiconductor coated electrode into cationic and anionic precursor solution each time followed by rinsing and drying) is referred as one SILAR cycle (Fig. 11.6B). The desired QDs growth depends upon the number of SILAR cycles, the rate of dipping, dipping time, reaction temperature, and concentration of precursor solutions. Compared to CBD, SILAR has less processing time and maintains close stoichiometry formation. However, QDs fabricated using SILAR face challenges as the method does not allow for a precise control of the QDs' particle sizes. The major problem is that the rate of recombination is quite high in the case of the SILAR deposited sample [125]. Recently, a new type of SILAR, named as Potential Induced Ionic Layer Adsorption and Reaction (PILAR), has been reported for the in situ synthesis and assembling of CdSe QDs into the mesoporous $TiO_2$ film. This enhanced the ion adsorption and assisted in high QD loading on the semiconductor coated electrode. In the PILAR process, adsorption of cadmium ion ($Cd^{2+}$) was done under an applied bias of electrochemical cells followed by rinsing and drying. Afterward, it was dipped into anionic (Se) precursor solution for completion of fabrication reaction of CdSe QDs. CdSe/$TiO_2$ assembly prepared through PILAR followed by SILAR has shown PCE up to 4.30% [126].

#### 11.3.3.3 Electrochemical deposition

ED method is widely used because of its simplicity, low energy consumption, ease control of size and shape, and low cost. This technique allows the growth of a thin layer semiconductor QDs onto a substrate. The whole process is carried out in the presence of an electric current. The substrate and reference substrate are immersed into a bath solution consisting of the salt precursor. On applying an electric field, positive charge ions are attracted toward the negatively charged substrate. Therefore, semiconductor thin film is deposited on the substrate. The ECD method is a facile, low-cost technique for producing semiconductor film of desired thickness. Rao et al. used the ECD technique for the deposition of CdS/CdSe QDs on $TiO_2$ NW array and achieved 4.20% of efficiency [127]. The whole process of deposition is completed in less than 1 hour. Recently Wang et al. demonstrated a single-step potentiostatic method for the electrodeposition of $Cu_2S$ nanoparticles onto the fluorine-doped tin oxide (FTO) electrode from an aqueous solution of $CuCl_2$ and thiourea to develop CEs QDSSCs. The $Cu_2S$-CE based QDSSCs exhibited a PCE as high as 4.24% with a $J_{sc}$, $V_{oc}$, and fill factor (FF) of 19.60 mA $cm^{-2}$, 0.445 V, and 48.62%, respectively, without any further optimization of photoanode [128].

#### 11.3.3.4 Electrophoretic deposition

In this technique, the electrophoretic bath is prepared by mixing polar/nonpolar solvent (e.g., toluene/acetonitrile) and colloidal solution of presynthesized QDs. Semiconductor coated electrode as a positive terminal and FTO glass as a negative terminal are immersed into the prepared electrophoretic bath and separated at a specified distance. ADC voltage is applied for a fixed period to deposit QDs on the positive electrode, e.g., semiconductor coated electrode (Fig. 11.6C). This ex situ approach can take advantage of the tremendous developments in controlling the growth of monodisperse and highly crystalline QDs of diverse semiconductor material. EPD was previously employed to deposit semiconductor [129–132], metallic [133], and insulating [134,135] nanoparticles on conductive substrates and polymers [136–138]. Salant et al. reported a facile fabrication of QDSSC by EPD of CdSe QDs onto conducting electrodes coated with mesoporous $TiO_2$ [139]. Smith et al. fabricated PVs by EPD of CdSe nanocrystals on flat $TiO_2$, yielding low conversion efficiencies [140]. Kamat et al. used EPD of carbon nanotube on the CdSe NPs composites to prepare SCs, also yielding low efficiencies [141,142]. Recently,

Kamazani et al. used EPD to deposit the $TiO_2$ layer on FTO glass substrate for a photonaode electrode of copper indium diselenide (CIS)-$Cu_2S$ QDSSCs with 2.01% of PCE [143].

#### 11.3.3.5 Molecular linker attachment

In molecular linker attachment (MLA), a bi-functional linker molecule, such as 3-MPA, is used for the attachment of presynthesized QDs to the semiconductor surface. The carboxylic acid group present in bi-functional linker molecule is attached to the semiconductor surface and on the other end of bi-functional linker molecule, thiol group interacts with the QDs (Fig. 11.6D). This approach enables the use of the selective size of presynthesized QDs. In the presynthesis method of QD, it is prepared usually through hot injection method using a suitable capping agent (surfactant), such as thioglycolic acid, MPA, trioctylphosphine (TOP), TOP oxide, oleic acid, etc. Capping agents assist in controlling the structural, morphological, size distributions, and optical characteristics of the QDs. Size and growth of the QDs are controlled through concentration of the capping agent in the precursor solution, reaction temperature, and reaction time. In QDSSCs, fabricated through MLA technique, electron transportation from the QDs to the semiconductor depends on electric properties of the linker molecules. Length of linker molecules affects the interaction between QDs and semiconductor [120,144,145].

#### 11.3.3.6 Direct adsorption

DA is an ex situ method carried out by simply immersing semiconductor coated electrode into the colloidal QDs solution for a specified time. QDs are deposited through DA without using any molecule linker or external DC voltage. DA was recently proposed for the deposition of monodisperse QDs without molecular linkers to the surface of the metal oxide nanostructure. However, only a low surface overage of approximately 14% was achieved with this method and the attachment mechanism remained unclear [120,121].

## 11.4 Counter electrode in quantum dot-sensitized solar cells

In QDSSCs, the choice of the CE is one of the essential points in achieving good PCE. The CE performs the important task of collecting photogenerated electrons from the external circuit and catalyzing them to reduce the

oxidized electrolyte species. Thus, the properties of the CE must be catalytically active toward the redox electrolyte [146]. The primary properties for the CE materials are excellent stability, good electron requirements, catalytic activity for redox couple reduction, and high conductivity for a charge. Various types of CEs have been fabricated, such as noble metals, metal sulfides, polymers, carbon, and carbon derivatives. Among them, platinum, due to its significant electro-catalytic property and ability to reduce redox couples in liquid electrolytes, is often regarded as the most reliable CE material [147]. However, Pt CE is unsuitable for polysulfide electrolytes mainly due to their strong chemisorption with $S^{2-}/S_n^{2-}$ couples (so-called poisoning effect), leading to a reduced chemical activity of the CE, leading to a reduced chemical activity and a reduced electrical conductivity which the CE [128]. Therefore, significant efforts have been made to develop a highly catalytic and stable Pt-free CE material, such as metal chalcogenides, carbon materials, and conducting polymers.

Recently, metal-chalcogenides, such as $Cu_2S$ [148–151], CuS [152,153], NiS [154,155], PbS [156], CoS [157], $FeS_2$ [157], and copper zinc tin sulphide [158] have been intensively exploited and found to be cost-effective alternatives to Pt CE. The use of metal-chalcogenides as CE for QDSSC exhibit better performance compared to Pt CE [150]. Among these materials, $Cu_2S$ CEs prepared by depositing $Cu_2S$ on brass foil provides high electrocatalytic activity in polysulfide reduction [149]. Nevertheless, continual corrosion would happen to $Cu_2S$ CEs when they are exposed to the polysulfide electrolyte [148]. In order to solve this problem, indium tin oxide (ITO) or FTO glass as a promising substrate for metal sulfide CE has been explored. Jiang et al. reported ITO@$Cu_2S$ tunnel junction NW arrays as efficient CEs for high PCE QDSSCs [159]. Zhao et al. through electrodeposition. prepared a $Cu_2S$ film on the FTO glass substrate ($Cu_2S$/FTO) as CEs in CdSe QDSSCs with PCE of 2.45% [160]. Shen et al. prepared counter $Cu_2S$ CE electrodes for CdSe QDSSCs by ion exchange of ZnS films deposited on porous ITO electrodes with a $Cu^+$ containing electrolyte solution. The as-prepared CdSe QDSSCs with the cuprous electrodes exhibit much higher photovoltaic characteristics than those with the Pt counterpart [161]. However, the charge carrier mobility is not significant in these CEs. Therefore, a challenge of optimizing the CE materials is to improve the conducting ability.

Apart from transition metal sulfides, carbonaceous materials have also received much attention as CE for QDSSCs due to their advantages of good conductivity, high surface area, and low cost. However, the

relatively slow intrinsic reaction kinetics of carbon with the polysulfide electrolyte leads to low PCE QDSSCs [162]. In order to overcome this problem of carbonaceous materials, some researchers have paid attention to the fabrication of carbon at an atomic level [162,163]. For example, the hollow core-mesoporous shell carbon CE has been synthesized for QDSSC applications, yielding higher conversion efficiency than those based on conventional Pt. The efficiency improvement is attributed to the superior structural characteristics, such as large specific surface area, high mesoporous volume, and particularly 3-D interconnected unique hierarchical nanostructure consisting of hollow macropore core, mesoporous shell, and interconnected large interstitial spaces between the packed spherical carbon particles. Dong et al. prepared N-doped carbon nanoparticles as effective CE catalysts, and they found an enhanced electrocatalytic activity of N-doped carbon by the additional electrons provided by the nitrogen dopant atoms as well as the active sites [164]. Meanwhile, the combination of carbonaceous materials with metal chalcogenides is also considered as a facile strategy to enhance the QDSSC performance. Recently, Subramanyan et al. reported Cuprous Sulfide@Carbon nanostructures-based CEs for QDSSCs. They prepared five CEs from $Cu_2S$ and carbon based materials including prepared $Cu_2S$, $Cu_2S$@-graphene oxide, $Cu_2S$@reduced graphene oxide, $Cu_2S$@functionalized multiwalled carbon nanotubes [165]. Among them, the $Cu_2S$@functionalized multiwalled carbon nanotubes composite CE based QDSSCs exhibited the highest PCE with $J_{sc}$ of 16.8 mA $cm^{-2}$ and $V_{oc}$ of $\sim$1 V. This CE also shows higher electrocatalytic activity toward the reduction of the oxidized sulfide species in the electrolyte, which is reflected in a lower charge transfer resistance, higher reduction current density, and a greater exchange current density. The Fermi level position of functionalized multiwalled carbon nanotubes is also conducive for accepting electrons from FTO. In addition, this electrode also showed a superior catalytic activity and a higher flat band potential, which enhanced its hydrogen evolution performance, in comparison to the other electrodes.

On the other hand, conducting polymers, such as polythiophene (PT), polypyrrole (PPy), and poly(3,4-ethylenedioxythiophene) (PEDOT) and polyaniline, owing to their high electron conductivity, low cost-availability, and the large electrochemical surface, have become promising candidates as CE materials for DSSCs. Yeh et al. prepared CEs using conducting polymers (PEDOT, PPy, and PT), and reported efficiencies of 1.35%, 0.09%, and 0.41% for the SCs with PEDOT, PT, and PPy CEs,

respectively [166]. The authors demonstrated that the promising efficiency of the cell with the PEDOT electrode is attributed to higher electrocatalytic activity, reduced charge transfer resistance at the CE and electrolyte interface, and the higher porosity and surface roughness of the PEDOT film. Yeh et al. used PT, PPy, and PEDOT as CEs for QDSSCs [167]. Among them, PEDOT-CE showed the best PCE (1.16%). This CE also showed the least charge transfer resistance ($R_{ct}$) value of 15.4 'Ω $cm^{-2}$ at the interface of the CE and electrolyte which is almost the same as s-Au electrode (16.4 'Ω $cm^{-2}$).

## 11.5 Electrolytes in quantum dot-sensitized solar cells

As the central component of a QDSSC, the electrolyte redox couple is essential to regenerate QDs and transport holes to the CE [168,169]. The efficiency of a QDSSC device is determined by its short $J_{sc}$, $V_{oc}$, and FF. $J_{sc}$ is dependent on the transport of the redox couple in the electrolyte [170]. FF can be affected by the catalyzing ability of the CE materials for the reduction of the redox couple [171]. And, $V_{oc}$ is significantly affected by the redox potential of the electrolyte and is determined by the energy difference between the Fermi level of the metal oxide ($TiO_2$, ZnO) electron acceptor and the redox potential of the electrolyte [172]. For the redox electrolyte to be effective, high solubility, high ionic mobility, and fast electron transfer kinetics are crucial. The most common electrolytes used in QDSSCs are aqueous polysulfide and an organic electrolyte with $I^-/I_3^-$ redox couple [117]. However, the $I^-/I_3^-$ redox couple is corrosive to most QDs, leading to degradation of QDSSC performance [23]. Thus, exploring an appropriate iodine-free electrolyte is critical for stable QDSSCs. The sulfide/polysulfide ($S^{2-}/S_n^{2-}$) redox couple in the aqueous electrolyte provides a stable environment for QDs. However, the QDSSCs employing the $S^2/S_n^{2-}$ redox couple with higher redox potential generate low $V_{oc}$ and very poor FF. Recently, a new electrolyte of the $Co^{2+}/Co^{3+}$ redox system was used to improve the $V_{oc}$ due to the relative low redox potential in comparison with the $S^2/S_n^{2-}$ redox couple; however, the photocurrents are still lower than that of the $S^2/S_n^{2-}$redox couple [173]. Besides, $Fe^{2+}/Fe^{3+}$ and $Fe(CN)_6^{5-}/Fe(CN)_6^{4-}$ redox systems were also investigated in CdS sensitized SCs [174]. Until now, the QDSSCs employing the $S^{2-}/S_n^{2-}$ redox couple have shown the highest efficiency [175]. The FF and $V_{oc}$ could be further increased by selecting an appropriate electrolyte. For example, replacing

the $S^{2-}/S_n^{2}$ redox couple with $[(CH_3)_4N]_2S/[(CH_3)_4N]_2S_n$ in an organic solvent yielded an impressive $V_{oc}$ of 1.2 V [176]. Solid-state and quasisolid hole conductors, such as spiro-OMeDAT and CuSCN, have been used to replace the liquid electrolyte. The difference between quasisolid and solid electrolytes is that quasisolid electrolytes still contain a molecular redox system, but the liquid has been solidified using a gel, polymer, etc. The purely solid electrolytes are based on molecular or polymeric holeconductors, and thus there is no extra redox system present [169].

## 11.6 Experimental background in quantum dot-sensitized solar cells

### 11.6.1 Current–voltage characteristics

IV curve is one of the most important and direct characterization methods to understand the overall performance of a SC. They are a pictorial representation of the performance of a SC or module. Light sources (artificial sunlight) developed on a laboratory level to simulate solar radiation whose illumination intensity is made to match the natural sunlight are called solar simulators. They can be used as a test system for SC material devices in order to study the overall performance of the SC. They provide a facility for controlling the electrical parameters in order to study the characteristics of the SC under study. The light obtained from the solar simulator is controlled in spectral content, spatial uniformity and temporal stability [177]. Based on the requirement, several types of solar simulators, like continuous, pulsed, and flashed are used. It also involves a variety of lamps, like a xenon arc lamp, metal halide arc lamp, quartz tungsten halogen lamp, and LED. LED-based solar simulators have an edge over others as they can be used over a wide range of wavelengths from UV–visible to IR at various power configurations [178]. The overall efficiency or performance of SCs are addressed by parameters like FF, open circuit voltage ($V_{oc}$), and short circuit current ($I_{sc}$) of the cell and they are most widely analyzed by IV characteristics. $V_{oc}$ corresponds to the maximum voltage provided by an illuminated photovoltaic device when no external load is connected and $I_{SC}$ is the current that flows in a photovoltaic device when illuminated and its electrodes are connected. In an ideal device, $V_{oc}$ is limited by radiative recombination [179]. Band gaps and potential drops on contacts, sub radiative band gaps within QDs [180] are factors that likely affect the recombination processes in the device, which, in turn, affect the $V_{oc}$ and $I_{sc}$. The generation of photocurrent in the QDSSCs

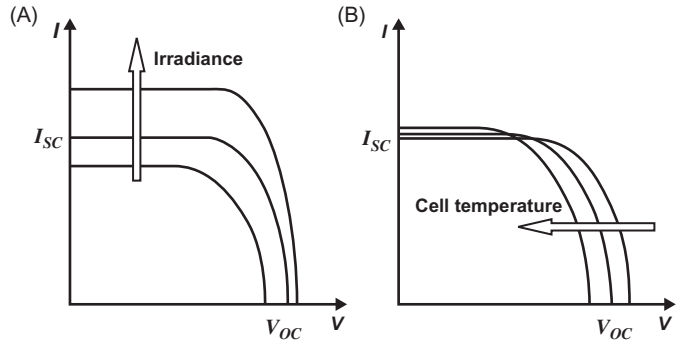


**Figure 11.7** Effect of (A) irradiation and (B) cell temperature on the performance of solar cells [185].

occurs when the sensitizer (QDs) absorbs the incident light photons and move through the network of interconnected oxide particles [181], resulting in ultra-fast electron injection into the CB of the electrode [182]. FF of the device is affected by the CE and electrolyte and takes a major share in the device performance [183,184]. The increase in temperature of the SCs decreases the band gap of the material, thus decreasing $V_{oc}$ linearly while $I_{sc}$ increases (slightly), as shown in Fig. 11.7 [185], and results in lower power output. Hence the temperature should be maintained at around 25°C. Apart from temperature, increase in illumination of solar irradiation source affects the performance for which $V_{oc}$ increases logarithmically and $I_{sc}$ increases linearly [186], resulting in large output current. Enhancement in $V_{oc}$ invariably increases the short circuit current and FF from which could be observed Fig. 11.8.

The other parameters, like the reverse-bias breakdown voltage of the diode, series resistance, and shunt resistance, can also be extracted from the dark IV curve measurements (in the absence of light). The area independent current is termed current density ($J_{sc}$), which is preferred in addressing overall performance of a cell. Modification of the photoanode increases the surface activation sites for electrons, with better photocurrent and $V_{oc}$. High conducting CEs with high electro catalytically active sites [148,187] can efficiently reduce the electrolytes thereby increasing the photocurrent and overall efficiency of the device.

## 11.6.2 Electrochemical impedance spectroscopy

Electrochemical impedance spectroscopy (EIS) is a powerful technique used to investigate the charge transfer and charge storage processes of an

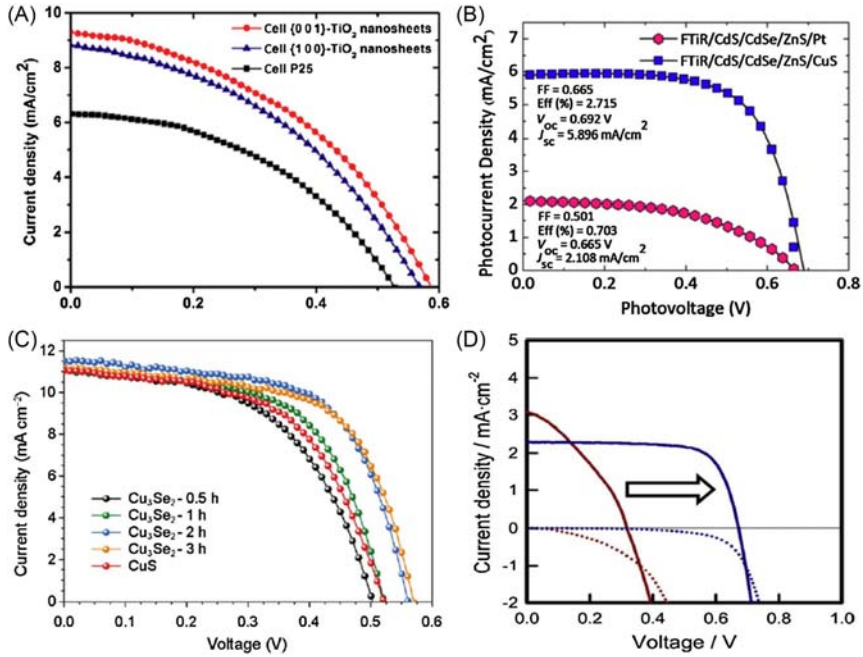


**Figure 11.8** Current density–voltage curves for, modification of anode with (A) nano sheets, (B) with 3-D $TiO_2$ flower, (C) selenides based counter electrode, (D) ferricyanide redox couple [188]. *3-D*, Three-dimensional.

electrical system. When EIS measurement is conducted, a sinusoidal AC potential with small amplitude is applied, which produces a measurable electric signal (impedance and phase angle) at the given frequency range. EIS, as a sensitive tool to for investigating electrochemical systems, has the advantage of separating interfacial processes at different frequency domains, and it is useful for analyzing the reaction mechanism of the electrode system [188–191]. Analysis of EIS spectra with equivalent electrical circuits in QDSSCs can help quantify the various contributions to the overall impedance, such as charge transfer resistance, solution resistance, double layer capacitance, and so on. Resulting impedance spectra can be fitted to an appropriate equivalent circuit, as shown in Fig. 11.9 [192]. In general, at least three internal resistances are found. Fig. 11.9B shows a Nyquist plot. The three semicircular shapes are assigned to impedances related to charge transport at the Pt CE ($Z_{Pt}$) in the high-frequency region (103–105 Hz), at the $TiO_2$/QD/electrolyte interface ($Z_{ct}$) in the middle-frequency region (100–103 Hz), and in the Warburg diffusion

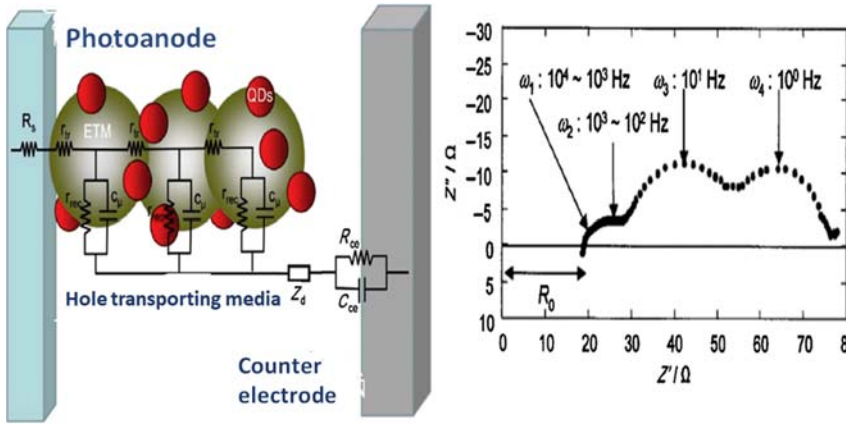


**Figure 11.9** (A) Equivalent circuit used to fit the EIS spectra. (B) A Nyquist plot showing each resistive element. *EIS*, Electrochemical impedance spectroscopy.

within the electrolyte ($Z_d$) in the low-frequency region (100−102 Hz), respectively. The resistance elements $R_{Pt}$, $R_{ct}$, and $R_d$ are described as the real parts of $Z_{Pt}$, $Z_{ct}$, and $Z_d$, respectively [193]. $R_s$ is the series resistance of the cell, including the transparent and conducting oxides sheet resistance, and $R_T$ is the electron transport resistance through the nanoparticle $TiO_2$ film. The frequency ($f$) at maximum imaginary components of each semicircle in a $Z''-Z'$ plot is the reciprocal of the time constant ($\tau$) for an equivalent circuit. Thus, the recombination lifetime ($\tau_r$) between the electrons in the $TiO_2$ and the oxidized form of the redox couples in the solution can be calculated by adopting the following equation [194].

$$\tau_r = \frac{1}{\omega_{max}} = \frac{1}{2\pi f} \tag{11.15}$$

where $\omega_{max}$ refers to the peak frequency of the second semiarc related to $R_{ct}$.

Capacitance measurement involves characterization of a SC similar to IV characteristics. Unlike IV where measurements are recorded as a function of AC, it can be studied as a function of the DC voltage, frequency, and time or AC voltage, as per the requirement. The capacitance measurements are made over voltage; frequency and time domain are described by the following techniques; The Quasistatic technique, which is a straightforward technique that involves applying a constant voltage and measuring current density. For different illumination intensity $V_{oc}$, $J_{sc}$ is recorded, which yields information about charge transport in the diode [195]. The harmonic technique, which is the second class of

optoelectronic characterization technique. Its involves the application of a frequency-dependent voltage/illumination and measurement of systems response [196]. The transient techniques involve an electrical pulse that is applied for which reading is measured with respect to time [197]. Capacitance vs. voltage is helpful in studying the doping concentration of the cell; capacitance-frequency provides information about charge trap densities in the PV substrate's depletion region and is also helpful in understanding the dynamic behavior of the SCs [198,199]. AC voltage capacitance technique, known as drive-level capacitance profiling, is used to determine the deep defect densities [200]. It also helps in determining the number of trap centers and the energy between the different states of the semiconductor material [201]. The results of the parameters obtained are plotted as complex numbers in the impedance plane in Nyquist plots, Cole-Cole plots, or complex impedance plots. The plot of $1/C^2$ vs. $V$ is a straight line that is called a Mott–Schottky plot [202,203], whose intercept on $X$-axis is $V$ called flat band potential and its slope gives the doping density $N_c$. They open a new way to record the nonstationary interfaces [204]. But they limit themselves only to chemical capacitance and do not take into account the electrostatic capacitance. The electrostatic capacitance is the capacitance over the depletion region that has very few free charge carriers or no charge carriers at all, and the chemical capacitance refers to the occupation of electronic states in semiconductor, which is governed by the Boltzmann distribution.

## 11.7 Summary and future prospects

Over the last few years, QDSSCs, which represent a type of next-generation of SCs, have attracted much attention due to their characteristic properties, such as processability, at low cost, feasibility to control light absorption spectrum in a wide region, and the possibility of multiple electron generations with theoretical conversion efficiency up to 44%. High PCE can be achieved through high-energy photon excitation. Today, the conversion efficiency of QDSSCs has greatly improved from less than 1% up to 12% in no more than ten years. However, the relatively low PCE is still not comparable to other photovoltaic devices. Several factors limit the overall PCE of QDSSCs such as narrow range absorption of the solar spectrum, the disparity between charge scavenging grate, recombination at interfaces, low QDs deposition on the metal oxide film, poor electrical transportation characteristics, photo-corrosion of the electrode, and low

FF due to the poor performance of the CE. By addressing these issues, optimizing the construction of QD sensitizers, CEs with superior catalytic activity, and redox coupled electrolyte can improve the performance of QDSSCs. Combination of diversified inorganic semiconductor QDs and passivation of QDs by organic and inorganic passivating agents can enhance the light absorption and electron excitation and reduce the recombination at the interface. Among them, the type-II core/shell structure can significantly increase the $V_{oc}$ arising from potential-induced degradation effects. On the other hand, highly ordered architectures of wide band gap semiconductors provide fast and efficient transfer of photogenerated electrons from QDs to the substrate.

In summary, for further development, future studies should focus on improving the QDSSCs' performance. Therefore, the future big leaps in QDSSCs will involve rational strategies to increase the $V_{oc}$ and FF values of the cell devices by optimizing the relevant active materials, developing more stable sensitizer layers and electrolytes or hole transporting materials for solid-state QDSSCs, and exploiting some techniques available for large-scale manufacture. For example, the design of new semiconductor QDs to broaden the absorption spectral region offers a range of new opportunities and challenges to improve the efficiency. Moreover, deeper research on surface treatment provides a new strategy to reduce the recombination. Also, further studies of CEs with high electrocatalytic ability are expected to be the breakthrough in the currently stagnant research field of QDSSCs. Much attention might be paid to the stability of QDSSCs, in which the weak penetration ability of polymer electrolytes and inferior electron conductivity limit the development. It is expected that exploring highly efficient solid-state SCs will be a persistent objective in the near future.

## Acknowledgments

The authors wish to thank the National Research Foundation (NRF), South Africa, under the Competitive Program for Rated Researchers (Grant no: 106060) and the University of Johannesburg, Faculty of Science Research Committee, and University Research Committee for financial support.

## References

[1] A. Foley, A.G. Olabi, Editorial. Renew. Sustain, Energy Rev 68 (2017) 1112–1114.
[2] N.L. Panwar, S.C. Kaushik, S. Kothar, Role of renewable energy sources in environmental protection: a review, Renew. Sustain. Energy Rev. 15 (2011) 1513–1524.

[3] S.K. Sahoo, Renewable and sustainable energy reviews solar photovoltaic energy progress in India, Renew. Sustain. Energy Rev. 59 (2016) 927–939.
[4] M. Grätzel, R. Janssen, D.B. Mitzi, E.H. Sargent, Materials interface engineering for solution-processed photovoltaics, Nature 488 (2012) 304–312.
[5] P.G.V. Sampaio, et al., Exploring the potential of a hybrid device combining solar water heating and molecular solar thermal energy storage, Energy Environ. Sci. 10 (2017) 728–734.
[6] A.K. Sleiti, Tidal power technology review with potential applications in Gulf Stream, Renew. Sustain. Energy Rev. 69 (2017) 435–441.
[7] V.K. Singh, S.K. Singal, Operation of hydro power plants—a review, Renew. Sustain. Energy Rev. 69 (2017) 610–619.
[8] G.K. Singh, Solar power generation by PV (photovoltaic) technology: a review, Energy 53 (2013) 1–13.
[9] N. Ali, A. Hussain, R. Ahmed, M.K. Wang, C. Zhao, B. Ul Haq, et al., Advances in nanostructured thin film materials for solar cell applications, Renew. Sustain. Energy Rev. 59 (2016) 726–737.
[10] W.A. Badawy, A review on solar cells from Si-single crystal to porous materials and quantum dots, J. Adv. Res. 6 (2015) 123–132.
[11] L.H. Lai, L. Protesescu, M.V. Kovalenko, M.A. Loi, Sensitized solar cells with colloidal PbS–CdS core–shell quantum dots, Phys. Chem. Chem. Phys. 16 (2014) 736–742.
[12] Z. Zheng, H. Ji, P. Yu, Z. Wang, Recent progress towards quantum dot solar cells with enhanced optical absorption, Nanoscale Res. Lett. 11 (2016) 266–272.
[13] W. Li, Z. Pan, X. Zhong, $CuInSe_2$ and $CuInSe_2$–ZnS based high efficiency "green" quantum dot sensitized solar cells, J. Mater. Chem. A 3 (2015) 1649–1655.
[14] J. Duan, H. Zhang, Q. Tang, B. Heb, L. Yu, Recent advances in critical materials for quantum dot-sensitized solar cells: a review, J. Mater. Chem. A 3 (2015) 17497–17510.
[15] D.H. Jara, S.J. Yoon, K.G. Stamplecoskie, P.V. Kamat, Size-dependent photovoltaic performance of $CuInS_2$ quantum dot-sensitized solar cells, Chem. Mater. 26 (2014) 7221–7228.
[16] J. Luo, J. Sun, P.C. Guo, Z.S. Yang, Y.X. Wang, Q.F. Zhang, Enhancement in efficiency of CdS/CdSe quantum dots-sensitized solar cells based on ZnO nanostructures by introduction of MnS layer, Mat. Lett. 215 (2018) 176–178.
[17] P.V. Kamat, Quantum dot solar cells. Semiconductor nanocrystals as light harvesters, J. Phys. Chem. C 112 (2008) 18737–18753.
[18] T. Takagahara, K. Takeda, Theory of the quantum confinement effect on excitons in quantum dots of indirect-gap materials, Phys. Rev. B 46 (1992) 15578–15581.
[19] F.W. Wise, Lead salt quantum dots: the limit of strong quantum confinement, Acc. Chem. Res. 33 (2000) 773–780.
[20] X. Zhao, C.M. Wei, L. Yang, M.Y. Chou, Quantum confinement and electronic properties of silicon nanowires, Phys. Rev. Lett. 92 (2004) 236805.
[21] A.L. Efros, M. Rosen, The electronic structure of semiconductor nanocrystals, Annu. Rev. Mater. Sci. 30 (2000) 475–521.
[22] A.C. Pasaran, T.L. Luke, D. Esparza, I. Zarazua, E.D.L. Rosa, R.F. Ramirez, et al., Photovoltaic properties of multilayered quantum dot/quantum rod sensitized $TiO_2$ solar cells fabricated by SILAR and electrophoresis, Phys. Chem. Chem. Phys. 17 (2015) 18590–18599.A.P. Alivisatos, Semiconductor clusters, nanocrystals, and quantum dots, Science 271 (1996) 933-937.
[23] Y.L. Lee, C.H. Chang, Efficient polysulfide electrolyte for CdS quantum dot-sensitized solar cells, J. Power Sour. 185 (2008) 584–588.

[24] A. Bisquert, M. Zaban, I. Greenshtein, Mora-sero determination of rate constants for charge transfer and the distribution of semiconductor and electrolyte electronic energy levels in dye-sensitized solar cells by open-circuit photovoltage decay method, J. Am. Chem. Soc. 126 (2004) 13550–13559.
[25] F.E. Doany, D. Grischkowsky, Measurement of ultrafast hot-carrier relaxation in silicon by thin-film-enhanced, timeresolved reflectivity, Appl. Phys. Lett. 52 (1988) 36–43.
[26] A.J. Nozik, Spectroscopy and hot electron relaxation dynamics in semiconductor quantum wells and quantum dots, Annu. Rev. Phys. Chem. 52 (2001) 193–231.
[27] F. Williams, A.J. Nozik, Irreversibilities in the mechanism of photoelectrolysis, Nature 271 (1978) 137–139.
[28] D.S. Boudreaux, F. Williams, A.J. Nozik, Hot carrier injection at semiconductor-electrolyte junctions, J. Appl. Phys. 51 (1980) 2158–2163.
[29] D.J. Robbins, Aspects of the theory of impact ionization in semiconductors, Phys. Stat. Sol. 79 (1980). 79 9–50.
[30] M. Wolf, R. Brendel, J.H. Werner, H.J. Queisser, Solar cell efficiency and carrier multiplication in Si1−xGex alloys, J. Appl. Phys. 83 (1998) 4213–4221.
[31] A.J. Nozik, Multiple exciton generation in semiconductor quantum dots, Chem. Phys. Lett. 457 (2008) 3–11.
[32] D. Harrison, R.A. Abram, S. Brand, Characteristics of impact ionization rates in direct and indirect gap semiconductors, J. Appl. Phys. 85 (1999) 8186–8192.
[33] S. Kolodinski, J.H. Werner, T. Wittchen, H.J. Queisser, Quantum efficiencies exceeding unity due to impact ionization in silicon solar cells, Appl. Phys. Lett. 63 (1993) 2405–2407.
[34] V.I. Klimov, Mechanisms for photogeneration and recombination of multiexcitons in semiconductor nanocrystals: implications for lasing and solar energy, J. Phys. Chem. B 110 (2006) 16827–16845.
[35] J.A. Dean, Lange's Handbook of Chemistry, 14th ed., McGraw-Hill, New York, 1992.
[36] R.C. Weast, Handbook of Chemistry and Physics, 56th ed., CRC, Cleveland, OH, 1975.
[37] M. Ye, X. Wen, M. Wang, J. Iocozzia, N. Zhang, C. Lin, et al., Recent advances in dye-sensitized solar cells: from photoanodes, sensitizers and electrolytes to counter electrodes, Mater. Today 18 (2015) 155–162.
[38] R. Swierk, K.P. Regan, J. Jiang, G.W. Brudvig, C.A. Schmuttenmaer, Rutile $TiO_2$ as an anode material for water splitting dye-sensitized photoelectrochemical cells, ACS Energy Lett. 1 (2016) 603–606.
[39] F. Lenzmann, J. Krueger, S. Burnside, K. Brooks, M. Grätzel, D. Gal, et al., Surface photovoltage spectroscopy of dye-sensitized solar cells with $TiO_2$, $Nb_2O_5$, and $SrTiO_3$ nanocrystalline photoanodes: indication for electron injection from higher excited dye states, J. Phys. Chem. B 105 (2001) 6347–6352.
[40] T.T.T. Pham, N. Maathews, Y.M. Lam, S. Mhaisalkar, Enhanced efficiency of dye-sensitized solar cells with mesoporous–macroporous $TiO_2$ photoanode obtained using ZnO template, J. Electron. Mater. 46 (2017) 3801–3807.
[41] Q. Chang, Z. Ma, J. Wang, Y. Yan, W. Shi, Q. Chen, et al., Graphene nanosheets@ZnO nanorods as three-dimensional high efficient counter electrodes for dye sensitized solar cells, Electrochim. Acta 151 (2015) 459–466.
[42] W.M.N.M.B. Wanninayake, K. Premaratne, R.M.G. Rajapakse, High efficient dye-sensitized solar cells based on synthesized $SnO_2$ nanoparticles, J. Nanomater. 2016 (2016) 1–8.
[43] Y. Zhang, J. Tian, K. Jiang, J. Huang, L. Zhang, H. Wang, et al., A novel method for fabrication of CdS quantum dot-sensitized solar cells, J. Mater. Sci. Mater. Electron. 28 (2017) 4103–14109.

[44] G.H. Carey, A.L. Abdelhady, Z. Ning, S.M. Thon, O.M. Bakr, E.H. Sargent, Colloidal quantum dot solar cells, Chem. Rev. 115 (2015) 12732–12763.
[45] M. Samadpour, Efficient CdS/CdSe/ZnS quantum dot sensitized solar cells prepared by ZnS treatment from methanol solvent, Sol. Energy 144 (2017) 63–70.
[46] L.Y. Chen, Y.T. Yin, T.Y. Ho, Y.Z. Chen, Sensitized solar cells via nanomaterials: a recent development in quantum dots-based solar cells, IEEE Nanotechnol. Mag. 8 (2014) 16–21.
[47] Y.-L. Lee, Y.S. Lo, Highly efficient quantum-dot-sensitized solar cell based on cosensitization of CdS/CdSe, Adv. Funct. Mater. 19 (2009) 604–609.
[48] J. Guocan, P. Zhenxiao, R. Zhenwei, J. Du, C. Yang, W. Wang, et al., Poly(vinyl pyrrolidone): a superior and general additive in polysulfide electrolytes for high efficiency quantum dot sensitized solar cells, J. Mater. Chem. A 4 (2016) 11416–11421.
[49] Z. Yang, C.Y. Chen, P. Roy, H.T. Chang, Quantum dot-sensitized solar cells incorporating nanomaterials, Chem. Commun. 47 (2011) 9561–9571.
[50] P.V. Kamat, Quantum dot solar cells. The next big thing in photovoltaics, J. Phys. Chem. Lett. 4 (2013) 908–918.
[51] I.J. Kramer, E.H. Sargen, The architecture of colloidal quantum dot solar cells: materials to devices, Chem. Rev. 14 (2014) 863–882.
[52] K. Surana, R.M. Mehra, B. Bhattacharya, H.W. Rhee, A.R. Polu, P.K. Singh, A comprehensive study of chalcogenide quantum dot sensitized solar cells with a new solar cell exceeding 1V output, Renew. Sustain. Energy Rev. 52 (2015) 1083–1092.
[53] Z. Li, L. Yu, Y. Liu, S. Sun, Efficient quantum dot-sensitized solar cell based on $CdS_xSe_{1-x}$/MnCdS/$TiO_2$ nanotube array electrode, Electrochim. Acta 153 (2015) 200–209.
[54] J. Tian, G. Cao, Semiconductor quantum dot-sensitized solar cells, Nano Rev. 4 (2013) 22578–22585.
[55] M. Kouhnavard, S. Ikeda, N.A. Ludin, N.B.A. Khairudin, B.V. Ghaffari, M.A. Mat-Teridi, et al., Renew. Sustain. Energy Rev. 37 (2014) 397–407.
[56] J. Qi, H. Xiong, G. Wang, H. Xie, W. Jia, Q. Zhang, et al., High-performance solar cells with induced crystallization of perovskite by an evenly distributed CdSe quantum dots seed-mediated underlayer, J. Power Sour. 376 (2018) 46–54.
[57] I. Robel, V. Subramanian, M. Kuno, P.V. Kama, Quantum dot solar cells. Harvesting light energy with CdSe nanocrystals molecularly linked to mesoscopic $TiO_2$ films, J. Am. Chem. Soc. 128 (2006) 2385–2393.
[58] A. Manjceevan, J. Bandar, Systematic stacking of PbS/CdS/CdSe multi-layered quantum dots for the enhancement of solar cell efficiency by harvesting wide solar spectrum, Electrochim. Acta 271 (2018) 567–575.
[59] C.A. Bauer, T.Y. Hamada, H. Kim, M.R. Johnson, M.J. Voegtle, M.S. Emrick, An integrated, multipart experiment: synthesis, characterization, and application of CdS and CdSe quantum dots as sensitizers in solar cells, J. Chem. Educ. 95 (2018) 1179–1186.
[60] Q. Chen, C. Zhou, X. Zhang, F. Gao, Y. Meng, C. Yao, et al., One-step aqueous synthesis of thioglycolic acid-CdTe:$Eu^{3+}$ quantum dots-sensitized $TiO_2$ nanotube solar cells, J. Appl. Electrochem. 48 (2018) 27–35.
[61] J. Li, Y. Zhang, T. Gao, C. Hu, T. Yao, Q. Yuan, et al., Quantum dot-induced improved performance of cadmium telluride (CdTe) solar cells without a Cu buffer layer, J. Mater. Chem. A 5 (2017) 4904–4911.
[62] U. Jabeen, T. Adhikari, D. Pathak, S.M. Shah, J.M. Nunzi, Structural, optical and photovoltaic properties of P3HT and Mn-doped CdS quantum dots based bulk hetrojunction hybrid layers, Opt. Mater. 78 (2018) 132–141.

[63] K. Veerathangam, M.S. Pandian, P. Ramasamy, Size-dependent photovoltaic performance of cadmium sulfide (CdS) quantum dots for solar cell applications, J. Alloys Compd. 735 (2018) 202–208.
[64] Z. Ning, H. Tian, C. Yuan, Y. Fu, H. Qin, L. Sun, et al., Solar cells sensitized with type-II ZnSe–CdS core/shell colloidal quantum dots, Chem. Commun. 47 (2011) 1536–1538.
[65] J. Hou, H. Zhao, F. Huang, L. Chen, Q. Wu, Z. Liu, et al., Facile one-step fabrication of $CdS_{0.12}Se_{0.88}$ quantum dots with a ZnSe/ZnS-passivation layer for highly efficient quantum dot sensitized solar cells, J. Mater. Chem. A 6 (2018) 9866–9873.
[66] A. Tubtimtae, M. Lee, G. Wang, $Ag_2Se$ quantum-dot sensitized solar cells for full solar spectrum light harvesting, J. Power Sour. 196 (2011) 6603–6608.
[67] J. Xue, J. Liu, S. Mao, Y. Wang, W. Shen, W. Wang, et al., Recent progress in synthetic methods and applications in solar cells of $Ag_2S$ quantum dots, Mater. Res. Bull. 106 (2018) 113–123.
[68] X. Hu, W. Xu, C. Chen, F. Tan, W. Zhang, Fabrication of $Ag_2S$ quantum dots decorated $TiO_2$ nanorod arrays for organic/inorganic hybrid solar cells, Mater. Lett. 204 (2017) 125–128.
[69] J. Vyskočil, A. Hospodková, O. Petříček, J. Pangrá, M. Zíková, J.O. Vetushka, GaAsSb/InAs/(In)GaAs type II quantum dots for solar cell applications, J. Cryst. Growth 464 (2017) 64–68.
[70] M. Omri, A. Sayari, L. Sfaxi, Fabrication and characterization of multi-layer InAs/InGaAs quantum dot p-i-n GaAs solar cells grown on silicon substrates, Appl. Phys. A 124 (2018) 74–79.
[71] S. Yang, P. Zhao, X. Zhao, L. Qua, X. Lai, InP and Sn:InP based quantum dot sensitized solar cells, Mater. Chem. A 3 (2015) 21922–21929.
[72] F. Eisner, A. Seitkhan, Y. Han, D. Khim, E. Yengel, A.R. Kirmani, et al., Solution-processed $In_2O_3$/ZnO heterojunction electron transport layers for efficient organic bulk heterojunction and inorganic colloidal quantum-dot solar cells, RRR Solar 7 (2018) 1800076–1800110.
[73] M.C. Portillo, J.A. Pulido, S.G. Hernánde, B.S.S. Cruz, S.A. Iniesta, R.G. Pérez, et al., Voc enhancement of a solar cell with doped $Li^+$-PbS as the active layer, Superlattices Microstruct. 18 (2018) 137–144.
[74] P.C.J. Pip Clark, D.C.J. Neo, R.A. Lazo, A.I. Williamson, I. Pis, S. Nappini, et al., Influence of multistep surface passivation on the performance of PbS colloidal quantum dot solar cells, Langmuir 34 (2018) 8887–8897.
[75] A.H.C. Khavar, A.R. Mahjoub, N. Taghavinia, Low-temperature solution-based processing to 7.24% efficient superstrate $CuInS_2$ solar cells, Sol. Energy 157 (2018) 581–586.
[76] Y. Hu, R. Patterson, R.L. Chin, J. Zheng, N. Song, L. Hu, et al., Potential for improved transport in core–shell $CuInS_2$ nanoparticle solar cells from an Ag surface termination, Cryst. Eng. Comm. 20 (2018) 3381–3387.
[77] M.R. Bergren, N.S. Makarov, K. Ramasamy, A. Jackson, R. Guglielmetti, H. McDaniel, High-performance $CuInS_2$ quantum dot laminated glass luminescent solar concentrators for Windows, ACS Energy Lett. 3 (2018) 520–525.
[78] E. Raphael, D.H. Jara, M.A. Schiavon, Optimizing photovoltaic performance in $CuInS_2$ and CdS quantum dot-sensitized solar cells by using an agar-based gel polymer electrolyte, RSC Adv. 7 (2017) 6492–6500.
[79] S.M. Kobosko, D.H. Jara, P.V. Kamat, $AgInS_2$–ZnS quantum dots: excited state interactions with $TiO_2$ and photovoltaic performance, ACS Appl. Mater. Interfaces 9 (2017) 33379–33388.

[80] C. Cai, L. Zhai, Y. Ma, C. Zou, L. Zhang, Y. Yang, et al., Synthesis of $AgInS_2$ quantum dots with tunable photoluminescence for sensitized solar cells, J. Power Sour. 341 (2017) 11–18.
[81] D. Esparza, I. Zarazúa, T.L. Luke, R. Carriles, A.T. Castro, E. De laRosa, Photovoltaic properties of $Bi_2S_3$ and CdS quantum dot sensitized $TiO_2$ solar cells, Electrochim. Acta 180 (2015) 486–492.
[82] M. Sugiyama, S. Aihara, Y. Shimamune, H. Katagiri, Influence of electron and proton irradiation on the soaking and degradation of $Cu_2ZnSnS_4$ solar cells, Thin Solid Films 642 (2017) 311–315.
[83] T. Chandel, V. Thakur, M.B. Zaman, S.K. Dwived, R. Poolla, Ultrasonically assisted sol-gel synthesis of nanocrystalline $Cu_2ZnSnS_4$ particles for solar cell applications, Mater. Lett. 212 (2018) 279–282.
[84] D.W. Jeong, J.Y. Kim, H.W. Seo, K.M. Lim, M.J. Ko, T.Y. Seong, et al., Characteristics of gradient-interface-structured ZnCdSSe quantum dots with modified interface and its application to quantum-dot-sensitized solar cells, Appl. Surf. Sci. 429 (2018) 16–22.
[85] G.Y. Kwak, T.G. Kim, S. Hong, A. Kim, M. HyoHa, K.J. Kim, Efficiency improvement of Si quantum dot solar cells by activation with boron implantation, Sol. Energy 164 (2018) 89–93.
[86] P. Sehgal, A.K. Narula, Enhanced performance of porphyrin sensitized solar cell based on graphene quantum dots decorated photoanodes, Opt. Mater. 79 (2018) 435–445.
[87] S. Diao, X. Zhang, Z. Shao, K. Ding, J. Jie, X. Zhang, 12.35% efficient graphene quantum dots/silicon heterojunction solar cells using graphene transparent electrode, Nano Energy 31 (2017) 359–366.
[88] H.K. Jun, M.A. Careem, A.K. Arof, Quantum dot-sensitized solar cells—perspective and recent developments: a review of Cd chalcogenide quantum dots as sensitizers, Renew. Sustain. Energy Rev. 22 (2013) 148–167.
[89] X. Zhang, Y. Zhang, L. Yan, C. Ji, H. Wu, Y. Wang, et al., High photocurrent PbSe solar cells with thin active layers, J. Mater. Chem. A 3 (2015) 8501–8507.
[90] Q. Wu, J. Hou, H. Zhao, Z. Liu, X. Yue, S. Pengc, et al., Charge recombination control for high efficiency CdS/CdSe quantum dot co-sensitized solar cells with multi-ZnS layers, Dalton Trans. 47 (2018) 2214–2221.
[91] K. Surana, I.T. Salisu, R.M. Mehra, B. Bhattacharya, A simple synthesis route of low temperature CdSe-CdS core-shell quantum dots and its application in solar cell, Opt. Mater. 82 (2018) 135–140.
[92] S. He, H. Lu, B. Li, J. Zhang, G. Zeng, L. Wu, et al., Study of CdTe/ZnTe composite absorbing layer deposited by pulsed laser deposition for CdS/CdTe solar cell, Mater. Sci. Semicond. Process 67 (2017) 41–45.
[93] M.A. Leontiadou, E.J. Tyrrell, C.T. Smith, D.E. Velazquez, R. Page, P. Brien, et al., Influence of elevated radiative lifetime on efficiency of CdSe/CdTe type II colloidal quantum dot based solar cells, Sol. Energy Mater. Sol. Cells 159 (2017) 657–663.
[94] A.M. Al-Zuhery, S.M. Al-Jawad, A.K. Al-Mouso, The effect of PbS thickness on the performance of CdS/PbS solar cell prepared by CSP, Optik 130 (2017) 666–672.
[95] S. Jindal, M. Giripunje, Potential effect of $CuInS_2$/ZnS core-shell quantum dots on P3HT/PEDOT:PSS, heterostructure based solar cell, Opt. Laser Technol. 103 (2018) 212–218.
[96] T.T. Johna, M. Mathew, C.S. Kartha, K.P. Vijayakumar, T. Abe, Y. Kashiwaba, $CuInS_2/In_2S_3$ thin film solar cell using spray pyrolysis technique having 9.5% efficiency, Sol. Energy Mater. Sol. Cells 89 (2005) 27–36.

[97] Z. Chen, W. Peng, K. Zhang, J. Zhang, X. Yang, Y. Numata, et al., Band alignment by ternary crystalline potential-tuning interlayer for efficient electron injection in quantum dot-sensitized solar cells, J. Mater. Chem. A 2 (2014) 7004–7014.
[98] Z. Pan, K. Zhao, J. Wang, H. Zhang, Y. Feng, X. Zhong, Near infrared absorption of $CdSe_xTe_{1-x}$ alloyed quantum dot sensitized solar cells with more than 6% efficiency and high stability, ACS Nano 7 (2013) 5215–5222.
[99] J. Yang, T. Oshima, W. Yindeesuk, Z. Pan, X. Zhong, Q. Shen, Influence of linker molecules on interfacial electron transfer and photovoltaic performance of quantum dot sensitized solar cells, J. Mater. Chem. A 2 (2014) 20882–20888.
[100] J. Luo, H. Wei, F. Li, Q. Huang, D. Li, Y. Luo, et al., Microwave assisted aqueous synthesis of core-shell $CdSe_xTe_{1-x}$–CdS quantum dots for high performance sensitized solar cells, Chem. Commun. 50 (2014) 3464–3466.
[101] H. McDaniel, N. Fuke, N.S. Makarov, J.M. Pietryga, V.I. Klimov, An integrated approach to realizing high-performance liquid-junction quantum dot sensitized solar cells, Nat. Commun. 4 (2013) 2887.
[102] Z. Pan, K. Zhao, J. Wang, H. Zhang, Y. Feng, X. Zhong, Near infrared absorption of $CdSe_xTe_{1-x}$ alloyed quantum dot sensitized solar cells with more than 6% efficiency and high stability, ASC Nano 6 (2013) 5215–5222.
[103] J. Du, Z. Du, J.S. Hu, Z. Pan, Q. Shen, J. Sun, et al., Zn − Cu − In − Se quantum dot solar cells with a certified power conversion efficiency of 11.6%, J. Am. Chem. Soc. 138 (2016) 4201–4209.
[104] W. Wang, W. Feng, J. Du, W. Xue, L. Zhang, L. Zhao, et al., Cosensitized quantum dot solar cells with conversion efficiency over 12%, Adv. Mater. 30 (2018) 1705746–1705752.
[105] W. Peng, J. Du, Z. Pan, N. Nakazawa, J. Sun, Z. Du, et al., Alloying strategy in Cu − In − Ga − Se quantum dots for high efficiency quantum dot sensitized solar cells, ACS Appl. Mater. Interfaces 9 (2017) 5328–5336.
[106] H. Sun, L. Wu, W. Wei, X. Qu, Recent advances in graphene quantum dots for sensing, Mater. Today 11 (2013) 433–442.
[107] H.S. Hojaghan, M.S. Niasari, Degradation of methylene blue as a pollutant with N-doped graphene quantum dot/titanium dioxide nanocomposite, J. Clean. Prod. 148 (2017) 31–36.
[108] J. Shen, Y. Zhu, X. Yang, C. Li, Graphene quantum dots: emergent nanolights for bioimaging, sensors, catalysis and photovoltaic devices, Chem. Commun. 48 (2012) 3686–3699.
[109] G. Liu, K. Zhang, K. Ma, A. Care, M.R. Hutchinsond, E.M. Goldys, Graphene quantum dot based "switch-on" nanosensors for intracellular cytokine monitoring, Nanoscale 9 (2017) 4934–4943.
[110] K. Tian, F. Nie, K. Luo, X. Zheng, J. Zheng, A sensitive electrochemiluminescence glucose biosensor based on graphene quantum dot prepared from graphene oxide sheets and hydrogen peroxide, J. Electroanal. Chem. 801 (2017) 162–170.
[111] M. Dutta, S. Sarkar, T. Ghosh, D. Basa, ZnO/graphene quantum dot solid-state solar cell, J. Phys. Chem. C 116 (2012) 20127–20131.
[112] Y. Qin, Y. Cheng, L. Jiang, X. Jin, M. Li, X. Luo, et al., Top-down strategy toward versatile graphene quantum dots for organic/inorganic hybrid solar cells, ACS Sustain. Chem. Eng. 3 (2015) 637–644.
[113] X. Li, M. Rui, J. Song, Z. Shen, H. Zeng, Carbon and graphene quantum dots for optoelectronic and energy devices: a review, Adv. Funct. Mater. 25 (2015) 4929–4947.
[114] S. Bak, D. Kim, H. Lee, Graphene quantum dots and their possible energy applications: a review, Curr. Appl. Phys. 16 (2016) 1192–1201.

[115] Y. Zhong, H. Zhang, D. Pan, L. Wang, X. Zhong, Graphene quantum dots photovoltage and efficiency enhancement in CdSe quantum dot solar cell sensitized solar cells, J. Eng. Chem. 24 (2015) 722–728.
[116] M.M. Tavakoli, H. Aashuri, A. Simchi, S. Kalytchuk, Z. Fan, Quasi core/shell lead sulfide/graphene quantum dots for bulk heterojunction solar cells, J. Phys. Chem. C 119 (2015) 18886–18895.
[117] S. Ruhle, M. Shalom, A. Zaban, Quantum-dot-sensitized solar cells, ChemPhysChem 11 (2010) 2290–2304.
[118] Y. Choi, M. Seol, W. Kim, K. Yong, Chemical bath deposition of stoichiometric CdSe quantum dots for efficient quantum-dot-sensitized solar cell application, J. Phys. Chem. C 118 (2014) 5664–5670.
[119] J. Qiu, B. Weng, W. Ge, L.L. McDowell, Z. Ca, Z. Shi, A broadband Pb-chalcogenide/CdS solar cells with tandem quantum-dots embedded in the bulk matrix (QDiM) absorption layers by using chemical bath deposition, Sol. Energy Mater. Sol. Cells 172 (2017) 117–123.
[120] D. Sharma, R. Jha, S. Kumar, Quantum dot sensitized solar cell: recent advances and future perspectives in photoanode, Sol. Energy Mater. Sol. Cells 155 (2016) 294–322.
[121] S. Gimenez, I. Mora-Sero, L. Macor, N. Guijarro, T. Lana-Villarreal, R. Gomez, et al., Nanotechnology 20 (2009) 295204.
[122] G. Zhu, L. Pan, T. Xu, Z. Sun, CdS/CdSe-cosensitized $TiO_2$ photoanode for quantum-dot-sensitized solar cells by a microwave-assisted chemical bath deposition method, ACS Appl. Mater. Interfaces 3 (2011) 3146–3151.
[123] L. Tao, Y. Xiong, H. Liu, W. Shen, High performance PbS quantum dot sensitized solar cells via electric field assisted in situ chemical deposition on modulated TiO2 nanotube array, Nanoscale 6 (2014) 931–938.
[124] Y. Choi, M. Seol, W. Kim, K. Yong, Chemical bath deposition of stoichiometric CdSe quantum dots for efficient quantum-dot-sensitized solar cell application, J. Phys. Chem. 118 (2014) 5664–5670.
[125] N. Syafiqah, M. Mustakim, C.A. Ubani, S. Sepeai, N.A. Ludin, M.A.M. Teridi, et al., Quantum dots processed by SILAR for solar cell applications, Sol. Energy 163 (2018) 256–270.
[126] J. Du, X. Meng, K. Zhao, Y. Li, X. Zhong, Performance enhancement of quantum dot sensitized solar cells by adding electrolyte additives, ACS Appl. Mater. Interfaces 6 (2014) 19378–19384.
[127] H. Rao, W. Wu, Y. Liu, Y. Xu, B. Chen, H. Chen, et al., CdS/CdSe co-sensitized vertically aligned anatase TiO2 nanowire arrays for efficient solar cells, Nano Energy 8 (2014) 1–8.
[128] J. Wang, M.M. Rahman, C. Ge, J.J. Lee, Electrodeposition of $Cu_2S$ nanoparticles on fluorine-doped tin oxide for efficient counter electrode of quantum-dot-sensitized solar cells, J. Ind. Eng. Chem. 62 (2018) 185–191.
[129] S.V. Mahajan, J. Cho, M.S.P. Shaffer, A.R. Boccaccini, J.H. Dickerson, Electrophoretic deposition and characterization of $Eu_2O_3$ nanocrystal carbon-nanotube heterostructures, J. Eur. Ceram. Soc. 30 (2010) 1145–1150.
[130] S.V. Mahajan, J.H. Dickerson, Dielectric properties of colloidal $Gd_2O_3$ nanocrystal films fabricated via electrophoretic deposition, Appl. Phys. Lett. 96 (2010) 113105.
[131] S. Ameen, M.S. Akhtar, S.G. Ansari, O.B. Yang, H.S. Shin, Electrophoretically deposited polyaniline/ZnO nanoparticles for P-N heterostructure diodes, Superlattices Microstruct. 46 (2009) 872–880.
[132] V. Svrcek, I. Turkevych, K. Hara, M. Kondo, Ordered titanium dioxide nanotubes filled with photoluminescent surfactant-free silicon nanocrystals, Nanotechnology 21 (2010) 215203.

[133] M.N. Patel, R.D. Williams, R.A. May, H. Uchida, K.J. Stevenson, K.K.P. Johnston, Electrophoretic deposition of Au nanocrystals inside perpendicular mesochannels of $TiO_2$, Chem. Mater. 20 (2008) 6029–6604.
[134] L. Grinis, S. Dor, A. Ofir, A. Zaban, Electrophoretic deposition and compression of titania nanoparticle films for dye-sensitized solar cells, J. Photochem. Photobiol. A 198 (2008) 52–59.
[135] B. Ferrari, A. Bartret, C. Baudin, Sandwich materials formed by thick alumina tapes and thin-layered alumina-aluminium titanate structures shaped by EPD, J. Eur. Ceram. Soc. 29 (2009) 1083–1092.
[136] M. Vidotti, S.I.C. de Torresi, Electrostatic layer-by-layer and electrophoretic depositions as methods for electrochromic nanoparticle immobilization, Electrochim. Acta 54 (2009) 2800–2804.
[137] M.Y. Gao, J.Q. Sun, E. Dulkeith, N. Gaponik, U. Lemmer, J. Feldmann, Lateral patterning of CdTe nanocrystal films by the electric field directed layer-by-layer assembly method, Langmuir 18 (2002) 4098–4102.
[138] J.Q. Sun, M.Y. Gao, J. Feldmann, Electric field directed layer-by-layer assembly of highly fluorescent CdTe nanoparticles, J. Nanosci. Nanotechnol. 1 (2001) 133–136.
[139] A. Salant, M. Shalom, I. Hod, A. Faust, A. Zaban, U. Banin, Quantum dot sensitized solar cells with improved efficiency prepared using electrophoretic deposition, ACS Nano 4 (2010) 5962–5968.
[140] N.J. Smith, K.J. Emmett, S.J. Rosenthal, Photovoltaic cells fabricated by electrophoretic deposition of CdSe nanocrystals, Appl. Phys. Lett. 93 (2008) 043504.
[141] P. Brown, P.V. Kamat, Quantum dot solar cells. Electrophoretic deposition of CdSe-C-60 composite films and capture of photogenerated electrons with nC(60) cluster shell, J. Am. Chem. Soc. 130 (2008) 8890–8891.
[142] B. Farrow, P.V. Kamat, CdSe quantum dot sensitized solar cells. Shuttling electrons through stacked carbon nanocups, J. Am. Chem. Soc. 131 (2009) 11124–11131.
[143] M.M. Kamazani, Z. Salehi, K. Motevalli, Enhancement of quantum dot-sensitized solar cells performance using $CuInS_2$–$Cu_2S$ nanocomposite synthesized by a green method, Appl. Phys. A 123 (2017) 691–698.
[144] Z. Pan, H. Zhang, K. Chang, Y. Hou, J. Hua, X. Zhong, Highly efficient inverted Type-I CdS/CdSe core/shell structure QD-sensitized solar cells, ACS Nano 6 (2012) 3982–3991.
[145] Z. Pan, I. Mora-Sero, Q. Shen, H. Zhang, Y. Li, K. Zhao, et al., High-efficiency "green" quantum dot solar cells, J. Am. Chem. Soc. 136 (25) (2014) 9203–9210.
[146] H. Zhang, J. Tong, W. Fang, N. Qian, Q. Zhao, Efficient flexible counter electrode based on modified graphite paper and in situ grown copper sulfide for quantum dot sensitized solar cells, ACS Appl. Energy Mater. 1 (2018) 1355–1363.
[147] S.S. Khalili, H. Dehghani, M. Afrooz, Composite films of metal doped CoS/carbon allotropes; efficient electrocatalyst counter electrodes for high performance quantum dot-sensitized solar cells, J. Colloid Interface Sci. 493 (2017) 32–41.
[148] K. Meng, G. Chen, K.R. Thampi, Metal chalcogenides as counter electrode materials in quantum dot sensitized solar cells: a perspective, J. Mater. Chem. A 3 (2015) 23074–23089.
[149] B. Yuan, Q. Gao, X. Zhang, L. Duan, L. Chen, Z. Mao, et al., Reduced graphene oxide (RGO)/$Cu_2S$ composite as catalytic counter electrode for quantum dot-sensitized solar cells, Electrochim. Acta 277 (2018) 50–58.
[150] Q. Shen, A. Yamada, S. Tamura, T. Toyoda, CdSe quantum dot-sensitized solar cell employing $TiO_2$ nanotubeworking-electrode and $Cu_2S$ counter-electrode, Appl. Phys. Lett. 97 (2010) 123107.

[151] Y.Y. Yang, Q.X. Zhang, T.Z. Wang, L.F. Zhu, X.M. Huang, Y.D. Zhang, et al., Novel tandem structure employing mesh-structured $Cu_2S$ counter electrode forenhanced performance of quantum dot-sensitized solar cells, Electrochim. Acta 88 (2013) 44–50.
[152] C.D. Sunesh, C.V.V.M. Gopi, M. Panthakkal, A. Muthalif, H.J. Kim, Y. Choe, Improving the efficiency of quantum-dot-sensitized solar cells by optimizing the growth time of the CuS counter electrode, Appl. Surf. Sci. 416 (2017) 446–453.
[153] C.D. Sunesh, C.V.V.M. Gopi, M. Panthakkal, A. Muthalif, H.J. Kim, Y. Choe, $H_3PO_4$ treated surface modified CuS counter electrodes with high electrocatalytic activity for enhancing photovoltaic performance of quantum dot-sensitized solar cells, Appl. Surf. Sci. Volume 440 (2018) 1022–1026.
[154] C.V.V.M. Gopi, S.S. Rao, S.K. Kim, D. Punnoose, H.J. Kim, Highly effective nickel sulfide counter electrode catalyst prepared by optimal hydrothermal treatment for quantum dot-sensitized solar cells, J. Power Sour. 275 (2015) 547–556.
[155] H.J. Kim, S.W. Kim, C.V.V.M. Gopi, S.K. Kim, S.S. Rao, M.S. Jeong, Improved performance of quantum dot-sensitized solar cells adopting a highly efficient cobalt sulfide/nickel sulfide composite thin film counter electrode, J. Power Sour. 268 (2014) 163–170.
[156] B.B. Jin, G.Q. Zhang, S.Y. Kong, X. Quan, H.S. Huang, Y. Liu, et al., Pulsed voltage deposited hierarchical dendritic PbS film as a highly efficient and stable counter electrode for quantum-dot-sensitized solar cells, J. Mater. Chem. C 6 (2018) 6823–6831.
[157] M. Que, W. Guo, X. Zhang, X. Li, Q. Hua, L. Dong, et al., Flexible quantum dot-sensitized solar cells employing CoS nanorod arrays/graphite paper as effective counter electrodes, J. Mater. Chem. A 2 (2014) 13661–13666.
[158] Y. Zhang, C. Shi, X. Dai, F. Liu, X. Fang, J. Zhu, Pyrolysis preparation of $Cu_2ZnSnS_4$ thin film and its application to counter electrode in quantum dotsensitized solar cells, Electrochim. Acta 118 (2014) 41–44.
[159] Y. Jiang, X. Zhang, Q.Q. Ge, B.B. Yu, Y.G. Zou, W.J. Jiang, et al., ITO@$Cu_2S$ tunnel junction nanowire arrays as efficient counter electrode for quantum-dotsensitized solar cells, Nano Lett. 4 (2014) 365–372.
[160] K. Zhao, H.J. Yu, H. Zhang, X.H. Zhong, J electroplating cuprous sulfide counter electrode for high-efficiency long-term stability quantum dot sensitized solar cells, Phys. Chem. C 18 (2014) 5683–5690.
[161] C. Shen, L. Sun, Z.Y. Koh, Q. Wang, Cuprous sulfide counter electrodes prepared by ion exchange for high-efficiency quantum dotsensitized solar cells, J. Mater. Chem. A 2 (2014) 2807–2813.
[162] B.Z. Fang, M. Kim, S.Q. Fan, J.H. Kim, D.P. Wilkinson, J. Ko, et al., Facile synthesis of open mesoporous carbon nanofibers with tailored nanostructure as a highly efficient counter electrode in CdSe quantum-dot-sensitized solar cells, J. Mater. Chem. 21 (2011) 8742–8748.
[163] M. Seol, E. Ramasamy, J. Lee, K. Yong, Highly efficient and durable quantum dot sensitized ZnO nanowire solar cell using noble-metal-free counter electrode, J. Phys. Chem. C 115 (2011) 22018–22024.
[164] J.H. Dong, S.P. Jia, J.Z. Chen, B. Li, J.F. Zheng, J.H. Zhao, et al., Nitrogen-doped hollow carbon nanoparticles as efficient counter electrodes in quantum dot sensitized solar cells, J. Mater. Chem. 22 (2012) 9745–9750.
[165] P. Subramanyam, P. Ghosal, M. Deepa, C. Subrahmanyam, Cuprous sulfide@-carbon nanostructures based counter electrodes with cadmium sulfide/titania photoanode for liquid junction solar cells, Electrochim. Acta 278 (2018) 374–384.

[166] S. Ahmad, J.H. Yum, Z. Xianxi, M. Grätzel, H.J. Butt, M.K. Nazeeruddin, Dye-sensitized solar cells based on poly(3,4-ethylenedioxythiophene) counter electrode derived from ionic liquids, J. Mater. Chem. 20 (2010) 1654.
[167] M.H. Yeh, C.P. Lee, C.Y. Chou, L.Y. Lin, H.Y. Wei, C.W. Chuc, R. Vittal, K. C. Ho, Conducting polymer-based counter electrode for a quantum-dot-sensitized solar cell (QDSSC) with a polysulfide electrolyte, Electrochim. Acta 57 (2011) 277–284.
[168] R. Dang, Y. Wang, J. Zeng, Z. Huang, Z. Feid, P.J. Dyson, Benzimidazolium salt-based solid-state electrolytes afford efficient quantum-dot sensitized solar cells, J. Mater. Chem. A 5 (2017) 13526–13534.
[169] H. Song, H. Rao, X. Zhong, Recent advances in electrolytes for quantum dotsensitized solar cells, J. Mater. Chem. A 6 (2018) 4895–4911.
[170] J.K. Sun, Y. Jiang, X. Zhong, J.S. Hu, L.J. Wan, Three-dimensional nanostructured electrodes for efficient quantum-dot-sensitized solar cells, Nano Energy 32 (2017) 130156.
[171] S. Jiao, J. Du, Z. Du, D. Long, W. Jiang, Z. Pan, et al., Nitrogen-doped mesoporous carbons as counter electrodes in quantum dot sensitized solar cells with a conversion efficiency exceeding 12%, J. Phys. Chem. Lett. 8 (2017) 559–564.
[172] M. Kouhnavard, S. Ikeda, N.A. Ludin, N.B. Ahmad Khairudin, B.V. Ghaffari, M. A. Mat-Teridi, et al., A review of semiconductor materials as sensitizers for quantum dot-sensitized solar cells, Renew. Sustain. Energy Rev. 37 (2014) 397–407.
[173] S.Y. Chae, Y.J. Hwang, O.S. Joo, Role of HA additive in quantum dot solar cell with $Co[(bpy)_3]^{2+/3+}$-based electrolyte, RSC Adv. 4 (2014) 26907–26911.
[174] Y. Tachibana, H.Y. Akiyama, Y. Ohtsuka, T. Torimoto, S. Kuwabata, CdS quantum dots sensitized $TiO_2$ sandwich type photoelectrochemical solar cells, Chem. Lett. 36 (2007) 88–95.
[175] K. Zhao, Z.X. Pan, I. Mora-Seró, et al., Boosting power conversion efficiencies of quantum-dot-sensitized solar cells beyond 8% by recombination control, J. Am. Chem. Soc. 137 (2015) 5602–5609.
[176] L. Li, X.C. Yang, J.J. Gao, H.N. Tian, J.Z. Zhao, A. Hagfeldt, et al., Highly efficient CdS quantum dot-sensitized solar cells based on a modified polysulfide electrolyte, J. Am. Chem. Soc. 133 (2011) 8458–8460.
[177] S. Chaudhuri, D. Bhattacharyya, A. Maity, A. Pal, Surface coatings for solar application, Mater. Sci. Forum 246 (1997) 181–206.
[178] M. Guvench, C. Gurcan, K. Durgin, D. MacDonald, Solar simulator and IV measurement system for large area solar cell testing, in: Proceedings of the 2004 American Society for Engineering Education Annual Conference & Exposition 9, 2004, p. 1.
[179] R. Sinton, A. Cuevas, A quasi-steady-state open-circuit voltage method for solar cell characterization, in: Proceedings of the 16th European Photovoltaic Solar Energy Conference, 2000.
[180] A.K. Rath, T. Lasanta, M. Bernechea, S.L. Diedenhofen, G. Konstantatos, Determination of carrier lifetime and mobility in colloidal quantum dot films via impedance spectroscopy, Appl. Phys. Lett. 104 (2014) 063504.
[181] Y. Wang, J.B. Asbury, T. Lian, Ultrafast excited-state dynamics of Re (Co) 3Cl (dcbpy) in solution and on nanocrystalline $TiO_2$ and $ZrO_2$ thin films, J. Phys. Chem. A 104 (2000) 4291–4299.
[182] L.M. Peter, Dye-sensitized nanocrystalline solar cells, Phys. Chem. Chem. Phys. 9 (2007) 2630–2642.
[183] H.J. Kim, B. Ko, C.V.V.M. Gopi, M.V. Haritha, Y.S. Lee, Facile synthesis of morphology dependent CuS nanoparticle thin film as a highly efficient counter electrode for quantum dot-sensitized solar cells, J. Electroanal. Chem. 791 (2017) 95–102.

[184] F. Ren, S. Li, C. He, Electrolyte for quantum dot-sensitized solar cells assessed with cyclic voltammetry, Sci. China Mater. 58 (2015) 490–495.
[185] M.E. Meral, F. Dinçer, A review of the factors affecting operation and efficiency of photovoltaic based electricity generation systems, Renew. Sustain. Energy Rev. 15 (2011) 2176–2184.
[186] D. Ghosh, G. Halder, A. Sahasrabudhe, S. Bhattacharyya, Microwave synthesized $Cu_xS$ and graphene oxide nanoribbon composite as highly efficient counter electrode for quantum dot sensitized solar cells, Nanoscale 8 (2016) 10632–10641.
[187] H. Yufeng, W. Jixiao Wang, H. Zhang, S. Zha, Q. Ma, Z. Wang, Electrochemical impedance spectroscopy (EIS): an efficiency method to monitor resin curing processes, Sens. Actuators 250 (2016) 78–86.
[188] J.K.R.G. Balakrishna, A review on electrical characterization techniques performed to study the device performance of quantum dot sensitized solar cells, Sol. Energy 159 (2018) 682–696.
[189] J.F. Rubinson, Y.P. Kayinamura, Charge transport in conducting polymers: insights from impedance spectroscopy, Chem. Soc. Rev. 38 (2009) 3339–3347.
[190] B.Y. Chang, S.M. Park, Electrochemical impedance spectroscopy, Annu. Rev. Anal. Chem. 3 (2010) 207–229.
[191] R.P. Venkatesh, B.J. Cho, S. Ramanathan, J.G. Park, Electrochemical impedance spectroscopy (EIS) analysis of BTA removal by TMAH during post Cu CMP cleaning process, J. Electrochem. Soc. 159 (2012) 447–452.
[192] J.W. Ondersma, T.W. Hamann, Impedance investigation of dye-sensitized solar cells employing outer-sphere redox shuttles, J. Phys. Chem. C 114 (2010) 638–645.
[193] L. Han, N. Koide, Y. Chiba, T. Mitate, Modeling of an equivalent circuit for dye-sensitized solar cells, Appl. Phys. Lett. 84 (2004) 2433–2435.
[194] R. Kern, R. Sastrawan, J. Ferber, R. Stangl, J. Luther, Modeling and interpretation of electrical impedance spectra of dye solar cells operated under open-circuit conditions, Electrochim. Acta 47 (2002) 4213–4225.
[195] K. Szendrei, W. Gomulya, M. Yarema, W. Heiss, M. Loi, PbS nanocrystal solar cells with high efficiency and fill factor, Appl. Phys. Lett. 97 (20) (2010) 203501.
[196] J.R. Macdonald, Impedance spectroscopy, Ann. Biomed. Eng. 20 (1992) 289–305.
[197] K.W. Johnston, A.G.P. Abraham, J.P. Clifford, S.H. Myrskog, S. Hoogland, H. Shukla, et al., Efficient Schottky-quantumdot photovoltaics: the roles of depletion, drift, and diffusion, Appl. Phys. Lett. 92 (2008) 122111.
[198] M. Igalson, C.P. Björkman, The influence of buffer layer on the transient behavior of thin film chalcopyrite devices, Sol. Energy Mater. Sol. Cells 84 (2004) 93–103.
[199] T. Walter, R. Herberholz, C. Müller, H. Schock, Determination of defect distributions from admittance measurements and application to Cu (In, Ga) $Se_2$ based heterojunctions, J. Appl. Phys. 80 (1996) 4411–4420.
[200] R. Green, Hall effect measurements in materials characterization, White Paper (2011) 3111.
[201] D. Bozyigit, V. Wood, Electrical characterization of nanocrystal solids, J. Mater. Chem. C 2 (2004) 3172–3184.
[202] J. Harper, X.D. Wang, I-V, CV and AC impedance techniques and characterizations of photovoltaic cells, in: The 7th National Conference on Functional Materials and Applications 92, 2010.
[203] S.M.N. Sze, K. Kwok, Physics of Semiconductor Devices, John Wiley & Sons, Hoboken, NJ, 2006.
[204] A.S. Bondarenko, G.A. Ragoisha, Variable Mott-Schottky plots acquisition by potentiodynamic electrochemical impedance spectroscopy, J. Solid State Electrochem. 9 (2005) 845–849.

## Further reading

M. Wolf, R. Brendel, J.H. Werner, H.J. Queisser, Solar cell efficiency and carrier multiplication in alloys, J. Appl. Phys. 83 (1998) 4213–4221.

M. Giersig, P. Mulvaney, Formation of ordered two dimensional gold colloid lattices by electrophoretic deposition, J. Phys. Chem. 97 (1993) 6334–6336.

M.P.A.M. Chozhidakath, D. Sunesh, Y. Choe, Improved photovoltaic performance of quantum dot-sensitized solar cells based on highly electrocatalytic Ca-doped CuS counter electrodes, J. Photochem. Photobiol. A 358 (2018) 177–185.

J. Xu, H. Xue, X. Yang, H. Wei, W. Li, Z. Li, et al., Synthesis of honeycomb-like mesoporous pyrite $FeS_2$ microspheres as efficient counter electrode in quantum dots sensitized solar cells, Small 10 (2014) 4754–4759.

This page intentionally left blank

# CHAPTER 12

# Perovskite solar cells

**Junming Li, Qiong Wang and Antonio Abate**
Helmholtz Center for Materials and Energy, Berlin, Germany

## Contents



## 12.1 Introduction

Halide perovskites were first used as visible-light sensitizers in dye-sensitize liquid junction solar cells with a power conversion efficiency (PCE) of 3%–4% in 2009 [1]. Halide perovskites exhibit outstanding optoelectronic properties that make this type of semiconductor a huge success in photovoltaic applications [2]. A long-term durable perovskite solar cell (PSC) with a PCE of 9.7% was reported in 2012. After that, tremendous research has been conducted, focusing on the optoelectronic application of halide perovskites as well as the investigation of the abnormal electronic properties of the materials [3]. Today, a certified PCE of 23.3% has been reported, which is comparable to single crystalline silicon

*Nanomaterials for Solar Cell Applications*
DOI: https://doi.org/10.1016/B978-0-12-813337-8.00012-6

(24.4%) and polycrystalline silicon solar cells (19.9%) [4,5]. The notable achievements in PSCs are attributed to the tunable bandgap of perovskites, spanning from 1.2 to 2.4 eV [6], long charge carrier diffusion length [7], development of new perovskite materials, and advances in perovskite film deposition. The stability of halide perovskites has been the main obstacle for the commercialization. Understanding the degradation mechanism of PSCs and the device architecture may give the answer for the long-term stability in PSCs. As presented in the follow section, we will give a brief introduction about the basic physical properties of these perovskite materials and the solar cells based on them.

## 12.2 Halide perovskite materials

### 12.2.1 Structural properties

Halide perovskites adopt the general chemical formula of $AMX_3$, where $A$ is the organic or inorganic cation, $M$ is the metal, and $X$ is the halogen. The stability of the crystal structure is highly dependent on the size of organic cation and the interaction between the organic cation and the corner-sharing $MX_6^{4-}$ octahedral. The Goldschmidt tolerance factor $t$ is a reliable empirical index to predict whether or not a stable perovskite structure can be formed or presented, defined in the following equation: [8]

$$t = \frac{r_A + r_X}{\sqrt{2}(r_A + r_M)} \tag{12.1}$$

where $r_A$, and $r_M$, and $r_X$ are the radii of the organic/inorganic cation, metal ion, and halide ions. In halide perovskites, the cell parameters increase as the halide changes from chlorine ($Cl^-$, $r_{Cl^-} = 1.81$ Å), bromine ($Br^-$, $r_{Br^-} = 1.96$ Å) to iodine ($I^-$, $r_{I^-} = 2.2$ Å). The most commonly used inorganic or organic monovalent cations include methylammonium ($MA^+$, $r_{MA^+} = 1.8$ Å) [9], formamidinium ($FA^+$, $r_{FA^+} = 1.9-2.2$ Å), rubidium ($Rb^+$, $r_{Rb^+} = 2.9$ Å), and cesium ($Cs^+$, $r_{Cs^+} = 3$ Å) [10–12]. The suitable divalent metal ions based on Eq. (12.1) include tin ($Sn^{2+}$, $r_{Sn^{2+}} = 1.1$ Å) and lead ($Pb^{2+}$, $r_{Pb^{2+}} = 1.19$ Å). When $t$ equals to 1, it induces a cubic symmetry and is composed of a backbone of a corner sharing $MX_6$-octahedral with cuboctahedra voids occupied by the A-cation, as shown in Fig. 12.1.

Most of the known halide perovskites have $t$ values in the range of 0.75–1.00 at room temperature, with an orthorhombic, rhombohedral,

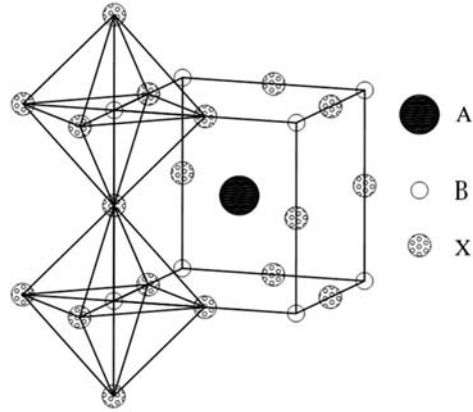


**Figure 12.1** Cubic perovskite structure of $AMX_3$, where *A* cation occupies the lattice corners, *M* cation occupies the interstitial site, and *X* anions occupy the lattice faces. *Adapted from literature G.E. Eperon, et al., Formamidinium lead trihalide: a broadly tunable perovskite for efficient planar heterojunction solar cells, Energy Environ. Sci. 7 (3) (2014) 982–988. ©2008 Wiley-VCH.*

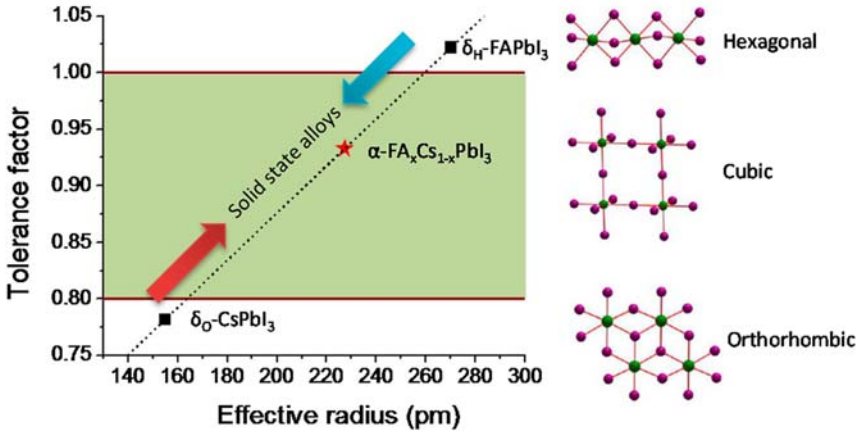


**Figure 12.2** Correlations between tolerance factor and halide perovskites crystal structures. *Adapted from literature Z. Li, et al., Stabilizing perovskite structures by tuning tolerance factor: formation of formamidinium and cesium lead iodide solid-state alloys, Chem. Mater. 28 (1) (2015) 284–292. ©2015 American Chemical Society.*

or tetragonal structure [14–17]. If *t* is larger than 1, this means that a non-perovskite phase will be formed. The correlation between the perovskite crystal structure and the tolerance factor is schematically illustrated in Fig. 12.2.

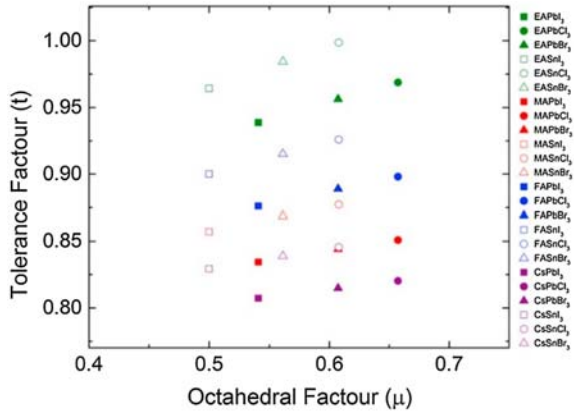


**Figure 12.3** Calculated octahedral factor and tolerance factors for various combinations of halide perovskites. *Adapted from literature Q. Chen, et al., Under the spotlight: the organic–inorganic hybrid halide perovskite for optoelectronic applications, Nano Today 10 (3) (2015) 355–396 [18].* ©*2015 Elsevier.*

Complementing the Goldschmidt tolerance factor, the octahedral factor $\mu$ was developed to assess the fit of $M$ cation into the $X_6$ octahedron, which is defined as: [13]

$$\mu = \frac{r_M}{r_X} \tag{12.2}$$

where $r_M$ and $r_X$ are the ionic radii of $M$ cation and $X$ anion, respectively. A plot of $\mu$ against $t$ of common halide perovskites can be constructed. Fig. 12.3 show a range of tolerance and octahedral factors that allow in a perovskite structure with different $A$, $M$, and $X$ ions.

## 12.2.2 Optoelectronic properties

Although the halide perovskites were studied a decade ago [19–21], only recently they are given enough attention after the successful application in solar cells. In addition to photovoltaic applications, halide perovskites are considered as the most compelling candidate for several optoelectronic applications, such as lasing [22,23], light emitting devices [24–28], and photodetector [29,30].

The operation of a solar cell starts with the light absorption of the photovoltaic material. Compared with conventional photovoltaic materials, the advantages of perovskite material include the high absorption coefficient, and the facile tunnability in their optical band gap. By adjusting

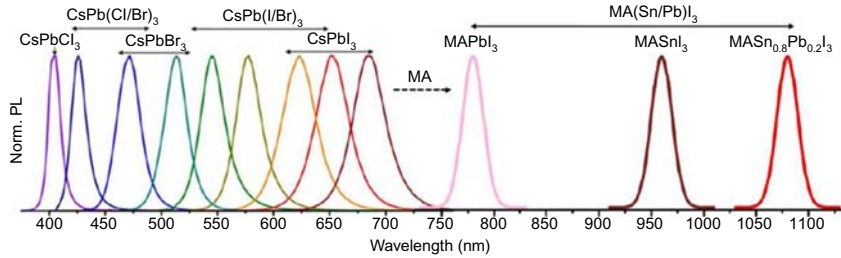


**Figure 12.4** Representative photoluminescence spectra of different compositions from the most blue $CsPbCl_3$ to the most redshifted $CH_3NH_3(Sn_{0.8}/Pb_{0.2})I_3$ perovskite. *Adapted from literature M. Saliba et al., Perovskite solar cells from the atomic to the film level, Angew. Chem. (2017) 2554–2569 [36].* ©*2017 Wiley-VCH.*

the radius of cations and ions in $AMX_3$, the optical band gap of perovskites can be tuned from 1.36 eV ($CH_3NH_3SnI_3$) to 3.06 eV ($CsPbCl_3$) [31–34]. Doping tin-perovskite with a small amount of lead leads to a further decrease in the optical band gap. The most lowest optical band gap is of 1.15 eV achieved by the lead-tin mix composition $CH_3NH_3Sn_{0.8}Pb_{0.2}I_3$ [35] (Fig. 12.4).

The absorption coefficient ($\alpha$) defines how efficient the material absorbs the light. In general, a semiconductor that has a direct band gap shows a higher absorption coefficient than an indirect semiconductor. For indirect bandgap material, the light abortion requires a phonon assisted transition. A direct bandgap doesn't need the additional phonon assisted transition, which usually results in a stronger absorption coefficient [37]. Halide perovskites used in photovoltaic are direct band gap materials that exhibit a strong absorption. The measurement of the absorption coefficient of $CH_3NH_3PbI_3$ is given in Fig. 12.5 [38]. The absorption coefficient of $CH_3NH_3PbI_3$ was estimated to be $1.5 \times 10^4\ cm^{-1}$ at 550 nm, indicating that the penetration depth for 550 nm light is approximately 0.66 μm, and it increases to 2 μm for a 700 nm light with the absorption coefficient of $0.5 \times 10^4\ cm^{-1}$. This means most of the visible light can be absorbed by $CH_3NH_3PbI_3$ film within a layer thinner than 2 μm. Nonlinear absorption, for example, two-photon absorption was also observed in perovskite materials [39,40], the multimodal absorption makes it possible to detect a wider range of light and used as photodetector.

When it is under illumination, the photogenerated charge carriers in a solar cell can be free electron–hole pairs or excitons depending on the nature of the photovoltaic material and the contacts. In particular, the exciton binding energy is an important factor for determining the device

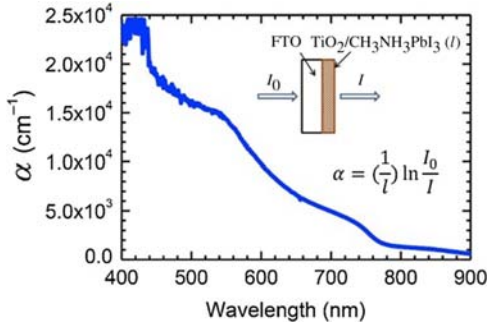


**Figure 12.5** The absorption coefficient as a function of wavelength for the $CH_3NH_3PbI_3$ coated on $TiO_2$ film. $\alpha$ was obtained from $\alpha = (1/l)\ln(I_0/I)$, where $I$, $I_0$, and $l$ are the transmitted light intensity, incident light intensity and $TiO_2$ film thickness, respectively. *Adopted from literature N.-G. Park, Perovskite solar cells: an emerging photovoltaic technology, Materials Today 18 (2) (2015) 65–72. ©2015 Elsevier.*

operation. Usually, if this value is comparable with the thermal energy (around 25 meV at room temperature), excitons will spontaneously dissociate to generate free charge carriers that can be readily collected. In halide perovskite semiconductors, the exciton binding energy is estimated within the range or close to the thermal energy [41,42], thus after light absorption, most free charge carriers are immediately available with no need of additional energy to separate them.

More interestingly, perovskite materials are found intrinsically to be doped with a similar concentration of electrons and holes, and a long balanced carrier diffusion length. For $CH_3NH_3PbI_3$, the electron diffusion length was estimated as 130 nm compared to 100 nm for the hole diffusion length [43]. $CH_3NH_3PbI_3$ prepared from chlorine containing precursors showed even longer diffusion lengths of over 1000 nm for both electrons and holes [38]. Moreover, Dong et al. found that the charge carrier diffusion length of $CH_3NH_3PbI_3$ single crystals exceeds 175 μm under 1 sun (100 mW $cm^{-2}$) illumination and is over 3 mm under weak light for both electrons and holes [44].

## 12.3 Perovskite solar cells

The definition of PSC is commonly used to indicate a large variety of devices employing halide perovskites as the light absorber sandwiched in between electron and hole selective contacts.

### 12.3.1 A historical overview

The PCE of PSCs has increased very rapidly from 3% in 2009 to over 22% nowadays [45]. The first work demonstrating the functioning perovskite-based solar cells was published in 2009, reporting a PCE of 3.8% using $CH_3NH_3PbI_3$ perovskite [1]. In this pioneering work, Kojima et al. demonstrated the perovskite as a sensitizer in a device resembling a dye-sensitized solar cell (DSSC, device structure is shown in Fig. 12.6 [46]), where the perovskite is depicted as a pigment absorbed on the mesoporous $TiO_2$ surface. In the following 2 years, though higher PCE (6.5%) was achieved [47], the stability of such a device structure was rather poor due to the dissolution of the perovskite soaked in the liquid electrolyte employed in the DSSC-like device.

A breakthrough was achieved in 2012 when Lee et al. [48]. and Kim et al. [3]. reported independently, using solid-state hole selective contact in replace of liquid electrolyte, which promoted the efficiency over 9%. After that. the PCE in PSC has experienced a fast enhancement. The growth in efficiency in PSCs in the recent 8 years is summarized in Fig. 12.7. The milestones given in Fig. 12.7 are contributed by the

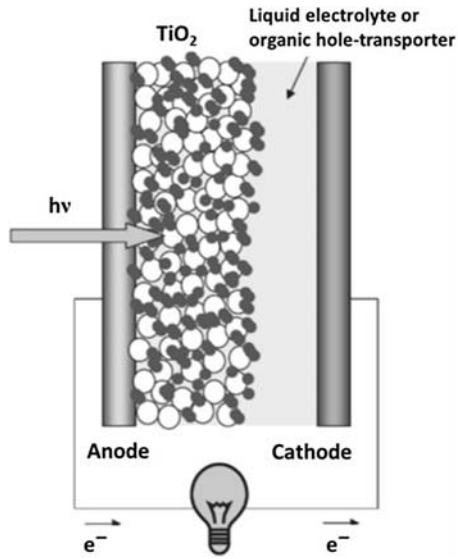


**Figure 12.6** Schematic of a dye-sensitized solar cell. The mesoporous $TiO_2$ (*white circles*) was covered by the dye moleculars (*dark gray dots*). *Adapted from literature H.J. Snaith, L. Schmidt-Mende, Advances in liquid-electrolyte and solid-state dye-sensitized solar cells, Adv. Mater. 19 (20) (2007) 3187–3200. ©2007 Wiley-VCH.*

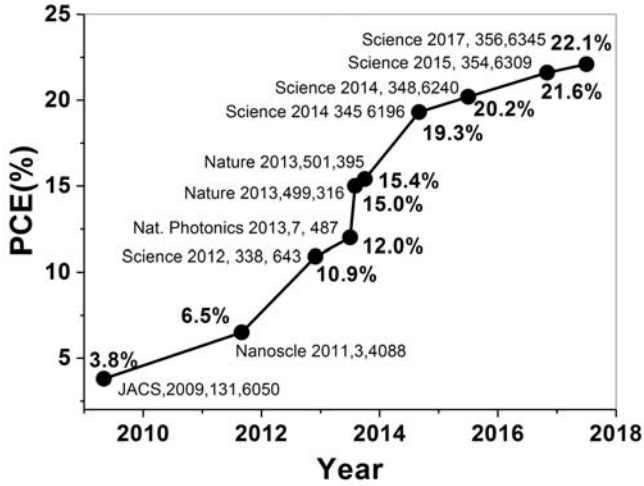


**Figure 12.7** PCE increased quickly from 3.8% to 22.1%. *PCE*, Power conversion efficiency.

following research groups: Heo et al. tried several polymeric hole selective contacts in $CH_3NH_3PbI_3$ PSCs, which lead to a PCE of 12%; [49] Burschka et al. modified the deposition method of perovskite layer using a two-step method, which leads to a PCE of 15.0%; [50] Liu et al. tried another deposition method via physical vapor deposition, which leads to a PCE of 15.4%; [51] Zhou et al. enhanced the conductive of $TiO_2$ by Yttrium-doping, which leads to a PCE of 19.3% for planar structured PSCs; [52] Yang et al. got a certified PCE of 20.2% via intermolecular exchange for $FAPbI_3$ PSCs; [32] Siliba et al. further promoted the PCE to 21.6% by using a quadruple cation perovskite system; [53] Yang et al. reported a certified PCE of 22.1% using iodide management in a double-cation perovskite system [45].

### 12.3.2 Device architectures

The device architectures refer to the choice of charge selective materials, the fabrication techniques, and the compatibility of each component. In general, two typical architectures can be constructed: mesoporous structured PSCs and planar structured PSCs. Until now, the record efficiency is 22.1% for mesoporous structured PSCs [45] and 20.8% for planar structured PSCs [54]. Meanwhile, depending on the flow direction of electrons in devices, PSCs can be classified into "n-i-p" structured and "p-i-n" structured. In "n-i-p" structured PSCs, electrons flow from the

perovskite layer to the beneath electron selective contact and get collected at the contacts where light illuminates on. In "p-i-n" structured PSCs, electrons flow from the perovskite layer to the top electron selective contact and get collected at the metal contact.

#### 12.3.2.1 Mesoporous structured n-i-p perovskite solar cells

The mesoporous structured n-i-p PSCs are composed of transparent conductive oxide, an electron selective layer (ESL), the perovskite active layer, a hole selective layer (HSL), and a metal contact electrode, as shown in Fig. 12.8. Different from planar structured PSCs, mesoporous structured PSCs contain a mesoporous inorganic layer on top of a planar ESL. The most commonly used inorganic metal oxide layer is $TiO_2$. Besides the $TiO_2$ nanoparticles, $TiO_2$ nanocrystals in other shapes (nanorod, nanowires, nanofibers, nanoflower, nanocones) have also been applied [55–63]. Other inorganic materials include $Fe_2O_3$ [64], $ZrO_2$ [65], $SiO_2$ [66–68], and $Zn_2SnO_4$ [69,70].

#### 12.3.2.2 Planar perovskite solar cells

Since the halide perovskites have good charge transport property and high absorption coefficient, mesoporous inorganic layer is not necessarily required to achieve a high PCE in PSCs. Indeed, planar structured PSCs have been developed as a successful architecture. Similar to mesoporous structured PSCs, planar PSCs comprise a transparent conductive electrode, a perovskite active layer, a HSL, an ESL, and the metal top electrode. Different from mesoporous structured PSCs, planar PSCs can be an "n-i-p" structure or a "p-i-n" structure. Because "n-i-p" structure adopts the similar electron flow direction as the DSSCs, it is also called regular

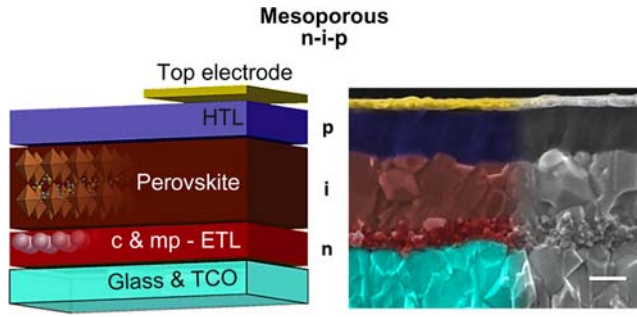


**Figure 12.8** Schematic diagram of a mesoporous structured PSCs structure [71]. *PSC*, Perovskite solar cell.

structured PSCs. Meanwhile, the "p-i-n" structure adopts the similar electron flow direction as the organic photovoltaics, it is also recognized as inverted structured PSCs.

#### 12.3.2.3 Regular planar (n-i-p) perovskite solar cells

The regular planar (n-i-p) structure (Fig. 12.9) is the natural evolution of the mesoscopic structure. The light also first enters the perovskite layer through the ESL layer. By delicately controlling the formation of the perovskite absorber, and the interface among the perovskite and the charge selective layers, high efficiencies can now be achieved without a mesoporous ESL. To date, the best regular planar (n-i-p) PSCs showed a 20.8% efficiency [54]. Although regular planar (n-i-p) PSCs have shown the high efficiency, they usually exhibit more $I-V$ hysteresis. Meanwhile, the organic HSL materials suffer from high cost, thus limiting the commercialization of PSCs.

Typically, the ESLs are compact n-type metal oxide layers, such as $SnO_2$ [72] and $TiO_2$ [52]. The most commonly used HSLs include Spiro-OMeTAD [73] and poly [bis(4-phenyl)(2,4,6-trimethylphenyl)amine] (PTAA) [74]. Other HSLs, such as cuprous thiocyanate (CuSCN) [75], and copper iodide (Cul) [76] also show a good performance in PSCs.

#### 12.3.2.4 Inverted planar (p-i-n) perovskite solar cells

In 2013, the inverted planar (p-i-n) PSCs was emerged as a new architecture. This type of PSC uses p-type and n-type materials as HSL and ESL, respectively, as shown in Fig. 12.10. The first inverted planar (n-i-p) PSCs was reported by Jeng et al; [77]. they reported PSCs where the indium tin oxide (ITO)/poly(3,4-ethylenedioxythiophene) poly(styrene-sulfonate) (PEDOT:PSS) substrate was used as the anode; a $CH_3NH_3PbI_3$/fullerene

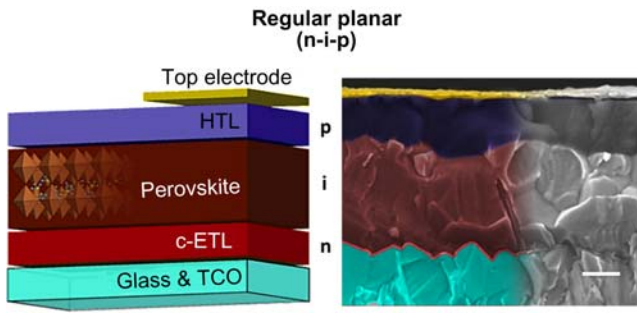


**Figure 12.9** Schematic diagram of regular planar (n-i-p) structure [71].

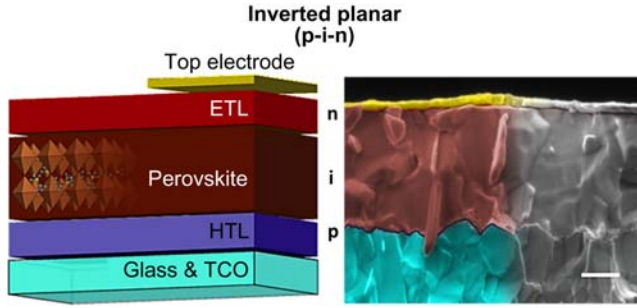


**Figure 12.10** Schematic diagram of inverted (p-i-n) structure [71].

($C_{60}$) layer was used as the active layer; a thin bathocuproine film was used as hole blocking layer, and aluminum as top cathode. The resulting cell provided a PCE of 3.0%. Although the PCE of the first inverted (p-i-n) PSC is low, this provides a new direction for developing highly efficient PSCs. In a short period of time, the PCE of inverted "p-i-n" structured PSCs has been enhanced to 16% with a remarkably high $V_{oc}$ of 1.05 eV [78]. A certified PCE of 20.59% was achieved by Zheng et al. in 2017 [79].

PEDOT:PSS and phenyl-$C_{61}$-butyric acid methyl ester (PCBM) are the most commonly used HSL and ESL, respectively, in inverted (p-i-n) PSCs. However, PEDOT:PSS is hygroscopic and acidic, which is detrimental to device long-term stability. To overcome this issue, PTAA and its analogs have been adopted in planar devices [80,81]. Small organic molecules that have good structure tunability are also promising for HSLs, Huang et al. reported a truxene-based HSL in which the planar and symmetrical truxene core promoted ordered molecular packing in the film, which resulted in an efficiency of 18.6% [82]. Besides organic materials, interests have been shown to inorganic materials. Park et al. successfully adopted $NiO_x$ as an HSL in PSCs and obtained a PCE of 19.2% [83]. Other p-type inorganic metal oxides, such as cuprous oxide ($Cu_2O$), copper oxide (CuO), copper doped chromium oxide (Cu doped $CrO_x$), molybdenum trioxide ($MoO_3$), and vanadium oxide ($V_2O_5$) have also been examined as HSLs in PSCs [84–89].

### 12.3.3 Deposition methods of perovskite films

The perovskite layer can be prepared using different deposition routes. Different deposition methods result in perovskite films of different grain sizes, electron and hole mobilities, concentration of defects in the bulk

and at the interfaces, and finally affect the photovoltaic efficiencies. In general, the deposition methods can be classified into two categories: one is vacuum deposition method and the other is solution-processed method.

#### 12.3.3.1 Vacuum deposition

In early works, high performance PSCs were achieved by vacuum deposition method. The idea is to allow the mixture of vapors of organic and inorganic species inside a high vacuum chamber where substrates are loaded. More specifically, in Liu's work [51], $CH_3NH_3I$ and $PbCl_2$ were simultaneously evaporated with a controlled molar ratio of 4:1. The dark reddish-brown color perovskite film was formed immediately after evaporation. The surface morphology of perovskite film and cross-sectional image of a complete device prepared using this method is given in Fig. 12.11 [51]. It shows a highly compact perovskite film with a good uniformity in the film thickness. Later, a sequential vacuum deposition of $PbCl_2$ followed by $CH_3NH_3I$ was demonstrated, using a substrate temperature of 75°C to enable $CH_3NH_3I$ diffusion into the $PbCl_2$ layer [90]. The resultant morphology is shown in Fig. 12.12. The main disadvantage of vacuum deposition method is that it demands high vacuum, which involves high energy consumption and hinders mass production [91].

#### 12.3.3.2 Solution-processed method

At the beginning of the development of PSCs, perovskite film was deposited from the precursor via one-step spin-coating method [3,48,92]. However, it is found that this method results in a poor film morphology. Then the two-step deposition method was developed, where $PbI_2$

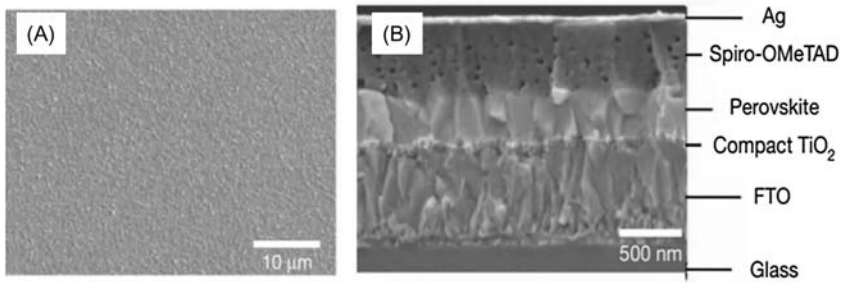


**Figure 12.11** SEM image of perovskite films fabricated by vacuum coevaporation (A) top view and (B) cross-section view. *Adapted from M. Liu, M.B. Johnston, H.J. Snaith, Efficient planar heterojunction perovskite solar cells by vapour deposition, Nature 501 (7467) (2013) 395. ©2013 Nature Publishing Group.*

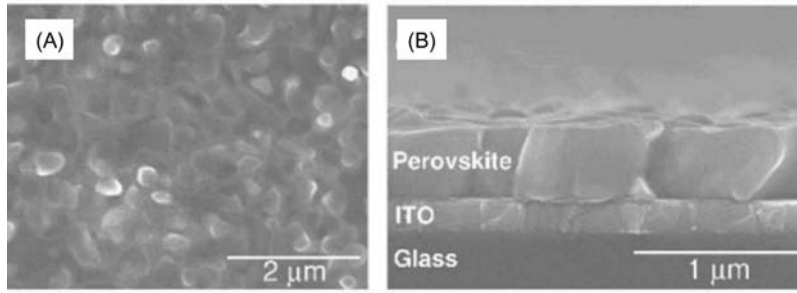


**Figure 12.12** SEM image of perovskite films fabricated by vacuum layer-by-layer evaporation: (A) top view and (B) cross-section view. *Adapted from C.W. Chen, et al., Efficient and uniform planar-type perovskite solar cells by simple sequential vacuum deposition, Adv. Mater. 26 (38) (2014) 6647–6652. ©2014 Wiley-VCH.*

dissolved in dimethylformamide (DMF) (*N*,*N*-dimethylformamide) was spin-coated onto the substrates, followed by immersion in $CH_3NH_3I$ in isopropanol solution [50,93,94]. This method helps to promote the film morphology of perovskite film with a good control of the formation of perovskite crystals, but it has some disadvantages as well. It is found that the transformation of lead iodide to perovskite may not be complete if the immersion time in $CH_3NH_3I$ in isopropanol is too short and the perovskite film may peel off from the substrates if the immersion time is too long.

Currently, the most popular solution-processed method is the antisolvent method [32,95]. Briefly, the antisolvent that has good miscibility with the solvent used in perovskite precursor but poor solubility for the perovskite material, such as chlorobenzene and toluene, when the solvent is dropped onto the perovskite solution deposited on the substrate during the spin-coating process. For this method, the choice of the antisolvent, the spin-coating speed, and the dripping time of antisolvent play critical roles in the final film morphology and the efficiency in the device. This method can give a very compact perovskite film, which leads to a high PCE [71]. More importantly, this method can be adopted by the mixed cations and mixed halides perovskites and can be easily applied in both a nitrogen filled glove box or in the air.

#### *12.3.3.3 Vapor-assisted solution deposition*

The vapor-assisted solution process is illustrated in Fig. 12.13 [117]. It involves two steps. First, $PbI_2$ is deposited on the substrate. Then, $CH_3NH_3I$ powder is kept near $PbI_2$ coated substrates inside a covered

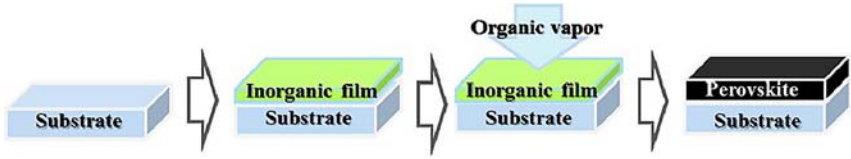


**Figure 12.13** Schematic illustration of vapor-assisted solution deposition method of $CH_3NH_3PbI_3$ perovskite film [96].

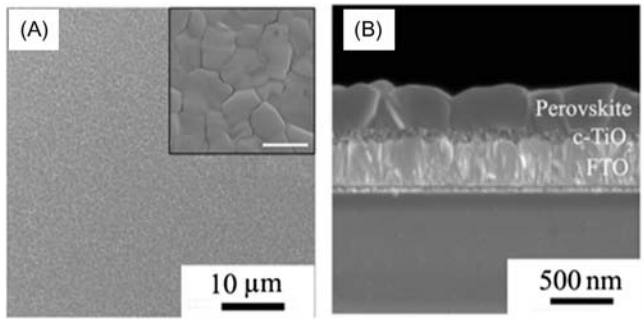


**Figure 12.14** SEM images of $CH_3NH_3PbI_3$ film deposited on $TiO_2$/FTO substrates by vapor-assisted solution process: (A) surface morphology (inset image with higher resolution, scale bar 1 μm) and (B) cross-sectional image. *Adapted from literature Q. Chen, et al., Planar heterojunction perovskite solar cells via vapor-assisted solution process, J. Am. Chem. Soc. 136 (2) (2013) 622–625. ©2013 American Chemical Society.*

petri dish placed on a hot plate at the temperature of 150°C. At this temperature, $CH_3NH_3I$ powder evaporates and forms $CH_3NH_3I$ vapor inside the petri dish, which reacts with the yellow $PbI_2$ film and forms a dark brown $CH_3NH_3PbI_3$ film in two hours. The resultant film morphology is given in Fig. 12.14. It shows that a compact and monolithic $CH_3NH_3PbI_3$ perovskite film can be formed using this method.

#### *12.2.3.3.4 Vacuum-flash assisted deposition*

Li et al. [97]. reported the vacuum-flash assisted deposition method for $FA_{0.81}MA_{0.15}PbI_{2.51}Br_{0.45}$ perovskite. The scheme of this method is illustrated in Fig. 12.15. Briefly, the perovskite precursor solution was first spin-coated on top of a mesoporous $TiO_2$ film, and then it was placed into a low vacuum chamber to remove the residual solvents, which led to the formation of a transparent orange film, a perovskite intermediate phase. Finally, after annealing at 100°C for 30 minutes, it formed a smooth, shiny, and highly crystalline perovskite layer. The film

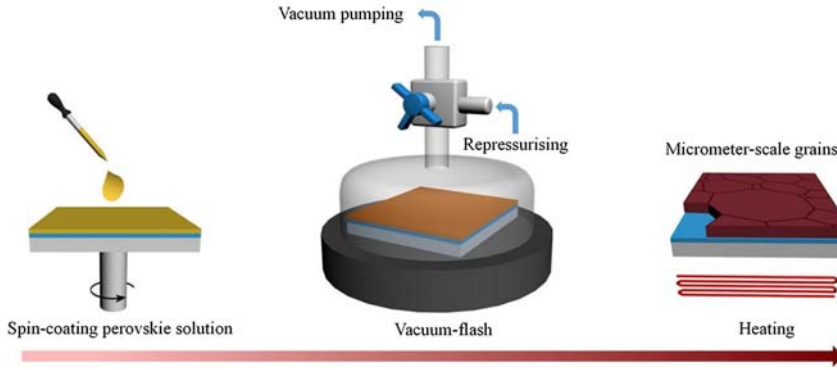


**Figure 12.15** Schematic illustration of vacuum flash-assisted solution deposition method. *Adapted from literature X. Li, et al., A vacuum flash-assisted solution process for high-efficiency large-area perovskite solar cells, Science 353 (6294) (2016) 58–62. ©2016 Science Publishing Group.*

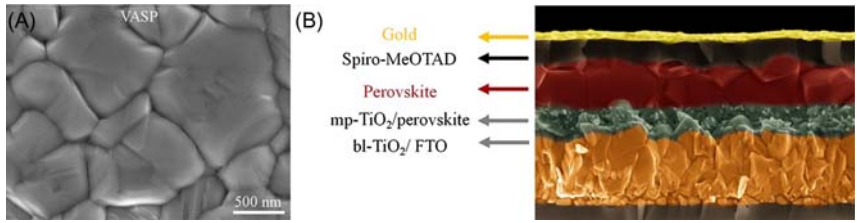


**Figure 12.16** (A) Surface morphology of perovskite films and (B) cross-sectional image of a complete device deposited by the vacuum-flash assisted method. *Adapted from literature X. Li, et al., A vacuum flash-assisted solution process for high-efficiency large-area perovskite solar cells, Science 353 (6294) (2016) 58–62. ©2016 Science Publishing Group.*

morphology of perovskite film deposited from this method is given in Fig. 12.16. More importantly, this method shows the potential for large scale deposition of perovskite film.

#### *12.3.3.5 Flash infrared annealing*

The flash infrared annealing (FIRA) method was recently developed by Sanchez et al. [98]. Different from the conventional solution deposition method, after spin-coating perovskite precursor on top of $TiO_2$/FTO substrates, the samples were placed under infrared lamps and radiated for several seconds. The scheme of this method is given in Fig. 12.17. Compared to the conventional annealing method, the infrared

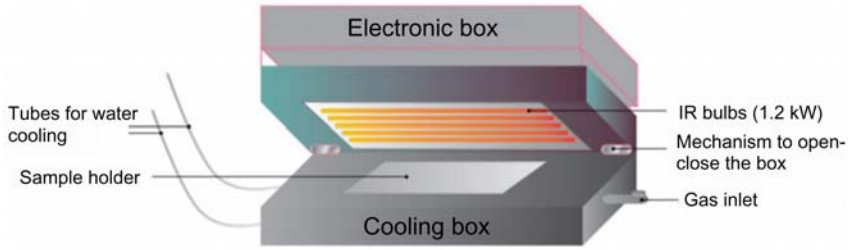


**Figure 12.17** Scheme of the FIRA method. *FIRA*, Flash infrared annealing. *Adapted from literature S. Sanchez, et al., Flash infrared annealing for antisolvent-free highly efficient perovskite solar cells, Adv. Energy Mater. 8 (2018) 1702915. ©2018 Wiley-VCH.*

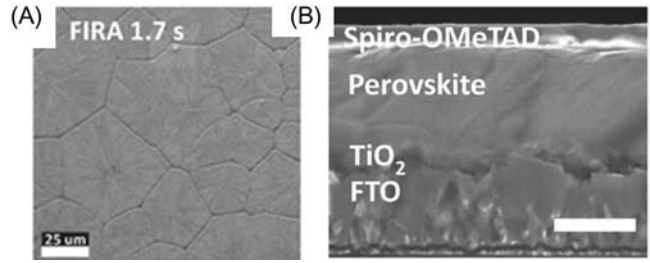


**Figure 12.18** (A) Surface morphology of perovskite film and (B) cross-sectional image of a complete device prepared from FIRA method. *FIRA*, Flash infrared annealing. *Adapted from literature S. Sanchez, et al., Flash infrared annealing for antisolvent-free highly efficient perovskite solar cells, Adv. Energy Mater. 8 (2018) 1702915. ©2018 Wiley-VCH.*

annealing is much faster and results in micrometer-sized grains, as shown in Fig. 12.18. Most importantly, the FIRA method shows the compatibility with flexible substrates as it does not require high temperature annealing. Also, it show great potential in large-scale deposition of perovskite films.

## 12.4 Characterization

### 12.4.1 Current–voltage characterization

As for any other photovoltaic technology, the main performance parameters derived from the current voltage ($JV$) characteristics include the short-circuit current density ($J_{SC}$) that is the highest current density extracted from an illuminated device, the open-circuit voltage ($V_{OC}$) that is the maximum voltage provided by an illuminated device, and the fill

factor (FF) that is the ratio of the maximum power from the solar cell to the product of $I_{SC}$ and $V_{OC}$. Finally, the PCE is calculated as the ratio of the electrical power output at the maximum power point divided by the incident light power.

For the *JV* measurement of PSCs, two different efficiencies might be obtained from the *JV* curve depending on the scan direction. As shown in Fig. 12.19, the forward scan (*red line*) where it scans from low voltage to high voltage results in a lower efficiency than the reverse scan (*black line*) where it scans from high voltage to low voltage. This phenomenon is called hysteresis. It have been found that the hysteresis is highly influenced by the electron and hole selective contact materials [99]. Jeon et al. [100] show that the hysteresis is particularly heavily for regular planar (n-i-p) PSCs. Several possible reasons for hysteresis have been proposed, such as ion migration [101], unbalanced charge collection rates [102], and ferroelectricity [103].

Due to the differences in the forward and reverse scan in *JV* measurement, the stabilized PCE measured from maximum power point tracking (MPPT) is required to report a valid value of PCE. The MPPT also helps to evaluate the stability or lifespans of PSCs, as will be discussed in the next section.

### 12.4.2 Estimation of device stability

In 2011, Reese et al. [105] proposed the idea of $T_{80}$, which refers to the period of time that it takes for a device to degrade to 80% of its initial efficiency. After this time, the device is considered to be needing replacement because more serious degradation mechanisms start kicking in. Although this idea was proposed for organic photovoltaics, the $T_{80}$ test is also useful for other photovoltaics because it helps to evaluate the lifetime energy yield (LEY) of one photovoltaic. LEY is defined in the following equation:

$$\mathrm{LEY} = \int_0^{T80} \mathrm{PCE}(t)dt. \tag{12.3}$$

For perovskite photovoltaics, the burn-in (nonrecoverable permanent degradation occurring at the beginning of the device operation) may be reversible [53,106] which has a significant impact on the LEY under real working conditions that involves day/night cycling [107]. Therefore, we should take the impact of the day/night cycling during aging into account

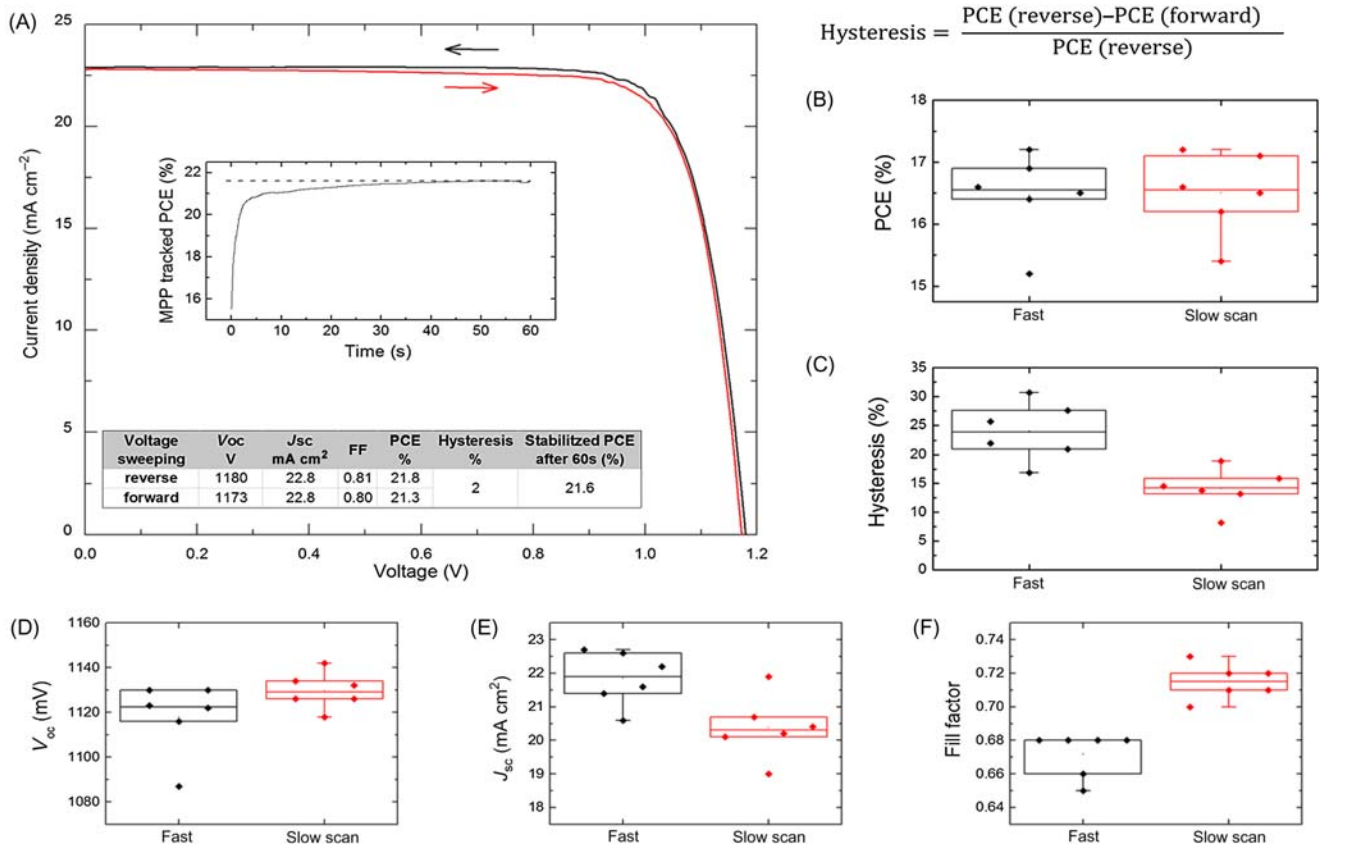


**Figure 12.19** Hysteresis and stabilized PCE. (A) *J*−*V* curves (forward and reverse) with a 2% hysteresis and an inset stabilized PCE of 21.6%. Adapted from literature [53], copyright Science Publishing Group. Major differences arise from using fast (100 mV s$^{-1}$) and slow scan (10 mV s$^{-1}$) rates, as displayed for 6 independent devices for the (B) PCE, (C) Hysteresis, (D) $V_{oc}$, (E) $J_{sc}$, and (F) FF (parameters extracted from the reverse scan, adapted from literature [104], copyright Royal Society of Chemistry). It is due to these differences that the slow scan speeds (10 mV s$^{-1}$) and MPP tracking, as shown in the inset in (A), have become required measurements for accurate PSC performance parameters evaluation. *MPP*, Maximum power point; *PCE*, power conversion efficiency; *PSC*, perovskite solar cells.

to provide a realistic economic prospect of PSCs. Thus, it is suggested that the aging test should consider the following key points:

- MPPT to avoid artificially inflated values from *JV* scans as described in Fig. 12.19.
- Testing time for at least 150 hours to pass the initial transient behavior and to estimate longer-term degradation as previously reported [104].
- Measuring the stabilized PCE after dark resting for several hours to distinguish between reversible and irreversible processes.

After MPPT, the device is left resting in the dark for more than 1 day. The changes in dark are then used to renormalize the decay curve, adding the "bonus/malus" efficiency collected during the dark rest. Thus, the $T_{s80}$ is defined as the $T_{80}$ of the renormalized MPP trace as depicted in Fig. 12.20. Accordingly, the LEY for PSCs needs to take multiple cycles into account; thus appreciating multiple reversible losses that significantly impact long-term energy yield (in contrast to previous photovoltaic (PV) materials).

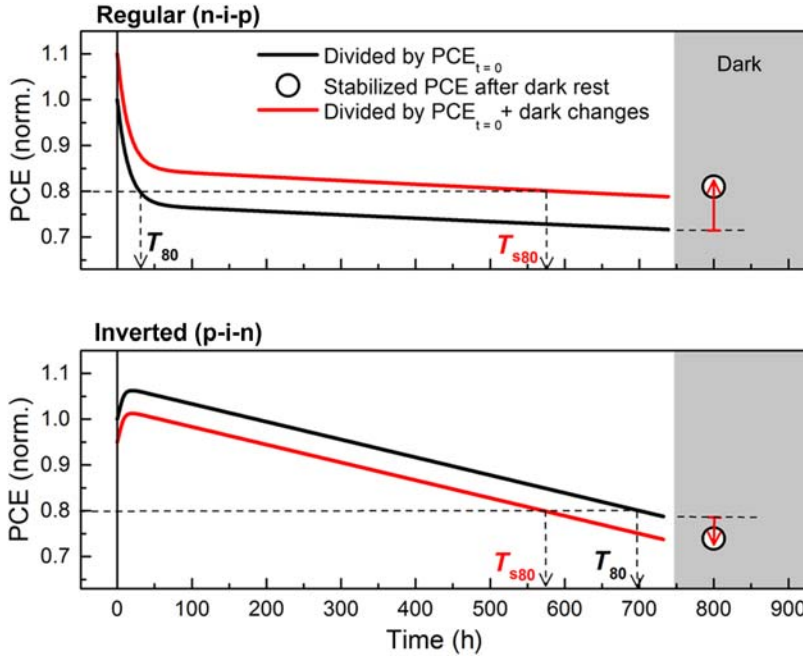


**Figure 12.20** Aging protocol for PSCs. Schematic of regular (n-i-p) (top panel) and inverted (p-i-n) (bottom panel) devices measured under MPP including changes after dark resting. In dark condition, the device is left at open circuit. $T_{s80}$ (corrected $T_{80}$) can be extracted from the MPP traces as depicted and used to compare the stability of perovskite to existing data from any solar cell technology. *MPP*, Maximum power point; *PSC*, perovskite solar cell.

## 12.5 Remaining challenges

Although the efficiency of PSCs has increased to over 20%, competitive to the established photovoltaic technologies, such as silicon solar cells and thin film solar cells, to make PSCs transfer from the intense laboratory research to outdoor commercialization, there are still two main challenges: (1) toxicity in lead perovskites and (2) long-term stability.

### 12.5.1 Toxicity of perovskite solar cells

Lead comprises more than 30% (mass ratio) in $CH_3NH_3PbI_3$ perovskite. Even though only small amount of perovskites are contained in PSCs, it can still bring harm to humans and the environment via long-term accumulation [108]. Lead halide perovskites form water-soluble compounds of lead, which can slowly, but inevitably, accumulate within the food chain and thus into the human body, as schematically depicted in Fig. 12.21 [109].

In order to develop low toxic PSCs, several alternative lead-free metal halide perovskites have been studied [110–117]. Tin is the most promising substitute for lead in the perovskite structure because of the similar electronic configuration and the similar ionic radius ($Pb^{2+}$: 119 pm and $Sn^{2+}$: 110 pm). Due to the smaller ionic radius of tin, the bandgap of Sn-based perovskites are lower than that of their lead counterparts, located in

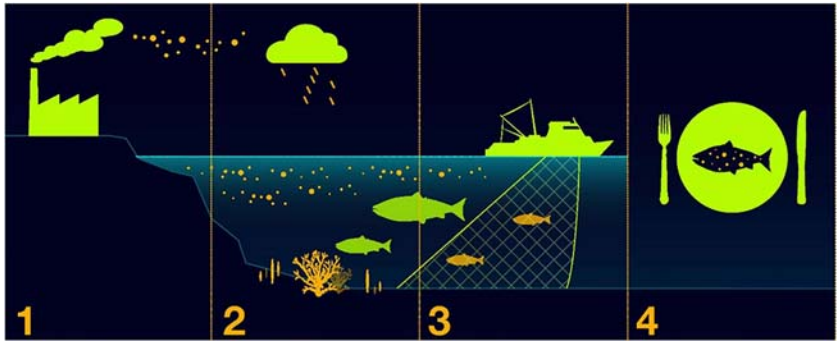


**Figure 12.21** Toxic heavy metals entering the food chain: (1) Industrial activates release metals in the environment; (2) Water transports metals into plants, which small fish consume; (3) Larger fish consume small contaminated fish; (4) Humans consume contaminated fish. Heavy metals accumulate up the food chain, thus more in human than in any species farther down in the chain. *Adapted from literature A. Abate, Perovskite solar cells go lead free, Joule 1 (4) (2017) 887. ©2017 Cell Publish Group and U.S. Environmental Protection Agency.*

the range of 1.2−1.5 eV [113,118]. As a result, a higher $J_{sc}$ is expected for tin-perovskites than lead-perovskites [6,119]. Noel et al. reported the first $CH_3NH_3SnI_3$-based PSCs in a mesoporous structure. They got a PCE of 6% for the champion device [111]. $CsSnI_3$ perovskite shows a small band gap of 1.27 eV, which leads to an ultra-high $J_{sc}$ of up to 27.67 mA $cm^{-2}$ [120]. So far, the record efficiency of tin-perovskite was reported by Zhao et al. who applied the mixed cation tin perovskite $[(FA)_{0.75}(MA)_{0.25}SnI_3]$ in PSCs and achieved a PCE of approximately 8% [116]. It is found that the mixed cation in tin perovskite results in a more compact and uniform perovskite film, which helps to enhance the stability of $Sn^{2+}$. The big challenge for tin-based PSCs is the easy oxidization of tin from $Sn^{2+}$ to $Sn^{4+}$. The appearance of $Sn^{4+}$ incudes defects in the PSCs and jeopardize the efficiency. To control the formation of $Sn^{4+}$, several attempts have been tried. Song et al. introduced the vapor of hydrazine during the preparation process of tin-perovskite, and he was able to reduce the content of $Sn^{4+}$ by 20% [121]. In another two works conducted by Chung et al. and Kumar et al. separately, they added $SnF_2$ to the perovskite precursor solution and managed to get a decent photovoltaic performance of tin-based PSCs [120,122].

## 12.5.2 Long-term stability of perovskite solar cells

One of the most important criteria for a commercial solar cell is the capacity of maintaining a stable power output under a standard working condition [123,124]. PSC without encapsulation have shown hundreds of hours of stability when they are stored in the dark and are measured every several hours or days. However, PSCs are found to degrade rapidly under continuous light illumination [125]. For a commercial solar cell, it expects to have a 25-year lifetime. In the following, we are going to discuss the degradation reasons for PSCs and the strategies developed so far to enhance the stability of PSCs.

### *12.5.2.1 Degradation of perovskites*

A deep understanding of the degradation mechanism of PSCs will be helpful to enhance the long-term stability [126−128]. As shown in Fig. 12.22, external factors, such as moisture, ultra violet (UV) light, oxygen, and heat can induce the degradation of PSCs and result in a lower efficiency. Particularly, it is found that perovskites are vulnerable to moisture. The possible decomposition mechanism of $CH_3NH_3PbI_3$ is suggested following the chemical reactions in 15.5−15.8. $CH_3NH_3PbI_3$ first

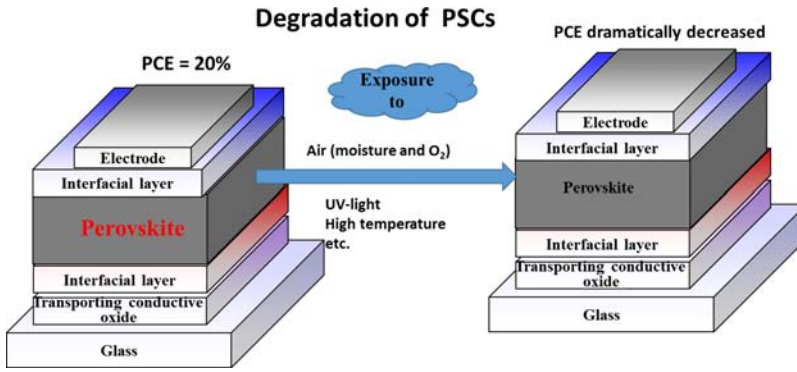


**Figure 12.22** Degradation of PSCs induced by external factors, such as moisture, $O_2$, UV-light, high temperature. *PSC*, Perovskite solar cell; *UV*, ultra violet.

decomposes into $PbI_2$ and $CH_3NH_3I$, and then $CH_3NH_3I$ decomposes into aqueous $CH_3NH_2$ and HI. The latter is then converted into iodine upon oxidation or photo excitation.

$$CH_3NH_3PbI_3(s) \leftrightarrow PbI_2(s) + CH_3NH_3I\ (aq) \tag{12.i}$$

$$CH_3NH_3(aq) \leftrightarrow CH_3NH_2(aq) + HI(aq) \tag{12.ii}$$

$$4HI(aq) + O_2(g) \leftrightarrow 2I_2(s) + 2H_2O(\text{presence of oxygen}) \tag{12.iii}$$

$$2HI \leftrightarrow H_2(g) + I_2(s)(\text{UV light}) \tag{12.iv}$$

The degradation mechanism by $O_2$ coupled with photogenerated electrons was proposed as the following:

$$CH_3NH_3PbI_3 + O_2^{\bullet -} \rightarrow CH_3NH_2 + PbI_2 + 1/2I_2 + H_2O\ (\text{deprotonation}) \tag{12.v}$$

The joint effect of moisture and oxygen lead to the fast degradation in efficiencies of PSCs [129].

#### *12.5.2.2 Degradation caused by electron selective layers and hole selective layers*

Inorganic ESLs and HSLs in general exhibit much better stability than their organic counterparts. As a result, we will mainly discuss the degradation caused by organic ESLs and HSLs. For example, PEDOT:PSS is found to bring some damage to the transparent oxide electrode because of

its acidity. Besides, PEDOT:PSS easily absorbs moisture from the ambient atmosphere. These two disadvantages of PEDOT:PSS contribute to the degradation in PSCs [87]. Another example is PCBM that shows excellent electron conductivity and demonstrates as a powerful ESL in PSCs. It is found that PCBM is not stable in ambient atmosphere due to the chemical states and band structure variation, which result in device degradation [130]. Another example is spiro-OMeTAD. It has been widely used in regular structured "n-i-p" PSCs with the presence of dopants, such as LiTFSI (bis(trifluoromethane)sulfonimide lithium salt) and tBP (4-*tert*-Butylpyridine). Although the doped spiro-OMeTAD shows a higher hole mobility and a better efficiency in PSCs, these dopants also can lead to degradation in PSCs as well. In particular, LiTFSI is hydrophilic and tends to absorb moisture when it is exposed to ambient air. Several dopant-free hole transport materials (HTMs) have been synthesized and applied in PSCs [131–134]. A better stability has been reported in these HTMs. Abate et al. [104] demonstrated that HTMs with higher thermal stability also contributes to the enhancement in stability of PSCs.

#### *12.5.2.3 Degradation caused by electrodes*

It was recently revealed that the corrosion of metal electrode (gold, silver, and aluminum) upon the reaction with halide facilitates the degradation of PSCs. Domanski et al. [135] intercalated an interlayer of chromium metal between the HSL and gold electrode, and they observed a significant enhancement in the stability of PSCs during the MPPT measurement. Back et al. introduced an amine-mediate metal electrode oxide interlayer between [6,6]-PCBM and silver [136].

## 12.6 Summary and outlook

In this chapter, we give an overview of the perovskite materials, their optical and electronic properties, and provide a discussion of the architecture, components and characterizations of PSCs. The remarkable optoelectronic properties of perovskites, such as broad light harvesting spectrum range, high absorption coefficient, low exciton binding energy, and low defects concentrations, together with the facile and versatile deposition methods, result in the huge success of PSCs and the fast development of this type of photovoltaic. We have to admit that due to the limitation of this chapter, we are not able to explore a detailed discussion of all the issues involved with PSCs. We are more focused on introducing

the general information of PSCs to a more broad range of readers. Although there are still some challenges for the future commercialization of PSCs, such as a short lifespan, we are convinced that *via* interfacial engineering under the assistance of encapsulation, PSCs will be one of the most promising photovoltaic technologies that will meet the energy demands of human beings.

## Reference


[1] A. Kojima, et al., Organometal halide perovskites as visible-light sensitizers for photovoltaic cells, J. Am. Chem. Soc. 131 (17) (2009) 6050–6051.
[2] N.-G. Park, T. Miyasaka, M. Grätzel, Organic–Inorganic Halide Perovskite Photovoltaics, Springer, 2016.
[3] H.-S. Kim, et al., Lead iodide perovskite sensitized all-solid-state submicron thin film mesoscopic solar cell with efficiency exceeding 9%, Sci. Rep. 2 (2012) 591.
[4] NREL Efficiency Chart, 2017. Available from: https://www.nrel.gov/pv/assets/images/efficiencychart.png (accessed 16.12.18).
[5] M.A. Green, et al., Solar cell efficiency tables (version 46), Prog. Photovoltaics Res. Appl. 23 (7) (2015) 805–812.
[6] W. Shockley, H.J. Queisser, *Detailed balance limit of efficiency of p-n junction solar cells*, Br. J. Appl. Phys. 32 (3) (1961) 510–519.
[7] G. Xing, et al., Long-range balanced electron-and hole-transport lengths in organic–inorganic CH3NH3PbI3, Science 342 (6156) (2013) 344–347.
[8] V.M. Goldschmidt, Die gesetze der krystallochemie, Naturwissenschaften 14 (21) (1926) 477–485.
[9] N.K. McKinnon, D.C. Reeves, M.H. Akabas, 5-HT3 receptor ion size selectivity is a property of the transmembrane channel, not the cytoplasmic vestibule portals, J. Gen. Physiol. 138 (4) (2011) 453–466.
[10] J.-H. Im, et al., Synthesis, structure, and photovoltaic property of a nanocrystalline 2H perovskite-type novel sensitizer (CH3CH2NH3) PbI3, Nanoscale Res. Lett. 7 (1) (2012) 353.
[11] T.M. Koh, et al., Formamidinium-containing metal-halide: an alternative material for near-IR absorption perovskite solar cells, J. Phys. Chem. C 118 (30) (2013) 16458–16462.
[12] G.E. Eperon, et al., Formamidinium lead trihalide: a broadly tunable perovskite for efficient planar heterojunction solar cells, Energy Environ. Sci. 7 (3) (2014) 982–988.
[13] C. Li, et al., Formability of ABX3 (X = F, Cl, Br, I) Halide Perovskites, Acta Crystallogr., Sect. B: Struct. Sci 64 (6) (2008) 702–707.
[14] M.A. Green, A. Ho-Baillie, H.J. Snaith, The emergence of perovskite solar cells, Nat. Photonics 8 (7) (2014) 506–514.
[15] W. Travis, et al., On the application of the tolerance factor to inorganic and hybrid halide perovskites: a revised system, Chem. Sci. 7 (7) (2016) 4548–4556.
[16] T. Sato, et al., Extending the applicability of the Goldschmidt tolerance factor to arbitrary ionic compounds, Sci. Rep. 6 (2016).
[17] Z. Li, et al., Stabilizing perovskite structures by tuning tolerance factor: formation of formamidinium and cesium lead iodide solid-state alloys, Chem. Mater. 28 (1) (2015) 284–292.

[18] Q. Chen, et al., Under the spotlight: The organic–inorganic hybrid halide perovskite for optoelectronic applications, Nano Today 10 (3) (2015) 355–396.
[19] C.K. Møller, A phase transition in cæsium plumbochloride, Nature 180 (4593) (1957) 981–982.
[20] C.K. Møller, Crystal structure and photoconductivity of caesium plumbohalides, Nature 182 (4647) (1958) 1436.
[21] D. Weber, CH3NH3PbX3, ein Pb(II)-system mit kubischer perowskitstruktur/CH3NH3PbX3, a Pb(II)-system with cubic perovskite structure, Zeitschrift für Naturforschung B 33 (12) (1978) 1443–1445.
[22] F. Deschler, et al., High photoluminescence efficiency and optically pumped lasing in solution-processed mixed halide perovskite semiconductors, J. Phys. Chem. Lett. 5 (8) (2014) 1421–1426.
[23] J.H. Park, et al., *Efficient CH3NH3PbI3 perovskite solar cells employing nanostructured p-type NiO electrode formed by a pulsed laser deposition*, Adv. Mater. 27 (27) (2015) 4013–4019.
[24] Z.-K. Tan, et al., Bright light-emitting diodes based on organometal halide perovskite, Nat. Nanotechnol. 9 (9) (2014) 687–692.
[25] L. Protesescu, et al., Nanocrystals of cesium lead halide perovskites (CsPbX3, X = Cl, Br, and I): novel optoelectronic materials showing bright emission with wide color gamut, Nano Lett. 15 (6) (2015) 3692–3696.
[26] H. Cho, et al., Overcoming the electroluminescence efficiency limitations of perovskite light-emitting diodes, Science 350 (6265) (2015) 1222–1225.
[27] G. Li, et al., Efficient light-emitting diodes based on nanocrystalline perovskite in a dielectric polymer matrix, Nano Lett. 15 (4) (2015) 2640–2644.
[28] J. Song, et al., *Quantum dot light-emitting diodes based on inorganic perovskite cesium lead halides (CsPbX3)*, Adv. Mater. 27 (44) (2015) 7162–7167.
[29] H. Lu, et al., *A self-powered and stable all-perovskite photodetector–solar cell nanosystem*, Adv. Funct. Mater. 26 (8) (2016) 1296–1302.
[30] J. Song, et al., *Monolayer and few-layer all-inorganic perovskites as a new family of two-dimensional semiconductors for printable optoelectronic devices*, Adv. Mater. 28 (24) (2016) 4861–4869.
[31] N. Pellet, et al., *Mixed-organic-cation Perovskite photovoltaics for enhanced solar-light harvesting*, Angew. Chem. Int. Ed. 53 (12) (2014) 3151–3157.
[32] W.S. Yang, et al., High-performance photovoltaic perovskite layers fabricated through intramolecular exchange, Science 348 (6240) (2015) 1234–1237.
[33] Y. Ogomi, et al., CH3NH3Sn x Pb (1−x) I3 Perovskite solar cells covering up to 1060 nm, J. Phys. Chem. Lett. 5 (6) (2014) 1004–1011.
[34] I.E. Castelli, et al., Bandgap calculations and trends of organometal halide perovskites, APL Mater. 2 (8) (2014) 081514.
[35] B. Zhao, et al., *High open-circuit voltages in tin-rich low-bandgap perovskite-based planar heterojunction photovoltaics*, Adv. Mater. 29 (2) (2017).
[36] M. Saliba, et al., Perovskite solar cells from the atomic to the film level, Angew. Chem. (2017) 2554–2569.
[37] T. Wang, et al., Indirect to direct bandgap transition in methylammonium lead halide perovskite, Energy Environ. Sci. 10 (2) (2017) 509–515.
[38] N.-G. Park, Perovskite solar cells: an emerging photovoltaic technology, Mater. Today 18 (2) (2015) 65–72.
[39] Y. Xie, et al., *Giant two-photon absorption in mixed halide perovskite CH3NH3Pb0. 75Sn0. 25I3 thin films and application to photodetection at optical communication wavelengths*, Adv. Opt. Mater. (2017).
[40] G. Walters, et al., Two-photon absorption in organometallic bromide perovskites, ACS Nano 9 (9) (2015) 9340–9346.

[41] A.M. Askar, K. Shankar, Exciton binding energy in organic–inorganic tri-halide perovskites, J. Nanosci. Nanotechnol. 16 (6) (2016) 5890–5901.
[42] K. Galkowski, et al., Determination of the exciton binding energy and effective masses for methylammonium and formamidinium lead tri-halide perovskite semiconductors, Energy Environ. Sci. 9 (3) (2016) 962–970.
[43] G. Xing, et al., Long-range balanced electron- and hole-transport lengths in organic–inorganic CH3NH3PbI3, Science 342 (6156) (2013) 344–347.
[44] Q. Dong, et al., Electron-hole diffusion lengths >175 μm in solution-grown CH3NH3PbI3 single crystals, Science 347 (6225) (2015) 967–970.
[45] W.S. Yang, et al., Iodide management in formamidinium-lead-halide–based perovskite layers for efficient solar cells, Science 356 (6345) (2017) 1376–1379.
[46] H.J., Snaith, L. Schmidt-Mende, *Advances in liquid-electrolyte and solid-state dye-sensitized solar cells*, Adv. Mater. 19 (20) (2007) 3187–3200.
[47] J.-H. Im, et al., 6.5% efficient perovskite quantum-dot-sensitized solar cell, Nanoscale 3 (10) (2011) 4088–4093.
[48] M.M. Lee, et al., Efficient hybrid solar cells based on meso-superstructured organometal halide perovskites, Science 338 (6107) (2012) 643–647.
[49] J.H. Heo, et al., Efficient inorganic–organic hybrid heterojunction solar cells containing perovskite compound and polymeric hole conductors, Nat. Photonics 7 (6) (2013) 486–491.
[50] J. Burschka, et al., Sequential deposition as a route to high-performance perovskite-sensitized solar cells, Nature 499 (7458) (2013) 316–319.
[51] M. Liu, M.B. Johnston, H.J. Snaith, Efficient planar heterojunction perovskite solar cells by vapour deposition, Nature 501 (7467) (2013) 395.
[52] H. Zhou, et al., Interface engineering of highly efficient perovskite solar cells, Science 345 (6196) (2014) 542–546.
[53] M. Saliba, et al., Incorporation of rubidium cations into perovskite solar cells improves photovoltaic performance, Science 354 (6309) (2016) 206–209.
[54] E.H. Anaraki, et al., Highly efficient and stable planar perovskite solar cells by solution-processed tin oxide, Energy Environ. Sci. 9 (10) (2016) 3128–3134.
[55] D.-Y. Son, et al., 11% efficient perovskite solar cell based on ZnO nanorods: an effective charge collection system, J. Phys. Chem. C 118 (30) (2014) 16567–16573.
[56] D. Bi, et al., Efficient and stable CH 3 NH 3 PbI 3-sensitized ZnO nanorod array solid-state solar cells, Nanoscale 5 (23) (2013) 11686–11691.
[57] M.H. Kumar, et al., Flexible, low-temperature, solution processed ZnO-based perovskite solid state solar cells, Chem. Commun. 49 (94) (2013) 11089–11091.
[58] X. Gao, et al., *Enhanced photovoltaic performance of perovskite CH 3 NH 3 PbI 3 solar cells with freestanding $TiO_2$ nanotube array films*, Chem. Commun. 50 (48) (2014) 6368–6371.
[59] J. Qiu, et al., *All-solid-state hybrid solar cells based on a new organometal halide perovskite sensitizer and one-dimensional $TiO_2$ nanowire arrays*, Nanoscale 5 (8) (2013) 3245–3248.
[60] K. Manseki, et al., *Mg-doped $TiO_2$ nanorods improving open-circuit voltages of ammonium lead halide perovskite solar cells*, RSC Adv. 4 (19) (2014) 9652–9655.
[61] D. Zhong, et al., *Synthesis of oriented $TiO_2$ nanocones with fast charge transfer for perovskite solar cells*, Nano Energy 11 (2015) 409–418.
[62] N. Islam, et al., *Mesoporous scaffolds based on $TiO_2$ nanorods and nanoparticles for efficient hybrid perovskite solar cells*, J. Mater. Chem. A 3 (48) (2015) 24315–24321.
[63] K. Mahmood, B.S. Swain, A. Amassian, *Highly efficient hybrid photovoltaics based on hyperbranched three-dimensional $TiO_2$ electron transporting materials*, Adv. Mater. 27 (18) (2015) 2859–2865.

[64] Q. Luo, et al., Discrete Iron(III) oxide nanoislands for efficient and photostable perovskite solar cells, Adv. Funct. Mater. 27 (34) (2017).
[65] D. Bi, et al., *Using a two-step deposition technique to prepare perovskite ($CH_3$ $NH_3$ $PbI_3$) for thin film solar cells based on $ZrO_2$ and $TiO_2$ mesostructures*, RSC Adv. 3 (41) (2013) 18762–18766.
[66] S.H. Hwang, et al., *Size-controlled $SiO_2$ nanoparticles as scaffold layers in thin-film perovskite solar cells*, J. Mater. Chem. A 2 (39) (2014) 16429–16433.
[67] X. Yu, et al., *Enhanced photovoltaic performance of perovskite solar cells with mesoporous $SiO_2$ scaffolds*, J. Power Sources 325 (2016) 534–540.
[68] K. Lee, et al., *Morphology-controlled mesoporous $SiO_2$ nanorods for efficient scaffolds in organo-metal halide perovskite solar cells*, Chem. Commun. 52 (22) (2016) 4231–4234.
[69] L.S. Oh, et al., *$Zn_2SnO_4$-based photoelectrodes for organolead halide perovskite solar cells*, J. Phys. Chem. C 118 (40) (2014) 22991–22994.
[70] S.S. Mali, C.S. Shim, C.K. Hong, *Highly porous zinc stannate ($Zn_2SnO_4$) nanofibers scaffold photoelectrodes for efficient methyl ammonium halide perovskite solar cells*, Sci. Rep. 5 (2015) 11424.
[71] M. Saliba, et al., How to make over 20% efficient perovskite solar cell in regular and inverted architectures, Chem. Mater. 30 (13) (2018) 4193–4201.
[72] W. Ke, et al., Low-temperature solution-processed tin oxide as an alternative electron transporting layer for efficient perovskite solar cells, J. Am. Chem. Soc. 137 (21) (2015) 6730–6733.
[73] A.T. Murray, et al., Modular design of SPIRO-OMeTAD analogues as hole transport materials in solar cells, Chem. Commun. 51 (43) (2015) 8935–8938.
[74] S.S. Mali, C.S. Shim, C.K. Hong, Highly stable and efficient solid-state solar cells based on methylammonium lead bromide (CH3NH3PbBr3) perovskite quantum dots, NPG Asia Mater. 7 (8) (2015) e208.
[75] P. Qin, et al., Inorganic hole conductor-based lead halide perovskite solar cells with 12.4% conversion efficiency, Nat. Commun. 5 (2014).
[76] J.A. Christians, R.C. Fung, P.V. Kamat, An inorganic hole conductor for organo-lead halide perovskite solar cells. Improved hole conductivity with copper iodide, J. Am. Chem. Soc. 136 (2) (2013) 758–764.
[77] J.Y. Jeng, et al., *CH3NH3PbI3 perovskite/fullerene planar-heterojunction hybrid solar cells*, Adv. Mater. 25 (27) (2013) 3727–3732.
[78] C.-H. Chiang, Z.-L. Tseng, C.-G. Wu, Planar heterojunction perovskite/PC 71 BM solar cells with enhanced open-circuit voltage via a (2/1)-step spin-coating process, J. Mater. Chem. A 2 (38) (2014) 15897–15903.
[79] X. Zheng, et al., Defect passivation in hybrid perovskite solar cells using quaternary ammonium halide anions and cations, Nat. Energy 2 (7) (2017) 17102.
[80] D. Zhao, et al., *High-efficiency solution-processed planar perovskite solar cells with a polymer hole transport layer*, Adv. Energy Mater. 5 (6) (2015).
[81] S. Ryu, et al., Voltage output of efficient perovskite solar cells with high open-circuit voltage and fill factor, Energy Environ. Sci. 7 (8) (2014) 2614–2618.
[82] C. Huang, et al., Dopant-free hole-transporting material with a C 3 h symmetrical truxene core for highly efficient perovskite solar cells, J. Am. Chem. Soc. 138 (8) (2016) 2528–2531.
[83] I.J. Park, et al., *Highly efficient and uniform 1 $cm^2$ perovskite solar cells with an electrochemically deposited NiOx hole-extraction layer*, ChemSusChem (2017).
[84] C. Zuo, L. Ding, *Solution-processed $Cu_2O$ and $CuO$ as hole transport materials for efficient perovskite solar cells*, Small 11 (41) (2015) 5528–5532.
[85] W. Yu, et al., *Ultrathin $Cu_2O$ as an efficient inorganic hole transporting material for perovskite solar cells*, Nanoscale 8 (11) (2016) 6173–6179.

[86] Y. Liu, et al., *$V_2O5$ nano-electrodes with high power and energy densities for thin film li-ion batteries*, Adv. Energy Mater. 1 (2) (2011) 194–202.
[87] J.H. Kim, et al., *High-performance and environmentally stable planar heterojunction perovskite solar cells based on a solution-processed copper-doped nickel oxide hole-transporting layer*, Adv. Mater. 27 (4) (2015) 695–701.
[88] A. Huang, et al., Achieving high-performance planar perovskite solar cells with co-sputtered co-doping NiOx hole transport layers by efficient extraction and enhanced mobility, J. Mater. Chem. C 4 (46) (2016) 10839–10846.
[89] P.L. Qin, et al., *Copper-doped chromium oxide hole-transporting layer for perovskite solar cells: interface engineering and performance improvement*, Adv. Mater. Interfaces 3 (14) (2016).
[90] C.W. Chen, et al., *Efficient and uniform planar-type perovskite solar cells by simple sequential vacuum deposition*, Adv. Mater. 26 (38) (2014) 6647–6652.
[91] J. Cui, et al., Recent progress in efficient hybrid lead halide perovskite solar cells, Sci. Technol. Adv. Mater. 16 (3) (2015) 036004.
[92] M.J. Carnie, et al., A one-step low temperature processing route for organolead halide perovskite solar cells, Chem. Commun. 49 (72) (2013) 7893–7895.
[93] A. Dualeh, et al., *Effect of annealing temperature on film morphology of organic–inorganic hybrid pervoskite solid-state solar cells*, Adv. Funct. Mater. 24 (21) (2014) 3250–3258.
[94] Y. Chen, T. Chen, L. Dai, *Layer-by-layer growth of CH3NH3PbI3 − xClx for highly efficient planar heterojunction perovskite solar cells*, Adv. Mater. 27 (6) (2015) 1053–1059.
[95] G.E. Eperon, et al., *Morphological control for high performance, solution-processed planar heterojunction perovskite solar cells*, Adv. Funct. Mater. 24 (1) (2014) 151–157.
[96] Q. Chen, et al., Planar heterojunction perovskite solar cells via vapor-assisted solution process, J. Am. Chem. Soc. 136 (2) (2013) 622–625.
[97] X. Li, et al., A vacuum flash-assisted solution process for high-efficiency large-area perovskite solar cells, Science 353 (6294) (2016) 58–62.
[98] S. Sanchez, et al., *Flash infrared annealing for antisolvent-free highly efficient perovskite solar cells*, Adv. Energy Mater. 8 (2018) 1702915.
[99] Y. Shao, et al., Origin and elimination of photocurrent hysteresis by fullerene passivation in CH3NH3PbI3 planar heterojunction solar cells, Nat. Commun. 5 (2014) 5784.
[100] N.J. Jeon, et al., Solvent engineering for high-performance inorganic–organic hybrid perovskite solar cells, Nat. Mater. 13 (9) (2014) 897–903.
[101] C. Eames, et al., Ionic transport in hybrid lead iodide perovskite solar cells, Nat. Commun. 6 (2015) 7497.
[102] V.W. Bergmann, et al., Real-space observation of unbalanced charge distribution inside a perovskite-sensitized solar cell, Nat. Commun. 5 (2014) 5001.
[103] J.M. Frost, K.T. Butler, A. Walsh, Molecular ferroelectric contributions to anomalous hysteresis in hybrid perovskite solar cells, APL Mater. 2 (8) (2014) 081506.
[104] A. Abate, et al., Silolothiophene-linked triphenylamines as stable hole transporting materials for high efficiency perovskite solar cells, Energy Environ. Sci. 8 (10) (2015) 2946–2953.
[105] M.O. Reese, et al., Consensus stability testing protocols for organic photovoltaic materials and devices, Sol. Energy Mater. Sol. Cells 95 (5) (2011) 1253–1267.
[106] H. Tan, et al., Efficient and stable solution-processed planar perovskite solar cells via contact passivation, Science 355 (6326) (2017) 722–726.
[107] K. Domanski, et al., Migration of cations induces reversible performance losses over day/night cycling in perovskite solar cells, Energy Environ. Sci. (2017).
[108] A. Babayigit, et al., Toxicity of organometal halide perovskite solar cells, Nat. Mater. 15 (3) (2016) 247–251.

[109] A. Abate, Perovskite solar cells go lead free, Joule 1 (4) (2017) 887.
[110] Z. Chen, et al., Schottky solar cells based on CsSnI3 thin-films, Appl. Phys. Lett. 101 (9) (2012) 093901.
[111] N.K. Noel, et al., Lead-free organic–inorganic tin halide perovskites for photovoltaic applications, Energy Environ. Sci. 7 (9) (2014) 3061–3068.
[112] F. Hao, et al., Lead-free solid-state organic–inorganic halide perovskite solar cells, Nat. Photonics 8 (6) (2014) 489–494.
[113] F. Hao, et al., Anomalous band gap behavior in mixed Sn and Pb perovskites enables broadening of absorption spectrum in solar cells, J. Am. Chem. Soc. 136 (22) (2014) 8094–8099.
[114] W. Liao, et al., *Lead-free inverted planar formamidinium tin triiodide perovskite solar cells achieving power conversion efficiencies up to 6.22%*, Adv. Mater. 28 (42) (2016) 9333–9340.
[115] F. Wang, et al., *Organic cation-dependent degradation mechanism of organotin halide perovskites*, Adv. Funct. Mater. 26 (20) (2016) 3417–3423.
[116] Z. Zhao, et al., *Mixed-organic-cation tin iodide for lead*-free perovskite solar cells with an efficiency of 8.12%, Adv. Sci. (2017).
[117] M. Zhang, et al., *Recent advances in low-toxic lead-free metal halide perovskite materials for solar cell application*, Asia Pac. J. Chem. Eng. 11 (3) (2016) 392–398.
[118] Z. Yang, et al., *Stable low-bandgap Pb–Sn binary perovskites for tandem solar cells*, Adv. Mater. 28 (40) (2016) 8990–8997.
[119] S. Rühle, Tabulated values of the Shockley–Queisser limit for single junction solar cells, Solar Energy 130 (2016) 139–147.
[120] M.H. Kumar, et al., *Lead-free halide perovskite solar cells with high photocurrents realized through vacancy modulation*, Adv. Mater. 26 (41) (2014) 7122–7127.
[121] T.-B. Song, et al., Importance of reducing vapor atmosphere in the fabrication of tin-based perovskite solar cells, J. Am. Chem. Soc. 139 (2) (2017) 836–842.
[122] S.J. Lee, et al., Fabrication of efficient formamidinium tin iodide perovskite solar cells throughsnf2–pyrazine complex, J. Am. Chem. Soc. 138 (12) (2016) 3974–3977.
[123] Y. Rong, et al., Beyond efficiency: the challenge of stability in mesoscopic perovskite solar cells, Adv. Energy Mater. 5 (20) (2015).
[124] T. Leijtens, et al., *Stability of metal halide perovskite solar cells.*, Adv. Energy Mater. 5 (20) (2015).
[125] S.D., Stranks, H.J. Snaith, Metal-halide perovskites for photovoltaic and light-emitting devices, Nat. Nanotechnol. 10 (5) (2015) 391–402.
[126] W. Chen, et al., Efficient and stable large-area perovskite solar cells with inorganic charge extraction layers, Science 350 (6263) (2015) 944–948.
[127] J. Cao, et al., Thiols as interfacial modifiers to enhance the performance and stability of perovskite solar cells, Nanoscale 7 (21) (2015) 9443–9447.
[128] Q. Jiang, et al., *Pseudohalide-induced moisture tolerance in perovskite CH3NH3Pb (SCN) 2I thin films*, Angew. Chem. 127 (26) (2015) 7727–7730.
[129] J.H. Noh, et al., Chemical management for colorful, efficient, and stable inorganic–organic hybrid nanostructured solar cells, Nano Lett. 13 (4) (2013) 1764–1769.
[130] J. You, et al., Improved air stability of perovskite solar cells via solution-processed metal oxide transport layers, Nat. Nanotechnol. 11 (1) (2016) 75–81.
[131] J. Liu, et al., A dopant-free hole-transporting material for efficient and stable perovskite solar cells, Energy Environ. Sci. 7 (9) (2014) 2963–2967.
[132] S. Kazim, et al., A dopant free linear acene derivative as a hole transport material for perovskite pigmented solar cells, Energy Environ. Sci. 8 (6) (2015) 1816–1823.

[133] P. Ganesan, et al., A simple spiro-type hole transporting material for efficient perovskite solar cells, Energy Environ. Sci. 8 (7) (2015) 1986–1991.
[134] Y. Liu, et al., Perovskite solar cells employing dopant-free organic hole transport materials with tunable energy levels, Adv Mater 28 (3) (2016) 440–446.
[135] K. Domanski, et al., Not all that glitters is gold: metal-migration-induced degradation in perovskite solar cells, ACS Nano 10 (6) (2016) 6306–6314.
[136] H. Back, et al., Achieving long-term stable perovskite solar cells via ion neutralization, Energy Environ. Sci. 9 (4) (2016) 1258–1263.

# CHAPTER 13

# Metal nanostructures for solar cells

**Saniat Ahmed Choudhury, Fatema Fairooz, Rashid Ahmed Rifat and Mustafa Habib Chowdhury**
Independent University, Bangladesh (IUB), Dhaka, Bangladesh

## Contents



*Nanomaterials for Solar Cell Applications*
DOI: https://doi.org/10.1016/B978-0-12-813337-8.00013-8

## 13.1 Section 1—Introduction

The need for discovering and developing novel and improved materials for attaining greater photovoltaic (PV) efficiency has been an intense focus of research since the inception of the idea that solar energy can be harvested to generate "clean" electricity [1,2]. The interaction of sunlight with materials and the subsequent generation of electricity is not a trivial phenomenon to manipulate. While power electronics and different post-energy-generation technologies do help in the usage of the generated electricity, one thing remains absolutely certain, only the improvement of materials and alterations of devices at the nanoscale with regard to their interaction with photons at the quantum level can truly provide significant progress toward greater cell efficiency [3–5]. This has proved to be a significant challenge, as limitations in material development and cell fabrication can prove to be a hindrance toward that goal [1–5]. To that end, research has always been focused on developing novel materials and nanostructures the unique properties of which would be beneficial in enhancing the optical and electrical activities of the PV cell. Metals, therefore, have been, and are currently studied extensively as a part of that research to identify and optimize properties that would assist in that goal [1–5].

The use of metals in PV technologies has not always been prevalent since the harvesting of solar energy became a viable option. While lithium was initially thought to be a suitable material for the electrode contacts responsible for carrying the generated electron–hole pairs and producing a current, it had a massive drawback: the lithium gradually seeped into the silicon and forced the p–n junction to travel further away from the surface and degrade the current generation efficiency of the PV cell [6–8]. This made lithium nonviable, and unsuitable for use with other metals as well. This also meant that scientists were forced to look for alternatives and they thus developed doped (arsenic and boron) semiconductors, namely silicon, to be used as electrical contacts [9].

However, as with most scientific discoveries, the theoretical possibility of using metals for PV purposes predates the development of the first commercially viable solar cell. A semiconductor-junction photo-sensitive cell made of copper and copper oxide junction was first suggested and developed by Wilhelm Hallwachs in 1904 as a part of his research that laid the foundation for "Hallwachs-Effekt," now called the photoelectric effect, and Albert Einstein's quantum light hypothesis [10,11].

Despite that, the use of metals in solar cells was essentially nonexistent until the development of gallium arsenide (GaAs) and its use in the production of heterostructure solar cells [12].

Gallium is a group 3 metal with transition metal properties (variable oxidation states), and can normally be found as gallium(III) in bauxite and zinc ores [13]. While it was discovered in 1875, its usage as a viable solar cell material was not discovered until 1970 by Zhores Alferov of the USSR ($Al_xGa_{1-x}As$-GaAs heterojunctions) [14]. Further research and development in the 1970s and 1980s led to GaAs based heterostructure solar cells having greater efficiencies than the conventional crystalline silicon solar cells [15]. Such was its positive impact in solar cell technology that, by the 1990s, it began to replace the use of silicon in the production of solar cells for satellites [16]. The use of GaAs in solar cells for space-based technologies, such as rovers and satellites, is prevalent even today. The highest recorded efficiencies for both single-junction and multi-junction solar cells are both GaAs based—28.8% for the former, while 32% for the latter (dual- and triple-junction solar cells based on GaAs with germanium and indium gallium phosphide layers) [17].

Since the 1970s, there was great progress in a branch of PV technology called dye-sensitized solar cells, a technology where the use of inert metals such as titanium and platinum has become a staple. This technology utilizes a finely powdered metal oxide layer covered in a photosensitive dye on an electrolyte bed [18]. The modern version of the dye-sensitized solar cell contains titanium dioxide nanoparticles that is coated with a molecular dye that absorbs sunlight, a structure that is very similar to chlorophyll in green leaves. As a part of the fabrication process, the titanium dioxide is submerged in an electrolyte solution that has been placed above a platinum-based catalyst. An anode (the titanium dioxide) and a cathode (the platinum) are placed on either side of a liquid conductor (the electrolyte), similar to a conventional alkaline battery [19].

While the use of cadmium in solar cell technology has also existed since the 1970s, the PV effect in cadmium selenide and cadmium sulfide was demonstrated by Audobert and Stora in 1932 [20]. While the first generation of thin-film solar cells was made from amorphous silicon, much greater efficiencies ($> 10\%$) was reached with a copper sulfide/cadmium sulfide complex in 1980 by Szedon, Biter, and Dickey at the Institute of Energy Conversion at the University of Delaware [21]. In 1992, the Ferekides Research Group at the University of South Florida developed a 15.9% efficient thin-film PV cell made of cadmium telluride

(CdTe), breaking the 15% barrier for the first time for this technology [22]. In many commercially viable thin-film solar technology and multi-junction solar cells today, CdTe is a staple. Another important metal from the same period as cadmium and the same group as gallium that is now widely used in second generation thin-film PVs and quantum dot solar cells is indium, mainly in the form of the semiconductor copper indium gallium selenide (CIGS) [23].

Since the early 2000s, however, a large portion of the interest in the use of metals in solar cells has been focused on a particular group of metal that exhibit a unique property called surface plasmon (SP) resonance. The interface between a metal and a dielectric/semiconductor can support SPs, which are collective oscillations of conduction-band electrons in metals and such oscillations occur at the interface of the metal and the dielectric. SPs can be excited to higher energy states in metallic nanostructures/nanoparticles, where it is localized and has limited spatial freedom, or along a continuous metal-dielectric interface called SP polaritons (SPP). They are able to propagate and restrict light at this interface. Plasmonic metals can not only improve the solar-cell efficiency by trapping or concentrating light in the absorber layer, but can also serve as a back contact or a cheap anti-reflective electrode in some configurations [24]. Metals such as silver, gold, and aluminum that have been found to exhibit these properties have also been identified as the most suitable metals for PV purposes. Despite this, the interest in plasmonic solar cells began to wane in the 2011–12 period due to increased research in organic solar cells [25]. However, that interest has recently been reignited due to the emerging concept of using plasmonics in thin-film technology, and their possible commercial viability [26].

This chapter on "Metal nanostructures for solar cells" will be divided into several portions that will deal with all of the above technologies. However, a significant amount of focus will be placed on "plasmonic solar cells." We will first discuss in detail CdTe, copper indium gallium selenide, GaAs in solar cells, and then move on to the use of tin or lead in perovskite solar cells and multi-junction solar cells.

The next section will then deal with fundamental physics behind plasmonics: the plasmon resonance phenomenon, metals exhibiting plasmon resonance, an introduction to plasmonic nanostructures, and a theoretical link between plasmonic nanostructures and solar cells.

We will then traverse to plasmonic properties necessary for metal nanostructures used with solar cells, plasmonic metals suitable for solar cell

applications, and possible plasmonic nanostructure configuration with solar cells—top, embedded, back, or a combination of all three.

The subsequent section will delve more into surface plasmonic nanostructures and the optimization physical parameters of these nanostructures for use in solar cells—parameters such as metal, diameter, pitch, shape, periodicity, and the effect of source polarization. Analysis of the extent of the optical and electrical enhancement of solar cells due to the presence of the plasmonic nanostructures will also be provided.

Finally, we will talk about the possibility of using plasmonic nanostructures embedded within the solar cell substrate, and the extent to which this concept can be made a reality.

## 13.2 Section 2—Photovoltaic technologies involving metals

### 13.2.1 Cadmium telluride

CdTe is a PV technology based on the use of a thin film (TF) of CdTe to absorb and convert sunlight into electricity [27–31]. CdTe is growing rapidly in acceptance and now represents the second most-utilized solar cell material in the world. The first still is silicon [27]. Solar panels based on CdTe are the first and only thin-film PV technology to surpass crystalline silicon PV in cost for a significant portion of the PV market, namely in multi-kilowatt systems [28].

CdTe-based PV is considered a thin-film technology because the active layers are just a few microns thick, or about a tenth the diameter of a human hair. CdTe is recognized as a very promising material for high efficiency, low-cost thin-film solar cells [29,30]. CdTe is a II–VI compound semiconductor with a direct optical bandgap of $\sim 1.5$ eV that is nearly optimally matched to the solar spectrum for PV energy conversion [29,30]. CdTe also has a high absorption coefficient, $>5 \times 10^5$/cm, which means that $\sim 99\%$ of photons with energy greater than the bandgap ($E_g$) can be absorbed within 2 μm of CdTe film [29,30]. Processing homogenous polycrystalline TFs of CdTe is less critical for CdTe than for many other compound semiconductors. The best small-area CdTe thin-film cells manufactured show more than 15% conversion efficiency, whereas large-area modules with aperture efficiencies in excess of 10% have also been reported [29].

A schematic of a typical CdTe solar cell is shown in Fig. 13.1. Transparent conducting oxide (TCO) layers such as $SnO_2$ or $Cd_2SnO_4$ are transparent to visible light and highly conductive to transport current

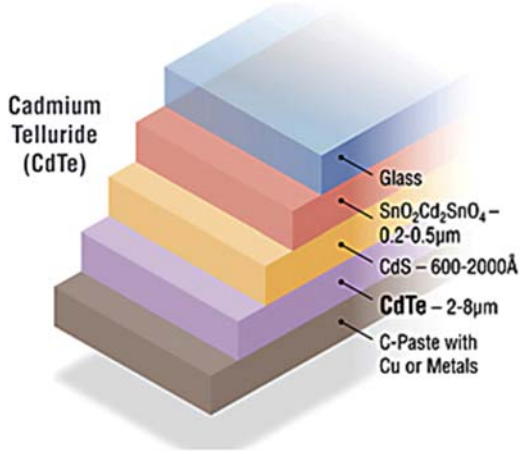


**Figure 13.1** Schematic illustration of a typical CdTe superstrate thin-film PV device. In this design, the layers of the device are deposited onto a glass "superstrate" that allows sunlight to enter. The sunlight passes through the glass and produces electrical current and voltage in the lower layers. *PV,* Photovoltaic. *Diagram reprinted with permission from The National Renewable Energy Laboratory (NREL).*

efficiently. Intermediate layers such as CdS help in both the growth and electrical properties between the TCO and CdTe. The CdTe film acts as the primary photo-conversion layer and absorbs most visible light within the first one or two microns of material. Together, the CdTe, intermediate, and TCO layers form an electric field that converts light absorbed in the CdTe layer into current and voltage [31]. Metal is placed on the back to form electrical contacts. In production, all these layers are deposited on incoming glass and processed into complete solar panels in just a few hours [32].

Due to its high optical absorptivity, the CdS film with a thickness of 0.1 μm can absorb approximately 63% of the incident radiation with energy greater than $E_g$ [33–35]. Higher short-circuit current densities ($J_{sc}$) can be achieved by, for example, reducing the CdS thickness to improve the blue response in the conventional CdS/CdTe device structure. However, reducing the CdS thickness can adversely impact device open-circuit voltage ($V_{oc}$) and fill factor (FF) [33,36]. Additionally, it is well known that the $CdCl_2$ treatment is important for making high-efficiency CdTe devices. This is because $CdCl_2$ treatment offers several substantial benefits such as, for example, increased grain size, grain-boundary passivation, increased CdS/CdTe interface alloying, and

reduced lattice mismatch between the CdS and CdTe layers. However, one disadvantage of the $CdCl_2$ treatment is that over-treatment can result in loss of adhesion. Hence, it is important to note that the adhesion problems can limit the optimal $CdCl_2$ treatment process, as well as device performance [33].

Research in CdTe dates back to the 1950s because, as highlighted earlier, it is almost perfectly matched to the distribution of photons in the solar spectrum in terms of optimal conversion to electricity [37]. Early leaders in CdS/CdTe cell efficiencies were General Electric in the 1960s, and then Kodak, Monosolar, Matsushita, and AMETEK [38–42].

Chu et al. made significant contributions in moving the efficiency of CdTe cells to above 15% in 1992, a critical level of success in terms of potential commercial competitiveness [22]. This was the first TF to reach this level, as verified at the National Renewable Energy Laboratory (NREL) [44].

Matsushita claimed an 11% module efficiency using close spaced sublimation and then dropped out of the technology. One possible explanation could possibly be the internal corporate pressures over cadmium, which is highly toxic [45]. A similar efficiency and fate eventually occurred at BP Solar, which dropped the technology in the early 2000s [46].

#### 13.2.1.1 Cell efficiency

Best cell efficiency has plateaued at 16.5% since 2001 (a record held by NREL) [47]. The opportunity to increase current has been almost fully exploited, but more difficult challenges associated with junction quality, with properties of CdTe and with contacting, have not been as successfully resolved [48].

Improved doping of CdTe and increased understanding of key processing steps (e.g., cadmium chloride recrystallization and contacting) are key to improving cell efficiency [49]. Since CdTe has the optimal band gap for single-junction devices, it may be expected that efficiencies regularly exceeding 20% (such as already shown in CIS alloys) should be achievable in mass produced CdTe cells [50]. In 2009, EMPA, the Swiss Federal Laboratories for Materials Testing and Research, demonstrated a 12.4% efficient solar cell on flexible plastic substrate [51].

#### 13.2.1.2 Low cost manufacturing

The major advantage of this technology is that the panels can be manufactured at lower costs than silicon-based solar panels. First Solar was the first

manufacturer of CdTe panels to produce solar cells for less than $1.00/W [52]. Some experts believe it will be possible to get the solar cell costs down to around $0.5/W [53]. With commodity-like margins and combined with balance-of-system costs, installed systems near $1.5/W seem achievable [54]. With sufficient levels of sunlight, this would allow such systems to produce electricity in the $0.06–$0.08/kW h range—or for less than fuel-based electricity costs [55].

#### 13.2.1.3 Advantages of cadmium telluride solar panels

CdTe panels have several advantages over traditional silicon technology. These include:

1. Ease of manufacturing: The necessary electric field, which makes turning solar energy into electricity possible, stems from properties of two types of cadmium molecules, cadmium sulfide, and CdTe. This means a simple mixture of molecules achieves the required properties, simplifying manufacturing compared to the multi-step process of joining two different types of doped silicon in a silicon solar panel [56].
2. Good match with sunlight: CdTe absorbs sunlight at close to the ideal wavelength, capturing energy at shorter wavelengths than is possible with silicon panels [57].
3. Cadmium is relatively abundant: It is produced as a by-product of other important industrial metals, such as zinc; consequently it has not had the wider price swings that have occurred in the past two years with silicon prices [58].

#### 13.2.1.4 Drawbacks

While price is a major advantage, there are some drawbacks to this type of solar panel, namely:

1. Lower efficiency levels: CdTe solar panels currently achieve an efficiency of 10.6%, which is significantly lower than the typical efficiencies of silicon solar cells [59].
2. Tellurium supply: While cadmium is relatively abundant, Tellurium (Te) is not. It is an extremely rare element (1–5 parts per billion in the Earth's crust) [60]. According to the United States Geological Survey, global tellurium production in 2007 was 135 metric tons [61]. Most of it comes as a by-product of copper, with smaller byproduct amounts from lead and gold. One gigawatt of CdTe PV modules would require about 93 metric tons of Te (at current efficiencies and

thicknesses), so the availability of tellurium will eventually limit how many panels can be produced with this material [62].

Since CdTe is now regarded as an important technology in terms of PV's future impact on global energy and environment, the issue of tellurium availability is significant. Recently, researchers have added an unusual twist: astrophysicists identify tellurium as the most abundant element in the universe with an atomic number over 40 [63]. This surpasses heavier materials like tin, bismuth, and lead, which are common. Researchers have shown that well-known undersea ridges (which are now being evaluated for their economic recoverability) are rich in tellurium and by themselves could supply more tellurium than we could ever use for all of our global energy [64]. It is not yet known whether this undersea tellurium is recoverable, nor whether there is much more tellurium elsewhere that can be recovered [65].

However, it has been suggested that the capacity for manufacturing thin-film PV solar cells from CdTe is very close to the maximum supply of tellurium available, or that may become available and that the ability of companies like First Solar to continue to expand at the rates at which they have been growing over the past several years will become increasingly difficult to maintain because of lack of available tellurium (even with recovery from recycling) [66].

#### *13.2.1.5 Toxicity of cadmium*

Cadmium is one of the top 6 deadliest and toxic materials known. However, CdTe appears to be less toxic than elemental cadmium, at least in terms of acute exposure [67].

This is not to say it is harmless. CdTe is toxic if ingested, if its dust is inhaled, or if it is handled improperly (i.e., without appropriate gloves and other safety precautions) [68]. The toxicity is not solely due to the cadmium content. One study found that the highly reactive surface of CdTe quantum dots triggers extensive reactive oxygen damage to the cell membrane, mitochondria, and cell nucleus [69]. In addition, the CdTe films are typically recrystallized in a toxic compound of cadmium chloride [70].

The disposal and long-term safety of CdTe is a known issue in the large-scale commercialization of CdTe solar panels [32]. Serious efforts have been made to understand and overcome these issues. Researchers from the U.S. Department of Energy's Brookhaven National Laboratory have found that large-scale use of CdTe PV modules does not present any risks to health and the environment, and recycling the modules at the end

of their useful life resolves any environmental concerns [71–73]. During their operation, these modules do not produce any pollutants, and, furthermore, by displacing fossil fuels, they offer great environmental benefits. CdTe PV modules appear to be more environmentally friendly than all other current uses of Cd.

The approach to CdTe safety in the European Union and China is, however, much more cautious: cadmium and cadmium compounds are considered as toxic carcinogens in EU, whereas Chinese regulations allow Cd products for export only [74,75]. The issue about regulating the use of CdTe is currently being discussed in Europe. At the present time, the most common opinion is that the use of CdTe in residential/industrial rooftop installations does not pose a major environmental problem. However, some groups have expressed concern about large utility-sized projects in the desert and the possibility of release of cadium gases or water table contamination [76,77].

#### *13.2.1.6 Ongoing research*

Research on CdTe focuses on several of today's challenges:

1. Boosting efficiencies by, among other things, exploring innovative TCOs that allow more light into the cell to be absorbed and that more efficiently collect the electrical current generated by the cell [78,79].
2. Studying mechanisms such as grain boundaries that can limit the voltage of the cell [78,79].
3. Understanding the degradation that some CdTe devices exhibit at contacts and then redesigning devices to minimize this phenomenon [78,79].
4. Designing module packages that minimize any outdoor exposure to moisture [78,79].
5. Engaging aggressively in both indoor and outdoor cell and module stress testing. For example, we propose to test thin-film modules in hot and humid climates [78,79].

### 13.2.2 Copper indium gallium selenide

Since its initial development, copper indium diselenide ($CuInSe_2$) thin-film technology has been considered promising for solar cells because of its favorable electronic and optical properties. It was later found that by substituting gallium (Ga) for indium (In), the bandgap can be increased from about 1.04 eV for copper indium diselenide (CIS) films to about

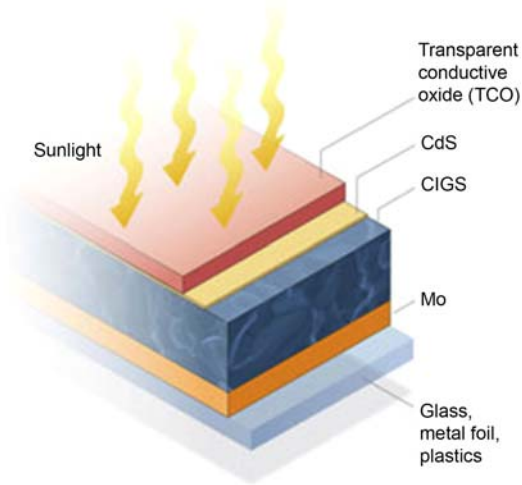


**Figure 13.2** Structure of a GaAs cell cell. *GaAs*, gallium arsenide. *Diagram reproduced with permission from IEEE J. Photovoltaics (X. Wang + et al.).*

1.68 eV for copper gallium diselenide (CGS) films [80–82]. Optimal devices have been fabricated with only a partial substitution of Ga for In, leading to a substantial increase in overall efficiency and more optimal bandgap. These solar cells are commonly known as a copper indium gallium diselenide [$Cu(In_xGa_{1-x})Se_2$], or CIGS, cells [83–85] (see Fig. 13.2).

Although laboratory-scale cell efficiencies have exceeded 20%, commercial CIGS modules typically have efficiencies between 12% and 14% [84,85].

The benefits of CIGS solar cells include:

- High absorption: This direct-bandgap material can absorb a significant portion of the solar spectrum, enabling it to achieve the highest efficiency of any thin-film technology [83–85].
- Tandem design: A tunable bandgap allows the possibility of tandem CIGS devices [83–85].
- Protective buffer layer: The grain boundaries form an inherent buffer layer, preventing surface recombination and allowing for films with grain sizes of less than 1 μm to be used in device fabrication [83–85].

#### 13.2.2.1 Production

Two of the low-cost deposition methods that produce the highest device and module efficiencies were developed in the 1980s. These methods are:

- Co-evaporation, in which precursor elements are allowed to sublimate in a high-vacuum environment and then re-deposit on a heated substrate [86].
- Precursor Reaction Processes, in which a precursor containing Cu and In/Ga is deposited at a low temperature by any of several processes, such as sputtering or electroplating. This is followed by a reactive annealing step in a Se compound, such as hydrogen selenide ($H_2Se$) or gaseous selenium (Se), to form CIGS films. This is also commonly known as two-stage deposition; a variant of this technique, three-stage deposition, is also commonly used [87].

After the CIGS deposition, the junction is formed by chemical-bath deposition of the n-type CdS layer. To finish the solar cell, a high-resistance zinc oxide (ZnO) layer and a high-conductivity n + -type ZnO layer are deposited by either sputtering or chemical-vapor deposition. Laser-scribing processes at different steps in the production process create the individual solar cells connected in series [86,87].

Alternative manufacturing techniques have been explored, such as reactive sputtering, magnetron sputtering (Cu, In, and Ga are sputtered while Se is evaporated), and electrodeposition [88]. However, co-evaporation and precursor reaction processes still remain the most popular (Fig. 13.2).

A major increase in device performance was achieved when the ceramic or borosilicate glass substrate was replaced by soda-lime glass. Although soda-lime glass was chosen because it has closer thermal expansion properties to CIGS, it was ultimately determined that the primary advantage of using soda-lime glass results from the diffusion of sodium (Na) ions from the glass into the CIGS absorber layer. Work is currently being done to identify the role of Na in improving CIGS performance and what tolerances CIGS has to the inclusion of Na. Current manufacturing techniques incorporate Na either from soda-lime glass or a separate Na source. Soda-lime glass has an added advantage of being less expensive than previous glass substrates [89,90]. The Na-induced increase in carrier concentration in CIGS has been suggested to be due to incorporation of Na onto In or Ga lattice sites, where it would directly act as an acceptor [89,90].

All high-efficiency CIS and CIGS devices use molybdenum (Mo) as the back contact primarily because of its work function and the high reflectivity of the Mo film. These films are typically deposited through direct-current (DC) sputtering [90]. The sputtering deposition process

requires precise pressure to control the stress in the film. Because of some inherent problems with the Mo back-contact, such as the possibility of a hole-blocking Schottky diode effect at the interface, other metals have been investigated to replace Mo, but have had limited success [91]. Furthermore, molybdenum has been found to be toxic to humans and other organisms alike [92].

### 13.2.3 Gallium arsenide

GaAs is a III–V semiconductor with a zinc blende crystal structure. GaAs solar cells were first developed in the early 1970s and have several unique advantages. GaAs is naturally robust to moisture and ultraviolet (UV) radiation, making it very durable [93,94]. It has a wide and direct band gap, which allows for more efficient photon absorption and high-output power density and, additionally, it has a low temperature coefficient and strong low light performance. GaAs naturally performs better at converting the sun's energy into electricity than other materials under normal conditions. Furthermore, GaAs solar cells deliver more energy in high heat or low light, two of the most common real-world conditions for solar cells [93,94].

In 1970, the first GaAs heterostructure solar cells were created by the team led by Zhores Alferov in the USSR [95]. In the early 1980s, the efficiency of the best GaAs solar cells surpassed that of conventional, crystalline silicon-based solar cells. In the 1990s, GaAs solar cells took over from silicon as the cell type most commonly used for PV arrays for satellite applications. Later, dual- and triple-junction solar cells based on GaAs with germanium and indium gallium phosphide layers were developed as the basis of a triple-junction solar cell, which held a record efficiency of over 32% and can operate also with light as concentrated as 2000 suns [96,97] (see Fig. 13.3). This kind of solar cell powers the rovers *Spirit* and *Opportunity*, which are exploring Mars' surface. Additionally, many solar cars utilize GaAs in solar arrays [98].

While the "layman" may not be familiar with GaAs, it has been used to build solar cells for over four decades. That is because the chemical and physical properties of GaAs make it the undisputed choice for high-efficiency solar cells. For this reason, the space program has used GaAs solar cells for over 25 years, starting with the Mir space station and continuing to this day, with virtually every space bound vehicle incorporating GaAs solar cells. These types of cells are also used in terrestrial solar

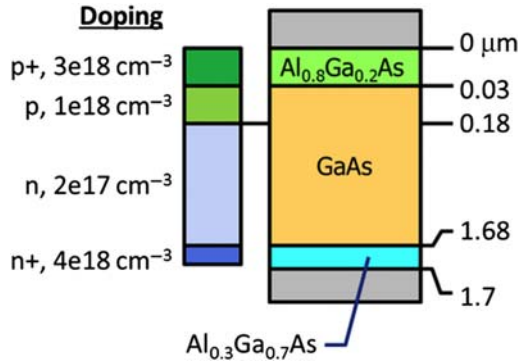


**Figure 13.3** Structure of a GaAs cell. Diagram reproduced with permission from IEEE J. Photovoltaics (X. Wang, et al.).

concentrating systems because of their ability efficiently to convert the sun's energy into electricity [99].

GaAs has the ability to deliver the highest energy conversion efficiencies, which is a measure of how much of the sun's energy is converted to electricity. In fact, all of the world records for high-efficiency solar cells are held by some form of a GaAs solar cell [96,97,100]. The unique properties of GaAs that lead to high efficiency include a direct band gap for efficient conversion of photons to electron–hole pairs. It turns out that the best GaAs solar cells operate very much like an LED, being almost equally capable of converting electricity to light as they are of converting light to electricity [97].

Under real-world conditions, where changing levels of illumination and temperature are common, GaAs is a true standout compared to other materials. GaAs operates near its full efficiency at levels of illumination that are only one tenth of a sun, a level where most semiconductor materials have long since stopped operating as efficient solar cells. GaAs also has a temperature coefficient that is a mere one fifth of silicon and only one third of CIGS or CdTe. That means that at high temperature, GaAs continues to deliver energy at near its rated output, while the energy output of a silicon cell declines by 30% or more [101]. The advantages of GaAs as a material for solar cell applications as discussed thus far can be summarized in the following manner [93–102].

1. *Low temperature coefficient*: the temperature coefficient is a measure of performance (efficiency) loss versus temperature relative to 25°C. Most widely used solar materials, such as Si, lose a lot of efficiency when the

temperature rises. GaAs, however, has a low temperature coefficient and thus experiences very little efficiency loss at higher temperatures [102].

2. *Good low-light performance*: In most solar cells, the energy available in weak illumination (low light) leaks away, but this does not happen in the case of high quality GaAs. The wide bandgap and low-defect crystal structure of GaAs solar cells also results in a lower leakage current and more rapid voltage buildup with illumination. Additionally, the wider bandgap of GaAs also means it is much better tuned to the wavelengths of LED and fluorescent light, relative to silicon. This is important because GaAs solar cells can therefore be used in an office or warehouse environment to generate solar power [102].
3. *High efficiency*: GaAs is the highest efficiency solar material currently available in the world. This means it produces more power for a given surface area than any other solar technology. This is very important when surface area is limited, such as on an aircraft, cars, or on small satellites. For example, triple junction GaAs solar is 37% + efficient while silicon solar is around 21% efficient at beat [102].
4. *Excellent UV radiation and moisture resistance*: GaAs is inherently resistant to damage from moisture, radiation, and ultraviolet light. These properties make GaAs an excellent choice for aerospace applications where there is increased UV and other forms of potentially harmful and detrimental radiation [102].
5. *Flexible and lightweight*: GaAs solar is highly efficient even when very thin layers are used, which keeps overall solar material weight low. Alta Devices uses a thin GaAs layer placed on a thin flexible substrate to maintain its lightweight and flexible properties. Si is not as good an absorber of sunlight, so a relatively thick layer is required, making it very brittle and heavier. Rigid brittle glass is usually placed on top of the silicon, which further increases weight.

One of the major problems with GaAs is that the material itself is expensive. However, it is possible to grow extremely thin layers of GaAs that use just minuscule amounts of material, keeping the cost down. At the same time, these thin layers of semiconductor material actually get more efficient as they become thinner. The opposite is true for most other solar cell technologies. And a side benefit of these thin cells is that they are completely flexible and can be incorporated into any of today's commercially available encapsulating materials. Even better, the flexible nature of these cells opens up the potential for a whole new generation of

innovation in solar cells from factors that can dramatically reduce the cost of solar electricity.

### 13.2.4 Perovskite solar cell

Halide perovskites are one of the most promising materials for delivery of the next generation of solar cells. Perovskite solar cells have enabled power conversion efficiency comparable with established technologies, such as silicon and CdTe [103,104]. Their stability is constantly improving and it is not difficult to believe that stability will soon reach market requirements. There remains a main concern about the toxicity of lead, a key constituent of all the better-performing perovskite solar cells so far demonstrated [104]. To tackle that, scientists have been working on developing lead-free, tin-based perovskite solar cells. Sn-based halide perovskite materials have attracted tremendous attention and have been employed successfully in solar cells. However, their high conductivities resulting from the unstable divalent Sn state in the structure cause poor device performance and poor reproducibility. Therefore, scientists used excess tin iodide ($SnI_2$) in Sn-based halide perovskite solar cells ($ASnI_3$, methylammonium, and formamidinium tin iodide as the representative light absorbers) combined with a reducing atmosphere to stabilize the $Sn^{2+}$ state [103]. Excess $SnI_2$ can disperse uniformly into the perovskite films and functions as a compensator as well as a suppressor of $Sn^{2+}$ vacancies, thereby effectively reducing the p-type conductivity. This process significantly improved the solar cell performances of all the $ASnI_3$ materials on mesoporous $TiO_2$. Optimized $CsSnI_3$ devices achieved a maximum power conversion efficiency of 4.81%, which is the highest among all inorganic Pb-free perovskite solar cells to date [103,104].

## 13.3 Section 3—Surface plasmon resonance

Metal nanostructures (e.g., nanoparticles) display a wide range of interesting and useful optical properties that have made them a primary focus of current fundamental and application driven research in a variety of applications. Such applications include, but are not limited to, biomedicine, diagnostics, healthcare, disease treatment, solar cells, and renewable energy, optical communication, etc. [105]. Fundamentally, metal nanoparticles bridge the gap between the bulk and the atomic level, and thus exhibit unique properties that are particular to this size range. Additionally, recent advances in nanotechnology has allowed for the

precise and affordable fabrication of a wide range of novel metal nanostructures the physical (e.g., morphological) and optical properties of which have been well characterized. Such metal nanostructures have now been functionalized for incorporation into a wide variety of devices [106–108]. These advances in fabrication techniques have also helped reduce nanoparticle size distribution, thus improving the morphological and optical properties of the nanoparticles by reducing the inhomogeneity problem [105].

The most widely used of these exploited optical properties of metal nanoparticles is the optical plasmon resonance that is associated with the collective oscillation of conduction band electrons that are confined in nanoparticles [105]. These collective but localized oscillation of conduction band electrons are known as SPs. At specific frequencies, these charge oscillations can be driven resonantly that can, under the right conditions, produce intense light fields near the metal and cause strong light scattering. The light concentration and scattering effects can be effectively harnessed to trap light inside, for example, the absorbing semiconductor layers of a solar cell and ultimately to enhance the power conversion efficiency of such "plasmonic solar cells." [109]

The resonance in nanoscale metallic structures is determined by multiple morphological factors such as, for example, the size, shape, and dielectric properties of the nanoparticle, and the physical, chemical, and electrical properties of its immediate environment, thus making it an attractive phenomenon to exploit in the design of, for example, novel solar cells (both traditional and thin-film) and also optically based biological or chemical sensors [109–119]. A qualitative explanation of plasmon resonance can be presented in the simplest case of a spherical metal nanoparticle as depicted in Fig. 13.4 [105]. When a small spherical metallic nanoparticle (note that metallic nanoparticles need not be limited to a spherical shape to support plasmon resonances) is irradiated by light, the oscillating electric field of the incident light, on impinging upon the metallic nanoparticle, can cause its conduction band electrons to oscillate coherently. In such conditions, the electron cloud in the metallic nanoparticle is displaced relative to the nuclei, and a restoring force arises from Coulombic attraction between electrons and nuclei that results in oscillation of the electron cloud relative to the nucleus [105,120]. This oscillation frequency is governed by several parameters. Four of the important parameters are the density of electrons, the effective electron mass, the shape, and size of the charge distribution. The collective oscillation of the

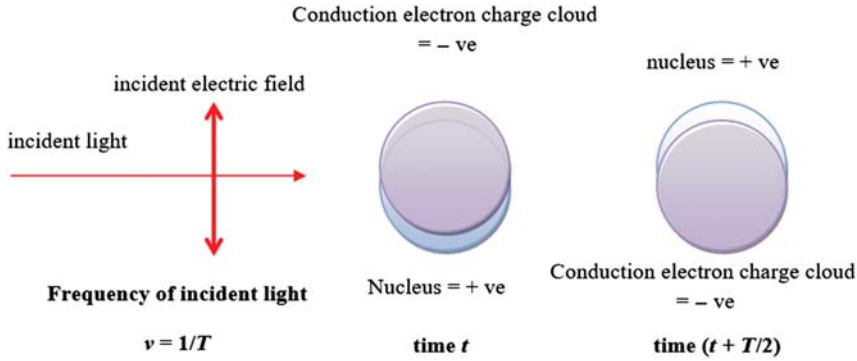


**Figure 13.4** Plasmon oscillations in spherical metal nanoparticles showing the displacement of the conduction electron charge cloud relative to the nuclei. Diagram reproduced with permission from Chowdhury Dissertation.

electrons is called the dipole plasmon resonance of the particle. For larger particles, higher modes of plasmon excitation can occur, such as the quadruple mode where half of the electron cloud moves parallel to the direction of the applied electric field and the other half moves antiparallel to the direction of the applied electric field [105,116,120]. For noble metal nanoparticles like silver and gold which, have completely filled d-orbitals and half filled s-orbitals, the plasmon frequency is also influenced by the electrons in the d-orbitals. The plasmon frequency can be related to the metal dielectric constant, which is a property that can be measured as a function of wavelength for bulk metal [105,116,120].

The frequencies and intensities of the localized SP (LSP) resonances are known to be sensitive to the dielectric properties of the medium [121–133], and, in particular, to the refractive index (RI) of matter in the extreme vicinity of the particle surface [121,122,125,126,134–138]. Measurements and simulations of nanoparticle LSP resonance sensitivity to both bulk and local RI, $n$, are a matter of current research [121–138]. As a matter of general observation, plasmon resonances have been found to shift to the red as $n$ is increased. More specifically, for a variety of nanoparticles, the peak wavelength of resonance, $\lambda_{max}$, has been found to increase linearly with $n$ [121–124,126–129]. However, the peak wavelength sensitivities of plasmons supported by nanoparticles of various sizes, shapes, and compositions differ greatly [114,121,123,127,129]. Considering only the RI sensitivities of the lowest-energy, dipolar resonances, values of $d\lambda_{max}/dn$ ranging from tens to hundreds of nanometers have been observed for various nanoparticles, such as, for example,

nanotriangles, nanoplates, nanorods, nanospheres, and nanoshells, interestingly with high-aspect-ratio particles and thin nanoshells having the higher sensitivities [121]. Examples of the variation of the plasmon resonance of silver nanoparticles of different shapes as shown by their respective extinction, scattering, and absorption spectra have been calculated (using a finite-difference time-domain technique) and shown in Fig. 13.5A–E [114].

When excited by incident irradiation (e.g., sunlight, laser light, LED light, etc.), SP excitation can result in scattering and giant enhancement of the electric fields around the metallic nanoparticle. Metal particles in the order of wavelength of light (mostly in the nm regime) basically act as miniature dipoles that can scatter the incident radiation, which can then be coupled to the modes of the underlying semiconductor in plasmonic solar cell applications [139]. Metals show this behavior because of the presence of relatively abundant free charge carriers. Highly doped semiconductors and metal oxides can also show similar plasmon effects but because of the relatively lower number of free charge carriers, their resonance is mostly limited to the infrared region. For small particles in the quasi-static limit, the scattering and absorption cross-sections are given by [139,140]:

$$C_{abs} = \frac{2\pi}{\lambda} lm[\alpha] \text{and} C_{sca} = \frac{1}{6\pi}\left(\frac{2\pi}{\lambda}\right)^4 |\alpha|^2 \tag{13.1}$$

Here $\alpha$ is the polarizability of the particle for a small spherical particle in vacuum, given by [139,140]:

$$\alpha = 3V\left[\frac{\frac{\varepsilon}{\varepsilon_m} - 1}{\frac{\varepsilon}{\varepsilon_m} + 2}\right] \tag{13.2}$$

where $V$ is the volume of the particle, $\varepsilon$ the permittivity of the metal and $\varepsilon_m$ the permittivity of the surrounding medium. The scattering efficiency $Q_{sca}$ is given by $Q_{sca} = C_{sca}/(C_{sca} + C_{abs})$. For frequencies near their resonance, these nanoparticles can have a scattering or absorption cross-section much larger than their geometric cross-section [144,145]. For example the scattering cross-section of a 100 nm silver nanoparticle can be ten times more than the geometric cross-section at the plasmon frequency [139].

The development of nonwafer-based TF PV devices (e.g., solar cells) in recent years has been one of the preferred routes to lower the material

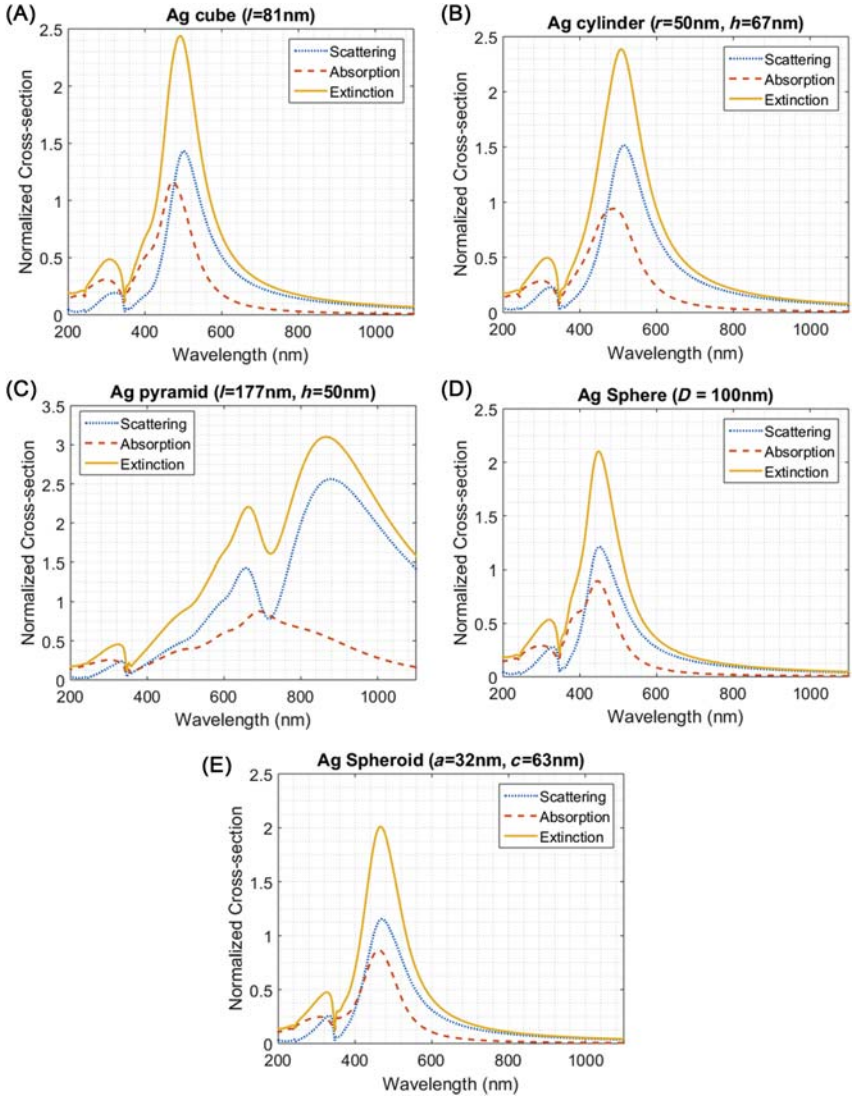


**Figure 13.5** Absorption, scattering and extinction spectra for the different nanoparticle shapes (A) cube, (B) cylinder, (C) pyramid, (D) sphere, and (E) spheroid. *Diagram reprinted with permission from IEEE Xplore (Choudhury et al.).*

costs of PV electricity and thus achieve grid parity [141–143]. TF cells can also allow higher conversion efficiencies than traditional thick-film cells due to improved conditions for carrier collection [141]. Hence, TF cells can potentially be supported on a wide variety of rigid (glass, building

facades, and rooftops, etc.) or flexible (plastics, etc.) inexpensive substrates, thereby extending PV solutions to a much wider range of consumer-oriented applications [141–145]. Nevertheless, TF PV technology is not yet sufficiently developed to be competitive with traditional crystalline silicon (c-Si) cells. While a remarkable 25.6% efficiency record has been achieved in a laboratory with 150 μm thick textured c-Si wafers [141,146], this value drops below 20% for a thickness around 40 μm and to even smaller values when using thinner layers [141,147]. So, the efficiencies of commercially available TF panels (~10%–13%) are still low in comparison with those of wafer-based Si (~15%–20%). The fundamental problem currently plaguing TF PV technology is that the required light absorption lengths are usually much higher than the carrier diffusion lengths in the TF materials. Therefore, the improvement of nonwafer-based cells relies on the development of effective light trapping and/or enhanced light absorption techniques that can successfully enable physically thin but optically thick absorbers with good material quality [141,147,148].

Many different techniques have been employed to increase the light absorption and current generation efficiency of thin-film solar cells. For example, nanostructures have been designed and implemented to be utilized in conjunction with PV cells [112,149–152]. Such structures can include, for example (but are not limited to), nanowire solar cells and quantum dot solar cells. These have been illustrated in Fig. 13.6. Nanostructured solar cells utilize different principles and materials to improve light coupling and/or light absorption efficiency within the PV cell itself. The nanoscale dimensions of these structures result in greater surface area to volume ratio, which in turn can increase the pathways for light coupling.

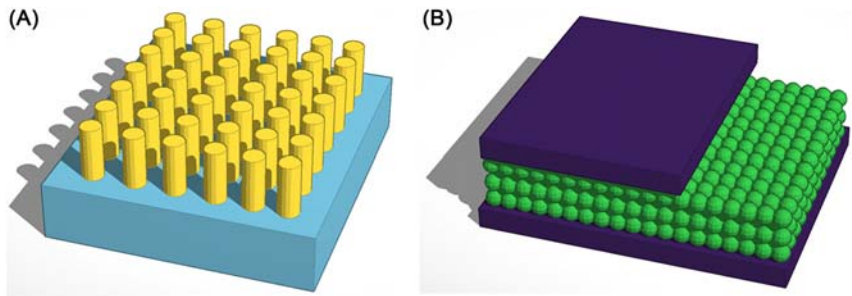


**Figure 13.6** Nanostructured solar cells (A) nanowire solar cells, and (B) quantum dot solar cells. *Diagram reprinted with permission from IEEE Xplore (Choudhury et al.).*

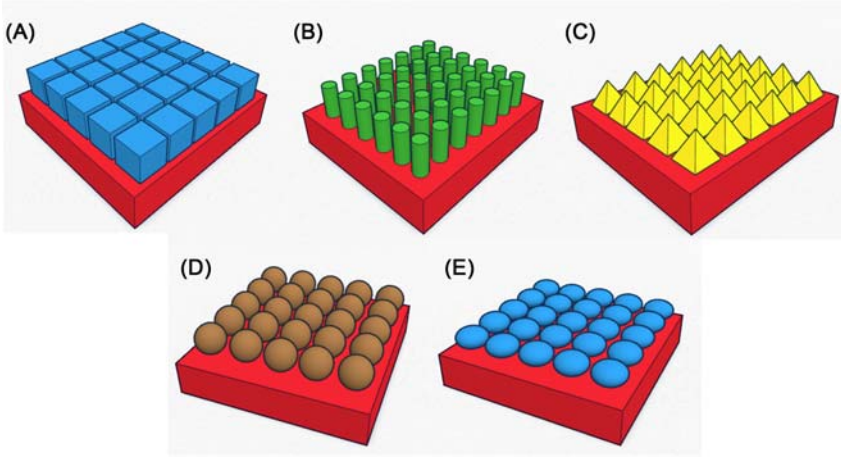


**Figure 13.7** Different shapes of plasmonic nanostructures analyzed—(A) cube, (B) cylinder, (C) pyramid, (D) sphere, and (E) spheroid. *Diagram reprinted with permission from IEEE Xplore (Choudhury et al.).*

Another method to improve the efficiency of thin-film solar cells is to use plasmonic nanoparticles/nanostructures of different kinds in various morphological configurations with the thin-film solar cells [24,112,153–161]. A simple example of such a plasmonic-solar cell (thin-film) configuration can be an ordered 2-D array of metallic nanoparticles placed on top of a silica coated silicon substrate as shown in Fig. 13.7A–E. This technique can simultaneously take advantage two phenomena, namely: (1) the high near-fields surrounding the nanostructures close to their SP resonance (SPR) frequency and; (2) the effective coupling to waveguide modes supported by the thin Si film through an optimization of the array properties, essentially to increase the light absorption/retention/trapping capability of the plasmonic-solar cell. The increased absorbed and retention of light in the absorbing Si layer of the solar cell leads to the increased possibility of charge carrier creation (increased absorbed photons = increased possibility of electron − hole pair creation), and thereby increases the current producing capability of the solar cell. It is important to note that absorption within the metal nanoparticles represents a possible and/or significant mechanism for loss of optical energy in the plasmon-enhanced solar photo-conversion process and needs to be considered in the design process for plasmonic-solar cells. However, for many materials—particularly those that by themselves exhibit poor optical absorption—the beneficial effects of electromagnetic

energy concentration in the semiconductor absorbing layer due to the plasmon resonance of metallic nanoparticles can by far outweigh additional losses caused by metal absorption. As discussed above, the SPR frequency of a metallic nanoparticle can be tuned across the UV, visible, and near-infrared parts of the electromagnetic spectrum through a choice of its size, shape, and dielectric environment. This notion has enabled broadband enhancements of the photocurrent across the wide solar spectrum.

Rapid developments in this area can be possible by the ability of current or future technologies to be able to fabricate metallic nanoparticles of various shapes and sizes with very high precision and accuracy in, for example, the morphological parameters of the metal nanoparticles and the purity of the metal. Additionally, such fabrication techniques must be cost-effective and environmentally friendly for use in industrial scales. Present lithographic techniques, like e-beam lithography (EBL) and focused ion beam (FIB) lithography, enable fabrication of nanoparticles with high precision [151]. However, both EBL and FIB are expensive techniques with high setup and maintenance costs. This makes EBL and FIB unsuitable for large-area processing as would be required for industrial production. Development of new techniques, such as nano-imprinting or soft lithography, is gaining popularity as a robust practical production process for plasmonic solar cells [151]. This technology in conjunction with existing nanoparticle/nanostructure deposition techniques (like thermal evaporation or sputtering) promises control of the size, shape, and distribution of the nanoparticles with accuracy at the nanoscale. This can allow more freedom for optimization irrespective of the nature of the semiconductor used [151].

Optimization of the various parameters mentioned earlier has not been easily done to date due to many variables involved, such as the current state of nanoparticle fabrication technologies. Hence it is important to develop alternate techniques to understand better the technology, in particular, the interaction of incident light with the metal nanoparticles and the surrounding environment [151]. Powerful computer simulation tools that can give realistic interpretations of results (accounting for the dielectric medium surrounding the particles and also the effect for the neighboring particles) are needed to predict the photocurrent enhancements to enable fabrication of optimal nanoparticle arrays for light trapping and/or enhanced light absorption applications in solar cells. Such computer tools are currently available in the market and include, for example, FDTD Solutions (Lumerical Solutions, Inc.), OptiFDTD (Optiwave Systems,

Inc), and COMSOL Multiphysics (COMSOL, Inc.), among others. Such tools can be implemented both on single computers and also on a distributed computing network, thus giving the user tremendous computing capability to generate high-quality results. The results of current research discussed thus far (and much more not alluded to here) in incorporating plasmonics into solar cell applications look very promising. It allows the drastic reduction in the thickness of the active semiconductor layer (absorbing layer) and simultaneously boosts the performance of solar cells fabrication from materials with poor charge carrier transport properties. Hence, there is high optimism that PV research will benefit immensely from plasmonics, thereby enabling the use of low quality low cost materials and fabricating solar cells with high performance and low cost [151].

## 13.4 Section 4—Plasmonic solar cells—metals and configuration

As has been explained, plasmonic technology used in conjunction with solar cells have to be optimized in such a manner as to provide the maximum contribution in terms of optical and electrical enhancement [e.g., short circuit current density ($J_{SC}$) and open-circuit voltage ($V_{OC}$)]. This means that, regardless of the kind of plasmonic nanostructure that we use for this purpose, their physical parameters have to be altered/modified with utmost scrutiny. The general problem of incorporating a metal into solar cells is that the beneficial effects are at times counteracted by an enhanced absorption of light inside the metal [162–166]. Consequently, at first the potential enhanced incident light absorption enhancement into the solar cells as the results of the metal has to compensate these losses prior to causing a positive net gain.

Scattering and absorption depend on the size of the particles. Metallic particles that are much smaller than the wavelength of light tend to absorb more and hence their extinction is dominated by absorption in the metal particles. Absorption dissipates heat and this property is utilized in applications like solar glazing, nanoscale lithography, and therapeutic applications [166,167]. However, as the size of the particles increases, their extinction is dominated by scattering (rather than absorption) and we take advantage of this property for our application of light trapping and/or enhanced absorption within the solar cells. Beyond certain limits, however, increasing the particle size leads to increased retardation effects and higher order

multipole excitation modes, which decreases the efficiency of the scattering process [165,166,168].

A whole range of possibilities exist for tuning of SPs. The resonance frequency of metal nanoparticles depends on the size, shape, particle material, and optical properties of the surrounding medium, namely RI [154,169–171]. In practice, larger-size particles deposited on a substrate tend to lose their spherical property and hence look more like ellipsoids, causing the resonance frequency to be redshifted because of the change in shape. The resonance frequency also gets redshifted when the dielectric function of the surrounding medium increases. For example, the bulk plasmon resonance in vacuum changes when the same metal particles are deposited on a substrate [154,169–171]. Furthermore, over-coating of the metal particles on a substrate can change the resonance. The particle material also affects the resonance frequency [154,169–171]. For example, for a particle size corresponding to the same deposited mass thickness of gold and silver, gold nanoparticles have a lower frequency resonance than silver nanoparticles. Alloying the two metals in the different ratios can yield resonances in between the resonances of the pure gold and silver particles [169]. The resonance can also be tuned using nanoshells that have a dielectric as the core and a metal as the shell [171]. The redshifting of resonance leads to an increase in scattering cross section at longer wavelengths that would be beneficial for increasing the absorption of solar cells because of the indirect band gap of silicon.

### 13.4.1 Silver

Silver nanoparticles absorb and scatter light with extraordinary efficiency. Their strong interaction with light occurs because the conduction electrons on the metal surface undergo a collective oscillation when they are excited by light at specific wavelengths. This oscillation is known as a SPR, and it causes the absorption and scattering intensities of silver nanoparticles to be much higher than identically sized nonplasmonic nanoparticle [154,170,172]. Silver nanoparticle absorption and scattering properties can be tuned by controlling the particle size, shape, and the local RI near the particle surface. Plasmonic properties of silver nanoparticles have been extensively studied for their superior performances that exceed those of other metals with a SPR in the visible range, like gold or copper [154]. In the past years, a number of applications based on the SPR of silver nanoparticles have been presented, in particular for

biosensing, surface-enhanced Raman scattering, and plasmon circuitry [154]. Several of these applications take advantage of the engineering of silver nanoparticles plasmonic response that depends on their size, shape, dielectric environment, and on mutual electromagnetic interactions among particles in close proximity [154].

Over the last decade, many efficient synthesis approaches have been developed that allow good control of silver nanoparticles size, shape, and structure [154]. On one hand, modeling plasmonic properties of silver nanoparticles can provide useful indications for the synthesis. On the other hand, correlating the silver nanoparticles plasmonic properties with their morphology is a fast and easy way for in situ monitoring of the synthesis by, for example, UV–visible spectroscopy [173]. This is very useful, for instance, in the early stages of wet chemistry synthesis, when many different chemicals are present in solution and sample preparation for transmission electron microscopy analysis poses serious concerns about particle modification.

The SPR of silver nanoparticles with high symmetry, like spheres or ellipsoids, can be calculated with good accuracy by analytical expressions developed in the frame of the Mie theory [173–176]. For instance, Mie theory can be used to obtain a good fitting of experimental UV–visible spectra of spherical gold and silver nanoparticles in solution and to evaluate the average size of the nanoparticles [154,170,171].

However, when particle symmetry is lowered, the exact solution of the electromagnetic problem is not possible, and numerical approaches are necessary [177]. One of the most frequently used numerical methods for the calculation of the SPR in metal nanoparticles is the finite difference time domain (FDTD) algorithm.

### 13.4.2 Optical properties of silver (experimental)

There have been multiple studies, using both different computational analyses and empirical examinations, on the plasmonic and/or optical properties of silver. The following study takes samples of silver nanoparticles and analyzes them for different optical phenomenon [154,170,171,177]. The transmittance and reflectance of the samples were measured in the wavelength range of 300–1200 nm using an integrating sphere setup. The results for the silver nanoparticle film with an average particle diameter of 80 nm (corresponding to a silver mass thickness of 12 nm) on glass are shown in Fig. 13.8. It can be seen that for most

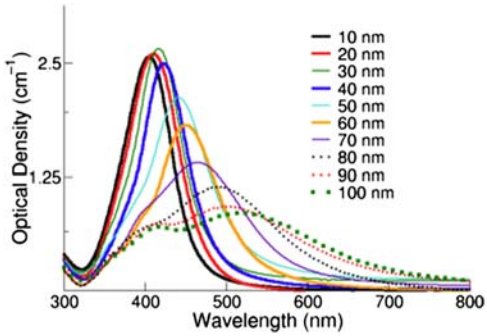


**Figure 13.8** Extinction (the sum of scattering and absorption) spectra of silver nanoparticles with diameters ranging from 10 to 100 nm at mass concentrations of 0.02 mg mL$^{-1}$. Nanoparticles have optical densities that are 50-times larger.). *Diagram reprinted with permission from nanoComposix.*

wavelengths, about 40% of the light is transmitted and about 15% is reflected. The remaining 45% of the light is absorbed. Because glass is known to absorb less than 2% percent of the light, it is concluded that most absorption occurs in the silver nanoparticles [154,170,171,177].

### 13.4.3 Gold

In recent decades, gold nanoparticles have been the subject of a vast and exponentially growing level of interest within the research community and thus the subject of a large amount of recent literature. As their name implies, the small size of gold nanoparticles is attractive for biomedical use in sensing, cellular imaging, drug delivery, and cancer therapy, but intensive research effort is also directed to chemical analysis and catalysis, electronics, and nonlinear optical processes. This broad range of applications fostered parallel research on a multitude of basic physical effects occurring in Au NPs [172,177].

There are three main reasons behind the success of gold nanoparticles in the arena of nanoscience and nanotechnology: (1) the high chemical and physical stability, also implying the intrinsic biocompatibility of gold nanostructures (colloidal gold has been exploited for curative purposes since the Middle Ages); (2) the ease of surface functionalization with organic and biological molecules; and (3) the multitude of optical properties related to SPs. In particular, gold nanoparticles have a large number of easily polarizable conduction electrons, which is a general prerequisite for preferential interaction with electromagnetic fields and the generation of

nonlinear optical phenomena [172,177]. In fact, compared to other organic and inorganic molecules or atoms (e.g., fluorescent molecules or scattering molecules), gold nanoparticles with size above 2 nm have a larger extinction cross-section, possibly reaching 100% of light-to-heat conversion efficiency, high photostability, and the ability to amplify the electromagnetic field at nanometric distance from the metal surface [177].

### 13.4.4 Optical properties of gold (experimental)

Gold nanoparticles' interaction with light is strongly dictated by their environment, size, and physical dimensions. Oscillating electric fields of a light ray propagating near a colloidal nanoparticle interact with the free electrons causing the collective oscillation of electron charge that is in resonance with the frequency of visible light. For small ($\sim$30 nm) monodisperse gold nanoparticles, the SPR phenomenon causes a significant absorption of light in the blue-green portion of the spectrum ($\sim$450 nm) while red light ($\sim$700 nm) is reflected, yielding a rich red color. As particle size increases, the wavelength of SPR related absorption shifts to longer, red-shifted wavelengths. Red light is then absorbed, and blue light is reflected, yielding solutions with a pale blue or purple color [172,177]. As particle size continues to increase toward the bulk limit, SPR wavelengths move into the IR portion of the spectrum and most visible wavelengths are reflected, giving the nanoparticles a murky translucent color. The SPR can be tuned by varying the size or shape of the nanoparticles, leading to particles with tailored optical properties for different applications [178,179].

### 13.4.5 Aluminum

Most plasmonics' work has involved the proposal and study of metallic nanostructures containing gold or silver. These noble metals exhibit plasmon resonances in the visible spectral region, and have convenient properties. For example, gold is relatively robust to oxidation. Silver, on the other hand, is less robust to oxidation but exhibits more narrow and intense plasmon resonances. However, as plasmonics continues to expand, researchers are reaching out beyond such noble metals to other possibilities. The plasmonic response of aluminum nanostructures, in particular, is beginning to be significantly explored by many groups [178–184].

One reason for the interest in aluminum plasmonics is that aluminum's plasma frequency is higher than that of gold or silver and this essentially

allows for significant SP responses to occur in the UV portion of the spectrum, whereas gold and silver typically involve visible plasmon resonances. This is relevant, for example, to applications of plasmonics ideas to the detection of organic and biological systems that exhibit strong UV absorptions and to photo catalysis. Furthermore, aluminum, as we all know, is a relatively economical and tunable material, which opens up more avenues for fabrication and mass production. It is furthermore a very stable metal, due to the formation of a self-limiting native oxide layer protecting the metal surface from further oxidation and from contaminants [178–184].

### 13.4.6 Optical properties of aluminum (experimental)

The plasmonic response of aluminum nanostructures should depend sensitively on both the presence of a surface oxide layer and the presence of a substrate. For a pure, isolated Al nanodisk with a diameter of 50 nm diameter, the scattering spectrum exhibits a single dipolar resonance at 210 nm (1). The addition of a 3 nm surface oxide (a characteristic thickness of the native Al oxide) red shifts the resonance by 15 nm and decreases the amplitude of the resonance. Placed on a dielectric substrate (e.g., $SiO_2$), the aluminum nanodisk plasmon resonance red shifts and weakens further, with the dipolar SPR shifting to 255 nm and a quadrupolar shoulder appearing as a distinct mode at even shorter wavelengths (higher frequencies) [184].

### 13.4.7 Plasmonic nanostructure configuration

Plasmonic structures can be incorporated with a solar cell in different manners, depending on the size and shape of the nanostructures, and the type of semiconductor used (Si, GaAs, CdTe, etc.). Because plasmonic nanostructures have been most effective with thin-film solar cell technology, the following configurations refer to this specific type of solar cell as reference.

#### *13.4.7.1 Plasmonic nanostructure on surface of substrate*

A plasmonic nanostructure can be placed on the surface of a solar cell. In its most common form as metallic nanoparticles, it has the capability to enhance absorption of incident light (e.g., sunlight) in the absorber layer (semiconductor substrate) by scattering the sunlight into the semiconductor substrate and reducing the reflection. If the plasmonic nanostructure is

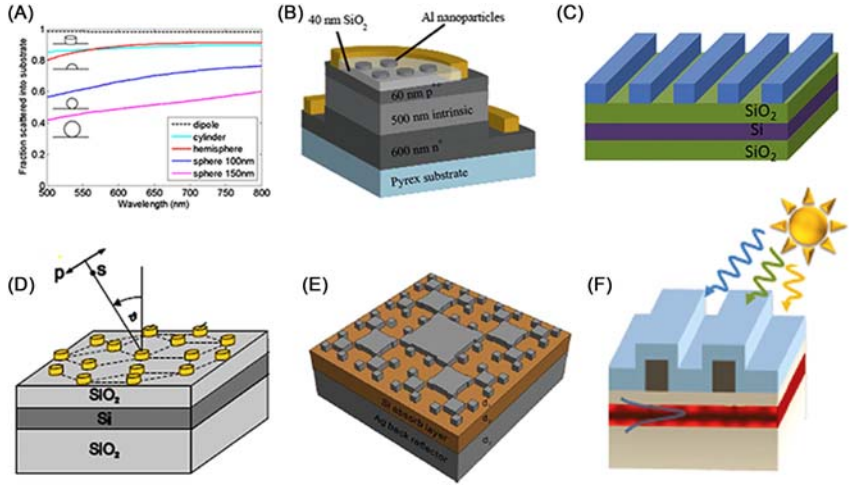


**Figure 13.9** Various metallic nanostructures on top of thin film solar cells. (A) Fraction of light scattered into the substrate for different sizes and shapes of Ag particles on Si; (B) Al nanoparticles placed on front of a thin Si film; (C) Ag strips on the top of Si thin film cell; (D) 2D quasiperiodic gold disks on top of the Si layer; (E) a fractal-like pattern of silver nano cuboids on top of Si thin film cell; (F) combination of anti-reflective (AR) coatings and gratings on top of ultrathin Si cell. *Diagrams reprinted with permission from: (A) AIP; (B) OSA; (D), (E) OSA; (F) ACS.*

in the form of a metallic mesh directly on the absorber layer, then it can serve both as a scatterer and an electrode.

The nanoparticle geometries in Fig. 13.9 can ensure optical enhancement by scattering the incident light into the absorber layer. Although the number of electron–hole pairs available for excitation in a TF substrate is much less than its thick film counterpart, metallic nanoparticles are able to excite them very efficiently because they efficiently scatter light into many different possible directions. If any light escapes the substrate, it can partially be scattered back by the metal nanoparticles. Although dielectric particles can also provide scattering, metallic counterparts are preferable because they have a much larger scattering cross section [178–184]. This means they can scatter light over an area much larger than their physical geometry. For example, the scattering cross section of a 20 nm Ag nanoparticle embedded in Si is 30 times larger than its geometric cross section, therefore small surface coverage with these particles can highly scatter the incident light (e.g., incident sunlight) [182]. Studies have shown that the type of metal, shape, size, and density of particles are important factors determining the scattering efficiency. However, very small particles suffer

from significant Joule heating losses and careful engineering is required to optimize metal loss versus scattering efficiency. Inexpensive and scalable fabrication techniques are required to make metal nanoparticles useful for solar cells. A simple way of forming a random array of metal nanoparticles is to evaporate a thin metal film and then heat it at a moderate temperature. The surface tension of the metal film causes the film to convert into a random array of nanoparticles [182]. A periodic array can also be made by employing a recently developed method of substrate conformal imprint lithography [179].

The plasmonic in-coupling geometries are not limited to nanoparticles. Arrays of periodic or aperiodic metal stripes or grids can also serve as very efficient couplers. An example of such a cell, decorated with a periodic array of thin silver stripes, is given in Pala et al. In this case, both LSPs and coupling into waveguide modes contribute to light trapping and enhanced absorption. Calculations show 43% enhancement in the short circuit current ($J_{SC}$) as compared to a cell without metallic stripes. If the stripes are placed directly on the absorber layer, then they can serve as an electrode at the same time [183].

Another promising in-coupling geometry is the random arrangement of metallic wires, which is an inexpensive alternative that serves both as an electrode and a scatterer. It can be fabricated over large areas through economic chemical synthesis approaches. Fig. 13.9 shows an example of such a film that has an optical transparency equivalent of better than that of metal-oxide TFs for the same sheet resistance [183].

#### 13.4.7.2 Plasmonic nanostructure embedded in substrate

Plasmonic nanoparticles can be embedded inside the absorber (Fig. 13.10). They behave as subwavelength lenses and enhance light absorption by concentrating the light locally. The amount of generated photocurrent in a solar cell is directly related to the light intensity inside the absorber layer. By embedding nanoparticles in the absorber region, one can benefit from strong light localization around metal nanoaparticles through the excitation of SPs, particularly when they are in resonance with the incident light. For efficient energy conversion from sunlight into photocurent, absorption of metallic nanoparticles must be much less than the absorber layer. This is the case for many of the organic and inorganic semiconductors. For example, colloidal Ag and Au nanoparticles are used as intermediate reflectors in organic solar cells [173–175,184]. The conversion efficiency of dye-sensitized solar cells has been enhanced by

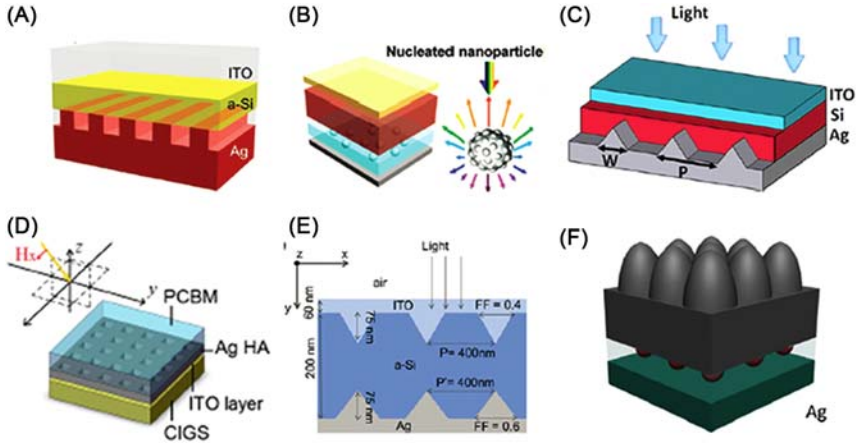


**Figure 13.10** (A) Ag gratings at the bottom of thin film Si; (B) nucleated Ag particles is embedded inside the ZnO layer at the rear side of the a-Si:H cell; (C) Ag triangular corrugations at the bottom of a 100 nm c-Si cell; (D) an Ag hole-array is inserted into a [6,6]-phenyl-$C_{61}$-butyric acid methyl ester (PCBM)/CIGS tandem solar cell; (E) Ag triangular gratings at the back side of cell and triangular indium tin oxide (ITO) gratings at the front a-Si cell; (F) the biomimetic silicon moth-eye structure combined with rear located Ag hemispherical particles in 2 μm thick c-Si cell. *Diagrams reprinted with permission from: (A) ACS; (B) ACS; (C) OSA; (D) OSA; (E) APS; (F) OSA.*

embedding gold nanodisks [184]. Other works have shown that embedding nanoparticles can also enhance the efficiency of many inorganic solar cells such as silicon cells [173–175,184].

#### *13.4.7.3 Plasmonic nanostructure on the back surface of substrate*

Metallic nanoparticles or corrugated metal films can be placed at the back surface of a cell (Fig. 13.11). In the case of a metallic film, SPPs are excited at the interface between the metal and the absorber (e.g., semiconductor), which can enhance the optical field concentration and also couple the incident light into the guided modes of the thin absorber. It can also serve as the back contact of the cell where charge carries are efficiently collected due to the very short distance they travel to reach the contact.

The plasmonic structure can be engineered and placed on the back surface of a solar cell where light is partially converted into SPP at the metal-absorber interface and partially coupled to waveguide modes of the absorber. Light travels along a much longer path in comparison to the physical thickness of the absorber, which can result in enormous

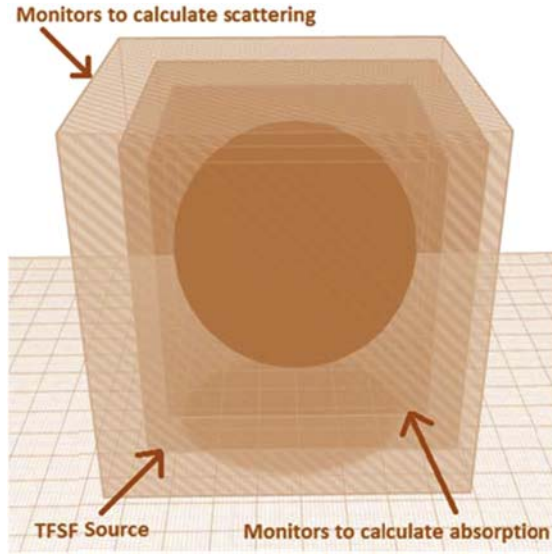


**Figure 13.11** Plasmonic resonance analysis setup. *Diagram reprinted with permission from IEEE Xplore (Choudhury et al.).*

absorption enhancements. In addition to light trapping, the plasmonic layer on the back surface of a cell can play the role of an electrode to collect charge carriers. Using SPPs to enhance absorption has been investigated in several organic and inorganic solar cell designs. For example, using a one-step direct imprinting process, plasmonic silver nano-dome arrays are incorporated in the back reflector of a dye-sensitized solar cell that results in 16% enhancement in short circuit current ($J_{SC}$) [176,185]. In another study, thin-film amorphous silicon is deposited on a textured metal back reflector, which shows a 26% photocurrent enhancement mainly in the near-infrared regime [176,185]. It should be noted that the effect of scattering and localization are simultaneously present with coupling into SPP and waveguide modes and good engineering is required to extract the maximum efficiency from these light-trapping mechanisms.

## 13.5 Section 5—Plasmonic nanostructures on the surface

The majority of research done in the field of plasmonic solar cells involved using plasmonic nanostructures on the top surface of the semiconductor substrate [154,162–171,177]. There may be a number of reasons why this is the case. For one, the nanostructures will be in direct

contact with the incoming solar radiation, and thus the possibility of effective plasmon scattering is much greater. From a fabrication standpoint, having the nanostructures on the surface of the substrate is preferable as well, as the fabrication complexity can be greatly reduced.

The placement of plasmonic nanostructures is simply the first task in achieving an effective solar cell—the physical nature of the nanostructures (e.g., various morphological parameters) themselves have to be adjusted to ensure greater optical absorption and electrical current generation within the PV substrate. The analysis of plasmonic structures by previous studies have demonstrated that the scattering and absorption resonance characteristics of these structures vary directly with their physical parameters [154,162–171,177]. Of course, greater scattering and lower absorption is the more desired phenomenon; the "focused" scattering radiation into (inside) the substrate would be an improved substitute for direct solar radiation in terms of greater optical absorption. However, greater scattering does not always lead to greater absorption within the substrate. The scattering has to occur with sufficient intensity and toward an appropriate direction, that is, toward or into the substrate. Hence, the physical parameters that have been found to have a significant impact on the plasmonic effect exhibited by metallic nanostructures are:

1. Size
2. Shape
3. Material
4. Periodicity
5. Pitch (distance between consecutive nanostructures)
6. Polarization of source radiation

A variation in each of the above parameters can cause a shift in the capability of a plasmonic nanostructure to enhance the optical absorption of a PV substrate. In this section, an analytical study is provided on how each of the parameters tabulated above affects plasmonic solar cells, and how it is possible to achieve greater energy conversion efficiencies by optimizing these parameters. Most of these analyses have been performed using the computational FDTD algorithm, particularly those developed by Lumerical Inc. While plasmonic nanostructures can be used with conventional thick-film solar cells, their preferred usage is with thin-film technology. The reason for this lies in the major disadvantage of thin-film solar cells: the reduced amount of semiconductor materials means that the potential number of electron–hole pairs that can be generated by incoming photons is much less than their thick-film counterparts. Hence, one

major way in which it can be improved is to enhance the "intensity" of the incoming radiation. Plasmonic nanostructures can be very useful when it comes to achieving this.

As mentioned previously, any variation in the physical parameters stated above can affect the plasmon resonance spectra of the metallic nanostructure, the intensity of scattering, and/or the direction of scattering. In order effectively to understand the extent of influence that each parameter can have, the following set of analyses must be performed [110–115]:

1. Plasmon resonance analysis—The purpose of this analysis is to identify the effect that the different parameters, namely material, size, and shape, have on the plasmon resonance phenomenon of the nanostructure. It is necessary to establish if a change in these parameters results in a change in the resonance peak location and/or intensity. To that end, the scattering and absorption spectrum of each of the metallic nanostructures with different physical parameters were analyzed and compared.
2. Absorption enhancement—To calculate this, radiation absorption in the first quarter portion from the top of the surface of the substrate with metallic nanostructures was calculated and divided by that of the substrate with no nanostructures, to generate the optical absorption enhancement factor, $g$. The reason for measuring optical absorption enhancement rather than raw absorption is to ensure that an optical energy absorption enhancement is actually taking place within the solar cell due to the presence of the metallic nanostructures.
3. Short circuit current density ($J_{SC}$) analysis—Studies that have been made for decades have shown that while an increase in optical enhancement can lead to greater electrical generation, the correlation between the two factors is never directly proportional. This can be attributed to the fact that increased electron–hole pair generation does not result in all of electrons contributing to the current generated from the solar cell, as a large portion can potentially undergo recombination before reaching the anode. Thus, to establish the extent to which optical absorption enhancement has resulted in electrical current generation of the different plasmonic solar cell configurations for this investigation, short circuit current density ($J_{SC}$) for each configuration was calculated. The $J_{SC}$ for the bare Si substrate was also measured for the purpose of comparison with that of solar cells with metallic nanostructures.

4. Near-field enhancement—In order further to relate the interaction of the incident electromagnetic field with the Si substrate due to the presence of the metallic nanostructure (array) with the optical absorption enhancements and electrical current generation enhancements, near-field images of each configuration were generated at the resonance wavelengths of the respective metal, which were recorded in the first analysis. Comparison of the near-field images of the bare Si substrate (i.e., dividing the former with the latter) was used to generate near-field enhancement images. These images demonstrate, in one format, the interaction of the electromagnetic field with the metallic nanostructure/Si substrate, and the variations of the field on the Si surface or within the Si surface, due to the interaction of the plasmonic metal nanostructure of different sizes/types/shapes/inter-particle distances with the incident radiation.

In the following pages, the variation of each parameter and its effect on the plasmonic nature of the nanostructures and the subsequent change in optical and electrical enhancement will be discussed in detail. In the following discussions, the plasmonic nanostructures have been used in conjunction with thin-film amorphous silicon substrate.

### 13.5.1 Size and material of nanostructures—plasmon resonance analysis

As has been stated in the previous section, the plasmonic resonance phenomenon varies greatly with the metal that is being used for the nanostructures. The three most effective metals for PV application are silver (Ag), gold (Au), and aluminum (Al). In order to understand the variation in the plasmon resonance phenomenon of the different metals at different sizes, in the results presented, the material was kept constant while the size of the nanostructure was changed. In the initial analysis, the nanostructure was chosen to be spherical in shape, so that variations in the shape can have no physical effect on the plasmonic resonance. The diameters of the metallic nanoparticles analyzed are 50, 100 and 200 nm. It is anticipated that this set of results can provide a sufficient amount of data to reach a proper conclusion regarding the correlation between the variation in diameter of the nanoparticles and the absorption enhancement of the PV cell.

The particles were separately and individually placed inside the simulation region (shown in Fig. 13.11), and the absorption, scattering, and extinction spectra were obtained as has been described elsewhere and

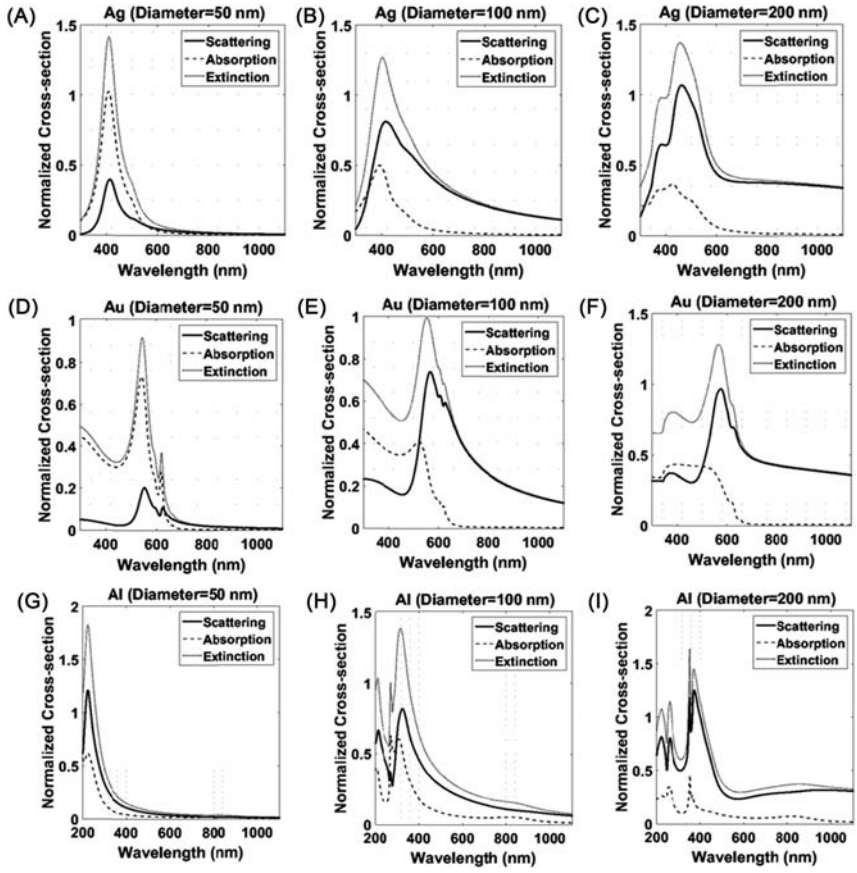


**Figure 13.12** Absorption, scattering and extinction spectra for (A) Ag nanoparticle of $D = 50$ nm, (B) Ag nanoparticle of $D = 100$ nm, (C) Ag nanoparticle of $D = 200$ nm, (D) Au nanoparticle of $D = 50$ nm, (E) Au nanoparticle of $D = 100$ nm, (F) Au nanoparticle of $D = 200$ nm, (G) Al nanoparticle of $D = 50$ nm, (H) Al nanoparticle of $D = 100$ nm, and (I) Al nanoparticle of $D = 200$ nm. *Diagram reprinted with permission from IEEE Xplore (Choudhury et al.).*

shown previously in Fig. 13.12 [110–115]. The analysis was done across a wide wavelength range of $\lambda = 300–1100$ nm for Ag and Au nanoparticles, and $\lambda = 200–1100$ nm for Al nanoparticles (as Al demonstrates resonance on the bluer region of the spectrum). The resultant spectra for each nanoparticle is analyzed in detail next.

It can be seen from the graphs for each respective Ag nanoparticle diameter that there is clearly a resonance peak occurring within a particular wavelength range. While the extinction spectra peak value remains

almost the same for increasing the diameters (with a slight red-shift for increasing nanoparticle size), the same cannot be said for the absorption and scattering graphs. It is clearly seen that for higher diameters, the magnitude of the resonant peak of the absorption graph decreases while that of the scattering graph increases. This is in agreement with the results of previous studies [154,162–171,177]. Furthermore, the peak of the extinction, scattering, and absorption spectra shifts toward the higher wavelength side of the spectra for increasing nanoparticle diameter. Overall, the resonance peak always lies within the wavelength range of 400–500 nm for Ag nanoparticles.

A similar trend to the one found for Ag nanoparticles can also be observed for Au nanoparticles, as shown in Fig. 13.12D–F. Once again, distinct peaks are seen for all diameters of Au nanoparticles, providing evidence to the fact that Au exhibits plasmonic resonance. The average peak values are lower than that of Ag, and the consequences of this becomes evident in the absorption enhancement calculations shown later. The absorption peak decreases, and the scattering peak increases, for increasing diameter. For Au, the peaks lie within the wavelengths 500 and 600 nm.

For the Al plasmon resonance calculations, the wavelength range studied was from 200 to 1100 nm, as it is well known that aluminum exhibits plasmonic resonance at the bluer portion of the electromagnetic spectrum. Once again, the same trends as before can be observed, as shown in Fig. 13.12G–I.

For all nine particles analyzed, it can be seen that there is a resonant wavelength at which the maximum absorption, scattering, and extinction occurs, as has been demonstrated in previous studies. For all three diameters of Ag, the resonant peak occurs between wavelengths 400 and 500 nm, that of Au is between wavelengths 500 and 600 nm, and that of Al is between 300 and 400 nm, an observation that is in agreement with results that have been previously generated. The resonance amplitude of the absorption spectra for particles of all three metals decreases as the metal diameter increases, and, concurrently, the resonance amplitude of the scattering spectra also increases. This is in agreement with known results [105–116,154,162–171]. Furthermore, a visible red shift in the absorption, scattering, and extinction spectra is observed for each successive increase in diameter. For Au, the fall in the absorption peak is much more pronounced, while for Al the variation is lower. Additionally, the extinction peak broadens for increasing diameters of the nanoparticles.

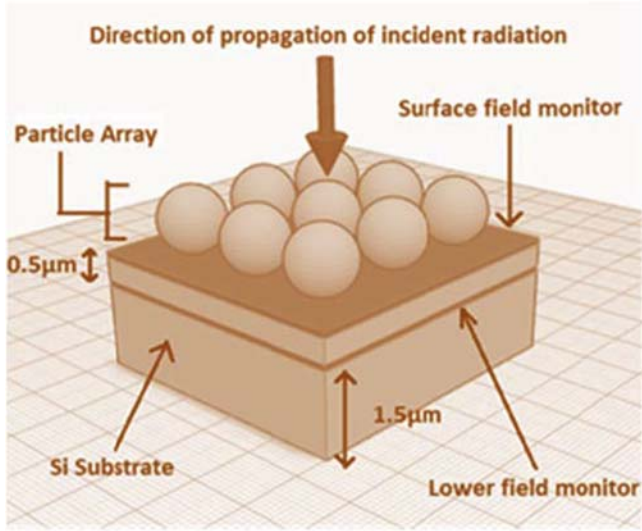


**Figure 13.13** Simulation setup for absorption enhancement analysis. *Diagram reprinted with permission from IEEE Xplore (Choudhury et al.).*

### 13.5.2 Absorption enhancement analysis

The absorption is calculated and described elsewhere. The resultant raw absorption spectra calculated for the Si substrate, both with the plasmonic nanoparticles and without the plasmonic nanoparticles, are applied to Eq. (13.3) below to obtain the wavelength-dependent absorption enhancement factor, $g$. The absorption enhancement factor, $g$, gives us an appropriate mathematical framework to analyze [110–115].

$$g = \frac{\text{Absorption across Si with metal nanoparticles}}{\text{Absorption across bare Si}} \tag{13.3}$$

The setup used for the simulations that is discussed here is illustrated in Fig. 13.13.

In order to ensure that the effect of the change in one parameter does not distort the data obtained for the observed variation in another parameter, only one parameter was changed at a time while the others were kept constant for the calculations discussed. This allowed the results to be more rigid and precise and adds to the credibility of the results discussed. The metal is kept constant while the diameter of the (spherical) nanoparticles periodically dispersed at a pitch of 300 nm (center–center) on top are varied, and the absorption enhancement factor ($g$) for each configuration

is calculated across their respective incident radiation spectra. This is repeated for all three metals. The pitch is then changed to 220 nm (center−center), and the above analysis is repeated once again.

The absorption enhancement analysis for Ag nanoparticles at both pitches is shown in Fig. 13.14A and B. The graphs show that there is almost no absorption enhancement (i.e., absorption enhancement factor $\sim 1$) for Si wafers topped with Ag particles of diameter of 50 nm. For the 300 nm pitch (Fig. 13.14), the absorption enhancement factor reaches a peak for the nanoparticle with diameter of 100 nm Ag at approximately $\lambda \sim 420$ nm and for diameter of 200 nm Ag at approximately $\lambda \sim 460$ nm, respectively, although no clear peaks for the diameter of 200 nm nanoparticles are identified. This can be related to the extinction spectra for Ag as shown in Fig. 13.14A−C as their plasmon resonance peaks lie approximately close to the same wavelengths. For the pitch of 220 nm, the absorption enhancement factor for diameter of 50 nm is approximately unity (i.e., "1"), and the peak $g$ factor for diameter of 100 nm is higher than it was for the pitch of 300 nm. Furthermore, it can be seen that the g factors for Ag nanoparticle with diameter of 200 nm are below 1 throughout the entire spectrum, from which it can be inferred that this should adversely influence the overall light coupling efficiency into the Si substrate.

The results for the Au nanoparticle configurations and the Al nanoparticle configurations are shown in Fig. 13.14C and D, and E and F, respectively. The results obtained for Au and Al nanoparticles are very similar in trend as it was for Ag. Al shows a slight difference in the fact that (A) its highest absorption enhancement peaks all lie on the lower wavelength portion, and (B) its 200 nm nanoparticles demonstrate higher absorption enhancement peaks than Ag or Au nanoparticles. However, for the major portion of absorption enhancement curve, the enhancement factor is well below 1, just as it was for Ag and Au.

For Au, the overall absorption is lower when compared to that of Ag or Al. While the nanoparticles with diameter of 50 nm configuration shows the same enhancement as those for Ag and Al, the 100 nm diameter configuration has a peak enhancement that is close to the plasmon resonance wavelength of Au. These show that the plasmonic nature of the metals involved have an inherent effect on the light coupling efficiency of the thin-film Si substrate. Of the three diameters of metal nanoparticles analyzed, nanoparticles with diameter of 100 nm are seen to provide the largest absorption enhancement of the incident radiation into the Si

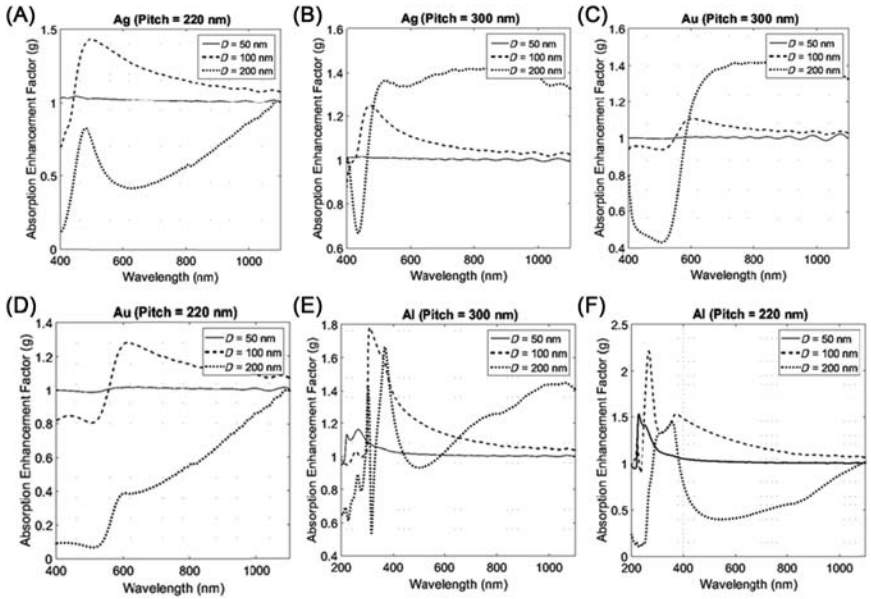


**Figure 13.14** Absorption enhancement factor spectra for (A) Ag (with pitch = 300 nm) and (B) Ag (with pitch = 200 nm), (C) Au (with pitch = 300 nm), (D) Au (with pitch = 200 nm), (E) Al (with pitch = 300 nm), and (F) Al (with pitch = 200 nm). *Diagram reproduced with permission from IEEE Xplore (Choudhury et al.).*

substrate for all of the metals that have been analyzed. Additionally, the variations in absorption and scattering of the metallic nanoparticle spectra have an essential influence on the light absorption enhancement from the "plasmonic-solar cell." As previously shown, the increase in diameter of the metallic nanoparticle causes the absorption of the particle to decrease, while increasing the scattering efficiency of the nanoparticles. Hence, a correlation between the scattering of the plasmonic nanoparticles and absorption enhancement in the Si substrate can be seen. It is possible that, for the nanoparticles with diameter of 200 nm metal nanoparticles, increased scattering of the incident radiation by the Ag and Au nanoparticles may be in a direction away from the Si substrate, thus leading to decreased absorption by the Si substrate [110–115].

### 13.5.3 Short circuit current density ($J_{SC}$) analysis

As has been stated previously, any enhancement in optical absorption might not cause a corresponding proportionate increase in electrical activity of the PV cell. This may be because of a number of reasons, including the fact that not all incident photons from the sunlight's radiation are able to generate an electron–hole pair because the photon does not have enough energy to cover the band-gap energy. Even if the energy is sufficient, the excess energy provided by the photon to the electron is used to navigate through the substrate, and this energy may not be enough to cover the entire path, and thus may result in the electron recombining with a corresponding hole. Although the use of thin-film does significantly reduce this required diffusion length for the electron to travel, the presence of less semiconductor material means that the number of possible electron–hole pairs generated may be lower than that of traditional thick-film solar cells. Thus, any analysis of nanostructured solar cells must be accompanied by a current generation analysis to find the extent to which the optical absorption enhancement has translated into electrical current output improvement. To that end, short circuit current density ($J_{SC}$) is calculated for several configurations of plasmonic nanoparticle arrays.

The short circuit current density ($J_{SC}$) for all of the plasmonic nanostructures discussed (with metals Ag, Au, and Al, and diameters of 50, 100, and 200 nm for pitch = 220 and 300 nm) are calculated for the entire spectrum, and illustrated in tabular form in Table 13.1. The highest increases in $J_{SC}$ have been highlighted in bold.

**Table 13.1** $J_{SC}$ of the nanoparticle array based Si solar cell for the entire solar spectrum (A) for pitch of 300 nm, and (B) for pitch of 220 nm.

| | Ag ($\lambda = 400-1100$ nm) | | Au ($\lambda = 400-1100$ nm) | | Al ($\lambda = 200-1100$ nm) | |
|---|---|---|---|---|---|---|
| **Structure** | $J_{SC}$ | **% Change** | $J_{SC}$ | **% Change** | $J_{SC}$ | **% Change** |
| ***(a) For pitch = 300 nm*** | | | | | | |
| No particles | 76.2793 | 0 | 76.2793 | 0 | 109.366 | 0 |
| $D = 50$ nm | 78.2283 | 2.555 | 76.5712 | 0.383 | 111.636 | 2.076 |
| **$D = 100$ nm** | **95.5242** | **25.230** | **76.6562** | **0.494** | **135.808** | **24.178** |
| $D = 200$ nm | 41.1047 | − 46.11 | 19.2681 | − 77.362 | 59.7525 | − 45.365 |
| ***(b) For pitch = 220 nm*** | | | | | | |
| No particles | 76.2793 | 0 | 76.2793 | 0 | 109.366 | 0 |
| $D = 50$ nm | 77.3442 | 13.961 | 76.4398 | 0.210 | 110.743 | 1.259 |
| **$D = 100$ nm** | **89.7007** | **17.595** | **77.0183** | **0.969** | **127.488** | **16.570** |
| $D = 200$ nm | 77.0193 | 0.970 | 48.9927 | -35.772 | 122.772 | 12.258 |

*Source*: Data in table taken with permission from IEEE Xplore (Choudhury et al.).

The $J_{SC}$ calculations were then repeated for a shorter wavelength range. This allows a more careful study on how the solar cell's electrical current generation varies with an incident radiation spectrum that is in the region around the plasmon resonance of each nanoparticle. Another reason for this is that a large portion of the sunlight that reaches the surface of earth after passing through the atmosphere has been reduced to be within this range of wavelength. The shortened wavelength ranges were where each metal nanoparticle exhibits plasmonic resonance, that is, 400−700 nm for Ag and Au, and 200−600 nm for Al. The results are tabulated in Table 13.2. Once again, the highest increases in $J_{SC}$ have been highlighted in bold [110−115].

The most significant rise in $J_{SC}$ is found to be for Ag nanoparticles with a diameter of 100 nm placed at a pitch of 220 nm for the 400−700 nm shortened wavelength range, which is in compliance with the results obtained through the absorption enhancement analysis. Furthermore, in conjunction with the results for the optical absorption enhancement, it is seen that $J_{SC}$ is reduced significantly for nanoparticles of diameter 200 nm and pitch of 220 nm. For the analysis with reduced spectrums of 400−700 nm for Ag and Au, the increase in $J_{SC}$ is lower. This can be attributed to the fact that the absorption enhancement is occurring across all the wavelengths (frequencies), and thus limiting the frequency range also lowers the percentage increase in $J_{SC}$ for the case of

**Table 13.2** $J_{SC}$ of the nanoparticle array based Si solar cell for the limited solar spectrum (a) for pitch of 300 nm, and (b) for pitch of 220 nm.

| | **Ag ($\lambda$ = 400 nm to 700 nm)** | | **Au ($\lambda$ = 400 nm to 700 nm)** | | **Al ($\lambda$ = 200 nm to 600 nm)** | |
|---|---|---|---|---|---|---|
| **Structure** | $J_{SC}$ | **% Change** | $J_{SC}$ | **% Change** | $J_{SC}$ | **% Change** |
| ***(a) For pitch = 300 nm*** | | | | | | |
| No particles | 64.1602 | 0 | 64.1602 | 0 | 60.0142 | 0 |
| $D = 50$ nm | 65.1141 | 1.487 | 63.8908 | − 0.420 | 61.1944 | 1.967 |
| **$D = 100$ nm** | **75.6064** | **17.840** | **59.8337** | **− 6.743** | **75.1950** | **25.295** |
| $D = 200$ nm | 59.2331 | − 7.679 | 26.0504 | − 59.398 | 61.7457 | 2.885 |
| ***(b) For pitch = 220 nm*** | | | | | | |
| No particles | 64.1602 | 0 | 64.1602 | 0 | 60.0142 | 0 |
| $D = 50$ nm | 65.8854 | 2.689 | 63.6557 | − 0.786 | 62.1060 | 3.486 |
| **$D = 100$ nm** | **79.7938** | **19.691** | **56.1374** | **− 12.504** | **81.4004** | **35.635** |
| $D = 200$ nm | 32.9415 | − 48.657 | 8.44858 | − 86.832 | 32.2894 | 32.389 |

*Source*: Data in table taken with permission from IEEE Xplore (Choudhury et al.).

Ag and Au. For Al, the opposite phenomenon occurs. This may be explained by the fact that the majority of the absorption enhancement for Al occurs in the limited incident spectrum range (i.e., $\lambda = 200-600$ nm range) [110–115].

## 13.5.4 Near-field enhancement analysis

Near-field images can help establish the relation between transmission of the electric field within/around the metallic nanoparticle and the Si substrate at the resonant wavelength of the particle, and the improved optical and electrical enhancements shown. To this end, near-field images are generated and presented for important physical parameters of Ag, Au, and Al nanoparticle to be able to visualize, compare, and contrast the electromagnetic interactions within the structures themselves, and thus establish a comprehensive link between the variation of the physical parameters of the plasmonic nanoparticles and the improvement in electrical activity. The approximate wavelength at which the nanoparticles of Ag, Au, and Al of all diameters displayed SPR were found to be $\lambda \sim 460$ nm for Ag, $\lambda \sim 560$ nm for Au, and $\lambda \sim 340$ nm for Al.

Three near-field images generated for each respective nanoparticle configuration are as follows: (1) the Si substrate illuminated by incident radiation without the particle at the given wavelength; (2) the Si substrate

with the respective metal nanoparticle particle at the given wavelength of incident radiation; and, (3) the enhancement image, which was calculated by dividing the raw data of the second image [calculated in (2)] with the raw data of the first image [calculated in (1)]. For the enhancement image, the color scale is in the log scale, and hence the areas that are dark red in color have an enhancement of over 1 in the log scale that corresponds to near-field enhancement of over $\times 10$ (over 10 fold).

A closer inspection of the near-field enhancement images shown in Fig. 13.5E show that in almost all of the cases demonstrated, a certain amount of EM field enhancement always makes its way into the substrate. For the images involving Ag (Fig. 13.15A–C), with diameters increasing with subsequent image, the highest optical enhancement in the absorber region is for the nanoparticle with a diameter 100 nm. The cell with the 50 nm diameter nanoparticle, while demonstrating EM interaction around it, shows almost no optical enhancement in the absorber region. This is expected, as the absorption enhancement and the electrical analysis have shown. However, for the 200 nm diameter Ag particle, the enhancement, though present, is lower than that of the nanoparticle with diameter 100 nm. This explains the trend found in the previous analysis. A significant portion of enhancement is seen around the nanoparticle, from which it can be inferred that although the larger nanoparticle is scattering more, the scattered radiation is spread outwards and not focused toward the Si substrate.

Comparing the near field of the Ag nanoparticles of the same the same size with that of Au (Fig. 13.15D and E) and Al (Fig. 13.15F), it can be observed that the enhancements are not as significant. With Ag, enhancements of at or up to a value of 1 is discernible, while no such enhancement is seen with Au or Al.

## 13.6 Section 6—Embedded plasmonic nanostructures

The use of plasmonic nanostructures on the surface (i.e., on top of the semiconductor surface) has been studied extensively, but embedding them inside the PV substrate is a practice that has yet to gain some momentum. Theoretically, it is a design concept that makes sense in terms of fundamental physics. Embedding the nanostructures inside the substrate means that they are in contact with the region for which optical absorption is of utmost priority [186]. As a result, the plasmonic nanostructures themselves must undergo minimal absorption to maximize the light absorption into

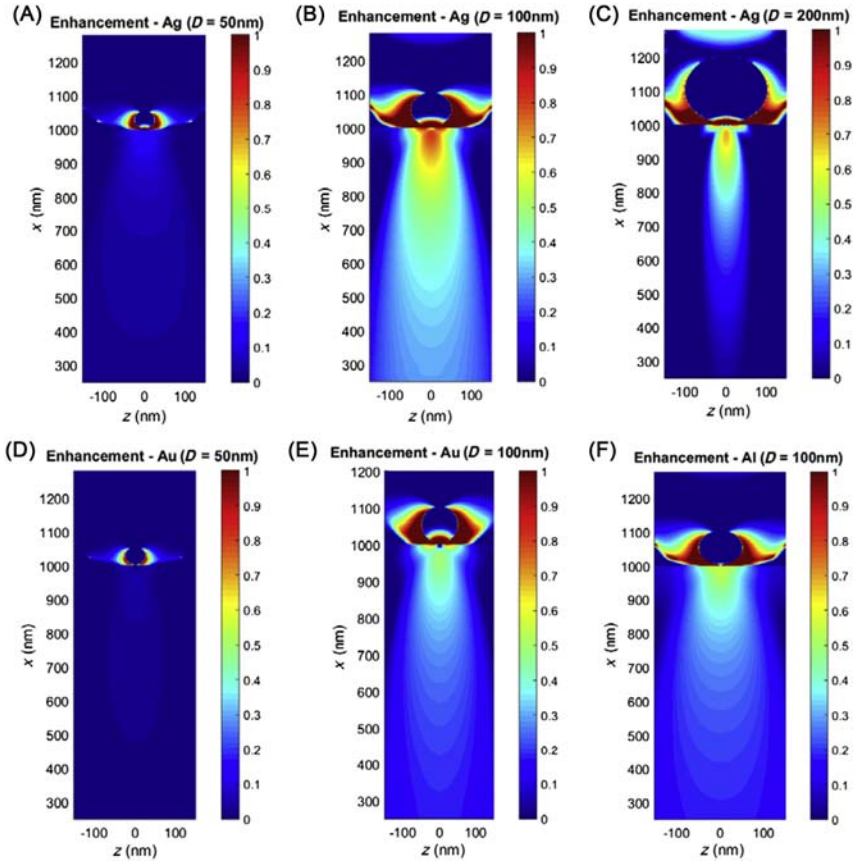


**Figure 13.15** Near-field enhancement images of (A) Ag with diameter 50 nm configuration at $\lambda = 460$ nm, (B) Ag with diameter 100 nm configuration at $\lambda = 460$ nm, (C) Ag with diameter 200 nm configuration at $\lambda = 460$ nm, (D) Au with diameter 50 nm configuration at $\lambda = 560$ nm, (E) Au with diameter 100 nm configuration at $\lambda = 560$ nm, and (F) Al with diameter 100 nm configuration at $\lambda = 340$ nm. *Diagram reproduced with permission from IEEE Xplore (Choudhury et al.).*

the semiconductor absorber layer (e.g., the Si substrate). Additionally, minimal absorption would mean greater scattering by the nanostructures, causing them to act very similar to reflectors [187,188]. The greater scattering can, in theory, lead to greater absorption in the substrate (absorber region). However, embedding the nanostructures inside the substrate can also mean that the metal is no longer in direct contact with the incident solar radiation, and would also reduce the amount of absorber substrate by taking up its space. Despite these drawbacks, there is a case to be made

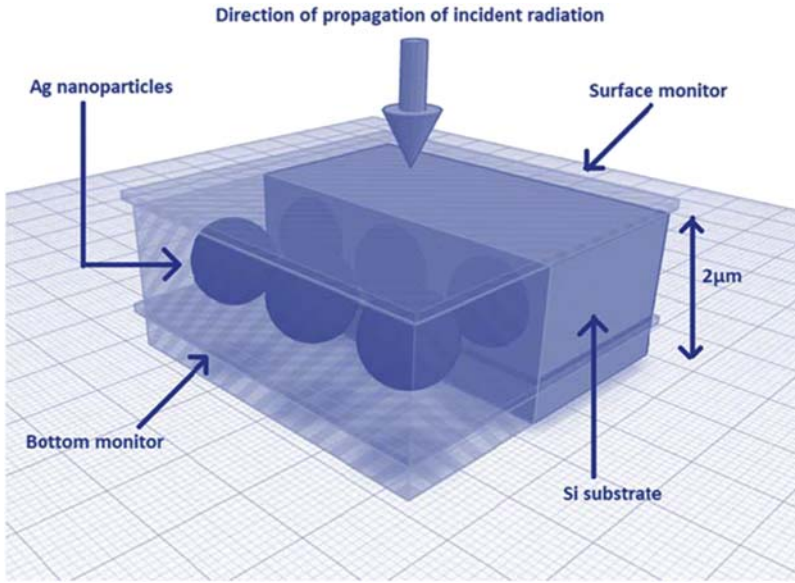


**Figure 13.16** Nanospheres embedded in Si substrate. *Diagram reprinted with permission from IEEE Xplore (Choudhury et al.).*

for embedding plasmonic metal nanostructures in the PV substrate in relation to enhancing the energy conversion efficiency of the solar cell (see Fig. 13.16).

Hence, because plasmonic nanostructures placed on the top surface of the substrate have proved to be so effective in enhancing the light absorption into the semiconductor substrate, the logical next step would be to analyze and optimize plasmonic nanostructures embedded within the Si substrate itself. However, as previously stated, the number of studies done in this area is limited [187–191]. Most of the research that has been done with embedded plasmonic nanostructures involves organic solar cells and dye-sensitized solar cells, while a limited amount of work has been done with Si cells. The purpose of this section of the chapter is to provide the basis for a fundamental understanding of this technique through simulation-based studies [187–191]. To ensure proper understanding, a fundamental relationship between key physical parameters of the embedded plasmonic nanostructures and the energy conversion efficiency of the thin-film amorphous silicon solar cells will be provided. For the sake of reducing analytical complexity and to keep in line with previous studies, only spherical nanostructures will be focused upon, and the type of

plasmonic metal used was limited to only Ag, as this has been previously found to yield the best results [191]. A working relationship between the physical parameters of these nanostructures, such nanoparticle size and the pitch, will also be expanded upon. Once again, the analyses that will be presented from different studies to formulate a rudimentary understanding of this technology are plasmon resonance analysis, absorption enhancement analysis, short circuit current density ($J_{SC}$) analysis, and near-field enhancement analysis (Fig. 13.16).

### 13.6.1 Plasmon resonance analysis

As has been the norm, the first task of any study involving plasmonic nanoparticles has been to observe and analyze the plasmonic resonance phenomenon of each metal nanoparticle inside the Si substrate, and identify the wavelength range where the resonance of each nanoparticle occurred. Thus, the extinction, scattering, and absorption spectra of incident radiation for each nanoparticle has to be studied thoroughly. The resonance spectra for four different nanoparticle sizes will be analyzed: diameters of 50, 100, 200, and 500 nm. The particles were separately and individually placed inside the Si substrate to replicate the particle being embedded in the substrate, and this entire structure was then analyzed. The analysis was done across a wavelength range of $\lambda = 400-1100$ nm, as it has been already established that Ag nanoparticles demonstrate plasmon resonance in this region. The resultant spectra from the simulations have been provided in Fig. 13.17.

For all four sizes of particles the resonant spectra of which been provided, it can be seen that there are multiple resonant peaks that occur at relatively similar wavelengths. The most pronounced peak is found to be around 810 nm for each nanoparticle, while a second, sharper peak is seen for each particle at different wavelengths: 950, 980, 1000, and 1010 nm for nanoparticles of diameter 50, 100, 200, and 500 nm, respectively.

A significant reason why there will be a difference in the scattering and absorption spectral behavior when compared to that of nanostructures in air is because Si is highly dispersive and absorbing in this frequency range. This proves to have a significant detrimental effect on the plasmon resonance of the metal nanoparticle embedded within the substrate, as the Si may, in fact, be absorbing the incident radiation. Such a phenomenon causes unexpected challenges to the calculation of the scattering and extinction spectra of the metal nanoparticles when embedded within the

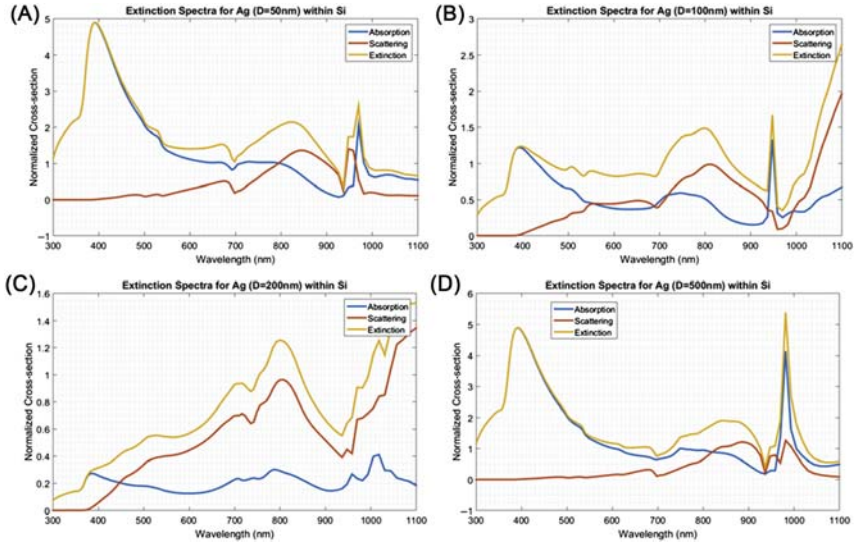


**Figure 13.17** Absorption, scattering and extinction spectra for (A) Ag nanoparticle of $D = 50$ nm, (B) Ag nanoparticle of $D = 100$ nm, (C) Ag nanoparticle of $D = 200$ nm, (D) Ag nanoparticle of $D = 500$ nm. *Diagram reprinted with permission from IEEE Xplore (Choudhury et al.).*

Si substrate. However, the presence of the resonance peaks does indicate that plasmon resonance is occurring at certain specific wavelengths.

## 13.6.2 Absorption enhancement

Following the plasmon resonance calculations, the logical progression is to analyze the efficacy of embedding plasmonic nanostructures on the optical absorption capability of the absorber layer, that is, silicon. To that end, each metal nanoparticle was placed as a periodic, horizontal array 0.5 μm below the surface of a 2 μm thick Si substrate, and then a plane wave was orthogonally directed toward the PV cell. Once again, to analyze optical absorption, the parameter absorption enhancement factor, $g$, was calculated for each respective nanoparticle size and pitch configurations.

The metal was kept constant (Ag), while the diameter of the nanoparticles periodically dispersed at a constant end-end pitch of 10 nm inside the Si substrate are varied (end-end pitch means the distance between neighboring nanoparticles was 10 nm from their respective edges), and the absorption enhancement factor (g) for each configuration is calculated across its respective incident radiation spectra. This is repeated for all four sizes of nanoparticles. The pitch (end-end) is then changed to 20 nm,

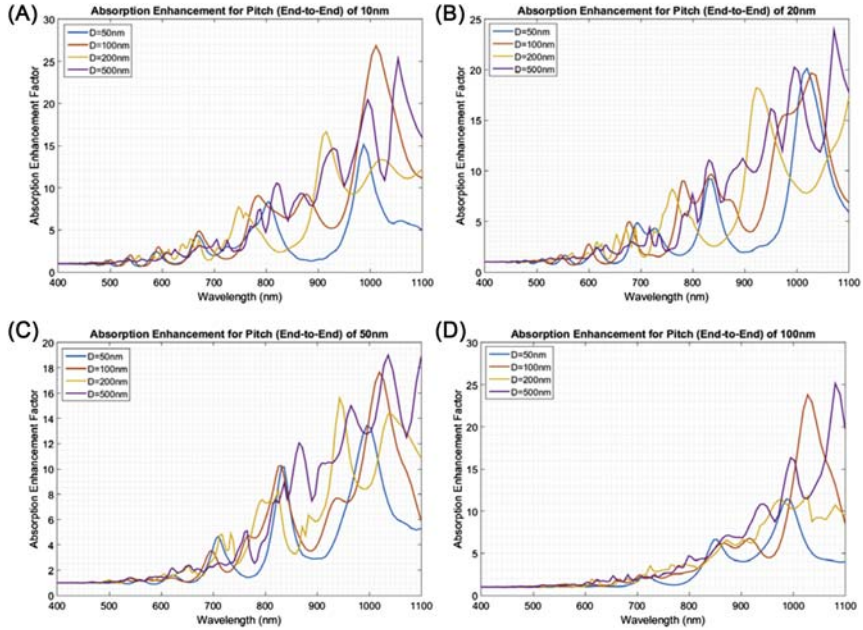


**Figure 13.18** Absorption enhancement factor spectra for (A) pitch (end-end) = 10 nm, (B) pitch (end-end) = 20 nm, (C) pitch (end-end) = 50 nm, and (D) pitch (end-end) = 100 nm. *Diagram reprinted with permission from IEEE Xplore (Choudhury et al.).*

50 nm, and 100 nm, and the above analysis is repeated for each Ag nanoparticle size. The absorption enhancement analysis for Ag nanoparticles embedded within the Si substrate for all sizes and pitches discussed above is shown in Fig. 13.18.

The graphs repeat a pattern that was observed in the plasmon resonance analysis, in that they demonstrate multiple absorption peaks. Once again, this phenomenon can be attributed to the dispersive and absorbing nature of the Si substrate in which the Ag nanoparticles are embedded. Because of this property, it is possible that the reflected radiation from the Ag–Si interface interfered with the original incident radiation and/or with each other. Thus, one plausible explanation can be that the constant constructive and destructive interferences results in the oscillating pattern as observed. It has to be noted here that the solar cells with nanoparticle diameter of 500 nm demonstrates the highest absorption enhancement when compared with the other configurations studied.

In order to understand these results further, the total absorption enhancement for the entire spectrum of each configuration has been

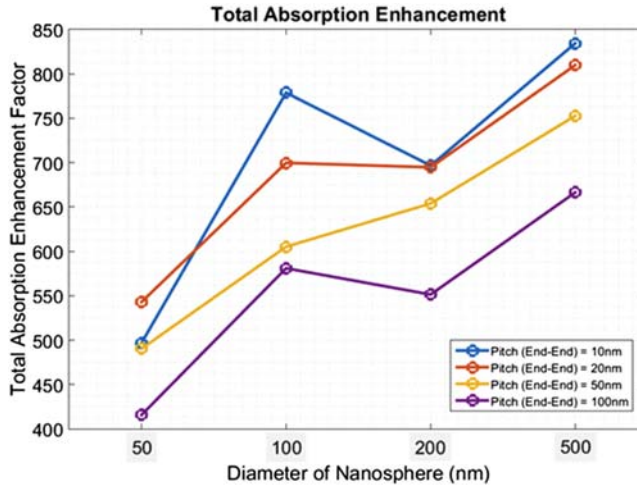


**Figure 13.19** Total absorption enhancement for different configurations. *Diagram reprinted with permission from IEEE Xplore (Choudhury et al.).*

analyzed and calculated as shown in previous studies, and the results are shown in Fig. 13.19 [191]. This has been achieved by taking the sum of each individual point on the absorption enhancement curve and plotting it in a single figure. A general pattern for all pitches arises from this graph arises—the nanoparticle with diameter of 50 nm shows the least total enhancement, then increases for diameter of 100 nm, decreases for diameter of 200 nm, and then shows the highest total enhancement for diameter of 500 nm. In addition to that, the general trend of the data in the figure shows the highest set of absorption enhancements is for the smallest end-end pitch, that is, 10 nm. This is an expected result and can be explained because for the nanoparticles closest together for the small pitch size, the neighboring metallic nanoparticles are able better plasmonically to couple with each other and also the incident and/or any scattered radiation.

### 13.6.3 Short circuit current density

The trend in $J_{SC}$ observed is very similar to that of total absorption enhancement graph, and has been demonstrated in graphical form in Fig. 13.20 so as to highlight this trend. In conjunction with the total absorption enhancement graph, the highest $J_{SC}$ is found to be for the smallest pitch (inter-particle distance). The increase in the amount of $J_{SC}$ generation is found to be significantly greater to that of previous analysis

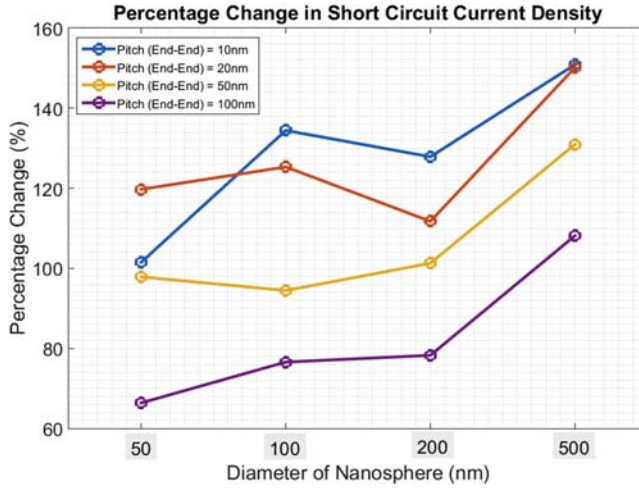


**Figure 13.20** Percentage change in $J_{SC}$ for different configurations. *Diagram reprinted with permission from IEEE Xplore (Choudhury et al.).*

where plasmonic nanostructures were placed on top of the Si substrate. This is an interesting result and suggests that embedding plasmonic metal nanostructures inside the Si substrate can be an effective approach to increase the light absorption efficiency of solar cells.

### 13.6.4 Near-field enhancement

The near field enhancement images for a selected few of the nanoparticle configurations have been provided in Fig. 13.21. As can be observed, there is a large amount of EM field enhancement inside the Si substrate. For smaller pitches, it can be seen that the enhancements from each nanoparticle is spread across neighboring particles, which can be indicative of strong plasmonic coupling between neighboring metal nanoparticles. The enhancement is not localized in a certain region, as well, they are spread above and below the nanoparticle array. Additionally, the enhancement above the nanoparticles is observed to be higher. A plausible explanation for this can be that the that radiation is constantly being reflected back and forth between the Si-air interface and the top portion of the Ag–Si interface, forming a cavity-like phenomenon that intensifies the electromagnetic fields due to constant constructive interference [191]. This may, in turn, result in enhanced optical absorption within the substrate, and can explain the observations made in absorption enhancement and short circuit current density portions of the analysis.

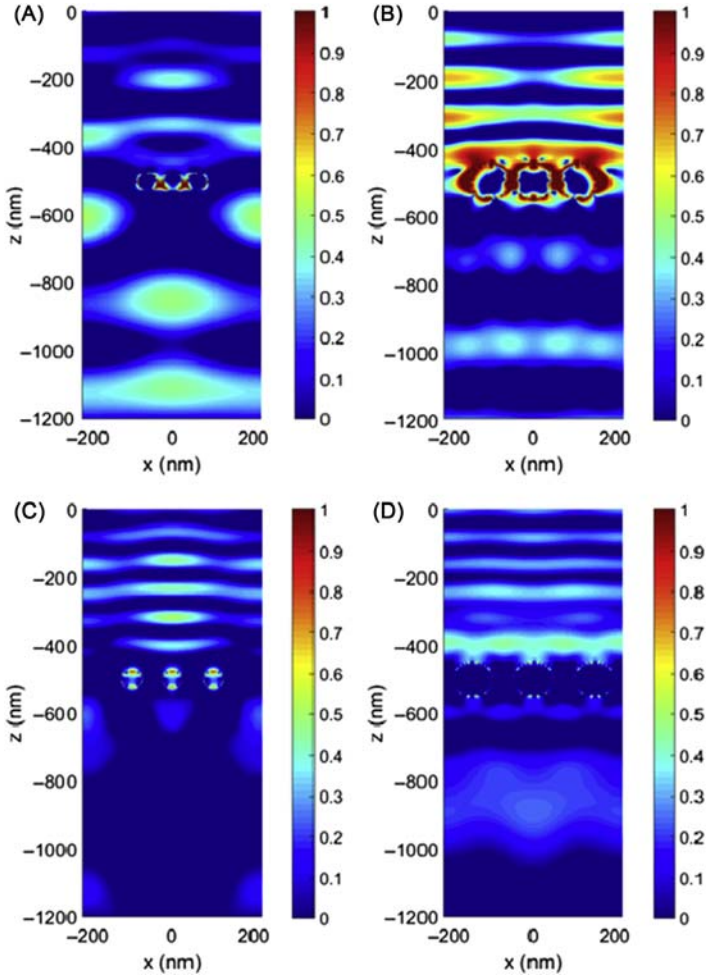


**Figure 13.21** Near-field enhancement image for (A) $D = 50$ nm and pitch = 10 nm, (B) $D = 100$ nm and pitch = 10 nm, (C) $D = 50$ nm and pitch = 20 nm, and (D) $D = 100$ nm and pitch = 20 nm. *Diagram reprinted with permission from IEEE Xplore (Choudhury et al.).*

The analysis provided in this section is largely based on computational methods, and thus do not provide an absolute understanding of this technology. A reason why computational methods have been preferred by different studies may be due to the complexity and high costs of fabricating and embedding plasmonic nanospheres within the semiconductor substrate, and maintaining the overall structural integrity of the solar cell. Despite this, however, this technology does show promise, and can prove

to be quite effective in improving the energy conversion efficiency of TF solar cells.

## 13.7 Section 7—Conclusion

The purpose of this chapter is to provide the reader with a comprehensive understanding of how the use of metals and metal nanostructures in solar cells has evolved since the harvesting of solar energy became a viable concept, and even before that the photosensitivity of different metals had been established. The use of metals in PV technology, despite being almost entirely absent in the early stages of the technology, has become particularly prevalent in recent times. The use of GaAs in expanding the horizon of solar cell efficiencies, CdTe proving to be a game changer when it came to thin-film PVs, and the advent of plasmonic nanostructures made of metals such as silver, gold, and aluminum are just a few of the examples provided in this chapter. While all of these technologies have proven to be milestones in the field, the chapter put a particular focus on plasmonic nanostructures because of how effective the concept has proven to be. The whole idea that an inherently unique property of a metal can be manipulated to increase the energy conversion efficiency of solar cells is, in itself, a startling concept. However, despite its complexity, plasmonic resonance has proven to be quite an effective phenomenon in enhancing solar cell efficiency. While the amount of published research in the field is quite substantial, the information is dispersed across different platforms in such a manner that to gather viable, relevant information can prove to be a daunting task indeed. With this chapter, however, it is hoped that a fundamental understanding of plasmonic metal nanostructures and their use in solar cells has been provided, and that a sufficiently encompassing image of the plasmonic solar cell technology has been portrayed.

## Acknowledgements

The authors would first like to express their deep gratitude to the Department of Electrical and Electronic Engineering and the Green Energy Research Center (GERC), Independent University, Bangladesh (IUB), for their continuous technical and financial support of the authors' research and for supporting the IUB Photonics Simulation Laboratory.

Special thanks are extended to Dr. M. Abdur Razzak, Past Head of the Department of Electrical and Electronic Engineering (2016–18), Associate Director of the Green

Energy Research Center (GERC), Independent University, Bangladesh (IUB), for his encouragement, lively discussions, and providing all the necessary logistical support for the authors' research. The authors cannot express their gratitude enough in this regard.

Finally, the authors would also like to thank Prof. Khosru Mohammad Salim, current head of the Department of Electrical and Electronic Engineering (2018–Present), Director of the Green Energy Research Center (GERC), Independent University, Bangladesh (IUB), for his enthusiasm and for providing the necessary financial support to ensure the continuation of the authors' research.

## References

[1] U. Eicker, E. Demir, D. Gürlich, Strategies for cost efficient refurbishment and solar energy integration in European Case Study buildings, Energy Build. Vol. 102 (2015) 237–249.
[2] J. Nelson, The Physics of Solar Cells., Imperial College Press, London, England, 2003.
[3] P. W ffel, Physics of solar cells, Principles to New Concepts, Wiley-VCH, New York, 2004.
[4] M.C. Beard, J.M. Luther, A.J. Nozik, The promise and challenge of nanostructured solar cells, Nat. Nanotechnol. 9 (2014) 951.
[5] S. Tetsuo, Nanostructured Materials for Solar Energy Conversion., Elsevier, 2006.
[6] Q., Yu, et al., High-efficiency dye-sensitized solar cells: the influence of lithium ions on exciton dissociation, charge recombination, and surface states, ACS Nano 4 (10) (2010) 6032–6038.
[7] A., Abate, et al., Lithium salts as "redox active" p-type dopants for organic semiconductors and their impact in solid-state dye-sensitized solar cells, Phys. Chem. Chem. Phys. 15 (2013) 2572–2579.
[8] L.M. Fraas, History of Solar Cell Development, Springer International Publishing, 2014.
[9] M. Ernst, A. Fell, E. Franklin, K.J. Weber, Characterization of recombination properties and contact resistivity of laser-processed localized contacts from doped silicon nanoparticle ink and spin-on dopants, IEEE J. Photovoltaics 7 (2) (2017) 471–478.
[10] R.A. Powell, Photoelectric effect: back to basics, Am. J. Phys. 46 (1978) 1046.
[11] S. Bose, The beginning of quantum statistics: a translation of "Planck's law and the light quantum hypothesis, Am. J. Phys. 44 (1976) 1056.
[12] B. Green, C. Weitzel, A brief history of GaAs technology at the GaAs IC symposium and a look ahead to the 2015 CSICS [Speakers' Corner], IEEE Microw. Mag. vol. 16 (no. 7) (2015) 120–123.
[13] M.P. Max Frenzel, T. Ketris, J.G. Seifert, On the current and future availability of gallium, Resour. Policy Volume 47 (2016) 38–50.
[14] Zh. I. Alferov, V.M. Andreev, M.B. Kagan, I.I. Protasov, V.G. Trofim, Solar-energy converters based on p-n $Al_xGa_{12x}As$-GaAs heterojunctions, Fiz. Tekh. Poluprovodn. 4, 2378 (Sov. Phys. Semicond. 4 (1971) 2047.
[15] Dong, Liang, et al., High-efficiency nanostructured window GaAs solar cells, Nano. Lett. 13 (10) (2013) 4850–4856.
[16] T.A. Cross, C.M. Hardingham, C.R. Huggins, S.P. Wood, GaAs solar panels for small satellites: performance data and technology trends, in: Conference Record of the Twenty Fifth IEEE Photovoltaic Specialists Conference – 1996, Washington, DC, 1996, pp. 277–282.

[17] E.M. Gaddy, Cost performance of multi-junction, gallium arsenide, and silicon solar cells on spacecraft, in: Conference Record of the Twenty Fifth IEEE Photovoltaic Specialists Conference – 1996, Washington, DC, 1996, pp. 293–296.
[18] Hans-Georg Steinrück, et al., The nanoscale structure of the electrolyte–metal oxide interface, Energy Environ. Sci. (2018). Advance Article.
[19] A. Hagfeldt, Brief overview of dye-sensitized solar cells, Ambio 41 (Suppl. 2) (2012) 151–155.
[20] S. Deambi. Solar PV Power: a global perspective. The Energy and Resources Institute (TERI), 2010.
[21] K.H. Norian, J.W. Edington, A device-oriented materials study of CdS and Cu2S films in solar cells, Thin Solid Films 75 (1) (1981) 53–65.
[22] T.L. Chu, et al., High efficiency thin film cadmium telluride solar cells, in: AIP Conference Proceedings, 268, 88, 1992.
[23] Y. Tang, in: N. Das (Ed.), Copper Indium Gallium Selenide Thin Film Solar Cells, Nanostructured Solar Cells, InTech, 2017.
[24] D. Derkacs, S.H. Lim, P. Matheu1, W. Mar, E.T. Yu, Improved performance of amorphous silicon solar cells via scattering from surface plasmon polaritons in nearby metallic nanoparticles, Appl. Phys. Lett. 89 (2006) 093103.
[25] X. Li, W.C.H. Choy, H. Lu, W.E.I. Sha, A.H.P. Ho, Efficiency enhancement of organic solar cells by using shape-dependent broadband plasmonic absorption in metallic nanoparticles, Adv. Func. Mater. 23 (21) (2013) 2728–2735.
[26] T. Li, L. Dai, C. Jiang, Design of efficient plasmonic thin-film solar cells based on mode splitting, J. Opt. Soc. Am. B 28 (2011) 1793–1797.
[27] S. Chu, A. Majumdar, Opportunities and challenges for a sustainable energy future, Nature 488 (7411) (2012) 294–303. 2012.
[28] J.R. Sites, Quantification of losses in thin-film polycrystalline solar cells, Sol. Energy Mater. Sol. Cells 2003 75 (1–2) (2003) 243–251.
[29] B.E. McCandless, K.D. Dobson, Processing options for CdTe thin film solar cells, Solar Energy 77 (6) (2004) 839–856. 2004.
[30] X. Li, R. Ribelin, Y. Mahathongdy, D. Albin, R. Dhere, D. Rose, et al., The effect of high-resistance $SnO_2$ on CdS/CdTe device performance, in: AIP Conference Proceedings 1999; 462(1), 1999
[31] J.M. Kephart, R.M. Geisthardt, Z. Ma, J. McCamy, W.S. Sampath, Reduction of window layer optical losses in CdS/CdTe solar cells using a float-line manufacturable HRT layer, in: 2013 39th IEEE Photovoltaic Specialists Conference (PVSC), Tampa, FL, 2013, pp. 1653–1657.
[32] D.E. Swanson, R.M. Geisthardt, J.T. McGoffin, J.D. Williams, J.R. Sites, Improved CdTe solar-cell performance by plasma cleaning the TCO layer, IEEE J. Photovoltaics 3 (2) (2013) 838–842.
[33] E. Klampaftis, D. Ross, K.R. McIntosh, B.S. Richards, Enhancing the performance of solar cells via luminescent down-shifting of the incident spectrum: a review, Solar Energy Mater. Solar Cells 93 (8) (2009) 1182–1194.
[34] S.D. Hodgson, W.S.M. Brooks, A.J. Clayton, G. Kartopu, V. Barrioz, S.J.C. Irvine, Enhancing blue photoresponse in CdTe photovoltaics by luminescent down-shifting using semiconductor quantum dot/PMMA films, Nano Energy 2 (1) (2013) 21–27.
[35] J. Zhou, X. Wu, G. Teeter, B. To, Y. Yan, R.G. Dhere, et al., CBD Cd1–xZnxS thin films and their application in CdTe solar cells, Phys. Status Solidi (B) 241 (3) (2004) 775–778.
[36] G. Kartopu, A.J. Clayton, W.S.M. Brooks, S.D. Hodgson, V. Barrioz, A. Maertens, et al., Effect of window layer composition in Cd1–xZnxS solar cells, Prog. Photovoltaics: Res. Appl. 22 (1) (2012) 18–23.

[37] X. Wu, Y. Yan, R.G. Dhere, Y. Zhang, J. Zhou, C. Perkins, et al., Nanostructured CdS: Ofilm: preparation, properties, and application, Phys. Status Solidi (C) 1 (4) (2004).
[38] X. Wu, R.G. Dhere, Y. Yan, I.J. Romero, Y. Zhang, J. Zhou, et al., High-efficiency polycrystalline CdTe thin-film solar cells with an oxygenated amorphous CdS (a-CdS:O) window layer, in: Photovoltaic Specialists Conference, 2002. Conference Record of the Twenty-Ninth IEEE. IEEE: New Orleans, LA, 2003, pp. 531–534.
[39] A. Gupta, K. Allada, S.H. Lee, A.D. Compaan, Oxygenated CdS window layer for sputtered CdS/CdTe solar cells, in: Materials Research Society Symposium Proceedings, 2003, vol. 763, pp. 341–346.
[40] Y.L. Soo, W.H. Sun, S.C. Weng, Y.S. Lin, S.L. Chang, L.Y. Jang, et al., Local environment surrounding S and Cd in CdS:O thin film photovoltaic materials probed by x-ray absorption fine structures, Appl. Phys. Lett. 89 (2006) 131908–1-131908-3.
[41] J.M. Kephart, R. Geisthardt, W.S. Sampath, Sputtered, oxygenated CdS window layers for higher current in CdS/CdTe thin film solar cells, in: 2012 38th IEEE Photovoltaic Specialists Conference (PVSC), Austin, TX, 2012, pp. 854–858.
[42] R. Asaba, K. Wakita, A. Kitano, Y. Shim, N. Mamedov, A. Bayramov, et al., Structure and optical properties of CdS:O thin films, Phys. Status Solidi (C) 10 (7–8) (2013) 1098–1101.
[43] D. Albin, R. Dhere, S. Glynn, W. Metzger, The direct correlation of CdTe solar cell stability with mobile ion charge generation during accelerated lifetime testing, in: 2009 34th IEEE Photovoltaic Specialists Conference (PVSC), Philadelphia, PA, 2009, pp. 001903–001908.
[44] C.R. Corwine, A.O. Pudov, M. Gloeckler, S.H. Demtsu, J.R. Sites, Copper inclusion and migration from the back contact in CdTe solar cells, Solar Energy Mater. Solar Cells 82 (4) (2004) 481–489.
[45] K.D. Dobson, I. Visoly-Fisher, G. Hodes, D. Cahen, Stabilizing CdTe/CdS solar cells with cucontaining contacts to p-CdTe, Adv. Mater. 13 (19) (2001) 1495–1499.
[46] B. Korevaar, R. Shuba, A. Yakimov, H. Cao, J. Rojo, T. Tolliver, Initial and degraded performance of thin film CdTe solar cell devices as a function of copper at the back contact, Thin Solid Films 519 (21) (2011) 7160–7163.
[47] P. Kobyakov, N. Schuh, K. Walters, V. Manivannan, W. Sampath, Continuous in-line processing of CdS/CdTe devices: process control using XRF and efficient heating, in: 2010 35th IEEE Photovoltaic Specialists Conference (PVSC), Honolulu, HI, 2010, pp. 780–785.
[48] R.C. Powell, Research leading to high-throughput manufacturing of thin-film CdTe PV modules, in: NREL Subcontract Report SR-520-39669, First Solar SR520-39669, National Renewable Energy Laboratory, 2006.
[49] D.A. Hanks, J.M. Kephart, K. Horsely, M. Blum, M. Mezher, L. Weinhardt, et al., Characterization of sulfur bonding in CdS:O buffer layers for CdTe-based thin-film solar cells, in: Preparation, 2014.
[50] H. Wilhelm, H.W. Schock, R. Scheer, Interface recombination in heterojunction solar cells: influence of buffer layer thickness, J. Appl. Phys. 109 (8) (2011) 084514–1-08514-6.
[51] R. Paternoster, R. Brame, P. Mazerolle, A. Piquero, Using the correct statistical test for the equality of regression coefficients, Criminology 36 (4) (1998) 859–866.
[52] M. Burgelman, P. Nollet, S. Degrave, Modelling polycrystalline semiconductor solar cells, Thin Solid Films 361-362 (2000) 527–532.
[53] M. Gloeckler, A.L. Fahrenbruch, J.R. Sites, Numerical modeling of CIGS and CdTe solar cells: setting the baseline, in: Proceedings of 3rd World Conference on Photovoltaic Energy Conversion, Osaka, Japan, 2003.

[54] T. Minemoto, T. Matsui, H. Takakura, Y. Hamakawa, T. Negami, Y. Hashimoto, et al., Theoretical analysis of the effect of conduction band offset of window/CIS layers on performance of CIS solar cells using device simulation, Solar Energy Mater. Solar Cells 67 (2001) 83–88.
[55] T. Minemoto, Y. Hashimoto, T. Satoh, T. Negami, H. Takakura, Y. Hamakawa, Cu(In,Ga)Se2 solar cells with controlled conduction band offset of window/Cu(In, Ga)Se2 layers, J. Appl. Phys. 89 (12) (2001) 8327–8330.
[56] J. Fritsche, T. Schulmeyer, D. Kraft, A. Thissen, A. Klein, W. Jaegermann, Utilization of sputter depth profiling for the determination of band alignment at polycrystalline CdTe/CdS heterointerfaces, Appl. Phys. Lett. 81 (2002) 2297–2299.
[57] K. Nishi, H. Ohyama, T. Suzuki, T. Mitsuyu, T. Tomimasu, Evaluation of the CdS/CdTe interface using free-electron laser internal photoemission technique, Appl. Phys. Lett. 70 (26) (1997) 3585–3587.
[58] J. Sites, J. Pan, Strategies to increase CdTe solar-cell voltage, Thin Solid Films 515 (15) (2007) 6099–6102.
[59] D. Albin, Y. Yan, M. Al-Jassim, The effect of oxygen on interface microstructure evolution in CdS/CdTe solar cells, Prog. Photovoltaics: Res. Appl. 10 (5) (2002) 309–322.
[60] M.A. Green, K. Emery, Y. Hisikawa, W. Warta, E.D. Dunlop, Solar cell efficiency tables (Version 45), Prog. Photovoltaics 23 (2015) 1–9.
[61] M. Topic, R. Geisthardt, J.R. Sites, Performance limits and status of single-junction solar cells with emphasis on CIGS, IEEE J. Photovoltaics 5 1 (2015) 360–365.
[62] W. Shockley, H.J. Queisser, Detailed balance limit of efficiency in P-N junction solar cells, J. Appl. Phys. 32 (no. 3) (1961) 510.
[63] T. Tiedje, E. Yablonovitch, G.D. Cody, B.G. Brooks, Limiting efficiency of silicon solar cells, IEEE Trans. Electron Devices. ED31. 5 (1984) 711–716.
[64] O.D. Miller, E. Yablonovitch, S.R. Kurtz, Strong internal and external luminescence as solar cells approach the Shockley-Queisser limit, IEEE J. Photovoltaics 2 (3) (Jul. 2012) 303–311.
[65] L.C. Hirst, N.J. Ekins-Daukes, Fundamental losses in solar cells, Prog. Photovoltaics 19 (3) (2011) 286–293.
[66] J.L. Balenzategui, A. Mart, The losses of efficiency in a solar cell step by step, in: Proc. 14th Eur. Photovoltaic Sol. Energy Conf. 1997, pp. 2374–2377.
[67] M.A. Green, Efficiency limits, losses, and measurement, Solar Cells., Prentice-Hall, Englewood Cliffs, NJ, 1982.
[68] Standard Tables for Reference Solar Spectral Irradiances, Direct Normal and Hemispherical on 37° Tilted Surface, ATSM G173-03, 2012.
[69] J. Kurnik, M. Jankovec, K. Brecl, M. Topic, Outdoor testing of PV module temperature and performance under different mounting and operational condition, Sol. Energy Mater. Sol. Cells 95 (2011) 373–376.
[70] T. Huld, R. Gottschalg, H.G. Beyer, M. Topic, Mapping the performance of PV modules, effects of module type and data averaging, Sol. Energy 84 (2010) 324–338.
[71] J. Kephart, R. Geisthardt, W.S. Sampath, Optimization of CdTe thin-film solar cell efficiency using a sputtered, oxygenated CdS window layer, Prog. Photovoltaics (2015). to be published.
[72] X. Wu, J.C. Keane, R.G. Dhere, C. DeHart, D.S. Albin, A. Duda, et al., 16.5%-efficient CdS/CdTe polycrystalline thin-film solar cell, in: Proc. 17th Eur. Photovoltaic Sol. Energy Conf. 2001, pp. 995–1000.
[73] M. Gloeckler, I. Shankin, Z. Zhao, CdTe solar cells at the threshold to 20% efficiency, IEEE J. Photovoltaics 3 4 (2013) 1389–1393.

[74] R. Geisthardt, Device Characterization of Cadmium Telluride Photovoltaics (Ph.D. dissertation), Dept. Phys., Colorado State Univ., Fort Collins, CO, 2014.
[75] K.-J. Hsiao, J.R. Sites, Electron reflector to enhance photovoltaic efficiency: Application to thin-film CdTe solar cells, Prog. Photovoltaics 20 (4) (2012) 486–489.
[76] P.S. Kobyakov, D.E. Swanson, J. Drayton, J.M. Raguse, K.L. Barth, W.S. Sampath, Progress towards a CdS/CdTe solar cell implementing an electron reflector, in: Proc. 39th IEEE Photovoltaic Spec. Conf. 2013, pp. 0386–0391.
[77] T.A. Gessert, J.N. Duenow, S. Ward, J.F. Geisz, B. To. Analysis of ZnTe:Cu/Ti contacts for crystalline CdTe, in: Proc. 40th IEEE Photovoltaic Spec. Conf. 2014, pp. 2329–2333.
[78] M. Gloeckler, Progress towards practical CdTe solar modules with 17% efficiency, in: Presented at the E-MRS 2014 Spring Meeting, Lille, France, 2014.
[79] R.M. Geisthardt, M. Topič, J.R. Sites, Status and potential of CdTe solar-cell efficiency, IEEE J. Photovoltaics vol. 5 (no. 4) (2015) 1217–1221.
[80] I. Repins, M.A. Contreras, B. Egaas, C. DeHart, J. Scharf, C.L. Perkins, et al., 19.9%-Efficient ZnO/CdS/CuInGaSe$_2$ solar cell with 81.2% fill factor, Prog. Photovoltaics: Res. Appl. 16 (2008) 235–239.
[81] M. Powalla, B. Dimmler, K.-H. Gross, CIS thin-film solar modules—an example of remarkable progress in PV, in: W. Palz, H.A. Ossenbrink, P. Helm (Eds.), Proceedings of the 20th European Photovoltaic Solar Energy Conference, WIP: Munich, Germany, 2005. p. 1689.
[82] P. Jackson, R. Wuerz, U. Rau, J. Mattheis, M. Kurth, T. Schloetzer, et al., High quality baseline for high efficiency, Cu(In1-xGax)Se2 solar cells, Prog. Photovoltaics: Res. Appl. 15 (2007) 507–519.
[83] U. Rau, K. Taretto, S. Siebentritt, Grain boundaries in Cu(In,Ga)(Se, S)$_2$ thin-film solar cells, Appl. Phys. A 96 (2009) 221–234.
[84] P.T. Erslev, J.W. Lee, W.N. Shafarman, J.D. Cohen, The influence of Na on metastable defect kinetics in CIGS materials, Thin Solid Films 517 (7) (2009) 2277–2281.
[85] H. Mönig, C.-H. Fischera, R. Caballero, C.A. Kaufmann, N. Allsop, M. Gorgoi, et al., Surface Cu depletion of Cu(In,Ga)Se2 films: an investigation by hard X-ray photoelectron spectroscopy, Acta Mater. 57 (12) (2009) 3645–3651.
[86] Y. Yan, K.M. Jones, J. Abushama, M. Young, S. Asher, M.M. AlJassim, et al., Microstructure of surface layers in Cu(In,Ga)Se2 thin films, Appl. Phys. Lett. 81 (2002) 1008.
[87] S.-H. Han, F.S. Hasoon, A.M. Hermann, D.H. Levi, Spectroscopic evidence for a surface layer in CuInSe$_2$:Cu deficiency, Appl. Phys. Lett. 91 (2007) 021904.
[88] M. Igalson, A. Urbaniak, M. Edoff, Reinterpretation of defect levels derived from capacitance spectroscopy of CIGSe solar cells, Thin Solid Films 517 (7) (2009) 2153–2157.
[89] J. Hedstrom, H. Ohlsen, M. Bodegard, A. Kylner, L. Stolt, D. Hariskos, et al., ZnO/CdS/Cu (In,Ga)Se$_2$ thin film solar cells with improved performance, in: Conference Record of the 23rd IEEE Photovoltaic Specialists Conference, 1993, pp. 364–371.
[90] D. Rudmann, Effects of Sodium on Growth and Properties of Cu(In, Ga)Se2 Thin Films and Solar Cells (Doctoral dissertation), Eidgenössische Technische Hochschule ETHZürich, No. 15576, 2004.
[91] D. Herrmann, et al., CIGS module manufacturing with high deposition rates and efficiencies, in: Presented at 40th IEEE PVSC, Denver, CO, June 8–13, 2014.

[92] X. Chen, B. Jia, Y. Zhang, M. Gu, Exceeding the limit of plasmonic light trapping in textured screen-printed solar cells using Al nanoparticles and wrinkle-like graphene sheets, Light Sci. Appl. (2013) 2.
[93] C.F. Guo, T. Sun, F. Cao, Q. Liu, Z. Ren, Metallic nanostructures for light trapping in energy-harvesting devices, Light Sci. Appl. 2014.
[94] E.D. Kosten, J.H. Atwater, J. Parsons, A. Polman, H.A. Atwater, Highly efficient GaAs solar cells by limiting light emission angle, Light Sci. Appl. (2013).
[95] B.M. Kayes, H. Nie, R. Twist, S.G. Spruytte, F. Reinhardt, et al., 27.6% conversion efficiency, a new record for single-junction solar cells under 1 sun illumination, in: Proceedings of 2011 37th IEEE Photovoltaic Specialists Conference; 19–24 June; Seattle, WA. IEEE: New York, 2011, pp. 000004–000008.
[96] M.A. Steiner, J.F. Geisz, I. García, D.J. Friedman, A. Duda, et al., Optical enhancement of the open-circuit voltage in high quality GaAs solar cells, J. Appl. Phys. 113 (2013) 123109.
[97] K. Lee, J.D. Zimmerman, T.W. Hughes, S.R. Forrest, Non-destructive wafer recycling for low-cost thin-film flexible optoelectronics, Adv. Funct. Mater. 24 (2014) 4284–4291.
[98] K. Lee, J.D. Zimmerman, X. Xiao, K. Sun, S.R. Forrest, Reuse of GaAs substrates for epitaxial lift-off by employing protection layers, J. Appl. Phys. 111 (2012) 033527.
[99] C.W. Cheng, K.T. Shiu, N. Li, S.J. Han, L. Shi, et al., Epitaxial lift-off process for gallium arsenide substrate reuse and flexible electronics, Nat. Commun. 4 (2013) 1577.
[100] J. Yoon, S. Jo, I.S. Chun, I. Jung, H.S. Kim, et al., GaAs photovoltaics and optoelectronics using releasable multilayer epitaxial assemblies, Nature 465 (2010) 329–333.
[101] M. Memarian, G.V. Eleftheriades, Light concentration using hetero-junctions of anisotropic low permittivity metamaterials, Light Sci. Appl. (2013).
[102] G.J. Bauhuis, P. Mulder, E.J. Haverkamp, J.J. Schermer, E. Bongers, et al., Wafer reuse for repeated growth of III–V solar cells, Prog. Photovoltaics Res. Appl. (2010).
[103] C.D. Bailie, M.G. Christoforo, J.P. Mailoa, et al., Semi-transparent perovskite solar cells for tandems with silicon and CIGS, Energy Environ. Sci. 8 (2015) 956–963.
[104] J.M. Ball, M.M. Lee, A. Hey, H.J. Snaith, Low-temperature processed meso-superstructured to thin-film perovskite solar cells, Energy Environ. Sci. 6 (6) (2013) 1739–1743.
[105] M.H. Chowdhury, The Use of Surface Enhanced Raman Spectroscopy (SERS) for Biomedical Applications, College Station, TX, USA, 2005.
[106] D.A. Stuart, A.J. Haes, C.R. Yonzon, E.M. Hicks, R.P. Van Duyne, Biological applications of localized surface Plasmon resonance phenomena, in: IEEE Proceedings on Nano Biotechnology: 2005, vol. 152, pp. 13–32.
[107] M. Brust, M. Walker, D. Bethell, D.J. Schiffrin, R. Whyman, Synthesis of thiol-derivatised gold nanoparticles in a two-phase liquid–liquid system, J. Chem. Soc. Chem. Commun. 23 (1994) 801–802.
[108] R.G. Freeman, K.C. Grabar, K.J. Allison, R.M. Bright, J.A. Davis, A.P. Guthrie, et al., Self-assembled metal colloid monolayers: an approach to SERS substrates, Science 267 (1995) 1629–1632.
[109] I. Thomann, B.A. Pinaud, Z. Chen, B.M. Clemens, T.F. Jaramillo, M.L. Brongersma, Plasmon enhanced solar-to-fuel energy conversion, Nano Lett. 11 (2011) 3440–3446.
[110] S.A.Choudhury, M.H.Chowdhury, The promise and challenge of enhancing solar cell efficiency using patterned nanostructures, in: First International Conference on

Advanced Information and Communication Technology; 2016; Chittagong (Bangladesh).
[111] S.A. Choudhury, M.H. Chowdhury, Optimizing the parameters of plasmonic metal nanoparticles to maximize the energy conversion efficiency of thin film solar cells, in: Third International Conference on Advanced Information and Communication Technology; 2016; MIST, Dhaka (Bangladesh).
[112] S.A. Choudhury, M.H. Chowdhury, Use of plasmonic metal nanoparticles to increase the light absorption efficiency of thin film solar cells, in: IEEE 4TH International Conference on Sustainable Energy Technologies; 2016; Hanoi (Vietnam).
[113] S.A. Choudhury, M.S. Munir, N. Nawshin, M.H. Chowdhury, Effect of varying the row and column size of periodic arrays of plasmonic nanoparticles on the energy conversion efficiency of thin film solar cells, in: International Conference on Electrical, Computer and Communication Engineering (ECCE); 2017; Dhaka (Bangladesh), pp. 44–49.
[114] S.A. Choudhury, N. Nawshin, M.H. Chowdhury, Influence of particle shape on the efficacy of plasmonic metal nanoparticles to enhance the energy conversion efficiency of thin film solar cells, in: IEEE Region Ten Conference(TENCON); 2017; Penang (Malaysia).
[115] S.A. Choudhury, R.A. Rifat, F. Fairooz, W. Mahdhiand, M.H. Chowdhury, On the possibility of using plasmonic metal nanoparticles embedded within the silicon substrate to enhance the energy conversion efficiency of silicon thin film solar cells, in: IEEE Region 10 Humanitarian Technology Conference (R10HTC); 2017; Dhaka (Bangladesh).
[116] U. Kreibig, M. Vollmer, Optical Properties of Metal Clusters., Springer-Verlag, New York, 1995.
[117] U. Kreibig, M. Gartz, A. Hilger, Mie resonances: Sensors for physical and chemical cluster interface properties, Ber. Bunsenges. Phys. Chem. 101 (1997) 1593–1604.
[118] A.J. Haes, W.P. Hall, L. Chang, W.L. Klein, R.P. Van Duyne, A localized surface plasmon resonance biosensor: First steps toward an assay for Alzheimer's disease, Nano Lett. 4 (2004) 1029–1034.
[119] A.J. Haes, L. Chang, W.L. Klein, R.P. Van Duyne, Detection of a biomarker for Alzheimer's disease from synthetic and clinical samples using a nanoscale optical biosensor, J. Am. Chem. Soc. 127 (2005) 2264–2271.
[120] K.L. Kelly, E. Coronado, L.L. Ahao, G.C. Schatz, The optical properties of metal nanoparticles: the influence of size, shape and dielectric environment, J. Phys. Chem. B 107 (2003) 668–677.
[121] M.M. Miller, A.A. Lazarides, Sensitivity of metal nanoparticle surface plasmon resonance to the dielectric environment, J. Phys. Chem. B 109 (2005) 21556–21565.
[122] A.J. Haes, S.L. Zou, G.C. Schatz, R.P. Van Duyne, Nanoscale optical biosensor: short range distance dependence of the localized surface plasmon resonance of noble metal nanoparticles, J. Phys. Chem. B 108 (2004) 6961–6968.
[123] T.R. Jensen, M.L. Duval, K.L. Kelly, A.A. Lazarides, G.C. Schatz, R.P. Van Duyne, J. Phys. Chem. B 103 (1999) 9846–9853.
[124] P. Hanarp, M. Kall, D.S. Sutherland, Optical properties of short range ordered arrays of nanometer gold disks prepared by colloidal lithography, J. Phys. Chem. B 107 (2003) 5768–5772.
[125] T.R. Jensen, M.D. Malinsky, C.L. Haynes, R.P. Van Duyne, Nanosphere lithography: tunable localized surface plasmon resonance spectra of silver nanoparticles, Phys. Chem. B 104 (2000) 10549–10556.
[126] M.D. Malinsky, K.L. Kelly, G.C. Schatz, R.P. Van Duyne, Chain length dependence and sensing capabilities of the localized surface plasmon resonance of silver

nanoparticles chemically modified with alkanethiol self-assembled monolayers, J. Am. Chem. Soc. 123 (2001) 1471–1482.
[127] J.J. Mock, D.R. Smith, S. Schultz, Local refractive index dependence of plasmon resonance spectra from individual nanoparticles, Nano Lett. 3 (2003) 485–491.
[128] G. Raschke, S. Brogi, A.S. Susha, A.L. Rogach, T.A. Klar, J. Feldmann, et al., Gold nanoshells improve single nanoparticle molecular sensors, Nano Lett. 4 (2004) 1853–1857.
[129] F. Tam, C. Moran, N. Halas, Geometrical parameters controlling sensitivity of nanoshell plasmon resonances to changes in dielectric environment, J. Phys. Chem. B 108 (2004) 17290–17294.
[130] A.C. Templeton, J.J. Pietron, R.W. Murray, P. Mulvaney, Solvent refractive index and core charge influences on the surface plasmon absorbance of alkanethiolate monolayer-protected gold clusters, J. Phys. Chem. B 104 (2000) 564–570.
[131] Y.G. Sun, Y.N. Xia, Analyst. UK: Cambridge 2003, vol. 128, pp. 686–691.
[132] N.G. Khlebtsov, L.A. Trachuk, A.G. Mel'nikov, The effect of the size, shape, and structure of metal nanoparticles on the dependence of their optical properties on the refractive index of a disperse medium, Opt. Spectrosc. 98 (2005) 77–83.
133 V.A. Bogatyrev, S.A. Vrublevsky, L.A. Trachuk, and N.G. Khlebtsov, Saratov Fall Meeting 2004: Coherent Optics of Ordered and Random Media IV, Zimnyakov, D. A., Ed., Proc. SPIE, 2005, vol. 5772, p. 11.
[134] A. Gole, C.J. Murphy, Polyelectrolyte-coated gold nanorods: synthesis, characterization and immobilization, Chem. Mater. 17 (2005) 1325–1330.
[135] N. Nath, A. Chilkoti, A colorimetric gold nanoparticle sensor to interrogate biomolecular interactions in real time on a surface, Anal. Chem. 74 (2002) 504–509.
[136] A.J. Haes, S.L. Zou, G.C. Schatz, R.P. Van Duyne, Nanoscale optical biosensor: short range distance dependence of the localized surface plasmon resonance of noble metal nanoparticles, J. Phys. Chem. B 108 (2004) 109–116.
[137] H.X. Xu, M. Kall, Modeling the optical response of nanoparticle-based surface plasmon resonance sensors, Sens. Actuat., B 87 (2002) 244–249.
[138] N.G. Khlebtsov, Optical models for conjugates of gold and silver nanoparticles with biomacromolecules, J. Quant. Spectrosc. Radiat. Transf. 89 (2004) 143–153.
[139] S. Pillai, M.A. Green, Plasmonics for photovoltaic, Solar Energy Mater. Solar Cells 94 (2010) 1481–1486.
[140] C.F. Bohren, D.R. Huffman, Absorption and Scattering of Light by Small Particles., Wiley-Interscience, New York, 1983.
[141] M.J. Mendes, S. Morawiec, T. Mateus, A. Lyubchyk, H. Águas, I. Ferreira, et al., Broadband light trapping in thin film solar cells with self-organized plasmonic nano-colloids, Nanotechnology (2015) 26.
[142] A. Luque, H.S. Status, trends, challenges and the bright future of solar electricity from photovoltaics. Handbook of Photovoltaic Science and Engineering, 2003.
[143] F. Priolo, T. Gregorkiewicz, M. Galli, T.F. Krauss, Silicon nanostructures for photonics and photovoltaics, Nat. Nanotechnol. 9 (2014) 19–32.
[144] H. Aguas, et al., Silicon thin film solar cells on commercial tiles, Energy Environ. Sci. 4 (2011) 4620–4632.
[145] S.A. Filonovich, et al., Hydrogenated amorphous and nanocrystalline silicon solar cells deposited by HWCVD and RF-PECVD on plastic substrates at 150 °C, J. Non-Crystal. Solids 354 (2008) 2376–2380.
[146] K. Masuko, et al., Achievement of more than 25% conversion efficiency with crystalline silicon heterojunction solar cell, IEEE J. Photovoltaics 4 (2014) 1433–1435.
[147] A. Bozzola, P. Kowalczewski, L.C. Andreani, Towards high efficiency thin-film crystalline silicon solar cells: the roles of light trapping and non-radiative recombinations, J. Appl. Phys. 115 (2014) 094501.

[148] M.G. Deceglie, et al., Design of nanostructured solar cells using coupled optical and electrical modeling, Nano Lett. 12 (2012) 2894–2900.
[149] M.C. Beard, J.M. Luther, A.J. Nozik, The promise and challenge of nanostructured solar cells, Nat. Nanotechnol. 5 (2014) 951–954.
[150] H. Zhou, Q. Dhen, G. Li, S. Luo, T. Song, H. Duan, et al., Interface engineering of highly efficient perovskite solar cells, Science 345 (2014) 542–546.
[151] S. Pillai, M.A. Green, Plasmonics for photovoltaic applications, Green/Solar Energy Mater. Solar Cells 94 (2010) 1481–1486.
[152] R. Hulstrom, R. Bird, C. Riordian, Spectral solar irradiance data sets for selected terestrial conditions, Solar Cells 15 (1985) 365–391.
[153] S.H. Lim, W. Mar, P. Matheu, D. Derkacs, E.T. Yu, Photocurrent spectroscopy of optical absorption enhancement in silicon photodiodes via scattering from surface plasmon polaritrons in gold nanoparticles, J. Appl. Phys. 101 (2007) 104309–1-104309-7.
[154] J.P. Kottmann, O.J.F. Martin, D.R. Smith, S. Schultz, Spectral response of plasmon resonant nanoparticles with a non-regular shape, Opt. Soc. Am. 6 (2000) 213–219.
[155] M.S. Tame, K.R. McEnery, Ş.K. Özdemir, J. Lee, S.A. Maier, M.S. Kim, Quantum plasmonics, Nat. Phys. 9 (2013) 329–340.
[156] K.L. Kelly, E. Coronado, L.L. Zhao, G.C. Schatz, The optical properties of metal nanoparticles: the influence of size, shape, and dielectric environment, J. Phys. Chem. B (2003) 668–677.
[157] M.A. Green, S. Pillai, Harnessing plasmonics for solar cells, Nat. Photonics 6 (2012) 130–132.
[158] X. Li, W.C.H. Choy, H. Lu, W.E.I. Sha, A.H.P. Ho, Efficiency enhancement of organic solar cells by using shape dependent broadband plasmonic absorption in metallic nanoparticles, Adv. Func. Mat. 23 (2013) 2728–2735.
[159] E.T. Yu, D. Derkacs, P. Matheu, D.M. Schaadt, Plasmonic nanoparticle scattering for enhanced performance of photovoltaic and photodetector devices, in: Plasmonics: Nanoimaging, Nanofabrication, and Their Applications IV, 2008.
[160] N.P. Hylton, X.F. Li, V. Giannini, K.-H. Lee, N.J. Ekins-Daukes, J. Loo, et al., Loss mitigation in plasmonic solar cells: aluminium nanoparticles for broadband photocurrent enhancements in GaAs photodiodes, Sci. Rep. (2013) 3.
[161] M.J. Mendes, S. Morawiec, T. Mateus, A. Lyubchyk, H. Aguas, I. Ferreira, et al., Broadband light trapping in thin film solar cells with self-organized plasmonic nanocolloids, Nanotechnology (2015) 26.
[162] Y.A. Akimov, W.S. Koh, K. Ostricov, TCO and light trapping in silicon thin film solar cells, Solar Energy 77 (2004) 917–930.
[163] Yu.A. Akimov, K. Ostrikov, E.P. Li, Surface plasmon enhancement of optical absorption in thin-film silicon solar cells, Plasmonics 4 (2009) 107–113.
[164] K.R. Catchpole, S. Pillai, Absorption enhancement due to scattering by dipoles into silicon waveguides, Appl. Phys. 100 (2006) 044504.
[165] K.P. Catchpole, A. Polman, Design principles for particle plasmon enhanced solar cells, Appl. Phys. Lett. 93 (2008) 191113.
[166] W.B. Ewe, H.S. Chu, E.P. Li, Volume integral equation analysis of surface plasmon resonance of nanoparticles, Opt. Soc. Am. 15 (2007) 18200–18208.
[167] C. Hägglund, M. Zäch, B. Kasemo, Enhanced charge carrier generation in dye sensitized solar cells by nanoparticle plasmons, Appl. Phys. Lett. 92 (2008) 013113.
[168] M.A. Green, Solar Cells: Operating Principles, Technology and System Applications, the University of New South Wales, Sydney, 1998.
[169] M. Hussein, F.M. Hameed, F.F.N. Areed, S.S.A. Obayya, Analysis of a novel decagonal semiconductor nanowire for solar cell applications, SPIE 9140 (2014) 1–6.

[170] B.S. Luk'yanchuk, M.I. Tribelsky, Z.B. Wang, Y. Zhou, M.H. Hong, L.P. Shi, et al., Extraordinary scattering diagram for nanoparticles near plasmon resonance frequencies, Appl. Phys. A 89 (2007) 259–264.
[171] J. Müller, B. Rech, J. Springer, M. Vanecek, Enhancement of optical absorption in thin-film solar cells through the excitation of higher-order nanoparticle plasmon modes, Opt. Express 17 (2009) 10195–10205.
[172] S. Pillai, K.R. Catchpole, T. Trupke, M.A. Green, Surface plasmon enhanced silicon solar cells, J. Appl. Phys. 101 (2007) 093105.
[173] S.Y. Abate, W.-T. Wu, S. Pola, Y.-T. Tao, Compact $TiO_2$ films with sandwiched Ag nanoparticles as electron-collecting layer in planar type perovskite solar cells: improvement in efficiency and stability, RSC Adv. 8 (14) (2018) 7847.
[174] B. Du, W. Yang, Q. Jiang, H. Shan, D. Luo, B. Li, et al., Plasmonic-functionalized broadband perovskite photodetector, Adv. Opt. Mater. (2018) 1701271.
[175] M. Que, L. Zhu, Y. Yang, J. Liu, P. Chen, W. Chen, et al., Tunable plasmon-enhanced broadband light harvesting for perovskite solar cells, J. Power Sources 383 (2018) 42.
[176] B.C. Moon, J.H. Park, D.K. Lee, N. Tsvetkov, I. Ock, K.M. Choi, et al., Broadband light absorption and efficient charge separation using a light scattering layer with mixed cavities for high-performance perovskite photovoltaic cells with stability, Small 13 (30) (2017) 1700418.
[177] S.S.A. Obayya, Computational Photonics., Wiley, 2011.
[178] D. Pinto, S.S.A. Obayya, Improved complex-envelope alternating-direction-implicit finite-difference-time-domain method for photonic-bandgap cavities, IEEE J. Lightwave Technol. 25 (1) (2007) 440–447.
[179] M. Westphalen, U. Kreibig, J. Rostalski, H. Lüth, D. Meissner, Metal cluster enhanced organic solar cells, Solar Energy Mater. Solar Cells 61 (2000) 97–105.
[180] H.R. Stuart, D.G. Hall, Island size effects in nanoparticle-enhanced photodetectors, Appl. Phys. 73 (1998) 3815–3817.
[181] B.J. Soller, D.G. Hall, Scattering enhancement from an array of interacting dipoles near a planar waveguide, J. Opt. Am. Soc. B 19 (2002) 2437–2448.
[182] S.W. Tong, C.F. Zhang, C.Y. Jiang, G. Ling, Q.D. Liu, E.T. Kang, et al., Improvement in the hole collection of polymer solar cells by utilizing gold nanoparticle buffer layer, Chem. Phys. Lett. 453 (2008) 73–76.
[183] S. Wu, W. Wang, K. Reinhardt, Y. Lu, S. Chen, Absorption enhancement in thin film silicon solar cells by two dimensional periodic nanopatterns, J. Nanophotonics 4 (2010) 1–6.
[184] C.L. Davies, M.R. Filip, J.B. Patel, T.W. Crothers, C. Verdi, A.D. Wright, et al., Bimolecular recombination in methylammonium lead triiodide perovskite is an inverse absorption process, Nat. Commun. 9 (2018) 1.
[185] Y. Cheng, C. Chen, X. Chen, J. Jin, H. Li, H. Song, et al., Considerably enhanced perovskite solar cells via the introduction of metallic nanostructures, J. Mater. Chem. A 5 (14) (2017) 6515.
[186] W. Zhang, M. Saliba, S.D. Stranks, Y. Sun, X. Shi, U. Wiesner, et al., Enhancement of perovskite-based solar cells employing core–shell metal nanoparticles, Nano Lett. 13 (9) (2013) 4505–4510.
[187] Z. Lu, X. Pan, Y. Ma, Y. Li, L. Zheng, D. Zhang, et al., Plasmonic-enhanced perovskite solar cells using alloy popcorn nanoparticles, RSC Adv. 5 (2015) 11175–11179.
[188] H.-L. Hsu, T.-Y. Juang, C.-P. Chen, C.-M. Hsieh, C.-C. Yang, C.-L. Huang, et al., Enhanced efficiency of organic and perovskite photovoltaics from shape-dependent broadband plasmonic effects of silver nanoplates, Sol. Energy Mater. Sol. Cells 140 (2015) 224–231.

[189] V. Myroshnychenko, J. Rodriguez-Fernandez, I. Pastoriza-Santos, A.M. Funston, C. Novo, P. Mulvaney, et al., Chem. Soc. Rev. 37 (2008) 1792.
[190] J. Burschka, N. Pellet, S.-J. Moon, R. Humphry-Baker, P. Gao, M.K. Nazeeruddin, et al., Sequential deposition as a route to high-performance perovskite-sensitized solar cells, Nature 499 (2013) 316–319. Available from: https://doi.org/10.1038/nature12340 [Crossref], [PubMed].
[191] P. Spinelli, A. Polman, Prospects of near-field plasmonic absorption enhancement in semiconductor materials using embedded Ag nanoparticles, Opt. Express 20 (S5) (2012).

## Further reading

Design of plasmonic thin-film solar cells with broadband absorption enhancements, Adv. Mater.29 (2009) 3504–3509.

This page intentionally left blank

# CHAPTER 14

# Electrolyte for dye-sensitized, quantum dots, and perovskite solar cells

**Sawanta S. Mali[1], Jyoti V. Patil[1,2], Hyungjin Kim[1], Pramod S. Patil[2] and Chang Kook Hong[1]**

[1]Polymer Energy Materials Laboratory, School of Applied Chemical Engineering, Chonnam National University, Gwangju, South Korea
[2]Thin Film Materials Laboratory, Department of Physics, Shivaji University, Kolhapur, India

## Contents



## 14.1 Introduction

Low-cost renewable energy source is the best choice toward an environmentally friendly technique. The photoelectrochemical solar cell is one of the low-cost, eco-friendly techniques to convert solar energy into electricity. After some preliminary exploration, O'Regan et al. demonstrated a new type of solar cell, known as dye-sensitized solar cells (DSSCs) [1].

*Nanomaterials for Solar Cell Applications*
DOI: https://doi.org/10.1016/B978-0-12-813337-8.00014-X

Because of the low cost, easy preparation, good performance, and environmental benign compared with conventional photovoltaic techniques, such as silicon (Si), copper indium gallium selenide, and cadmium telluride (CdTe) solar cells [2,3], the DSSCs have aroused intense interest. Furthermore, instead of using a dye absorber, if we replace it with semiconductor quantum dots (QDs), then these devices are called QD-sensitized solar cells (QDSSC). This device possesses some distinct advantages, such as ease in fabrication, size-dependence properties of QDs with tunable band gaps, high extinction coefficients, and potential of high power conversion efficiency (PCE). This is due to the generation of multiple excitons by the impact-ionization effect in QDs [4–9]. Therefore QDSSC is another type of low-cost photovoltaics. On the other hand, if we replace QDs with organic–inorganic metal halides (ABX) perovskite absorber with solid-state electrolyte, then perovskite solar cells (PSCs) term arouses [10–12]. Nowadays, the PSCs attract as much attention due to their boomed efficiency within a very short of period [13–17]. The abovementioned three types of low-cost photovoltaics, the redox couples either electrolyte or hole-transporting materials (HTMs) play a key role in order to achieve best PCE. Therefore this third-generation technology has been regarded as one of the most prospective solar cell types in PV technologies. This chapter focuses the importance of electrolytes in abovementioned low-cost photovoltaics with different absorber layers.

### 14.1.1 Importance of an electrolyte

The electrolyte is one of the most crucial components in low-cost photovoltaics because it is responsible for the inner charge carrier transport between electrodes and continuously regenerates the absorber and itself during cell operation. The electrolyte has great influence on the light-to-electric conversion efficiency and long-term stability of the devices. The solar cell parameters, such as open circuit voltage ($V_{oc}$), short-circuit current density ($J_{sc}$), and fill factor (FF), are mostly dependent on electrolyte, electrode–electrolyte interfaces [18]. It is well known that the $J_{sc}$ of the device is strongly affected by the transport of the redox couple components in the electrolyte, while FF can be affected by the diffusion of charge carrier in electrolyte and the charge transfer resistance on the electrolyte/electrode interface. The device voltage is significantly affected by the redox potential of the electrolyte. Therefore for high-performance solar cells, many aspects such as morphology of the

electrode, type of electrolyte, and additives doping have been studied in order to improve the performance and stability. Fig. 14.1 demonstrated the different type of low-cost solar cells that require different electrolytes. In case of DSSCs, iodine redox couples ($I^-/I_3^-$), while in QDSSCs, sulfide/polysulfide ($S^{2-}/S_n^{2-}$) electrolytes have been used so far [19]. In case of PSCs, usually additives doped 2,2',7,7'-Tetrakis[N,N-di(4-methoxyphenyl)amino]-9,9'-spirobifluorene (spiro-MeOTAD) and poly[bis(4-phenyl)(2,4,6-trimethylphenyl)amine] (PTAA)-based HTM have been used. These electrolyte materials provide a pure ionic conductivity between the positive and the negative electrodes in an electrochemical device. The key role of electrolyte is to serve as the charge transport medium in the form of ions between two electrodes. Following properties are necessary in order to prepare ideal electrolytes for low-cost photovoltaics [20]:

1. The electrolytes must be able to transport the charge carriers between photoanode and counter electrode.
2. The electrolytes must guarantee fast diffusion of charge carriers (higher conductivity) and produce good interfacial contact with the electrode and the counter electrode.
3. The electrolytes must have long-term stabilities, including chemical, thermal, optical, electrochemical, and interfacial, and protect the sensitizer from degradation and desorption.

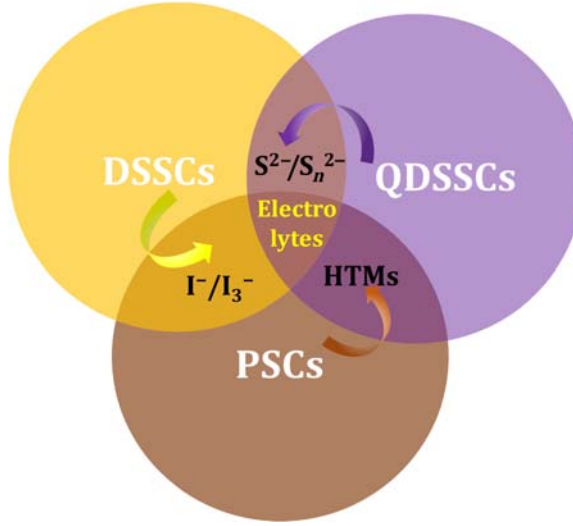


**Figure 14.1** Different types of low-cost photovoltaics and their electrolytes.

4. The electrolytes should not exhibit a significant absorption in the range of visible light.

The electrolytes can be classified into three different types according to their physical states, such as liquid electrolytes, quasi-solid electrolytes, and solid-state conductors (herein HTM). In addition, there are various subcategories of electrolytes depending on their solvents, such as ionic liquid (IL), organic—inorganic nature, and polymer electrolyte.

### 14.1.2 Role of dyes on dye-sensitized solar cells

In DSSCs, dye or sensitizers play a key role in order to absorb solar radiation. The ideal dye should fulfill the following criteria in order to produce higher efficiency. The energy levels between $TiO_2$ and electrolyte should be matched, it should not be agglomerate and dye should have excellent light, thermal, and electrochemical stability. Besides, a sensitizer should have carboxyl and hydroxyl group that is required for good binding with the semiconductor, shows maximum absorbance from visible to near infrared region of solar radiations, and not degrade fast. There are three types of dye sensitizers, such as metal complex sensitizers, metal-free organic (indoline) dye, and nature dyes. However, so far metal complex—based dyes demonstrated record efficiency.

## 14.2 Electrolytes for dye-sensitized solar cells

Schematic illustration of the structure of DSSC is shown in Fig. 14.2. Generally, DSSCs consist of three parts: the dye-sensitized wide band metal oxide (mostly, $TiO_2$) or other nanocrystalline porous film photoanode on a transparent conducting oxide (TCO) glass substrate, an electrolyte solution penetrating throughout the $TiO_2$ film, and the platinized TCO as a counter electrode. In the operation, the sunlight is absorbed by the dye molecules that excite electrons from highest occupied molecular orbital to lowest unoccupied molecular orbital, and the excited-state electrons are quickly injected into the conduction band (CB) of the $TiO_2$. These electrons percolate through the $TiO_2$ film and are collected by the conducting substrate. The original state of the dye is subsequently restored by electron donation from the electrolyte, usually an organic solvent containing redox system, such as the iodide/triiodide redox couple. The regeneration of the sensitizer by iodide intercepts the recapture of the CB electron by the oxidized dye. The iodide is regenerated, in turn, by the reduction of triiodide at the counter electrode, the circuit being

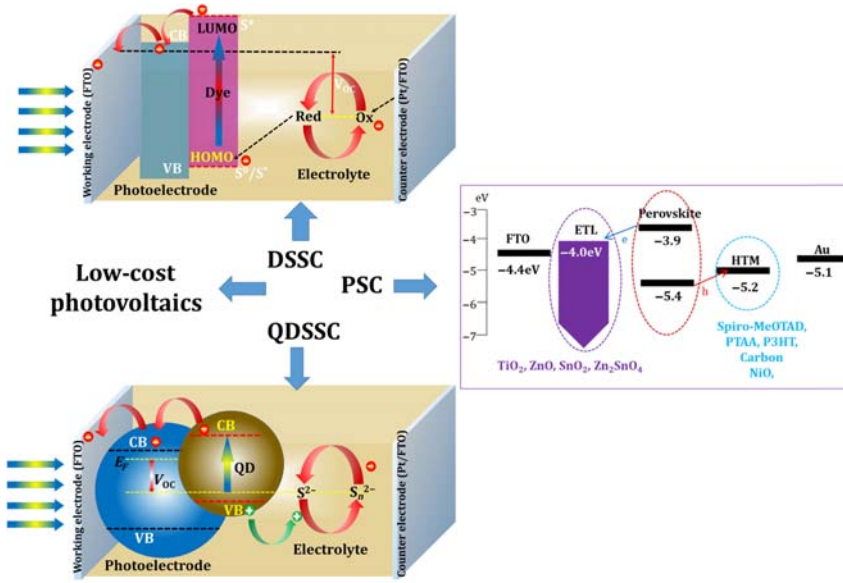


**Figure 14.2** Different types of low-cost photovoltaics and their energy level diagrams.

completed via electron migration through the external load. The voltage generated under illumination corresponds to the difference between the Fermi level of the electron in the solid and the redox potential of the electrolyte [21]. This process is very similar to the photosynthetic process in plants where chlorophyll absorbs photons but does not participate in charge transfer, the photoreceptor and charge carrier are implemented by different components in DSSCs.

### 14.2.1 Electron transfer processes in dye-sensitized solar cells

DSSCs are PEC devices where several electron transfer (ET) processes are in parallel and in competition. Since the highest energy conversion efficiencies have been reported for a nanocrystalline $TiO_2$ film sensitized with ruthenium polypyridyl complexes and permeated with $I^-/I^{3-}$ as the electrolyte, the following discussion will primarily focus on DSSCs with this configuration. Fig. 14.3 shows the typical time constants of processes involved in such a DSSC device. Upon illumination, the sensitizer is photoexcited in a few femtoseconds (Eq. 14.1) and electron injection is ultrafast from $S^*$ to $TiO_2$ (Eq. 14.2) on the subpicosecond timescale, where they are rapidly ($<10$ fs) thermalized by lattice collisions and

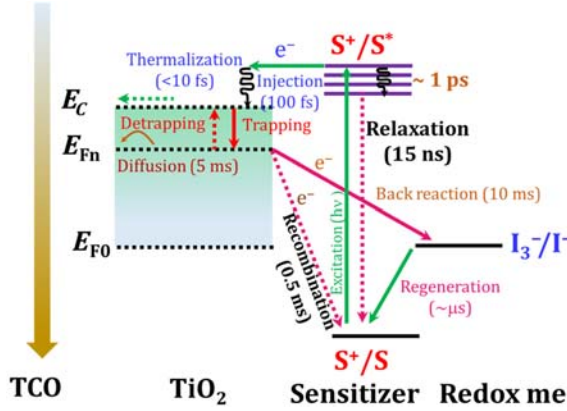


**Figure 14.3** Dynamics of different electron transfer processes for forward reactions and dark/back reaction in the conversion of light-to-electric power by DSSCs with iodine/triiodide electrolyte under working conditions. The numbers in parentheses are representative values for each process. *DSSC*, Dye-sensitized solar cell.

phonon emissions. The nanosecond-ranged relaxation of S* (Eq. 14.3) is rather slow compared to injection, ensuring the injection efficiency to be unity. The ground state of the sensitizer is then recuperated by $I^-$ in the microsecond domain (Eq. 14.4), effectively annihilating $S^+$ and intercepting the recombination of electron in $TiO_2$ with $S^+$ (Eq. 14.5) that happens in the millisecond time range. This is followed by the two most important processes—electron percolation across the nanocrystalline film and the redox capture of the electron by the oxidized relay (back reaction, Eq. 14.6), $I^{3-}$, within milliseconds or even seconds. The similarity in time constants of both processes induces a practical issue on achieving high conversion efficiencies in DSSC. In a simple model, an electron collecting efficiency at short-circuit can be defined as $\Phi_{col} = k_{trans}/(k_{trans} + k_{rec})$, where $k_{trans}$ and $k_{rec}$ are the first-order rate constants for the electron transportation and the back reaction, respectively, indicating that a fast electron transportation in $TiO_2$ and a slower back reaction are preferable.

Photoexcitation

$$S|TiO_2 + h\nu \rightarrow S*|TiO_2 \tag{14.1}$$

Charge injection

$$S* \left|TiO_2 \rightarrow S^+\right|TiO_2 + e_{cb}^-(TiO_2) \tag{14.2}$$

Relaxation

$$S* | TiO_2 \rightarrow S | TiO_2 \tag{14.3}$$

Regeneration

$$S^+ | TiO_2 + 2\Gamma \rightarrow S | TiO_2 + I_2^{-*} \tag{14.4}$$

Recombination

$$S^+ \left| TiO_2 + e^-(TiO_2) \rightarrow S \right| TiO_2 \tag{14.5}$$

Back reaction

$$e^-(TiO_2) + I_2 \rightarrow I_2^{-*} \tag{14.6}$$

These DSSC processes are required reactions for completing the light-to-electric conversion. In case of recombination and back/dark reactions, which result in charge carrier recombination that hampers the efficiency. However, these dark reactions do not have a significant negative effect owing to their slower reaction speed compared with that of the required processes.

As per as electrolyte concern, usually it contains an organic solvent containing a redox mediator, such as iodide/triiodide ($I^-/I_3^-$) redox couple for the recovery of dye and the regeneration of electrolyte itself during operation. The DSSCs' electrolytes are mainly classified in three different categories:

1. liquid electrolytes;
2. quasi-solid-state electrolytes; and
3. solid-state transport materials (ionic or hole transport materials).

### 14.2.2 Liquid electrolyte

There are various chemical compounds that have been studied rigorously and it has been concluded that the polar organic solvents and ILs are most suitable for ideal electrolytes. Table 14.1 represents the physical parameters of most popular frequently used organic solvents for the electrolytes in DSSCs. Table 14.2 shows details of DSSC electrolytes with various compositions and their respective efficiency. In the case of $I^-/I_3^-$ electrolyte, the hole transportation through electrolyte takes place in the following order. Initially, the dye regeneration can be represented as

**Table 14.1** Frequently used organic solvents for electrolytes and their physical parameters.

| Name of the solvent | Melting point (°C) | Boiling point (°C) | Viscosity (cP) | Dielectric constant | Donor number |
|---|---|---|---|---|---|
| Water | 0 | 100 | 0.89 | 78 | 18 |
| Ethanol | −114 | 78 | 1.08 | 25 | 29 |
| Dimethyl carbonate | 4.6 | 91 | 59 at 20°C | 3.107 | – |
| Diethyl carbonate | −74.3 | 126 | 0.75 | 2.805 | – |
| Acetonitrile | −44 | 82 | 0.33 at 30°C | 36 | 14.1 |
| Propionitrile | −93 | 118 | 0.39 at 30°C | 27 at 20°C | 16.1 |
| Butyronitrile | −112 | 139 | 0.78 at 19°C | 21 | – |
| Valeronitrile | −96 | 287 | 5.3 | 37 | – |
| 3-Methoxy-propionitrile | −29 | 164 | 2.5 | 36 | 16.1 |
| Ethylene carbonate | −63 | 238 | 90 | 90 | 16.4 |
| Propylene carbonate | −36 | 241 | 2.5 | 64 | 15.1 |
| γ-Butyrolactone | −44 | 204 | 1.7 | 42 | 18 |
| *N*-methyl-oxazolidinone | 15 | 270 | 2.5 | 78 | – |
| *N*-methylpyrrolidone | −24 | 203 | 1.65 | 32.2 | 27.3 |

**Table 14.2** Literature survey on various electrolytes for dye-sensitized solar cells.

| Photoanode | Sensitizer | Electrolyte (composition) | $J_{sc}$ (mA cm$^{-2}$) | $V_{oc}$ (V) | FF | PCE (%) | Reference |
|---|---|---|---|---|---|---|---|
| $TiO_2$ | N719 | $I^-/I_3^-$; 0.5 M tetrapropylammonium iodide, 0.02 M KI, 0.04 M $I_2$ | 10 | 0.685 | 0.76 | 7.9 | [1] |
| $TiO_2$ | Oligothiophene | $I^-/I_3^-$; 1 M DMII, 30 mM $I_2$, 50 mM LiI, 0.5 M TBP, 0.1 GNCS in ACN, VN | 15.35 | 0.722 | 0.728 | 8.06 | [22] |
| $TiO_2$ | C217 | $I^-/I_3^-$; solvent-free DMII/1-ethyl-3-methylimidazolium iodide/1-ethyl-3-methylimidazolium tetracyanoborate/$I_2$/*N*-butylbenzimidazole/GNCS (molar ratio:12/12/16/1.67/3.33/0.67) | 16.1 | 0.803 | 0.759 | 9.8 | [23] |
| $TiO_2$ | C219 | $I^-/I_3^-$; EL01: 1.0 M DMII, 50 mM LiI, 30 mM $I_2$, 0.5 M TBP, and 0.1 M GNCS in ACN/VN (85/15) EL02:DMII/EMII/EMITCB/$I_2$/TBP/GNCS (molar ratio: 12/12/16/1.67/3.33/0.67), where the iodide and triiodide concentrations are 3.18 and 0.24 M, respectively | 17.94 | 0.770 | 0.730 | 10.1 | [24] |
| ZnO | N3 | $I^-/I_3^-$; 0.5 M tetrabutylammoniumiodide, 0.1 M LiI, 0.1 M $I_2$, 0.5 M TBP in ACN | 18.7 | 0.635 | 0.451 | 5.4 | [25] |

(*Continued*)

**Table 14.2** (Continued)

| Photoanode | Sensitizer | Electrolyte (composition) | $J_{sc}$ (mA cm$^{-2}$) | $V_{oc}$ (V) | FF | PCE (%) | Reference |
|---|---|---|---|---|---|---|---|
| $YF_3$:$Eu^{3+}$(5 wt.%) $TiO_2$ | N719 | $I^-/I_3^-$; 0.6 M tetrabutylammoniumiodide, 0.1 M LiI, 0.1 M $I_2$, 0.5 M TBP in ACN | 14.894 | 0.787 | 0.661 | 7.741 | [26] |
| $Zn_2SnO_4$ | SJ-ET1 | $I^-/I_3^-$; 0.7 M PMII, 0.03 M $I_2$, 0.1 M GSCN, and 0.5 M TBP in ACN/VN (85/15 v/v) | 12.2 | 0.71 | 0.72 | 6.3 | [27] |
| $TiO_2$ | DN350 | $I^-/I_3^-$; 0.1 M LiI, 0.6 M butylmethylimidazolium iodide, 0.05 M $I_2$, 0.05 M TBP | 14.70 | 0.650 | 0.62 | 5.92 | [28] |
| $TiO_2$ | N719 | $I^-/I_3^-$; 0.7 M PMII, 0.03 M $I_2$, 0.1 M GSCN, and 0.5 M TBP in ACN/VN (85/15 v/v) | 8.42 | 0.574 | 0.65 | 3.90 | [21] |
| $TiO_2$ | N719 | $I^-/I_3^-$; 0.7 M PMII, 0.03 M $I_2$, 0.1 M GSCN, and 0.5 M TBP in ACN/VN (85/15 v/v) | 17.17 | 0.6125 | 0.647 | 7.16 | [29] |
| $TiO_2$ | C239 | $Co^{2+}/Co^{3+}$; 0.25 M $Co(bpy)_3(TFSI)_2$, 0.05 M $Co(bpy)_3(TFSI)_3$, 0.1 M LiTFSI, 0.5 M TBP in ACN | 6.91 | 1.05 | 0.76 | 5.5 | [30] |
| $TiO_2$ | C240 | | 12.17 | 0.99 | 0.75 | 9.0 | [30] |
| $TiO_2$ | C218 | | 13.01 | 0.950 | 0.76 | 9.4 | [30] |
| $TiO_2$ | C241 | | 12.92 | 0.860 | 0.72 | 8.0 | [30] |
| $TiO_2$ | C241 | $Co^{2+}/Co^{3+}$; 0.25 M $Co(bpy)_3(TFSI)_2$, 0.05 M $Co(bpy)_3(TFSI)_3$, 0.1 M LiTFSI, 0.5 M TBP in ACN | 13.53 | 0.960 | 0.72 | 9.3 | [31] |

| | | | | | | | |
|---|---|---|---|---|---|---|---|
| $TiO_2$ | C252 | $Co^{2+}/Co^{3+}$; 0.25 M $Co(bpy)_3(TFSI)_2$, | 15.41 | 0.861 | 0.714 | 9.5 | [32] |
| $TiO_2$ | C253 | 0.05 M $Co(bpy)_3(TFSI)_3$, 0.1 M LiTFSI, 0.5 M TBP in ACN | 12.25 | 0.745 | 0.734 | 6.7 | [32] |
| $TiO_2$ | Y123 | $Co^{2+}/Co^{3+}$; 0.25 M $Co(bpy)_3(TFSI)_2$, | 13.06 | 0.998 | 0.774 | 10.08 | [33] |
| $TiO_2$ | SM371 | 0.06 M $Co(bpy)_3(TFSI)_3$, 0.1 M | 15.9 | 0.960 | 0.79 | 12.0 | [34] |
| $TiO_2$ | SM315 | LiTFSI, 0.5 M TBP in ACN | 18.1 | 0.91 | 0.78 | 13.0 | [34] |
| $TiO_2$ | FNE45 | $I^-/I_3^-$; 0.6 M DMPI0mI, 0.1 M LiI, 0.05 M $I_2$, 0.5 M TBP | 14.60 | 0.676 | 0.75 | 7.40 | [35] |
| $TiO_2$ | FNE46 | $I^-/I_3^-$; 0.6 M DMPI0mI, 0.1 M LiI, 0.05 M $I_2$, 0.5 M TBP | 16.16 | 0.682 | 0.75 | 8.27 | [35] |
| $TiO_2$ | FNE46 (ssDSSCs) | $I^-/I_3^-$ in PVDF-HFP 5 wt.%; 0.1 M LiI, 0.1 M $I_2$, 0.6 M DMPImI, 0.5 M TBP, MPN | 15.68 | 0.632 | 0.720 | 7.14 | [35] |
| $TiO_2$ | FNE60 (ssDSSCs) | $I^-/I_3^-$ in PVDF-HFP; 0.1 M LiI, 0.1 M $I_2$, 0.6 M DMPIiM, TBP, MPN | 13.97 | 0.656 | 0.67 | 6.1 | [36] |
| $TiO_2$ | FNE61 (ssDSSCs) | $I^-/I_3^-$ in PVDF-HFP; 0.1 M LiI, 0.1 M $I_2$, 0.6 M DMPIiM, TBP, MPN | 9.23 | 0.620 | 0.68 | 3.9 | [36] |
| $TiO_2$ | FNE62 (ssDSSCs) | $I^-/I_3^-$ in PVDF-HFP; 0.1 M LiI, 0.1 M $I_2$, 0.6 M DMPIiM, TBP, MPN | 17.59 | 0.682 | 0.68 | 8.2 | [36] |
| $TiO_2$ | FNE63 (ssDSSCs) | $I^-/I_3^-$ in PVDF-HFP; 0.1 M LiI, 0.1 M $I_2$, 0.6 M DMPIiM, TBP, MPN | 10.81 | 0.641 | 0.70 | 4.9 | [36] |
| $TiO_2$ | Z907Na | 0.2 M $I_2$, 0.5 M NMBI in PMImI/EMImTCM (vol. ratio 1/1) | 12.8 | 0.752 | 0.764 | 7.4 | [37] |

(*Continued*)

**Table 14.2** (Continued)

| Photoanode | Sensitizer | Electrolyte (composition) | $J_{sc}$ (mA cm$^{-2}$) | $V_{oc}$ (V) | FF | PCE (%) | Reference |
|---|---|---|---|---|---|---|---|
| $TiO_2$ | Z907 | 0.2 M $I_2$, 0.14 M GuanSCN, 0.5 M TBP in PMImI/EMImSCN (vol. ratio 13/7) | 13.3 | 0.746 | 0.72 | 7.0 | [38] |
| $TiO_2$ | K19 | 0.8 M PMImI, 0.15 M $I_2$, 0.1 M GuanSCN, 0.5 M NMBI in MPN | 15.1 | 0.747 | 0.699 | 8.0 | [39] |
| $TiO_2$ | K60 | 0.2 M $I_2$, 0.5 M NMBI, 0.1 M GuanSCN in REImI/REImTFSI (vol. ratio 13/7) | 13.54 | 0.700 | 0.717 | 6.8 | [40] |
| $TiO_2$ | D149 | 0.2 M $I_2$ in PMImI/EMImTFSI/ EMImTf (vol. ratio 2/2/1) | 16.13 | 0.612 | 0.676 | 6.67 | [41] |
| $TiO_2$ | D205 | 1 M PMII, 0.1 M 4-OH-TEMPO, 0.01 M $NOBF_4$, 0.2 M LiTFSI, 0.5 M NBB in MPN | 17.4 | 0.710 | 0.580 | 7.2 | [42] |
| $TiO_2$ | C106 | 1 M DMII, 0.15 M $I_2$, 0.5 M NBB, 0.1 M GuNCS, 50 mM NaI in BN | 17.9 | 0.733 | 0.760 | 10.0 | [43] |

*DSSC*, Dye-sensitized solar cell; *GNCS*, guanidine thiocyanate; *NMBI*, *N*-methylbenzimidazole; *PCE*, power conversion efficiency; *PVDF-HFP*, poly(vinylidenefluoride-co-hexafluoropropylene); *TBP*, 4-tert-butylpyridine; VN, valeronitrile.

$$D^+ + I^- \xrightarrow{\text{Dyeregenration}} D + I_3^- \tag{14.7}$$

This process contains a series of successive reactions on the $TiO_2$ interface

$$D^+ + I^- \rightarrow [D\cdots I] \xrightarrow{I_2^-} D + I_2^{-\bullet} \xrightarrow{I_2^{-\bullet}} D + I_3^- + I^- \tag{14.8}$$

$$D + I_2^{-\bullet} \rightarrow [I_2\cdots D] \xrightarrow{I^-} D + I_3^- \tag{14.9}$$

The regenerative cycle of electrolytes is completed by the conversion of $I_3^-$ to $I^-$ ions on the counter electrode. The counter electrode must have catalytic activity to ensure rapid reaction and low overpotential and, in this sense, Pt is a suitable counter electrode material. However, many other counter electrodes, including $Cu_2ZnSnS_4$ (CZTS), have been used as a counter electrode for DSSCs [21]. Accordingly, many researchers developed a variety of dyes, mesoporous metal oxides, counter electrolytes, and electrolytes, and developed efficient DSSCs with $\geq$13% efficiency. Table 14.1 shows the milestones in DSSCs and their electrolyte compositions.

After the investigation of Gratzel cell, it has become a popular low-cost solar cell over the last three decades. A number of approaches have been reported to fabricate different nanostructure of $TiO_2$, such as single crystal, nanorod; wire; tube arrays, nanospheres that include template-assisted method, electrochemical anodic oxidation method, spray pyrolysis technique, chemical vapor deposition, hydrothermal and solvothermal method, anodized aluminum oxide (AAO) template-assisted sol–gel method, AAO template-assisted electrodeposition method, electrochemical anodic oxidation of pure titanium sheet, eggshell membrane template, electrospinning, and chemical treatment of fine $TiO_2$ particles.

The DSSC was theoretically studied by Smestad in 1994 and he concluded that at least 10% conversion efficiency with voltages of over 1 V are possible with Ru trinuclear complexes at AM 1.5 [44]. The Gratzel cell was verified by Hagfeldt et al. in 1994 [45] and they have showed 7% efficient using Gratzel procedure under 1000 W $m^{-2}$ light from an ELH lamp. They concluded that the practical problems in the preparation procedure of the DSSC modules have so far made long term stability tests impossible.

Long-term stability testing of DSSCs was studied by Sommeling et al. [46] in 2004. They have prepared mesoporous $TiO_2$ using hydrothermal technique. In short, titanium isopropoxide is hydrolyzed in water. After peptization at 80°C, a colloidal $TiO_2$ solution is obtained, containing

$TiO_2$ particles with a size in the range of a few nanometers. The $TiO_2$ colloid is transferred from the aqueous solution into a terpineol/ethylcellulose mixture to obtain a screen printable paste using a pearl mill. They claimed that constant heating in the dark at 85°C leads to a severe decrease in performance that is somehow reversible, that is, the efficiency of degraded cells can be restored by continuous illumination of ~1 Sun at moderate temperatures. No major changes in short-circuit currents occur during the period of testing (~1200 hours), although the decrease in $V_{oc}$ for these cells during this test is ~10%, resulting in an overall decrease in efficiency of 12%–15%.

Fuke et al. [47] investigated the $TiCl_4$ treatment to $TiO_2$ photoanode and its effect on open circuit voltage. The sintered nanocrystalline $TiO_2$ films were treated with an aqueous solution of 50 mM $TiCl_4$ and stored in an oven at 70°C for 20 minutes. Raman spectroscopy revealed that the dye penetrates all the way though the nanocrytalline $TiO_2$ film and the amount of dye absorption was unchanged in spite of a decreased pore size in the $TiO_2$ film due to the $TiCl_4$ treatment. The $TiCl_4$-treated device facilitates decrease in the impedance related to electron transport between $TiO_2$ particles and an increase in electron lifetime within the nanocrystalline $TiO_2$ film. This indicates that the main factor responsible for the enhancement of the short-circuit current is the improvement of electron transport and electron lifetime in the nanocrystalline $TiO_2$ film. An overall energy conversion efficiency of 8.9% was achieved for the $TiCl_4$-treated electrodes.

Mali et al. synthesized anatase $TiO_2$ nanofibers with various diameters by electrospinning technique [48]. The electrospinning feeding rate has been varied from 1.0, 1.5, 2.0, and 2.5 mL $h^{-1}$ in order to control the diameter of $TiO_2$ nanofibers. Fig. 14.4A–D shows the SEM micrographs of the $TiO_2$ nanofibers deposited at 1.0, 1.5, 2.0, and 2.5 mL $h^{-1}$. The right side images show respective highly magnified field emission scanning electron microscopic (FESEM) micrographs of single nanofibers. The $TiO_2$ nanofibers having smooth uniform surface with 296 nm diameter deposited at 1.0 mL $h^{-1}$ feeding rate. Fig. 14.4B shows FESEM image of $TiO_2$ nanofiber deposited at 1.5 mL $h^{-1}$ feed rate. These nanofibers exhibit straight and smooth nanofiber having 421 nm diameters. Further increased feed rate from 2.0 to 2.5 mL $h^{-1}$ led to the observation that the diameter of the nanofibers changes from 435 to 639 nm, respectively, as shown in Fig. 14.4C and D. These results are ascribed to the higher feeding rate results in larger diameter of the $TiO_2$ nanofibers. The 1.0 mL $h^{-1}$

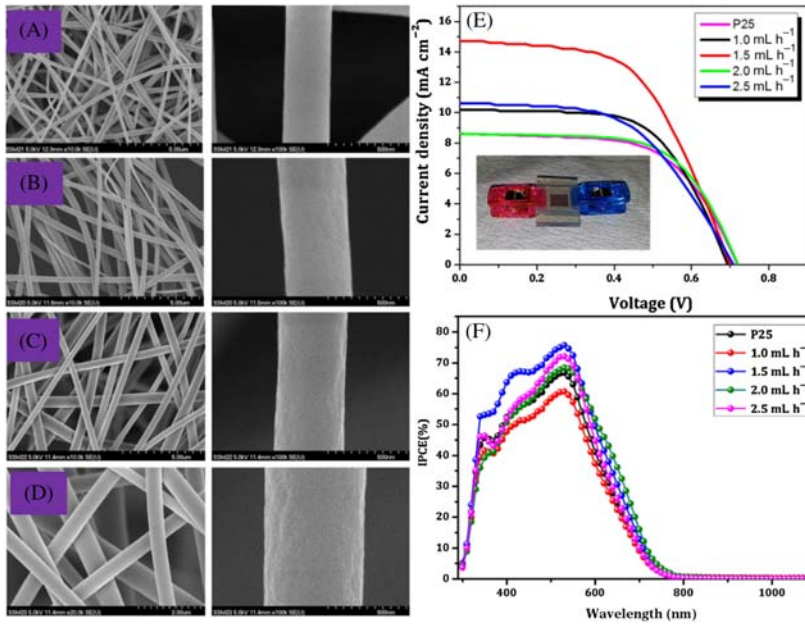


**Figure 14.4** ***$TiO_2$ nanofiber–based DSSCs*** (A) FESEM images of synthesized anatase $TiO_2$ nanofibers deposited by different feed rate: (A) 1.0 mL h$^{-1}$, (B) 1.5 mL h$^{-1}$, (C) 2.0 mL h$^{-1}$, and (D) 2.5 mL h$^{-1}$. Right side images show respective higher magnified images of single nanofiber. (E) *J–V* curves of the DSSCs assembled from $TiO_2$ nanofibers under simulated AM 1.5 solar light (100 mW cm$^{-2}$). Inset shows photograph of fabricated DSSC devices. (F) IPCE spectra of DSSCs based on $TiO_2$ nanofiber photoanode deposited at different feed rate. *DSSC*, Dye-sensitized solar cell; *FESEM*, field emission scanning electron microscopic; *IPCE*, incident-photon-to-current conversion efficiency. *Reproduced from Elsevier (2015). S.S. Mali, C.S. Shim, H.J. Kim, J.V. Patil, D.H. Ahn, P.S. Patil, et al., Electrochim. Acta 166 (2015) 356–366.*

synthesized $TiO_2$ nanofiber–based DSSC produces $\eta = 4.09\%$ ($J_{sc} = 8.62$ mA cm$^{-2}$, $V_{oc} = 0.719$ V, FF = 0.63). The 1.5 mL h$^{-1}$ sample shows $\eta$ of 5.39% ($J_{sc} = 13.32$ mA cm$^{-2}$, $V_{oc} = 0.698$ V, FF = 0.55). In the case of $TiO_2$, nanofiber deposited at 2.0 mL h$^{-1}$shows $J_{sc} = 10.59$ mA cm$^{-2}$, $V_{oc} = 0.706$ V, and FF = 0.54. The conversion efficiency of this sample comes to be 4.23%, while the nanofibers spun at 2.5 mL h$^{-1}$ show 4.55% PCE ($J_{sc} = 10.21$ mA cm$^{-2}$, $V_{oc} = 0.694$ V, FF = 0.61). From above the discussion, it is clear that the sample deposited at 1.5 mL h$^{-1}$ feed rate shows the highest conversion efficiency of 5.39% that is much higher than that of other feeding rates. These results are also confirmed by incident photon-to-current conversion efficiency analysis.

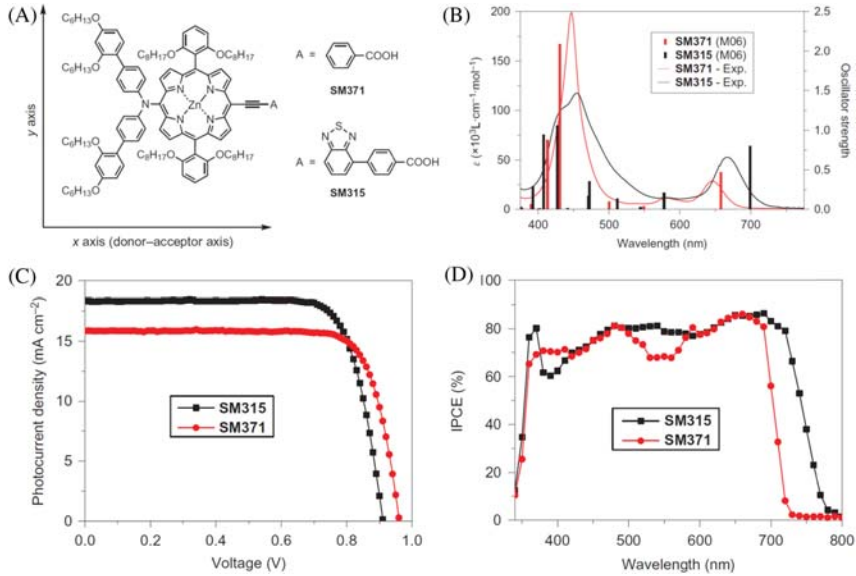


**Figure 14.5** (A) The structures are coded SM371 and SM315. They both feature a porphyrin core and a bulky bis(2′,4′-bis(hexyloxy)-[1,1′-biphenyl]-4-yl)amine donor. Their acceptor groups differ, with SM315 featuring a benzothiadiazole group. (B) The experimental spectra (in tetrahydrofuran (THF)) are shown as continuous lines and the theoretical electronic transitions are shown as bars for both SM371 and SM315. Theoretical data were computed using LR-TDDFT/M06/IEFPCM(THF).(C) Photovoltaic performance of devices made with SM371 and SM315. (A) *J*–*V* curve under AM 1.5 G illumination (1000 W $m^{-2}$) and (D) photocurrent action spectrum for SM371 and SM315. *(Reproduced from Nature Publishing Group (2014). D.R. MacFarlane, M. Forsyth, Adv. Mater. 13 (95) (2001) 7.*

In 2014 the highest 13% efficiency was achieved for a DSSC device via the molecular engineered porphyrin sensitizers, coated SM315, which have properties of a donor-π-bridge-acceptor, high light-harvesting properties with better electrolyte compatibility [34]; here 7 μm mesoporous $TiO_2$ film as a photoanode, and an electrolyte having $[Co(bpy)_3]^{2+/3+}$ redox couple employed in device fabrication (Fig. 14.5).

## 14.2.3 Quasi-solid-state electrolytes

In order to solve the problem of liquid electrolytes, researchers selected another type, known as quasi-solid-state electrolytes. This quasi-solid-state electrolyte provides better stability and sealing ability with high ionic conductivity and smooth interfaces. However, still the quasi-solid-state type DSSCs (QS-DSSC) lag behind in efficiency as compared to liquid-type

electrolytes. The term "quasi" means it is neither solid nor liquid substance that can have ability of ionic charge transportation. This state is intermediate between liquid and solid material containing a macromolecular or supramolecular nanoaggregates. The prepared semisolid substance has both cohesive and diffusive properties. Therefore these types of electrolytes provide better stability than liquid electrolytes. The quasi-solid-state electrolytes are prepared in three different ways: (1) thermoplastic materials, (2) implementation of inorganic gelators with composite electrolytes, and (3) IL-based electrolytes solidified with the help of inorganic gelators or organic polymers additives. Based on their preparation method and composition of the electrolytes, the quasi-solid-state electrolytes are further classified into four subcategories.

1. thermoplastic polymer–based electrolytes;
2. thermosetting polymer–based electrolytes;
3. inorganic materials–polymer composite–based electrolytes; and
4. IL-based electrolytes.

Usually some ILs are plastic solids at room temperature yet still maintain reasonable conductivity [49], and are called thermoplastic polymers. While others can be transformed into soft, elastomeric solids at room temperature by the addition of small amounts (~5%) of a suitable polymer, called as thermosetting polymers [50].

#### 14.2.3.1 Thermoplastic polymer–based electrolytes

Cao et al. used this thermoplastic polymer–based electrolyte for quasi-solid-state DSSCs for the first time [51]. In this type of quasi-solid-state electrolytes, polymer matrix is mixed with liquid electrolyte to form a viscous gel or sol. Furthermore, the viscosity of the sol could be optimized using solvent. It is also called a plastizer. This sol or gel type of electrolyte showed temperature-dependent physical properties; therefore this is called a thermoplastic polymer–based electrolyte. Usually, including poly(ethyleneoxide) (PEO), poly(acrylonitrile) (PAN), poly(vinylpyrrolidinone) (PVP), polystyrene, poly(vinyl chloride), poly(vinylidene ester), poly (vinylidene fluoride) (PVDF), and poly(methyl methacrylate) (PMMA), is used as polymer matrix, which plays a gelator role.

After the first successful report, Wu et al. [52] used the unique composition of thermoplastic electrolyte containing polymer host/solvent/ionic conductor with polyblend electrolyte [PVP/polyethylene glycol (PEG) + KI + $I_2$] results in $V_{oc}$ of 0.698 V, $J_{sc}$ of 9.77 mA $cm^{-2}$, FF of 0.59 and PCE of 4.01%. Yang et al. used PMMA polymer gel electrolyte with

odium iodide and iodine as source of $I^-/I_3^-$. The optimized device showed 4.78% PCE with $V_{oc}$ of 0.778 V, $J_{sc}$ of 10.07 mA $cm^{-2}$ and FF of 0.61 [53]. Shi et al. used a high molecular weight PEO ($MW = 2 \times 10^6$ g $mol^{-1}$) as a polymer host to gelate liquid electrolyte and form a polymer gel electrolyte; the QS-DSSC with the polymer electrolyte (PEO 10 wt.%) that showed a conversion efficiency of 6.12% and 10.11% under 100 and 30 mW $cm^{-2}$ illumination, respectively [54]. PAN helps to make homogeneous hybrid electrolyte and matrix for structural stability of salts and plastics-based electrolytes. The PAN-based DSSC exhibits 7.23% PCE [55,56].

#### *14.2.3.2 Thermosetting polymer–based electrolytes*

The organic molecule chemical or covalent cross-linking molecules converted into three-dimensional polymer network in the presence of liquid electrolyte and become an irreversible solid. Therefore these types of electrolytes are called thermosetting polymer–based electrolytes. Due to their unique thermal and chemical stability, these types of polymer electrolytes exhibit a long-term photovoltaic stability with high performance [57,58]. The thermosetting polymer electrolytes can be prepared by three different methods:

1. light-induced in situ polymerization method [59];
2. heat-induced in situ polymerization method [60]; and
3. liquid electrolyte adsorption method [61].

Komiya et al. [62] used poly(ethylene oxide-*co*-propylene oxide) trimethacrylate (oligomer) with three polymerizable reactive groups as a gel electrolyte precursor and injected it into the assembled cells. The three-dimensional polymer network was formed in the device by employing heat treatment at 90°C for 90 minutes. Interestingly, these QS-DSSCs with this thermosetting polymer–based electrolytes (TSPE) showed larger open circuit voltage, with 8.1% PCE, than conventional liquid electrolytes based DSSCs. Furthermore, Wang et al. prepared a necklace-like polymer gel electrolyte containing latent and chemically cross-linked gel electrolyte precursors and demonstrated 7.72% PCE [63].

In the case of in situ surface-induced polymerization method, Park et al. [64] used the nanocrystalline $TiO_2$ surface-induced cross-linking polymerization and demonstrated that it resulted in the formation of the encapsulation of the $TiO_2$ particles. The fabricated devices exhibit ~8.1% PCE with an excellent stability during heating at 65°C more than 30 days [65]. These performance characteristics were superior to those obtained

from a conventional DSSC (7.5%→3.5%) prepared in a similar condition. Furthermore, the surface-induced cross-linking polymerization of methyl methacrylate and 1,6-hexanediol diacrylate on the surfaces of nanocrystalline $TiO_2$ particles in order to prepare nanoporous network polymer with 10.6% efficiency which is 20% higher was more stable than conventional DSSCs [66].

Recently, Dong at al. synthesized the structurally interconnected block copolymer by the oligomerization of poly(oxyethylene)-segmented diamine and 4,40-oxydiphthalic anhydride, followed by a late-stage curing to generate amide–imide cross-linked gels [67]. The optimized 76.8% of absorbed liquid by weight in the polymer gel showed 9.48% efficiency, which was superior to conventional DSSCs (8.84%).

#### 14.2.3.3 Inorganic materials–polymer composite–based electrolytes

When inorganic oxide materials, such as $TiO_2$, $SiO_2$, $Al_2O_3$, ZnO, or carbon material, are used as gelator for liquid-type electrolyte, then this term arises. The main aim of this type of electrolyte is to improve the mobility of low-conducting polymer by introducing these inorganic materials. In 1998 Scrosati and Croce et al. first proposed the addition of inorganic nanoparticles into polymer electrolytes to change the physical state and conductivity of electrolytes [68–70]. It is observed that the previous conductivity ($10^{-4}$–$10^{-8}$ S cm$^{-1}$) of unfilled PEO–$LiClO_4$ electrolytes (at 80°C–30°C) were reached up to $10^{-4}$ S cm$^{-1}$ at 50°C and $10^{-5}$ S cm$^{-1}$ at 30°C after the addition of addition of $TiO_2$ and $Al_2O_3$ nanopowders. This promising conductivity enhancement was attributed to the enlargement of the amorphous phase in the electrolytes. Therefore after this study, $TiO_2$ or different inorganic nanoparticles were extensively applied to improve the states and ionic conductivities.

#### 14.2.3.4 Ionic liquid–based electrolytes

The salts that are liquid at room temperature are now commonly called ILs. The high thermal stability, negligible vapor pressure, wide electrochemical window, no combustion, nontoxicity, and unusual dissolving capability of room temperature IL are widely explored in various applications, especially in the field of organic synthesis, catalysis, separation, and good solvents for DSSCs [71]. These ILs have been known for more than 100 years; however, their unique properties have only come to light in the past two decades. The morphologies of wide band gap semiconductors are tailored by using ILs as designer solvents. Due to these unique

applications, these ILs have received much attention in recent years. Several are now well known in the research community, for example, ethyl ammonium nitrate ($[EtNH_3][NO_3]$), which has a melting point of 12°C, was first described in 1914 [72]. Typically, ILs consist of nitrogen-containing organic cations and inorganic anions with unique and tunable properties that can be adjusted by selecting appropriate ions for a specific need. This unique ability to tune the properties, often with just selection of the ions rather than covalent modification, makes ILs attractive for a range of applications, from materials science to electrochemistry and from catalysis to medicinal chemistry. As discussed above, ILs are composed of cations and anions. Generally, the cations are bulky, ammonium or phosphonium salts or heteroaromatics, with low symmetry, weak intermolecular interactions, and low charge densities. However, the anions are generally divided in to the halide/pseudohalide anions and the complex anions.

As they are nonvolatile and nonflammable, have high thermal stability, and are relatively inexpensive to manufacture, ILs are now finding applications in chemical synthesis, catalysis, separation technology, and the fabrication of conventional electrochemical devices [73]. The high thermal stability, higher viscosities ($10^{-2}$–100 Pa s) of ILs than either aqueous ($<10^{-3}$ Pa s) or organic ($\sim 6 \times 10^{-3}$ Pa s) electrolytes at room temperature, negligible vapor pressure, high ionic conductivity, and wide electrochemical window make them attractive novel environmental friendly solvents [74]. When compared with other electrolytes, some ILs also have the advantage that they can be obtained in a very dry state, making them especially suitable for applications in electrochemical systems from which moisture must be excluded over long periods of operation. ILs were used as suitable reaction media for organic syntheses, catalysis, separation, and polymerization. Due to these unique properties, ILs acts as a beneficial solvent for the fast crystal nucleation with uniform nanoparticle size and well-crystallized structure [75–77].

Initially, Wang et al. prepared a quasi-solid IL electrolyte with the help of mixing poly(vinylidenefluoride-co-hexafluoropropylene) (PVDF-HFP) (10 wt.%) with IL electrolyte containing iodine and *N*-methylbenzimidazole in 1-methyl-3-propylimidazolium iodide and demonstrated 5.3% for QS-DSSCs. It is noted that these results are almost identical when pristine without PVDF-HFP liquid electrolyte was used. These observations revealed that there is no adverse effect on the conversion efficiency in presence of polymer, which may be attributed to the

contribution by a Grotthus-type electron exchange mechanism in viscous polymer electrolytes [78]. Similarly, Shi et al. used a solvent-free eutectic melt-based electrolyte, DMII/EMImI/EMImB$(CN)_4$/$I_2$/NBB/GNCS (mol. ratio 12/12/16/1.67/3.33/0.67), to fabricate a QS-DSSC with C103 dye, yielding a record efficiency of 8.5%. Moreover, the device sustained more than 90% of its initial performance when subjected to accelerate testing for 1000 hours at 60°C under full sunlight soaking [79].

The application of quasi-solid-state electrolyte improves the long-term stability of DSSCs; however, the efficiencies of general QS-DSSCs are lower than that of DSSCs with liquid electrolytes as a result of the inferior mass-transfer rates of the redox couples in the highly viscous medium and high ET resistance at the electrolyte/electrode interfaces owing to imperfect wetting of electrode pores with the electrolyte. Various quasi-solid electrolytes, including thermoplastic polymer electrolytes, thermosetting polymer electrolytes, composites polymer electrolytes, and IL electrolytes, have different features. By optimizing and designing some QS-DSSCs based on the quasi-solid electrolytes, besides better long-term stability, one also can obtain high photovoltaic performances. Accordingly, the quasi-solid-state electrolyte is a prospective candidate in highly efficient and stable DSSCs.

## 14.3 Electrolytes for quantum dot sensitized solar cells

The unique size-dependent optical property of QD, QDSSC, is another promising candidate in low-cost photovoltaic technology. The device configuration of QDSSC is very similar to DSSC but instead of dyes, the QDs have been used as a light-absorbing material. Usually, chalcogenide QDs such as CdS, CdSe, and CdTe are used as a light absorber because of its better stability and size-dependent optical absorption coefficient. The basic device configuration with energy level diagram has been represented in Fig. 14.6. Once this device illuminates under light, the absorbed QDs on the wide band gap photoanodes can harvest light with respect to QDs' size and band gap. The light absorption generates the photoexcited electrons, which are subsequently injected from the CB of the QDs into the CB of the wide band gap semiconductor such as $TiO_2$ or ZnO. These electrons further are quickly transferred to the external circuit through the TCO substrate to produce electricity. On the other hand, the holes are synchronously produced by the photoexcitation process in the valence band of the QDs, which are immediately transferred to the redox

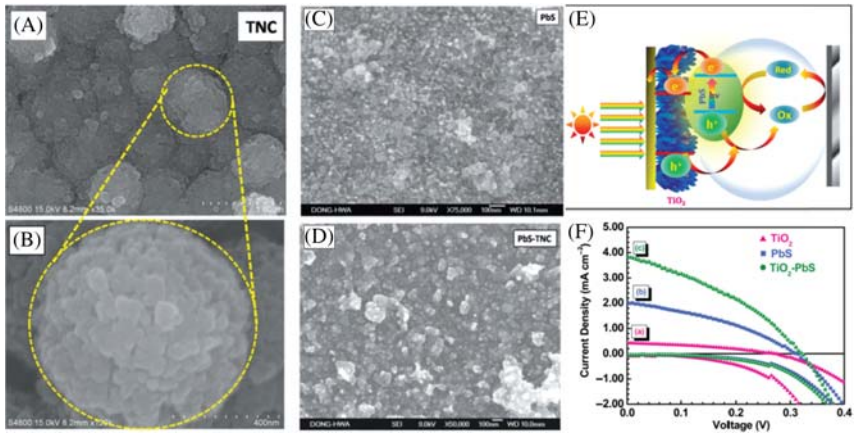


**Figure 14.6** FESEM images of (A and B) $TiO_2$ nanocorals, (C) PbS, and (D) PbS−TNC thin films. (E) An artistic representation of the PbS-sensitized $TiO_2$ nanocoral thin films with an accompanying energy level diagram (F) *J*−*V* curves for (A) the TNC, (B) PbS, and (C) the PbS−TNC samples. *FESEM*, Field emission scanning electron microscopic. *Reproduced from Royal Society of Chemistry (2012). Dalton Trans. 41 (2012) 6130−6136; S.S. Mali, H.J. Kim, P.S. Patil, C.K. Hong, Dalton Trans. 42 (2013) 16961−16967.*

electrolyte to oxidize it. The oxidized electrolyte is restored by the electrons in the counter electrode (CE) from the external circuit back to the cycling circuit in the cell. The solar cells parameters, such as current density, strongly depends on QDs light's harvesting ability and interfaces between electrolyte−electrode interfaces, while the $V_{oc}$ is depending on redox potential of the electrolyte.

Hydrothermal is one of the most promising techniques for the synthesis of hierarchical $TiO_2$. We have synthesized $TiO_2$ nanocoral-like morphology using hydrothermal technique and CdS QDs were synthesized by the successive ionic layer adsorption and reaction (SILAR) method (Fig. 14.6A−D). The cell was fabricated using a standard two-electrode configuration, comprised of PbS−$TiO_2$/F:$SnO_2$/glass as the photoanode.

$$\text{Glass/FTO/TNC/NaOH/Pt/FTO} \tag{14.10}$$

$$\text{Glass/FTO/PbS/Na}_2\text{S} + \text{NaOH} + \text{S/Pt/FTO} \tag{14.11}$$

$$\text{Glass/FTO/TNC} - \text{PbS/Na}_2\text{S/Pt/FTO} \tag{14.12}$$

The bare $TiO_2$ electrode exhibits a PCE ($\eta$) of 0.004% with $J_{sc} = 50\ \mu A\ cm^{-2}$, $V_{oc} = 0.234$ V, and FF = 0.32. The bare PbS electrode shows $J_{sc} = 2.01\ mA\ cm^{-2}$ and $V_{oc} = 0.312$ V with 0.63% efficiency. However, a drastic change in the photoelectrochemical performance was observed for the PbS−$TiO_2$ electrode with $J_{sc} = 3.84\ mA\ cm^{-2}$, $V_{oc} = 0.322$ V, and FF = 0.49. The $\eta$ of the cell is ~1.23% under illumination with a light intensity of 100 mW $cm^{-2}$, which is comparable with the performance of other PbS-sensitized solar cell systems (Fig. 14.6F). The significant enhancement of the PEC due to quantum sized PbS particles produced by the SILAR technique may effectively charge separately under visible illuminations and constrains the electron−hole recombination centers, which results in enhancement of the performance of such electrodes [80]. Table 14.3 shows the literature survey of QDSSCs based on various QDs and photoanodes. However, so far only polysulfide with few additives has been used as an electrolyte for QDSSCs based solar cells.

Very similar to redox electrolytes in DSSCs, the polysulfide ($S_2/S_n^{2}$) is the medium to transfer charge between working photoanodes and counter electrodes for the regeneration of oxidized QDs [100]. These electrolytes are playing a key role in terms of efficiency and stability of QDSSCs. Due to poor stability of QDs in iodide/triiodide ($I/I_3$) coupled polysulfide ($S_2/S_n^{2}$), redox couple aqueous solution electrolyte is used for QDSSCs [101]. Due to the relatively high redox potential of the polysulfide redox couple, the QDSSCs show relatively low open circuit voltage. Therefore there are many aspects needed to optimize the QDSSCs, which includes concentration of the redox mediator [102], introducing additives such as $SiO_2$, [103] PEG, [104] PVP, [105] and guanidine thiocyanate [106], and using a modifying solvent [107].

Mali et al. used an aqueous chemical growth route to grow vertically aligned ZnO nanorod arrays on a fluoride doped tin oxide (FTO) coated glass substrate. These nanorods were further sensitized with cadmium sulfide (CdS) QDs by a SILAR technique (Fig. 14.7A−H). Fig. 14.7I shows a schematic representation of a QDSSC based on the CdS−ZnO architecture with electron transport mechanism. For photoelectrochemical measurements, the $S^{2-}/S_n^{2-}$ redox electrolyte has been used. The CdS QD deposited at 10 SILAR sample ($CS_{10}$) shows a $J_{sc}$ of 1.95 mA $cm^{-2}$ and $V_{oc}$ of 0.580 V, FF of 0.48 results in 0.46% PCE. The champion cells having 40 SILAR cycles ($CS_{40}$) showed $J_{sc}$ of 5.61 mA $cm^{-2}$ results in 1.22% PCE. The 1D ZnO morphology is very useful due to the fast ET

**Table 14.3** Literature survey on various electrolytes for low-cost photovoltaics quantum dot sensitized solar cells.

| Photoanode | Quantum dot absorber | Electrolyte | $J_{sc}$ (mA cm$^{-2}$) | $V_{oc}$ (V) | FF | PCE (%) | Reference |
|---|---|---|---|---|---|---|---|
| $TiO_2$ | CdS | $S^{2-}/S_n^{2-}$ | 1.04 | 0.378 | 0.53 | 0.72 | [81] |
| $TiO_2$ | CdSe/ZnS | $S^{2-}/S_n^{2-}$ | 15.54 | 0.563 | 0.61 | 5.53 | [82] |
| $TiO_2$ | CdSe/ZnS/$SiO_2$ | $S^{2-}/S_n^{2-}$ | 16.95 | 0.591 | 0.50 | 5.01 | [83] |
| $TiO_2$ | CdS/CdSe | $S^{2-}/S_n^{2-}$ | 19.32 | 0.531 | 0.586 | 6.011 | [84] |
| $TiO_2$ | CdS/CdSe ZnS | $S^{2-}/S_n^{2-}$ | 10.81 | 0.689 | 0.62 | 4.61 | [85] |
| ZnO | CdS/CdSe | $S^{2-}/S_n^{2-}$ | 17.3 | 0.627 | 0.383 | 4.15 | [86] |
| ZnO | CdS/CdSe | $S^{2-}/S_n^{2-}$ | 16.0 | 0.620 | 0.49 | 4.86 | [87] |
| ZnO | CdS | $S^{2-}/S_n^{2-}$ | 5.61 | 0.585 | 0.49 | 1.61 | [88] |
| $TiO_2$/ZnO | CdS/CdSe | $S^{2-}/S_n^{2-}$ | 19.19 | 0.517 | 0.54 | 5.38 | [89] |
| ZnO/$TiO_2$ | CdS/CdSe | $S^{2-}/S_n^{2-}$ | 15.34 | 0.659 | 0.53 | 5.36 | [90] |
| ZnO/Ag NPs/$TiO_2$ | CdS/CdSe | $S^{2-}/S_n^{2-}$ | 15.65 | 0.744 | 0.508 | 5.92 | [91] |
| ZnO/g-$C_3N_4$ | CdS | $S^{2-}/S_n^{2-}$ | 11.1 | 0.650 | 0.34 | 2.43 | [92] |
| ZnO/$Zn_2SnO_4$ | CdS/CdSe | $S^{2-}/S_n^{2-}$ | 11.32 | 0.492 | 037 | 2.08 | [93] |
| $TiO_2$/MgO/$Al_2O_3$ | CdS/CdSe | $S^{2-}/S_n^{2-}$ | 11.4 | 0.630 | 0.56 | 3.25 | [94] |
| $SnO_2$ | CdS/CdSe/ZnS | $S^{2-}/S_n^{2-}$ | 7.5 | 0.587 | 0.562 | 2.5 | [95] |
| $TiO_2$ | CdSe | $S^{2-}/S_n^{2-}$ | 16.31 | 0.664 | 0.675 | 7.30 | [96] |
| $TiO_2$ | CdSeTe | $S^{2-}/S_n^{2-}$ | 21.36 | 0.703 | 0.646 | 9.71 | [96] |
| $TiO_2$ | ZCISe | $S^{2-}/S_n^{2-}$ | 26.36 | 0.768 | 0.610 | 12.34 | [96] |
| $TiO_2$ | PbS/CuS CQDs | P3HT (HTM) | 20.7 | 0.600 | 0.65 | 8.07 | [97] |
| $TiO_2$ | PbS | P3HT (HTM) | 14.2 | 0.470 | 0.429 | 2.9 | [98] |
| $TiO_2$ | ZnCuInSe | $S^{2-}/S_n^{2-}$ | 25.25 | 0.739 | 0.622 | 11.61 | [99] |

*CQD*, Colloidal quantum dot; *HTM*, hole-transporting material; *P3HT*, poly(3-hexylthiophene); *PCE*, power conversion efficiency; *ZCISe*, Zn−Cu−In−Se.

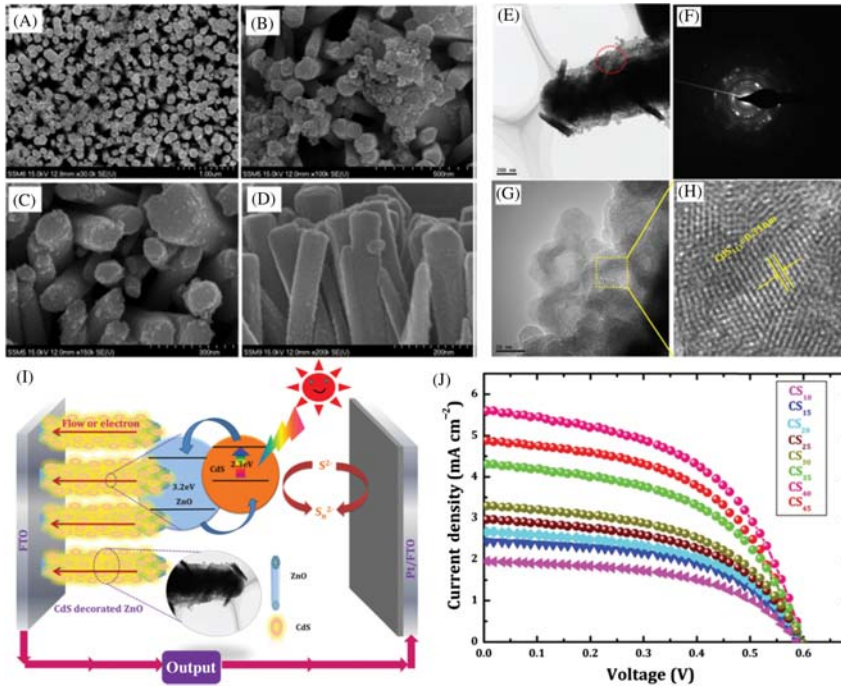


**Figure 14.7** (A–C) SEM images of the CdS-sensitized ZnO nanorods at different magnifications. (D) Cross-sectional FESEM image of the ZnO/CdS core shell. (E–H) TEM image of the CdS-sensitized ZnO nanorod, (F) selective area electron diffration (SAED) pattern of CdS–ZnO sample, and (G and H) high-resolution TEM images of the CdS-sensitized ZnO nanorods. (I) Schematic illustration of the CdS-coated ZnO nanorod architecture synthesized by an aqueous chemical growth and SILAR technique. (J) *J–V* characteristics of the CdS–ZnO photoelectrodes at different cycles. *FESEM*, Field emission scanning electron microscopic; *SILAR*, successive ionic layer adsorption and reaction. *Reproduced from The Royal Society of Chemistry (2013). Dalton Trans. 42 (2013) 16961–16967; G. Jiang, Z. Pan, Z. Ren, J. Du, C. Yang, W. Wang, et al., J. Mater. Chem. A 4 (2016) 11416–11421.*

through 1D nanostructures, effective high surface area via the vertical arrangement, and the very smooth surface to the CdS QDs [88].

Yu et al. developed a new recipe for the synthesis of polysulfide electrolyte with tetraethyl orthosilicate (TEOS) additives and demonstrated >12% PCE [96]. The investigated QD light-harvesting materials, including OAm-capped CdSe, CdSeTe, and Zn–Cu–In–Se (ZCISe) oil-soluble QDs, were synthesized by SILAR method. QD sensitizers were immobilized on $TiO_2$ mesoporous film electrodes by pipetting mercaptopropionic acid (MPA) or thioglycolic acid (TGA)-capped QD aqueous

solution onto the film electrodes. After QD loading, the photoanodes were rinsed with water and ethanol sequentially. ZnS passivation layers were then coated on the QD-sensitized photoanodes by immersing the electrodes into a 0.1 M $Zn(OAc)_2$ methanol solution and 0.1 M $Na_2S$ aqueous solution alternately. They concluded that the champion cell having pristine polysulfide electrolyte showed highest PCE for a champion cell was $\eta$ of 10.27% efficiency with $V_{oc}$ of 0.629 V, $J_{sc}$ of 26.91 mA $cm^{-2}$, and FF of 0.607. On the other hand, if $Cu_2S$/Brass counter electrode is used with pristine polysulfide electrode, then efficiency was enhanced up to 11.75% ± 0.38% with $V_{oc}$ of 0.743 V, $J_{sc}$ of 25.84 mA $cm^{-2}$, and FF of 0.612 V. Further, author used 6 vol.% TEOS modified electrolyte and it shows $V_{oc}$ of 0.768 V, $J_{sc}$ of 26.36 mA $cm^{-2}$, and FF of 0.610 yielded 12.34% ± 0.21% PCE (Fig. 14.8). The average PCE of ZCISe-based QDSSCs was boosted to a new record of 12.3% under standard measurement conditions with 6 vol.% TEOS in the polysulfide electrolyte at a staying time of 24 hours.

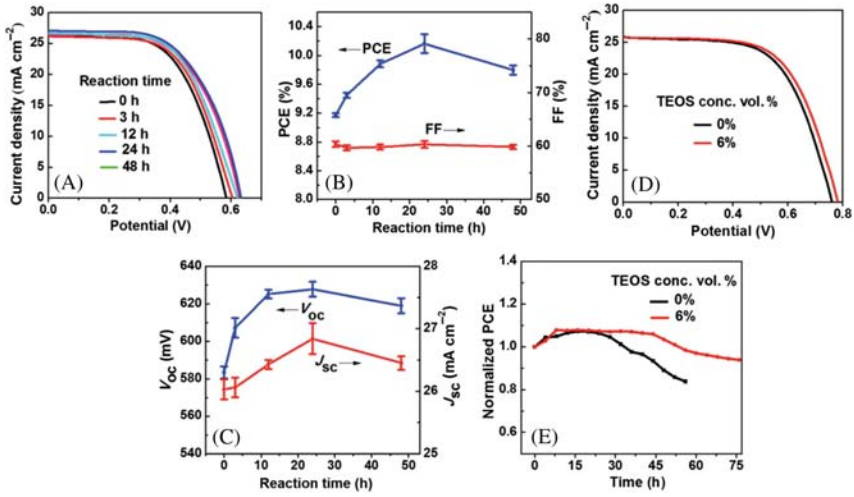


**Figure 14.8** (A) *J*–*V* curves of champion ZCISe QDSSCs with 6 vol.% TEOS in the modified polysulfide electrolyte at various staying times; (B) dependence of average PCE and FF on the staying time of modified electrolyte; and (C) dependence of average $V_{oc}$ and $J_{sc}$ on the staying time of modified electrolyte. (D) *J*–*V* curves of ZCISe QDSSCs using MC/Ti CEs with 0 and 6 vol.% TEOS in the modified polysulfide electrolyte at a staying time of 24 h. (E) Normalized PCE of CdSe QDSSCs with (6 vol.%) and without TEOS in the electrolyte. *PCE*, Power conversion efficiency; *TEOS*, tetraethyl orthosilicate; *ZCISe*, Zn–Cu–In–Se. *Reproduced from The Royal Society of Chemistry (2017). J. Mater. Chem. A 5 (2017) 14124–14133; J. Yu, W. Wang, Z. Pan, J. Du, Z. Ren, W. Xue, et al., J. Mater. Chem. A 5 (2017) 14124.*

Im et al. fabricated multiple layered PbS colloidal QD (CQD)-sensitized photovoltaic cells using poly(3-hexylthiophene) (P3HT) as HTMs [63]. Authors obtained the multiple layers of PbS CQD by the repeated spin-coating of oleic-acid-capped PbS CQD solution and 1 wt.% 1,2-ethanedithiol (EDT) on to mp-$TiO_2$ (Fig. 14.9A and B). Here, EDT molecules exhibit two modes of interactions. In addition, the P3HT layer was deposited by the spin-coating process, followed by poly(3,4-ethylenedioxythiophene)-poly(styrenesulfonate) (PEDOT:PSS) deposition in order to improve the better contact. They may be attached to PbS CQDs monodentately bridging different PbS CQDs. Author's study revealed that the $J_{sc}$ gradually increases as the post-EDT treatment time increases and becomes saturated over 16 hours of posttreatment, which is also confirmed by external quantum efficiency (EQE), as shown in Fig. 14.9C. This increment stem from the improved charge transport in multiply layered PbS CQDs and/or efficient charge injection from PbS CQDs into the CB of mp-$TiO_2$ due to the mono- or bi-dentately chelated EDT molecules on the PbS CQDs via the post-EDT treatment. The optimized results revealed that 2.9% efficiency with $J_{sc}$ of 14.2 mA $cm^{-2}$, $V_{oc}$ of 0.470 V, and FF of 0.47 Fig. 14.9D.

Park et al. used a novel technique for the synthesis of CuS anchored PbS QDs by rapid injection of a sulfur precursor into a lead precursor solution followed by cation exchange of Pb with Cu ions [97]. Here CuS acts as surface plasmon resonance centers by the existence of vacancies in CuS in the near infrared region. Authors developed CuS (PbS[CuS]QDs) and fabricated a QDSSCs using P3HT as a HTM. The optimized solid-state QDSSC devices produce a high PCE of 8.07% with $V_{oc}$ of 0.6 V, $J_{sc}$ of 20.7 mA $cm^{-2}$, and FF 65%.

The addition of inorganic metal oxide nanoparticles in polysulfide can improve the further conductivity. Therefore Wei et al. used $SiO_2$ nanoparticles into the polysulfide electrolyte that can enable the formation of an energy barrier for the recombination at the photoanode/electrolyte interface results in a higher electron collection efficiency and a longer electron lifetime results in 11.23% efficiency [103]. It is also noted that the $V_{oc}$ can be further improved by using alternative redox couples, such as $[Co(o\text{-phen})_3]^{2+/3+}$, $[Fe(CN)_6]^{3-/4-}$, and Mn poly(pyrazolyl)borate with relatively low redox potentials [108,109].

Although the QDSSCs are now crossing 11% PCE, but still they are suffering from poor stability of chalcogenide materials and liquid-type electrolytes. Therefore very similar to QS-DSSC, the quasi-solid-state and

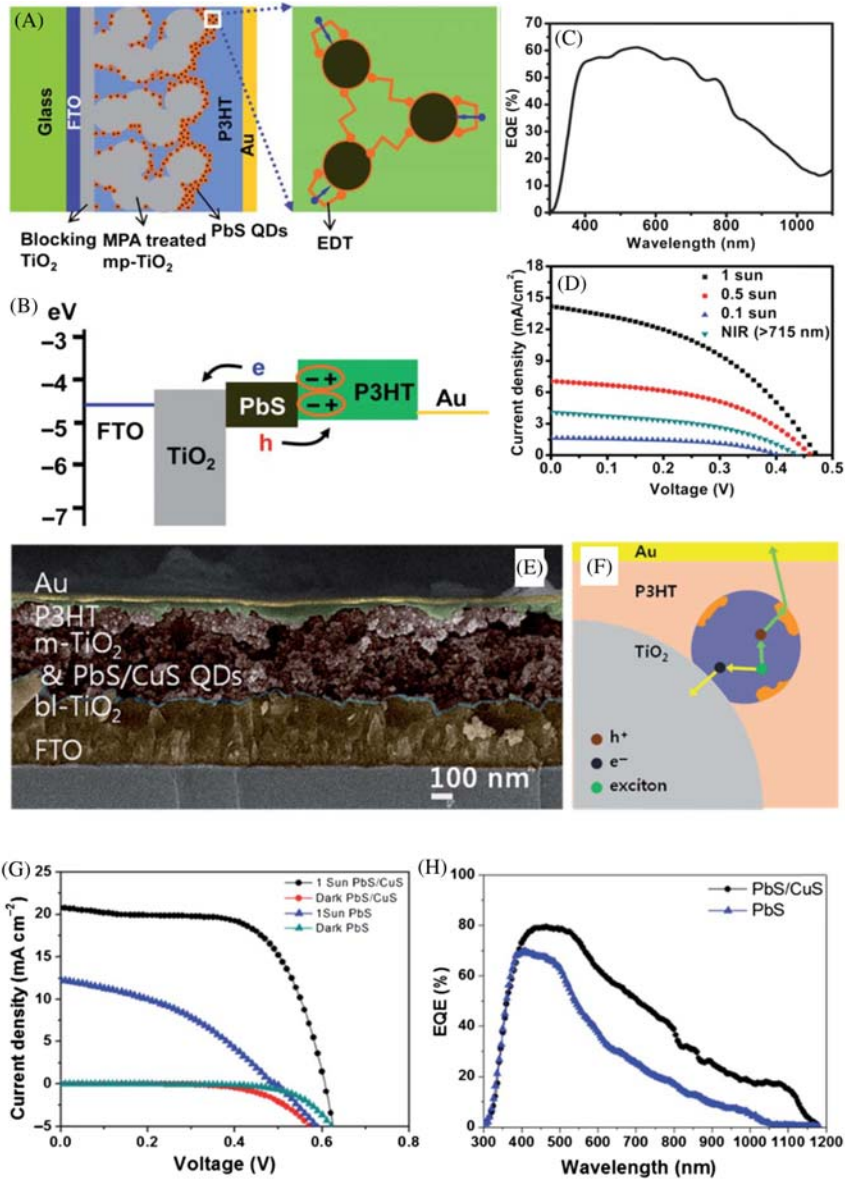


**Figure 14.9** (A) Schematic illustration of the device structure and (B) the energy level diagram. (A) Short-circuit current density ($J_{sc}$) of a PbS20 device with post-EDT treatment time in 10 wt.% EDT solution, (B) EQE, and (C) EQE spectrum of PbS20-EDT16h sample (D) $J-V$ curves with illuminated sun intensity. A PbS20-EDT16h was used for EQE and $J-V$ measurements. (E) SEM cross-sectional images of QDSSCs. (F) Illustration of the proposed working mechanism; generated excitons by light

solid-state electrolytes have been developed as well. In particular, the ILs, [110] gel electrolytes [111,112], and hydrogel electrolytes [113,114] containing redox couples are commonly used as quasi-solid-state electrolytes.

Recently, Feng et al. developed by solidifying a polysulfide aqueous solution using sodium carboxymethylcellulose with superabsorbent and water-holding capability. The fabricated quasi-solid-state QDSSCs yielded 9% PCE [115]. On the other hand, for fully solid-state electrolytes, including various HTMs, such as 2,20,7,70-tetrakis(*N*,*N*-di-4-methoxyphenylamino)-9,90-spirobifluorene (spiro-MeOTAD), [116], P3HT, [98] 3,3000-didodecylquaterthiophene (QT12), [117], PVP, [118] 214, and PEO-PVDF [119] have been successfully employed in solid-state QDSSCs and are now crossing 8% PCE.

## 14.4 Ternary $CuInSe_xS_{2-x}$-based solar cells

Considering the low toxicity and low cost, low-toxicity $CuInSe_xS_{2-x}$ QDs open a new area in QDSSCs. The $CuInSe_xS_{2-x}$ is promising light-absorbing materials due to its tunable band gap from 1.0−1.5 eV, high absorption coefficient, excellent charge transporting properties, and, most importantly, low cost and low toxicity [120−122]. With a controlled hot-injection method, McDaniel synthesized pyramid shaped $CuInSe_xS_{2-x}$ QDs and demonstrated 3.45% efficiency with $J_{sc}$ of 10.5 mA $cm^{-2}$, $V_{oc}$ of 0.550 V, and FF of 0.604 [123]. Authors also pointed out the ZnS passivation may substantially improve the device efficiency up to >5.13%: the certified 5.13% with $J_{sc}$ of 17.565 mA $cm^{-2}$, $V_{oc}$ of 0.540 V, and FF of 54.00% [124]. On a similar aspect, Pan et al. introduced a term "Green" QDs with certified 6.66% PCE. Controlled reaction medium results in ∼5 nm CIS QDs, which is passivated with ZnS interfacial layer (herein CIS-Z). With this wide absorption range of QDs, CIS-Z-based QDSSC configuration with high QD loading and

illumination are rapidly separated into free charge carriers. (G) *I*−*V* curve of pristine PbS QDSSCs and PbS[CuS] QDSSCs. (H) EQE spectra of pristine PbS QDSSCs and PbS [CuS] QDSSCs. The EQE spectrum of PbS[CuS] QDSSCs shows improved efficiency over the 400 nm region, especially in the 1100 nm region. *EDT*, 1,2-Ethanedithiol; *QD*, quantum dot. *(A−C) Reproduced from The Royal Society of Chemistry (2017). Energy Environ. Sci. 4 (2011) 4181; S.H. Im, H. Kim, S.W. Kim, S.W. Kim, S.I. Seok, Energy Environ. Sci. 4 (2011) 4181. (E−H) Reproduced from The Royal Society of Chemistry (2016). J. Mater. Chem. A 4 (2016) 785−790; J.P. Park, J.H. Heo, S.H. Im, S.-W. Kim, J. Mater. Chem. A 4 (2016) 785−790.*

with the benefit of the recombination reduction with type-I core/shell structure boosts the PCE of Cd- and Pb-free QDSSC to a record of 7.04% (with certified efficiency of 6.66%) under AM 1.5 G 1 Sun irradiation [125]. Similarly, Kim et al. developed a SILAR method for optimizing the ZnS overlayer and demonstrated 8.10% PCE [126] ultrasmall CIS QDs (~4 nm) with different thickness of ZnS overlayer prepared from 7 SILAR cycles results in $J_{sc}$ of 26.93 mA $cm^{-2}$, $V_{oc}$ of 0.528 V, and FF of 0.57 yielded 8.10% PCE.

## 14.5 Electrolytes for perovskite solar cells

Methylammonium lead halide (MAPbX) (X = I, Br, or Cl)-based PSCs open new approaches for the fabrication of efficient and stable solid-state sensitized solar cells. The pioneering work on alkali-metal lead and tin halides was performed by Wells [127]. The chemical formula of the compound that he used was $CsPbX_3$ (X = Cl, Br, or I). However, 94 years later, Poglitsch et al. successfully replaced cesium (Cs) with methylammonium cations ($CH_3NH_3^+$) and studied various compositions of the first three-dimensional organic–inorganic hybrid perovskites by tuning their crystal structures and phases into what can be referred to as $ABX_3$ [128]. The first perovskite light harvester was demonstrated successfully by Miyasaka with 3.8% and 3.1% PCE for $MAPbI_3$ and $MAPbBr_3$-based PSCs [129]. After successful synthesis of $MAPbI_3$ perovskite QDs, Im et al. demonstrated a 6.5% PCE via the ex situ method [130] followed by all solid-state PSC using spiro-MeOTAD as a HTM Burschka et al. in 2013 demonstrated 13% PCE [131] (Table 14.4).

The HTM is also playing a key role in order to improve the $V_{oc}$ of the PSCs. Fig. 14.10A–D shows a schematic of the typical device architectures that we used, and respective energy level diagrams for the PSCs with spiro-MeOTAD and PTAA HTMs [156]. In a typical PSC, the absorber layer is sandwiched between the electron transporting layer (ETL) and hole transporting layer (HTL). The compact titanium oxide blocking layer (Bl-$TiO_2$), with or without the mesoporous scaffold ($TiO_2$), acts as the ETL. The HTM and the counter electrode (Au, Ag, or Al) are the key components of the HTL. When the light illuminates the device, the absorbing material absorbs the photons to generate the electron–hole pair excitons. Then, the excitons dissociate at the $TiO_2$/perovskite interface. The dissociated electrons flow toward the $TiO_2$ CB to FTO, whereas the holes travel through the HTM layer and reach the Au

**Table 14.4** Literature survey on various electrolytes for perovskite solar cells.

| Photoanode | Sensitizer | Electrolyte or HTM | $J_{sc}$ (mA cm$^{-2}$) | $V_{oc}$ (V) | FF | PCE (%) | Reference |
|---|---|---|---|---|---|---|---|
| $TiO_2$ | $MAPbBr_3$ | LiBr and $Br_2$ | 5.57 | 0.960 | 0.59 | 3.13 | [10] |
| $TiO_2$ | $MAPbI_3$ | LiI and 0.075 M $I_2$ | 11.0 | 0.61 | 0.57 | 3.81 | [10] |
| $TiO_2$ | $MAPbI_3$ | $3I/I_3^-$ | 15.82 | 0.706 | 0.586 | 6.54 | [11] |
| $TiO_2$ | $MAPbI_3$ | Spiro-MeOTAD + LiTFSI + TBP | 20.0 | 0.993 | 0.73 | 15.0 | [12] |
| $TiO_2$ | $MAPbI_{3-x}Cl_x$ | Spiro-MeOTAD + LiTFSI + TBP + FK209 | 22.8 | 1.13 | 0.75 | 19.3 | [13] |
| $TiO_2$ | $MAPbI_3$ | Py-C + LiTFSI + TBP + FK209 | 20.2 | 0.890 | 0.69 | 12.4 | [132] |
| $TiO_2$ | $MAPbI_3$ | Po-spiro-MeOTAD + LiTFSI + TBP | 21.2 | 1.02 | 0.77 | 16.7 | [133] |
| $TiO_2$ | $MAPbI_3$ | H111 + LiTFSI + TBP + FK102 | 19.8 | 1.08 | 0.72 | 15.4 | [134] |
| $TiO_2$ | $MAPbI_3$ | KTM3 + LiTFSI + TBP + FK269 | 13.0 | 1.08 | 0.78 | 11.0 | [135] |
| $TiO_2$ | $MAPbI_3$ | T103 + LiTFSI + TBP + FK102 | 20.3 | 0.99 | 0.62 | 12.4 | [136] |
| $TiO_2$ | $MAPbI_3$ | Triazine-Th-OMeTPA | 20.7 | 0.92 | 0.66 | 12.5 | [137] |
| $TiO_2$ | $MAPbI_3$ | Triazine-Ph-OMeTPA | 19.1 | 0.93 | 0.61 | 10.9 | [137] |
| $TiO_2$ | $MAPbI_3$ | MeO-DATPA + H-TFSI + Et4N-TFSI | 16.4 | 0.96 | 0.560 | 8.8 | [138] |
| $TiO_2$ | $MAPbI_3$ | TPBC | 19.3 | 0.94 | 0.72 | 13.1 | [139] |
| $TiO_2$ | $MAPbBr_{3-x}Cl_x$ | CBP + LiTFSI + TBP | 4.0 | 1.150 | 0.46 | 2.7 | [140] |
| $TiO_2$ | $MAPbI_{3-x}Cl_x$ | X19 + LiTFSI + TBP | 17.1 | 0.76 | 0.58 | 7.6 | [141] |
| $TiO_2$ | $MAPbI_3$ | X51 + LiTFSI + TBP + FK209 | 19.8 | 0.96 | 0.70 | 13.3 | [142] |
| $TiO_2$ | $MAPbI_{3-x}Cl_x$ | P3HT + LiTFSI + D-TBP | 19.1 | 0.98 | 0.66 | 12.4 | [143] |
| $TiO_2$ | $MAPbI_3$ | PCBTDPP + LiTFSI + TBP | 13.9 | 0.83 | 0.48 | 5.6 | [144] |
| $TiO_2$ | $MAPbI_3$ | PDPPDBTE + LiTFSI + TBP | 14.4 | 0.86 | 0.75 | 9.2 | [145] |

(*Continued*)

**Table 14.4** (Continued)

| Photoanode | Sensitizer | Electrolyte or HTM | $J_{sc}$ (mA cm$^{-2}$) | $V_{oc}$ (V) | FF | PCE (%) | Reference |
|---|---|---|---|---|---|---|---|
| $TiO_2$ | $MAPbI_3$ | TFB + LiTFSI + TBP | 17.5 | 0.960 | 0.65 | 10.9 | [146] |
| $TiO_2$ | $MAPbI_3$ | PANI + LiTFSI + TBP | 18.0 | 0.88 | 0.40 | 6.3 | [147] |
| $TiO_2$ | $MAPbI_{3-x}Br_x$ | Spiro-MeOTAD + LiTFSI + TBP | 20.77 | 1.108 | 0.69 | 45.88 | [148] |
| $Au/TiO_2$ | $MAPbI_3$ | Spiro-MeOTAD + LiTFSI + TBP | 21.63 | 0.986 | 0.70 | 14.92 | [149] |
| $Li/TiO_2$ | $(FAPbI_3)_{0.85}$ $(MAPbBr_3)_{0.15}$ | Spiro-MeOTAD + LiTFSI + FK209 + TBP | 23.0 | 1.114 | 0.74 | 19.3 | [150] |
| $Li:SnO_2$ | $MAPbI_3$ | Spiro-MeOTAD + LiTFSI + TBP | 23.27 | 1.106 | 0.7071 | 12.20 | [151] |
| $TiO_2$ | $CsI_{0.05}\{(FAPbI_3)_{0.85}$ $(MAPbBr_3)_{0.15}\}_{0.95}$ | Spiro-MeOTAD + LiTFSI + TBP | 22.69 | 1.1132 | 0.748 | 21.06 | [152] |
| $TiO_2$ | RbI:CsI:MAFA | Spiro-MeOTAD + LiTFSI + FK209 + TBP | 22.5 | 1.186 | 0.77 | 20.6 | [153] |
| $TiO_2$ | $(FAPbI_3)_{0.85}$ $(MAPbBr_3)_{0.15}$ | Spiro-MeOTAD + LiTFSI + FK209 + TBP | 24.6 | 1.16 | 0.73 | 20.8 | [154] |
| $La:BaSnO_3$ | $MAPbI_3$ | PTAA + LiTFSI + TBP | 23.4 | 1.120 | 0.813 | 21.3 | [155] |

*HTM*, Hole-transporting material; *P3HT*, poly(3-hexylthiophene); *PCE*, power conversion efficiency; *PTAA*, poly[bis(4-phenyl)(2,4,6-trimethylphenyl)amine]; *TBP*, 4-tert-butylpyridine.

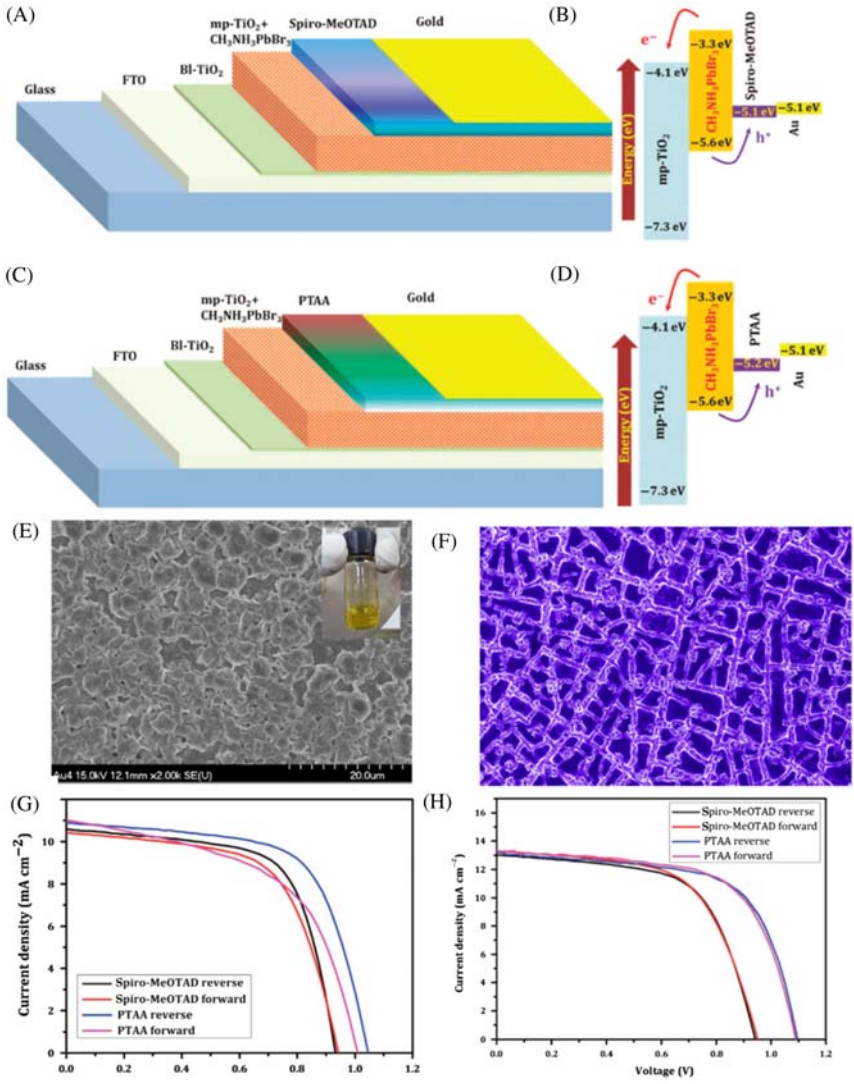


**Figure 14.10** Device configurations and energy level diagrams of $MAPbBr_3$-based PSCs (A and B) spiro-MeOTAD-based devices. (C and D) PTAA. (E) Top view of perovskite solar deposited by solvent engineering process (F) after deposition of spiro-MeOTAD HTM. (G and H) *J*−*V* curves of the forward and reverse bias sweeps and the respective *J*−*V* curves for spiro-MeOTAD and PTAA. *HTM*, Hole-transporting material; *PSC*, perovskite solar cell; *PTAA*, poly[bis(4-phenyl)(2,4,6-trimethylphenyl)amine]. *(A−D, G, H) Reproduced from Nature Publishing Group (2015). Z. Pan, I. Mora-Sero, Q. Shen, H. Zhang, Y. Li, K. Zhao, et al., J. Am. Chem. Soc. 136 (2014) 9203−9210. (E) Reproduced from Royal Society of Chemistry (2016). J.Y. Kim, J. Yang, J.H. Yu, W. Baek, C.-H. Lee, H.J. Son, et al., ACS Nano 9 (2015) 11286−11295. (F) Reproduced from Elsevier (2015). H.L. Wells, Z. Anorg. Chem. 3 (1893) 195.*

counter electrode. Fig. 14.10E shows surface morphology of the perovskite layer [150] and Fig. 14.10F shows after the deposition of spiro-MeOTAD HTM [157]. The surface morphology revealed that the spiro-MeOTAD HTM is uniformly deposition over the perovskite layer. The mp-$TiO_2$ layer was deposited at 5000 rpm and the $MAPbBr_3$−DMSO solution was spin cast at 1000 (10 seconds) and 5000 (45 seconds) rpm, respectively. Fig. 14.10G and H shows typical $J-V$ plots of the optimized ~2−3 nm $MAPbBr_3$ QD devices that are based on spiro-MeOTAD and PTAA HTMs in forward and reverse scan modes. The FTO/Bl-$TiO_2$/mp-$TiO_2$ + $MAPbBr_3$(≤3 nm)/spiro-MeOTAD/Au-based perovskite exhibits a PCE of 7.66% and 7.61% for the forward and reverse scan modes, respectively. In case of the standard spiro-MeOTAD-based devices, the forward scan exhibits the following parameters: $V_{oc} = 0.951$ V, $J_{sc} = 11.68$ mA $cm^{-2}$, FF = 0.69, and $\eta = 7.66\%$. The reverse scan shows similar characteristics: PCE = 7.61% ($V_{oc} = 0.932$ V, $J_{sc} = 11.50$ mA $cm^{-2}$, and FF = 0.71).

In 2013 Gratzel et al. used sequential the deposition method for the fabrication of $MAPbI_3$ perovskite absorber layer for mesoscopic type and spiro-MeOTAD-based HTM and demonstrated 13% PCE (Fig. 14.11E). After this report, Park et al. used a single-step process for the synthesis of $MAPBI_3$ perovskite layer and demonstrated 9.7% PCE for mesoscopic type PSCs (Fig. 14.11F−H) [11]. The stability has been improved up to 500 hours using spiro-MeOTAD based HTM. However, Seok at al. introduced the solvent engineering process in order to make highly uniform textured perovskite thin films with large grains and demonstrated 16.2% using mixed halide perovskite $MAPb(I_{1-x}Br_x)_3$ ($x = 0.1-0.15$) absorber layer with no hysteresis [14]. Bi et al. tuned the amount of $PbI_2$ in mixed halide $FAPbI_3$ + $MAPbBr_3$ perovskite and demonstrated 20.8% PCE using spiro-MeOTAD based HTM (Fig. 14.10J) [154]. Very recently, Shin et al. developed the La-doped $BaSnO_3$ oxide perovskite structure and using PTAA as a HTM and demonstrated >21.3% PCE with good stability (Fig. 14.10K) [16]. Further, the iodine management produced 22.1% PCE [17].

## 14.6 Role of dopant in solid-state hole-transporting materials for perovskite solar cells

In order to control the type of the conductivity and charge mobility of organic and inorganic materials, electronic doping play a key role.

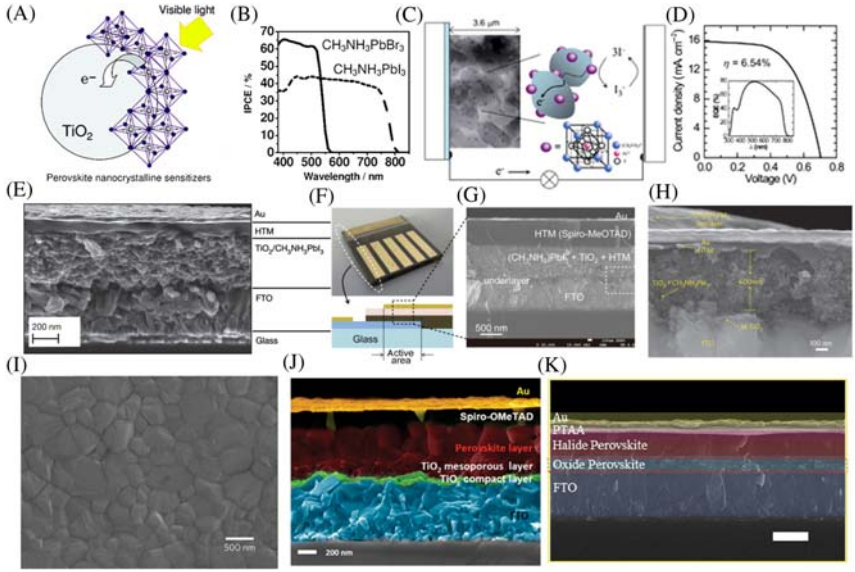


**Figure 14.11** Evolution of PSCs from liquid-type electrolyte to solid-state hole-transporting materials. (A) Schematic representation of perovskite/$TiO_2$ interface (B) EQE spectra for MAPbBr3 and MAPbI3 perovskites (C) proposed mechanism for liquid type perovskite solar cells (D) J-V characteristics for MAPbI3 perovskite. Inset shows its EQE spectrum. (E) Cross-sectional SEM micrograph of perovskite device obtained from two-step deposition. (F) Photograph of perovskite device and (G) its cross-sectional SEM (H) cross-sectional SEM of perovskite device based on polymeric HTM (I) top-view of solvent engineering processed perovskite thin film. (J) Cross-sectional SEM of bi-layered PSC. (K) Cross-sectional image of oxide perovskite based PSC. *PSC*, Perovskite solar cell. *The respective figures were reprinted with permission from respective publishers.*

Usually, p-type doping and n-type doping, that is, donor and acceptor species, can be optimized by reduction or oxidation process. The key parameter for efficient doping is therefore the position of the ionization potential or electron affinity of the dopant with respect to the host's energy levels. Grätzel et al. developed a new recipe for p-type doing using Co(III) complexes in order to improve the overall performance of DSSCs [158]. Two new Co(III) complexes, namely, tris(2-(1*H*-pyrazol-1-yl)-4-tert-butylpyridine)cobalt(III), tris-(bis(trifluoromethylsulfonyl)imide), and bis(2,6-di(1*H*-pyrazol-1-yl)pyridine)cobalt(III) tris(bis(trifluoromethylsulfonyl)-imide), commonly known as FK209 and FK269 were synthesized by Co(II) complexes as dopants. From this it is clear that the properties of the dopant can be easily adjusted by modifying the organic ligands and/or

the counter ion. The doping with 10% FK209 yielded $V_{oc}$ of 0.941 V, $J_{sc}$ of 9.1 mA cm$^{-2}$, and FF of 0.73 results in 6.2% PCE. Juarez-Perez et al. studied the influence of dopant on morphological and transport properties of spiro-MeOTAD [159]. They found that the main role of 4-tert-butylpyridine (TBP) is to prevent phase segregation of LiTFSI and spiro-MeOTAD, resulting in a homogeneous hole transport layer. These properties are critical for charge transport in the HTM bulk film as well as at the perovskite/HTM and HTM/electrode interfaces and for efficient solar cell performance. On the other hand, Abate et al. developed protic ILs as p-dopant for spiro-MeOTAD HTM and demonstrated three times higher conductivity using bis(trifluoromethanesulfonyl)imide (HTFSI) doping [160].

## 14.7 Role of additives

Additives are one of the most important components in electrolyte. It is also noted that for both solid-state HTM and liquid-type electrolyte additives are playing a crucial role. For the first time, TBP was used as an additive in electrolyte by Gratzel et al., resulting in a substantial increment in $V_{oc}$ of DSSCs. Usually, nitrogen-containing heterocyclic compounds, including analogues and derivatives of pyridine, alkylaminopyridine, alkylpyridine, benzimidazole, pyrzaole, quinoline, and so on, have been used as promising additives in liquid-type electrolytes [161–164].

## 14.8 Future aspects in solid-state electrolytes

The development of DSSCs, QDSSCs, and PSCs are most promising low cost, easy preparation, and environment benign photovoltaic technologies, becoming a promising alternative to conventional photovoltaic devices. The redox couple, known as electrolyte, is playing a key role in the improvement of performance. However, proper doping is needed in order to achieve high open circuit voltage with minimum back reaction. The PCE of DSSCs has greatly improved, up to 13%, by using unique composition of electrolyte and dye absorber. In the case of QDSSCs, the initial $<$1% PCE has now reached 12% with the help of different QDs, passivation layers, counter electrodes, and electrolytes.

## 14.9 Conclusion and outlook

In this chapter we have discussed the state-of-the-art of low-cost photovoltaic technology that includes DSSCs, QDSSCs, and PSCs. The stability of DSSCs, as well as QDSSCs, is a major issue and that can be solved by using quasi-solid-state or solid-state electrolytes. Although the thermosetting-based devices showed higher stability than conventional liquid-based electrolyte, there is still efficiency lagging behind. Therefore this is the right pathway for the new researcher to develop more stable and efficient electrolyte for low-cost solar cells. In the case of PSCs, certified efficiency has been demonstrated only for small molecule-based HTM, such as spiro-MeOTAD. The $V_{oc}$ of the device can be improved by precise doping of LiTFSI and FK209 additives. However, still these HTMs are expensive and having low stability. Therefore the future big-leaf in low-cost photovoltaic technology is to develop unique composition of electrolyte that facilitates the high efficiency as well as stability at low cost.

## Acknowledgment

This research work was supported by The Leading Human Resource Training Program of Regional Neo Industry through the National Research Foundation of Korea (NRF), funded by the Ministry of Science, ICT, and future Planning (Grant Number) (NRF-2016H1D5A1909787). This research is also supported by the National Research Foundation of Korea (NRF) (NRF-2017R1A2B4008117). This work was also supported by Korea Research Fellowship Program through the National Research Foundation of Korea (NRF), funded by the Ministry of Science, ICT, and Future Planning (2016H1D3A1909289) for an outstanding overseas young researcher.

## References

[1] B. O'Regan, M. Grätzel, Nature 353 (1991) 737–740.
[2] D. Chapin, C. Fuller, G.J. Pearson, Appl. Phys. 25 (1954) 676.
[3] M. Green, K. Emery, Y. Hishikawa, W. Warta, E. Dunlop, Prog. Photovoltaics Res. Appl. 22 (2014) 1.
[4] N.S. Lewis, Science 315 (2007) 798–801.
[5] R.D. Schaller, M.A. Petruska, V.I. Klimov, Appl. Phys. Lett. 87 (2005) 253102.
[6] P.V. Kamat, J. Phys. Chem. C 112 (2008) 18737–18753.
[7] V. Gonzaalez-Pedro, X. Xu, I. Mora-Seroo, J. Bisquert, ACS Nano 4 (2010) 5783.
[8] W. Ma, S.L. Swisher, T. Ewers, J. Engel, V.E. Ferry, H.A. Atwater, et al., ACS Nano 5 (2011) 8140–8147.
[9] D. Segets, J.M. Lucas, R.N.K. Taylor, M. Scheele, H. Zheng, A.P. Alivisatos, et al., ACS Nano 6 (2012) 9021–9032.

[10] A. Kojima, K. Teshima, Y. Shirai, T. Miyasaka, J. Am. Chem. Soc. 131 (2009) 6050–6051.
[11] (a) J.-H. Im, C.-R. Lee, J.W. Lee, S.-W. Park, N.-G. Park, Nanoscale 3 (2011) 4088–4093. (b) H.-S. Kim, C.-R. Lee, J.-H. Im, K.-B. Lee, T. Moehl, A. Marchioro, et al., Sci. Rep. 2 (2012) 591.
[12] J. Burschka, N. Pellet, S.-J. Moon, R. Humphry-Baker, P. Gao, M.K. Nazeeruddin, et al., Nature 499 (2013) 316.
[13] H. Zhou, Q. Chen, G. Li, S. Luo, T. Song, H.-S. Duan, et al., Science 345 (2014) 542–546.
[14] N.J. Jeon, J.H. Noh, Y.C. Kim, W.S. Yang, S. Ryu, S.I. Seok, Nat. Mater. 13 (2014) 897–903.
[15] N.J. Jeon, J.H. Noh, W.S. Yang, Y.C. Kim, S. Ryu, J. Seo, et al., Nature 517 (2015) 476–480.
[16] S.S. Shin, E.J. Yeom, W.S. Yang, S. Hur, M.G. Kim, J. Im, et al., Science 356 (2017) 167–171.
[17] W.S. Yang, B.W. Park, E.H. Jung, N.J. Jeon, Y.C. Kim, D.U. Lee, et al., Science 356 (2017) 1376–1379.
[18] M. Gratzel, Nature 414 (2001) 338.
[19] I. Mora-Sero, S. Gimenez, F. Fabregat-Santiago, R. Gomez, Q. Shen, T. Toyoda, et al., Acc. Chem. Res. 42 (2009) 1848–1857.
[20] J. Wu, Z. Lan, J. Lin, M. Huang, Y. Huang, L. Fan, et al., Chem. Rev. 115 (2015) 2136–2173.
[21] S.S. Mali, P.S. Patil, C.K. Hong, ACS Appl. Mater. Interfaces 6 (2014) 1688–1696.
[22] J. Liu, R. Li, X. Si, D. Zhou, Y. Shi, Y. Wang, et al., Energy Environ. Sci. 3 (2010) 1924–1928.
[23] G. Zhang, H. Bala, Y. Cheng, D. Shi, X. Lv, Q. Yu, et al., Chem. Commun. (2009) 2198–2200.
[24] W. Zeng, Yiming Cao, Yu Bai, Yinghui Wang, Yushuai Shi, Min Zhang, et al., Chem. Mater. 22 (2010) 1915–1925.
[25] Qifeng Zhang, Tammy P. Chou, Bryan Russo Samson, A. Jenekhe, Angw Guozhong Cao, Chemie Int. 47, 2008, pp. 2402–2406.
[26] Jihuai Wu, Jiangli Wang, Jianming Lin, Yaoming Xiao, Gentian Yue, et al., Sci. Rep. 3 (2013) 2058.
[27] Daesub Hwang, Jun-Su Jin, Horim Lee, Hae-Jin Kim, Heejae Chung, Dong Young Kim, et al., Sci. Rep. 4 (2014) 7353.
[28] Chang Su Shim, Sawanta S. Mali, Ryota Aokie, et al., RSC Adv. 5 (2015) 91708–91715.
[29] Muhammad M. Mirza, Felix J. Schupp, Jan A. Mol, Donald A. MacLaren, G. Andrew, D. Briggs, et al., Sci. Rep. 3 (2013) 3004.
[30] Mingfei Xu, Min Zhang, Mariachiara Pastore, Renzhi Li, Filippo De Angelis, Peng Wang, Chem. Sci. 3 (2012) 976–983.
[31] Ning Cai, Jing Zhang, Mingfei Xu, Min Zhang, Peng Wang, Adv. Funct. Mater. 23 (2013) 3539–3547.
[32] Jing Zhang, Zhaoyang Yao, Yanchun Cai, Lin Yang, Mingfei Xu, Renzhi Li. Min Zhang, et al., Energy Environ. Sci. 6 (2013) 1604–1614.
[33] Jun-Ho Yum, Etienne Baranoff, Florian Kessler, Thomas Moehl, Shahzada Ahmad, Takeru Bessho, et al., Nat. Commun. 3 (2012) 631.
[34] S. Mathew, A. Yella, P. Gao, R. Humphry-Baker, B.F. Curchod, N. Ashari-Astani, et al., Nat. Chem. 6 (2014) 242–247.
[35] Xuefeng Lu, Quanyou Feng, Tian Lan, Gang Zhou, Zhong-Sheng Wang, Chem. Mater. 24 (2012) 3179–3187.

[36] Tian Lan, Xuefeng Lu, Lu Zhang, Yijing Chen, Gang Zhou, Zhong-Sheng Wang, J. Mater. Chem. A 3 (2015) 9869–9881.
[37] Peng Wang, Bernard Wenger, Robin Humphry-Baker, Jacques-E. Moser, Joël Teuscher, Willi Kantlehner, et al., J. Am. Chem. Soc. 127 (2005) 6850.
[38] A Binary Ionic Liquid Electrolyte to Achieve ≥7% Power Conversion Efficiencies in Dye-Sensitized Solar Cells, Chem. Mater. 16 (2004) 2694.
[39] Peng Wang, C.édric Klein, Robin Humphry-Baker, Shaik M. Zakeeruddin, Michael Grätzel, Appl. Phys. Lett. 86 (2005) 123508.
[40] Zhaofu Fei, Daibin Kuang, Dongbin Zhao, Cedric Klein, Wee Han Ang, Shaik M. Zakeeruddi, et al., Inorg. Chem. 45 (2006) 10407–10409.
[41] S. Ito, S. M. Zakeeruddin, R. Humphry-Baker, P. Liska, R. Charvet, P. Comte, et al., Adv. Mater. 18 (2006) 1202.
[42] Xiaojian Chen, Dan Xu, Lihua Qiu, Shichao Li, Wei Zhang, Feng Yan, J. Mater. Chem. A 1 (2013) 8759–8765.
[43] Frédéric Sauvage, Sarine Chhor, Arianna Marchioro, Jacques-E. Moser, Michael Graetzel, Am. Chem. Soc. 133 (2011) 13103.
[44] G. Smestad, Sol. Energy Mater. Sol. Cells 32 (1994) 273.
[45] A. Hagfeldt, B. Didriksson, T. Palmqvist, H. Lindström, S. Södergren, H. Rensmo, et al., Sol. Energy Mater. Sol. Cells 31 (1994) 481.
[46] P.M. Sommeling, M. Späth, H.J.P. Smit, N.J. Bakker, J.M. Kroon, J. Photochem. Photobio. A Chem. 164 (2004) 137.
[47] N. Fuke, R. Katoh, A. Islam, M. Kasuya, A. Furube, A. Fukui, et al., Energy Environ. Sci. 2 (2009) 1205.
[48] S.S. Mali, C.S. Shim, H.J. Kim, J.V. Patil, D.H. Ahn, P.S. Patil, et al., Electrochim. Acta 166 (2015) 356–366.
[49] D.R. MacFarlane, M. Forsyth, Adv. Mater. 13 (95) (2001) 7.
[50] X. Gao, F. Lu, B. Dong, T. Zhou, Y. Liu, L. Zheng, RSC Adv. 5 (2015) 63732.
[51] F. Cao, G. Oskam, P. Searson, J. Phys. Chem. 99 (1995) 17071.
[52] J. Wu, P. Li, S. Hao, H. Yang, Z. Lan, Electrochim. Acta 52 (2007) 5334.
[53] H. Yang, M. Huang, J. Wu, Z. Lan, S. Hao, J. Lin, Mater. Chem. Phys. 110 (2008) 38.
[54] Y. Shi, C. Zhan, L. Wang, B. Ma, R. Gao, Y. Zhu, et al., Phys. Chem. Chem. Phys. 11 (2009) 4230.
[55] A. Stephan, Eur. Polym. J. 42 (2006) 21.
[56] O. Ileperuma, G. Kumara, H. Yang, K. Murakami, J. Photochem. Photobiol. A 217A (2011) 308.
[57] M. Kang, K. Ahn, J. Lee, J. Power Sources 180 (2008) 896.
[58] Z. Lan, J. Wu, S. Hao, J. Lin, M. Huang, Y. Huang, Energy Environ. Sci. 2 (2009) 524.
[59] T. Kato, A. Okazaki, S. Hayase, Chem. Commun. (2005) 363.
[60] M. Parvez, I. In, J. Park, S. Lee, S. Kim, Sol. Energy Mater. Sol. Cells 95 (SI) (2011) 318.
[61] Z. Tang, J. Wu, Q. Liu, Z. Lan, L. Fan, J. Lin, et al., Electrochim. Acta 55 (2010) 4883.
[62] R. Komiya, L. Han, R. Yamanaka, A. Islam, T. Mitate, J. Photochem. Photobiol. A 164 (2004) 123.
[63] Z. Tang, Q. Liu, Q. Tang, J. Wu, J. Wang, S. Chen, et al., Electrochim. Acta 58 (2011) 52.
[64] S. Park, J. Lim, I. Song, N. Atmakuri, S. Song, Y. Kwon, et al., Adv. Energy Mater. 2 (2012) 219.
[65] S. Park, I. Song, J. Lim, Y. Kwon, J. Choi, S. Song, et al., Energy Environ. Sci. 6 (2013) 1559.

[66] S. Park, J. Lim, Y. Kwon, I. Song, J. Choi, S. Song, et al., Adv. Energy Mater. 3 (2013) 184.
[67] R.-X. Dong, S.-Y. Shen, H.-W. Chen, C.-C. Wang, P.-T. Shih, C.-T. Liu, et al., J. Mater. Chem. A 1 (2013) 8471.
[68] F. Croce, G. Appetecchi, L. Persi, B. Scrosati, Nature 394 (1998) 456.
[69] F. Croce, L. Persi, F. Ronci, B. Scrosati, Solid State Ionics 135 (2000) 47.
[70] A. Clemente, S. Panero, E. Spila, B. Scrosati, Solid State Ionics 85 (1996) 273.
[71] N. Yu, L. Gong, H. Song, Y. Liu, D. Yin, J. Solid State Chem. 180 (2007) 799.
[72] P. Walden, Bull. Acad, Imper. Sci. (St. Petersburg) 1800 (1914) 405–422.
[73] M. Freemantle, Chem. Eng. News 78 (2000) 37.
[74] S.S. Mali, C.A. Betty, P.N. Bhosale, P.S. Patil, C.K. Hong, Sci. Rep. 4 (2014) 5451.
[75] J. Lemus, J. Palomar, M.A. Gilarranz, J.J. Rodriguez, Adsorption 17 (2011) 561.
[76] C. Han, S. Ho, Y. Lin, Y. Lai, W. Liang, Y.C. Yang, Micropor. Mesopor. Mater. 131 (2010) 217.
[77] L.W.L. Chang, B. Zhao, Z.Y. Gaosong, S.W. Zheng, Inorg. Chem. 47 (2008) 1443.
[78] P. Wang, S. Zakeeruddin, I. Exnar, M. Gratzel, Chem. Commun. (2002) 2972.
[79] D. Shi, N. Pootrakulchote, R. Li, J. Guo, Y. Wang, S. Zakeeruddin, et al., Phys. Chem. C 112 (2008) 17046.
[80] S.S. Mali, S.K. Desai, S.S. Kalagi, C.A. Betty, P.N. Bhosale, R.S. Devan, et al., Dalton Trans. 41 (2012) 6130–6136.
[81] S.S. Mali, S.K. Desai, D.S. Dalavi, C.A. Betty, P.N. Bhosale, P.S. Patil, Photochem. Photobiol. Sci. 10 (2011) 1652–1658.
[82] Zhonglin Du, Hua Zhang, Huili Bao, Xinhua Zhong, J. Mater. Chem. A 2 (2014) 13033–13040.
[83] Haitao Zhou, Lin Li, Dianli Jiang, Yingbing Lu, Kai Pan, RSC Adv. 6 (2016) 67968–67975.
[84] Y.-F. Xu, W.Q. Wu, Hua-Shang Rao, Hong-Yan Chen, Dai-Bin Kuang, Cheng-Yong Su, Nano Energy 11 (2015) 621–630.
[85] Hui Huang, Lei Pan, Chiew Keat Lim, Hua Gong, Jun Guo, Man Siu Tse, et al., Small 9 (2013) 3153–3160.
[86] Minsu Seol, Heejin Kim, Youngjo Tak, Kijung Yong, Chem. Commun. 46 (2010) 5521–5523.
[87] Tridip Ranjan Chetia, Mohammad Shaad Ansari, Mohammad Qureshi, ACS Appl. Mater. Interfaces 7 (2015) 13266–13279.
[88] S.S. Mali, H.J. Kim, P.S. Patil, C.K. Hong, Dalton Trans. 42 (2013) 16961–16967.
[89] Hao-Lin Feng, Wu-Qiang Wu, Hua-Shang Rao, Long-Bin Li. Dai-Bin Kuang, Cheng-Yong Su, J. Mater. Chem. A 3 (2015) 14826–14832.
[90] Bin Bin Jin, Ye Feng Wang, Jing Hui Zeng, Chem. Phys. Lett. 660 (2016) 76–80.
[91] Haifeng Zhao, Fei Huang, Juan Hou, Zhiyong Li, Qiang Wu, Haibin Cao, et al., ACS Appl. Mater. Interfaces 8 (2016) 26675–26682.
[92] Tridip Ranjan Chetia, Mohammad Shaad Ansari, Mohammad Qureshi, J. Mater. Chem. A 4 (2016) 5528–5541.
[93] Long-Bin Li, Yu-Fen Wang, Hua-Shang Rao, Wu-Qiang Wu, Ke-Nan Li, Cheng-Yong Su, et al., ACS Appl. Mater. Interfaces 5 (2013) 11865–11871.
[94] D. Punnoose, C.H.S.S. Pavan Kumar, H.W. Seo, M. Shiratani, A.E. Reddy, S. Srinivasa Rao, et al., New J. Chem. 40 (2016) 3423–3431.
[95] Zhang Lan, Lu Liu, Miaoliang Huang, Jihuai Wu, Jianming Lin, J. Mater. Sci. Mater. Electron. 26 (2015) 7914–7920.
[96] J. Yu, W. Wang, Z. Pan, J. Du, Z. Ren, W. Xue, et al., J. Mater. Chem. A 5 (2017) 14124.
[97] J.P. Park, J.H. Heo, S.H. Im, S.-W. Kim, J. Mater. Chem. A 4 (2016) 785–790.

[98] S.H. Im, H. Kim, S.W. Kim, S.W. Kim, S.I. Seok, Energy Environ. Sci. 4 (2011) 4181.
[99] Jun Du, Zhonglin Du, Jin-Song Hu, Zhenxiao Pan, Qing Shen, Jiankun Sun, et al., J. Am. Chem. Soc. 138 (2016) 4201–4209.
[100] M. Wu, X. Lin, Y. Wang, T. Ma, J. Mater. Chem. A 3 (2015) 19638–19656.
[101] J. Duan, H. Zhang, Q. Tang, B. He, L. Yu, J. Mater. Chem. A 3 (2015) 17497–17510.
[102] Y. Liao, J. Zhang, W. Liu, W. Que, X. Yin, D. Zhang, et al., Nano Energy 11 (2015) 88–95.
[103] H. Wei, G. Wang, J. Shi, H. Wu, Y. Luo, D. Li, et al., J. Mater. Chem. A 4 (2016) 14194–14203.
[104] J. Du, X. Meng, K. Zhao, Y. Li, X. Zhong, J. Mater. Chem. A 3 (2015) 17091–17097.
[105] G. Jiang, Z. Pan, Z. Ren, J. Du, C. Yang, W. Wang, et al., J. Mater. Chem. A 4 (2016) 11416–11421.
[106] C.-Y. Chou, C.-P. Lee, R. Vittal, K.-C. Ho, J. Power Sources 196 (2011) 6595–6602.
[107] L. Li, X. Yang, J. Gao, H. Tian, J. Zhao, A. Hagfeldt, et al., J. Am. Chem. Soc. 133 (2011) 8458–8460.
[108] Z. Ning, C. Yuan, H. Tian, Y. Fu, L. Li, L. Sun, et al., J. Mater. Chem. 22 (2012) 6032–6037.
[109] K. Meng, P.K. Surolia, O. Byrne, K.R. Thampi, J. Power Sources 275 (2015) 681–687.
[110] V. Jovanovski, V. Gonzalez-Pedro, S. Gimenez, E. Azaceta, G. Cabanero, H. Grande, et al., J. Am. Chem. Soc. 133 (2011) 20156–20159.
[111] W. Feng, Y. Li, J. Du, W. Wang, X. Zhong, J. Mater. Chem. A 4 (2016) 1461–1468.
[112] H. Kim, I. Hwang, K. Yong, ACS Appl. Mater. Interfaces 6 (2014) 11245–11253.
[113] Z. Yu, Q. Zhang, D. Qin, Y. Luo, D. Li, Q. Shen, et al., Electrochem. Commun. 12 (2010) 1776–1779.
[114] Z. Huo, L. Tao, S. Wang, J. Wei, J. Zhu, W. Dong, et al., J. Power Sources 284 (2015) 582–587.
[115] W. Feng, L. Zhao, J. Du, Y. Li, X. Zhong, J. Mater. Chem. A 4 (2016) 14849–14856.
[116] H. Lee, H.C. Leventis, S.-J. Moon, P. Chen, S. Ito, S.A. Haque, et al., Adv. Funct. Mater. 19 (2009) 2735–2742.
[117] I. Barcelo, J.M. Campina, T. Lana-Villarreal, R. Gomez, Phys. Chem. Chem. Phys. 14 (2012) 5801–5807.
[118] J. Duan, Q. Tang, Y. Sun, B. He, H. Chen, RSC Adv. 4 (2014) 60478–60483.
[119] Y. Yang, W. Wang, J. Power Sources 285 (2015) 70–75.
[120] W. Shockley, H.J. Queisser, J. Appl. Phys. 32 (1961) 510–519.
[121] M. Booth, A.P. Brown, S.D. Evans, K. Critchley, Chem. Mater. 24 (2012) 2064–2070.
[122] A. Rockett, Thin Solid Films 480 (2005) 2–7.
[123] H. McDaniel, N. Fuke, J.M. Pietryga, V.I. Klimov, J. Phys. Chem. Lett. 4 (2013) 355–361.
[124] H. McDaniel, N. Fuke, N.S. Makarov, J.M. Pietryga, V.I. Klimov, Nat. Commun. 4 (2013) 2887. Available from: https://doi.org/10.1038/ncomms3887.
[125] Z. Pan, I. Mora-Sero, Q. Shen, H. Zhang, Y. Li, K. Zhao, et al., J. Am. Chem. Soc. 136 (2014) 9203–9210.
[126] J.Y. Kim, J. Yang, J.H. Yu, W. Baek, C.-H. Lee, H.J. Son, et al., ACS Nano 9 (2015) 11286–11295.

[127] H.L. Wells, Z. Anorg. Chem. 3 (1893) 195.
[128] A. Poglitsch, et al., J. Chem. Phys. 11 (1987) 87.
[129] A. Kojima, K. Teshima, Y. Shirai, T. Miyasaka, J. Am. Chem. Soc. 131 (17) (2009) 6050–6051.
[130] J.-H. Im, et al., Nanoscale 3 (2011) 4088.
[131] J. Burschka, et al., Nature 316 (2013) 499.
[132] Nam Joong Jeon, Jaemin Lee, Jun Hong Noh, Mohammad Khaja Nazeeruddin, Michael Grätzel, Sang Il Seok, J. Am. Chem. Soc. 135 (2013) 19087–19090.
[133] Nam Joong Jeon, Hag Geun Lee, Young Chan Kim, Jangwon Seo, Jun Hong Noh, Jaemin Lee, et al., J. Am. Chem. Soc. 136 (2014) 7837.
[134] Hairong Li Kunwu Fu, Pablo P. Boix, Lydia H. Wong, Anders Hagfeldt, Michael Grätzel, Subodh G. Mhaisalkar, et al., ChemSusChem 7 (2014) 3420–3425.
[135] Thirumal Krishnamoorthy, Fu Kunwu, Pablo P. Boix, Hairong Li, Teck Ming Koh, Wei Lin Leong, et al., J. Mater. Chem. A 2 (2014) 6305–6309.
[136] Anurag Krishna, Dharani Sabba, Hairong Li, Jun Yin, Pablo P. Boix, Cesare Soci, et al., Chem. Sci. 5 (2014) 2702–2709.
[137] K. Do, H. Choi, K. Lim, H. Jo, J.W. Cho, M.K. Nazeeruddin, et al., Chem. Commun. 50 (2014) 10971–10974.
[138] Antonio Abate, Miquel Planells, Derek J. Hollman, Vishal Barthi, Suresh Chand, Henry J. Snaith, et al., Phys. Chem. Chem. Phys. 17 (2015) 2335.
[139] Yakun Song, Songtao Lv, Xicheng Liu, Xianggao Li, Shirong Wang, Huiyun Wei, et al., Chem. Commun. 50 (2014) 15239.
[140] Eran Edri, Saar Kirmayer, Michael Kulbak, G. Hodes, David Cahen, J. Phys. Chem. Lett. 5 (2014) 429–433.
[141] Bo Xu, Esmaeil Sheibani, Peng Liu, Jinbao Zhang, Haining Tian, Nick Vlachopoulos, et al., Adv. Mater. 26 (2014) 6629–6634.
[142] Sang Do Sung, Min Soo Kang, In Taek Choi, Hong Mo Kim, Hyoungjin Kim, MunPyo Hong, et al., Chem. Commun. 50 (2014) 14161.
[143] Yunlong Guo, Chao Liu, Kento Inoue, Koji Harano, Hideyuki Tanaka, Eiichi Nakamura, J. Mater. Chem. A 2 (2014) 13827.
[144] Bing Cai, Yedi Xing, Zhou Yang, Wen-Hua Zhang, Jieshan Qiu, Environ. Sci. 6 (2013) 1480.
[145] Jin Hyuck Heo, Sang Hyuk Im, Jun Hong Noh, et al., Nat. Photonics 7 (2013) 486–491.
[146] Zonglong Zhu, Yang Bai, Harrison Ka, Hin Lee, Cheng Mu, Teng Zhang, et al., Adv. Funct. Mater. 24 (2014) 7357.
[147] M.S. Sadia Ameen, H.-K.Seo Akhtar, Hyung-Shik Shin, Langmuir 30 (2014) 12786.
[148] S.S. Mali, A.I. Inamdar, H.S. Im, S.E. Shim, C.K. Hong, Nanoscale 9 (2017) 3095–3104.
[149] S.S. Mali, C.S. Shim, H.J. Kim, P.S. Patil, C.K. Hong, Nanoscale 8 (2016) 2664–2677.
[150] Fabrizio Giordano, Antonio Abate, Juan Pablo Correa Baena, Michael Saliba, Taisuke Matsui, Sang Hyuk Im, et al., Nat. Commun. 7 (2016) 10379.
[151] Minwoo Park, Jae Yup Kim, Hae Jung Son, Chul-Ho Lee, Seung Soon Jang, Min Jae Ko, Nano Energy 26 (2016) 208–215.
[152] Michael Saliba, Taisuke Matsui, Ji-Youn Seo, Konrad Domanski, Juan-Pablo Correa-Baena, Mohammad Khaja Nazeeruddin, et al., Energy Environ. Sci. 9 (2016) 1989–1997.
[153] M. Saliba, et al., Science 354 (2016) 206.
[154] D. Bi, W. Tress, M.I. Dar, P. Gao, J. Luo, C. Renevier, et al., Sci. Adv. 2 (2016) e1501170. Available from: https://doi.org/10.1126/sciadv.1501170.

[155] Seong Sik Shin, Eun Joo Yeom, Woon Seok Yang, Seyoon Hur, Min Gyu Kim, Jino Im, et al., Science 356 (6334) (2017) 167–171.
[156] S.S. Mali, C.S. Shim, C.K. Hong, NPG Asia Mater. 7 (2015) e208.
[157] S.S. Mali, C.S. Shim, P.S. Patil, C.K. Hong, Mater. Today 18 (2015) 172.
[158] J. Burschka, F. Kessler, M.K. Nazeeruddin, M. Grätzel, Chem. Mater. 25 (2013) 2986–2990.
[159] E.J. Juarez-Perez, M.R. Leyden, S. Wang, L.K. Ono, Z. Hawash, Y. Qi, Chem. Mater. 28 (2016) 5702–5709.
[160] A. Abate, D.J. Hollman, J. Teuscher, S. Pathak, R. Avolio, G. D'Errico, et al., J. Am. Chem. Soc. 135 (2013) 13538–13548.
[161] F. Bella, A. Sacco, D. Pugliese, M. Laurenti, S. Bianco, J. Power Sources 264 (2014) 333.
[162] H. Kusama, Y. Konishi, H. Sugihara, H. Arakawa, Sol. Energy Mater. Sol. Cells 80 (2003) 167.
[163] H. Kusama, H. Arakawa, Sol. Energy Mater. Sol. Cells 81 (2004) 87.
[164] H. Kusama, H. Arakawa, J. Photochem. Photobiol. A 162 (2004) 441.

This page intentionally left blank

CHAPTER 15

# Polymer nanocomposites for solar cells: research trends and perspectives

**Iliya E. Kuznetsov[1], Alexander V. Akkuratov[1] and Pavel A. Troshin[1,2]**
[1]Institute for Problems of Chemical Physics of Russian Academy of Sciences, Chernogolovka, Russian Federation
[2]Skolkovo Institute of Science and Technology, Moscow, Russian Federation

Contents



## 15.1 Introduction

### 15.1.1 Organic solar cells as a basis of a promising photovoltaic technology

Solar energy has a primary importance among all renewable energy resources. Indeed, the energy delivered from the Sun to the Earth surface in one hour well exceeds the annual demand of the present population of our planet. Photovoltaic (PV) devices allow for direct conversion of the solar energy to electricity. The power conversion efficiencies (PCEs) of the best laboratory crystalline silicon solar cells reach 26.7%, while the

*Nanomaterials for Solar Cell Applications*
DOI: https://doi.org/10.1016/B978-0-12-813337-8.00015-1

large area PV modules are 2–3% less efficient [1]. However, massive implementation of silicon solar cells has been long time limited by their high cost. For instance, the crystalline silicon modules can be installed at the cost of 1–3 USD per every watt of energy generated at maximal (peak) solar irradiance (denoted as watt-peak, $W_p$) [2]. Recently, solar-generated electricity became cheaper than the energy produced by combustion of fossil fuel, at least in Dubai with over 300 sunny days per year and pretty high average insolation [3]. For other most populated areas in the world, silicon PVs can hardly compete with the conventional energy sources. Therefore, mostly political rather than economic aspects drive the development and implementation of the PV technology.

To shift the paradigm on the world energy market, the cost of the solar-generated electricity should fall to 20 cents per $W_p$ and below, which is the target for the 3rd generation PV technologies currently under development [2]. There has been a big expectation for organic solar cells, which can potentially deliver moderate PCEs of 10%–15% in combination with ultra-low module costs (20–40 USD $m^{-2}$) and decent operation lifetimes of 10–20 years. These benchmarks are expected to be achieved for organic solar cells within a decade. Indeed, certified PCEs of 11%–12% were reported in 2017–2018 for single junction cells based on organic materials, while small modules delivered PCE of ~10% [1]. Lifetimes of 7–15 years were projected for conjugated polymer-based devices using accelerated tests [4,5]. Helatek declared extrapolated lifetimes of >25 years for the organic PV product based on low molecular weight materials [6]. Further advancement of organic solar cells with respect to efficiency, lifetime, module design, and production technologies might lead to a breakthrough in the renewable energies. Many researchers believe that organic PV will make the dream come true by decreasing the cost of the solar-generated electricity well below the threshold dictated by current low prices for fossil fuels.

In this review, we will highlight the main research trends in the design of bulk heterojunction organic solar cells based on fullerene-polymer nanocomposites. The content of this review and provided citations are organized for didactical purposes only and do not reflect the chronology of the research in the field and/or have any claim of completeness. We also intentionally do not cover substantial progress achieved in the field by introducing non-fullerene acceptor materials, which was summarized in the recent reports on that topic [7–9].

### 15.1.2 Architecture and operation principle of bulk heterojunction solar cells

The bulk heterojunction organic solar cells were invented in 1992 and attracted enormous attention of the researchers for the next decades [10–12]. According to the bulk heterojunction concept, p-type and n-type materials are mixed together and organized at the nanoscale to form the three-dimensional interpenetrating networks. A schematic layout of the organic bulk heterojunction solar cell is shown in Fig. 15.1. The active layer of this device represents the composite of the electron donor (p-type, hexagons) and electron acceptor (n-type, spheres) materials, which are split apart in small clusters. The idealized ordering of these nanometer-sized domains shown in the drawing enables efficient generation of positive and negative charge carriers and their transport in opposite directions toward respective electrodes. Actually, the massively increased interface between the p-type and n-type materials represents the strongest advantage of the bulk heterojunction solar cells over the planar junction devices known before [13].

Both p-type and n-type materials absorb photons under illumination producing the corresponding excitons. The vast majority of these excitons are formed inside nanoclusters of pristine p-type and n-type semiconductors and have to diffuse to the donor/acceptor interface (p/n heterojunction), where charge separation takes place, producing the charge carriers. Therefore, the size of the grains formed by the phases of pristine p- and

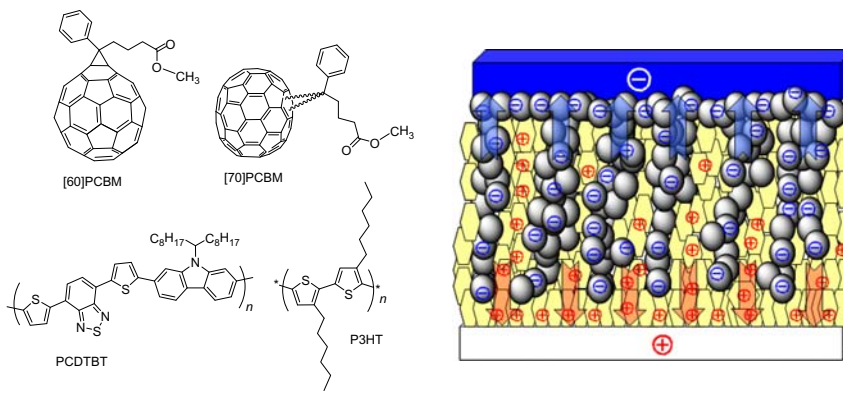


**Figure 15.1** Schematic layout of the ideal organic bulk heterojunction solar cell. Electron donor materials (*hexagons*) are generally represented by conjugated polymers (e.g., P3HT or PCDTBT), while the fullerene derivatives, such as [60]PCBM and [70]PCBM, are usually applied as acceptor components (*spheres*).

n-type materials should be comparable to the exciton diffusion lengths in organic semiconductors (5–20 nm) [14–16]. Splitting of excitons to mobile charge carriers in organic solar cells can be very efficient if the morphology of the bulk heterojunction layer is optimized. This fact is manifested in the experimental observation of ~100% internal quantum efficiency (IQE) for some bulk heterojunction solar cells [17].

The energy levels of the p- and n-type materials should be properly aligned for efficient generation of charge carriers. Generally, HOMO and LUMO levels of the donor must lie at least 0.3 eV higher in energy as compared to the same frontier orbitals of the acceptor in order to provide a sufficient driving force for the charge separation. However, using some non–fullerene acceptors might allow one to reduce the aforementioned energy offset down to 0.1 eV or even lower while keeping the high efficiency of the photoinduced charge generation [18–20]. Therefore, the rationally designed non-fullerene acceptors enable minimal energy losses and, consequently, might provide increased open circuit voltages and higher efficiencies in PV cells, which represents their strongest advantage over the conventional fullerene derivatives.

Photoinduced electron transfer in bulk heterojunction systems usually produces hole and electron pairs, where charges remain bound by the coulombic attraction forces (so-called geminate polaron pairs [21–23]). There are many factors, which are believed to affect the splitting of the geminate polaron pairs to the mobile charge carriers. Among them, the built-in electric field induced by the difference in the work functions of the electrode materials, the excessive energy of photons (compared to the band gap of the blend) released as a heat as well as the potential jump at the p/n heterojunction probably provide the strongest contributions [24].

Positive and negative charge carriers should be transported in opposite directions and collected at the respective electrodes of the PV cell. To achieve efficient charge transport, both p-type and n-type materials should have high and balanced charge carrier mobilities. Additionally, the composite morphology should be ideal, providing direct paths to the electrodes and possessing minimal number or even no dead-ends. The concentration of traps for charge carriers in the active layer and at the active layer/electrode interfaces should be minimized. Finally, the electrodes must have proper work functions: hole-collecting electrode should match HOMO of the p-type component, while the electron-collecting electrode should be aligned with respect to the LUMO of the n-type material. The selectivity of the electrodes and their collection efficiency

can be enhanced using various buffer (inter)layers represented by organic and inorganic p-type and n-type semiconductors, some dopants, molecules with high dipole moments, etc. There are some specialized reviews covering the progress in the design of buffer layer materials for organic solar cells [25–28]. We emphasize that all the aforementioned conditions should be satisfied in order to suppress the bimolecular recombination of charge carriers and enable their facile collection thus delivering high photon-to-current conversion efficiencies in organic solar cells.

The above-presented operation principle of organic bulk heterojunction solar cells was significantly simplified for didactical purposes. Interested readers are referred to the specialized reviews and monographs providing more comprehensive overview of this topic [29–34].

### 15.1.3 Characterization of organic photovoltaic cells and their main parameters

Organic PV cells are usually characterized by measuring their current density–voltage characteristics ($J-V$ curves) in dark and under illumination. The illumination should simulate the real solar light spectrum AM1.5G (Air Mass 1.5 Global) with the best possible precision, which is a big challenge. The characteristics of the instruments used for this purpose (solar simulators) depend a lot on the optical design, implemented light source (e.g. metal-halogen or xenon lamp, sulfur plasma lamp, LEDs, etc.), output power, temperature, etc. Moreover, the parameters of even the most precise AAA type solar simulators can evolve rapidly due to e.g., lamp aging effects or simply after replacing the lamp. All these technical issues dramatically affect the accuracy of the measurements, leading sometimes to severe exaggerations appearing in the reports (see below). To rationalize a possible error, one should regularly measure the spectrum of the light provided by the solar simulator, compare it with the standard AM1.5G spectrum, and evaluate the mismatch factors considering the spectral response of the cell. The detailed guidelines for proper characterization of organic solar cells can be found elsewhere [35,36].

The intensity of the light provided by the solar simulator should be set to 100 mW $cm^{-2}$, generally using a calibrated cell with a known spectral response matching well the spectral response of the experimental cell. The measured PV cell should be kept and equilibrated at 25°C. While sweeping the voltage and recording the current, one can obtain the experimental $I-V$ characteristic. The voltage sweep direction and sweeping rate sometimes can be also important: this is a particular case of perovskite

solar cells, which exhibit strong hysteresis in their current–voltage characteristics [37]. This means that the same device can deliver PCE of 6% or 15%, just depending on the measurement conditions. Fortunately, the hysteresis in the current–voltage characteristics of organic solar cells appears only in very exotic cases.

The next challenge is converting the measured current to the correct current density, which requires accurate assessment of the device active area. In principle, this can be done well by direct measurements. Alternatively, the active area size can be confined by using the specific substrate and shadow mask (used for top electrode deposition) geometries. Many groups recommend applying the mask with a defined window on top of the transparent electrode of the PV device [38,39]. Indeed, this approach can be useful, though some additional errors can appear, especially in case of small "window" sizes and while using thick substrates [40].

Thus, the accurate measurements should result in the current density-voltage characteristics recorded in dark and under simulated AM1.5G illumination. These characteristics can deliver all the main parameters of the PV device: short circuit current density $J_{sc}$, open circuit voltage $V_{oc}$, fill factor (FF), and the PCE of the device ($\eta$ or PCE). Definitions of all these parameters are shown in Fig. 15.2. The PCE of the PV cell is calculated as electrical power produced by the device divided by the power of the light irradiating the device active area. The electrical power is a maximal product of the current density and voltage in the fourth quadrant. The current density and voltage at the maximal power point (MPP) on the $J-V$ curve are defined as $J_{max}$ and $V_{max}$, respectively.

To complete characterization of the PV device, one should measure its spectral response defined by external quantum efficiency (EQE) spectrum also known as incident photon to collected electron efficiency (IPCE) spectrum. Illumination of the device with a monochromatic light of a known intensity (lock-in technique allows to apply simultaneously also a background white light bias) generates photocurrent, which delivers information on the number of charge carriers collected at the electrodes. Dividing the number of the collected electrons by the number of incident photons gives us EQE (IPCE) values at each wavelength, which can be expressed in percent. For instance, EQE = 80% at the wavelength $\lambda$ means that the device generates in average 80 electrons per 100 incident photons at this wavelength (see example in Fig. 15.2). Recalculating the average number of charge carriers produced by the device per every

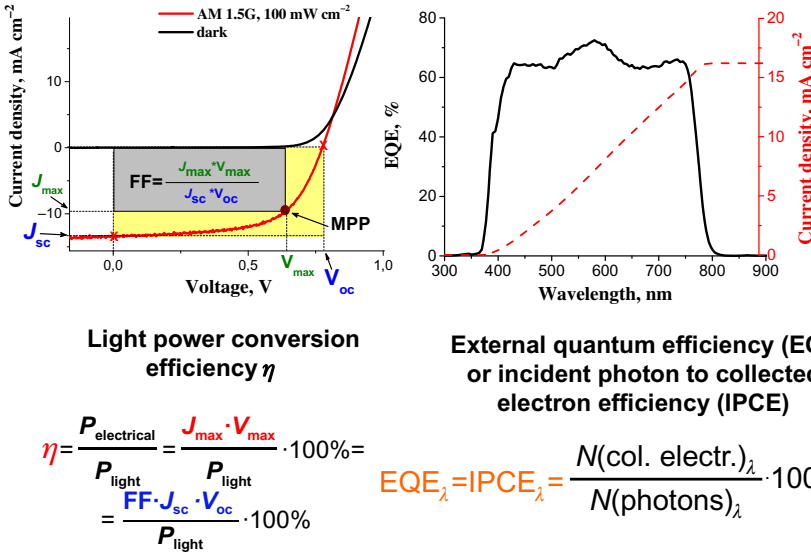


**Figure 15.2** Current density-voltage characteristics of a photovoltaic cell measured in dark and under illumination with definitions of the main parameters: $J_{sc}$, $V_{oc}$, FF, $\eta$, MPP, $J_{max}$, and $V_{max}$ (left). EQE (IPCE) spectrum of a photovoltaic cell and its integral over the reference AM1.5G spectrum giving a good estimation of the short circuit current density (right). *EQE*, external quantum efficiency; *IPCE*, incident photon to collected electron efficiency; *MPP*, maximal power point.

absorbed (but not incident) photon gives IQE. IQE is always higher than EQE because the latter does not account for the optical losses (e.g. scattering, reflection). However, one should keep in mind that correct assessment of IQE is usually a big challenge.

Integration of the EQE spectrum of a PV device over the reference AM1.5G solar irradiation spectrum provides a very good estimation of the device short circuit current density (Fig. 15.2). However, the adequate comparison of the "integrated $J_{sc}$" with the $J_{sc}$ value obtained from the $J$–V measurements with the solar simulator can be drawn only in the case when the EQE spectrum was measured under the white light bias of the same intensity (100 mW cm$^{-2}$). Background white light bias option might not be available on some EQE measurement setups. In that case, one should keep in mind that applying light bias almost always results in some minor or even considerable reduction of the EQE values, particularly due to the bimolecular recombination effects [41,42]. Therefore, the $J_{sc}$ value obtained by the integration of the "dark" EQE spectrum (recorded without light bias) should be considered as an upper estimation

for the realistic short circuit current density, which can be obtained from $J-V$ measurements at the solar simulator. In should be emphasized that $J_{sc}$ value obtained by the integration of the EQE spectrum should always be reported along with the solar cell parameters extracted from the current–voltage characteristics.

## 15.2 Improving fundamental parameters of organic solar cells using rational material design

### 15.2.1 Short circuit current density

The short circuit current density in organic PV cells is limited by a number of photons absorbed in the active layer of the device. Therefore, the active layer materials should exhibit broad absorption spectra and high extinction coefficients to harvest the solar light efficiently. Absorption edges of some conjugated polymers are presented in Fig. 15.3 in comparison with the solar irradiation spectrum and crystalline silicon band gap. It is clear that achieving high current densities in organic PV devices requires materials with low band gaps. The design of low-band-gap electron donor materials capable of the efficient light harvesting has been one of the most intensively developing research directions during the last decade [51–59].

Polymer chemists made a real breakthrough in the field, introducing many different types of very promising low-band-gap polymer structures. More or less all of them rely on the "push-pull" concept featuring conjugated polymers with alternating electron donor and electron acceptor moieties. The examples shown in Fig. 15.3 illustrate that the band gaps of organic p-type semiconductors can be engineered to a large extent. The lowest band gaps can be typically achieved by combining strong electron donor and strong electron acceptor blocks in a single polymer chain as in the case of polymers **P7** and **P8**. In principle, the short circuit current density should continuously increase with decreasing the optical band gap of the photoactive material (*solid integral line* in Fig. 15.3). However, the experimental results sometimes show considerable deviations from the theory. To understand the realistic trend, we analyzed the PV characteristics for 527 different conjugated polymers presented in the literature. Fig. 15.4 shows the dependence of the maximal reported short circuit current density on the band gap of the applied conjugated polymer. According to the general expectations, $J_{sc}$ increases almost linearly following the decrease in the polymer band gap from 2.5 to 1.6 eV. The

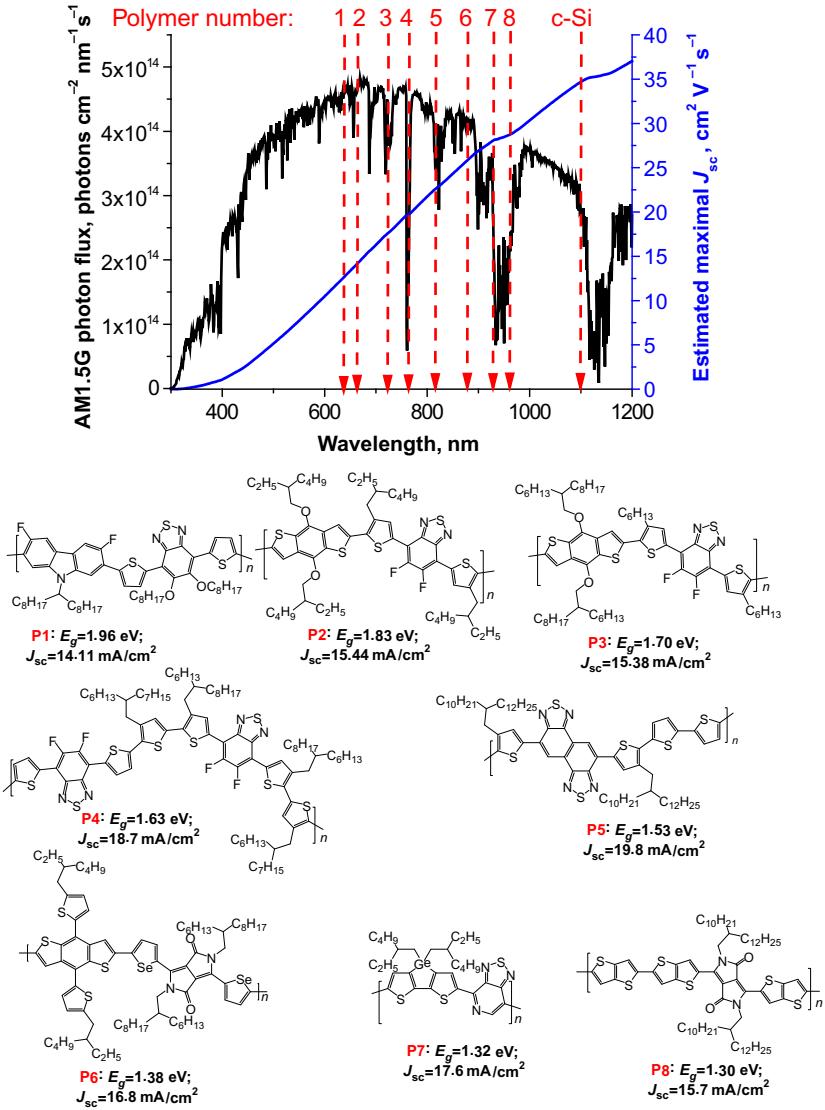


**Figure 15.3** Absorption edges of exemplary conjugated polymers **P1**–**P8** and crystalline Si given versus solar irradiation AM1.5G spectrum and molecular structures of these polymers with the reported experimental band gap and $J_{sc}$ values [43–50].

maximal short circuit current densities were reported for the polymers with the band gaps ranging from 1.45 to 1.65 eV.

Surprisingly, the materials with even lower band gaps failed to deliver improved current densities. This unusual behavior can be explained by

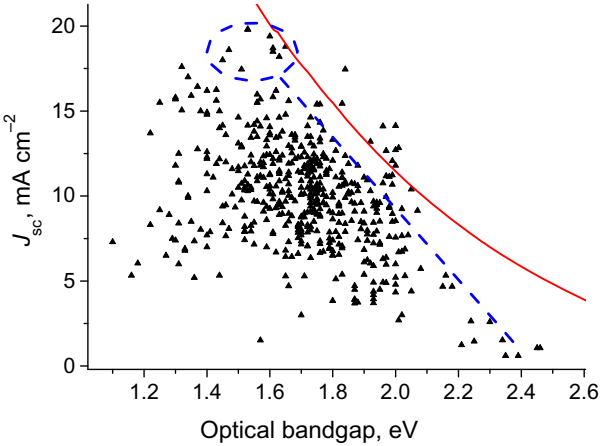


**Figure 15.4** Experimental short circuit current density values reported in the literature for 527 conjugated polymers plotted as a function of the material band gap. Solid line represents estimation of the maximal achievable $J_{sc}$, while dashed line represents a realistic relationship between the optimal experimental $J_{sc}$ values and material $E_g$.

the fact that reducing the band gap of conjugated polymers makes them much more sensitive to doping with oxygen and other aggressive chemical species. Therefore, synthesis and purification of polymers with the band gaps of 1.0−1.4 eV represents a big challenge to chemists. Most probably, all the materials with $E_g < 1.4$ eV reported in the literature were partially doped, which affected their PV performance. It should be noticed that doping results in the appearance of persistent radical species, which serve as traps facilitating recombination of charge carriers [60,61].

Solid line given in Fig. 15.4 represents a realistically achievable short circuit current density for material with the certain band gap $E_g$ under assumption that the corresponding solar cells demonstrate rectangular shaped photocurrent response with EQE = 80%. One should keep in mind that transparency of conventional ITO glass reaches 86% at maximum, while PEDOT:PSS or other charge transport materials introduce additional parasitic absorption losses. On top of that, organic photoactive films of optical thickness usually never absorb 100% of light (realistic optical densities are in the range of 0.6−0.8), which is another source of optical loss. Recombination of charge carriers (germinal and bimolecular) also reduces EQE of devices. Therefore, the used EQE = 80% value is well justified and can be considered as a realistic maximum for organic solar cells besides a very few seldom examples. Therefore, more or less all

points located above this solid line represent experimental errors resulting from exaggeration of the short-circuit current density of the cells. For instance, it is theoretically virtually impossible to reach $J_{sc} = 14.2$ mA cm$^{-2}$ for the material with the $E_g = 1.97$ eV or, in another example, obtain $J_{sc} = 17.5$ mA cm$^{-2}$ for the material with the $E_g = 1.85$ eV. The dashed line shown in Fig. 15.4 can be considered as a good realistic relationship between the experimentally achievable $J_{sc}$ values and $E_g$. Considering the fact that photocurrent response of organic solar cells almost never has a rectangular shape and average EQE within the material absorption range is usually below 80%, the experimental points located above dashed line and below solid line should also be treated with a suspicion.

To summarize, considering the data presented in Fig. 15.4, we can recommend polymer chemists focus on designing conjugated polymers with the band gaps of 1.45–1.65 eV for achieving the highest short-circuit current densities and probably also PCEs in solar cells.

### 15.2.2 Open circuit voltage

The maximal achievable open circuit voltage in bulk heterojunction organic solar cells is proportional to the energy offset between the HOMO level of the donor material (p-type component) and the LUMO level of the acceptor (n-type component) (Fig. 15.5) [62]. This dependence was well illustrated using sets of fullerene derivatives with different LUMO energy levels and electron donor polymers with different HOMO energy levels [63,64].

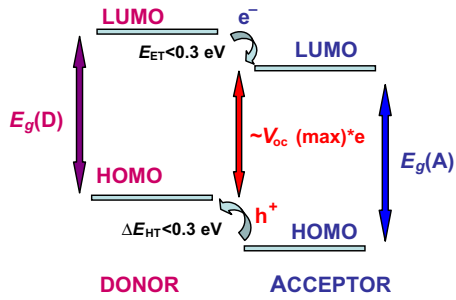


**Figure 15.5** Typical energy level alignment in the optimized donor/acceptor bulk heterojunction system.

According to the empirical model of Vandewal et al. [65], the experimental open circuit voltage can be well estimated using the following equation:

$$V_{oc}(\text{exp}) \approx E_g/q - 0.43\ \text{V} \tag{15.1}$$

where $q$ is the elementary charge and $E_g$ is a band gap of the charge transfer (CT) state formed in the polymer/fullerene system. It should be emphasized that CT states are almost always formed in the fullerene/polymer blends under illumination and their dissociation is considered as the main pathway for generation of free charge carriers [66,67].

The band gap of the CT state is generally ca. 0.1−0.2 eV smaller compared to the LUMO(A)−HOMO(D) offset. Therefore, Eq. (15.1) can be transformed to a more convenient equation [Eq. (15.2)]:

$$V_{oc}(\text{exp}) \approx [\text{LUMO(A)} - \text{HOMO(D)}]/\text{q} - (0.53 - 0.63)\text{V} \tag{15.2}$$

A linear correlation between the experimental $V_{oc}$ values and energy of the CT state is generally observed for both fullerene/polymer and fullerene/small molecular donor systems [68,69]. It is notable that this dependence is valid for all planar and bulk heterojunction device configurations fabricated using either fullerene or non-fullerene acceptor materials as illustrated in Fig. 15.6A.

The most precise expression (15.3) for the open circuit voltage was derived by Vandewal et al. in the framework of Marcus theory [70]:

$$V_{oc} = \frac{E_{CT}}{q} + \frac{kT}{q}\text{In}\left(\frac{J_{sc}h^3c^2}{fq2\pi(E_{CT} - \lambda)}\right) + \frac{kT}{q}\text{In}(\text{EQE}_{EL}) \tag{15.3}$$

In this equation, $E_{CT}$ corresponds to the energy (band gap) of the interfacial CT state, $k$ is Boltzmann constant, $T$ is the absolute temperature, $q$ is elementary charge, and $h$ and $c$ are Planck constant and speed of light in a vacuum, respectively. The reorganization energy $\lambda$ associated with the CT absorption process can be estimated experimentally from the alignment of the CT state absorption and emission spectra as illustrated in [65,70]. Parameter $f$ defines the CT absorption strength and is proportional to the density of the DA pairs and efficiency of the D and A coupling in CT state (see details in [70]). $\text{EQE}_{EL}$ is the EQE of electroluminescence of the PV device and usually stays in the range of $10^{-6}$.

The non-radiative open circuit voltage losses $\Delta V_{nr}$ represented by the $kT/q \times \ln(\text{EQE}_{EL})$ component in Eq. (15.3) have been explored in detail recently [69]. It was found that $\Delta V_{nr}$ depends on the band gap of the CT

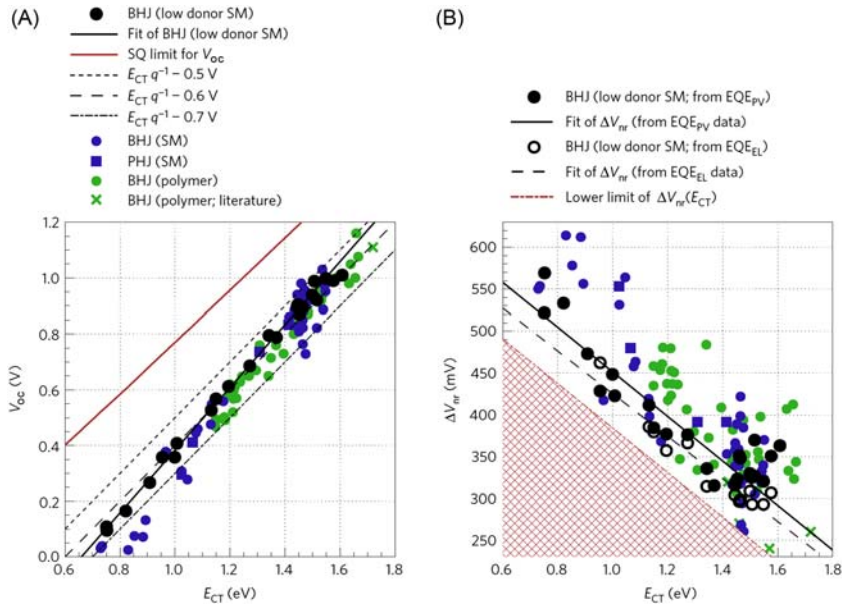


**Figure 15.6** The correlation of the experimental open circuit voltage with the band gap of the CT state ($E_{CT}$) (A). The upper solid line in (A) shows the ideal $V_{oc}$ (based on Shockley-Queisser assumptions) as a function of $E_{CT}$. The value of intrinsic non-radiative recombination losses $\Delta V_{nr}$ plotted as a function of $E_{CT}$ (B). Filled symbols show data calculated from $EQE_{PV}$ and open symbols correspond to data measured by $EQE_{EL}$. The dash dotted line laying at the hypotenuse of the filled right triangle indicates an empirical lower limit of $\Delta V_{nr}$ as a function of $E_{CT}$. Circles show BHJ organic solar cells, whereas squares represent PHJ devices. *BHJ*, Bulk heterojunction; *CT*, charge transfer; *EQE*, external quantum efficiency; *PHJ*, planar heterojunction; *SM*, small molecule *Image reproduced with permission from J. Benduhn, K. Tvingstedt, F. Piersimoni, S. Ullbrich, Y. Fan, M. Tropiano et al., Intrinsic non-radiative voltage losses in fullerene-based organic solar cells, Nat. Energy 2 (2017) 17053.*

state as shown in Fig. 15.6B. Practically useful band gaps below 1.7 eV are associated with the non-radiative voltage losses of >250 mV. Most importantly, these losses were correlated with the electron-vibration coupling and can be considered as intrinsic characteristic of all organic materials. If this hypothesis is correct, then $\Delta V_{nr}$ can hardly be avoided or even essentially suppressed using rational material design. According to Shockley and Queisser, the upper limit for the PCE of an ideal single-junction solar cell is about 34%, assuming that it has EQE of 100% above the band gap of the semiconductor and non-radiative recombination is absent. The intrinsic non-radiative recombination reported in [69] reduces the ultimate PCE of a single-junction organic solar cell down to ~25.5%.

Considering the energy diagram shown in Fig. 15.5, the maximal open circuit voltage is strongly affected by the $\Delta E_{ET}$ value, which is called a driving force for charge separation. It is commonly believed that for the fullerene-polymer systems, the driving force should be in the range of 0.3 eV [64]. However, by using non-fullerene acceptors, one probably can reduce the driving force to ~50 meV while keeping high quantum efficiency of the charge separation [18–20,71].

The vast majority of the conjugated polymers designed to date were explored in organic solar cells still using conventional fullerene-based acceptor materials. Achieving high open circuit voltages in these systems requires tailoring the frontier energy levels of conjugated polymers to match the LUMO energies of [60]PCBM or [70]PCBM. In particular, the LUMO of the polymer should be fixed ~0.3 eV higher in energy than that of the fullerene acceptor component. Lower is the HOMO energy of the polymer, higher is the open circuit voltage of the PV cell. However, materials with deep-lying HOMO levels have relatively wide band gap, which negatively affects the short circuit current density (see Section 15.2.1). Therefore, some compromise is required to get balanced $V_{oc}$ and $J_{sc}$ values and achieve high PCE as discussed below (Section 15.2.4).

Very intense research in the design of various conjugated polymers produced multiple promising structures delivering open circuit voltages close to 1 V or even a bit higher. The examples presented in Fig. 15.7 illustrate the power of the chemical design of novel organic materials. Indeed, chemists can do fine tuning of optoelectronic properties of organic photoactive materials that is hardly possible to the same extent for inorganic semiconductors.

Fig. 15.8 shows statistical analysis of the open circuit voltage values reported in the literature for 632 conjugated polymers with different HOMO energies [51]. It is seen from this figure that $V_{oc}$ increases almost linearly following the evolution of HOMO energies from −4.8 eV down to −5.5 eV. However, the vast majority of the polymers with HOMO energies of −5.7 to −5.9 eV showed lower open circuit voltages. Poor charge carrier collection at the ITO/PEDOT:PSS electrode (effective work function of ~5.1 eV) in the case of conjugated polymers with $E_{HOMO} < -5.6$ eV might be considered as the most probable reason for the observed behavior.

It should be also noted that the energy gap $\Delta E_{HT}$ (consider Fig. 15.5) becomes lower than 0.3 eV for the conjugated polymers with HOMO

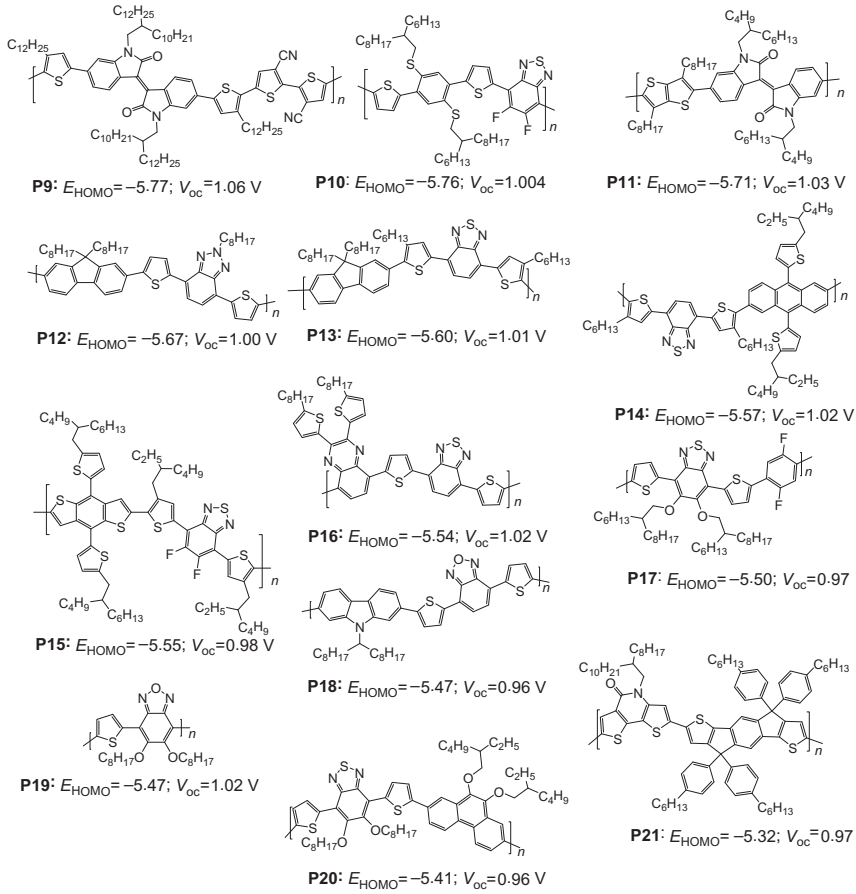


**Figure 15.7** Molecular structures of conjugated polymers delivering high open circuit voltages in organic solar cells. *Data are taken from [72–84].*

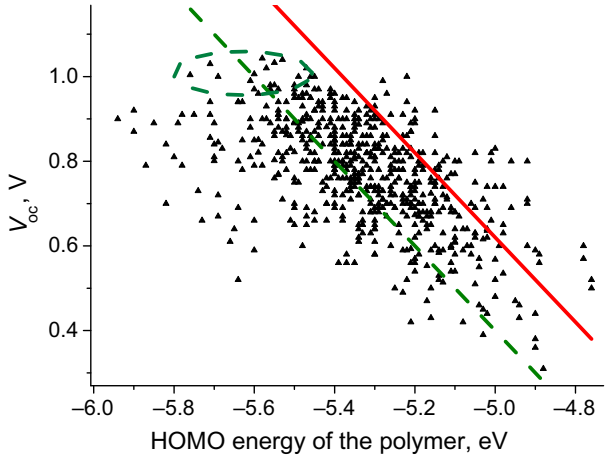


**Figure 15.8** Experimental $V_{oc}$ values reported in the literature for 632 conjugated polymers plotted as a function of the material HOMO energy.

energies below −5.7 eV while using conventional fullerene-based acceptors. Insufficiently high driving force for the hole transfer might severely affect efficiency of the charge carrier generation leading to low short circuit current densities and other parameters of PV cells.

Particular attention should be paid to the solid line shown in Fig. 15.8, which gives the most optimistic open circuit voltage estimation for bulk heterojunction solar cells based on conjugated polymers and fullerene-based acceptors. We used equation 2 above and assumed that PCBM has LUMO energy of −3.80 eV [85] and the system has minimal realistic voltage loss of 0.53 V. Therefore, all experimental points located above the solid line might be true only if some alternative acceptor material (e.g., non-fullerene or fullerene bis-adducts with reduced electron affinity) was implemented in the blend. Reports for PCBM-based solar cells delivering that high open circuit voltages in combination with decent EQEs > 40% should be considered with a strong suspicion.

Dashed line in Fig. 15.8 gives realistic estimation for the open circuit voltage of organic solar cells using the empiric formula provided by Scharber: $q \times V_{oc} = E_{HOMO}$ (polymer) − 4.6 eV [86]. We do not see a very good match between the experimental data and the model, presumably due to the fact that precise $E_{HOMO}$ estimation is very challenging and leads to large scattering of the data among publications coming from different research teams. The accuracy of the estimated energy values might depend significantly on the used technique (e.g., cyclic voltammetry vs photoelectron spectroscopy) and the experimental conditions. It is seen that the area between dashed and solid lines is strongly populated, therefore this corridor can be considered as a good estimation for open circuit voltage of optimized bulk heterojunction organic solar cells.

As a main conclusion from the data presented in Figs. 15.5 and 15.8, we can recommend researchers to focus on designing conjugated polymers with HOMO energy levels ranging between −5.5 and −5.6 eV and band gaps of 1.45−1.64 eV. These characteristics can deliver high efficiencies in single junction organic solar cells, if a number of other requirements are satisfied (e.g., optimal blend morphology, high charge carrier mobilities, etc.).

### 15.2.3 Fill factor

The FF of PV devices depends strongly on the charge transport characteristics of the photoactive blend and CT through the interfaces between the

active layer and the electrodes. To minimize the interface losses, the energy levels of the charge transport layers and work functions of the electrode materials have to be well aligned to facilitate collection of both types of charge carriers [87].

The optimization of the charge carrier transport in the photoactive blends is a much more complicated task. It is known that reasonably high FFs can be obtained only for the systems where electron and hole mobilities are balanced in the photoactive blend (means close to each other as much as possible) [88,89]. This requirement can be satisfied only by optimizing both the charge carrier mobilities of pristine materials and the morphology of the composite films. The electron mobilities of pristine fullerene derivatives such as [60]PCBM and [70]PCBM are reasonably high and stay within the range of $10^{-3}$–$10^{-1}$ $cm^2\,V^{-1}\,s^{-1}$, depending on the experimental conditions and techniques used for the measurements [90,91]. The hole mobilities in conjugated polymers change significantly depending on the peculiarities of their molecular structures and their chemical purity.

Typically, crystalline conjugated polymers exhibit higher charge carrier mobilities compared to amorphous materials. Therefore, one of the research trends in the polymer chemistry is improving the crystallinity of the designed materials. One should consider the regioregularity of the polymer chain, the length and the shape of the solubilizing alkyl chains, their relative positions in the polymer chain, and also the size and properties of the planar conjugated system itself. For example, it is known that regiorandom P3HT exhibits very poor crystallinity (if any) in contrast to the regioregular head-to-tail P3HT, which is a fairly crystalline material. Therefore, it is not surprising that regiorandom P3HT shows few orders of magnitude lower charge carrier mobility compared to the regioregular one [92].

Another example can be provided by the polymers **P22** and **P23**, which differ from each other mainly by the positions of the solubilizing alkyl chains (Fig. 15.9) [93]. One can see that simple shift of the octyl groups from one position to another in the thiophene rings dramatically changes the optoelectronic properties of the resulting polymers. The band gap of the polymer **P23** is more than 0.5 eV higher compared to the very similar polymer **P22**. Optical properties of **P23** suggest the lack of conjugation in the main polymer chain, which might result from its twisting due to the unfavorable steric interactions between the solubilizing alkyl side chains. One can expect that polymer **P23** will be amorphous in solid

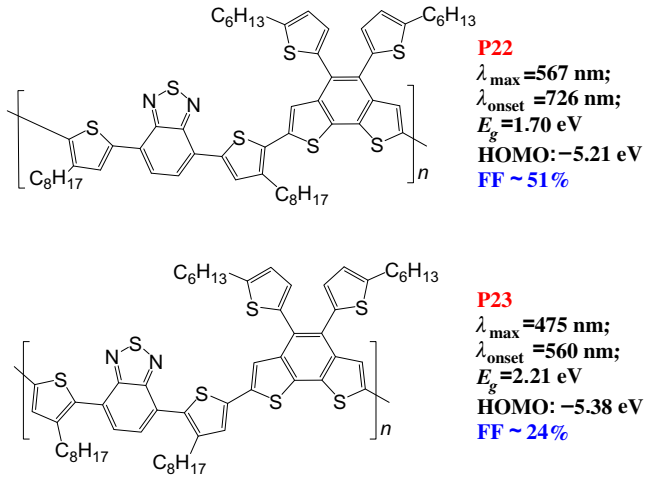


**Figure 15.9** Molecular structures of polymers **P22** (planar and ordered) and **P23** (twisted and disordered) and some of their physicochemical characteristics and fill factors reached in organic solar cells based on these polymers.

state (since the main chain is not planar), while polymer **P22** might give crystalline films. A similar effect of the solubilizing side chains on the optical, electronic, and PV properties of conjugated polymers was also reported in [94].

The packing of the polymer chains in the solid films is also affected by the length and shape of the solubilizing alkyl groups and their relative orientation. A series of polymers with identical backbone and different localization of the solubilizing 2-ethylhexyl side chains has been reported recently [95]. It was shown that shifting the alkyl substituents in the monomer can change the material band gap from 1.65 to 1.9 eV, charge carrier mobility from $2.8 \times 10^{-4}$ to $2.4 \times 10^{-5}$ $cm^2\,V^{-1}\,s^{-1}$, and FF in solar cells from 63% to 31% (Fig. 15.10). This example illustrates clearly that unfavorable steric interactions among the solubilizing alkyl side chains induce strong tilting of the polymer backbone, which affects badly optical and charge transport properties of the material and leads to significant reduction in the device FF. Therefore, highly planar polymer chains should be designed to boost charge transport and improve FF.

Other very nice illustrations of the side chain effect on the crystal structure of the conjugated polymers and their PV performance have been reported for a family of benzodithiophene-thienothiophene copolymers [96]. It was shown that solubilizing alkyl groups affect the distances among the polymer chains in the crystalline π−π stack. Decrease in these

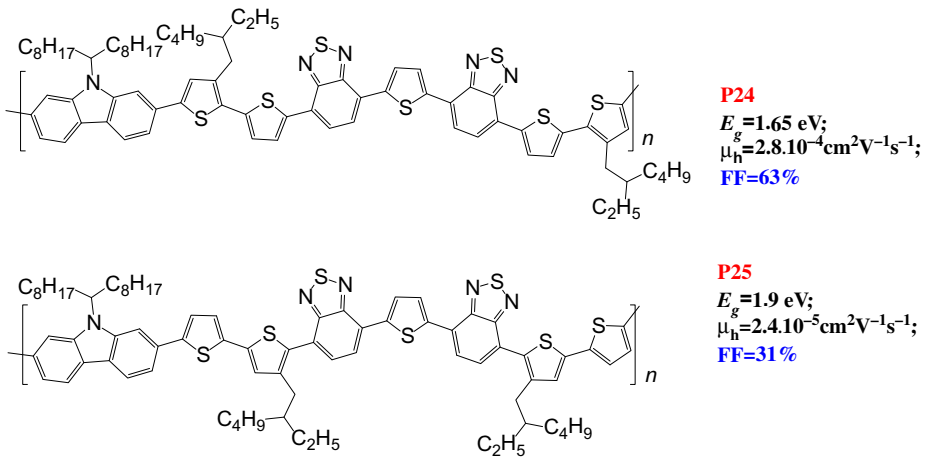


**Figure 15.10** Two extreme polymer structures reported in [95] with the most planar (**P24**) and twisted (**P25**) molecular backbones and some their physicochemical characteristics.

distances improves electronic coupling between the neighboring polymer chains in the stack and increases charge carrier mobilities. It was mentioned above that conjugated polymers with higher hole mobilities give improved FFs and PCEs in organic solar cells. These considerations are fully supported by experimental results presented in [96], which showed a linear correlation of the device FFs with the distances between the polymer chains in the π-stack (π-distance, Fig. 15.11).

One of the possible ways to increase the crystallinity of the target conjugated polymer is introducing a large planar conjugated system in the main polymer chain. This approach was pursued successfully by few research groups reported synthesis and investigation of a number of promising conjugated polymers [97–103].

It was demonstrated that substitution of the bridge carbon atom in cyclopentadithiophene system with silicon dramatically improves crystallinity of the conjugated polymers and their charge carrier mobilities. One of the most illustrative examples is provided by the conjugated polymers **P7-C** and **P7-Si** (Fig. 15.12) [104]. The repeating units of these two polymers differ by just one atom. However, this minor structural difference leads to major changes in the material properties. Grazing X-ray diffraction revealed that polymer **P7-Si** is a highly crystalline material in contrast to **P7-C**, which is completely amorphous. Good crystallinity of **P7-Si** leads to higher hole mobilities in thin films as compared to **P7-C**, which also resulted in the superior PV performance (PCE: 5.2% *vs* 3.2%) and, particularly, higher FF values (61% *vs* 47%).

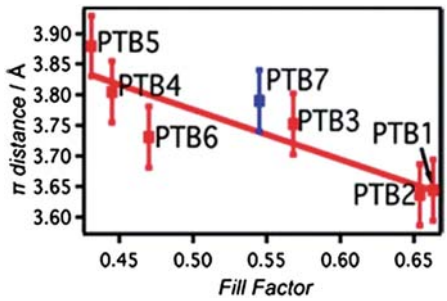


**Figure 15.11** The experimentally established relationship between the π-distance in the polymer stack and FF achieved in solar cells. *Image reproduced with permission from J.M. Szarko, J. Guo, Y. Liang, B. Lee, B.S. Rolczynski, J. Strzalka, et al., When function follows form: effects of donor copolymer side chains on film morphology and BHJ solar cell performance, Adv. Mater. 22 (2010) 5468–5472.*

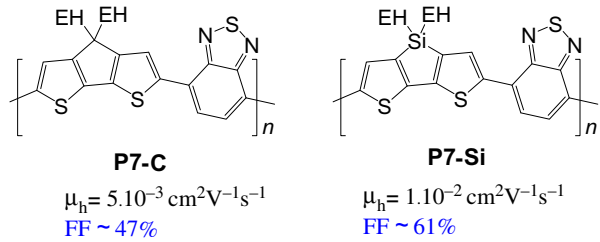


**Figure 15.12** Molecular structures of two conjugated copolymers showing the effect of the bridging atom on the charge transport properties of the material and FF values reached in photovoltaic devices. *FF*, Fill factor.

The presented examples illustrate the potential of using molecular design to control geometry of the polymer chain, induce or inhibit crystallization of the material in solid films, provide required charge carrier mobilities, and the chain packing behavior to attain sufficiently high FFs in organic PV devices. It should be emphasized that at the present status of the research in organic PVs, we cannot predict FFs of the devices (besides few rare examples) considering just the molecular structures and properties of the materials. Generally, the FFs of 65%–75% can be achieved for the best optimized organic PV cells.

### 15.2.4 Power conversion efficiency

PCE of organic solar cells is defined by the product of the short circuit current, open circuit voltage, and FF (Fig. 15.2). The maximal short circuit current density of any PV device can be estimated numerically considering the overlap between the absorption spectrum of the device active layer of a certain thickness and the solar AM1.5 emission spectrum [105–107]. Taking into account that the contribution of the fullerene component to the active layer absorption is not that strong (especially when derivatives of $C_{60}$ are used), one can use the absorption spectrum of pristine polymer for such kind of modeling. In cases when [70]fullerene derivatives or non-fullerene acceptor materials with complementary absorption spectra are used, higher currents can be reached due to contributions coming from both p- and n-type materials [7–9]. The open circuit voltage achievable for a certain pair of donor (conjugated polymer) and acceptor materials can be estimated using Eq. (15.2) or Eq. (15.3) if the correct values of the HOMO and LUMO energies and other numerical parameters are available for the system.

Extensive modeling was performed by many groups, which allowed estimating ultimate efficiencies of single-junction and double-junction organic bulk heterojunction cells [108–110]. For a single junction cell, Scharber et al. proposed an illustrative model using the band gap of the donor component and offset between the LUMO level energies of the donor and acceptor materials as the most important variables. Using standard estimations for $J_{sc}$(max) and $V_{oc}$ and assuming reasonable FF (FF = 65%) and EQE (EQE = 65%) values, the authors calculated theoretically achievable PCE as shown in Fig. 15.13A.

This diagram suggests that optimal electron donor material should have a band gap of ~1.5 eV, which corresponds to the absorption band edge of ~820 nm. At the same time, the offset between the LUMO level energies of the donor and acceptor components should be minimized to 0.2–0.3 eV to enable maximal $V_{oc}$ achievable for the system. In the case if [60]PCBM or [70]PCBM are used as electron acceptor counterparts (both have LUMO ~ −3.85 eV), the optimal electron donor conjugated polymer should have LUMO energy of −3.55 eV and HOMO energy of −5.15 eV (assuming offset of 0.2 eV). These values might be used as rough guidelines by the polymer chemists working on the design of novel conjugated polymers for PV applications.

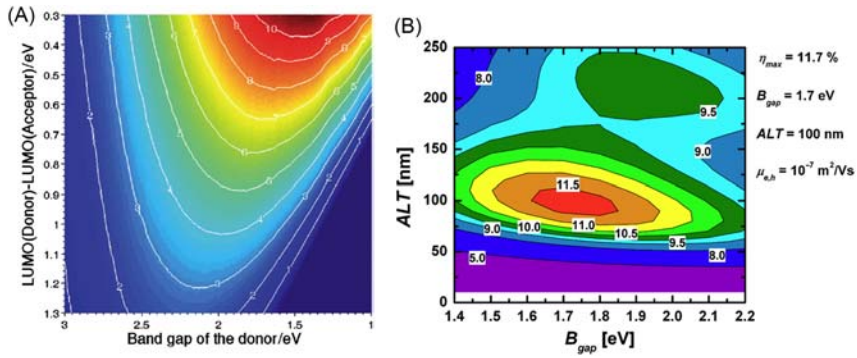


**Figure 15.13** Diagrams illustrating estimated ultimate power conversion efficiency of single junction organic solar cells as a function of fundamental optoelectronic characteristics of the used materials and active layer thickness following Scharber (A) and Kotlarski and Blom (B) *The artwork is reproduced with permission from M.C. Scharber, D. Muhlbacher, M. Koppe, P. Denk, C. Waldauf, A.J. Heeger, et al., Design rules for donors in bulk-heterojunction solar cells – towards 10 % energy–conversion efficiency, Adv. Mater. 18 (2006) 789–794; J.D. Kotlarski, P.W.M. Blom, Ultimate performance of polymer:fullerene bulk heterojunction tandem solar cells, Appl. Phys. Lett. 98 (2011) 053301.*

In the model presented in Refs. [108,109], no special attention was paid to the photoactive film thickness required to absorb certain number of photons, the charge carrier mobilities in the composite films, and the effect of the both parameters on the charge collection at the electrodes and the FF of the device. More extensive modeling has been performed later by Kotlarski and Blom [110]. It is seen from Fig. 15.13B that optimal material should have a band gap of 1.7 eV and the active layer thickness should be around 100 nm. Under these optimal conditions the solar cell can produce $J_{sc} = 15.65$ mA cm$^{-2}$, $V_{oc} = 1.0$ V, FF = 74.3%, and the PCE of 11.7%. Authors of this work used −3.8 eV for LUMO energy of PCBM. If we stay with this value, the optimal polymer material should have LUMO at −3.5 eV and HOMO at −5.2 eV. The second efficiency maximum of 9.9% was found for the systems with the polymer band gap of 1.9 V (similar to the band gap of P3HT) and the active layer thickness of 200 nm.

It is very likely that on-grid applications of organic solar cells will become feasible only when the module efficiencies reach 12% in combination with the lifetime of 10 years and the cost well below 100 USD m$^{-2}$ [111]. The PCEs of single cells have to be pushed up to 14%–16% to meet this severe module efficiency requirement. Single junction devices can hardly produce 14%–16% efficiencies, particularly on large area, due to the aforementioned fundamental limitations. Therefore, the research community pays more and more attention to tandem organic solar cells, especially the double junction devices. Theoretical modeling suggests that indeed double-junction organic solar cells can produce PCEs of 14%–15% if optical and electronic properties of the materials in both subcells are optimized.

The diagram shown in Fig. 15.14A suggests that the highest tandem efficiency can be reached using subcells composed of the materials with the band gaps of ∼1.63 and ∼1.23 eV (the first maximum) or ∼1.77 and ∼1.33 eV (the second maximum) [109]. Somewhat different modeling results for double-junction organic solar cells were reported by Kotlarski and Blom [110]. First of all, they confirmed that in the optimal situation, the front cell (one which is closer to transparent electrode) should have a wider band gap compared to the back cell (one which is closer to the reflecting metal electrode). The optimal band gap for the front cell donor component was estimated to be between 1.85 and 2.0 eV and the optimal active layer thickness was around 150 nm. At the same time, the back cell should have the band gap of 1.50–1.65 eV and the thickness of the light absorbing layer has to be nearly 90 nm. The fully

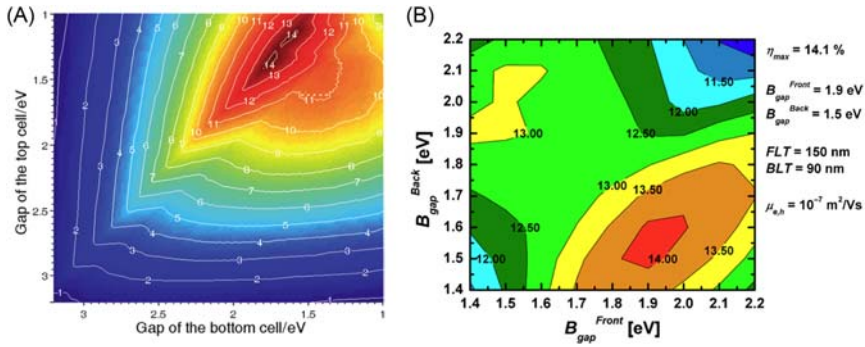


**Figure 15.14** Diagrams illustrating estimated ultimate power conversion efficiency of double junction tandem organic solar cells depending on the optical properties of two absorber materials used in bottom and top subcells following Scharber (A) and Kotlarski and Blom (B). *The artwork is reproduced with permission from T. Ameri, G. Dennler, C. Lungenschmied, C.J. Brabec, Organic tandem solar cells: a review, Energy Environ. Sci. 2 (2009) 347–363; J.D. Kotlarski, P.W.M. Blom, Ultimate performance of polymer:fullerene bulk heterojunction tandem solar cells, Appl. Phys. Lett. 98 (2011) 053301.*

optimized devices might produce PCEs slightly above 14.0% (Fig. 15.14B). The second efficiency maximum was obtained for the system where the front cell materials have smaller band gap ($E_g = 1.45–1.55$ eV) compared to the back cell components ($E_g = 1.9–2.1$ eV). However, the thickness of the front cell active layer (40 nm) should be much smaller compared to the back cell active layer (200 nm) to provide the maximal efficiency of 13.1%.

While the general knowledge on the mechanisms of the organic solar cell operation and related loss processes was accumulated, it became clear that the diagrams shown in Figs. 15.13 and 15.14 are not fully correct. In particular, they are based on assumption of the unrealistically small voltage losses (0.3 eV from the HOMO(D)–LUMO(A) energy offset). Therefore, Scharber revised his model and assumed realistic open-circuit voltage loss of 0.7 eV based on the empiric relationship of Janssen et al., suggesting that organic bulk heterojunction systems with voltage loss of less than 0.7 V fail to deliver EQE > 70% [112]. The updated Scharber model is also built with the assumption of EQE of 70% and FFs of the optimized devices of 70% [86].

According to the model (Fig. 15.15), electron donor materials should possess a band gap of 1.2–1.7 eV and HOMO energy ranging from −5.7 to −5.3 eV. The energy levels of the acceptor component should be aligned in a way resulting in the minimal open circuit voltage losses (see

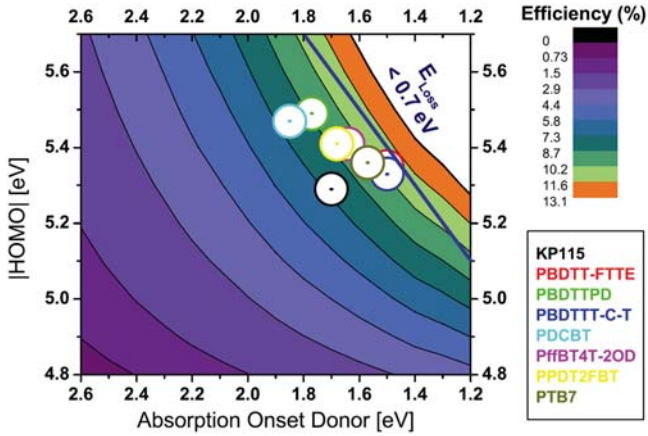


**Figure 15.15** Updated Scharber diagram illustrating the theoretical potential of various electron donor polymers: the maximal achievable PCE is shown as a function of the bandgap (Absorption Onset Donor or $E_g$) and HOMO energy of the material. Positions of some promising conjugated polymers actively investigated in the field are illustrated with the circles. *The artwork is reproduced with permission from M.C. Scharber, On the efficiency limit of conjugated polymer: fullerene-based bulk heterojunction solar cells. Adv. Mater. 28 (2016) 1994–2001.*

above). Materials with the optimal electronic characteristics can provide PCEs of about 12%–13% in single-junction solar cells. Even though we are not aware of revised models reported for double-junction organic solar cells, it is quite clear that their ultimate efficiencies can reach 15%–16% or even go higher.

The presented modeling results provide very useful guidelines for material chemists working on the design of novel photoactive electron donor and electron acceptor materials for bulk heterojunction organic solar cells. It becomes more or less clear what kind of electronic and optical properties one should attain synthesizing, for instance, new donor polymer, which is supposed to be used in organic solar cells in combination with the fullerene-based material [60]PCBM or alternative non-fullerene acceptor materials.

We have analyzed experimental characteristics of organic solar cells based on >730 different conjugated polymers reported in the literature and reconstructed a counter plot similar to that presented by Scharber (Fig. 15.16). It should be emphasized that the Scharber model estimates only the theoretical potential of organic materials with variable electronic characteristics. Practically, the vast majority of the experimentally investigated polymers failed to deliver expected characteristics due to many

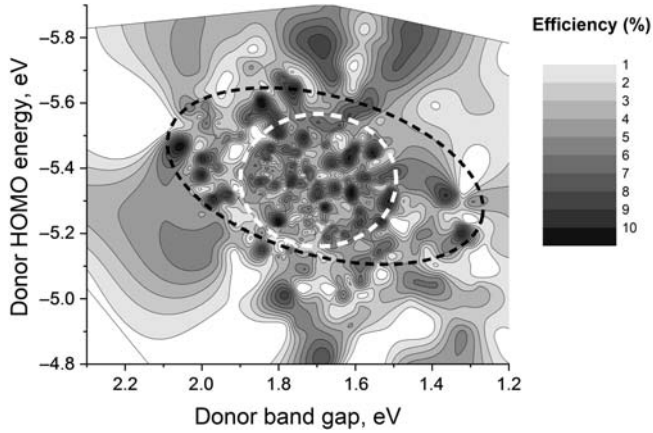


**Figure 15.16** Contour diagram built based on 730 experimental data points collected from the literature illustrating optimal optoelectronic characteristics of electron donor conjugated polymers for achieving high power conversion efficiencies in organic solar cells.

reasons, such as unbalanced active layer morphology, insufficient purity of the materials leading to trapping and recombination of charge carriers, formation of barriers, and the electrode/active layer interfaces preventing efficient extraction of charges. Therefore, the diagram in Fig. 15.16 represents a grayish sea (solar cell PCE $<4\%$) with some dark islands (PCE $>7\%$) corresponding to the successful materials.

The ellipse shown with a black dashed line is surrounding the experimental points corresponding to the record high efficiencies of $>10\%$. Considering this area, one can conclude that the best solar cell efficiencies can be delivered by low band-gap polymers ($E_g$ down to 1.3 eV) with high HOMO energies of $-5.2$ eV as well as wide band-gap polymers ($E_g \sim 2.1$ eV) with deeper lying HOMO levels (below $-5.4$ eV) when they are combined with low band-gap non-fullerene acceptors. The white dashed line is surrounding the area on the diagram with the highest probability of achieving high PCEs for certain polymers used in solar cells. The boarders of this "high probability area" are defined by the band gap values of 1.5–1.85 eV and HOMO energies within the range of $-5.25$ to $-5.5$ eV. We believe that these parameters can be considered as a good indication for materials scientists working on the design of novel materials for organic PVs.

Table 15.1 gives an overview of the selected examples of conjugated polymers delivering high efficiencies in organic solar cells. The results are

**Table 15.1** Some examples of high-efficiency organic solar cells based on conjugated polymers with variable HOMO energy levels and band gaps.

| Polymer | Acceptor | $E_{HOMO}$, eV | $E_g$, eV | $V_{oc}$, V | $J_{sc}$, mA cm$^{-2}$ | FF, % | $\eta$, % | $\eta_{teor.}$, %[a] | $\eta/\eta_{teor.}$[b] | Ref. |
|---|---|---|---|---|---|---|---|---|---|---|
| **P26** | [60]PCBM | − 5.41 | 1.66 | 0.77 | 17.2 | 70.8 | 9.4 | 8.7−10.2 | 0.92 | [113] |
| **P27** | [60]PCBM | − 5.47 | 1.68 | 0.77 | 16.55 | 72.7 | 9.3 | 8.7−10.2 | 0.91 | [113] |
| **P28** | [60]PCBM | − 5.34 | 1.65 | 0.77 | 17.1 | 73.0 | 9.6 | 7.3−8.7 | 1.10 | [47] |
| **P28** | [70]PCBM | − 5.34 | 1.65 | 0.77 | 18.4 | 74.0 | 10.5 | 7.3−8.7 | 1.21 | [47] |
| **P28** | [60]TCPM | − 5.34 | 1.65 | 0.75 | 17.4 | 74.0 | 9.7 | 7.3−8.7 | 1.11 | [47] |
| **P28** | [70]TCBM | − 5.34 | 1.65 | 0.77 | 18.8 | 75.0 | 10.8 | 7.3−8.7 | 1.24 | [47] |
| **P28** | [60]PCPM | − 5.34 | 1.65 | 0.77 | 17.7 | 76.0 | 10.4 | 7.3−8.7 | 1.19 | [47] |
| **P28** | ICMA | − 5.34 | 1.65 | 0.78 | 16.4 | 77.0 | 9.8 | 7.3−8.7 | 1.13 | [47] |
| **P28** | NCMM | − 5.34 | 1.65 | 0.76 | 17.7 | 70.0 | 9.4 | 7.3−8.7 | 1.08 | [47] |
| **P28** | ICMM | − 5.34 | 1.65 | 0.78 | 17.0 | 70.0 | 9.3 | 7.3−8.7 | 1.07 | [47] |
| **P28** | MOPFP | − 5.34 | 1.65 | 0.76 | 17.2 | 69.0 | 9.2 | 7.3−8.7 | 1.06 | [47] |
| **P28** | [60]PCBE | − 5.34 | 1.65 | 0.78 | 17.1 | 67.0 | 9.2 | 7.3−8.7 | 1.06 | [47] |
| **P28** | NCMA | − 5.34 | 1.65 | 0.77 | 17.7 | 67.0 | 9.1 | 7.3−8.7 | 1.05 | [47] |
| **P29** | [70]PCBM | − 5.37 | 1.57 | 0.82 | 15.7 | 71.0 | 9.14 | 8.7−10.2 | 0.90 | [114] |
| **P30** | [70]PCBM | − 5.20 | 1.63 | 0.77 | 18.2 | 74.0 | 10.4 | 5.8−7.3 | 1.42 | [47] |
| **P30** | [60]PCPM | − 5.20 | 1.63 | 0.76 | 18.6 | 69.0 | 9.6 | 5.8−7.3 | 1.31 | [47] |
| **P31** | [70]PCBM | − 5.27 | 1.59 | 0.78 | 16.04 | 74.0 | 9.18 | 7.3−8.7 | 1.06 | [115] |
| **P32** | [70]PCBM | − 5.50 | 1.90 | 0.97 | 14.0 | 72.0 | 9.8 | 7.3−8.7 | 1.13 | [116] |
| **P33** | [70]PCBM | − 5.31 | 1.61 | 0.82 | 18.5 | 64.1 | 9.7 | 7.3−8.7 | 1.11 | [117] |
| **P34** | [70]PCBM | − 5.31 | 1.61 | 0.82 | 18.7 | 68.3 | 10.5 | 7.3−8.7 | 1.21 | [117] |
| **P35** | [70]PCBM | − 5.46 | 1.60 | 0.81 | 19.4 | 65.5 | 10.6 | 10.2−11.6 | 0.91 | [118] |
| **P36** | [70]PCBM | − 5.24 | 1.53 | 0.76 | 19.8 | 68.0 | 10.1 | 7.3−8.7 | 1.16 | [47] |
| **P36** | [60]PCPM | − 5.24 | 1.53 | 0.73 | 18.8 | 67.0 | 9.3 | 7.3−8.7 | 1.07 | [47] |
| **P37** | [70]PCBM | − 5.32 | 1.62 | 0.75 | 16.98 | 70.1 | 9.04 | 8.7−10.2 | 0.89 | [119] |

(*Continued*)

**Table 15.1** (Continued)

| Polymer | Acceptor | $E_{HOMO}$, eV | $E_g$, eV | $V_{oc}$, V | $J_{sc}$, mA cm$^{-2}$ | FF, % | $\eta$, % | $\eta_{teor.}$, %[a] | $\eta/\eta_{teor.}$[b] | Ref. |
|---|---|---|---|---|---|---|---|---|---|---|
| **P38** | [70]PCBM | − 5.34 | 1.61 | 0.76 | 19.08 | 74.1 | 10.8 | 8.7−10.2 | 1.06 | [119] |
| **P39** | [70]PCBM | − 5.42 | 1.62 | 0.74 | 18.92 | 73.5 | 10.31 | 8.7−10.2 | 1.01 | [120] |
| **P40** | [70]PCBM | − 5.43 | 1.64 | 0.72 | 18.46 | 69.7 | 9.28 | 8.7−10.2 | 0.91 | [120] |
| **P41** | [70]PCBM | − 5.28 | 1.68 | 0.77 | 23.8 | 67.0 | 12.25 | 7.3−8.7 | 1.40 | [121] |
| **P42** | [70]PCBM | − 5.15 | 1.84 | 0.75 | 17.5 | 70.0 | 9.2 | 4.4−5.8 | 1.59 | [122] |
| **P43** | [70]PCBM | − 5.33 | 1.51 | 0.80 | 17.46 | 67.9 | 9.48 | 8.7−10.2 | 0.93 | [123] |
| **P44** | [70]PCBM | − 5.45 | 1.62 | 0.86 | 16.4 | 62.2 | 9.0 | 10.2−11.6 | 0.78 | [124] |
| **P45** | [70]PCBM | − 5.23 | 1.59 | 1.00 | 14.79 | 61.1 | 9.07 | 7.3−8.7 | 1.04 | [125] |
| **P46** | [70]PCBM | − 5.44 | 1.56 | 0.89 | 15.1 | 71.0 | 9.58 | 10.2−11.6 | 0.83 | [126] |
| **P47** | [70]PCBM | − 5.45 | 1.75 | 0.92 | 15.4 | 66.0 | 9.4 | 7.3−8.7 | 1.08 | [127] |
| **P48** | [70]PCBM | − 5.56 | 1.81 | 0.93 | 12.97 | 74.5 | 9.02 | 8.7−10.2 | 0.88 | [128] |
| **P49** | [70]PCBM | − 5.40 | 1.73 | 0.85 | 14.38 | 74.2 | 9.13 | 7.3−8.7 | 1.05 | [129] |
| **P50** | ITIC | − 5.32 | 1.93 | 0.89 | 17.43 | 61.5 | 9.53 | 4.4−5.8 | 1.64 | [130] |
| **P51** | i−IEICO−4F | − 5.26 | 1.52 | 0.85 | 22.86 | 67.9 | 13.2 | N/A | N/A | [131] |
| **P52** | m−MeIC | − 5.40 | 1.96 | 0.92 | 18.45 | 69.2 | 11.73 | N/A | N/A | [132] |
| **P53** | INIC1 | − 5.38 | 2.0 | 0.93 | 16.6 | 64.3 | 9.9 | N/A | N/A | [133] |
| **P53** | INIC2 | − 5.38 | 2.0 | 0.90 | 17.6 | 66.8 | 10.6 | N/A | N/A | [133] |
| **P53** | INIC3 | − 5.38 | 2.0 | 0.86 | 19.44 | 67.4 | 11.2 | N/A | N/A | [133] |
| **P54** | [70]PCBM | − 5.37 | 1.76 | 0.87 | 15.06 | 70.4 | 9.22 | 7.3−8.7 | 1.06 | [134] |
| **P55** | [70]PCBM | − 5.31 | 1.70 | 0.89 | 15.53 | 70.9 | 9.8 | 7.3−8.7 | 1.13 | [135] |
| **P56** | [70]PCBM | − 5.43 | 2.00 | 0.96 | 14.1 | 74.7 | 10.1 | 5.8−7.3 | 1.38 | [136] |
| **P56** | ITIC−Th | − 5.43 | 2.00 | 0.97 | 15.5 | 68.1 | 10.3 | 5.8−7.3 | 1.41 | [136] |
| **P57** | [70]PCBM | − 5.28 | 1.83 | 0.96 | 13.45 | 71.0 | 9.25 | 5.8−7.3 | 1.27 | [137] |
| **P58** | [70]PCBM | − 5.35 | 1.77 | 0.90 | 14.9 | 73.0 | 9.8 | 7.3−8.7 | 1.13 | [138] |
| **P59** | IT−M | − 5.23 | 1.8 | 0.95 | 15.53 | 72.2 | 11.3 | N/A | N/A | [139] |
| **P59** | m−MeIC | − 5.23 | 1.8 | 0.84 | 18.16 | 69.7 | 10.68 | N/A | N/A | [132] |

| | | | | | | | | | | |
|---|---|---|---|---|---|---|---|---|---|---|
| **P59** | NFBDT | − 5.23 | 1.8 | 0.87 | 17.85 | 67.2 | 10.42 | N/A | N/A | [140] |
| **P59** | NFBDT−Me | − 5.23 | 1.8 | 0.91 | 17.3 | 70.0 | 11.00 | N/A | N/A | [140] |
| **P59** | NFBDT−F | − 5.23 | 1.8 | 0.79 | 19.3 | 69.5 | 10.62 | N/A | N/A | [140] |
| **P59** | IDT2Se | − 5.23 | 1.8 | 0.88 | 17.31 | 59.8 | 9.11 | N/A | N/A | [141] |
| **P59** | IDT2Se−4F | − 5.23 | 1.8 | 0.79 | 21.35 | 65.4 | 11.03 | N/A | N/A | [141] |
| **P59** | IDIDT−C8 | − 5.23 | 1.8 | 0.97 | 15.81 | 65.9 | 10.1 | N/A | N/A | [142] |
| **P60** | ITIC | − 5.35 | 1.81 | 0.94 | 14.86 | 66.5 | 9.28 | N/A | N/A | [143] |
| **P61** | [70]PCBM | − 5.43 | 1.83 | 0.92 | 13.28 | 77.4 | 9.43 | 7.3−8.7 | 1.08 | [144] |
| **P62** | ITIC | − 5.46 | 1.82 | 0.87 | 17.60 | 65.4 | 10.04 | N/A | N/A | [145] |
| **P63** | [70]PCBM | − 5.61 | 1.85 | 0.97 | 14.7 | 67.5 | 9.72 | 8.7−10.2 | 0.95 | [125] |
| **P63** | IT−4F | − 5.61 | 1.85 | 0.88 | 20.88 | 71.3 | 13.1 | N/A | N/A | [146] |
| **P64** | [70]PCBM | − 5.36 | 1.85 | 0.92 | 14.1 | 75.0 | 9.74 | 5.8−7.3 | 1.33 | [99] |
| **P65** | O−IDTBR | − 5.47 | 2.05 | 1.08 | 16.3 | 63.6 | 11.2 | N/A | N/A | [147] |
| **P66** | ITIC | − 5.31 | 1.97 | 1.00 | 14.04 | 65.5 | 9.25 | N/A | N/A | [148] |
| **P66** | IT−M | − 5.31 | 1.97 | 0.98 | 14.9 | 62.2 | 9.1 | N/A | N/A | [149] |
| **P66** | POIT−M | − 5.31 | 1.97 | 0.97 | 15.4 | 65.1 | 9.7 | N/A | N/A | [149] |
| **P66** | MOIT−M | − 5.31 | 1.97 | 0.96 | 17.5 | 68.8 | 11.6 | N/A | N/A | [149] |
| **P67** | ITIC | − 5.31 | 1.69 | 0.90 | 16.88 | 69.2 | 10.52 | N/A | N/A | [150] |
| **P68** | [70]PCBM | − 5.50 | 1.73 | 0.90 | 14.0 | 74.0 | 9.2 | 8.7−10.2 | 0.90 | [151] |
| **P68** | ITIC | − 5.50 | 1.73 | 0.94 | 15.4 | 66.0 | 9.6 | N/A | N/A | [151] |
| **P69** | [70]PCBM | − 5.44 | 1.55 | 0.86 | 16.0 | 65.0 | 9.02 | 10.2−11.6 | 0.78 | [152] |
| **P70** | [70]PCBM | − 5.3 | 1.51 | 0.80 | 17.99 | 70.6 | 10.2 | 8.7−10.2 | 1.00 | [153] |
| **P71** | [70]PCBM | − 5.65 | 1.75 | 0.85 | 15.3 | 70.0 | 9.21 | 10.2−11.6 | 0.79 | [154] |
| **P72** | [70]PCBM | − 5.50 | 1.80 | 0.98 | 13.65 | 75.6 | 10.15 | 7.3−8.7 | 1.16 | [155] |
| **P73** | [70]PCBM | − 5.1 | 1.6 | 0.72 | 17.7 | 71.0 | 9.1 | 4.4−5.8 | 1.57 | [156] |

[a]Power conversion efficiency estimated using the Scharber model and the diagram shown in Fig. 15.15.
[b]Experimentally achieved efficiency normalized to the maximal value of the theoretically expected efficiency according to the Scharber model.

arranged in a way showing first the performance of the solar cells comprising conventional fullerene-based acceptors ([60]PCBM and [70]PCBM) and moving to less-conventional fullerene derivatives and non-fullerene acceptors. Molecular structures of the polymers and acceptor materials are given in Figs. 15.17, 15.18, and 15.19, respectively.

We believe that for didactic purposes it is worthy to compare the experimentally obtained parameters of the devices with those predicted using the Scharber model, considering the fundamental properties of the materials ($E_g$, HOMO energy, etc.). Practically useful can be the $\eta/\eta_{\text{teor.}}$ ratio, given in one of the last columns of the table. If this parameter is below 1, this means that further optimization might be carried out to boost the efficiency of the device, based on a certain material to the

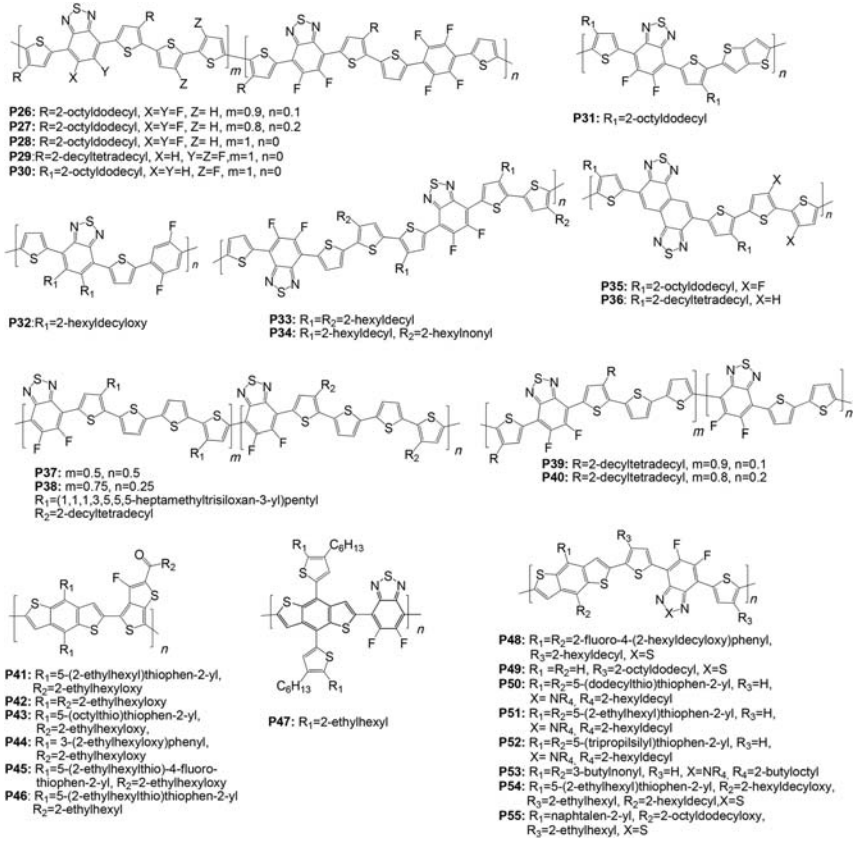


**Figure 15.17** Molecular structures of conjugated polymers **P26**–**P55** delivering high power conversion efficiencies in organic solar cells.

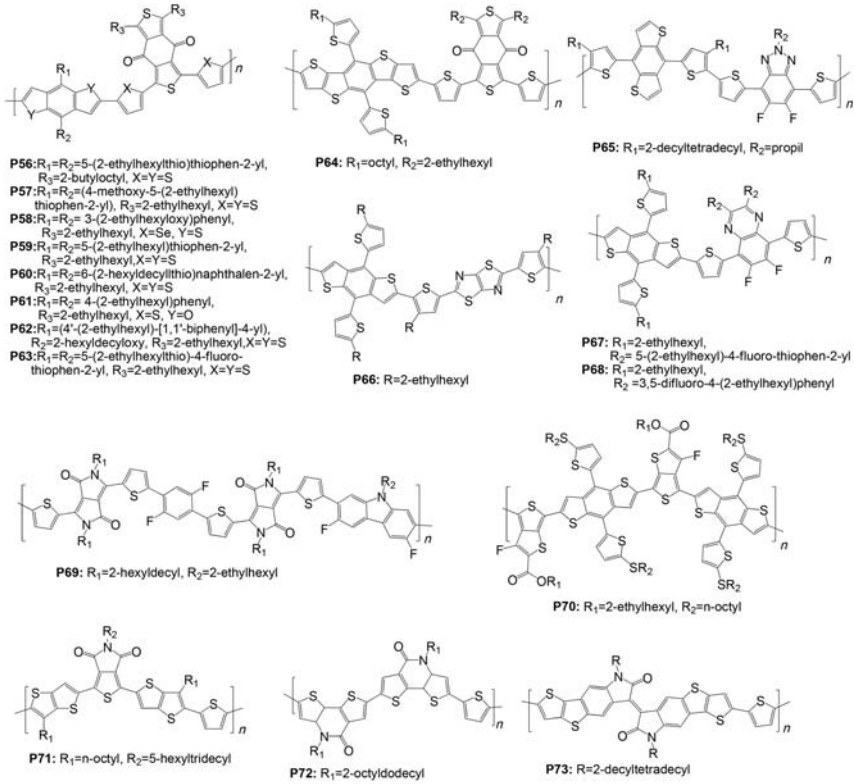


**Figure 15.18** Molecular structures of conjugated polymers **P56**–**P73** delivering high power conversion efficiencies in organic solar cells.

theoretical limit. On the contrary, materials showing $\eta/\eta_{\text{teor.}} > 1$ might be extensively optimized, thus delivering higher EQE and FF than implemented in the Scharber's model (70% each, see above). Alternatively, in some cases the solar cell parameters could be overestimated due to technical errors, which resulted in a number of unrealistically high efficiencies reported in the literature. This aspect has been already emphasized while considering the collections of the literature data points presented in Figs. 15.4 and 15.8 above. It is clear that the Scharber model can hardly be used in a correct way for the systems comprising non-fullerene acceptors, which might have even lower band gaps than donor polymers.

To summarize, there is no doubt that organic solar cells start to demonstrate impressive PCEs well exceeding 10%. In particular, recent reports on achieving 13.2% [157] and 17.3% [158] in single- and double-junction devices, respectively, all based on organic materials, are very inspiring.

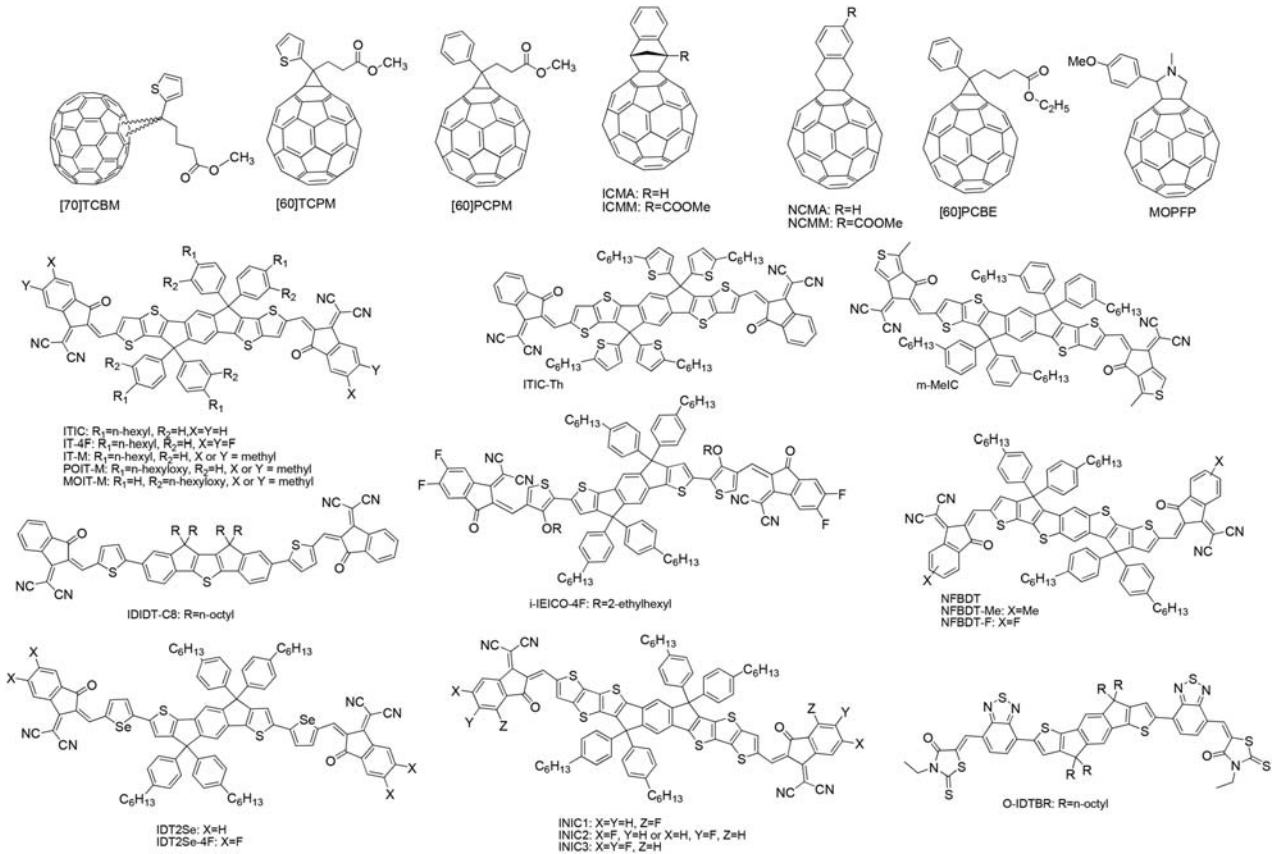


**Figure 15.19** Molecular structures of acceptor components delivering high power conversion efficiencies in organic solar cells.

These psychological barrier-breaking reports can be considered as a beginning of a renaissance of organic PVs, especially in the view of the fact that the main competing perovskite technology faced severe stability problems. However, considering the fact that the vast majority of publications report uncertified organic solar cell efficiencies, we strongly believe that interested readers will be doing a homework on their critical analysis following the major guidelines presented in this chapter.

## 15.3 Summary and outlook

Intense design of a diverse variety of new organic semiconductor materials, mostly the conjugated polymers, and their exploration as light harvesting components in organic solar cells led to significant improvement of our understanding of these systems. In particular, severe voltage losses of 0.8−1.0 eV were revealed and associated with the formation of CT states between donor and acceptor components of the blend and non-radiative relaxation processes [69]. It is very unlikely that careful material design will allow researchers to bring the offset between the organic absorber band gap and $q \times V_{oc}$ (q is elementary charge) below 0.7 eV [112]. If these considerations are correct, the efficiency of the single junction organic solar cells is limited to the level of 13%−16% (if ultra-high EQE and FF $>>$ 70% are reached), which is still hardly sufficient for launching large-scale production and entering on-grid PV market.

Another important obstacle is related to the fact that most efficient material combinations designed to date show insufficient stability or/and demonstrate significant efficiency roll-off while switching from laboratory small-area techniques to the industrially relevant roll-to-roll coating technologies. On top of that, high cost of the best-performing conjugated polymers ranging from hundreds to thousands of USD per-gram hampers the pilot R&D activities related to the optimization of large-area multilayer coating processes, device encapsulation, continuous quality control, etc., which slows the transition of polymer PVs to the large industry.

To sum up, principally new materials are urgently required now to address simultaneously a set of challenges presented in Fig. 15.20.

In spite of the long list of the aforementioned obstacles, we are confident that organic PVs sooner or later will make a significant impact on the PV market and multiple spheres of our life. Organic solar cells have

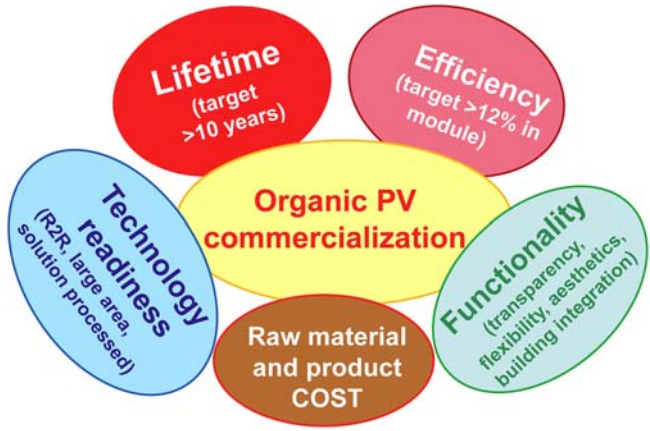


**Figure 15.20** Major challenges, which have to be addressed primarily through the advanced material design in order to accomplish the transition of organic photovoltaics technology from research labs to the world PV market. *PV*, Photovoltaic.

numerous advantages, which allow one to apply them in the areas where conventional solar panels based on rigid inorganic materials cannot work efficiently: e.g., semitransparent solar cells for smart windows, flexible solar cells integrated in textile, electronic skin, food package, etc. It is possibile to attain any arbitrary color and shape for organic solar cells, e.g., make devices in the form of a plant leaf, which makes organic PVs appealing for various aesthetic designs, which are intensively developed and commercialized by OPVIOUS (former Belectric OPV) company [159]. In contrast to standard inorganic PV modules, organic solar cells efficiently can harvest low-intensity diffuse light and demonstrate PCEs $>20\%$ under fluorescent or LED white light, enabling their multiple in-door applications [160].

Considerable success was also achieved in the field of building-integrated organic PVs (BIOPV). In particular, Heliatek company within the last 2 years received in total $>100$ million euro in investments for development of BIOPV using their new technology of small molecular multi-junction organic solar cells. Implementation of this technology will improve energy balance of buildings, while maintaining their aesthetic appearance. Lightweight and flexible "HeliaFilm" solar cells allow easy and relatively cheap approach to transforming roofs and facades of the buildings in one large-area collector of sunlight [161].

To conclude, organic PVs are starting to shape our future and we will be observing this continuously increasing impact within the next decades.

## Acknowledgment

This work was supported by the Russian Science Foundation (grant No. 18−13−00205) and Russian Ministry for Science and Education (project No. 0089-2019-0010).

## References

[1] M.A. Green, Y. Hishikawa, E.D. Dunlop, D.H. Levi, J. Hohl-Ebinger, A.W.Y. Ho-Baillie, Solar cell efficiency tables (version 51), Prog. Photovolt: Res. Appl 26 (2018) 3−12.
[2] S.J.C. Irvine, C. Candelise, in: S.J.C. Irvine (Ed.), Energy and Environment Series, Royal Society of Chemistry, Cambridge, 2014, pp. 1−26.
[3] <https://www.bloomberg.com/news/articles/2016-12-15/world-energy-hits-a-turning-point-solar-that-s-cheaper-than-wind> (last accessed 14.08.18).
[4] R.F. Service, Outlook brightens for plastic solar cells, Science 332 (2011) 293.
[5] W.R. Mateker, I.T. Sachs-Quintana, G.F. Burkhard, R. Cheacharoen, M.D. McGehee, Minimal long-term intrinsic degradation observed in a polymer solar cell illuminated in an oxygen-free environment, Chem. Mater. 27 (2015) 404−407.
[6] <http://www.heliatek.com/en/solar-films/technical-data> (accessed 06.01.18).
[7] S. Li, W. Liu, C.-Z. Li, M. Shi, H. Chen, Efficient organic solar cells with non-fullerene acceptors, Small 13 (2017) 1701120.
[8] N. Liang, W. Jiang, J. Hou, Z. Wang, New developments in non-fullerene small molecule acceptors for polymer solar cells, Mater. Chem. Front. 1 (2017) 1291−1303.
[9] W. Chen, Q. Zhang, Recent progress in non-fullerene small molecule acceptors in organic solar cells (OSC), J. Mater. Chem. C 5 (2017) 1275−1302.
[10] N.S. Sariciftci, A.J. Heeger, U.S. Patent 5331183.
[11] N.S. Sariciftci, L. Smilowitz, A.J. Heeger, F. Wudl, Photoinduced electron transfer from a conducting polymer to buckminsterfullerene, Science 258 (1992) 1474−1476.
[12] G. Yu, J. Gao, J.C. Hummelen, F. Wudl, A.J. Heeger, Polymer photovoltaic cells: enhanced efficiencies via a network of internal donor-acceptor heterojunctions, Science 270 (1995) 1789−1791.
[13] C.W. Tang, Two-layer organic photovoltaic cell, Appl. Phys. Lett. 48 (1986) 183−185.
[14] M. Theander, A. Yartsev, D. Zigmantas, V. Sundstrom, W. Mammo, M.R. Andersson, et al., Photoluminescence quenching at a polythiophene/C60 heterojunction, Phys. Rev. B 61 (2000) 12957−12963.
[15] D.E. Markov, C. Tanase, P.W.M. Blom, J. Wildeman, Simultaneous enhancement of charge transport and exciton diffusion in poly(p-phenylene vinylene) derivatives, Phys. Rev. B 72 (2005) 045217.
[16] D.E. Markov, E. Amsterdam, P.W.M. Blom, A.B. Sieval, J.C. Hummelen, Accurate measurement of the exciton diffusion length in a conjugated polymer using a heterostructure with a side-chain cross-linked fullerene layer, J. Phys. Chem. A 109 (2005) 5266−5274.
[17] S.H. Park, A. Roy, S. Beaupre, S. Cho, N. Coates, J.S. Moon, et al., Bulk heterojunction solar cells with internal quantum efficiency approaching 100%, Nat. Photonics 3 (2009) 297−302.
[18] Y. Li, D. Qian, L. Zhong, J.-D. Lin, Z.-Q. Jiang, Z.-G. Zhang, et al., A fused-ring based electron acceptor for efficient non-fullerene polymer solar cells with small HOMO offset, Nano Energy 27 (2016) 430−438.

[19] J. Liu, S. Chen, D. Qian, B. Gautam, G. Yang, J. Zhao, et al., Fast charge separation in a non-fullerene organic solar cell with a small driving force, Nat. Energy 1 (2016) 16089.
[20] Z. Zhang, W. Liu, T. Rehman, H.-X. Ju, J. Mai, X. Lu, et al., Energy-level modulation of non-fullerene acceptors to achieve high-efficiency polymer solar cells at a diminished energy offset, J. Mater. Chem. A 5 (2017) 9649–9654.
[21] V.D. Mihailetchi, L.J.A. Koster, J.C. Hummelen, P.W.M. Blom, Photocurrent generation in polymer-fullerene bulk heterojunctions, Phys. Rev. Lett. 93 (2004) 216601.
[22] A.C. Morteani, P. Sreearunothai, L.M. Herz, R.T. Phillips, R.H. Friend, C. Silva, Exciton regeneration at polymeric semiconductor heterojunctions, Phys. Rev. Lett. 92 (2004) 247240.
[23] L.J.A. Koster, E.C.P. Smiths, V.D. Mihailetchi, P.W.M. Blom, Device model for the operation of polymer/fullerene bulk heterojunction solar cells, Phys. Rev. B 72 (2005) 085205.
[24] J. Nelson, Diffusion-limited recombination in polymer-fullerene blends and its influence on photocurrent collection, Phys. Rev. B 67 (2003) 155209.
[25] Z. Yin, J. Wei, Q. Zheng, Interfacial materials for organic solar cells: recent advances and perspectives, Adv. Sci 3 (2016) 1500362.
[26] F. Huang, H. Wu, Y. Cao, Water/alcohol soluble conjugated polymers as highly efficient electron transporting/injection layer in optoelectronic devices, Chem. Soc. Rev. 39 (2010) 2500–2521.
[27] R. Steim, F.R. Kogler, C.J. Brabec, Interface materials for organic solar cells, J. Mater. Chem. 20 (2010) 2499–2512.
[28] L.–M. Chen, Z. Xu, Z. Hong, Y. Yang, Interface investigation and engineering - achieving high performance polymer photovoltaic devices, J. Mater. Chem. 20 (2010) 2575–2598.
[29] P.W.M. Blom, V.D. Mihailetchi, L.J.A. Koster, D.E. Markov, Device physics of polymer: fullerene bulk heterojunction solar cells, Adv. Mater. 19 (2007) 1551–1566.
[30] P. Kumar, in: C.R.C. Press (Ed.), Organic Solar Cells: Device Physics, Processing, Degradation, and Prevention, Taylor & Francis Group, Boca Raton, FL, 2017.
[31] W.C.H. Choy (Ed.), Organic Solar Cells: Materials and Device Physics, Springer, London; New York, 2013.
[32] C. Brabec, V. Dyakonov, U. Scherf (Eds.), Organic Photovoltaics, Wiley-VCH Verlag GmbH & Co. KGaA, Weinheim, Germany, 2008.
[33] S.-S. Sun, N.S. Sariciftci (Eds.), Organic Photovoltaics: Mechanisms, Materials, and Devices, Taylor & Francis, Boca Raton, FL, 2005.
[34] J. Nelson, The Physics of Solar Cells, Imperial College Press, 2003.
[35] G. Li, V. Shrotriya, J. Huang, Y. Yang, Measurement issues of organic solar cell, in: Z.H. Kafafi, P.A. Lane (Eds.), Proc. SPIE 7052, Organic Photovoltaics IX, 70520E (3 September 2008); doi: 10.1117/12.799607.
[36] H.J. Snaith, How should you measure your excitonic solar cells? Energy Environ. Sci. 5 (2012) 6513.
[37] E.L. Unger, E.T. Hoke, C.D. Bailie, W.H. Nguyen, A.R. Bowring, T. Heumüller, et al., Hysteresis and transient behavior in current-voltage measurements of hybrid-perovskite absorber solar cells, Energy Environ. Sci. 7 (2014) 3690–3698.
[38] D. Gupta, M. Bag, K.S. Narayan, Area dependent efficiency of organic solar cells, Appl. Phys. Lett. 93 (2008) 163301.
[39] A. Cravino, P. Schilinsky, C.J. Brabec, Characterization of organic solar cells: the importance of device layout, Adv. Funct. Mater. 17 (2007) 3906–3910.
[40] L.J. Rozanski, C.T.G. Smith, K.K. Gandhi, M.J. Beliatis, G.D.M.R. Dabera, K.D.G. I. Jayawardena, et al., A critical look at organic photovoltaic fabrication

methodology: defining performance enhancement parameters relative to active area, Sol. Energy Mater. Sol. Cells 130 (2014) 513–520.
[41] T.J.K. Brenner, Y. Vaynzof, Z. Li, D. Kabra, R.H. Friend, C.R. McNeill, White-light bias external quantum efficiency measurements of standard and inverted P3HT:PCBM photovoltaic cells, J. Phys. D 45 (2012) 415101.
[42] S.R. Cowan, J. Wang, J. Yi, Y.-J. Lee, D.C. Olson, J.W.P. Hsu, Intensity and wavelength dependence of bimolecular recombination in P3HT:PCBM solar cells: a white-light biased efficiency study, J. Appl. Phys. 113 (2013) 154504.
[43] H. Wei, Y.-H. Chao, C. Kang, C. Li, H. Lu, X. Gong, et al., High-efficiency large-bandgap material for polymer solar cells, Macromol. Rapid Commun. 36 (2015) 84–89.
[44] J. Lee, S.B. Jo, M. Kim, H.G. Kim, J. Shin, H. Kim, et al., Donor-acceptor alternating copolymer nanowires for highly efficient organic solar cells, Adv. Mater. 26 (2014) 6662.
[45] N. Wang, Z. Chen, W. Wei, Z. Jiang, Fluorinated benzothiadiazole-based conjugated polymers for high-performance polymer solar cells without any processing additives or post-treatments, J. Am. Chem. Soc. 135 (2013) 17060–17068.
[46] H. Hu, K. Jiang, G. Yang, J. Liu, Z. Li, H. Lin, et al., Terthiophene-based D − A polymer with an asymmetric arrangement of alkyl chains that enables efficient polymer solar cells, J. Am. Chem. Soc. 137 (2015) 14149–14157.
[47] Y. Liu, J. Zhao, Z. Li, C. Mu, W. Ma, H. Hu, et al., Aggregation and morphology control enables multiple cases of high-efficiency polymer solar cells, Nat. Commun. 5 (2014) 5293.
[48] L. Dou, W.-H. Chang, J. Gao, C.-C. Chen, J. You, Y. Yang, A selenium-substituted low-bandgap polymer with versatile photovoltaic applications, Adv. Mater. 25 (2013) 825–831.
[49] C.P. Yau, Z. Fei, R.S. Ashraf, M. Shahid, S.E. Watkins, P. Pattanasattayavong, et al., Influence of the electron deficient co-monomer on the optoelectronic properties and photovoltaic performance of dithienogermole-based co-polymers, Adv. Funct. Mater. 24 (2014) 678–687.
[50] I. Meager, R.S. Ashraf, S. Rossbauer, H. Bronstein, J.E. Donaghey, J. Marshall, et al., Alkyl chain extension as a route to novel thieno[3,2-*b*]thiophene flanked diketopyrrolopyrrole polymers for use in organic solar cells and field effect transistors, Macromolecules 46 (2013) 5961–5967.
[51] H. Zhou, L. Yang, W. You, Rational design of high performance conjugated polymers for organic solar cells, Macromolecules 45 (2012) 607–632.
[52] C. Duan, F. Huang, Y. Cao, Recent development of push-pull conjugated polymers for bulk-heterojunction photovoltaics: rational design and fine tailoring of molecular structures, J. Mater. Chem. 22 (2012) 10416–10434.
[53] Z.-G. Zhang, J. Wang, Structures and properties of conjugated donor-acceptor copolymers for solar cell applications, J. Mater. Chem. 22 (2012) 4178–4418.
[54] Y. He, W. Hong, Y. Li, New building blocks for π-conjugated polymer semiconductors for organic thin film transistors and photovoltaics, J. Mater. Chem. C 2 (2014) 8651–8661.
[55] F. Meyer, Fluorinated conjugated polymers in organic bulk heterojunction photovoltaic solar cells, Prog. Polym. Sci. 47 (2015) 70–91.
[56] H. Luo, Z. Liu, D. Zhang, Conjugated D-A terpolymers for organic field-effect transistors and solar cells, Polym. J. 50 (2018) 21–31.
[57] X. Liu, Y. Yan, Y. Yao, Z. Liang, Ternary blend strategy for achieving high- efficiency organic solar cells with nonfullerene acceptors involved, Adv. Funct. Mater. 28 (2018) 1802004.

[58] H. Mori, Y. Nishihara, Low-bandgap semiconducting polymers based on sulfur-containing phenacene-type molecules for transistor and solar cell applications, Polym. J. 50 (2018) 615–625.
[59] W. Huang, P. Cheng, Y.M. Yang, G. Li, Y. Yang, High-performance organic bulk-heterojunction solar cells based on multiple-donor or multiple-acceptor components, Adv. Mater. 30 (2018) 1705706.
[60] D. Susarova, N.P. Piven, A.V. Akkuratov, L.A. Frolova, M.S. Polinskaya, S. Ponomarenko, et al., ESR spectroscopy as a powerful tool for probing the quality of conjugated polymers designed for photovoltaic applications, Chem. Commun. 51 (2015) 2239–2241.
[61] L.A. Frolova, N.P. Piven, D.K. Susarova, A.V. Akkuratov, S.D. Babenko, P.A. Troshin, ESR spectroscopy for monitoring the photochemical and thermal degradation of conjugated polymers used as electron donor materials in organic bulk heterojunction solar cells, Chem. Commun. 51 (2015) 2242–2244.
[62] C.J. Brabec, A. Cravino, D. Meissner, N.S. Sariciftci, T. Fromherz, M.T. Rispens, et al., Origin of the open circuit voltage of plastic solar cells, Adv. Funct. Mater. 11 (2001) 374.
[63] F.B. Kooistra, J. Knol, F. Kastenberg, L.M. Popescu, W.J.H. Verhees, J.M. Kroon, et al., Increasing the open circuit voltage of bulk-heterojunction solar cells by raising the LUMO level of the acceptor, Org. Lett. 9 (2007) 551–554.
[64] B.D. Paulsen, J.C. Speros, M.S. Claflin, M.A. Hillmyer, C.D. Frisbie, Tuning of HOMO energy levels and open circuit voltages in solar cells based on statistical copolymers prepared by ADMET polymerization, Polym. Chem. 5 (2014) 6287–6294.
[65] K. Vandewal, A. Gadisa, W.D. Oosterbaan, S. Bertho, F. Banishoeib, I. Van Severen, et al., The relation between open-circuit voltage and the onset of photocurrent generation by charge-transfer absorption in polymer: fullerene bulk heterojunction solar cells, Adv. Funct. Mater. 18 (2008) 2064–2070.
[66] J. Lee, K. Vandewal, S.R. Yost, M.E. Bahlke, L. Goris, M.A. Baldo, et al., Charge transfer state versus hot exciton dissociation in polymer − fullerene blended solar cells, J. Am. Chem. Soc. 132 (2010) 11878–11880.
[67] K. Vandewal, S. Albrecht, E.T. Hoke, K.R. Graham, J. Widmer, J.D. Douglas, et al., Efficient charge generation by relaxed charge-transfer states at organic interfaces, Nat. Mater. 13 (2014) 63–68.
[68] K.R. Graham, P. Erwin, D. Nordlund, K. Vandewal, R. Li, G.O. Ngongang Ndjawa, et al., Re-evaluating the role of sterics and electronic coupling in determining the open-circuit voltage of organic solar cells, Adv. Mater. 25 (2013) 6076–6082.
[69] J. Benduhn, K. Tvingstedt, F. Piersimoni, S. Ullbrich, Y. Fan, M. Tropiano, et al., Intrinsic non-radiative voltage losses in fullerene-based organic solar cells, Nat. Energy 2 (2017) 17053.
[70] K. Vandewal, K. Tvingstedt, A. Gadisa, O. Inganäs, J.V. Manca, Relating the open-circuit voltage to interface molecular properties of donor:acceptor bulk heterojunction solar cells, Phys. Rev. B 81 (2010) 125204.
[71] V.C. Nikolis, J. Benduhn, F. Holzmueller, F. Piersimoni, M. Lau, O. Zeika, et al., Adv. Energy Mater. 7 (2017) 1700855.
[72] S.-F. Liao, C.-T. Chen, C.-Y. Chao, Isoindigo-dicyanobithiophene-based copolymer for high performance polymer-fullerene solar cells reaching 1.06 V open circuit voltage and 8.36% power conversion efficiency, ACS Macro Lett. 6 (2017) 969–974.
[73] X. Xu, P. Cai, Y. Lu, N.S. Choon, J. Chen, X. Hu, et al., Synthesis and characterization of thieno[3,2-*b*]thiophene-isoindigo-based copolymers as electron donor and

hole transport materials for bulk-heterojunction polymer solar cells, J. Polym. Sci. A 51 (2013) 424–434.
[74] J.-M. Jiang, P.-A. Yang, T.-H. Hsieh, K.-H. Wei, Crystalline low-band gap polymers comprising thiophene and 2,1,3-benzooxadiazole units for bulk heterojunction solar cells, Macromolecules 44 (2011) 9155–9163.
[75] L. Zhang, C. He, J. Chen, P. Yuan, L. Huang, C. Zhang, et al., Bulk-heterojunction solar cells with benzotriazole-based copolymers as electron donors: largely improved photovoltaic parameters by using PFN/Al bilayer cathode, Macromolecules 43 (2010) 9771–9778.
[76] N. Blouin, M. Leclerc, Poly(2,7–carbazole)s: structure-property relationships, Acc. Chem. Res. 41 (2008) 1110–1119.
[77] L. Ai, X.H. Ouyang, Q.D. Liu, S.Y. Wang, R.X. Peng, A. Islam, et al., Effective side chain selection for enhanced open circuit voltage of polymer solar cells based on 2D-conjugated anthracene derivatives, Dyes Pigm. 115 (2015) 73–80.
[78] G. Li, C. Kang, C. Li, Z. Lu, J. Zhang, X. Gong, et al., Planar conjugated polymers containing 9,10-disubstituted phenanthrene units for efficient polymer solar cells, Macromol. Rapid Commun. 35 (2014) 1142–1147.
[79] W. Li, R. Qin, Y. Zhou, M. Andersson, F. Li, C. Zhang, et al., Tailoring side chains of low band gap polymers for high efficiency polymer solar cells, Polymer 51 (2010) 3031–3038.
[80] J. Lee, M. Kim, B. Kang, S.B. Jo, H.G. Kim, J. Shin, et al., Side-chain engineering for fine-tuning of energy levels and nanoscale morphology in polymer solar cells, Adv. Energy Mater 4 (2014) 1400087.
[81] M.A. Uddin, T.H. Lee, S. Xu, S.Y. Park, T. Kim, S. Song, et al., Interplay of intramolecular noncovalent coulomb interactions for semi-crystalline photovoltaic polymers, Chem. Mater. 27 (2015) 5997–6007.
[82] M.L. Keshtov, A.R. Khokhlov, S.A. Kuklin, F.C. Chen, A.Y. Nikolaev, E.N. Koukaras, et al., Synthesis of alternating D–A1–D–A2 terpolymers comprising two electron-deficient moieties, quinoxaline and benzothiadiazole units for photovoltaic applications, Polym. Chem. 7 (2016) 4025–4035.
[83] S.-J. Ko, Q.V. Hoang, C.E. Song, M.A. Uddin, E. Lim, S.Y. Park, et al., High-efficiency photovoltaic cells with wide optical band gap polymers based on fluorinated phenylene-alkoxybenzothiadiazole, Energy Environ. Sci. 10 (2017) 1443–1455.
[84] W. Gao, T. Liu, M. Hao, K. Wu, C. Zhang, Y. Sun, et al., Dithieno[3,2-b:2′,3′-d] pyridin-5(4*H*)-one based D-A type copolymers with wide bandgap up to 2.05 eV to achieve solar cell efficiency up to 7.33%, Chem. Sci. 7 (2016) 6167–6175.
[85] Y. Matsuo, Development of fullerene derivatives with high LUMO level through changes in π-conjugated system shape, Pure Appl. Chem. 84 (2012) 945–952.
[86] M.C. Scharber, On the efficiency limit of conjugated polymer: fullerene-based bulk heterojunction solar cells, Adv. Mater. 28 (2016) 1994–2001.
[87] W. Tress, K. Leo, M. Riede, Influence of hole-transport layers and donor materials on open-circuit voltage and shape of *I-V* curves of organic solar cells, Adv. Funct. Mater. 21 (2011) 2140–2149.
[88] V.D. Mihailetchi, J. Wildeman, P.W.M. Blom, Space-charge limited photocurrent, Phys. Rev. Lett. 94 (2005) 126602.
[89] W. Tress, A. Petrich, M. Hummert, M. Hein, K. Leo, M. Riede, Imbalanced mobilities causing S-shaped IV curves in planar heterojunction organic solar cells, Appl. Phys. Lett. 98 (2011) 063301.
[90] T.D. Anthopoulos, C. Tanase, S. Setayesh, E.J. Meijer, J.C. Hummelen, P.W.M. Blom, et al., Ambipolar organic field-effect transistors based on a solution-processed methanofullerene, Adv. Mater. 16 (2004) 2174–2179.

[91] B. Ebenhoch, S.A.J. Thomson, K. Genevičius, G. Juška, I.D.W. Samuel, Charge carrier mobility of the organic photovoltaic materials PTB7 and PC71BM and its influence on device performance, Org. Electron. 22 (2015) 62–68.
[92] R. Mauer, M. Kastler, F. Laquai, The impact of polymer regioregularity on charge transport and efficiency of P3HT:PCBM photovoltaic devices, Adv. Funct. Mater. 20 (2010) 2085–2092.
[93] H. Zhou, L. Yang, S. Xiao, S. Liu, W. You, Donor-acceptor polymers incorporating alkylated dithienylbenzothiadiazole for bulk heterojunction solar cells: pronounced effect of positioning alkyl chains, Macromolecules 43 (2010) 811–820.
[94] E. Wang, M. Wang, L. Wang, C. Duan, J. Zhang, W. Cai, et al., Donor polymers containing benzothiadiazole and four thiophene rings in their repeating units with improved photovoltaic performance, Macromolecules 42 (2009) 4410–4415.
[95] A.V. Akkuratov, D.K. Susarova, D.V. Novikov, D.V. Anokhin, Y.L. Moskvin, A. V. Chernyak, et al., A strong influence of the positions of solubilizing alkyl side chains on optoelectronic and photovoltaic properties of TTBTBTT-based conjugated polymers, J. Mater. Chem. C 3 (2015) 1497–1506.
[96] J.M. Szarko, J. Guo, Y. Liang, B. Lee, B.S. Rolczynski, J. Strzalka, et al., When function follows form: effects of donor copolymer side chains on film morphology and BHJ solar cell performance, Adv. Mater. 22 (2010) 5468–5472.
[97] J.-S. Wu, Y.-Y. Lai, Y.-J. Cheng, C.-Y. Chang, C.-L. Wang, C.-S. Hsu, A new sp2–sp2 dialkylethylene-bridged heptacyclic ladder-type arene for high efficiency polymer solar cells, Adv. Energy Mater. 3 (2013) 457–465.
[98] I.H. Jung, J.-H. Kim, S.Y. Nam, C. Lee, D.-H. Hwang, S.C. Yoon, A di(1-benzothieno)[3,2-b:2′,3′-d]pyrrole and isoindigo-based electron donating conjugated polymer for efficient organic photovoltaics, J. Mater. Chem. C 4 (2016) 663–667.
[99] L. Huo, T. Liu, X. Sun, Y. Cai, A.J. Heeger, Y. Sun, Single junction organic solar cells based on a novel wide-bandgap polymer with efficiency of 9.7%, Adv. Mater. 27 (2015) 2938–2944.
[100] Y. Cai, X. Xue, G. Han, Z. Bi, B. Fan, T. Liu, et al., Novel π-conjugated polymer based on an extended thienoquinoid, Chem. Mater. 30 (2018) 319–323.
[101] Y. Deng, W. Li, L. Liu, H. Tian, Z. Xie, Y. Geng, et al., Low bandgap conjugated polymers based on mono-fluorinated isoindigo for efficient bulk heterojunction polymer solar cells processed with non-chlorinated solvents, Energy Environ. Sci. 8 (2015) 585–591.
[102] P. Guo, G. Luo, Q. Su, J. Li, P. Zhang, J. Tong, et al., Boosting up performance of inverted photovoltaic cells from bis(alkylthien−2−yl) dithieno[2,3-*d*:2′,3′-*d*′] benzo[1,2-b:4′,5′-*b*′] di thiophene-based copolymers by advantageous vertical phase separation, ACS Appl. Mater. Interfaces 9 (2017) 10937–10945.
[103] C.L. Chochos, N. Leclerc, N. Gasparini, N. Zimmerman, E. Tatsi, A. Katsouras, et al., The role of chemical structure in indacenodithienothiophene-alt-benzothiadiazole copolymers for high performance organic solar cells with improved photo-stability through minimization of burn-in loss, J. Mater. Chem. A 5 (2017) 25064–25076.
[104] M.C. Scharber, M. Koppe, J. Gao, F. Cordella, M.A. Loi, P. Denk, et al., Influence of the bridging atom on the performance of a low-bandgap bulk heterojunction solar cell, Adv. Mater. 22 (2010) 367–370.
[105] H. Hoppe, S. Shokhovets, G. Gobsch, Inverse relation between photocurrent and absorption layer thickness in polymer solar cells, Phys. Stat. Sol 1 (2007) R40–R42 (RRL).
[106] H. Hoppe, N.S. Sariciftci, *Polymer solar cells*, p. 1-86, in Photoresponsive Polymers II, in: S.R. Marder, K.-S. Lee (Eds.), Advances in Polymer Science, Publ.: Springer Berlin-Heidelberg, 2008.

[107] P.A. Troshin, H. Hoppe, A.S. Peregudov, M. Egginger, S. Shokhovets, G. Gobsch, et al., [70]Fullerene-based materials for organic solar cells, ChemSusChem 4 (2011) 119–124.
[108] M.C. Scharber, D. Muhlbacher, M. Koppe, P. Denk, C. Waldauf, A.J. Heeger, et al., Design rules for donors in bulk-heterojunction solar cells – towards 10% energy–conversion efficiency, Adv. Mater. 18 (2006) 789–794.
[109] T. Ameri, G. Dennler, C. Lungenschmied, C.J. Brabec, Organic tandem solar cells: a review, Energy Environ. Sci. 2 (2009) 347–363.
[110] J.D. Kotlarski, P.W.M. Blom, Ultimate performance of polymer:fullerene bulk heterojunction tandem solar cells, Appl. Phys. Lett. 98 (2011) 053301.
[111] Polymer Solar Cells Market: BIPV Segment by Application Projected to be a Highly Attractive Segment During the Forecast Period: Global Industry Analysis (2012–2016) and Opportunity Assessment (2017–2027); <https://www.future-marketinsights.com/reports/polymer-solar-cells-market>.
[112] W. Li, K.H. Hendriks, A. Furlan, M.M. Wienk, R.A.J. Janssen, High Quantum Efficiencies in polymer solar cells at energy losses below 0.6 eV, J. Am. Chem. Soc. 137 (2015) 2231.
[113] X. Liao, L. Zhang, L. Chen, X. Hu, Q. Ai, W. Ma, et al., Room temperature processed polymers for high-efficient polymer solar cells with power conversion efficiency over 9%, Nano Energy 37 (2017) 32–39.
[114] J.W. Jo, J.W. Jung, E.H. Jung, H. Ahn, T.J. Shin, W.H. Jo, Fluorination on both D and A units in D-A type conjugated copolymers based on difluorobithiophene and benzothiadiazole for highly efficient polymer solar cells, Energy Environ. Sci. 8 (2015) 2427.
[115] S. Zhang, B. Yang, D. Liu, H. Zhang, W. Zhao, Q. Wang, et al., Correlations among chemical structure, backbone conformation, and morphology in two highly efficient photovoltaic polymer materials, Macromolecules 49 (2016) 120–126.
[116] S. Ko, Q.V. Hoang, C.E. Song, M.A. Uddin, E. Lim, S.Y. Park, et al., High-efficiency photovoltaic cells with wide optical band gap polymers based on fluorinated phenylene-alkoxybenzothiadiazole, Energy Environ. Sci. 10 (2017) 1443.
[117] H. Hu, K. Jiang, G. Yang, J. Liu, Z. Li, H. Lin, et al., Terthiophene-based D-A polymer with an asymmetric arrangement of alkyl chains that enables efficient polymer solar cells, J. Am. Chem. Soc. 137 (2015) 14149.
[118] J. Lee, D.H. Sin, B. Moon, J. Shin, H.G. Kim, M. Kima, et al., Highly crystalline low-bandgap polymer nanowires towards high-performance thick-film organic solar cells exceeding 10% power conversion efficiency, Energy Environ. Sci. 10 (2017) 247.
[119] X. Liu, L. Nian, K. Gao, L. Zhang, L. Qing, Z. Wang, et al., Low band gap conjugated polymers combining siloxaneterminated side chain and alkyl side chain: a side chain engineering achieving large active layer processing window for PCE > 10% in polymer solar cells, J. Mater. Chem. A 5 (2017) 17619–17631.
[120] I. Shin, H. ju Ahn, J.H. Yun, J.W. Jo, S. Park, S. Joe, et al., High-performance and uniform 1 $cm^2$ polymer solar cells with D1–A–D2–A–type random terpolymers, Adv. Energy Mater. 8 (2018) 1701405.
[121] J. Huang, H. Wang, K. Yan, X. Zhang, H. Chen, C.-Z. Li, et al., Highly efficient organic solar cells consisting of double bulk heterojunction layers, Adv. Mater. 29 (2017) 1606729.
[122] Z. He, C. Zhong, S. Su, M. Xu, H. Wu, Y. Cao, Enhanced power-conversion efficiency in polymer solar cells using an inverted device structure, Nat. Photon. 6 (2012) 591–595.
[123] L. Ye, S. Zhang, W. Zhao, H. Yao, J. Hou, Highly efficient 2D-conjugated benzodithiophene-based photovoltaic polymer with linear alkylthio side chain, Chem. Mater. 26 (2014) 3603–3605.

[124] W. Li, B. Guo, C. Chang, X. Guo, M. Zhang, Y. Li, Efficient polymer solar cells based on a copolymer of meta-alkoxy-phenyl-substituted benzodithiophene and thieno[3,4-*b*]thiophene, J. Mater. Chem. A 4 (2016) 10135–10141.
[125] Z. Du, X. Bao, Y. Li, D. Liu, J. Wang, C. Yang, et al., Balancing high open circuit voltage over 1.0 V and high short circuit current in benzodithiophene-based polymer solar cells with low energy loss: a synergistic effect of fluorination and alkylthiolation, Adv. Energy Mater. 8 (2018) 1701471.
[126] C. Cui, Z. He, Y. Wu, X. Cheng, H. Wu, Y. Li, et al., High-performance polymer solar cells based on a 2D-conjugated polymer with an alkylthio side-chain, Energy Environ. Sci. 9 (2016) 885–891.
[127] J. Subbiah, B. Purushothaman, M. Chen, T. Qin, M. Gao, D. Vak, et al., Organic solar cells using a high-molecular-weight benzodithiophene-benzothiadiazole copolymer with an efficiency of 9.4%, Adv. Mater. 27 (2014) 702.
[128] N. Wang, W. Chen, W. Shen, L. Duan, M. Qiu, J. Wang, et al., Novel donor-acceptor polymers containing o-fluoro-p-alkoxyphenyl-substituted benzo[1,2-*b*:4,5-*b*′]dithiophene units for polymer solar cells with power conversion efficiency exceeding 9%, J. Mater. Chem. A 4 (2016) 10212–10222.
[129] W. Chen, M. Xiao, L. Han, J. Zhang, H. Jiang, C. Gu, et al., Unsubstituted benzodithiophene-based conjugated polymers for high-performance organic field-effect transistors and organic solar cells, ACS Appl. Mater. Interfaces 8 (2016) 19665–19671.
[130] H. Bin, Z.-G. Zhang, L. Gao, S. Chen, L. Zhong, L. Xue, et al., Non-fullerene polymer solar cells based on alkylthio and fluorine substituted 2D-conjugated polymers reach 9.5% efficiency, J. Am. Chem. Soc. 138 (2016) 4657–4664.
[131] W. Wang, B. Zhao, Z. Cong, Y. Xie, H. Wu, Q. Liang, et al., Nonfullerene polymer solar cells based on a main-chain twisted low-bandgap acceptor with power conversion efficiency of 13.2%, ACS Energy Lett. 3 (2018) 1499–1507.
[132] Z. Luo, G. Li, W. Gao, K. Wu, Z.-G. Zhang, B. Qiu, et al., A universal nonfullerene electron acceptor matching with different band-gap polymer donors for high-performance polymer solar cells, J. Mater. Chem. A 6 (2018) 6874–6881.
[133] S. Dai, F. Zhao, Q. Zhang, T.-K. Lau, T. Li, K. Liu, et al., Fused nonacyclic electron acceptors for efficient polymer solar cells, J. Am. Chem. Soc. 139 (2017) 1336–1343.
[134] C. Gu, D. Liu, J. Wang, Q. Niu, C. Gu, B. Shahid, et al., Alkylthienyl substituted asymmetric 2D BDT and DTBT-based polymer solar cells with a power conversion efficiency of 9.2%, J. Mater. Chem. A 6 (2018) 2371–2378.
[135] D. Liu, C. Gu, J. Wang, D. Zhu, Y. Li, X. Bao, et al., Naphthalene substituent via β-position linkage: an effective extended conjugated moiety can make a decent trade-off between optical band gap and open circuit voltage in symmetry breaking benzodithiophene based polymer solar cells, J. Mater. Chem. A 5 (2017) 9141–9147.
[136] T. Liu, X. Pan, X. Meng, Y. Liu, D. Wei, W. Ma, et al., Alkyl side-chain engineering in wide-bandgap copolymers leading to power conversion efficiencies over 10%, Adv. Mat. 29 (2017) 1604251.
[137] W. Huang, M. Li, L. Zhang, T. Yang, Z. Zhang, H. Zeng, et al., Molecular engineering on conjugated side chain for polymer solar cells with improved efficiency and accessibility, Chem. Mater. 28 (2016) 5887–5895.
[138] Z. Xu, Q. Fan, X. Meng, X. Guo, W. Su, W. Ma, et al., Selenium-containing medium bandgap copolymer for bulk heterojunction polymer solar cells with high efficiency of 9.8%, Chem. Mater. 29 (2017) 4811–4818.
[139] R. Peng, Z. Liu, Q. Guan, L. Hong, W. Song, Q. Wei, et al., Highly efficient non-fullerene polymer solar cells enabled by novel non-conjugated small-molecule cathode interlayers, J. Mater. Chem. A 6 (2018) 6327–6334.

[140] X. Ke, B. Kan, X. Wan, Y. Wang, Y. Zhang, C. Li, et al., Substituents on the end group subtle tuning the energy levels and absorptions of small-molecule nonfullerene acceptors, Dyes Pigm. 155 (2018) 241–248.
[141] Z. Liang, M. Li, X. Zhang, Q. Wang, Y. Jiang, H. Tian, et al., Near-infrared absorbing non-fullerene acceptors with selenophene as π bridges for efficient organic solar cells, J. Mater. Chem. A 6 (2018) 8059–8067.
[142] R. Hou, M. Li, S. Feng, Y. Liu, L. Wu, Z. Bi, et al., Fused pentacyclic electron acceptors with four cis-arranged alkyl side chains for efficient polymer solar cells, J. Mater. Chem. A 6 (2018) 3724–3729.
[143] G. Huang, J. Zhang, N. Uranbileg, W. Chen, H. Jiang, H. Tan, et al., Significantly enhancing the efficiency of a new light-harvesting polymer with alkylthio naphthyl substituents compared to their alkoxyl analogs, Adv. Energy Mater. 8 (2018) 1702489.
[144] L. Huo, T. Liu, B. Fan, Z. Zhao, X. Sun, D. Wei, et al., Organic solar cells based on a 2D benzo[1,2-*b*:4,5-*b*′]difuran-conjugated polymer with high-power conversion efficiency, Adv. Mater. 27 (2015) 6969–6975.
[145] T. Zhu, D. Liu, K. Zhang, Y. Li, Z. Liu, X. Gao, et al., Rational design of asymmetric benzodithiophene based photovoltaic polymers for efficient solar cells, J. Mater. Chem. A 6 (2018) 948–956.
[146] W. Zhao, S. Li, H. Yao, S. Zhang, Y. Zhang, B. Yang, et al., Molecular optimization enables over 13% efficiency in organic solar cells, J. Am. Chem. Soc. 139 (2017) 7148–7151.
[147] S. Chen, Y. Liu, L. Zhang, P.C.Y. Chow, Z. Wang, G. Zhang, et al., A wide-bandgap donor polymer for highly efficient non-fullerene organic solar cells with a small voltage loss, J. Am. Chem. Soc. 139 (2017) 6298–6301.
[148] B. Xiao, J. Song, B. Guo, M. Zhang, W. Li, R. Zhou, et al., Improved photocurrent and efficiency of non-fullerene organic solar cells despite higher charge recombination, J. Mater. Chem. A 6 (2018) 957–962.
[149] W. Su, Q. Fan, X. Guo, J. Chen, Y. Wang, X. Wang, et al., Significant enhancement of the photovoltaic performance of organic small molecule acceptors via side-chain engineering, J. Mater. Chem. A 6 (2018) 7988–7996.
[150] S. Xu, X. Wang, L. Feng, Z. He, H. Peng, V. Cimrová, et al., Optimizing the conjugated side chains of quinoxaline based polymers for nonfullerene solar cells with 10.5% efficiency, J. Mater. Chem. A 6 (2018) 3074–3083.
[151] T. Wang, T.-K. Lau, X. Lu, J. Yuan, L. Feng, L. Jiang, et al., A medium bandgap D-A copolymer based on 4-alkyl-3,5-difluorophenyl substituted quinoxaline unit for high performance solar cells, Macromolecules 51 (2018) 2838–2846.
[152] Y. Liu, G. Li, Z. Zhang, L. Wu, J. Chen, X. Xu, et al., An effective way to reduce energy loss and enhance open-circuit voltage in polymer solar cells based on a diketopyrrolopyrrole polymer containing three regular alternating units, J. Mater. Chem. A 4 (2016) 13265–13270.
[153] H. Yao, W. Zhao, Z. Zheng, Y. Cui, J. Zhang, Z. Wei, et al., PBDT-TSR: a highly efficient conjugated polymer for polymer solar cell with regioregular structure, J. Mater. Chem. A 4 (2016) 1708–1713.
[154] J.-H. Kim, J.B. Park, I.H. Jung, A.C. Grimsdale, S.C. Yoon, H. Yang, et al., Well-controlled thieno[3,4-*c*]pyrrole-4,6-(5*H*)-dione based conjugated polymers for high performance organic photovoltaic cells with the power conversion efficiency exceeding 9%, Energy Environ. Sci. 8 (2015) 2352–2356.
[155] H. Li, D. He, P. Mao, Y. Wei, L. Ding, J. Wang, Additive-free organic solar cells with power conversion efficiency over 10%, Adv. Energy Mater. 7 (2017) 1602663.
[156] W. Yue, R.S. Ashraf, C.B. Nielsen, E. Collado-Fregoso, M.R. Niazi, S.A. Yousaf, et al., A thieno[3,2-*b*][1]benzothiophene isoindigo building block for additive-and

annealing-free high-performance polymer solar cells, Adv. Mater. 27 (2015) 4702–4707.
[157] Z. Fei, F.D. Eisner, X. Jiao, M. Azzouzi, J.A. Röhr, Y. Han, et al., An alkylated indacenodithieno[3,2-*b*]thiophene-based nonfullerene acceptor with high crystallinity exhibiting single junction solar cell efficiencies greater than 13% with low voltage losses, Adv. Mater. 30 (2018) 1705209.
[158] L. Meng, Y. Zhang, X. Wan, C. Li, X. Zhang, Y. Wang, et al., Organic and solution-processed tandem solar cells with 17.3% efficiency, Science 361 (2018) 1094–1098.
[159] <http://www.opvius.com/> (last accessed 14.08.18).
[160] H. Yin, J.K.W. Ho, S.H. Cheung, R.J. Yan, K.L. Chiu, X. Hao, et al., Designing a ternary photovoltaic cell for indoor light harvesting with a power conversion efficiency exceeding 20%, J. Mater. Chem. A 6 (2018) 8579–8585.
[161] <https://www.heliatek.com/de/> (last accessed 14.08.18).

PART V

# Nano-carbon materials-based solar cells

This page intentionally left blank

# CHAPTER 16

# Graphene and carbon nanotube-based solar cells

**Xiaoxiao Lin**[1,2] **and Peng Gao**[1,2]
[1]CAS Key Laboratory of Design and Assembly of Functional Nanostructures, and Fujian Key Laboratory of Nanomaterials, Fujian Institute of Research on the Structure of Matter, Chinese Academy of Sciences, Fuzhou, P.R. China
[2]Laboratory of Advanced Functional Materials, Xiamen Institute of Rare Earth Materials, Haixi Institute, Chinese Academy of Sciences, Xiamen, P.R. China

## Contents



## 16.1 Introduction

Energy shortages are rapidly becoming a reality due to the exhaustible reserves of conventional and non-renewable fossil fuels. The byproducts of these sources combusting into the atmosphere, resulting in a massive release of harmful gases into the atmosphere, making clean, renewable energy source more desirable. Solar energy is a clean and inexhaustible power source [1–4]. Solar cells have attracted tremendous attention as efficient energy conversion devices (Fig. 16.1). Silicon materials have been dominating the platform of solar cells since the beginning of the photovoltaic technology. In recent years, with the development of third generation solar cells, nanocarbon materials, especially graphene and carbon

*Nanomaterials for Solar Cell Applications*
DOI: https://doi.org/10.1016/B978-0-12-813337-8.00016-3

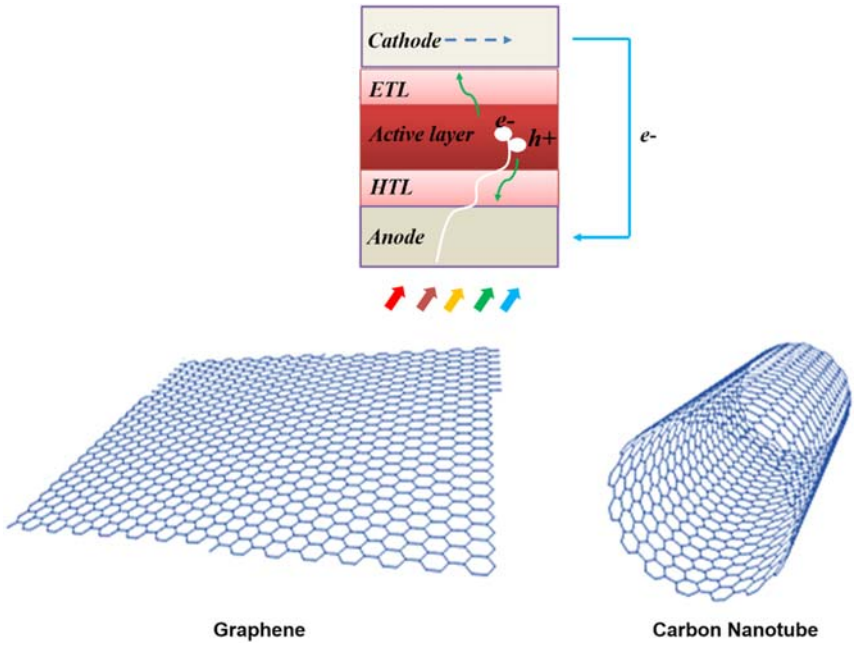


**Figure 16.1** Contains a schematic illustration of the typical structure of a solar cell with graphene and carbon nanotube.

nanotubes (CNTs) [2,5–8], started to be the focus of study. Thanks to the merits of carbon materials, such as being an abundant resource, having easy functionality, and a fast charge transfer rate [9,10], they are vital components in a multitude of applications, such as catalysis or catalysis support, gas separation, supercapacitor, electrode materials, etc. [11,12]. In this regard, graphene-based solar cells using CNTs as transporting layers or electrodes, have attracted considerable attention as portable energy conversion devices that have a variety of applications [13–20] (Fig. 16.1).

### 16.1.1 Graphene properties and advantages

This section contains an introduction to the properties and advantages of graphene and graphene derivatives. Graphene is structurally a single layer graphite with one carbon atom of thickness. The interaction force between graphite layers is weak and can easily exfoliate to form a graphene sheet. The resulting graphene is formed by hexagon shaped arrangement of carbon atoms connected by sp [2] bonds, that can be extended indefinitely in a two-dimensional space [21–24]. Since

graphene has outstanding chemical, physical, electrical and optical properties, it became an ideal candidate for use in many industrial and scientific fields. Recently, there is an increasing tendency to use graphene in the photovoltaic industry particularly in perovskite solar cells (PSC), due to the high efficiency and low fabrication cost [25–27]. It has been reported that graphene can successfully be applied to many parts of a solar cell, including the electrode, active layer, and interfacial layers [28–30]. There are also many reports about the improved efficiencies from graphene modified solar cells compared with the referenced counterparts.

### 16.1.2 Carbon nanotubes

Reports about CNTs were first issued by Iijima at the NEC Corporation using high-resolution transmission electron microscopy (TEM) in 1991 [31]. CNTs are mainly made up of hexagonally oriented carbon atoms with a cylindrical structure, that is often ascribed to a tubular shaped graphene after being rolled up [31]. CNTs have similar properties to graphene, such as; being chemically and thermally stable, mechanically robust, uniquely porous, and highly conductive. CNTs consist of single-wall CNT (SWCNTs) and multiwall CNTs (MWCNTs). SWCNTs are structurally the simplest CNT with typical diameters in the range of 0.4–3 nm. MWCNTs comprise several co-axially arranged SWCNTs with different radii and an intertube distance close to the interplane distance in graphite (0.34–0.35 nm). Moreover, MWCNTs can be synthesized with diameters as large as 100 nm [32], and the length of the two kinds of CNTs can be controlled during the growth process [33]. With the rapid development of nanotechnology, CNTs have become necessary components in many applications, such as electronic devices [34], supercapacitors [18], catalysis [35], photonics [36], and more. In terms of solar cells, CNTs find applications such as conductive and transparent electrodes, hole collection and transport layer, etc. [37].

## 16.2 Graphene-based solar cells

Converting sunlight directly to electrical energy using solar cells is one of the most promising, highly scalable solutions[38]. Great efforts have been made to improve the efficiency of the photon to electricity conversion, leading to significantly enhanced device performance of photovoltaic systems over the past few decades [39–42]. Graphene, with its unique properties, including high transparency in the broad wavelength region,

ultrahigh carrier mobilities, chemical, and mechanical robustness, has found applications as a transparent electrode and other device components in solar cells [43,44]. Furthermore, graphene-based materials used as transparent electrodes instead of indium tin oxide (ITO) applied in PSCs, have a greater power conversion efficiency (PCE) of over 17% [45]. In this section, we will focus on recent advances in solar cells based on graphene materials.

### 16.2.1 Graphene as a transparent electrode for solar cells

ITO or fluorine-doped tin oxide (FTO) is usually employed as transparent electrode materials in conventional solar cells [46–49]. However, the resource of indium element is rare and expensive. The brittle nature of metal oxides makes them easy to crack, which largely limits the applications of ITO (or FTO) in flexible electrode materials [50,51]. Graphene-based materials on the other hand, possess excellent properties, including the abundance of carbon sources, easy functionality, high electrical conductivity, low sheet resistance, and high optical transparency. Graphene has the potential to replace ITO electrodes as the transparent electrode material used for solar cells. Since 2008, graphene derivatives have taken greater roles in photovoltaic applications. However, those devices have shown instability under dark conditions and poor initial PCE of 0.4%–1% [8,52], which probably resulted from the high sheet resistance of graphene oxide (GO) with low dispersion. To solve the problem, De Arco, et al. reported that continuous, highly flexible, transparent graphene films obtained by chemical vapor deposition (CVD) and applied as transparent conductive electrodes (TCEs) in organic photovoltaic cells as shown in Fig. 16.2 [53], showed a PCE of 1.18% with the graphene anode, which was very close to that of an ITO reference electrode (PCE = 1.27%). Also, the CVD made graphene is transferred to flexible polyethylene terephthalate (PET) substrates, giving excellent flexibility with a maximum bending ability up to 138 degrees, while the ITO-based devices showed poor flexibility of only 60 degrees.

Subsequently, Park et al. used graphene-based materials as a flexible anode and cathode in polymer solar cells and achieved PCEs of 6.1% and 7.1% [54]. They fabricated flexible polymer solar cells on polyethylene naphthalate (PEN) substrate and the device remained good condition after 100 bending cycles. However, compared to the reference ITO electrode, the PCE of solar cells with graphene-based electrode was still inefficient

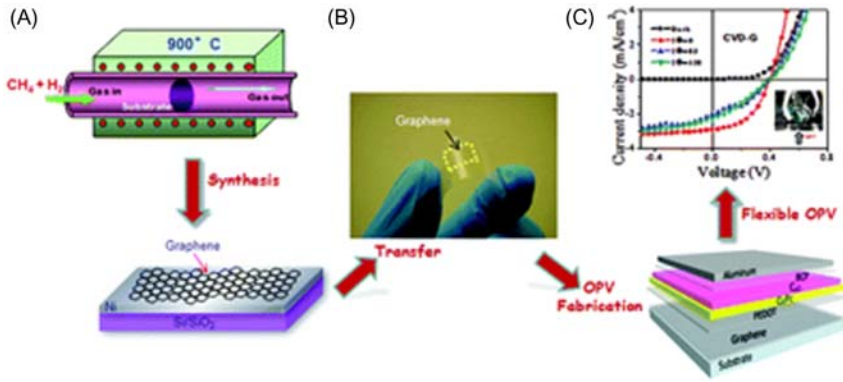


**Figure 16.2** Contains the following: (A) Preparing the process and construction of the heterojunction organic solar cell fabricated with graphene as an anodic electrode: CVD graphene/PEDOT/CuPc/C60/BCP/Al. (B) Schematic of the CVD graphene transfer process onto transparent substrate. (C) Current density versus the voltage characteristics of CVD graphene [53]. *CVD*, Chemical vapor deposition; *PEDOT*, poly (3,4-ethylene dioxythiophene).

because of the poor charge transportability from the active layers into the graphene electrode. Studies have shown that graphene can be miscible with other highly conductive materials such as Au or Ag metals to improve conductivity and carrier transport as hybrid electrodes. Yusoff et al. assembled Au-doped single-layer graphene nanoribbons (SLGNRs) as the transparent electrode in ITO-free tandem polymer solar cells. The sheet resistance of the SLGNRs (Au-doped) transparent electrode ranged from 350 to 221 $\Omega\,sq^{-1}$. The data also revealed that soluble $AuCl_3$ can successfully be used to dope SLGNRs, and the sheet resistance can be adjusted by controlling doping concentration [55]. Recently, Ye et al. used the Ag nanowire (AgNW)-graphene hybrid film as a TCE and compared it with the pristine AgNWs electrode. The sheet resistance of AgNW-graphene TCE was sharply reduced to 14.9 $\Omega\,sq^{-1}$ and showed good transmittance and outstanding stability with anti-corrosion refrainment [56].

Improving the PCE of solar devices must include making full use of the solar spectrum with the lowest cost. Currently, silicon-based solar cells are the most popular photovoltaic technology that is available on the market due to the abundance of natural resources, high efficiency, and long-term stability [57]. So far, solar cell devices based on crystalline silicon materials reached a maximum PCE of around 25% and became the dominating material used for products in the commercial market. Regardless of

the quick reduction of module price in recent years, silicon solar cells are still costly due to the complicated fabrication processes necessary and the harsh conditions involved[4,58]. Therefore, organic/silicon hybrid solar cells have drawn a great deal of attention due to the low cost of manufacturing at moderate temperatures [59,60]. Additional improvement in environmental stability is still needed and is a prerequisite to enhance the chance of real applications [61].

Graphene quantum dots (GQDs) are made of monolayered or less-layered graphene, and are a few nanometers in diameter. The GQDs have a unique edge and quantum-confinement effects, making unique and distinctive from traditional graphene and quantum dots [62]. Zero-dimensional GQDs are promising for optoelectronic and energy storage applications owing to size-dependent band gap and tunable chemical properties [63–65]. Diao et al. demonstrated solution-processed GQDs for highly efficient GQDs/n-silicon heterojunction solar cells [66] (Fig. 16.3). The GQDs layer could be used as a hole transport layer (HTL), to accelerate the separation of photogenerated electron–hole pairs. It could also serve as an electron transporting layer (ETL) to avoid the carrier recombination at the anode [67]. In addition, they used graphene as the TCE to guarantee the efficient light absorption and carrier collection. GQDs/n-silicon heterojunction solar cell exhibited a PCE record of 12.35% under AM 1.5G irradiation. Due to the high chemical stability and physical robustness of GQDs and graphene, the devices also

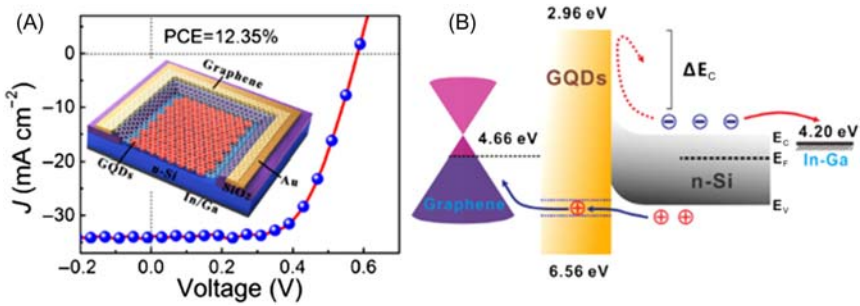


**Figure 16.3** Shows the following: (A) Schematic illustration of the GQDs/Si heterojunction solar cell with graphene film on top of the transparent electrode. *J–V* curves of the GQDs/Si solar cell measured (B) Energy band diagram of the GQDs/Si heterojunction device with graphene transparent electrode. $\Delta E_c$ represents the offset between the $E_c$ of Si and LUMO of GQDs [66]. *GQDs*, Graphene quantum dots.

exhibited excellent stability in air. It is likely that high-performance and low-cost photovoltaics could become a reality with the advances in the high-efficiency GQDs/Si heterojunction solar cells [66].

Since the pioneering work by Grätzel et al. [1] the unprecedented dye-sensitized solar cells (DSSCs) have been seen as a candidate to replace silicon-based solar cells, owing to their low cost, ease of assembly, and growing PCE values. DSSCs are generally made of mesoporous anatase $TiO_2$ film loaded with sensitizers, a transparent electrode such as ITO or FTO, a transparent conductive counter electrode with platinum as a reductive catalyst, and finally , an electrolyte, usually containing a redox couple of $I^-/I_3^-$ [68]. To date, DSSCs have achieved a respectable high PCE of 15%. The effort is still being made to further improve the PCE of DSSCs since the electrode materials in the state-of-the-art DSSCs are costly and not recyclable, especially the counter electrode. The precious metal platinum is usually applied as a counter electrode with high catalytic activity and high conductivity to catalyze the reduction reaction of $I_3^-$ to $I^-$ for iodine-based electrolytes. Its high cost and depletable resource largely limit its wide applications. The efforts to exploit new counter electrode materials with lower expense for DSSCs is imperative and urgent. There are more stable and cheaper materials like carbon, that can be used for the replacement of Pt-based counter electrodes.

As previously discussed, graphene has many advantages including super flexibility, high transmittance, high electrical conductivity, thermal and chemical stability, as well as multiformity of synthesis. Moreover, graphene's work function (5.0 eV) is near Au (5.1 eV), which makes carbon an ideal candidate for a PSC back electrode. In this regard, many groups have created various solutions to replace Pt-based counter electrodes with graphene-based materials to produce cost-effective DSSCs devices. Roy-Mayhew et al. provided a functionalized graphene sheet with the prototypically defective sites as DSSCs counter cathode. As shown in Fig. 16.4, the modified graphenes contained oxygen functional groups, such as hydroxyls and carbonyls at the surface. By controlling the amount of oxygen functional groups in the graphene sheets using thermal treatment, the C/O ratio of the functionalized graphene sheets can be changed. Furthermore, the current density-voltage curves exhibited the differences in the performances of DSSC devices with functionalized graphene sheets and platinum counter electrodes. It was apparent that the device with functionalized graphene sheets showed almost equivalent PCE (4.99%) to that of platinum counter electrodes (5.48%) based devices [69].

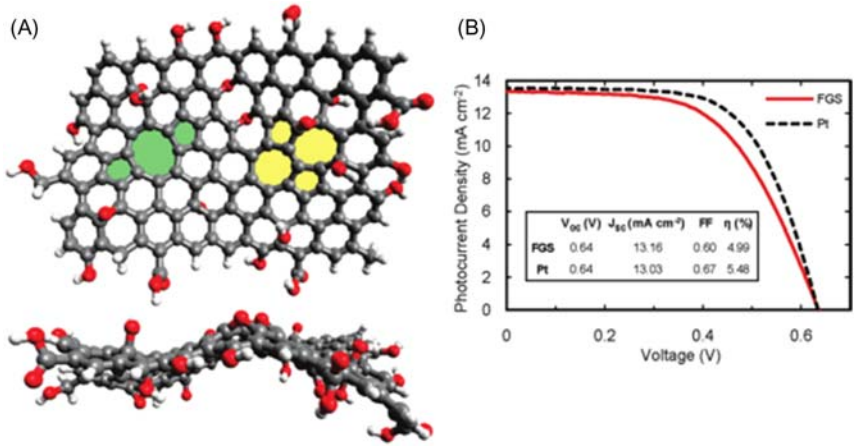


**Figure 16.4** Contains the following: (A) Schematic of functional groups and lattice defects on an FGS. Side view emphasizing the topography of the sheet. (B) *J*–*V* curve characteristics of DSSCs using thermally decomposed chloroplatinic acid and $FGS_{13}$ counter electrodes measured in Iodolyte AN-50 electrolyte. The active area is 0.39 $cm^2$ [69]. *DSSCs*, Dye-sensitized solar cells.

Later research shows that some groups designed nickel oxide nanoparticles loaded on graphene in DSSCs devices and utilized as an electrocatalyst counter electrode [70,71]. The pulsed laser ablation method was used to prepare the material in an inert nitrogen atmosphere, however, the synthesis of high-quality homogeneous metal nanoparticles uniformly distributed on the surface of graphene faces a huge challenge due to the quick chemical reduction rate and other complicated processes accompanied by a reduction reaction. Expensive equipment such as a vacuum chamber, makes it difficult to develop a sustainable and economic process. Dao et al. [71]. exploited dry plasma reduction to easily, continuously, uniformly, and stably synthesize the NiO-NP–RGO compound with simultaneously reduced Ni precursor ions and GO [71–73]. This method breaks the obstacle in the experimental condition aforementioned and makes the process sustainable. Additionally, the evidence from the energy dispersive spectrometer, X-ray diffraction spectrometer, and X-ray photoelectron spectroscopy (XPS) measurements suggested the formation of NiO, that was well dispersed on the surface of RGO, with a low degree of aggregation. The result was confirmed by TEM in cooperations with SEM analysis, revealing that the NiO-NPs were 1.5 nm on average smaller than the typical sizes of 14.2 and 25 nm formed by pulsed laser ablation [70] and thermal decomposition [74] respectively. The DSSC device

with NiO-NP−RGO nanohybrid-coated counter electrode exhibits a PCE of 7.42% (±0.10%), which is superior to those of the devices with GO-coated and RGO-coated and NiO-NP-immobilized counter electrodes respectively [4.48% (±0.12%), 5.18% (±0.11%) and 1.53% (±0.15%)]. The electrochemical impedance spectroscopy (EIS) produced Nyquist plots of DSSCs with the NiO-NP−RGO nanohybrid-coated, GO-coated, RGO-coated, NiO-NP-immobilized and Pt-sputtered counter electrodes. The study shows that the charge transfer resistance (Rct) of the NiO-NP−RGO nanohybrid-coated electrode was 1.93 $\Omega$ cm$^2$ smaller than other counter electrodes, which is quite equal to that of the Pt-sputtered electrode (1.22 $\Omega$ cm$^2$). The photocurrent−voltage ($I-V$) characteristics of DSSCs was also tested with the NiO-NP−RGO counter electrode which was in comparison to that of the conventional Pt-sputtered counter electrode at the same condition.

Water is always used as the solvent and reaction medium to facilitate reaction during the hydrothermal process. The hydrothermal method is cost-effective and green at ambient atmosphere, atmospheric pressure, and low temperature. With continuous development, a hydrothermal method is in expansion and becoming better with more experience. It is likely to gain attention in the technology and industry fields because of low-cost, high-efficiency, facile process with relatively mild conditions, especially in the carbonization process via hydrothermal technique. Moreover, auxiliary precursors are ready to dope carbon matrix with heteroatomic (O, N, P, B) and transform it into a functional carbon material with the hydrothermal approach.

Contradictory, in 2014, Kannan et al. first reported nitrogen and sulfur co-doped graphene (NSG) nanosheet as a counter electrode with a synergistically enhanced performance for DSSCs using a convenient hydrothermal method. They systematically investigated its electrocatalytic activity of the NSG towards the $I_3^-/I^-$ redox reaction, which showed favorable electrocatalytic activity, high electronic conductivity, and resistance to the corrosive $I_3^-/I^-$ electrolyte [75]. In their report, they used thiourea as a source for both nitrogen and sulfur heteroatoms to synthesize nitrogen and sulfur dual-doped graphene (NSG) nanosheets via one-step hydrothermal method, as illustrated in Fig. 16.5, then applied it as a counter electrode material for DSSCs. Thiourea was then decomposed into hydrogen sulfide, isothiocyanic acid, ammonia and carbodiimide [76] during the hydrothermal treatment, which allowed the materials to be formed with a high content of sulfur and nitrogen. At the same time, the

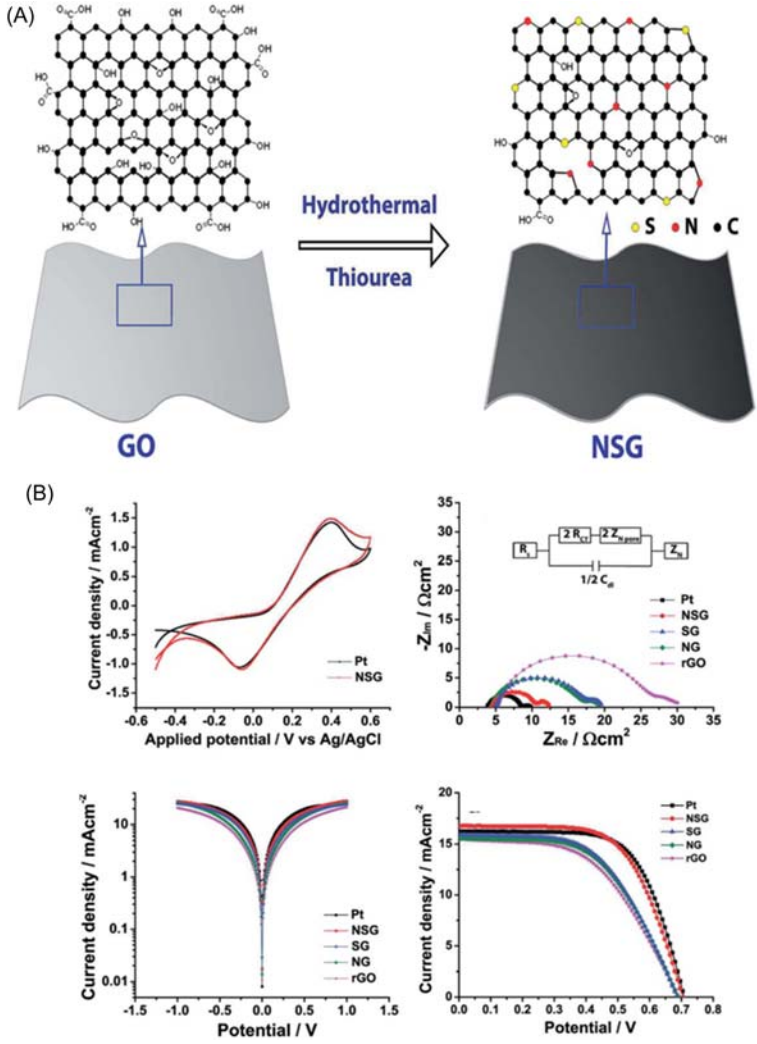


**Figure 16.5** Contains the following: (A) Schematic illustration of the synthesis of NSG nanosheets from GO and thiourea using a simple hydrothermal method. (B) Electrochemical performances of different counter electrodes: CV curves of NSG and Pt electrodes obtained at a scan rate of 50 mV $s^{-1}$ using Pt wire and $Ag/Ag^{+}$ as a counter and reference electrodes, respectively; Nyquist plots of different counter electrodes using symmetric cells; Tafel polarization curves of different counter electrodes using symmetric cells; Photocurrent−voltage curves of DSSCs with different counter electrodes under one-sun illumination [75]. *DSSCs*, Dye-sensitized solar cells; *NSG*, nitrogen and sulfur co-doped grapheme.

materials showed that nitrogen and sulfur heteroatoms were highly distributed throughout the graphene nanosheet. The composition of doped nitrogen includes pyridinic, pyrrolic, and graphitic species. The doped sulfur was present in the C−S−C state via high-resolution XPS spectra. The analysis showed the content of nitrogen and sulfur in the NSG sample was 2.02 and 2.54 at% from the XPS spectrum, and successfully implied that the nitrogen and sulfur heteroatoms were incorporated into the graphene sheet. For reference, they also calculated the C/O ratios of NSG and GO samples were 9.75 and 1.91 respectively from the XPS spectra, which further explained that the graphene nanosheets' oxide groups were in reduction reaction during the co-doping process. Importantly, the electrochemical measurements were comprehensively carried out to evaluate the photovoltaic performance using nitrogen and sulfur dual-doped graphene (NSG) nanosheets as the counter electrode in DSSCs device, such as cycle-voltage curves, Nyquist plots. Moreover, the PCE with the NSG counter electrode was 7.42%, close to that of the Pt counter electrode (7.56%); its performance excelled greater than that of the single nitrogen or sulfide-doped graphene counter electrodes. As shown in Fig. 16.5, the CV curves of NSG and Pt electrodes obtained at a scan rate of 50 mV $s^{-1}$ all exhibited conspicuous redox peaks at approximately −0.05 and 0.39 V (an Ag/AgCl as a reference electrode), which relates to the reduction of triiodide to iodide.

Electronegativity of a carbon atom is lower than that of an nitrogen atom. Its atomic size is smaller than the sulfur atom, thus doping with them led to structural modifications for better electrocatalytic activity. As previously mentioned, the difference in electronegativity between nitrogen and carbon is the same as the structural distortion caused by the sulfur bigger atomic size attributed to the synergistic effect of the high charge polarization and then modified the charge and spin density of graphene. That was the first time that nitrogen and sulfide dual-doping of graphene applied on the counter electrode performance in DSSCs device via green and straightforward hydrothermal approach, made new and promising methods to accelerate the photovoltaic performance of DSSCs.

Platinum-based materials are very popular as counter electrodes in DSSCs devices because of unique conductivity and excellent catalytic activity. Although, platinum-free solar cells' efficiency with these hybrids was still lower than that of cells with a platinum counter electrode, it

lacked a useful structure to generate a synergistic effect in the hybrid materials. $NiS_2$/reduced GOs (rGO) have been proven to have better catalytic activity, higher conductivity, and higher PCE compared to the single-component materials in DSSCs devices [77]. Sequentially, Bi et al. designed a quasi-core−shell nitrogen-doped graphene/cobalt sulfide conductive catalyst to improve the DSSCs device with a higher PCE, up to 10.71% based on a platinum-free counter electrode. The material consists of a core of CoS nanoparticles coated with a shell of ultrathin N-doped graphene layers that act as conductive paths, in order to overcome the problem of low conductivity [77].

Recently, Casaluci et al. demonstrated graphene ink used as a counter electrode for fabrication of large-area DSSC modules with a viable spray coating method. The graphene-based ink was obtained by liquid phase exfoliation from graphite and was sprayed on a transparent conductive oxide (TCO) substrate, achieving a graphene-based electrode with a large area ($>90\ cm^2$) and semi-transparent (transmittance 44%), instead of platinum-based counter electrode material [78]. The graphene ink was deposited in DMF on FTO substrate and kept at a low temperature of 100°C, then a post-heat treatment to 400°C under inert nitrogen atmosphere was applied. Consequently, the graphene-based large area DSSC device was examined by electrochemical measurements to estimate photovoltaic performance. Further insights into electrical resistance and ion diffusion of the graphene ink electrodes can be attained, based on the frequency dependent impedances from the EIS curves (the Nyquist plot). It is evident that the semicircle radius of a sample FTO is smaller than that of FTO/graphene and FTO/Pt, suggesting that FTO/graphene has a lower interface contact resistance. From the reference group cell (see Fig. 16.6B) the two devices with graphene-based and platinum-based counter electrodes all displayed the first semicircle in $I_3^-/I^-$ liquid electrolyte sandwiched measured in the 20 Hz−1 MHz range. Afterward a large-area (43.2 $cm^2$ active area) DSSC module with the graphene-based counter electrode was fabricated, with a PCE of 3.5%. The spray coating approach presented in this article is an all-printed, flexible, cost-effective approach, using large-area and transparent graphene-based counter electrode photovoltaic devices on random substrates.

With the rapid and successful developments of solar cells, PSCs have drawn more attention in photovoltaic fields over the decades years, owing to the economic expense, high-efficiency (≥20%), and pure solution-processed properties. Presently it is desirable in our daily lives for

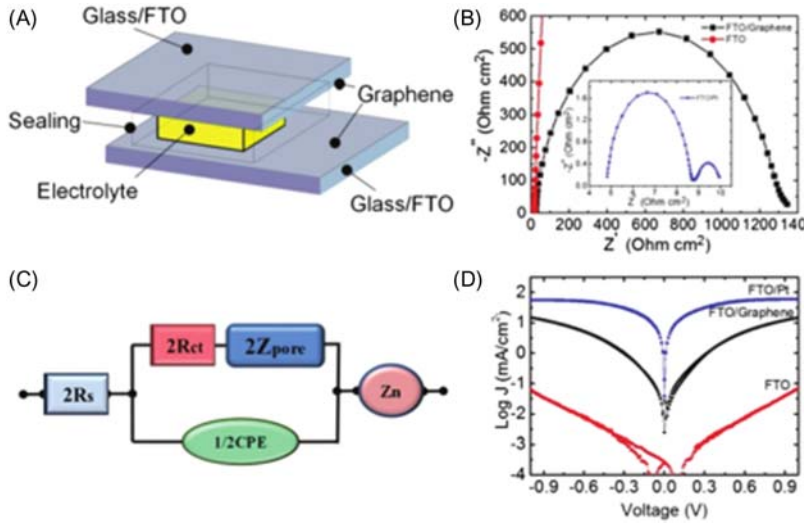


**Figure 16.6** Contains the following: (A) Schematic of a dummy cell for EIS measurements. (B) Nyquist plots of FTO (*left straight line*) and FTO−graphene (*Semicircle line*) CEs measured in the 20 Hz−1 MHz range. The inset contains the EIS plot of a dummy cell fabricated with Pt CE. (C) Equivalent circuit is used for data fitting. (D) Tafel plot is used for the dummy cell assembled with FTO, FTO/graphene, and FTO/Pt [78]. *EIS*, electrochemical impedance spectroscopy.

portable and wearable PSCs due to their high specific power density and flexibility. The traditional structure of PSCs is usually the n−i−p architecture with high performance, such as electron transport materials ($TiO_2$ or $Al_2O_3$), perovskite adsorptive material, and hole transport material [79−81]. The mesoporous $TiO_2$ or planar heterojunction structure is employed in PSCs. During the process of the metal oxide film's preparation, the temperature requirement is over 450°C, which is incompatible with flexible substrates limited to low-cost manufacturing. Earlier researchers [82] designed the p−i−n (ITO)/PEDOT:PSS/$CH_3NH_3PbI_3$ ($MAPbI_3$)/PCBM/gold (Au) architecture with a PCE of 18.1% at relatively low temperature, which is still inferior to the n−i−p devices using metal oxide for electron transport layers. However, p−i−n PSCs revealed low hysteresis behavior at the low processing temperature and facile manufacturing processes compared to that of n−i−p devices and aroused a wide range of research interests [79,83−85]. Docampo et al. first introduced the flexible PSCs with a PCE of 6.4% by employing the p−i−n inverted architecture device during a low-temperature solution-process in 2013 [86]. Kim et al. applied a compact TiOx layer to flexible PSCs using

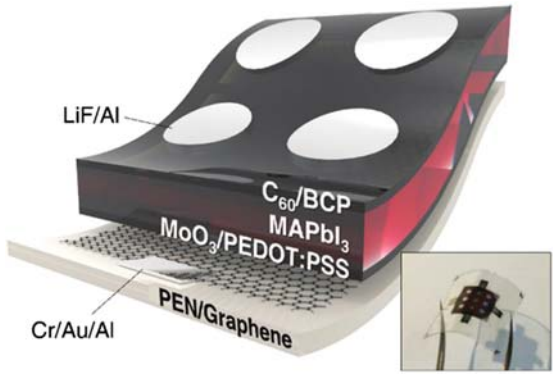


**Figure 16.7** Contains the device structure of graphene-based flexible PSC [88]. *PSC,* Perovskite solar cells. *Inset image: photograph of a complete device.*

a low-temperature processable atomic layer deposition method and achieved a much improved PCE of 12.2% in 2015 [87]. The devices are often used ITO on plastic substrates as a transparent anode. The expense of the ITO-based transparent electrode is high-cost and unsustainable, but it is unrealistic to bend the devices and generate cracks due to lack of mechanical brittleness. Yoon et al. proposed the transfer of single layer CVD graphene, doped with few nanometers thick $MoO_3$, on a thin PEN film. The p-type doping induced by the $MoO_3$ increased not only the conductivity of the graphene, but also improved the wettability that allowed the most uniform deposition of the HTL onto it (Fig. 16.7). Although the PCE of the graphene-based PSC was lowered from 17.3% to 16.8%, the flexibility was improved. The bending stability of the graphene-based PSCs was impressive, after 1000 bending cycles with a bending radius of 4 mm, the PCE remained more than 90% of its original value [88] (Table 16.1).

### 16.2.2 Graphene as an electron transporting layer for solar cell

Sandwiched structure with a TCE (anode, such as ITO), a low-work-function metal cathode (Au, Ag), and an adsorptive and active layer (such as thick $CH_3NH_3PbI_3$ film) is representative of solar cells devices. Many factors dramatically affect the solar cells' stability, such as adsorptive layer and electrode. The humidity and oxygen degrade the cathode material. The interfaces between them are electron/hole transport layers which, to a great extent, determine the performance of solar cells. Metal oxides such

**Table 16.1** Photovoltaic performance of solar cell devices with graphene-based electrodes.

| Electrode materials | $T^{a}$ (%) | Rs ($\Omega$ sq$^{-1}$) | Bending cycles/ radius | PCE (%) | Devices | Ref. |
|---|---|---|---|---|---|---|
| CVD-Graphene | 72 | 230 | | 1.18 | Organic Photovoltaics | [53] |
| CVD-Graphene | 92 | 300 | 100/5 mm | 7.1 | Organic Photovoltaics | [54] |
| CVD-Graphene | 90 | 140 ± 35 | | 12.02 | PSC | [43] |
| SLGNRs (Au-doped) | 90 | 350–221 | | 8.48 | Tandem OPV | [55] |
| AgNW–graphene | 88 | 14.9 | | 8.12 | Organic solar cell | [56] |
| CVD-Graphene | 88–90 | 290 | | 12.35 | GQDs/n-silicon heterojunction solar cells | [66] |
| Functional graphene sheets | | | | 5.0 | DSSCs | [89] |
| N-doped graphene/cobalt sulfide | | | | 10.71 | DSSCs | [77] |
| Graphene–NiO | | 2.92 | | 7.42 | DSSCs | [71] |
| MWNT@rGONR | | 14.46 ± 1.08 | | 6.91 | DSSCs | [90] |
| Graphene ink | 44 | | | 3.5 | DSSCs | [78] |
| Reduced graphene oxide | 82 | 51 | 1000/2 mm | 8.32 | Organic solar cell | [91] |
| Graphene (doped $MoO_3$) | 75–80 | 501 ± 43 | 1000 | 14.2 | PSC | [92] |
| Graphene (doped $MoO_3$) | 97 | 500 | | 17.1 | PSC | [45] |
| Graphene (doped $MoO_3$) | 97 | 552 ± 24.2 | 5000/2 mm | 16.8 | PSC | [88] |
| Reduced graphene | | 8.94 | | 4.5 | Quantum-dot-sensitized solar cells | [93] |

*CVD*, Chemical vapor deposition; *DSSCs*, dye-sensitized solar cells; *GQDs*, graphene quantum dots; *OPV*, organic photovoltaic cells; *PSC*, perovskite solar cells; *SLGNRs*, single-layer graphene nanoribbons.

[a]Transparency

as $Al_2O_3$, $TiO_2$ or $ZrO_2$ are used as the ETL are common with high-efficiency solar cells [94]. The metal oxide performs very well as an electron transport layer, the fabrication is always in high temperature-processing demand, which is a disadvantage of low-cost production. Worse still, a large hysteresis with the sweep direction existed in the device of $TiO_2$/active layer/p-type HTL [95,96]. Therefore, various approaches to seek low-temperature manufacturing for preparing conductive ETL have been examined [83,97]. One unusual approach to synthesize and use the phenyl-C61-butyric acid methyl ester (PCBM) as ETL in PSCs [85,86,94,98,99] was investigated by an earlier group of researchers. As an alternative to the electron transport layer, the organic molecular PCBM was applied in p−i−n PSCs, which has many advantages such as low hysteresis behavior, low processing temperature, inexpensive fabrication. Organic materials are usually more susceptible to degradation in thermal and oxygen atmosphere and have lower conductivity, which leads to the devices' poor stability and low efficiency. Graphene has gained wide attraction in applications used for energy conversion and storage, such as photovoltaics, lithium-sulfide batteries, supercapacitors, and more, with remarkably high charge mobility and electronic conductivity. Moreover, graphene is proven to be not only one of the strongest materials [23], but has also demonstrated unique properties, including perfect thermal conductivity and superior optical transmittance [100−102]. To solve the problems of ETL, graphene-based materials are integrated into the device structure to enhance the charge extraction and transfer at the electrodes, enhancing solar cells with a higher PCE [103] or longer-term stability [104]. Owing to the lowered fabrication cost, bulk heterojunction (BHJ) polymer solar cells have gained appeal and are believed to be easily made via roll-to-roll solution processes on flexible substrates. It is common to use ZnO or $TiO_2$ to extract electrons in polymer solar cells with the demand for UV light soaking better performance although the improvement is not durable and tends to decrease [105,106]. $Cs_2CO_3$ was reported as another possibility for a cathode buffer because of good electron injection and easy manufacturing process [107,108]. However, the device of the $Cs_2CO_3$-modified solar cell was missing the hole blocking ability, so that significantly increased the recombination of electrons and holes at the interface between the electrode and polymer active layer, which damaged the active polymer layer accompanied with low efficiency and instability [109]. GQDs, used as a graphene derivative, due to its unique property such as controllable band gap and size, are widely used in

organic/inorganic hybrid solar cells as well as in QD-sensitized solar cells. Functional GQDs can be modified to tune optical and electrical properties of GQDs. In 2014, Yang et al. designed GQDs − $Cs_2CO_3$ as the electron elective material in inverted polymer solar cells. The research showed that the device based on GQDs − $Cs_2CO_3$ as ETLs showed an improvement in PCE and stability, which can be attributed to efficient electron-extraction, leakage suppression, and retarded Cs + ion diffusion at the buffer/polymer interface [64], as seen in Fig. 16.8. Moreover, the group provided a thermal-annealing-free, solution-processable method for producing ETL in inverted polymer solar cells, which largely reduced the manufacturing expense of solar cells. In fact, the efficiency of the device based GQDs − $Cs_2CO_3$ as ETL is lower than that of mesoporous $TiO_2$ as ETL in polymer solar cells which need a high-temperature sintering process.

Recently, the $SnO_2$ and $TiO_2$ nanocrystalline, used as an effective ETL with a low-temperature process and applied in the planar PSCs, have achieved a certified efficiency of >20%, which is almost equivalent to the efficiency of commercial monocrystalline silicon solar cells [110,111]. However, $SnO_2$ exuded serious hysteresis with the sweep direction and weakened the polymer solar cells' performance because of

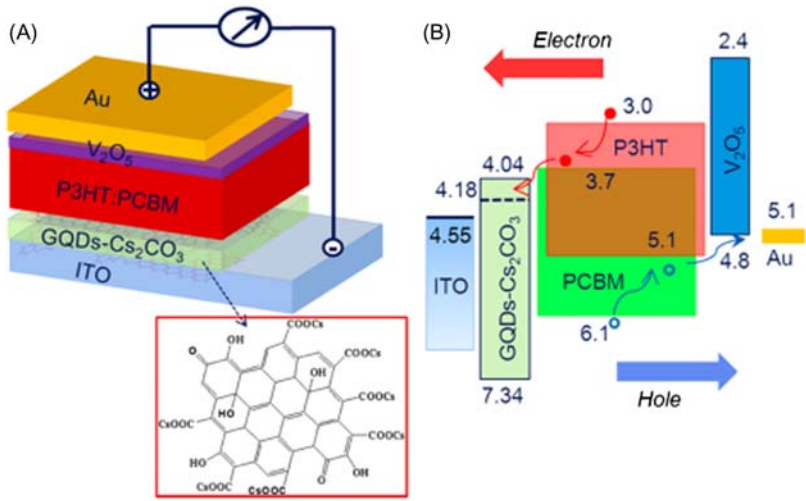


**Figure 16.8** Contains the following: (A) Schematic structure of inverted BHJ PSCs. (B) Energy band diagram of an inverted polymer solar cell with the GQDs−$Cs_2CO_3$ buffer layer [64]. *BHJ*, Bulk heterojunction; *GQDs*, graphene quantum dots; *PSCs*, perovskite solar cells.

numerous trap states in low-temperature solution processed. Xie et al. attempted to add a spot of GQDs into $SnO_2$ with the purpose of improving the electronic properties via a facile treatment [112], as shown in Fig. 16.9. In their research, the conduction band of $SnO_2$ was lower than that of GQDs, which enabled the transfer of electrons from GQDs to $SnO_2$ with no energy barrier. The photogenerated electrons in GQDs were delivered to the conductive band of $SnO_2$, so then the electron traps in $SnO_2$ were effectively filled and the conductivity of $SnO_2$ was improved. This improved the efficiency of electron extraction and diminish the recombination at the interface between the electrodes and the active layer. The device based on $SnO_2$: GQDs, as ETL could yield a mean PCE of up to 19.2% ± 1.0% and the steady-state efficiency output, is found to be 20.23% with minimal $J-V$ hysteresis. The study provided an affordable way to accelerate the performance of PSCs using enhancing the electronic properties of $SnO_2$.

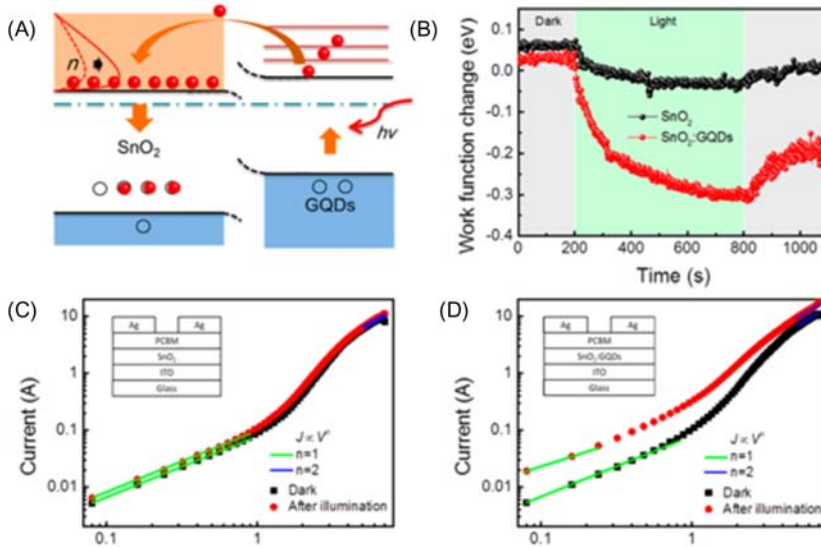


**Figure 16.9** Shows the following: (A) A schematic of the hot electron transfer from GQDs to $SnO_2$ under illumination. (B) Work function change of the $SnO_2$ and $SnO_2$: GQDs under dark and then exposed to light. The HOPG is used as a standard sample, and the work function (WF) is 4.6 eV. The relative WF of HOPG measured by kelvin probe force microscopy (KPFM) is ~0.25 eV. Electron traps and mobility of (C) $SnO_2$ and (D) $SnO_2$: GQDs determined by the SCLC method [112]. *GQDs*, Graphene quantum dots; *HOPG*, highly ordered pyrolytic graphite; *SCLC*, space-charge-limited current.

Metal oxides such as $TiO_x$ and $ZnO_x$ [97,113–115], are mostly assembled in state-of-the-art organic photovoltaic cells (OPV) devices as the ETLs, which always requires high annealing temperatures to promote crystallization which is detrimental to fabricate the portable and flexible device. Beliatis et al. addressed these problems, for example, how to balance the low-temperature solution process and ETL with high electrical mobility, excellent optical transparency, the use of low-cost commercial metal oxides ($TiO_2$ and ZnO) and how to incorporate facile roll to roll deposition to synthesize well-defined crystal structure with high transparency [113]. The experiment manufactured novel hybrid ETLs that where chemically modified metal oxides with rGO layers, and tuned the electrical and optical properties to ensure superior performance. Comprehensive research was utilized with new hybrid materials used as ETLs to fabricate solar cell devices with an air stable polymer system: poly[*N*-9″-heptadecanyl-2,7-carbazole-alt-5,5-(4′,7′-di-2-thienyl-′,1′,3′benzothiadiazole)] PCDTBT/[6,6]-phenyl C70-butyric acid methyl ester ($PC_{70}BM$) as the active layer. An increase was obtained in PCE of 8.38%, compared to when pristine metal oxides were used as electron transport layers. Furthermore, the efficiency of the device based the hybrid ZnO-RGO and $TiO_2$-RGO is 6.72% and 6.57% as electron transport layers with the sizeable active area (28.3 $mm^2$), respectively.

During the same period, Wang et al. [97] reported graphene and $TiO_2$ nanocomposites as the electron collection layers in meso-superstructure PSCs using an economical and solution-processing deposition. In the study, they were able to fabricate the overall device at temperatures below 150°C, thanks to outstanding charge-collection in the graphene nanoflakes nanocomposites. These devices that had an application of hybrid ZnO or $TiO_2$-RGO as ETL showed excellent photovoltaic performance, with the efficiency is as high as 15.6%. They further proved that graphene-based nanocomposites as ETL have the crucial role to develop the market of low-cost solar cells. With the rapid development of solution-processable graphene, the approach to chemical exfoliation allowed the easy and facile functionalization in the processing of graphene, scaling its applications in the various layers of solution-processable solar cells [116,117]. PSCs with PCE over 22% have become more popular in the scientific and industrial fields due to the impressive technological development in recent research [118]. It is necessary and urgent to optimize the PSCs device operation and stability further, then improve the performance. From this perspective, Cho et al. [115],

thoroughly investigated the character of rGO in hybrid PSCs. They mixed rGO with the mesoporous $TiO_2$ (m-$TiO_2$) matrix as ETL, and the device achieved a notable PCE of 19.54%. That emphasized the role of rGO with and Li-treated free m-$TiO_2$, which improved transport and injection of photoexcited electrons. Graphene-based materials, especially rGO, has been applied in various solar cell devices in multiform [97,119–121], which effectively avoids the charge recombination and decreases the leakage currents [122–124]. They systematically discussed rGO as three different roles in the PSCs as shown in Fig. 16.10. The study shows whether the introduction to the rGO flakes in each layer affected the devices' performance. Furthermore, they compared devices with and without Li treatment where the m-$TiO_2$ layer is treated with a solution of lithium bistrifluoromethanesulfonimidate (Li-TFSI) in acetonitrile before the deposition of the perovskite layer to confirm the effect of rGO in the ETL. From Figures A–C, we can see that rGO was introduced into the m-$TiO_2$ layer as ETL, the mixed perovskite layer as an active layer, and spiro-OMeTAD layer as an HTL, The corresponding energy level diagrams are shown in Fig. 16.10D–F [125,126]. The research conducted a systematic investigation of the role of rGO applied to PSCs, proving rGO played a positive role when mixed with the m-$TiO_2$ layer in enhancing the electron transporting.

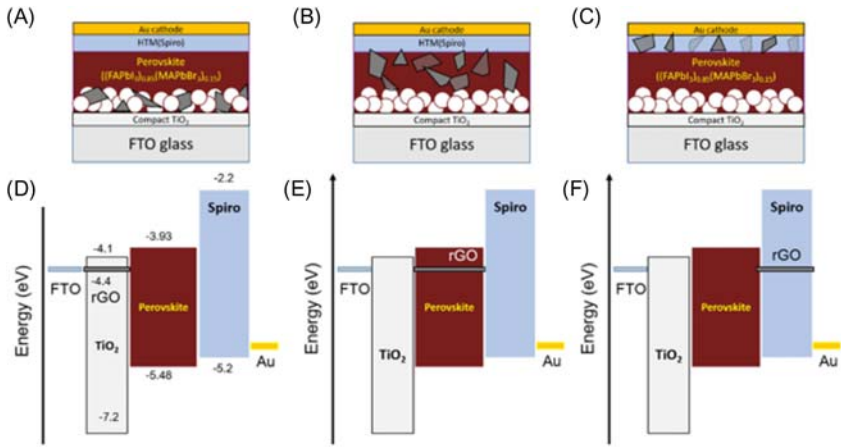


**Figure 16.10** Contains an illustration of the solar cells architectures fabricated with rGO in each layer: (A) m-$TiO_2$ + rGO, (B) perovskite + rGO, and (C) spiro-OMeTAD + rGO. (D–F) The corresponding diagram contains the energy level of the three devices. The energy levels are based on the individual materials in the solar cell. Also, under illumination there will be a relative shift [115].

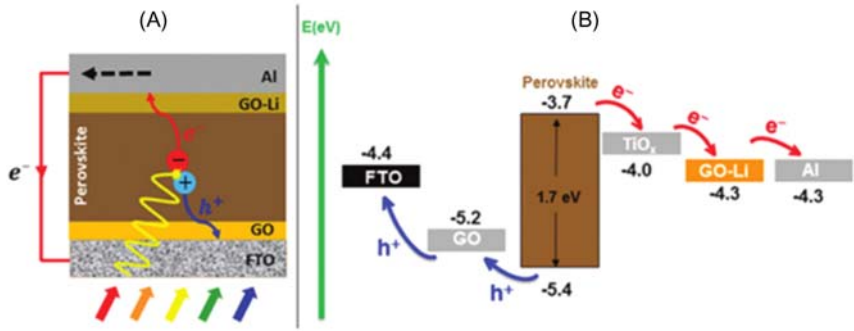


**Figure 16.11** Contains the following: (A) Schematic illustration of the inverted PSC structure employed in the present work and (B) energy level diagram showing possible charge transfer in the inverted planar PSC device with GO as the hole transport layer and GO-Li as the electron transport layer [128]. *PSC*, Perovskite solar cells.

Following the research of graphene being used as ETL, Agresti et al. [127] and Nouri et al. [128] reported that lithium-neutralized GO (GO-Li) was the ETL applied in PSCs. Surprisingly, Nouri et al. adopted an inverted p–i–n architecture in PSCs where GO was studied as the HTL and Li-doped GO as the Nouri under ambient conditions, shown in Fig. 16.11A, mostly for in cost reduction [128]. The Li-modified GO as ETL in the solar cell device got an efficiency of 10.5%, where synergetic effect existed between GO-Li and Ti-based sol. In fact, the energy levels of the perovskite and the Al electrode matched properly, as shown in Fig. 16.11B. The GO and GO-Li films' work functions were 5.2 and 4.3 eV respectively. It is essential to have proper work functions in electron and hole selective layers in PSC to overcome interfacial energy barriers between the electrodes and the active perovskite layer to prevent back recombination at the interfaces [129,130]. Recently, devices are being made by employing NiO/GO and Li-modified GO/$TiO_x$ as a hole and electron transporters in p–i–n PSCs, respectively. In comparison with the FTO/PEDOT:PSS/ Perovskite /PCBM/ Al device, the FTO/NiO/GO/Perovskite/GO-Li/$TiO_x$/Al device was markedly more stable than the latter [131]. In summary, they presented a strategy that adopted GO-based as an HTL and Li-modified GO as an ETL in an inverted p–i–n architecture and matched well with the perovskite active layer; and boosted a dual-role graphene-based material applied in solar cells in a low-cost and efficient method (Table 16.2).

**Table 16.2** Properties of graphene-based as electron transporting materials in solar cells.

| ETM | $J_{sc}$ (mA cm$^{-2}$) | $V_{oc}$ (V) | FF (%) | PCE (%) | Devices | Ref. |
|---|---|---|---|---|---|---|
| ZnO-RGO | 12.54 | 0.91 | 58.91 | 6.72 | Organic photovoltaics | [113] |
| $TiO_2$-RGO | 11.66 | 0.90 | 62.07 | 6.57 | | |
| $SnO_2$-GQDs | 23.05 | 1.134 | 77.8 | 20.31 | PSC | [112] |
| | 22.97 | 1.135 | 75.4 | 19.68 | | |
| rGO-PCBM | 22.92 | 0.85 | 65.8 | 12.82(13.50) | Planar inverted PSCs | [132] |
| GQDs-$Cs_2CO_3$ | 9.18 | 0.585 | 60.1 | 3.23 | Inverted polymer solar cells | [64] |
| GO-Li | 13.2 | 0.89 | 0.60 | 7.1 | Inverted PSCs | [128] |
| GO-Li-Ti-based sol | 15.6 | 0.91 | 0.72 | 10.2 | | |
| $TiO_2$-RGO | 9.71 ± 0.50 | 0.51 ± 0.01 | 47.4 ± 2.26 | 2.32 ± 0.07 | Inverted hybrid bulk-heterojunction solar cells | [114] |
| GO-Li | − 19.61 | 0.859 | 70.3 | 11.8 | PSC | [127] |
| m-$TiO_2$ + rGO | 21.984 | 1.11 | 80 | 19.54 | PSC | [115] |
| $TiO_2$ + graphene | 21.9 | 1.04 | 0.73 | 15.6 | PSC | [97] |

*GQDs*, Graphene quantum dots; *PSC*, perovskite solar cells.

### 16.2.3 Graphene as HTL for solar cells

Whether utilizing electron transporting materials or HTL, there is a difference in the performance and stability of solar cell devices regarding morphology and conductivity between the contacted interlayers. The basic request for an effective HTL is an appropriate energy level to promote hole transfer and hamper electrons to prevent electron−hole recombination on the anode selectively. Also, the potential to solution processability for the HTL is beneficial for scalable and low-cost device manufacturing [133,134]. Spiro-OMeTAD (2,2′,7,7′-tetrakis (*N*,*N*-di-*p*-methoxyphenylamine) 9,9′-spirobifluorene) is the first and representative HTL in solid-state DSSCs reported by Bach [3] and Grätzel et al. [135]. As previously mentioned, a new upsurge in PSCs is in the making, owing to the superior efficiency of over 22% in less than a decade, which suggests the possibility of having access to low-cost photovoltaics conversion and low energy consumption. HTLs are also in a revolution, accompanied by 'perovskite fever' [136]. The following are several important roles that HTLs play in solar cells: [137] (1) Hinders the electron transfer to the anode as physical/energy barrier between the anode and the perovskite layer [138], (2) Efficiently extracts the hole and transfer to the anode [139], (3) Affects the open voltage circuit [140−142], and (4) Suspends the degradation at the interface between metal (Au) and perovskite layer where there is no HTL [143,144]. Past research shows that the spiro-OMeTAD always requires being mixed with additives such as *tert*-butylpyridine (t-BP) to enhance its limited conductivity in order to improve the device performance [145]. In fact, *tert*-butylpyridine (t-BP) can dissolve and destroy the perovskite layer because of its soluble polarity [146]. Furthermore, the expense of spiro-OMeTAD and the noble metal is very high, which largely limits large industrial application. Subsequently, poly(3,4-ethylene dioxythiophene)−polystyrene sulfonate (PEDOT:PSS) emerged and was popularly applied in inverted PSCs with high efficiency due to the proper energy level, good mobility, and good transparency in visible and near-infrared regions [27]. However, like most organic materials, PEDOT:PSS lacked durability when exposed to oxygen and humidity, compared with inorganic materials [147]. Furthermore, PEDOT:PSS is high in acidity and hygroscopic accounting for device instability [148]. CuSCN [148], $NiO_x$ [149] and other inorganic substances have been designed into inverted PSCs as HTLs and have achieved favorable efficiency. Nevertheless, even CuSCN or $NiO_x$-based PSCs had some shortcomings: (1) the device based on CuSCN as HTL lack of stability; (2) the

device based on $NiO_x$ needed high-temperature treatment and vacuum-based processing [150]. Graphene materials have been well noted and is popular, with unique electrical, optical, thermal, and mechanical properties because of its two-dimensional nanostructure and morphology [21,151]. In 2014, Liu et al. was the first to report that graphene oxide nanoribbon (GOR) synthesized from SWCNTs with the posttreatment of $H_2SO_4$ and $KMnO_4$, could be applied in polymer solar cells as a remarkable HTL [152]. As the shown in Fig. 16.12 , the GOR's HOMO level nearly equates to that of the poly(3-hexylthiophene) (P3HT), the donor material, which is useful in improving hole transporting. Also, the relatively large energy barrier between the LUMO of GOR and that of phenyl-C61-butyric acid methyl ester (PCBM), the acceptor material, can effectively avoid possible charge combination at the anode. GOR revealed ideal energy levels as an efficient HTL. Moreover, another advantage for GOR is as HTL with weak absorption in the visible range, which may also be beneficial to the absorptive layer in polymer solar cells because of high transmittance [153]. The device based GOR and PEDOT:PSS as

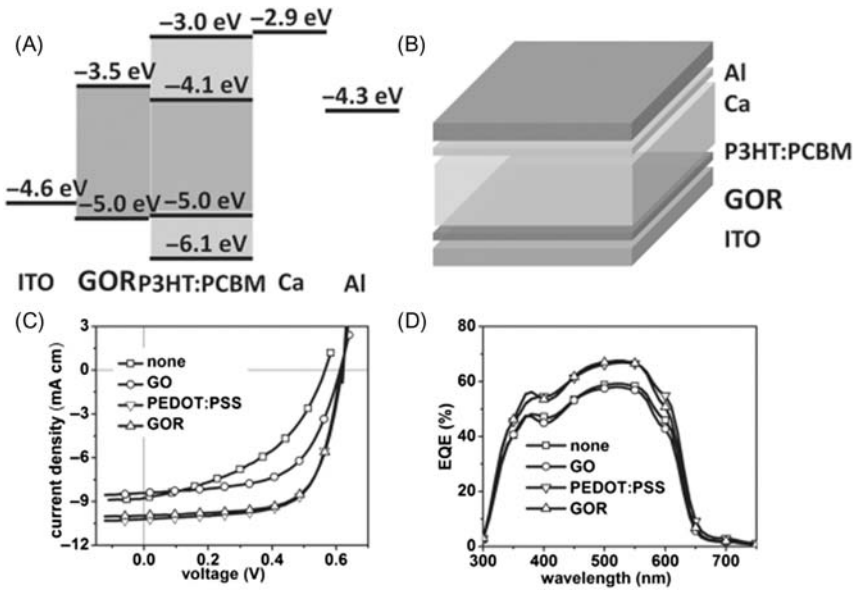


**Figure 16.12** Contains the following: Device energy level alignment (A) and device structure (B) of the GOR-based PSC device. Current density-voltage ($J-V$) curves (C) and external quantum efficiency (EQE) curves (D) under AM 1.5G illumination of the PSCs without and with PEDOT:PSS, GO or GOR as the HTL [152]. *PEDOT:PSS*, Poly(3,4-ethylene dioxythiophene)—polystyrene sulfonate; *PSC*, perovskite solar cells.

HTL achieved a PCE of 4.14% and 4.16%, respectively; which confirmed that the strategy provides a novel method for carbon-based materials with low-cost and highly-effective solar cells.

In 2017 Yang et al. introduced a solution-processed GO with a proper work function and conductivity as HTL in metal organometal halide PSCs by controlling the thickness, the schematic of the device configuration is shown in Fig. 16.13 [154]. The device GO-based as HTL with 2 nm thickness GO obtained the best PCE of 16.5% with no hysteresis. Furthermore, the GO-based as HTL device expressed superior stability than those of a commonly used organic-based HTL, which maintained a performance of >80% of their initial efficiency over 2000 h under high humidity and continuous light soaking. In Fig. 16.13B, observe the roughness of GO film at 0.59 nm, which is smaller than that of the PEDOT:PSS film (1.53 nm) using atomic force microscopy (AFM), which is beneficial to form a better interlayer between the perovskite layer and HTL. Using the ultra-violet photoelectron spectra (UPS)

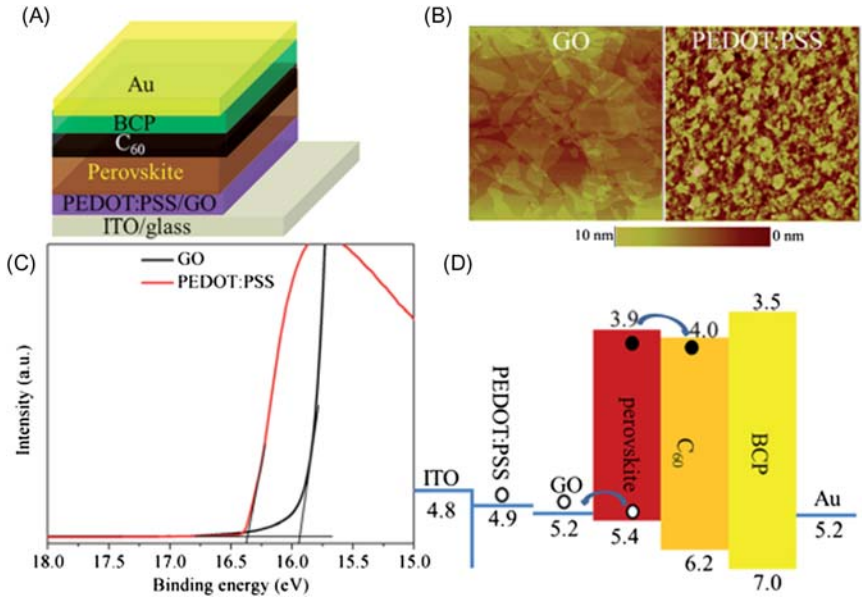


**Figure 16.13** Contains the following: (A) Device architecture of PSCs with PEDOT:PSS or GO as the hole-transporting layer, (B) AFM images of GO and PEDOT:PSS film on ITO glass with scan size of $2 \times 2\ \mu m$, (C) UPS spectra of PEDOT:PSS and GO spin-coated on an ITO glass substrate, (D) energy diagrams of PSCs (schematic) [154]. *AFM*, Atomic force microscopy; *PEDOT:PSS*, poly(3,4-ethylene dioxythiophene)–polystyrene sulfonate; *PSC*, perovskite solar cells.

measurement (Fig. 16.12C and D) to analyze the work function of GO (5.2 eV) and PEDOT:PSS (4.9 eV), the research suggested that GO was more capable of forming a p-type contact with the perovskite active layer. They also proved that the photogenerated holes in perovskite are preferably transferred to GO and competed with that of PEDOT:PSS because the GO's energy level matched well with the perovskite by photoluminescence (PL) spectroscopy and transient photocurrent measurement. That is to say, GO is more likely to efficiently extract the holes from perovskite active layers and decrease electron and hole recombination. With the increasing thickness of GO, the carrier extraction efficiency decreased because of the poor conductivity of between GO layers. The research showed us an economic and high-efficient way, without any other posttreatment, to employ soluble GO as HTL in solar cells under room temperature-processed and mild condition, which improved stability in the light soaking test.

Based on the works previously mentioned, Jokar et al. investigated the films of GO and rGO as efficient p-type HTL for inverted planar heterojunction PSCs (ITO/GO or rGO)/$MAPbI_3$/PCBM/Ag, as shown in Fig. 16.14. The devices showed the efficiencies of 16%, higher than those

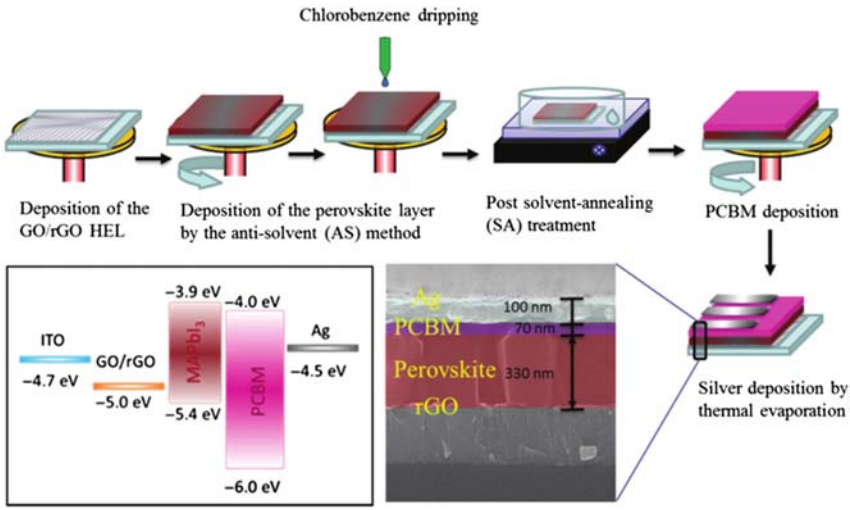


**Figure 16.14** Contains the device fabrication layer by layer for a perovskite layer produced with a combined AS and SA approach. The side-view SEM image shows the PHJ PSC device structure, with each layer labeled in a separate color. The inset box shows a potential-energy level diagram for each component [157]. *AS*, Antisolvent; *SA*, solvent-annealing.

made of GO and poly(3,4-ethenedioxythiophene): poly(styrene sulfonate) films. A perovskite layer was deposited with a typical antisolvent (AS) method [155] followed by solvent-annealing (SA) treatment [156]. The device rGO-based as HTL possesses super flexibility and retained 70% performance over 150 bending cycles [157]. The rate to extract and deliver hole is faster for the GO/methylammonium lead-iodide perovskite (PSK) film than for the other rGO/PSK films, which resulted from the significantly improved hole extraction from PSK to GO, while effectively blocking the charge recombination at the GO/PSK interface, indicated by photoluminescence (PL) spectroscopy and transient photocurrent measurement.

Functionalized graphene is active in photovoltaic fields because of unique tunable properties such as the ability to coordinate interactions with perovskite layer in solar cells, facilitating the charge extraction and transport from perovskite to graphene [158]. Cao et al. designed a functionalized nanographene with tunable energy level by doping perthiolated trisulfurannulated hexa-peri-hexabenzocoronene (TSHBC) and applying it as HTL in PSCs with higher efficiency of 12.8% in pristine form, compared to that of graphene improved up to 14.0% [30] as shown in Fig. 16.15. Furthermore, they proved that the HTL's HOMO levels are important in the performance of PSCs and tunable by adjusting the thickness of TSHBC homologs. The device based thiolated nanographene used as HTL shows outstanding stability under AM 1.5 illumination in humidity of about 45% without encapsulation, owing to the hydrophobic TSHBC. These findings encourage researchers to further exploit graphene as HTL in various solar cells by means of edge functionalization and core-structure modulation. This work also suggests the possibility of using functional graphene materials, and indicate graphene-based material such as graphene nanoribbons and graphene sheets can be functionalized and thiolated to assemble in solar cells as HTL (Table 16.3).

### 16.2.4 Graphene in electron acceptor materials in active layers of a solar cell

Using different active components over the decades, the solar cell could be classified as follows: silicon solar cells, polymer solar cells, organic solar cells, plastic solar cells, and PSCs. The active layer in a solar cell is very crucial to the whole device. Whether utilizing the single crystal silicon solar cells or the recent PSCs, the expense of devices is high and not sustainable. The key to solving the current problem is to find cleaner and

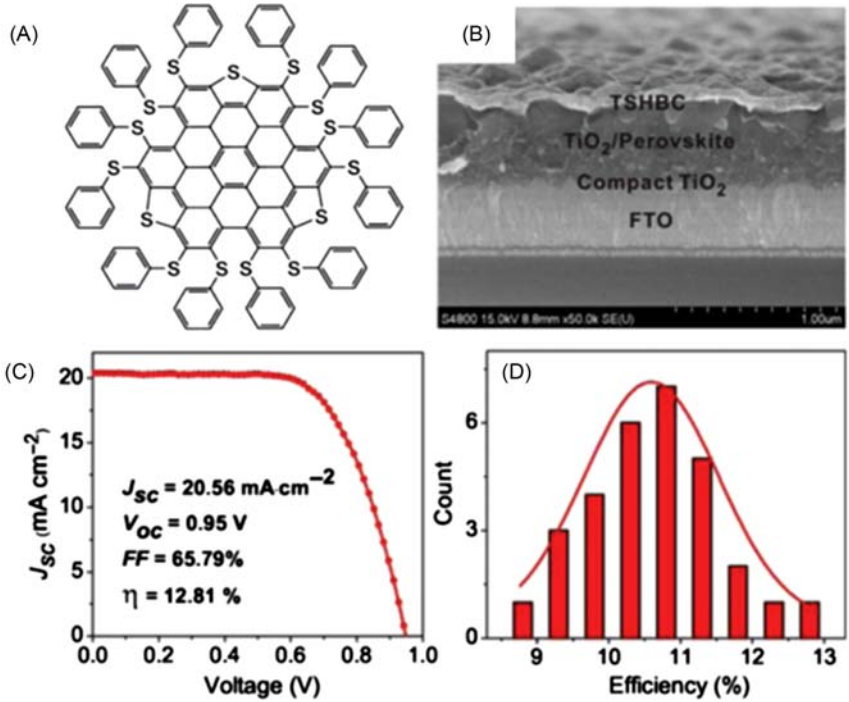


**Figure 16.15** (A) Structures of TSHBC. (B) Cross-sectional SEM image of the device of FTO/$TiO_2$/perovskite/TSHBC film. (C) Best *I–V* characteristics. (D) Comparison of the performance distributions of 30 individual devices of the cells [30]. *TSHBC*, Trisulfurannulated hexa-peri-hexabenzocoronene.

lower energy consumption components. Carbon materials are known to be abundant in nature and may be a viable alternative.

In 2008 Liu et al. were the first to experiment with solution-processable functionalized graphene (SPF Graphene) material as an electron-accepter with poly(3-hexylthiophene) (P3HT) or poly(3-octylthiophene) (P3OT) as donor material in BHJ solar cells where the device structure is ITO/PEDOT:PSS/P3OT:graphene/LiF/Al [7,167,168]. As shown in Fig. 16.16, adding graphene to the P3OT induces a significant decrease of the photoluminescence of the P3OT, indicating a substantial electron/energy transfer from the P3OT to the graphene. The device based on a graphene electron acceptor in active layer showed the best performance with a PCE of 1.4%, an open-circuit voltage of 0.92 V, short-circuit current density of 4.2 mA $cm^{-2}$, and a fill factor of 0.37 using simulated 100 mW $cm^{-2}$ AM 1.5 G illumination. The research uncovered a new and creative way to employ graphene as an acceptor material

**Table 16.3** Properties of graphene-based as HTLs in solar cells.

| HTL | $J_{sc}$ (mA cm$^{-2}$) | $V_{oc}$ (V) | FF (%) | PCE (%) | Devices | Ref. |
|---|---|---|---|---|---|---|
| GO | 20.2 | 1.04 | 73 | 15.1 | PSCs | [159] |
| Functionalized graphene | 18.06 | 1.08 | 77 | 15.2 | PSCs | [29] |
| Fluorinated reduced graphene oxide (MFGO) | 19.2 | 1.01 | 76.2 | 14.7 | PSCs | [160] |
| Reduced GO-sheet | 22.1 | 0.962 | 77 | 16.4 | PSCs | [157] |
| SWNT/GO/PMMA | 19.4 | 0.95 | 72 | 13.3 | PSCs | [161] |
| GO | 15.6 | 0.91 | 72 | 10.2 | PSCs | [128] |
| GO | 17.46 | 1.00 | 71 | 12.4 | PSCs | [162] |
| Graphene oxide nanoribbon | 9.96 | 0.62 | 67 | 4.14 | Polymer solar cells | [152] |
| Sulfonic acid GO | 15.3 | 0.75 | 63 | 7.18 | Polymer solar cells | [163] |
| GO-Cl | 13.65 | 0.88 | 54.7 | 6.56 | Organic photovoltaic | [123] |
| F-GQDs | 10.65 | 0.89 | 67 | 6.30 | Polymer solar cells | [164] |
| rGO | 11.5 | 0.95 | 60.54 | 6.62 | PSCs | [165] |
| TSHBC-graphene | 20.56 | 0.95 | 65.79 | 12.81 | PSCs | [30] |
| GO/PEDOT:PSS | 15.75 | 0.84 | 73.56 | 9.74 | PSCs | [166] |
| GO | 21.6 | 1.00 | 76.2 | 16.5 | PSCs | [154] |

*GQDs*, Graphene quantum dots; *PEDOT:PSS*, poly(3,4-ethylene dioxythiophene)−polystyrene sulfonate; *PMMA*, poly(methyl methacrylate); *PSC*, perovskite solar cells; *TSHBC*, trisulfurannulated hexa-peri-hexabenzocoronene.

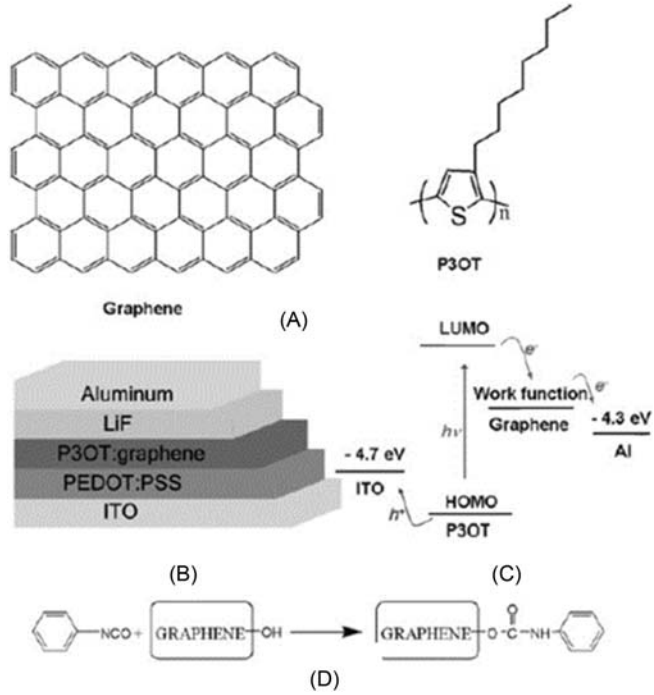


**Figure 16.16** Contains the following: **(**A) The idealized chemical structures of graphene and P3OT. (B) Schematic of the device with P3OT/graphene thin film as the active layer and the structure ITO (c. 17 V $sq^{-1}$)/PEDOT:PSS (40 nm)/P3OT: graphene (100 nm)/LiF (1 nm)/Al (70 nm). (C) Energy level diagram of P3OT and SPF Graphene. (D) Schematic representation of the reaction of phenyl isocyanate with graphene oxide to form SPF Graphene [7]. *PEDOT:PSS*, Poly(3,4-ethylene dioxythiophene)–polystyrene sulfonate.

in an organic BHJ solar cell active layer with P3HT and P3OT as an electron donor under organic solution-process. The active layer using graphene and P3OT/P3HT as an electron acceptor and donor materials, matches up well in BHJ solar cell devices. Consequently it prompted the use of graphene in the active layer.

GQDs represent a single-layer to tens of layers of graphene that is less than 30 nm. GQDs have particular properties such as quantum-confinement effects and edge effects. The properties makes GQDs distinct from both conventional quantum dots and graphene [62]. In fact, GQDs were made as a sensitizer in a DSSC with an efficiency of $<0.1\%$, hampering further application [169]. GQDs have been widely used as an electron acceptor analogous to fullerenes accompanied by an active layer

of poly(3-hexylthiophene) (P3HT) in organic photovoltaics [170,171], but the performance is inferior to that of fullerenes, due to the lower electron affinity and inappropriate assembly morphology. Zhu et al. [172] inserted an ultrathin GQD layer using a facile electrochemical method [173], between the perovskite layer and $TiO_2$ layer as shown in Fig. 16.17, and increased efficiency in PSCs from 8.81% to 10.15%. The addition of the GQDs, caused a strong quenching of perovskite photoluminescence at 760 nm. The research reported that GQDs can function as a superfast electron tunnel for optoelectronic devices, and they redefined the role of facilitating the electron transfer from the perovskite absorber to the current collector. That is in addition to its conventional role as an electron acceptor in OPV cells; which opens a new path to further solar cell development.

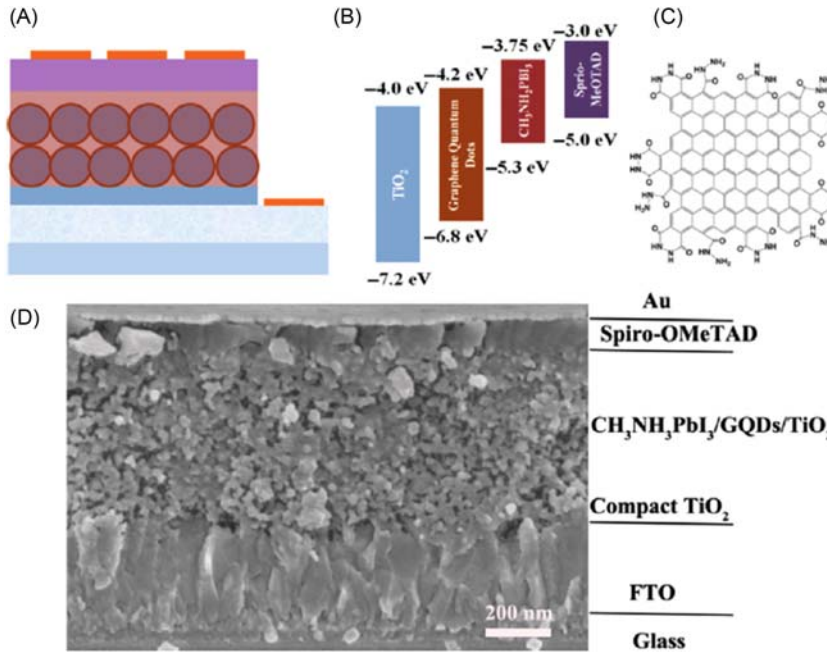


**Figure 16.17** Schematic representation of the typical full device structure (A), where the mesoporous oxide is loaded with GQDs and then without, the energy band alignment is relative to the vacuum (B), the edge-modified GQD structure is determined using theoretical calculations (C), (D) the cross-sectional SEM image of a complete photovoltaic device based on the $CH_3NH_3PbI_3$/GQDs/$TiO_2$ structure, with scale bar: 200 nm [172]. *GQDs*, Graphene quantum dots.

## 16.3 Carbon nanotube-based solar cells

The work function for metallic CNTs is in the range of 4.5−5.1 eV, approximately the same as ITO 4.4−4.9 eV [174]. CNT possesses high transmittance in the visible and near-infrared regime and excellent conductivity, high thermal stability, and mechanically robustness [175]. Metallic nanotubes are preferable for electrode applications due to high conductivity [176]. In contrast, semiconducting CNTs are preferable as charge selective contacts in solar cells since they possess much longer charge carrier lifetimes. Their metallic counterparts act as charge carrier recombination centers [177]. Originally, CNTs were employed as electron acceptors with low efficiency in photovoltaic solar cells used in combination with conjugated polymers in organic solar cells [178,179]. The p-type characteristic of CNTs has also been thoroughly used for injunctions with an n-type silicon [28]. The 'p−n junction' has recently demonstrated a power-conversion efficiency of up to 17.0% [180]. The p-type CNTs were within a work function range of 4.7−5.1 eV under ambient conditions, and served as a potential HTL for PSCs [181]. Recently, reports have been made about the advances of CNT-based materials that are being used in solar cells. The following section contains a detailed discussion about the advancement.

### 16.3.1 Carbon nanotubes as transparent electrodes for solar cells

In 2004, Wu et al. [182] first reported single-wall CNTs as a new class of transparent conducting electrode, comparable to ITO. Since then, CNTs have been widely employed as electrodes in various solar cells, such as organic solar cells, DSSCs and so forth [183−188].

Klinger et al. [176] designed fantastic solar cells using CNTs only, with semiconducting nanotubes as a photoactive layer, CNTs as a counter electrode, and a liquid electrolyte through a redox reaction. The whole device was low-cost with neither noble metal electrodes such as In or Pt, or dye for photo-conversion using a spray-paint technique. The performance with a lower concentration of CNTs on an active semiconducting electrode was better than cells with a higher concentration of nanotubes, which was caused by the presence of metallic nanotubes which offered a short for photoexcited electrons. That explains the concept of CNT-only solar cells and provides a more economical and environmentally friendly way to assemble solar cells for low-cost manufacturing, but efficiency is in

great need of improvement for industry use. Recently, Luo et al. [189] reported that all-carbon-electrode-based endurable flexible PSCs fabricated with and without spiro-OMeTAD hole conductors showed PCEs of 11.9% and 8.4%, respectively, which increases evidence of the potential of an all-carbon-electrode-based as shown in Fig. 16.18.

DSSCs are available for photovoltaic conversion because of low-cost, semi-transparency, and the ability to manufacture them easily. The widely used on the cathode is Platinum nanoparticles, which extends development time and increases costs. Many efforts have been made to find

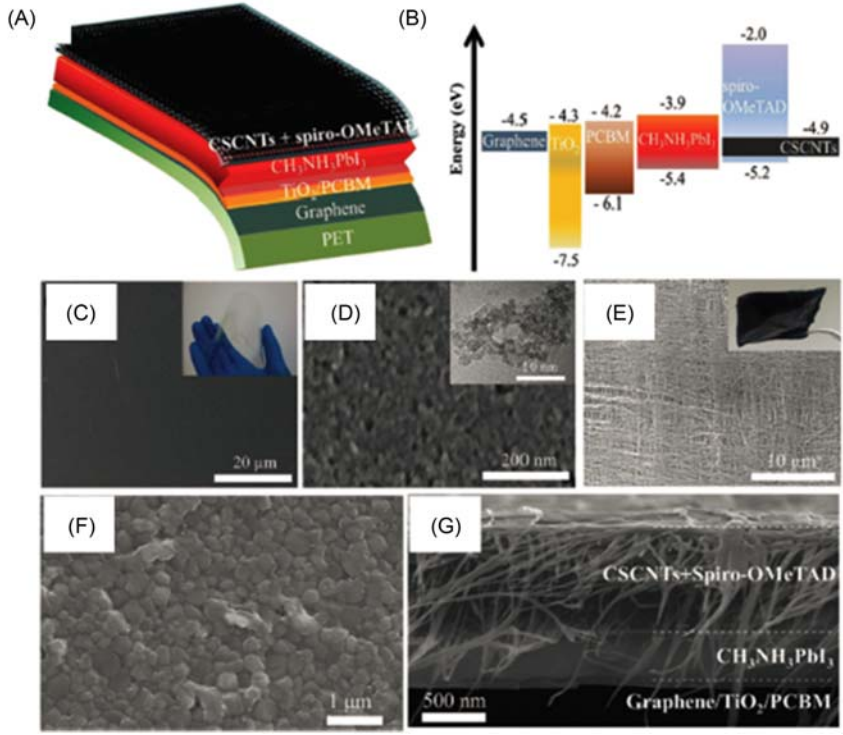


**Figure 16.18** Contains the following: (A) Device architecture of the all-carbon-electrode-based flexible PSCs. (B) Energy levels of the various device layers in the PSCs. Top view SEM images of (C) graphene/PET, (D) $TiO_2$, (E) cross-stacking carbon nanotubes (CSCNTs), (F) perovskite film deposited on $TiO_2$—PCBM/graphene/PET substrate. (G) The cross-sectional SEM image of the all-carbon-electrode-based flexible PSCs. Insets in panels (C) and (E) show the photograph of the as-fabricated CSCNTs and graphene/PET, respectively. Inset in panel (D) is the TEM image of the low-temperature prepared $TiO_2$ [189]. *PET*, Polyethylene terephthalate; *PSC*, perovskite solar cells.

replacement materials for the Pt catalyst. Research has focused on carbon-based materials due to the natural abundance, low cost, environmentally benign properties, and reasonable catalytic effects [89,186,190,191]. Vertically aligned CNTs have the properties in high order, easily controllable, and more, which makes them promising for applications [192–194]. Dong et al. [195] replaced the conventional Pt electrode with vertically aligned few-walled CNTs (VAFWCNTs)/graphene as a novel cathode in DSSCs, as shown in Fig. 16.19A. This (VAFWCNTs)/graphene cathode possesses a lower charge transfer resistance and lower contact resistance between the catalyst and the substrate compared to that of Pt/FTO cathode. The flexibility of CNTs/graphene/Ni cathode makes it employable on flexible organic substrate, attracting lots of attention regarding its use in portable and low-weight devices. The performances of VAFWCNTs/graphene hybrid cathode and the Pt-based cathode in DSSCs is 8.2% and 6.4%, respectively. Research has shown that it is inexpensive and easy to manufacture solar cells with the application of a flexible VAFWCNTs/graphene cathode.

In 2015, Jeon et al. [196] introduced SWCNT films doped with $MoO_x$ as electron-blocking transparent electrodes for flexible organic solar cells by direct and dry deposition. This method was directly prepared with CNT electrode through SWCNTs grown by an aerosol CVD technique [197]. Their process was without surfactant and induced fewer defects than other solution-based processes [198,199]. $MoO_3$ doping

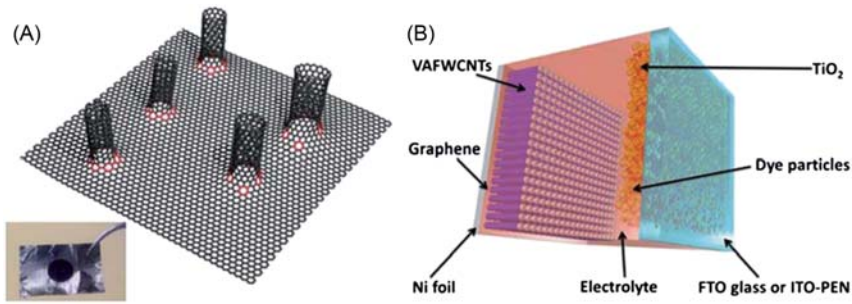


**Figure 16.19** Contains the following: Schematic diagram of the fabricated DSSCs. (A) Schematic structure of the VAFWCNTs/graphene. The rings are indicated by different color represent the seven-membered rings that seamlessly fuse the planar graphene and tubular CNTs. However, the CNTs are tens of microns long, whereas the graphene is <1 nm thick. The inset is an image of the VAFWCNTs/graphene (*black circle*) on the Ni foil cathode. The diameter of the black circle is 6 mm. (B) Schematic diagram of the DSSC with VAFWCNTs/graphene on Ni foil as the cathode [195]. *DSSCs*, Dye-sensitized solar cells; *VAFWCNTs*, vertically aligned few-walled CNTs.

[200] was more stable than other reported dopants. Also, thieno[3,4-*b*] thiophene/benzodithiophene (PTB7) [201], the low band gap polymer, was employed in the photoactive layer without thermal annealing treatment, which enabled it to be used on flexible substrates [202]. As Fig. 16.20 shows, the devices are made up of P3HT-based cells (glass/SWCNT/$MoO_x$/P3HT:mix-PCBM/LiF/Al) and the most optimized

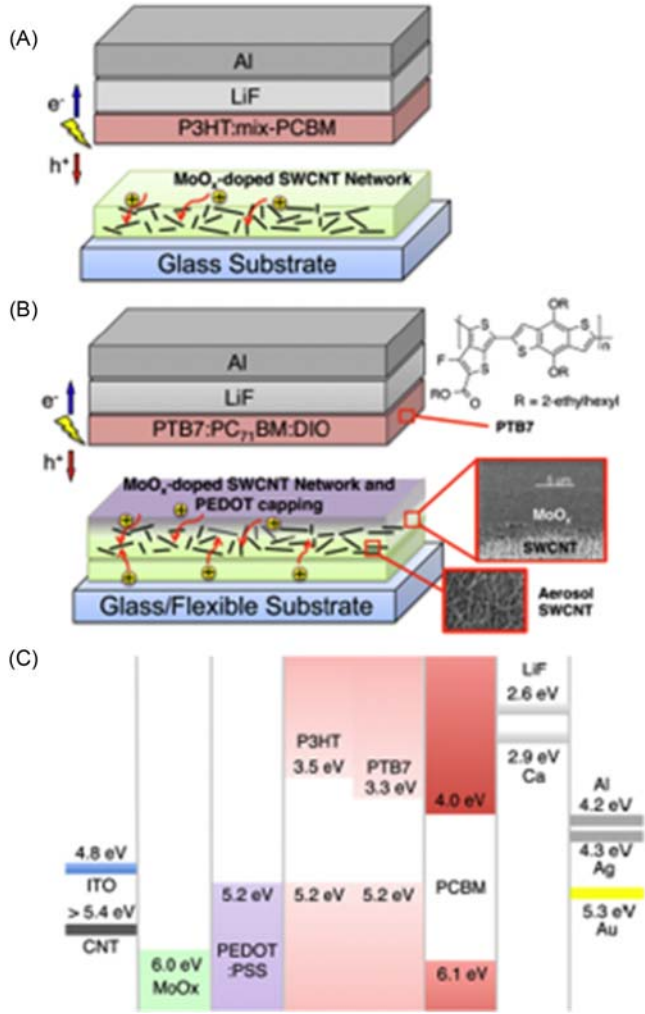


**Figure 16.20** Contains the following: SWCNT OSC configurations of (A) P3HT-based cells (glass/SWCNT/$MoO_x$/P3HT:mix-PCBM/LiF/Al) and (B) the most optimized device that gave high efficiency (glass or flexible substrate/ $MoO_x$/SWCNT/$MoO_x$/PEDOT:PSS/PTB7:PC71BM/LiF/Al). (C) Energy band alignment diagram of SWCNT OSCs [196]. *PEDOT:PSS*, poly(3,4-ethylene dioxythiophene)—polystyrene sulfonate.

device (glass or flexible substrate/ $MoO_x$/SWCNT/$MoO_x$/PEDOT:PSS/PTB7:PC71BM/LiF/Al) architectures. An investigation of the work function by photoelectron yield spectroscopy was also performed. The Fermi levels gap between SWCNT and $MoO_3$ was narrowed by thermal doping, and as seen in Figure C, the work function of pristine SWCNT films on the glass is 4.86 eV, which increased by 0.54 eV after thermal annealing with $MoO_3$. The organic solar cell device based on SWCNT as an electrode shows a PCE of 6.04%. Recently, Jeon et al. [92] began a new effort to apply CNTs and graphene with dopant $MoO_3$ used as transparent carbon electrodes in flexible inverted PSCs. The research included measuring the devices based carbon materials electrodes in photovoltaic performance and mechanical resilience using various techniques. The PCEs of ITO, the CNT, and graphene-based solar cells were 17.8%, 12.8%, and 14.2%, respectively. The performances with $MoO_3$ doped CNTs as a transparent electrode doubled the improvement.

PSCs are universal in the poor long-term thermal stability that fails to the aid in commercialization. Considerable amounts of Au from the electrode diffuse across the HTL into the perovskite active layer, which leads to the primary loss of device performance during an elevated temperature process [203]. Dabera et al. designed chemically and mechanically robust SWCNT as transparent hole extracting in BHJ organic photovoltaics electrodes with a simple drop cast method [204]. However, the treatment is with thermal annealing and acid treatment, which achieved a low efficiency of 4.4%. PCE based CNTs are comparable to PCEs. This is achieved using ITO-based reference devices with the same parameters, implying the potential of the single-wall nanotube (SWNT) electrodes as an ITO replacement toward the realization of an all carbon solar cell. Recently, Aitola et al. employed FTO/compact $TiO_2$/mesoporous $TiO_2$/perovskite/SWCNT-Spiro-OMeTAD structure to investigate the performance based on CNTs electrode, as shown in Fig. 16.21A [205]. The process of fabricating the SWCNT solar cells includes cutting the SWCNT film on filter paper and transferring it on top of perovskite with some pressure. A bit of chlorobenzene was used to densify the SWCNT film. The second film was transferred to the prepared film, one by one. Spiro-OMeTAD solution was painted on the SWCNT film with drop casting. Stability testing was then applied to an Au-based device with a PCE of 18.4% and a SWCNT-based device with a PCE of 15.0%. During the stability test a temperature of 60°C in the $N_2$ atmosphere and 1 sun equivalent white LED illumination was applied and the devices

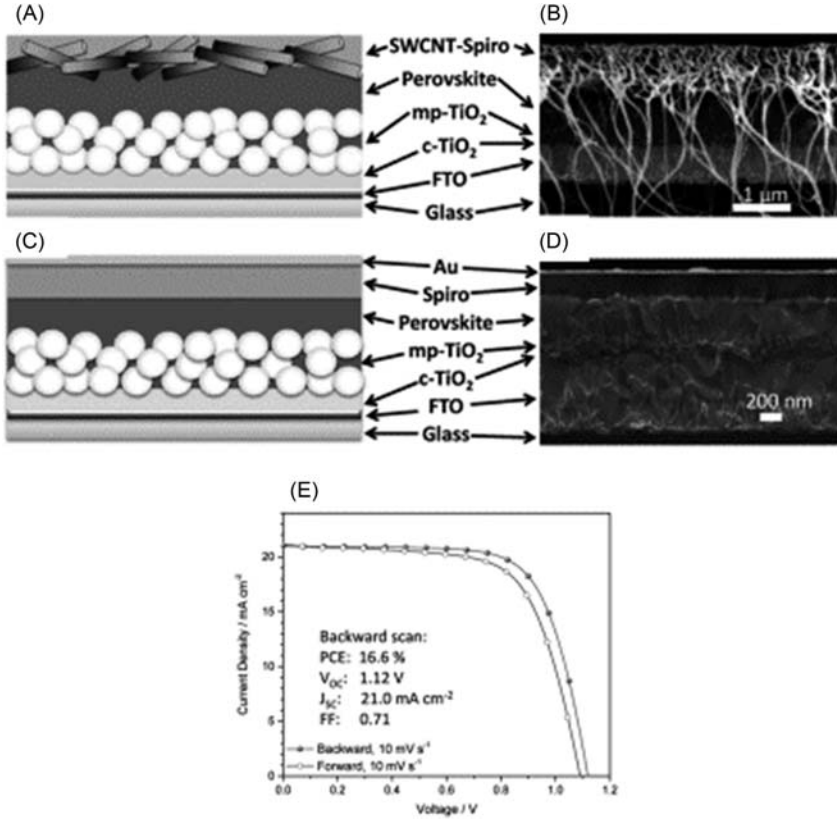


**Figure 16.21** Contains the following: (A) Schematics and (B) cross-sectional SEM image of the SWCNT-contacted device. The carbon nanotube 'whiskers' in front of the SEM image are due to sampling preparation. (C) Schematics and (D) cross-sectional SEM image of the standard Au contacted device (with spin-coated Spiro-OMeTAD HTM). (E) The *J*–*V* curve of a device that yielded a 16.0% average efficiency (average of the backward and forward scans) [205]. *SWCNT*, Single wall carbon nanotube.

showed only a modest linear efficiency loss, which led to an estimated lifetime of 580 hours. For comparison, the standard PCSs with an Au electrode exhibited a significant, rapid efficiency loss, mainly due to the ion migration of gold in the structure contained in Table 16.4.

## 16.3.2 Carbon nanotubes as HTL for solar cells

State-of-the-art HTLs that are commonly used, such as 2,2,7,-7-tetrakis (*N*,*N*-di-*p*-methoxyphenylamine)-9,9-spirobifluorene(Spiro-OMeTAD) and

**Table 16.4** Photovoltaic performance of solar cell devices with carbon nanotubes-based electrodes.

| Electrodes | $J_{sc}$ (mA cm$^{-2}$) | $V_{oc}$ (V) | FF (%) | PCE (%) | Devices | Ref. |
|---|---|---|---|---|---|---|
| CNT-dripping | 18.97 | 1.00 | 71 | 13.57 | PSCs | [206] |
| Carbon/SWCNTs | 21.26 | 1.01 | 69 | 14.7 | PSCs | [207] |
| MWCNTs | 15.6 | 0.88 | 75 | 10.3 | PSCs | [208] |
| SWNT/$MoO_3$(2 nm)/PEDOT:PSS | 17.5 | 0.96 | 76 | 12.8 | PSCs | [92] |
| CSCNTs | 20.25 | 0.89 | 65 | 11.9 | PSCs | [189] |
| SWCNT | 20.3 | 1.1 | 61 | 15.5 | PSCs | [209] |
| SWCNT | 21 | 1.12 | 71 | 16.6 | PSCs | [205] |
| Pod(N)-FeNi | 16.16 | 0.745 | 73.21 | 8.82 | DSSCs | [210] |
| VAFWCNTs/graphene on Ni foil | 13.86 | 0.72 | 64 | 8.2 | DSSCs | [195] |
| RG-CNT | 12.86 | 0.78 | 61.3 | 6.17 | DSSCs | [211] |
| TiN-CNTs | 12.74 | 0.75 | 57 | 5.41 | DSSCs | [212] |
| s-SWCNTs | 12.32 | 0.68 | 52.14 | 4.4 | BHJ solar cells | [204] |
| SWCNTs-MoOx | 13.7 | 0.72 | 61 | 6.04 | Organic solar cells | [196] |

*DSSCs*, Dye-sensitized solar cells; *MWCNT*, multiwall carbon nanotube; *PEDOT:PSS*, poly(3,4-ethylene dioxythiophene)−polystyrene sulfonate; *PSC*, perovskite solar cells; *SWCNT*, single wall carbon nanotube; *SWNT*, single-wall nanotube; *VAFWCNT*, vertically aligned few-walled carbon nanotube.

organic poly(3-hexylthiophene) (P3HT), or poly(triarylamine) (PTAA) to assemble high efficiency solar cell devices. Spiro-OMeTAD as an HTL further improves the PCE of solar cells because of the low electrical conductivity and complicated synthetic route resulting in higher costs. The organic HTL is intolerant to thermal and instability. Doping is often used to improve the mobility and conductivity of the pristine HTL. Habisreutinger et al. made systematic efforts to enhance the conductivity of HTMs (spiro-OMeTAD and P3HT) by mixing or laminating the pristine HTMs with SWNTs, shown in Fig. 16.22. First, the HTL in perovskite is made of a P3HT/SWNT layer filled with poly(methyl methacrylate) (PMMA) matrix [213]. They utilized the architecture and achieved a device PCE up to 15.3% with an average efficiency of 10% ± 2%. Observations included noticing a substantial retardation in thermal

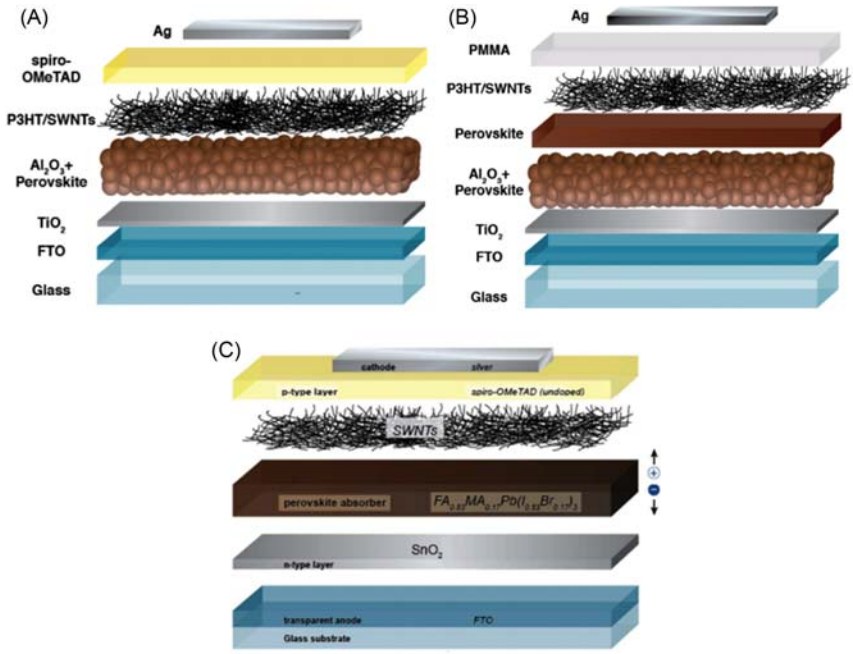


**Figure 16.22** Contains the schematic architecture of a device (A) with a P3HT/SWNT layer underneath the hole transport material (spiro-OMeTAD) matrix [213]. (B) With composite composed of a P3HT/SWNT layer in-filled with a PMMA matrix as hole-transporting structure [214]. (C) With a solution-processed $SnO_2$ layer, $FA_{0.83}MA_{0.17}Pb(I_{0.83}Br_{0.17})_3$ as perovskite absorber, a dense multilayer of polymer-wrapped SWNT, and a sequentially deposited layer of undoped spiro-OMeTAD [215]. *PMMA*, Poly (methyl methacrylate); *SWNT*, single-wall nanotube.

degradation and the resistance to water ingress, which was remarkably enhanced. Then they stratified the two-layer architecture of neat spiro-OMeTAD and P3HT/SWNT to form a highly efficient p-type charge transporter. This device performed at an efficiency of 15.4% [214]. Recently, the use of previous composites was adopted as hole transport, which changed the perovskite layer to a double mixed composition [215]. Shown in Fig. 16.22 is the dopant-free planar n–i–p PSC shown with a high PCE of 18.8%. Summarily, the research provided a series of work with the CNTs HTL which shows that even with dopant-free, it is not a sustainable HTM for long-term possibly due to its morphological instability.

As previously mentioned, MWCNTs incorporated with a P3HT composite is to increase the fill factor and mobility in the HTL for the enhancement in PSC [216,217]. Lee et al. [218] designed a hierarchical intermediate layer of pure spiro-OMeTAD between the perovskite and the as HTL in PSCs, in reference to that of spiro-OMeTAD/MWCNTs layers using toluene drop-casting method. The PSCs were fabricated by a low-temperature solution process (<100°C). As shown in Fig. 16.23, with a small amount of MWCNTs in spiro-OMeTAD, both the carrier concentration and mobility of the HTL was improved. The hole selectivity decreased, creating an undesirable back-electron passage because of the large work function (c. 4.6 eV) of MWCNTs in spiro-OMeTAD/MWCNTs [217]. In between the hierarchical construction of the perovskite and the spiro-OMeTAD/MWCNTs layers, an intermediate layer of pure spiro-OMeTAD was inserted, which effectively blocked electron transport from $CH_3NH_3PbI_3$ to spiro-OMeTAD/MWCNTs. This resulted in PSCs with a maximum PCE increased from 12.8% to 15.1%. (MWCNT concentration = 2 wt%). The PSCs were fabricated by a low-temperature solution process, further decreasing the per-Watt cost.

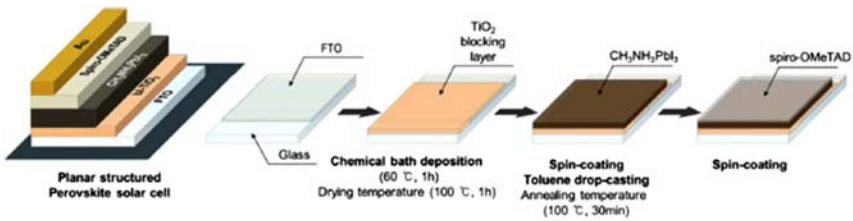


**Figure 16.23** Contains a schematic of the planar PSC fabricated by the solution method using a temperature of <100°C [218]. *PSC*, perovskite solar cells.

Due to the conduction band (CB) bottom of semiconducting SWNTs ($\sim -4.1$ eV from vacuum level) being lower than that of $CH_3NH_3PbI_3$ ($\sim -3.9$ eV), it is a likely occurrence to shunt leakage in porous SWNT networks. That could cause substantial photovoltaic losses resulting from carrier recombination. Such recombination losses significantly decrease the efficiency of solar cells. It is good for the solar cells' performance to have an electron-blocking barrier layer. GO can be applied as an electron-blocking layer [219]. Wang et al. [161] reported a combination of SWNTs with GO, when compacted with PMMA as an efficient and stable HTL for organo-lead iodide PSCs, as shown in Fig. 16.24. The photovoltaic conversion efficiency of 13.3% was achieved in the organo-lead iodide PSC due to the complementary properties of CNTs and GO. The significant improvement of photovoltaic performance stability in the PSCs using CNTs/GO/polymethyl methacrylate was demonstrated and compared with the use of typical organic HTL of 2,2,7,7-tetrakis-(*N*, *N*-di-4-methoxyphenylamino)-9,9-spirobifluorene in air condition (Table 16.5).

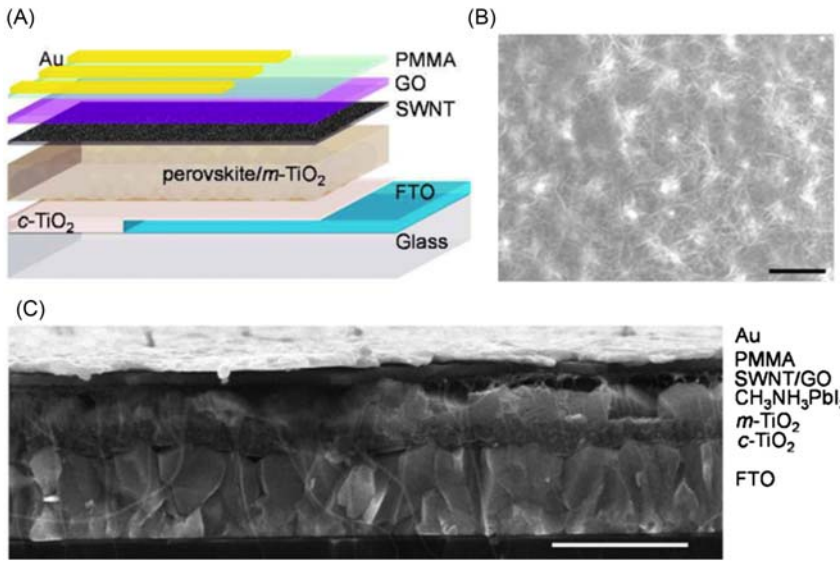


**Figure 16.24** Contains the following: (A) Schematic of an organo-lead iodide perovskite/SWNT/GO/PMMA solar cell. (B) Top-view SEM image of an SWNT film on a perovskite thin film. (C) Cross-sectional SEM image of a perovskite/SWNT/GO/PMMA solar cell. The scale bar in each figure is 1 μm [161]. *PMMA*, Poly(methyl methacrylate); *SWNT*, single-wall nanotube.

**Table 16.5** Properties of carbon nanotube (CNT)-based HTLs in solar cells.

| HTM | $J_{sc}$ (mA cm$^{-2}$) | $V_{oc}$ (V) | FF (%) | PCE (%) | Devices | Ref. |
|---|---|---|---|---|---|---|
| CNT/spiro-OMeTAD | 18.1 | 1.00 | 55 | 9.9 | PSCs | [220] |
| P3HT/SWCNT-spiro-OMeTAD | 21.4 | 1.02 | 71 | 15.4 | PSCs | [214] |
| SWNTs spiro-OMeTAD | 22.07 | 1.14 | 75 | 18.9 | PSCs | [215] |
| SWNT/GO/PMMA | 17.7 | 0.97 | 60 | 10.4 | PSCs | [161] |
| MWCNT/spiro-OMeTAD | – | – | – | 15.1 | PSCs | [218] |

*PMMA*, Poly(methyl methacrylate); *PSC*, perovskite solar cells; *SWNT*, single-wall nanotube.

## 16.4 Conclusions and outlook

In this chapter, recent developments of graphene and CNTs-based photovoltaic applications such as DSSCs, organic photovoltaics, and PSCs have been discussed. Graphene and CNTs show promise in securing a vital role in manufacturing low-cost solar cells. That is due to highly flexible properties, abundant carbon sources, and high thermal/chemical stability, compared to traditional devices. The flexible transparent electrodes are not only applied in solar cells, but also in flexible touch screens, displays, printable electronics, flexible transistors, and memory[221] In recent years many researchers have proven that graphene, whether grown by CVD or solution synthesized, functionalized or dopant, has found a niche roles in various components of solar cells, and have had improvements in performance. Graphene-based transparent electrodes in solar cells show low sheet resistance, high efficiency, and super flexibility compared to ITO-based photovoltaics. In particular, GQDs have the exciting potential to create a new challenge [66,170]. Also, graphene-based ETLs in solar cells is cost-efficient and can be processed at low temperatures in a solution-processable way. They provide enhanced electron transport because of proper energy levels relative to the electrodes and the active perovskite layer, and prevent back recombination at the interfaces [128–130]. Furthermore, graphene-based HTL in solar cells provides the appropriate energy level to promote hole transfer and selectively hamper electrons to prevent electron–hole recombination on the anode. Because of its unique two-dimensional nanostructure and morphology, device stability can be improved toward oxygen and humidity with unique electrical, optical,

thermal, and mechanical properties [21,151]. Finally, graphene-based electron acceptor materials for active layers have the ability to extract electron/energy from the P3OT [167,168]. The research of graphene-based electron acceptors in the active layer of a solar cell is underway. Like graphene, CNTs have been recently active in the field of material science and engineering, specifically those with a focus on electronic and optoelectronic applications, such as PSCs [6,18,176,222,223]. It is key to fabricate electrodes based on abundant and sustainable elements with an easily processable method. CNTs are considered a promising replacement for conventional TCO because of the properties they exhibit, such as low resistance, high conductivity, superior flexibility, and ability to be fabricated with simple techniques [204,220,224,225]. CNTs are ideal candidates for solar cells, with chemical and mechanical stability, that are beneficial for device performance. Surprisingly, CNT used as electrodes in PSC instead of the metal electrode without additional HTM, yielded a PCE of 9.1% (record 11%) [26]. However, more often CNTs are mixed or laminated with P3HT [213–215] or Spiro-OMeTAD [218] to function as hybrid HTL in solar cells and reach a high efficiency of 18.8% in dopant-free planar n–i–p PSCs. As previously summarized, several very promising approaches that utilize the unique properties of graphene and CNTs to improve the performance in a diverse set of photovoltaic devices have been reported. The era of low-cost and highly efficient carbon-based solar cells is coming.

## References

[1] B. O'Regan, M. Grätzel, A low-cost, high-efficiency solar cell based on dye-sensitized colloidal $TiO_2$ films, Nature 353 (1991) 737–740. Available from: https://doi.org/10.1038/353737a0.

[2] H. Ago, K. Petritsch, M.S.P. Shaffer, A.H. Windle, R.H. Friend, Composites of carbon nanotubes and conjugated polymers for photovoltaic devices, Adv. Mater. 11 (1999) 1281–1285. Available from: http://dx.doi.org/10.1002/(SICI)1521-4095(199910)11:15<1281::AID-ADMA1281>3.0.CO;2-6.

[3] U. Bach, Solid-State Dye-Sensitized Mesoporous $TiO_2$ Solar Cells, Swiss Federal Institute of Technology Lausanne, 2000. Available from: http://dx.doi.org/10.5075/epfl-thesis-2187.

[4] M. Grätzel, Photoelectrochemical cells, Nature 414 (2001) 338–344. Available from: https://doi.org/10.1038/35104607.

[5] D.B. Romero, M. Carrard, W. De Heer, L. Zuppiroli, A carbon nanotube/organic semiconducting polymer heterojunction, Adv. Mater. 8 (1996) 899–902. Available from: https://doi.org/10.1002/adma.19960081105.

[6] K. Suzuki, M. Yamaguchi, M. Kumagai, S. Yanagida, Application of carbon nanotubes to counter electrodes of dye-sensitized solar cells, Chem. Lett. 32 (2003) 28–29. Available from: https://doi.org/10.1246/cl.2003.28.
[7] Z. Liu, Q. Liu, Y. Huang, Y. Ma, S. Yin, X. Zhang, et al., Organic photovoltaic devices based on a novel acceptor material: graphene, Adv. Mater. 20 (2008) 3924–3930. Available from: https://doi.org/10.1002/adma.200800366.
[8] J. Wu, H.A. Becerril, Z. Bao, Z. Liu, Y. Chen, P. Peumans, Organic solar cells with solution-processed graphene transparent electrodes, Appl. Phys. Lett. 92 (2008). Available from: https://doi.org/10.1063/1.2924771.
[9] A.A. Balandin, Thermal properties of graphene and nanostructured carbon materials, Nat. Mater. 10 (2011) 569–581. Available from: https://doi.org/10.1038/nmat3064.
[10] P. Gao, D. Konrad, S. Aghazada, M.K. Nazeeruddin, Molecular engineering of functional materials for energy and opto-electronic applications, Chim. Int. J. Chem. 69 (2015) 253–263. Available from: https://doi.org/10.2533/chimia.2015.253.
[11] X.-X. Lin, B. Tan, L. Peng, Z.-F. Wu, Z.-L. Xie, Ionothermal synthesis of microporous and mesoporous carbon aerogels from fructose as electrode materials for supercapacitors, J. Mater. Chem. A 4 (2016) 4497–4505. Available from: https://doi.org/10.1039/C6TA00681G.
[12] Y. Liu, B. Huang, X. Lin, Z. Xie, Biomass-derived hierarchical porous carbons: boosting the energy density of supercapacitors via an ionothermal approach, J. Mater. Chem. A 5 (2017) 13009–13018. Available from: https://doi.org/10.1039/C7TA03639F.
[13] T. Kuila, A.K. Mishra, P. Khanra, N.H. Kim, J.H. Lee, Recent advances in the efficient reduction of graphene oxide and its application as energy storage electrode materials, Nanoscale 5 (2013) 52–71. Available from: https://doi.org/10.1039/C2NR32703A.
[14] S. Giri, D. Ghosh, C.K. Das, Growth of vertically aligned tunable polyaniline on graphene/$ZrO_2$ nanocomposites for supercapacitor energy-storage application, Adv. Funct. Mater. 24 (2014) 1312–1324. Available from: https://doi.org/10.1002/adfm.201302158.
[15] W. Tu, Y. Zhou, Z. Zou, Versatile graphene-promoting photocatalytic performance of semiconductors: basic principles, synthesis, solar energy conversion, and environmental applications, Adv. Funct. Mater. 23 (2013) 4996–5008. Available from: https://doi.org/10.1002/adfm.201203547.
[16] C. Hu, L. Song, Z. Zhang, N. Chen, Z. Feng, L. Qu, Tailored graphene systems for unconventional applications in energy conversion and storage devices, Energy Environ. Sci. 8 (2015) 31–54. Available from: https://doi.org/10.1039/C4EE02594F.
[17] A.S. Aricò, P. Bruce, B. Scrosati, J.-M. Tarascon, W. van Schalkwijk, Nanostructured materials for advanced energy conversion and storage devices, Nat. Mater. 4 (2005) 366–377. Available from: https://doi.org/10.1038/nmat1368.
[18] M.F.L. De Volder, S.H. Tawfick, R.H. Baughman, A.J. Hart, Carbon nanotubes: present and future commercial applications, Science (80-.) 339 (2013) 535–539. Available from: https://doi.org/10.1126/science.1222453.
[19] A.R. bin, M. Yusoff, L. Dai, H.-M. Cheng, J. Liu, Graphene based energy devices, Nanoscale 7 (2015) 6881–6882. Available from: https://doi.org/10.1039/C5NR90062J.
[20] D. Chen, H. Zhang, Y. Liu, J. Li, Graphene and its derivatives for the development of solar cells, photoelectrochemical, and photocatalytic applications, Energy Environ. Sci. 6 (2013) 1362. Available from: https://doi.org/10.1039/c3ee23586f.
[21] M.J. Allen, V.C. Tung, R.B. Kaner, Honeycomb carbon: a review of graphene, Chem. Rev. 110 (2010) 132–145. Available from: https://doi.org/10.1021/cr900070d.

[22] A.C. Ferrari, J.C. Meyer, V. Scardaci, C. Casiraghi, M. Lazzeri, F. Mauri, et al., Raman spectrum of graphene and graphene layers, Phys. Rev. Lett. 97 (2006) 187401. Available from: https://doi.org/10.1103/PhysRevLett.97.187401.
[23] C. Lee, X. Wei, J.W.J.W. Kysar, J. Hone, Measurement of the elastic properties and intrinsic strength of monolayer graphene, Science (80-) 321 (2008) 385–388. Available from: https://doi.org/10.1126/science.1157996.
[24] F. Bonaccorso, L. Colombo, G. Yu, M. Stoller, V. Tozzini, A.C. Ferrari, et al., Graphene, related two-dimensional crystals, and hybrid systems for energy conversion and storage, Science (80-) 347 (2015). Available from: https://doi.org/10.1126/science.1246501. 1246501–1246501.
[25] K. Wang, C. Liu, T. Meng, C. Yi, X. Gong, Inverted organic photovoltaic cells, Chem. Soc. Rev. 45 (2016) 2937–2975. Available from: https://doi.org/10.1039/C5CS00831J.
[26] K. Yan, Z. Wei, J. Li, H. Chen, Y. Yi, X. Zheng, et al., High-performance graphene-based hole conductor-free perovskite solar cells: Schottky junction enhanced hole extraction and electron blocking, Small. 11 (2015) 2269–2274. Available from: https://doi.org/10.1002/smll.201403348.
[27] C.-H. Chiang, C.-G. Wu, Bulk heterojunction perovskite—PCBM solar cells with high fill factor, Nat. Photonics 10 (2016) 196–200. Available from: https://doi.org/10.1038/nphoton.2016.3.
[28] X. Li, Z. Lv, H. Zhu, Carbon/silicon heterojunction solar cells: state of the art and prospects, Adv. Mater. 27 (2015) 6549–6574. Available from: https://doi.org/10.1002/adma.201502999.
[29] H. Chen, Y. Hou, C.E. Halbig, S. Chen, H. Zhang, N. Li, et al., Extending the environmental lifetime of unpackaged perovskite solar cells through interfacial design, J. Mater. Chem. A 4 (2016) 11604–11610. Available from: https://doi.org/10.1039/C6TA03755K.
[30] J. Cao, Y.-M.M. Liu, X. Jing, J. Yin, J. Li, B. Xu, et al., Well-defined thiolated nanographene as hole-transporting material for efficient and stable perovskite solar cells, J. Am. Chem. Soc. 137 (2015) 10914–10917. Available from: https://doi.org/10.1021/jacs.5b06493.
[31] P.M. Ajayan, S. Lijima, Smallest carbon nanotube, Nature 358 (1992) 23. Available from: https://doi.org/10.1038/358023a0.
[32] R.A. Hatton, A.J. Miller, S.R.P. Silva, Carbon nanotubes: a multi-functional material for organic optoelectronics, J. Mater. Chem. 18 (2008) 1183. Available from: https://doi.org/10.1039/b713527k.
[33] H.W. Zhu, Direct synthesis of long single-walled carbon nanotube strands, Science (80-) 296 (2002) 884–886. Available from: https://doi.org/10.1126/science.1066996.
[34] J. Li, C. Papadopoulos, J.M. Xu, M. Moskovits, Highly-ordered carbon nanotube arrays for electronics applications, Appl. Phys. Lett. 75 (1999) 367–369. Available from: https://doi.org/10.1063/1.124377.
[35] Y. Yan, J. Miao, Z. Yang, F.-X. Xiao, H. Bin Yang, B. Liu, et al., Carbon nanotube catalysts: recent advances in synthesis, characterization and applications, Chem. Soc. Rev. 44 (2015) 3295–3346. Available from: https://doi.org/10.1039/C4CS00492B.
[36] S. Yamashita, Photonic applications of carbon nanotube and graphene, in: Int. Conf. Fibre Opt. Photonics, OSA, Washington, D.C., 2012: p. T3B.1. doi:10.1364/PHOTONICS.2012.T3B.1.
[37] D.S. Hecht, L. Hu, G. Irvin, Emerging transparent electrodes based on thin films of carbon nanotubes, graphene, and metallic nanostructures, Adv. Mater. 23 (2011) 1482–1513. Available from: https://doi.org/10.1002/adma.201003188.
[38] M. Green, Operating Principles, Technology, and System Applications (1982) 274.

[39] G. Dennler, M.C. Scharber, C.J. Brabec, Polymer-fullerene bulk-heterojunction solar cells, Adv. Mater. 21 (2009) 1323–1338. Available from: https://doi.org/10.1002/adma.200801283.
[40] L. Lu, T. Zheng, Q. Wu, A.M. Schneider, D. Zhao, L. Yu, Recent advances in bulk heterojunction polymer solar cells, Chem. Rev. 115 (2015) 12666–12731. Available from: https://doi.org/10.1021/acs.chemrev.5b00098.
[41] J. Wu, Z. Lan, J. Lin, M. Huang, Y. Huang, L. Fan, et al., Electrolytes in dye-sensitized solar cells, Chem. Rev. 115 (2015) 2136–2173. Available from: https://doi.org/10.1021/cr400675m.
[42] L. Liang, P. Gao, Lead-free hybrid perovskite absorbers for viable application: can we eat the cake and have it too? Adv. Sci. 5 (2018) 1700331. Available from: https://doi.org/10.1002/advs.201700331.
[43] P. You, Z. Liu, Q. Tai, S. Liu, F. Yan, Efficient semitransparent perovskite solar cells with graphene electrodes, Adv. Mater. 27 (2015) 3632–3638. Available from: https://doi.org/10.1002/adma.201501145.
[44] I.-Y. Jeon, M.J. Ju, J. Xu, H.-J. Choi, J.-M. Seo, M.-J. Kim, et al., Edge-fluorinated graphene nanoplatelets as high performance electrodes for dye-sensitized solar cells and lithium ion batteries, Adv. Funct. Mater. 25 (2015) 1170–1179. Available from: https://doi.org/10.1002/adfm.201403836.
[45] H. Sung, N. Ahn, M.S. Jang, J.-K. Lee, H. Yoon, N.-G. Park, et al., Transparent conductive oxide-free graphene-based perovskite solar cells with over 17% efficiency, Adv. Energy Mater. 6 (2016) 1501873. Available from: https://doi.org/10.1002/aenm.201501873.
[46] H. Schmidt, H. Flügge, T. Winkler, T. Bülow, T. Riedl, W. Kowalsky, Efficient semitransparent inverted organic solar cells with indium tin oxide top electrode, Appl. Phys. Lett. 94 (2009) 243302. Available from: https://doi.org/10.1063/1.3154556.
[47] T.C. Wei, C.C. Wan, Y.Y. Wang, Poly(*N*-vinyl-2-pyrrolidone)-capped platinum nanoclusters on indium-tin oxide glass as counterelectrode for dye-sensitized solar cells, Appl. Phys. Lett. 88 (2006) 103122. Available from: https://doi.org/10.1063/1.2186069.
[48] T. Kawashima, T. Ezure, K. Okada, H. Matsui, K. Goto, N. Tanabe, FTO/ITO double-layered transparent conductive oxide for dye-sensitized solar cells, J. Photochem. Photobiol. A: Chem. 164 (2004) 199–202.
[49] C. Sima, C. Grigoriu, S. Antohe, Comparison of the dye-sensitized solar cells performances based on transparent conductive ITO and FTO, Thin Solid Films 519 (2010) 595–597. Available from: https://doi.org/10.1016/j.tsf.2010.07.002.
[50] X. Hu, L. Chen, Y. Zhang, Q. Hu, J. Yang, Y. Chen, Large-scale flexible and highly conductive carbon transparent electrodes via roll-to-roll process and its high performance lab-scale indium tin oxide-free polymer solar cells, Chem. Mater. 26 (2014) 6293–6302. Available from: https://doi.org/10.1021/cm5033942.
[51] C. Sachse, N. Weiß, N. Gaponik, L. Müller-Meskamp, A. Eychmüller, K. Leo, ITO-free, small-molecule organic solar cells on spray-coated copper-nanowire-based transparent electrodes, Adv. Energy Mater. 4 (2014) 1300737. Available from: https://doi.org/10.1002/aenm.201300737.
[52] G. Eda, Y.Y. Lin, S. Miller, C.W. Chen, W.F. Su, M. Chhowalla, Transparent and conducting electrodes for organic electronics from reduced graphene oxide, Appl. Phys. Lett. 92 (2008) 233305. Available from: https://doi.org/10.1063/1.2937846.
[53] L. Gomez De Arco, Y. Zhang, C.W. Schlenker, K. Ryu, M.E. Thompson, C. Zhou, Continuous, highly flexible and transparent graphene films by chemical vapor deposition for organic photovoltaics, ACS Nano 4 (2010) 2865–2873. Available from: https://doi.org/10.1021/nn901587x.

[54] H. Park, S. Chang, X. Zhou, J. Kong, T. Palacios, S. Gradečak, Flexible graphene electrode-based organic photovoltaics with record-high efficiency, Nano. Lett. 14 (2014) 5148–5154. Available from: https://doi.org/10.1021/nl501981f.
[55] A.R. bin Mohd Yusoff, D. Kim, F.K. Schneider, W.J. da Silva, J. Jang, Au-doped single layer graphene nanoribbons for a record-high efficiency ITO-free tandem polymer solar cell, Energy Environ. Sci. 8 (2015) 1523–1537. Available from: https://doi.org/10.1039/C5EE00749F.
[56] N. Ye, J. Yan, S. Xie, Y. Kong, T. Liang, H. Chen, et al., Silver nanowire–graphene hybrid transparent conductive electrodes for highly efficient inverted organic solar cells, Nanotechnology 28 (2017) 305402. Available from: https://doi.org/10.1088/1361-6528/aa7723.
[57] N.S. Lewis, Toward cost-effective solar energy use, Science (80-.) 315 (2007) 798–801. Available from: https://doi.org/10.1126/science.1137014.
[58] C. Battaglia, A. Cuevas, S. De Wolf, High-efficiency crystalline silicon solar cells: status and perspectives, Energy Environ. Sci. 9 (2016) 1552–1576. Available from: https://doi.org/10.1039/C5EE03380B.
[59] Q. Liu, R. Ishikawa, S. Funada, T. Ohki, K. Ueno, H. Shirai, Highly efficient solution-processed poly(3,4-ethylenedio-xythiophene):poly(styrenesulfonate)/crystalline-silicon heterojunction solar cells with improved light-induced stability, Adv. Energy Mater. 5 (2015) 1500744. Available from: https://doi.org/10.1002/aenm.201500744.
[60] S. Wu, W. Cui, N. Aghdassi, T. Song, S. Duhm, S.-T. Lee, et al., Nanostructured Si/organic heterojunction solar cells with high open-circuit voltage via improving junction quality, Adv. Funct. Mater. 26 (2016) 5035–5041. Available from: https://doi.org/10.1002/adfm.201600441.
[61] M. Graetzel, R.A.J. Janssen, D.B. Mitzi, E.H. Sargent, Materials interface engineering for solution-processed photovoltaics, Nature 488 (2012) 304–312. Available from: https://doi.org/10.1038/nature11476.
[62] X. Yan, B. Li, L. Li, Colloidal graphene quantum dots with well-defined structures, Acc. Chem. Res. 46 (2013) 2254–2262. Available from: https://doi.org/10.1021/ar300137p.
[63] J.K. Kim, M.J. Park, S.J. Kim, D.H. Wang, S.P. Cho, S. Bae, et al., Balancing light absorptivity and carrier conductivity of graphene quantum dots for high-efficiency bulk heterojunction solar cells, ACS Nano 7 (2013) 7207–7212. Available from: https://doi.org/10.1021/nn402606v.
[64] H. Bin Yang, Y.Q. Dong, X. Wang, S.Y. Khoo, B. Liu, Cesium carbonate functionalized graphene quantum dots as stable electron-selective layer for improvement of inverted polymer solar cells, ACS Appl. Mater. Interfaces 6 (2014) 1092–1099. Available from: https://doi.org/10.1021/am404638e.
[65] D.W. Chang, H.-J. Choi, A. Filer, J.-B. Baek, Graphene in photovoltaic applications: organic photovoltaic cells (OPVs) and dye-sensitized solar cells (DSSCs), J. Mater. Chem. A 2 (2014) 12136. Available from: https://doi.org/10.1039/C4TA01047G.
[66] S. Diao, X. Zhang, Z. Shao, K. Ding, J. Jie, X. Zhang, 12.35% efficient graphene quantum dots/silicon heterojunction solar cells using graphene transparent electrode, Nano Energy 31 (2017) 359–366. Available from: https://doi.org/10.1016/j.nanoen.2016.11.051.
[67] A. El Fatimy, R.L. Myers-Ward, A.K. Boyd, K.M. Daniels, D.K. Gaskill, P. Barbara, Epitaxial graphene quantum dots for high-performance terahertz bolometers, Nat. Nanotechnol. 11 (2016) 335–338. Available from: https://doi.org/10.1038/nnano.2015.303.
[68] P. Gao, M. Grätzel, M.D.K. Nazeeruddin, Chapter 6. Chemistry of sensitizers for dye-sensitized solar cells, Adv. Concepts Photovoltaics (2014) 186–241. Available from: https://doi.org/10.1039/9781849739955-00186.

[69] J.D. Roy-Mayhew, D.J. Bozym, C. Punckt, I.A. Aksay, Functionalized graphene as a catalytic solar cells, ACS Nano 4 (2010) 6203–6211. Available from: https://doi.org/10.1021/nn1016428.
[70] R. Bajpai, S. Roy, N. Koratkar, D.S. Misra, NiO nanoparticles deposited on graphene platelets as a cost-effective counter electrode in a dye sensitized solar cell, Carbon N. Y. 56 (2013) 56–63. Available from: https://doi.org/10.1016/j.carbon.2012.12.087.
[71] V.-D. Dao, L.L. Larina, K.-D. Jung, J.-K. Lee, H.-S. Choi, Graphene–NiO nanohybrid prepared by dry plasma reduction as a low-cost counter electrode material for dye-sensitized solar cells, Nanoscale 6 (2014) 477–482. Available from: https://doi.org/10.1039/C3NR04871C.
[72] V.-D. Dao, H.-S. Choi, Dry plasma synthesis of a MWNT–Pt nanohybrid as an efficient and low-cost counter electrode material for dye-sensitized solar cells, Chem. Commun. 49 (2013) 8910. Available from: https://doi.org/10.1039/c3cc42151a.
[73] V.-D. Dao, L. Van Nang, E.-T. Kim, J.-K. Lee, H.-S. Choi, Pt nanoparticles immobilized on CVD-grown graphene as a transparent counter electrode material for dye-sensitized solar cells, ChemSusChem 6 (2013) 1316–1319. Available from: https://doi.org/10.1002/cssc.201300353.
[74] W. Lv, F. Sun, D.M. Tang, H.T. Fang, C. Liu, Q.H. Yang, et al., A sandwich structure of graphene and nickel oxide with excellent supercapacitive performance, J. Mater. Chem. 21 (2011) 9014–9019. Available from: https://doi.org/10.1039/c1jm10400d.
[75] A.G. Kannan, J. Zhao, S.G. Jo, Y.S. Kang, D.-W. Kim, Nitrogen and sulfur co-doped graphene counter electrodes with synergistically enhanced performance for dye-sensitized solar cells, J. Mater. Chem. A 2 (2014) 12232–12239. Available from: https://doi.org/10.1039/C4TA01927J.
[76] S. Wang, Q. Gao, J. Wang, Thermodynamic analysis of decomposition of thiourea and thiourea oxides, J. Phys. Chem. B 109 (2005) 17281–17289. Available from: https://doi.org/10.1021/jp051620v.
[77] E. Bi, H. Chen, X. Yang, W. Peng, M. Grätzel, L. Han, A quasi core–shell nitrogen-doped graphene/cobalt sulfide conductive catalyst for highly efficient dye-sensitized solar cells, Energy Environ. Sci. 7 (2014) 2637–2641. Available from: https://doi.org/10.1039/C4EE01339E.
[78] S. Casaluci, M. Gemmi, V. Pellegrini, A. Di Carlo, F. Bonaccorso, Graphene-based large area dye-sensitized solar cell modules, Nanoscale 8 (2016) 5368–5378. Available from: https://doi.org/10.1039/C5NR07971C.
[79] J.M. Ball, M.M. Lee, A. Hey, H.J. Snaith, Low-temperature processed meso-superstructured to thin-film perovskite solar cells, Energy Environ. Sci. 6 (2013) 1739. Available from: https://doi.org/10.1039/c3ee40810h.
[80] J.H. Heo, S.H. Im, J.H. Noh, T.N. Mandal, C.-S. Lim, J.A. Chang, et al., Efficient inorganic–organic hybrid heterojunction solar cells containing perovskite compound and polymeric hole conductors, Nat. Photonics 7 (2013) 486–491. Available from: https://doi.org/10.1038/nphoton.2013.80.
[81] G.E. Eperon, V.M. Burlakov, P. Docampo, A. Goriely, H.J. Snaith, Morphological control for high performance, solution-processed planar heterojunction perovskite solar cells, Adv. Funct. Mater. 24 (2014) 151–157. Available from: https://doi.org/10.1002/adfm.201302090.
[82] J.H. Heo, H.J. Han, D. Kim, T.K. Ahn, S.H. Im, Hysteresis-less inverted CH 3 $NH_3$ $PbI_3$ planar perovskite hybrid solar cells with 18.1% power conversion efficiency, Energy Environ. Sci. 8 (2015) 1602–1608. Available from: https://doi.org/10.1039/C5EE00120J.
[83] D. Liu, T.L. Kelly, Perovskite solar cells with a planar heterojunction structure prepared using room-temperature solution processing techniques, Nat. Photonics 8 (2013) 133–138. Available from: https://doi.org/10.1038/nphoton.2013.342.

[84] D. Yang, R. Yang, J. Zhang, Z. Yang, S. (Frank) Liu, C. Li, High efficiency flexible perovskite solar cells using superior low temperature $TiO_2$, Energy Environ. Sci. 8 (2015) 3208–3214. Available from: https://doi.org/10.1039/C5EE02155C.
[85] J. You, Z. Hong, Y. (Michael) Yang, Q. Chen, M. Cai, T.-B. Song, et al., Low-temperature solution-processed perovskite solar cells with high efficiency and flexibility, ACS Nano 8 (2014) 1674–1680. Available from: https://doi.org/10.1021/nn406020d.
[86] P. Docampo, J.M. Ball, M. Darwich, G.E. Eperon, H.J. Snaith, Efficient organometal trihalide perovskite planar-heterojunction solar cells on flexible polymer substrates, Nat. Commun. 4 (2013) 2761. Available from: https://doi.org/10.1038/ncomms3761.
[87] B.J. Kim, D.H. Kim, Y.-Y. Lee, H.-W. Shin, G.S. Han, J.S. Hong, et al., Highly efficient and bending durable perovskite solar cells: toward a wearable power source, Energy Environ. Sci. 8 (2015) 916–921. Available from: https://doi.org/10.1039/C4EE02441A.
[88] J. Yoon, H. Sung, G. Lee, W. Cho, N. Ahn, H.S. Jung, et al., Superflexible, high-efficiency perovskite solar cells utilizing graphene electrodes: towards future foldable power sources, Energy Environ. Sci. 10 (2017) 337–345. Available from: https://doi.org/10.1039/C6EE02650H.
[89] J.D. Roy-Mayhew, D.J. Bozym, C. Punckt, Ia Aksay, Functionalized graphene as a catalytic counter electrode in dye-sensitized solar cells, ACS Nano 4 (2010) 6203–6211. Available from: https://doi.org/10.1021/Nn1016428.
[90] M.-H. Yeh, L.-Y. Lin, C.-L. Sun, Y.-A. Leu, J.-T. Tsai, C.-Y. Yeh, et al., Multiwalled carbon nanotube@reduced graphene oxide nanoribbon as the counter electrode for dye-sensitized solar cells, J. Phys. Chem. C 118 (2014) 16626–16634. Available from: https://doi.org/10.1021/jp412542d.
[91] X. Hu, X. Meng, J. Xiong, Z. Huang, X. Yang, L. Tan, et al., Roll-to-roll fabrication of flexible orientated graphene transparent electrodes by shear force and one-step reducing post-treatment, Adv. Mater. Technol. 2 (2017) 1700138. Available from: https://doi.org/10.1002/admt.201700138.
[92] I. Jeon, J. Yoon, N. Ahn, M. Atwa, C. Delacou, A. Anisimov, et al., Carbon nanotubes versus graphene as flexible transparent electrodes in inverted perovskite solar cells, J. Phys. Chem. Lett. 8 (2017) 5395–5401. Available from: https://doi.org/10.1021/acs.jpclett.7b02229.
[93] V.D. Dao, Y. Choi, K. Yong, L.L. Larina, H.S. Choi, Graphene-based nanohybrid materials as the counter electrode for highly efficient quantum-dot-sensitized solar cells, Carbon N. Y. 84 (2015) 383–389. Available from: https://doi.org/10.1016/j.carbon.2014.12.014.
[94] O. Malinkiewicz, A. Yella, Y.H. Lee, G.M. Espallargas, M. Graetzel, M.K. Nazeeruddin, et al., Perovskite solar cells employing organic charge-transport layers, Nat. Photonics 8 (2013) 128–132. Available from: https://doi.org/10.1038/nphoton.2013.341.
[95] N.J. Jeon, J.H. Noh, Y.C. Kim, W.S. Yang, S. Ryu, S. Il Seok, Solvent engineering for high-performance inorganic-organic hybrid perovskite solar cells, Nat. Mater. 13 (2014) 897–903. Available from: https://doi.org/10.1038/nmat4014.
[96] H.J. Snaith, A. Abate, J.M. Ball, G.E. Eperon, T. Leijtens, N.K. Noel, et al., Anomalous hysteresis in perovskite solar cells, J. Phys. Chem. Lett. 5 (2014) 1511–1515. Available from: https://doi.org/10.1021/jz500113x.
[97] J.T.-W. Wang, J.M. Ball, E.M. Barea, A. Abate, J.A. Alexander-Webber, J. Huang, et al., Low-temperature processed electron collection layers of graphene/$TiO_2$ nanocomposites in thin film perovskite solar cells, Nano Lett. 14 (2014) 724–730. Available from: https://doi.org/10.1021/nl403997a.

[98] J.-Y.Y. Jeng, Y.-F.F. Chiang, M.-H.H. Lee, S.-R.R. Peng, T.-F.F. Guo, P. Chen, et al., $CH_3$ $NH_3$ $PbI_3$ perovskite/fullerene planar-heterojunction hybrid solar cells, Adv. Mater. 25 (2013) 3727–3732. Available from: https://doi.org/10.1002/adma.201301327.

[99] S. Sun, T. Salim, N. Mathews, M. Duchamp, C. Boothroyd, G. Xing, et al., The origin of high efficiency in low-temperature solution-processable bilayer organometal halide hybrid solar cells, Energy Environ. Sci. 7 (2014) 399–407. Available from: https://doi.org/10.1039/C3EE43161D.

[100] S. Chen, Q. Wu, C. Mishra, J. Kang, H. Zhang, K. Cho, et al., Thermal conductivity of isotopically modified graphene, Nat. Mater. 11 (2012) 203–207. Available from: https://doi.org/10.1038/nmat3207.

[101] A.A. Balandin, S. Ghosh, W. Bao, I. Calizo, D. Teweldebrhan, F. Miao, et al., Superior thermal conductivity of single-layer graphene, Nano Lett. 8 (2008) 902–907. Available from: https://doi.org/10.1021/nl0731872.

[102] R.R. Nair, P. Blake, A.N. Grigorenko, K.S. Novoselov, T.J. Booth, T. Stauber, et al., Fine structure constant defines visual transparency of graphene, Science (80-) 320 (2008). Available from: https://doi.org/10.1126/science.1156965. 1308–1308.

[103] M. Acik, S.B. Darling, Graphene in perovskite solar cells: device design, characterization and implementation, J. Mater. Chem. A 4 (2016) 6185–6235. Available from: https://doi.org/10.1039/c5ta09911k.

[104] A. Agresti, S. Pescetelli, B. Taheri, A.E. Del Rio Castillo, L. Cinà, F. Bonaccorso, et al., Graphene-perovskite solar cells exceed 18% efficiency: a stability study, ChemSusChem 9 (2016) 2609–2619. Available from: https://doi.org/10.1002/cssc.201600942.

[105] Z. Lin, C. Jiang, C. Zhu, J. Zhang, Development of inverted organic solar cells with $TiO_2$ interface layer by using low-temperature atomic layer deposition, ACS Appl. Mater. Interfaces 5 (2013) 713–718. Available from: https://doi.org/10.1021/am302252p.

[106] S. Trost, K. Zilberberg, A. Behrendt, A. Polywka, P. Görrn, P. Reckers, et al., Overcoming the "light-soaking" issue in inverted organic solar cells by the use of Al:Zno electron extraction layers, Adv. Energy Mater. 3 (2013) 1437–1444. Available from: https://doi.org/10.1002/aenm.201300402.

[107] Z. Xu, L.-M. Chen, G. Yang, C.-H. Huang, J. Hou, Y. Wu, et al., Vertical phase separation in poly(3-hexylthiophene): fullerene derivative blends and its advantage for inverted structure solar cells, Adv. Funct. Mater. 19 (2009) 1227–1234. Available from: https://doi.org/10.1002/adfm.200801286.

[108] Y.-I. Lee, J.-H. Youn, M.-S. Ryu, J. Kim, H.-T. Moon, J. Jang, Electrical properties of inverted poly(3-hexylthiophene): Methano-fullerene [6,6]-phenyl C71-butyric acid methyl ester bulk hetero-junction solar cell with $Cs_2CO_3$ and $MoO_3$ layers, Sol. Energy Mater. Sol. Cells 95 (2011) 3276–3280. Available from: https://doi.org/10.1016/j.solmat.2011.07.008.

[109] G. Cheng, W.-Y. Tong, K.-H. Low, C.-M. Che, Thermal-annealing-free inverted polymer solar cells using $ZnO/Cs_2CO_3$ bilayer as electron-selective layer, Sol. Energy Mater. Sol. Cells 103 (2012) 164–170. Available from: https://doi.org/10.1016/j.solmat.2012.04.022.

[110] Q. Jiang, L. Zhang, H. Wang, X. Yang, J. Meng, H. Liu, et al., Enhanced electron extraction using SnO2 for high-efficiency planar-structure $HC(NH_2)_2PbI_3$-based perovskite solar cells, Nat. Energy 2 (2016) 16177. Available from: https://doi.org/10.1038/nenergy.2016.177.

[111] H. Tan, A. Jain, O. Voznyy, X. Lan, F.P. García de Arquer, J.Z. Fan, et al., Efficient and stable solution-processed planar perovskite solar cells via contact

passivation, Science (80-) 355 (2017) 722–726. Available from: https://doi.org/10.1126/science.aai9081.

[112] J. Xie, K. Huang, X. Yu, Z. Yang, K. Xiao, Y. Qiang, et al., Enhanced electronic properties of $SnO_2$ via electron transfer from graphene quantum dots for efficient perovskite solar cells, ACS Nano 11 (2017) 9176–9182. Available from: https://doi.org/10.1021/acsnano.7b04070.

[113] M.J. Beliatis, K.K. Gandhi, L.J. Rozanski, R. Rhodes, L. McCafferty, M.R. Alenezi, et al., Hybrid graphene-metal oxide solution processed electron transport layers for large area high-performance organic photovoltaics, Adv. Mater. 26 (2014) 2078–2083. Available from: https://doi.org/10.1002/adma.201304780.

[114] A. Morais, J.P.C. Alves, F.A.S. Lima, M. Lira-Cantu, A.F. Nogueira, Enhanced photovoltaic performance of inverted hybrid bulk-heterojunction solar cells using $TiO_2$/reduced graphene oxide films as electron transport layers, J. Photonics Energy 5 (2015) 057408. Available from: https://doi.org/10.1117/1.JPE.5.057408.

[115] K.T. Cho, G. Grancini, Y. Lee, D. Konios, S. Paek, E. Kymakis, et al., Beneficial role of reduced graphene oxide for electron extraction in highly efficient perovskite solar cells, ChemSusChem 9 (2016) 3040–3044. Available from: https://doi.org/10.1002/cssc.201601070.

[116] Z. Yin, J. Zhu, Q. He, X. Cao, C. Tan, H. Chen, et al., Graphene-based materials for solar cell applications, Adv. Energy Mater. 4 (2014) 1300574. Available from: https://doi.org/10.1002/aenm.201300574.

[117] N. Balis, E. Stratakis, E. Kymakis, Graphene and transition metal dichalcogenide nanosheets as charge transport layers for solution processed solar cells, Mater. Today 19 (2016) 580–594. Available from: https://doi.org/10.1016/j.mattod.2016.03.018.

[118] M.A. Green, Y. Hishikawa, W. Warta, E.D. Dunlop, D.H. Levi, J. Hohl-Ebinger, et al., Solar cell efficiency tables (version 50), Prog. Photovoltaics Res. Appl. 25 (2017) 668–676. Available from: https://doi.org/10.1002/pip.2909.

[119] G.S. Han, Y.H. Song, Y.U. Jin, J.-W. Lee, N.-G. Park, B.K. Kang, et al., Reduced graphene oxide/mesoporous $TiO_2$ nanocomposite based perovskite solar cells, ACS Appl. Mater. Interfaces 7 (2015) 23521–23526. Available from: https://doi.org/10.1021/acsami.5b06171.

[120] M. Batmunkh, C.J. Shearer, M.J. Biggs, J.G. Shapter, Solution processed graphene structures for perovskite solar cells, J. Mater. Chem. A 4 (2016) 2605–2616. Available from: https://doi.org/10.1039/C5TA08996D.

[121] J.-S. Yeo, R. Kang, S. Lee, Y.-J. Jeon, N. Myoung, C.-L. Lee, et al., Highly efficient and stable planar perovskite solar cells with reduced graphene oxide nanosheets as electrode interlayer, Nano Energy 12 (2015) 96–104. Available from: https://doi.org/10.1016/j.nanoen.2014.12.022.

[122] C.-H. Jung, Y.-J. Noh, J.-H. Bae, J.-H. Yu, I.-T. Hwang, J. Shin, et al., Polyacrylonitrile-grafted reduced graphene oxide hybrid: An all-round and efficient hole-extraction material for organic and inorganic-organic hybrid photovoltaics, Nano Energy 31 (2017) 19–27. Available from: https://doi.org/10.1016/j.nanoen.2016.11.003.

[123] E. Stratakis, K. Savva, D. Konios, C. Petridis, E. Kymakis, Improving the efficiency of organic photovoltaics by tuning the work function of graphene oxide hole transporting layers, Nanoscale 6 (2014) 6925–6931. Available from: https://doi.org/10.1039/C4NR01539H.

[124] G. Kakavelakis, D. Konios, E. Stratakis, E. Kymakis, Enhancement of the efficiency and stability of organic photovoltaic devices via the addition of a lithium-neutralized graphene oxide electron-transporting layer, Chem. Mater. 26 (2014) 5988–5993. Available from: https://doi.org/10.1021/cm502826f.

[125] J.P. Correa Baena, L. Steier, W. Tress, M. Saliba, S. Neutzner, T. Matsui, et al., Highly efficient planar perovskite solar cells through band alignment engineering, Energy Environ. Sci. 8 (2015) 2928–2934. Available from: https://doi.org/10.1039/C5EE02608C.

[126] J. Seo, N.J. Jeon, W.S. Yang, H. Shin, T.K. Ahn, J. Lee, et al., Effective electron blocking of CuPC-doped Spiro-OMeTAD for highly efficient inorganic-organic hybrid perovskite solar cells, Adv. Energy Mater. 5 (2015) 1501320. Available from: https://doi.org/10.1002/aenm.201501320.

[127] A. Agresti, S. Pescetelli, L. Cinà, D. Konios, G. Kakavelakis, E. Kymakis, et al., Efficiency and stability enhancement in perovskite solar cells by inserting lithium-neutralized graphene oxide as electron transporting layer, Adv. Funct. Mater. 26 (2016) 2686–2694. Available from: https://doi.org/10.1002/adfm.201504949.

[128] E. Nouri, M.R. Mohammadi, P. Lianos, Inverted perovskite solar cells based on lithium-functionalized graphene oxide as an electron-transporting layer, Chem. Commun. 53 (2017) 1630–1633. Available from: https://doi.org/10.1039/C6CC09876B.

[129] W. Chen, Y. Wu, Y. Yue, J. Liu, W. Zhang, X. Yang, et al., Efficient and stable large-area perovskite solar cells with inorganic charge extraction layers, Science (80-) 350 (2015) 944–948. Available from: https://doi.org/10.1126/science.aad1015.

[130] J. Shi, X. Xu, D. Li, Q. Meng, Interfaces in perovskite solar cells, Small 11 (2015) 2472–2486. Available from: https://doi.org/10.1002/smll.201403534.

[131] E. Nouri, M.R. Mohammadi, P. Lianos, Improving the stability of inverted perovskite solar cells under ambient conditions with graphene-based inorganic charge transporting layers, Carbon N. Y. 126 (2018) 208–214. Available from: https://doi.org/10.1016/j.carbon.2017.10.015.

[132] G. Kakavelakis, T. Maksudov, D. Konios, I. Paradisanos, G. Kioseoglou, E. Stratakis, et al., Efficient and highly air stable planar inverted perovskite solar cells with reduced graphene oxide doped PCBM electron transporting layer, Adv. Energy Mater. 7 (2017) 1602120. Available from: https://doi.org/10.1002/aenm.201602120.

[133] R. Steim, F.R. Kogler, C.J. Brabec, Interface materials for organic solar cells, J. Mater. Chem. 20 (2010) 2499. Available from: https://doi.org/10.1039/b921624c.

[134] H.-L. Yip, A.K.-Y. Jen, Recent advances in solution-processed interfacial materials for efficient and stable polymer solar cells, Energy Environ. Sci. 5 (2012) 5994. Available from: https://doi.org/10.1039/c2ee02806a.

[135] F. Fabregat-Santiago, J. Bisquert, L. Cevey, P. Chen, M. Wang, S.M. Zakeeruddin, et al., Electron transport and recombination in solid-state dye solar cell with spiro-OMeTAD as hole conductor, J. Am. Chem. Soc. 131 (2009) 558–562. Available from: https://doi.org/10.1021/ja805850q.

[136] W. Zhou, Z. Wen, P. Gao, Less is more: dopant-free hole transporting materials for high-efficiency perovskite solar cells, Adv. Energy Mater. 8 (2018) 1702512. Available from: https://doi.org/10.1002/aenm.201702512.

[137] Z.H. Bakr, Q. Wali, A. Fakharuddin, L. Schmidt-Mende, T.M. Brown, R. Jose, Advances in hole transport materials engineering for stable and efficient perovskite solar cells, Nano Energy 34 (2017) 271–305. Available from: https://doi.org/10.1016/j.nanoen.2017.02.025.

[138] W. Tress, N. Marinova, O. Inganas, M.K. Nazeeruddin, S.M. Zakeeruddin, M. Graetzel, The role of the hole-transport layer in perovskite solar cells – reducing recombination and increasing absorption, in: 2014 IEEE 40th Photovolt. Spec. Conf., IEEE, 2014, pp. 1563–1566. doi:10.1109/PVSC.2014.6925216.

[139] L. Zhu, J. Xiao, J. Shi, J. Wang, S. Lv, Y. Xu, et al., Efficient $CH_3NH_3PbI_3$ perovskite solar cells with 2TPA-*n*-DP hole-transporting layers, Nano Res. 8 (2015) 1116–1127. Available from: https://doi.org/10.1007/s12274-014-0592-y.

[140] S. Chen, Y. Hou, H. Chen, M. Richter, F. Guo, S. Kahmann, et al., Exploring the limiting open-circuit voltage and the voltage loss mechanism in planar $CH_3NH_3PbBr_3$ perovskite solar cells, Adv. Energy Mater. 6 (2016) 1–9. Available from: https://doi.org/10.1002/aenm.201600132.

[141] N.K. Elumalai, A. Uddin, Open circuit voltage of organic solar cells: an in-depth review, Energy Environ. Sci. 9 (2016) 391–410. Available from: https://doi.org/10.1039/C5EE02871J.

[142] Y. Shao, Y. Yuan, J. Huang, Correlation of energy disorder and open-circuit voltage in hybrid perovskite solar cells, Nat. Energy 1 (2016) 15001. Available from: https://doi.org/10.1038/nenergy.2015.1.

[143] H. Back, G. Kim, J. Kim, J. Kong, T.K. Kim, H. Kang, et al., Achieving long-term stable perovskite solar cells via ion neutralization, Energy Environ. Sci. 9 (2016) 1258–1263. Available from: https://doi.org/10.1039/C6EE00612D.

[144] Y. Kato, L.K. Ono, M.V. Lee, S. Wang, S.R. Raga, Y. Qi, Silver iodide formation in methyl ammonium lead iodide perovskite solar cells with silver top electrodes, Adv. Mater. Interfaces 2 (2015) 1500195. Available from: https://doi.org/10.1002/admi.201500195.

[145] J.H. Noh, N.J. Jeon, Y.C. Choi, M.K. Nazeeruddin, M. Grätzel, S. Il Seok, Nanostructured $TiO_2/CH_3NH_3PbI_3$ heterojunction solar cells employing spiro-OMeTAD/Co-complex as hole-transporting material, J. Mater. Chem. A 1 (2013) 11842. Available from: https://doi.org/10.1039/c3ta12681a.

[146] H. Wang, Y. Liu, M. Li, H. Huang, H.M. Xu, R.J. Hong, et al., Multifunctional $TiO_2$ nanowires-modified nanoparticles bilayer film for 3D dye-sensitized solar cells, Optoelectron. Adv. Mater. Rapid Commun. 4 (2010) 1166–1169. Available from: https://doi.org/10.1039/b000000x.

[147] J. You, L. Meng, T. Song, T. Guo, Y. (Michael) Yang, W.-H. Chang, et al., Improved air stability of perovskite solar cells via solution-processed metal oxide transport layers, Nat. Nanotechnol. 11 (2015) 75–81. Available from: https://doi.org/10.1038/nnano.2015.230.

[148] S. Ye, W. Sun, Y. Li, W. Yan, H. Peng, Z. Bian, et al., CuSCN-based inverted planar perovskite solar cell with an average PCE of 15.6%, Nano Lett. 15 (2015) 3723–3728. Available from: https://doi.org/10.1021/acs.nanolett.5b00116.

[149] X. Yin, P. Chen, M. Que, Y. Xing, W. Que, C. Niu, et al., Highly efficient flexible perovskite solar cells using solution-derived $NiO_x$ hole contacts, ACS Nano 10 (2016) 3630–3636. Available from: https://doi.org/10.1021/acsnano.5b08135.

[150] M. Jung, Y.C. Kim, N.J. Jeon, W.S. Yang, J. Seo, J.H. Noh, et al., Thermal stability of CuSCN hole conductor-based perovskite solar cells, ChemSusChem 9 (2016) 2592–2596. Available from: https://doi.org/10.1002/cssc.201600957.

[151] K.S. Novoselov, Electric field effect in atomically thin carbon films, Science (80-) 306 (2004) 666–669. Available from: https://doi.org/10.1126/science.1102896.

[152] J. Liu, G.-H. Kim, Y. Xue, J.Y. Kim, J.-B. Baek, M. Durstock, et al., Graphene oxide nanoribbon as hole extraction layer to enhance efficiency and stability of polymer solar cells, Adv. Mater. 26 (2014) 786–790. Available from: https://doi.org/10.1002/adma.201302987.

[153] G. Eda, G. Fanchini, M. Chhowalla, Large-area ultrathin films of reduced graphene oxide as a transparent and flexible electronic material, Nat. Nanotechnol. 3 (2008) 270–274. Available from: https://doi.org/10.1038/nnano.2008.83.

[154] Q.-D. Yang, J. Li, Y. Cheng, H.-W. Li, Z. Guan, B. Yu, et al., Graphene oxide as an efficient hole-transporting material for high-performance perovskite solar cells with enhanced stability, J. Mater. Chem. A 5 (2017) 9852–9858. Available from: https://doi.org/10.1039/C7TA01752A.

[155] M. Xiao, F. Huang, W. Huang, Y. Dkhissi, Y. Zhu, J. Etheridge, et al., A fast deposition-crystallization procedure for highly efficient lead iodide perovskite thin-film solar cells, Angew. Chem. Int. Ed 53 (2014) 9898–9903. Available from: https://doi.org/10.1002/anie.201405334.

[156] Z. Xiao, Q. Dong, C. Bi, Y. Shao, Y. Yuan, J. Huang, Solvent annealing of perovskite-induced crystal growth for photovoltaic-device efficiency enhancement, Adv. Mater. 26 (2014) 6503–6509. Available from: https://doi.org/10.1002/adma.201401685.

[157] E. Jokar, Z.Y. Huang, S. Narra, C. Wang, V. Kattoor, C. Chung, et al., Anomalous charge-extraction behavior for graphene-oxide (GO) and reduced graphene-oxide (rGO) films as efficient p-contact layers for high-performance perovskite solar cells, Adv. Energy Mater. 8 (2018) 1701640. Available from: https://doi.org/10.1002/aenm.201701640.

[158] Z. Liu, S.P. Lau, F. Yan, Functionalized graphene and other two-dimensional materials for photovoltaic devices: device design and processing, Chem. Soc. Rev. 44 (2015) 5638–5679. Available from: https://doi.org/10.1039/C4CS00455H.

[159] W. Li, H. Dong, X. Guo, N. Li, J. Li, G. Niu, et al., Graphene oxide as dual functional interface modifier for improving wettability and retarding recombination in hybrid perovskite solar cells, J. Mater. Chem. A 2 (2014) 20105–20111. Available from: https://doi.org/10.1039/C4TA05196C.

[160] J. Yeo, C.-H. Lee, D. Jang, S. Lee, S.M. Jo, H. Joh, et al., Reduced graphene oxide-assisted crystallization of perovskite via solution-process for efficient and stable planar solar cells with module-scales, Nano Energy 30 (2016) 667–676. Available from: https://doi.org/10.1016/j.nanoen.2016.10.065.

[161] F. Wang, M. Endo, S. Mouri, Y. Miyauchi, Y. Ohno, A. Wakamiya, et al., Highly stable perovskite solar cells with an all-carbon hole transport layer, Nanoscale 8 (2016) 11882–11888. Available from: https://doi.org/10.1039/C6NR01152G.

[162] Z. Wu, S. Bai, J. Xiang, Z. Yuan, Y. Yang, W. Cui, et al., Efficient planar heterojunction perovskite solar cells employing graphene oxide as hole conductor, Nanoscale 6 (2014) 10505. Available from: https://doi.org/10.1039/C4NR03181D.

[163] S.-S. Kim, S.-I. Na, J.-S. Yeo, J.-M. Yun, Y.-S. Jung, D.-Y. Kim, et al., Sulfonic acid-functionalized, reduced graphene oxide as an advanced interfacial material leading to donor polymer-independent high-performance polymer solar cells, J. Mater. Chem. A 2 (2014) 292–298. Available from: https://doi.org/10.1039/c3ta13647g.

[164] Z. Ding, Z. Hao, B. Meng, Z. Xie, J. Liu, L. Dai, Few-layered graphene quantum dots as efficient hole-extraction layer for high-performance polymer solar cells, Nano Energy 15 (2015) 186–192. Available from: https://doi.org/10.1016/j.nanoen.2015.04.019.

[165] A.L. Palma, L. Cinà, S. Pescetelli, A. Agresti, M. Raggio, R. Paolesse, et al., Reduced graphene oxide as efficient and stable hole transporting material in mesoscopic perovskite solar cells, Nano Energy 22 (2016) 349–360. Available from: https://doi.org/10.1016/j.nanoen.2016.02.027.

[166] D.-Y. Lee, S.-I. Na, S.-S. Kim, Graphene oxide/PEDOT:PSS composite hole transport layer for efficient and stable planar heterojunction perovskite solar cells, Nanoscale 8 (2016) 1513–1522. Available from: https://doi.org/10.1039/C5NR05271H.

[167] Q. Liu, Z. Liu, X. Zhang, L. Yang, N. Zhang, G. Pan, et al., Polymer photovoltaic cells based on solution-processable graphene and P3HT, Adv. Funct. Mater. 19 (2009) 894–904. Available from: https://doi.org/10.1002/adfm.200800954.

[168] J.Y. Kim, K. Lee, N.E. Coates, D. Moses, T.-Q. Nguyen, M. Dante, et al., Efficient tandem polymer solar cells fabricated by all-solution processing, Science (80-) 317 (2007) 222–225. Available from: https://doi.org/10.1126/science.1141711.
[169] X. Yan, X. Cui, B. Li, L.S. Li, Large, solution-processable graphene quantum dots as light absorbers for photovoltaics, Nano Lett. 10 (2010) 1869–1873. Available from: https://doi.org/10.1021/nl101060h.
[170] Y. Li, Y. Hu, Y. Zhao, G. Shi, L. Deng, Y. Hou, et al., An electrochemical avenue to green-luminescent graphene quantum dots as potential electron-acceptors for photovoltaics, Adv. Mater. 23 (2011) 776–780. Available from: https://doi.org/10.1002/adma.201003819.
[171] V. Gupta, N. Chaudhary, R. Srivastava, G.D. Sharma, R. Bhardwaj, S. Chand, Luminscent graphene quantum dots for organic photovoltaic devices, J. Am. Chem. Soc. 133 (2011) 9960–9963. Available from: https://doi.org/10.1021/ja2036749.
[172] Z. Zhu, J. Ma, Z. Wang, C. Mu, Z. Fan, L. Du, et al., Efficiency enhancement of perovskite solar cells through fast electron extraction: the role of graphene quantum dots, J. Am. Chem. Soc. 136 (2014) 3760–3763. Available from: https://doi.org/10.1021/ja4132246.
[173] M. Zhang, L. Bai, W. Shang, W. Xie, H. Ma, Y. Fu, et al., Facile synthesis of water-soluble, highly fluorescent graphene quantum dots as a robust biological label for stem cells, J. Mater. Chem. 22 (2012) 7461. Available from: https://doi.org/10.1039/c2jm16835a.
[174] B.B. Parekh, G. Fanchini, G. Eda, M. Chhowalla, Improved conductivity of transparent single-wall carbon nanotube thin films via stable postdeposition functionalization, Appl. Phys. Lett. 90 (2007) 121913. Available from: https://doi.org/10.1063/1.2715027.
[175] E. Arici, S. Karazhanov, Carbon nanotubes for organic/inorganic hybrid solar cells, Mater. Sci. Semicond. Process. 41 (2016) 137–149. Available from: https://doi.org/10.1016/j.mssp.2015.07.086.
[176] C. Klinger, Y. Patel, H.W.C. Postma, Carbon nanotube solar cells, PLoS One 7 (2012) 1–9. Available from: https://doi.org/10.1371/journal.pone.0037806.
[177] J.M. Holt, A.J. Ferguson, N. Kopidakis, B.A. Larsen, J. Bult, G. Rumbles, et al., Prolonging charge separation in P3HT − SWNT composites using highly enriched semiconducting nanotubes, Nano Lett. 10 (2010) 4627–4633. Available from: https://doi.org/10.1021/nl102753z.
[178] E. Kymakis, Ga.J. Amaratunga, Carbon nanotubes as electron acceptors in polymeric photovoltaic, Rev. Adv. Mater. Sci. 10 (2005) 300–305. Available from: https://doi.org/10.1063/1.1428416.
[179] A.F. Nogueira, B.S. Lomba, Ma Soto-Oviedo, C.R.D. Correia, P. Corio, Ca Furtado, et al., Polymer solar cells using single-wall carbon nanotubes modified with thiophene pedant groups, J. Phys. Chem. B 111 (2007) 18431–18438. Available from: https://doi.org/10.1021/jp074979n.
[180] F. Wang, D. Kozawa, Y. Miyauchi, K. Hiraoka, S. Mouri, Y. Ohno, et al., Considerably improved photovoltaic performance of carbon nanotube-based solar cells using metal oxide layers, Nat. Commun. 6 (2015) 6305. Available from: https://doi.org/10.1038/ncomms7305.
[181] S.N. Habisreutinger, R.J. Nicholas, H.J. Snaith, Carbon nanotubes in perovskite solar cells, Adv. Energy Mater 7 (2017) 1601839. Available from: https://doi.org/10.1002/aenm.201601839.
[182] Z. Wu, Transparent, conductive carbon nanotube films, Science (80-) 305 (2004) 1273–1276. Available from: https://doi.org/10.1126/science.1101243.
[183] A. Du Pasquier, H.E. Unalan, A. Kanwal, S. Miller, M. Chhowalla, Conducting and transparent single-wall carbon nanotube electrodes for polymer-fullerene solar

cells, Appl. Phys. Lett. 87 (2005) 1–3. Available from: https://doi.org/10.1063/1.2132065.
[184] M.W. Rowell, M.A. Topinka, M.D. McGehee, H.J. Prall, G. Dennler, N.S. Sariciftci, et al., Organic solar cells with carbon nanotube network electrodes, Appl. Phys. Lett. 88 (2006) 233506. Available from: https://doi.org/10.1063/1.2209887.
[185] A. Kongkanand, R.M. Domínguez, P.V. Kamat, Single wall carbon nanotube scaffolds for photoelectrochemical solar cells. Capture and transport of photogenerated electrons, Nano Lett. 7 (2007) 676–680. Available from: https://doi.org/10.1021/nl0627238.
[186] E. Ramasamy, W.J. Lee, D.Y. Lee, J.S. Song, Spray coated multi-wall carbon nanotube counter electrode for tri-iodide (I3-) reduction in dye-sensitized solar cells, Electrochem. Commun. 10 (2008) 1087–1089. Available from: https://doi.org/10.1016/j.elecom.2008.05.013.
[187] V.C. Tung, L.M. Chen, M.J. Allen, J.K. Wassei, K. Nelson, R.B. Kaner, et al., Low-temperature solution processing of graphene-carbon nanotube hybrid materials for high-performance transparent conductors, Nano Lett. 9 (2009) 2513. Available from: https://doi.org/10.1021/nl9001525.
[188] F. Hao, Z. Wang, Q. Luo, J. Lou, J. Li, J. Wang, et al., Highly catalytic cross-stacked superaligned carbon nanotube sheets for iodine-free dye-sensitized solar cells, J. Mater. Chem. 22 (2012) 22756. Available from: https://doi.org/10.1039/c2jm35095e.
[189] Q. Luo, H. Ma, Q. Hou, Y. Li, J. Ren, X. Dai, et al., All-carbon-electrode-based endurable flexible perovskite solar cells, Adv. Funct. Mater. 28 (2018) 1706777. Available from: https://doi.org/10.1002/adfm.201706777.
[190] S.I. Cha, B.K. Koo, S.H. Seo, D.Y. Lee, Pt-free transparent counter electrodes for dye-sensitized solar cells prepared from carbon nanotube micro-balls, J. Mater. Chem. 20 (2010) 659–662. Available from: https://doi.org/10.1039/B918920C.
[191] J.G. Nam, Y.J. Park, B.S. Kim, J.S. Lee, Enhancement of the efficiency of dye-sensitized solar cell by utilizing carbon nanotube counter electrode, Scr. Mater. 62 (2010) 148–150. Available from: https://doi.org/10.1016/j.scriptamat.2009.10.008.
[192] L. Qu, L. Dai, Gecko-foot-mimetic aligned single-walled carbon nanotube dry adhesives with unique electrical and thermal properties, Adv. Mater. 19 (2007) 3844–3849. Available from: https://doi.org/10.1002/adma.200700023.
[193] X. Zhang, K. Jiang, C. Feng, P. Liu, L. Zhang, J. Kong, et al., Spinning and processing continuous yarns from 4-inch wafer scale super-aligned carbon nanotube arrays, Adv. Mater. 18 (2006) 1505–1510. Available from: https://doi.org/10.1002/adma.200502528.
[194] S. Li, Y. Luo, W. Lv, W. Yu, S. Wu, P. Hou, et al., Vertically aligned carbon nanotubes grown on graphene paper as electrodes in lithium-ion batteries and dye-sensitized solar cells, Adv. Energy Mater. 1 (2011) 486–490. Available from: https://doi.org/10.1002/aenm.201100001.
[195] P. Dong, Y. Zhu, J. Zhang, F. Hao, J. Wu, S. Lei, et al., Vertically aligned carbon nanotubes/graphene hybrid electrode as a TCO- and Pt-free flexible cathode for application in solar cells, J. Mater. Chem. A 2 (2014) 20902–20907. Available from: https://doi.org/10.1039/C4TA05264A.
[196] I. Jeon, K. Cui, T. Chiba, A. Anisimov, A.G. Nasibulin, E.I. Kauppinen, et al., Direct and dry deposited single-walled carbon nanotube films doped with $MoO_x$ as electron-blocking transparent electrodes for flexible organic solar cells, J. Am. Chem. Soc. 137 (2015) 7982–7985. Available from: https://doi.org/10.1021/jacs.5b03739.
[197] A.G. Nasibulin, A. Kaskela, K. Mustonen, A.S. Anisimov, V. Ruiz, S. Kivistö, et al., Multifunctional free-standing single-walled carbon nanotube films, ACS Nano 5 (2011) 3214–3221. Available from: https://doi.org/10.1021/nn200338r.

[198] Y. Zhou, L. Hu, G. Grüner, A method of printing carbon nanotube thin films, Appl. Phys. Lett. 88 (2006) 123109. Available from: https://doi.org/10.1063/1.2187945.
[199] C. Lim, D.-H. Min, S.-B. Lee, Direct patterning of carbon nanotube network devices by selective vacuum filtration, Appl. Phys. Lett. 91 (2007) 243117. Available from: https://doi.org/10.1063/1.2824575.
[200] S.L. Hellstrom, M. Vosgueritchian, R.M. Stoltenberg, I. Irfan, M. Hammock, Y.B. Wang, et al., Strong and stable doping of carbon nanotubes and graphene by $MoO_x$ for transparent electrodes, Nano Lett. 12 (2012) 3574–3580. Available from: https://doi.org/10.1021/nl301207e.
[201] K.P. Loh, S.W. Tong, J. Wu, Graphene and graphene-like molecules: prospects in solar cells, J. Am. Chem. Soc. 138 (2016) 1095–1102. Available from: https://doi.org/10.1021/jacs.5b10917.
[202] Z. He, C. Zhong, S. Su, M. Xu, H. Wu, Y. Cao, Enhanced power-conversion efficiency in polymer solar cells using an inverted device structure, Nat. Photonics 6 (2012) 593–597. Available from: https://doi.org/10.1038/nphoton.2012.190.
[203] K. Domanski, J.-P.P. Correa-Baena, N. Mine, M.K. Nazeeruddin, A. Abate, M. Saliba, et al., Not all that glitters is gold: metal-migration-induced degradation in perovskite solar cells, ACS Nano 10 (2016) 6306–6314. Available from: https://doi.org/10.1021/acsnano.6b02613.
[204] G.D.M.R. Dabera, M.R.R. Prabhath, K.T. Lai, K.D.G.I. Jayawardena, F.L.M. Sam, L.J. Rozanski, et al., Does electronic type matter when single-walled carbon nanotubes are used for electrode applications? Adv. Funct. Mater. 25 (2015) 4520–4530. Available from: https://doi.org/10.1002/adfm.201501394.
[205] K. Aitola, K. Domanski, J.-P. Correa-Baena, K. Sveinbjörnsson, M. Saliba, A. Abate, et al., High temperature-stable perovskite solar cell based on low-cost carbon nanotube hole contact, Adv. Mater. 29 (2017) 1606398. Available from: https://doi.org/10.1002/adma.201606398.
[206] J. Ryu, K. Lee, J. Yun, H. Yu, J. Lee, J. Jang, Paintable carbon-based perovskite solar cells with engineered perovskite/carbon interface using carbon nanotubes dripping method, Small (2017) 1701225. Available from: https://doi.org/10.1002/smll.201701225.
[207] H. Li, K. Cao, J. Cui, S. Liu, X. Qiao, Y. Shen, et al., 14.7% efficient mesoscopic perovskite solar cells using single walled carbon nanotubes/carbon composite counter electrodes, Nanoscale 8 (2016) 6379–6385. Available from: https://doi.org/10.1039/C5NR07347B.
[208] Z. Wei, H. Chen, K. Yan, X. Zheng, S. Yang, Hysteresis-free multi-walled carbon nanotube-based perovskite solar cells with a high fill factor, J. Mater. Chem. A 3 (2015) 24226–24231. Available from: https://doi.org/10.1039/C5TA07714A.
[209] K. Aitola, K. Sveinbjörnsson, J.-P. Correa-Baena, A. Kaskela, A. Abate, Y. Tian, et al., Carbon nanotube-based hybrid hole-transporting material and selective contact for high efficiency perovskite solar cells, Energy Environ. Sci. 9 (2016) 461–466. Available from: https://doi.org/10.1039/C5EE03394B.
[210] X. Zheng, J. Deng, N. Wang, D. Deng, W.-H. Zhang, X. Bao, et al., Podlike N-doped carbon nanotubes encapsulating FeNi alloy nanoparticles: high-performance counter electrode materials for dye-sensitized solar cells, Angew. Chem. Int. Ed. 53 (2014) 7023–7027. Available from: https://doi.org/10.1002/anie.201400388.
[211] G. Zhu, L. Pan, T. Lu, T. Xu, Z. Sun, Electrophoretic deposition of reduced graphene-carbon nanotubes composite films as counter electrodes of dye-sensitized solar cells, J. Mater. Chem. 21 (2011) 14869. Available from: https://doi.org/10.1039/c1jm12433a.

[212] G.R. Li, F. Wang, Q.W. Jiang, X.P. Gao, P.W. Shen, Carbon nanotubes with titanium nitride as a low-cost counterelectrode material for dye-sensitized solar cells, Angew. Chem. – Int. Ed. 49 (2010) 3653–3656. Available from: https://doi.org/10.1002/anie.201000659.

[213] S.N. Habisreutinger, T. Leijtens, G.E. Eperon, S.D. Stranks, R.J. Nicholas, H.J. Snaith, Carbon nanotube/polymer composites as a highly stable hole collection layer in perovskite solar cells, Nano Lett. 14 (2014) 5561–5568. Available from: https://doi.org/10.1021/nl501982b.

[214] S.N. Habisreutinger, T. Leijtens, G.E. Eperon, S.D. Stranks, R.J. Nicholas, H.J. Snaith, Enhanced hole extraction in perovskite solar cells through carbon nanotubes, J. Phys. Chem. Lett. 5 (2014) 4207–4212. Available from: https://doi.org/10.1021/jz5021795.

[215] S.N. Habisreutinger, B. Wenger, H.J. Snaith, R.J. Nicholas, Dopant-free planar n–i–p perovskite solar cells with steady-state efficiencies exceeding 18%, ACS Energy Lett. 2 (2017) 622–628. Available from: https://doi.org/10.1021/acsenergylett.7b00028.

[216] H. Chen, X. Pan, W. Liu, M. Cai, D. Kou, Z. Huo, et al., Efficient panchromatic inorganic–organic heterojunction solar cells with consecutive charge transport tunnels in hole transport material, Chem. Commun. 49 (2013) 7277. Available from: https://doi.org/10.1039/c3cc42297f.

[217] J.M. Lee, J.S. Park, S.H. Lee, H. Kim, S. Yoo, S.O. Kim, Selective electron- or hole-transport enhancement in bulk-heterojunction organic solar cells with N- or B-doped carbon nanotubes, Adv. Mater. 23 (2011) 629–633. Available from: https://doi.org/10.1002/adma.201003296.

[218] J. Lee, M.M. Menamparambath, J.-Y. Hwang, S. Baik, Hierarchically structured hole transport layers of spiro-OMeTAD and multiwalled carbon nanotubes for perovskite solar cells, ChemSusChem 8 (2015) 2358–2362. Available from: https://doi.org/10.1002/cssc.201403462.

[219] G.-K. Lim, Z.-L. Chen, J. Clark, R.G.S. Goh, W.-H. Ng, H.-W. Tan, et al., Giant broadband nonlinear optical absorption response in dispersed graphene single sheets, Nat. Photonics 5 (2011) 554–560. Available from: https://doi.org/10.1038/nphoton.2011.177.

[220] Z. Li, S. a Kulkarni, P.P. Boix, E. Shi, A. Cao, K. Fu, et al., Laminated carbon nanotube networks for metal electrode-free efficient perovskite solar cells, ACS Nano 8 (2014) 6797–6804. Available from: https://doi.org/10.1021/nn501096h.

[221] Y. He, W. Chen, C. Gao, J. Zhou, X. Li, E. Xie, An overview of carbon materials for flexible electrochemical capacitors, Nanoscale 5 (2013) 8799. Available from: https://doi.org/10.1039/c3nr02157b.

[222] S. Yamashita, A. Martinez, B. Xu, Carbon nanotube and graphene for photonic applications, in: G.S. Subramania, S. Foteinopoulou (Eds.), 2013: p. 88080Q. doi:10.1117/12.2023742.

[223] S. Collavini, J.L. Delgado, Carbon nanoforms in perovskite-based solar cells, Adv. Energy Mater. 7 (2017) 1601000. Available from: https://doi.org/10.1002/aenm.201601000.

[224] H. Alturaif, Z. ALOthman, J. Shapter, S. Wabaidur, Use of carbon nanotubes (CNTs) with polymers in solar cells, Molecules 19 (2014) 17329–17344. Available from: https://doi.org/10.3390/molecules191117329.

[225] K.S. Lee, W.J. Lee, N.-G. Park, S.O. Kim, J.H. Park, Transferred vertically aligned N-doped carbon nanotube arrays: use in dye-sensitized solar cells as counter electrodes, Chem. Commun. 47 (2011) 4264. Available from: https://doi.org/10.1039/c1cc10471c.

# CHAPTER 17

# Fullerene-based solar cells

**Takeo Oku**
Department of Materials Science, The University of Shiga Prefecture, Hikone, Japan

## Contents



## 17.1 Introduction

A carbon (C) element is generated by the nuclear fusion of He nuclei in fixed stars. A huge amount of carbon atoms exists in the whole universe. Life activity such as photosynthesis and carbon compounds such as $CO_2$ and $C_6H_{12}O_6$ play an important role. Carbon has various hollow-cage nanostructures such as $C_{60}$, giant fullerenes, nanocapsules, onions, nanopolyhedra, cones, cubes, horns, and nanotubes. These C nanostructures show different physical properties and the potential of studying materials of low dimensions within an isolated environment is present. By controlling the size, layer numbers, helicity, compositions, and included clusters, the cluster-included C nanocage structures with a band-gap energy of 0−1.7 eV, and nonmagnetism are expected to show various electronic, optical, and magnetic properties such as Coulomb blockade, photoluminescence, superparamagnetism, and photovoltaic effects [1−8]. $C_{60}$-based

*Nanomaterials for Solar Cell Applications*
DOI: https://doi.org/10.1016/B978-0-12-813337-8.00017-5

fullerene/polymer solar cells especially, have been investigated and reported [9–13]. These organic solar cells can be fabricated with printing methods and in ordinary atmospheric conditions. They have the potential for use in lightweight, flexible, inexpensive, and large-scale solar cells [14–23]. Recently, the efficiencies of fullerene-based solar cells was increased to more than 10% [24–32].

Nanostructures of fullerene-based solar cells are described in this research. The investigation utilized transmission electron microscopy, electron diffraction and X-ray diffraction. These are closely related with the photovoltaic properties. Electronic structures of the molecules were investigated using molecular orbital calculations. Energy levels of the solar cells were also discussed.

## 17.2 Organic solar cells and excitons

A photovoltaic mechanism of organic solar cells is shown in Fig. 17.1. The light is absorbed in the donor (D) layers, such as phthalocyanine and poly[3-hexylthiophene] (P3HT), and electrons are excited to form excitons from the energy levels of the highest occupied molecular orbital (HOMO) to the lowest unoccupied molecular orbital (LUMO), as shown in Fig. 17.1A. Then, the excitons diffuse to the donor–acceptor (DA) interface, then the charges are separated at the interface, as indicated in Fig. 17.1B. Separated electrons are transported in the acceptor (A), such as fullerene, and holes are transported in the donor to the electrodes and the current flows.

Four factors that determine conversion efficiencies of organic solar cells are exciton generation efficiency $\eta_1$, exciton transport efficiency $\eta_2$,

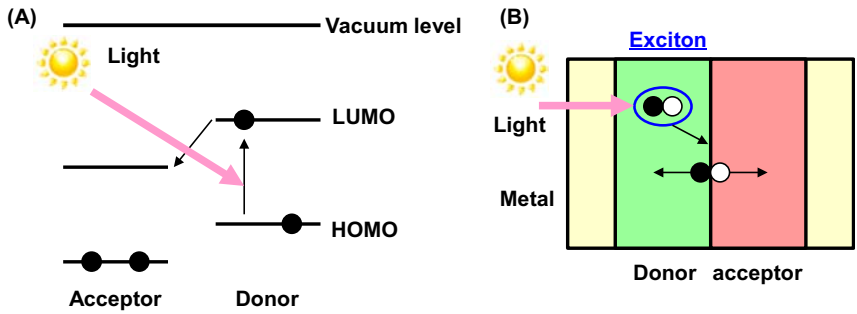


**Figure 17.1** Photovoltaic mechanism of organic solar cell. (A) Energy levels and (B) cross section of the cell.

charge separation efficiency $\eta_3$, and carrier transport efficiency $\eta_4$, as shown in Fig. 17.2. Since whole efficiency is calculated by multiplying the four efficiencies, all the efficiencies should be high [33]. Although the $\eta_1$ and $\eta_3$ values are high for the organic solar cells, the $\eta_2$ and $\eta_4$ values are low because of the very short diffusion length of the excitons. One weak point of the organic solar cells is a low conversion efficiency, which is due to the recombination of excitons produced by light irradiation. For the photovoltaic solar cells, excitons are generated by light irradiation. The excitons are separated to electrons and holes and transported to each electrode to generate potential difference. However, if the electrons and holes of the excitons are recombined before their arrival at the electrode, light is emitted by the recombination, and generates no electric power. One of the origins of the recombination of the organic solar cells is its low carrier mobility. It takes too much time for the generated excitons to reach the pn junction for the carrier separation, and the excitons recombine on the way to the pn junction or metal electrodes. In addition, since sizes of excitons of organic materials are small, they tend to recombine.

An exciton is a pair of excited electrons and an excited hole restricted by the electrostatic Coulomb force. It is an electrically neutral quasiparticle that exists in semiconductors and insulators, as shown in Fig. 17.3. The Coulomb force is expressed as follows ($\varepsilon$: relative permittivity):

$$F = \frac{1}{4\pi\varepsilon\varepsilon_0}\frac{q_1 q_2}{r^2} \tag{17.1}$$

The exciton is regarded as an elementary excitation that can transport energy without transporting electric charge [33]. The current of solar cells flows only when the exciton is separated into an electron and a hole. Excitons are introduced physically from excited waves in a wave function of biding state of electrons on the conduction band, and holes on the

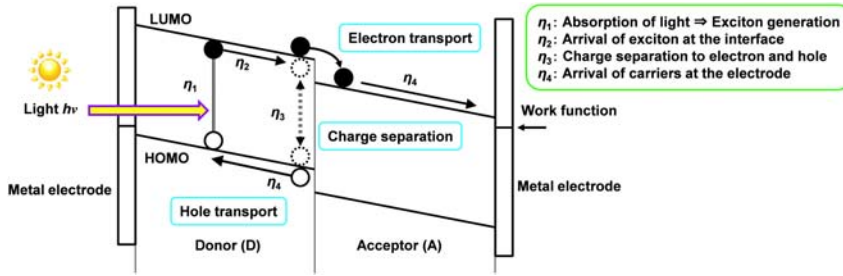


**Figure 17.2** Carrier separation and carrier transport in organic solar cells.

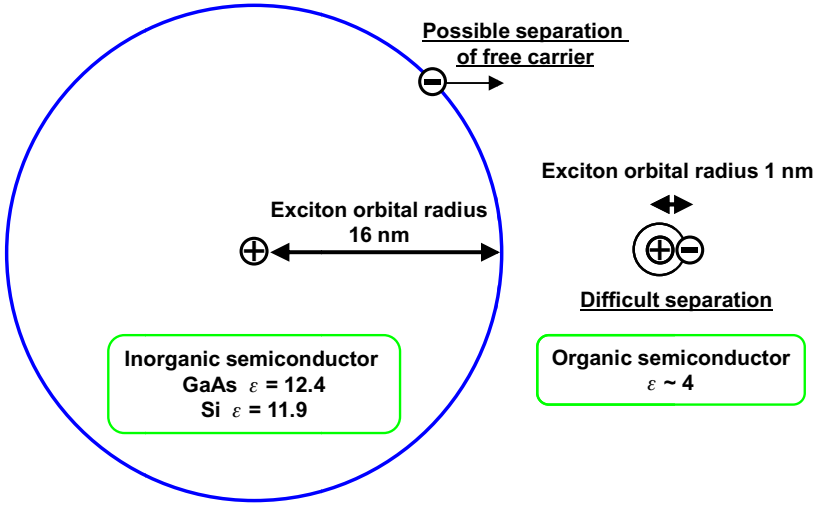


**Figure 17.3** Excitons of inorganic and organic semiconductors.

valence band. Frenkel excitons and Mott–Wannier excitons are limited models of the excited waves. Actual excitons have intermediate states between these excitons.

Mott–Wannier excitons (weak binding of an electron and a hole) have a broader wave function in an excited state compared to the lattice constants. The excited state is a spread state at a lattice point. An electron and a hole are in a bound state with weak restriction. An excited state like the Mott–Wannier excitons spread in crystals such as various ionic crystals and ionic semiconductors.

Frenkel excitons (comparatively strong binding of an electron and a hole) have a narrower wave function of the excited state when compared with the lattice constants. The excited state is similar to the excited states of atoms or ions. An excited state like the Frenkel excitons spread resonantly through lattice points with a certain wavenumber in organic-molecular crystals.

The energy required for the exciton generation is lower than the bandgap energy because of the binding energy between an electron and a hole, and the exciton being in a stable state. A sharp reflection peak can be observed at lower energy than that of interband transition. Excitons that spread in the hard, nondeformed lattice are called free excitons and can transport freely in the crystal. Self-restraint excitons that spread in the vibrating lattice localize at a certain position by the interaction with the lattice vibration.

## 17.3 Bulk-heterojunction

One of the improvements of organic solar cells is with DA proximity in devices by using blends of donor-like and acceptor-like molecules or polymers, which are called DA bulk-heterojunction solar cells [34–39], as shown in Fig. 17.4A. The previous organic solar cells consisted of a simple *pn* heterojunction. The bulk-heterojunction is a *pin* junction that consists of a mixture intrinsic semiconductor layer (*i*-layer) between *p*- and *n*-type semiconductors. For a fullerene-based system, *p*-type molecular crystals are surrounded by amorphous fullerene matrix.

When light is irradiated on the junction, excitons are generated around the p-type molecular/fullerene interface, that consists of a bulk-hetero mixture layer. The excitons can reach the DA or pn junction by transporting several nm. Electrons and holes are separated to *n*-layer and *p*-layer at the interface, respectively. Each carrier transports through the connected crystals and matrix to the electrode, and current flows. Conversion efficiencies of the cell can be described as a carrier generation efficiency times a carrier transport efficiency, as illustrated in Fig. 17.4B.

Ordinary heterojunction solar cells are high efficiency if the carrier mobility and electrical conductivity of the D and A layers are high. However, only the excitons generated near the D/A interface contribute to the photocurrent. The interfacial area of bulk-heterojunction is so large

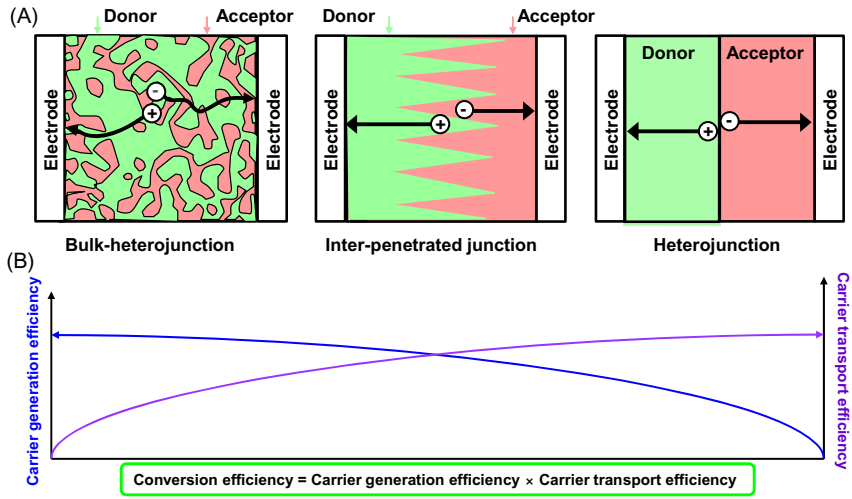


**Figure 17.4** (A) Main device structures proposed for organic solar cells. (B) Conversion efficiencies and carrier generation/transport efficiencies.

that the carriers are separated effectively, but the carrier transport pass is complicated, and the carrier cannot be taken away from the cells. An interpenetrated structure would be more effective for the carrier generation and carrier transport research on new structures such as nanorods and nanotubes is in progress.

## 17.4 Poly[3-hexylthiophene]:6,6-phenyl $C_{61}$-butyric acid methyl ester

$C_{60}$-based polymer/fullerene solar cells have been investigated and significant improvements of photovoltaic efficiencies are mandatory for usage in future solar power plants. Characterization of polymer/fullerene bulk-heterojunction solar cells using different organic polymers is presented in this section. P3HT and poly[2-methoxy-5-(20-ethylhexoxy)-1,4-phenylenevinylene] (MEH-PPV) were used for p-type semiconductors and 6,6-phenyl $C_{61}$-butyric acid methyl ester (PCBM) was used for the n-type one. Device structures were produced and efficiencies and spectral responsivity were investigated.

A thin layer of polyethylenedioxythiophene doped with polystyrene–sulfonic acid (PEDOT:PSS) (Sigma Aldrich) was spin-coated on precleaned indium tin oxide (ITO) glass plates. Then, semiconductor layers were prepared on a PEDOT:PSS layer with spin coating, using a mixed solution of P3HT, MEH-PPV and PCBM in 1,2-dichlorobenzene. The weight ratio of P3HT:PCBM and MEH-PPV:PCBM was 1:8. The thickness of the blended device was approximately 150 nm. After annealing at 100°C for 30 minutes in $N_2$ atmosphere, aluminum (Al) metal contacts with a thickness of 100 nm were evaporated as a top electrode. A schematic diagram of the present solar cells is shown in Fig. 17.5A [15].

The typical current density–voltage ($J-V$) characteristics of a P3HT/PCBM structure in the dark and under illumination is shown in Fig. 17.5A. Although no photocurrent is observed for the dark, photocurrent over 5 mA $cm^{-2}$ is observed under illumination. $J-V$ characteristics of both MEH-PPV/PCBM and P3HT/PCBM solar cell structures are shown in Fig. 17.5A. Each structure shows characteristic curves for open-circuit voltage and short-circuit current. Measured parameters of these solar cells are summarized in Table 17.1. A solar cell with a P3HT/PCBM structure provided power convergent efficiency of 1.03%, a fill factor of 0.53, and a short circuit current density of 5.18 mA $cm^{-2}$, which

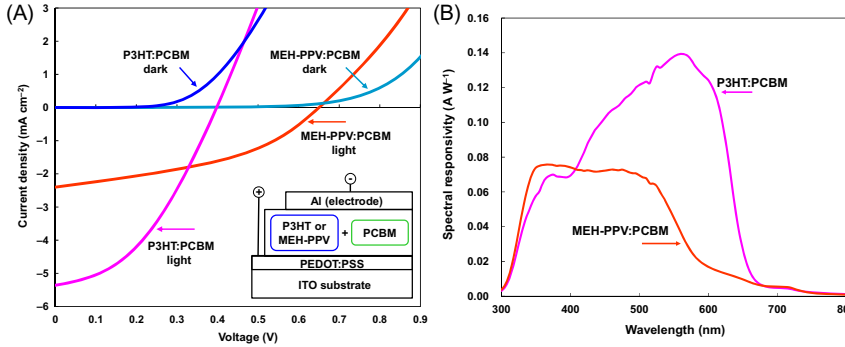


**Figure 17.5** (A) Measured *J*–*V* characteristic of P3HT:PCBM and MEH-PPV:PCBM structure in the dark and under illumination. (B) Spectral photoresponses of the solar cells. *MEH-PPV*, Poly[2-methoxy-5-(20-ethylhexoxy)-1,4-phenylenevinylene]; *P3HT*, poly [3-hexylthiophene]; *PCBM*, 6,6-phenyl $C_{61}$-butyric acid methyl ester.

**Table 17.1** Measured parameters of solar cells.

| ETL | $J_{SC}$ (mA cm$^{-2}$) | $V_{OC}$ (V) | FF | $\eta$ (%) |
|---|---|---|---|---|
| P3HT:PCBM | 5.18 | 0.37 | 0.53 | 1.03 |
| MEH-PPV:PCBM | 2.59 | 0.70 | 0.42 | 0.75 |

*ETL*, Electron transport layer; *MEH-PPV*, poly[2-methoxy-5-(20-ethylhexoxy)-1,4-phenylenevinylene]; *P3HT*, poly[3-hexylthiophene]; *PCBM*, 6,6-phenyl $C_{61}$-butyric acid methyl ester.

is better than that of a MEH-PPV/PCBM device. Although the MEH-PPV/PCBM structure showed a higher open-circuit voltage of 0.70 V.

Fig. 17.5B shows the measured spectral photoresponses of the solar cells. The MEH-PPV/PCBM structure shows a high photoresponse in the range of 300–600 nm, while the P3HT/PCBM shows higher spectral responsivity in the range of 400–650 nm, which corresponds to 3.1 and 1.9 eV, respectively. Optimization of the nanocomposite structure with P3HT and MEH-PPV would increase the efficiencies of the solar cells.

Electronic structures of the molecules were calculated. Energy levels of the LUMO of PCBM are shown in Fig. 17.6A. The LUMO levels are observed around $C_{60}$ molecule with high electron negativity. Energy levels of the HOMO of P3HT and MEH-PPV are shown in Fig. 17.6B and C, respectively. HOMO levels are observed around the five and six-membered rings in the main-chain structures of the polymers, which is due to the charge transfer from the sulfur and oxygen atoms, respectively. Effective formation and separation of excitons in the P3HT/PCBM

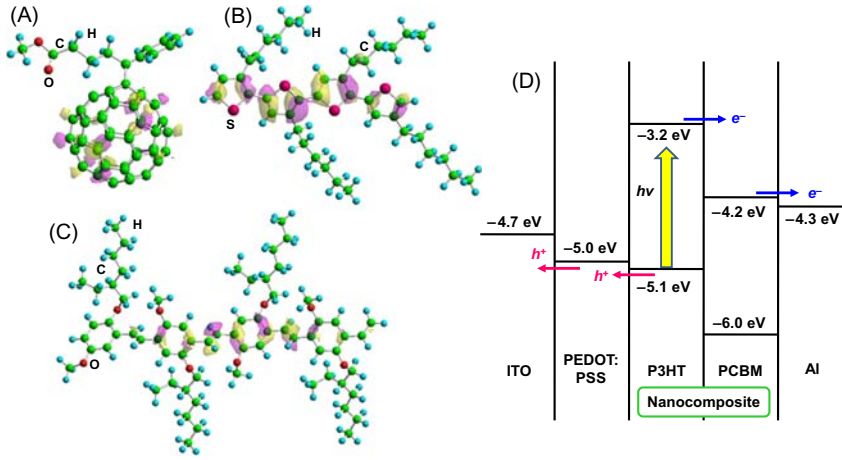


**Figure 17.6** Calculated (A) LUMO levels of PCBM and HOMO levels of (B) P3HT and (C) MEH-PPV. (D) Energy level diagram of P3HT/PCBM solar cell. *HOMO*, Highest occupied molecular orbital; *LUMO*, lowest unoccupied molecular orbital; *MEH-PPV*, poly[2-methoxy-5-(20-ethylhexoxy)-1,4-phenylenevinylene]; *P3HT*, poly[3-hexylthiophene]; *PCBM*, 6,6-phenyl $C_{61}$-butyric acid methyl ester.

system is due to the nanocomposite structure, as reported previously [18]. Energy levels of LUMO of P3HT are around sulfur atoms, and the separated carriers transfer from P3HT to $C_{60}$. Interdiffusion of PCBM into the P3HT network leads to the existence of $C_{60}$ molecules within the exciton diffusion radius of the P3HT network.

An energy-level diagram of P3HT/PCBM solar cells is summarized as shown in Fig. 17.6D. Previously reported values [23,40–42] were used for the energy levels of the figures by adjusting them to the present work. An energy gap of 1.9 eV, which is an estimated value from Fig. 17.5B, is used for the model. The relation between $V_{OC}$ and polymer oxidation potential was reported as follows:

$$V_{OC} \sim e^{-1}|D_{HOMO} - A_{LUMO}| - 0.3\ (\mathrm{V}) \tag{17.2}$$

where $e$ is the elementary charge [41,42]. The value of 0.3 V is an empirical factor and this is enough for efficient charge separation [43]. The present model agrees with this equation, and control of the energy levels is important to increase the efficiency. Combination of the present solar cells and boron nitride nanomaterials with various direct band gaps might be effective for an increase in efficiencies [44]. The performances of the present solar cells is also due to the nanoscale structures of the polymer materials. The control and structure must be investigated further.

## 17.5 Phthalocyanine dimer

Phthalocyanines, which have photovoltaic properties, heat resistance, light stability, chemical stability and high optical absorption at visible range, are used as an oxidation catalyst, catalyst of fuel cells and solar cells. Many studies on the metal phthalocyanine (MPc) monomers have been performed [45,46] and the properties are different by changing central metal and chemical substitution. The organic–inorganic hybrid device structures were produced and nanostructure, electronic property, and optical absorption were investigated. When the nearest neighbor two phthalocyanines with substituent such as amino group and hydroxy group are connected by hydrogen bridged substituent, high photoconduction was observed [47,48]. However, few phthalocyanine dimers have been reported and high photoconduction can be expected from the covalently bridged phthalocyanine dimers. The purpose is to fabricate and characterize phthalocyanine dimer/fullerene HJ solar cells. Here, μ-oxo bridged gallium phthalocyanine (GaPc) dimer is used for p-type semiconductors, and fullerene with excellent electron affinity is used for the n-types. The molecular orbital of GaPc dimer and fullerene was investigated as solar cell material [23].

GaPc monomer with axial Cl ligand was investigated for a comparison. The measured $J-V$ characteristic of the ITO/PEDOT:PSS/GaPc dimer/$C_{60}$/Al solar cell and ITO/PEDOT:PSS/GaPc/$C_{60}$/Al showed a characteristic curve for open circuit voltage and short circuit current density. All of the parameters showed improvement using GaPc dimer compared to the GaPc monomer. Fig. 17.7A shows a measured optical absorption of GaPc dimer, $C_{60}$ and GaPc dimer/$C_{60}$ cells [49]. The solar cells show a wide optical absorption ranging from 320 to 800 nm, which corresponds to 3.8 and 1.5 eV, respectively. The absorption spectrum of the GaPc dimer was similar to that of the monomer, however a new peak was observed at $\sim$450 nm. Fluorescence (FL) spectra of GaPc dimer and GaPc dimer/$C_{60}$ thin films are shown in Fig. 17.7B, with and excitation wave length of 300 nm. FL peak of GaPc dimer disappeared after formation of GaPc dimer/$C_{60}$ HJ thin film. It was believed that carriers could effectively be transported from GaPc dimer to $C_{60}$.

Fig. 17.7C contains a structure of μ-oxo-bridged GaPc dimer that is used here. Two GaPc planes are parallel to one another and the rotational degrees are 41.35 [49,50]. The plane distance between GaPc monomer is $\sim$0.34 nm. When the nearest neighbor two phthalocyanines is arranged

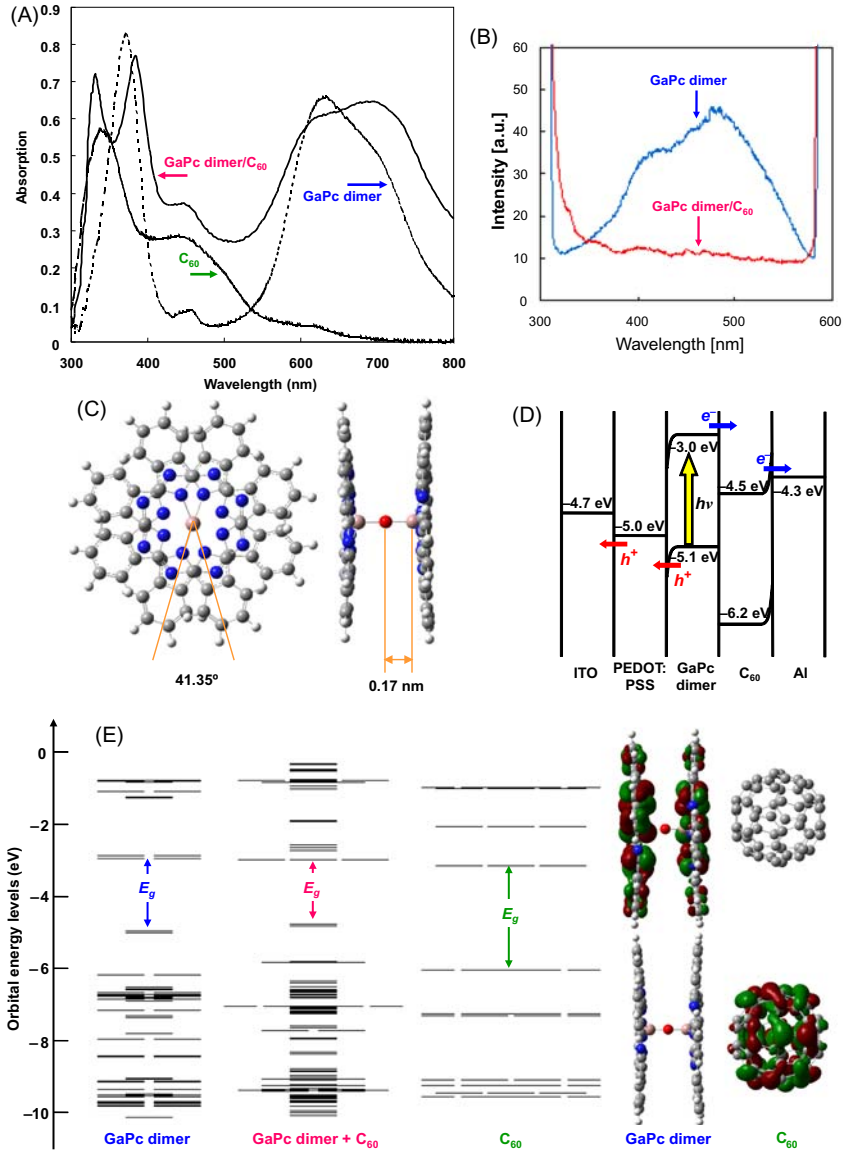


**Figure 17.7** (A) Optical absorption and (B) fluorescence spectra of GaPc dimer/$C_{60}$ solar cells. (C) Structure of GaPc dimer. (D) Energy level diagram of GaPc dimer/$C_{60}$ solar cells. (E) Electronic structure of GaPc dimer and $C_{60}$. *GaPc*, Gallium phthalocyanine.

with hydrogen bridged substituent, high photoconduction can be expected for the covalently bridged phthalocyanine dimer.

The energy level diagram and electronic structures of the solar cell were calculated and summarized as shown in Fig. 17.7D and E. The HOMO and LUMO levels of GaPc, and HOMO and LUMO of two phthalocyanine monomers were stirred and piled up, respectively. The interaction of the two phthalocyanine monomers is not able to be confirmed. Carriers could transport from −4.5 to −4.3 eV by hopping conduction. Fig. 17.7E shows HOMO and LUMO energy levels of the GaPc dimer with $C_{60}$ after structural optimization using DFT/6−31G*. Electronic densities of LUMO, LUMO + 1, and LUMO + 2 are localized for the fullerene side, while the HOMO is localized for the GaPc-dimer side, which suggests electron transfer between the GaPc dimer and fullerene. Similar localization of frontier orbital was reported for the other donor-fullerene systems [51,52]. A schematic diagram of the energy levels of the GaPc dimer, $C_{60}$, and GaPc with $C_{60}$ showed that the LUMO levels of the GaPc dimer with $C_{60}$ are comparable to the LUMO levels of fullerene, and the HOMO levels of the GaPc dimer with $C_{60}$ are close to the HOMO levels of GaPc dimer. However, the symmetry of the GaPc dimer seems to be lowered because of decreasing degeneracy, which is due to the interaction with $C_{60}$.

Although the energy gap and energy level of the GaPc dimer were hardly changed by dimerization, the power conversion efficiency was significantly improved. It is known that the π electron system is enhanced by dimerization and high career mobility can be expected. Since enhancing the π electron system was not confirmed by dimerization here, the improvement of efficiency is believed to have been caused by the molecular orientation and crystallinity that were improved by ordered array due to dimerization, which led to the decrease of career recombination. As a result, open-circuit voltage was greatly improved, which led to the high conversion efficiency.

The X-ray diffraction pattern of a GaPc dimer layer showed a peak of lattice spacing of 1.27 nm. Various crystallizations of a μ-oxo bridged GaPc dimer have been reported [47,48]. When the crystallographic structure is different, initial surface potential, photosensitivity, and residual surface potential are also different. Further crystallographic structure must be investigated in the future.

## 17.6 ZnTPP:$C_{60}$

Fabrication and characterization of porphyrin:$C_{60}$ bulk hetero junction (BHJ) solar cells is discussed in this section. 5,10,15,20-tetraphenyl-21,23H-porphin zinc (ZnTPP) was used for p-type semiconductors [16,53] and $C_{60}$ was used for the n-type semiconductors. Porphyrin has high optical absorption in the visible spectrum and high hole mobility [54–56] and was expected to form cocrystallites [57,58] with $C_{60}$ that would be suitable for the BHJ structure [59,60]. The second purpose is to investigate an effect of electron transport layer (ETL). 3,4,9,10-Perylenetetracarboxylic dianhydride (PTCDA) is a perylene derivative with a simple structure, which was reported to be used in solar cells [61]. For this research, PTCDA was used as the ETL for porphyrin/$C_{60}$ BHJ solar cells. The ETL prevents hole transfer between the active layer and electrode, and improvement of conversion efficiency was expected with the introduction of the ETL. A thin layer of PEDOT:PSS was spin coated on precleaned ITO glass plates. The PEDOT:PSS served as a hole transport layer (HTL) for an electron blocking layer. Semiconductor layers were then prepared on a PEDOT:PSS layer by spin coating using a mixed solution of $C_{60}$, ZnTPP in 1 mL dichlorobenzene. The total weight of ZnTPP:$C_{60}$ was 18 mg, and the weight ratio of ZnTPP:$C_{60}$ was changed in the range of 1:9–5:5. The thickness of the blended device was ~150 nm. To increase efficiencies, PTCDA with a thickness of ~20 nm was also added over the active layers. After annealing at 100°C for 30 minutes in $N_2$ atmosphere, PTCDA was evaporated between the active layer and the metal layer. Finally, Al metal contacts were evaporated as a top electrode.

Fig. 17.8A and B shows the optical absorption of $C_{60}$, ZnTPP, ZnTPP:$C_{60}$ and ZnTPP:$C_{60}$/PTCDA BHJ solar cells, respectively. The ZnTPP:$C_{60}$/PTCDA structure provided higher absorption in the range of 300–800 nm (which correspond to 4.0 and 1.5 eV, respectively), compared with the ZnTPP:$C_{60}$ structure.

Measured $J-V$ characteristic of ZnTPP:$C_{60}$ BHJ solar cells under illumination are shown in Fig. 17.8C. The BHJ indicates one layered composite structure with p and n-type semiconductors, which is denoted as ZnTPP:$C_{60}$. The effects of the PTCDA addition to the ZnTPP:$C_{60}$ BHJ solar cells were also investigated, which is denoted as ZnTPP:$C_{60}$/PTCDA. Each structure shows a characteristic curve for open circuit voltage and short circuit current. The current density of ZnTPP:$C_{60}$ increased

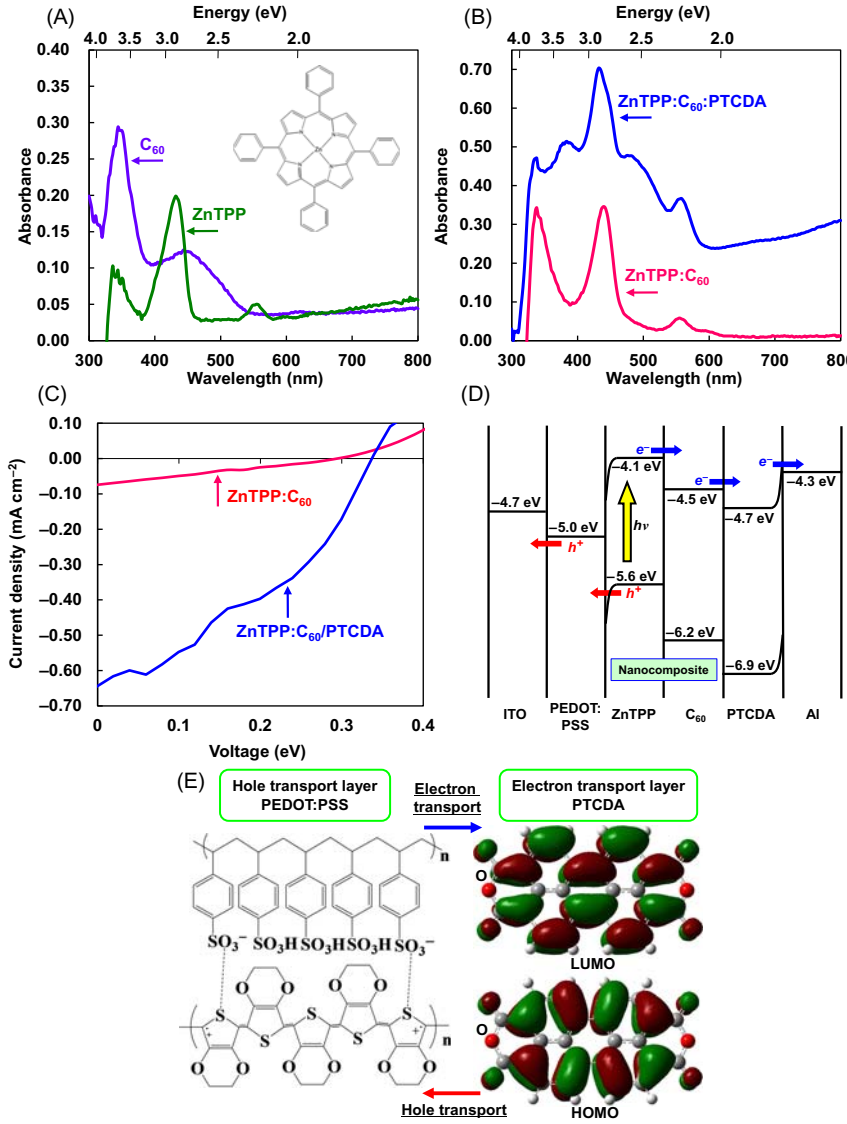


**Figure 17.8** Absorbance spectra of (A) $C_{60}$, ZnTPP and (B) ZnTPP:$C_{60}$ BHJ solar cells. (C) Measured *J*−*V* characteristic of ZnTPP:$C_{60}$ BHJ solar cells under illumination. (D) Energy level diagram of ZnTPP/$C_{60}$ solar cell. (D) Carrier transfer of ETL and HTL. *ETL*, Electron transport layer; *HTL*, hole transport layer.

with the PTCDA addition, and the best efficiency was obtained with the ZnTPP:$C_{60}$/PTCDA sample. Exciton migration of $C_{60}$ can efficiently be suppressed using PTCDA. Exciton would be generated for both ZnTPP/$C_{60}$ and $C_{60}$/PTCDA interfaces, which results in the increase in conversion efficiency, as shown in Fig. 17.8C. Schematic illustration of electron and hole transport is shown in Fig. 17.8D and E.

X-ray diffraction patterns of ZnTPP and ZnTPP:$C_{60}$ BHJ layers are shown in Fig. 17.9A and B, respectively. In Fig. 17.9A, diffraction peaks corresponding to ZnTPP crystal are observed. After formation of the ZnTPP:$C_{60}$ BHJ layer, the diffraction peaks corresponding to ZnTPP disappeared, and $C_{60}$ peaks were observed, as shown in Fig. 17.9B. In

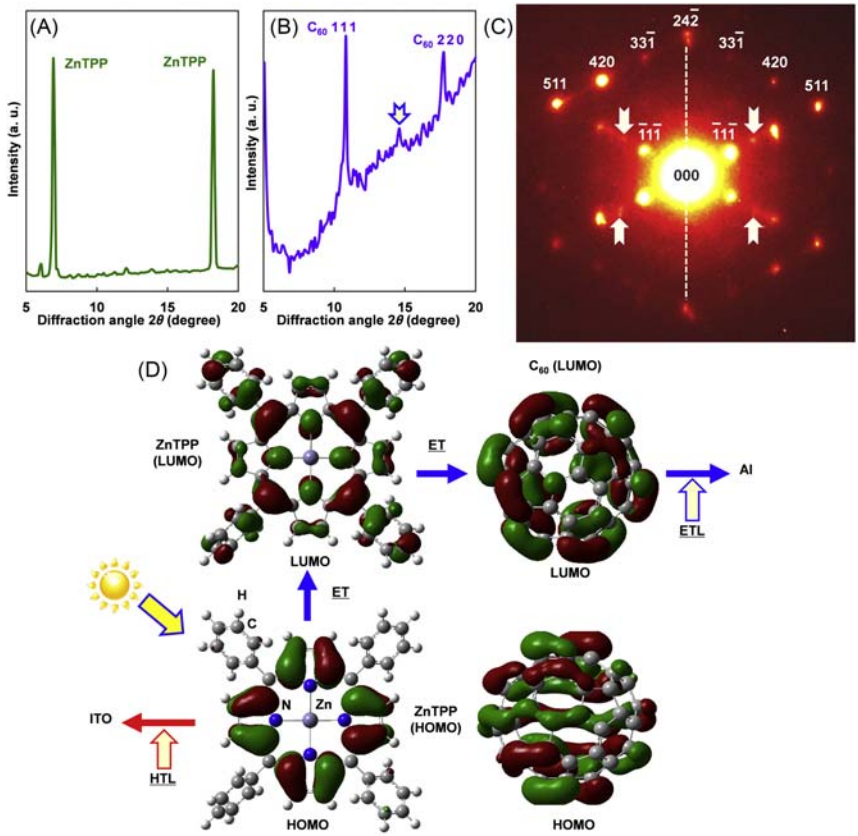


**Figure 17.9** (A) X-ray diffraction pattern of (A) ZnTPP and (B) ZnTPP:$C_{60}$ BHJ layer. (C) Electron diffraction pattern of ZnTPP:$C_{60}$ BHJ layer. (D) ET of ZnTPP/$C_{60}$ system. *ET*, Electron transport.

addition, a new diffraction peak is observed as indicated with an arrow, and is believed to be porphyrin/$C_{60}$ cocrystallites [57,58]. Fig. 17.9C contains an electron diffraction pattern of the ZnTPP:$C_{60}$ BHJ layer, taken along the [ − 123] direction of $C_{60}$. A twin structure with the (112) twin plane is observed in Fig. 17.9C, as indicated by a dotted line. Diffraction spots, which correspond to cocrystallites of ZnTPP:$C_{60}$, are also observed as indicated by arrows.

Since the microstructure of the ZnTPP and $C_{60}$ BHJ layer is strongly dependent on the weight ratio of these, it is necessary to control the microstructure to form cocrystallites of ZnTPP:$C_{60}$. In the present work, higher efficiencies were obtained for the ZnTPP:$C_{60}$ sample with a weight ratio of 3:7, which is suitable for cocrystallite formation, as observed in weak reflections in X-ray and electron diffraction patterns. Recombination of electrons of $C_{60}$ and holes of ZnTPP would occur in the BHJ layer with intermittent cocrystallite structure. If continuous cocrystallite structures form perpendicular to the thin film, it is believed that recombination of electrons and holes can be suppressed, which will lead to improvement of conversion efficiency.

An energy level diagram, carrier transfer of ETL, and HTL of the ZnTPP/$C_{60}$/PTCDA solar cell are summarized as shown in Fig. 17.9D. The incident direction of light is from the ITO side. The energy barrier would exist near the semiconductor/metal interface [62,63]. Electronic charge-transfer separation was caused by light irradiation from the ITO substrate side. Electrons are transported to an Al electrode and holes are transported to an ITO substrate. The $V_{OC}$ of organic solar cells is reported to be determined by the energy gap, as indicated by Eq. (17.2). The present experimental data of $V_{OC}$ indicated smaller values compared to the calculations from the equation, which might be due to the voltage descent at the metal/semiconductor interface. Control of the energy level is also important to increase the efficiency.

## 17.7 Diamond:$C_{60}$

Fabrication and characterization of $C_{60}$/phthalocyanine based BHJ and HJ solar cells are presented in this section. $C_{60}$ and fullerenol [$C_{60}(OH)_{10-12}$] were used for n-type semiconductors, and nanodiamond (ND) and MPc derivatives were used for p-type semiconductors. A schematic diagram of the present $C_{60}$/phthalocyanine based BHJ and HJ solar cells is shown in Fig. 17.10A. A thin layer of PEDOT:PSS was spin coated on precleaned

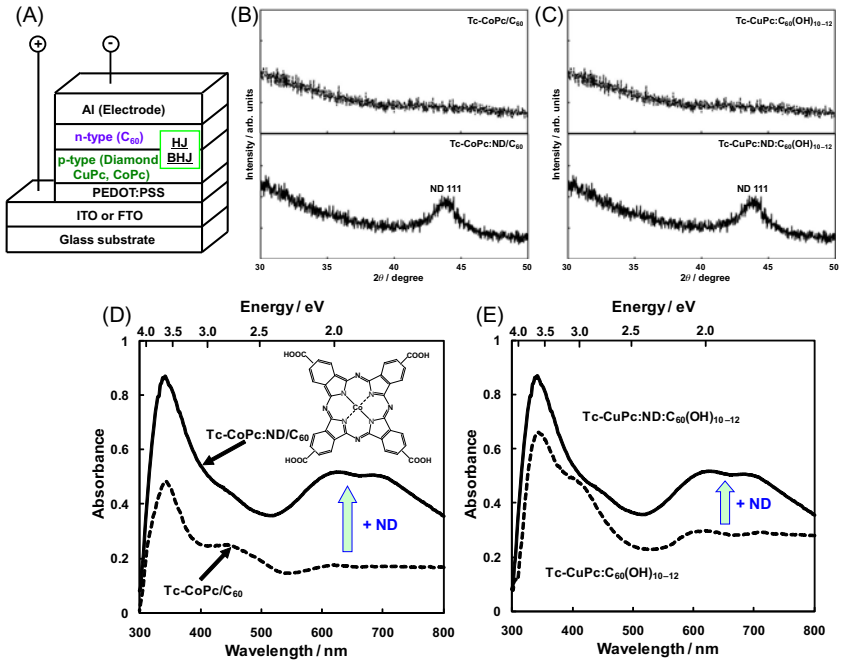


**Figure 17.10** (A) Device structure of MPc:ND/$C_{60}$ cells. X-ray diffraction patterns of (B) Tc-CoPc:ND/$C_{60}$ and Tc-CuPc/$C_{60}$ layers and (C) Tc-CuPc:ND:$C_{60}(OH)_{10-12}$ and Tc-CuPc:$C_{60}(OH)_{10-12}$ layers. Optical absorption spectra of (D) Tc-CoPc:ND/$C_{60}$ and Tc-CoPc/$C_{60}$ layers and (E) Tc-CuPc:ND:$C_{60}(OH)_{10-12}$ and Tc-CuPc:$C_{60}(OH)_{10-12}$ layers. *MPc*, Metal phthalocyanine; *ND*, nanodiamoond; *Tc-CoPc*, tetra carboxy phthalocyaninate cobalt; *Tc-CuPc*, copper tetrakis (4-cumylphenoxy) phthalocyanine.

ITO glass plates. The PEDOT:PSS was used as an electron blocking layer for hole transport. Two types of solution for p-type semiconductors were produced [64,65].

The first was produced by ND and tetra carboxy phthalocyaninate cobalt (Tc-CoPc) in deionized water. The solution for n-type semiconductors was prepared by dissolving $C_{60}$ in 1,2-dichlorobenzene. On the thin layer of PEDOT:PSS, p-type semiconductor layers were prepared by spin coating a mixed solution of Tc-CoPc and ND in deionized water. The NDs were dispersed in the Tc-CoPc thin film. The n-type semiconductor layers were deposited on top of the p-type semiconductor layer by spin coating a $C_{60}$ solution in 1,2-dichlorobenzene.

The second was also produced by copper tetrakis (4-cumylphenoxy) phthalocyanine (Tc-CuPc), fullerenol [$C_{60}(OH)_{10-12}$] and ND in deionized water. On a thin layer of PEDOT:PSS, semiconductor layers were

prepared by spin coating with a mixed solution of Tc-CuPc, $C_{60}(OH)_{10-12}$ and ND in deionized water. The NDs were obtained using the bead milling method in water [66,67] and dispersed in the active layer.

Fig. 17.10B and C shows X-ray diffraction (XRD) patterns of diamond powder and the present thin film. In Fig. 17.10D, diffraction peaks of the diamond powder were confirmed as 111, 220, and 311 of the diamond structure. In Fig. 17.10D and E, diffraction peaks corresponding to diamond are observed for the Tc-CoPc:ND/$C_{60}$ and Tc-CuPc:ND:$C_{60}(OH)_{10-12}$ sample. The average particle sizes of the ND were calculated to be 4.5 and 5.5 nm with Scherrer's formula.

Measured parameters of diamond based thin films indicated that the thin film structure with ND provided a higher cell performance on the $J_{SC}$ values than that of thin film structure without ND. Fig. 17.10D and E shows optical absorption spectra of the ND based thin films. A solid line and a dashed line show thin film structure with ND and thin film structure without ND respectively. These thin films provided photo absorption in the range of 300–800 nm. Thin film structure with ND indicates a higher optical absorption compared to thin film structure without ND. The optical absorption property of the thin film was improved by adding the ND to the active layer.

Fig. 17.11A is a TEM image of the $C_{60}$ layer, and the lattice image of $C_{60}$ {111} is observed. Fig. 17.11B is an electron diffraction pattern of $C_{60}$ layer, and the diffraction peaks of $C_{60}$ are observed. $C_{60}$ also has an fcc structure with a lattice parameter of $a = 1.42$ nm. Fig. 17.11C is a high-resolution electron microscopy (HREM) image of the Tc-CoPc:ND composite layer. In Fig. 17.11C the lattice image of diamond {111} is observed. Tc-CoPc shows dark contrast in the image. Fig. 17.11D is an electron diffraction pattern of the Tc-CoPc:ND composite layer, and diffraction peaks of diamond 111, 220, 311 are observed. Diamond powder has an fcc structure with a lattice parameter of $a = 0.357$ nm. Since no diffraction peak of Tc-CoPc was observed, Tc-CoPc has an amorphous structure. Fig. 17.11E is a TEM image of the Tc-CuPc:ND:$C_{60}(OH)_{10-12}$ composite layer. The TEM image indicated ND with the size of 4–6 nm, indicated by arrows, agrees well with the XRD results. Fig. 17.11F contains an electron diffraction pattern of the active layer, and diffraction peaks of diamond 111, 220, 311 are observed. Since no diffraction peaks of Tc-CuPc and $C_{60}(OH)_{10-12}$ were observed, Tc-CuPc and $C_{60}(OH)_{10-12}$ would have amorphous structures. An advantage for the

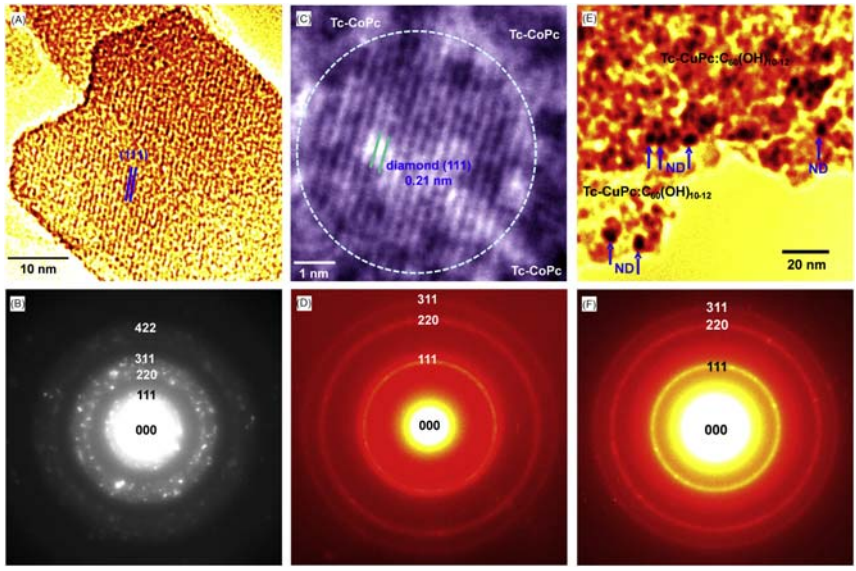


**Figure 17.11** (A) TEM image and (B) electron diffraction pattern of $C_{60}$ layer. (C) HREM image and (D) electron diffraction pattern of Tc-CoPc:ND layer. (E) TEM image and (F) electron diffraction pattern of Tc-CuPc:ND:$C_{60}(OH)_{10-12}$ layer. *ND*, Nanodiamoond; *Tc-CoPc*, tetra carboxy phthalocyaninate cobalt; *Tc-CuPc*, copper tetrakis (4-cumylphenoxy) phthalocyanine.

nanocomposite structure is the increase in p/n HJ interface. However, due to the disarray of the donor/acceptor microstructure, electrons and holes could not be transported smoothly by carrier recombination at the electronic acceptor/Al interface and at the PEDOT:PSS/electronic donor interface respectively. To solve the problems, introduction of a layer preventing carrier recombination and improvement of crystalline structure with few defects are needed. In the present work, ND-based solar cells were fabricated and characterized. For the carbon based solar cells in previous works, thin films were fabricated by a chemical vapor deposition method [68,69]. In the present work, solar cells with $C_{60}$, $C_{60}(OH)_{10-12}$ and MPc as an organic semiconductor, and diamond particles and ND as an inorganic semiconductor were fabricated by a spin coating method, which is a low cost method.

The $J_{SC}$ values of the cells with ND increased compared to those without ND. In addition, optical absorption spectra of the cells with ND were higher than those without ND in the range of 600−800 nm. A bandgap energy of diamond is originally ~5.5 eV and carrier mobility

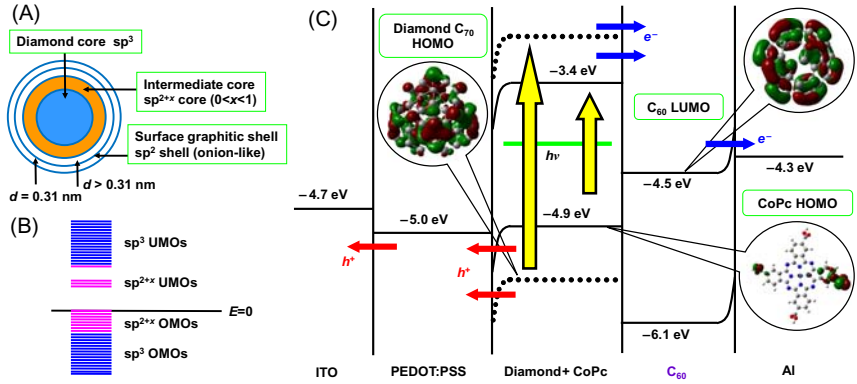


**Figure 17.12** (A) Structure of nanodiamond cluster. (B) Schematic OMOs and UMOs levels of diamond cluster. (C) Energy level diagram of diamond:CoPc/$C_{60}$ solar cell. *OMO*, Occupied molecular orbital; *UMO*, unoccupied molecular orbital.

would be low. However, the ND would have a core shell structure as shown in Fig. 17.12A, which indicates that the surface of the ND is covered by graphene sheets with $sp^2$ hybridized orbital, and there is an intermediate layer between the ND core and the graphene sheets. If the ND has a three layered structure, the ND have various bandgap energies as shown in Fig. 17.12B, and light with various wavelengths can be absorbed by the ND [23]. The XRD results also show lattice distances of ~3.2 Å, which is related to the intermediated layers. The energy level diagram of the cell with ND is shown in Fig. 17.12C, and the carrier is transported by hopping mechanism.

## 17.8 Ge nanoparticles

Fabrication and characterization of fullerene based solar cells with Ge nanoparticles are presented in this section. Tc-CuPc was used for p-type semiconductors as shown in Fig. 17.13A, and $C_{60}$ was used for n-type semiconductors. In addition, Ge(IV) bromide ($GeBr_4$) was added to the solar cells for the formation of Ge based quantum dots to increase the photovoltaic efficiencies [70]. Device structures were produced, and efficiencies, optical absorption, and nanostructures were investigated.

A thin layer of PEDOT:PSS (Sigma Aldrich Corp.) was spin coated on precleaned ITO glass plates. Then, semiconductor layers were prepared on a PEDOT:PSS layer by spin coating using a mixed solution of $C_{60}$, Tc-CuPc and $GeBr_4$ in 1 mL *o*-dichlorobenzene. Weight ratio of Tc-

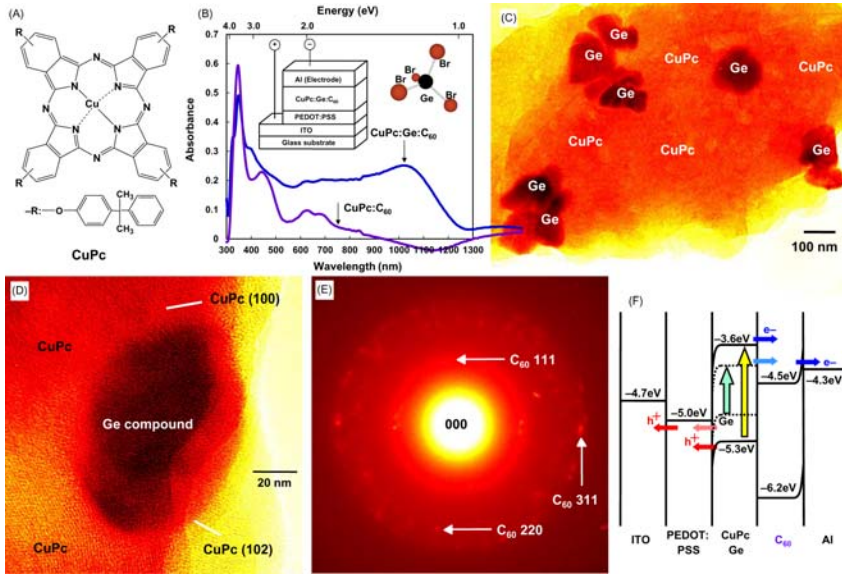


**Figure 17.13** (A) Molecular structure of CuPc. (B) Absorption spectra of Tc-CuPc:Ge:$C_{60}$ and Tc-CuPc:$C_{60}$ bulk heterojunction structure. (C) TEM image, (D) enlarged image and (E) electron diffraction pattern of Tc-CuPc:Ge:$C_{60}$ bulk heterojunction layer. (F) Energy level diagram of Tc-CuPc:Ge:$C_{60}$ solar cell. *Tc-CuPc*, Copper tetrakis (4-cumylphenoxy) phthalocyanine.

CuPc:$C_{60}$ was 1:8 (2 mg:16 mg), and 0.03 mL of $GeBr_4$ was added to the solution [70]. The thickness of the blended device was ~150 nm. A schematic diagram of the Tc-CuPc:$C_{60}$ BHJ and HJ solar cells with a Tc-CuPc/$C_{60}$ structure is shown in Fig. 17.13B. To increase efficiencies, $GeBr_4$ was also added in the Tc-CuPc layers for both structures. After annealing at 100°C for 30 minutes in $N_2$ atmosphere, Al metal contacts with a thickness of 100 nm were evaporated as a top electrode.

The BHJ indicates one layered composite structures with p and n-type semiconductors, which is denoted as Tc-CuPc:$C_{60}$. The common HJ solar cell that has two separated layers was also investigated for comparison, and was denoted; Tc-CuPc/$C_{60}$. The measured open circuit voltages of Tc-CuPc:$C_{60}$ and Tc-CuPc/$C_{60}$ increased several times by $GeBr_4$ addition and slight increases were also observed for short circuit current density for both structures. Fig. 17.13B shows optical absorption of Tc-CuPc:Ge:$C_{60}$ and Tc-CuPc:$C_{60}$ BHJ solar cells. The Tc-CuPc:Ge:$C_{60}$ structure provided higher photo-absorption in the range of 500−1200 nm (which corresponds to 2.5 and 1.0 eV, respectively), compared with the

Tc-CuPc:$C_{60}$ structure. An energy gap between HOMO and LUMO for $C_{60}$ is 1.7 eV, which corresponds to absorbance of 730 nm [71].

A TEM image of the Tc-CuPc:Ge:$C_{60}$ BHJ layer is shown in Fig. 17.13C. Nanoparticles consisting of a Ge element, which has the largest atomic number, and is in present solar cells are observed in the Tc-CuPc layer. An enlarged TEM image is shown in Fig. 17.13D, and lattice fringes of Tc-CuPc are observed. The nanoparticle with Ge compounds is denoted as Ge comp. An electron diffraction pattern of the Tc-CuPc:Ge:$C_{60}$ BHJ layer is shown in Fig. 17.13E, and many diffraction spots and rings corresponding to $C_{60}$ 111, 220, and 311 can be observed, which indicates microcrystalline structures of $C_{60}$. Dispersion of Ge based nanoparticles is effective for optical absorption in the range of 500−1200 nm. Although Ge has a band gap energy of 0.7 eV as indicated in Fig. 17.13F, optical absorption was observed in the range of 2.5 and 1.0 eV in the present work, which was due to Ge compound formation and nanodispersion effect of the nanoparticles, as reported in the previous work [72]. Interpenetrating DA network has a large interfacial area, which could be effective in charge generation. Since the microstructures of Tc-CuPc and $C_{60}$ were disordered, recombination of electrons of $C_{60}$ and holes of Tc-CuPc would occur. Then the ordered column-like structure would be suitable for carrier transport. If continuous nanocomposite structures are perpendicular to the thin film, the recombination of electrons and holes could be avoided, and the conversion efficiency of the solar cells would increase.

Quantum dot solar cells, including intermediate band structures, are one of the candidates of high efficiency solar cells [73−78]. In this work, efficiencies of the solar cells was increased by the formation of Ge based nanoparticles. The present solution technique is a very simple and cost effective method for the formation of nanoparticles. To improve the efficiencies, arrangement of the quantum dots and the control of size distribution is necessary. Combination of the present solar cells and copper oxide nanomaterials with various direct band gaps or other organic materials might also be effective to increase efficiencies [79,80]. The performance of current solar cells is also be due to the nanoscale structures.

## 17.9 Polysilane-system

Polysilane is a p-type semiconductor and has been used as an electrical conductive material in photovoltaic systems [81−85]. Polysilanes are

known as σ-conjugate polymers, with a hole mobility of $10^{-4}$ $cm^2$ $V^{-1}$ $s^{-1}$. Although polysilanes could be applied to p-type semiconductors on organic thin-film solar cells, few studies on polysilane solar cells have been reported [82,86–88].

The purpose is to fabricate and characterize bulk heterojunction solar cells with polysilane and fullerenes of $C_{60}$ and PCBM. $C_{60}$ was selected as a good electronic acceptor material for the devices. Spin-coating is a low-cost method and essential for mass production of solar cells. The following four types of polysilane were used in this work: dimethyl-polysilane (DMPS), poly(methyl phenyl silane) (PMPS), poly(phenyl silane) (PPSi), and decaphenyl cyclopentasilane (DPPS). Fig. 17.14A and B shows the solar cell structures and molecular structures of the DMPS, PMPS, PPSi, and DPPS used to fabricate bulk-heterojunction and heterojunction solar cells, respectively [89]. ITO glass plates were cleaned in an ultrasonic bath with acetone and methanol, and then dried with nitrogen gas. A thin layer of polyethylendioxythiophen doped with poly(3,4-ethylene

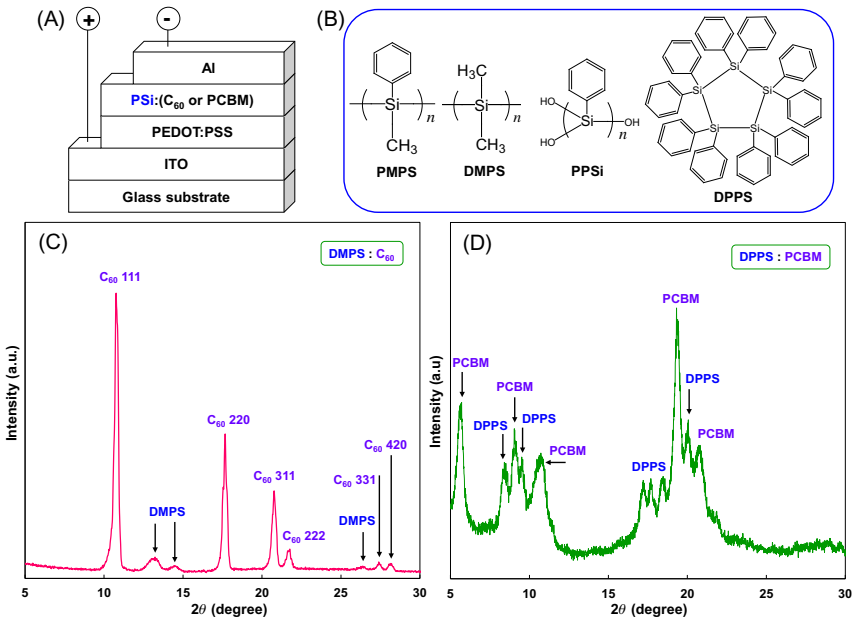


**Figure 17.14** Structures of (A) ITO/PEDOT:PSS/polysilane:($C_{60}$ or PCBM)/Al bulk heterojunction solar cells. (B) Molecular structures of polysilanes. XRD patterns of (C) DMPS:$C_{60}$ and (D) DPPS:PCBM thin films. *DMPS*, Dimethyl-polysilane; *DPPS*, decaphenyl cyclopentasilane; *ITO*, indium tin oxide; *PCBM*, 6,6-phenyl $C_{61}$-butyric acid methyl ester.

dioxythiophene):poly(styrene sulfonate) (PEDOT:PSS) was spin-coated on the ITO substrates. Then, semiconductor layers were prepared on a PEDOT:PSS layer by spin-coating using mixture solutions of DMPS, PMPS, PPSi or DPPS, and $C_{60}$ or PCBM in 1 mL *o*-dichlorobenzene. The total weight of $C_{60}$:PMPS, $C_{60}$:PPSi, $C_{60}$:DPPS, or PCBM:DPPS was 10 mg, the weight ratio of $C_{60}$:PMPS, $C_{60}$:PPSi, or $C_{60}$:DPPS was 8:2, and the weight ratio of PCBM:DPPS was 7:3. The total weight of $C_{60}$:DMPS was 19 mg, and the weight ratio of $C_{60}$:DMPS was 16:3. Another type of thin-film solar cell was prepared as follows: Aluminum (Al) metal contacts were evaporated as a top electrode. Finally, the devices were annealed at 140°C for 30 minutes in $N_2$ atmosphere.

The $J-V$ characteristics of the solar cell showed open-circuit voltage and short-circuit current. The measured parameters of the present solar cells are summarized in Table 17.2. A solar cell with the DMPS/$C_{60}$ structure provided of 0.020%, which was better than those of other polysilane-based devices with $C_{60}$. A solar cell with the DPPS/PCBM structure also provided of 0.032%.

XRD patterns of DMPS:$C_{60}$ and DPPS:PCBM thin films are shown in Fig. 17.14C and D, respectively. The diffraction patterns showed several diffraction peaks, which corresponded to DMPS, $C_{60}$, DPPS, and PCBM, as indicated in the figures.

Fig. 17.15A and B shows a TEM image and an electron diffraction pattern of the DMPS:$C_{60}$ composite thin film, respectively. In Fig. 17.15A, nanoparticles consisting of the Si element in the $C_{60}$ matrix can be observed. The electron diffraction pattern in Fig. 17.15B shows many diffraction spots and Debye–Scherrer rings, which indicates the microcrystalline structures of $C_{60}$ and DMPS. Fig. 17.15C and D shows a HREM image and an electron diffraction pattern of DPPS:PCBM bulk

**Table 17.2** Measured parameters of the present solar cells.

| Active layer | $J_{SC}$ (mA cm$^{-2}$) | $V_{OC}$ (V) | FF | $\eta$ (%) |
|---|---|---|---|---|
| DMPS:$C_{60}$ | 0.42 | 0.15 | 0.31 | 0.020 |
| PMPS:$C_{60}$ | 0.045 | 0.10 | 0.25 | $1.2 \times 10^{-4}$ |
| PPSi:$C_{60}$ | $7.0 \times 10^{-5}$ | $2.5 \times 10^{-3}$ | 0.26 | $1.2 \times 10^{-8}$ |
| DPPS:$C_{60}$ | $5.0 \times 10^{-3}$ | 0.050 | 0.24 | $6.0 \times 10^{-5}$ |
| DPPS:PCBM | 0.24 | 0.40 | 0.34 | 0.032 |

*DMPS*, Dimethyl-polysilane; *DPPS*, decaphenyl cyclopentasilane; *PCBM*, 6,6-phenyl $C_{61}$-butyric acid methyl ester; *PMPS*, poly(methyl phenyl silane); *PPSi*, poly(phenyl silane).

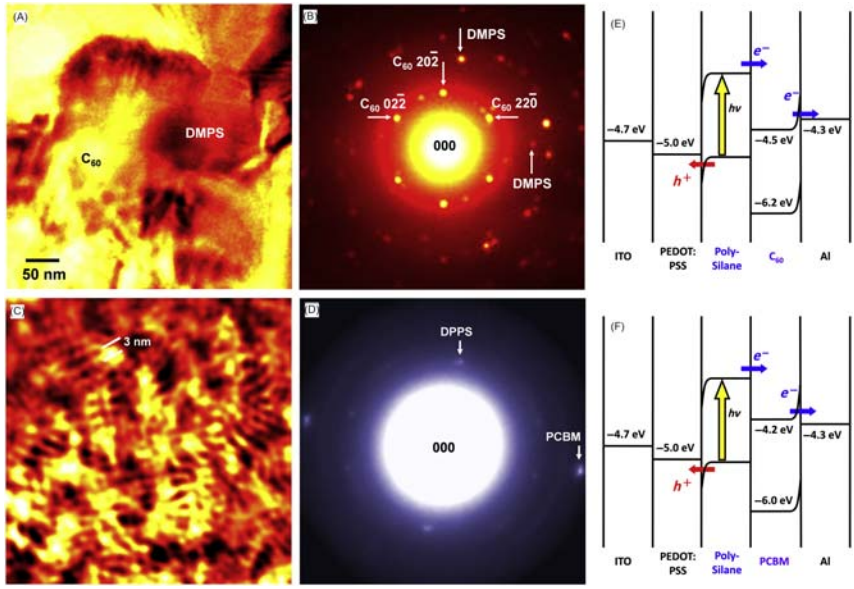


**Figure 17.15** (A) TEM image and (B) electron diffraction pattern of DMPS:$C_{60}$ thin film. (C) TEM image and (D) electron diffraction pattern of DPPS:PCBM. Energy level diagrams of (E) polysilane:$C_{60}$ and (F) DPPS:PCBM solar cells. *DMPS*, Dimethyl-polysilane; *DPPS*, decaphenyl cyclopentasilane; *PCBM*, 6,6-phenyl $C_{61}$-butyric acid methyl ester.

heterojunction thin films, respectively. In Fig. 17.15D the diffraction spots corresponding to DPPS and PCBM were observed. The HREM image in Fig. 17.15C indicates that the DPPS:PCBM thin films have a nanocomposite structure, which has a lamella structure with a periodicity of ~3 nm. Optimization of the nanocomposite structure of DPPS:PCBM could increase the conversion efficiency of the solar cells.

The energy level diagrams of the present polysilane-based solar cells are summarized in Fig. 17.15E and F. In this work the $V_{OC}$ of DPPS is higher than that of PMPS, which would indicate that the HOMO−LUMO levels are different. Mixing $C_{60}$ with polysilanes could suppress the recombination of photo-separated charge carriers by promoting the electron transfer from polysilanes.

The present DPPS-based solar cells were compared with other silicon-based solar cells such as amorphous silicon solar cells prepared by inductively coupled plasma chemical vapor deposition and a spin-coating method, as listed in Table 17.3. The present solar cells fabricated with a spin-coating method have a simple fabrication process and better cost

**Table 17.3** Comparison of silicon-based solar cells.

| Material | $\eta$ (%) | Fabrication process | Reference |
|---|---|---|---|
| Amorphous Si | 9.6 | ICP-CVD | [90] |
| PMPS:$C_{60}$ | 0.33 | Spin-coating | [88] |
| PSi-Phth:$C_{60}$ | 0.013 | Spin-coating | [82] |

*ICP-CVD*, Inductively coupled plasma chemical vapor deposition; *PMPS*, poly(methyl phenyl silane).

performance. The low conversion efficiency of the present solar cells could be due to the high electrical resistance and carrier recombination caused by defects. Further improvement is necessary.

In summary, polysilane-based solar cells were fabricated using a mixture solution of DMPS, PMPS, PPSi, DPPS, $C_{60}$, and PCBM, and characterized by electrical measurements and microstructural analyses. Bulk heterojunction devices of DMPS:$C_{60}$ and DPPS:PCBM provided photovoltaic properties. XRD and TEM results indicated that the DMPS:$C_{60}$ and DPPS:PCBM layers had nanocomposite structures. Energy level diagrams of the present solar cells were presented, and carrier transport mechanisms were discussed.

## 17.10 6,6-Phenyl $C_{61}$-butyric acid methyl ester:poly[3-hexylthiophene] with silicon phthalocyanine or silicon naphthalocyanine

MPcs and metal naphthalocyanines (MNc) are groups of small molecular materials with Q-band absorption in the red to near-infrared range, with have high optical and chemical stabilities, and photovoltaic properties. They are used as donor materials for organic solar cells. Heterojunction solar cells using copper phthalocyanine and fullerene were fabricated by an evaporation method, and the power conversion efficiency was $\sim$3% [91]. The characteristics such as electronic conductivity, crystalline structure, and absorption range were investigated by changing a central metal [92–95]. Organic solar cells such as those using P3HT and PCBM exhibit good incident photon-to-current conversion efficiency and fill factor. The device performance of such polymer solar cells can be affected by the preparation condition, such as the annealing temperature, concentration of starting material, and film thickness. The addition of third components such as phthalocyanines, naphthalocyanines, and low-band-gap polymers is expected to absorb light that the P3HT and PCBM cannot collect. In

particular, phthalocyanines absorb near-infrared light and the effects of silicon phthalocyanine, silicon naphthalocyanine, or germanium phthalocyanine on the P3HT:PCBM system were investigated [96–100]. MPc and MNc can be dissolved in organic solvents, and application to the device process using a spin-coating method is possible with the solubilization.

Fabrication and characterization of bulk heterojunction polymer solar cells with an inverted structure using PCBM, P3HT, soluble tetrakis(tert-butyl)[bis(trihexylsiloxy)silicon phthalocyanine] (SiPc) and tetrakis(tert-butyl)[bis(trihexylsiloxy)silicon naphthalocyanine] (SiNc) is presented in this section. SiPc or SiNc was added as the third component for the PCBM:P3HT solar cells, as shown in Fig. 17.16A [101,102]. The polarity of charge collection is reversed from conventional devices in the inverted structure [103–105], which is expected to provide stable devices in air. Layered structures of bulk heterojunction solar cells with the inverted structure are denoted as ITO/$TiO_x$/PCBM:P3HT(SiPc or SiNc)/PEDOT:PSS/Au.

The device performance of the present solar cell doped with SiPc was improved compared to that of the PCBM:P3HT. A solar cell with a PCBM:P3HT(SiPc, 3 wt.%) structure provided $\eta$ of 0.768%, which was better than those of other devices in this work [101]. The maximum $\eta$ lies for SiPc concentrations between 3 and 7 wt.%. The stability of inverted-structure solar cells with a PCBM:P3HT(SiPc) active layer was also investigated. $J-V$ characteristics of the device were measured after a 1 week exposure to ambient atmosphere, as listed in Table 17.4, and the devices exhibited stability in air. The conversion efficiency slightly increased upon exposure to air for 1 week. Similar increases in efficiencies were observed in previous works [106,107]. The morphology of the solar cells could be improved, leading to improved carrier mobility and a decreased energy barrier of the metal/semiconductor interface. Devices maintained similar conversion efficiencies after 2 weeks of exposure to air.

External quantum efficiency (EQE) spectra of PCBM:P3HT(SiPc) solar cells are shown in Fig. 17.16B. EQE peaks were observed at ~680 nm for the solar cell with SiPc. If SiPc aggregates exist in the P3HT domain, no charge separation occurs, and if the SiPc exists in the PCBM domain, charge transfer does not occur. Therefore, the power conversion efficiency would be improved only when SiPc exists at the PCBM:P3HT interface. Since the peaks of EQE for SiPc were observed at ~680 nm, SiPc would exist at the PCBM:P3HT interface. Internal quantum efficiencies of PCBM:P3HT(SiPc) solar cells were calculated

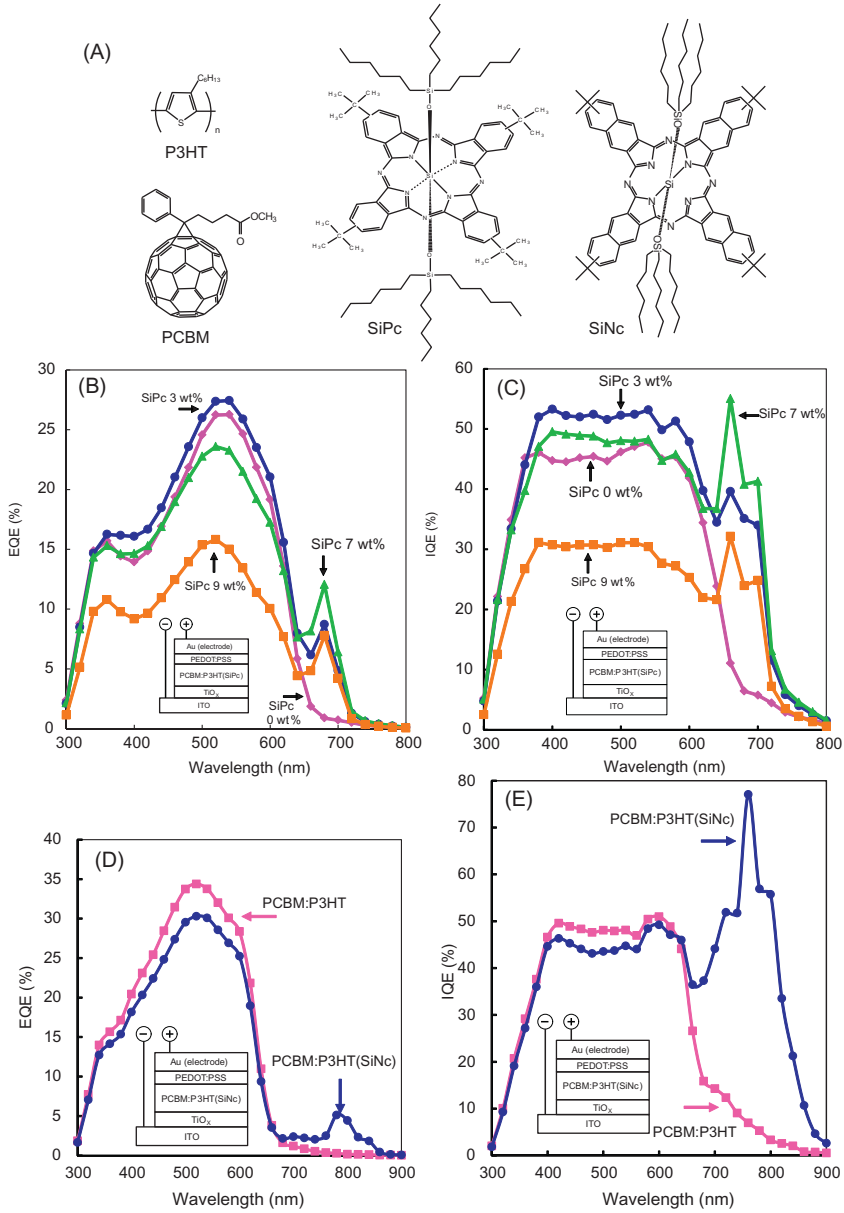


**Figure 17.16** (A) Molecular structures of P3HT, PCBM, SiPc, and SiNc. (B) EQE and (C) IQE spectra of PCBM:P3HT(SiPc) solar cells. (D) EQE and (E) IQE spectra of PCBM:P3HT (SiPc) solar cells. *P3HT*, Poly[3-hexylthiophene]; *PCBM*, 6,6-phenyl $C_{61}$-butyric acid methyl ester; *SiNc*, silicon naphthalocyanine; *SiPc*, silicon phthalocyanine.

**Table 17.4** Measured parameters of 6,6-phenyl $C_{61}$-butyric acid methyl ester:poly[3-hexylthiophene] (silicon phthalocyanine, 1 wt.%) solar cell.

| Sample | $J_{SC}$ (mA cm$^{-2}$) | $V_{OC}$ (V) | FF | $\eta$ (%) |
|---|---|---|---|---|
| As-prepared | 3.4 | 0.50 | 0.41 | 0.69 |
| After 1 week | 3.4 | 0.59 | 0.52 | 1.05 |
| After 2 weeks | 3.1 | 0.57 | 0.53 | 0.95 |

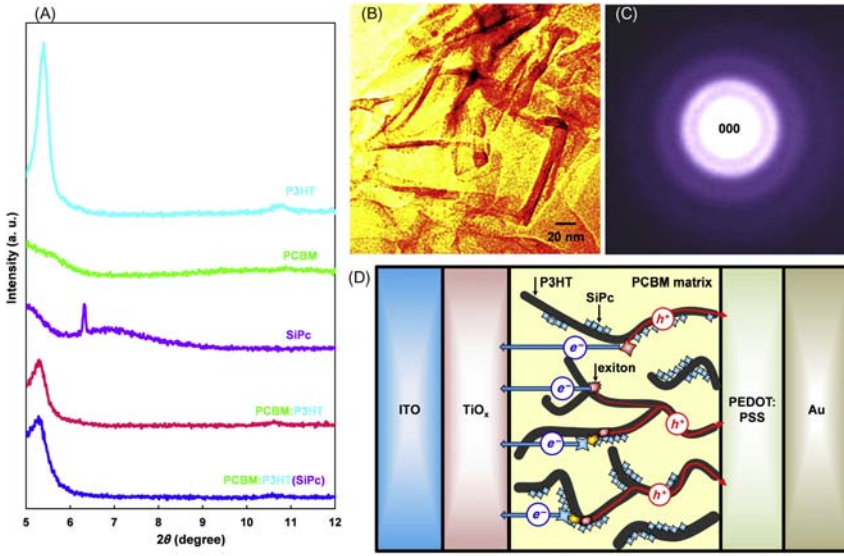


**Figure 17.17** (A) XRD patterns of P3HT, PCBM, SiPc, PCBM:P3HT, and PCBM:P3HT (SiPc) thin films. (B) TEM image and (C) electron diffraction pattern of PCBM:P3HT (SiPc) thin film. (D) Schematic interfacial structure of PCBM:P3HT(SiPc) solar cell. *P3HT*, Poly[3-hexylthiophene]; *PCBM*, 6,6-phenyl $C_{61}$-butyric acid methyl ester; *SiPc*, silicon phthalocyanine.

from the EQE, as shown in Fig. 17.16C. A relatively higher internal quantum efficiency (IQE) is observed for the PCBM:P3HT(SiPc) solar cells in the range of 640–700 nm. EQE spectra of PCBM:P3HT(SiNc) solar cells are also shown in Fig. 17.16D, which indicates an EQE peak ~800 nm. IQE spectra of the PCBM:P3HT(SiNc) solar cell is shown in Fig. 17.16E, which also indicates higher IQE in the range of 700–900 nm, that is effective for photovoltaic devices.

XRD patterns of PCBM, P3HT, SiPc, PCBM:P3HT, and PCBM:P3HT(SiPc) thin films are shown in Fig. 17.17A. Diffraction peaks are observed for P3HT and SiPc, which indicate crystalline structures. No

sharp diffraction peak is observed for PCBM, which indicates that the PCBM has an amorphous structure. For the PCBM:P3HT(SiPc) and PCBM:P3HT thin films, diffraction peaks due to P3HT are weaker and broader than that of the single P3HT phase, and no sharp peak due to SiPc is observed. This indicates that P3HT has nanocrystalline structures dispersed in the amorphous PCBM, and the SiPc molecules without a crystalline structure would exist at the PCBM/P3HT interface. No sharp diffraction peak is observed for SiNc, which also indicates the PCBM: P3HT(SiNc) thin films have a similar structure.

A TEM image and an electron diffraction pattern of the PCBM:P3HT (SiPc) thin film are shown in Fig. 17.17B and C, respectively [101]. In Fig. 17.17B, P3HT nanowires are observed in the amorphous PCBM matrix. The electron diffraction pattern in Fig. 17.17C shows a halo-like intensity, which indicates the amorphous and nanocrystalline structures, which agrees well with the XRD results shown in Fig. 17.17A.

An interfacial structure model and an energy level diagram of the present PCBM:P3HT(SiPc) solar cells are summarized and illustrated in Figs. 17.17D and 17.18A, respectively. In Fig. 17.17D, P3HT nanowires are dispersed in the PCBM amorphous matrix, which was confirmed by XRD and TEM analyses. Since an increase in photocurrent originating from the SiPc was observed, it is believed that the SiPc molecules are located at the PCBM/P3HT interface. The localization of SiPc molecules at the PCBM/P3HT interface would be due to the insolubility of SiPc both in P3HT nanowires and the PCBM matrix. When the amount of SiPc addition increased, the efficiencies decreased, which indicated that

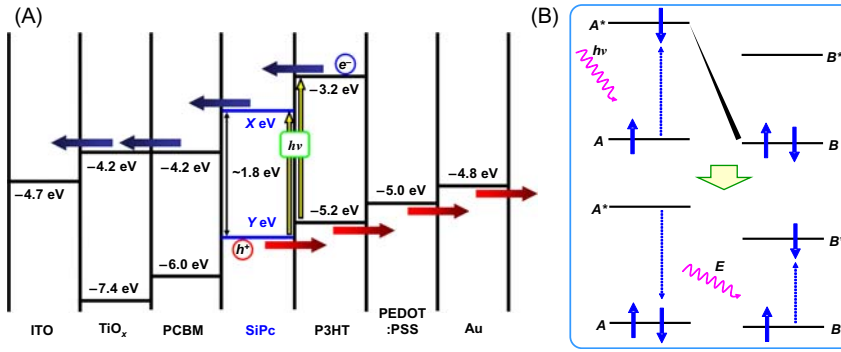


**Figure 17.18** (A) Energy level diagram of PCBM:P3HT(SiPc) solar cell. (B) Schematic illustration of Förster resonance energy transfer mechanism. *P3HT*, Poly[3-hexylthiophene]; *PCBM*, 6,6-phenyl $C_{61}$-butyric acid methyl ester; *SiPc*, silicon phthalocyanine.

the single-layer localization of SiPc at the PCBM/P3HT interface would be effective for conversion efficiencies. There would be two mechanisms for the increase in efficiencies caused by the SiPc addition. Additional absorption of SiPc directly contributes to the increase in $J_{SC}$, which was observed in EQE and IQE spectra at 680 nm in Fig. 17.16B and C, respectively. In addition, the EQE and IQE intensities in the range of 400−600 nm were increased by the SiPc addition, which could be explained by the Förster energy transfer from P3HT to SiPc [108,109], as shown in Fig. 17.18B. For the cell with the inverted structure, electrons are transported to an ITO substrate, and holes are transported to the Au electrode. Electrons could be transported only when the value of the LUMO for SiPc ($X$ eV) is $-4.2 \leq X \leq -3.2$ eV, and holes could be transported only when the value of the HOMO for SiPc ($Y$ eV) is $Y \leq -5.2$ eV. Control of HOMO and LUMO of the phthalocyanine is required for the polymer solar cells. Since a molecule exists in monomeric molecule, a bulky molecular structure is required, and the present SiPc has a suitable structure. Control of HOMO and LUMO becomes possible by following the exchange of a central metal and the introduction of a substituent group. Addition of silicon naphthalocyanine to PCBM:P3HT bulk heterojunction solar cells also showed a higher conversion efficiency [101] than that shown in this study, which is due to the different compositions of PCBM:P3HT.

In summary, PCBM:P3HT(SiPc) and PCBM:P3HT(SiNc) bulk heterojunction solar cells with an inverted structure were fabricated and characterized. The photovoltaic properties of the solar cells were improved by the SiPc addition and were near stable after 2 weeks of exposure in air. Microstructural analysis showed that the P3HT nanowires were dispersed in the amorphous PCBM matrix, and it is believed that SiPc or SiNc molecules are located at the PCBM/P3HT interface. EQE and IQE spectra of the PCBM:P3HT(SiPc) solar cell showed peaks at ∼680 nm, and the intensities of EQE and IQE in the range of 400−600 nm were increased by the SiPc addition. The increase in conversion efficiency by the SiPc addition can be explained with the direct charge transfer from SiPc to PCBM and Förster energy transfer from P3HT to SiPc. PCBM:P3HT(SiNc) solar cells also showed higher values at the near-infrared region (∼800 nm), which indicated that the enhancement of the solar cell performance is possible by the SiNc addition.

## 17.11 Summary

Fabrication and nanostructures of fullerene-based solar cells with phthalocyanines, ND, porphyrin, Ge, polysilane, and P3HT were reviewed in this article. Photovoltaic behavior including charge separation and transfer was described on the basis of the nanostructures of the bulk heterojunction solar cells. It is necessary for the development of organic solar cells to characterize the microstructures in nanoscopic scale [110]. Recently, perovskite solar cells are widely studied as organic-inorganic solar cells [111–113], and fullerene-based nanomaterials can also be applied to perovskite solar cells as ETLs and capping layers for the perovskite phase [114–116]. Further research on the fullerene introduced perovskite solar cells will be done.

## Acknowledgments

The author would like to acknowledge many colleagues for experimental help and useful discussion as follows: Atsushi Suzuki, Tsuyoshi Akiyama, Kenji Kikuchi, Taisuke Matsumoto, Akihiro Takeda, Akihiko Nagata, Junya Nakagawa, Kazumi Yoshida, Haruto Maruhashi, Tatsuya Noma, Kazuma Kumada, Satoru Hori, Shiomi Kikuchi, Katsuhisa Tokumitsu, Yasuhiro Yamasaki, Mika Nakamura, Masahiro Yamada, Sakiko Fukunishi, Kazufumi Kohno, Yasuhiko Hayashi, Tetsuo Soga, and Eiji Ōsawa.

## References

[1] Z. Li, Z. Liu, H. Sun, C. Gao, Superstructured assembly of nanocarbons: fullerenes, nanotubes, and graphene, Chem. Rev. 115 (2015) 7046–7117.
[2] M. Gong, T.A. Shastry, Y. Xie, M. Bernardi, D. Jasion, K.A. Luck, et al., Polychiral semiconducting carbon nanotube–fullerene solar cells, Nano Lett. 14 (2014) 5308–5314.
[3] A.-M. Dowgiallo, K.S. Mistry, J.C. Johnson, O.G. Reid, J.L. Blackburn, Probing exciton diffusion and dissociation in single-walled carbon nanotube–$C_{60}$ heterojunctions, J. Phys. Chem. Lett. 7 (2016) 1794–1799.
[4] M. Gong, T.A. Shastry, Q. Cui, R.R. Kohlmeyer, K.A. Luck, A. Rowberg, et al., Understanding charge transfer in carbon nanotube–fullerene bulk heterojunctions, ACS Appl. Mater. Interfaces 7 (2015) 7428–7435.
[5] T. Salim, H.-W. Lee, L.H. Wong, J.H. Oh, Z. Bao, Y.M. Lam, Semiconducting carbon nanotubes for improved efficiency and thermal stability of polymer–fullerene solar cells, Adv. Funct. Mater. 26 (2016) 51–65.
[6] H. Hanaei, M.K. Assadi, R. Saidur, Highly efficient antireflective and self-cleaning coatings that incorporate carbon nanotubes (CNTs) into solar cells: a review, Renew. Sustain. Energy Rev. 59 (2016) 620–635.

[7] T. Oku, T. Hirano, M. Kuno, T. Kusunose, K. Niihara, K. Suganuma, Synthesis, atomic structures and properties of carbon and boron nitride fullerene materials, Mater. Sci. Eng. B 74 (2000) 206–217.
[8] T. Oku, I. Narita, A. Nishiwaki, N. Koi, K. Suganuma, R. Hatakeyama, et al., Formation, atomic structures and properties of carbon nanocage materials, Top. Appl. Phys. 100 (2006) 187–216.
[9] N.S. Sariciftci, L. Smilowitz, A.J. Heeger, F. Wudl, Photoinduced electron transfer from a conducting polymer to buckminsterfullerene, Science 258 (1992) 1474–1476.
[10] H. Hoppe, N.S. Sariciftci, Organic solar cells: an overview, J. Mater. Res. 19 (2004) 1924–1945.
[11] S. Günes, H. Neugebauer, N.S. Sariciftci, Conjugated polymer-based organic solar cells, Chem. Rev. 107 (2007) 1324–1338.
[12] L.-M. Chen, Z. Hong, G. Li, Y. Yang, Recent progress in polymer solar cells: manipulation of polymer:fullerene morphology and the formation of efficient inverted polymer solar cells, Adv. Mater. 21 (2009) 1434–1449.
[13] C.J. Brabec, S. Gowrisanker, J.J.M. Halls, D. Laird, S. Jia, S.P. Williams, Polymer–fullerene bulk-heterojunction solar cells, Adv. Mater. 22 (2010) 3839–3856.
[14] Y. Hayashi, I. Yamada, S. Takagi, A. Takasu, T. Soga, T. Jimbo, Influence of structure and $C_{60}$ composition on properties of blends and bilayers of organic donor-acceptor polymer/$C_{60}$ photovoltaic devices, Jpn. J. Appl. Phys. 44 (2005) 1296–1300.
[15] T. Oku, S. Nagaoka, A. Suzuki, K. Kikuchi, Y. Hayashi, H. Inukai, et al., Formation and characterization of polymer/fullerene bulk heterojunction solar cells, J. Phys. Chem. Solids 69 (2008) 1276–1279.
[16] T. Oku, T. Noma, A. Suzuki, K. Kikuchi, S. Kikuchi, The effects of exciton-diffusion blocking layers on pentacene/$C_{60}$ bulk heterojunction solar cells, J. Phys. Chem. Solids 71 (2010) 551–555.
[17] Y.H. Lin, P.C. Yang, J.S. Huang, G.D. Huang, I.J. Wang, W.H. Wu, et al., High-efficiency inverted polymer solar cells with solution-processed metal oxides, Sol. Energy Mater. Sol. Cells 95 (2011) 2511–2515.
[18] W. Ma, C. Yang, X. Gong, K. Lee, A.J. Heeger, Thermally stable, efficient polymer solar cells with nanoscale control of the interpenetrating network morphology, Adv. Funct. Mater. 15 (2005) 1617–1622.
[19] M. Granström, K. Petritsch, A.C. Arias, A. Lux, M.R. Andersson, R.H. Friend, Laminated fabrication of polymeric photovoltaic diodes, Nature 395 (1998) 257–260.
[20] T. Oku, A. Takeda, A. Nagata, T. Noma, A. Suzuki, K. Kikuchi, Fabrication and characterization of fullerene-based bulk heterojunction solar cells with porphyrin, $CuInS_2$, diamond and exciton-diffusion blocking layer, Energies 3 (2010) 671–685.
[21] M. Manceau, D. Angmo, M. Jørgensen, F.C. Krebs, ITO-free flexible polymer solar cells: from small model devices to roll-to-roll processed large modules, Org. Electron. 12 (2011) 566–574.
[22] L. Dou, J. You, J. Yang, C.C. Chen, Y. He, S. Murase, et al., Tandem polymer solar cells featuring a spectrally matched low-bandgap polymer, Nat. Photonics 6 (2012) 180–185.
[23] T. Oku, A. Takeda, A. Nagata, H. Kidowaki, K. Kumada, K. Fujimoto, et al., Microstructures and photovoltaic properties of $C_{60}$ based solar cells with copper oxides, $CuInS_2$, phthalocyanines, porphyrin, PVK, nanodiamond, germanium and exciton diffusion blocking layers, Mater. Technol. 28 (2013) 21–39.

[24] J. You, L. Dou, K. Yoshimura, T. Kato, K. Ohya, T. Moriarty, et al., A polymer tandem solar cell with 10.6% power conversion efficiency, Nat. Commun. 4 (2013) 1446.
[25] Y. Liu, C.-C. Chen, Z. Hong, J. Gao, Y. Yang, H. Zhou, et al., Solution-processed small-molecule solar cells: breaking the 10% power conversion efficiency, Sci. Rep. 3 (2013) 3356.
[26] Y. Liu, J. Zhao, Z. Li, C. Mu, W. Ma, H. Hu, et al., Aggregation and morphology control enables multiple cases of high-efficiency polymer solar cells, Nat. Commun. 5 (2014) 5293.
[27] C.-C. Chen, W.-H. Chang, K. Yoshimura, K. Ohya, J. You, J. Gao, et al., An efficient triple-junction polymer solar cell having a power conversion efficiency exceeding 11%, Adv. Mater. 26 (2014) 5670–5677.
[28] J.-D. Chen, C. Cui, Y.-Q. Li, L. Zhou, Q.-D. Ou, C. Li, et al., Single-junction polymer solar cells exceeding 10% power conversion efficiency, Adv. Mater. 27 (2015) 1035–1041.
[29] C. Liu, C. Yi, K. Wang, Y. Yang, R.S. Bhatta, M. Tsige, et al., Single-junction polymer solar cells with over 10% efficiency by a novel two-dimensional donor–acceptor conjugated copolymer, ACS Appl. Mater. Interfaces 7 (2015) 4928–4935.
[30] H. Zhou, Y. Zhang, C.-K. Mai, S.D. Collins, G.C. Bazan, T.-Q. Nguyen, et al., Polymer homo-tandem solar cells with best efficiency of 11.3%, Adv. Mater. 27 (2015) 1767–1773.
[31] A.R.M. Yusoff, D. Kim, H.P. Kim, F.K. Shneider, W.J. Silva, J. Jang, A high efficiency solution processed polymer inverted triple-junction solar cell exhibiting a power conversion efficiency of 11.83%, Energy Environ. Sci. 8 (2015) 303–316.
[32] Z. Zheng, S. Zhang, J. Zhang, Y. Qin, W. Li, R. Yu, et al., Over 11% efficiency in tandem polymer solar cells featured by a low-band-gap polymer with fine-tuned properties, Adv. Mater. 28 (2016) 5133–5138.
[33] T. Oku, Solar Cells and Energy Materials, Walter de Gruyter, Berlin, 2017.
[34] G. Yu, A.J. Heeger, Charge separation and photovoltaic conversion in polymer composites with internal donor/acceptor heterojunctions, J. Appl. Phys. 78 (1995) 4510–4515.
[35] F. Padinger, R.S. Rittberger, N.S. Sariciftci, Effects of postproduction treatment on plastic solar cells, Adv. Funct. Mater. 13 (2003) 85–88.
[36] T. Oku, N. Kakuta, A. Kawashima, K. Nomura, R. Motoyoshi, A. Suzuki, et al., Formation and characterization of bulk hetero-junction solar cells using $C_{60}$ and perylene, Mater. Trans. 49 (2008) 2457–2460.
[37] K. Nomura, T. Oku, A. Suzuki, K. Kikuchi, G. Kinoshita, The effects of exciton-diffusion blocking layers on pentacene/$C_{60}$ bulk heterojunction solar cells, J. Phys. Chem. Solids 71 (2010) 210–213.
[38] Y. Liang, Z. Xu, J. Xia, S.T. Tsai, Y. Wu, G. Li, et al., For the bright future—bulk heterojunction polymer solar cells with power conversion efficiency of 7.4%, Adv. Mater. 22 (2010) E135–E138.
[39] L. Yang, H. Zhou, S.C. Price, W. You, Parallel-like bulk heterojunction polymer solar cells, J. Am. Chem. Soc. 134 (2012) 5432–5435.
[40] L.J.A. Koster, V.D. Mihailetchi, P.W.M. Blom, Ultimate efficiency of polymer/fullerene bulk heterojunction solar cells, Appl. Phys. Lett. 88 (2006) 093511–093513.
[41] M.C. Scharber, D. Mühlbacher, M. Koppe, P. Denk, C. Waldauf, A.J. Heeger, et al., Design rules for donors in bulk-heterojunction solar cells – towards 10% energy-conversion efficiency, Adv. Mater. 18 (2006) 789–794.

[42] J.L. Brédas, D. Beljonne, V. Coropceanu, Charge-transfer and energy-transfer processes in pi-conjugated oligomers and polymers: a molecular picture, Chem. Rev. 104 (2004) 4971–5004.
[43] R. Ulbricht, S.B. Lee, X. Jiang, K. Inoue, M. Zhang, S. Fang, et al., Transparent carbon nanotube sheets as 3-D charge collectors in organic solar cells, Sol. Energy Mater. Sol. Cells 91 (2007) 416–419.
[44] T. Oku, I. Narita, N. Koi, A. Nishiwaki, K. Suganuma, M. Inoue, et al., Boron nitride nanocage clusters, nanotubes, nanohorns, nanoparticles, and nanocapsules, in: Y.K. Yap (Ed.), B-C-N Nanotubes and Related Nanostructures, *Springer*, 2009, pp. 149–194.
[45] K.S. Yook, B.D. Chin, J.Y. Lee, B.E. Lassiter, S.R. Forrest, Vertical orientation of copper phthalocyanine in organic solar cells using a small molecular weight organic templating layer, Appl. Phys. Lett. 99 (2011) 043308.
[46] S. Mori, M. Nagata, Y. Nakahata, K. Yasuta, R. Goto, M. Kimura, et al., Enhancement of incident photon-to-current conversion efficiency for phthalocyanine-sensitized solar cells by 3D molecular structuralization, J. Am. Chem. Soc. 132 (2010) 4054–4055.
[47] Y. Yamasaki, K. Takaki, Synthesis of μ-oxo-bridged hetero-metal phthalocyanine dimer analogues and application for charge generating material in photoreceptor, Dyes Pigm. 70 (2006) 105–109.
[48] Y. Yamasaki, K. Kuroda, K. Yakaki, Synthesis of new polymorphs of μ-oxo-meta (III) phthalocyanine dimers and their photoconductive properties, J. Chem. Soc. Jpn. Chem. Ind. Chem. 12 (1997) 887–898.
[49] A. Takeda, A. Minowa, T. Oku, A. Suzuki, K. Kikuchi, Y. Yamasaki, Formation and characterization of phthalocyanine dimer/$C_{60}$ solar cells, Prog. Nat. Sci. Mater. Int. 21 (2011) 27–30.
[50] A. Takeda, T. Oku, A. Suzuki, Y. Yamasaki, Theoretical study of gallium phthalocyanine dimer-fullerene complex for photovoltaic device, J. Mod. Phys. 2 (2011) 966–969.
[51] H. Mizuseki, N. Igarashi, R.V. Belosludov, A.A. Farajian, Y. Kawazoe, Theoretical study of phthalocyanine–fullerene complex for a high efficiency photovoltaic device using *ab initio* electronic structure calculation, Synth. Met. 138 (2003) 281–283.
[52] A.J. Hameed, Theoretical investigation of a phthalocyanine–fulleropyrrolidine adduct and some of its metallic complexes, J. Mol. Struct. Theochem. 764 (2006) 195–199.
[53] K. Takahashi, N. Kuraya, T. Yamaguchi, T. Komura, K. Murata, Three-layer organic solar cell with high-power conversion efficiency of 3.5%, Sol. Energy Mater. Sol. Cells 61 (2000) 403–416.
[54] T. Hasobe, H. Imahori, P.V. Kamat, T.K. Ahn, S.K. Kim, D. Kim, et al., Photovoltaic cells using composite nanoclusters of porphyrins and fullerenes with gold nanoparticles, J. Am. Chem. Soc. 127 (2005) 1216–1228.
[55] Q. Sun, L. Dai, X. Zhou, L. Li, Q. Li, Bilayer- and bulk-heterojunction solar cells using liquid crystalline porphyrins as donors by solution processing, Appl. Phys. Lett. 91 (2007) 253505.
[56] T. Hasobe, A.S.D. Sandanayaka, T. Wada, Y. Araki, Fullerene-encapsulated porphyrin hexagonal nanorods. An anisotropic donor–acceptor composite for efficient photoinduced electron transfer and light energy conversion, Chem. Commun. (2008) 3372–3374.
[57] T. Ishii, N. Aizawa, R. Kanehama, M. Yamashita, K. Sugiura, H. Miyasaka, Cocrystallites consisting of metal macrocycles with fullerenes, Coord. Chem. Rev. 226 (2002) 113–124.

[58] D.V. Konarev, A.Y. Kovalevsky, X. Li, I.S. Neretin, A.L. Litvinov, N.V. Drichko, et al., Synthesis and structure of multicomponent crystals of fullerenes and metal tetraarylporphyrins, Inorg. Chem. 41 (2002) 3638–3646.
[59] W.J. Belcher, K.I. Wagner, P.C. Dastoor, The effect of porphyrin inclusion on the spectral response of ternary P3HT:porphyrin:PCBM bulk heterojunction solar cells, Sol. Energy Mater. Sol. Cells 91 (2007) 447–452.
[60] P.C. Dastoor, C.R. McNeill, H. Frohne, C.J. Foster, B. Dean, C.J. Fell, et al., Understanding and improving solid-state polymer/$C_{60}$-fullerene bulk-heterojunction solar cells using ternary porphyrin blends, J. Phys. Chem. C 111 (2007) 15415–15426.
[61] Y.N. Berredjem Karst, L. Cattin, A. Lakhdar-Toumi, A. Godoy, G. Soto, F. Diaz, et al., The open circuit voltage of encapsulated plastic photovoltaic cells, Dyes Pigm. 78 (2008) 148–156.
[62] T. Oku, H. Wakimoto, A. Otsuki, M. Murakami, NiGe-based ohmic contacts to n-type GaAs. I. Effects of in addition, J. Appl. Phys. 75 (1994) 2522–2529.
[63] T. Oku, M. Furumai, C.J. Uchibori, M. Murakami, Formation of WSi-based ohmic contacts to n-type GaAs, Thin Solid Films 300 (1997) 218–222.
[64] A. Nagata, T. Oku, K. Kikuchi, A. Suzuki, Y. Yamasaki, E. Osawa, Fabrication, nanostructures and electronic properties of nanodiamond-based solar cells, Prog. Nat. Sci. 20 (2010) 38–43.
[65] A. Nagata, T. Oku, A. Suzuki, K. Kikuchi, S. Kikuchi, Fabrication and photovoltaic property of diamond:fullerene nanocomposite thin films, J. Ceram. Soc. Jpn. 118 (2010) 1006–1008.
[66] E. Ōsawa, Recent progress and perspectives in single-digit nanodiamond, Diamond Relat. Mater. 16 (2007) 2018–2022.
[67] M.V. Korobova, N.V. Avramenko, A.G. Bogachev, N.V. Rozhkova, E. Osawa, Nanophase of water in nano-diamond gel, J. Phys. Chem. C 111 (2007) 7330–7334.
[68] T. Soga, T. Kokubu, Y. Hayashi, T. Jimbo, Effect of rf power on the photovoltaic properties of boron-doped amorphous carbon/n-type silicon junction fabricated by plasma enhanced chemical vapor deposition, Thin Solid Films 482 (2005) 86–89.
[69] K.M. Krishna, M. Umeno, Y. Nukaya, T. Soga, T. Jimbo, Photovoltaic and spectral photoresponse characteristics of n-*C*/p-*C* n-C/p-C solar cell on a *p*-silicon substrate, Appl. Phys. Lett. 77 (2000) 1472–1474.
[70] T. Oku, K. Kumada, A. Suzuki, K. Kikuchi, Effects of germanium addition to copper phthalocyanine/fullerene-based solar cells, Cent. Eur. J. Eng. 2 (2012) 248–252.
[71] J. Yang, T.Q. Nguyen, Effects of thin film processing on pentacene/$C_{60}$ bilayer solar cell performance, Org. Electron. 8 (2007) 566–574.
[72] T. Oku, T. Nakayama, M. Kuno, Y. Nozue, L.R. Wallenberg, K. Niihara, et al., Formation and photoluminescence of Ge and Si nanoparticles with oxide layers, Mater. Sci. Eng. B B74 (2000) 242–247.
[73] G. Conibeer, M. Green, R. Corkish, Y. Cho, T. Fangsuwannarak, E. Pink, et al., Silicon nanostructures for third generation photovoltaic solar cells, Thin Solid Films 511–512 (2006) 654–662.
[74] A. Martí, N. López, E. Antolín, E. Cánovas, C. Stanley, C. Farmer, et al., Novel semiconductor solar cell structures: the quantum dot intermediate band solar cell, Thin Solid Films 511–512 (2006) 638–644.
[75] S.H. Choi, H. Song, I.K. Park, J.H. Yum, Synthesis of size-controlled CdSe quantum dots and characterization of CdSe–conjugated polymer blends for hybrid solar cells, J. Photochem. Photobiol., A 179 (2006) 135–141.
[76] A.J. Nozik, Quantum dot solar cells, Physica E 14E (2002) 115–120.

[77] P. Brown, P.V. Kamat, Quantum dot solar cells. Electrophoretic deposition of CdSe–$C_{60}$ composite films and capture of photogenerated electrons with $nC_{60}$ cluster shell, J. Am. Chem. Soc. 130 (2008) 8890–8891.
[78] S. Emin, S.P. Singh, L. Han, N. Satoh, A. Islam, Colloidal quantum dot solar cells, Sol. Energy 85 (2011) 1264–1282.
[79] T. Oku, R. Motoyoshi, K. Fujimoto, T. Akiyama, B. Jeyadevan, J. Cuya, Structures and photovoltaic properties of copper oxides/fullerene solar cells, J. Phys. Chem. Solids 72 (2011) 1206–1211.
[80] T. Oku, K. Nomura, A. Suzuki, K. Kikuchi, Effect of perylenetetracarboxylic dianhydride layer as a hole blocking layer on photovoltaic performance of poly-vinylcarbazole:$C_{60}$ bulk heterojunction thin films, Thin Solid Films 520 (2012) 2545–2548.
[81] S. Silence, J. Scott, F. Hache, E. Ginsbrug, P. Jenkner, R. Miller, et al., Poly(silane)-based high-mobility photorefractive polymers, J. Opt. Soc. Am. B10 (1993) 2306–2312.
[82] A. Rybak, J. Jung, W. Ciesielski, J. Ulanski, Photovoltaic effect in novel polysilane with phenothiazine rings and its blends with fullerene, Mater. Sci. Pol. 24 (2006) 527–534.
[83] M. Kakimoto, H. Kashihara, T. Kashiwagi, T. Takiguchi, Visible light photoconduction of poly(disilanyleneoligothienylene)s and doping effect of $C_{60}$, Macromolecules 30 (1997) 7816–7820.
[84] Y. Haga, Y. Harada, Photovoltaic characteristics of phthalocyanine-polysilane composite films, Jpn. J. Appl. Phys. 40 (2001) 855.
[85] A. Watanabe, O. Ito, Photoinduced electron transfer between $C_{60}$ and polysilane studied by laser flash photolysis in the near-IR region, J. Phys. Chem. 98 (1994) 7736–7740.
[86] S. Kim, C. Lee, M.H. Jin, Fourier-transform infrared spectroscopic studies of pristine polysilanes as precursor molecules for the solution deposition of amorphous silicon thin-films, Sol. Energy Mater. Sol. Cells 100 (2012) 61–64.
[87] T. Shimoda, Y. Matsuki, M. Furusawa, T. Aoki, I. Yudasaka, H. Tanaka, et al., Solution-processed silicon films and transistors, Nature 440 (2006) 783–786.
[88] J. Lee, C. Seoul, J. Park, J. Youk, Fullerene/poly(methylphenylsilane) (PMPS) organic photovoltaic cells, Synth. Met. 145 (2004) 11–14.
[89] T. Oku, J. Nakagawa, M. Iwase, A. Kawashima, K. Yoshida, A. Suzuki, et al., Microstructures and photovoltaic properties of polysilane-based solar cells, Jpn. J. Appl. Phys. 52 (2013) 04CR07.
[90] J.Y. Huang, C.Y. Lin, C.-H. Shen, J.-M. Shieh, B.-T. Dai, Low cost high-efficiency amorphous silicon solar cells with improved light-soaking stability, Sol. Energy Mater. Sol. Cells 98 (2012) 277–282.
[91] P. Peumans, S.R. Forrest, Very-high-efficiency double-heterostructure copper phthalocyanine/$C_{60}$ photovoltaic cells, Appl. Phys. Lett. 79 (2001) 126.
[92] L. Li, Q. Tang, H. Li, W. Hu, X. Yang, Z. Shuai, et al., Organic thin-film transistors of phthalocyanines, Pure Appl. Chem. 80 (2008) 2231–2240.
[93] N.M. Bamsey, A.P. Yuen, A.M. Hor, R. Klenkler, J.S. Preston, R.O. Loutfy, Integration of an M-phthalocyanine layer into solution-processed organic photovoltaic cells for improved spectral coverage, Sol. Energy Mater. Sol. Cells 95 (2011) 1970–1973.
[94] N.M. Bamsey, A.P. Yuen, A.M. Hor, R. Klenkler, J.S. Preston, R.O. Loutfy, Heteromorphic chloroindium phthalocyanine films for improved photovoltaic performance, Sol. Energy Mater. Sol. Cells 95 (2011) 2937–2940.

[95] D.Y. Kim, F. So, Y. Gao, Aluminum phthalocyanine chloride/$C_{60}$ organic photovoltaic cells with high open-circuit voltages, Sol. Energy Mater. Sol. Cells 93 (2009) 1688–1691.
[96] S. Honda, S. Yokoya, H. Ohkita, H. Benten, S. Ito, Light-harvesting mechanism in polymer/fullerene/dye ternary blends studied by transient absorption spectroscopy, J. Phys. Chem. C 115 (2011) 11306–11317.
[97] S. Honda, H. Ohkita, H. Benten, S. Ito, Selective dye loading at the heterojunction in polymer/fullerene solar cells, Adv. Energy Mater. 1 (2011) 588–598.
[98] S. Honda, H. Ohkita, H. Benten, S. Ito, Multi-colored dye sensitization of polymer/fullerene bulk heterojunction solar cells, Chem. Commun. 46 (2010) 6596–6598.
[99] T. Oku, S. Nose, K. Yoshida, A. Suzuki, T. Akiyama, Y. Yamasaki, Fabrication and characterization of silicon naphthalocyanine, gallium phthalocyanine and fullerene-based organic solar cells with inverted structures, J. Phys. Conf. Ser. 433 (2013) 012025.
[100] K. Yoshida, T. Oku, A. Suzuki, T. Akiyama, Y. Yamasaki, Fabrication and characterization of PCBM:P3HT bulk heterojunction solar cells doped with germanium phthalocyanine or germanium naphthalocyanine, Mater. Sci. Appl. 2013 (4) (2013) 1–5.
[101] T. Oku, S. Hori, A. Suzuki, T. Akiyama, Y. Yamasaki, Fabrication and characterization of PCBM:P3HT:silicon phthalocyanine bulk heterojunction solar cells with inverted structures, Jpn. J. Appl. Phys. 53 (2014) 05FJ08.
[102] T. Oku, K. Yoshida, A. Suzuki, T. Akiyama, Y. Yamasaki, Fabrication and characterization of PCBM:P3HT bulk heterojunction solar cells doped with silicon naphthalocyanine, Phys. Status Solidi C 10 (2013) 1836–1839.
[103] F.C. Krebs, Air stable polymer photovoltaics based on a process free from vacuum steps and fullerenes, Sol. Energy Mater. Sol. Cells 92 (2008) 715–726.
[104] B. Walker, C. Kim, T.Q. Nguyen, Small molecule solution-processed bulk heterojunction solar cells, Chem. Mater. 23 (2011) 470–482.
[105] H.Y. Lin, W.C. Huang, Y.C. Chen, H.H. Chou, C.Y. Hsu, J.T. Lin, et al., BODIPY dyes with β-conjugation and their applications for high-efficiency inverted small molecule solar cells, Chem. Commun. 48 (2012) 8913–8915.
[106] T. Kuwabara, T. Nakayama, K. Uozumi, T. Yamaguchi, K. Takahashi, Highly durable inverted-type organic solar cell using amorphous titanium oxide as electron collection electrode inserted between ITO and organic layer, Sol. Energy Mater. Sol. Cells 92 (2008) 1476–1482.
[107] A. Takeda, T. Oku, A. Suzuki, T. Akiyama, Y. Yamasaki, Fabrication and characterization of fullerene-based solar cells containing phthalocyanine and naphthalocyanine dimers, Synth. Met. 177 (2013) 48–51.
[108] S.R. Scully, P.B. Armstrong, C. Edder, J.M. Fréchet, M.D. McGehee, Long-range resonant energy transfer for enhanced exciton harvesting for organic solar cells, Adv. Mater. 19 (2007) 2961–2966.
[109] S. Honda, T. Nogami, H. Ohkita, H. Benten, S. Ito, Improvement of the light-harvesting efficiency in polymer/fullerene bulk heterojunction solar cells by interfacial dye modification, ACS Appl. Mater. Interfaces 1 (2009) 804–810.
[110] T. Oku, Structure Analysis of Advanced Nanomaterials, Walter de Gruyter, Berlin, 2014.
[111] A. Kojima, K. Teshima, Y. Shirai, T. Miyasaka, Organometal halide perovskites as visible-light sensitizers for photovoltaic cells, J. Am. Chem. Soc. 131 (2009) 6050–6051.

[112] J.H. Im, C.R. Lee, J.W. Lee, S.W. Park, N.G. Park, 6.5% Efficient perovskite quantum-dot-sensitized solar cell, Nanoscale 3 (2011) 4088–4093.
[113] T. Oku, Y. Ohishi, N. Ueoka, Highly (100)-oriented $CH_3NH_3PbI_3(Cl)$ perovskite solar cells prepared with $NH_4Cl$ using an air blow method, RSC Advances 8 (2018) 10389–10395.
[114] J.-Y. Jeng, Y.-F. Chiang, M.-H. Lee, S.-R. Peng, T.-F. Guo, P. Chen, et al., $CH_3NH_3PbI_3$ perovskite/fullerene planar-heterojunction hybrid solar cells, Adv. Mater. 25 (2013) 3727–3732.
[115] Y. Shao, Z. Xiao, C. Bi, Y. Yuan, J. Huang, Origin and elimination of photocurrent hysteresis by fullerene passivation in $CH_3NH_3PbI_3$ planar heterojunction solar cells, Nat. Commun. 5 (2014) 5784.
[116] Q. Xue, Z. Hu, J. Liu, J. Lin, C. Sun, Z. Chen, et al., Highly efficient fullerene/perovskite planar heterojunction solar cells via cathode modification with an amino-functionalized polymer interlayer, J. Mater. Chem. A 2 (2014) 19598–19603.

# CHAPTER 18

# Metal-assisted chemical etching–based nanostructured silicon solar cells

**Fatima Toor[1], Wenqi Duan[1], Bingtao Gao[1] and Marcie Black[2]**
[1]Electrical and Computer Engineering Department, University of Iowa, Iowa City, IA, United States
[2]Advanced Silicon Group, Lincoln, MA, United States

## Contents



## 18.1 Introduction

Metal-assisted catalyzed etching (MACE)-fabricated nanowires (NWs) provide improved antireflection (AR) and light trapping functionality when compared to the traditional technique of texturing the surface by introducing iso-textured [1] and multimicron scale features [2] and subsequently coating the surface with a dielectric interference coating [such as plasma-enhanced chemical vapor deposited (PECVD) silicon (Si) nitride ($SiN_x$)]. The resulting lower reflection and improved light trapping can

*Nanomaterials for Solar Cell Applications*
DOI: https://doi.org/10.1016/B978-0-12-813337-8.00018-7

lead to higher short circuit currents. In addition, NW cells can have higher fill factors and voltages than traditionally processed cells, leading to increased solar cell efficiency. NW processing also significantly reduces the amount of material removed compared with traditional texturing, which is important for those thin crystalline Si (c-Si) technologies where removal of several microns of Si can be problematic, i.e., removing a significant fraction of a thin device [3]. Eliminating a major step such as PECVD can also help in thin wafer processing where device yield issues are exacerbated. For traditional solar cells, the NW formation process can be one-sided, and so the back surface of the cell can remain flat, providing additional energy conversion efficiency improvement.

## 18.2 Motivation for industrial applications of metal-assisted catalyzed etching–based solar cells

The industry had to overcome several challenges to adopt MACE-based c-Si solar cells, [4] When the technology was first being explored for commercialization one concern, was that the nanostructures generated by the MACE process could not stay intact during the doping process. The nanostructures generated a graded index surface on c-Si surface and turned into a black surface, hence the name, "black Si" (bSi). Based on various research reports [5,6], it has been demonstrated that nanostructures generated on the c-Si surface through the MACE process survive the high temperature diffusion-based doping process needed for emitter formation in solar cells. Therefore nanotexturing can be conducted before diffusion, enabling a shorter and higher throughput diffusing process. If texturing is done before the diffusion process, the diffusion process must span a long time to obtain junction depths that are deep enough for the junction below the nanostructure, after the nanostructure is etched into the silicon. However, if diffusion is done after nanotexturing, the dopants, for example, POCl3, can begin diffusing at the exposed base of the NWs. So the diffusion depth only has to be the desired depth below the NW array. That leads to more standard diffusion times versus diffusion times that can be hours-long if the texture is completed after diffusion. The shorter diffusion time is important to keeping manufacturing costs low. There are many concerns about the small features of the nanotexture increasing the surface area and resulting in an unavoidably high surface recombination, which would negatively impact the solar cell performance. This was resolved with a combination of device design and optimization of the

geometry in the MACE process-based nanostructures [7,8]. Other issues such as screen printing on the nanotexture [9] and using metal without degradation of solar cell performance were also resolved.

Since several key issues were resolved for bSi commercial scale adoption, some leading solar photovoltaic (PV) cell manufacturers have adopted the technology to create high-efficiency PV products. For example, Trina Solar, one of the leading solar cell manufacturers in China, set a new efficiency record April 2016 using bSi solar cells of 23.5% in a large-area, monocrystalline, square silicon wafer that was 156 millimeters in size [10]. Another leading Chinese solar cell producer, GCL System Integration Technology (GCL-SI), improved the peak efficiency of its multicrystalline Si (mc-Si) PERC cells with a bSi texture on diamond-wire-sawn wafers to 21.6% in 2018 [11]. A much wider adoption of bSi is expected in the coming years and more advanced solar cell concepts that incorporate bSi nanotexture will be introduced in the market.

## 18.3 Optical properties

This section contains discussions about how geometry of the NW arrays affect the array's optical reflection, as well as an exploration of light trapping. The silicon nanostructures on the surface of the solar cell act as an AR coating that increases light absorption and sequentially lowers reflection. The specific geometry of the NW array affects both light trapping and the quality of the AR coating. Low reflection due to a nanostructured surface is not challenging to achieve. Research groups have previously demonstrated a spectrum-weighted-average reflectivity ($R_{ave}$) below 0.1%. The challenging part is being able to achieve low surface recombination, which leads to high solar cell efficiency and, low reflection. Very long wires that have small diameters give low reflection and perform poorly in a device. Any light that is absorbed at the wire tips recombine in the NW before reaching the junction and are unable to be collected. However, there are wire geometries that can obtain low reflection and high efficiency in solar cells.

The absorption and reflection as a function of NW length are detailed in this section, along with a focus on the minimum NW length that achieves low reflection, since it is the wire length that will result in the lowest recombination, retaining low reflection. Also discussed are the differences in the mechanisms of bSi and traditional AR layers, and how the different physics involved results in very different optical properties.

Unlike traditional quarter-wavelength $SiN_x$ AR coatings [12], the bSi [13–16] surface exhibits low broadband reflection. Contrary to traditional AR coatings that depend on a certain wavelength and a given angle of incidence for destructive interference, bSi has a graded index of refraction that results in low reflection from wavelengths of the ultraviolet (UV), visible (VIS), to the near-infrared (NIR) regions, relevant to the solar radiation. The NW diameters are smaller than the wavelengths of light and therefore interact with the incident UV–VIS–NIR photons. The incident light experiences an index of refraction that is a composite of the indexes of the refraction of Si nanostructures and surrounding material, such as air. This causes a gradual change in the index of refraction on the bSi surface, as illustrated in Fig. 18.1A. The further the light penetrates into the bSi surface, the higher the percentage of Si present in the nanostructure, leading to a slow varying index of refraction, which can be from that of the surrounding material to that of Si. bSi provides low reflection for incident light at a wide range of angles of incidence and a wide range of wavelengths.

The optical properties of Si NWs can be affected by wire diameter, length, and filling ratio, as well as the periodicity of the Si NW array. There are many groups that have simulated Si NWs' optical properties [17–20]. For example, Lin and Povinelli [17] performed in depth analysis of an optimal partially aperiodic vertical Si NW array using the random walk algorithm to design a structure that maximizes PV absorption, shown in Fig. 18.2. Compared to a periodic structure it was found that aperiodicity provides a dramatic absorption enhancement, improving efficiency 2.35 times.

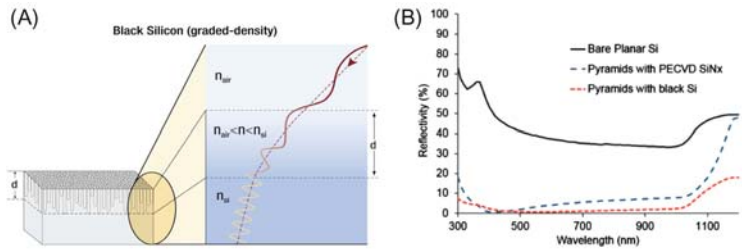


**Figure 18.1** (A) Schematic of the graded index of refraction on the black silicon surface. (B) Reflectivity versus wavelength for bare Si (*solid*), pyramids with PECVD $SiN_x$ coating (*long dashes*), and pyramids with bSi nanostructured bSi coating (*short dashes*). *bSi*, Black silicon; *PECVD*, plasma-enhanced chemical vapor deposited. *Reprinted from F. Toor, et al., Metal assisted catalyzed etched (MACE) black Si: optics and device physics. Nanoscale 8 (34) (2016) 15448–15466.*

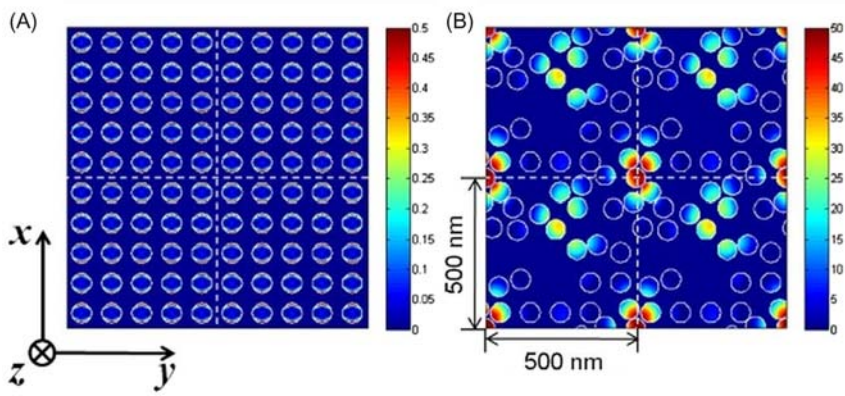


**Figure 18.2** Absorption profile of (A) periodic and (B) optimal aperiodic Si NW structures at a horizontal cross section 0.233 μm below the top surface of the NW array. White dashed lines indicate boundaries between super cells. *Reprinted from C. Lin, M. Povinelli, Optimal design of aperiodic, vertical silicon nanowire structures for photovoltaics, Opt. Express 19 (S5) (2011) 1148—1154.*

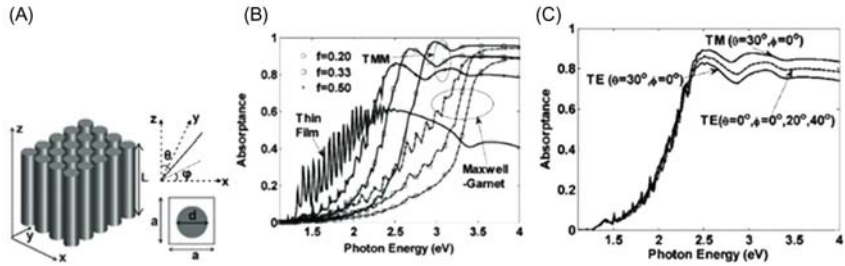


**Figure 18.3** (A) Schematic drawing of the periodic Si NW structure. The parameters are as follows: length *L*, period *a*, and diameter *d*. In the figure, $\theta$ and $\phi$ are the zenith and azimuthal angles, respectively. (B) Absorptance of Si NWs obtained by TMM and Maxwell—Garnet approximation as a function of various filling ratios. (C) Angular dependence on absorptance for an NW structure with $d = 80$ nm, $a = 100$ nm, and $L = 2.33$ μm. The absorptance curves of $\phi = 0$, 20, and 40 degrees are overlapped. *TMM*, Transfer matrix method. *Reprinted from L. Hu, G. Chen, Analysis of optical absorption in silicon nanowire arrays for photovoltaic applications, Nano Lett. 7 (11) (2007) 3249—3252.*

A detailed numerical analysis performed by Hu et al. [21] shows the optical absorption of periodic Si NW arrays based on wire diameter, length, and filling ratio. Those results were then compared to thin Si films. The period NW schematic is shown in Fig. 18.3A. The incoming radiation is defined by the zenith ($\theta$) and azimuthal ($\phi$) angles. The

structure is defined by three parameters: lattice period $a$, wire diameter $d$, and wire length $L$. MACE is able to fabricate NWs with diameters between 50 and 80 nm. That is included in this study. The transfer matrix method (TMM) and the solutions were used to the full wave vector Maxwell's equations to take into account wave effects. TMM is a finite difference frequency domain method; a transfer matrix relates the fields on one side of a unit cell to the other end. The frequency range of interest was 1.1−4 eV since most above-band-gap photons in Si-based materials concentrate in this range. The permittivity of SI shows dispersion in this range.

Compared to thin films analysis found that NW array based solar cells have intrinsic AR effects, increasing short wavelength absorption as shown in Fig. 18.3B. The Maxwell−Garnett approach is invalidated in Fig. 18.3B, since the electromagnetic interaction between NWs is not trivial. NW structures have low broadband reflection without specially designed AR coatings, unlike thin films. The polarization effects of periodic NW arrays were also considered, where the electric field's normal incidence ($\theta = 0$ degree) was polarized along the $x$-axis ($\phi = 0$ degree). The NW structure was almost isotropic for wavelengths of interest in the $xy$ plane since the difference between TE polarized light ($\phi = 0$, 20, 40 degrees) was negligible, as shown in Fig. 18.3C. For an oblique incidence ($\theta = 30$ degrees), TM polarization has an electric field component along the wire axis, facilitating absorption. Thus TM polarization has higher absorption than TE polarization in this case. This shows that NWs have high broadband, wide-angle absorption and are polarization insensitive within VIS wavelengths.

### 18.3.1 Fill fraction versus optical properties of Si nanowires

The term "fill fraction" refers to the Si NW array density. The percentage of the area covered by Si is measured by using a top view scanning electron microscope (SEM) image of the NW array. The light is reflected when the index of refraction changes in the direction of light propagation. Therefore in order to achieve high solar cell performance, the NW array geometry must be optimized. In this case, light can be reflected off the top surface and base of the NW arrays. If an array is too dense (high fill fraction), it causes light to reflect off the NW array−air interface because the change in index of refraction of the two materials is too significant. If an array is too sparse (low fill fraction), it means the light reflects off the

base of the array due to the large change in index of refraction at the transition from NW to Si. Optimal NW density for low reflection can be found for a specific NW length, roughness, and wire tapering.

Varying the fill fraction of the array can be done by adjusting the MACE process. The SEM images of the top surface of three samples with different FFs are shown in Fig. 18.4A. The reflection spectra as a function of wavelength of the three samples are shown in Fig. 18.4B. Fig. 18.4C shows the spectra weighted reflection average of 8 samples of varying FF. Initially, with increasing fill fraction, the reflection decreases, but at a fill fraction of about 32% the reflection starts to increase. A fill fraction of 32% exhibits the lowest reflection for this NW geometry. The reflection profile of the 32% fill fraction sample in Fig. 18.4B shows that there is low broadband reflection for all wavelengths, meaning minimal light is

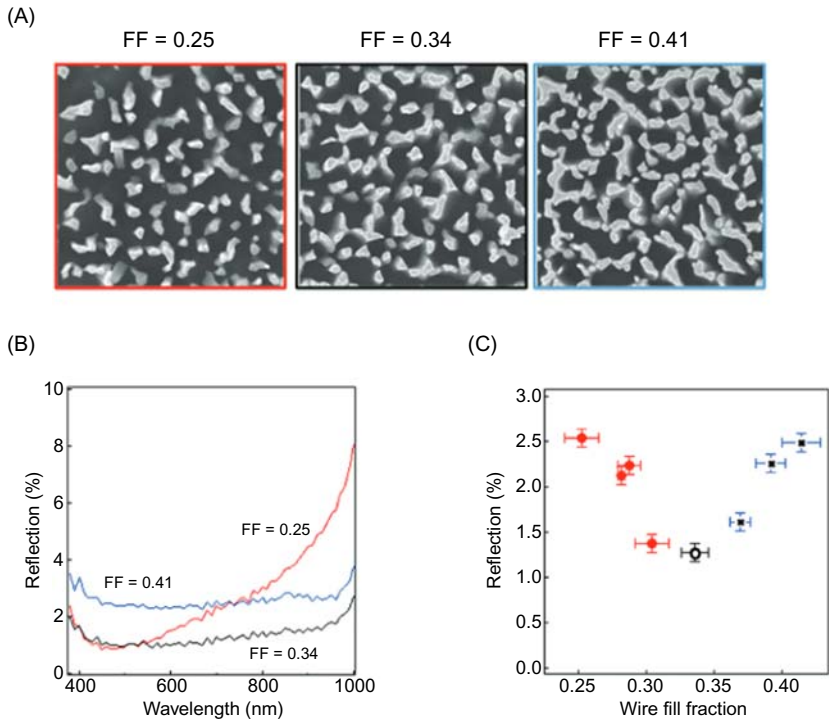


**Figure 18.4** (A) Top surface SEM images of three NW arrays with fill fraction (FF) of 0.25, 0.34, and 0.41; (B) reflection profiles of the three NWs with FF of 0.25, 0.34, and 0.41; and (C) spectrum weighted reflection versus FF. *SEM*, Scanning electron microscope; *FF*, fill fraction. *Reprinted from F. Toor, et al., Metal assisted catalyzed etched (MACE) black Si: optics and device physics. Nanoscale 8 (34) (2016) 15448–15466.*

reflected at each wavelength. Fill fraction of 25% shows reflection high in the IR wavelengths. In this case, light reflects off the base of the NWs with minimal reflection off the front. For the 41% fill fraction sample, there is relatively high reflection across the spectrum, meaning incident light sees a large change in the index of refraction when entering the NW array [5]. Therefore all wavelengths are reflected from the air−Si NW interface.

### 18.3.2 Geometric optics of multiscale textured black Si

The most common front-surface texture in c-Si solar cells is a micron-scale pyramid texture obtained by utilizing alkaline anisotropic etching [1], which is then covered with vacuum-deposited dielectric silicon nitride ($SiN_x$) AR coating. Etching bSi nanotextures on pyramid textured c-Si surfaces is one technique researchers are using to obtain extremely low reflection (~1.5%) without utilizing a vacuum-deposited AR coating. Toor et al. [22] measured a dramatic decrease in reflection after etching nanopores on top of pyramids on c-Si surfaces. The geometrical optics effect of multiscale textured bSi surface is shown in Fig. 18.5A. The light absorption was enhanced due to the incident light bouncing multiple times on the surface. For varying bSi etch times on both planar and pyramid textured surfaces, the $R_{ave}$ was calculated from 350 to 1000 nm, as shown in Fig. 18.5B. As shown on the plot, with a planar surface, at least 3 minutes of etching time is needed to reach a $R_{ave}$ value below 2%. After 3 minutes of etching, the density grade depth $d$ is approximately 250 nm. For a pyramid textured surface, 1.5 minutes of etching is required

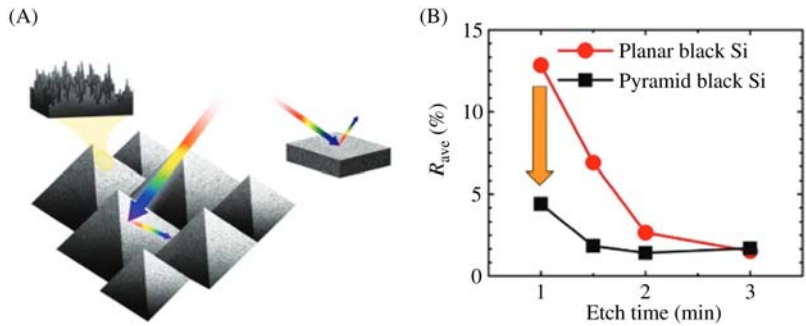


**Figure 18.5** (A) Schematic of the geometrical optics of nanostructured black Si surfaces etched on microtextured pyramids versus planar surface, where the pyramid enhances solar light absorption due to the two bounces of the incident light. (B) $R_{ave}$ (%) versus different etch times for planar and the pyramid textured black Si.

to reach a $R_{ave}$ of 1.8%, which had $d \sim 100$ nm. After 2 minutes of etching, the $R_{ave}$ is 1.4% and $d \sim 150$ nm. Therefore multiscale textured Si showed low reflectivity even at a much smaller nanoporous layer depth, compared to a planar surface.

Lee et al. [23] investigated how NWs etched into pyramid textured Si surfaces affected the power-conversion efficiency (PCE). Solar cells based on nine different NW etching times (0, 1, 2, 3, 4, 5, 7, 10, and 15 minutes) were fabricated and the performance of each cell was tested. The short circuit current density ($J_{sc}$), open circuit voltage ($V_{oc}$), fill factor and PCE were compared to find the optimal etching time for the highest performing cell. The surface morphologies after etching are shown on the cross section and surface view SEM images in Fig. 18.6. Research shows that when the etching time was longer than 10 minutes, the NWs tended to collapse, as shown in Fig. 18.6H and I. A maximum PCE of 15.39% was achieved at 2 minutes of electroless etching time. Without NW,

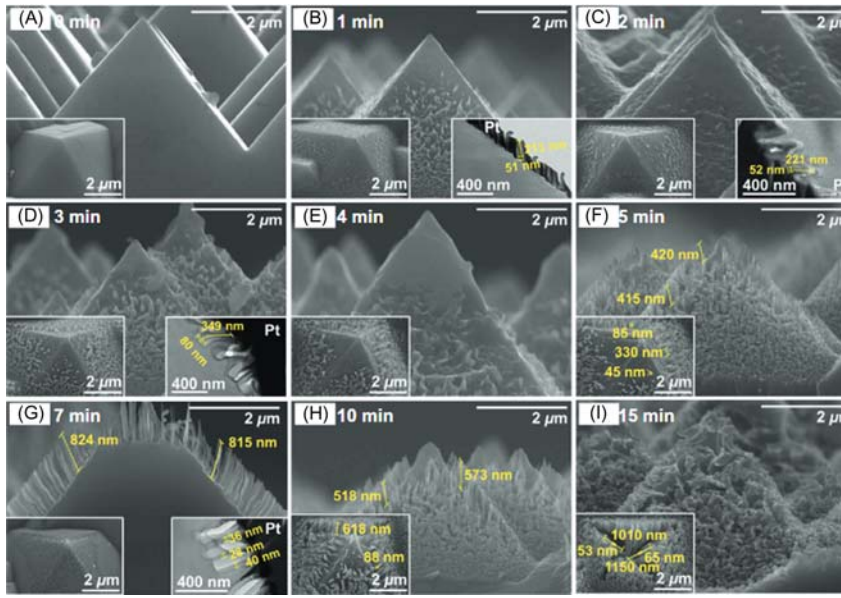


**Figure 18.6** The surface morphology of silicon nanowires on pyramid textured silicon surface depending on electroless etching time: (A) 0 min, (B) 1 min, (C) 2 min, (D) 3 min, (E) 4 min, (F) 5 min, (G) 7 min, (H) 10 min, and (I) 15 min. *Reprinted from F. Toor, et al., Metal assisted catalyzed etched (MACE) black Si: optics and device physics. Nanoscale 8 (34) (2016) 15448–15466; I.J. Lee, U. Paik, J.G. Park, Solar cell implemented with silicon nanowires on pyramid-texture silicon surface, Solar Energy 91 (2013) 256–262.*

another sample pyramid textured solar cell had a PCE of 14.00%. The 2 minutes etch produced NWs around 52 nm in diameter and 221 nm in height. When the pyramids were etched for a longer time, all elements of PV performance decreased due to the rapidly decreasing effective minority carrier recombination lifetime.

### 18.3.3 Light trapping

Presently, c-Si dominates the solar cell market and yields the highest efficiency single junction solar cells, however, c-Si wafers have poor absorption, limiting efficiency, and are not ideal for thin film solar cells. To address this issue, different light trapping methods are the focus in attaining thin film high-efficiency c-Si solar cells. Light trapping is the effect of an increase in optical path length inside a device so that a photon incident on a solar cell can bounce around many times before escaping the cell, creating a higher probability of being absorbed to contribute to electricity production. Traditional c-Si devices achieve light trapping generally by etching pyramids on the Si surface. Compared to flat surfaces, ideally rough surface optical path length can be enhanced up to $4n^2$ times, where $n$ is the index of refraction. The limit is known as the Lambertian limit. Therefore for Si, which has a refractive index $n \sim 3.5$, the path length can be increased by approximately 50 times, compared to a flat Si surface. Many researchers have experimented with light trapping using various nanostructures on the Si surface to enhance light absorption [3,5,24].

Han and Chen [25] used group theory to optimize the design of three nanostructures (pyramids, skewed pyramids, and nanorods), in order to achieve the highest possible absorptance at normal incidence and averaged over all directions of incidence over a broad wavelength range. The optical absorption of optimized pyramid textured, skewed pyramid textured, and nanorod textured Si surfaces are contained in Fig. 18.7A–C respectively. Averaged over all directions of incidence, this demonstrated that nanorods with nonsymmetric tapered tops exhibit absorptance close to the Lambertian limit.

Toor et al. [5] measured combined absorption of 1 μm long NWs on a 3 μm thick Si wafer, shown as the black line in Fig. 18.8. A range of possible absorption coefficients is shown in the shaded region. The lower limit represents single-pass absorptance. The upper limit is the Lambertian limit. Regarding the calculations, it is assumed that no reflection is from the front surface and calculated using the bulk Si thickness plus the NW

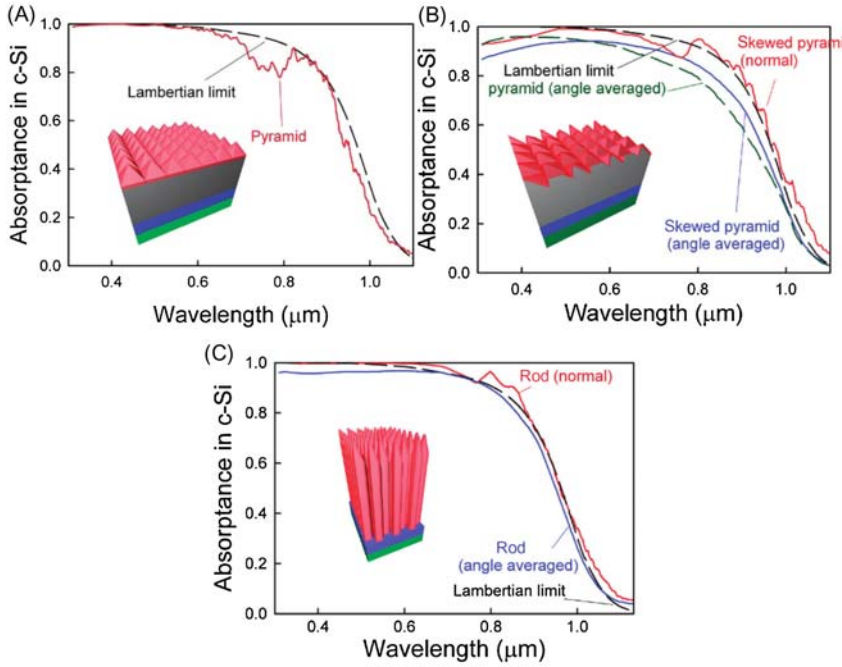


**Figure 18.7** (A) Absorptance of a pyramid structure. A *solid line* represents absorptance of a pyramid structure. The base of the pyramid has a height and length of 566 and 800 nm, respectively. There is a layer of 90 nm thick $Si_3N_4$ (*solid*) coated on the pyramids. The c-Si film thickness is 2.012 μm and a $SiO_2$ layer of 717 nm thickness is placed between the Si and the Ag back reflector at the bottom. (B) Absorptance of a skewed pyramid structure at normal incidence is shown (*solid line*) and averaged over all directions of incidence (*solid line*). Angle-averaged absorptance of the pyramid structure (A) is also shown (*dashed line*). The skewed pyramid height and the longer side of its base are 636 and 900 nm, respectively. The 90 nm $Si_3N_4$ layer is coated on the skewed pyramids. The c-Si film thickness is 2.012 μm and a $SiO_2$ layer of thickness 741 nm is placed between the Si and the Ag back reflector. (C) Absorptance of the nanorod structure with skewed pyramids on top shown at normal incidence (*solid line*) and averaged over all directions of incidence (*solid line*). The pyramid height and the longer side of the base are 1125 and 450 nm, respectively. The length of the rod of the rectangular cross section is 6.508 μm. A 90 nm $Si_3N_4$ layer (red) is coated on the tapered rods. A layer of $SiO_2$ with a thickness of 953 nm is placed between the Si rod and the Ag back reflector. The equivalent film thickness is 1.768 μm. The spectrum was averaged over $\Delta\lambda/\lambda^2 \sim 0.05\ \mu m^{-1}$ in order to smooth out the narrow peaks. The *dashed line* represents the Lambertian limit of a c-Si film of equal thickness. *Reprinted from S.E. Han, G. Chen, Toward the Lambertian limit of light trapping in thin nanostructured silicon solar cells, Nano Lett 10 (11) (2010) 4692–4696.*

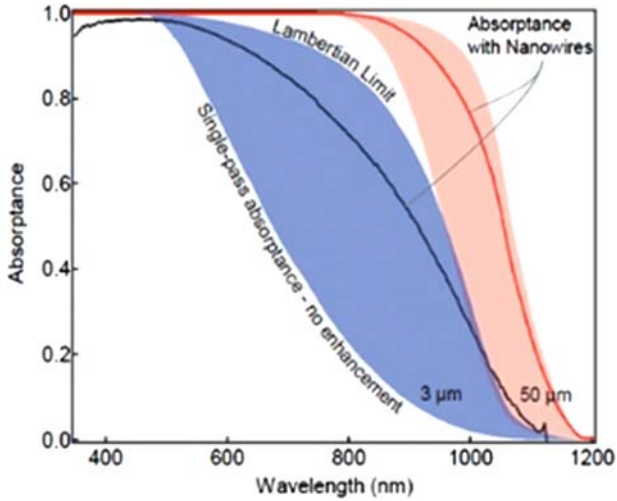


**Figure 18.8** Absorptance as a function of wavelength of incident light. Absorption enhancement of the NWs on 3 μm thick Si wafer (measured, *black line*) and 50 μm Si [extrapolated, *red line* (gray line in print version)]. *Reprinted from F. Toor, et al., Metal assisted catalyzed etched (MACE) black Si: optics and device physics. Nanoscale 8 (34) (2016) 15448–15466.*

length. The Si refractive index was used to define the NW region, but in reality the NW region should have a smaller refractive index due to the etched region having both air and Si. Both of these assumptions will give the largest absorptance possible for the Lambertian limit. Since the absorptance exceeds the Lambertian limit close to the bandgap, the NW etched Si surface has excellent light trapping properties. Extrapolating from the 3 μm data, the absorptance for 1 μm long NWs on a 50 μm thick Si wafer is estimated. Due to the large absorption values, the IR response is better, and essential for thin c-Si solar cells.

## 18.4 Device design

The benefit of the excellent optical properties of NWs is clear, but the electrical performance of NW based c-Si solar cells can suffer because of high recombination induced by the nanostructures, and without careful design can lead to a significant drop in solar cell performance. The increased surface area of Si NWs relative to planar Si is the main reason for shorter carrier lifetime right in and slightly below the surface of the NWs. Recent studies have shown that with appropriate device designs, it

is possible to take advantage of the low surface reflection, as well as maintain the carrier lifetime at an acceptable level for NW Si solar cells.

### 18.4.1 Trade-off between blue light quantum efficiency and reflection

NW solar cells have a high absorption of light. A high performance solar cell also requires a high portion of light generated carriers to be collected before recombination. One inherent property of high-surface-area NW textures is the high ratio of dangling bonds that are on the surface. Since many of the photogenerated excess carriers are closer to the surface of the nanotexture than to the p–n junction which resides in the bulk and collects carriers, some of the photogenerated carriers recombine on the surface before being collected as current. In addition, during doping, the entire surface of the NWs contacts the dopant atmosphere ($POCl_3$, for example, for phosphorous doping) and the wires end up being heavily doped. Heavy doping leads to higher recombination because of Auger recombination. As a result, the excess carriers in NWs are further hindered from being collected in the region. If the metal leftover during MACE is not cleaned thoroughly, it sits in the bottom of the NWs and could diffuse into the bulk in the following diffusion and firing processing. So, if the standard fabrication process for planar solar cells is used for NW solar cells, it will result in low open circuit voltage ($V_{oc}$), low short circuit current density ($J_{sc}$), and low overall efficiency of the cells.

Blue light cannot penetrate deep into the bulk of Si, which means that most of the blue light is absorbed in the NWs as shown in Fig. 18.9A. Since the NWs can have a high recombination rate, the quantum efficiency of the NW solar cells can be low in the short wavelength region, usually $<600$ nm. Shown in Fig. 18.9B is the internal quantum efficiency (IQE) in terms of wavelength of a planar solar cell and an NW solar cell that is suffering from high surface recombination. The poor blue response corresponds to a noneffective collection of photocarriers on or near the surface. Since the NWs not only absorb blue light, but also some parts of longer wavelength light, the nanotextured solar cell has an overall suppressed IQE of 350–800 nm, compared to the solar cell with a planar front surface.

In order to make high-efficiency nanotextured solar cells, the trade-off between low reflection, higher surface area, and Auger recombination velocity has to be understood and balanced thoroughly [14]. By sacrificing extremely low reflection and carefully adjusting the fabrication process for

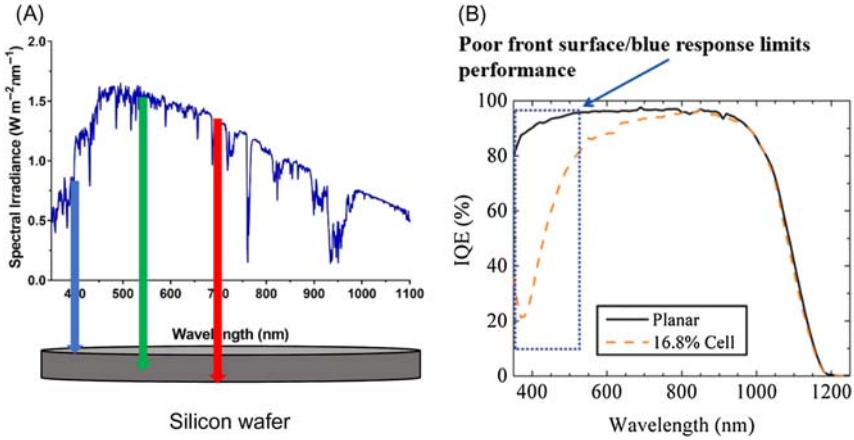


**Figure 18.9** (A) Schematic of the highest absorption areas of light with different wavelengths, where the short wavelength (300–450 nm) light is absorbed near the front surface. (B) The IQE spectra of a solar cell with a planar front surface and a 16.8% efficiency nanotextured cell with high front-surface recombination. *IQE*, Internal quantum efficiency.

best performance, it is possible to make nanostructured solar cells that perform better than standard cells.

## 18.4.2 Minimizing surface area

High surface recombination is a byproduct of large surface area solar cells. Therefore the first step to make high-efficiency solar cells is to make the surface area as small as possible. The surface area of NWs can be reduced by decreasing the NW length, density, and diameter. Surface roughness and taper can also affect the surface area of the NW array. The change of nanostructure morphology is not trivial, since it usually involves modification of the recipe composition or additional treatment. The most commonly used method for surface area reduction is to create shorter NW arrays. Decreasing the NW length linearly reduces the surface area and recombination. As NW length reaches the wavelength of light, decreasing the NW length inevitably decreases the thickness of the graded index layer and weakens the light trapping property. However, it is possible to minimize the surface area of the nanostructure keep relatively low reflection.

Shorter NW arrays can be achieved by modifying the black etch or by performing postetch processing. During the etch, the NW length can be shortened by decreasing the thickness of plated metal, etchant

concentration, etch time, ambient temperature, or by changing the source of $O_2$. The length of the NWs generally has a linear dependence on etch time, but insufficient etch time could change the morphology of the nanostructure. There is an optimal etch time where the expected nanostructure and reflectivity can be maintained while the surface area is kept minimum. Once the nanostructures are made, they can still be affected by the following processing steps. For example, a phosphorous doping using Ammonium dihydrogen phosphate ($NH_4H_2PO_4$: ADP) as source can be conducted after etching to form a highly n-doped emitter on the slightly p-doped Si wafer. However, the standard spin on dopant processing can largely damage the delicate NWs as shown in Fig. 18.10A and B. A more protective proximity doping method can be used to preserve the nanostructure, producing only a 10% length decrease and slight curling of NWs as shown in Fig. 18.10C and D [26]. Decrease in length is attributed to the removal of phosphosilicate glass that is generated by firing the mixture of Si and ADP on the surface.

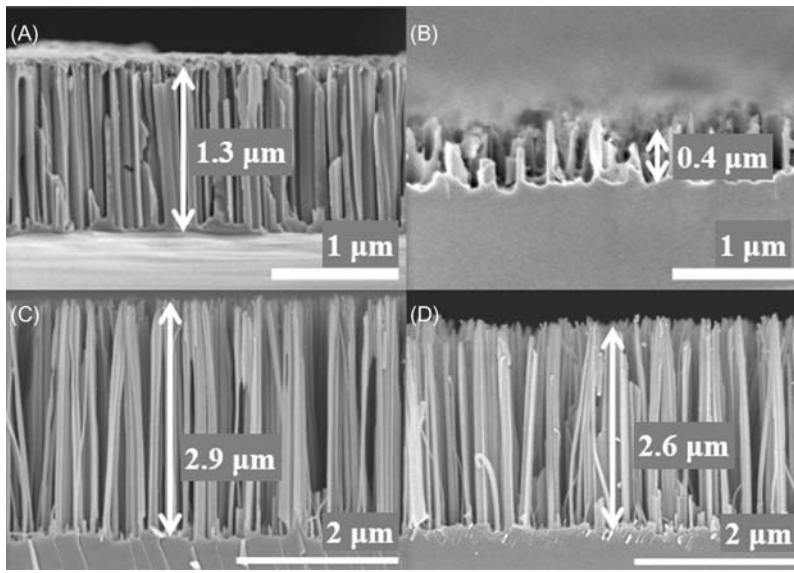


**Figure 18.10** The effect of different emitter doping methods on length of NW arrays, indicated by cross-sectional SEM images of black silicon before (A) and after (B) SOD processing, and before (A) and after (B) proximity doping. *SEM*, Scanning electron microscope; *SOD*, spin on dopant. *Reprinted from W. Duan, et al., Performance enhancement techniques for the front and back of nanostructured "black silicon" solar cells, SPIE J. Photon Energy 8 (2018) 11.*

Fig. 18.11A shows an example of thickness of nanoporous layer ($d_E$) as a function of black etch time and processed solar cell samples ($d_{SC}$) [22]. After the solar cell fabrication steps, the depth of nanopores $d_{SC}$ decreases about one-third of its as-etched value $d_E$, which is mainly due to the consumption of Si during thermal oxidation. Although the thickness is linearly dependent on etch time, the larger error bars for $d_{SC}$ values than $d_E$ indicate that the consequent thickness reduction varies from pore to pore. The optical and electrical performance of solar cells is only related to the nanostructures after the final step, so only the final nanostructure geometry matters. Presented in Fig. 18.11B, IQE (electrons collected per photon absorbed) of the black Si solar cells as well as the planar black Si control; the Fig. 18.11B inset plots the IQE at 450 nm versus black etch time. The IQE spectra shows that the blue response improves linearly as the black etch time and nanoporous layer depth decrease, indicating that nanostructures are important for surface recombination. Ref. [14] shows that the best fit by PC1D [27] simulation to the black Si IQE data are obtained by representing the nanostructured zone as an electrically "dead layer" of thickness, $d_{PC1D}$. The representative dead layer thickness shown in Fig. 18.11B, $d_{PC1D}$, is thicker than $d_{SC}$ but thinner than $d_E$. The following two factors may contribute to the nanoporous layer acting as a

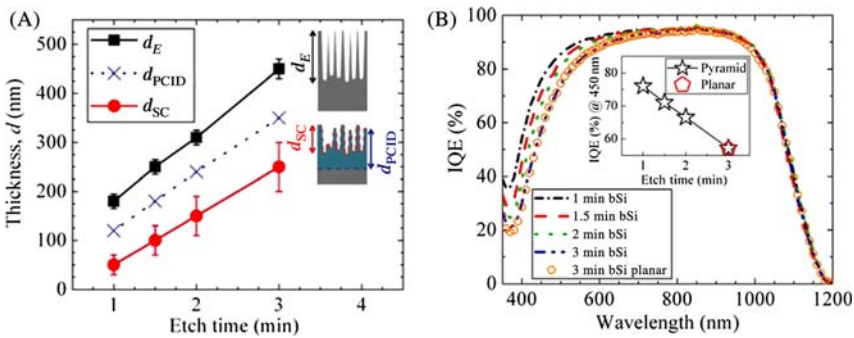


**Figure 18.11** (A) The thickness $d$ of the nanoporous layer as a function of black etch time, for as-etched, $d_E$ (*square*), processed solar cell, $d_{SC}$ (*circle*), and the electrically "dead" layer thickness as predicted by the PC1D solar cell simulation software, $d_{PC1D}$ (*cross*). The insert shows a schematic depiction of the effect of solar cell processing on the nanoporous layer. (B) IQE spectrum of black Si solar cells for different black etch times on pyramids compared to a 3 min black etched planar solar cell. The inset shows IQE at 450 nm as a function of black etch time. *IQE*, Internal quantum efficiency. *Reprinted from F. Toor, et al., Multi-scale surface texture to improve blue response of nanoporous black silicon solar cells, Appl. Phys. Lett. 99 (10) (2011) 103501.*

recombination active layer with no PV response in the black Si cells: (1) surface recombination due to the high surface area of the nanoporous layer and (2) Auger recombination due to heavy emitter doping which is caused by heavy in-diffusion of phosphorus from the high nanostructured surface area. Shallower nanopores reduce both the surface and Auger recombination to dramatically improve the blue response in thinner black Si layers. While black etching shorter nanopores is easy, preserving superior optical and electrical properties for the processed solar cell is challenging. A solar cell must be designed by the final performance of solar cell, rather than the figures of merit in each step. The optimal process flow must be adjusted when there are changes in processing methods, equipment, sequence, and even environment. Simulations can guide the development; however, finding the best nanopore geometry can only be optimized with experience, trial and error.

### 18.4.3 Junction placement

Black et al. [28] reported that in addition to optimizing the length of the NWs, high-efficiency NW, solar cells require that the pn junction is *below* the base of the nanotexture in bulk Si. This separates the depletion region where recombination is enhanced, from potential defects at the surface of the NW. Both electrons and holes are present in large concentrations in the depletion region, and so recombination centers are especially effective here [28]. Placing the junction below the NWs also reduces the total area of the junction, reducing the dark current, and improving device performance.

Many researchers are looking at radial junctions, in order to take advantage of the short distance that carriers need to travel to the junction in this device design [29]. The devices have the potential to capture hot carriers and have efficiencies above the traditionally used single bandgap limit. However, since the junction area of the devices is large, in order for the design to result in a high-efficiency cell, the junction needs to be high quality. Currently, it is not possible to make high quality radial junctions in manufacturing. For this research a concentration is placed on device designs that have the junction below the NWs.

Since the junction should be below the NW array, the junction needs to be formed either after the NW formation, or be deep enough so the NWs can be etched into the surface without the etch reaching the junction. The challenge with forming a junction prior to etching the NW is that the time in the diffusion furnace to form the junction increases as the

square of the junction depth. For deep junctions, the throughput of the cell process is limited by the diffusion process to form the junction. When the junction is formed post-NW formation, the dopant diffuses between the NWs and dopes the exposed uneven surface at the base of the NW array. Doping after the NW formation requires doping diffusion times comparable to those used in the standard process. However, when the NWs are formed prior to the diffusion, the wafers need to be cleaned to ensure that metal is not being driven into the cell. This research has found that the procedure for using a metal etch, combined with a preclean process prior to the dopant diffusion, was sufficient to remove the metallic impurities used in the MACE process. Most researchers and bSi solar cell manufacturers now form the NWs prior to diffusion doping [14,30–32].

### 18.4.4 Surface passivation

A good surface passivation is crucial to obtain high-efficiency solar cells with or without nanostructures. The abrupt change of lattice period at the interface causes the formation of dangling bonds, serving as a site for free carriers to recombine. Meanwhile, the highly doped nanotextured region represents an electrically "dead layer" that cannot participate in carrier collection due to its low lifetime [14]. An effective surface passivation is required for nanostructured solar cells. By passivating the surface of the cell, the surface recombination velocity (SRV) is minimized in many ways. The amount of dangling bonds on the surface can be reduced by a forming gas anneal or dielectric layer growth like thermal grown silicon dioxide ($SiO_2$), plasma-enhanced chemical vapor deposited (PECVD) $SiN_x$, and atomic-layer-deposited (ALD) aluminum oxide ($Al_2O_3$). These surface layers allow dangling bonds to connect with either H atoms or other dielectric molecules. That reduces the surfaces' effectiveness by serving as a recombination site and electrically passivates the surface. The Auger recombination on the highly doped surface can be mitigated by lowering the doping level or by removing the corresponding volume of heavily doped silicon. Alternatively, an even higher doped region can be formed on the surface, so that a high–low junction is formed where the minority carriers are repelled from the surface.

Generally, higher doping levels correspond to a higher recombination velocity. A proper doping level is needed for junction formation, especially for NW solar cells, the doping concentration in NWs is a very important parameter. So, it is critical to measure the surface doping of the

solar cell and optimize it. A commonly used but indirect measurement is the emitter sheet resistance, which is a single parameter that provides an overall characterization of the cell as a function of doping concentration and junction depth. The basic assumption for validating four-point-probe sheet resistance measurement is that the current path between each neighboring probe is the same. This condition no longer holds true for nanostructured solar cells since the textures cannot be periodic for broadband low reflectivity. Some other more expensive and time-consuming methods, including secondary ion mass spectroscopy and spreading resistance profiling, can measure the doping profile in terms of depth, but are not applicable to all types of nanotextures (especially NW arrays). An estimation can be made by measuring doping profiles of sister samples that have been through the same processing, but without a nanotexture. Sheet resistance can also be measured on the backside of the nanostructured cell if the Si wafer is double-side polished and no metal exists on both sides.

In order to lower the doping level of the surface, an extra etching step can be utilized after emitter doping to remove the highly doped layer on the top. This etch can be done by dipping the cell in an alkaline solution like potassium hydroxide (KOH). Tetramethylammonium hydroxide (TMAH) is another option in which iron oxide particle residue, in connection with the KOH etching, are avoided on the Si surface [33]. Reflection increase is expected after the TMAH etching, but the nanostructured solar cell with comparable effective lifetime ($\tau_{eff}$) to polished solar cells can be fabricated. That was the method used in this research and cells with an overall efficiency of 18.2% without the standard PECVD $SiN_x$ AR coating was achieved [34]. Standard passivation dielectrics for traditional solar cells like PECVD $SiN_x$, $SiO_2$, and ALD $Al_2O_3$ can still be used to passivate the surface of NW solar cells. Jura et al. [7] reported that an NW solar cell fabricated by conventional processing, including using PECVD $SiN_x$ as passivation and AR layer, results in a 0.4% efficiency improvement when compared to standard multicrystalline cells. A comparison of carrier lifetime as a function of carrier concentration between polished Si and an ALD $Al_2O_3$ passivated NW solar cell is shown in Fig. 18.12 [35]. The NWs are etched on one side of the double-side polished, 1–5 Ω cm p-type 280 μm thick float zone Si wafer, and both sides are passivated. The minority carrier lifetime is ~500 μs at an injection level of $10^{15}$ $cm^{-3}$, which corresponds to SRV < 53 cm $s^{-1}$ at the bottom of NWs. Jura et al. approximate in [7] that the SRV at the same interface of the conventionally processed NW cells is ~ 49 cm $s^{-1}$.

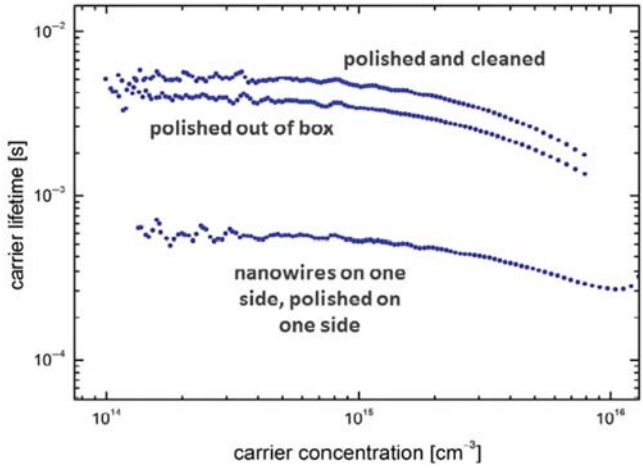


**Figure 18.12** Minority carrier lifetime versus carrier concentration for a polished uncleaned wafer, a polished cleaned wafer, and an NW silicon wafer with both sides passive by $Al_2O_3$ using a Levitech ALD tool. *ALD*, Atomic-layer-deposited. *Reprinted from F. Toor, et al., Metal assisted catalyzed etched (MACE) black Si: optics and device physics. Nanoscale 8 (34) (2016) 15448–15466.*

### 18.4.5 Contacting nanowires

The NW solar cells can be contacted via conventional contacting methods including screen printing and electroplating. Screen printing is robust, cheap, and with high throughput, it is recognized as a commonly used industrial metallization technique. Electroplating is an alternative to screen plating, but since it usually involves photolithography or laser patterning as a pretreatment for $SiN_x$ removal, its cost and complexity are increased, and the application is limited.

Due to special morphology, screen printing is expected to have difficulties on nanostructured surface. Fragile NWs are easily broken when the squeegee moves across the surface to remove the excess paste, or consumed during the firing processing to evaporate the organic materials, similar to what happens during doping in Fig. 18.10. Some research groups have made nanotextured solar cells that suffered from high series resistance and low shunt resistance because the emitter was shorted by the Ag paste [36]. However, recent studies have successfully shown that higher fill factors, higher sheet resistance, and higher efficiency over conventional solar cells can be achieved using standard screen printing processing [9]. The two opposite results in Refs. [36,9] are the consequences of different NW length and shape of those nanostructures, where the success in

Ref. [9] has fabricated solar cells with shorter and more rigid NWs (from 150 to 450 nm) than the single micron NWs in [36]. The structural strength can be enhanced with denser and shorter NWs, so that the nanostructures can survive through the mechanical and thermal stresses of the screen printing process.

Meanwhile, the formation process of contact on nanotextures must be fully understood before effective improvements can be made. During the firing of the metal paste, the metal fingers form a glass layer as well. Therefore the current is flowing from the emitter to contact through the glass layer by tunneling effect and contact conductivity is affected. Generally, the thinner the glass layer and the larger the concentration of metal atoms inside the glass, the lower the contact resistivity. Cabrera et al. [37] studied the surface topography dependence of contact formation of screen-printed Ag, where the contact conductance and the fill factor can be kept sufficiently high if the pyramid-like texture is sharp and high enough to poke through the glass layer and form a direct contact with Ag, as shown in Fig. 18.13. The dopant level and pyramid height are also impacting factors on contact performance, but a good contact can still be achieved without high doping and height after the direct contact between the metal (Fig. 18.13B and C) and Si has been achieved [37].

As previously stated, the contact conductivity can be enhanced by the NW arrays, which can improve the performance of the solar cells. Toor et al. [5] reported an example of NWs higher than the glass layer, as shown in Fig. 18.14A. The Ag crystallites can still be found at the tip of NWs when the finger is removed in Fig. 18.14B, indicating a strong adhesion of Ag on Si. More quantitative works must be done to optimize the contact resistance. Since the goal is to make the best results for fabricated solar cells after all steps are completed, the doping profile and other parameters must be adjusted together with contacting to get the best performance.

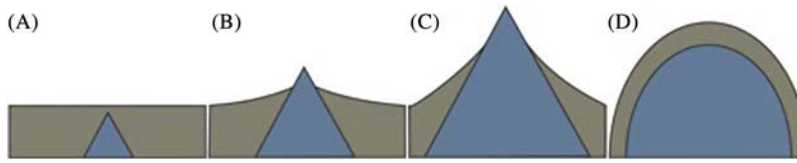


**Figure 18.13** A schematic of glass layer distribution of screen-printed Ag contact on pyramid-like nanotextured silicon surface for different surface topographies including sharp pyramids (A) lower, (B) just above, and (C) further higher than thickness of glass, and a rounded pyramid. *Reprinted from E. Cabrera, et al., Influence of surface topography on the glass coverage in the contact formation of silver screen-printed Si solar cells, IEEE J. Photovolt. 3(1) (2013) 102–107.*

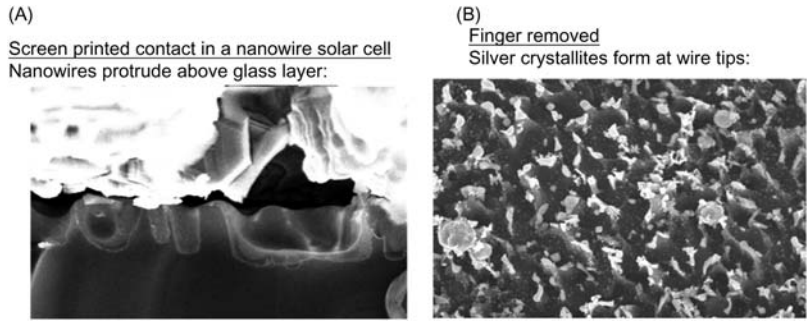


**Figure 18.14** SEM images (A) showing that the NWs are protruding from the glass and probably contacting the Ag directly; (B) after Ag fingers being removed, indicating that the Ag crystallites are strongly adhering on the tips of NWs. *SEM*, Scanning electron microscope. *Reprinted from F. Toor, et al., Metal assisted catalyzed etched (MACE) black Si: optics and device physics, Nanoscale 8 (34) (2016) 15448–15466.*

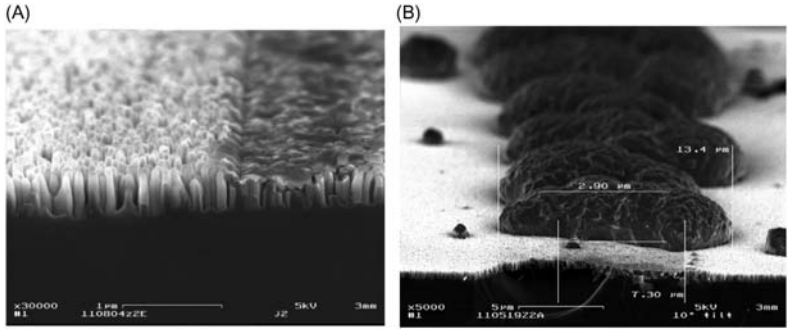


**Figure 18.15** Cross-sectional SEM images showing that (A) an area of $Al_2O_3$ coated Si has been removed by a metal comb and (B) a continuous line of Cu has been electroplated on the exposed Si. *SEM*, Scanning electron microscope. *Reprinted from M.R. Black, et al., US8852981B2: Electrical Contacts to Nanostructured Areas, Advanced Silicon Group Inc., 2014.*

Electroplating is another important contacting method for NW solar cells, and is employed by several groups [38–40]. The standard electroplating process includes the removal of dielectric passivation layer, deposition of seed metal like nickel (Ni) or copper (Cu), and the electroplating of metal contact fingers, usually made of Ag. The width of fingers in the method can be as thin as 25–50 μm so that the shading losses of electroplated contact are less than those of the screen-printed contact. In order to reduce processing cost and complexity, another contacting method that does not use photolithography has been developed by Black et al. [41], where the tips of NWs and the coated $Al_2O_3$ passivation layer are removed with a metal comb, as seen in Fig. 18.15A. The remaining part

of NWs and bulk Si are exposed so that the seed metal can be electroplated directly onto them. The continuous Cu metal line is generated, as shown in Fig. 18.15B.

### 18.4.6 Nanowire solar cell efficiency results

Designed properly, solar cells with nanotextures, NWs, or bSi can exhibit higher efficiency than their standard process solar cell counterparts. The current record bSi solar cell fabricated by Savin et al. [16] has 22.1% efficiency and uses cryogenic deep reactive ion etching (RIE) to form the nanostructured Si surface and interdigitated back contact cell design. A 17.9% mc-Si NW solar cell using RIE was fabricated by Chen et al. [42]. Table 18.1 contains a compiled list of high solar cell efficiency measurements achieved utilizing the MACE process to create a nanostructured

**Table 18.1** Efficiencies of solar cells fabricated using the MACE process with Ag, Au, and Cu metal catalysts.

| Author(s) | Metal catalyst | Substrate types | $J_{sc}$ (mA cm$^{-2}$) | $V_{oc}$ (mV) | FF (%) | $\eta$ (%) |
|---|---|---|---|---|---|---|
| Jin et al. [43] | Ag | DWS mc-Si 243.36 cm$^2$ | 39.2 | 667 | 79.1 | 20.7 |
| Zhang et al. [44] | Ag | DWS p-Si (100) 243.36 cm$^2$ | 38.5 | 647 | 80.9 | 20.2 |
| Irishika et al. [45] | Ag | p-Si 25 cm$^2$ | 41.6 | 613 | 77.6 | 19.8 |
| Zhuang et al. [46] | Ag | DWS p-Si (mc-Si) 243.36 cm$^2$ | 38.4 | 641 | 78.4 | 19.3 |
| Su et al. [47] | Ag | DWS mc-Si 243.36 cm$^2$ | 37.6 | 634 | 80.1 | 19.1 |
| Jura et al. [7] | Ag | p-Si (100) 182.41 cm$^2$ | 36.5 | 646 | 80.5 | 19.0 |
| Yang et al. [48] | Cu | p-Si (100) 243.36 cm$^2$ | 37.5 | 638 | 78.8 | 18.9 |
| Wang et al. [49] | Ag | DWS mc-Si | 36.9 | 637 | 80.3 | 18.9 |
| Zheng et al. [50] | Ag/Cu | DWS p-Si (mc-Si) 243.36 cm$^2$ | 36.8 | 632 | 80.2 | 18.7 |
| Ye et al. [51] | Ag | p-Si (mc-Si) 243.36 cm$^2$ | 36.7 | 634 | 79.3 | 18.4 |
| Wang et al. [52] | Ag | p-Si (100) | 41.3 | 598 | 75.1 | 18.2 |
| Oh et al. [34] | Ag | p-Si (100) | 36.5 | 628 | 79.6 | 18.2 |
| Jiang et al. [53] | Ag | p-Si 243.36 cm$^2$ | 36.3 | 632 | 79.1 | 18.1 |
| Jura et al. [7] | Ag | p-Si (mc-Si) 243.36 cm$^2$ | 36.0 | 634 | 79.2 | 18.0 |
| Toor et al. [22] | Au | p-Si (100) 1 cm$^2$ | 35.6 | 615 | 78.2 | 17.1 |
| Toor et al. [54,55] | Cu | p-Si (100) 1 cm$^2$ | 36.6 | 616 | 75.4 | 17.0 |

DWS, Diamond wire sawn.

Si surface. Jura et al. [7], using a silver (Ag) catalyst for the MACE process, demonstrated an 18.0% cell on a mc-Si wafer, made with and measured by Hareon Solar, a large commercial manufacturer. The group has also demonstrated a record 19.0% efficient NW cell on a c-Si wafer, processed and measured at the Georgia Institute of Technology [7]. Jin et al. [43] holds the record for fabricating a mc-Si solar cell using Ag-catalyzed MACE at 20.69% efficiency. The group achieved this efficiency by producing an inverted pyramid-like texture on a mc-Si wafer followed by RIE etching. Using copper (Cu) as the catalyst in a one-step texturization process, Yang et al. [48] fabricated a record c-Si solar cell with 18.87% efficiency. Toor et al. [22], using a gold (Au) catalyst for the MACE process and combining micro–nano dual-scale surface texture, have demonstrated a record 17.1% Au c-Si solar cell.

## 18.5 Concluding remarks

The nonvacuum wet etching-based MACE process holds great promise for large scale industrial deployment with its simple process flow and fast etching rate. The MACE process forms nanopores on the Si surface that resulted in a smooth refractive index transition from air to bulk Si. Consequently, very low reflectance, less than 1%, can be achieved over a broadband of wavelengths and different polarizations, and has been realized with bSi. By carefully varying the process parameters, a wide range of surface morphologies can be created with a high degree of control. In addition to bSi use in conventional Si solar cells, the bSi process is being explored in the next generation of solar cell technologies, such as thin kerfless c-Si [56], n-type [57], and back contact [16]. There are already commercial solar PV panels based on bSi technology in the market. The economic and technical advantages of this technique promise a bright future for this technology that is already being adopted by large solar cell manufacturers.

## References

[1] P. Campbell, M.A. Green, Light trapping properties of pyramidally textured surfaces, J. Appl. Phys. 62 (1) (1987) 243–249.
[2] Y.-T. Cheng, et al., Efficiency improved by acid texturization for multi-crystalline silicon solar cells, Solar Energy 85 (1) (2011) 87–94.
[3] K. Wang, et al., Absorption enhancement in ultrathin crystalline silicon solar cells with antireflection and light-trapping nanocone gratings, Nano Lett. 12 (3) (2012) 1616–1619.

[4] M.R. Black, I. William, B. Rever, Black Silicon: there's more than meets the eye, 2017 [cited 2019]. Available from: <https://www.pv-tech.org/guest-blog/black-silicon-theres-more-than-meets-the-eye>.
[5] F. Toor, et al., Metal assisted catalyzed etched (MACE) black Si: optics and device physics, Nanoscale 8 (34) (2016) 15448–15466.
[6] F. Toor, et al., Nanostructured silicon via metal assisted catalyzed etch (MACE): chemistry fundamentals and pattern engineering, Nanotechnology 27 (41) (2016) 412003.
[7] M.P. Jura, et al., Conventionally-processed silicon nanowire solar cells demonstrating efficiency improvement over standard cells, in: Photovoltaic Specialist Conference (PVSC), 2014 IEEE 40th, 2014.
[8] F. Modawar, et al., in: U. PTO (Ed.), US20150340526A1: Nanowire Device With Alumina Passivation Layer and Methods of Making Same, Advanced Silicon Group, 2011.
[9] M. Jura, et al., in: U. PTO (Ed.), US9768331: Screen Printing Electrical Contacts to Nanowire Areas, Advanced Silicon Group USA, 2017.
[10] What are black silicon solar cells? 2016 [cited 2019]. Available from: <https://www.trinasolar.com/us/resources/blog/black-silicon-solar-modules-powerful-and-pleasing-design>.
[11] EU PVSEC: "Multicrystalline silicon will not die", 2018 [cited 2019]. Available from: <https://www.pv-magazine.com/2018/09/28/eu-pvsec-multicrystalline-silicon-will-not-die/>.
[12] J. Zhao, M.A. Green, Optimized antireflection coatings for high-efficiency silicon solar cells, IEEE Trans. Electr. Dev. 38 (8) (1991) 1925–1934.
[13] M. Otto, et al., Black silicon photovoltaics, Adv. Opt. Mater. 3 (2) (2015) 147–164.
[14] H.-C. Yuan, et al., Efficient black silicon solar cell with a density-graded nanoporous surface: optical properties, performance limitations, and design rules, Appl. Phys. Lett. 95 (12) (2009) 123501.
[15] H.M. Branz, et al., Nanostructured black silicon and the optical reflectance of graded-density surfaces, Appl. Phys. Lett. 94 (23) (2009) 231121.
[16] H. Savin, et al., Black silicon solar cells with interdigitated back-contacts achieve 22.1% efficiency, Nat. Nano 10 (7) (2015) 624–628.
[17] C. Lin, M. Povinelli, Optimal design of aperiodic, vertical silicon nanowire structures for photovoltaics, Opt. Exp. 19 (S5) (2011) 1148–1154.
[18] C. Lin, M. Povinelli, Optical absorption enhancement in silicon nanowire arrays with a large lattice constant for photovoltaic applications, Opt. Exp. 17 (22) (2009) 19371–19381.
[19] M. Kelzenberg, et al., Enhanced absorption and carrier collection in Si wire arrays for photovoltaic applications, Nat. Mater. 9 (3) (2010) 239–244.
[20] L.Y. Cao, et al., Semiconductor nanowire optical antenna solar absorbers, Nano Lett. 10 (2) (2010) 439–445.
[21] L. Hu, G. Chen, Analysis of optical absorption in silicon nanowire arrays for photovoltaic applications, Nano Lett. 7 (11) (2007) 3249–3252.
[22] F. Toor, et al., Multi-scale surface texture to improve blue response of nanoporous black silicon solar cells, Appl. Phys. Lett. 99 (10) (2011) 103501.
[23] I.J. Lee, U. Paik, J.G. Park, Solar cell implemented with silicon nanowires on pyramid-texture silicon surface, Solar Energy 91 (2013) 256–262.
[24] E. Garnett, P. Yang, Light trapping in silicon nanowire solar cells, Nano Lett. 10 (3) (2010) 1082–1087.
[25] S.E. Han, G. Chen, Toward the Lambertian limit of light trapping in thin nanostructured silicon solar cells, Nano Lett. 10 (11) (2010) 4692–4696.
[26] W. Duan, et al., Performance enhancement techniques for the front and back of nanostructured "black silicon" solar cells, SPIE J. Photon. Energy 8 (2018) 11.

[27] P.A. Basore, D.A. Clugston, PC1D version 4 for Windows: from analysis to design, in: Conference Record of the Twenty Fifth IEEE Photovoltaic Specialists Conference—1996, 1996.
[28] B.A. Buchine, F. Modawar, M.R. Black, in: USPTO (Ed.), US8450599B2: Nanostructured Devices, Bandgap Engineering Inc, 2013.
[29] B. Kayes, H. Atwater, N. Lewis, Comparison of the device physics principles of planar and radial p-n junction nanorod solar cells, J. Appl. Phys. 97 (11) (2005) 114302.
[30] S. Koynov, M.S. Brandt, M. Stutzmann, Black multi-crystalline silicon solar cells, Phys. Status Solidi-Rapid Res. Lett. 1 (2) (2007) R53–R55.
[31] B.K. Nayak, V.V. Iyengar, M.C. Gupta, Efficient light trapping in silicon solar cells by ultrafast-laser-induced self-assembled micro/nano structures, Prog. Photovolt. 19 (6) (2011) 631–639.
[32] C. Wu, et al., Near-unity below-band-gap absorption by microstructured silicon, Appl. Phys. Lett. 78 (13) (2001) 1850–1852.
[33] C.B. Nielsen, et al., Particle precipitation in connection with KOH etching of silicon, J. Electrochem. Soc. 151 (5) (2004) G338–G342.
[34] J. Oh, H.-C. Yuan, H.M. Branz, An 18.2%-efficient black-silicon solar cell achieved through control of carrier recombination in nanostructures, Nat. Nano 7 (11) (2012) 743–748.
[35] G. Dingemans, W. Kessels, Recent progress in the development and understanding of silicon surface passivation by aluminum oxide for photovoltaics, in: Proceedings of the 25th European Photovoltaic Solar Energy Conference, Valencia, Spain, 2010.
[36] T. Yehua, et al., Characterization of the nanosized porous structure of black Si solar cells fabricated via a screen printing process, J. Semiconductors 33 (6) (2012) 064007.
[37] E. Cabrera, et al., Influence of surface topography on the glass coverage in the contact formation of silver screen-printed Si solar cells, IEEE J. Photovolt. 3 (1) (2013) 102–107.
[38] V.A. Chaudhari, C.S. Solanki, A novel two step metallization of Ni/Cu for low concentrator c-Si solar cells, Solar Energy Mater. Solar Cells 94 (12) (2010) 2094–2101.
[39] J.D. Lee, et al., The investigation of one step annealing for plated Ni/Cu contact solar cells, Renew. Energy 42 (2012) 1–3.
[40] P.N. Vinod, The electrical and microstructural properties of electroplated screen-printed Ag metal contacts in crystalline silicon solar cells, RSC Adv. 3 (33) (2013) 14106–14113.
[41] M.R. Black, et al., US8852981B2: Electrical Contacts to Nanostructured Areas, Advanced Silicon Group Inc., 2014.
[42] W.H. Chen, F.C.N. Hong, 0.76% absolute efficiency increase for screen-printed multicrystalline silicon solar cells with nanostructures by reactive ion etching, Solar Energy Mater. Solar Cells 157 (2016) 48–54.
[43] J.S. Jin, et al., > 20.5% diamond wire sawn multicrystalline silicon solar cells with maskless inverted pyramid like texturing, IEEE J. Photovolt. 7 (5) (2017) 1264–1269.
[44] C.Y. Zhang, et al., Fabrication of 20.19% efficient single-crystalline silicon solar cell with inverted pyramid microstructure, Nanoscale Res. Lett. 13 (2018) 91.
[45] D. Irishika, et al., Improvement of conversion efficiency of silicon solar cells by submicron-textured rear reflector obtained by metal-assisted chemical etching, Solar RRL 1 (7) (2017).
[46] Y.F. Zhuang, et al., Broadband spectral response of diamond wire sawn me-Si solar cell with omnidirectional performance and improved appearance, Solar Energy Mater. Solar Cells 179 (2018) 372–379.

[47] G.Y. Su, et al., The influence of black silicon morphology modification by acid etching to the properties of diamond wire sawn multicrystalline silicon solar cells, IEEE J. Photovolt. 8 (4) (2018) 937–942.
[48] L. Yang, et al., 18.87%-efficient inverted pyramid structured silicon solar cell by one-step Cu-assisted texturization technique, Solar Energy Mater. Solar Cells 166 (2017) 121–126.
[49] S.L. Wang, et al., Effect of surface structure on electrical performance of industrial diamond wire sawing multicrystalline Si solar cells, Int. J. Photoenergy 2018 (2018) 4.
[50] C.F. Zheng, et al., High-efficient solar cells by the Ag/Cu-assisted chemical etching process on diamond-wire-sawn multicrystalline silicon, IEEE J. Photovolt. 7 (1) (2017) 153–156.
[51] X.Y. Ye, et al., 18.45%-efficient multi-crystalline silicon solar cells with novel nanoscale pseudo-pyramid texture, Adv. Funct. Mater. 24 (42) (2014) 6708–6716.
[52] W.C. Wang, et al., Surface passivation of efficient nanotextured black silicon solar cells using thermal atomic layer deposition, ACS Appl. Mater. Interfaces 5 (19) (2013) 9752–9759.
[53] Y. Jiang, et al., Nanostructured multi-crystalline silicon solar cell with isotropic etching by HF/KMnO4, Phys. Status Solidi A—Appl. Mater. Sci. 214 (5) (2017).
[54] F. Toor, H.M. Branz, Copper-Assisted, Anti-Reflection Etching of Silicon Surface., National Renewable Energy Laboratory, Golden, CO, 2014.
[55] F. Toor, J. Oh, H.M. Branz, Efficient nanostructured 'black' silicon solar cell by copper-catalyzed metal-assisted etching, Prog. Photovolt.: Res. Appl. 23 (10) (2015) 1375–1380.
[56] D.M. Powell, et al., Effective lifetimes exceeding 300 μs in gettered p-type epitaxial kerfless silicon for photovoltaics, Appl. Phys. Lett. 103 (26) (2013) 263902.
[57] W.-K. To, et al., Fabrication of n-type mesoporous silicon nanowires by one-step etching, Nano Lett. 11 (12) (2011) 5252–5258.

This page intentionally left blank

# Index

*Note*: Page numbers followed by "*f*" and "*t*" refer to figures and tables, respectively.

## D

## F



## G

## H



## I



## J



## K

## L



## M

## N

## O

## P

## Q



## R



## S

## T

## Z

# NANOMATERIALS FOR **SOLAR CELL APPLICATIONS**

EDITED BY
SABU THOMAS, EL HADJI MAMOUR SAKHO, NANDAKUMAR KALARIKKAL, SAMUEL OLUWATOBI OLUWAFEMI, JIHUAI WU

Nanomaterials have emerged over the last decades as the new building blocks to construct solar cell assemblies. The need to develop high-efficiency and cost-effective materials for solar cells is growing, and nanomaterials provide an opportunity for the development of new methods to approach solar energy conversion with a flexible and promising material platform.

***Nanomaterials for Solar Cell Applications*** provides a review of the recent developments in the field of nanomaterials-based solar cells. It has been reported that the efficiency of nanomaterials in solar cells is dependent on their shape, size, and structure. Therefore, this book accounts the developments in the synthesis and characterizations of these nanomaterials for solar cells. The book opens with a discussion on the fundamentals of nanomaterials for solar cells, including a discussion on the life-cycle assessments and characterization techniques. It then follows with a review of the various types of solar cells: thin film; metal-oxide, nanowire, nanorod and nanoporous materials, and concludes with nanocarbon materials. In addition, it includes a review of quantum dot-sensitized, perovskite, and polymer nanocomposites-based solar cells.

### Key Features

- Provides well–organized approach to the use of nanomaterials for solar cell applications
- Discusses the synthesis, characterization, and applications of traditional and new materials
- Includes coverage of emerging nanomaterials such as graphene, graphene-derivatives, and perovskites

### About the Editors

**Professor Sabu Thomas** is a professor of polymer science and technology, and honorary director of the International and Inter University Centre for Nanoscience and Nanotechnology, School of Chemical Sciences, Mahatma Gandhi University, India.

**Dr. El Hadji Mamour Sakho** is a postdoctoral researcher in the Department of Chemical Sciences (formerly Applied Chemistry), University of Johannesburg, South Africa.

**Dr. Nandakumar Kalarikkal** is an associate professor and head of Advanced Materials Laboratory, School of Pure and Applied Physics, and also a senate member of the International and Inter University Centre for Nanoscience and Nanotechnology, Mahatma Gandhi University, India.

**Professor Samuel Oluwatobi Oluwafemi** is a professor at the department of Chemical Sciences (formerly Applied Chemistry), University of Johannesburg, Doornfontein Campus, South Africa.

**Professor Jihuai Wu** is a professor of chemistry and materials and the vice president at Huaqiao University, China.

ISBN 978-0-12-813337-8
9 780128 133378

ELSEVIER elsevier.com/books-and-journals